Pengfei Zhao
Zhuangzhi Ye
Min Xu
Li Yang   *Editors*

# Advanced Graphic Communication, Printing and Packaging Technology

Proceedings of 2019 10th China Academic Conference on Printing and Packaging

Springer

# Lecture Notes in Electrical Engineering

## Volume 600

The book series *Lecture Notes in Electrical Engineering* (LNEE) publishes the latest developments in Electrical Engineering—quickly, informally and in high quality. While original research reported in proceedings and monographs has traditionally formed the core of LNEE, we also encourage authors to submit books devoted to supporting student education and professional training in the various fields and applications areas of electrical engineering. The series cover classical and emerging topics concerning:

- Communication Engineering, Information Theory and Networks
- Electronics Engineering and Microelectronics
- Signal, Image and Speech Processing
- Wireless and Mobile Communication
- Circuits and Systems
- Energy Systems, Power Electronics and Electrical Machines
- Electro-optical Engineering
- Instrumentation Engineering
- Avionics Engineering
- Control Systems
- Internet-of-Things and Cybersecurity
- Biomedical Devices, MEMS and NEMS

For general information about this book series, comments or suggestions, please contact leontina.dicecco@springer.com.

To submit a proposal or request further information, please contact the Publishing Editor in your country:

**China**

Jasmine Dou, Associate Editor (jasmine.dou@springer.com)

**India, Japan, Rest of Asia**

Swati Meherishi, Executive Editor (Swati.Meherishi@springer.com)

**Southeast Asia, Australia, New Zealand**

Ramesh Nath Premnath, Editor (ramesh.premnath@springernature.com)

**USA, Canada:**

Michael Luby, Senior Editor (michael.luby@springer.com)

**All other Countries:**

Leontina Di Cecco, Senior Editor (leontina.dicecco@springer.com)

**\*\* Indexing: The books of this series are submitted to ISI Proceedings, EI-Compendex, SCOPUS, MetaPress, Web of Science and Springerlink \*\***

More information about this series at http://www.springer.com/series/7818

Pengfei Zhao · Zhuangzhi Ye ·
Min Xu · Li Yang
Editors

# Advanced Graphic Communication, Printing and Packaging Technology

Proceedings of 2019 10th China Academic Conference on Printing and Packaging

Springer

*Editors*
Pengfei Zhao
China Academy of Printing Technology
Beijing, China

Min Xu
China Academy of Printing Technology
Beijing, China

Zhuangzhi Ye
China Academy of Printing Technology
Beijing, China

Li Yang
China Academy of Printing Technology
Beijing, China

# 2019 10th China Academic Conference on Printing and Packaging

**Date**: November 14–17, 2019
**Location**: Xi'an, China

**Sponsors**

China Academy of Printing Technology
Beijing Institute of Graphic Communication
Shaanxi University of Science and Technology

**Support**

Chinese Society for Imaging Science and Technology

**Organizers**

Key Laboratory of Environmental Protection Technology for Printing Industry, China Academy of Printing Technology
Editorial Department of Digital Printing, China Academy of Printing Technology
School of Printing and Packaging Engineering, Beijing Institute of Graphic Communication
College of Bioresources Chemical and Materials Engineering, Shaanxi University of Science and Technology
Printing Technology Professional Committee of Chinese Society for Imaging Science and Technology

**Co-sponsors**

Faculty of Printing, Packaging Engineering and Digital Media Technology, Xi'an University of Technology
School of Media and Design, Hangzhou Dianzi University
College of Light Industry and Engineering, South China University of Technology
School of Light Industry Science and Engineering, Qilu University of Technology (Shandong Academy of Science)
School of Printing and Packaging, Wuhan University
State Key Laboratory of Modern Optical Instrumentation, Zhejiang University
College of Light Industry Science and Engineering, Tianjin University of Science and Technology
Light Industry College, Harbin University of Commerce

College of Communication and Art Design, University of Shanghai for Science and Technology
School of Light Industry and Chemical Engineering, Dalian Polytechnic University
College of Materials Science and Engineering, Beijing University of Chemical Technology
School of Packaging and Material Engineering, Hunan University of Technology
School of Food and Chemical Engineering, Beijing Technology and Business University
School of Mechanical Engineering, Tianjin University of Commerce
College of Material Science and Engineering, Zhengzhou University
School of Materials and Chemical Engineering, Henan University of Engineering
College of Engineering, Qufu Normal University
College of Light Industry Science and Engineering, Nanjing Forestry University
School of Mechanical Engineering, Jiangnan University
Shanghai Publishing and Printing College
School of Media and Communication, Shenzhen Polytechnic
College of Communications, National Taiwan University of Arts

## Conference Executive Committee

### Chairman

Xueke Luo (President of Beijing Institute of Graphic Communication, Vice Chairman of Printing and Printing Equipment Industries Association of China)
Jianzhong Ma (President of Shaanxi University of Science and Technology)
Pengfei Zhao (President of China Academy of Printing Technology)

### Vice Chairman

Jialing Pu (Vice President of Beijing Institute of Graphic Communication)
Zhijian Li (Vice President of Shaanxi University of Science and Technology)
Zhuangzhi Ye (Vice President of China Academy of Printing Technology)

### Honorary Chairman

Desen Qu (Former President of Beijing Institute of Graphic Communication)
Tingliang Chu (Former President of China Academy of Printing Technology, Executive Vice Chairman of the Printing Technology Association of China)
Wencai Xu (Former Vice President of Beijing Institute of Graphic Communication, Vice Chairman of the Printing Technology Association of China)

### Secretary-General

Xianfu WEI (Dean of School of Printing and Packaging Engineering, Beijing Institute of Graphic Communication)

Guodong Liu (Director of Department of Printing Engineering, College of Bioresources Chemical and Materials Engineering, Shaanxi University of Science and Technology)

Min Xu (Director of Industry Development Research Department, China Academy of Printing Technology)

## Conference Academic Committee

**Chairman**

Deren Li (Academician of Chinese Academy of Sciences, Academician of China Engineering Academy, Academician of International Eurasian Academy of Sciences, Academician of New York Academy of Sciences, Academician of International Academy of Astronautics, Professor of Wuhan University, Director of State Key Laboratory of Information Engineering in Surveying, Mapping and Remote)

**Vice Chairman**

Guangnan Ni (Academician of China Engineering Academy, Researcher of Institute of Computing Technology Chinese Academy of Sciences, Board Chairperson of Chinese Information Processing Society of China)

Kefu Chen (Academician of China Engineering Academy, Professor of South China University of Technology, Director of Academic Committee of State Key Laboratory of Pulp and Paper Engineering)

Songlin Zhuang (Academician of China Engineering Academy, Director and Professor of School of Optical-Electrical and Computer Engineering of University of Shanghai for Science and Technology, Optical Expert)

Jinping Qu (Academician of China Engineering Academy, Professor of South China University of Technology, Director of National Engineering Research Center of Novel Equipment for Polymer Processing, Director of the Key Laboratory for Polymer Processing Engineering of Ministry of Education)

**Commissioners**

Yuri Andreev (Head of Moscow State University of Printing Arts)

Stephen W. Bigger (Doctor, Professor, Vice President of Faculty of Engineering and Science of Victoria University)

Congjun Cao (Doctor, Professor of Xi'an University of Technology)

Guorong Cao (Doctor, Professor of Beijing Institute of Graphic Communication)

Guangxue Chen (Doctor, Professor of South China University of Technology)

Hong Chen (Professor of Beijing Institute of Graphic Communication)

Yunzhi Chen (Doctor, Professor of Tianjin University of Science and Technology)

Kamal Chopra (Professor, President of All India Federation of Master Printers)

Fuqiang Chu (Doctor, Professor of Qilu University of Technology (Shandong Academy of Science))

Tingliang Chu (Professorial Senior Engineer of China Academy of Printing Technology)

Changqing Fang (Doctor, Professor of Xi'an University of Technology)

Patrick Gane (Doctor, Professor of Printing Technology at the School of Chemical Technology, Aalto University)

Phil Green (Professor of Colour Imaging, London College of Communication)

Aran Hansuebsai (Doctor, Associate Professor of Chulalongkorn University)

Jon Yngve Hardeberg (Doctor, Professor of Norwegian University of Science and Technology)

Roger D. Hersch (Doctor, Professor of Computer Science and Head of the Peripheral Systems Laboratory at the Ecole Polytechnique Fédérale de Lausanne (EPFL))

Mathias Hinkelmann (Doctor, Professor of Stuttgart Media University)

Thomas Hoffmann-Walbeck (Professor of the Faculty of Print and Media Technology, Stuttgart University of Media)

Min Huang (Doctor, Professor of Beijing Institute of Graphic Communication)

Yungcheng Hsieh (Doctor, Professor of National Taiwan University of Arts)

Jeroen Guinée (Doctor, Associate Professor of Leiden University)

Kaida Xiao (Doctor, University Academic Fellow of University of Leeds)

Takashi Kitamura (Doctor, Professor of Graduate School of Advanced Integration Science, Chiba University)

Shijun Kuang (Consultant Engineer of China National Pulp and Paper Research Institute, Chief Engineer)

Jose Maria Lagaron (Doctor, Professor, Leader and Founder of the Group Novel Materials and Nanotechnology for Food Related Applications at the Institute of Agrochemistry and Food Technology of the Spanish Council for Scientific Research)

Benjamin Lee (Professor, Director of Department of Technology, California State University)

Houbin Li (Doctor, Professor of Wuhan University)

Luhai Li (Doctor, Professor of Beijing Institute of Graphic Communication)

Zhijian Li (Doctor, Professor of Shaanxi University of Science and Technology)

Maohai Lin (Doctor, Associate Professor of Qilu University of Technology (Shandong Academy of Science))

Haoxue Liu (Doctor, Professor of Beijing Institute of Graphic Communication)

Guodong Liu (Doctor, Associate Professor of Shaanxi University of Science and Technology)

Yanan Liu (Doctor, Engineer of China Academy of Printing Technology)

Zhen Liu (Professor of University of Shanghai for Science and Technology)

Dongming Lu (Doctor, Professor of Zhejiang University)

M. Ronnier Luo (Doctor, Professor of University of Leeds, Director of Color and Image Science Center)

Xiufeng Ma (Professor of Qufu Normal University)

Xuesong Mei (Doctor, Professor from Xi'an Jiaotong University)

Wanbin Pan (Doctor, Associate Professor of Hangzhou Dianzi University)

Zhigeng Pan (Doctor, Professor of Hangzhou Normal University)

Pierre Pienaar (Professor, President of the World Packaging Organization)

Luciano Piergiovanni (Professor of the Department of Food, Environmental and Nutritional Sciences, Faculty of Agricultural and Food Sciences, University of Milan)

Ngamtip Poovarodom (Doctor, Associate Professor of Department of Packaging and Materials Technology of Faculty of Agro-Industry, Kasetart University)

Jialing Pu (Doctor, Professor of Beijing Institute of Graphic Communication)

Yuansheng Qi (Doctor, Professor of Beijing Institute of Graphic Communication)

Alexander Roos (Professor of Stuttgart Media University)

Yanlin Song (Doctor, Professor of Institute of Chemistry, Chinese Academy of Sciences)

Zhihui Sun (Professor of Harbin University of Commerce)

Zhengning Tang (Doctor, Professor of Jiangnan University)

Fei Tao (Doctor, Professor of Beihang University)

Anita Teleman (Doctor, Research Manager of Printing Solutions at the Research Institute Innventia, Sweden)

Yuemin Teng (Professor of Shanghai Publishing and Printing College)

Junfei Tian (Doctor, Professor of South China University of Technology)

Alexander Tsyganenko (Professor of Media Industry Academy)

Philipp Urban (Head of Emmy-Noether Research Group, Institute of Printing Science and Technology, Technische Universität Darmstadt)

Howard E. Vogl (Visiting Professor of Rochester Institute of Technology)

Xiaoxia Wan (Doctor, Professor of Wuhan University)

Haiqiao Wang (Doctor, Professor of Beijing University of Chemical Technology, Doctoral supervisor)

Lijie Wang (Professor of Shenzhen Polytechnic)

Qiang Wang (Doctor, Professor of Hangzhou Dianzi University, Doctoral supervisor)

Yiqing Wang (Doctor, Professor of Xi'an Jiaotong University)

Xianfu Wei (Doctor, Professor of Beijing Institute of Graphic Communication)

Yan Wei (Doctor, Professor of Tsinghua University, Beijing Institute of Graphic Communication)

Jimei Wu (Doctor, Professor of Xi'an University of Technology)

Punan Xie (Professor of Beijing Institute of Graphic Communication)

Xiulan Xin (Doctor, Professor of Beijing Technology and Business University)

Jinlin Xu (Professor of Xi'an University of Technology)

Wencai Xu (Professor of Beijing Institute of Graphic Communication)

Bin Yang (Doctor, Researcher of Peking University)

Haigen Yao (Professor of Shanghai Publishing and Printing College)

Yadong Yin (Doctor, Professor of University of California, Riverside)

Haiyan Zhang (Professor of Xi'an University of Technology)

Lijing Zhang (Doctor, Overseas Distinguished Experts of Taishan Scholar, Distinguished Professor of Qilu University of Technology (Shandong Academy of Science))

Pengfei Zhao (Senior Engineer of China Academy of Printing Technology)
Xiuping Zhao (Professor of Tianjin University of Science and Technology)
Yunfei Zhong (Professor of Hunan University of Technology)
Shisheng Zhou (Doctor, Professor of Xi'an University of Technology, Doctoral supervisor)
Yingquan Zou (Doctor, Professor of Beijing Normal University, Doctoral supervisor)

**Reviewers**

Congjun Cao (Doctor, Professor of Xi'an University of Technology)
Shaozhong Cao (Doctor, Professor of Beijing Institute of Graphic Communication)
Guangxue Chen (Doctor, Professor of South China University of Technology)
Yun Chen (Doctor, Engineer of China Academy of Printing Technology)
Fuqiang Chu (Doctor, Professor of Qilu University of Technology (Shandong Academy of Science))
Yi Fang (Doctor, Teacher of Beijing Institute of Graphic Communication)
Yabo Fu (Doctor, Associate Professor of Beijing Institute of Graphic Communication)
Shanshan Gao (Doctor, Associate Professor of Qingdao University of Science and Technology)
Jing Geng (Doctor, Associate Professor of Xi'an University of Technology)
Minghui He (Doctor, Associate researcher of South China University of Technology)
Beiqing Huang (Associate Professor of Beijing Institute of Graphic Communication)
Junyan Huang (Master, Professor of Dalian Polytechnic University)
Min Huang (Doctor, Professor of Beijing Institute of Graphic Communication)
Zhen Huang (Doctor, Professor of Tianjin University of Commerce)
Xiaoshan Jiang (Doctor, Associate Professor of Beijing Institute of Graphic Communication)
Houbin Li (Doctor, Professor of Wuhan University)
Shi Li (Doctor, Teacher of Hangzhou Dianzi University)
Shuangyang Li (Doctor, Associate Professor of Beijing Technology and Business University)
Zhijian Li (Doctor, Professor of Shaanxi University of Science and Technology)
Zhijiang Li (Doctor, Associate Professor of Wuhan University)
Jing Liang (Lecturer of Dalian Polytechnic University)
Maohai Lin (Doctor, Associate Professor of Qilu University of Technology (Shandong Academy of Science))
Guodong Liu (Doctor, Associate Professor of Shaanxi University of Science and Technology)
Haoxue Liu (Doctor, Professor of Beijing Institute of Graphic Communication)
Qiang Liu (Doctor, Associate Professor of Wuhan University)
Yanan Liu (Doctor, Engineer of China Academy of Printing Technology)
Zhuang Liu (Doctor, Associate Professor of Harbin University of Commerce)

Lixin Lu (Doctor, Professor of Jiangnan University)
M. Ronnier Luo (Doctor, Professor of Zhejiang University)
Yalin Miu (Associate Professor of Xi'an University of Technology)
Ming Mu (Master, Engineer of China Academy of Printing Technology)
Yuansheng Qi (Doctor, Professor of Beijing Institute of Graphic Communication)
Zhanjun Si (Professor of Tianjin University of Science and Technology)
Haiqiao Wang (Doctor, Professor of Beijing University of Chemical Technology)
Haiwen Wang (Doctor, Associate Professor of Quzhou University)
Mengmeng Wang (Doctor, Associate Professor of Jiangnan University)
Qiang Wang (Doctor, Professor of Hangzhou Dianzi University)
Yigang Wang (Doctor, Professor of Hangzhou Dianzi University)
Xianfu Wei (Doctor, Professor of Beijing Institute of Graphic Communication)
Jimei Wu (Doctor, Professor of Xi'an University of Technology)
Dehong Xie (Doctor, Teacher of Nanjing Forestry University)
Xiulan Xin (Doctor, Professor of Beijing Technology and Business University)
Zhuofei Xu (Doctor, Teacher of Xi'an University of Technology)
Fazhong Zhang (Doctor, Engineer of China Academy of Printing Technology)
Gaimei Zhang (Doctor, Professor of Beijing Institute of Graphic Communication)
Zhengjian Zhang (Doctor, Associate Professor of Tianjin University of Science and Technology)
Yuanlin Zheng (Doctor, Associate Professor of Xi'an University of Technology)
Ming Zhu (Doctor, Associate Professor of Henan Institute of Engineering)

# Preface

"2019 10th China Academic Conference on Printing and Packaging & Forum of Technology Integration Innovation Development", one of the series "China Academic Conference on Printing and Packaging" which is mainly hosted by China Academy of Printing Technology, was held on November 14–17, 2019, in Xi'an, China. The conference was co-hosted by China Academy of Printing Technology, Beijing Institute of Graphic Communication and Shaanxi University of Science and Technology, and co-organized by Key Laboratory of Environmental Protection Technology for Printing Industry of China Academy of Printing Technology, Editorial Department of Digital Printing, School of Printing and Packaging Engineering of Beijing Institute of Graphic Communication, College of Bioresources Chemical and Materials Engineering of Shaanxi University of Science and Technology and Printing Technology Professional Committee of Chinese Society for Imaging Science and Technology.

By far, "China Academic Conference on Printing and Packaging (CACPP)" and its series of events have been held for ten sessions since the first session in 2010, and have already become the most influential academic exchange activities in printing and packing fields in China.

In recent years, the printing and packaging industry of China has been keeping a stable growth, by the end of 2018, the total output value of China printing industry has topped to RMB 1.27 trillion, increasing by 5.4%. The total number of enterprises is 98,000, and the number of employees reaches 2.704 million. The speed of development has bottomed out and rebounded, the trend of controlling quantity and improving quality is obvious, the new kinetic energy keeps growing, and the new window period effect is emerging. "Greening, digitalization, intelligence, and integration" is becoming the development direction of China's printing industry. Scientific research and innovation is playing a leading role. Both universities and enterprises are committed to new technologies, new materials and new equipment. The research on new technologies has produced many scientific research results. In order to promote the transformation and application of research results in the actual production, the conference also hosted "Forum of Technology Integration Innovation Development", set up the exchanges session between the enterprise technology

demands and scientific results of universities, to explore new ideas and new approaches of industrialization of scientific research application, to widen research channel of the innovation technical teams and the research institutes, to accelerate comprehensive collaborative innovation in production, education, research and application, to create printing and packaging industry innovation chain, and to realize comprehensive promotion of innovation capacity building in printing and packaging fields.

The conference invited Martti Toivakka, full professor and head of the Laboratory of Paper Coating and Converting at ÅboAkademi University, Finland; Eduard Neufeld, the managing director of Fogra Research Institute for Media Technologies; Martin Dreher, Director and General Manager of DFTA Technology Center, Stuttgart, Germany; Xuesong Mei, Professor from Xi'an Jiaotong University, to make keynote speeches "Novel Paper-based Applications through Printing and Coating of Functional Materials", "Current trends in printing standardization research", "Status, News and Innovations in Flexographic Printing" and "Research Progress and Application of Mobile Operating Robot". Moreover, the conference also invited distinguished Prof. Fei Tao from Beihang University, Prof. Junfei Tian from South China University of Technology, Prof. Changqing Fang from Xi'an University of Technology, Associate Prof. Wanbin Pan from Hangzhou Dianzi University as outstanding young scholars to make speeches respectively. At the same time, the participants had oral presentations, academic exchanges and latest research achievement communication on color science, image processing, digital media, printing innovation materials, packaging innovation materials, etc. on 4 panel discussion meetings.

The conference received 220 papers this year, among which 118 were selected to be published on Lecture Notes in Electrical Engineering (LNEE) (ISSN: 1876-1100) by Springer.

Here we greatly acknowledge all the organizations that offered great support for the conference and they are: the Printing Technology Association of China, Chinese Society for Imaging Science and Technology, School of Printing and Packaging of Wuhan University, College of Communication and Art Design of University of Shanghai for Science and Technology, School of Media and Design of Hangzhou Dianzi University, College of Light Industry and Engineering of South China University of Technology, Faculty of Printing, Packaging Engineering and Digital Media Technology of Xi'an University of Technology, School of Light Industry Science and Engineering of Qilu University of Technology (Shandong Academy of Science), Light Industry College of Harbin University of Commerce, College of Light Industry Science and Engineering of Tianjin University of Science and Technology, State Key Laboratory of Modern Optical Instrumentation of Zhejiang University, School of Mechanical Engineering of Jiangnan University, School of Light Industry and Chemical Engineering of Dalian Polytechnic University, School of Packaging and Material Engineering of Hunan University of Technology, College of Engineering of Qufu Normal University, School of Mechanical Engineering of Tianjin University of Commerce, School of Materials and Chemical Engineering of Henan University of Engineering, College of Light Industry Science and Engineering of Nanjing Forestry University, College of Materials Science and Engineering of

Beijing University of Chemical Technology, College of Material Science and Engineering of Zhengzhou University, School of Food and Chemical Engineering of Beijing Technology and Business University, Shenzhen Polytechnic, Shanghai Publishing and Printing College, College of Communications of Taiwan University of Arts.

We would like to express our gratitude to the 40 experts from China, Germany, Britain, American and Japan for reviewing and recommending papers for the conference with strict standards.

We also thank Springer for offering us an international platform for publishing.

We look forward to our reunion at 2020 11th China Academic Conference on Printing and Packaging.

October 2019                                                                        Edited by
                                                    Key Laboratory of Environmental Protection
                                                      Technology for Printing Industry
                                                     China Academy of Printing Technology
                                                                          Beijing, China

# Contents

Image Processing Technology

Digital Media Technology

## Printing Engineering Technology

**Packaging Engineering Technology**

**Mechanical Engineering Technology**

**Information Engineering and Artificial Intelligence Technology**

## Film and Related Material Technology

## Novel Functional Material Technology

# Color Science and Technology

# Experiment Based No-Reference Objective Image Quality Metric for Testing Performance of Different Tone Mapped Images

Muhammad Usman Khan, Imran Mehmood,
and Ming Ronnier Luo[✉]

State Key Laboratory of Modern Optical Instrumentation, Zhejiang University,
Hangzhou, China
m.r.luo@zju.edu.cn

**Abstract.** Subjective image quality assessment for a large database is a lengthy and tiring process. The task becomes more complicated when the testing of tone-mapped images is desired as it is not possible to directly display HDR content on standard displays, hence unavailability of reference images for comparison. This limits the quality evaluation methods to comparative or categorical judgement. For this study, we used the comparative judgement method to subjectively test the performance of images tone-mapped by different operators against each other on eight different visual image appearance attributes. Attributes having a higher correlation with overall image preference scores are used to develop the proposed no-reference image quality metric. Results of the psychophysical experiment and performance of the resulting metric are reported here.

**Keywords:** Tone mapping operators · Visual image appearance attributes · No-reference image quality metric · Image quality assessment

## 1 Introduction

There are two general ways to determine the quality of an image, subjective and objective. Subjective evaluation involves human subjects which determine the perceived quality of the images showed to them. For tone-mapped images usually reference high dynamic range (HDR) images are not available for observers to compare with, so subjective evaluation can be carried out via comparative judgement (comparing different tone-mapped versions of a single scene against each other and rank according to observer preferences) or categorical judgement (ask the observers to score the displayed images on a predefined scale using memory references for objects present in the scene) methods. Objective evaluation is done by using Image Quality Metrics (IQMs) which basically are mathematical models to determine the quality of images.

Objective IQMs can be classified into three types [1]; full reference, reduced reference and no-reference image quality methods. Full reference image quality metrics compare parameters from a reference image with those from a test image. MSE [2],

SSIM [3], TMQI [4], FSITM [5] are some popular FR-IQMs. Reduced reference metrics use limited reference parameters from test images.

No-reference image quality metrics (NR-IQMs), as the name suggests, do not require a reference image to estimate its quality instead it performs the desired task either in a pre-defined or in a complete blind way. The former algorithms try to determine predefined distortions in the image like jpeg distortions proposed in [6] and blurring artifacts proposed in [7], where the strength of distortions present in the image determine the divergence of image quality from the best. The later type of algorithms, complete blind NR-IQMs, are based on visual image appearance attributes which are basically motivated by the human visual system (HVS) characteristics of viewing and determining the image quality.

Mittal et al. proposed naturalness image quality evaluator (NIQE) in [8], which is based on first constructing a collection of "Quality-Aware" features which are derived from natural scene statistics (NSS) model and then fitting them to a multivariate Gaussian (MVG) model. Quality is of the image is expressed as distance between MVG fit to NSS features.

Integrated local NIQE proposed by Zhang et al. [9] is an improvement over NIQE [8] model. It includes three additional quality-aware features in addition to the NSS features in NIQE [8]. Also, IL-NIQE uses local MVG models which are compared to local quality-aware features for each patch of the test image to compute local quality scores. Local quality scores then pooled to get a single quality score.

Gong et al. [10] developed a model based on visual image appearance attributes to predict image quality for natural and non-natural scenes under different viewing environments. It considers naturalness and clearness as attributes for determining the quality of natural scenes and colorfulness and clearness for determining the quality of non-natural scene images. The model needs to be trained on psychophysical data to get parameters for its attributes which are different for different viewing conditions. For natural images, Gong et al. [10] model needs natural image regions (sky, grass/trees and skin etc.) from reference image for comparison to calculate naturalness, hence it can be classified as reduced reference IQM.

Due to large scale use of digital display media, every single user sees and perceive the quality of images without a reference image. This necessitates the development of an NR-IQM which (1) relies on the HVS characteristics to perceive the quality of images using visual image appearance attributes and (2) is generalized enough to predict the quality on any database without the need of training.

The next section explains the psychophysical experiment performed to get the data to develop an NR-IQM, followed by results and discussions on model performance. The conclusions are drawn in the end.

## 2   Experiment and Model Development

Test images for the subjective evaluation experiment contain ten HDR images from RIT HDR image database [11]. Images were tone-mapped for displaying purpose using six TMOs namely; Drago's adaptive logarithmic mapping [12], Reinhard and Devlin's photoreceptor-based operator [13], Reinhard's photographic tone reproduction

operators (Local and Global operators) [14], Schlick's quantization function [15] and Ward's histogram adjustment operator [16]. All ten images tone-mapped using Reinhard's photographic tone-reproduction global operator are shown in Fig. 1.
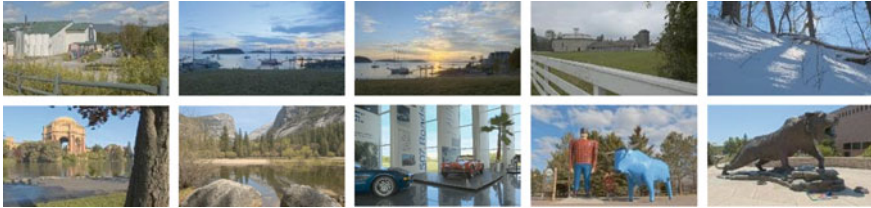


**Fig. 1.** Sample images from RIT HDR image database [11] tone-mapped using Reinhard Local [14] tone-mapping operator

For subjective evaluation, comparative judgement method was adopted. Images of the same scene were displayed in pairs on a calibrated NEC PW272 display in dark surroundings. Maximum luminance level of the display was set at 287 cd/m$^2$. 20 observers (12 males and 8 females), aged between 21–33, evaluated the image pairs on the basis of eight evaluation criteria namely luminance contrast ($C_L$), color contrast ($C_C$), brightness (Q), colorfulness (M), shadow details ($D_S$), highlight details ($D_H$), naturalness (N) and preference (P). All the observers passed the Ishihara test for color deficiency. In total 26400 assessments (((15 pairs × 10 scenes) + 10% repeatability) × 8 evaluation criteria × 20 observers) were carried out to test the performance of six TMOs and to get the most significant visual image attributes to determine the image quality.

Reliability of subjective assessment was verified via inter and intra-observer variability using the coefficient of variation. For intra-observer variability, best observer gave 0.07 while worst observer gave 0.33 CV value. For inter-observer variability, best CV value was 0.16 while the worst was 0.21.

Observer's scores for each criterion from the psychophysical judgements were transformed to Z-scores (higher the better) and are plotted in Fig. 2. Results suggest
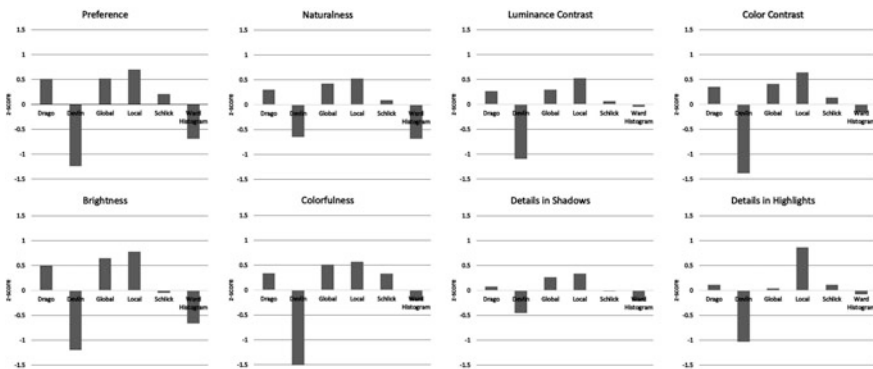


**Fig. 2.** Results of the psychophysical assessment presented in terms of z-scores

that the Reinhard Local operator [14] was overall best in tone reproduction of HDR images. This was followed by Reinhard Global operator [14]. Drago's operator [12] ranked third, Schlick's operator [15] ranked fourth. Ward's [16] and Reinhard-Devlin [13] operators ranked fifth and sixth in all evaluation criteria, respectively.

The most important attribute preference (P) was directly correlated to overall image quality i.e., the most preferred images would have higher quality and vice versa. The decision of observers to assess the preference was highly influenced by a number of visual image appearance attributes such as naturalness (N), colorfulness (M), brightness (Q), contrast (C) and details in highlights ($D_H$) and shadows ($D_S$). Given the availability of psychophysical data, the relationship between image preference and other attributes was developed which gives Pearson linear correlation coefficient of 0.971.

In order to develop a statistical model which can calculate appearance attribute values from the images to estimate its quality, the following considerations were made. (1) Naturalness (N), as proposed by Choi et al. [17], can be calculated using a function including colorfulness (M), shadow details ($D_S$) and luminance contrast ($C_L$) (sharpness was used in original model), hence it was dropped from the final model due to duplication. (2) Attributes of color contrast ($C_C$) and highlight details ($D_H$) were dropped from the model and will be incorporated in a future version of our IQM. The proposed image quality metric, which consists of four attributes ($C_L$, Q, M and $D_S$), is expressed as:

$$IQ = 0.829C_L + 0.195Q + 0.0012M + 0.937D_S - 1.309 \tag{1}$$

The constants were determined using linear regression of psychophysical preference (P) and statistical data of image appearance attributes of luminance contrast ($C_L$), brightness (Q), colorfulness (M) and shadow details ($D_S$). Brightness (Q) and colorfulness (M) in Eq. 1 can be obtained directly from color appearance model CAM16-UCS [18]. Luminance contrast ($C_L$) was calculated as follows

$$C_L = -0.986C_{L13} + 2.701C_{L9} - 0.784C_{L5} + 0.051 \tag{2}$$

where $C_{Lw}$ is the luminance contrast ($C_L$), proposed by Calabria and Fairchild in [19], used here for different image regions of sizes $13 \times 13$, $9 \times 9$ and $5 \times 5$. $C_{Lw}$ is defined as

$$C_{L_w} = -0.007\kappa_L + 0.039\kappa_C + 0.007\kappa_S + 0.539 \tag{3}$$

where $\kappa_L$, $\kappa_C$ and $\kappa_S$ are standard deviations of image lightness, chroma and high-passed lightness channels. Shadow details ($D_S$) was calculated as follows

$$D_S = 0.22D_{S13} - 0.394D_{S9} + 0.215D_{S5} - 0.331 \tag{4}$$

$D_{Sw}$ in the above equation was calculated using the clearness model of Gong et al. [10]. It first calculates $\Delta J_w$, the mean squared deviation of the edge detected dark pixels (pixels with $J < 42$ which corresponds to 10% of maximum display luminance) from their neighbouring pixels. $\Delta J_w$ is defined as

$$\Delta J_w\left(k,r\right)=\left(\frac{\sum_{i=-N}^{N}\sum_{j=-N}^{N}[J(k-i,r-j)-J(k,r)]^2}{(2N+1)^2}\right)^{\frac{1}{2}} \tag{5}$$

$\Delta J_w$ was calculated for image regions of sizes $13 \times 13$, $9 \times 9$ and $5 \times 5$ around the detected pixels. $D_{Sw}$ is the mean of $\Delta J_w$ overall edge detected pixels.

To optimize the parameters in Eq. (1), images were divided into training and testing data. 70% of the images were selected as training data and the 30% images were selected as testing data. Parameters were optimized using linear regression by maximizing the correlation between image statistical data and psychophysical preference scores. The performance was evaluated by implementing the developed model on the test data. The process of optimizing the parameters was repeated ten times by randomly selecting the images as training data. Ten sets of optimized parameters were obtained which gave the minimum and maximum correlation values of 0.52 and 0.72 respectively when evaluated on their respective test data. Parameters mentioned in Eq. (1) are averaged parameters for all ten optimizations.

## 3   Results and Discussions

Pearson linear correlation coefficient (PLCC), Spearman's Rank Order Correlation Coefficient (SRCC) and standardized residual sum of squares (STRESS) were used as evaluation criteria to test the performance of proposed IQM. PLCC is the linear correlation, SRCC is the correlation between ranks of objective and subjective data. STRESS is a measure of disagreement between observed and calculated data.

In Fig. 3, predicted IQ scores are plotted against observed data for the test images using prediction from all ten optimization rounds. In the figure, vertically spaced points are the predictions for the same image with different optimization parameters. Best optimization results obtained for testing data have PLCC value of 0.72 whereas SRCC and STRESS values are 0.71 and 12.26 respectively. On the other hand, least optimized PCC, SRCC and STRESS values for testing data are 0.52, 0.37 and 14.64 respectively.

Figure 4 shows the observed vs predicted IQ scores using average parameters from all ten optimization rounds. In this case, the model is tested on all images used in the experiment. These predicted IQ scores have PLCC and SRCC values of 0.764 and 0.760 respectively. This predicted data has STRESS value of 11.5. These results show that the proposed IQM, that uses image appearance attributes to blindly predict the test image quality, was reliable.
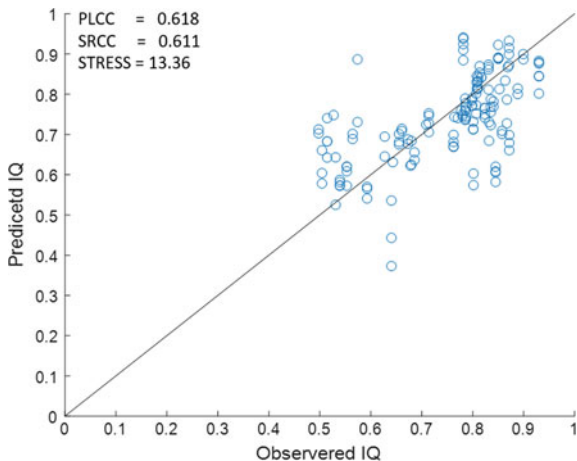
**Fig. 3.** Combined predicted versus observed IQ scores on test images using ten set of optimized parameters
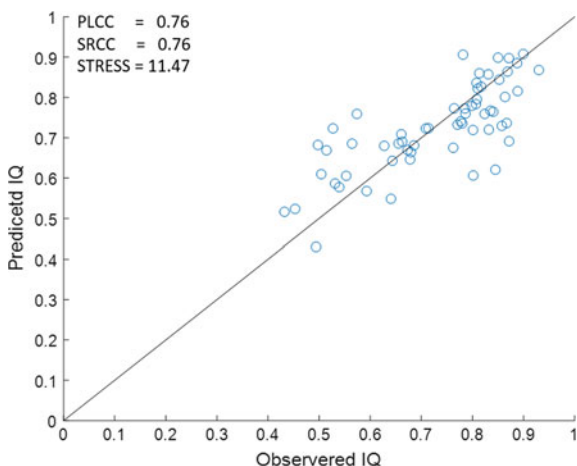


**Fig. 4.** Predicted versus observed IQ scores on all images using Eq. (1)

## 4   Conclusions

We proposed a no-reference image quality metric for the applications where the reference image was not available for comparison. Psychophysical data for developing the model were obtained from the subjective analysis of tone-mapped images. The obtained data were used to determine the necessary image appearance attributes of an image. The image appearance attribute values in the proposed model were obtained by applying the CAM16-UCS models on the test images. Evaluation results showed the

effectiveness of the proposed model. However, the proposed model was the basic version, and it was applied to the tone-mapped outdoor natural scenes. Further analysis of the IQM is in progress to test the effectiveness of IQM on other available databases. To further improve the performance of the model, the inclusion of color contrast ($C_C$) and highlight details ($D_H$) attributes is in progress.

# References

1. Reinhard E, Heidrich W, Debevec P et al (2012) High dynamic range imaging, 2nd edn. Morgan Kaufmann, Burlington, MA, pp 438–439
2. Wang Z, Bovik AC (2009) Mean squared error: love it or leave it? A new look at signal fidelity measures. IEEE Signal Process Mag 26(1):98–117
3. Wang Z, Bovik AC, Sheikh HR et al (2004) Image quality assessment: From error visibility to structural similarity. IEEE Trans Imag Process 13(4):600–612
4. Yeganeh H, Wang Z (2013) Objective quality assessment of tone-mapped images. IEEE Trans Image Process 22(2):657–667
5. Nafchi HZ, Shahkolaei A, Moghammadam RF (2015) FSITM: A feature similarity index for tone-mapped images. IEEE Signal Process Lett 22(8):1026–1029
6. Wang Z, Sheikh HR, Bovik AC (2002) No-reference perceptual quality assessment of JPEG compressed images. In: IEEE international conference on image processing, pp 477–480
7. Caviedes J, Oberti F (2004) A new sharpness metric based on local kurtosis, edge and energy information. Signal Process Image Commun 19:147–161
8. Mittal A, Soundararajan R, Bovik AC (2013) Making a completely blind image quality analyzer. IEEE Signal Process Lett 22(3):209–212
9. Zhang L, Zhang L, Bovik AC (2015) A feature-enriched completely blind local image quality analyzer. IEEE Trans Image Process 24(8):2579–2591
10. Gong R, Xu H, Luo MR et al (2015) Comprehensive model for predicting perceptual image quality of smart mobile devices. Appl Opt 54:85–95
11. Fairchild MD (2007) The HDR photographic survey. In: Color and imaging conference, Society for Imaging Science and Technology, pp 233–238
12. Drago F, Myszkowski K, Annen T et al (2003) Adaptive logarithmic mapping for displaying high contrast scenes. Comput Graph Forum 22(3):419–426
13. Reinhard E, Devlin K (2005) Dynamic range reduction inspired by photoreceptor physiology. IEEE Trans Vis Comput Graph 11(1):13–24
14. Reinhard E, Stark M, Shirley P et al (2002) Photographic tone reproduction for digital images. ACM Trans Graph 21(3):267–276
15. Schlick C (1995) Quantization techniques for visualization of high dynamic range pictures. In: Sakas G, Müller S, Shirley P (eds) Photorealistic rendering techniques: focus on computer graphics (Tutorials and perspectives in computer graphics). Springer, Berlin, Heidelberg, pp 7–20
16. Ward G, Rushmeier H, Piatko C (1997) A visibility matching tone reproduction operator for high dynamic range scenes. IEEE Trans Vis Comput Graph 3(4):291–306
17. Choi SY, Luo MR, Pointer MR et al (2008) Predicting perceived colorfulness, contrast, naturalness and quality for color images reproduced on a large display. In: 16th color imaging conference, IS&T and SID, pp 158–164

18. Li C, Li Z, Wang Z et al (2017) Comprehensive color solutions: CAM16, CAT16, and CAM16-UCS. Color Res Application 42(6):703–718
19. Calabria AJ, Fairchild MD (2003) Perceived image contrast and observer preference II. Empirical modeling of perceived image contrast and observer preference data. J Imaging Sci Technol 47(6):494–508

# Correlations Between Colour Discrimination and Colour Quality Metrics

Ying Liu[1], Lianjiang Rao[2], Zheng Huang[1], Hanwen Gong[1],
Xinwei Wu[1], and Qiang Liu[1(✉)]

[1] School of Printing and Packaging, Wuhan University, Wuhan, China
liuqiang@whu.edu.cn
[2] WAC Lighting, Shanghai, China

**Abstract.** Nowadays, many studies are trying to propose a measure for characterizing the colour discrimination of human vision. Our previous work conducted three sets of colour discrimination experiments using the Farnsworth - Munsell (FM) 100 Hue Test under lighting conditions with different correlated colour temperatures, illumination levels and Duv values. In this study, the Pearson correlation coefficients between observers' average error score and 27 typical colour quality metrics were computed based on the three sets of experimental data. The results show that among these metrics, CDI, CSA, GAI, GAI-RA and FSCI have stronger correlations with colour discrimination for most lighting conditions, and relatively, CQI-1, DSI(D65) and Snuetral perform better.

**Keywords:** Colour discrimination · FM-100 Hue Test · Colour quality metric · Pearson correlation coefficient

## 1 Introduction

For several decades, the Commission International de l' Eclairage (CIE) General Colour Rendering Index (CRI) Ra [1] has been recommended as the standard criterion for assessing colour quality of light sources. But in recent years, many researchers have agreed that describing colour quality of a light source with only one metric is not sufficient, and a full description of light quality should include many different aspects, such as fidelity [1, 2], preference [3–8], naturalness [9, 10], vividness [11–13], harmony [14] and discrimination [8, 15]. Among them, colour discrimination refers to the ability of human eyes to distinguish the difference between hue, brightness and saturation [16]. Nowadays, many new metrics have been proposed. Therefore, exploring the effectiveness of colour quality metrics in characterizing colour discrimination has become a hot topic at home and abroad [17–21]. For example, in a recent study of Jiang et al. [15], a new metric defined as cone sensitivity difference (CSD), based on the cone cell sensitivity was proposed to describe the colour discrimination property of a light source, and they conducted visual experiments to assess the performance of the new CSD metric and conventional colour quality metrics such as Ra, Qa, Qg and CDI.

In this study, based on the data of three FM-100 Hue Tests, which were carried out under different lighting conditions in our previous work [8, 20, 21], the Pearson

correlation coefficients between observers' average error score and 27 typical colour quality metrics were calculated. The purpose of this study is mainly to study the correlations between various indexes and colour discrimination.

## 2 Experimental Method

### 2.1 Experimental Setup

In the first experiment, five spectral power distributions (SPDs) of CCTs ranging from 2500 K to 6500 K, with a constant illuminance (200 lx), were generated [8]. In the second experiment, a set of five SPDs, which have similar CCT and illuminance level (5500 K, 500 lx), different Duv values ranged from −0.02 to 0.02 (0.01 interval), were used [20]. In the third experiment, the light sources were six SPDs of 3000 K, 200 lx, different Duvs ranged from −0.015 to 0.010 (0.005 interval) [21]. The SPDs of the experimental light sources are shown in Fig. 1, and the colorimetric parameters were calculated, together with typical colour quality measures, as shown in Table 1. For additional information on experimental environment and devices, please refer to our previous articles [8, 20, 21].

### 2.2 Experimental Design and Procedure

A group of 42 observers (21 females and 21 males, 18–28 years old, with a mean of 22.3 years) were recruited for the first FM-100 Hue Test experiment, while 24 subjects (12 males and 12 females, 17–32 years old, with a mean of 20.2 years), participated in the second and third experiments. All of them are students of Wuhan University and have passed the Ishihara Color Vision Test.

The FM-100 Hue Test consists of 93 colour samples with consistent brightness and saturation, but with a gradient pattern in hue. Among them, 85 movable samples are divided into 4 boxes and each of the boxes has one fixed sample at each end as a reference. The colours of the four boxes are respectively red-green (85 ∼ 1∼21), green-blue (22 ∼ 42), blue-purple (43 ∼ 63), purple-red (64 ∼ 84), thus covering the Munsell hue circle. For each sample, an integer number is marked on its underside to identify its original position. To carry out the test, each of the four boxes of samples should be sorted into a continuous hue order. The farther the observer arranges the hue chess from the position where it should be placed, the higher the error score is, indicating that the colour discrimination of the sample region is worse. After the observer completes the test, the error score was calculated according to the calculation method shown in Eq. (1), where $X_n$ represents the number of the hue chess placed by the observer at the nth position of the hue chess. Such calculations can be automatically implemented by the FM-100 Hue Test scoring software provided by X-Rite [22].

$$ErrorScore = \sum_n \left( |X_{n+1} - X_n| + |X_n - X_{n-1}| - 2 \right), \; n = 1, 2, \ldots, 85 \quad (1)$$

(a). 2500 K~6500 K, 200 lx

(b). 5500 K, 500 lx

(c). 3000K, 200 lx
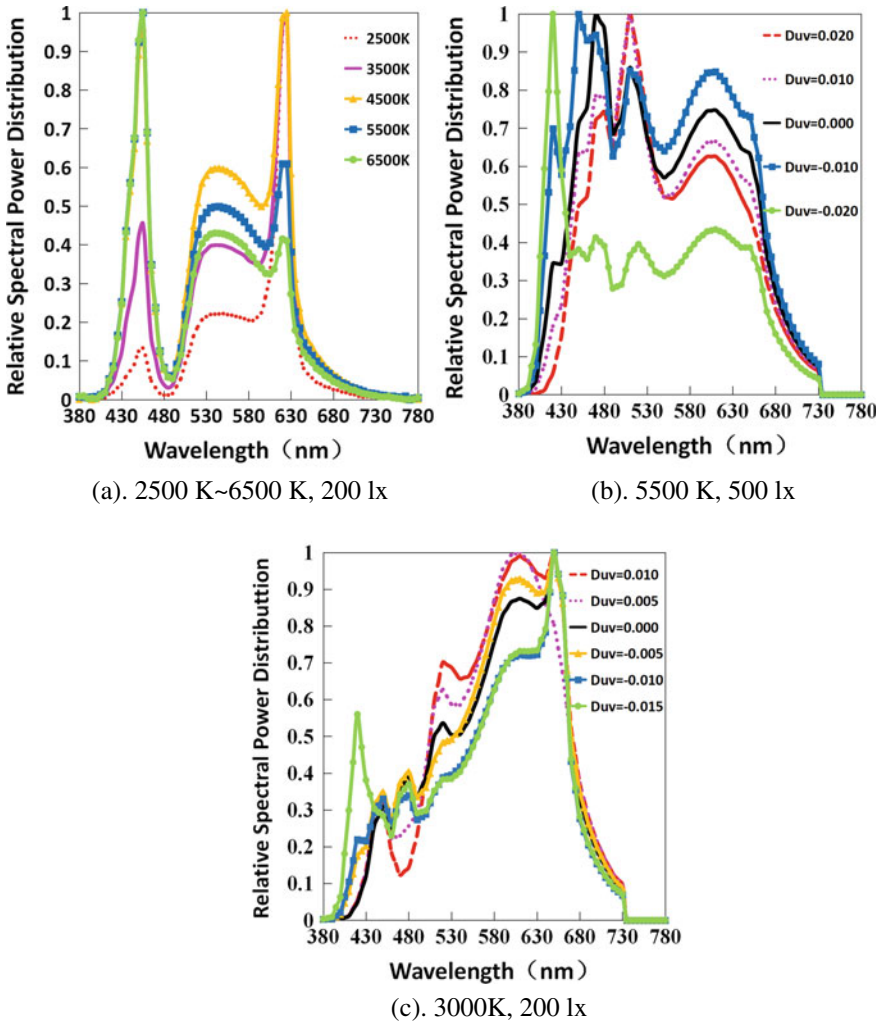
**Fig. 1.** Relative spectral power distributions of experimental light sources

The three sets of experiments followed the same procedure, more details can be found in our other articles [8, 20, 21]. In total, we obtained 1896 groups of data sets from three experiments, which lasted about 133 h.

**Table 1.** Colorimetric properties of the experimental SPDs and the corresponding values of typical colour quality metrics

| ID | The first experiment (2500–6500 K, 200 lx) | | | | | The second experiment (5500 K, 500 lx) | | | | | The third experiment (3000 K, 200 lx) | | | | | |
|---|---|---|---|---|---|---|---|---|---|---|---|---|---|---|---|---|
| | 2445 | 3451 | 4471 | 5538 | 6637 | 5484 | 5591 | 5500 | 5518 | 5576 | 3097 | 3085 | 3073 | 2998 | 3019 | 3034 |
| CCT | 2445 | 3451 | 4471 | 5538 | 6637 | 5484 | 5591 | 5500 | 5518 | 5576 | 3097 | 3085 | 3073 | 2998 | 3019 | 3034 |
| Duv | −0.003 | −0.005 | −0.007 | −0.007 | −0.008 | 0.020 | 0.010 | 0.000 | −0.010 | −0.020 | 0.010 | 0.005 | 0.000 | −0.005 | −0.010 | −0.015 |
| u' | 0.278 | 0.241 | 0.223 | 0.212 | 0.206 | 0.192 | 0.198 | 0.207 | 0.214 | 0.222 | 0.244 | 0.246 | 0.248 | 0.252 | 0.254 | 0.255 |
| v' | 0.528 | 0.507 | 0.486 | 0.470 | 0.457 | 0.498 | 0.487 | 0.477 | 0.468 | 0.457 | 0.532 | 0.527 | 0.520 | 0.515 | 0.507 | 0.500 |
| CRI | 91 | 89 | 84 | 81 | 79 | 89 | 89 | 89 | 91 | 87 | 91 | 90 | 95 | 93 | 95 | 94 |
| GAI | 50 | 78 | 91 | 96 | 97 | 75 | 87 | 95 | 105 | 117 | 44 | 50 | 58 | 64 | 74 | 83 |
| FSCI | 28 | 57 | 67 | 70 | 70 | 87 | 91 | 94 | 97 | 99 | 75 | 77 | 81 | 83 | 85 | 89 |
| Qa(v9.0.3) | 87 | 85 | 80 | 76 | 73 | 82 | 86 | 91 | 97 | 92 | 90 | 91 | 95 | 92 | 93 | 92 |
| Qf(v9.0.3) | 82 | 81 | 78 | 73 | 70 | 82 | 85 | 91 | 94 | 86 | 91 | 92 | 95 | 92 | 90 | 86 |
| Qg(v9.0.3) | 96 | 92 | 87 | 83 | 81 | 91 | 96 | 100 | 105 | 112 | 92 | 93 | 97 | 100 | 105 | 109 |
| Qp(v7.4) | 113 | 107 | 103 | 101 | 98 | 81 | 86 | 94 | 101 | 102 | 88 | 90 | 95 | 95 | 99 | 100 |
| FCI(CAM02) | 107 | 102 | 94 | 87 | 81 | 96 | 96 | 99 | 97 | 93 | 113 | 111 | 120 | 119 | 122 | 119 |
| CDI | 73 | 114 | 133 | 139 | 142 | 110 | 126 | 138 | 153 | 171 | 65 | 73 | 85 | 93 | 108 | 122 |
| CSA | 0.034 | 0.048 | 0.056 | 0.06 | 0.062 | 0.055 | 0.059 | 0.062 | 0.065 | 0.069 | 0.035 | 0.038 | 0.041 | 0.043 | 0.047 | 0.051 |
| CPI | 142 | 139 | 131 | 126 | 123 | 139 | 139 | 138 | 141 | 135 | 143 | 142 | 148 | 145 | 149 | 146 |
| CAM02-UCS | 85 | 84 | 80 | 75 | 73 | 81 | 85 | 90 | 94 | 83 | 93 | 92 | 95 | 92 | 91 | 87 |
| CRI2012 | 83 | 84 | 82 | 78 | 77 | 87 | 91 | 94 | 97 | 88 | 93 | 93 | 96 | 94 | 95 | 91 |
| MCRI | 89 | 90 | 89 | 87 | 85 | 83 | 87 | 91 | 93 | 93 | 86 | 87 | 90 | 90 | 91 | 91 |
| Rf | 81 | 81 | 77 | 74 | 72 | 82 | 85 | 88 | 95 | 83 | 92 | 92 | 93 | 92 | 93 | 87 |
| Rg | 110 | 106 | 102 | 101 | 99 | 92 | 96 | 98 | 104 | 111 | 98 | 96 | 97 | 100 | 103 | 106 |
| ΔC* | 2.58 | 1.75 | 1.26 | 1.37 | 1.4 | −2.13 | −0.78 | 0.03 | 1.34 | 3.08 | −2.37 | −1.98 | −0.65 | 0.01 | 1.32 | 2.12 |
| CQI-1 | 169 | 175 | 179 | 180 | 182 | 173 | 180 | 187 | 191 | 191 | 167 | 168 | 174 | 173 | 175 | 175 |
| CQI-2 | 1434 | 1672 | 1971 | 2386 | 2803 | 1782 | 2053 | 2160 | 2389 | 2704 | 849 | 911 | 1133 | 1217 | 1446 | 1587 |

*(continued)*

**Table 1.**  (*continued*)

| ID | The first experiment (2500–6500 K, 200 lx) | | | | | The second experiment (5500 K, 500 lx) | | | | | The third experiment (3000 K, 200 lx) | | | | | |
|---|---|---|---|---|---|---|---|---|---|---|---|---|---|---|---|---|
| GAI-RA | 70 | 84 | 89 | 90 | 90 | 82 | 88 | 92 | 98 | 102 | 68 | 70 | 77 | 78 | 85 | 89 |
| GVI | 81 | 89 | 90 | 90 | 88 | 92 | 92 | 89 | 88 | 86 | 80 | 78 | 79 | 77 | 78 | 78 |
| DSI(D65) | 78 | 81 | 82 | 82 | 82 | 88 | 90 | 91 | 94 | 89 | 84 | 85 | 85 | 86 | 88 | 85 |
| Snuetral | 0.66 | 3.72 | 6.44 | 7.83 | 8.07 | 2.07 | 4.31 | 6.84 | 7.91 | 6.87 | 1.53 | 1.92 | 2.36 | 2.45 | 2.71 | 2.78 |
| WS | 0.16 | 0.45 | 0.74 | 0.99 | 1.13 | 0.26 | 0.42 | 0.69 | 1.10 | 1.85 | 0.18 | 0.22 | 0.28 | 0.33 | 0.43 | 0.56 |
| Percent tint | 0.66 | 0.10 | 0.43 | 0.89 | 1.26 | 0.07 | 0.32 | 0.56 | 0.87 | 1.30 | 0.70 | 0.60 | 0.47 | 0.35 | 0.18 | 0.04 |

# 3    Results and Discussion

## 3.1    Colour Discrimination in Different Lighting Conditions

The results of the three colour discrimination experiments are shown in Table 2. The results indicate that when the illuminance level is 200 lx, there is an optimum CCT of 5500 K, at which observers were found to get the lowest average error score (AES), meaning that they exhibited the greatest capability for colour discrimination. Then, under the optimal CCT (5500 K), and the illuminance was increased to 500 lx, we found that the observers' AES was significantly reduced. However, under low CCT and illumination (3000 K, 200 lx), the observers' AES is higher than that under high CCT and illumination (5500 K, 500 lx), which means that properly increasing colour temperature and illumination level is beneficial to enhance the colour discrimination of human vision. Simultaneously, through the second and third experiments, we also found that whether the lighting condition is low CCT and low illumination or high CCT and high illumination, the best colour discrimination is obtained when the Duv value is negative.

**Table 2.** The observers' average error score of the three colour discrimination experiments

| *The first experiment (2500–6500 K, 200 lx)* | | | | | |
|---|---|---|---|---|---|
| ID | 2500 K | 3500 K | 4500 K | 5500 K | 6500 K |
| Average Error Score | 104 | 63 | 45 | 36 | 40 |
| *The second experiment (5500 K, 500 lx)* | | | | | |
| ID | Duv = 0.020 | Duv = 0.010 | Duv = 0.000 | Duv = −0.010 | Duv = −0.020 |
| Average Error Score | 20 | 14 | 15 | 11 | 17 |
| *The third experiment (3000 K, 200 lx)* | | | | | |
| ID | Duv = 0.010 | Duv = 0.005 | Duv = 0.000 | Duv = −0.005 | |
| Duv = −0.010 | | | | Duv = −0.015 | |
| Average Error Score | 49 | 47 | 43 | 36 | |
| 34 | 31 | | | | |

## 3.2    Correlation Analysis

27 typical colour quality metrics were computed, including the CIE Color Rendering Index (CRI) [1], Gamut Area Index(GAI) [23], Full Spectrum Colour Index (FSCI) [24], Colour Quality Scale (CQS: Qa, Qf, Qp, Qg) [25], Feeling of Contrast Index (FCI) [26], Colour Discrimination Index (CDI) [16], Cone Surface Area (CSA) [27], Color Preference Index (CPI) [28], Cone Sensitivity Difference (CSD) [15], CRI-CAM02UCS [29], CRI2012 [30], Memory Colour Rendering Index (MCRI) [31], IES TM-30 (Rf and Rg) [32], CIE-Rf [19], Mean Chroma Shift of CQS ($\Delta C^*$) [11–13], two combined metrics named Colour Quality Index (respectively denoted as CQI1 and

CQI2) [11, 13], the arithmetic mean value of GAI and CRI [10], Gamut Volume Index (GVI) [33], Daylight Spectrum Index (DSI) [34], Degree of neutrality (Sneutral) [35], White Sensation (WS) [36], Percent tint [37]. And then the Pearson correlation coefficients between the metrics and observers' average error score were calculated and listed in Table 3.

As mentioned above, lower observers' average error score represents stronger colour discrimination, so the correlation coefficient between the index and the average

**Table 3.** Pearson correlation coefficients of 27 typical colour quality metrics with the observers' average total error score obtained from the experiments

| ID | The first experiment (2500–6500 K, 200 lx) | | The second experiment (5500 K, 500 lx) | | The third experiment (3000 K, 200 lx) | | Overall r |
|---|---|---|---|---|---|---|---|
| | Pearson $r$ | p | Pearson $r$ | p | Pearson $r$ | p | |
| CRI | 0.8828 | 0.0473 | −0.6311 | 0.2536 | −0.6981 | 0.1230 | −0.15 |
| GAI | −0.9974 | 0.0002 | −0.4123 | 0.4903 | −0.9756 | 0.0009 | −0.80 |
| FSCI | −0.9960 | 0.0003 | −0.5171 | 0.3723 | −0.9767 | 0.0008 | −0.83 |
| Qa(v9.0.3) | 0.8535 | 0.0658 | −0.7630 | 0.1335 | −0.3464 | 0.5012 | −0.09 |
| Qf(v9.0.3) | 0.7809 | 0.1189 | −0.8351 | 0.0784 | 0.6033 | 0.2048 | 0.18 |
| Qg(v9.0.3) | 0.9164 | 0.0286 | −0.3542 | 0.5587 | −0.9735 | 0.0010 | −0.14 |
| Qp(v7.4) | 0.9501 | 0.0133 | −0.5382 | 0.3494 | −0.9505 | 0.0036 | −0.18 |
| FCI(CAM02) | 0.8658 | 0.0578 | −0.3568 | 0.5556 | −0.7845 | 0.0646 | −0.09 |
| CDI | −0.9960 | 0.0003 | −0.3944 | 0.5111 | −0.9718 | 0.0012 | −0.79 |
| CSA | −0.9865 | 0.0019 | −0.4143 | 0.4880 | −0.9677 | 0.0016 | −0.79 |
| CPI | 0.8799 | 0.0491 | −0.5024 | 0.3884 | −0.6238 | 0.1857 | −0.08 |
| CSD | 0.9774 | 0.0041 | −0.4406 | 0.4577 | −0.1682 | 0.7500 | 0.12 |
| CRI-CAM02UCS | 0.8161 | 0.0920 | −0.8835 | 0.0469 | 0.7038 | 0.1186 | 0.21 |
| CRI2012 | 0.6659 | 0.2198 | −0.9083 | 0.0329 | 0.1703 | 0.7470 | −0.02 |
| MCRI | 0.5328 | 0.3552 | −0.6312 | 0.2535 | −0.9136 | 0.0109 | −0.34 |
| Rf | 0.7937 | 0.1089 | −0.8853 | 0.0458 | 0.5043 | 0.3077 | 0.14 |
| Rg | 0.9524 | 0.0124 | −0.3043 | 0.6186 | −0.8952 | 0.0159 | −0.08 |
| CIE-Rf | 0.8030 | 0.1018 | −0.8460 | 0.0708 | 0.5043 | 0.3077 | 0.15 |
| △C* | 0.9797 | 0.0034 | −0.3607 | 0.5509 | −0.9791 | 0.0006 | −0.12 |
| CQI-1 | −0.9742 | 0.0050 | −0.6276 | 0.2570 | −0.8792 | 0.0210 | −0.83 |
| CQI-2 | −0.8169 | 0.0914 | −0.3683 | 0.5419 | −0.9725 | 0.0011 | −0.72 |
| GAI-RA | −0.9948 | 0.0004 | −0.4767 | 0.4168 | −0.9609 | 0.0023 | −0.81 |
| GVI | −0.9184 | 0.0276 | 0.2624 | 0.6698 | 0.6564 | 0.1568 | 0.00 |
| DSI(D65) | −0.9876 | 0.0017 | −0.9304 | 0.0218 | −0.6098 | 0.1986 | −0.84 |
| Snuetral | −0.9748 | 0.0048 | −0.7213 | 0.1690 | −0.9446 | 0.0045 | −0.88 |
| WS | −0.9234 | 0.0252 | −0.1809 | 0.7709 | −0.9475 | 0.0041 | −0.68 |
| Percent tint | −0.3177 | 0.6025 | −0.3252 | 0.5934 | 0.9802 | 0.0006 | 0.11 |

The metrics with correlation coefficients close to −0.8 or less than −0.8 are underlined and bolded

error score is expected to be closed to −1, meaning that the higher the metric value, the lower the average error score and the better the colour discrimination.

The data shown in Table 3 reveal that the same index has different correlations with the observers' average error score under different lighting conditions. For example, CRI-CAM02UCS showed stronger positive correlations in the first ($r = 0.8161$) and third experiment ($r = 0.7038$), while in the second experiment, it showed a significant negative correlation ($r = -0.8835$). We assumed that such indexes could not characterize the colour discrimination well.

In addition, as shown in Table 3, these colour quality metrics performed differently between high CCT, high illumination (5500 K, 500 lx) and low CCT, low illumination (3000 K, 200 lx). There were some indexes which only performed well under lighting conditions with high CCT and high illumination level, such as Qf(v9.0.3), Rf, CIE-Rf, CRI2012 and CRI-CAM02UCS, whose Pearson correlation coefficients were close to or less than −0.8, and most with a p value less than 0.05. However, other indexes that performed well under low CCT and low illumination, such as, Qg(v9.0.3), Qp(v7.4), Rg, $\triangle$C*, CQI-2 and WS, were not well under high CCT and high illumination.

In summary, CDI, CSA, GAI, GAI-RA and FSCI performed well in the multiple CCTs or low CCT and low illumination, but the negative correlations in the lighting condition of high CCT and high illumination were not strong enough. Overall, DSI (D65), Snuetral and CQI-1 exhibited relatively stable and strong negative correlations with the observers' average error score, regardless of the lighting conditions. In our previous studies, we found that for the scenarios with multiple CCTs ranging from 2500 K to 5500 K people indeed got better colour discrimination under whiter lightings, while for CCTs higher than 5500 K it seemed that they appeared too cold to distinguish [7, 8]. We guess the fact that Snuetral performs a significant negative correlation with the observers' average error score may be related to the relationship between the whiteness of a light source and colour discrimination, which still needs further study.

## 4    Conclusions

In this paper, to explore the correlations between colour discrimination and colour quality metrics, 27 typical colour quality metrics of 16 SPDs used in our previous studies were calculated, and the Pearson correlation coefficients of these metrics with the observers' average error score obtained from the three sets of experiments were studied. The results of colour discrimination experiments indicate that higher correlated colour temperatures and illumination levels are beneficial for improving colour discrimination. In addition, a negative Duv value can also produce better colour discrimination. Through correlation analysis, we found that CDI, CSA, GAI, GAI-RA, FSCI, CQI-1, DSI(D65) and Snuetral have relatively stronger correlations with colour discrimination, and in which Snuetral performs best. The authors believes that the findings of this study may contribute to establishing an index that effectively characterizes colour discrimination.

**Compliance with Ethical Standards**

**Conflict of Interest**: The authors declare that they have no conflict of interest.

**Ethical approval**: All procedures performed in studies involving human participants were in accordance with the ethical standards of the school of printing and packaging, Wuhan University and with the 1964 Helsinki declaration and its later amendments or comparable ethical standards.

**Informed consent**: Informed consent was obtained from all individual participants included in the study.

# References

1. Nickerson D, Jerome CW (1965) Color rendering of light sources: CIE method of specification and its application. Illum Eng 60:262
2. Davis W, Ohno Y (2010) Color quality scale. Opt Eng 49:033602–033602–033616
3. Wei M, Houser KW (2016) What is the cause of apparent preference for sources with chromaticity below the blackbody locus? Leukos 12:95–99
4. Huang Z, Liu Q, Westland S, Pointer MR, Luo MR, Xiao K et al (2018) Light dominates colour preference when correlated colour temperature differs. Light Res Technol 50:995–1012
5. Liu Q, Huang Z, Pointer MR et al (2018) Evaluating colour preference of lighting with an empty light booth. Light Res Technol 50:1249–1256
6. Huang Z, Liu Q, Pointer MR et al (2019) White lighting and colour preference, Part 1: Correlation analysis and metrics validation. Light Res Technol 147715351882478
7. Huang Z, Liu Q, Luo MR et al (2019) The whiteness of lighting and colour preference, Part 2: a meta-analysis of psychophysical data. Light Res Technol. https://doi.org/10.1177/1477153519837946
8. Huang Z, Liu Q, Liu Y et al (2019) Best lighting for jeans, part 1: Optimising colour preference and colour discrimination with multiple correlated colour temperatures. Light Res Technol 51(8):1208–1223
9. Jost-Boissard S, Fontoynont M, Blanc-Gonnet J (2009) Perceived lighting quality of LED sources for the presentation of fruit and vegetables. J Mod Opt 56:1420–1432
10. Jost-Boissard S, Avouac P, Fontoynont M (2015) Assessing the colour quality of LED sources: naturalness, attractiveness, colourfulness and colour difference. Light Res Technol 47:769–794
11. Khanh T, Bodrogi P, Vinh Q et al (2016) Colour preference, naturalness, vividness and colour quality metrics, Part 1: experiments in a room. Light Res Technol. https://doi.org/10.1177/1477153516643359
12. Khanh T, Bodrogi P (2016) Colour preference, naturalness, vividness and colour quality metrics, Part 3: experiments with makeup products and analysis of the complete warm white dataset. Light Res Technol. https://doi.org/10.1177/1477153516669558
13. Khanh T, Bodrogi P, Vinh Q et al (2016) Colour preference, naturalness, vividness and colour quality metrics, Part 2: Experiments in a viewing booth and analysis of the combined dataset. Light Res Technol. https://doi.org/10.1177/1477153516643570

14. Szabó F, Bodrogi P, Schanda J (2009) A colour harmony rendering index based on predictions of colour harmony impression. Light Res Technol 41:165–182
15. Jiang L, Jin P, Lei P (2015) Color discrimination metric based on cone cell sensitivity. Opt Express 23:A741–A751
16. Thornton WA (1972) Color-discrimination index. J Opt Soc Am 62:191–194
17. Royer MP, Houser KW, Wilkerson AM (2012) Color discrimination capability under highly structured spectra. Color Res Appl 37:441–449
18. Esposito T, Houser K (2017) A new measure of colour discrimination for LEDs and other light sources. Light Res Technol 51(1):5–23
19. Jost S, Cauwerts C, Avouac P (2017) CIE 2017 color fidelity index Rf: a better index to predict perceived color difference? J Opt Soc Am A: Opt Image Sci, Vis 35(4):B202–B213
20. Huang Z, Liu Q, Luo MR et al (2019) Best lighting for jeans: optimising colour preference and colour discrimination. In: 29th Quadrennial session of the CIE, June 2019
21. Liu Y, Rao L, Zhong X et al (2019) Verification of Farnworth-Munsell 100 Hue Test on color discrimination quantification under different lighting conditions (in Chinese). China Illum Eng J (in press)
22. Vingrys AJ, King-Smith PE (1988) A quantitative scoring technique for panel tests of color vision. Investig Ophthalmol Vis Sci 29:50–63
23. Freyssinier JP, Rea M (2010) A two-metric proposal to specify the color-rendering properties of light sources for retail lighting. In: SPIE optical engineering + applications. SPIE, p 6
24. Rea M (2004) NLPIP lighting answers: light sources and color. Rensselaer Polytechnic Institute; National Lighting Product Information Program, Troy, NY. http://www.lrcrpiedu/nlpip/publicationDetailsasp?id=901&type=2
25. Davis W, Ohno Y (2010) Color quality scale. Opt Eng 49:033602–033616
26. Hashimoto K, Yano T, Shimizu M et al (2007) New method for specifying color-rendering properties of light sources based on feeling of contrast. Color Res Appl 32:361–371
27. Fotios S, Levermore GJ (1997) Perception of electric light sources of different colour properties. Int J Light Res Technol 29:161–171
28. Thornton WA (1974) A validation of the color-preference index. J Illum Eng Soc 4:48–52
29. Luo MR (2011) The quality of light sources. Color Technol 127:75–87
30. Smet KAG, Schanda J, Whitehead L (2013) CRI2012: a proposal for updating the CIE colour rendering index. Light Res Technol 45:689–709
31. Smet KAG, Ryckaert WR, Pointer MR et al (2010) Memory colours and colour quality evaluation of conventional and solid-state lamps. Optics Express 18:26229–26244
32. David A, Fini PT, Houser KW et al (2015) Development of the IES method for evaluating the color rendition of light sources. Optics Express 23:15888–15906
33. Liu Q, Huang Z, Xiao K et al (2017) Gamut Volume Index: a color preference metric based on meta-analysis and optimized colour samples. Opt Express 25:16378–16391
34. Acosta I (2017) Daylight Spectrum Index: Development of a New Metric to Determine the Color Rendering of Light Sources. Int J Eng Technol 9(6):442–447
35. Kevin A, Geert D, Peter H (2014) Chromaticity of unique white in object mode. Opt Express 22:25830–25841
36. Wang Q, Xu H, Cai J (2015) Chromaticity of white sensation for LED lighting. Chin Opt Lett 13:073301
37. Rea MS, Freyssinier JP (2015) White lighting: a provisional model for predicting perceived tint in "white" illumination. Color Res Appl 39:466–479

# Analysis on Color Rendering Performance of Digital Acquisition System for Grotto Murals

Lingjun Kong[1(✉)] and Huoyong Xie[2]

[1] Printing and Packaging Engineering Department, Shanghai Publishing and Printing College, Shanghai, China
`908641376@qq.com`
[2] Shanghai Commercial Digital Printing Co., Ltd, Shanghai, China

**Abstract.** On the basis of ensuring the physical safety of the grotto murals, high-fidelity digitalization of the murals is the basis for the scientific protection, permanent preservation, continuation and inheritance of grotto murals. This paper aims to study the color rendering performance and applicability of the planar digital acquisition system for the murals. The color rendering performance of four acquisition systems were detected and analyzed by simulating the planar digital acquisition scene in the grotto temple and its shooting conditions. The results show that the color gamut of each acquisition system is much larger than those of sRGB and Adobe RGB color space, and the systems of scanning back combined with LED light have better color rendering accuracy and larger color gamut than the systems consisting of digital back and fluorescent light. The four acquisition systems are competent for the digitalization of grotto murals, and the systems of set 4 and set 2 are especially recommended.

**Keywords:** Grotto mural · Planar digital acquisition · Color rendering accuracy · Color gamut

## 1 Introduction

Grotto murals are non-renewable human precious historical and cultural resources, the use of high-tech digital technology means to digitally acquire, archive and reproduce the grotto murals is a new scientific and effective way to protection, permanent preservation, continuation and inheritance of the murals, which has a very important practical significance, and gets more and more attention from the state and the general concern of the international community. The relevant research is still in the initial developing stage [1].

In the digitalization process of grotto murals, the light source, digital acquisition equipment and the working environment should not cause any physical damage to the murals, and ensure that the captured images effectively restore and reproduce the original features of the murals [2]. Obviously, choosing the right digital acquisition system is important, where the color rendering performance of the system is the key.

The paper simulates the digital acquisition scene of grotto murals to study the color rendering performance from the aspects of color gamut and color rendering accuracy

for the digital acquisition systems, which provide the basis for research and production practices such as digital acquisition, scientific protection and permanent preservation of grotto murals.

## 2  Experimental Equipment and Conditions

A digital acquisition system is made up of acquisition equipment and light sources, the CCD working mode of the equipment and color temperature, color rendering index (CRI) of light source etc. are the main influencing factors to the color rendering performance of the system. The paper simulates the practice to digitalize grotto murals, and selects four systems combined with different acquisition equipment and light sources for the experiment.

### 2.1  Digital Acquisition Equipment

In the digitalization of grotto murals, only SLR camera (also called digital back) and scanning back can be applied to high-precision acquisition of the image data without direct contact with the murals [3]. Digital back contains an array of CCDs, has smaller size and less weight than scanning back, it can be installed on a small tripod. Digital back has fast working speed, but its pixels are usually lower than those of scanning back. Scanning back uses line-by-line CCD scanning mode, and its overall working speed is much slower than digital back's.

Any acquisition equipment can be used freely in the large space, but the acquisition system with scanning back is not suitable in narrow channels due to the large size of its holder, which should be stable enough to keep the scanning back perfectly still during the exposure time. As a result, companies typically have more than one system for mural digitalization. This paper takes three acquisition equipments used by Shanghai Commercial Digital Printing Co., Ltd. for the experiment, which are Phase One IQ180 digital back, Phase One Power FX+ scanning back and Rencay Archive scanning back.

### 2.2  Light Sources

Fluorescent lamp and LED light are selected as light sources, and fluorescent lamp has two types, OSRAM DULUX L 55 W/954 and SHO Light 55 W 5400 K, which are arranged in parallel by six lamp tubes and installed in a lamp box. The LED light source is composed of an array of LED beads.

The color temperature of two fluorescent lamps is 5400 k and LED light are 5000 K, their spectral power distribution (SPD) curves are showed in Fig. 1. We can see that two types of the fluorescent lamps have very similar SPD curves, with maximum spectral energy in 540–550 nm and 610 nm, while the LED light has maximum spectral energy around 450–460 nm. The CRI of OSRAM DULUXL 55 W/954 is 90 with xy color coordinate (0.3320, 0.3485). The CRI of SHO Light 55 W is 94 with xy color coordinate (0.3398, 0.3538). The CRI of LED light is 97 with xy color coordinate (0.3323, 0.3350).
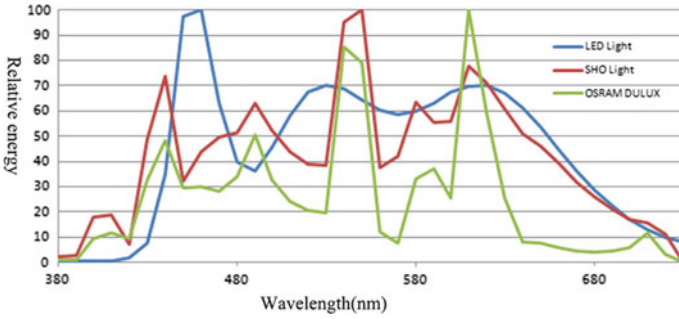
**Fig. 1.** Spectral power distribution curves of the light sources

Although the three acquisition equipment and three light sources can be combined to form nine acquisition systems, not every combination is reasonable, the paper takes the combination of digital back and fluorescent lamp, the combination of scanning back and LED light source as the research objects based on our experience of actual digitalization of the murals, and here generates four sets of acquisition system, as shown in Table 1.

**Table 1.** Composition of digital acquisition systems for the experiment

| System No. | The combinations of acquisition equipment and light source |
|---|---|
| Set 1 | Phase One IQ180 digital back and OSRAM DULUX L 55 W/954 light source |
| Set 2 | Phase One IQ180 digital back and SHO Light source |
| Set 3 | Phase One Power FX+ scanning back and LED light source |
| Set 4 | Rencay Archive scanning back and LED light source |

### 2.3   Related Software

GretagMacbeth Digital ColorChecker® SG test chart is used as color reference and benchmark, CIELAB of each patch is measured under D50 illuminant and 2° field of view by X-Rite spectrodensitymeter. ICC files of the digital acquisition systems are generated by GretagMacbeth ProfileMaker 5.05 software, GretagMacbeth ProfileEditor and Online software ICCView is used to view and compare the color gamut.

## 3   Detection Method

In order to know the color rendering performance of the acquisition systems, we simulate the acquisition conditions in the grotto temples. The test chart, light source and acquisition equipment are arranged in place according to Fig. 2. The light sources are adjusted to emit light uniformly in the acquisition area, and the acquisition equipment is placed at the focus distance by adjusting the shooting distance.
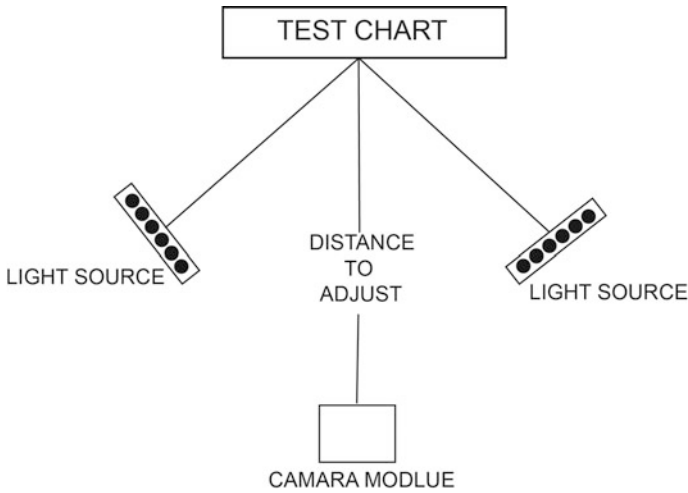
**Fig. 2.** Schematic layout of digital acquisition scene

According to the exposure standard information provided by the software to select exposure and using ISO 50 and customized white balance, shoot the Digital ColorChecker® SG test chart without any special effect, and save the image as TIFF format in uncompressed way.

The captured image of Digital ColorChecker® SG test chart is opened in Photoshop software, and each color patch is processed with average blur filter separately. Then ICC files of the digital acquisition systems are created by ProfileMaker software, and the color differences between the color patches of the captured image and the standard test chart are calculated. The color gamut volumes of the digital acquisition systems are calculated through ICCView software.

## 4  Results and Analysis

### 4.1  Color Gamut

Figure 3 shows that the gamut of four acquisition systems, each of them takes sRGB color space as the reference. The hollow grid area in the graph represents the gamut of the acquisition system. The other color filling area is the gamut of sRGB color space, whose total color volume is 899,157 cubic color units according to the report of ICCView software [4], and the color volumes of the four acquisition systems are shown in Table 2.

We can see from Table 2 that the color gamut of four acquisition systems are much larger than that of sRGB color space, and also larger than that of Adobe RGB color space with color volume of 1,311,023 cubic color units. Among them, Set 1 and Set 2 have similar color rendering ability, while Set 3 and Set 4 have similar color rendering ability. Furthermore, the color rendering capability of Set 3 and Set 4 are higher than those of Set 1 and Set 2, reflecting that the acquisition system consisting of scanning
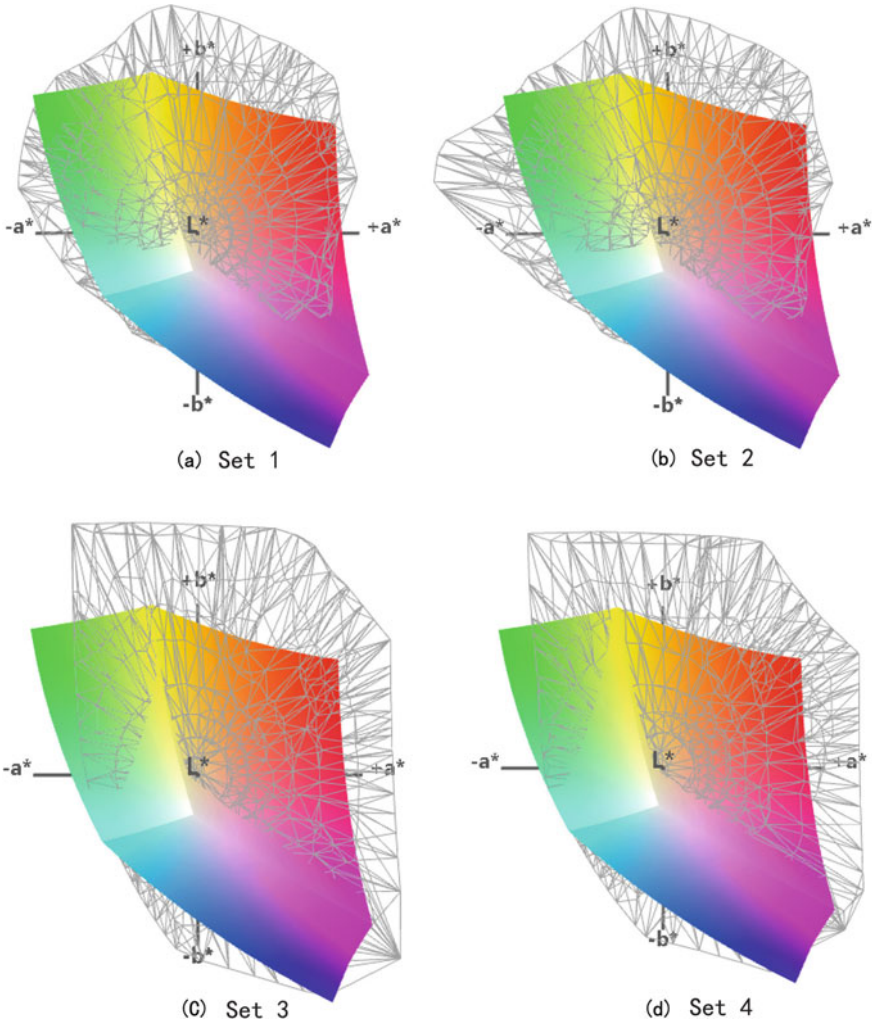
**Fig. 3.** Gamut of four acquisition systems compared with sRGB

**Table 2.** The rendered color volume of four acquisition systems

| System No. | Color volume (cubic color units) |
|------------|----------------------------------|
| Set 1      | 1,391,433                        |
| Set 2      | 1,483,061                        |
| Set 3      | 1,680,033                        |
| Set 4      | 1,722,020                        |

back and LED light source is superior to the acquisition system consisting of digital back and fluorescent lamps, because of the higher CRI of LED light and CCD of the scanning back. Similarly, the color gamut of Set 2 is larger than that of Set 1 because of the higher CRI of SHO fluorescent lamp. The color gamut of Set 4 is larger than that of Set 3, which shows that Rencay Archive scanning back has better color rendering ability than Phase One Power FX+ scanning back.

Figure 4 shows that $a^*b^*$ graph of the four acquisition systems. From Fig. 4, we can easily find out that the colors can be captured by the first two systems are very similar, and have big difference with those of the last two systems. Set 1 and Set 2 can capture brighter green and cyan, while Set 3 and Set 4 have stronger acquisition performance in red, magenta and blue, which maybe result from the SPD characteristic of the LED lamp and fluorescent lamps.
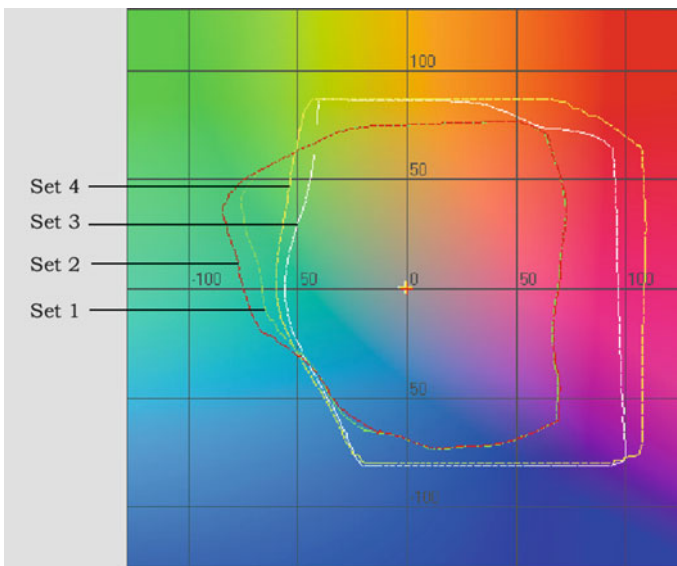


**Fig. 4.** $a^*b^*$ graph of four color gamut

## 4.2   Color Rendering Accuracy

The CIELAB values of each color patch in the captured image and the measured CIELAB values of Digital ColorChecker® SG test chart are compared and described by $\Delta E_{ab}$. The cumulative relative frequency (CRF) curves of the color differences of the four systems are shown in Fig. 5, and the statistic data are listed in Table 3.

The color difference statistics in Table 3 show that Set 3 and Set 4 have higher color rendering accuracy than Set 1 and Set 2, with the average $\Delta E_{ab}$ less than 3.5 and $\Delta E_{ab}$ of 90% patches are less than 6.5. Among them, Set 4 is the best system; Set 1 and Set 2 are almost the same. The results are consistent with those of the results of color
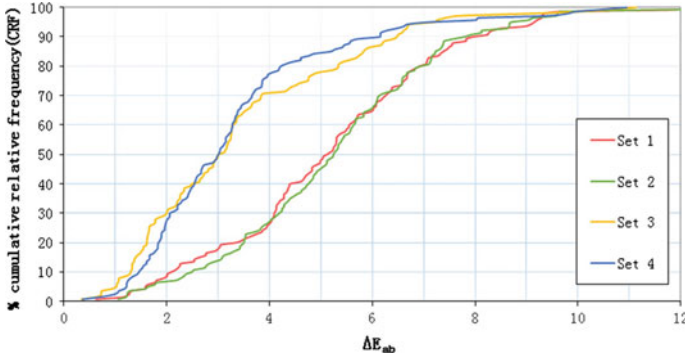
**Fig. 5.** Comparison of color rendering accuracy of four sets

**Table 3.** The rendered color volumes of four acquisition systems

| $\Delta E_{ab}$ | Set 1 | Set 2 | Set 3 | Set 4 |
|---|---|---|---|---|
| Average | 5.20 | 5.30 | 3.45 | 3.36 |
| Max | 12.60 | 16.23 | 11.13 | 10.95 |
| 90% Patches | $\leq 7.96$ | $\leq 7.79$ | $\leq 6.48$ | $\leq 6.15$ |

gamut, which shows that the system with larger color gamut also have better color rendering accuracy.

## 5   Conclusions

The four acquisition systems used in this study have large color gamut, the systems with scanning back and LED light source have high color rendering accuracy, and the systems with digital back and fluorescent lamp have acceptable color rendering accuracy. Among the four systems, the system consisting of Rencay Archive scanning back and LED light source has the best color rendering performance. Furthermore, Since Rencay Archive scanning back has faster working speed than Phase One Power FX+ scanning back, we recommend to use the acquisition system of Rencay Archive scanning back and LED light as long as the grotto temple space is permitted, and apply the combination of digital back with SHO fluorescent light in the narrow space of grotto temple such as swing channels.

# References

1. Wang M (2017) The digital regeneration of the mural art of Kizil grottoes. Digital Printing:29–31
2. Xie H (2013) Introduction to the key technical flow of digital and reductive replication of Grottoes murals. Digital Printing:31–33
3. Zhang X, Zheng X (2018) On the digitization of the mural of Kizil Grottoes in Xinjiang. Printing Field:41–46
4. ICCView (2019) Germany, 45131 Essen, Veronikastr. 40. https://www.iccview.de. Accessed 4 Sept 2019

# Testing of Colour Quality Models Using Colour Preference Assessment Results

Jiamin Shen and Ming R. Luo[(⊠)]

State Key Laboratory of Modern Optical Instrumentation, Zhejiang University,
Zhejiang, China
m.r.luo@zju.edu.cn

**Abstract.** Various experimental datasets have been accumulated to evaluate colour quality metrics. However, most of the datasets did not cover the comprehensive set of lighting parameters. This results in that the metrics developed can only predict limited lighting conditions. This paper describes an experiment for assessing the colour quality of 48 sets of LED lighting conditions in terms of preference. The results were first used to test individual colour quality metrics (CQMs). Later, those better ones were combined to form the regression models to fit the experimental data. The results showed that the models to include colour fidelity metric, colour gamut metric, chroma-shift metric and correlated colour temperature (CCT in K) can predict visual results well.

**Keywords:** Colour quality metrics · Colour preference

## 1 Introduction

Colour quality considers different aspects of lighting settings, e.g. colour naturalness [1, 2], colour preference [1, 2] and colourful attractiveness [3, 4]. Colour preference considers how an observer likes the colour appearance of the coloured objects under the testing light source. In the previous studies, researchers found that the metrics of colour fidelity [5], the size of colour gamut [6, 7], chroma-shift between the testing and reference illuminants [8], CCT [1, 2, 9, 10], the distance of the light source from the Planckian locus (Duv) [9, 11–14] and the illuminance level [15–18] can all have an impact on colour preference, naturalness and colourfulness impression.

Various experimental datasets have been accumulated to evaluate CQMs. However, most of the datasets only covered limited lighting parameters. This results in that the metrics developed from those datasets can only predict limited lighting conditions. This was the motivation of the current work to conduct experiments to include all possible viewing conditions to test all available CQMs.

## 2    Experimental Methods

### 2.1    Light Sources

In the experiment, we used a multi-spectral tunable LED system for achieving different parameters. The parameters studied included 2 luminance levels (100 cd/m$^2$, 200 cd/m$^2$), 3 CCTs (3600 K, 5000 K, 6500 K), 2 Duv levels (−0.015, 0.000), 2 levels of colour fidelity (IES Rf value of 75, 90), and 2 levels of colour gamut sizes (IES Rg value of 95, 115). In total, there were 48 light settings.

### 2.2    Samples and Experimental Environment

The experiment was carried out in a living room environment. Familiar fruits and vegetables were placed on a table covered by a black tablecloth. Figure 1 shows the real experimental scene. Figure 2 shows the objects assessed visually by observers. A multi-spectral tunable LED system was installed in the ceiling on top of the table. Observers could adjust their sitting position slightly to make sure they could see all the samples simultaneously.



**Fig. 1** Experimental situation

Observers were instructed to judge the overall appearance of objects on the table, rather than each individual object. A 6-point categorical judgment method was used for each attribute (naturalness, colourfulness and preference). For example, 'very unnatural', 'unnatural', 'a little unnatural', 'a little natural', 'natural' and 'very natural' correspond to scores of −3, −2, 1, 1, 2, 3, respectively. Only the preference results are reported here.

**Fig. 2** Samples assessed in the experiment

### 2.3 Procedures

There were 8 light settings for one of the six CCT-luminance levels. Table 1 shows the 8 light settings for one CCT-luminance level. The light settings had similar CCT and similar luminance level.

**Table 1** Eight light settings for one CCT-luminance level

| Luminance(cd/m$^2$) | CCT (K) | Duv | Rf | Rg |
|---|---|---|---|---|
| 93.2 | 5035 | 0.0001 | 75.7 | 90.0 |
| 93.1 | 5117 | −0.0144 | 74.1 | 90.6 |
| 96.7 | 5058 | 0.0001 | 76.8 | 112.2 |
| 94.6 | 5186 | −0.0131 | 76.7 | 112.4 |
| 93.4 | 5050 | 0.0008 | 85.3 | 92.5 |
| 93.6 | 5096 | −0.0099 | 83.0 | 92.9 |
| 96.1 | 5159 | 0.0002 | 83.8 | 112.2 |
| 94.2 | 5098 | −0.0139 | 87.5 | 111.1 |

In total, there were 18 observation sessions (i.e. 6 CCT-luminance levels × 3 attributes). Observer only judged one colour quality percept at the same time, for example, naturalness, colourfulness or preference.

Within one observation session, each observer first adapted to the light source which was set close to the Planckian locus. They were then having 2 min' adaptation. Subsequently, one light source with same CCT-luminance level was presented. After 20 s' adaptation, observers observed the colour appearance of the samples and marked a cross onto the scale at a piece of paper corresponding to a particular judgment. Observers then repeated the above procedures for the other light settings with similar CCT and similar luminance level.

Twenty-five observers took part in the study, including 12 males and 13 females.

## 3   Results

The coefficient of variation (CV) was used to quantify inter-observer variability. It was found that the inter-observer variability results for twenty-five observers ranged from 17 to 35 with a mean value of 25.

The preference results were used to test the performance of the representative individual CQMs, including colour gamut (GAI [19], FCI [20], Rg [21]), colour fidelity (Ra [22], R9 [22], Rf [21]), chroma shift (Rcs,h1 [23]), memory colour index (MCRI) [24] and colour quality scale (Qa) [25]. Note that all the IES TM 30 metrics were calculated using CAM16-UCS [26]. As shown in Fig. 3, MCRI performed the best, followed by the colour gamut metrics (GAI, Rg and FCI), Qa, Rcs,h1 and colour fidelity based metrics the worst (Rf, Ra, R9). This implies that colour preference percept is closer to colour gamut metrics than colour fidelity metrics as also found by many other researchers. However, it can be concluded all metrics did not predict well to the visual data. The highest r value is 0.49.
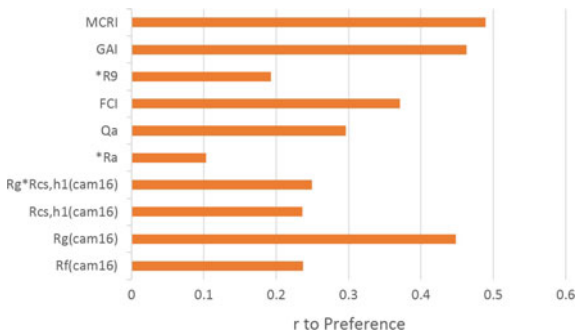


**Fig. 3** Pearson correlation coefficients (r) calculated between the metrics' predictions and the preference results. Negative values were marked with '*'

## 4   Modelling

As mentioned earlier, individual metrics did not predict well. From the other studies such as those by Royer et al. [27] and Wang and Xu [28], they found that to build regression models including some selective individual CQMs. Table 2 shows the correlation coefficients between the preference visual results and the regression CQMs, which are linear combination of colour preference metrics. The results are given in the column named 'R1'. The results clearly showed that the regression models in general performed better than individual CQMs. It can be seen that Ra and GAI, together with the metrics proposed by IES TM 30 also give better performance.

**Table 2** Correlation coefficients r between the visual results and regression CQMs

| Regression model | R1 | R2 |
|---|---|---|
| Rf, Rg, and Rcs,h1 + Rcs,h1$^2$ + Rcs,h1$^3$ | 0.49 | 0.58 |
| Rf and Rcs,h1 + Rcs,h1$^2$ + Rcs,h1$^3$ | 0.41 | 0.55 |
| Rf, Rg, Rcs,h1 and Rg*Rcs,h1 | 0.48 | 0.57 |
| Rcs,h1 + Rcs,h1$^2$ + Rcs,h1$^3$ | 0.39 | 0.44 |
| Ra and FCI | 0.31 | 0.33 |
| Rf and Rg | 0.48 | 0.56 |
| Ra and R9 | 0.28 | 0.35 |
| Ra and GAI | 0.54 | 0.64 |

Since luminance and CCT parameters could have an impact on visual results, Eqs. (1) and (2) proposed by Khanh et al. [2, 29] were integrated to form a new model, i.e. E (luminance) × E(CCT) × regression model. The results are given in 'R2' column in Table 2. It can be seen that there is a large improvement of r values in R2 than R1 column. This indicates that the luminance and CCT light settings do have a large impact to the visual results.

$$E(\text{luminance}) = a_1 + a_2 \bullet \log(\text{luminance} - a_3) \tag{1}$$

$$E(\text{CCT}) = b_1 + b_2 \bullet \text{CCT} + b_3 \bullet \text{CCT}^2 \tag{2}$$

## 5  Conclusions

An experimental dataset including a comprehensive set of viewing parameters was obtained and the results were used to test promising individual CQMs. It was found the colour gamut metrics outperformed colour fidelity metrics. MCRI gave overall best performance. However, when considering the regression models including individual metrics, their performance improved. Further improvement was achieved by integrating the functions to include luminance and CCT. The results seem to imply that a generic regression model including different individual CQMs can be established, for which the coefficients in the model would be different for different applications.

## 6  Compliance with Ethical Standards

**Conflict of Interest:** The authors declare that they have no conflict of interest.
**Ethical approval:** All procedures performed in studies involving human participants were in accordance with the ethical standards of Zhejiang University and national research committee and with the 1964 Helsinki Declaration and its later amendments or comparable ethical standards.
**Informed consent:** Informed consent was obtained from all individual participants included in the study.

# References

1. Khanh TQ, Bodrogi P, Vinh QT, Stojanovic D (2017) Colour preference, naturalness, vividness and colour quality metrics—Part 1: experiments in a real room. Lighting Res and Technol 49:697–713
2. Khanh TQ, Bodrogi P, Guo X et al (2017) Colour preference, naturalness, vividness and colour quality metrics, Part 5: a colour preference experiment at 2000 lx in a real room. Lighting Research and Technology, first published online 20 October
3. Jost-Boissard S, Avouac P, Fontoynont P (2015) Assessing the colour quality of LED sources: naturalness, attractiveness, colourfulness and colour difference. Lighting Res and Technol 47:769–794
4. Durmus D, Davis W (2017) Object color naturalness and attractiveness with spectrally optimized illumination. Opt Express 25:12839–12850
5. Commission Internationale de l'Éclairage (2017) CIE 2017 Color Fidelity Index for accurate scientific use, CIE Publication, 224
6. Islam MS, Dangol R, Hyvärinen M et al (2013) User preferences for LED lighting in terms of light spectrum. Light Res Technol 45:641–665
7. Dangol R, Islam MS, Hyvärinen M et al (2015) User acceptance studies for LED office lighting: preference, naturalness and colourfulness. Light Res Technol 47:36–53
8. IES (Illuminating Engineering Society) (2015) IES method for evaluating light source color rendition, IES TM-30-15
9. Royer MP, Wilkerson A, Wei M (2018) Human perceptions of colour rendition at different chromaticities. Light Res Technol 50:965–994
10. Huang Z, Liu Q, Westland S et al (2018) Light dominates colour preference when correlated colour temperature differs. Light Res Technol 50:995–1012
11. Li H, Luo MR, Liu XY et al (2016) Evaluation of colour appearance in a real lit room. Light Res Technol 48:412–432
12. Bodrogi P, Guo X, Stojanovic D et al (2018) Observer preference for perceived illumination chromaticity. Color Research and Application, Early View
13. Wang Y, Wei M (2018) Preference among light sources with different Duv but similar colour rendition: a pilot study. Lighting Research and Technology 50:1013–1023
14. Wei M, Houser KW (2016) What is the cause of apparent preference for sources with chromaticity below the blackbody Locus? LEUKOS 12:95–99
15. Wei M, Bao W, Huang HP (2018) Consideration of light level in specifying light source color rendition. LEUKOS, published online on 11 May
16. Wei M (2018) Maintaining color preference under different LIGHT Levels. Presented at the 15th China International Forum on Solid State Lighting, Shenzhen, China, 23–25 Oct.
17. Khanh TQ, Bodrogi P, Guo X, et al (2018) Towards a user preference model for interior lighting Part 2: experimental results and modelling. Light Res Technol, published online on December 13
18. Smet KA et al (2017) Study of chromatic adaptation using memory color matches. Opt Express 25(7):8350–8365
19. Rea MS, Freyssinier JP (2008) Color rendering: a tale of two metrics. Color Res Appl 33:192–202
20. Hashimoto K, Yano T, Shimizu M et al (2007) New method for specifying color-rendering properties of light sources based on feeling of contrast. Color Res Appl 32:361–371
21. David A, Fini PT, Houser KW et al (2015) Development of the IES method for evaluating the color rendition of light sources. Opt Express 23:15888–15906

22. Commission Internationale de l'Éclairage (1995) Method of measuring and specifying colour rendering properties of light sources, CIE Publication 13.3-1995. Vienna: CIE
23. Royer MP, Wilkerson A, Wei M et al (2017) Human perceptions of colour rendition vary with average fidelity, average gamut, and gamut shape. Light Res Technol 49:966–991
24. Smet KAG, Ryckaert WR, Pointer MR et al (2012) A memory colour quality metric for white light sources. Energy Build 49:216–225
25. Davis W, Ohno Y (2010) Color quality scale. Opt Eng 49:033602
26. Li C, Li Z, Wang Z et al (2017) Comprehensive color solutions: CAM16, CAT16 and CAM16-UCS. Color Res Appl 42:703–718
27. Royer MP, Wei M, Wilkerson A et al (2019) Experimental validation of colour rendition specification criteria based on ANSI/IES TM-30-18. Light Res Technol
28. Zhang F, Xu H, Feng H (2017) Toward a unified model for predicting color quality of light sources. Appl Opt 56(29):8186
29. Khanh TQ, Bodrogi P, Guo, X et al (2018) Towards a user preference model for interior lighting Part 1: concept of the user preference model and experimental method. Light Res Technol, December 13

# Improved Spectral Reflectance Reconstruction Algorithm Based on Matrix $R$ Method

Xiaojie Hu, Yusheng Lian[(⊠)], Yang Jin, Zixin Lin, Yanxing Liu,
Min Huang, Meng Wang, and Guannan He

Printing and Packaging Institute, Beijing Institute of Graphic Communication,
Beijing, China
`lianyusheng@126.com`

**Abstract.** To solve the problem of information loss in multispectral image color reproduction, a new algorithm for reconstructing spectral reflectance is proposed. Based on the traditional matrix $R$ theory, the improved method is obtained by combing ICA and smoothing pseudo-inverse method. We choose the standard color target Color Checker 24 and IT8.7/4 as training and test samples respectively and design the reconstruction experiment. By calculating the spectrum and chromaticity accuracy of ICA, the traditional matrix $R$ and the proposed method, the effect of the new algorithm is verified. The results show that the improved method's spectrum error and chromaticity error of the training and test color samples are significantly lower than the other two methods. That is, the proposed method improves the spectral information loss of the reconstructed spectrum in the spectral image acquisition system of the multichannel digital camera. It has important significance for solving the problem of mesmerism, and realizing the true color reproduction of the object in the changing observation environment.

**Keywords:** Spectral reflectance reconstruction · Matrix $R$ · ICA ·
Smoothing pseudo-inverse method

Spectral reflectance doesn't change with illuminant, observer and other conditions. It can be used as a stable feature to describe objects' surface color, and applied in the industrial fields such as color reproduction and digital museum [1]. How to effectively reconstruct spectral reflectance of an image is an important research topic on the basis of obtaining the chromaticity value with traditional camera.

The method proposed by MIA Elrifai to reconstruct spectral reflectance is the direct pseudo-inverse method [2]. Based on principal component analysis (PCA) [3], it mainly compress the data information, that is, to reduce the dimension, but the independence of each component can't be guaranteed. Independent component analysis (ICA) achieves dimension reduction based on high order statistics of high dimensional spectra. It is different from PCA in that it doesn't require the source to be Gaussian [4], and the obtained components remain statistically independent [5]. In 2007, $R$ matrix method was developed to reconstruct spectra and it simultaneously achieved better colorimetric performance for a defined illuminant and observer [6, 7]. The advantages

of chromaticity and spectra transformation are combined in the method. Tristimulus values and spectral reflectance were predicted by colorimetric transformation from multi-channel camera signals and by a spectra transformation from the same signals respectively. Then, fundamental stimulus can be obtained from the predicted tristimulus values and the metameric black can be obtained from the estimated spectral reflectance, based on the Wyszecki hypothesis Mesmerism black [6]. They are used together to reconstructed reflectance.

However, the pseudo-inverse method has a low accuracy in calculating the mesmerism black spectrum, and the non-independence of the feature vectors extracted by PCA method makes the decomposition lack of practical significance, thus reducing the typicality of the extracted features. Therefore, the pseudo-inverse and PCA method are not adopted in this paper [8]. We used ICA method to reconstruct the metamerism black spectrum, and smooth matrix is added to improve the traditional matrix $R$ method. The improved algorithm improves the accuracy of reconstruction. Results show that the improved method has higher accuracy in color measurement compared with the traditional matrix $R$ method and ICA method.

# 1 Improved Matrix $R$ Method

After spectroscopic imaging system captures an object, it outputs a multi-channel image associated with the camera's color space [2]. This process can be expressed by Formula (1) where $Q$ is a spectral feature matrix of the system, $G$ is a digital response output of the camera channel of the scene and $R^*$ represents spectral reflectance matrix. Spectral reflectance reconstruction is to estimate the spectral reflectance of the scene in the case of known correlation characteristics and multi-channel images output by the camera, that is, to find the transformation matrix $Q$ of Formula (2), where $Q^+ = (Q^T Q)^{-1} Q^T$ and $Sv$ is reconstructed spectral reflectance matrix.

$$G = QR^* \tag{1}$$

$$Sv = Q^+ G \tag{2}$$

## 1.1 ICA Method and Smooth Inversion Method

ICA is a statistical method of signal processing, which is a generalization of PCA [9, 10]. If the observed signal is represented by $X = (x_1, x_2, x_N)^T$ (a series of discrete spectral reflectance) and the source (independent component) is represented by $S = (s_1, s_2, s_M)^T$, the independent components satisfy the assumption of statistical independence and both have zero mean [4]. Hybrid matrix is represented by $A$, and each column represents a feature. Signal source $S$ is mixed with hybrid matrix $A$ to get mixed signal $X$, then the ICA model can be expressed as Formula (3) [5].

$$X = AS \tag{3}$$

ICA is to find the separation matrix $W = (w_1, w_2, w_M)^T$ so that $Y_i^T = w_i^T X \sim S_i^T$ is the $i$th independent component when only the components of $X$ and $S$ are independent of each other, but $A$ and $S$ are unknown. Then the ICA matrix can be expressed as Formula (4), where $Y = (y_1, y_2, y_M)^T, N \geq M$ ($M$ is the number of independent components) and $S$ contains at most one component subject to a Gaussian distribution.

$$Y = WX \tag{4}$$

The ICA system used in this paper is the Fast ICA system developed by the Information and Computer Science Laboratory of the Helsinki University of Technology (Finland). The algorithm uses a fixed-point algorithm developed by the laboratory. Spectral reflectance can be expressed as Formula (5), where $Y$ is the independent component matrix; $U$ is the transformation matrix.

$$Sv = YU \tag{5}$$

According to equation Formula (4), U can be written as Formula (6), where $Y^+ = (Y^T Y)^{-1} Y^T$.

$$U = Y^+ Sv \tag{6}$$

Substitute Formula (2) into Formula (6) to get Formula (7), and the corresponding output $G'$ is obtained through the shooting of the training color samples set by the camera.

$$U = Y^+ Q^+ G' \tag{7}$$

$U$ can be obtained from the training color samples set, then

$$Q^+ = YUG'^+ \tag{8}$$

Substitute Formula (8) into Formula (2), the spectral reflectance estimate is shown in Formula (9).

$$Sv = YUG'^+ G \tag{9}$$

The smooth inversion method is based on the fact that the spectral reflectance curve is smooth [11]. On the basis of the pseudo-inverse method, a smoothing factor is added, and a regular matrix $M$ is used as a smooth constraint of the spectral characteristics of the system to improve reconstructed spectral reflectance's smoothness. $\varepsilon$ is a small constant and used to correct $M$ (Fig. 1).

$$M = \begin{bmatrix} 1 & -2 & 1 & 0 & \cdots & & & & \\ -2 & 5 & -4 & 1 & 0 & \cdots & & & \\ 1 & -4 & 6 & -4 & 1 & 0 & \cdots & & \\ 0 & 1 & -4 & 6 & -4 & 1 & 0 & \cdots & \\ \cdots & \cdots & \cdots & \cdots & \cdots & \cdots & \cdots & \cdots & \cdots \\ & & & 1 & -4 & 6 & -4 & 1 & \cdots \\ & & & & 1 & -4 & 6 & -4 & 1 \\ & & & & & 1 & -4 & 5 & -2 \\ & & & & & & 1 & -2 & 1 \end{bmatrix} + \varepsilon I$$

**Fig. 1.** The M matrix

## 1.2  Improved Matrix R Method

The workflow of the improved matrix $R$ method is shown in Fig. 2.
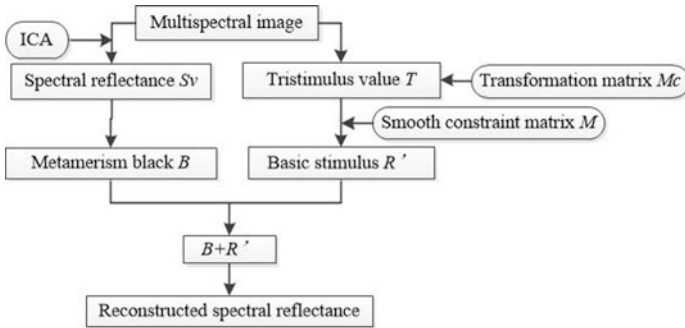


**Fig. 2.** The workflow of the improved matrix R method

The matrix $R$ method [2, 8, 12], which defines the $R$ matrix as: $R = A(A^TA)^{-1}A^T$. $A = kLV$, where $k$ is the color adjustment factor, $L$ is the spectral power distribution of the illumination source, and $V$ is the standard chromaticity observer color matching equation. $A$ is an orthogonal projection factor. Decompose the spectral reflectance $S$ by the matrix $R$ to the basic stimulus $R'$, then $R' = RSv$. $Sv$ and the $T$ satisfy $T = A^TSv$. After added matrix $M$, $R'$ can be written as Formula (10).

$$R' = M^{-1}A(A^TM^{-1}A)^{-1}T \tag{10}$$

$T = McG$, $G$ is the response value in the multi-spectral imaging system, then the basic stimulus $R'$ can be calculated. The metamerism black $B$ is the difference between $S$ and $R'$ is as shown in Formula (11).

$$B = Sv - R' = (I - R)Sv \qquad (11)$$

The spectral reflectance $Sv$ can be obtained by the ICA method. So the reconstructed spectral reflectance is as shown in Formula (12).

$$Sv' = B + R' \qquad (12)$$

## 2   Experiment and Results

To verify the effectiveness of the algorithm, the spectral reflectance and tristimulus values of the standard color target IT8.7/4 were measured using an Eye One-Is is spectrophotometer. The Sony camera acquired the three-channel response values, with a total of 1617 color samples. The wavelength range is 380–730 nm at 10 nm intervals; the corresponding tristimulus value data is measured under the illumination D65 and the standard observer CIE 1931 standard observer function. We selected Color Checker 24 as the training color samples (TCS) set, and standard color samples target IT8.7/4 including 1617 color blocks as the TCS set. The transformation matrices $Q^+$ and $Mc$ can be calculated from TCS data. The reconstruction accuracy of improved method, traditional matrix $R$ method and ICA method was analyzed and compared.
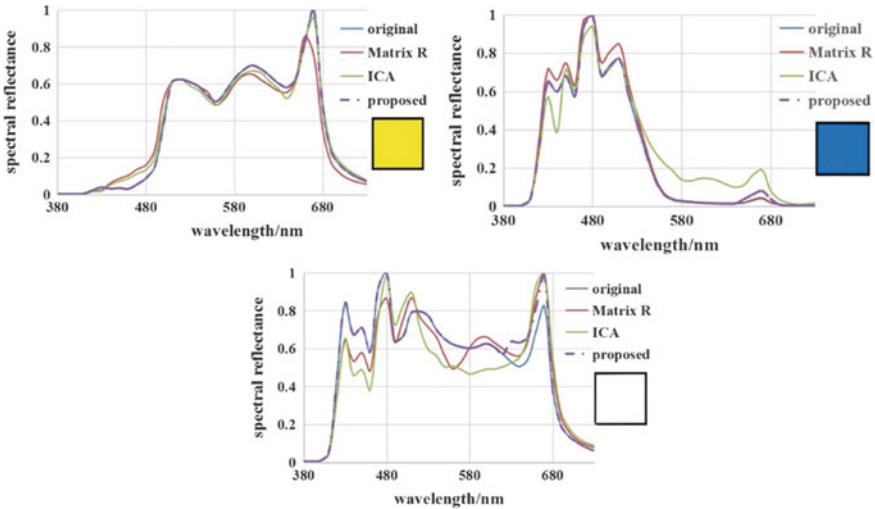


**Fig. 3.** Partial color blocks' reconstruction spectral reflectance in TCS

Part of the TCS' reconstruction spectrum curve is shown in Fig. 3. The three colors are Yellow, Cyan and White as shown in the color block below the legend. These color blocks contain three primary colors red, green and blue.

**Table 1.** Comparison of spectral reflectance reconstruction in terms of *RMES* and $DE_{a*b*}$

| Method | *RMSE* | | | $DE_{a*b*}$ | | |
|---|---|---|---|---|---|---|
| | Min | Max | Mean | Min | Max | Mean |
| ICA | 0.0033 | 0.5635 | 0.1674 | 0.3724 | 2.1427 | 1.7724 |
| Matrix *R* | 0.0031 | 0.6322 | 0.1647 | 0.3715 | 2.2568 | 1.5682 |
| proposed | 0.0029 | 0.6287 | 0.1507 | 0.3670 | 2.0013 | 0.8550 |

In Fig. 3, TCS's spectral reflectance curve (green curve) reconstructed by ICA method has the lowest fitting degree with the original curve. It is higher in the long wavelength and there is no fixed trend in the blue-green band. For matrix *R* method (red curve), it fits better than ICA, but it's also not ideal in the blue-green band. The figure clearly illustrates that the spectrum reconstructed by the proposed method is the closest to the original spectrum, though the reconstructed curve is slightly higher around 670 nm. Overall, matrix *R* method is better than ICA. Next, reconstruction accuracy of the three methods is quantitatively analyzed by test samples through CIE94 $DE_{a*b*}$ [13] and *RMSE* [14] (Table 1).

Compared with ICA and traditional matrix *R* method, *RMSE'* mean value of m the proposed method is reduced by 0.0167 and 0.014 respectively, and the maximum and minimum values also slightly reduce. Matrix *R* method is better than ICA for its mean and minimum values of *RMSE* are smaller than ICA. The CIE94 $DE_{a*b*}$ statistics of the three methods are relatively small. The maximum value is also smaller than the human eye recognition threshold (i.e., less than 3 color difference units) indicating that the reconstructed spectral reflectance's color accuracy can be tolerated in human vision. Besides, the proposed method is the lowest of the three methods in terms of maximum, minimum and mean values and the algorithm also has obvious advantages in color reproduction.

## 3 Conclusions

Based on the traditional matrix *R* spectral reconstruction method, the metamerism black spectrum is obtained by ICA, and the smooth matrix is added to calculate the basic color stimulation, then the improved matrix *R* method is obtained. After the spectrum reconstruction algorithm was trained by Color Checker 24 which contains 24 color samples, the transformation matrix used to reconstruct spectral reflectance from the response values is obtained. We took the standard color target IT8.7/4 which contains 1617 color blocks as the test color samples set and reconstructed the spectrum of it. The reconstruction accuracy were evaluated from the *RMSE* and CIE94 $DE_{a*b*}$. Compared with ICA and the traditional matrix *R* method, the *RMSE'* mean value of the proposed method is 0.1507, it reduced by 0.0167 and 0.014 respectively. Its mean chromaticity accuracy CIE94 $DE_{a*b}$ is 0.8850, and the maximum value is only 2.0013. Whether it is maximum, minimum or mean value, it is improved over the other two methods. The results show that the spectral accuracy and chromaticity accuracy of the reconstruction are better than the traditional matrix *R* method and ICA method.

# References

1. Xie DH, Wang XX, Liu Q, Zhu WF (2016) Research on tristimulus reconstruction spectrum method based on iterative tikhonov normalization. Spectrosc Spectr Anal 36(1):201–205
2. Wang Y (2010) A study of key technologies in multispectral image color reproduction. XiDian University
3. Zabalza J, Ren JC, Liu Z, Marshall S (2014) Structured covariance principal component analysis for real-time onsite feature extraction and dimensionality reduction in hyper spectral imaging. Appl Opt 53(20):4440–4449
4. Zhang XY, Yang WP, Zhou HT et al (2007) Muti-spectral reconstruction based on the method of independent component analysis (ICA). Opt Tech 33(3):390–394
5. Wang YF, Tang ZN (2014) Dimensional reduction methodbased on combination of PCA and ICA. Opt Tech 40(2):180–183
6. Zhao YH, Berms RS (2007) Image based spectral reflectance reconstruction using Matrix R method. Color Res Appl 32(5):343–351
7. He SH, Liu Z, Chen Q (2014) Research of spectral dimension reduction method based on matrix R theory. Acta Opt Sin 34(2):325–333
8. Zhang CE, Han F, Gao T, et al (2018) The improved spectral reflectance reconstruction algorithm based on matrix R method. Light Ind Sci Technol 34(7):73–75+88
9. Asif K, Intaek K (2008) Sparse kernel independent component analysis for blind source separation. J Opt Soc Korea 12(3):121–125
10. Min W, Zhang Y, Cheng JL, Zhou JL (2010) Stability and chaos analysis for an ICA algorithm. Comput Math Appl 60(6):1810–1827
11. Pratt W, Mancill C (1976) Spectral estimation techniques for the spectral calibration of a color image scanner. Appl Opt 15(1):73–75
12. Wang K, Wang HQ, Wang Z, Zhang Y, Yin Y (2018) Spectral reflectance reconstruction based on improved matrix R method. Chin J Liquid Cryst Disp 33(4):338–346
13. Wang HZ (2009) Study of color vision discrimination characteristics and color-difference evaluation. Zhejiang University
14. Yang P (2009) Study of approaches to spectral reflectance reconstruction based on digital camera 29(5):1176–1180

# Research on Colour Visual Preference of Light Source for Black and White Objects

Wei Chen[1], Zheng Huang[1], Lianjiang Rao[2], Zhen Hou[1], and Qiang Liu[1(✉)]

[1] School of Printing and Packaging, Wuhan University, Wuhan, China
liuqiang@whu.edu.cn
[2] WAC Lighting, Shanghai, China

**Abstract.** Many studies now use coloured objects when discussing lighting colour preference, but rarely involve black and white objects. In this study, nine CCTs were adopted to illuminate three groups of black and white objects (a group of black and white birds, a group of black and white statues and four black and white photographs). Thirty observers, 16 males and 14 females, were invited to give their visual preference for experimental black and white objects, and to judge whether they prefer black bird/statue or white bird/statue. The results show that light dominates colour preference and black and white objects have no significant effect on the preference. And the three-dimensional objects can strengthen the conclusion that light dominates preference compared with two-dimensional objects. In research about preferring black or white objects, there are no difference of lighting, as well as gender difference. The difference of objectdoes not exist in black and white bird experiment but exist in black and white statue experiment.

**Keywords:** Black and white objects · Visual preference · Correlated colour temperature

## 1 Introduction

Colour preference of lighting is one of the most important topics in current field of lighting application since the overall colour quality may have a close relationship with human visual appreciation of the lit scene [1, 2], and many studies discuss its influencing factors and quantitative characterization methods. Coloured objects are always used in many researches [3–6], but the effects of black and white objects are not discussed. Therefore, this work studies the effects of black and white objects on visual preference at different correlated colour temperatures (CCTs).

## 2 Experimental Method

### 2.1 Experimental Setup

All experiments were carried out in a standard light booth lightCube in the darkroom, with the inner wall of the light booth being coated with medium-grey matt paint. The

lights used in the experiment were generated by LEDCube. The light source has 9 CCTs (2500–6500 K, 500 K interval), and the illuminance is 200 lx. The spectral power distributions (SPDs) for the light sources measured by an X-Rite i1 Pro 2 spectrophotometer are shown in Fig. 1.
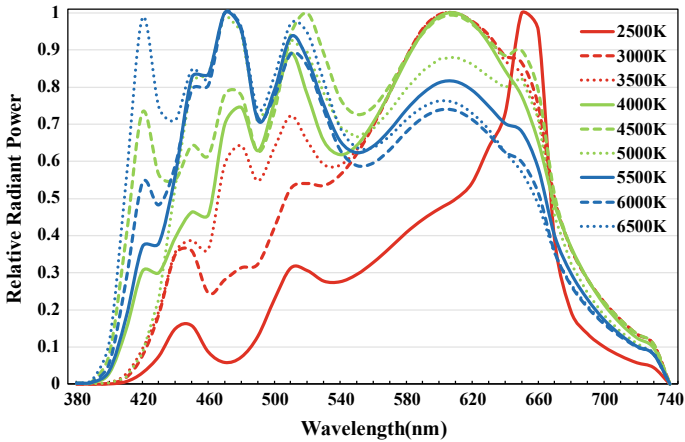


**Fig. 1.** Relative spectral power distributions of experimental light source

## 2.2    Experimental Design

The experimental objects are a group of black and white statues, a group of black and white birds and four photographs (reproductions), as shown in Fig. 2.
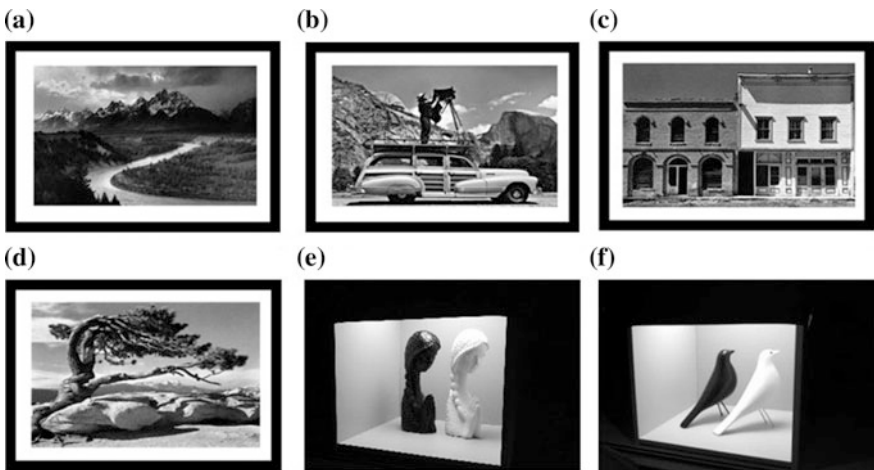


**Fig. 2.** Different objects adopted in the psychophysical experiment. **a–d** Black and white photographs, **e** black and white statues, **f** black and white birds

Thirty observers (fourteen females and sixteen males) participated in the visual experiment. All of them are students of Wuhan University and their ages range from 18 to 38, with a mean of 22.63 years. All the observers passed the Ishihara Colour Vision Test while none of them was informed of the research intent in advance.

The experiment used two evaluation scales, whiteness evaluation and preference evaluation. Whiteness evaluation: the participants were asked to respond with $-3$, $-2$, $-1$, 0, 1, 2, 3, respectively denoting strongly not white, moderately not white, slightly not white, unable to determine, slightly white, moderately white and strongly white. Preference evaluation: the participants were asked to respond with $-3$, $-2$, $-1$, 0, 1, 2, 3, respectively denoting strongly dislike, moderately dislike, slightly dislike, neutral, slightly like, moderately like and strongly like.

## 2.3   Experimental Procedure

Upon arrival, the participant was asked to sign a consent form and carry out the Ishihara Test. Then, the experimenter asked the observer to put on a grey coat so that there would be no colour light reflected from his/her coloured clothes onto the test object.

When the observer sat in front of the light booth to adjust the height of the chair and adapt to the darkroom environment, the experimenter introduced the experiment to the observer. The order of the nine CCTs was random in the experiment.

At the very beginning, using a randomly selected CCT, the observer was asked to give whiteness evaluation of the empty light booth, and then preference evaluation. The CCT was then changed and the above steps were repeated until all nine CCTs were evaluated. Next, the experiment of black and white statues, black and white birds, and four black and white photographs (one at a time) was conducted. Additionally, in the black and white statue experiment, observers were asked to judge whether they prefer white statue or black statue. The same is true of the black and white bird experiment.

# 3   Result and Discussion

## 3.1   Effects of Object Characteristics on Preference

The average preference ratings of black and white objects are shown in Fig. 3. And the standard deviation of preference ratings is shown in Fig. 4.

The three-dimensional objects in the experimental objects are black and white statues and black and white birds. The two-dimensional objects are four black and white photographs.

As can be seen from Fig. 3, the observers prefer the two-dimensional objects at low CCTs and prefer the three-dimensional objects at high CCTs (more obvious from the average values). The reason for this phenomenon may be that a three-dimensional object has one more dimension than a two-dimensional object, which allows the three-dimensional object to transmit more light information to the observers through different angles (multi-dimension) reflection. Therefore, the observers are more susceptible to the influence of the light source when rating the three-dimensional objects. That is, the
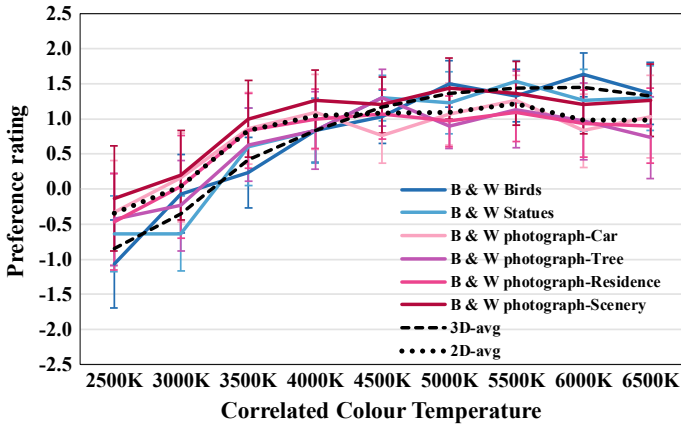
**Fig. 3.** Average colour preference ratings of black and white objects with regard to different CCTs. The error bars are 95% confidence intervals
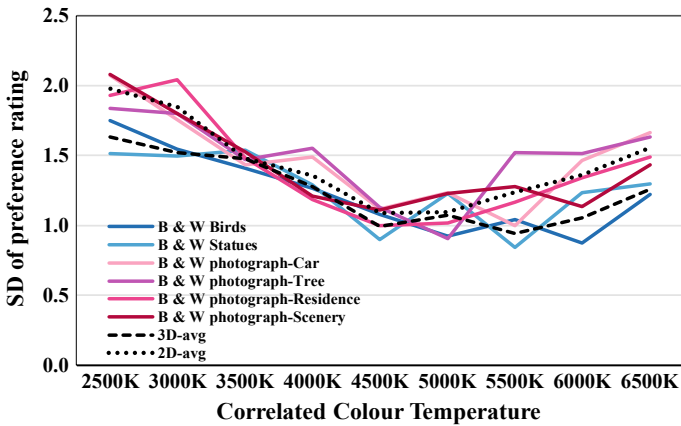


**Fig. 4.** Standard deviation of ratings of black and white objects with regard to different CCTs

three-dimensional objects strengthen the conclusion that light dominates preference when CCT differs [7, 8]. Low CCTs are generally unpopular while high CCTs are preferred. This coincides with the fact that the three-dimensional objects score lower at low CCTs while score higher at high CCTs than the two-dimensional objects.

It can be seen from Fig. 4 that at all CCTs, the standard deviations of the ratings of the three-dimensional objects are smaller than those of the two-dimensional objects. That is, the observers are more likely to give an accurate evaluation of the three-dimensional objects. The reason for this phenomenon may be that the three-dimensional object has one more dimension than the two-dimensional object, so more object information can be transmitted to the observers. The more accurately the observer knows about an object, the more likely it is to make an extreme judgment and

the less likely it is to have a medium preference rating [7]. Therefore, the standard deviations of three-dimensional objects are lower than those of two-dimensional objects.

From the ratings of three-dimensional objects in Fig. 3, first it can be seen from each light source that the ratings of black and white birds and black and white statues are similar at nine CCTs, indicating that the difference between the two types of objects has no significant effect on the preference ratings. Secondly, from the perspective of scoring trend, the ratings of black and white birds and black and white statues both increase rapidly from 2500 to 4500 K and flatten from 5000 to 6500 K with slight fluctuations, indicating that light dominates preference when CCT differs [7]. In general, the three-dimensional objects have no significant effect on the preference ratings and the light dominates colour preference.

From the ratings of two-dimensional objects in Fig. 3, first of all, it can be clearly seen from each light source that the object "B & W photography—Scenery" scores the highest at almost CCTs. The possible reason is that the content of the photograph has an impact on the preference. Observers prefer scenes with spatial levels. The "Scenery" has a longer visual extension and a better layering, giving people a feeling of variety, so observers prefer it. Secondly, from the perspective of scoring trend, the ratings of black and white photographs increase rapidly from 2500 to 4000 K and flatten from 4500 to 6500 K with slight fluctuations. Due to the dominant effect of light, the influence of two-dimensional objects on the preference is not significant.

## 3.2   Preference Analysis of Selecting Black or White Objects

The number of people who prefer black objects or white objects is shown in Fig. 5. For black and white birds, the number of people who prefer black bird can be regard as equal to that who prefer white bird at different CCTs. There are no difference of object and lighting. In addition, among the observers who like black bird or white bird, the number of men and women is almost the same. That is, there is no gender difference. The effects of light and gender on preferring black bird or white bird were tested by RM-ANOVA. The p values were both greater than 0.05, indicating no significant effects. The influence of the object was measured by t test, and the Significance value p was also greater than 0.05.

For black and white statues, the white statue is always preferred by more observers than black statue at different CCTs. There is no difference of lighting but exist difference of object. Meanwhile, among observers who prefer white statue or black statue, the difference between the number of men and women is not great. That is, there is no gender difference. The $p$ values of light and gender were both greater than 0.05 while the p value of object is much less than 0.05, which proves the above conclusion.

The reason for this may be that black bird and white bird are both common to people so that they are equally liked. But for black and white statues, the white statue resembles plaster statue, which is more common than the black statue, so people will prefer familiar white statue [7]. In addition, the black statue reflects less light, so the details and stereoscopic effect of the face are worse than the white statue.
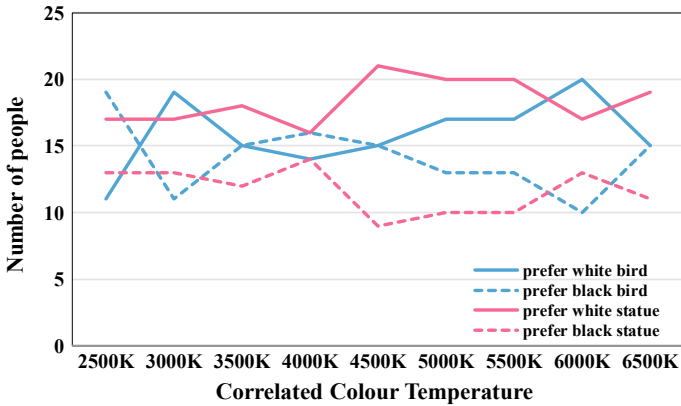
**Fig. 5.** Number of people who prefer black objects or white objects

### 3.3 Contrastive Analysis of Black and White Objects and Coloured Objects

The coloured objects used in the experiments of multiple CCTs and 200 lx illuminance in our former work [7, 9] are shown in Fig. 6 (left). It should be noted that the experimental light sources used for the coloured objects (hue 9 LEDs) are 2500–6500 K, but the SPDs are different from those used for black and white objects. Although the experimental light sources are different, the scoring trend is consistent.
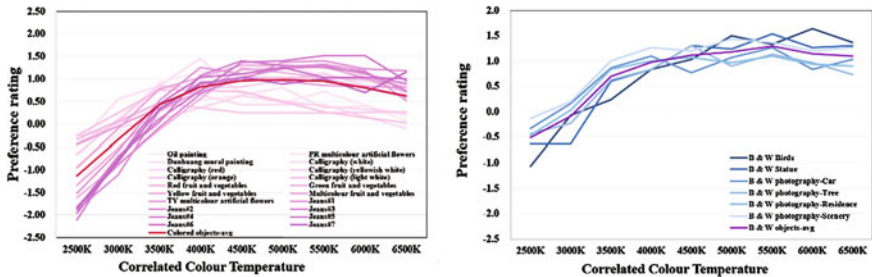


**Fig. 6.** Preference ratings of coloured objects (left) and black and white objects (right)

It can be seen from Fig. 6 that the conclusion of light dominating preference when CCT differs [7] is still valid for both black and white objects and coloured objects. Meanwhile, the black and white objects and the coloured objects have similar rating trends. It can be said that there is little difference in the perception of preference between black and white objects and coloured objects in multiple CCTs. This may be due to the fact that the influence of light is so great that the objects with or without colour have less effect on preference.

## 4 Conclusions

This paper studies the effects of black and white objects on colour preference. The results indicate that since the three-dimensional objects transmit more object information and light information than two-dimensional objects, the standard deviations of ratings of three-dimensional objects are lower than those of two-dimensional objects at any CCT. And the three-dimensional objects score lower at low CCT and score higher at high CCT. That is, the observer's subjective judgment is more significant. In addition, the influences of three-dimensional objects and two-dimensional objects on preference ratings are not significant due to light dominating colour preference. Based on the individual preference analysis of black and white objects, for the black and white bird experiment, the number of people who like white bird is about the same as that who like black bird. There are no differences of object and lighting, as well as gender difference. When it comes to black and white statues, more people prefer the white statue to the black statue at different CCTs. There is difference of object but no difference of lighting and gender. Comparing the black and white object experiments with the previously performed coloured object experiments, the results show that at the multiple CCTs, there is little difference in people's preference perception between black and white objects and coloured objects.

## References

1. Islam MS, Dangol R, Hyvärinen M et al (2013) User preferences for LED lighting in terms of light spectrum. Light Res Technol 45:641–665
2. Lin Y, Wei M, Smet KAG et al (2017) Colour preference varies with lighting application. Light Res Technol 49:316–328
3. Tang Y, Lu D, Xun YJ, et al (2018) The influence of individual color preference on LED lighting preference. Lecture notes in electrical engineering, vol 477, pp 77–87
4. Khanh TQ, Bodrogi P, Vinh QT et al (2018) Colour preference, naturalness, vividness and colour quality metrics, Part 4: Experiments with still life arrangements at different correlated colour temperatures. Light Res Technol 50(6):862–879
5. Narendran N, Deng L (2002) Color rendering properties of LED light sources. In: Proceedings of SPIE—The International Society for Optical Engineering. https://doi.org/10.1117/12.452574

6. Feltrin F, Leccese F, Hanselaer P, et al (2017) Analysis of painted artworks' color appearance under various lighting settings. In: 2017 17th IEEE international conference on environment and electrical engineering and 2017 1st IEEE industrial and commercial power systems Europe. https://doi.org/10.1109/eeeic.2017.7977574
7. Huang Z, Liu Q, Westland S et al (2018) Light dominates colour preference when correlated colour temperature differs. Light Res. Technol 50(7):995–1012
8. Liu Q, Huang Z, Pointer MR et al (2018) Evaluating colour preference of lighting with an empty light booth. Light Res. Technol 50(8):1249–1256
9. Huang Z, Liu Q, Liu Y et al (2018) Best lighting for jeans, part 1: optimising colour preference and colour discrimination with multiple correlated colour temperatures. Light Res. Technol. https://doi.org/10.1177/1477153518816125

# Research on Color Vision Anomaly Under Light Source of Color LEDs

Pengfei Wang[1(✉)], Yawen Li[2], and Haiwen Wang[3]

[1] College of Software Technology, Zhejiang University, Hangzhou, China
noah-wang@foxmail.com
[2] Pan Tianshou Academy of Architecture Arts and Design, Ningbo University, Ningbo, China
[3] College of Teacher Education, Quzhou University, Quzhou, China

**Abstract.** Under light sources with different spectral composition, human eye has different visual perceptions of colors, which has a great impact on high fidelity reproduction of colors under special environmental conditions. To explore effects of different common color LEDs on color perception of human eye, we conducted a color identification experiment by using 4 common color light-emitting diodes as a light source. CIEDE2000 was used to calculate color difference between color perceived by human eye under color LED light source and standard light source. Also, subjective evaluation of color perception difference was given by experiment participants. The results show that the color difference between yellow and green LED sources and standard light source is generally smaller than that of the red and blue LED sources. And this difference is not constant, it will decrease as observation time increases. The study of human visual characteristics under different color LED sources provides a theoretical supplement for high-fidelity reproduction of images under special spectral light sources.

**Keywords:** Color LED light source · Color reproduction · Color vision · Special spectral light source

## 1 Introduction

Current researches on color discrimination ability can be divided into two categories: study of illuminants characteristics and physiological characteristics. According to the first type of researches, as color temperature is lower than 6500 K, the tester's color discrimination ability increases with LED color temperature and becomes the strongest at 5000 K [1, 2]. According to Bezold-Brücke effect, relationship between color seen by human eye and the actual wavelength is not constant, but changes as illuminance changes [3]. As illuminance increases, ability to distinguish colors of human eye is enhanced [4]. Holter et al. found visual function can adapt to illuminants, and expression of visual proteins become different [5]. Hu et al. found monochromatic light

changes the visual cells of guinea pigs to adapt to environment [6]. Toshihiko found main spectrum of white LED is blue light which is easy to damage color discrimination ability [7].

However, there is a lack of research in context of color LED illuminants. Therefore, experiments are designed to reveal and quantify color vision anomalies under color LED illuminants. This effect may give a glance to understand human vision differently. In reality, it is necessary to identify and quantify these effects to guide lighting engineering and safety design of cinemas, bars, darkroom, etc. Difference in color perception can be calculated by CIEDE2000 formula [8].

## 2    Metamerism and Quantization Method

The problem to be discussed in this paper is effects of special spectral illuminants on color perception of human eye and law of color perception variation in this environment. Therefore, when variables controlled, color under colored LED is matched to the closest color on standard display by human eye. Then record its Lab value. Control group repeated above steps under standard illuminant. Quantized color difference can be obtained by calculating Lab value by CIEDE2000 between experimental and control group. Give conclusions by explaining the processed data. Also, observer's subjective evaluation was used as an important supplement.

Samples of same wavelength have different color appearances under different environmental conditions. This phenomenon is called metamerism. In addition, different color appearances caused by different characteristic of different observers are also called metamerism. Quantitative analysis of the difference in color appearance under different conditions can calculate the size of the metamerism phenomenon [9]. David et al. believe that the quantitative discrimination of quantitative observers should focus on comparing the difference between the observer's final perceived and perceived object wavelengths, rather than their absolute differences [10]. Therefore, the size of the observer's metamerism is adopted in this experiment, as Formula (1).

$$OM = \max \overline{(\Delta E_{y,P_j})} \tag{1}$$

Among them, $\Delta E_{y,P_j}$ represents the difference between the color perceived by the $i$-th observer in the experiment and standard color, y represents calculation method of color difference, the CIEDE2000 color difference calculation method is generally used to quantify color difference. The maximum value of the average value of the color difference is obtained in a total of P experiments. CIEDE2000 formula is as (2) [8].

$$\Delta E_{00} = \sqrt{\left(\frac{\Delta L'}{K_L S'_L}\right)^2 + \left(\frac{\Delta C'}{K_C S'_C}\right)^2 + \left(\frac{\Delta H'}{K_H S'_H}\right)^2 + R_T \left(\frac{\Delta C'}{K_C S'_C}\right)\left(\frac{\Delta H'}{K_H S'_H}\right)} \tag{2}$$

# 3 Color Discrimination Experiment Under Color LED

## 3.1 Experiment Condition and Procedure

Color samples are extracted in sections from visible light. In order to ensure that the experiment has a certain representativeness, wavelength is randomly extracted from region of 380–420, 430–450, 450–470, 480–500, 520–560, 550–600, 600–620, 630–640, and 660–780 nm. And, research is aimed at human eye's perceived color anomaly and pay attention to objective difference. So, colors which are perceived differently were added in. Common color LEDs were chosen to simulate daily situation. The luminous flux of deployed red, blue, yellow and green LEDs are 73, 134, 563 and 527 lm.

Sixteen normal color-conscious young subjects were organized to conduct experiments. Among them, each observation subject completed at least a blank control experiment and four experimental group experiments. In addition, 25% of the subjects were assigned to repeat the experiment, and the repeated experiments needed to performed the control group and 2 random experimental groups 2–4 times. Average color Lab value was recorded. This experiment was carried out 116 times. The specific information of the observed subject are shown in the Table 1.

**Table 1.** Summary of specific characteristics data of the experimental

| Experiment name | Percentage of male (%) | Age scope | Number of experiments |
|---|---|---|---|
| Blank | 53.6 | 20–23 | 28 |
| Ex(R) | 52.4 | 20–23 | 21 |
| Ex(B) | 53.3 | 20–23 | 26 |
| Ex(Y) | 48.1 | 20–23 | 21 |
| Ex(G) | 57.7 | 20–23 | 20 |

Specific experiment process is as follows.

(1) Print out the color sample as Fig. 1. Then, place it under standard light source and common color LEDs. Color appearance is shown in Fig. 2.
(2) Match color perceived by human eyes under color LEDs to the most similar one shown in standard display in standard observation box.
(3) Record Lab value of color shown in standard displays.

## 3.2 Data Processing

Substituting the Lab value obtained by observer's match into Formula (2), we quantified the color difference of human eye perception between color LEDs and standard light source. Substituting the data calculated by Formula (2) into Formula (1) to obtain the metachromatic size. Then, draw a polyline chart by the data calculated by Formula (1), as shown in Fig. 3.

**Fig. 1.** Segmentally randomly selected color sample
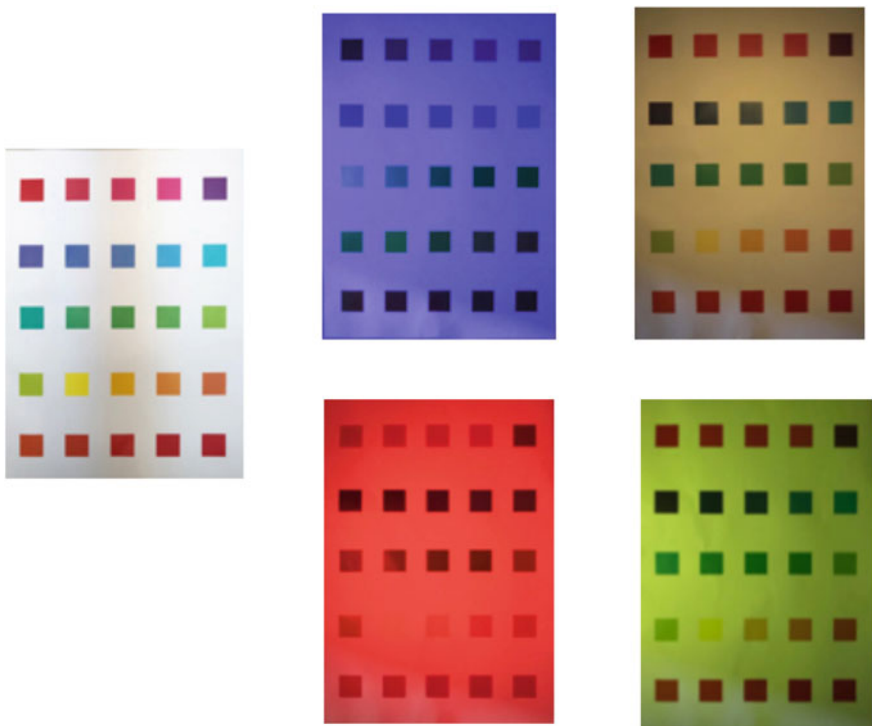


**Fig. 2.** Color appearance of sample in the environment of standard illuminant and color LEDs

At the end of this experiment, observers subjectively evaluate perceived color difference. 13 observers supposed the color difference under yellow and green LED light source is lower than the red and blue one. They also affirmed that the perceived illuminance and color difference is smaller than absolute difference measured by color density meter. This situation is even more pronounced after a period of observation.
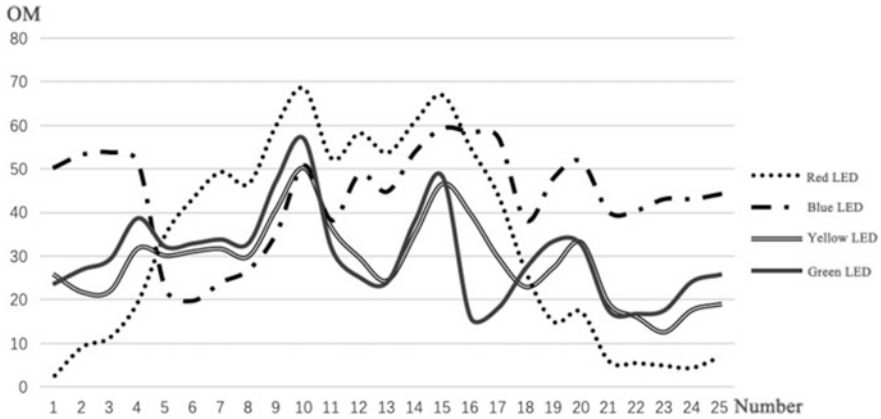
**Fig. 3.** OM between perceived color under LED standard illuminants

That is, the color vision anomaly generated under the condition of the special spectral light source gradually decreases as the observation time increases.

## 4   Conclusions

After introducing factors that influence color discrimination ability of human eyes, analysing current research conclusions, and proposing a new factors which is special spectral illuminants. Therefore, this study designed a color matching experiment, CIEDE2000 formula and the OM formula were used, under common color LED and simulated conditions of color anomaly of human eye in a special lighting environment to quantify the size of color difference. At the end, explains were given to identify variation of this difference.

According to processed data supplemented by the subjective evaluation of the observers, following main conclusions are drawn:

(1)  Compared with the red and blue LED spectral light sources, human eyes are easier to distinguish color under yellow and green ones, colors are better reproduced.
(2)  Under the special spectral light source, human eye will produce color vision abnormalities. However, this color vision anomaly is not constant, but gradually decreases as the observation time increases. The human eye will constantly change with the environment to adapt to spectrum change.

In experimental design, only a few common color LEDs were selected. Comprehensive effects of illuminance and color temperature of special spectral light sources were not studied. Also, the change of color vision anomaly with time is not quantitatively analyzed under special spectral light source. Therefore, there is still room for research on visual variability mechanism of human eye color in special spectral source, and medical and biological mechanism of it needs to be researched.

# References

1. Pardo PJ, Cordero EM, Suero MI, Pérez ÁL (2012) Influence of the correlated color temperature of a light source on the color discrimination capacity of the observer. J Opt Soc Am A Opt Image Sci Vis 29(2):209–215
2. Pardo PJ, Suero MI et al (2014) Optimization of the correlated color temperature of a light source for a better color discrimination. J Opt Soc Am A 31(4):A121
3. Walraven PL (1961) On the bezold-brücke phenomenon. J Opt Soc Am A 51(10): 1113–1116
4. Shimomura K, Saunders F, Kusuda M et al (2012) Effects of color and illuminance level on the legibility of colored letters for older people. J Color Sci Assoc Jpn 36:15–26
5. Hölter P, Kunst S, Wolloscheck T et al (2012) The retinal clock drives the expression of kcnv2, a channel essential for visual function and cone survival. Invest Ophthalmol Vis Sci 53(11):6947–6954
6. Hu M, Hu Z, Xue L et al (2011) Guinea pigs reared in a monochromatic environment exhibit changes in cone density and opsin expression. Exp Eye Res 93(6):804–809
7. Uedaabbac T (2009) Eye damage control by reduced blue illumination. Exp Eye Res 89 (6):863–868
8. Li C, Luo MR (2017) Revisiting the weighting function for lightness in the ciede2000 colour-difference formula. Color Technol 133(4):273–282
9. Akbarinia A, Gegenfurtner KR (2018) Color metamerism and the structure of illuminant space. J Opt Soc Am A: 35(4):B231
10. Long DL, Fairchild MD (2014) Modeling observer variability and metamerism failure in electronic color displays. J Imag Sci Technol 58(3):30402-1–30402-14(14)

# An Analysis of the Influence of Measurement Illuminant Conditions on the Printing Color Appearance

Yanfang Xu$^{(\boxtimes)}$, Zengyun Yan, Biqian Zhang, and Xiu Li

Beijing Institute of Graphic Communication, Beijing, China
`xuyanfang63@l63.com`

**Abstract.** There are four different light source conditions of M0, M1, M2 and M3 in the current spectrophotometer, the previous printing color test mainly uses the M0 measurement condition corresponding to illuminant A. In order to explore the suitable color measurement conditions for printing with fluorescent brightener substrate, this article is based on CMC(l:c) color difference, comparing the consistency between M1 and M0 source conditions and visual perception color difference for blue, magenta, yellow, red, green and blue and other representative color prints through subjective evaluation experiments. The results show that the CMC(2:1) color difference of M0 chromaticity does not conform to the visual color difference for the coated paper and the standard observation condition of illuminant D50 commonly used in the printing industry, while the compliance of CMC(2:1) color difference of the M1 chromaticity with visual perception is 67%, which is above the CIEDE2000 color difference with 46% and CIE $L^*a^*b^*$ color difference with 28% on M1 condition.

**Keywords:** M0 and M1 chromaticity · Color difference · Subjective evaluation · Compliance

## 1 Introduction

In the printing industry, the M0 color measurement condition does not define the amount of ultraviolet light. In order to reasonably measure the chromaticity value of the fluorescent brightening agent prints, the spectral power distribution of the illumination source should match the CIE illuminant D50, which is called M1 condition [1].

In this paper, the applicability of the color difference index of the spot color used in the printing of the milk carton of Yili Company in China is analyzed. The degree of conformity of color difference and visual color difference in M0 and M1 condition is analyzed to clarify the reasonable choice of M measurement conditions in industrial.

In the experiment, 17 spot colors commonly used in the milk carton of Yili Company were selected as the research object. By making a plurality of color sample groups with different color difference from the spot color standard and multiple levels of color difference, the numerical values of the color difference of M0 and M1 and the difference in visual difference are used to analyze the degree of conformity of different M conditions and different color difference.

## 2   Color Samples Production

### 2.1   Production Method

The experiment uses color management technology to print out the color samples [1]. The methods and steps are as follows:

Step 1: Create a printer color profile.

Step 2: Make color samples with the same color difference of the standard color. According to the CIE $L^*a^*b^*$ color chromaticity value of the standard sample, the color sample with a certain color difference range is changed with brightness, saturation and hue, and a printable RGB value is formed.
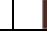
Step 3: Making a square patch RGB image of a certain size and Printing out.

### 2.2   Production of Color Samples

The Epson Style 7908 printer and 210g coated paper were selected as the printing device and material. And the output profile was created by using software X-rite Monaca.

Thereafter, the 17 spot color's CIE $L^*a^*b^*$ chromaticity in M0 condition of the milk carton of Yili Company commonly used as the standard samples were measured. The color map of the CIE $L^*a^*b^*$ chromaticity values in the printer gamut is shown in Table 1.

**Table 1.** The selected seventeen standard sample colors

| No. | 1 | 2 | 3 | 4 | 5 | 6 | 7 | 8 | 9 |
|---|---|---|---|---|---|---|---|---|---|
| Color | | | | | | | | | |
| No. | 10 | 11 | 12 | 13 | 14 | 15 | 16 | 17 | |
| Color | | | | | | | | | |

Then, for each color samples, its CIE $L^*a^*b^*$ value is converted to RGB value using the printer profile. Next, generate a plurality of RGB values around the seventeen definite RGB values, and use the printer profile to convert them into CIE $L^*a^*b^*$ value, then calculate the CIE $L^*a^*b^*$ color difference with the standard. Finally, a certain color difference range is set, and CIE $L^*a^*b^*$ and RGB within the range are extracted as color samples having a certain color difference from the standard. There were $0 \sim 0.6$, $1.00 \sim 1.05$, $1.50 \sim 1.55$, $2.00 \sim 2.05$, $2.50 \sim 2.55$ and $3.00 \sim 3.05$ and other segmented $\Delta E_{ab}^*$ color samples selected, and $200 \sim 300$ color samples corresponding to each standard sample were selected.

Finally, the selected RGB value of the color samples are printed as a square patch image with a side length of 5 cm as shown in Fig. 1.

**Fig. 1.** Printed samples

## 3 Color Sample Grouping and Color Difference Evaluation

### 3.1 Chroma Measurement and Grouping

The CIE chromaticity values under the circumstances of the M0 and M1 conditions, the D50 illuminant, and the 10° viewing angle were measured with the i1Pro spectrophotometer for each of 17 color's 200–300 color samples.

Since the color difference of CIEDE94 has been abolished [2], three common color difference of CIEDE2000, CIECMC and CIE $L^*a^*b^*$ are selected, which are respectively recorded as $\Delta E_{00}$, CMC(l:c) and $\Delta E_{ab}^*$ It has been given by theory [2] that the CMC(l:c) color difference parameter is suitable for l = 2 and c = 1 in the evaluation of large color difference such as acceptability chromatic aberration. Therefore, the CMC(l:c) color difference is taken as CMC(2:1).

First, it is found that among the selected 17 standard color, there is no difference between M0 and M1 of color number 11–17. The reason why the chromaticity of M1 and M0 is different is the fluorescence effect of the substrate. Among the 17 spot color standards selected for the experimental work, the 7 color of the number 11–17 have the same M1 chromaticity and the same M0 chromaticity. Therefore, only the 1 to 10 spot color are used in the experiment.

Then the color sample is sorted according to the CMC(2:1) color difference of M0 chromaticity and standard sample, and then select the color samples of the same color difference of M0 as a group. Due to the large number of color samples, each color of the standard can find multiple color groups with different levels of color difference. As shown in Table 2, for the standard sample 6, 8 color samples were selected according to the color difference of M0 chromaticity CMC(2:1). At the last line also gives the M1 chromatic aberration corresponding to the same color gradation. Thus, each standard color has 8–9 color samples with different color difference.

As seen from Table 2 that the color difference of M1 chromaticity is no longer the same for a group of color samples with the same chromatic aberration of M0, and some of the differences are smaller, and some of the differences are larger.

**Table 2.** Different color difference of standard sample 6

| Group No. | 1 | 2 | 3 | 4 | 5 | 6 | 7 | 8 |
|---|---|---|---|---|---|---|---|---|
| Color samples No. | A2 B23 B10 C38 | B18 B32 B49 B50 | B51 B43 D40 | B53 C29 D10 | B52 C2 D3 | D21 D30 E18 | E20 D6 E35 | E39 E43 E17 |
| $\Delta L^*$ (M0) | −0.01 −1.02 −0.74 1.33 | −0.83 0.49 −0.18 −0.16 | 0.89 −0.46 1.57 | 0.12 −0.44 −1.45 | −0.19 −0.29 1.24 | −0.30 0.35 −0.73 | 1.89 0.85 −0.73 | 0.09 0.70 1.94 |
| $\Delta C_{ab}^*$ (M0) | 1.46 −0.22 1.28 −0.57 | 1.02 0.60 −1.24 −1.11 | −1.93 −2.2 −0.05 | −2.66 −1.04 2.14 | −3.79 3.55 3.32 | −0.23 −2.91 2.70 | 3.26 4.98 −2.15 | −2.21 −2.99 5.28 |
| $\Delta H$ (M0) | 0.17 −0.56 0.16 0.27 | -0.64 −0.84 −0.69 0.76 | −0.65 0.55 −1.00 | −0.89 1.54 −0.98 | −0.67 0.95 −0.97 | 2.41 1.90 −1.96 | 1.87 −0.64 −2.43 | −2.88 −2.67 1.14 |
| CMC(2:1) (M0) | 0.68 | 0.82 | 1.13 | 1.45 | 1.82 | 2.13 | 2.36 | 2.72 |
| CMC(2:1) (M1) | 0.68 0.68 0.69 0.82 | 0.82 0.82 1.18 0.92 | 1.57 1.19 1.61 | 2.03 1.45 1.45 | 2.20 1.82 1.81 | 2.13 2.19 2.14 | 2.34 2.36 2.43 | 3.72 3.13 3.63 |

## 3.2 Subjective Evaluation

For the grouping shown in Table 2, the subjective evaluation is completed to judge the color differences between a group of color samples with its standard sample, as follows:

(1) Place each sets of color samples close to their standards in the Standard light source observation box with D50 source, 2000 lx illuminance;
(2) Observe each set of color samples and finds two color samples with the largest and smallest color difference perceived. The scene of observation is shown in Fig. 2;
(3) Comparison of the perceived maximum and minimum color difference samples with their corresponding M1 chromaticity CMC(2:1) color difference. And the ratio of the group number of the sample group, their visually difference are uniformity with the CMC(2:1) color difference, with total group number is considered as correct rate.

From the $1 \sim 10$ standard, it is found that when the color difference between the M0 chromaticity and the standard CMC(2:1) is smaller (about 0.6), the color difference between the color samples and the standard is not perceived, which is consistent with the fact that many studies have found discernable color difference values below 1 [3–6]. For all other color groups, the average of 8 observations gives the correct rate of M1 chromaticity CMC(2:1) value and visual chromatic aberration as shown in Fig. 3. It can

**Fig. 2.** Observation scene
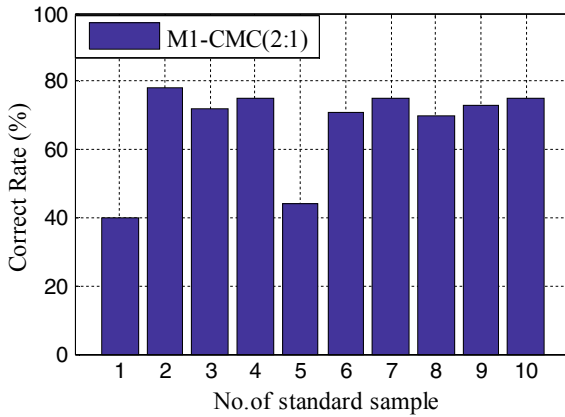


**Fig. 3.** Correct rate of M1 chromaticity CMC(2:1)

be seen that the correct rate of the eight samples is between 75 and 80%, with an average of 67%; but the lower of the standards 1 and 5 is about 40%.

## 3.3 Analysis of Results

First, the results in Fig. 3 show that the CMC(2:1) color difference under M1 can better match the perceived color difference, compared to the M0 condition. Therefore, in any print color measurement of the substrate containing the fluorescent brightening agent, M1 condition should be used.

Secondly, the comparison between the correct rates of different color formula is shown in Fig. 4. It can be seen that, except for the standard 9, the correct rate of $\Delta E_{00}$ value is lower than that of the CMC(2:1), with an average of 46%, which is 31% lower than that of CMC(2:1) value of 67%. And $\Delta E_{ab}^*$ is the lowest with an average value of 28%.
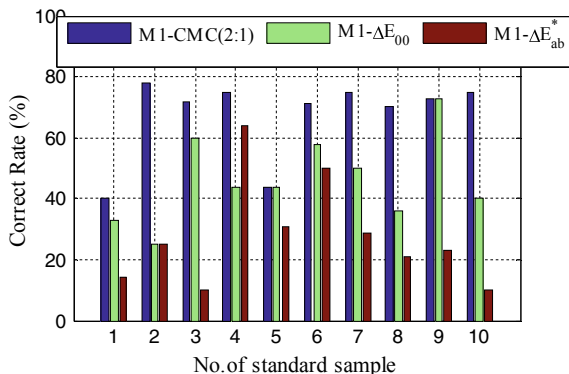
**Fig. 4.** Correct rate of M1 chromaticity the CMC(2:1), $\Delta E_{00}$, and $\Delta E_{ab}^*$

A number of studies have shown that CIEDE2000 color difference $\Delta E_{00}$ has the highest degree of compliance with vision, followed by CMC(1:1) color difference, and the worst is $\Delta E_{ab}^*$ color difference [3–6]. Theoretically, the $\Delta E_{00}$ is only suitable for the case where the $\Delta E_{ab}^*$ value is less than 5. However, our research here contains large chromatic aberration with $\Delta E_{ab}^*$ greater than 5. Therefore, the result that the CMC(2:1) value is more advantageous than the $\Delta E_{00}$. In fact, some companies have adopted CMC (2:1) color difference in color quality control.

The result there is still the lowest degree of compliance between $\Delta E_{ab}^*$ chromatic aberration and visual perception, which again indicates the inapplicability of $\Delta E_{ab}^*$ chromatic aberration. However, the color difference is still used in printing standards.

## 4   Conclusions

The experimental results show that the M1 chromatic aberration can more accurately reflect the influence of the substrate fluorescence whitening effect on visual chromatic aberration, which can be applied in the evaluation of print color quality. In addition, the experimental results also show that CMC(2:1) color difference based on M1 chromaticity is better than CIEDE2000 chromatic aberration, while CIE $L^*a^*b^*$ color difference is relatively the worst for large color difference evaluation.

## References

1. Xu Y (2011) Color management principle and application. Printing Industry Press, Beijing
2. Hu W, Tang S, Zhu Z (2007) Principle and application of modern color technology. Beijing Science and Technology Co Ltd, Beijing
3. Wang Z, Xu H (2007) Study of color discrimination threshold using CRT display part II: evaluation of classical color-difference formulae. ACTA Optic Asinica 27(7):1344–1348

4. Huang M, Liu H, Liao N (2009) Study on just-noticeable color difference discrimination threshold by using printed samples I: analysis of visual evaluation experimental data. Acta Optic Asinica 29(5):1431–1436
5. Huang M, Liu H, Liao N (2009) Study on just-noticeable color difference discrimination threshold by using printed samples II: analysis and evaluation of color difference formulae. Acta Optic Asinica 29(6):1740–1745
6. Li W, Zhang E, Liu H (2013). Research on smaller color-difference evaluation of digital proofing machine. Mech Sci Technol Aerosp Eng 32(6):928–931+936

# Study on the Effectiveness of Colour Quality Metrics in Preference Prediction at Different Illuminance Levels

Wei Chen[1], Lianjiang Rao[2], Zheng Huang[1], Zhen Hou[1], and Qiang Liu[1(✉)]

[1] School of Printing and Packaging, Wuhan University, Wuhan, China
liuqiang@whu.edu.cn
[2] WAC Lighting, Shanghai, China

**Abstract.** Now many studies discuss the preferred correlated colour temperature (CCT) as well as the validity of colour quality metrics. However, most of them were implemented under a constant illuminance (E) level. In this study, three E levels (50, 200, 600 lx) and three CCT levels (3500, 5000, 6500 K) were adopted to illuminate six single-coloured decorative birds. Twenty participants, ten males and ten females, were invited to respond with their visual preference of the colour of the experimental birds. The purpose of this work is mainly to discuss the validity of colour preference metrics at different E levels, as well as to provide reference for the exhibition of artwork of monochromatic colours. Based on the subjective preference data, twenty-six colour quality metrics of light source were evaluated in this study. The results indicate that at different E levels, the average subjective preference increases with CCT, but the combination of high E level and high CCT will lead to a decline in preference due to over-whiteness-perception. In addition, the validity of metrics also varies with E levels while in general many metrics are highly correlated with the subjective preference.

**Keywords:** Illuminance · Correlated colour temperature · Colour preference · Colour metrics

## 1 Introduction

Colour preference of lighting is one of the most important topics in current field of lighting application and many studies discuss its influencing factors and quantitative characterization methods. Studies show that E and CCT have a great influence on colour preference of lighting. However, many current studies discuss which light of different CCT people prefer and the validity of colour preference metrics only at a constant E level [1–11]. The impact of E on the validity of metrics is not discussed. In order to solve this problem, this paper conducted a psychophysical study to test whether E levels affect preferred CCT and the validity of colour preference metrics.

## 2   Method

### 2.1   Experimental Setup

All the experiments were carried out in a light booth, as shown in Fig. 1, whose walls and floor were painted with medium-grey matt paint (Munsell N7). The size of the booth was 50 cm × 50 cm × 60 cm (W × D × H).



**Fig. 1.** Experimental scene of the visual experiments

Nine different lights were generated by an LEDcube spectrally-tunable smart lighting system, which was provided by Changzhou Thouslite Ltd. The light sources had 3 CCT values (3500, 5000, 6500 K) and 3 E levels (50, 200, 600 lx). The spectral power distributions (SPDs) for the light sources measured by an X-Rite i1 Pro 2 spectrophotometer are shown in Fig. 2. The colorimetric parameters of the experimental light sources were calculated, together with typical colour quality measures, as shown in Table 1.

### 2.2   Experimental Design

The experimental objects are six decorative birds with similar shape and size (approximately 10 cm × 37 cm × 28 cm). The birds were of monochromatic colours (red, green, blue, yellow, black and white) with high saturation.

Twenty observers (ten females and ten males) participated in the visual experiments. All of them are students of Wuhan University and their ages range from 17 to 22, with a mean of 19.1 years. All the observers passed the Ishihara Color Vision Test while none of them was informed of the research intent in advance.
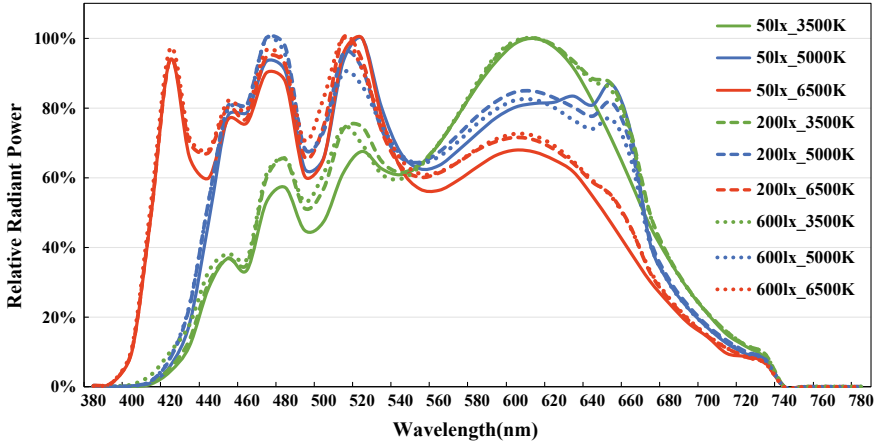
**Fig. 2.** Relative spectral power distributions of experimental light source

**Table 1.** Key information of the experimental light sources

| Normalised illuminance (lx) | 50 | | | 200 | | | 600 | | |
|---|---|---|---|---|---|---|---|---|---|
| Normalised CCT (K) | 3500 | 5000 | 6500 | 3500 | 5000 | 6500 | 3500 | 5000 | 6500 |
| Measured illuminance (lx) | 52 | 48 | 52 | 203 | 210 | 204 | 603 | 600 | 602 |
| Measured CCT (K) | 3412 | 4956 | 6624 | 3523 | 5005 | 6520 | 3529 | 5102 | 6604 |
| x | 0.4139 | 0.3471 | 0.3106 | 0.4078 | 0.3452 | 0.3130 | 0.4050 | 0.3425 | 0.3116 |
| y | 0.4023 | 0.3606 | 0.3283 | 0.4002 | 0.3538 | 0.3251 | 0.3934 | 0.3524 | 0.3240 |
| u′ | 0.2365 | 0.2093 | 0.1967 | 0.2334 | 0.2106 | 0.1995 | 0.2344 | 0.2094 | 0.1990 |
| v′ | 0.5173 | 0.4893 | 0.4676 | 0.5155 | 0.4858 | 0.4663 | 0.5123 | 0.4847 | 0.4655 |
| Duv | 0.0032 | 0.0037 | 0.0039 | 0.0036 | 0.0011 | 0.0011 | 0.0012 | 0.0014 | 0.0012 |
| CRI(Ra) | 91 | 90 | 95 | 92 | 90 | 94 | 92 | 90 | 93 |
| GAI | 59 | 88 | 101 | 62 | 90 | 102 | 65 | 90 | 102 |
| Qa(9.0.3) | 91 | 90 | 94 | 90 | 92 | 94 | 91 | 92 | 94 |
| Qf(9.0.3) | 91 | 89 | 93 | 90 | 92 | 93 | 91 | 92 | 93 |
| Qg(9.0.3) | 92 | 99 | 102 | 93 | 99 | 102 | 94 | 99 | 102 |
| Qp(7.4) | 90 | 91 | 96 | 90 | 94 | 96 | 91 | 94 | 96 |
| FSCI | 83 | 92 | 95 | 85 | 92 | 96 | 87 | 92 | 96 |
| CPI | 143 | 140 | 147 | 144 | 140 | 146 | 143 | 141 | 145 |
| FCI(CAM02) | 111 | 105 | 88 | 112 | 103 | 90 | 111 | 103 | 90 |
| CDI | 86 | 129 | 147 | 90 | 130 | 148 | 95 | 131 | 149 |
| CSA | 0.0428 | 0.0584 | 0.0661 | 0.0441 | 0.0589 | 0.0662 | 0.0455 | 0.0593 | 0.0665 |
| CRI-CAM02UCS | 90 | 87 | 94 | 89 | 90 | 95 | 90 | 90 | 94 |
| CRI2012 | 92 | 91 | 97 | 92 | 91 | 97 | 93 | 94 | 97 |
| MRCI | 89 | 91 | 90 | 89 | 91 | 90 | 89 | 91 | 90 |
| Rf | 87 | 86 | 94 | 87 | 86 | 94 | 88 | 87 | 94 |

<div align="right">(<i>continued</i>)</div>

**Table 1.** (*continued*)

| Normalised illuminance (lx) | 50 | | | 200 | | | 600 | | |
|---|---|---|---|---|---|---|---|---|---|
| Rg | 93 | 98 | 101 | 93 | 97 | 101 | 94 | 97 | 101 |
| $\triangle C^*$ | 1.73 | 0.13 | 0.31 | 1.47 | 0.06 | 0.39 | 1.18 | 0.17 | 0.36 |
| CQI1 | 173 | 184 | 190 | 174 | 185 | 190 | 174 | 185 | 190 |
| CQI2 | 1078 | 1929 | 2627 | 1163 | 1959 | 2602 | 1214 | 1977 | 2628 |
| GAI-RA | 75 | 89 | 98 | 77 | 90 | 98 | 78 | 90 | 98 |
| GVI | 81 | 91 | 92 | 82 | 90 | 91 | 81 | 90 | 91 |
| Snuetral | 2.82 | 5.38 | 6.67 | 3.01 | 6.03 | 7.19 | 3.36 | 6.08 | 7.20 |
| WS | 0.30 | 0.52 | 0.65 | 0.31 | 0.59 | 0.74 | 0.35 | 0.60 | 0.74 |
| Percent tint | 0.41 | 0.25 | 0.91 | 0.38 | 0.33 | 0.94 | 0.31 | 0.36 | 0.96 |
| DSI (D65) | 86 | 88 | 93 | 86 | 89 | 94 | 87 | 90 | 94 |

A 7-point rating method was employed for quantifying the colour preference of the observers. That is, the participants were asked to respond with −3, −2, −1, 0, 1, 2, 3, respectively denoting strongly dislike, moderately dislike, slightly dislike, neutral, slightly like, moderately like and strongly like.

## 2.3 Experimental Procedure

Upon arrival, the participant was asked to sign a consent form and carry out the Ishihara Test. Then, the experimenter asked the observer to put on a grey coat so that there would be no colour light reflected from his/her coloured clothes onto the test object.

After leading the observer to the booth, the experimenter asked him/her to adjust the height of the chair to make sure that the lighting module in the booth could not be seen. In this experiment, the light sources with low E levels (50 lx) were evaluated first and then the middle (200 lx) and high (600 lx) levels. At the very beginning, with a randomly selected light from 50 lx and a randomly selected colour bird, a training section was provided to help the observer to get used to the evaluation process.

After the training session, the formal experiment began with the subgroup of 50 lx light sources. Using a randomly selected CCT, the participant was first asked to rate his/her visual colour preference of the empty booth (such a judgment was conducted first in every E-CCT scenario) and then of the 6 colour birds (one at a time, with a random order). When the observer announced that they had finished their rating (for the last bird) and confirmed the results, the experimental lighting was changed. Meanwhile, when all the trials for a constant illuminance had been completed, the visual judgment workflow described above was repeated for next illuminance subgroup.

## 2.4 Analysis of Colour Preference Metrics

In this study, twenty-six typical colour preference metrics were involved, which include Duv, the CIE Color Rendering Index (CRI) [12], Gamut Area Index(GAI) [13], Full Spectrum Colour Index (FSCI) [14], Colour Quality Scale (CQS: Qa, Qf, Qp, Qg) [15], Feeling of Contrast Index (FCI) [16], Colour Discrimination Index (CDI) [17],

Cone Surface Area (CSA) [18], Color Preference Index (CPI) [19], CRI-CAM02UCS [20], CRI2012 [21], IES TM-30 (Rf and Rg) [22], Memory Colour Rendering Index (MCRI) [7], Gamut Volume Index (GVI) [23], Sneutral [24], White Sensation (WS) [25], Percent tint [26], Daylight Spectrum Index (DSI) [27], mean chroma shift of CQS (ΔC*) advocated by Khanh et al. [8–11], the arithmetic mean value of GAI and CRI [6, 28] as well as two combined metrics named Colour Quality Index (respectively denoted as CQI1 [8] and CQI2 [9]).

## 3    Result and Discussion

### 3.1    Analysis of Preference at Different E and CCT

The overall result is summarized in Fig. 3. In general, the average subjective ratings increase with CCT at different E levels.
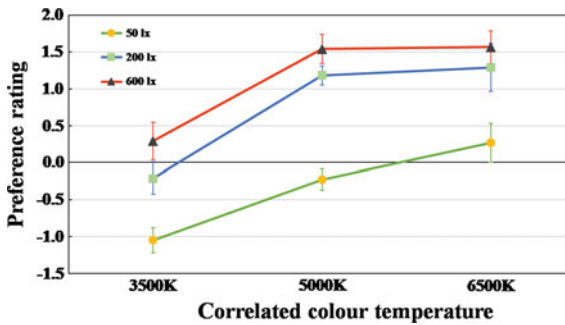


**Fig. 3.** Average colour preference ratings of six birds with regard to different CCT and E levels. The error bars are 95% confidence intervals

For the low E level (50 lx), the subjective preference increases remarkably with CCT. The evaluation at low and middle CCT shows *dislike* and the preference at high CCT is also not high. Because the lighting environment is too dark, people do not like the yellow light of low CCT. It is known that the higher the CCT is, the whiter it feels. So, at low E level, people do not like the yellow light of low CCT while prefer white light of high CCT.

For the middle E level (200 lx), the preference at low CCT also shows *dislike* while at middle and high CCT, it shows *like*. An increase of CCT from 3500 to 5000 K sharply raises the score but tend to show a smaller increase at 6500 K. In fact, at 5000 K, the ratings of some objects even appear higher than those at 6500 K. Since the light of high CCT feels whiter, when E is enough high, it may impair the preference because of too white.

For the high E level (600 lx), the preference at low CCT is not high and at middle and high CCT, it appears stronger *like* than 200 lx. But there is almost no difference in ratings between 5000 and 6500 K, because the ambient light is brighter at this time, the effect of being too white to like is more prominent.

Although the observers are required to focus on the color appearance of the objects, it seems that the perception of final lighting environment greatly affects the visual preference. Whatever the E level, people are not very fond of low CCT compared to middle and high CCT.

In brief, the result suggests that the E level has an effect on the preferred CCT, which is consistent with the finding of Khanh [29, 30]. When discussing this topic, such a factor should be considered carefully. It is not always the case that the higher the CCT is, the more people like it. Sometimes, the high CCT is not necessarily the favorite one at high E level.

## 3.2    Correlation Analysis

Table 2 summarizes the performance of twenty-six metrics in terms of the Pearson correlation coefficient (r) between metrics prediction and preference ratings of each E level.

**Table 2.** Pearson correlation coefficient between metric predictions and average preference ratings

| Color quality metric | 50 lx | 200 lx | 600 lx | Overall |
|---|---|---|---|---|
| Duv | 0.9953 | −0.9979 | 0.4851 | 0.1608 |
| CRI(Ra) | 0.6054 | 0.0328 | 0.1524 | 0.2635 |
| GAI | 0.9968 | 0.9712 | 0.9505 | 0.9728 |
| Qa(9.0.3) | 0.6127 | 0.8707 | 0.8260 | 0.7698 |
| Qf(9.0.3) | 0.3695 | 0.8307 | 0.7941 | 0.6648 |
| Qg(9.0.3) | 0.9966 | 0.9702 | 0.9302 | 0.9657 |
| Qp(7.4) | 0.8970 | 0.9446 | 0.9008 | 0.9141 |
| FSCI | 0.9930 | 0.9662 | 0.9368 | 0.9653 |
| CPI | 0.4820 | −0.0994 | 0.0221 | 0.1349 |
| FCI(CAM02) | −0.9139 | −0.8340 | −0.8125 | −0.8535 |
| CDI | 0.9968 | 0.9712 | 0.9504 | 0.9728 |
| CSA | 0.9988 | 0.9650 | 0.9470 | 0.9703 |
| CRI-CAM02UCS | 0.4719 | 0.7338 | 0.6245 | 0.6101 |
| CRI2012 | 0.7167 | 0.4935 | 0.6679 | 0.6260 |
| MCRI | 0.6200 | 0.8318 | 0.8573 | 0.7697 |
| Rf | 0.6911 | 0.5325 | 0.3961 | 0.5399 |
| Rg | 0.9966 | 0.8645 | 0.7848 | 0.8820 |
| $\Delta$C* | 0.9852 | 0.9857 | 0.9466 | 0.9725 |
| CQI1 | 0.9999 | 0.9623 | 0.9523 | 0.9715 |
| CQI2 | 0.9961 | 0.9219 | 0.8954 | 0.9378 |
| GAI-RA | 1.0000 | 0.9471 | 0.9266 | 0.9579 |
| GVI | 0.9459 | 0.9988 | 0.9963 | 0.9803 |
| Snuetral | 0.9991 | 0.9786 | 0.9637 | 0.9805 |
| WS | 1.0000 | 0.9594 | 0.9411 | 0.9668 |
| Percent tint | 0.6191 | 0.4921 | 0.5728 | 0.5613 |
| DSI(D65) | 0.9554 | 0.8290 | 0.8150 | 0.8665 |

As shown in the table, each metric shows different correlations at different E levels. For instance, the correlation of MCRI increases with E levels, while Rg has a high correlation at low E level than at high E level [31]. The correlation of CRI-CAM02UCS at middle E level is higher than the other two while the correlation of CRI2012 is lower at middle E level. The above indicates that the E level has a certain impact on the performance of metrics.

At 50 lx, only FCI has a negative correlation and the correlations of Qf (r = 0.37), CRI-CAM02UCS (r = 0.47) and CPI (r = 0.48) are relatively low. Other metrics are highly correlated with preference ratings, WS (r = 1) and GAI-RA (r = 1) have the highest correlations.

At 200 lx, Duv, CPI and FCI perform poorly and performance of CRI (r = 0.03), Percent tint (r = 0.49), CRI2012 (r = 0.49) and Rf (r = 0.53) is not good enough. At this E level, GVI performs best.

At 600 lx, FCI is still negatively correlated with preference ratings. The metrics of low correlations are CPI (r = 0.02), CRI (r = 0.15), Rf (r = 0.4), Duv (r = 0.48) and Percent tint (r = 0.57). GVI still performs best as it does at 200 lx.

Overall, FCI performs poorly and is extremely negatively correlated with preference ratings at all E levels, which may be attributed to the distribution of color samples and the method of calculating the color gamut. GVI performs very well at every E level, which again demonstrates its role in predicting preference of lighting [23]. In addition, the metrics based on the colour difference (CRI, CRI-CAM02UCS, Qa, Qp, Qf, CRI2012, Rf, CPI and $\Delta C^*$) perform poorly compared with other measures while CPI and CRI have the worst performance among these metrics. The only two exceptions are Qp and $\Delta C^*$, which exhibit relatively better correlations. CRI is defective in predicting colour preference of lighting, which is consistent with many current research results [2, 32]. The reasons for the poor performance of the colour difference based metrics is that their intent is to evaluate fidelity rather than colour preference and they are not comparable at different CCTs since they are related to different reference sources.

## 4   Conclusions

This paper investigates the preferred CCT and validity of colour preference metrics at different E levels by conducting a series of psychophysical studies. The results indicate that the average subjective preference increases with CCT at different E levels. But the combination of high E level and high CCT will lead to a decline in preference due to over-white. At 50 lx, there is no over-white effect because the ambient light is too dark and the preference increases remarkably with CCTs. At 200 and 600 lx, an increase of CCT from 3500 to 5000 K sharply raises the score but tend to show a smaller increase at 6500 K because of the over-white effect. Therefore, when choosing the preferred CCT, the impact of E level should be taken into consideration. In addition, the results reveal that the validity of colour preference metrics varies with E levels. For the low E level (50 lx), WS and GAI-RA show the best correlation with the subject preference while for the middle (200 lx) and high (600 lx) E levels, GVI is the best. Overall, many

metrics, including Sneutral, GVI, GAI, CDI, $\Delta C^*$, CQI1, CSA, WS, Qg, FSCI, GAI-RA, CQI2 and Qp, are highly correlated with the subjective preference.

# References

1. Liu Q, Huang Z, Liu Y et al (2018) Best lighting for jeans, Part 1: Optimizing colour preference and colour discrimination with multiple correlated colour temperatures. Res Technol, Light. https://doi.org/10.1177/1477153518816125

2. Narendran N, Deng L (2002) Color rendering properties of LED light sources. In: Proceedings of SPIE—The International Society for Optical Engineering. https://doi.org/10.1117/12.452574

3. Nascimento SMC, Masuda O (2014) Best lighting for visual appreciation of artistic paintings—experiments with real paintings and real illumination. JOSA 31(4):214–219

4. Huang Z, Liu Q, Westland S et al (2018) Light dominates colour preference when correlated colour temperature differs. Light Res Technol 50(7):995–1012

5. Feltrin F, Leccese F, Hanselaer P, et al (2017) Analysis of painted artworks' color appearance under various lighting settings. In: 2017 17th IEEE international conference on environment and electrical engineering and 2017 1st IEEE industrial and commercial power systems Europe. https://doi.org/10.1109/eeeic.2017.7977574

6. Smet K, Ryckaert WR, Pointer MR et al (2011) Correlation between color quality metric predictions and visual appreciation of light sources. Opt Express 19(9):8151–8166

7. Smet KAG, Ryckaert WR, Pointer MR et al (2010) Memory colours and colour quality evaluation of conventional and solid-state lamps. Opt Express 18(25):26229–26244

8. Khanh TQ, Bodrogi P, Vinh QT et al (2017) Colour preference, naturalness, vividness and colour quality metrics, Part 1: experiments in a room. Light Res Technol 49(6):697–713

9. Khanh TQ, Bodrogi P, Vinh QT et al (2017) Colour preference, naturalness, vividness and colour quality metrics, Part 2: experiments in a viewing booth and analysis of the combined dataset. Light Res Technol 49(6):714–726

10. Khanh TQ, Bodrogi P (2018) Colour preference, naturalness, vividness and colour quality metrics, Part 3: experiments with makeup products and analysis of the complete warm white dataset. Light Res Technol 50(2):218–236

11. Khanh TQ, Bodrogi P, Vinh QT et al (2018) Colour preference, naturalness, vividness and colour quality metrics, Part 4: experiments with still life arrangements at different correlated colour temperatures. Light Res Technol 50(6):862–879

12. Nickerson D, Jerome CW (1965) Color rendering of light sources: CIE method of specification and its application. Illum Eng 60:262–271

13. Freyssinier JP, Rea M (2002) A two-metric proposal to specify the color-rendering properties of light sources for retail lighting. Proc SPIE. https://doi.org/10.1117/12.863063
14. Rea M, Deng L, Wolsey R (2004) NLPIP lighting answers: light sources and color. Polytechnic Institute
15. Davis W, Ohno Y (2010) Color quality scale. Opt Eng 49(3)
16. Hashimoto K, Yano T, Shimizu M et al (2007) New method for specifying color rendering properties of light sources based on feeling of contrast. Color Res Appl 32(5):361–371
17. Thornton WA (1972) Color-discrimination index. J Opt Soc Am 62(2):191–194
18. Fotios SA (1997) The perception of light sources of different colour properties. Doctor of Philosophy Thesis, UMIST, United Kingdom
19. Thornton WA (1974) A validation of the color-preference index. J Illum Eng Soc 4(1):48–52
20. Luo MR (2011) The quality of light sources. Color Technol 127(2):75–87
21. Smet KA, Schanda J, Whitehead L et al (2013) CRI2012: a proposal for updating the CIE colour rendering index. Light Res Technol 45(6):689–709
22. David A, Fini PT, Houser KW et al (2015) Development of the IES method for evaluating the color rendition of light sources. Opt Express 23(12):15888–15906
23. Liu Q, Huang Z, Xiao K et al (2017) Gamut volume index: a color preference metric based on meta-analysis and optimized colour samples. Opt Express 25(14):16378–16391
24. Kevin A, Geert D, Peter H (2014) Chromaticity of unique white in object mode. Opt Express 22(21):25830–25841
25. Wang Q, Xu H, Cai J (2015) Chromaticity of white sensation for LED lighting. Chin Opt Lett 13(7)
26. Rea MS, Freyssinier JP (2015) White lighting: a provisional model for predicting perceived tint in "white" illumination. Color Res Appl 39(5):466–479
27. Acosta I (2017) Daylight spectrum index: development of a new metric to determine the color rendering of light sources. In: Proceedings of the international conference on civil and urban engineering, Prague, Czech Republic, 14 March 2017, vol. 9, pp. 442–447
28. Jost-Boissard S, Avouac P, Fontoynont M (2014) Assessing the colour quality of LED sources: naturalness, attractiveness, colourfulness and colour difference. Light Res Technol 47(7):769–794
29. Khanh T, Bodrogi P, Guo X, et al (2018) Towards a user preference model for interior lighting Part 1: concept of the user preference model and experimental method. Light Res Technol. https://doi.org/10.1177/1477153518816469
30. Khanh T, Bodrogi P, Guo X, et al (2018) Towards a user preference model for interior lighting. Part 2: experimental results and modelling. Light Res Technol. https://doi.org/10.1177/1477153518816474
31. Wei M, Bao W, Huang H-P (2018) Consideration of light level in specifying light source color rendition. LEUKOS. https://doi.org/10.1080/15502724.2018.1448992
32. Dangol R, Islam M, Lisc MH et al (2013) Subjective preferences and colour quality metrics of LED light sources. Light Res Technol 45(6):666–688

# The Performance of Color Matching Functions in Different Field Sizes

Chunli Guo[1], Min Huang[1(✉)], Chunjie Shi[2], and Yonghui Xi[1]

[1] School of Printing and Packaging Engineering, Beijing Institute of Graphic Communication, Beijing, China
huangmin@bigc.edu.cn
[2] College of Network Communication, Zhejiang Yuexiu University of Foreign Languages, Shaoxing, China

**Abstract.** In order to investigate the performance of different color matching functions (CMFs) in different field sizes, a series of color matching experiments with different field sizes were conducted based on two displays with different primary colors. Eighteen observers with normal color vision were organized to match the CIE recommended 5 color stimuli on the matched displays. The mean CIEDE2000 color difference between target and matched colors was calculated and used to evaluate the performance of different CMFs. Observer variability ellipses were also employed to evaluate observer variability. The results indicated that the CIE2006 CMFs had the best performance in each field size. For different field sizes, the observer variability was the largest with 2° and the smallest with 29° performed by the observer variability ellipses.

**Keywords:** Color matching functions · Color matching experiment · Field size · Observer variation

## 1 Introduction

CIE recommended CIE1931 and CIE1964 color matching functions (CMFs) to represent average human color vision properties with different field sizes. In 2006, CIE proposed CIE2006 physiological observer model to predict the individual cone fundamentals with the field size ranged from 1° and 10°, and aged from 20 and 80. With the development of digital technology and people's demand for large-screen displays, the size of electronic display devices is growing, such as computer, mobile phone, LED displays and so on. In different viewing size, observers will have different color perception.

Recently, many researchers studied on the relationship of field sizes and color perception. Hu and Houser [1] found that observers were less sensitive to shorter wavelengths while higher sensitivities to the longer wavelengths under the large-field conditions. Kutas and Bodrogi [2] indicated that "size effect" was significant by conducting a color matching experiment using a large (85°) homogeneous self-luminous visual stimulus and a 2°/10° stimulus. Xiao et al. [3, 4] found that when increasing the stimulus size, the colors will appear to be lighter and more colorful with little change in hue. Then Xiao et al. [5] introduced two models that could transform the color

appearance of a stimulus having a viewing field of 2° to that associated with a range of viewing fields. The above studies showed that field size could affect the color appearance. It is useful to know that how about the performances of CIE proposed CMFs beyond 10° or ranging from 1 to 10°?

In this study, a series of color matching experiments with different field sizes (2°, 4°, 10°, 22°, 29°) were conducted based on the two displays with different primary colors. Eighteen observers with normal color vision were organized to match the CIE recommended 5 color stimuli on the matched displays. The CIEDE2000 values between target colors and matched colors were calculated to evaluate the performance of CIE1931, CIE1964 and CIE2006 CMFs.

## 2   Color Matching Experiment

### 2.1   Displays

EIZO-CG19 LCD display (called EIZO) and QUATO-220ex LED display (called QUATO) were chosen as the target display and matched display in the experiments. The spectral power distributions (SPDs), measured by Photo Research 655 spectrometer (PR655) were shown in Fig. 1. The correlative color temperature, luminance of the target and matched displays were set as 6309 and 6188 K, 110.5 and 110.6 cd/m$^2$ measured by PR655.
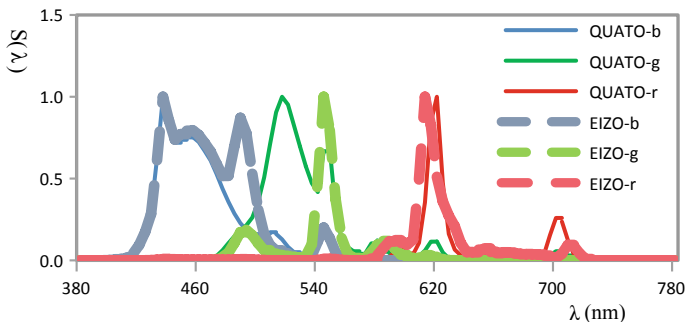


**Fig. 1.**  Relative SPDs of the primary colors of the displays

### 2.2   Color Stimuli

Five colors, proposed by CIE, were selected and displayed on the target display. The CIELAB color differences between the four corners and the center point of the target display were within 2.0. The CIELAB color differences between CIE proposed values and experimental colorimetric values of 5 colors were shown in Table 1. "Target" represented the CIE proposed values under D65 and 10°. "1931" and "1964" meant the values calculated by CIE1931 CMFs and CIE1964 CMFs, respectively. In the following calculation, in 2° and 4° filed size, the CIE 1931 CMFs were used and CIE1964 CMFs were employed in the remaining field size conditions.

**Table 1.** CIE proposed values and experimental colorimetric values of 5 colors

| Colors | Categories | $L^*$ | $a^*$ | $b^*$ | $\Delta E_{ab}^*$ |
|--------|-----------|-------|-------|-------|-------------------|
| Gray   | Target    | 62.00 | 0.00  | 0.00  | –    |
|        | 1931      | 61.48 | 0.09  | −0.28 | 0.60 |
|        | 1964      | 62.55 | −0.11 | 0.35  | 0.66 |
| Red    | Target    | 44.00 | 37.00 | 23.00 | –    |
|        | 1931      | 43.73 | 36.96 | 22.27 | 0.78 |
|        | 1964      | 44.15 | 36.68 | 22.51 | 0.61 |
| Yellow | Target    | 87.00 | −7.00 | 47.00 | –    |
|        | 1931      | 87.26 | −7.07 | 46.79 | 0.34 |
|        | 1964      | 87.57 | −7.18 | 46.99 | 0.60 |
| Green  | Target    | 56.00 | −32.00| 0.00  | –    |
|        | 1931      | 56.43 | −31.69| 0.51  | 0.73 |
|        | 1964      | 56.03 | −31.68| −0.24 | 0.40 |
| Blue   | Target    | 36.00 | 5.00  | −31   | –    |
|        | 1931      | 36.47 | 5.23  | −31.02| 0.53 |
|        | 1964      | 35.67 | 4.40  | −30.80| 0.72 |

## 2.3 Different Field Size Conditions

The experimental setup was shown in Fig. 2. Five field size conditions can be obtained by the fixed observation distance (equals to 50 cm) and different size of the stimuli. The corresponding parameters are shown in Table 2.
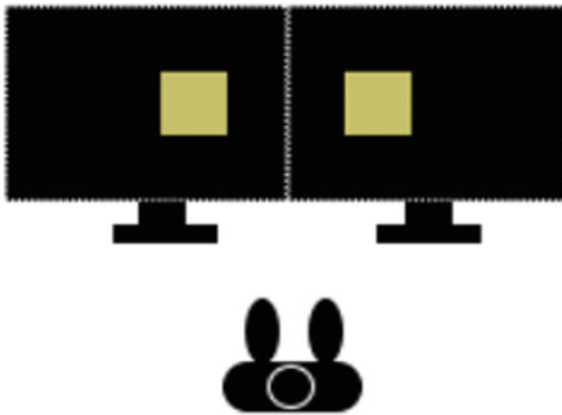


**Fig. 2.** Diagram of visual experiment

**Table 2.** Field sizes and the corresponding stimuli sizes

| Field size (°) | 2 | 4 | 10 | 22 | 29 |
|---|---|---|---|---|---|
| Side length (cm) | 1.74 | 3.50 | 8.54 | 19.44 | 24.50 |

The visual experiments were carried out in the dark room and a black mask $(Y^*_{10} = 4.72)$ with an open window was used to cover the entire screen. The displays must be worked for 2 h before the real color matching experiment to ensure the stable working condition. The observers were asked to adjust the RGB channels on the QUATO display to match the colors displayed on EIZO. The corresponding spectral data would be measured by PR655 spectroradiometer as soon as the observers finished the color matching experiments.

Eighteen observers (2 males and 16 females) with normal color vision were organized to carry out the visual experiments. All of them are students with the average age of 19. Each observer participated in color matching experiments with 5 field sizes at different time periods, and there were 5 colors in each field size. In total, 450 (=18 observers × 5 colors × 5 filed sizes) groups of data were collected.

## 3   Data Analysis

### 3.1   Performance of Different CMFs

The mean CIEDE2000 values between the target and matched colors after CAT16 [6] were calculated by the CIE1931, 1964, CIE2006 CMFs. The smaller the values were, the better the performance of the CMFs. When CIE2006 CMFs were used to calculate the CIEDE2000 values, the actual age of the observers and field size were employed. If the age was less than 20 or the field size exceeded 10°, it was counted as 20 and 10°, respectively. It could be shown in Fig. 4. The values of CIEDE2000 were ranging from 1.10 to 4.95. Note that the values were the average of the 5 colors. Horizontal coordinate represented each observer with different filed size conditions. 1–18 represented the observers in 2°, 19–36 represented observers in 4°, ..., 73–90 meant observers in 29°. The frequencies of the minimum value of CIEDE2000 values under different field size conditions using different CMFs were counted, as shown in Table 3 (Fig. 3).

**Table 3.** Frequencies of the minimum of CIEDE 2000 values using different CMFs

| Field size | CIE1931 CMFs | CIE1964 CMFs | CIE2006 CMFs | In total |
|---|---|---|---|---|
| 2° | 5 | 2 | 11 | 18 |
| 4° | 1 | 3 | 14 | 18 |
| 10° | 2 | 5 | 11 | 18 |
| 22° | 3 | 4 | 11 | 18 |
| 29° | 1 | 3 | 14 | 18 |
| In total | 12 | 17 | 61 | 90 |
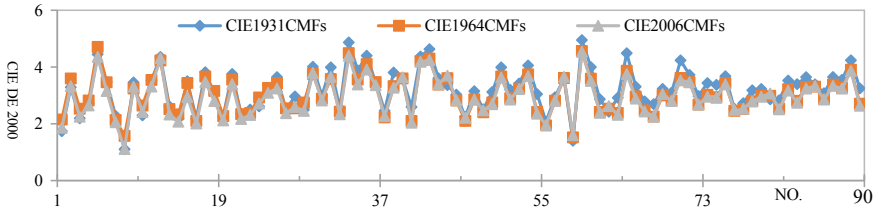
**Fig. 3.** CIEDE2000 values using 3 CMFs under different field size conditions

It can be seen that CIE2006 CMFs has the highest frequency with the smallest CIEDE2000 values under any field size, which implied that CIE2006 CMFs outperform others in each field size condition.

### 3.2    Observer Variability in Different Field Sizes

In the color matching experiments, 18 observers matched 5 colors in different field sizes (90 data sets). The covariance inverse matrix parameters of $a^*$ and $b^*$ values of the matching data calculated by 3 CMFs were used to obtain the observer variability elliptic parameters and then plotted the observer variability ellipses, as shown in Fig. 4. The ellipses were used to investigate the observer variability in different field sizes. Note that these ellipses were drawn after being magnified 3 times.

From Fig. 4, it can be seen that there was a positive correlation between the area of the ellipse and the observer variation. For 3 CMFs, the observer variability was similar and the smallest ellipse area was 29° field size. It indicated that all the CIE recommended CMFs were the most accurate to induce matching results in larger (29°) field size while the most sensitive to induce matching inaccuracies in small field sizes. It also found that the observer variability calculated using CIE2006 CMFs was slightly shifted to the direction of $-a^*$ axis from CIE1931 and CIE1964 CMFs at red with 2° and 4° field size conditions.

## 4    Conclusions

In order to investigate the performances of different CMFs in different field sizes, a series of visual experiments were conducted based on 5 colors with two displays with different color primaries. Eighteen observers with normal color vision were organized to carry out the visual experiments in the dark room. The results indicated that the CIE2006 CMFs had the best performance in each field size. For different field sizes, the

(a) CIE1931CMFs

(b) CIE1964 CMFs

(c) CIE2006 CMFs
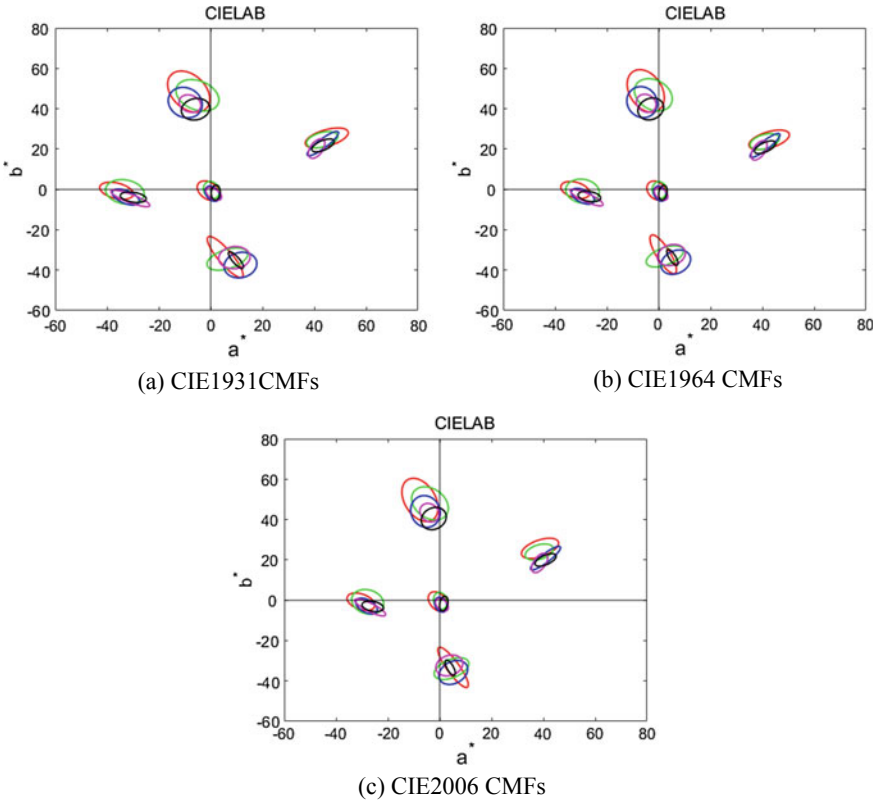
**Fig. 4.** Distribution of observer variability ellipse in a*-b* plane using 3 CMFs (2°:red; 4°:green; 10°:blue; 22°:magenta; 29°:black)

observer variability was the largest with 2° performed by the observer variability ellipses, which indicate that in small field size, all the CIE recommended CMFs were most sensitive to induce matching inaccuracies.

**Compliance with Ethical Standards.**
**Conflict of Interest**: The authors declare that they have no conflict of interest.
**Ethical approval**: All procedures performed in studies involving human participants were in accordance with the ethical standards of the school of printing and packaging engineering, Beijing Institute of Graphic Communication and with the 1964 Helsinki declaration and its later amendments or comparable ethical standards.
**Informed consent**: Informed consent was obtained from all individual participants included in the study.

# References

1. Hu X, Houser KW (2006) Large-field color matching functions. Color Res Appl 31:18–29
2. Kutas G, Bodrogi P (2008) Color appearance of a large homogenous visual field. Color Res Appl 33:45–54
3. Xiao K, Luo MR, Li C et al (2010) Colour appearance of room colours. Color Res Appl 35:284–293
4. Xiao K, Luo MR, Li C et al (2011) Investigation of colour size effect for colour appearance assessment. Color Res Appl 36:201–209
5. Xiao K, Luo MR, Li C (2012) Colour size effect modelling. Color Res Appl 37:4–12
6. García PA, Huertas R, Melgosa M, Cui G (2007) Measurement of the relationship between perceived and computed color differences. J Opt Soc Am A 24(7):1823–1829

# To Build a Novel HDR/WCG Display Model

Dalin Tian, Cheng Ji, Xinye Shi, Haoyu Zhou,
and Ming Ronnier Luo[(✉)]

State Key Laboratory of Modern Optical Instrumentation, Zhejiang University,
Hangzhou, China
m.r.luo@zju.edu.cn

**Abstract.** Recently the High Dynamic Range (HDR) display has been a focused topic in display area, especially with the development of Organic Light Emitting Diode (OLED) technique and Quantum Dot Liquid Crystal Display (QD-LCD) technique, it has been possible to achieve a higher luminance and lower black level in commercial product application. However, currently the OLED display or QD-LCD display could attain a peak luminance for around 500–800 cd/m$^2$, which is better than traditional Liquid Crystal Display (LCD) but far away from BT.2020 standard expectation. To reach a higher luminance, Helge Seetzen et al. had built a novel LCD-DLP display model, using a Digital Light Projector to replace the conventional LCD's backlight, and using the LCD panel as color controller, which could display impressive high dynamic range images. But the disadvantages were that the system was complex, and the color gamut was smaller than common commercial displays. So in this study, an LCD-DLP display prototype was firstly built and optimized, then the display was calibrated and measured. Finally we proposed to use the color filter to enlarge the color gamut.

**Keywords:** High dynamic range · Wide color gamut · Liquid crystal display · Digital imaging projector

## 1 Introduction

The high dynamic range (HDR) display is becoming the most popular trend to replace the standard dynamic range (SDR) display, which is widely used in the daily life. The dynamic range is defined based on human vision. For human eyes perception, the luminance range from $10^{-3}$ to $10^6$ cd/m$^2$ could be accepted [1]. However, only a small part in this range, from around 1 to 100 cd/m$^2$, could be covered by SDR commercial display, like Liquid Crystal Display F(LCD). As we all know the contrast of a display equals to the ratio of its highest and lowest luminance. For the LCD display, the dynamic range depends on its transparency of its liquid crystal color filter. The backlight of the LCD won't affect the overall contrast because it's uniform, no matter how the backlight luminance is changed, the dark pixels and the bright pixels will be influenced simultaneously, which means it won't improve the contrast. Consequently, the images and videos in SDR display are not as real and natural as feelings of real world, especially for the detail loss in high brightness and blackness scene.

Comparing with the SDR display, a much higher brightness and lower black level could be attained in HDR display, like the Organic Light Emitting Diode (OLED) display and Quantum Dot Liquid Crystal Display (QD-LCD). In previous study [2], the luminance range of these two products were measured. The OLED display could achieve a luminance range from 0.0005 cd/m$^2$ to around 430 cd/m$^2$, and the QD-LCD could achieve from 0.76 to 670 cd/m$^2$. They were proved to have a better overall image quality than traditional LCD display [3], but compared with the HDR standard BT.2020, the peak luminance of those displays is still not enough.

Helge Seetzen et al. [4] had proposed two solutions to realize HDR standard, which are based on the idea that, using an LCD panel as an optical filter which transparency is programmable, to modulate a low-resolution image from a second display, which is achromatic but has extremely high dynamic range. The first solution is the Liquid Crystal Display- Digital Light Projector (LCD-DLP) system, using the DLP to replace the backlight of the LCD. If the contrast of LCD is $c_1$, and DLP is $c_2$, considering that the overall contrast of a whole system is the product of the contrast of each component, the contrast of the LCD-DLP system is $c_1 * c_2$, which is apparently improved. The second system is similar with the first one, using the LED panel as the backlight and LCD panel as color filter, so it's an LCD-LED system. These two systems were proved to have impressive appearances in dynamic range, but their color performances had not been tested, i.e. the color gamut, color accuracy, etc.

This study is based on the LCD-DLP system. We firstly developed and optimized the LCD-DLP system, then the calibration and characterization were made on this display to test its color display appearance. After that a proposal was conducted to enlarge its color gamut.

## 2   System Establishing

The whole system consisted of a liquid crystal panel, a digital projector which color wheel module was removed, a Fresnel Lens and a diffuser. The schematic of the whole system is shown in Fig. 1.
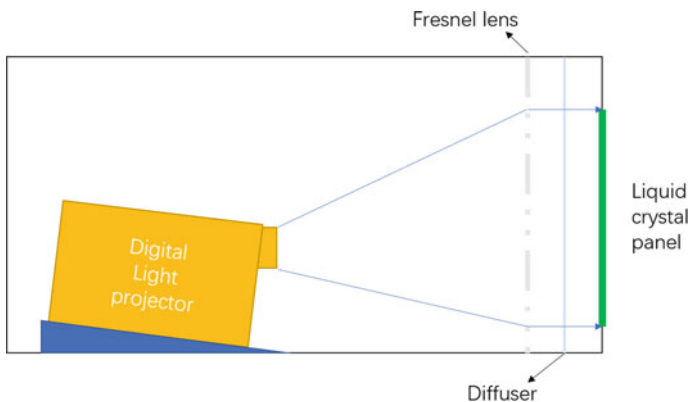


**Fig. 1.** Schematic of LCD-DLP system

Followings are the descriptions and concrete assembling details of each components.

## 2.1    Liquid Crystal Display (LCD) Panel

The LCD utilized in this system was disassembled from an old Apple iPad 3. This panel was manufactured by LG Display and the model number was LP097QX1. This display was 9.7 in. with 200 mm width and 150 mm height. The resolution of this display was 2048 * 1536. It consisted a uniform backlight, a liquid crystal panel, and several optical light modulation layers between them. After the backlight went through the first polarizer, the color could be controlled by changing the polarization state of the liquid crystal panel. Even though the polarization direction of light and liquid crystal could be orthogonal, the transmittance of the panel was not zero, the light was still able to pass it. Consequently the luminance of the darkest color is about 1 cd/m$^2$, and its brightest white was approximately 300 cd/m$^2$. Considering the liquid crystal panel was only needed in this study to control the colors, the backlight, polarizer, and other optical layers were removed carefully. Afterwards, the LCD panel was driven by a Retina iPad Display Port Driver, which provided a DP input to be connected with the graphics card in computer.

## 2.2    Digital Light Projector (DLP)

The digital light projector used in this system was Optoma X600 projector. The maximum illumination of this projector could be 6000l m, which was very bright and suitable for this design. The resolution of this projector was 1024 × 768. Since we intended to use the projector as a programmable backlight, it was not supposed to display colors. Thus the color filters inside the projector could only cause unnecessary loss of light. To further improve the illumination, the color wheel of this projector was carefully removed, so the projector could only project images with neutral colors and the brightness was much higher.

## 2.3    Fresnel Lens and Diffuser

Because of the characteristics of the DLP, the light projected from the DLP's lens was divergent, therefore after the light went through the LCD the colors could be shifted due to the distortion. Thus, the Fresnel lens and the diffuser were used to focus and align the light projected from the DLP. The focal length of the Fresnel lens was around 400 mm. Both components were placed between the DLP and LCD.

All components were well aligned to avoid the light loss and color distortion. Besides, compensation algorithm was used to match the neutral images projected by the DLP and colors displayed by LCD, which is similar with Seetzen's experimental solution. The optical transfer function was firstly measured and simulated, then the reverse function was integrated into the driver to compensate the distortion. Further details were well explained in Seetzen's research and wouldn't be discussed here considering it wasn't the main point. The actual structure was shown in Fig. 2.

**Fig. 2.** Inner situation of the display

After the whole system was assembled and well-tuned, the test HDR images were correctly displayed, as shown in Fig. 3. The contrast was too impressively high to be captured in one exposure with camera.



**Fig. 3.** Same test HDR image captured in different exposure

## 3   Measurement

The LCD-DLP was calibrated and measured after the HDR images were successfully displayed. Firstly the luminance response of the DLP was measured using Konica Minota CS-2000a spectroradiometer. All the pixels in LCD were set to [255, 255, 255] to show a white color. The output luminance of DLP was controlled from minimum to maximum to measure the luminance response. The response curve was shown in Fig. 4.

The maximum luminance was measured to be approximately 8500 cd/m$^2$, which was also the maximum luminance of the whole system. It was far much higher than OLED or QD-LCD displays.

Due to the control of projector's luminance, the input and output luminance difference of single colors could be measured. The ratio of luminance difference ($\Delta L$) and
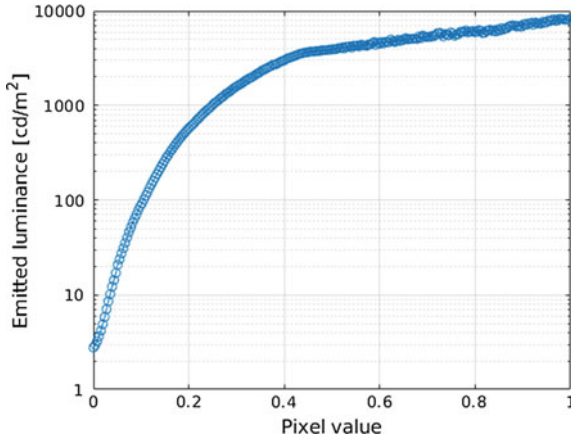
**Fig. 4.** DLP luminance response curve

input luminance (L), i.e. the luminance difference ratio $\Delta L/L$ was shown in Fig. 5. Color of marks represented the color with different luminance measured. Results indicated that the average luminance difference was about 0.01, which implied the luminance information could be accurately reappeared.
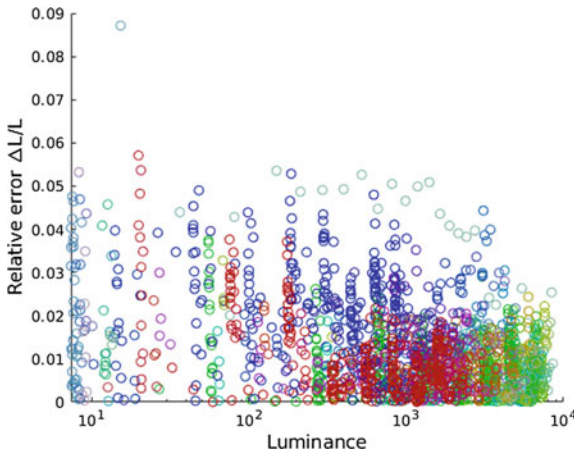


**Fig. 5.** Relative luminance error $\Delta L/L$

Secondly the response curve of LCD was measured. The input of DLP was set to maximum luminance and the channel input of LCD was increased from 0 to 255, including R, G, B, and grey scales. The response curve was shown in Fig. 6. The color of the curve represented the color of the channel.
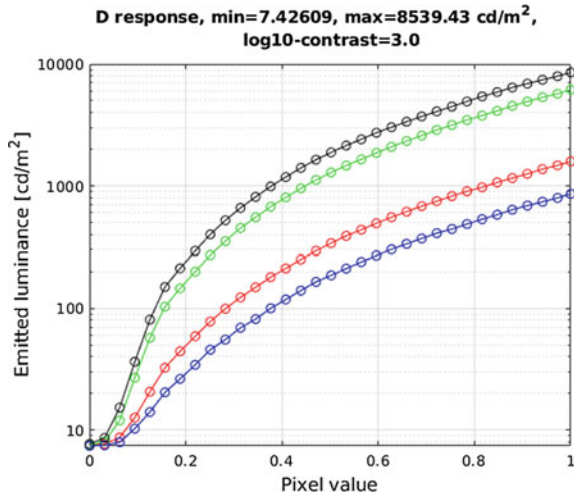
**Fig. 6.** LCD luminance response curve

Similar maximum luminance was attained in this measurement, because both results were measured under the condition of DLP maximum luminance and LCD [255, 255, 255]. The minimum luminance was measured to be around 1 cd/m$^2$ under the condition of minimum DLP luminance and [0, 0, 0] LCD input. Hence, the contrast of this display was 8500, while its log10 contrast was 3.93.

The color gamut was measured afterwards. The tristimulus XYZ was measured with value 255 of three channels separately. Then the results were transferred to CIE 1931-xy values, as shown in Fig. 7. The Rec.2020 and Rec.709 gamut was also shown in this figure. Results implied that the gamut of this HDR display was closed to Rec.709 due to the limitation of LCD.
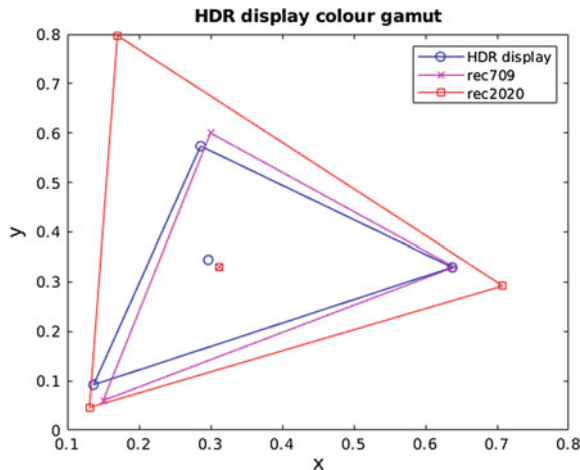


**Fig. 7.** Color gamut of LCD-DLP display

## 4   Gamut Enlarge Proposal

Wide Color Gamut (WCG) is also a significant scale of displays. Wider color gamut means more saturated colors. The gamut of OLED and QD-LCD are closed to DCI-P3 color gamut. Hence, how to enlarge the color gamut of this LCD-DLP HDR display is a valuable question. Adrian Kitai [5] described a method to use narrow band color filters designed by Kodak to enlarge the color gamut of LCD display. The narrow bandpass color filters could cover the wavelength of red, green, blue colors, so the FWHM of the spectrum output of R, G, and B will be narrow. As a result, the colors are more saturated and the color gamut is enhanced.

Similar method could be used to enlarge the LCD-DLP display's color gamut. The fundamental idea is to integrate a multiple narrow bandpass color filter in front of the projector to reshape the spectrum of the projected light. Nevertheless, some study indicates that if the color spectrum peak is too narrow, observer metamerism effect will be more serious. Thus, further measurements and psychophysical experiments would be conducted in the next stage.

## 5   Conclusions

An LCD-DLP display prototype was firstly built and optimized. Afterwards the display was calibrated and measured. The peak luminance of this display was about 8500 cd/m$^2$, and the blackness was 1 cd/m$^2$. The contrast is 8500 and log10 contrast is 3.93. The color gamut is closed to Rec709. A color gamut enhancement method was proposed.

## References

1. Barten P (1992) Physical model for the contrast sensitivity of the human eye. Proc SPIE 1666:57–72
2. Tian D, Xu L, Luo MR (2019) The characterization of HDR OLED display. Electron Imaging 10:IQSP-326
3. Baek Y, Kim H, Park S, Kim Y (2008) Colorimetric characteristics evaluation of OLED and LCD. In: International meeting on information display, 2008, pp 509–512
4. Seetzen H, Heidrich W, Stuerzlinger W et al (2004) High dynamic range display systems. ACM Trans Graph 23(3):760–768
5. Kitai A (2008) Luminescent materials and applications. Wiley, pp 137–141

# A New Auto-brightness Control Technology for Mobile Terminal Under Various Ambient Illumination

Zhaojing Xu, Cuihua Dong$^{(\boxtimes)}$, and Qing Wang

School of Light Industry Science and Technology, Key Laboratory of Green
Printing & Packaging Materials and Technology in Universities of
Shandong (Qilu University of Technology), Jinan, China
`xiaodong77llll@l63.com`

**Abstract.** The mobile terminal as a phone or a pad would be influenced by the ambient illumination when it was used in different scenarios. In order to keep good visibility, the screen backlight luminance needs to be adjusted in accordance with the ambient illumination. The high ambient lighting conditions were taken into account in this paper to find out a more universal Auto-Brightness Control (ABC) technology. The perceptual brightness of 20 test images displayed on the mobile phone were visually evaluated via categorical judgment method under six levels of ambient illumination (from dark up to 20000 lx) with six levels of screen backlight luminance. The experimental results show that the score of perceptual brightness and ambient contrast ratio (ACR) were in logarithmic relation, which has stronger relation with optimum luminance of mobile terminal. Therefore, a new ABC Technology was proposed to automatically adjust the display luminance in mobile devices to maintain visibility under various ambient illumination.

**Keywords:** High ambient illumination · Screen backlight luminance ·
Perceptual brightness · Auto-brightness control technology

## 1 Introduction

Nowadays, the mobile terminal such as a phone or a pad is used not only indoors but also outdoors because of their portability. And the change of ambient light can dramatically affect perceptions for the images or articles displayed on the mobile terminal [1]. In reality, however, ambient light is inevitable no matter indoors or outdoors [2]. Thus, how to keep good visibility under different ambient lighting conditions is a practically important concern. In order to solve this problem, the screen backlight luminance needs to be adjusted in accordance with the ambient illumination [3, 4]. Therefore, auto brightness control (ABC) technology has been widely used to automatically adjust the screen backlight luminance of mobile terminals to maintain visibility under various ambient lighting conditions [5, 6]. At present, the researches of the ABC Technology under high ambient illumination are very limited. Therefore, the high ambient lighting conditions were taken into account in this paper to find out a more universal ABC technology. Besides, it is generally known that ACR has already been

widely used to evaluate the sunlight readability of LCDs contrast ratio, which is also an important parameter to quantitatively evaluate a display performance. Therefore, ACR could be applied in this study to investigate the ABC Technology.

## 2 Experiments

In this study, the ambient illumination levels were set to 0, 500, 2000, 5000, 10000 and 20000 lx, which were simulated by a set of LED lighting modules with a CCT of approximately 5300 K. A mobile phone was employed to test the perceptual brightness. The perceptual brightness was assessed by a five-point categorical judgment (1 = Intolerable, 2 = Just tolerable, 3 = Just acceptable, 4 = General satisfied, 5 = Extremely satisfied). Moreover, the 20 test images were adopted, which were comprised of the standard images from Kodak image database and the common images browsing on mobile phone such as game, landscape buildings, webpage and so on. The screen backlight luminance levels of mobile phone were set to 3, 119, 236, 351, 467 and 583 cd/m$^2$, which were measured using a spectrophotometer of Konica Minolta CS2000 when the mobile phone screen presented the white patch under darkroom, as shown in Fig. 1. The viewing angle for mobile phone screen was 10° * 14° with the viewing distance of 40 cm between the eyes of observes and the center of the screen. The visual experiment was conducted by a panel of 10 observers who is contained with the five male and five females and their average age was 26.5 years old. All of them had normal color vision, and underwent a training session to learn the evaluated estimations before the formal experiment.
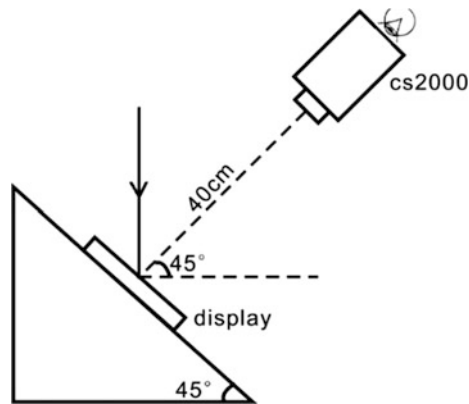


**Fig. 1.** A graphical expression of the psychophysical and measure experiment

The experiment was carried out in a darkroom. After a 2-min dark adaptation and a 1-min light adaptation, each observer was asked to evaluate the perceptual brightness of 20 test images under the 36 test lighting conditions (combination of six ambient illumination levels and six screen backlight luminance levels) which were presented to

the observers in random order. In total, 7200 judgments were performed in the whole visual experiment, i.e., 1 estimations × 20 images × 6 ambient light levels × 6 mobile phone screen backlight luminance levels × 10 observers.

## 3   Results and Discussion

### 3.1   Observer Variation

To test the validity of the estimations, coefficient of variation (CV) was employed, which would verify the agreement between ten observers in this research. The CV of the perceptual brightness was 27.69, which imply that the observers performed effectively for the perceptual brightness [7–9]. In general, the observer variations were accepted, which ensured the credibility of the experimental data.

### 3.2   Data Analysis of Categorical Judgment Method and ACR Calculation

The original numerical category scales of the perceptual brightness are grade marks actually rather than the equal interval scale, which cannot be used for data analysis. Therefore, these data must be transformed into the equal interval scale values (SV) before the further data analysis [8].

As mentioned above, ambient contrast ratio (ACR) is a significant parameter quantitatively evaluated a display performance [10–12]. In this research, $M_W$ and $M_K$, the measurements which were obtained as Fig. 1 shown, were used to calculate ACR value which is equivalent to the original formula [11, 13]. Then the ACR can be described as Eq. (1):

$$ACR = \frac{M_w}{M_k} \tag{1}$$

Here, Mw and Mk are the luminance that actually enter the human eye which includes the luminance of screen backlight and the luminance of reflecting ambient light on the mobile phone screen.

Figure 2 illustrates that the normalized SV of perceptual brightness when the ACR value changes under five levels of ambient illumination. There was an upward trend in the normalized SV of perceptual brightness with the increase of ACR. In addition, there was an obvious logarithmic relationship of perceptual brightness and ACR. Hence, the ACR would be taken the logarithm for the relationship between the IQ and ACR, as expressed in Eq. (2).

$$Y = \frac{0.228529 + 0.399455 \times R \times X + 0.01023 \times X - 0.20014 \times R \times X^2}{0.2331 \times X + 0.3349} \tag{2}$$

where X denotes ambient illumination, Y is screen backlight luminance and R is the reflectance of the mobile phone screen.
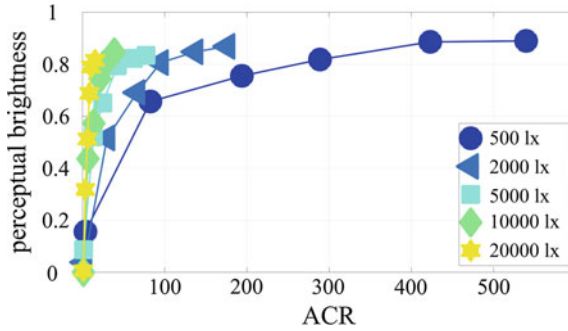
**Fig. 2.** Normalized scale value of perceptual brightness when the ACR value changes under five levels of ambient illumination

Figure 3 shows the fitting curve of perceptual brightness scores when the test image displayed on the mobile phone under the five levels of ambient illumination. The scattered point represents the experimental data and the solid line is the fitting curve. Therefore, the $R^2$ of modeling is 0.9815, which illustrated the feasibility of the model in this research. The normalized SV of ambient illumination levels which are 500, 2000, 10000, and 20000 lx were used to train the model and the data of ambient illumination level which is 5000 lx were used to test the model. And the average error between measured data and predicted data is 7.296%, which is a satisfaction agreement is obtained although errors exist.
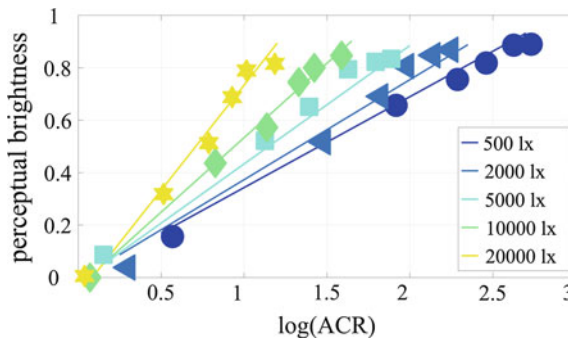


**Fig. 3.** Fitting image of perceptual brightness scores under the five levels of ambient illumination

## 4    Conclusions

In this study, a new Auto-Brightness Control (ABC) Technology based on the ACR was proposed to automatically adjust the display luminance in mobile devices to maintain visibility under various ambient illumination, which also could apply to find out the ambient illumination value suitable for image display effect.

# References

1. Wang Y, Wang X, Jie L (2017) Color appearance phenomena under high ambient illumination optik. Int J Light Electron Opt 145(S0030402617307878
2. Choi SY, Luo R, Pointer M (2007) Color appearance of a display changes under various illumination conditions
3. Kim M, Jeon DH, Kim JS et al (2018) Optimum display luminance depends on white luminance under various ambient illuminance conditions. Opt Eng 57(2):1
4. Kim SR, Lee SH, Jeon DH et al (2017) Optimum display luminance dependence on ambient illuminance. Opt Eng 56(1):017110
5. Mantiuk R, Rempel AG, Heidrich W (2009) Display considerations for night and low-illumination viewing. In: Proceedings of the symposium on applied perception in graphics & visualization
6. Kim JS, Kim SR, Lee SW (2018) A new auto-brightness control technology for transparent displays. In: 2018 IEEE international conference on consumer electronics (ICCE)
7. Trickey KA (2015) Structural models of coefficient of variation matrices. Dissertations & theses, Gradworks
8. Rui G, Xu H, Wang B et al (2012) Image quality evaluation for smart-phone displays at lighting levels of indoor and outdoor conditions. Opt Eng 51(8):4001
9. Rui G, Xu H, Wang Q et al (2013) Investigation of perceptual attributes for mobile display image quality. Opt Eng 52(8):083104
10. Jiun-Haw L, Xinyu Z, Yi-Hsin L et al (2005) High ambient-contrast-ratio display using tandem reflective liquid crystal display and organic light-emitting device. Opt Express 13 (23):9431–9438
11. Dobrowolski JA, Sullivan BT, Bajcar RC (1992) Optical interference, contrast-enhanced electroluminescent device. Appl Opt 31(28):5988–59896
12. Kelley EF (2012) Display daylight ambient contrast measurement methods and daylight readability. J Soc Inform Display 14(11):1019–1030
13. Tan G, Chen H, Wu ST (2017) Ambient contrast ratio of LCDs and OLED displays. Opt Express 25(26):33643

# Chinese Skin Colour Preference of Different Genders

Mengmeng Wang[1] and Jing Cao[2,3(✉)]

[1] School of Digital Media, Jiangnan University, Wuxi, China
mngmngwang@163.com
[2] Graduate School of Creative Industry Design, National Taiwan University of
Arts, Taipei, China
872027708@qq.com
[3] School of Media and Design, Hangzhou Dianzi University, Hangzhou, China

**Abstract.** Skin colour preference was widely studied. But limited research investigated the preferred skin colour of different genders. This study investigated the skin colour preference of the Chinese female and male based on the Leeds Liverpool skin colour database (LLSC). An facial image of Chinese female and an image of Chinese male were used in this study. Twenty-five skin colours with different skin whiteness and hue angle were rendered to these two images. A psychophysical experiment was carried out to determine the skin colour preference. Twenty-four observers were participated. The result shows that the gender of the observer have limited influence on the judgement of the skin colour preference. This study found that the preferred skin colour for different gender is different. The Chinese male with darker skin colour and Chinese female with whiter skin colour was preferred. Reddish skin colour were preferred for both genders.

**Keywords:** Skin colour · Colour preference · Skin whiteness · Psychophysics experiment

## 1 Introduction

Skin colour is an important identity of the human being. The preference of the skin colour lead the new product development in the cosmetic and digital imaging industry. The skin colour preference is depend on ones' culture background. For Asians, light skin colour is preferred. So the skin whitening products and light shade of foundations are demand greatly. The people appeared in the photo with lighter skin colour is preferred. In contrast, the tan skin colour is preferred by Europeans. The skin products that related to tan the skin are demand. The tan skin colour appeared in the photo is preferred. The relationship between skin colour preference and the skin colour attributes, such as CIELAB values, are needed for industries and also interested the researchers. Lots of research were carried out to investigate this relationships. Some researchers observed the real human face under different illuminates. They found that the preferred skin colour of the Japanese female was higher in saturation and reddish in hue compared to their actual skin colour [1]. Other researchers set up experiments

based on the digital facial images. They found that the preferred skin colour of Chinese was slightly more reddish than the actual skin colour [2]. Some researchers investigate the preferred skin colour by using printed facial image. They found that the preferred skin colour of Chinese was redder than the preferred skin colour of the Japanese [3]. Most of the research was used female subject or facial images to investigate the preferred skin colour. Also, limited research investigated the agreement between the female and male observers at the skin colour preferences.

CIELAB is widely used for accurate colour description and comparison. It is also used in skin colour preference research. Skin whiteness is an attribute which commonly used to describe skin colour. Previous research found that the whiter skin colour was preferred by the Japanese [4]. But limited research investigates the relationship between skin whiteness and preferred skin colour.

This study aimed to investigate the Chinese skin colour preference of different genders. Instead of using CIELAB value, skin whiteness and hue angle were used to determine the property of the preferred skin colour. The skin whiteness was gained through a skin whiteness index proposed by Wang et al. [5].

## 2 Methodology

The Leeds Liverpool Skin Colour database (LLSC) contained skin colour information of 188 subjects from 4 different ethnicities which are Chinese, Caucasian, South Asian and African. These skin colour information including facial images and skin colour reflectance of five facial locations. Two facial images, included one Chinese female image (OF) and one Chinese male image (OM), are selected out from the LLSC and used in this study. The ranges of the Chinese skin colour in skin whiteness and hue angles are determined through the Chinese skin colour reflectance in LLSC. To be noticed, the skin whiteness is determined through the skin whiteness formula that proposed by Wang et al. [5]. Twenty-five skin colour with different skin whiteness and hue angle combination were selected out based on these ranges. The distribution of the selected skin colour is shown in Fig. 1.

The range of the selected skin colours covered the whole Chinese skin colour gamut, as shown in Fig. 1. These 25 skin colours replaced the skin colour of the two selected facial images and generated 50 new images. These new images were used in the experiment.

A psychophysical experiment was used to investigate the skin colour preference. The paired comparison method was used in this study. The experimental interface is shown in Fig. 2.

Two images with same face but different skin colours were displayed, as shown in Fig. 2. The observer was sit in the dark room and was asked to select the preferred facial image from the displayed two images. In total, six hundred pair of images were judged. Six repeat pairs of images were also included to determine the intra-observer variation. Another six paired of images results were selected out to determine the inter-observer variation. Twenty-four observers, including twelve Chinese females and twelve Chinese males, were participated. The experimental results were converted into z-score then used to determine the skin colour preference of different genders.
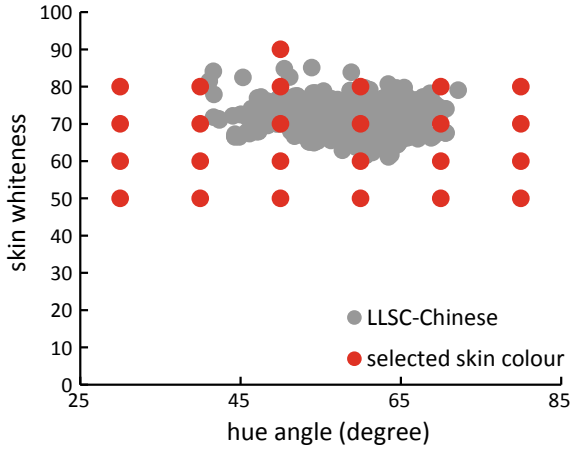
**Fig. 1.** Selected skin colour (red dot) and the Chinese skin colour range in LLSC (grey dots)
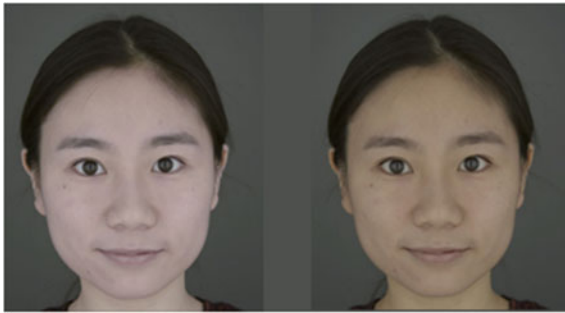


**Fig. 2.** Experimental interfaces

## 3    Result and Analysis

### 3.1    Inter-observer Variation and Intra-observer Variation

Wrong decision (WD%) is used to determine the intra-observer variation and inter-observer variation. The intra-observer variation was accessed by the repeat judgements of six pairs of stimuli images in each session. The inter-observer variation was calculated to investigate the variation of the judgement between observers. The WD% of the intra-observer variation and inter-observer variation are listed in Table 1.

**Table 1.** Intra-observer variation and inter-observer variation (WD%)

| Intra-observer variation (WD%) | Inter-observer variation (WD%) |
| --- | --- |
| 16% | 21% |

In Table 1, the inter-observer variation is larger than the intra-observer variation which is a common finding. The WD% of the intra-observer variation indicated that the observers gave a consistent response in the experiment. This validated the experimental results.

The one-way ANOVA analysis was used to determine the significance of the correlation between the skin colour preference and two skin colour attributes. The results are listed in Table 2.

**Table 2.** Significance of the correlation (p) of the skin colour preference and skin whiteness or hue angle

|  | Skin whiteness | Hue angle |
|---|---|---|
| Skin colour preference | 0.012* | 0.033* |

*indicates a *p*-value 0.05

A *p*-value no greater than 0.05 indicates that the scale has a significant impact on the results. So the skin whiteness and hue angle have significant influence to the skin colour preference, as the results listed in the Table 2.

## 3.2    Agreement Between Female and Male Observers

The correlation coefficient (*r*) was used to determine the agreement between the female and male Chinese observers at judging OF image and OM image respectively. The results are shown in Table 3.

**Table 3** The *r* of the judgement between two genders with images varied in whiteness and hue angle.

| Attributes | Images | | |
|---|---|---|---|
|  | OF | OM | Mean |
| Skin whiteness | 0.76 | 0.95 | 0.86 |
| Hue angle | 0.99 | 0.94 | 0.97 |

The mean *r* value listed in the Table 3 shows that the female and male observer have good agreement at skin colour preference. This indicated that the gender of the observer have limited impact on the skin colour preference judgement. The agreement of the preferred Chinese female's skin colour whiteness is poorest (*r* = 0.76). This indicated that the female and male observers were less agreeable to the preferred Chinese female skin colour whiteness. Overall, the female and male observers have better agreement in terms of the hue angle (average *r* = 0.97) than the whiteness (average *r* = 0.86).

### 3.3    Final Results Versus Whiteness Versus Hue

The experimental results (z-scores) with the same skin whiteness/hue angle were averaged first. Then, they were plotted in the line chart to investigate the trend of the variation of skin colour preference in terms of skin whiteness and hue angle, as shown in Fig. 3. The red line and the blue line in the figure were the experimental results of OF images and OM images, respectively.



(a). skin whiteness

(b). hue angle
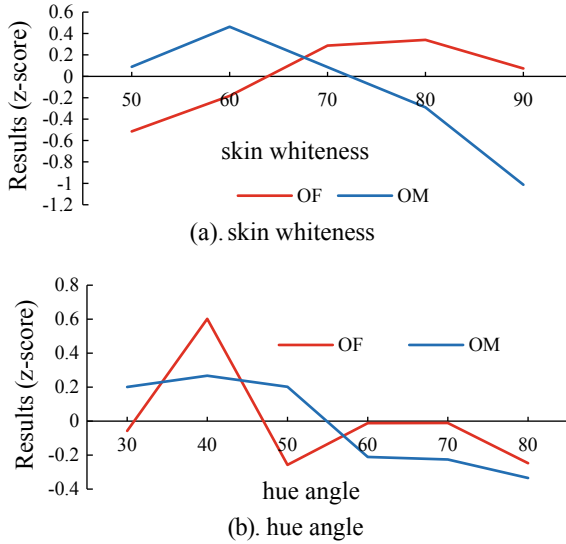
**Fig. 3.**  Response of the observers to the OF and OM images with different

The trend of lines in Fig. 3 shows that the preferred skin colour for Chinese male and female are different. For the skin whiteness, Chinese male and female have opposite trend. Chinese male with skin whiteness less than 70 was preferred. Chinese female with skin whiteness more than about 65 was found to be preferred. The most preferred skin whiteness were found to be 60 and 80, for Chinese male and female respectively. This indicated that the Chinese male with darker skin and the Chinese female with whiter skin are preferred. For the hue angle of the skin colour, both gender's skin colour were both found to be preferred when hue angle is 40°. The Chinese male have larger range of hue angle (30°–50°) found out to be the preferred skin colour. This indicated that reddish skin colour is preferred for both gender.

## 4   Conclusions

The Chinese skin colour preference of different genders was investigated in this study. Based on the LLSC database, twenty-five skin colours, which cover the LLSC Chinese skin colour gamut, were selected to use. These skin colours were rendered to two facial

images, including one Chinese female image and one Chinese male image. The psychophysical experiment results showed that the Chinese skin colour preference of different gender is not the same. The darker skin colour is preferred by the Chinese male. The whiter skin colour is preferred by the Chinese female. Reddish skin colour is preferred by both gender. The preferred skin colours' hue angle range of Chinese male is wider than the Chinese female.

**Compliance with Ethical Standards**

**Conflict of Interest**: The authors declare that they have no conflict of interest.

**Ethical approval**: All procedures performed in studies involving human participants were in accordance with the ethical standards of the school of digital media, Jiangnan University and approved by the university research ethical committee and with the 1964 Helsinki declaration and its later amendments or comparable ethical standards. The images and skin colour information are from Leeds Liverpool Skin Colour Database.

**Informed consent**: Informed consent was obtained from all individual participants included in the study.

# References

1. Yano T, Hashimoto K (1997) Preference for Japanese complexion color under illumination. Color Res Appl 22(4):269–274
2. Zeng H, Luo R (2013) Colour and tolerance of preferred skin colours on digital photographic images. Color Res Appl 38(1):30–45
3. Fan Y, Deng P, Tsuruoka H et al (2011) On the preferred flesh color of Japanese and Chinese and the determining factors investigation of the younger generation using method of successive categories and semantic differential method. J Soc Photogr Sci Technol Jpn 73:31–38
4. Yoshikawa H, Kikuchi K, Yaguchi H et al (2012) Effect of chromatic components on facial skin whiteness. Color Res Appl 37(4):281–291
5. Wang M, Luo MR, Xiao K (2017) The impact of skin colour on facial impressions. AIC 2017 Jeju:89–89

# Yellow Color Acquisition of Old Yellowed Book Based on Color Management with Small Color Gamut

Junfeng Li[⊠], Shiwei Liu, and Miaoxin Li

School of Packaging and Printing Engineering, Henan University of Animal Husbandry and Economy, Zhengzhou, China
ljf@hnuahe.edu.cn

**Abstract.** The existing scanning device mostly adopts the standard color cards with large color gamut for color management. It is difficult to accurately acquire the yellow color of old yellowed books. This study aims to establish a color management method based on small color gamut to achieve an accurate recording of the yellow color of old books. The color values of old books are collected first. Then a standard color card with small color gamut that can cover the yellow color of the book is prepared. The standard color card is utilized as a tool to perform color management on scanning device, realizing an accurate collection of the yellow color. The experimental results show that the color difference between the yellow color acquired and the actual color of the book is significantly smaller than that of color management with large color gamut. This method can also be applied to color management of products such as bronze, ceramics and wood.

**Keywords:** Color management · Small color gamut · Old yellowed book · Scanning device

## 1 Introduction

The yellow color of old yellowed books can give readers a sincere historical feeling. It is necessary to accurately record the characteristic yellow when digitizing old books. Traditional method utilizes color-managed scanning devices with high spatial resolution to digitize old books [1]. The color management of the devices usually adopts standard color cards (e.g., IT8.7/2, ColorChecker Classic) as color standards to calibrate and characterize the color of the devices [2, 3]. It can represent all colors indiscriminately and device-independently when converting the device-dependent RGB color into CIELAB color space since the color patches of the standard color cards span a large color gamut in the CIELAB color space. However, it is difficult to accurately acquire the yellow color of old yellowed books because the yellow colors of old books only span a small color in the space.

This work introduces a method to accurately record the yellow color of old yellowed books based on color management with small color gamut. The method to prepare the standard color card with small color gamut and the process to manage the

color of the scanning device with the prepared card will be introduced in Sect. 2. Section 3 gives the experimental results of the proposed method. Comparisons with color management based on standard color card, IT8.7/2, with large color gamut will also be shown in this section. At last, conclusions relating to this work will be drawn in Sect. 4.

## 2 Methods

### 2.1 Preparation of the Standard Color Card with Small Color Gamut

The color (CIELAB) value of the old yellowed book to be digitalized is measured by a spectrophotometer (e.g., GretagMacbeth SpectroEye) first. Then this value is used as center point and sample colors ($\Delta E_{76} \leq 10$ under CIE Standard Illuminant D65 for the CIE 10° Standard Observer) around this reference center uniformly in the CIELAB color space. Apparently, these sampled colors have a small color gamut and enclose the color of the old yellowed book in the CIELAB color space.

An old yellowed book was measured by the GretagMacbeth SpectroEye mentioned above. Its CIELAB color value obtained is $L^* = 89$, $a^* = 0$ and $b^* = 16$. Then 540 colors around the reference center point were selected in this work as the standard color. These colors were prepared into 1 cm * 1 cm color patches in Photoshop and then stored in digital TIFF format. All color patches were arranged as a 27 * 20 matrix as shown in Fig. 1.
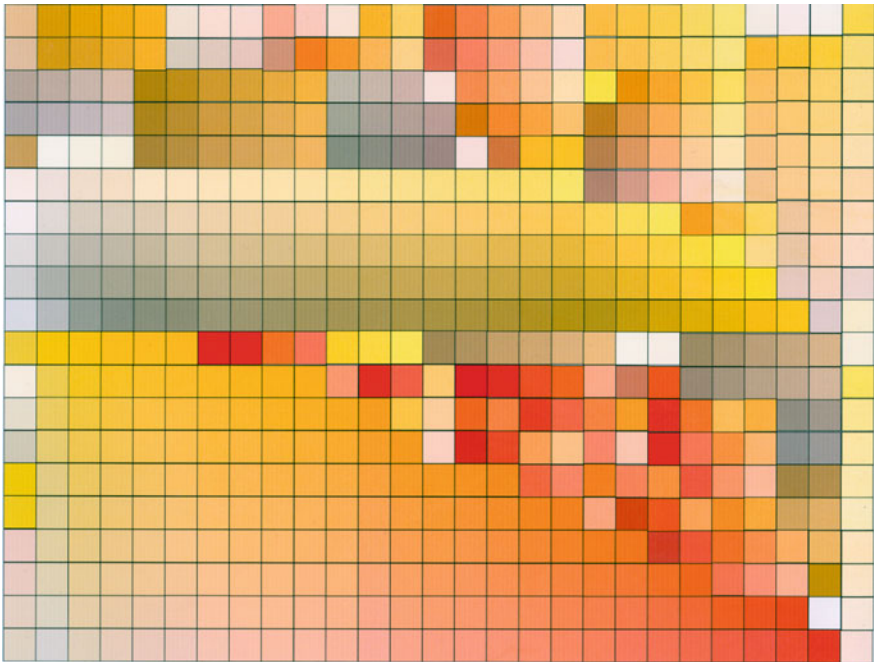


**Fig. 1.** 540 digital color patches prepared

Color management of scanning devices requires object standard color card. Thus the digital color card designed in Fig. 1 needs to be printed by a color-managed printer. It's important to note that the printer should be color-managed first. This work applied the traditional color management process [4, 5] to control the color of the printer. The printer used in this work is a EPSONSTYLUS PRO8900 printer. The color patches were printed on matt paper with a size of 29.7 cm × 420 cm (A3).

The color values of the printed color patches were measured by the GretagMecbeth SpectroEye. Then these color values are imported in a TXT file. It is worth mentioning that the values measured are numbered and formatted according to the requirement of ProfileMaker 5.0.

As mentioned above, the color patches were arranged as a 27 * 20 matrix, so this work adopted 27 pieces of color data as a set and a total of twenty sets of data were obtained. Here we applied A1, A2, A3 … A27, B1, B2, B3 … B27, C1 … T26, T27 to arrange the data, as shown in Fig. 2.

## 2.2 Generation of ICC Profile for Scanning Device with the Prepared Standard Color Card

As the special standard color card with small color gamut and its color values in the TXT file compatible to ProfileMaker 5.0 were prepared, the ICC profile of the scanning device can be prepared. ProfileMaker 5.0 was used to make the ICC profile of the scanning device in this work.

The process to make the ICC profile with the prepared standard color card is similar with that of traditional standard color cards. First, the scanning device captures the standard color card to obtain the digital image of the card. Then the prepared TXT file and the scanned image of the prepared standard color card is imported into ProfileMaker 5.0. Lastly, click on the start button and a special ICC profile will be generated.

## 3   Results

In order to test the effectiveness of the proposed method, a scanner produced by Microtek company with the model called ScanMakeri800plus is applied as the acquisition device. Two ICC profiles are generated by ProfileMaker 5.0 with the perceptual rendering intent. One is generated from the traditional standard color card, IT8.7/2, the other is generated from the standard color card prepared in this work.

The old book mentioned above is selected as testing samples to acquire its color. It is digitalized first by the scanner to get its digital image. Photoshop is used to embed the two ICC profiles into the digital image respectively. Then two color-managed images can be obtained. In other words, one image's color is managed by the traditional standard color card and another is by the prepared color card. The color values obtained by different profiles are listed in Table 1.

The color values obtained by the two profiles are compared with the original color value of the book. Lightness, hue, chroma and color difference under CIE Standard Illuminant D65 for the CIE 10° Standard Observer are selected as evaluation indexes.

```
LGOROWLENGTH 27
CREATED          "4/27/2019"  # Time: 20:40
INSTRUMENTATION    "Unknown"
MEASUREMENT_SOURCE    "Illumination=D50      ObserverAngle=2?WhiteBase=Abs         Filter=Unknown"
KEYWORD          "SampleID"
KEYWORD          "SampleName"
BEGIN_DATA_FORMAT
SampleID SampleName        XYZ_X   XYZ_Y   XYZ_Z   Lab_L   Lab_a   Lab_b   LAH_A   LAH_H
END_DATA_FORMAT
NUMBER_OF_SETS 540
BEGIN_DATA
1        A1        57.11    59.72    16.97    81.69    -1.19    50.37    50.38    91.35
2        A2        72.09    74.37    62.12    89.09    0.79     -0.74    1.08     316.87
3        A3        70.44    71.3     60.34    87.63    3.61     -1.52    3.92     337.17
4        A4        70.64    72.58    57.85    88.24    1.39     2.06     2.49     55.99
5        A5        62.4     66.34    24.6     85.16    -3.61    40.81    40.97    95.06
6        A6        58.43    60.99    20.47    82.37    -0.96    43.94    43.95    91.25
7        A7        55.53    56.73    16.56    80.03    2.06     48.46    48.5     87.57
8        A8        53.81    54.04    14.86    78.48    4.37     49.97    50.16    85
9        A9        51.67    50.63    13.98    76.45    7.57     48.74    49.32    81.17
10       A10       61.24    61.17    37.33    82.47    5.3      16.25    17.09    71.94
11       A11       53.55    50.87    23.39    76.6     11.84    28.27    30.65    67.28
12       A12       46.75    41.17    14.15    70.29    20.83    37.66    43.04    61.05
13       A13       42.15    34.15    10.06    65.08    29.97    40.63    50.49    53.59
14       A14       34.72    26.64    5.89     58.63    33.99    45.69    56.95    53.35
15       A15       56.19    57.29    19.23    80.34    2.33     43.03    43.09    86.9
16       A16       49.33    47.84    10.47    74.72    8.82     55.92    56.61    81.04
17       A17       66.4     67.05    50.04    85.53    3.87     5.76     6.94     56.1
18       A18       58.93    56.34    40.19    79.8     11.32    7.82     13.76    34.64
19       A19       51.1     45.73    25.6     73.37    19.39    18.69    26.93    43.95
20       A20       64.2     63.68    48.18    83.79    6.42     4.91     8.08     37.41
21       A21       64.78    64.61    48.79    84.28    5.62     5.04     7.55     41.89
22       A22       63.39    64.85    48.5     84.4     1.94     5.59     5.92     70.86
23       A23       47.25    46.16    8.99     73.65    7.75     59.06    59.57    82.52
24       A24       43.13    42.11    8.38     70.94    7.58     56.6     57.11    82.37
25       A25       39.25    38.28    6.53     68.22    7.49     59.35    59.82    82.81
26       A26       35.91    34.86    5.96     65.63    7.82     57.46    57.99    82.25
27       A27       48.49    47.56    25.61    74.54    7.3      20.7     21.95    70.57
28       B1        58.73    61.33    24.63    82.55    -1.01    36.26    36.27    91.6
29       B2        55.04    56.44    14.28    79.86    1.53     53.82    53.84    88.37
30       B3        53.16    53.25    12.78    78.02    4.69     54.69    54.89    85.1
31       B4        51.49    50.62    12.24    76.45    7.14     53.51    53.98    82.4
32       B5        63.04    66.71    27.83    85.35    -2.95    35.53    35.65    94.75
33       B6        59.4     61.82    23.06    82.81    -0.51    39.61    39.61    90.74
34       B7        56.42    57.84    18.66    80.65    1.58     44.79    44.82    87.98
35       B8        53.81    53.83    16.63    78.36    4.88     45.43    45.69    83.87
36       B9        51.99    50.97    15.76    76.66    7.54     44.57    45.2     80.4
```

**Fig. 2.** Format of the TXT file for the prepared standard color card

**Table 1.** Color values obtained by different profiles

|          | $L^*$ | $a^*$ | $b^*$ |
|----------|-------|-------|-------|
| Original | 89    | 0     | 16    |
| IT8.7/1  | 91    | 2     | 12    |
| Proposed | 90    | 1     | 16    |

The results are listed in Table 2. It is apparent that the color acquisition accuracy of the proposed method is significantly better than that of the traditional method.

**Table 2.**  Result Comparisons of prepared color card and IT8.7/1

|          | $\Delta L^*$ | $\Delta a^*$ | $\Delta b^*$ | $\Delta h^*$ | $\Delta C^*$ | $\Delta E_{76}$ |
|----------|------|------|------|------|------|------|
| IT8.7/1  | 1    | 2    | 4    | 9.46 | 3.83 | 4.58 |
| Proposed | 1    | 1    | 0    | 3.58 | 0.03 | 1.41 |

## 4    Conclusions

A color management method based on small color gamut to achieve the accurate recording of the yellow color of old yellowed books is proposed in this work. A color card with small color gamut is prepared first based on the color of old yellowed book. Then the card is used to perform color management on the scanning device to realize an accurate acquisition of the book's yellow color. Experimental results indicate the effectiveness of the proposed method. It is notable that the proposed method can also be applied to color management of products that have small color gamut, such as bronzes, ceramics and woods.

## References

1. Delaney JK, Conover DM, Dooley KA et al (2018) Integrated x-ray fluorescence and diffuse visible-to-near-infrared reflectance scanner for standoff elemental and molecular spectroscopic imaging of paints and works on paper. Herit Sci 6(1):31
2. Bühler P, Schlaich P, Sinner D (1998) Digitales colormanagement. Springer, Berlin
3. Gershbock R (1991) Image acquisition: quality control for document image scanners. In: Proceedings of the SPIE 10259. Standards for electronic imaging systems. San Jose, CA, United States
4. Guo G, Xu Y, Li Q (2010) Scanner color chart making and its application in printing color conversion. In: International conference on measuring technology & mechatronics automation. Changsha City, China
5. Sharma A (2006) Methodology for evaluating the quality of icc profiles: scanner, monitor, and printer. J Imaging Sci Technol 50(5):469–480

# Research Review of Color Appearance Phenomenon and Models

Qifeng Chen[1], Xue Li[1], Linyi Chen[1], Guangxue Chen[1(✉)], and Fushou Yin[2]

[1] Key Laboratory of Pulp and Paper, South China University of Technology, Guangzhou, China
chengx@scut.edu.cn
[2] Guangzhou Hengyuan Printing Co., Ltd., Guangzhou, China

**Abstract.** Color appearance models are of significance for researching in the area of color science, especially the cross-media color reproduction and transfer of images. These models can be used to solve series of problems with color appearance phenomenon, such as color contrast and chromatic adaptation, and can also be used to accurately predicted the perceptual attributes of color appearance under various viewing conditions included light source, illumination level, visual background and medium. In this article, a research review of color appearance models are provided with the illustration of the definition, the characteristics and suitable range, and a summary of the basic framework and development process, application values and areas are also included in this paper with the problems of color appearance models to be solved, aiming to offer the references for the same trades working in color transfer and reproduction related fields.

**Keywords:** Color appearance phenomenon · Color appearance model · Human color vision

## 1 Introduction

In the International Commission on Illumination (CIE) standard colorimetric, the color stimulus based on reflecting materials is defined very strictly. It should be viewed in specific conditions with illumination level, uniform background, medium and view geometry, and the color differences are approximate perceived by calculating the length from one stimulus to another in the color space CIELAB [1]. While virtually the changes with color appearance under different conditions cannot be provided with a numberical description due to the non-uniform CIE color space on vision [2]. Thus, the color appearance models are constantly developed by related scientists, which can be used to predicted the perceptual attributes of color appearance accurately, and taking the color appearance phenomenon into consideration, such as chromatic adaptation and color contrast etc.

Color appearance is defined as the perceptual attributes of color stimuli which is related to complicated visual stimulus and varies viewing conditions. Such a series of attributes include brightness, lightness, colorfulness, chroma, saturation, and hue, are

playing important roles. In terms of the theory of Wyszecki [3], a single color attribute is presented individually, the practical threats of colorimetry are made quite obvious, due to the subjective factors with observers illumination, medium or background. The detail descriptions of attributes are as following:

(1) **Hue**. As one of the judgments of Munsell color order system with the fundamental scaling, the hue is shown by a roundness devided into ten parts of color perception [4]. In fact, in terms of the NCS system, the color appearance can be specified by its similarity to essential color based on different scaling [3].

(2) **Chroma**. It is referred to a numerical scale with maximum and minimum values, which minimum chroma is zero represented a white, or black. With the extending for the chroma numbers, the perception of color will be more evident. On the chroma scaling, two coordinate distances are represented coordinate variations in perceived chroma [5].

(3) **Lightness**. The lightness can also be called the value, is defined on a numerical scaling, in which ranges from zero appointed to have the equal lightness as black, and to ten appointed to have the equal lightness as white for the same color [5].

(4) **Brightness, Colorfulness and Saturation**. To give the color appearance illustrations, these attributes are provides with a kind of transformations between some colors and scaling [6]. Included are scales for brightness (a receptive degree of lightness based on human vision), colorfulness (a absolute value for a color stimuli), and saturation (relative proportion of the colorfulness to brightness based on a stimuli of human color vision, expressed in Formula (1)).

$$S = {C}/{B} \qquad (1)$$

When the lowest-level sensory responses of an average human observer are factored in, the phenomenon of color appearance has been entered [7]. More complex visual stimulus can not be illustrated by physical measurements or illumination easily and independently [1]. Besides, some phenomenon of colorimetry have been provided really and truly with characteristics beyond description in human daily life. For example, the scenes usually appear more darker and colorless contrast on an overcast day than on a sunny day [2], or stars disappear from sight during the day time [2].

Some significant phenomenons of color appearance with human color vision are listed as following:

(1) **Bezold-Brücke Hue Effect**. The Bezold-Brücke phenomena, refers to the situation in which the hue of visual stimulus will change when the illumination increases, was defined by Brücke. It is yellower at yellow-green spots and high luminance with the enhance of hue [8]. In addition, the theoretical hue shift is a function of comparison of hues in the color mixture system, it is the matter with displays and other devices, if the hue doesn't shift.

(2) **Shift Abney Effect**. A bundle of monochromatic light, when mixed with white light, not only becomes desaturated but also changes in hue in terms of the Abney effect. Abney published a quantitative study of this effect that has been named after him. The effect describes hue shifts as a function of purity [9]. At that time,

Abney's white was produced by a carbon-arc lamp with a color temperature of nearly 3700 K [10]. However, the choice of white light is crucial when used for adaptations or color-plus-white experiments [11].

(3) **Helmholtz-Kohlrausch Effect**. For a specific color source, the H-K effect is the influence of color purity on the perceived brightness that not only depend on the tristimulus Y value, but also can enhance color saturation with the constant luminance. The so-called Helmholtz- Kohlrausch effect can be provided with the empirical significance of differently saturated colors, which is also related with the description of brightness or luminance discrepancies [12].

(4) **Hunt Effect and Stevens Effect**. Some colors occurs more saturated to the light-adapted eye than to the dark-adapted eye [13], such as the color appearance of objects is more soft and bright in the summer afternoon than in the evening, which are described by Hunt. It refers to the brightness of color perception will arise when the level of illuminance is arose, and for the same image, it is explained that the enhance of brightness of illuminance can influence color contrast in terms of Stevens effect.

In addition, some example of color appearance phenomenon related with images are lightness contrast, crispening, hue spreading, color constancy and color memory. etc.
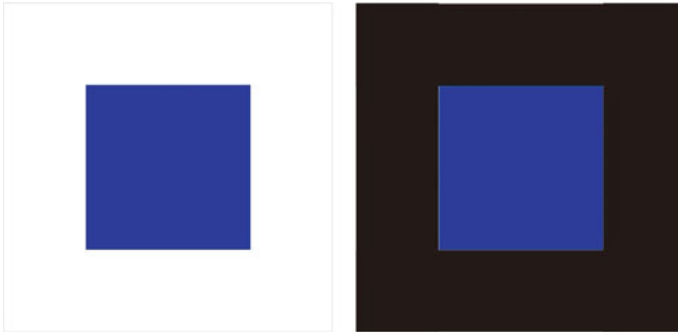


**Fig. 1.** Demonstration of simultaneous lightness contrast

As can be seen from the Fig. 1, two small blue squares of different lightness, higher on the dark background and lower on the light background, in spite of the fact that they are the same lightness when calculated from their spectral reflectance (physically identical). Moreover, Fig. 2 demonstrates hue spreading, a blurry light-blue annulus in the figure can be observed although the stimulus consists of only gray and blue lines on a uniform white background [14, 15].

More recently, the color appearance model is playing an important role in the modern color research, especially the image appearance model (iCAM) which allows images to reproduce and transfer between two different mediums, and view in different environments [2]. This work provides a review of the description of color appearance
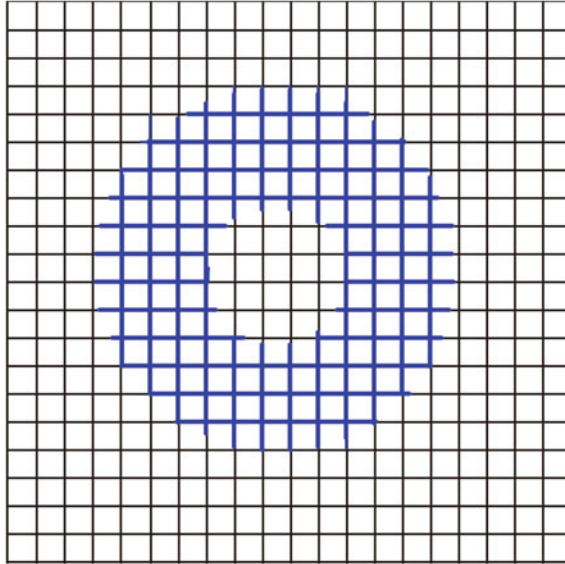
**Fig. 2.** Demonstration of hue spreading phenomenon

science, including its phenomenon, development process of models and practical application, and related flow framework are also discussed.

## 2    Color Appearance Models with Basic Framework

Based on the basic colorimety, the color appearance models aim to extend these basal color measurement technologies mathematical model to illustrate the color difference perceptions and color of stimulus in complex viewing environments. Such models have been founded in the late twentieth centuries. There are many models that have been proposed from the CIELAB color space to the iCAM model, among them, CIECAM02 is the symbolic model in modern colorimety.

### 2.1    Early Models Developed from CIELAB

The CIELAB is a color space that coordinates referred to the 1976 L*a*b*, and it is the prototype of color appearance model because the perceived attributes and their correlates of color can be calculated well from L* (lightness), a* (redness-greenness) and b* (yellowness-blueness) [16]. Figure 3 illustrates the calculation process in which the CIEXYZ values for a stimulus and a white under perfect viewing environments are convert into color appearance in the CIELAB coordinates as approximate connections. Firstly, inputting CIE XYZ values of stimulus and an ideal white, XnYnZn, and then a von Kries-type model of chromatic adaptation acts on the tristimulus values that are standardized to the white point [1]. A cube-root function is represented the standardized values that are controlled to a non-linearity compression, as shown in Formula 2.

Finally, combining with these compressed signals, the values of perception that include L*, a* and b* are expressed by these correlates [2].
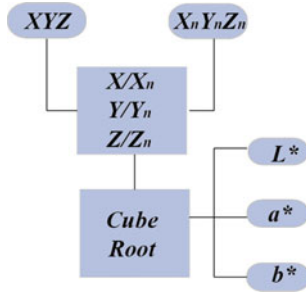


**Fig. 3.** Flow chart of computation of CIELAB coordinates

$$\begin{cases} L* = 116\left(Y/Y_n\right)^{1/3} - 16 \\ a* = 500\left[\left(X/X_n\right)^{1/3} - \left(Y/Y_n\right)^{1/3}\right] \\ b* = 200\left[\left(Y/Y_n\right)^{1/3} - \left(Z/Z_n\right)^{1/3}\right] \end{cases} \quad (2)$$

However, in the CIELAB, the color differences and tolerances cannot be represented as simple distances so simply, because of the space is non-uniform [17]. Some early attempts have been made to develop the color appearance models with a quantitative calculation in the early 1990s. At first, more quantified models were extended by RWG Hunt in 1982, which is called Hunt color appearance model [18, 19], and by Y. Nayatani and his coworkers, which is called Nayatani color appearance model. Afterwards [20, 21], RLAB color appearance model were proposed by Professor Fairchild on the foundation of color adaptation in 1993, then LLAB color appearance model is proposed by M. R. Luo and coworkers. There is also neural models such as the ATD model proposed by Guth [22, 23]. Another color appearance model is the Retinx theory proposed by E. Land that considers a special distribution of all pixels in the field of view [24].

## 2.2 CIECAM97s Color Appearance Model

Figure 2 illustrated the asymmetric matching framework of the CIECAM97s color appearance model, which shows two stages [5].

In the first stage, starting with computing the CIEXYZ tristimulus coordinates of a test stimuli with the information of light, and next step is to transform the tristimulus to the cone responses of adaptation under a standardized viewing conditions, and output

these adapted cone responses depends on the context that specifying parameters set by users, it can be illustrated in the sigmoidal nonlincarity figure [5]. In the second stage, an illustration of the transformation between color appearance attributes and adapted cone responses is given. It is opponent process model that counts in which these signals are divided into achromatic (A), yellow/blue (Y/B), red/green (R/G), each of them could be provided a set of adapted cone signals, and then transformed the six attributes' values (Fig. 4).
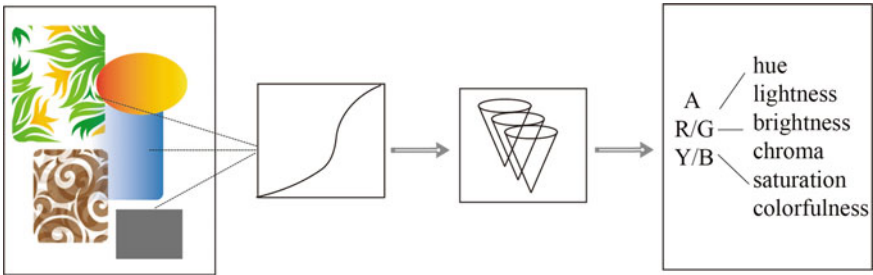


**Fig. 4.** Flow chart of CIECAM97s, as used to predict color appearance attributes

In general, the research of CIECAM97s bridges basic visual processing with applying on color order system, which takes a various of complex factors into context, such as the adapted of state of observer, the shape and size of stimulus and its global surroundings, and further studies are needed to be done.

### 2.3    CIECAM02 Color Appearance Model

A basic chart framework of the description of CIECAM02 is shown in Fig. 5. Mainly, some complex factors are considered with the levels of luminance and the relative luminance of surroundings [1]. Through the CAT02, an implicit reference viewing
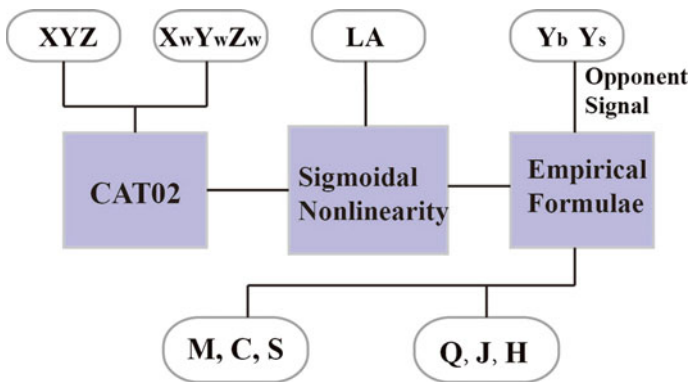


**Fig. 5.** Basic framework of CIECAM02 with additional input information and output correlates

environment on corresponding colors can be inputted. Those results, outputting computational attributes of chroma (C), brightness (Q), colorfulness (M), lightness (J), saturation (S), and hue (H) through inemperical formulae.

What's more, they still have several issues are not addressed [25], in which can cause the different position between spectrum locus and physiological cone primaries, and it is difficult to acquire the action of primary octant adaptation [26].

## 2.4  Image Color Appearance Model—iCAM

When the image is transferred and reproduced across different media or display, its color can not be accurately expressed. The object of image color appearance model (iCAM) was to predicted the appearance of complicated conditions and images for practical applications [27]. The framework and initial implementation of the model are presented with examples that illustrate its phenomenon for chromatic adaptation, color difference, appearance scales crispening, spreading, HDR image rendering, and image quality measurement [15].

All the input observation conditions of the iCAM color appearance model are obtained from the image, which framework is classified as two parts. In the first part, to input these tristimulus values that are switched into chromatic adaptation transformation, called CAT02 by a series of computational process. After completing color adaptation, the X'Y'Z' is switched into Image Processing Transform (IPT) [28], which the flow as is illustrated in Fig. 6  [29].



**Fig. 6.**  Flow chart of iCAM to creat IPT color gamut mapping model

Currently, the new iCAM06 color appearance model has been recommended. Combining with the characteristic of uniform color space about color appearance model, the Pixels could be treated as independent color stimuli with consistent viewing conditions, and also can be used for complex image stimuli [27]. It is expected that the implementation of this model framework will be refined as new data become available. What's more, the CAM16 color appearance model with great predictions of color correlates for many application has been given, which can produce high quality and visual experimental results [30]. As a more comprehensive current color appearance model, CAM16 has the applicability of adapt the augmented reality (AR) environments [31].

# 3   Application and Values of Color Appearance Models

Such color appearance models have been required for practical applications, which not only could be utilized for image collection and related instrumentation in the industry, but also applied with cross-media color reproduction of image.

Firstly, these models are researched on smart display or image capture, in which continuous functions to calculate different surround parameters. It is widely used for mobile phones, PDA and Portable DVD players [32]. They are small and convenient to be carried around and viewed under various surround conditions.

What's more, on the application field of color management technologies, it is divided into CMS (color management systems), CAD (computer-aided design), CCM (computer color matching system), low-light image system, and truly transfer of information for color handlers [33]. To make sure the consistent color appearance of image, an accurate calculating of the corresponding colors under different media and observation conditions should be provided [34]. It is common to see that the soft proofing of the screen can also not be separated from color management system based on color appearance models [35].

Thirdly, the color appearance model can be carried out non-linear color correction, device characterization, color adaptive conversion and device gamut mapping on the foundation of traditional chroma matching technology [36]. Some related research on the influence between color compression and correction are given to match some factors.

Finally, it is possible to extend the use of color appearance models to describe image quality metric, combining with a uniform color space that corresponds with perceptual appearance. A color difference metric also allows to calculate meaningful changes between standard material, and a reproduction of this color. It can be typically achieved by predicting the quality difference between two images. Meanwhile, using their framework as a video quality metric is similar to the image quality metric [37], and it can output in perceptually meaningful terms, such as changes in lightness, saturation, or sharpness.

# 4   Conclusions

The characteristic color appearance mode is widely utilized in various areas of application in daily life or industrial production, such as standardized CIECAM97s, CIE-CAM02, and iCAM that are based on traditional colorimetry [38]. Each color appearance model has its own representative framework and contents, with the capacity of transforming from color stimuli of a spatially-simple under specify viewing conditions to practical color appearance attributes that include chroma, saturation, brightness, lightness, and colorfulness.

In this article, a review of popular color appearance models recently used with the illustration of single model framework characteristics, combining with the actual influence of color appearance phenomena on human color vision and viewing conditions [1]. Finally, the application fields and values of these common models are given, mainly performed with the images transfer and cross-media color reproduction. It has

been further studied that advances in color appearance models would require more rigorous treatment of spatial appearance phenomenon and a great deal of visual data.

# References

1. Fairchild MD (2005) Color appearance models. Wiley, Chichester
2. Fairchild MD (2013) Color appearance models. Wiley
3. Wyszecki G (1973) Current developments in colorimetry. AIC Color 73:21–51
4. Plataniotis KN, Venetsanopoulos AN (2000) Color image processing and applications. Springer, February 18
5. Shevell SK (ed) (2003) The science of color. Elsevier
6. Johnson GM, Fairchild MD (2003) Measuring images: differences, quality, and appearance. In: Human vision and electronic imaging VIII, vol 5007. International society for optics and photonics, pp 51–60
7. Brainard DH (2003) Color appearance and color difference specification. Sci Color 5:191–216
8. Walraven PL (1961) On the Bezold-Brücke phenomenon. JOSA 51(10):1113–1116
9. Kurtenbach W, Sternheim CE, Spillmann L (1984) Change in hue of spectral colors by dilution with white light (Abney effect). JOSA A 1(4):365–372
10. Abney W (1910) On the changes in hue of spectrum colours by dilution with white light. Proc R Soc London 83:120–127
11. Larimer J, Krantz DH, Cicerone CM (1975) Opponent process additivity. I: red/green equilibria. Vision Res 14:1127–1140
12. Nayatani Y (1998) A colorimetric explanation of the Helmholtz–Kohlrausch effect. Color Research & Application: Endorsed by Inter-Society Color Council, The Colour Group (Great Britain), Canadian Society for Color, Color Science Association of Japan, Dutch Society for the Study of Color, The Swedish Colour Centre Foundation, Colour Society of Australia, Centre Français de la Couleur 23(6):374–378
13. Donofrio RL (2011) The Helmholtz-Kohlrausch effect. J Soc Inform Display 19(10):658–664
14. Hunt RWG (1950) The effects of daylight and tungsten light-adaptation on color perception. J Opt Soc Am 40:362–371
15. Fairchild MD, Johnson GM (2004) The iCAM framework for image appearance, image differences, and image quality. J Electron Imaging 13:126–138
16. Imai FH (2009) Reviewing state-of-the-art imaging modalities and its potential for biomedical applications. J Dent 37S:e7–14
17. Richter K (1980) Cube-root color spaces and chromatic adaptation. Color Res Appl 5:25–43
18. Hunt RWG (1982) A Model of colour vision for predicting colour appearance. Color Res Appl 7(2):297–314
19. Hunt RWG (1994) An improved predictor of colourfulness in a model of colour vision. Color Res Appl 19:23–33
20. Nayatani Y, Takahama K, Sobagaki H et al (1982) On exponents of a nonlinear model of chromatic adaptation. Color Res Appl 7:34–45

21. Nayatani Y, Hashimoto K, Takahama K et al (1987) Whitenessblackness and brightness response in a nonlinear color appearance model. Color Res Appl 12:121–127

22. Guth SL (1994) Further applications of the ATD model for color vision. Proc SPIE 2414:12–26

23. Guth SL (1995) ATD model for color vision I: background. Proc SPIE 2170:149–162

24. McCann JJ, McKee SP, Taylor TH (1976) Quantitative studies in Retinex theory. Vis Res 15:445–458

25. Moroney N Fairchild MD, Hunt RWG et al (2002) The CIECAM02 color appearance model. In: Color and imaging conference, no (1). Society for Imaging Science and Technology, pp 23–27

26. Brill MH, Süsstrunk S (2008) Repairing gamut problems in CIECAM02: a progress report. Color Res Appl 33(5):424–426

27. Fairchild MD, Johnson GM (2002) Meet iCAM: a next-generation color appearance model. In: Color and imaging conference, no 1. Society for Imaging Science and Technology, pp 33–38

28. Liu Z, Lu L, Tsai S (2009) The research on mechanism of color management system based on iCAM color appearance model [J]. Comput Math Appl 57(11–12):1829–1834

29. Ebner F, Fairchld MD (1998) IPT development and testing of a color space (IPT) with improved hue uniformity. In: Proceedings of IS&T/SID 6th color imaging conference, IS&T, pp 8–13

30. Luo MR, Pointer MR (2018) CIE colour appearance models: a current perspective. Light Res Technol 50(1):129–140

31. Hassani N, Murdoch MJ (2019) Investigating color appearance in optical see-through augmented reality. Color Res Appl 44(4):492–507

32. Park YK, Li CJ, Luo MR et al (2007) Applying CIECAM02 for mobile display viewing conditions. In: Color and imaging conference, no 1. Society for Imaging Science and Technology, pp 169–173

33. Qingfen T (2014) Research on color digital image color difference evaluation based on iCAM framework. Zhejiang University

34. Hongyong J (2018) Application of color appearance model in cross-media image replication. Packag Eng 39(23):224–230

35. Li C (2011) Research on color matching of paper digital proofing and screen soft proofing. Shandong Institute of Light Industry

36. Mantiuk R, Mantiuk R, Tomaszewska A et al (2009) Color correction for tone mapping. In: Computer graphics forum, vol 28, no 2. Blackwell Publishing Ltd, Oxford, UK, pp 193–202

37. Fairchild MD (2010) The perceptibility of video artifacts: a perspective from color science. In: 5th international workshop on video processing and quality metrics

38. Ibraheem NA, Hasan MM, Khan RZ et al (2012) Understanding color models: a review. ARPN J Sci Technol 2(3):265–275

# Study on Effect of Device Link Profile in Color Management

Yan Liu[(✉)], Xiaozhu Mou, and Pengfei Cheng

Printing and Packaging Engineering Department, Shanghai Publishing and
Printing College, Shanghai, China
sppcly@163.com

**Abstract.** This paper studies the effect of Device Link Profile in the color
management. To solve the color reproducibility in the color conversion, the
Device Link profile is established in ColorThink Pro 3. Through the analysis and
comparison of the color difference, visual perception and the different K channel
setting with the use of Device Link profile and standard ICC profile, it is found
that Device Link can save ink, improve printing suitability and improve the
accuracy of color reproduction. This indicates that Device Link is very effective
in color conversion.

**Keywords:** Device Link profile · Color management · K channel

## 1 Introduction

In the evaluation of printing quality, the accurate reproduction of the original color is
one of the decisive factors. ISO/TS10128 proposes three methods to adjust repro-
duction system to the ISO 12647-2, which are: TVI, gray balance and Device Link [1].
At present, the certification methods of printing standardization, such as PSO and G7,
mostly use TVI or gray balance as the process control method and rarely use Device
Link control method [2]. The Device Link control method is to establish a Device Link
profile of two devices by software, and to associate ICCs of different devices, omitting
the PCS space, and directly establishing a mapping relationship between the source
color space and the target color space. It can ensure the color consistency of two
devices [3]. Device Link, as a means of process control with unique advantages in color
reproduction, has corresponding modules designed by ProfileMakers, Printopen and
other software. However, there are few examples of practical applications and it needs
to be further studied. This paper uses ColorThink Pro 3 as an example software to
establish and optimize Device Link profile and evaluate the color reproduction per-
formance of Device Link Profile [4].

## 2  Experiments

### 2.1  Experimental Equipment and Materials

Software: ColorThink Pro 3, Excel,Adobe Photoshop CC2017; ICC profiles: CGATS21_CRPC3.icc, CGATS21_CRPC7.icc [5]; Test files: IT874_CMYK_1617. txt, SPPC_testblock (designed by Yan Liu).

### 2.2  Experimental Principle and Methodology

#### 2.2.1  Experimental Principle

In the workflow of color management, it is generally necessary to go through the profile connection space (PCS) when converting the source color space to target color space (see Fig. 1) [6]. In this conversion mode, when the color information is converted from PCS to the target device space, the single-channel color information may be lost during the conversion because the connection with the source color space cannot be established. That is, the color printed by single K is overprinted by four colors, which leads to the loss of layer details, black dirty and other problems. The reason is that the connection space for the standard ICC color conversion is usually a device-independent space, usually a LAB color space or XYZ color space. The device link technology differs from the standard ICC in the principle of color conversion. The device link profile does not need to go through the PCS space for color conversion, and directly establishes the connection between the source and target device color space (see Fig. 2). When the source and target profiles are created, the two profiles already contain the information of the connection space. The process of establishing the Device Link profile is equivalent to constructing the correspondence of color data in a color space. Device Link profile can save ink, improve printing suitability and improve the accuracy of color reproduction between devices.
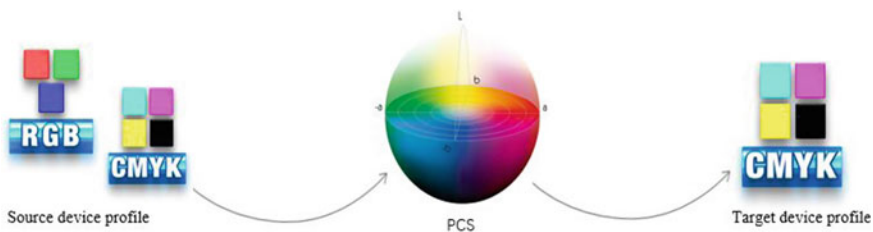


**Fig. 1.**  Principle of standard ICC



**Fig. 2.**  Principle of Device Link

### 2.2.2  Methodology

This paper studied the color difference and visual perception between the standard ICC workflow and Device Link. The two workflows are established in ColorThink Pro 3. CGATS21_CRPC3.ICC and CGATS21_CRPC7.ICC are represented two different CMYK color Spaces. The cumulative relative frequency curve CRF and 95% chromatic aberration data are compared and analyzed in ColorThink Pro 3 [7]. The color difference is calculated by CIEDE2000 [8]. To the further study, the Device Link Profile (preserve clean K channel and without preserve clean K channel) are set up. The database of test block (SPPC_testblock) is compared by using the two different Device Link profiles. Then in Photoshop CC2017, the test chart is configured with the Device Link Profile generated in two ways, and the visual effects are compared and analyzed.

## 3  Results

### 3.1  Comparison of Standard ICC and Device Link

### 3.1.1  Creating Device Link Profile

The Device Link profile is created in ColorThink Pro 3. (1) Click ColorSmarts Guide. (2) Select Profile > Create DVL > Next. (3) Add Source (CRPC3) > Add Destination (CRPC7) > Next. (4) Display Profile Linker > Build Link (see Fig. 3). You can find that a Device Link profile no longer goes through the PCS. It becomes a pair-wise color conversion for color proofing or ink optimization uses.
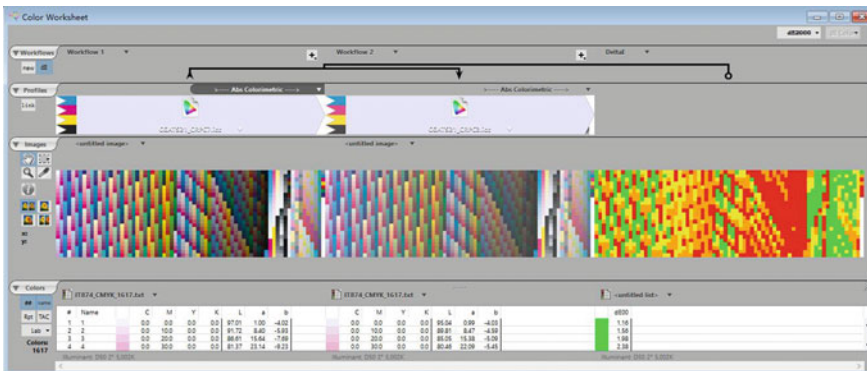


**Fig. 3.** Workflow of standard ICC

### 3.1.2  Color Conversion of Device Link

Color Conversion of Device Link is operated in ColorThink Pro 3. (1) Open IT8.7/4 list and apply DVL (CRPC3-to-CRPC7).icc. (2) Add CRPC7.icc to obtain the first Lab list. (3) Add IT8.7/4 list and apply CRPC3.icc to obtain the second Lab list using Absolute Colorimetric rendering. (4) Click $\Delta E_{00}$ and assess the color difference map.

### 3.1.3    Color Conversion of Standard ICC

Color Conversion of standard ICC is operated in ColorThink Pro 3. (1) Open the IT8.7/4 list in a color worksheet and apply CRPC7.icc. (2) Add the IT8.7/4 list and apply CRPC3.icc. (3) Click $\Delta E_{00}$ and observe the large color difference map.

### 3.1.4    Results

1. In standard ICC, Without DVL, color differences between the CRPC3 profile and the CRPC7 profile are large (see Fig. 3). With DVL, color differences between the CRPC7 and the CRPC3 dataset are small (see Fig. 4). The database of 95th percentile $\Delta E00$ of two workflows (see in Table 1) and the CRF distribution (see in Fig. 5) are very different.
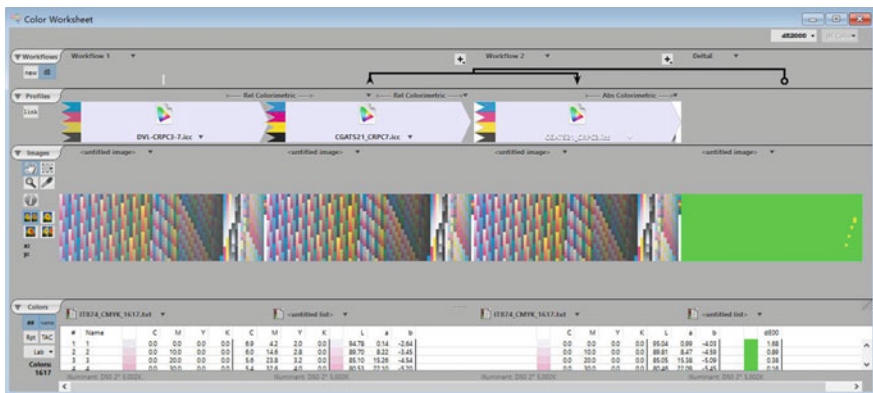


**Fig. 4.** Workflow of Device Link

**Table 1.** Color difference of standard ICC and Device Link

| CRPC3-to-CRPC7 | Standard ICC | With DVL |
|---|---|---|
| 95th percentile $\Delta E_{00}$ | 15.5 | 0.2 |
| Average $\Delta E_{00}$ | 7.4 | 0.1 |

2. In standard ICC, Without DVL, the sRGB-to-CRPC7 image shows high chroma than the sRGB-to-CRPC3 image (see in Fig. 6. The image in the red box on the left represents the CRPC3 visual effect,the right one represents the CRPC7). By applying DVL to CRPC3, the CRPC3-to-CRPC7 image, output from CRPC7, matches the CRPC3 image (see in Fig. 7. The image in the red box on the left represents the CRPC3 visual effect, the right one represents the DVL CRPC3-CRPC7).
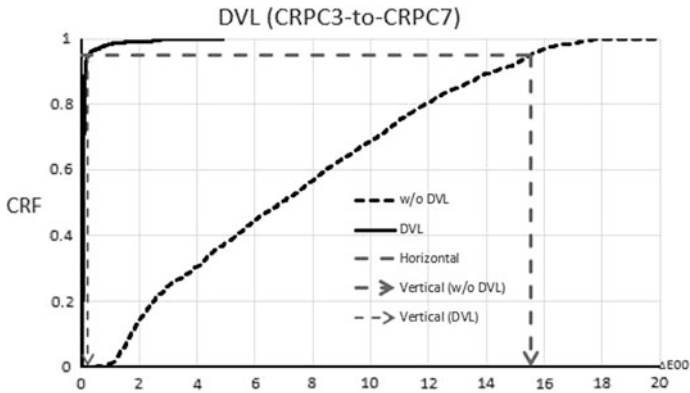
**Fig. 5.** CRF of standard ICC and Device Link



**Fig. 6.** Visual difference of standard ICC (without DVL)



**Fig. 7.** Visual difference of DVL

### 3.2 Effect of K Channel Setting on DVL

When using the Device Link method for color conversion, more precise control of the color conversion of each channel can be performed, and the purity of the color information of each channel can be ensured. Take the setting of the K channel in ColorThink Pro 3 as an example to compare the changes before and after the K channel is preserved.

In order to study the color conversion difference before and after the K channel is preserved, a test patch SPPC_testblock is designed. The test patch contains monochromatic 100% CMY and 11 steps of a single K color patch. The test color block is converted by using the two different Device Link profiles (preserved K channel and not preserve K channel), and the data result is shown in Table 2. Through the database

of conversion comparison, it can be seen that the conversion of the color patches reserved K channel, the K color patches of the single channel of each level are still reproduced by a single black, and the CMY single channel color patches are reproduced by four colors because it is not set. Without the single K channel setting, all the monochromes are produced by four-color overprinting, which increases the difficulty of registration and needs more ink supplies. In addition, when the color separation setting requirements are different, the value obtained by the K channel conversion will also change, which can meet more printing requirements.

**Table 2.** Database of test color block by two different Device Link profile

|   | SPPC_testblock | | | | DVL | | | | DVL (Preserve K) | | | |
|---|---|---|---|---|---|---|---|---|---|---|---|---|
|   | C | M | Y | K | C | M | Y | K | C | M | Y | K |
| 1 | 100 | 0 | 0 | 0 | 80.9 | 11.9 | 0.7 | **0.8** | 80.9 | 11.9 | 0.7 | **0.8** |
| 2 | 0 | 100 | 0 | 0 | 2.9 | 78.5 | 11.9 | **2.0** | 2.9 | 78.5 | 11.9 | **2.0** |
| 3 | 0 | 0 | 100 | 0 | 5.4 | 5.9 | 79.2 | **0.4** | 5.4 | 5.9 | 79.2 | **0.4** |
| 4 | 0 | 0 | 0 | 100 | 62.5 | 56.0 | 52.6 | **41.7** | 0.0 | 0.0 | 0.0 | **85.0** |
| 5 | 0 | 0 | 0 | 90 | 60.2 | 53.0 | 49.8 | **34.6** | 0.0 | 0.0 | 0.0 | **81.2** |
| 6 | 0 | 0 | 0 | 80 | 56.4 | 48.6 | 45.8 | **26.9** | 0.0 | 0.0 | 0.0 | **76.2** |
| 7 | 0 | 0 | 0 | 70 | 51.6 | 43.5 | 40.8 | **19.9** | 0.0 | 0.0 | 0.0 | **69.0** |
| 8 | 0 | 0 | 0 | 60 | 47.0 | 38.7 | 36.0 | **13.7** | 0.0 | 0.0 | 0.0 | **62.0** |
| 9 | 0 | 0 | 0 | 50 | 42.3 | 34.0 | 31.3 | **8.4** | 0.0 | 0.0 | 0.0 | **55.0** |
| 10 | 0 | 0 | 0 | 40 | 37.2 | 29.5 | 26.5 | **4.2** | 0.0 | 0.0 | 0.0 | **47.0** |
| 11 | 0 | 0 | 0 | 30 | 31.1 | 24.3 | 21.1 | **1.3** | 0.0 | 0.0 | 0.0 | **38.8** |
| 12 | 0 | 0 | 0 | 20 | 23.6 | 18.1 | 14.6 | **0.1** | 0.0 | 0.0 | 0.0 | **30.0** |
| 13 | 0 | 0 | 0 | 10 | 15.2 | 11.4 | 7.6 | **0.0** | 0.0 | 0.0 | 0.0 | **20.2** |
| 14 | 0 | 0 | 0 | 5 | 9.5 | 7.0 | 4.0 | **0.0** | 0.0 | 0.0 | 0.0 | **12.8** |

To further study in vision difference, open the test block sppc_testblock in photoshop CC2017. Edit/Convert to Profile and select Device Link with two different Device Link profiles and then select Edit/Specify Profile, here take the CGARTS_CRPC7 as an example, and then view the K channel of the file with two different conversion methods, the results are shown in Fig. 8.
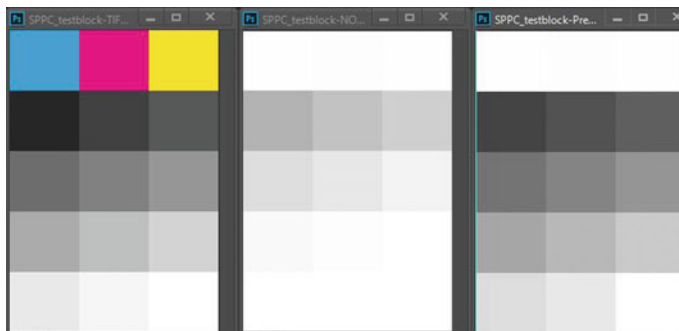


**Fig. 8.** SPPC_testblock and without/with preserve K channel (from left to right)

It can be clearly seen from the graphical effect that when the Preserve clean K channel is used, the converted test block K channel reproduces the single K color of the original test chart well. When K channel isn't preserved, the single K in the converted test chart will be obtained by CMYK four-color overprinting. So the K value is small in the single K channel, especially in the places of 5%, 10% and 20%K.

## 4    Conclusions

This paper starts with the working principle of standard ICC and Device Link, analyzes the difference between the two color conversion methods, and compares the difference between the standard ICC and Device Link from the data and visual aspects. And the data and vision difference of two Device Link profiles with/without "Preserve clean K channel" are studies. It can be concluded that Device Link can be used to establish mapping relationships between different devices, independently control the K channel, save ink usage, and the level details. In terms of color reproduction, Device Link is better than standard ICC both in color difference data and visual perception.

## References

1. ISO/TS 10128:2009 (2009) Graphic technology—methods of adjustment of the colour reproduction of a printing system to match a set of characterization data
2. You BZ (2018) Research on printing standardization and its extension based on ISO/PAS 15339. Xi'an University of Technology, Xi'an
3. Li XY (2012) Discussion on three color control methods of ISO/TS 10128. Print Qual Stand 3:19–22
4. Liu Y, Chung R (2018) Quantifying reproducible brand colors in four-color printing. Packag Eng 17:223–227
5. ICC profile registry. http://www.color.org/registry/index.xalter
6. Liu WH (2009) Discussion on device link profile. Guangdong Print 4:16–18
7. Liu Y, Gu P, Li ST (2018) Research on reproduction of brand colors on hi-fi color printing. Adv Graph Commun Print Packag 4:157–162
8. IS0/CIE 1664–6:2014(E)colorimetry-part 6:CIEDE2000 colour-difference formula

# Experimental Research on the Theoretical Basis of Density Balance Equation

Ganghu Cheng, Lina Jiang[(✉)], Shenglan Han, and Weiguo Jiao

Faculty of Printing, Packaging Engineering and Digital Media Technology,
Xi'an University of Technology, Xi'an, China
`1479620263@qq.com`

**Abstract.** The density balance equation is widely used in the field of printing engineering. It has the reputation of color reproduction equation and is a classic density balance analysis model and method. However, as two important theoretical bases of density equilibrium equation, density scale and additive setting, its correctness and reliability are challenged in both scientific research and engineering applications, and there are frequent objective data and phenomena that are contrary to the linear equilibrium equation. In response to this problem, based on the author's previous theoretical analysis and relying on laboratory equipment, this paper carried out in-depth experimental investigation and analysis. With the help of laboratory equipment, the use of the same paper, ink, carried out 10 different mesh parameters of the self-set test version of digital printing experiments. Based on the data of 8 color gray ladder density detection of 12-stage segmentation, the density ratio and additive were investigated and analyzed. The research shows that under all screening parameters, the density proportionality and additivity Settings have errors. And the error size and trend will change with the change of screening parameters.

**Keywords:** Density balance · Equation screening parameters · Density additivity · Density proportionality

## 1 Statement of Problem

The mask equation, the gray balance equation, and the color reproduction equation [1–4] under the density system, that is, the color printing density balance equation [5–8], which collectively referred to as the density linear equation, are used in electronic color separation, plate color correction, spot color ink configuration [9–13], and graying during printing operations. Balance detection control [14] plays an irreplaceable positive role [1, 6] and is an important tool for color printing process operation and quality analysis under the density system. The additivity and proportionality of density are the two basic theoretical pillars of the linear equation of density.

In the long-term scientific experiments and production practices, the frequently encountered problems of density additivity and proportional failure have been plagued by the industry and have long attracted people's attention. However, so far, people still think that addition of density and proportionality are the two basic laws that continue to be used [2]. So, whether it is caused by the unsatisfactory printing materials in actual

printing (including experiments) or by the flaws in the scientific existence of the model, it seems that this problem has not attracted enough attention of the industry and deserves our textual research.

In view of this, this paper carried out an experimental analysis based on digital printing system.

## 2   Experimental Design and Data Acquisition

A four-color printing test plate was designed for 8-color gray scale with 12-level segmentation. Printing experiments were carried out on a digital printing press (the test version was omitted, because this study only involved the gray scale), and the relevant data was measured in the laboratory using an X-Rite spectrophotometer. In order to eliminate random interference, each screening method extracts 10 consecutive samples, and the density data of each color block is averaged after measurement. Examples of experimental data are shown in Table 1. Among them, the experimental conditions include: AM screening (the first screening mode, simplified as one, the same below), linear network, 120lpi; screening angle: yellow, magenta, green, black 15, 75, 0, 45 degrees, respectively. Paper white density: $Dwr = 0.12$, $Dwg = 0.09$, $Dwb = 0.06$.

The experimental data of the other nine kinds of screening conditions are similar, which is limited to space, and will not be repeated here. Generally speaking, there is no singularity in the experimental data, and the data changes are continuous and smooth as a whole.

## 3   Experimental Analysis of Density Proportionality

As we all know, the actual ink is not pure, so the ink density is different from the primary and secondary density. At the same time, the proportional setting of density is also produced, that is when the dot area ratio of each monochrome ink is different, the density values measured by red, green and blue filters maintain a proportional (linear) relationship with each other. In other words, the ratio of secondary density to primary density of each color ink is constant. This is the proportion of ink density. The experimental curve of density proportionality drawn from the data in Table 1 is shown in Figs. 1 and 2. Dyr/Dyb in the figure represents the ratio of red to blue density of yellow block; Dmr/Dmg represents the ratio of red to green density of magenta block; Dcg/Dcr represents the ratio of green to red density of green block, and so on.

(1)  Proportional experimental curve under AM screening
    For the first mode of screening, according to the experimental data in Table 1, the relationship curve shown in Fig. 1 can be obtained.
(2)  Proportional experimental curve under FM screening
    Proportionality relationship of FM screening with shape size of 25 Fig. 2.

Of course, the experimental data of other screening methods can also obtain similar relationship curves. As can be seen from Figs. 1 and 2.

**Table 1.** Test results of spectral density of 8-color grey scale with 12-level segmentation

| Different patch density | | Area ratio | | | | | | | | | | |
|---|---|---|---|---|---|---|---|---|---|---|---|---|
| | | 5% | 10% | 20% | 30% | 40% | 50% | 60% | 70% | 80% | 90% | 100% |
| C | Dcg | 0.076 | 0.085 | 0.105 | 0.122 | 0.152 | 0.179 | 0.211 | 0.252 | 0.286 | 0.329 | 0.398 |
| | Dcr | 0.108 | 0.139 | 0.201 | 0.242 | 0.318 | 0.386 | 0.484 | 0.609 | 0.727 | 0.897 | 1.14 |
| | Dcb | 0.048 | 0.049 | 0.057 | 0.063 | 0.077 | 0.085 | 0.092 | 0.107 | 0.118 | 0.131 | 0.151 |
| M | Dmb | 0.056 | 0.071 | 0.108 | 0.146 | 0.197 | 0.233 | 0.256 | 0.307 | 0.379 | 0.452 | 0.647 |
| | Dmg | 0.098 | 0.135 | 0.214 | 0.296 | 0.388 | 0.463 | 0.537 | 0.631 | 0.808 | 1.023 | 1.523 |
| | Dmr | 0.08 | 0.085 | 0.097 | 0.107 | 0.129 | 0.14 | 0.146 | 0.154 | 0.187 | 0.189 | 0.233 |
| Y | Dyb | 0.07 | 0.091 | 0.129 | 0.174 | 0.212 | 0.242 | 0.286 | 0.374 | 0.534 | 0.623 | 0.966 |
| | Dyg | 0.068 | 0.07 | 0.073 | 0.077 | 0.081 | 0.083 | 0.088 | 0.095 | 0.112 | 0.114 | 0.136 |
| | Dyr | 0.075 | 0.076 | 0.077 | 0.078 | 0.08 | 0.079 | 0.081 | 0.083 | 0.091 | 0.09 | 0.098 |
| K | Deb | 0.093 | 0.146 | 0.253 | 0.384 | 0.503 | 0.646 | 0.806 | 1.011 | 1.242 | 1.571 | 1.884 |
| | Deg | 0.107 | 0.153 | 0.25 | 0.371 | 0.483 | 0.619 | 0.765 | 0.949 | 1.156 | 1.444 | 1.76 |
| | Der | 0.115 | 0.159 | 0.255 | 0.376 | 0.488 | 0.623 | 0.768 | 0.947 | 1.151 | 1.435 | 1.752 |
| R | Drb | 0.087 | 0.115 | 0.201 | 0.279 | 0.352 | 0.423 | 0.503 | 0.63 | 0.534 | 1.023 | 1.493 |
| | Drg | 0.101 | 0.138 | 0.226 | 0.307 | 0.392 | 0.466 | 0.544 | 0.638 | 0.799 | 1.006 | 1.462 |
| | Drr | 0.082 | 0.085 | 0.103 | 0.115 | 0.125 | 0.139 | 0.146 | 0.165 | 0.168 | 0.189 | 0.234 |
| G | Dgb | 0.076 | 0.095 | 0.14 | 0.19 | 0.223 | 0.275 | 0.309 | 0.381 | 0.506 | 0.591 | 0.788 |
| | Dgg | 0.078 | 0.087 | 0.11 | 0.132 | 0.156 | 0.189 | 0.221 | 0.255 | 0.299 | 0.337 | 0.402 |
| | Dgr | 0.109 | 0.137 | 0.199 | 0.245 | 0.303 | 0.371 | 0.467 | 0.566 | 0.67 | 0.809 | 0.965 |
| B | Dbb | 0.06 | 0.078 | 0.121 | 0.16 | 0.233 | 0.237 | 0.275 | 0.321 | 0.369 | 0.439 | 0.574 |
| | Dbg | 0.106 | 0.152 | 0.244 | 0.335 | 0.492 | 0.513 | 0.604 | 0.718 | 0.875 | 1.093 | 1.503 |
| | Dbr | 0.112 | 0.151 | 0.219 | 0.278 | 0.255 | 0.435 | 0.538 | 0.665 | 0.78 | 0.94 | 1.278 |
| BK | Deb | 0.088 | 0.122 | 0.196 | 0.276 | 0.397 | 0.397 | 0.465 | 0.554 | 0.709 | 0.848 | 1.087 |
| | Deg | 0.109 | 0.153 | 0.244 | 0.337 | 0.494 | 0.494 | 0.581 | 0.683 | 0.823 | 1.005 | 1.281 |
| | Der | 0.113 | 0.147 | 0.214 | 0.273 | 0.341 | 0.411 | 0.49 | 0.59 | 0.695 | 0.833 | 0.974 |

(1)  Whether C ink, M ink or Y ink, the ratio of primary density to secondary density decreases with the increase of area ratio, which has no relationship with screening and is consistent with theoretical analysis.

(2)  Whether C ink, M ink or Y ink, the ratio of primary density to secondary density varies in a certain range, but the variation range is different. The change range of Y ink (Take Fig. 1 as an example) is the largest, the ratio of primary density to secondary density decreases from 1.1 to 0.1 that of C ink is the second from 0.44 to 0.13, and that of M ink is the smallest from 0.6 to 0.4.

(3)  Whether it is C ink, M ink or Y ink, the ratio of primary density to secondary density does not conform to the proportional setting. If we continue to use the proportional setting, it will inevitably lead to errors. Obviously, the biggest error is Y ink, because the change range of its proportional relationship is the largest, followed by C ink, and the smallest is M ink.
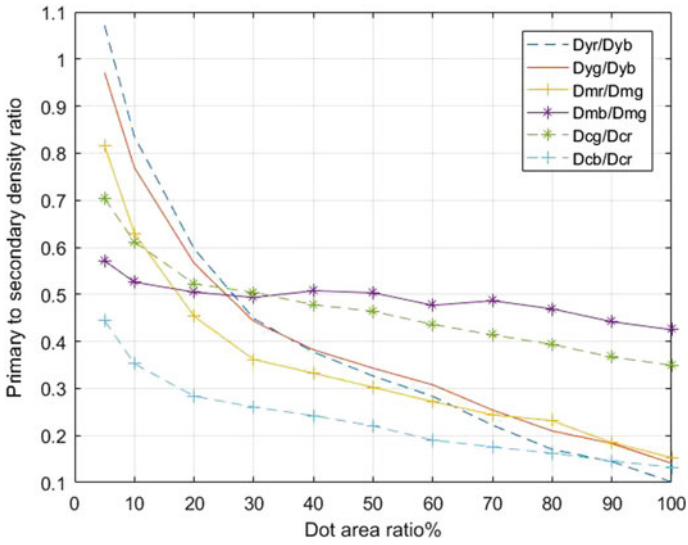
**Fig. 1.** Primary and secondary density ratio of ink monochrome scale (one)
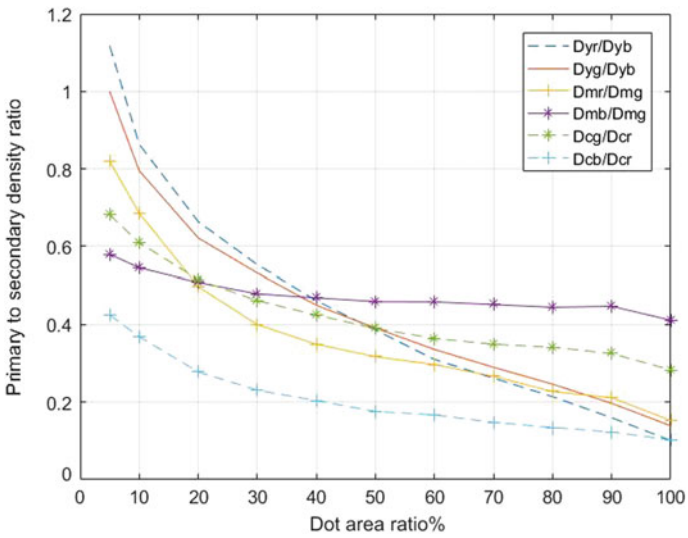


**Fig. 2.** Primary and secondary density ratio of ink monochrome scale (nine)

## 4   Experimental Analysis of Density Additivity

The printing industry believes that the composite density of three-color ink overprint is equal to the sum of the density of each monochromatic, which is the additivity of density. The additivity is based on the relationship of the inter-layer transmitted light

flux of the ink overlay, which proves that it can be defined only by density. However, in actual printing, when several kinds of ink are superimposed, the density value of the superimposed block measured with the same filter is often significantly smaller than the sum of the density values of the monochrome ink. The experimental curves of density additivity drawn from the data in Table 1 are shown in Figs. 3, 4 and 5 as follows: Dgr and Dgr1 represent the measured red density of color blocks, the superimposed red density of product and yellow; Dgg and Dgg1 represent the measured green density of color blocks and the superimposed green density of green and yellow; Dbb and Dbb1 represent the measured blue density of color blocks, the superimposed blue density of product and blue density of product, and so on.
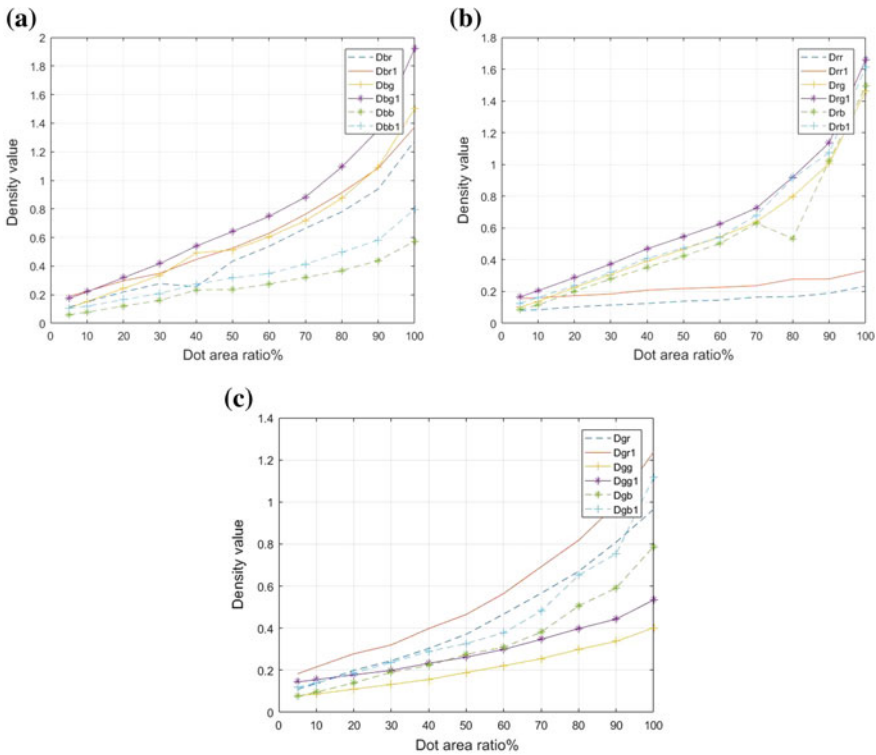


**Fig. 3.** Comparison curve between synthetic density and measured density of red, green and blue tricolor blocks (screening one). **a** Trend of blue block density. **b** Trend of red block density. **c** Trend of green block density
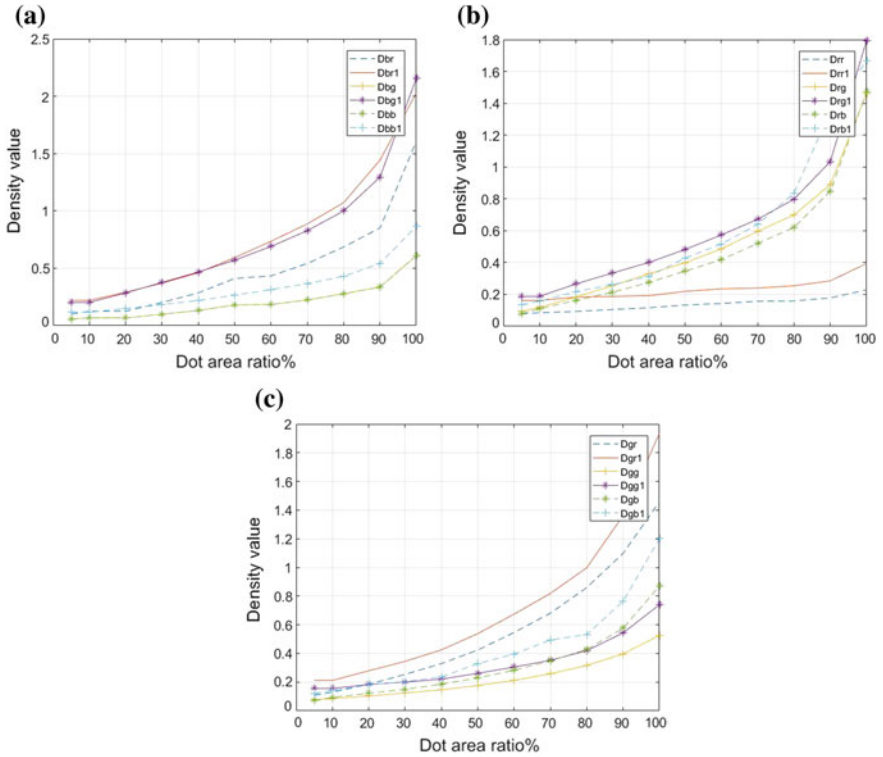
**Fig. 4.** Comparison curve between synthetic density and measured density of red, green and blue tricolor blocks (ten). **a** Trend of blue block density. **b** Trend of red block density. **c** Trend of green block density
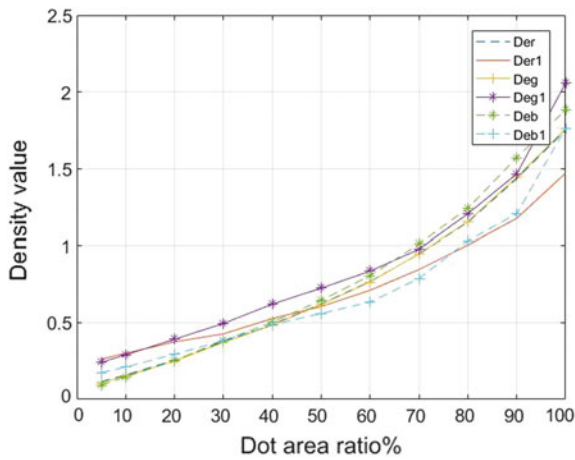


**Fig. 5.** The comparison curve between the measured density and the synthetic grey density of three colors (blue, magenta, yellow) (screening one)

## 4.1 Additive Experimental Analysis of Experimental Data Based on Inter-color (I.E. Red, Green and Blue) Scales

(1) Additivity experimental curve under AM screening (one)
(2) Additivity experimental curve of FM screening (shape size 45).

## 4.2 Additivity Experiment Analysis Based on Grey Scale Experiment Data

(1) AM screening (the first screening method, see Table 1 data)
(2) FM screening (shape size 25).

Similar curves can be obtained from the experimental data of other screening modes.

As can be seen from Figs. 3, 4, 5 and 6.
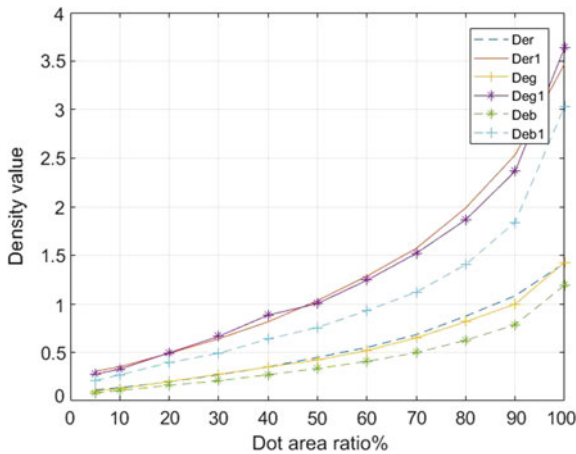


**Fig. 6.** Comparison curve between the measured density and the synthetic grey density of three colors (blue, magenta, yellow) (screening nine)

(1) Whether R, G, B or multi-color BK blocks, their primary and secondary densities increase nonlinearly with the increase of dot area ratio, which is consistent with the theory.
(2) Whether it is an R color block, a G color block, a B color block, or a complex color BK color block, and the primary density or the secondary density, the composite density is greater than the measured density. Strictly speaking, the additivity does not exist, and there is a certain error in the additivity setting.
(3) The magnitude of additive error varies with the change of dot area ratio, and in this experiment, the additive error increases with the increase of dot area ratio on the whole.

(4) The magnitude of additive error is affected by the mode of screening. In this experiment, FM screening is less than AM screening.

(5) The additivity error varies depending on the position of the color patch in the color gamut. This experimental study found that in terms of inter-color R, G, and B, the most additive error is red R, and the smallest is blue B, the green G additivity error is centered.

(6) In the complex color BK synthetic density: the effective influence of each monochromatic density varies due to the screen pattern (compared with Figs. 5 and 6), resulting in density loss (additive error), and the order of error influence is: B, G, R.

## 5 Research Conclusion

Density linear equation is established by density additivity and simplified by proportional setting. However, doubts about the additivity and proportionality of density have been difficult to relieve. Based on this, digital printing experiments and experimental data acquisition are carried out on the basis of the color density of 8-color gray scale, laboratory equipment and equipment. The contrast density data of the inter-color and multi-color ladders and the comparative analysis of the additive density of the additive are studied experimentally. The errors of density proportionality and additivity are investigated experimentally. Research indicates:

(1) No matter which monochrome scale is blue C, magenta M and yellow Y, the ratio of primary density to secondary density varies with the dot area ratio, and there is no proportional feature.

(2) Whether it is red R, blue B, and green G, both primary and secondary densities, the synthetic densities are higher than the measured densities of the corresponding printing blocks, and there is no strict additivity.

(3) No matter which monochrome scale is blue C, magenta M and yellow Y, the errors caused by the setting of proportionality are variable, depending on the dot area ratio, paper density and ink characteristics and other factors.

(4) Whether R color block, G color block, B color block or multi-color BK color block, the error caused by additivity setting is variable, which is controlled by many factors, such as dot area ratio, screening parameters, and color coordinates of color block.

## References

1. Hu CF (1993) Printing color and chromatics. Printing Industry Press, Beijing
2. Zheng YL, Zhou SS (2013) Printing chromatology, 3rd edn. Printing Industry Press, Beijing
3. Liu X (2016) Printing technology. Chemical Industry Press
4. Wang Q, Liu QX, Li ZJ (2007) Principle and methods of colouring. Printing Industry Press, Beijing

5. Chen B (2018) Analysis of digital density image quality density detection method, vol 45, no 03. Yunnan Chemical Industry Co., Ltd., pp 89–90
6. Huang YH (2017) Application analysis of grey balance in digital printing quality control. Light Ind Technol 33(11):113–114
7. Li N, Li XD (2017) Grey balance in color restoration. Guangdong Print 04:21–24
8. Zeng TY, Shao X, Wang ZH (2015) Quality control and evaluation of printing based on grey balance. J Packag 7(04):41–46
9. Qu T (2015) Research on the method of quality density detection for digital printing image. Print Qual Stand 12:39–41
10. Guo LH, Lei Y (2013) Analysis of the influence of ink thickness on the accuracy of ink matching based on mask equation. J Shaanxi Univ Sci Technol (Natural Science Edition) 31 (02):14–16+22
11. Guo LH, Duan XJ, Reng LF et al (2016) Research on color matching model for myopia prevention based on mask equation. J Shaanxi Univ Sci Technol (Natural Science Edition) 34(04):31–34+53
12. Moorthy AK, Su C-C, Mittal A et al (2012) Subjective evaluation of stereoscopic image quality. Sig Process Image Commun 28(8):870–883
13. Guo LH (2007) Analysis of the precision of the ink distribution of the mask equation. Packag Eng 06:73–74
14. Shen R, Chen W, Wang CC (2015) Study on the influencing factors and control methods of printing gray balance. Print Qual Stand 05:28–32

# Reference Images Development for Evaluation of Tone Mapping Operators

Imran Mehmood, Muhammad Usman Khan,
Muhammad Farhan Mughal, and Ming Ronnier Luo[(✉)]

State Key Laboratory of Modern Optical Instrumentation, Zhejiang University,
Hangzhou, China
m.r.luo@zju.edu.cn

**Abstract.** High Dynamic Range (HDR) imaging has been deployed in many multimedia devices recently. Various tone mapping operators (TMOs) have been developed which transform HDR radiance to the display devices. The objective of this study is to develop reference images for subjective evaluation of TMOs and full reference image quality metrics. For this purpose two psychophysical experiments were conducted. In the first experiment, high quality reference images were obtained containing the right features of colourfulness, sharpness and contrast. The reference images were used to evaluate the TMOs in subjective and objective assessments. In the second experiment, five popular TMOs were evaluated subjectively. It was found that Reinhard's photographic tone reproduction based local TMO performed best among the five TMOs. Three full reference image quality metrics SSIM, CIELAB (2:1) and S-CIELAB were used to evaluate structural similarity and colour image quality of those TMOs. Their results showed that the three metrics agreed well with the visual results.

**Keywords:** High dynamic range · Tone mapping · Image quality · Reference image

## 1 Introduction

For almost all the natural scenes, the difference in intensity between the brightest and darkest part is much higher than the differences of capturing and displaying devices. Although HDR display devices are available yet they have limited practical capability and are usually very expensive. TMOs provide solution to this problem by projecting the HDR luminance to that of the display device luminance range while preserving the contrast [1]. A number of TMOs have been developed for this purpose. These are broadly classified as global and local operators. The global operators have overall better contrast and they are fast in processing whereas the local operators produce more details and they are slower [2]. However, during tone mapping, the information loss and degradation of contrast severely effects the quality of the tone mapped image therefore assessments of TMOs is significantly important. The objective assessments of TMOs have been categorized into three types: no reference, full reference and reduced reference image quality metrics (IQMs). In full reference IQM, a reference image is

available for comparison. In the reduced reference IQMs, a specific set of features of reference images must be available for quality measurements. In no reference IQM, there is no information of the reference image. All the image quality attributes should base on the image itself, therefore, it is also called blind IQM. In this study, three full reference; CEIALB (2:1) [3], S-CIELAB and SSIM [4] objective IQMs were used.

In the full reference IQMs, reference image forms an important part. There are many standard range image databases available such as USC-SIPI image data-base, Kodak lossless true colour image suite [5, 6] but no such database is available for HDR images. The objective of this study was to develop high quality HDR reference images and to evaluate TMOs by subjective and objective methods.

## 2    Methodology

The aim of the Experiment 1 was to develop a database of high quality images. First of all, 10 natural images with quite high dynamic range were selected form Fairchild's database at Rochester Institute of Technology for rendering purpose. Various TMOs were implemented [7–10] and it was found that local tone mapping version of photographic tone reproduction operator (PTR Local) [8] performed best among all of them. Hence, it was chosen as the baseline TMO. Each RGB HDR radiance map from the database was converted to XYZ coordinates and luminance was mapped to the displayable range using this TMO. Tone mapped XYZ coordinates were transformed to CIELCh space and three attributes colourfulness, contrast and sharpness were used to produce perceptually high quality rendered images.

The colourfulness and contrast are two main attributes for high quality images. Colourfulness enhancement is necessary to improve image aesthetics. It is a measure of colour quality. The chroma channel of the $L^*C_{ab}^*h_{ab}$ space was used to enhance the colourfulness linearly.

Kaur et al. studied several contrast enhancement techniques [11]. The most effective and popular method for contrast enhancement is histogram equalization (HE). Clip limit adaptive histogram equalization (CLAHE) method [12] was used both to overcome the saturation of contrast produced by HE and to render images.

Unsharp masking technique was implemented to render the image sharpness. In unsharp masking, the Gaussian blurred image was subtracted from the original image called mask of the image. To create sharpening effect, this mask was added to the original image.

For each of the three attributes, five rendered images were generated which contained the original image, a perceptually best image, a perceptually worst but acceptable image and two images in between latter two. The image with maximum acceptable effect was selected visually such that adding more effect of the scale would produce defects or unnaturalness. For example, in case of image sharpness, one original image was used, one image with perceptually high sharpness, one with maximum acceptable sharpened image and the other two images had little lower and little higher sharpness as compared to the perceptually high image. For generating various sharpened image, standard deviation of the Gaussian's distribution was used to produce various blurring effects. For contrast

enhancement, clip limit of the CLAHE was varied to get different rendered images. The colorfulness rendering was achieved by in-creasing Chroma linearly.

It was mentioned earlier that five rendered images for each scale were generated for each of the ten original images. Therefore a total of 1,250 images were processed. Twenty percent of the images were repeated to calculate the intra-observer variably. In total 1,500 images were generated for Experiment 1.

The experiment was conducted in a dark room where the calibrated display was located. It was placed 45 cm away from the observer. Each observer passed Ishihara Test to ensure that they had normal colour vision. The observers were asked to judge the quality of the image either "Low Quality" or "High Quality". Twenty observer, 6 females and 14 males participated in the experiment. The mean age and standard deviation of the observers were 25.7 and 3.54 respectively. Each observer did 1,500 judgments and total judgments were 30,000 i.e. 5 (colourfulness) $\times$ 5 (sharpness) $\times$ 5 (contrast) $\times$ 10 (images) + 250 (repeatable images) $\times$ 20 (observers).

Experiment 1 was conducted to develop high quality reference images which were to be used in the evaluation of TMOs in the second experiment. It is explained in the next section that how the reference images were selected by analyzing the data of Experiment 1. In Experiment 2, five popular TMOs, Drago's adaptive logarithmic tone mapping (ALTM) [7], Reinhard photo-graphic tone reproduction based global (PTR Global) and local operators (PTR Local) [8], and Reinhard's and Devlin's dynamic range reduction inspired by photoreceptor physiology (DRR) [9] and Schilik's quantization (Quantization) [10] method were evaluated. The same ten images from RIT database were tone mapped and best versions for each TMO were selected under the experimental conditions. Total fifty images were selected for five TMOs. These tone mapped images were named as test images and the high quality images resulted from Experiment 1 were used as reference images. To analyze the variability of the observer, 10% images were repeated. Therefore, total number of images for Experiment 2 was 72. Categorical judgment based six points scale was defined to test the images difference between the reference images and the tone mapped images. The six categories were "No Difference", "Just Noticeable Difference", "Small Difference", "Acceptable difference", "Large Difference" and "Extremely Large Difference. These six categories were assigned numbers from 1 to 6 respectively.

Experiment 2 was conducted under the same display conditions as that of Experiment 1. A pair of test and reference images were displayed for each observer to make judgments in 1–6 categories. The position of the test and reference images were arranged randomly. In total, 20 observer, 5 females and 15 males, participated in the experiment with mean age of 27.35 and standard deviation of 8.6. Total number of assessments made in this experiment was 1,440.

## 3   Results and Discussion

The inter-observer and intra-observer variability were calculated for both the experiments to check the consistency of the observers. For Experiment 1, number of wrong decisions (WD) for each observer were calculated by evaluating the accuracy of the observers when they repeated their rating of the same image. Intra-observer variability

was defined as total number of WD divided by total number of decisions. The best and worst case observer had values 0.136 and 0.296 respectively with mean of 0.190. The coefficient of variation was calculated to check the intra-observer variability. The best and worst values were 0.21 and 0.30 CV respectively with mean of 0.26 CV. For Experiment 2, CV values were calculated to analyze the inter-observer and intra-observer variability. For inter observer, the best and worst values were 0.19 and 0.278 CV respectively with mean of 0.32 CV. For intra-observer variability, the best and worst values were 0.26 CV and 0.32 CV respectively with mean of 0.29 CV.

The raw data form Experiment 1 was transformed to Z-score using Torgerson's law [13]. The images with positive and negative Z-scores were considered as high quality and low quality images respectively. Using this criteria, 158 out 1250 rendered images were found as high quality images. Ten images with highest Z-score from each set of scenes were selected as reference images. Figure 1 shows four out of ten reference images. It was obvious that the reference images were more colourful, with higher contrast and sharpness as compared to the original tone mapped images. Further, it was also noticed from the Z-scores that, none of the original tone mapped image was selected as high quality image which shows that observer did not like straightforward tone mapped images.



|  Reference  |  ALTM  |  PTR Local  |  DRR  |  PTR Global  |  Quantization  |
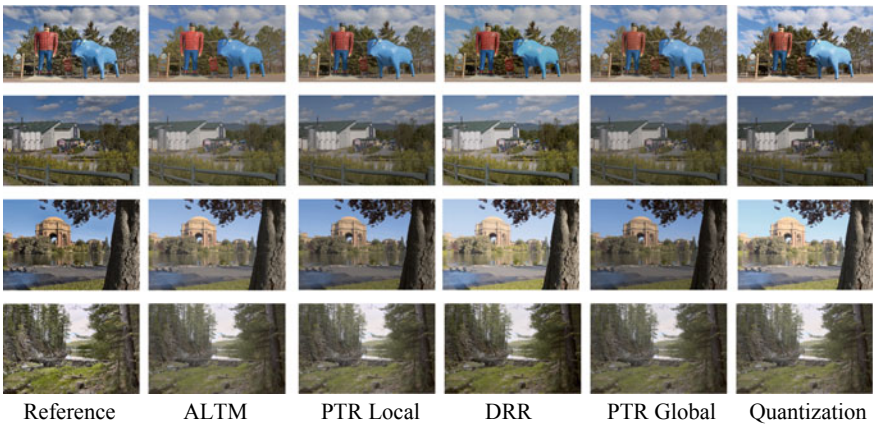
**Fig. 1.** Reference Images versus tone mapped images

From Experiment 2, the raw data was used to analyze the ranking of the TMOs using 6 point categorical judgment scales. Firstly, the mean ranking was calculated and then rearranged to present the score as zero and one (those from 1 to 3 and from 4 to 6, respectively). Table 1 shows the normalized mean ranking of the operators. Higher ranking corresponds to less difference from the reference images. Table 1 shows that PTR Local operator had the highest number ranking making it as top TMO. There are two reasons: firstly the reference images were developed using this operator, secondly, the PTR Local operator produced more details as compared to the other studied TMOs. The ALTM was ranked second. It was observed that ALTM produced higher contrast

as compared to the other TMOs but it is a global operator therefore it produces less details, consequently it was ranked after the PTR Local in subjective assessments. PTR Global operator was ranked third followed by Schilik's and DRR.

**Table 1.** Ranking of TMOs using subjective and objective methods.

|  | Mean ranking | CIELAB(2:1) $\Delta E^*_{ab}$ | S-CIELAB $\Delta E^*_{ab}$ | SSIM score |
|---|---|---|---|---|
| ALTM | 0.3725 | 8.6397 | 10.6823 | 0.9057 |
| PTR local | 0.4183 | 7.8606 | 10.0407 | 0.9196 |
| DRR | 0.2117 | 10.3480 | 12.1853 | 0.8746 |
| PTR global | 0.3467 | 8.7487 | 10.8824 | 0.8905 |
| Quantization | 0.2383 | 9.9308 | 11.8391 | 0.8906 |

For objective evaluation of the TMOs, CIELAB (2:1), S-CIELAB and SSIM was used. The input to each of the method was reference image and test image. In CIELAB (2:1), the $\Delta L^*$ is divided by two. As lightness difference is less weighted, CIELAB $\Delta E^*_{ab}$ is not well correlated with perceived image difference. The spatial extension of CIELAB called S-CIELAB was used. In the opponent colour space the red-green and yellow-blue planes were strongly blurred with Gaussian 2-D filter but the luminance was slightly blurred. Then CIELAB $\Delta E^*_{ab}$ was applied. For CIELAB (2:1) $\Delta E^*_{ab}$ and S-CIELAB $\Delta E^*_{ab}$, greater number means more image difference from the reference image. Table 1 indicates that PTR Local has lowest $\Delta E^*_{ab}$ and DRR has highest $\Delta E^*_{ab}$ therefore both CIELAB (2:1) and S-CILEAB agree well with the subjective rankings. SSIM was used to evaluate structural similarity between reference and tone mapped images. In case of SSIM score, greater higher number means more structural similarity with the reference images. SSIM also agreed with subjective ranking for the case of ALTM, PTR Local and DRR but it ranks PTR Global and Quantization methods almost equal. To find out which objective method is more close to the subjective assessment, mean image difference and SSIM score for each image is plotted with respect to mean image ranking in Fig. 2a, b, c values show that each objective method had strong correlation with subjective assessment.



(a) Correlation between SSIM score and mean image ranking

(b) Correlation between S-CIELAB(2:1) $\Delta E^*$ab and mean image ranking

(c) Correlation between CIELAB $\Delta E^*$ab and mean image ranking
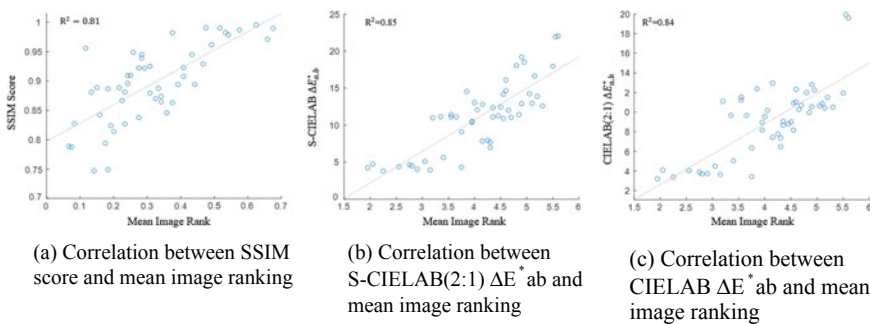
**Fig. 2.** Mean image difference and SSIM score for each image

## 4    Conclusions

In this research work two psychophysical experiments were conducted and TMOs were evaluated by subjective and objective methods. In Experiment 1, perceptually high quality reference images were developed. The images had more colorfulness, sharpness and contrast as compared to the original images. The reference images were used for the evaluation of five TMOs in the Experiment 2. It was found that PTR Local operator ranked first, followed by ALTM, PTR Global, Quantization method and DRR. Three full reference objective image quality metrics SSIM, CIELAB (2:1) and S-CIELAB were also used to evaluate TMOs. It was found that each objective method strongly agreed with the subjective assessments.

**Compliance with Ethical Standards. Conflict of Interest**: The authors declare that they have no conflict of interest.

**Ethical approval**: All procedures performed in studies involving human participants were in accordance with the ethical standards of the College of Optical Science and Engineering, Zhejiang University and with the 1964 Helsinki declaration and its later amendments or comparable ethical standards.

**Informed consent**: Informed consent was obtained from all individual participants included in the study.

## References

1. Mantiuk R, Daly S, Kerofsky L (2008) Display adaptive tone mapping. ACM Trans Graph (TOG) 27(3):68
2. Yoshida A, Blanz V, Myszkowski K, Seidel HP (2005) Perceptual evaluation of tone mapping operators with real-world scenes. In: Electronic imaging, international society for optics and photonics, pp 192–203
3. Luo MR (2002) CIE Division 8: a servant for the imaging industry. In: Colour science and imaging technologies, international society for optics and photonics, vol 4922, p 51
4. Wang Z, Bovik AC, Sheikh HR et al (2004) Image quality assessment: from error visibility to structural similarity. IEEE Trans Image Process 13(4):600–612
5. Weber AG (1997) The USC-SIPI image database version 5, USC-SIPI report, 315, 1
6. Franzen R (1999) Kodak lossless true color image suite. http://r0k.us/graphics/kodak, 4
7. Drago F, Myszkowski K, Annen T et al (2003) Adaptive logarithmic mapping for displaying high contrast scenes. Comput Graph Forum 22(3):419
8. Reinhard E, Stark M, Shirley P et al (2002) Photographic tone reproduction for digital images. ACM Trans Graph (TOG) 21(3):267
9. Reinhard E, Devlin K (2005) Dynamic range reduction inspired by photoreceptor physiology. IEEE Trans Vis Comput Graph 13
10. Schlick C (1995) Quantization techniques for visualization of high dynamic range pictures. Photorealistic rendering techniques. Springer, Berlin, Heidelberg, pp 7–20

11. Kaur M, Kaur J, Kaur J (2011) Survey of contrast enhancement techniques based on histogram equalization. Int J Adv Comput Sci Appl 2(7)
12. Reza AM (2004) Realization of the contrast limited adaptive histogram equalization (CLAHE) for real-time image enhancement. J VLSI Signal Process Syst Signal Image Video Technol 38(1):35
13. Torgerson WS (1958) Theory and methods of scaling, pp 205–286

# The Influence of Database Establishment on Color Difference in Computer Color Matching

Shiyu Chen, Maohai Lin[✉], and Kaiyang Sang

Key Laboratory of Green Printing & Packaging Materials and Technology in Universities of Shandong (Qilu University of Technology), School of Light Industry Science and Engineering, Qilu University of Technology, Jinan, China
mhlin@vip.163.com

**Abstract.** In order to establish a more accurate Lithography database and reduce the color difference of computer color matching, the Lithographic suitability meter was used to establish a database under different conditions of substrate material, ink ratio and printing speed, so as to explore the influence of various factors on color difference in this experiment. The X-Rite Color Master was used to output color scheme to print sample strips that could produce color differences. The experimental results showed that the database created by the top part of the laser printing paper is relatively better and its color difference fluctuates around 3. The increase in the proportion of the ink not only makes the color difference smaller, but also reduces the fluctuation range of the color difference.

**Keywords:** Lithography · Color matching · Database · Color difference

## 1   Introduction

In today's lean production environment, the key for color technology advancement was that could be faster and better to provide customers with accurate color formulas. In the past, the time of color matching was increased by a number of coloring work, various complicated materials and the effect of printing process, which could lead to the result of color matching that are random, not universal, learnable and learnable. The drawbacks of the previous artificial color matching have been improved because of the appearance of computer that gradually becomes an important assistant for color matching, which is the development trend of printing ink color matching [1]. Nowadays, the research and development of computer color matching systems in foreign countries are relatively better and have achieved remarkable achievements. More accurate and complex optical models and algorithmic techniques have been proposed, for example the Sanderson correction and neural network technology with surface reflectivity, which could improve the efficiency of calculating color difference [2]. Since the 1990s, a variety of color matching systems have been developed, such as the X-Rite Color ITM Match color matching system. Ink color theory research and software development were researched relatively later in China. Through continuous

exchanges and in-depth research with foreign countries, a CFS complex spectrum ink color matching system was developed by China Printing Science and Technology Research Institute [3]. Nowadays, Chinese computer color matching technology is also in a state of rapid development.

The establishment of computer aided color matching database is the first step and an important part of computer aided color matching technology [4]. The database refers to the characteristic information of all raw materials entered in advance to achieve computer color matching. The characteristic of database production are especially important for the performance of color matching systems. Without a good database, accurate recipes cannot be obtained. Jianghao Liu of the Beijing Institute of Printing has studied a single database. This paper will explore the influence of printing materials, printing speed and the number of basic proportions on color difference through various databases [5].

## 2    Experiment

### 2.1    Establishment of the Basic Database

#### 2.1.1    Basic Ink Blending

It is necessary to make a base ink strip from light to dark before color matching. In this test, yellow, magenta, cyan, and black inks and varnish were used and the proportion of ink was obtained by weighing and then printed. The total proportion was set to 18, which can be compared with the colour difference of 10 proportional databases, as shown in Table 1.

**Table 1.** Ten and eighteen ink proportion division

| Quantity | Scale (%) | | | | | | | | | |
|---|---|---|---|---|---|---|---|---|---|---|
| 10 | 2 | 4 | 8 | 16 | 24 | 32 | 45 | 55 | 64 | 99 |
| 18 | 2 | 4 | 8 | 16 | 24 | 32 | 45 | 55 | 64 | 99 |
|  | 6 | 12 | 20 | 28 | 38 | 50 | 72 | 90 | / | / |

#### 2.1.2    Color Measurement and Database Establishment

Nine databases were created by the X-Rite portable spectrophotometer to measure the top, middle and lower positions of the three base color strips.

### 2.2    Standard Colors Matching Experiment

After the database was established, a standard color matching experiment was required. Seven standard colors were selected by spectrophotometer on standard chromatography [6]. The C30Y50, C20M80K50, M60Y50K10, C60Y10, M30Y70, C50M50, C80Y80 were selected respectively as the standard color to use 9 kinds of databases for computer color matching in order to get the formula and strip printing.

### 2.2.1 Comparison of Seven Standard Color Differences in Three Substrate Databases

The comparison of the color matching of the three substrate databases for the seven standard colors was shown in Fig. 1a, b. The stability analysis was shown in Fig. 1c.
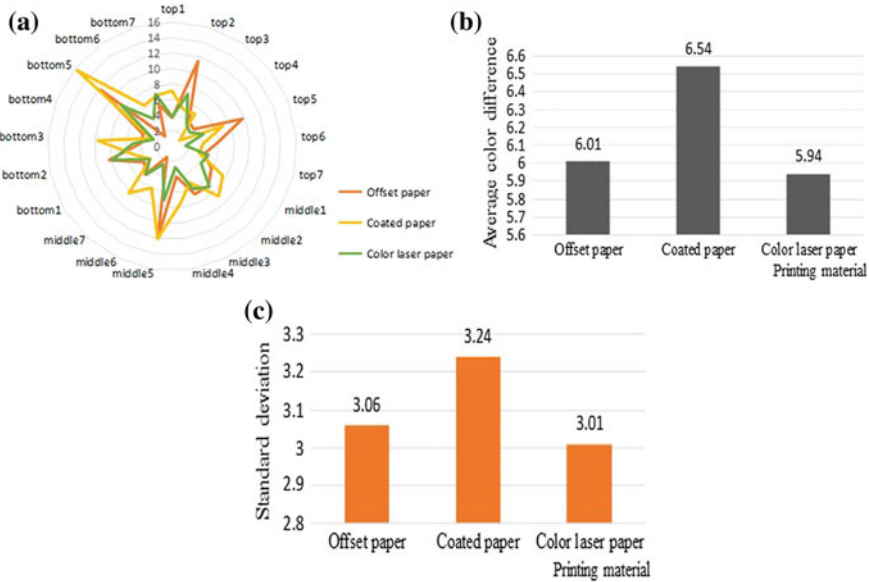


Fig. 1. Comparison of seven color matching data of three kinds of substrate databases

Through the above three graphs analysis, it can be concluded that the database of laser printing paper is relatively better and its average color difference is small and stable.

From the perspective of the substrate [7], various characteristics of the paper could affect the reproduction of printing color. The absorbency of paper is an important factor that can affect the color difference. If the ink absorption of the paper is too large, the color gloss of the paper will be poor, the density of the printing color will be decreased. At the same time, the gloss of the surface of paper is another significant factor; papers with lower gloss can achieve higher print densities when the same ink layer thickness is printed on the paper. In this paper, the laser printing paper has less ink absorption, higher gloss and higher smoothness. So the color difference was measured by the database corresponding to the laser printing paper was relatively smaller.

### 2.2.2 Comparison of Seven Standard Color Differences in Three Printing Speed Databases

The color differences of the top, middle and lower positions of the strips of the seven standard colors were shown in Fig. 2a, b. The stability analysis was shown in Fig. 2c.
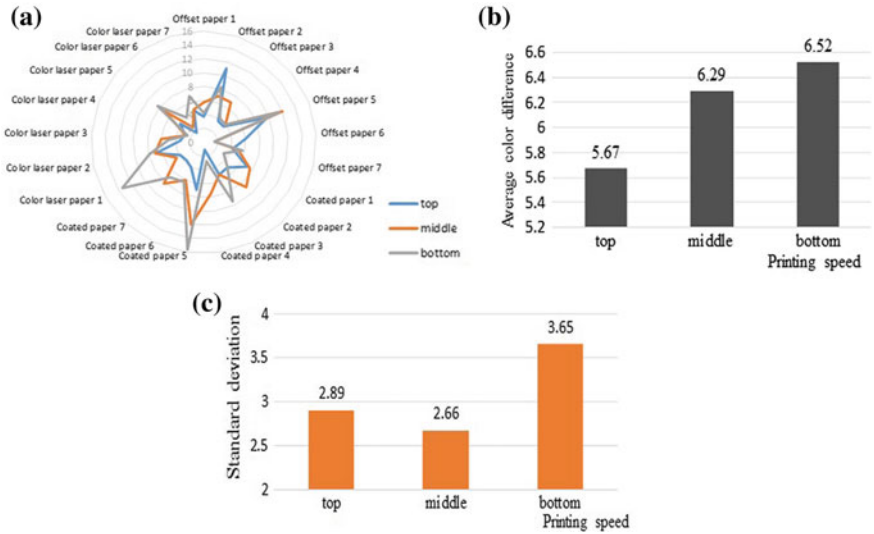
**Fig. 2.** Comparison of seven color matching data of three printing speed databases

By analyzing the radar chart, its mean and standard deviation, it can be concluded that the slowest printing speed of the database has a relatively smaller effect on the color difference from the three printing speeds. But the stability is less than the central speed.

In terms of printing speed, the process of printing a color strip is essentially a process in which the ink layer is split and transferred between the ink roller and the substrate. This process involves the transfer rate of the ink. The faster the printing speed, the shorter the time the ink is in the embossing zone, which lead to the ink layer was shallower and affected color difference. The printing speeds corresponding to the top, middle and lower positions of the strip are different. The lower the position is, the faster the speed is. Therefore, the color ink transfer rate corresponding to the color strip with lower printing speed is higher and the color difference of the formula obtained by this database will be smaller.

### 2.2.3 Comparison of Seven Standard Color Differences for Two Orders of Magnitude Proportional Spline Database

On the basis of 9 kinds of 10 basic ratio databases, the number of basic scale bars is increased to 18, and the color matching analysis of the two orders of magnitude for the seven standard colors was shown in Fig. 3.

The Fig. 3 was shown that the color difference corresponding to the 10 scale spline databases was 1, and the color difference corresponding to the 18 scale spline databases was 2. It can be seen from Fig. 3 that the database of increasing the basic scale spline had a significant improvement in the color matching compared with the original 10 scale spline databases, and the color difference 2 is decreased several points compared the higher points of the color difference 1. The color difference volatility of the 7
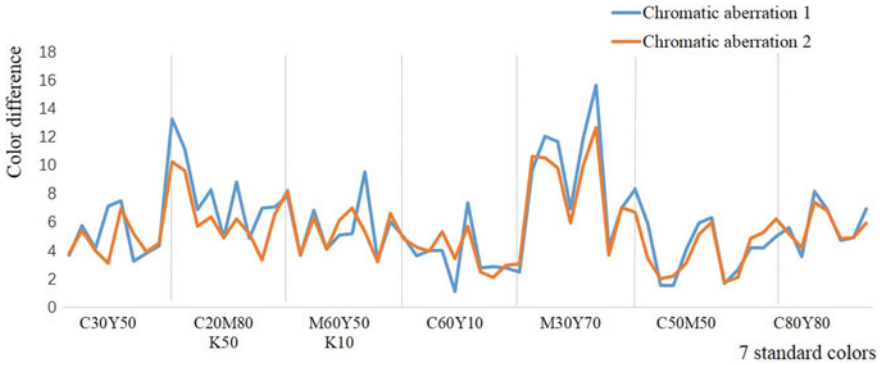
**Fig. 3.** Comparison of color differences between 10 scale spline databases and 18 scale spline databases for 7 color schemes

standard colors corresponding to the 18 scale spline database was relatively lower and the color difference is smoother than before.

### 2.3   Influencing Factors Analysis

The appearance of the paper is affected by the absorbency of the paper and the gloss of the standard color. Laser paper has lower ink absorption and higher smoothness, so the color difference of this database is smaller. The printing speed is related to the ink transfer rate. Slower database color matching is more accurate than the other two speeds; the 18-scale basic spline database has more color information than the 10-scale database, resulting in a smaller color difference [8].

## 3   Conclusions

Based on the X-Rite color matching system, this paper explored the influence of different databases on the final color difference by establishing the ink color matching database and measuring the color difference. The color difference analysis of seven standard colors were compared in this paper by three kinds of printing materials, three printing speeds and the number of two basic proportional splines. It was concluded that from these three factors, the corresponding database on the upper part of the spline of laser printing paper is more accurate. Moreover, 18 basic ratios are better than 10 proportional databases in color matching, with reduced fluctuation and relatively smaller influence on color difference.

# References

1. Zhu Y, Zhao Y, Wang H et al (2017) Application and development trend of computer color measurement and color matching in printing and dyeing. J Chengdu Text Coll 34(02):220–222
2. Liu W, Gengsheng H, Qi W (2009) Printing color science. Chemical Industry Press, Beijing
3. Wei J, Peng M, Li Q et al (2018) Evaluation of a novel computer color matching system based on the improved back-propagation neural network model. J Prosthodont 27(8)
4. Zhang G, Wang M, Yang A (2019) Application of computer color matching in precise formula dyeing of polyester fabrics. Dye Finish Technol 41(02):23–27
5. Liu J, Wei X (2010) Establishment of color matching ink color matching database. J Beijing Inst Graph Commun 18(02):6–8
6. Lü Z, Wang X (2011) Research on accurate preparation scheme of color master ink based on color master. Packag Eng 32(13):74–78
7. Yang L (2019) The effect of paper quality characteristics on color reproduction. Print Today 03:67–68
8. Wang C (2010) Analysis of the causes of color difference in multi-color printing. Technol Mark 79–80

# Research on Yellow Reproduction of Antique Books Based on Small Color Gamut

Shiwei Liu[1(✉)], Junfeng Li[1], Quanhui Tian[2], and Ming Zhu[3]

[1] School of Packaging and Printing Engineering, Henan University of Animal Husbandry and Economy, Zhengzhou, China
hnzzlsw@163.com
[2] Department of Printing and Packaging Engineering, Shanghai Publishing and Printing College, Shanghai, China
[3] Department of Materials and Chemical Engineering, Henan University of Engineering, Zhengzhou, China

**Abstract.** In order to accurately reproduce the yellow color of old books on monitor, in this paper we collected the color value of old books and prepared a color card whose color gamut is narrow but can include the color of old books. Then we made a display ICC profile according to the traditional color management steps, and measured the color value of old books displayed on the monitor which was embedded the narrow gamut ICC profile. Statistics indicate that the color value of old books displayed on the monitor embedded the narrow gamut ICC profile is closer to the color value of real old books. Compared with the traditional color management that the color value of old books is displayed on the monitor embedded the common ICC profile, it shows that our color management process based on small color gamut can achieve a perfect effect to the yellow reproduction of the old books on monitor.

**Keywords:** Small gamut · Old books · Color card · Color management

## 1 Introduction

Nostalgic style has become a fashion, and the "old" of the past has become a "new" of the present [1]. Old books are rustic, with the characteristics of The Times, and this rustic in this era of flowers and flowers is very important [2].

The paper color of old books is getting more and more attention as an important appearance index, If we want to retain these memories, retain these feelings, maybe we can use some modern technology to reproduce the color of old books [3, 4]. Therefore, it is very necessary to reproduce accurately the colors of ancient books by using color management technology [5].

In this paper, we take the old books as the object, the purpose is to find a better method to make the display screen can accurately match colors of old books.

## 2    Experiment Process

The purpose of color management is to reproduce the yellow color of old book accurately. The experiment is divided into two parts, first, the traditional ICC profile was used to reproduce color on monitor [4–9]. The second time, a narrow gamut ICC profile was used to reproduce color on monitor. The process of the two parts is the same, but the color gamut has changed.

### 2.1    Large Color Gamut Color Management

First, open the scanned photo of the old book by Photoshop. Then select the "color Settings" options in the "edit" menu [10–14], and select the traditional display properties file, as shown in Fig. 1.



**Fig. 1.**  Position of "Color Settings" options

Select 10 points of yellow part in the picture on the monitor, the 10 points must near the corresponding point on the book (the position of the corresponding point was showed in Fig. 1, and the corresponding point lab value is (86, 1, 17), calculates the color difference between the 10 points lab value in the monitor and the corresponding point lab value in the book. Table 1 shows the lab value of the 10 points and the ΔE under CIE Standard Illuminant D50 for the CIE 10° Standard Observer.

### 2.2    Small Gamut Color Management

#### 2.2.1    Color Card of Small Gamut

The Lab value range of color card includes the color point of the ancient book and the sampling points around the color point of the ancient book. The Lab value of the ancient book was tested by spectrophotometer. The lab of the surrounding points takes

**Table 1.** Lab value of 10 points and the ΔE between display and the book real Lab

| Points | L | a | b | $\Delta E^2$ | $\Delta E$ |
|---|---|---|---|---|---|
| 1 | 89 | −1 | 19 | 17 | 4.12 |
| 2 | 88 | 1 | 20 | 13 | 3.60 |
| 3 | 86 | −1 | 19 | 8 | 2.82 |
| 4 | 91 | 2 | 18 | 27 | 5.19 |
| 5 | 87 | −1 | 20 | 14 | 3.74 |
| 6 | 90 | −1 | 17 | 20 | 4.47 |
| 7 | 89 | 2 | 16 | 11 | 3.31 |
| 8 | 91 | 2 | 19 | 30 | 5.47 |
| 9 | 88 | 1 | 19 | 8 | 2.82 |
| 10 | 90 | 1 | 18 | 17 | 4.12 |
| | | | | Average of $\Delta E$ | 3.96 |

an interval of 8 from the Lab value of sampling point. It is worth noting that if the sample spacing is too small, the color card data would be very large; if the change value is too large, the color could not be accurately expressed in detail around the sampling point.

At last, the color card is composed of 540 color blocks, and the gamut includes the color range of ancient books, the color card we arranged is shown in Fig. 2.
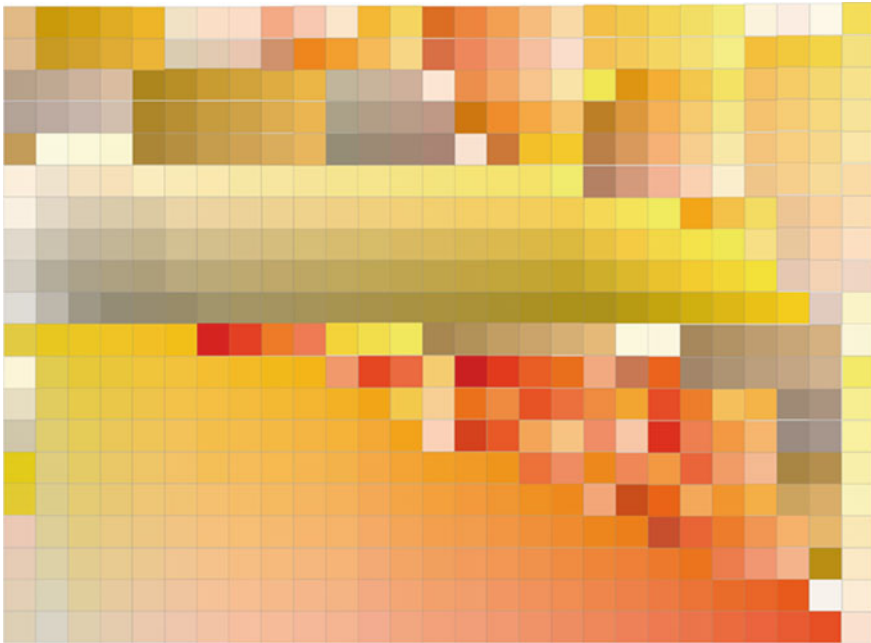


**Fig. 2.** Small gamut color card we arranged

Finally, the Lab value of the color block was converted into RGB value by PS software, the new txt file of monitor reference data file consists of all the color blocks RGB value according to ProfileMaker software encoding format, and the txt file was put in the folder under the path C:/ProgramFiles(x86)/XRite/ProfileMaker/ Professional5.0.10/ReferenceFiles/Monitor, in order to make the monitor profile of small color gamut.

### 2.2.2 ICC Profile of Small Gamut

After calibrating the monitor, open ProfileMaker and select the reference data txt file of the small color gamut just made in the interface of "Monitor options". And the option "measurement data" of ProfileMaker was measured by Xrite Eye-One. Finally, the ICC profile was completed to and put the file in the local disk C/Windows/System32/spool/drivers/color.

### 2.2.3 Color Difference Calculation

Calculate the color difference between display Lab and the book real Lab,the process is the same as the traditional color management process. The only difference is that when selecting the ICC profile in Photoshop, select the monitor profile made by the small color gamut, and the results are shown in Table 2.

**Table 2.** Lab value of 10 points and the $\Delta E$ between display and the book real Lab

| Points | L | a | b | $\Delta E^2$ | $\Delta E$ |
|--------|-----|----|----|-------------------|------|
| 1 | 85 | 1 | 17 | 1 | 1 |
| 2 | 86 | 1 | 18 | 1 | 1 |
| 3 | 87 | 1 | 16 | 2 | 1.14 |
| 4 | 86 | 2 | 18 | 2 | 1.14 |
| 5 | 86 | −1 | 17 | 4 | 2 |
| 6 | 87 | 1 | 17 | 1 | 1 |
| 7 | 86 | 1 | 16 | 1 | 1 |
| 8 | 85 | 2 | 18 | 3 | 1.73 |
| 9 | 88 | 1 | 19 | 8 | 4.89 |
| 10 | 86 | 1 | 15 | 4 | 2 |
| | | | | Average of $\Delta E$ | 1.69 |

## 3 Results

Contrast the data in Tables 1 and 2, we found that the $\Delta E$ is smaller by using the ICC profile of small gamut color card then using the traditional color management. the average color difference $\Delta E$ is 1.69, which is basically imperceptible to human eye, the experimental results show that the small color gamut ICC profile is effective in the color transfer process of old books, can achieve the perfect color reproduction effect.

Although small gamut color management is effective, it would be better if the following two details were improved.

The establishment of a small gamut color card: we used 540 color blocks to establish the color card. If the smaller the lab interval of the color blocks is, the more color blocks there are, the smaller the final color difference will be.

Calibration of monitor: Due to various factors, there may be errors in the display calibration, we can perform two or more calibrations of the monitor, and perhaps get better results.

## 4    Conclusions

In this paper, we propose a new method to achieve an accurate reproduction of the yellow in ancient books. The yellow color in ancient books is chosen as the sampling point, and 540 color blocks are used to make a small gamut color card by a certain interval. Then a monitor ICC profile is made to reproduce the yellow color of ancient books. Experimental data show that the proposed method performs better than the traditional color management significantly and can reproduce the yellow color of ancient books accurately. It is notable that the proposed method can also be applied to color management of products that have small color gamut, such as bronzes, ceramics and woods.

## References

1. National Post Office (2016) Express industry development "13th five-year plan" [EB], 12
2. Li Y (2014) Space design and analysis of the old bookstore. Master's thesis, Hebei University, Hebei, China
3. Zhang Y, Yan Q (2007) Calibration and characterization of display. Prepress Technology 9:49
4. Liang G (2016) Research on real-time color management method of display. Master's thesis, Hefei University of Technology, Anhui, China
5. Bruce FC, Murphy F (2005) Bunting real world color management. Beijing Electronics Industry Press, Beijing
6. Liu S (2016) Research on ICC color feature file generation method of display equipment. Master's thesis, Southeast University, Shanghai, China
7. Zheng Y, Yang S, Zhou S, Cao C (2005) Uniformity of CIE1976 LAB chromatic aberration formula. Packag Eng 26(2):48–49
8. Ma Z, Zhang L (1998) Analysis of components and typical workflow of color management system. Print Today 3:74–75
9. Zhou S (1997) Advanced color science. Printing Industry Press, Beijing

10. Li H (1994) Principle and application of color technology. Science Press, Beijing
11. Hu C (1993) Printing color and chromaticity. Printing Industry Press, Beijing
12. Du G (1993) Printing color science. Printing Industry Press, Beijing
13. Tang S (1990) Chromaticity. Beijing Institute of Technology Press, Beijing
14. Tian T (1995) Color engineering. Xi'an Jiaotong University Press, Xi'an

# Analysis of Color Gamut in Color 3D Printing

Liang Zheng[(⊠)], Chunmei Li, and Shengwei Yang

Printing and Packaging Engineering Department, Shanghai Publishing and
Printing College, Shanghai, China
`zg_zg@l63.com`

**Abstract.** At present, color 3D printing technology has been applied in many
fields, such as 3DP-based gypsum powder printing technology, plastic-based
FDM printing technology, paper-based LOM printing technology, PolyJet
printing technology and so on. All of these can realize mixed color 3D printing
including gradient color. PolyJet printing technology is the most representative
techonology. The purpose of this paper is to measure and analyze the gamut of
color PolyJet printing technology. The research method is to print standard color
target by color 3D printing equipment. The gamut of color 3D printing is
obtained by measuring and calculating. The gamut of color 3D printing is
compared with that of color inkjet printing on paper surface in order to analyze
the color rendering characteristics of color 3D printing results. The results show
that color 3D printing technology can display mixed colors including gradient
colors, but the color gamut is smaller than color inkjet printing on the surface of
paper. In particular, the appearance of light-tone colors and high-saturation
colors is still a big gap between 3D printing and color inkjet.

**Keywords:** 3D printing · PolyJet printing technology · Gamut · Color
reproduction

## 1 Introduction

With the application of new materials and technologies, 3D printing technology has
broken through the limitation of single materials and realized simultaneous printing of
multiple materials and colors, so as to process the colored texture and mapping of the
surface and complete the printing and molding of sophisticated models [1–3]. At present, the common color 3D printing technologies on the market include plastic-based
FDM (Fused Deposition Modeling) technology, paper-based LOM (Laminated Object
Manufacturing) technology, powder-based 3DP (Three-Dimensional Printing) technology and photosensitive polymer injection-based PolyJet technology [4, 5], which can
realize mixed color 3D printing including gradient color. Among them, the first three
technologies all spray color ink onto the molding material, and only the PolyJet technology based on photopolymer injection directly injects the color molding material to
complete the molding process [4–6]. Research on PolyJet technology has been carried
out, such as introducing the PolyJet monochrome 3D printing process [7], studying the
surface quality and dimensional accuracy of PolyJet monochrome 3D printing [8], and
studying the variation of raw material consumption during printing [9].

As mentioned earlier, PolyJet color 3D printing technology sprays the final molding material, which is a color photopolymer. The color of the photopolymer directly determines the color of the final molding result. The purpose of this paper is to measure the gamut of PolyJet color 3D printing technology and analyze the color rendering characteristics of PolyJet color 3D printing technology, which will play a reference role in promoting the application of PolyJet color 3D printing.

## 2    Principle of PolyJet Color 3D Printing Technology

The principle of PolyJet color 3D printing is shown in Fig. 1. The liquid photopolymer is sprayed onto the bench by a piezo nozzle. At the location where printing is desired, the color of the current layer is identified and the corresponding color of photopolymer is ejected to form a photopolymer liquid layer of a given thickness having a geometric profile. The liquid photopolymer on the workbench is then cured by ultraviolet light from an ultraviolet lamp. After the curing is completed, the workbench is precisely lowered by a forming layer thickness, and then a second layer of liquid photopolymer is cured. This cycle is repeated multiple times to bring the overall thickness and shape to the design requirements [10, 11].
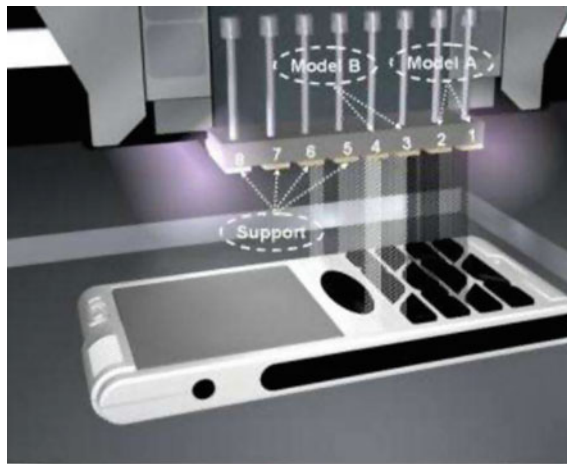


**Fig. 1.**  Principle of PolyJet 3D printing technology

In the process of PolyJet color 3D printing, photosensitive polymer materials of various colors can be directly ejected from corresponding nozzles. White, black, yellow, green and magenta are the five basic colors. The other colors are mixed by the three primary colors according to different ratios 0. This process is very similar to inkjet printing.

PolyJet technology also supports voxel printing. The voxel model is obtained by voxelization of the model. By transforming the mesh model into a solid object and

filling the whole model with voxels, see Fig. 2 [12]. PolyJet technology printers can be installed with a variety of materials at the same time. In addition to the color printing of different color materials, it is also possible to achieve a mixture of materials of different hardnesses, which is what the designer wants to achieve.
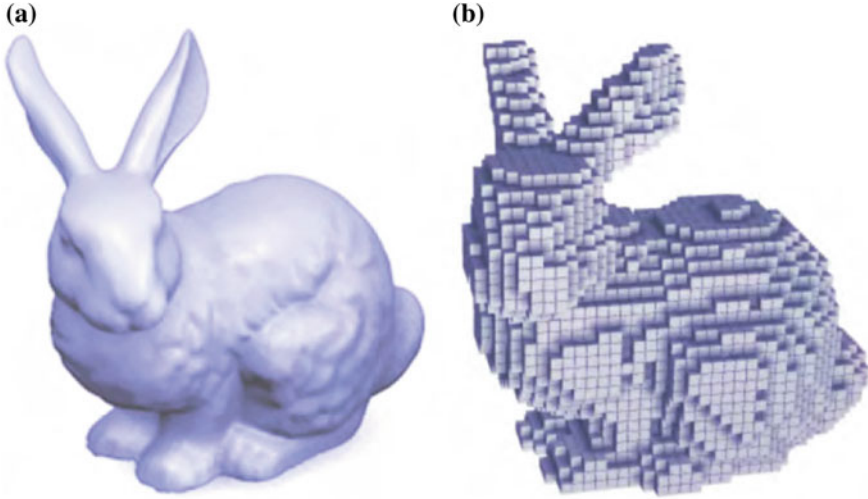


**Fig. 2.** Voxel printing diagram, **a** is the original model, **b** is the voxel model

## 3    Experimental Design

A flat rectangular cuboid model was created and printed with white photosensitive polymer on PolyJet 3D printing equipment. The thickness of the model is about 3 mm to ensure that the color measurement did not transmit light. The IT8.7-3 CMYK standard color target is printed on the surface of the model by mapping method. Figure 3 is a physical picture of the printed results.

The same IT8.7-3 CMYK standard color target was printed on matt digital proofing paper using an EPSON 9910 inkjet printer.

The color data of color 3D printing results and color inkjet printing results were measured by EyeOne Pro, and the corresponding gamut was calculated and generated by Gretag Macbeth ProfileEditor. By comparing the two gamuts, the color rendering characteristics of color 3D printing results are analyzed. It is emphasized here that the results of color 3D printing are not post-processed.
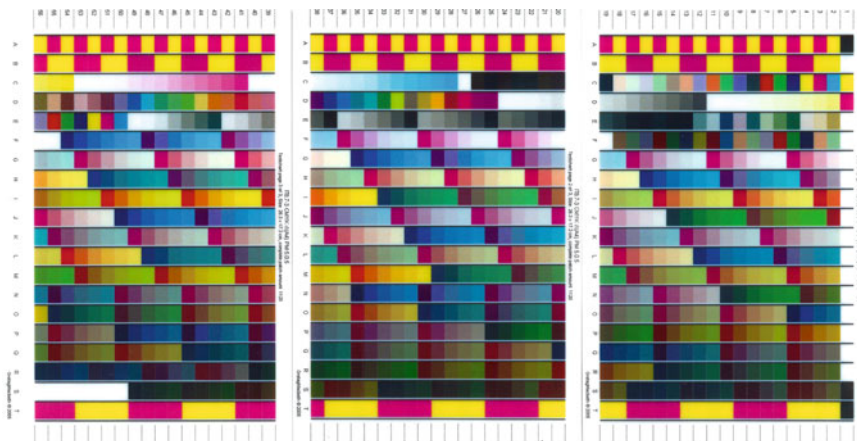
**Fig. 3.** IT8.7-3 CMYK standard color target printed by PolyJet 3D Printing technology

## 4    Result Analysis

### 4.1    Overall Color Gamut Comparison Analysis

Figure 4 shows the two color gamuts calculated and generated by the Gretag Macbeth ProfileEditor, where the color gamut of the inkjet print is displayed in translucent. It can be seen that, overall, the color gamut of the PolyJet color 3D printing technology is smaller than that of the inkjet printing, especially the gamut of bright and dark parts is significantly smaller than that of inkjet printing.
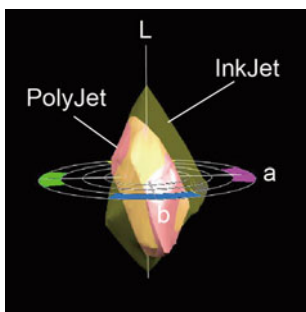


**Fig. 4.** Color gamut comparison between inkjet printing and color 3D printing

Analysis of the reasons for the obvious difference in brightness is mainly due to the whiteness of the inkjet printing paper is higher than the whiteness of the white photopolymer as the substrate; the cause of the difference in color saturation is mainly caused by the color characteristics of the color photopolymer. This conclusion can be confirmed by the difference of color data between Matt digital proofing paper and white

photopolymer, as well as the difference of color data of blue, magenta, yellow and black patches by inkjet printing and 3D printing. Table 1 shows the comparison of printing substrates and primary color data between inkjet printing and 3D printing. Among them, the white data of inkjet printing comes from Matt digital proofing paper and the white data of 3D printing comes from white photopolymer.

**Table 1.** Comparison of inkjet printing and 3D printing material and primary color data

|  |  | C | M | Y | K | W |
|---|---|---|---|---|---|---|
| InkJet | L* | 42.73 | 42.67 | 82.16 | 10.31 | 93.20 |
|  | a* | −32.92 | 75.73 | 5.02 | 2.23 | 1.91 |
|  | b* | −57.02 | 0.98 | 107.68 | 0.74 | −4.35 |
| 3D printing | L* | 36.17 | 33.60 | 63.18 | 17.33 | 81.10 |
|  | a* | −24.81 | 51.07 | −4.62 | −0.27 | −5.31 |
|  | b* | −37.76 | 9.25 | 73.39 | −1.32 | −3.78 |

In addition, the color gamut of color 3D printing is significantly smaller than that of inkjet printing on paper surface, because the surface gloss is affected by rough surface without post-processing. The influence of post-processing on the gamut of color 3D printing will be studied in the future.

## 4.2    Analysis of Coloring Characteristics of Different Lightness

Figure 5 shows gamuts of 3/4 lightness (L* = 75), intermediate lightness (L* = 50), and 1/4 lightness (L* = 25), respectively. It can be seen that the gamut of PolyJet color 3D printing has the following characteristics:
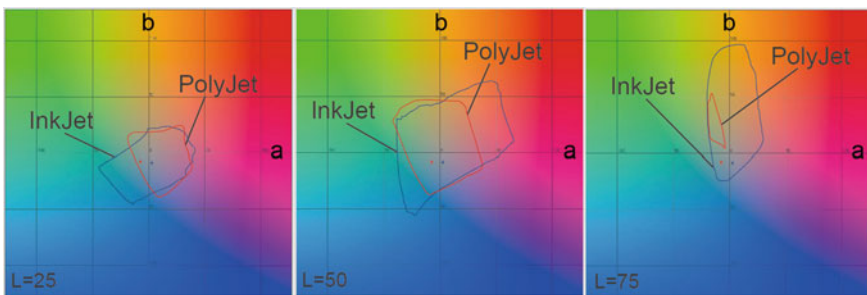


**Fig. 5.** Color rendering characteristics under different lightness

(1)  The difference between dark gamut and ink-jet printing gamut is smaller than that between bright gamut and ink-jet printing gamut.
(2)  In the high- lightness range, PolyJet color 3D printing is relatively poor in red, orange, purple and other colors, but it is better for yellow and green.

(3)  In the low-lightness range, PolyJet color 3D printing has poor rendering of cyan and blue tones, but better rendering of red and purple tones, especially for purple, even beyond the gamut of inkjet printing.

(4)  In the medium lightness range, PolyJet color 3D printing is more balanced for each color tone, with no obvious weakness, and the purple tone is slightly better than inkjet printing.

Figure 6 and Fig. 7 show the gamuts of dark and bright tones, respectively. In the dark part, when L = 12, the gamut of color 3D printing shrinks to very small, and when L = 10, the gamut shrinks to zero. This shows that for colors with L value less than 10, color 3D printing can hardly be rendered. In the bright part, when L = 77, the gamut of color 3D printing shrinks to very small, and when L = 78, the gamut shrinks to zero. This shows that for colors with L value greater than 78, color 3D printing can hardly be rendered.
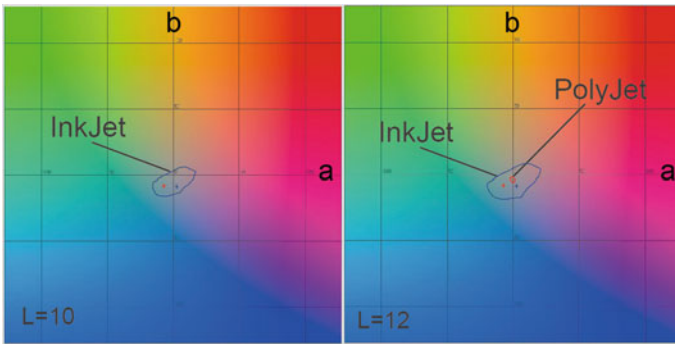


**Fig. 6.** Dark tone gamuts
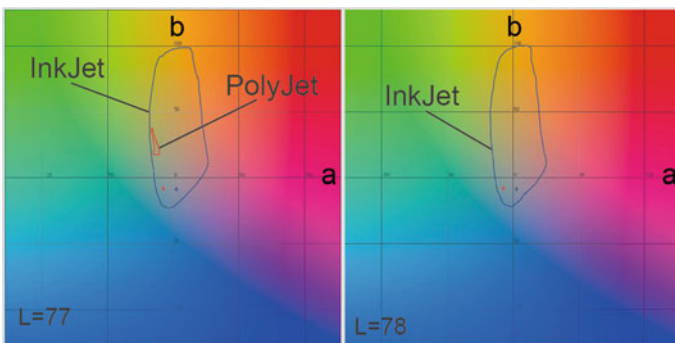


**Fig. 7.** Bright tone gamuts

In comparison, color 3D printing has better rendering capabilities for dark tones than for bright tones.

## 5  Conclusions

By comparing the gamut of PolyJet color 3D printing with that of inkjet printing on paper surface, the following conclusions can be drawn.

(1) PolyJet color 3D printing technology can present mixed colors including gradient, but its gamut is smaller than that of paper surface color inkjet printing. It is mainly manifested in the inadequacy of the rendering ability of extremely bright, extremely dark and highly saturated colors.
(2) PolyJet color 3D printing technology has different ability to present different tones with different brightness. It is better for high-lightness yellow, green and low-lightness red and purple, and relatively low for high- lightness red, orange, purple and low- lightness cyan and blue.
(3) Color 3D printing technology is more capable of rendering dark colors than for bright colors.

The above conclusion is obtained in the case where the result of color 3D printing is not post-processed. The effect of post-processing on the color rendering of color 3D printing will be explored in future studies.

## References

1. Yusheng S, Lichao Z, Yu B (2015) The development of 3D printing technology and its software implementation. Sci Sin Inf 45(2):197–203
2. Shuoping C, Heping YI, Zhihong L et al (2016) The 3D printing polymers and their printing technologies. Mater Rev
3. Dai L, Hong XY (2014) The development of 3D print technology. Appl Mech Mater 644–650:4856–4859
4. Yuan J, Zhu M, Xu B et al (2018) Review on processes and color quality evaluation of color 3D printing. Rapid Prototyp J 24(2):409–415
5. Stanić M, Lozo B, Muck T et al (2008) Color measurements of three-dimensional ink-jet prints. In: International conference on digital printing technologies
6. Stanic M, Lozo B (2010) Permanence and color stability in 3D ink-jet printing. Is & T Reporter 541–544(4)
7. Yanping H (2016) Practice of 3D printing technology in higher vocational education. Autom Instrum
8. Youlai X, Ai D, Zhiyong X et al (2016) 3D printing technology for the fabrication of micro target components. High Power Laser Part Beams
9. Zhouyi L, Hanyu S (2017) Material consumption analysis of square ring formed by polyjet color 3D printing. J Ordnance Equip Eng

10. Dong-Fang LI, Ji-Min C, Yan-Ping Y et al (2015) Development and application of stereo lithography apparatus. J Beijing Univ Technol
11. Lu G (2016) Development Review on 3D printing technology. Ind Technol Innov 6:1288–1292
12. Wenpeng XU, Longtao M, Shouming H et al (2018) Construction of support structure based on voxelization models for 3D printing. J Graph

# Study on the Influencing Factors of Color Reproduction in Color 3D Printing

Chunmei Li[✉], Liang Zheng, and Ying Xiao

Department of Graphic Communication, Shanghai Publishing and Printing
College, Shanghai, China
`lichunmeil206@sina.com`

**Abstract.** Development of the color 3D printing technology has greatly expanded the application field of 3D printing although color performance of color 3D printing is not satisfied. The influencing factors of color reproduction in color 3D printing were studied in this paper. Firstly, the printing principle and relative merits of different color 3D printing technologies were compared and the 3D printing technology with the highest degree of color reduction was found. Then, this color 3D printing technology was used to study the influencing factors of color reproduction. By comparing different standard color blocks, it was found that the number of printing layers has the greatest influence on color reproduction in color 3D printing. The relationship curves of the number of printing layers, hue, brightness, saturation and chromatic aberration were obtained through experiments. This study can provide the best color reproduction scheme for the color 3D printing technology.

**Keywords:** Color 3D printing · Color reproduction · Chromatic aberration

## 1 Introduction

Recently 3D printing technology is well developed. Compare to conventional production processing 3D printing technology has many advantages: lower costs, less time, saving material, individual customization, accurate replication, complex structure produced directly without assembly, etc. [1].

With the expansion of application fields, more requirements are put forward for 3D printing technology. For example, those industries such as product design, medical care, cultural relic restoration and jewelry manufacturing have special color requirements for models. But only monochrome or only two-color products could be printed in most early 3D printers [2–5]. In order to meet the demands of market color 3D printing technology has gradually been developed. However, different 3D technologies have different color expression when the products have been printed [6–9]. The basis of color reproduction and color measurements methodology, as well as the color permanence or color stability, are described and discussed in 3D ink-jet printing [10]. A novel thermoforming-based coloring technique was proposed to solving the problem of air pockets in concave regions and discoloration in overly stretched regions [11].

In this paper different types of color 3D printing technologies were listed. At the same time the printing principles, advantages and disadvantages of different color 3D

printing technologies were compared. The 3D printing technology with the highest color restoration degree was determined. Then this 3D printing technology was used to find the factors affecting color reproduction. Different standard color blocks were printed for comparison in the experiment. The test data were studied to find the relationship between the print layer number and hue, brightness, saturation and color difference. This result can provide an optimal scheme for color 3D printing.

## 2    Compare of Different Color 3D Printing Technologies

Based on the different printing principles and materials there are five kinds of color 3D printings on the market: FDM (fused deposition modeling), LOM (laminated object manufacturing), 3DP (3-dimension printing), Polyjet 3D Printing, SLM (selective laser melting) or SLS (selective laser sintering).

### 2.1    FDM Color Printing

FDM is widely applied as a cheap and convenient 3D printing technology. Most materials used by FDM printers are PLA and ABS. At the beginning, there were many different colored materials, but only one colored material could be used when printed because the FDM printer has generally only one printing nozzle. So the printed products were monochrome. In order to meet the demand of color products the printing equipment has been transformed from a single nozzle printer to a double nozzle printer. So the two-color products could be printed at the same time. But the model was still only two colored. The gradient material was developed by researchers and then the product could be printed in a gradient color. But where a particular color appears in the model could not be controlled. The latest technology is to print the white model first and then the white model should be painted with the inkjet printer, but the brightness and saturation of the color on the model are not satisfied because that the ink doesn't blend well with the base.

### 2.2    LOM Color Printing

The simple sheets of A4 are used in LOM color printing machine to build up 3D objects. The consumables are A4 paper, water soluble adhesive and cutting knife. The software which controls the printer takes the digital 3D data that to be made and slices it into layers equal to the thickness of the A4, approximate 0.1 mm. The depth of the cutting knife is accurately set and this can ensure a perfect cut every time.

First the outer outline of the layer model was printed by a color inkjet printer on both sides of each piece of paper (the outline is colored and has a certain width), and then all the printed paper were put into the paper tray. A sheet of paper is pasted on the build plate at first. The sequence within each layer for the 3D printer is as follows: (1) Deposit adhesive on the top layer; (2) Pull-in and place the next sheet; (3) Press the layers against heat plate; (4) Cut along the center of the colored outer contour into the new top layer using a cutting knife. Then repeat the step (1)–(4) until the object is

finished. Finally the waste parts should be removed. The product can be finished in a number of ways such as hardened, plated, coated, sealed and cast if it is necessary.

### 2.3    3DP Color Printing

Powder-like materials such as sandstone powder, clay powder, glass powder, bone powder, tire fragments and even sawdust, can be used as 3DP printing materials. The binder mixed with colorants is the main factors which contribute to create full-color 3d models.

### 2.4    Polyjet Color Printing

The raw CMYK materials similar to that of inkjet printing were developed in polyjet color printing. And these colored raw materials can be configured with each other to form more than 500,000 colors. At the same time these materials can also be flexible. So the polyjet color printing technology can produce a wide range of color products: ultra-real prototypes with stunning visual effects, soft-touch parts, medical models with perfect vision and tactile fidelity.

### 2.5    SLM or SLS Color Printing

SLM and SLS technology are relatively mature in aerospace, medical implantation, automobile parts, etc. The materials are metals. The color of a model mainly depends on the natural color of molding materials, such as gold, silver and copper. The surface color of the model can be controlled by mixing different proportions of liquid metals. The technology is already being used in jewelry industry.

   Compared with these five color printing technologies, the inkjet printer was used to add colors to the original materials in FDM, LOM and 3DP. The color of a product depends on the degree of integration between ink and the original materials. The color restoration is not satisfied but the cost is lower. The color of SLS products depends on the color of the metal itself. In addition to the jewelry industry other applications do not have high requirements in color. They pay more attention to the mechanical properties of products. Polyjet color printing is the only one technology that the raw materials with their own colors are used. These materials can be mixed to form new colors just like the ink of the inkjet printer. There are so many kinds of colors beyond our imagination, and the hardness of materials can also be controlled. At the rest of this paper Polyjet color printing technology will be taken into account to print test samples and the factors that affect the color reduction degree should been find out.

## 3    Experiments

### 3.1    Equipment, Scheme and Test Instrument

The test samples are designed as follows: first, the white 150 layers were printed as the background layers. On this base 10 steps are printed and each step has 10 layers. The size of each step section is 50 mm*60 mm. Due to the limit of size of the printer the 10

steps are divided into two parts for printing. The test samples are printed in CMYK four colors.

As mentioned above, the test sample is printed by polyjet color 3D printing technology. The printer is Stratasys J750 and there are two options of printing layer thickness of this printer: 0.014 mm and 0.028 mm respectively. The testing blocks are printed with 0.014 mm layer thickness, and the printed samples are shown in Fig. 1. Figure 2 is the test instruments named X-rite Exact used in the experiment.
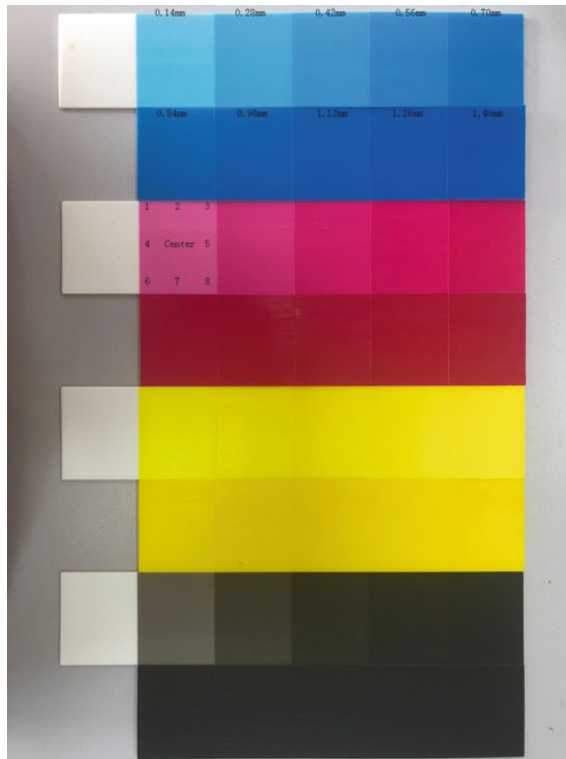


**Fig. 1.** Testing blocks

## 3.2 Data Curves

Eight points are chosen on each step (Fig. 1 point 1–8). Hue (H), lightness or value (L), saturation or chroma (C) of every point are measured and the average value of these 8 points is calculated as the value of this step. Then the values of different steps are compared. The relationship between hue and thickness is shown in Fig. 3. The relationship between brightness and thickness is shown in Fig. 4.

The relationship between saturation and thickness is shown in Fig. 5. Magenta block is chosen as a representative to find the evaluation between the eight points and the central point which is shown in Fig. 6.

**Fig. 2.** Testing instrument
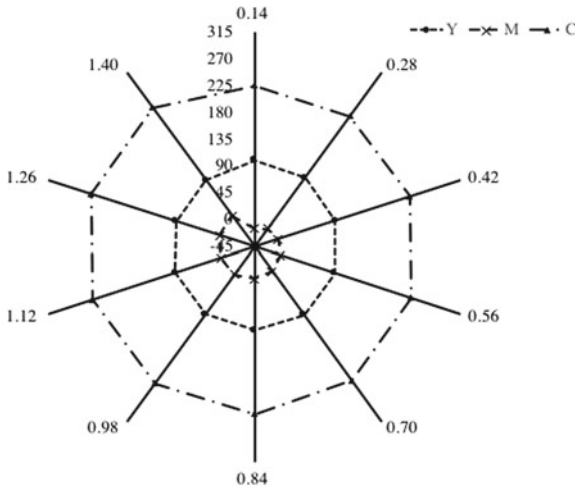


**Fig. 3.** Relationship between hue and thickness
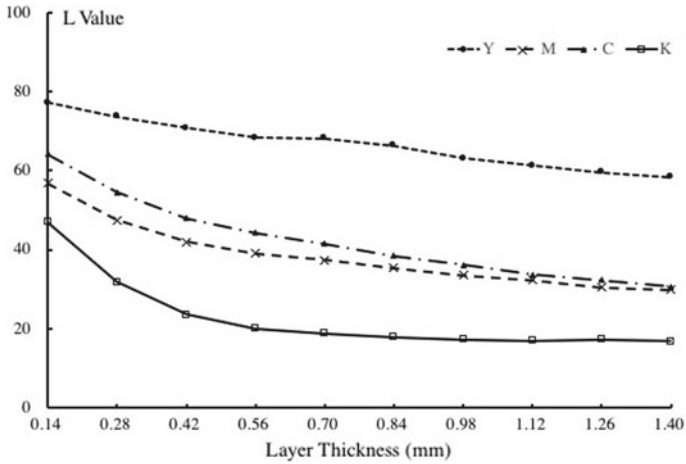
**Fig. 4.** Relationship between lightness and thickness
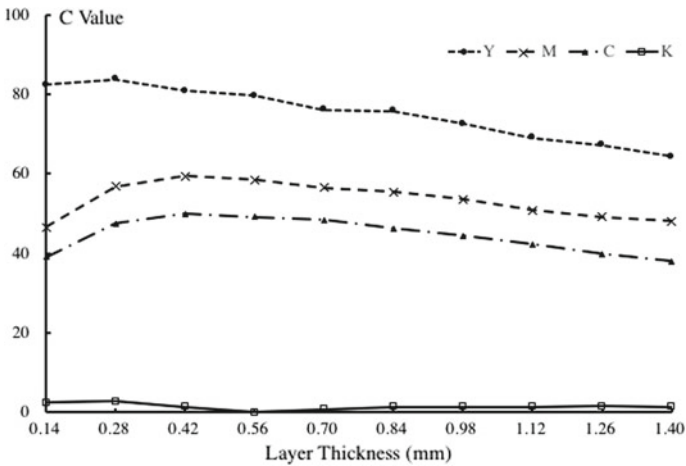


**Fig. 5.** Relationship between saturation and thickness

### 3.3    Discussion

In order to ensure the authenticity of the data, the sample blocks have not gone through any post-processing.

Figure 3 shows that the hue of CMY is basically a concentric circle. This conforms to the basic law of color. And the error of magenta is slightly larger.

Figure 4 shows that the brightness decreases with the increase of printing thickness. When the printing thickness is less than 0.56 mm the brightness decreases quickly. At other side when the printing thickness is more than 0.56 mm, the brightness decreases gradually.
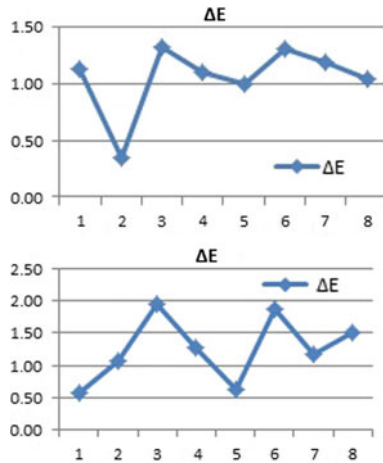
**Fig. 6.** The evaluation between the 8 points and the central point

Figure 5 shows that the change of the saturation of black s is not obvious when the print thickness increases. The maximum saturation of yellow should occur under highest brightness. The saturation of yellow must decrease with the printing thickness.

When the printing thickness is less than 0.42–0.56 mm the saturations of magenta and blue are increased. When the printing thickness is more than 0.42–0.56 mm the saturations of magenta and cyan are decreased. This is also in line with the color law described in Munsell Color System.

When the printing thickness is less than 0.56 mm the color concentration and the saturation increase as the printing thickness increases. When the printing thickness exceeds 0.56 mm the brightness of the color decreases, so does the saturation as the printing thickness increases. That is to say, the maximum saturation of magenta and cyan occurs when the brightness is relatively value.

Figure 6 shows that the evaluation between the 8 points and the central point is exceed 1 because there is no any post-processing.

According to the analysis of the experimental data, when the printing thickness is below 0.56 mm, the color change is relatively large; when the printing thickness is above 0.56 mm, the color change becomes smaller and tends to be stable. Therefore the default color printing thickness of J750 is 1 mm which will be reduced by about 0.5 mm with the addition of later polishing. So that the best color satisfaction can be obtained.

## 4   Conclusions

In this paper 5 types of color 3D printing technologies are listed. Polyjet 3D printing technology has the highest color restoration degree. Different standard color blocks are printed for comparison in the experiment. The test data was studied to find the relationship between the printing thickness and hue, brightness, saturation. It is concluded

that the maximum saturation of yellow should occur under highest brightness. The maximum saturation of magenta and cyan occurs when the brightness is 0.56 mm. Therefore the default color printing thickness of J750 is 1 mm which will be reduced by about 0.5 mm with the addition of later polishing. So that the best color satisfaction can be obtained. This result can provide an optimal scheme for color 3D printing.

Further, if we need to repair cultural relic, replicate and design complex anatomical structures (inside and out), create color stop motion animation models in the exact color shades and variations, etc., traditional mapping method(the thickness of the color layer is fixed) cannot achieve good results. So voxel files must be designed to achieve voxel printing using the relationship between printing thickness and hue, brightness, and saturation.

# References

1. Li C, Xiao Y, Zhen L (2018) Design and realization of a support bracket for medical test tubes based on 3D printing. In: Advances in graphic communication, printing and packaging. Lecture notes in electrical engineering, vol 543, pp 513–520
2. Sahi SE, Jiang Y, Spence AD (2009) Oriented 3-D inkjet printing. Comput Aided Des Appl 6(3):399–406
3. Stanic M, Lozo B, Svetec DG (2012) Colorimetric properties and stability of 3D prints. Rapid Prototyp J 18(2):120–128
4. Sugavaneswaran M, Arumaikkannu G (2014) Modeling for randomly oriented multi material additive manufacturing component and its fabrication. Mater Des 54(4):779–785
5. Dimitrov D, Schreve K, Beer ND (2006) Advances in three dimensional printing-state of the art and future perspectives. Rapid Prototyp J 12(3):136–147
6. He L, Chen G (2015) Color 3D printing based on UV ink-jet technology. Packag Eng 36 (9):134–138
7. Liu Y, Yao S, Jiao Y et al (2018) Improving the Surface coloring effect of 3D printing model based on UV ink-jet system. Packag Eng 39(5):196–202
8. Gibson I, Ming LW (2001) Colour RP. Rapid Prototyp J 7(4):212–216
9. Wang DX, Leng HW, Chen S (2007) Recent advances in colour rapid prototyping. Int J Precis Technol 1(1):133–138
10. Stanic M, Lozo B (2010) Color and permanence issues in 3D ink-jet printing. In: MIPRO 2010, Opatija, Croatia, pp 274–277
11. Zhang Y, Tong Y, Zhou K (2017) Coloring 3D printed surfaces by thermoforming. IEEE Trans Vis Comput Graph 23(8):1924–1935

# Image Processing Technology

# Region of Interest Extraction Based on Convolution Neural Networks for Image Linear Distortion Correction

Jianjun Zhao[(✉)] and Xiangru Ren

School of Printing and Packaging, Wuhan University, Wuhan, China
jjzhao@whu.edu.cn

**Abstract.** Image linear distortion, which causes tortuosity and texture loss in the image, is a fundamental problem in computer vision. In the correction processing, extracting the region of interest is the core technology. The commonly used methods include several steps which require the complicated interactive operation before perspective transformation. In this paper, we propose an accurate and fast region of interest extraction method based on convolution neural networks(ROI Net), which directly exploits and extracts the region of interest after mass dataset training without manual interactions. As a result, we can simplify the steps and provide more accurate parameters to complete the follow-up perspective transformation work, contributing to the image linear distortion correction. The experimental results can demonstrate that the algorithm proposed in the paper is state-of-the-art and accurate.

**Keywords:** Image distortion correction · Region of interest · Convolution neural networks

## 1 Introduction

Because of the wide-angle lenses, technical characteristics of the optical converters or the motion of the recording camera or the object [1], there usually exists image linear distortion, affecting the quality of the image, which is a problem worth exploring in computer vision. In order to resolve the image linear distortion, several methods had been proposed. The ordinarily used methods require numerous steps including edge detection [2–4], corner extraction [5] and perspective transformation [6, 7], which require manual interaction [8], leading to the result errors. The other commonly used method is based on finding areas of the image that match a template [9] ,which is the core difficulty of image distortion correction, namely extracting the region of interest. In addition, we have learned that Convolution neural networks have been widely applied in the image processing, such as the recognition of face [10, 11], for the reason that it is more intelligent and accurate, but it is seldom used in image distortion correction. In view of such a situation, this paper focuses on the extraction of interested region based on convolution neural networks. We design an appropriate convolution module to form our network. With the loss function, the well-trained data sets supply more accurate parameters to finish the following perspective transformation, thus

reducing the intervention errors and improving the accuracy and efficiency of Image Linear Distortion Correction.

## 2   Convolution Neural Networks for ROI Extraction

### 2.1   Network Architecture

CNN model mainly includes input layer, convolution layer, pooling layer, full connection layer and output layer [12, 13]. The popular models are proposed such as VGG [14], ResNet [15] etc. In this paper, we design an appropriate network architecture shown in Fig. 1, which follows the two principles. The first one is to pay attention to the area of the whole ROI; and the other one is to learn as more local information as possible to distinguish the ROI area from the background area. In order to guarantee that the ROI area can be correctly detected by the network, we adapt the network architecture combining the global feature extractor and local feature extractor. The global feature extractor is responsible for learning the outline information of ROI, which attaches little importance to the specific details. Therefore, it uses the extended convolution to increase the receptive field of this part rapidly, thus ensuring the extraction of the global information of the image ROI. Meanwhile, we refer to the densely connected convolution networks (Dense Net) [16–18], this paper also designs a local feature extractor to guarantee the correct ROI extraction, by which we can learn the details of the image very well.
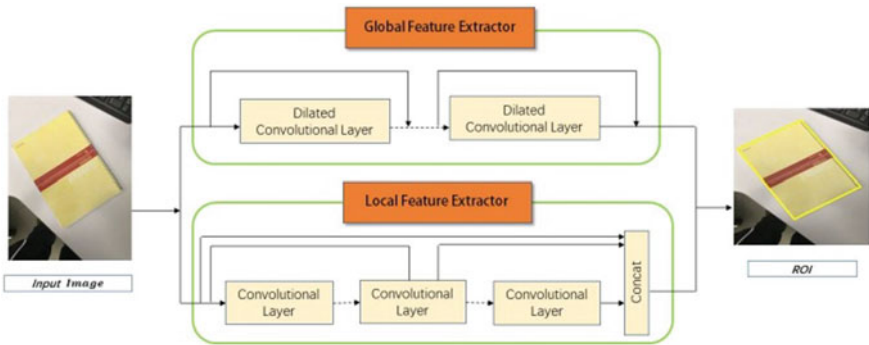


**Fig. 1.**  The network architecture we design for ROI extraction

Unlike the method of detecting saliency region [19–21], we need to pay more attention to the extraction of ROI instead of the recognition of the saliency region in the image. For example, in the Fig. 2. what we learn is the area where the card is located, rather than the specific content such as portrait and text detection. In saliency region detection, it cares more about the salient objects and background regions; as a result, more objects may be detected, which is not necessary in linear correction.

**Fig. 2.** The image of examples

## 2.2 Loss Function

We draw on the cross entropy loss function [22] to design the loss function for our own network. However, different from the original one, in this paper, we remove the fusion layer of the cross entropy loss function, for the reason that it is not necessary in our network. For each image, we drive the output node values to 0 or 1 depending on the target values [18]. 0 represents that there is no interesting feature at this pixel, while 1 means that the pixel contains all the region of interest. Finally the loss function can be deduced

In Formula (1), the training dataset is (X, Y), the test dataset is (X′, Y′), X and X′ belong to the same distribution. Assuming that Y′ equals 1, X′ is over-sampled in α ratio on X, and X′ is over-sampled in β ratio on X when Y′ equals 0.

$$H(p, q) = \frac{1}{N} \sum_{i=0}^{N} -\alpha y_i \log \hat{y}_i - \beta (1 - y_i) \log(1 - \hat{y}_i) \tag{1}$$

## 2.3 Training

Training is an important problem for extracting the region of interest. We use the structure of Dense Net for reference. Each layer can access to the gradients directly from the cross entropy loss function and the original input signal, thus realizing the implicit deep monitoring [23]. Through training, the latter layers can achieve the input information from the former existing layers, which also establish the connection between different layers. As a result, it strengthens the spread of the feature [22] and uses the feature more effectively.

## 2.4    Experiments

We compare the method based on ROI Net and the commonly used way. The common method detects the edge of the image first, and then extracts the feature points by the ORB (oriented FAST and rotated BRIEF) algorithm to in the image. Finally it uses the convex hull algorithm to extract the ROI [24]. Shown in Fig. 3, we take three samples as example, and can observe that the experiment results based on ROI Net are superior to the original method apparently. Meanwhile, it can save time when processing a large number of pictures, which shows our method to extract the ROI is more efficient.
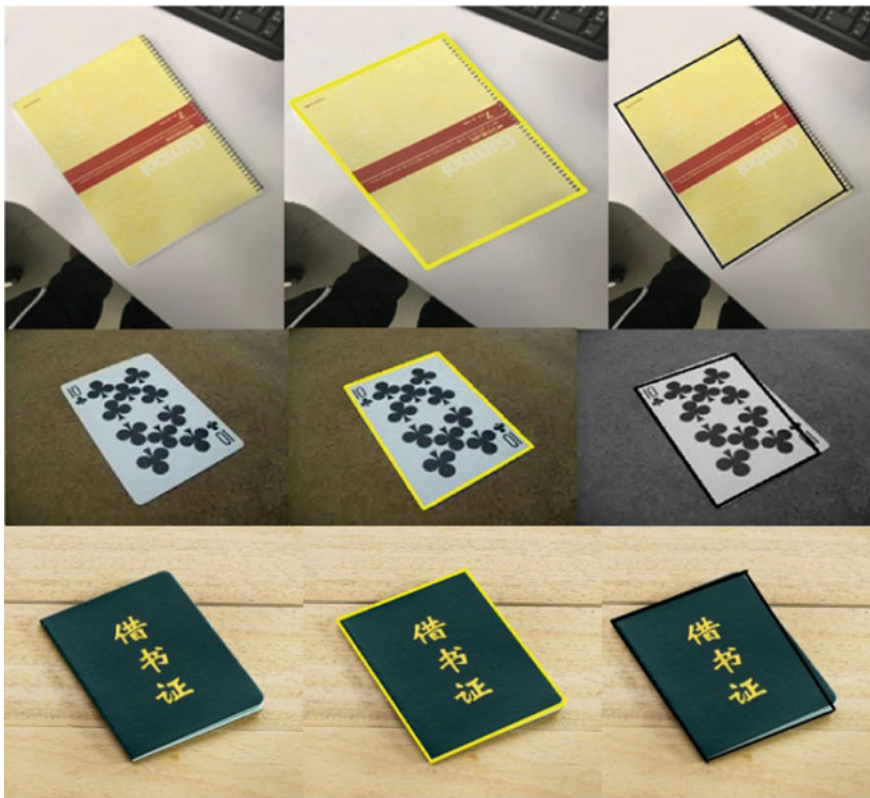


**Fig. 3.**  The architecture of ROI Net. Input the image and generate the output the ROI

## 3    Perspective Transformation

Perspective transformation is a coordinate transformation with perspective property from view space to target space [25]. The core of this step is to achieve the perspective transformation matrix. Based on the extraction of the ROI, we obtain the four coordinate values of the vertexes $(x_1, y_1)$, $(x_2, y_2)$, $(x_3, y_3)$, $(x_4, y_4)$, according to the corresponding coordinate $(u_1, v_1)$, $(u_2, v_2)$, $(u_3, v_3)$, $(u_4, v_4)$, and then we can use the

perspective parameter to correct the distortion. Figure 4 shows the process of the image being corrected.
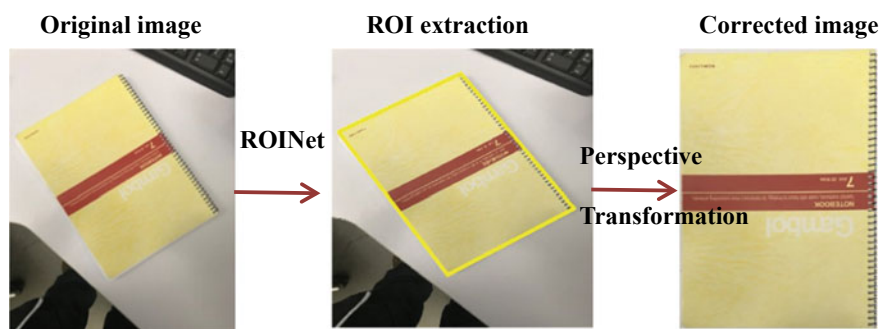


**Fig. 4.** The process of correct the image linear distortion

## 4 Conclusions

In this paper, we integrate the Convolution neural networks with region of interest extraction to improve the image linear distortion correction. The proposed approach, ROI Net, learns to adaptively extract the region. We design a special module with global feature extractor and local feature extractor to help train and improve the performance. And then we use the perspective transformation by perspective matrixes to conduct the distortion correction. By experiments, we can conclude that the method based on CNN is superior to the commonly used ways in the ROI extraction, which can decrease the manual interaction and improve the accuracy and efficiency.

## References

1. Karnaukhov VN, Kober VI (2017) Analysis of linear distortion characteristics in problems of restoration of multispectral images. J Commun Technol Electron 62(12):1464–1469
2. Liu Y, Cheng M-M, Hu X et al (2017) Richer convolutional features for edge detection. In: IEEE conference on computer vision and pattern recognition, pp 5872–5881
3. Wang L, Shen Y, Liu H, Guo Z. An Accurate and efficient multi-category edge detection method. Elsevier B.V. https://doi.org/10.1016/j.cogsys.2019.06.002
4. Jing J (2012) Image geometric distortion correction based on edge detection algorithm, smart factory. 1606-5123[2012] 10-0080-04
5. Zhu Z, Wang X, Liu Q et al. Analysis of the extraction accuracy of the corner point of the camera using polarization imaging. In: SPIE—The International Society for Optical Engineering. https://doi.org/10.1117/12.2512023

6. Wenli T (2017) Document image calibration recovery algorithm based on Hough line detection and two-dimensional perspective transformation. Electron Meas Technol. https://doi.org/10.19651/j.cnki.emt.2017.09.024

7. Han B, Yang D (2018) Research on normalization of printed image based on transmission transform. In: Computer engineering and applications

8. Yingchao M, Zhongping Z, Huaqiang Y et al (2017) Automatic detection of particle size distribution by image analysis based on local adaptive canny edge detection and modified circular Hough transform. Micron. https://doi.org/10.1016/j.micron.2017.12.002

9. Lihua W, Shang Q, Sun Y et al (2019) A self-adaptive correction method for perspective distortions of image. Front Comput Sci 13(3):588–598

10. Zhang JW, Shen W, Wu ZD (2019) Recognition of face privacy protection using convolutional neural networks. J Image Graph 24(05):0744–0752

11. Taigman Y, Yang M, Renato M et al (2014) Deep face: closing the gap to human-level performance in face verification. In: Proceedings of IEEE conference on computer vision and pattern recognition, vol 2014. IEEE, Columbus, pp 1701–1708

12. Zheng Y, Li G, Li Y (2019) Survey of application of deep learning in image recognition. Comput Eng Appl 55(12):20–36

13. Minghai Y, Zhen Y (2019) Research on real-time defect detection method based on lightweight convolutional neural network. Comput Meas Control

14. Simonyan K, Zisserman A (2014) Very deep convolutional networks for large-scale image recognition. arXiv:1409.1556

15. He K, Zhang X, Ren S et al (2016) Deep residual learning for image recognition. In: Computer vision and pattern recognition. IEEE, pp 770–778

16. Kewei W, Gao Y, Ma H et al (2018) A deep generative directed network for scene depth ordering. Vis Commun Image Represent. https://doi.org/10.1016/j.jvcir.2018.12.034

17. Qirui Y (2019) Fire image recognition algorithm based on improved densenet network. J Comput Appl Softw

18. Huang G, Liu Z, van der Maaten L, Weinberger KQ. Densely connected convolutional networks. https://arxiv.org/pdf/1608.06993.pdf

19. Yiliang N, Jixiang D, Yang L (2018) Image retrieval based on convolution feature map fusion and saliency detection. J Huaqiao Univ (Nat Sci)

20. Xin L, Leiting C, Hongbin C (2018) Salient object detection algorithm based on structure-sensitive deep neural network. Appl Res Comput. https://doi.org/10.3969/j.issn.1001-3695.2018.01.0064

21. Liu S-T, Wang H-N, Wang Z. Image target segmentation method based on fuzzy entropy and salient region extraction. SPIE—The International Society for Optical Engineering. https://doi.org/10.1117/12.2503165

22. de Li Z, Lu X, Cui G (2019) Cost function selection and performance evaluation for digital image recognition. Electron Opt Control. http://kns.cnki.net/kcms/detail/41.1227.TN.20190422.1527.002.html

23. Lee C-Y, Xie S, Gallagher P et al (2015) Deeply supervised nets. In: AISTATS

24. Zefenga Y, Xianyib C, Lua X (2018) Study on detection of ROI based on ORB and minimum convex hull. Appl Res Comput. https://doi.org/10.3969/j.issn.1001-3695.2018.10.071

25. Wei A, Hong L, Hui X et al (1999) Projective transformation and affine transformation in pattern recognition. Syst Eng Electron

# Research on Image Output Method Based on Optical Fiber Array Features

Xueying Wang[(✉)], Qiang Wang, and Genfu Yang

School of Media and Design, Hangzhou Dianzi University, Hangzhou, China
`812513427@qq.com`

**Abstract.** In the fields of plate printmaking and digital printing, the combination of laser dots and scanning technologies have become increasingly popular for half-tone image output. Targeting the external drum laser scanning imaging system based on optical fiber array, an optical microfiber array with a distance technology suitable for various laser scanning devices is proposed in this paper, which solves the key problems of imaging separation, black scanning area and short focal depth. In addition, a half-tone image output method is designed, which can achieve screen rulings over 175 lines per inch, satisfying the high precision image output requirements of digital plate making and printing.

**Keywords:** Optical fiber array · Laser · Image output · Scanning method

## 1 Introduction

Well known by the industry, the printing plate is a key device for determining the quality and efficiency in the whole printing process. In order to improve the speed and efficiency, the laser scanning imaging system mainly adopts the technique of multi-channel optical fibers without distance to increase the number of scanned dots in each trial. However, there are some new problems with this technology, such as imaging separation, black scanning area and short focal depth.

Over the last 10 years, domestic scholars have achieved half-tone image output by choosing optical fiber array and optical fiber mode based on hardware. While foreign scholars have mainly focused on laser dot array and image scanning method. This method combines scanning motion control based on hardware and laser dot control based on software to output high precision image, which better outputs half-tone images in high precision and efficiency. The combination of software and hardware to develop laser scanning imaging module and its control system has become a research focus at home and abroad.

This paper presents a new solution using optical microfiber with a diameter less than 10 μm as the laser transmission medium that combines laser dot array with distance and half-tone image scanning method together. This solution effectively resolves the problems of imaging dot separation, black scanning area, low imaging resolution and short focal depth in laser scanning imaging system.

## 2   Principle of Laser Dot Scanning Imaging

Currently, the main way of digital image output combines a drum of circular motion with a laser dots array of linear motion. The fast-rotating drum is engraved track by track by writing a helical line of precisely defined cells on its surface using direct laser ablation [1], as shown in Fig. 1. In laser scanning imaging system, the scanning array is composed of a group of closely arrayed optical fibers. The arrangement of optical fibers directly determines the accuracy of imaging points and the quality of half-tone image.
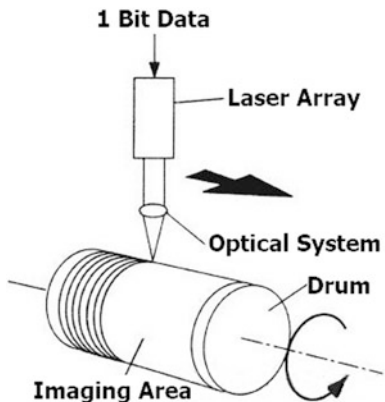


**Fig. 1.**   Imaging principle of external drum

### 2.1   Standard Optical Fibers Array Without Distance

Presently, the technology of closely arrayed optical fibers mainly utilizes standard fibers as transmission medium. The standard fiber has a cladding layer of 125 μm in diameter and a core of 62.5 μm in diameter. Because each optical fiber transmits a laser, the laser beams pass through optical lenses to form dot arrays on the imaging surface, as shown in Fig. 2.
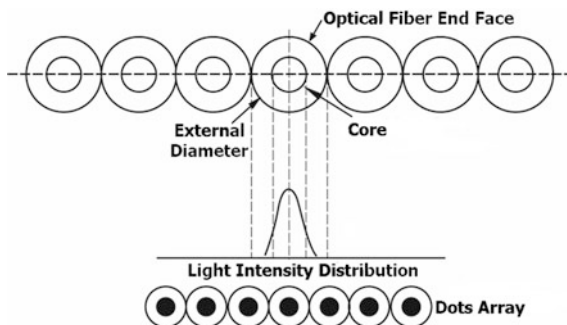


**Fig. 2.**   Dots array of standard optical fibers

As depicted in Fig. 2, the cladding diameter of standard fiber is larger than the core diameter, causing the laser energy to centralize in very small center area [2, 3]. Even if the optical fibers are in very close alignment, there will be certain distances between light dots, causing the appearance of black areas in scanning process. If defocusing is used to enlarge the diameter of the light dot, the energy of the light dot edge will be weakened, and the image quality will be affected [4]. When optical fibers are closely arrayed with slope angel, the laser dots can be controlled by delay circuit to form light dots without distance, but the output image will produce geometric distortion if the setting for slope angle is not appropriate [5].

### 2.2 Optical Microfibers Array with Distance

In 2003, Tong et al. [6] introduced a two-step drawing process for micro/nano optical fiber by using a flame-heated fiber drawing method. The fiber diameter is less than 50 nm with this technique. The optical microfiber with a diameter of 5 to 10 μm is applied in optical fiber array since it has good diameter uniformity and surface quality. The cladding of optical microfiber is covered with air around itself and the light is transmitted through the whole diameter range. If one optical microfiber is in direct contact with another microfiber, the light from one will enter the other, allowing the two lights to interfere with each other. Therefore, it is important to ensure that there is some distance between optical microfibers to avoid the interference.

## 3 Image Scanning Based on Dot Array with Distance

This section proposes an image scanning technology based on optical microfibers array with distance. This technology not only avoids mutual interference between lasers but also improves image resolution effectively.

### 3.1 Equidistant Dot Array

In equidistant dot array, the distance is fixed between light dots. The quantity of light dots and the distance between them are two key problems. N and m are used to represent the number and adjacent distance of light dots. Considering that there are 8 lasers ($N = 8$), the array is illustrated in Fig. 3. Lasers are labeled with integers from 1 to 8, and the center distance between adjacent dots is 3 ($m = 3$).
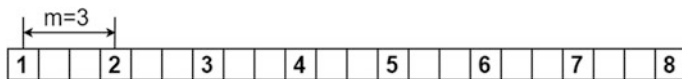


**Fig. 3.** Equidistant dots array ($N = 8, m = 3$)

The radial direction of drum is chosen as the main scanning direction. The direction perpendicular to the scanning plane is called the sub-scanning direction [7]. The imaging route of each laser is a spiral on the drum surface. If the rotation of the drum

and the motion of lasers are matched, the drum rotates in a circle while each laser moves N units in sub-scanning direction. During an exposure period of four circles of drum rotation, the images are output five times. Figure 4 illustrates each image result on the same line. Figure 5 illustrates the final image result on the same line after an exposure period. It is obvious that the edge regions on both sides have some gaps, while the center region without gap is continuous.
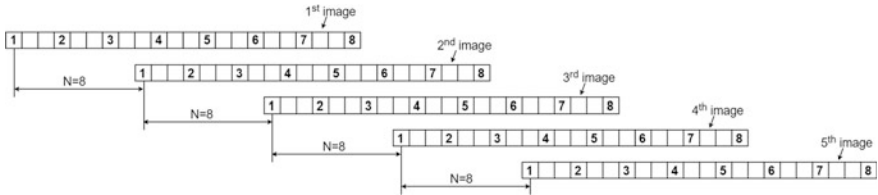


**Fig. 4.** Each image result on same line

## 3.2 Non-equidistant Dot Array

In non-equidistant dots array, the distance is variable between light dots. The variable distance should be selected according to the actual situation. In order to produce non-equidistant dot array, it is feasible to move the position of the light equidistant dot array. The distance of movement is defined as the following:

$$D_m = K \times N, \tag{1}$$

where K is an integer and N is the number of lasers.

According to Eq. (1), the light dots in Fig. 4 are rearranged. It is obvious that $N = 8$. The process of dot movement is reported in Table 1. The result of movement is shown in Fig. 6, which depicts that the center distance between adjacent dots is different. Figure 7 illustrates the result of each image on the same line during an exposure period of four circles of drum rotation. Figure 8 illustrates the final image result on the same line. The edge regions on both sides are discontinuous while the center region is continuous. These results are similar to those obtained in equidistant dot array.

## 4  Image Scanning Method Based on Non-equidistant Dot Array

This section presents an image scanning method using a device with eight lasers and non-equidistant array in Fig. 6. It is used to print $16 \times 32$ pixels matrix. The result of drum rotation during a period of four circles is shown in Fig. 9.

According to the light dots sequence, number 8 begins to fill pixels, and numbers from 7 to 1 subsequently follows. During the first period, numbers from 8 to 5 fill purple, brown, blue and green pixels separately, while numbers from 4 to 1 have not begun to fill pixels. The drum rotates a circle as each laser moves eight units in the sub-

**Table 1.** Process of dots movement

| Number in Fig. 3 | Value of $D_m$ | Description | Result in Fig. 6 |
|---|---|---|---|
| 1 | $D_m = 0 \times 8 = 0$ | No movement | 1 |
| 2 | $D_m = 0 \times 8 = 0$ | No movement | 3 |
| 3 | $D_m = 0 \times 8 = 0$ | No movement | 4 |
| 4 | $D_m = (-1) \times 8 = -8$ | Moves eight units to the left | 2 |
| 5 | $D_m = (+1) \times 8 = +8$ | Moves eight units to the right | 7 |
| 6 | $D_m = 0 \times 8 = 0$ | No movement | 5 |
| 7 | $D_m = 0 \times 8 = 0$ | No movement | 6 |
| 8 | $D_m = 0 \times 8 = 0$ | No movement | 8 |



**Fig. 5.** Final image result on same line



**Fig. 6.** Non-equidistant dots array ($N = 8$)
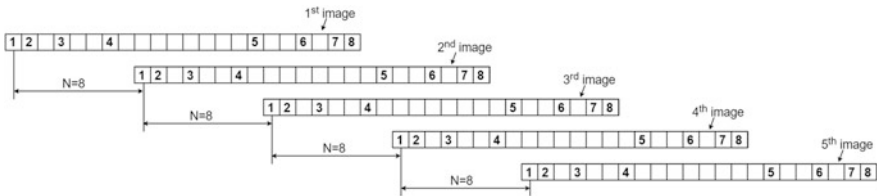


**Fig. 7.** Each image result on same line



**Fig. 8.** Final image result on same line

scanning direction. After several circles, the $16 \times 32$ pixels matrix will be fully filled, as shown in Fig. 10. Each pixel unit is only filled once. The data strings for Fig. 9 are encoded, the results of which are listed in Table 2. The positive numbers of coordinates in the Table 2 represent light dots in matrix and the negative numbers represent light
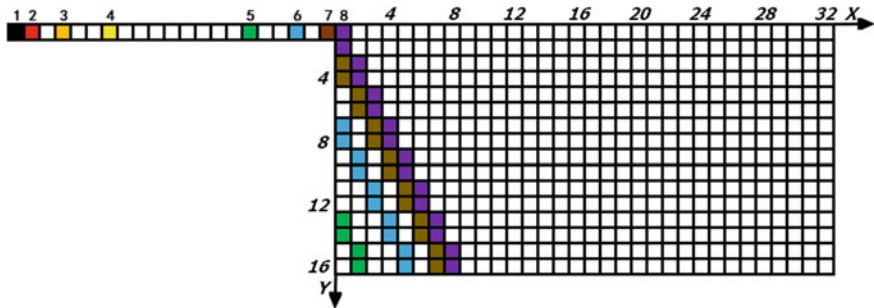
**Fig. 9.** Printed result during a period
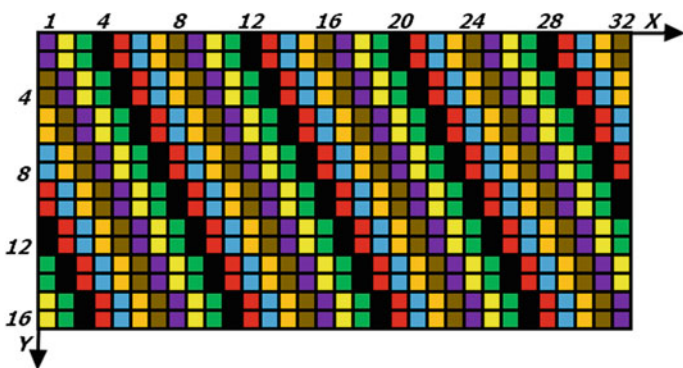


**Fig. 10.** Final printed result

dots out of matrix. The data strings during other circle are obtained with the same method.

## 5  Conclusions

This paper analyzes the principle of image scanning while introducing the technology of optical fibers array. The proposed scanning method satisfies the application needs of high precision and resolution based on optical microfiber with 5 to 10 μm in diameter. The combination of optical microfibers array with distance and imaging scanning method effectively resolves the problems of image spots separation, black scanning area, and short focal depth. Theory and technical foundations are established for the imaging scanning system and optical microfibers array with 64, 128 and more than 128 lasers, as guidance function is provided for the development of half-tone imaging output system.

**Table 2.** The results of data strings during first circle

| Group number | Data strings | | | | | | | |
|---|---|---|---|---|---|---|---|---|
| | Laser number | | | | | | | |
| | 1 | 2 | 3 | 4 | 5 | 6 | 7 | 8 |
| 1 | (–21, 1) | (–20, 1) | (–18, 1) | (–15, 1) | (–6, 1) | (–3, 1) | (–1, 1) | (1, 1) |
| 3 | (–20, 1) | (–19, 1) | (–17, 1) | (–14, 1) | (–5, 1) | (–2, 1) | (1, 1) | (2, 1) |
| 5 | (–19, 1) | (–18, 1) | (–16, 1) | (–13, 1) | (–4, 1) | (–1, 1) | (2, 1) | (3, 1) |
| 7 | (–18, 1) | (–17, 1) | (–15, 1) | (–12, 1) | (–3, 1) | (1, 1) | (3, 1) | (4, 1) |
| 9 | (–17, 1) | (–16, 1) | (–14, 1) | (–11, 1) | (–2, 1) | (2, 1) | (4, 1) | (5, 1) |
| 11 | (–16, 1) | (–15, 1) | (–13, 1) | (–10, 1) | (–1, 1) | (3, 1) | (5, 1) | (6, 1) |
| 13 | (–15, 1) | (–14, 1) | (–12, 1) | (–9, 1) | (1, 1) | (4, 1) | (6, 1) | (7, 1) |
| 15 | (–14, 1) | (–13, 1) | (–11, 1) | (–8, 1) | (2, 1) | (5, 1) | (7, 1) | (8, 1) |

# References

1. Henning G, Burdening S, Neuenschwander B (2011) Laser micro structuring and processing in printing industry. In: CLEO—laser science to photonic applications. IEEE
2. Kien FL, Liang JQ, Hakuta K et al (2004) Field intensity distributions and polarization orientations in a vacuum-clad sub wavelength-diameter optical fiber. Opt Commun 242(4–6):445–455
3. Balykin VI, Hakuta K, Le Kien F et al (2004) Atom trapping and guiding with a subwavelength-diameter optical fiber. Phys Rev A 70(1)
4. Xing J, Fan J, Zhang J, Chen D (2010) Design of laser dense fiber of heat-sensitive CTP. Packag Eng 31(23):85–88
5. Hou F, Liang J, Guo P et al (2007) Manufacturing of high accuracy and density linear optical fiber array. Microfab Technol
6. Tong L, Gattass R, Ashcom JB et al (2003) Subwavelength-diameter silica wires for low-loss optical wave guiding. Nature 426(6968):816–819
7. Kataoka K (2008) Analysis of banding problem in multiple beam scanning system of laser printer. Opt Rev 15(4):196–203

# Study on Image Retrieval Method for Color Information

Anda Yong[✉], Qiang Wang, and Chengcheng Jiang

School of Media and Design, Hangzhou Dianzi University, Hangzhou, China
657434964@qq.com

**Abstract.** According to the research on image retrieval method for color information, this paper compares several mainstream image retrieval methods for color information, and mends the problem that local segmentation of color space is not accurate enough and the traditional similarity measurement methods cross the weights of different color channel. Through the use of general histogram method and cumulative histogram method for image retrieval of MTM color space and HSV color space, the retrieval results show that the cumulative histogram method is more effective.

**Keywords:** Image retrieval · Color space · Cumulative histogram

With the development of technology and society, the number of multimedia images is increasing rapidly. Since color is an important visual information on image and it can distinguish different kinds of objects, it is important to content-based image retrieval. At present, compared with the traditional text retrieval, the image retrieval method for color information has broken through the bottleneck of traditional text retrieval annotated images of large workload, strong subjectivity and low accuracy. But there are still problems of the local segmentation of color space is not accurate enough and the traditional similarity measurement methods cross the weights of different color channel [1, 2].

This paper aims at the shortcomings of the existing image retrieval method for color information,and puts forward the improvement project of general histogram method and cumulative histogram method. This experiment yields good results in MTM color space and HSV color space.

## 1 Principles of Image Retrieval for Color Information

### 1.1 Representation of Image Color Features

Color is the most direct visual feature to describe the image and color histogram is the most common method for color feature expression [3]. Color histogram can describe the color distribution of image according to the occurrence frequency of image pixel [4], as shown in Eq. (1):

$$H(i) = \frac{Sum(i)}{N} \, (i = 0, 1, \ldots, L - 1) \tag{1}$$

Among them, $I$ is the Eigen value of the image, $L$ is the number of Eigen values, $Sum(i)$ is the number of pixels in the image with the Eigen value $i$, $N$ is the total number of pixels in the image.

## 1.2  Quantification and Measurement of Color Features

When calculating color histogram, the color space is firstly divided into each small color space through color quantization [5], where each space is a handle of the histogram, the number of pixels in each small color space is counted and the color histogram of the image appears finally.

In this paper, $Q$ and $K$ are assumed to be $D$imensional feature sequences of image to be retrieved and the candidate image. The Euclidean distance method is adopted for distance measurement, and its formula is shown in Eq. (2):

$$D(Q, K) = \sqrt{\sum_{i=1}^{N} (q_i - k_1)^2} \tag{2}$$

## 2  Method of Image Retrieval

### 2.1  Conversion of Color Space

There are several typical expressions of color space, such as HSV, RGB, CMYK, YUV and MTM [6]. Among them, MTM is designed based on human visual perception and is more conform to the human visual characteristics, HSV is an intuitionist color model for users and can reflect people's color perception and differentiation better. The experimental contrast is under the HSV and MTM.

(1)  RGB to HSV

HSV color space is composed of three components: tone, saturation and luminance. It is closer to the visual features of human eyes and more intuitionistic. The conversion formulas from RGB to HSV are shown in Eqs. (3)–(5):

$$H = \begin{cases} arccos \dfrac{(R-G)+(R-B)}{2\sqrt{(R-G)^2+(R-B)(G-B)}} & B \leq G, R \neq G \text{ or } R \neq B \\ 2\pi - arccos \dfrac{(R-G)+(R-B)}{2\sqrt{(R-G)^2+(R-B)(G-B)}} & B \geq G \end{cases} \tag{3}$$

$$S = \frac{\max(R, G, B) - \min(R, G, B)}{max(R, G, B)} \tag{4}$$

$$V = \frac{\max(R, G, B)}{255} \tag{5}$$

(2)  RGB to MTM [7]

MTM color space describes color through three dimensions, brightness, hue, chromaticity, which is more in line with human visual characteristics. The conversion formulas from RGB to MTM are shown in Eqs. (6)–(9):

$$\begin{cases} X = 1.020 * (0.608R + 0.174G + 0.2B) \\ Y = 0.299R + 0.587G + 0.144B \\ Z = 0.8742 * (0.066G + 1.112B) \end{cases} \tag{6}$$

Assuming that $V(x) = 11.6x^{1/3} - 1.6$:

$$\begin{cases} M_1 = V(X) - V(Y) \\ M_2 = 0.4 * [V(Z) - V(Y)] \\ M_3 = V(Y) \end{cases} \tag{7}$$

$$\begin{cases} S_1 = (a + b \times \cos\theta) \times M_1 \\ S_2 = (c + d \times \sin\theta) \times M_2 \end{cases} \tag{8}$$

Among them, $\theta = \tan^{-1}(M_1/M_2)$, a = 8.880, b = 0.966, c = 8.025, d = 2.558, the calculated result is:

$$\begin{cases} H_m = \tan^{-1} S_1/S_2 \\ S_{m=}(S_1^2 + S_2^2)^{1/2} \\ V_m = M_3 \end{cases} \tag{9}$$

## 2.2   Improvement of Color Space Quantization Method

The quantization of color space is usually divided into six non-overlapping local color spaces [8]. Figure 1 is divided into six spaces, (0, 60), (60, 120), (120, 180), (180, 240), (240, 300), (300, 360). Each color is divided into two local spaces, such as red is divided into two spaces, (0, 60) and (60, 360).
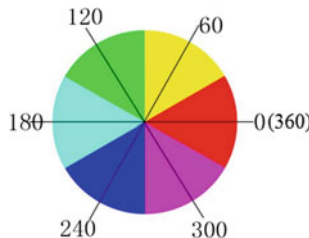


**Fig. 1.**  HSV color wheel

A closer look at Fig. 2 reveals that the chromatic aberration in two pictures 'upper and lower parts are both 40, but bring great differences in subjective feelings. According to theoretical analysis, dividing H, S and V into 12 color spaces can better experimental results.
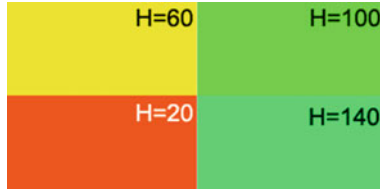


**Fig. 2.** Contrast with HSV color space chromatic aberration of 40

### 2.3   Improvement of Similarity Measurement Method

According to the problem of traditional similarity measurement method, equal-weight method for each color channel can achieve better experimental results. In this paper, Euclidean distance of three color channels in HSV and MTM color space is calculated and then the Euclidean distance sum is compared to determine the similarity of the retrieved image, as shown in Eq. (10):

$$D(Q,K) = \sqrt{\sum_{i=1}^{N}(Q(H_i) - K(H_i))^2} + \sqrt{\sum_{i=1}^{N}(Q(S_i) - K(S_i))^2} + \sqrt{\sum_{i=1}^{N}(Q(V_i) - K(V_i))^2}$$

$$(10)$$

## 3   Analysis of Experimental Results

### 3.1   Objective Data Analysis

(1)  "Horse Database" retrieval results

Three images are selected as images to be retrieved. The retrieval results are shown in Tables 1 and 2. In this paper, HSVG is HSV color space general histogram retrieval method, HSVC is HSV color space cumulative histogram retrieval method, MTMG is MTM color space general histogram retrieval method, MTMC is MTM color space cumulative histogram retrieval method.

**Table 1.** Precision results (unit: percent)

| Horse database | Picture 1 | Picture 2 | Picture 3 |
|---|---|---|---|
| HSVG | 50.0 | 60.0 | 50.5 |
| HSVC | 60.0 | 70.0 | 70.0 |
| MTMG | 40.0 | 50.0 | 40.0 |
| MTMC | 50.0 | 60.0 | 60.0 |

**Table 2.** Recall ratio results (unit: percent)

| Horse database | Picture 1 | Picture 2 | Picture 3 |
|---|---|---|---|
| HSVG | 55.5 | 54.5 | 41.7 |
| HSVC | 66.7 | 63.6 | 58.3 |
| MTMG | 44.4 | 45.5 | 33.3 |
| MTMC | 55.5 | 54.5 | 50.0 |

(2)  Conclusion

In tabular data, the number of retrieved images is 10 and the three images to be retrieved have 9, 11 and 12 related images respectively. Therefore, this paper comes to the conclusion that the cumulative histogram method is better than the general histogram method in HSV and MTM color spaces. For general histogram method, MTM does not have as good retrieval effect as HSV. For the cumulative histogram method, HSV and MTM are similar, even slightly inferior.

### 3.2  Subjective Data Analysis
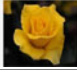
(1)  "Flower Data base" retrieval results

An image with obvious colors is selected from the flower database and retrieved by four different methods. Table 3 is the retrieval results of each method.

(2)  Conclusion

The results shows that: the results of HSV color space general histogram retrieval method, MTM color space general histogram retrieval method and MTM color space cumulative histogram retrieval method are not ideal, the main tone of the retrieval results has changed earlier; the result of retrieval is more accurately and effectively in HSV color space cumulative histogram retrieval method.

**Table 3.** Retrieval results of 4 methods

| Image to be retrieved | Retrieval methods | Retrieval results |
|---|---|---|
|  | HSVG |  |
| | HSVC |  |
| | MTMG |  |
| | MTMC |  |

## 4   Conclusions

This paper compares several mainstream image retrieval methods. Aiming at the problems that local segmentation of color space is not accurate enough and the overlapping of the weights of different color channels, the paper proposes to divide the color space into 12 equal parts to make the division of color space more accurate, and to improve the method of equal weights for each color channel. The conclusion is: the cumulative histogram retrieval method is better than the general histogram method; among the four image retrieval methods studied in this paper, cumulative histogram method in HSV color space has the best retrieval effect. The improved scheme and method that are compared in this paper provide new ideas and valuable evidence for the development of image retrieval method for color information in the future.

## References

1. Min JI (2002) A qualitative approach to content-based image retrieval with histogram. J Liaoning Norm Univ
2. Asiyan H, Haimiti A (2012) Comparative research of image retrieval based on text and content. J Cap Norm Univ (Nat Sci Ed) 33(4):6–9
3. Xing X, Shangluo University SEM (2015) Research and application of color image retrieval based. Electron Test
4. Aman Ma (2015) Study on image retrieval method based on color and edge direction histogram. J WuYi Univ 34(9):26–29
5. Qian Y (2016) Color image retrieval methods fast improvement research and simulation. Comput Simul
6. Zhan H, Wang H, He J et al (2014) Content-based image retrieval. Mod Electron Tech (7)
7. Miyahara M (1988) Mathematical transform of (R, G, B) color data to munsell (H, S, V) color data. Proc SPIE Int Soc Opt Eng 1001(3):650–657
8. Qilong S, Mingliang Z (2016) HSV color space quantization image retrieval method for tibetan Carpe. Comput Eng Softw 37(3)

# Image Restoration of Dun Huang Murals Based on Auto-encoder Generative Adversarial Neural Network

Zhengguang Song, Wenjie Xuan, Jia Liu, Yudan Li,
and Liqin Cao[(✉)]

School of Printing and Packaging, Wuhan University, Wuhan, China
clq@whu.edu.cn

**Abstract.** Dun Huang mural is an important part of Dun Huang art. Digital restoration for Dun Huang mural is significant and meaningful. At present, the restoration of Dun Huang mural mainly relies on manual work, which takes a lot of time and is limited by work experience. Although, the existing restoration methods perform well in painting for small missing region, there are disadvantages for large missing regions with semantic information. To solve these problems, Auto-encoder Generative Adversarial Nets (AGAN) was proposed for image restoration of Dun Huang Murals in this paper. In AGAN, the fully connected layer was replaced by the dilated convolution layer, which benefits the reconstruction of image with large scale missing. The experiments are executed over the Dun Huang dataset, and the results show that the restoration images based on AGAN were more realistic and natural. Compared with other traditional methods, our method achieved a better performance quantitatively and qualitatively.

**Keywords:** Dunhuang Murals · Generative Adversarial Nets · Image restoration · Cultural relics protection

## 1 Introduction

Due to the environmental erosion of the millennium and the destruction of modern humans, some of the Dun Huang murals are seriously damaged [1], and the restoration work is imminent. The traditional method is to repair artificially, which is not only time consuming but also inefficient. Therefore, many restoration projects of Dun Huang murals are difficult, and the digital restoration work of murals is of great significance [2].

Classical image completion methods, such as Fast Marching Method (FMM) [3], Criminisi algorithm [4], and Statistics of Similar Patches [5], are based on the existing pixels or texture of the image. These methods utilize the edge of the missing portion and gradually generate pixels or patches. However, these methods are limited to recovering images with overall information, especially with semantic information. According to the limitation, these traditional machine learning methods also show disadvantages in completing relatively complex content such as faces [6].

With the rapid development of deep learning technology in recent years, many advanced deep learning algorithms and frameworks provide many new ideas for tasks in the field of computer vision, especially in the field of image completion. Convolution neural network performs well in extracting image feature information [7], and auto encoder can be used for data reconstruction and demising [8]. The generative adversarial network model [9] proposed by Good fellow et al. introduced the idea of game theory and effectively improves the quality of image completion. Later, the dilated convolution [10], Res Net [11] and other methods were proposed for image completion, which further enhanced the quality of image completion and accelerated the network's convergence.

In this paper, auto encoder-GAN for facial image restoration of Dun Huang murals is proposed, which includes a generator and two discriminators. The generator based on auto encoder consists of an encoder and a decoder [12]. It can reconstruct missing region and details of an image with texture synthesis technology [13]. In addition, we introduced dilated convolution layers and the structure of Res Net in the generator. Experimental results show that our method outperforms typical completion methods on Dun Huang murals dataset.

## 2 Auto Encoder Generative Adversarial Neural Network

### 2.1 Principle of Image Completion Based on GAN

The architecture of our model is based on the auto encoder generated model [14]. The dataset is facial images of Dun Huang murals, hereinafter referred to as DMF image. The "damaged" images simulated by adding mask to the original images are used to train the network. The masked image can be completed by encoding-decoding process [15]. The architecture introduces a global discriminator and a local discriminator for judging the authenticity of the restored image and the original image [6]. The generator and discriminator are optimized alternately to make the discriminator unable to judge whether the result is real or not. Then the best completion is achieved, which means the restored image reaches the same fidelity as the original image [16]. To cope with the larger damaged region, we use the dilated convolution layer to replace the fully connected layer, so that the convolution layer can obtain a larger receptive field [17]. At the same time, the structure of Res Net is used to accelerate the convergence speed of the network, which is also helpful to improve the quality of restored images.

### 2.2 Network Structure

It includes a generator and two discriminators. The generator based on auto encoder consists of encoder and decoder. Two discriminators are local discriminator and global discriminator. The generator and two discriminators conduct iterative training alternately to achieve best performance.

Figure 1 is the structure of our proposed network. The overall completion process of the image completion network model is as follows:
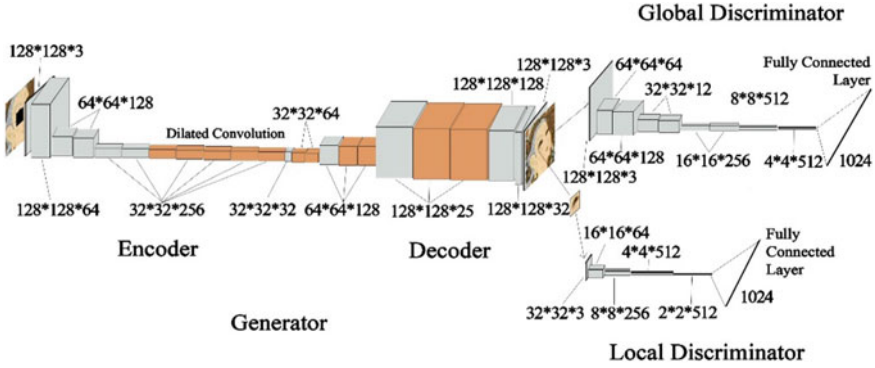
**Fig. 1.** Network structure model

**Encoder**: The encoder takes the RGB color channels DMF image with 128 * 128 pixels and a mask with 32 * 32 pixels in the central region as input data. Leaky Rectified Linear Unit (LRe LU) is the activation function:

$$f(x) = \begin{cases} x, x \geq 0 \\ ax, x < 0 \, and \, 0 \leq a \leq 1, \, a \in C \end{cases} \tag{1}$$

The size of convolution and dilated convolution layers is 32 * 32 * 256. The loss of encoder is the sum of the loss of auto encoder structure reconstruction, the loss of coding and the loss of generative adversarial neural network. It is defined as

$$Loss_{encoder} = MSE(x, y) + MSE(X, Y) + G(Y) \tag{2}$$

$$G(Y) = E[\log(1 - (D \cdot G)(Y))] \tag{3}$$

where x is the encoding of the real image X, y is the encoding of the completed image Y. MSE(X,Y) represents the mean square error between X and Y. E expresses expectation. G(Y) is the loss of the generator, and $(D \cdot G)(Y)$ presents the probability that the image generated by the generator spoofs the discriminator successfully.

The loss function of code-discriminator only includes the loss of the discriminator in GAN.

$$Loss_{code-disciminator} = D(x')$$

$$D(x') = E_{x \sim P_{data}}[\log D(x')] + E_{z \sim P_z}[\log(1 - D(G(z')))]$$

x' represents the masked image, and z' represents the coding of the masked image.

**Decoder**: The output of the encoder is the input of the decoder for image reconstruction. The decoder generates the preliminary completed image. The loss of

generator is the sum of the loss of auto encoder structure reconstruction and the loss of GAN, which is defined as:

$$Loss_{generator} = MSE(X, Y) + G(x') \tag{4}$$

$$G(x') = E[\log(1 - (D \cdot G)(x'))] \tag{5}$$

where x′ is the encoding of the image X′ to be completed, X is the real image, and Y is the completed image.

**Discriminator**: The local completed image is the part of preliminary completed image which corresponds to the masked region of damaged image. The masked region of the damaged image is replaced with the local completed image, and the combined image is called the global completed image. The local completed image is the input of the local discriminator and the global completed image is the input of the global discriminator. The specific structure is as follows:

(1) The first seven layers of the global discriminator are convolution layers, which are activated by LReLU function, and the last layer is the fully connected layer. The loss of the global discriminator is calculated as

$$Loss_{global-discriminator} = DIS(X, Y) \tag{6}$$

where DIS(X, Y) measures the distance between the original image X and the completed Y. The purpose of minimizing the loss function is to improve the ability of distinguishing the images of discriminator. The goal of the optimizing generator is to get a more similar distribution according to the real image.

(2) The first four layers of the local discriminator are convolution layers, and the fifth layer is a fully connected layer. The structure of local discriminator is similar to the global discriminator, and the loss of the local discriminator is defined as

$$Loss_{local-discriminator} = DIS(x_l, y_l) \tag{7}$$

where $l$ expresses local. Similar to the function of the global discriminator, the local discriminator only distinguishes the local image, which contains the completed region.

During the training process, the generator and two discriminators conduct iterative training alternately. The parameters in the network constantly approach the optimal value, the discriminator's ability reaches the optimum, and the probability of generator spoofing successfully also reaches the maximum. The result is that the distribution of the generated images (completed) is very close to the distribution of real images. Meanwhile, each layer of the network is normalized, and Res Net is introduced to speed up the training process.

## 3    Experiment and Result Analysis

### 3.1    Data Set Acquisition and Experimental Environment

The dataset of our work consists of three parts. First, some images of Dun Huang murals are obtained by web crawler on the Internet. Second, high-resolution digital images of Dun Huang murals from e-commerce websites are purchased. Third, some digital images are obtained from e-books about Dun Huang murals. After preparing the original data, the after-processing of the data were produced including the following steps.

Firstly, the operation of manually filtering data is implemented to remove irrelevant data. Then the facial recognition algorithm is used to extract the faces in the images using Open CV. After that, the irrelevant data was removed through manual screening. Later, the image size was uniformly modified to 128 * 128 pixels, and the image was mirrored to expand the data set.

Finally, we obtained a total of 9,162 DMF images with 128 * 128 pixels. We masked those pictures for training. The mask with size of 32 * 32 pixels is located on the center of each image. Those masked images are simulation data to train the network.

The experimental environment and parameters we used are shown in the following table.

| Input size | 128 * 128 |
|---|---|
| Output size | 128 * 128 |
| Learning rate | 0.0001 |
| Batch size | 9 |
| epoch | 4 |
| GPU | Nvidia GTX 1080Ti (11G) |
| Operating system | Ubuntu 16.04 |
| Programming language | Python 3.4 |
| Deep learning framework | Tensor Flow 1.2.1 |

### 3.2    Experimental Results and Analysis

We introduced simulated data set to train and test the image completion quality of the network, and selected the FMM [3], Criminals algorithm [4], Statistics of Similar Patches [5] as comparison.

The main principle of FMM [3] is to produce pixels at the edge of the missing region and fill inward one circle after another until the image is completely restored.

Criminals algorithm [4] is to decide the priority of contour to be filled. The patch with the highest priority is filled with the patch with the highest similarity in the known region. Those filled patches are considered as known afterwards. The patch with secondary priority is then filled. Loop this process until the image is completed.

When matching similar patches in the image, the patch offset statistics are sparsely distributed: most patches have similar offsets. Moreover, several prominent peaks are

formed in the statistics. This explicit offset describes the way the pattern is of the biggest possibility to be repeated, providing a reliable clue to the completion of the missing region. These offsets can predict the completion of linear structures, textures, and repeating objects [5].

It shows the results of image completion on the DMF images data set by different methods. The mask is located in the center of the image. Due to different facial postures, the location of masks in different images is random. In the first column, the right eye is blocked; in the other images, the nose is blocked.

As showed in Fig. 2, our approach shows ability of producing contents that not exist in the images and completing broken images and performs obviously better than other methods. The completed images of our approach can be more realistic and visually natural. For example, first column of results of the others methods fail to complete the missed right eye. The reason is that FMM is based on peripheral pixels, Criminals algorithm and Statistics of Similar Patches are based on the known patches which are similar to the region to be completed. The essence of them is to fill empty regions with what is already given, and there is no way to generate something that doesn't exist. However, the method proposed in this paper can learn structural features of the mural face and completed the other eye after training. In addition, due to the existence of local discriminator, the transition between the completed region and the surroundings of the original image is natural, without obvious color and texture mutation. The results of our method are very similar to the real images.

To further analyze our method, three evaluating indexes of image quality are used to evaluate the experimental results objectively. Mean Square Error (MSE) [18] and Peak Signal to Noise Ratio (PSNR) [18], are both based on the difference between pixels of images. The smaller the MSE value is, the better the completed effect is. The larger the PSNR is, the better result is, which indicates a smaller pixel difference between images. Structural Similarity Index (SSIM) [18] measures the structural similarity of images from three aspects: brightness, contrast and structure. The higher the SSIM value is, the more similar the two images are in structure and the better the completion effect is.

Table 1 shows the results of different methods calculated by three evaluation indexes, which are obtained by comparing the generated images with the real images. As showed in Table 1, the MSE value of our method is obviously lower than those obtained by other methods, and the PSNR is higher. It indicates that our method gets the smallest pixel difference from the real image, and the closest color to the real image. By combining self-encoding with generating an anti-neural network, the details of the image can be better done and the results closer to the original image can be obtained. It means it has a higher global consistency. In addition, the SSIM value obtained by our method is the highest, indicating that the generated image is more similar to the real image in structure. That's to say, our method has better performance of the structure. The reason is that our method can complete restoration according to the image semantics and produce elements that should exist in missing region with higher local consistency.

From Fig. 2 and Table 1, we can conclude that our image completion method gets better results than the other methods mentioned in this paper in facial completion of Dun Huang murals.

a. Original Image

b. Image with Mask

c. Our approaches

d. Criminisi algorithm

e. Statistics of Similar Patches

**Fig. 2.** Comparison of experimental results

f. FMM

**Fig. 2.** (*continued*)

**Table 1.** Comparison of results of different methods

|                              | MSE    | PSNR  | SSIM  |
|------------------------------|--------|-------|-------|
| Ours                         | 26.99  | 33.84 | 0.964 |
| Criminals algorithm          | 79.11  | 30.52 | 0.953 |
| Statistics of similar patches | 104.98 | 29.33 | 0.956 |
| FMM algorithm                | 130.06 | 27.94 | 0.950 |

## 4   Conclusions

In this paper, we proposed a new network which included a global discriminator and a local discriminator in the GAN, and the generator consisted by an encoder and a decoder. The generator and two discriminators optimize alternately to generate repaired image that is realistic and visually natural. Compared with manual repair, our method greatly reduces the time and improves the work efficiency. Moreover, our approach reduced the influence brought by staff's subjectivity. The experimental results indicated that our method could generate naturally contents that not existed in the image before in painting compared with other algorithms. The repaired image has higher global and local consistency. However, our method has some disadvantages at the present stage. Limited by the small data set, the performance of the network cannot be fully utilized. Better results can be expected if more data is utilized to train our network.

# References

1. Jinshi F (2008) Dunhuang standing forever—exploring the preservation of Dunhuang Grotto. Art & Design
2. Shuwen W, Yanhong L, Wei H, Xiaoping Y, Jianfang J (2009) Challenges in the digital image restoration of Dunhuang frescoes. J Northwest Univ Natl (Nat Sci Ed) 30(2):42–49
3. Alexandru T (2004) An image inpainting technique based on the fast marching method. J Graph Tool 9(1)
4. Criminisi A, Pérez P, Toyama K (2003) Object removal by exemplar-based inpainting. Computer vision and pattern recognition. In: Proceedings. IEEE Computer Society Conference on Computer Vision and Pattern Recognition
5. Kaiming H, Jian S (2014) Image completion approaches using the statistics of similar patches. IEEE Trans Pattern Anal Mach Intell 36(12)
6. Li Y, Liu S, Yang J, Yang MH (2017) Generative face completion. IEEE Conference on Computer Vision and Pattern Recognition
7. Ke X (2012) Research on application of convolutional neural network in image recognition. Zhejiang University
8. Vincent P, Larochelle H, Lajoie I et al (2010) Stacked denoising autoencoders: learning useful representations in a deep network with a local denoising criterion. J Mach Learn Res 11(12):3371–3408
9. Goodfellow I, Pouget-Abadie J, Mirza M, Xu B, Warde-Farley D, Ozair S, Courville A, Bengio Y (2014) Generative adversarial nets. In: NIPS
10. Gu J, Wang Z, Kuen J, Ma L, Shahroudy A, Shuai B, Liu T, Wang X, Wang L, Wang G, Cai J (2015) Recent advances in convolutional neural networks. arXiv:1512.07108
11. He K, Zhang X, Ren S, et al (2016) Deep residual learning for image recognition. In: IEEE conference on computer vision and pattern recognition. IEEE Computer Society, pp 770–778
12. Goodfellow I, Bengio Y, Courville A (2017) Deep learning. MIT Press, pp 429–430
13. Shaochun F, Shuntian L (2009) Regional texture synthesis based image inpainting. J Electron Inf Technol 31(6):1319–1322
14. Guo L, Jieyu Z, Zhongzhi S (2010) Image categorization of integrated, generative models and discriminative methods. Acta Electron Sin 38(5):1141–1145
15. Doersch C (2016) Tutorial on variational autoencoders. Arxiv Tech Report, June
16. Iizuka S, Simo-Serra E, Ishikawa H (2017) Globally and locally consistent image completion. ACM Trans Graph 36(4):1–14
17. Yandong L, Zongbo HL, Hang (2016) Survey of convolutional neural network. Comput Appl 36(9):2508–2515
18. Shuqin L, Lifang W, Gong Y, Xingsheng L (2011) Overview of image quality assessment. China Sci Technol Pap Online 6(7):501–506

# Optimal Tone Reproduction of Different Oil Painting Style Images

Jing Geng[(✉)] and Congjun Cao

Faculty of Printing, Packaging Engineering and Digital Media Technology,
Xi'an University of Technology, Xi'an, China
`gengjing_qianye@l63.com`

**Abstract.** The stylization of image art has become more and more familiar as a booming field, and has attracted the interest of many scholars. This paper summarizes the influence of different stroke textures on the optimal tone curve of stylized images, and analyzes the degree of preference of different styles of stylized images. It is concluded that the optimal tone reproduction curve of oil painting stylized images is universal. The conclusion provides a direction for further study of image stylization.

**Keywords:** Optimum tone reproduction · Oil painting · Non-photorealistic rendering · Brush strokes

## 1 Introduction

Tone reproduction, which reflects the input-output characteristics of an image, is a very important quality factor for the evaluation of image printing systems. Technique of continuous-tone [1] to express tone by the concentration of pigment has a long history of several tens of thousands of years as seen in paleolithic cave paintings of Lascaux and Altamira. On the other hand, line-drawing and dot-drawing, in which only binary of inked or not inked is used [1], was introduced into our drawing technique, first in Pre-Renaissance [5]. In the previous study [4], optimum tone reproduction was investigated for rendering photographic images with the impressionism style of Monet. In order to verify whether the proposed method is valid in more general cases, this study is to explore the influence of different painters' brush texture on optimum tone reproduction of oiled paintings.

## 2 Experiment

### 2.1 Photographs Used in the Paper

Considering the proportion of different subjects, landscape and the portraits of the characters, occupy a large proportion in the subject matter of oil painting. Therefore, two landscape photographs and two portrait photographs were used in this study. The landscape photographs are the landscape of the author's school. The characters are colleagues of the author's (Fig. 1).

Landscape1          Landscape2          Portrait1          Portrait2

**Fig. 1.** Original photographs used for preparation of oil painting like images

Histogram can show the color distribution and brightness of a photograph in the form of distribution map, providing statistical data of color and brightness. As shown in Fig. 2, the corresponding gray histogram of each photo.



Landscape 1's          Landscape 2's          Portrait 1's          Portrait 2's
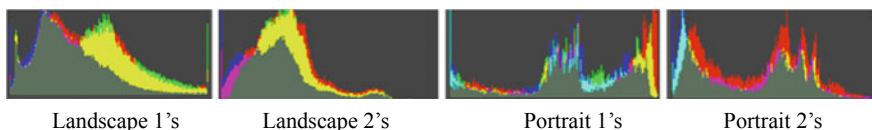
**Fig. 2.** Corresponding gray histogram of each photo

## 2.2    Setting of Tone Reproduction Curves

As shown in the figure below, curves marked 1 which is regarded as an optimum one for photographs [2], curves marked 2–9 have darker tones, curves marked 10 have lighter tones, ones with high contrast in the middle tone (Fig. 3; curve11, curve12), one with lower maximum density (Fig. 3; curve13) were set.
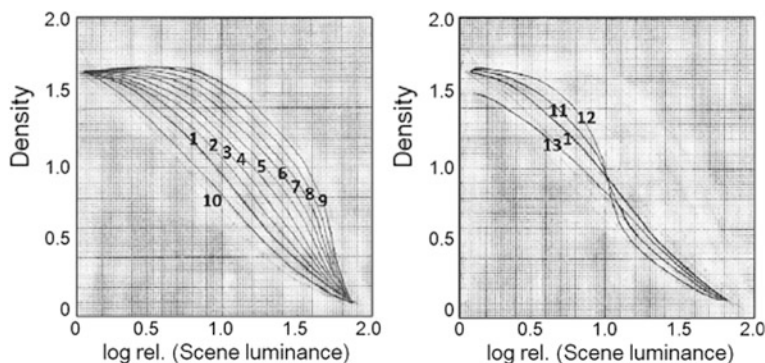


**Fig. 3.** Tone reproduction curves of the samples

## 2.3    Production Method of Oil Painting-Stylized Images

### 2.3.1    Brush Stroke

Brush strokes refer to the marks produced by the painter in the process of painting. In Figs. 4, 5 and 6 author just selects textures from regions containing background objects, and those textures are visually similar. If a texture is selected from the Cypress in Fig. 6, longer brushes may have brush stroke directions and spectral properties quite different from the one selected from the starry sky.



**Fig. 4.**  Seurat's



256pixels* 256pixels
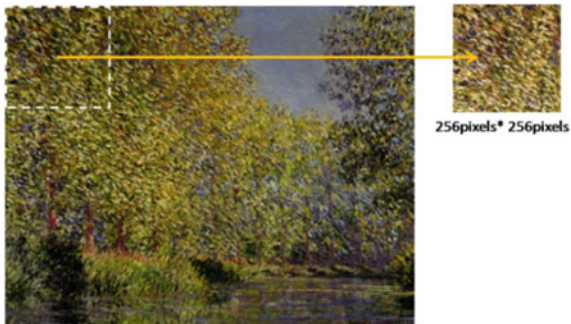
**Fig. 5.**  Monet's

**Fig. 6.**  Van Gogh's

### 2.3.2  Application of Brush Strokes

Authors used the previous algorithm [1] to render photographic images with styles associated with selected textures and adjusted tone reproduction.

### 2.4  Optimum Tone Reproduction

Tone reproduction is the relationship between the scene luminance and image density. The tone reproduction of the images after capturing is different. For example, in the case of insufficient exposure, tone reproduction is adjusted to a uniform standard. Figure 7 (③) shows the optimum tone reproduction of a digital photo [2]. In Fig. 7 (③), the horizontal axis represents the lightness of the scene when the original digital photo was taken. The illuminated objects usually have a very wide distribution of lightness, therefore, it is generally expressed in a logarithmic form. Vertical coordinates represent the density of print output.
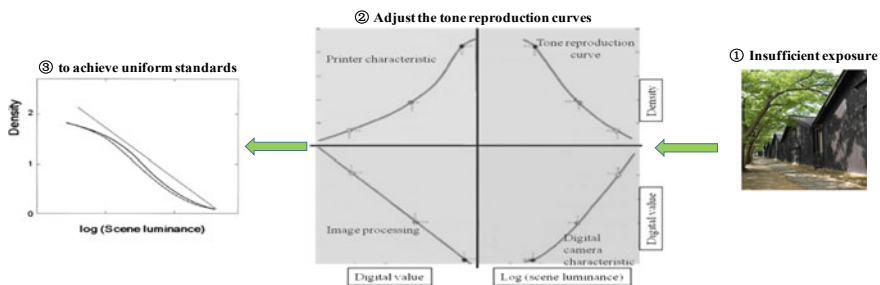


**Fig. 7.**  Optimum tone reproduction

## 2.5    Evaluation Method: A Method of Psychometric Scaling for a Ranking Scale

Because it is made up of a sequence of scales, the method of psychometric scaling is one of the scale constitution method. Compared with student-t-test, the accuracy of the normalized-rank approach is relatively low, but it involves a lighter workload for the experimenter [3].

The testers observed the sample images visually, and ranked the images, the criterion was degree of popularity. According to this experiment, images were evaluated under a fluorescent D50 lamp with high color rendering properties up to 700 lx. The size of the printed image is 12 cm*16 cm.

The Images were placed on the table. In this experiment, 65 students aged from 20 to 30 are chosen as testers. The distance between testers and images was not limited.

# 3    Result and Discussion

## 3.1    Seurat Style Image

### 3.1.1    Results of Landscape1

According to the tests results of the evaluation, the ranking of the corresponding images of each curve is calculated; the corresponding scale values of each curve are obtained from this data. In order to convert the ranking of evaluation results into numerical values, the ranking values are calculated (Figs. 8 and 9).
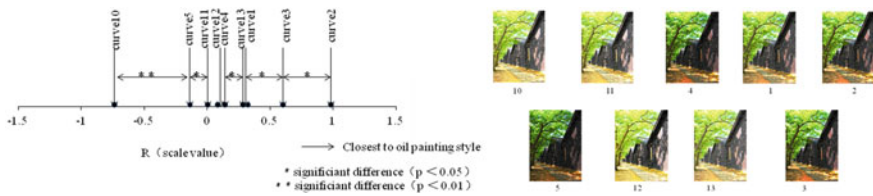


**Fig. 8.**    Result of Landscape1 (Seurat style image)
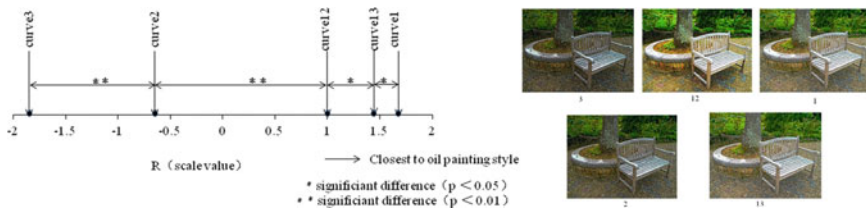


**Fig. 9.**    Result of Landscape2 (Seurat style image)

In this experiment, the larger the scale value, the more you can feel the image of "popularity". The obtained scale value was tested by student-t-test and was carried out for both 1 and 5% of the risk rate. The scale values of each stimulus were arranged in a number of straight lines. As shown in Fig. 10, to indicate the statistical significance difference between the curves.
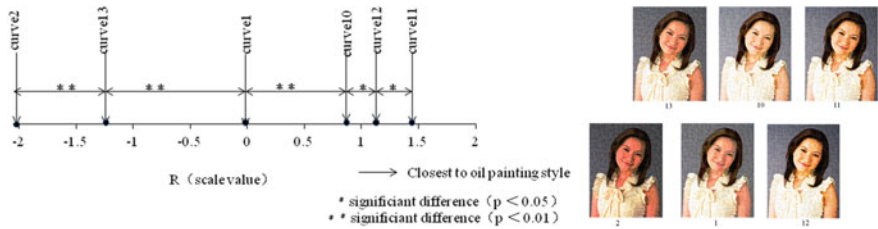


**Fig. 10.**  Result of Portrait1 (Seurat style image)

The results of student-t-test show that all scale value of curves' have significant difference except for curve11, curve12 and curve4. The scale value of curve2 is the largest. That is, the darkened tone reproduction is considered to be the best for Landscape1. A slightly more darker curve3, is less significant than curve2 at the risk rate of 5%.

### 3.1.2    Results of Landscape2

The number of stimuli depends on the specific image, the contrast and brightness of Landscape2 is not high. Therefore, we provides only 5 images which corresponding to curve1, 2, 3, 12, 13. There is a significant difference between curve12 and curve2, as well as curve2 and curve3, at a p-value of 1%. It can be speculated that the overall brightness of the image has some connection with the selection of the optimum tone curve.

### 3.1.3    Results of Portrait1

From here we can see, for high-key subject, the contrast to high brightness tone curve is less than low brightness tone curve. The result of stimulus10 also gets a high score which is similar to the result of Monet's in previous paper (Fig. 11).
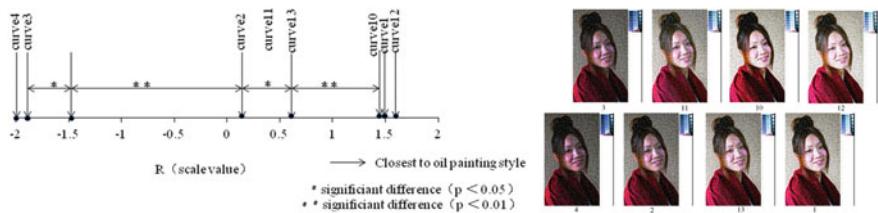


**Fig. 11.**  Result of Portrait2 (Seurat style image)

### 3.1.4    Results of Portrait2

For stimulus 12, the contrast to high brightness tone curve gets a high score. This result is similar to the Monet's, which was published previously.

## 3.2    Monet Style Images

### 3.2.1    Results of Landscape1

The larger the scale value, the more you can feel the image of "popularity". Curve2 corresponds to the largest scale and is considered the most favorite one. Compared with curve2, there is a significant difference between curve1 and curve2 at a p-value of 5% (Fig. 12).
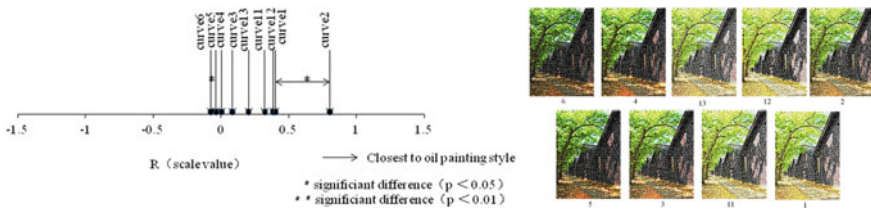


**Fig. 12.**  Result of Landscape1 (Monet style image)

### 3.2.2    Results of Landscape2

Curve1 corresponds to the largest scale and is considered the most favorite one. It shows a similar trend with the Seurat style image (Fig. 13).
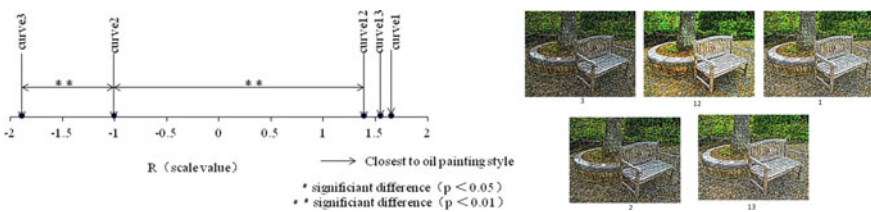


**Fig. 13.**  Result of Landscape2 (Monet style image)

### 3.2.3    Results of Portrait1

The result is completely different between landscape and portrait. Curve12 and curve11 obtained high scores, which means, the high brightness contrast of the whole image is welcome by the objective testers. The focus is mainly on the texture of the portrait's face, which directly influences the final effect of the whole image (Fig. 14).

### 3.2.4    Results of Portrait2

There is a very similar trend with Portrait1 (Fig. 15).
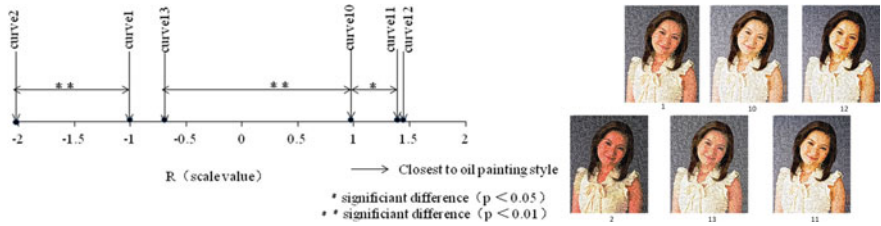
**Fig. 14.** Result of Portrait1 (Monet style image)
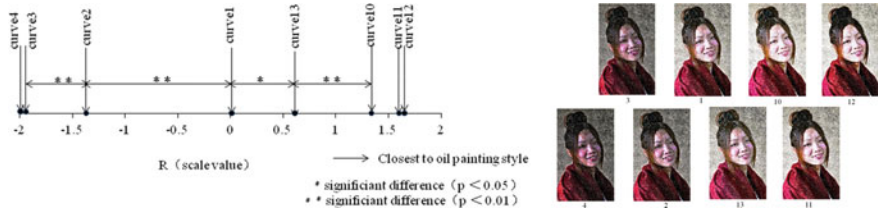


**Fig. 15.** Result of Portrait2 (Monet style image)

### 3.3    Van Gogh-Style Images

#### 3.3.1    Results of Landscape1

The scale value of curve2 is also the largest. That is, the darkened tone reproduction is considered to be the best for Landscape1 (Fig. 16).
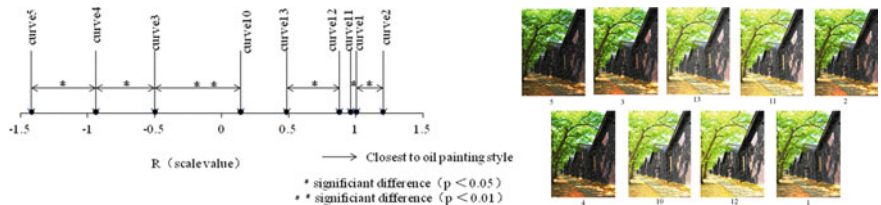


**Fig. 16.** Result of Landscape1 (Gogh style image)

#### 3.3.2    Results of Landscape2

Tone reproduction curve12 is considered the best. This result is different from Seurat and Monet. There is a significant difference between curve12 and curve13, the curve2 and the curve3, at a p-value of 1%. Curve2 and curve3 were placed at the end (Fig. 17).

**Fig. 17.** Results of Landscape2 (Gogh style image)

## 4 Conclusions

It can be seen from the above results that there is little difference in the trends of the optimum tone reproduction curve. The brightness of digital photographs has an impact on the results of landscape paintings and portraits. Shadowed Landscape1, no matter which artist's brush strokes, the results are in a higher concentration of images than the optimum tone reproduction of digital photographs'. Curve1, curve2 and curve13 are selected for Landscape2 which with low contrast brightness. However, in Seurat style images, curve1 was chosen as the first (favorite image) with the premise of having significant difference. The best tone of oil painting style image in Seurat's brush strokes is the same as that of digital photographs. In Portrait, the brighter tone than curve1 is selected not curve13 but curve10. This reveals that in Portrait, the highest concentration of black (thick black) can be printed. Curve11 and curve12, which depict the details of the highlights better than curve1, were selected. On the other hand, the highlight (skin), brighter curve10 was selected, only the image of shaded Portrait2. As an effect of strokes, Monet, with clear texture, chooses a more relaxed and powerful tone (curve12 of Portrait1). In Portrait2, you can't see any difference. As an effect of strokes, Monet, with clear texture, a more contrast tone (curve12 of Portrait1) was chosen. In Portrait2, you can't see significant difference. Although the three images are different in style, texture spectrum energy and other factors are different. It can be seen that the optimum tone reproduction of oil paintings is universal.

# References

1. Adams JM, Dolin PA (2001) Printing technology. 5th edn. Delmar
2. Engeldrum PG (2000) Psychometric scaling: a toolkit for imaging systems development. Imcotek Press, Winchester
3. Geng J, Shimizu H, Aoki N et al (2012) Optimum tone reproduction for oil paintings. Soc Photogr Imaging Jpn 75(5):389–395
4. Ivins JWM (1953) Prints and visual communication. Harvard University Press, Cambridge
5. Nelson CN (1977) The theory of the photographic process, 4th edn. Macmillan, New York, pp 557–558

# Study on Image Graying Method for Defect Detection of Area Elements in Map Printing

Siyang Liu, Ruizhi Shi[✉], and Bing Sun

Institute of Geospatial Information, Information Engineering University,
Zhengzhou, China
ruizhishi@sina.com, 875128290@qq.com

**Abstract.** In order to realize the automation of quality inspection in map printing, the development of quality inspection system based on machine vision is the dominant solution. Combining with the characteristics of map printing, the reason why it is difficult to identify the defects of light-colored area elements in the existing mainstream detection products was analyzed. It is mainly the color characteristics of map printing paper that causes the failure of the general grayscale algorithm. In this study, the image of printed matter to be detected was collected and the grayscale information of the image was obtained. The difference of grayscale between the area elements and the paper background in each channel of RGB was compared, and then the weights of each channel were defined to enhance the contrast between the defects of area elements and the paper background in the grayed image. The improved method was tested and verified in actual production. The experimental results showed that the improved weighted graying algorithm can effectively solve the problem that the low-saturation area elements cannot be recognized by the defect detection algorithms, which improved the efficiency of the whole map quality detection and proved the superiority of the solution.

**Keywords:** Map printing · Defect detection · Image graying algorithm · Machine vision

## 1 Introduction

To solve the outstanding problems in actual production, low efficiency of manual inspection and unstable quality control of map prints, the current efficient solution is to build a defect detection system based on machine vision. It is difficult for the existing graphic defect detection system to detect the defects of area elements in map printing, whether the light-colored areas such as water system and vegetation are missing or not, whether the regional edges are complete or not. Through the experimental analysis, it can be concluded that the main reason for the undetectable defect of area elements is the small contrast between area elements and paper background.

Combining with the production requirements for the speed of the processing system, based on the industrial standard gray (NTSC) method, this paper studies how to adjust the weights of each factor in R, G, B channel by the color information of the map, improve the differences of channel weight, reduce the channel weight whose

difference is small, finally obtain high- contrast gray image and provide the high quality image for the further image analysis and defect recognition.

## 2   Graying Method in Industrial Production

In the printing detection system, it is generally necessary to grayscale the image after image acquisition, so as to prepare for further image analysis and defect recognition. Considering the actual production demand, the requirements of the defect detection system for graying algorithm are mainly simple, fast, highly targeted and fast response speed. The ultimate goal is to highlight the defect to the maximum extent on the basis of retaining certain image details.

Aiming at the above requirements, the existing printing quality detection system of commonly used graying methods are one single component method, the maximum value method, average method, the industrial standard gray method, HLS model algorithm [1–4]. If set Gray as image gray value, R, G, B component values respectively, and the scope for [0, 255], $W_R W_G W_B$ separately for each component weight, value range of [0, 1] and $W_R + W_G + W_B = 1$, the calculating formula of each respectively Table 1.

**Table 1.** Grayscale methods commonly used in printing quality detection system

| Method | Calculate formula | Establishment condition |
|---|---|---|
| One single component method | $Gray = W_R R + W_G G + W_B B$ | Consider one component $W_R = 1$, $W_G = W_B = 0$ |
| The maximum value method | $Gray = \max(R, G, B)$ | |
| Average method | $Gray = W_R R + W_G G + W_B B$ | |
| The industrial standard gray method | $Gray = W_R R + W_G G + W_B B$ | $W_R = W_G = W_B = 1/3$ |
| HLS model algorithm | $Gray = [\max(R, G, B) + \min(R, G, B)]/2$ | $W_R = 0.299$, $W_G = 0.587$, $W_B = 0.114$ |

No matter which expression method is adopted for the above five graying algorithms, they all meet the following requirements:

$$Gray = W_R R + W_G G + W_B B \tag{1}$$

The differentiation of each algorithm mainly depends on the value of $W_R W_G W_B$, that is, how to allocate the weights of the three channels of R, G and B. Among the five algorithms, one single component method, the maximum method, the mean method and the HLS model algorithm run fast, but there are serious distortion and color information loss. The grayscale method of industrial Standards is suitable for the visual

characteristics of human eyes [2] and can better retain image details. It is a grayscale method proposed by the National Television Standards Committee (NTSC) of the United States, so it is also known as the NTSC method. NTSC is widely used in grayscale processing of other color images, such as grayscale printing and printing of color images [5].

Firstly, the author adopted the NTSC method to grayscale the map sample, as it was shown in Fig. 1, and the grayscale values were shown in Table 2.
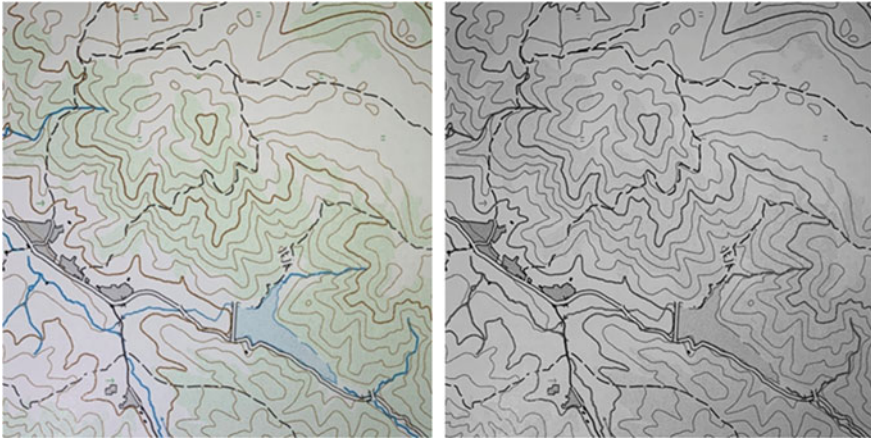


**Fig. 1.** Gray the map sample by NTSC method

**Table 2.** Grayscale values of each element in the sample after graying by NTSC method

| Factor | Average gray-value difference(with paper) |
|---|---|
| Black | 120 |
| Brown | 89 |
| Blue (area element) | 17 |
| Green (area element) | 3 |

It can be seen from the experimental results that the obtained grayscale image, especially the difference between the green area element and the background, is too small. It is likely that the difference is smaller than the threshold of the subsequent region segmentation algorithm, making the region segmentation algorithm insensitive and unable to correctly distinguish the green area element from the paper background. Through preliminary analysis, it is found that the NTSC method makes use of the physiological characteristics of human eyes' sensitivity to green, and the proportion of green channel in grayscale is relatively high. If the difference between the green channel and the background is the smallest, it is inevitable that the difference between green channel and background after grayscale is relatively small. In addition, although the color standard of map prints is fixed, it is difficult to avoid the environmental

changes and mechanical errors in each link of the actual production. In addition, the detection system itself needs to face different batches of maps with different color matching ratios, which requires the flexibility of gray-scale algorithm.

Therefore, this paper intends to start from the color characteristics of map prints, analyze the color information of images to be detected, and design a group of weights suitable for the detection of map defects, in order to improve the current situation that it is difficult to detect defects in general dyeing printing, in order to ensure the running speed of the algorithm and not change the calculation mode.

## 3   Weight-Adjustment Graying Method

The most prominent feature of NTSC method is that it conforms to human visual perception. However, for the detection of map prints, the grayscale images are still processed by the machine, and the main goal is not to get the images with the best visual perception, but to increase the difference between the target and background of defects, so as to facilitate the subsequent detection and processing of defects. Based on the idea of NTSC method to determine channel weights by considering visual perception, this paper plans to adjust the algorithm weights for map printing detection. Through the statistical collection of the RGB value of the map image to be detected, the differences between the map elements and the paper background in the three channels of RGB were calculated, and how to adjust the weights of the three channels of RGB was studied, so as to increase the contrast between the area elements after grayscale and the paper and highlight the elements to be detected. Its grayscale model is shown in Fig. 2.
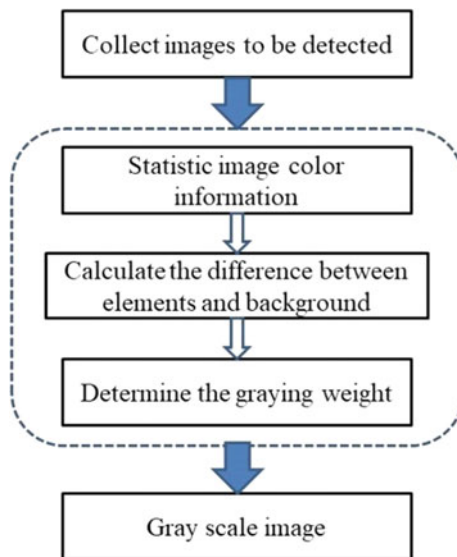


**Fig. 2.** Gray-scale model of weight adjustment

### 3.1   Statistic Image Color Information

Basic scale topographic map has particularity, both on the element characteristics and color in terms of color, on the specific drawings are black, brown, blue, green, red, purple six color printing, the color effect is shown in Fig. 3.
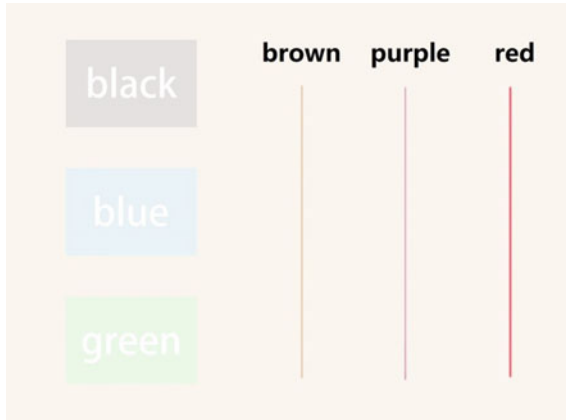


**Fig. 3.**  Line map six spot color simulation

According to the author's preliminary analysis on the use of color and paper for maps, except for the green area element, other areas have very big differences with the paper in at least two channels of RGB. Therefore, this paper intends to isolate the green spreading area and mainly study the relationship between the green elements area and the RGB value of paper.

Before getting the color information of the image need to be detected, the first step is to classify the detected image's green area element and background. Since the variety of colors used in basic scale topographic map are fixed, and at least one standard is required to classify each element and background, HSB color space is proposed in this study for classification and color information statistics. According to the definition of HSB color space, H represents hue and can be used to distinguish color information. Based on the size of their color gamut, H value can represent the types of various colors in RGB space. Theoretically, different elements and backgrounds in H channel can be clearly distinguished. Besides, the image to be detected is obtained by stable image acquisition equipment. The illumination intensity of each area of the map is basically the same. The gray scale of each area in the image to be detected is relatively uniform. With the analysis above, this paper uses H channel information to classify elements and backgrounds. The specific implementation methods are as follows:

(1)  Traverse the collected template image and classify all pixels in the image according to H value. i and j are used to represent the coordinate positions of pixels in different areas of H channel, I represents the horizontal coordinate and j represents the vertical coordinate.

(2) Set the green area element as $G(i_G, j_G)$. $G(i_G, j_G)$ is the target area, and all the pixels in the paper belong to the background area $P(i_P, j_P)$.

Until then, the general classification of the elements and background is completed.

## 3.2 Calculate the Difference Between Elements and Background

The green area element region set $G(i_G, j_G)$ and background set $P(i_P, j_P)$ obtained in Sect. 2.1 were converted from HSB mode to RGB mode, and three groups of target and background results were obtained corresponding to three channels respectively. Then execute two-step calculation:

(1) The average grayscale of pixels in the green and background region;
(2) The grayscale mean difference between the green and the background region in R, G and B channels is $D_R$, $D_G$ and $D_B$.

Thus, the difference between elements and background is calculated.

## 3.3 Determine the Graying Weight

The grayscale mean difference obtained in Sect. 2.2 is used to adjust the weights of the three channels in the grayscale algorithm. The basic idea of determining grayscale method is:

(1) Analyze the RGB value information of the image to be detected, calculate the RGB difference between each element and the paper, and determine the minimum average difference and the maximum average difference. Minimum average and maximum difference respectively represent the sensitivity of the region segmentation algorithm and fault tolerance, due to the defect detection process is to follow the quality evaluation standard, in does not affect the interpretation of the situation, individual small defects can be ignored, so need in the actual production according to the quality of different batch map specific Settings. In this method, they are mainly used to judge the difference and similarity between channels.
(2) When the mean difference of a channel is much larger than that of the other two channels, there is obvious difference between the target and background in the channel, and the channel information is directly used as the grayscale result;
(3) When there is no channel with maximum difference among the three channels, the similarity among the three channels is judged. If the mean difference of the three channels is very close, the NTSC method is adopted for grayscale; Otherwise, according to the proportion of the mean difference corresponding to the three channels, the weight value is redistributed to grayscale the image.
(4) In order to avoid image distortion, the weights of the three channels after redistribution add up to 1.

Based on the above ideas, take the case of $D_R > D_G > D_B$ as an example to introduce the algorithm implementation process. Firstly, the minimum mean difference is defined as $D_{min}$ and the maximum mean difference as $D_{max}$. At the same time, the following equation is defined:

$$D_1 = D_R - D_G, \ D_2 = D_G - D_B \tag{2}$$

If $D_1 + D_2 < D_{min}$ exists, it indicates that there is similarity among the three channels, then NTSC method is adopted for image graying. If $D_1 + D_2+ <D_{min}$ does not exist, determine whether $\{D_1 > D_2$ and $D_1 > D_{max}\}$ are true. If true, it means that the gray mean difference of R channel is far greater than that of G channel and B channel. Select R channel information for graying, that is, the weight distribution of the three channels of RGB is 1, 0 and 0 successively.

If the two conditions are not satisfied, it indicates that there is no simple rule to follow for the information of the three channels of RGB. Then, weighted average is carried out according to the mean difference corresponding to the three channels, and the weight values of the three channels $W_R$, $W_G$ and $W_B$ can be obtained through normalization processing:

$$W_R = \frac{D_R}{D_R + D_G + D_B}, \ W_G = \frac{D_G}{D_R + D_G + D_B}, \ W_B = \frac{D_B}{D_R + D_G + D_B}$$

The objects represented by the line map are not fixed, such as forest land, sea area, city and other different areas, the distribution of its elements and the proportion of each spot color will have great changes. Although considering that the distribution changes of detection objects will have a decisive impact on the selection of algorithm, quality control links are interspersed in the whole map printing production process. Even if the print has certain quality fluctuations, it is controlled within a certain range. Therefore, the above three cases can basically satisfy the grayscale treatment of defect detection system theoretically.

## 4   Experimental Verification

The purpose of the experiment is to compare the difference between the graying method proposed in this paper and the NTSC graying method on the contrast between each element and paper. The experimental design was as follows: three kinds of production batch were selected, the algorithm program was written by VC++ 6.0 combined with open CV2.4, and the color information of each group of images was counted. Two methods were used to grayscale the image and the gray difference between the area elements and background was compared. According to repeated tests in actual production, $D_{min} = 5$ and $D_{max} = 20$ were set to ensure the accuracy of the defect detection algorithm. The experimental results were shown in Tables 3 and 4.

**Table 3.** Difference of gray mean between NTSC method and the method in this paper indifferent batch processing

| Gray mean difference (with background) | NTSC | | | Ours | | |
|---|---|---|---|---|---|---|
| | Batch1 | Batch2 | Batch3 | Batch1 | Batch2 | Batch3 |
| Black | 119 | 114 | 105 | 131 | 122 | 118 |
| Brown | 99 | 87 | 75 | 125 | 93 | 82 |
| Blue (area element) | 15 | 20 | 9 | 10 | 21 | 9 |
| Green (area element) | 2 | 3 | 10 | 14 | 10 | 16 |

**Table 4.** Average grayscale of NTSC method and this method in different batch processing

| Average grayscale | NTSC | | | Ours | | |
|---|---|---|---|---|---|---|
| | Batch1 | Batch2 | Batch3 | Batch1 | Batch2 | Batch3 |
| Black | 86 | 75 | 74 | 95 | 80 | 73 |
| Brown | 106 | 107 | 106 | 101 | 109 | 109 |
| Blue (area element) | 190 | 169 | 170 | 216 | 181 | 182 |
| Green (area element) | 203 | 186 | 169 | 212 | 192 | 175 |
| Background | 205 | 189 | 179 | 226 | 202 | 191 |

Analysis of the experimental results showed that, in general, after graying of batch 1 and batch 2 by NTSC method, although all the black, brown and blue elements can meet the system's calibration requirements of mean difference, the mean difference of the green area element was less than the system's minimum mean difference, and the comparison between the green area element and background was too small. The graying effect of each element in batch 3 is ideal, and each element between backgrounds can meet the system requirements. The grayscale images obtained by the method presented in this paper showed very stable experimental results. No matter in which batch, all the color elements had a large mean difference, which was far greater than the system calibration mean difference.

Considering application, not only the contrast relation between each element and the background should be measured, but also the difference between each element should be analyzed in combination with the difference between each element, so the experiment should also compare whether the mean difference between each element can meet the requirement of minimum mean difference. Therefore, the specific gray values of the two methods were shown in Table 4.

The experimental data showed that although the NTSC method satisfy the system requirements in batch 3, but the difference between blue area element and green area element was 1, which was too close. Blue area element represent rivers, lakes, oceans, while green represent forest land, grass, etc. This often occurs in the form of edge connection in map composition, that is, in the gray-scale image segmentation, defect detection and other image processing, the problem will cause the target adhesion, make each factor can't be accurately separate, leading to a significant decline in defect detection accuracy. Therefore, the method proposed in this paper could better meet the needs of map defect detection.

## 5   Conclusions

Aiming at the problems of missing printing and misprinting of area elements in map printing, this paper proposed a new image graying method for defect detection of area elements in map printing, based on the analysis of the existing image graying methods. And the comparison experiment with NTSC method was carried out. The results showed that, compared with NTSC method, the weight-adjustment graying method

showed a certain stability in different batches of map image processing, which could improve the contrast between image area elements and background, provide high-quality images for later image processing.

# References

1. Zhang YJ (1999) Image processing and analysis (volume I). Tsinghua University Press, Beijing, pp 82–85
2. Zhang QF, Yang HB, Ren ZD, Li H (2011) Research on fast high-fidelity gravy-scale method for colon images. J ZhengZhou Univ (Science) 43(03):66–69
3. Liu M, Xue XS, Liu GW, Liu Z, CaiH (2008) Gray-scale algorithm of contrast enhancement colour image. J Changchun Univ Sci Technol (Nat Sci Edition), 41(05):70–74
4. Gu MH, SuB B, Wang MM et al (2019) Overview of colour image greying algorithm. Comput Appl Res 36(05):1286–1292
5. Zhou JH, Peng FT (2006) A selective method of image gravy-scale. Comput Eng 20:198–200

# Blind Image Quality Assessment Based Automatical Motion Blur Restoration Algorithm

Haojie Lou[1,2], Yehong Chen[1(✉)], and Qing Wang[1]

[1] School of Light Industry Science and Engineering, QiLu University of Technology, ShanDong Academy of Sciences, Jinan, China
`chenyh@spu.edu.cn`
[2] Faculty of Printing, Packaging and Digital Media Technology, Xi'an University of Technology, Xi'an, China

**Abstract.** Image quality has a profound influence on human visual information acquisition. For the distorted image with motion blur, how to restore the image accurately is a difficult problem. Firstly, this paper introduces the cause of motion blur, establishes the degradation model, and finally restores the image with wiener filter and blind image quality index. In previous studies, the original image will be used as a reference when the wiener filter is used to remove ambiguity. By finding the minimum mean square error, the image of good quality can be found. In this paper, no-reference image quality index is used to measure the image quality. A series of relations between image blur parameters and image quality index T (L, α) is obtained. These data points are fitted, and then the optimal data are selected to find the extreme point. The parameters corresponding to the extreme point are used to restore the image. By searching for the best quality index value, the automatic optimization of image definition is finally achieved, and the sharp image is obtained. Experiments show that our method improves the restoration performance than some part of the state method.

**Keywords:** Image deblurring · No-reference image quality assessment · Motion blur

## 1 Intrduction

The image blurring problem caused by the relative motion between the camera and object in the imaging process is one of the most common image degradation problems. Image blurring will affect the subsequent image processing work and bring difficulties to the late image analysis and recognition work. The traditional image deblurring method is to estimate the PSF (Point Spread Function) of the image, and then use the deconvolution method to achieve the purpose of image deblurring. After years of research, the method based on wiener filter can achieve image restoration effectively, but there is still room for improvement.

The original image was used as a reference image when the wiener filter method was used for deblurring. By finding the minimum mean square error, the image with the best quality can be found. Nathan [1] proposed the inverse filtering method, which made an important contribution to the field of image restoration technology at that time. However, the inverse filtering method has some shortcomings. Especially when the noise is unknown or cannot be separated. It's anti-noise performance is worse. To overcome this problem, Wiener put forward a new recovery filter [2].

The goal of deblurring is achieved by minimizing the mean square error between them. Compared with inverse filtering, wiener filter has many advantages. Firstly, it has a great improvement in noise resistance. But wiener filter needs to use the signal to noise ratio of the image as a parameter, so the estimation of the signal to noise ratio is an important part of image restoration. Later, domestic scholars also proposed a lot of improved wiener filter deblurring methods: for example, Yang [3] used a constant array to replace the noise signal power ratio in the research and get improvement of image restoration based on wiener filter. The advantage of this algorithm is that it can optimize and improve the ringing effect of images. Based on the restoration of wiener filter, Liang and Luo [4] combined with the genetic algorithm, proposed an algorithm based on genetic self-adaptive wiener filter to remove the motion blur of real images as much as possible, and the effect was better than the traditional wiener filter. Jiang et al. [5] used the angle estimation based on Gabor filtering, and the autocorrelation algorithm was utilized to solve the motion scale. This algorithm provides a new method to estimate fuzzy angle. Xiao et al. [6] proposed an adaptive fuzzy angle estimation method, which can adaptively select the Hough transform or Radon transform to obtain the detection results of fuzzy direction according to the accumulated value of polar diameter as the judgment basis. After the fuzzy direction is estimated, the method calculates the image quality index, and finally selects the most suitable fuzzy direction value adaptively, which is more convenient and fast for automatic restoration.

Implementation of the deblurring involves the quality evaluation of reconstructed images, which are the basis of automatic parameter selection. Our method is similar to [6], but we implement a no-reference image quality index to measure the degree of image blurring, which expands the application scope of this method. Experiments show that our proposed method improving the performance of image restoration.

## 2   Related Works

### 2.1   General Motion Blurring Model

When shooting an object with a camera, if the motion speed of the object exceeds the speed of shooting, there is relative motion between the object and the camera that will result in motion blur of the image be shotted. The motion fuzzy image model can be approximately simulated by a linear system model. The general linear simulation model is shown in the Fig. 1.
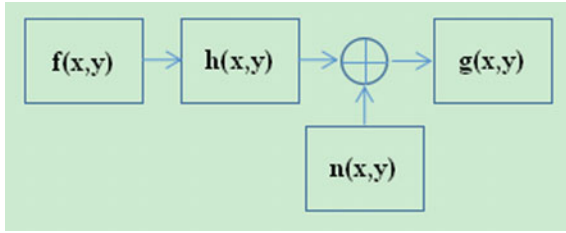
**Fig. 1.** A general motion blurring model

Function f(x, y) simulates the initial clear image, h(x, y) represents the corresponding spatial domain representation of the degradation system, n(x, y) represents the image noise, and g(x, y) represents the degraded fuzzy image.

$$g(x, y) = f(x, y) * h(x, y) + n(x, y) \tag{1}$$

x and y respectively represent the position of pixels in the image. And "*" represents the convolution operation. According to the characteristics of uniform linear motion, the point diffusion function h (x, y) can be expressed by the formula:

$$h(x, y) = \begin{cases} \frac{1}{L}, 0 \leq x \leq L\cos\alpha, & 0 \leq y \leq x\tan\alpha \\ 0 & otherwise \end{cases} \tag{2}$$

where L represents the fuzzy length of the point diffusion function, and $\alpha$ is the included angle with respect to the horizontal direction of 0°. Therefore, estimating the fuzzy angle and fuzzy length becomes the key points of fuzzy image restoration. We can perform the same operations in the frequency domain, where convolution is replaced by multiplication.

$$G(i, j) = F(i, j)H(i, j) + N(i, j) \tag{3}$$

If we knew the values of H and N, we could recover F by writing the above equation as:

$$F(i, j) = (G(i, j) - N(i, j))/H(i, j) \tag{4}$$

Errors N will appear on the image output in different ways depending on the type of disturbance in the signal. The noise modelling and noise removing are an important part of image restoration. In order to make things simple, we just estimate the fixed noise type for this paper, hence, we can choose the most appropriate method for reducing the effects.

A matrix corresponding to the transformation of the blur should be created, and the noise can be removed by adaptive filtering. A Wiener filter (a type of linear filter) which tailoring itself to the local image variance can be used to an image, and Wiener2 is the mat lab function which encapsulates a wiener filter, which works best when the noise is constant-power ("white") additive noise, such as Gaussian noise. In this paper, we apply Wiener2 to an image has had Gaussian noise added, and with estimated L and $\alpha$.

## 2.2    Estimation of Fuzzy Angle

This paper only considers blur caused by linear moving. When a motion blur occurs in an image, it will leave a blur trace in a certain direction in Frequency domain energy spectrums, which can be used to judge the magnitude of the blur angle Fig. 2.
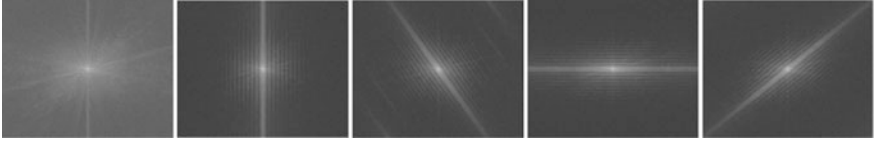


**Fig. 2.** FFT transformation images of series of Degraded image with motion blur. The left is from the original image, motion blur simulation is done by the rest images, the simulated length is 40, and the simulated angle for the rest from left to right, top to bottom are 0, 30, 90 and 135

Fuzzy angle estimation will be detected by Hough transform. So first analyze how to detect the size of fuzzy angle with Hough change. Therefore, we first convert above energy spectrums into polar coordinate space and express it by the formula:

$$r = \sqrt{x^2 + y^2} \tag{5}$$

$$\alpha = \tan^{-1}(y/x) \tag{6}$$

where r stands for polar diameter and $\alpha$ for polar angle. Because in polar space, polar coordinates on a line correspond to the same polar angle but radius r is different. Therefore, from the fuzzy trace, the maximum number of points with different diameters r and certain pole angle was found and the value of this was the size of the fuzzy angle $\alpha$ We used the algorithm from [6] to calculate this fuzzy angle.

## 2.3    Estimation of Fuzzy Length

After estimating the motion blur angle, the next task is to find the corresponding blur length, that is, the number of pixels blurred in the image.

The Fourier transform expression of motion blur can be expressed with fuzzy length L and fuzzy angle $\alpha$, the size of the fuzzy function is described by the periodic zero point on the u axis, and the zero point is obtained at u = $\pm 1/L$, $\pm 2/L$, $\pm 3/L$… respectively.

In other words, there are periodic intersecting zeroes in H = (u, v). if the noise N is ignored, the Fourier transform of the image G you see is equal to the Fourier transform of the Point Spread Function H times the Fourier transform of the original image F. We can find the lines in G (u, v) that is perpendicular to the direction of motion. By finding the zero of G (u, v), along that direction, we can find the fuzzy length. We used the algorithm from [6] to calculate this fuzzy length.

## 2.4   No-Reference Image Quality Index

How to determine if the fuzzy image is restored to the clearest statement is another important problem in the process of image restoration. Because real world noise is hard to be modeled, the above method can only estimate the approximate fuzzy angle and fuzzy length, which are deviated from real world situations. In order to avoid missing some possible trace of blur, we got a set of $\alpha$ and L pairs. Therefore, this paper uses an image quality index without reference to get the functional relations of the three variables of fuzzy Angle $\alpha$, fuzzy length L and image quality index T, and finds more accurate values of fuzzy Angle and fuzzy length through automatic optimization.

According to the paper [7], we have implemented an image quality index T without reference to measure the degree of image blurring. The calculation method is as follows:

The image is denoted as f(x, y), which has M rows and N columns, so the absolute value of the horizontal gradient of each pixel is denoted as:

$$D_h(x, y) = |f(x, y+1) - f(x, y-1)| \tag{7}$$

Therefore, the average value of the whole image is:

$$D_{h-mean} = \frac{1}{MN} \sum_{x=1}^{M} \sum_{y=1}^{N} D_h(x, y) \tag{8}$$

After that, we detected the horizontal edge pixel $E_h(x, y)$ through the following steps:

$$C_h(x, y) = \begin{cases} Dh(x, y), & Dh(x, y) > Dh - mean \\ 0 & otherwise \end{cases} \tag{9}$$

$$E_h(x, y) = \begin{cases} 1, & C_h(x, y) > C_h(x, y-1) \, and \, C_h(x, y) > C_h(x, y+1) \\ 0 & otherwise \end{cases} \tag{10}$$

where 1 represents the edge and 0 represents the non-edge region. The vertical edge pixels can also be represented in the same way. Then, whether the edge pixel corresponds to the fuzzy edge is detected. Equations (11) and (12) are used to determine the ratio value of the fuzzy pair.

Blur can be seen as a ambiguity $A_h(x, y)$, it is expressed as follows:

$$A_h(x, y) = \frac{1}{2} \times ((f(x, y+1) + (f(x, y-1)) \tag{11}$$

The horizontal fuzzy intensity $B_{Rh}$ (x, y) is shown as follows:

$$BR_h(x, y) = \frac{|f(x, y) - A_h(x, y)|}{A_h(x, y)} \tag{12}$$

In the same way, $B_{Rv}$ could be estimated in the vertical direction using equations. The larger value between $B_{Rv}$ and $B_{Rh}$ is selected for final decision, which is called inverse blurriness. The clearer the image, the bigger the inverse blurriness. The judgment expression of fuzzy pixel B (x, y) is as follows:

$$B(x,y) = \begin{cases} 1, \max(BR_h, BR_v) > T_{Hb} \\ 0, \qquad\qquad\qquad otherwise \end{cases} \tag{13}$$

## 3 Our Proposed Algorithm

Our algorithm use the fuzzy angle and length estimates function proposed in paper [6], then intensively sampling near the estimated parameter. The wiener filter is used to realize image deblur, and the evaluation of the restored image is based on paper [7], which proposed a kind of metrics for image blur quality evaluation. Let me briefly describe our algorithm as following:

The input of algorithm is g(x, y), and the output of algorithm is f(x, y).

After estimating the motion blur angle and length of the motion blur image, the Point Spread Function (PSF) of the image can be created.

PSF = fspecial ('motion', LEN, THETA);

Then, the PSF of the image was converted into the optical transfer function H by using the MATLAB function OTF = psf2otf (PSF, size(FBL)). FBL is the image after median filtering and Fourier transform.

Finally, the fuzzy image can be restored by wiener filter, is known as least square filtering, and its mathematical expression is:

$$M(u,v) = \frac{H^*(u,v)}{[|H(u,v)|^2 + P_n(u,v)P_f(u,v)]} \tag{14}$$

where, H(u, v) is the optical action function, $H^*(u, v)$ is the conjugate of the optical action function, $P_n(u, v)$ is the power spectrum of noise, $P_f(u, v)$ is the power spectrum of the input image, so the restored image can be expressed as:

$$f(m,n) = F^{-1}[G(u,v)M(u,v)] \tag{15}$$

Ten sampling points near the estimated fuzzy angle $\alpha$ and fuzzy length L are selected, and image quality index IQA is calculated for groups of experimental data. Surface fitting is carried out by means of linear interpolation.

Finally select optimized fuzzy parameters, the realization of image restoration.

## 4    Experiments and Discussions

In this paper, a fuzzy image of a fuzzy Angle of 45° and a fuzzy length of 40 images is adopted for the experiment. The method proposed by us optimizes the method proposed based on paper [6] by using no-referenced image quality indexes. Paper [6] uses PSNR to estimate noise signals, which have certain limitations.

Around the estimated parameters of fuzzy angle α and fuzzy length L, ten nearest neighbor data points were sampled at intervals of one. The image quality index IQA is calculated on deblur results from these grides of parameters. Surface fitting is carried out by means of linear interpolation on experimental data.

**Table 1.**  Measured IQA index based on a grids of sampling points around the estimated motion parameters α and L

| α / L | 40 | 41 | 42 | 43 | 44 | 45 | 46 | 47 | 48 | 49 |
|---|---|---|---|---|---|---|---|---|---|---|
| 33 | 0.7942 | 0.7969 | 0.7946 | 0.7971 | 0.8084 | 0.8087 | 0.8151 | 0.8069 | 0.7974 | 0.7988 |
| 34 | 0.7946 | 0.7916 | 0.7876 | 0.7939 | 0.8117 | 0.8119 | 0.8126 | 0.8012 | 0.7974 | 0.8007 |
| 35 | 0.7891 | 0.7863 | 0.7842 | 0.7942 | 0.8038 | 0.8012 | 0.8074 | 0.801 | 0.7992 | 0.7927 |
| 36 | 0.7903 | 0.7881 | 0.7905 | 0.7805 | 0.7933 | 0.7965 | 0.8077 | 0.7931 | 0.7931 | 0.7929 |
| 37 | 0.7963 | 0.7849 | 0.7833 | 0.7768 | 0.7947 | 0.7932 | 0.7992 | 0.7875 | 0.7945 | 0.7967 |
| 38 | 0.7963 | 0.7883 | 0.7888 | 0.7789 | 0.7854 | 0.7807 | 0.7955 | 0.7871 | 0.7846 | 0.7911 |
| 39 | 0.7949 | 0.7922 | 0.7943 | 0.7768 | 0.7752 | 0.7751 | 0.7907 | 0.7775 | 0.7869 | 0.7859 |
| 40 | 0.8109 | 0.8025 | 0.7891 | 0.7821 | 0.7843 | **0.7732** | 0.7761 | 0.7761 | 0.7872 | 0.7899 |
| 41 | 0.8122 | 0.8053 | 0.8037 | 0.7972 | 0.7876 | 0.7746 | 0.7825 | 0.7759 | 0.7850 | 0.7822 |
| 42 | 0.8108 | 0.8133 | 0.8116 | 0.7981 | 0.7922 | 0.7888 | 0.7849 | 0.7736 | 0.7828 | 0.7875 |

In Table 1, the image quality index IQA was calculated for the 100 groups of experimental data, and the curved surface was fitted through the linear interpolation method to get the following figure.

It can be clearly seen from Fig. 3, that the surface has an extreme point. The corresponding fuzzy Angle and fuzzy length are estimated. According to the data in Table 2, there is a certain gap between the estimated value and the actual value of the unimproved wiener filtering de-fuzzing method, and the improved wiener filtering method based on the no-reference image quality evaluation method can estimate the fuzzy Angle and fuzzy length more effectively.

**Table 2.**  Actual and estimated values of wiener filter PDF parameters

| Deblur method | Simulate motion angle/length | Deblur parameters angle/length |
|---|---|---|
| Paper [6] | 45/40 | 44/38 |
| Our proposed | 45/40 | 45/40 |
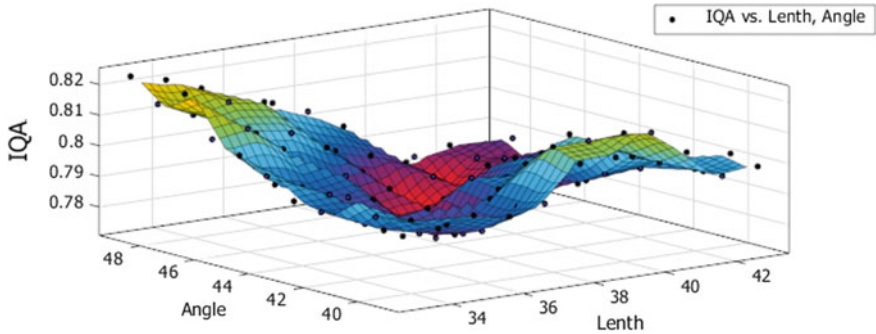
**Fig. 3.** Fitted convex face which map IQA on grids of experimental deblur estimated parameters

It can realize the optimized restoration of motion blur accurately. In Fig. 4, (a) is the original blur image, (b) is the wiener filter restoration image, and (c) is our proposed method that is based on the no-reference quality index. It can be seen that wiener filter restoration method based on no-reference image quality index has a better effect.



(a) a blurred image          (b) deblurring from[6]          (c) our method
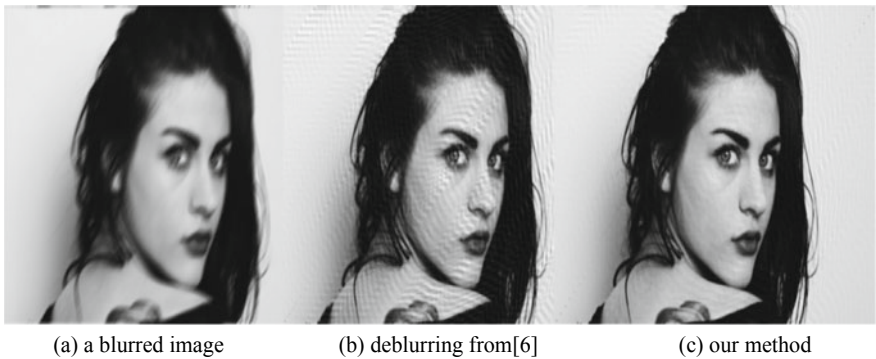
**Fig. 4.** Comparision of our proposed method with method from paper [6]

## 5   Conclusions

It has been proved by scholars that the method based on wiener filter can achieve image restoration effectively, but the accuracy of this method often depends on the accuracy of fuzzy Angle and fuzzy length estimation. According to the obtained PSF parameters, wiener filter is used to obtain the restored image. On this basis, the motion angle and length are optimized by using the image quality index. The traditional full reference image quality index evaluation method needs to use the original clear image data. However, the original clear image of a blurry image is often unknown. Therefore, this paper will evaluate the image quality obtained by different estimation parameters without reference, and then select the best extreme point of image quality. The

corresponding fuzzy Angle and fuzzy length are the optimal parameters for image restoration. Experiments show that this method has greatly improved the accuracy and the restoration effect.

# References

1. Hu W, Xue J, Zheng N (2012) PSF estimation via gradient domain correlation. IEEE Trans Image Process 1:386–392
2. Jin F, Bin Z, Xuan S (2011) Image restoration based on wiener filter. J Commun Univ China 04:19–23
3. Yan Y, Jian H (2012) Research and improvement of wiener filter image restoration technology. Sci Technol Eng 12(29):7611–7615
4. Xiao L, Xiao S (2017) Wiener filter image defuzzing algorithm based on genetic adaptive. J Guangxi Teachers Educat Univ 35(04):17–23
5. Jian J, Min Z, Mei Q (2012) Wiener filter based on Gabor to deblur. J Hefei Univ Technol 35(08):1026–1029
6. Zhen X, Shu Y, Shuang L (2017) Motion fuzzy instrument image restoration algorithm based on improved wiener filter. Electr Measurement Instrument 54(02):88–91
7. Kerouth F, Serir A (2011) A No-reference quality metric for measuring image blur in wavelet domain. Int J Digital Informat Wireless Commun 1(4):767–776

# Research on a Slice-Based Voxelization Method

Yanxing Liu, Yusheng Lian$^{(\boxtimes)}$, Yang Jin, Xiaojie Hu, Yongle Hu,
and Guannan He

School of Printing and Packaging Engineering, Beijing Institute of Graphic
Communication, Beijing, China
`lianyusheng@126.com`

**Abstract.** Model voxelization is an important part of three-dimensional (3D) printing. A slice-based voxelization method of 3D model is proposed in this paper. This method discretizes the 3D model both in the height direction and slice plane to realize the voxelization of the model. The 3D model is sliced with the same thickness in Z direction to discretize the height dimension of the model, and the polygonal contour in the slice plane of the 3D model is obtained, which is the intersection of the slice plane with the polygonal mesh of the 3D model surface. The contours are pixelated using Brenham's algorithm to realize discretization of the model contours in each slice plane. The experimental results show that the voxelization method is simple, the computation speed is suitable for daily tasks, and the model can be reproduced well.

**Keywords:** 3D model · Voxelization · Slice · Discretization

## 1   Introduction

3D printing is a technology to realize 3D model manufacturing by stacking or removing modeling materials layer by layer [1]. In order to realize the reproduction of 3D model,voxelization is an important and necessary step to process data of 3D model before printing. During voxelization process, the internal descriptive data can be calculated and the information of the 3D model is acquired. A dataset that can reproduce the complete 3D model is generated [2]. Finally, the driver of the 3D printer outputs the voxel dataset to reproduce the model.

   At present, as a research hotspot, with more and more research achievements on voxelization, more and more algorithms can convert the data of the 3D model into voxel data that can drive the 3D printing process. The quality of voxelization algorithm determines whether the 3D model can be reproduced with high precision and thus retains more details of the model. Duan [3] presents a voxelization method based on octree. The voxel data of the model is obtained based on octree to subdivide the model. Tian and Xue [4] present a novel approach to voxelization method in radial extent filling, based on replacing 3D sampling with two-dimensional plane-filling algorithm. Laine [5] proposed a voxelization method based on topological structure. The method is based on intersecting the input primitives against intersection targets in the voxel grid. Martin et al. [6] proposed an out-of-core voxel method based on GPU, which can

effectively process models with high resolution. Different from these above methods, we propose a new voxelization method-A slice-based voxelization method in this paper, which implements voxelization by processing the 3D model from the two dimensions of Z direction and X/Y slice plane.

## 2   Voxelization

In the voxelization method proposed in this paper, the 3D model is firstly slicedwith same thickness in the Z-axis direction. And the polygonal contour in the slice plane of the 3D model is obtained, which is the intersection of the slice plane with the polygonal mesh of the 3D model surface. Then, the slice plane is rasterized. And all the lines between the intersection points in the slice plane are pixelated by the Brenham's algorithm to realize discretization of the model surface contours in each slice plane. The flow chart of voxelization algorithm is shown in Fig. 1.
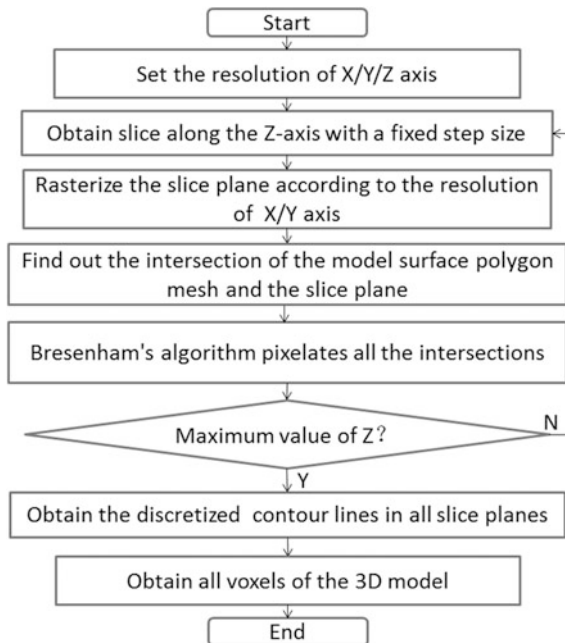


**Fig. 1.** Flow chart of voxelization algorithm

### 2.1   Slice and Rasterization

The thickness of each sliceis determined according to the set Z-axis resolution. The 3D model is sliced withfixed step size along the Z-axis from small to large coordinates, and the step size $m$ of the slice may also be called the height of voxel, $m$ can be represented as:

$$m = \frac{H_Z}{R_Z} \tag{1}$$

where in

$H_Z$ is the height of the model;

$R_Z$ is the Z-axis resolution.

The area of each slice $S_P$ is fixed; it is the projected area of the model in the Z-axis direction.

When a slice of the model is obtained, the slice layer is rasterized. Based on the value of X/Y resolution, the slice is processed into mesh layer with fixed size. $S_0$ represents the area of a grid, which is also the cross-sectional area of a voxel. The formula for$S_0$ is

$$S_0 = \frac{w}{R_X} * \frac{h}{R_Y} \tag{2}$$

where in

$w$ is the width of the slice plane;

$h$ is the height of the slice plane;

$R_X$ is the X-axis resolution;

$R_Y$ is the Y-axis resolution.

The diagram of 3D model slice and rasterization is shown in Fig. 2.
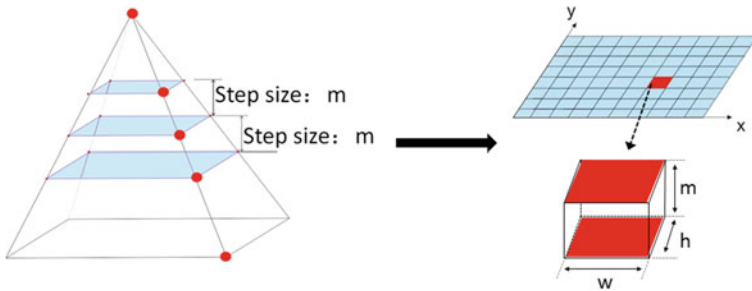


**Fig. 2.** Slice and rasterization

## 2.2 Draw the Contour of the Model

The surface of the 3D model consists of a large number of polygon facets, each of which is constructed by several vertices.Therefore, to draw the contour line of the surface of the model in the slice plane, it is necessary to find the intersection between the edge of the polygon facet and the slice plane. And the positional relationship between the edge of the polygon and slice plane has four positions relations possible. Suppose the coordinates of two vertices A and B are $(x_1, y_1, z_1)$ and $(x_2, y_2, z_2)$ respectively, and the height coordinate of the slice layer is $z_0$,the four position relations can be represented as:

$$z_1 > z_0 > z_2 \text{ or } z_2 > z_0 > z_1 \tag{3}$$

$$z_1 = z_0 > z_2 \text{ or } z_2 = z_0 > z_1 \tag{4}$$

$$z_1 > z_2 = z_0 \text{ or } z_2 > z_1 = z_0 \tag{5}$$

$$z_1 = z_2 = z_0 \tag{6}$$

According to the above analysis, the intersection of the edges of the polygons with the slice plane is found, and the intersection on the slice plane is pixelated by the Brenham's algorithm to realize discretization of the model surface contours in the slice plane. Finally, the closed figure on the slice plane is drawn, which is the contour line of the model surface on the slice at a certain Z value, as showed in Fig. 3.



**Fig. 3.** Contour of the model surface ata certain Z value

When the drawing of contour lines in the slice plane is finished, it is identified that pixelate on the slice plane is completed. Therefore, voxelization of the model is completed when the contour lines of all slice planes from small to large coordinates along the Z-axis have drawn.

## 3   Experimental Results

In this paper, two models of a quadrilateral pyramid and airplane are voxelized. In order to visualize the voxelization, a very low resolution of 2.54 dpi in X/Y/Z direction is applied. The printing size of the pyramid model is 10 cm × 10 cm × 10 cm, so the model consists of 10 × 10 × 10 voxels. Each X/Y image includes 10 ×10 pixels, and the model has 10 slice planes with thickness of 10,000 microns. The voxels are obtained by running the voxelization program. The result is shown in Fig. 4.

As is shown in the figure above, in the left figure is the image of each slice plane of the model after voxelization from bottom to top of the model. The white area is the contour of the model surface, the gray area is the internal voxels of the model, while the black part is the slice plane. The figure on the right shows the voxelization effect of the quadrilateral pyramid with 10 voxel plane. Due to the small resolution, only 10 slice planes are generated, so we can only reproduce the shape of the pyramid without reproducing its details in the figure.
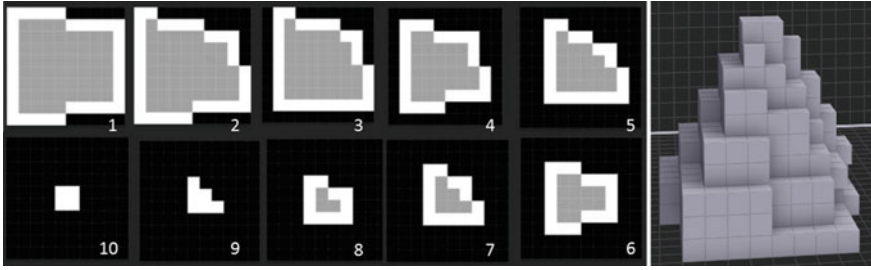
**Fig. 4.** Slice of the quadrilateral pyramid after voxelization (left) and voxelization model (right)

The voxelization program, which applies the algorithm proposed in this paper, has high operation efficiency. The test are carried out on a laptop PC, which equips an Intel ®i5-2600 CPU@3.4 GHz (4 physical cores), 4G RAM. Table 1 shows the voxelization time of the model with different resolutions.

**Table 1.** Voxelization parameters and computing time

| Model | Facets | Slices | Z-axis resolution/dpi | X/Y resolution/dpi | Time/s |
|---|---|---|---|---|---|
| Airplane | 2366 | 1851 | 400 | 400 | 111.43 |
| | 2366 | 2777 | 600 | 400 | 161.34 |

It can be seen from the above table that the computation speed of the proposed algorithm is fast, and the time of voxelization is proportional to the resolution. Therefore, the computation costs of the algorithm largely depend on the value of the resolution. From the test results, this method can be used in practical tasks.

## 4 Conclusions

In this paper, a slice-based voxelization method is proposed, which processes the 3D model from the two dimensions of Z direction and X/Y slice plane. Firstly, this method slices 3D models at the same thickness in Z direction to realize the discretization of the height dimension of the model. And the polygonal contour in the slice plane of the 3D model is obtained, which is the intersection of the slice plane with the polygonal mesh of the 3D model surface. Secondly, the slice plane is rasterized. Based on the X/Y resolution value, the slice is processed into mesh plane with fixed size. Then, the contour is pixelated using the Brenham's algorithm to realize discretization of the model contours in each slice plane. Finally, all the voxels of the 3D model are obtained. The voxelization algorithm proposed in this paper is simple, easy to implement, and has a fast processing speed. It has advantages in dealing with the voxelization tasks of 3D models. The experimental results show that the voxelization speed of the 3D model can meet the requirement of practical application, and the voxelization effect is also better.

# References

1. Shahrubudin N, Lee TC, Ramlan R (2019) An overview on 3d printing technology: technological, materials, and applications. Proscenia Manufact 35:1286–1296
2. Jacobs PF (1996) Stereo lithography and other RP&M technologies-from rapid prototyping to rapid tooling. Society of Manufacturing Engineers, USA
3. Duan W (2017) A fast voxelization method based on octet. Microcomput Appl 36(11):91–101
4. Tian F, Xia X (2013) The Voxelization and homogenization methods of high-resolution volumetric 3D display. J Comput Aided Design Graphics 25(09):1304–1311
5. Laine S (2013) A topological approach to voxelization. Comput Graph Forum 32(4):77–86
6. Martin P, Andreas K (2015) Grid-free out-of-core voxelization to sparse voxel cortexes on GPU. Conference on High-Performance Graphics, ACM: 95–103

# Digital Media Technology

# Study on Gesture Recognition Method for Special Effects

Ruze Zhuang[✉], Qiang Wang, and Shi Li

School of Media and Design, Hangzhou Dianzi University, Hangzhou, China
1143924475@qq.com

**Abstract.** Visual-based gesture recognition products for special effects at the moment are of poor gesture diversity and low recognition accuracy. Given the above problems, this study proposes a gesture recognition method based on positioning of key points of the hand. The method realizes the recognition of specific gestures by discriminating the five-finger state, and can feedback different special effects according to the recognition results of different gestures in real time. Problems of weak anti-interference ability and self-occlusion of key points in gesture recognition technology are solved through the method, this method also effectively improves the gesture recognition accuracy and diversity.

**Keywords:** Gesture recognition · Particle effect · Hand key points · Human computer interaction

## 1 Introduction

Gesture recognition is a method of understanding human body language through computer algorithms, which can build a bridge between man and machine. Recently, research on gesture recognition technology has inspired various recognition ideas and methods. In 2006, Double proposed a method of implementing gesture recognition based on gesture shape and texture features [1]. In 2008, Hang Zhou exploited the support vector machine classification to achieve gesture recognition [2]. In 2012, Yi Li used Kinect to achieve the acquisition of depth image and hand positioning to realize gesture recognition [3]. In 2013, Lei Yang realized gesture recognition based on hand edge contour detection [4], while the recognition was susceptible to complex background environment. In 2016, Lizhi Zhang et al. realized static gesture recognition through "Hidden Markov Model" [5], there is a certain error in the gestures with little differences in morphology when recognizing.

In light of shortcomings of the existing gesture recognition methods, this paper brings forth a gesture recognition method based on hand key points detection, and uses particle effects as a criterion for recognition results. The method of this paper apparently lowers the influence of complex background environment and improves identification accuracy and ductility.

## 2 Relevant Technical Principles

### 2.1 Multiview Hand Key Points Detection

For mentioned problems, on the basis of the "iterative algorithm of multi-view hand key points detection with deep learning" developed by Simon from Carnegie Mellon University [6], this paper creates a high-precision hand detection model through the multi-view bootstrapping [7]. It solves occlusion problem of certain key points in specific gesture images taken from different angles. To be specific, firstly, use the high-definition camera to shoot the hands from 31 different perspectives and establish a small number of initial image data sets containing key points. The neural network is used to train the image data sets to obtain the sketch of detection model. Secondly, for images with serious occlusion, build 3D position of key points based on camera pose and project it into 2D image position points of different viewing angles. Thirdly, combine the 2D images containing key points and the initial training set to obtain a new one, and improve the accuracy of key points detection through the iterative training detection model that can generate 21 hand key points, as shown in Figs. 1 and 2.
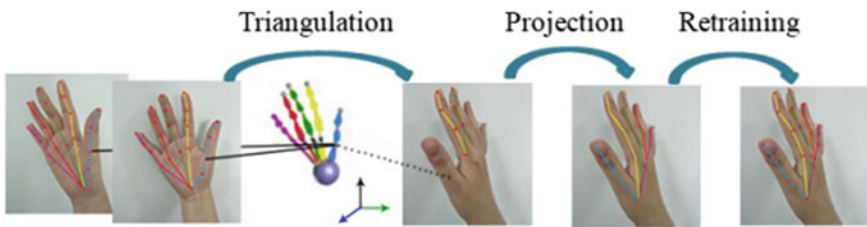


**Fig. 1.** Iterative process of multitier hand key points detection

### 2.2 Gesture Recognition Method

Mainly based on location information between key points, the gesture recognition method determines the specific category of gestures according to the state of each finger—"bending", "half bending" and "stretching".

#### 2.2.1 Key Points

Figure 2 depicts distribution of 21 key points of the hand. Relevant research shows that in morphological gesture transformation, seven key points, including 0, 1, 2, 5, 9, 13 and 17, have a relatively small changing range in relative position, which can be considered as the reference points. In different gestures, the positions of five key fingertip points, including 4, 8, 12, 16 and 20, vary greatly. The relative position relationship between them and the stable reference is often selected to identify the state of each finger and realize specific gesture recognition.

In this paper, experiments were designed to calculate detection accuracy of key points through three gestures—"five fingers straight", "five fingers half bent to grasp" and "five fingers bent to make a fist". Each gesture experiment includes 100 sample

**Fig. 2.** Hand key points

images. The average correct rate of key points detection for each gesture was further identified by calculating the correct rate of each image key points detection, and its formulas are shown in Eqs. (1) and (2):

$$\alpha_k = r_k/n * 100\% \tag{1}$$

$$\overline{\alpha} = \left(\sum_{k=1}^{100} \alpha_k\right)\Big/100 \tag{2}$$

where $\alpha_k$ is the correct detection rate of key points in the KTH picture, $r_k$ is the correct detection number of key points in the KTH picture, $n$ is the total number of key points, and $\overline{\alpha}$ is the average accuracy rate of key points detection.

According to the results shown in Table 1, key points detection accuracy rates of the three gesture states are all higher than 90%. It shows the position information of key points can be used as the discrimination condition of gestures.

**Table 1.** Key points recognition rate of three gestures

| Gesture categories | Fingers straight | Fingers half bent | Fingers bend and clench |
|---|---|---|---|
| Average accuracy ($\overline{\alpha}$) | 97% | 94% | 93% |

### 2.2.2   Location Relation of Key Points

The gesture recognition method is to identify the finger state through the relative positional relationship of the key points. The distance between the camera and the hand does not change the proportional relationship between the key points when images are collected. Therefore, this paper uses such relation to quantify the relative positional relationship of the key points, and designs experiments to optimize the proportional relationship of the 21 key points in the three states: straightening, bending and half-bending. (as shown in Tables 2 and 3).

**Table 2.** Calculation formula of five-finger state proportion relation

| Finger | Thumb | Index finger | Middle finger | Ring finger | Little thumb |
|---|---|---|---|---|---|
| Proportion | $q_1 = d_{0-4}/d_{0-2}$ | $q_2 = d_{0-8}/d_{0-5}$ | $q_3 = d_{0-12}/d_{0-9}$ | $q_4 = d_{0-16}/d_{0-13}$ | $q_5 = d_{0-20}/d_{0-17}$ |

**Table 3.** Identifies the optimal range of each finger in three states

| State\Finger | Thumb | Index finger | Middle finger | Ring finger | Little thumb |
|---|---|---|---|---|---|
| Bend | $q_1 < 1.10$ | $q_2 < 0.65$ | $q_3 < 0.60$ | $q_4 < 0.70$ | $q_5 < 0.80$ |
| Half bent | $1.10 < q_1 < 1.30$ | $0.65 < q_2 < 1.30$ | $0.60 < q_3 < 1.20$ | $0.70 < q_4 < 1.25$ | $0.80 < q_5 < 1.25$ |
| Straight | $q_1 > 1.40$ | $q_2 > 1.80$ | $q_3 > 1.90$ | $q_4 > 1.80$ | $q_5 > 1.70$ |

Table 3 shows that the states of five fingers can be discriminated and the recognition of the specific gesture can be realized by constraining the proportional range of the distance between the key points.

## 3 Design and Implementation of Gesture Recognition and Special Effect Application

Taking Visual Studio 2017 and Open CV 3.41 as the development tools, this paper designs and implements recognition of 10 different gestures in C++ language, and designs different particle effects to feedback the recognition results for generating interactive effects. The flow of system design is shown in Fig. 3.
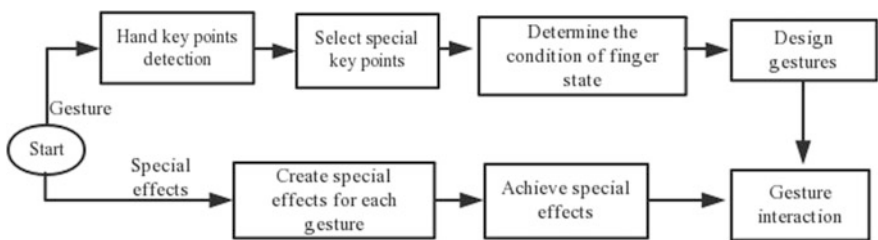


**Fig. 3.** System design and implementation flow chart

### 3.1 Gesture Recognition Module

This paper designs 10 gestures and a gesture recognition method based on Open CV. The value range of the distance relationship between the key points is used as a discrimination condition for gesture recognition. The judging conditions of 10 gestures are shown in Table 4.

**Table 4.** Judging conditions of 10 gestures

| S/N | Gestures | The discriminant conditions |
|---|---|---|
| 1 | OK | $1.10 < q_1 < 1.30$ && $0.65 < q_2 < 1.30$ && $q_3 > 1.9$ && $q_4 > 1.8$ && $q_5 > 1.7$ |
| 2 | Good | $q_1 > 1.40$ && $q_2 < 0.65$ && $q_3 < 0.60$ && $q_4 < 0.70$ && $q_5 < 0.80$ |
| 3 | Heart | $q_1 > 1.40$ && $q_2 > 1.1$ && $q_3 < 0.60$ && $q_4 < 0.70$ && $q_5 < 0.80$ |
| 4 | Love | $q_1 > 1.40$ && $q_2 > 1.8$ && $q_3 < 0.60$ && $q_4 < 0.70$ && $q_5 > 1.7$ |
| 5 | Fist | $q_1 < 1.10$ && $q_2 < 0.65$ && $q_3 < 0.60$ && $q_4 < 0.70$ && $q_5 < 0.80$ |
| 6 | Grab | $1.10 < q_1 < 1.30$ && $0.65 < q_2 < 1.30$ && $0.60 < q_3 < 1.20$ && $0.70 < q_4 < 1.25$ && $0.80 < q_5 < 1.25$ |
| 7 | Victory | $q_1 < 1.10$ && $q_2 > 1.8$ && $q_3 > 1.9$ && $q_4 < 0.70$ && $q_5 < 0.80$ |
| 8 | Click | $q_1 < 1.10$ && $q_2 > 1.8$ && $q_3 < 0.60$ && $q_4 < 0.70$ && $q_5 < 0.80$ |
| 9 | 666 | $q_1 > 1.40$ && $q_2 < 0.65$ && $q_3 < 0.60$ && $q_4 < 0.70$ && $q_5 > 1.7$ |
| 10 | Push | $q_1 > 1.40$ && $q_2 > 1.8$ && $q_3 > 1.9$ && $q_4 > 1.8$ && $q_5 > 1.7$ |

## 3.2 Particle Effects and Display

This paper verifies each gesture recognition result through different effects, recognizes a specific gesture and generates a corresponding effect to achieve gesture interaction. Part of the gestures are shown in Table 5.

**Table 5.** Special effect feedback and its effect display

| S/N | Gestures | Effect display | S/N | Gestures | Effect display |
|---|---|---|---|---|---|
| 1 | OK |  | 4 | Love |  |
| 2 | Victory |  | 5 | Good |  |
| 3 | 666 |  | 6 | Push |  |

## 4 Comparison of Experimental Results

This paper designs two experiments to compare advantages and disadvantages of this application and other special effects products of gesture recognition in terms of recognition accuracy and diversity.

## 4.1 Comparison of Gesture Recognition Accuracy

This paper designs a comparative experiment on accuracy of three gestures—"heart", "good" and "666" with 200 gesture sample images in each group (120 correct gestures

and 80 incorrect ones). The method designed in this paper (method A) is compared with the template matching gesture recognition method based on edge contour extraction (method B). The experimental results are shown in Table 6.

**Table 6.**  Comparison of gesture recognition accuracy

| Gestures/method | Heart | | | Good | | | 666 | | | Total | | |
|---|---|---|---|---|---|---|---|---|---|---|---|---|
| | R1 (%) | R2 (%) | R (%) | R1 (%) | R2 (%) | R (%) | R1 (%) | R2 (%) | R (%) | R1 (%) | R2 (%) | R (%) |
| Method A | 91 | 97 | 94 | 95 | 95 | 95 | 93 | 97 | 95 | 93 | 97 | 95 |
| Method B | 83 | 90 | 86 | 96 | 75 | 88 | 96 | 85 | 92 | 92 | 83 | 89 |

Among them, R1 is the recognition rate of the correct gesture. R2 is the recognition rate of the wrong gesture, and R is the comprehensive recognition accuracy.

The experimental data suggests the recognition rate of method A regarding correct gestures is basically the same as that of method B, while the former has a lower misjudgment rate and higher comprehensive recognition accuracy.

## 4.2    Comparison of Gesture Types

At present, the existing gesture recognition special effects interactive products, including FU Camera, TikTok and QQ, are mostly realized by method B. This paper designs an experiment to compare the gestures recognized by the gesture recognition method implemented in this paper with the gestures recognized by the above similar products, the experimental results are shown in Table 7.

**Table 7.**  Comparison of gesture types

| S/N | Product | The recognized gesture | Amount |
|---|---|---|---|
| 1 | The design of this paper | OK, good, heart, love, fist, grab, victory, click, 666, push | 10 |
| 2 | FU Camera | Heart, fuels, 666, good, hands folded, love, fists show MOE | 7 |
| 3 | TikTok | Push | 1 |
| 4 | QQ | Heart, palms up, push | 3 |

The results show that gesture recognition method implemented in this paper is more advantageous than other similar products in the number of identifiable gestures, so it enjoys stronger extensibility on gesture recognition.

## 5   Conclusions

Gesture recognition technology is a hot research topic in computer vision and intelligent application. This paper proposes a gesture recognition method based on positioning of key points of the hand, and uses special effects to feedback the recognition results. It also analyzes advantages and disadvantages of this paper and the current similar technical products through two contrast experiments. The experimental data presents higher recognition accuracy and stronger recognition ductility of the method. It can also improve the user experience and meet the growing demand for entertainment interactions.

## References

1. Doublet J (2006) Contact less hand recognition using shape and texture features. Int Conf Signal Process 3(2):26–30
2. Zhou H (2008) Research on gesture recognition based on computer vision. Beijing Jiaotong University, Beijing
3. Li Y (2012) Hand gesture recognition using Kinect. In: IEEE 3rd international conference on software engineering and service science, Beijing, China
4. Yang L, Sui Y, Yao L (2013) Static gesture recognition and detection combined with skin color segmentation and hand shape matching algorithm. Inf Commun 23(4):4–6
5. Zhang L, Huang J, Huang D et al (2016) Markov static gesture recognition combining local features and global features. Comput Sci 43(11A):247–251
6. Simon T, Joo H, Matthews I et al (2017) Hand keypoint detection in single images using multiview bootstrapping. CVPR 4645–4653
7. Ballan L, Taneja A, Gall J et al (2012) Motion capture of hands in action using discriminative salient points. ECCV 234–238

# Design of Mobile APP for Printing Pricing Based on Android

Yuke Huo[1], Wenjie Yang[1(✉)], and Shaozhong Cao[2]

[1] School of Printing and Packaging Engineering, Beijing Institute of Graphic Communication, Beijing, China
584767862@qq.com
[2] Beijing Key Laboratory of Signal and Information Processing for High-End Printing Equipment, Beijing Institute of Graphic Communication, Beijing, China

**Abstract.** In this paper an android-based APP for printing pricing is designed aiming to assist enterprises in mobile business processing. The technical scheme includes Eclipse + ADT platform, XML language to design the foreground interface, Java language for business logic processing and SQLite for database. The main function is the management of product, its parts and process information, and pricing of the required process and materials of each component.

**Keywords:** Printing pricing · Android · Mobile APP

## 1 Introduction

With the development of mobile Internet technology, the popularity of android smart phones and the gradual maturity of its open source technology, Android phones and apps have a good application prospect. Moreover, the idea of "Internet +" is gradually applied in printing enterprises. For example, the combination of mobile Internet technology and printing can better assist the display of enterprise information, broaden business, and shorten the distance with users [1]. The pricing is an important part of enterprise management, in which the convenience and accuracy of pricing process directly affect the production efficiency and profits. Based on this, the mobile application and pricing are combined to design APP for printing enterprises, which aims to assist enterprises not to be restricted by time and place and facilitate the management of information.

## 2 Demand Analysis

The formation of complete printed matter needs to go through a series of processes including pre-press, printing and post-press binding, etc. due to the influence of different printing parameters, the pricing items are small and trivial, and the materials and processes of each part will lead to different pricing results. For example, the pre-press mainly includes design, plate-making and other processes; printing includes monochrome printing, double-color printing and other choices; binding includes binding,

horse-riding binding and other ways. Obviously, information needs to be recorded if the price of each process is to be calculated.

On the one hand, the pricing needs to calculate the total cost of materials and processes, which are from many aspects in enterprise management. Based on this, basic information such as process category, pricing items, and material information such as paper name and price, are recorded to establish the price book, which can be used as a reference standard for enterprises and customers to view. That is to design a price book module. On the other hand, the printing product is from the customer needs, it is necessary to record product information and customer's choices of the material and process. Therefore, the pricing module is designed to be managed in three parts: product, part and process information. The system use case diagram is shown in Fig. 1.
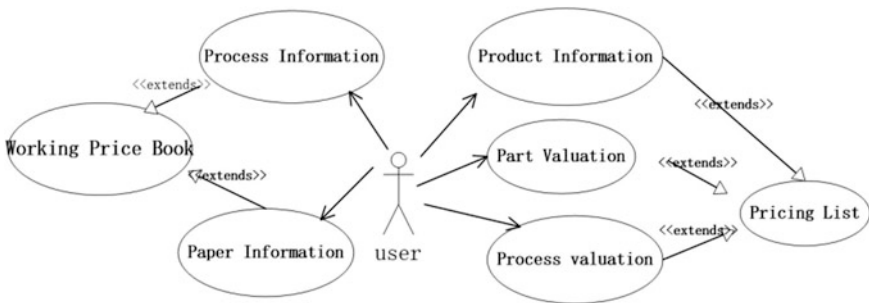


**Fig. 1.** Use case diagram

## 3 System Design

### 3.1 Technical Solution

Due to the advantages of open source and standardization, Android develops rapidly [2]. In terms of technology, in this paper Eclipse + ADT platform is used to build the development environment, XML technology is widely used in interface design, and Java is widely used to realize functions in the background. The Java has the advantages of security, simplicity and dynamic characteristics [3]. In this APP development, the "Activity" and "Intent" components are used as a whole, and the "Activity" is the only component of android that directly interacts with users [4], which is used for interface display and data transfer between interfaces through the "Intent", and also including "Fragment" grouping and modular management to UI components [5].

### 3.2 Interface Design

In this paper XML and View component are adopted to implement the interface. According to the functional requirements, it mainly includes three Fragment layouts: "Working Price Book", "Price List" and "Me". Then, the view component uses "Fragment Tab Host" to fill in the main activity, and realizes the free switching between layouts through "Fragment Layout", where the "Tab Page Indicator" expands

the work price book into two "view pagers": process and paper. Similarly, the price list is expanded into three parts: product, part and process information. The interface is shown in Fig. 2.
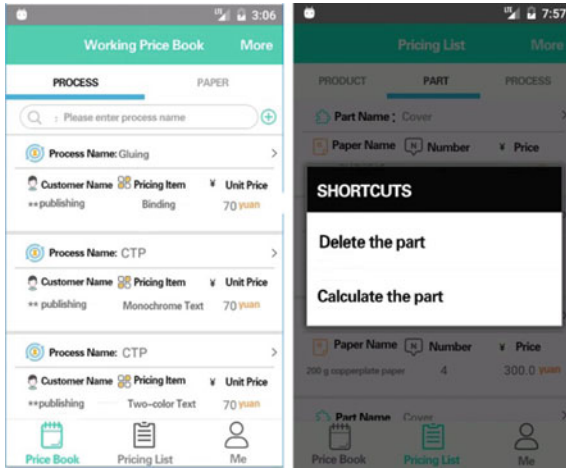


**Fig. 2.** System interface

### 3.3 Database Design

In this paper SQLite is adopted, which is a lightweight database. It has the following advantages: support SQL language, small size, fast computing speed, less resources, no need to install and configure [4]. Its data relationship is shown in Fig. 3.
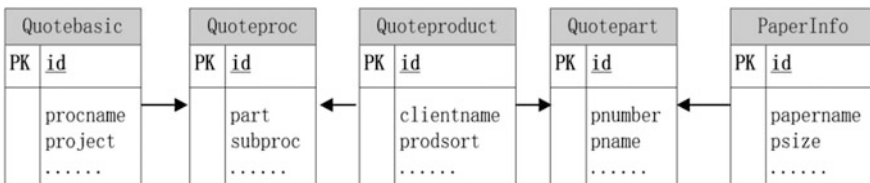


**Fig. 3.** Pricing relational data model

### 3.4 Functional Module Design

The main modules are following.

Working price book module: The price book is the reference standard in the process of pricing. Since the pricing step requires the reference of the process and the basic price of paper and other data, so we use "Viewpager" sliding switching to manage them separately.

Pricing list module: It is to management product, part, process information and pricing of materials and process. The interface and function are similar to the price book module. Because of the individualized orders from costumers, different parts have different material and process choices, each order needs pricing individually. Each material or process pricing is the quantity multiplied by unit price. The quantity is calculated by the product quantity and its processing process, and the unit price is taken from the price book. The function class diagram is shown in Fig. 4.



**Fig. 4.** Function class diagram

## 4   System Implementation

This paper aims to design an android-based mobile application with C/S structure. Because of the C/S mode guarantees a friendly human-computer interaction and improves the practicability and safety of the system [6]. Therefore, it can better assist enterprises in pricing. The sequence diagram of system realization of pricing process is shown in Fig. 5. So, the following is the functional realization of each module.

Working price book module, process and paper are managed separately. The process interface displays the key information of each process, such as name, pricing item, etc., for users to browse briefly. The function also has data query, update and delete; its paper interface displays paper name, size, amount and other information, also can carry out data maintenance. In order to facilitate user's operation, "Option Menu" is used to monitor user options, to graphical functions.

Pricing list module, the product module mainly records the product parameters of the customer commissioned printing, such as the type and format of the printed product; part module records customer requirements for the type and amount of paper required for text, cover, and interstitial printing. In the process of valuation, "Spinner" is used to display the paper and its price data from the price book, so as to calculate the total cost of materials; Process model, which is used to record the process required by customers for printing, including the selection and parameters of pre-press, printing and binding processes. As well, the data is taken from the price book to complete the calculation of the total cost of the process.
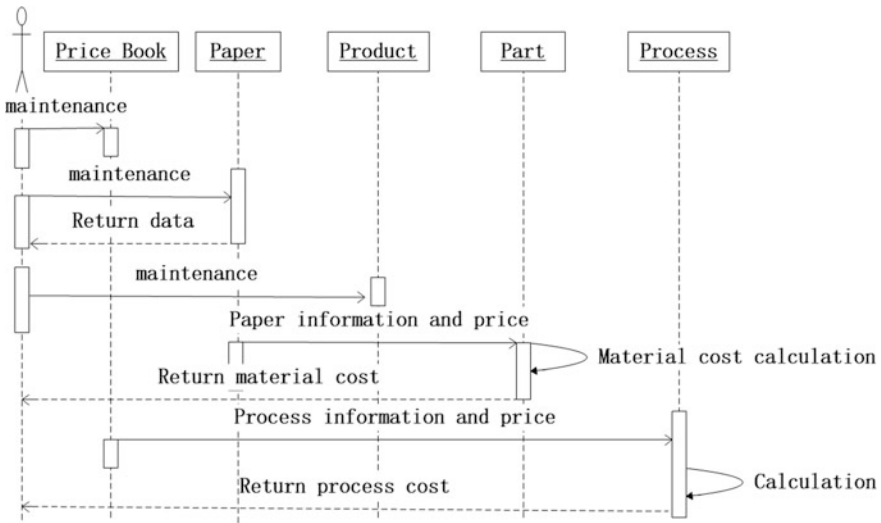
**Fig. 5.** Sequence diagram of pricing

## 5  Conclusions

This paper mainly introduces the design process of mobile application in printing enterprise, and designs the price book and pricing list module based on the personalized characteristics of printing materials, so as to assist the realization of PC terminal functions and the processing of mobile business. Its functions mainly include displaying process and paper information, specifying basic working price, recording product, component and process information by customer entrusted, and calculating the total cost of materials and processes required by components.

## References

1. Zhang Y (2015) Talking about the role of mobile app application in enterprise management. Papers Collection of Tianjin Television Technology Research Association 2015 Conference
2. Wang J (2017) Design and development of personnel management system based on android. Wuhan University of Engineering
3. Zhang Hong long (2018) Mobile phone software development of android system. Electron Technol Softw Eng 137(15):44
4. Zhou X (2018) Design and implementation of educational system client based on android. Univ Electron Sci Technol
5. Li G (2013) Crazy android handout
6. Pan H (2017) Design and implementation of financial management system based on C/S mode. Autom instrum 5:174–176

# Production and Experience of VR Roaming System in History Museum of Tianjin University of Science and Technology

Zheng Zhou[1], Zhanjun Si[2(✉)], and Ruiling He[1]

[1] College of Light Industrial Science and Engineering, Tianjin University of Science and Technology, Tianjin, China
[2] College of Artificial Intelligence, Tianjin University of Science and Technology, Tianjin, China
`szj@tust.edu.cn`

**Abstract.** In order to create an interactive VR campus roaming system, it is easy to display the campus landscape, publicize the campus image, and introduce the campus history, so that students and teachers can break through the time and space browse the school history museum. Taking Tianjin University of Science and Technology History Museum as a virtual space, using 3ds Max for creating model and mapping, rendering, processing UI pictures with Photoshop, combining JavaScript and C# language for editing human-computer interaction script, and finally completing the roaming system on Unity3D platform. Get a school history museum model that is scaled down by the entity school history museum by modeling. It can realize web browsing, provide a user-friendly GUI interface, and realize the roaming of the school history museum through the keyboard and mouse. The establishment of the VR roaming system of the school history museum enables visitors to enjoy the campus scenery without leaving home. At the same time, it provides a platform for the digital construction of Tianjin University of Science and Technology.

**Keywords:** Virtual roaming · 3ds max · Three dimensional modeling · Unity3d

## 1 Introduction

Virtual roaming is an important branch of virtual reality technology. The 3I features of virtual reality technology—immersion, interactivity and conception—satisfy people's pursuit of digital and informationized life, and make the virtual roaming system more effective and have great development prospects [1]. At present, various technical fields have paid more and more attention to the effect of virtual roaming systems, and the demand for virtual roaming technology applications has become more extensive.

## 2    Development Software Introduction

3ds Max is a PC-based, feature-rich 3D computer graphics software produced by Autodesk and one of the world's top 3D modeling software. This article uses 3ds Max 2014 to complete the 3D model building, mapping and rendering of the Tianjin University of Science and Technology.

Developed by Unity Technologies of the United States, Unity3D is a fully integrated professional game engine for developing 3D and 2D video games and simulations for computers, consoles and mobile devices. This article uses Unity3D 5.5 to complete the interactive and roaming functions of the roaming system.

Developed and released by Adobe, Adobe Photoshop is the most widely used image processing software in the world, referred to as "PS". This article uses Adobe Photoshop CC 2017 to process some old photos with yellowing, wrinkles, and breakage.

Adobe Illustrator is a vector graphics editor developed and marketed by Adobe, which has unique advantages in vector graphics production and text layout. This article uses Adobe Illustrator CC 2015 to complete some unique vector graphics, background image gradients and text layout.

## 3    Design Ideas and Framework of VR Roaming System in School History Museum

The scene design of the VR roaming system of the school history hall is divided into five parts, which are called "Preface Hall", "Hebei Institute of Light Industry", "Tianjin Institute of Light Industry", "Tianjin University of Science and Technology", and "Looking into the Future". In the overall school history hall roaming system production ideas, according to the implementation order can be divided into: the preparatory process, modeling the school history museum with 3ds Max software, mapping and rendering the school history museum models in 3ds Max, importing the model into Unity to build the scene, writing scripting language to achieve interaction, adding background music, making roaming, making the main interface, and detect the expected effect. The overall flow chart of the VR roaming system of the Tianjin University of Science and Technology History Museum is shown in Fig. 1.

## 4    Design and Production of VR Roaming System in School History Hall

### 4.1    Construction of 3D Model of School History Museum

The establishment of 3D models through 3ds Max is the most important part of the design of the roaming system of Tianjin University of Science and Technology. It is necessary to determine the dimensions of the various parts of the school history museum model before modeling. The construction of the entire school history museum model is mainly divided into five parts: "Preface Hall", "Hebei Institute of Light
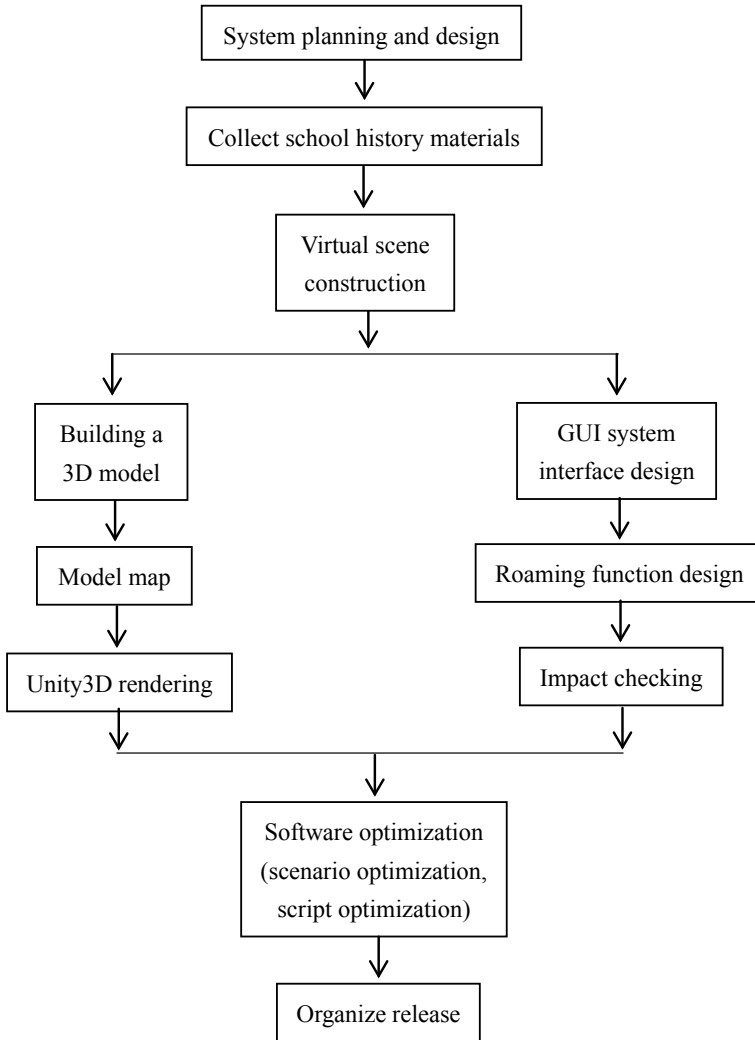
**Fig. 1.** Thought flow chart

Industry", "Tianjin Institute of Light Industry", "Tianjin University of Science and Technology", and "Looking into the Future", including the construction of models such as walls, panels, display cabinets, display stands, curved screens and stone columns. The overall model of the completed school history hall is shown in Fig. 2.

## 4.2 UI Interface Production

The production of the UI interface is the key to the roaming system. A good UI interface will give users a more intuitive and convenient operation experience. Before entering the VR roaming of Tianjin University of Science and Technology, we need to

**Fig. 2.** Overall model of the school history hall

create a welcome interface. With the Twin Towers of Tianjin University of Science and Technology as the background, we can make a UI button picture in Photoshop and pull the picture into Button created by Unity, and write the jump page code to realize the interactive function.

The five exhibition halls of the school history hall roaming system can be accessed by the code of the jump page. When we click on the corresponding exhibition hall from the display page, then we can start roaming from this exhibition hall. Roaming is done using the first person perspective camera in Unity. We need to create a new scene and put the school history museum model into it, then import the Rigid Body FPS Controller camera and put it in the corresponding exhibition hall to start the display and roaming of the corresponding exhibition hall.

After creating the UI interface, scripts are used to write interactive functions, interactions need to be realized include: clicking on the introduction of characters, scene conversion of the school history museum, clicking on voice prompts, roaming selection and other functions. The main interface is shown in Fig. 3.

### 4.3    Audio Import

When we enter the roaming, the background music will play automatically, and it will pause when the background music icon is clicked. First we need to convert the imported audio and video format to the format supported by Unity3D, and then do the following.

Create a new folder in the Assets panel of Unity3D. Let's name it sound and drag the audio into it. Then create a new empty object in the Hierarchy column, click Add Component under the Inspector panel of the empty object, then select Audio-Audio Source, and drag the audio under the sound folder directly into the Audio Clip to

**Fig. 3.** Main interface display

complete the import of the music component. Finally, put the audio in the resource file into the Audio Clip and finish assigning it. At this time, in the system, audio playback can be controlled by Play, Stop, Pause, etc., in Audio Source [2].

### 4.4 Production of Scene Roaming

When the user enters the display page of the roaming system of the school history museum, there will be a selection interface, which is "automatic roaming" and "manual roaming". Selecting the automatic roaming page will directly enter the roaming scene to roam in the order of the specified route. Selecting manual roaming requires controlling the first person to convert the angle of view and the angle of movement through

the keyboard WSAD button and mouse. Users can choose their own roaming scene. Partial roaming scene conversion codes are as follows. You can add the following code where you want to jump to the scene and add the scene name in parentheses.

Scene Manager. Load Scene ("shoudongmanyou") [3].

The roaming page is set with an end button, and the user can opt out of roaming at any time. The roaming scene is shown in Fig. 4.



**Fig. 4.** Roaming scene

The first person roaming is set, so that the roaming implementation controls the first person to convert the viewing angle and movement by pressing the button WSAD and the mouse. The viewing angle can be controlled by creating a camera. The process of creating a camera is as follows: first select the Create command in the Hierarchy column, click Camera to create it, and name it First person, complete the first person camera setting, and adjust the camera's perspective slightly. Next, right-click in the Project panel to create a C# script for writing the mouse-controlled camera view change, name it mouse look and double-click to open and write the script. After writing, drag the script into the first person camera in the Scene view, and view the effect. Click the play button to find that the camera can only switch the angle of view through the mouse and cannot move. The mobile function can be implemented by writing a scripting language to control the keys on the keyboard.

## 5    Testing and Optimization

After the preliminary production of the school history museum roaming system, it is necessary to carry out the test. First of all, we need to pay attention to whether the model, texture, material is lost, whether the multimedia playback is normal, whether

the overall scene effect is normal, whether there is a stuck phenomenon in the roaming process, and perform collision detection.

The number of faces used in the 3D model construction is proportional to the memory occupied by the file. The more the number of faces, the larger the memory, the slower the rendering process, and the lower the roaming speed, which has many adverse effects on the overall system construction. Therefore, some repeated lines and faces need to be deleted during scene optimization to reduce unnecessary file memory consumption.

In the process of writing a scripting language, the assignment of the scripting language may be repeated or confusing, which may easily lead to page jump errors. In the optimization process, first check whether the code logic is correct, there may be multiple times of code with similar functional effects, so we need to streamline it. In addition, when creating a new script in the Assets directory, the script will include an Update method that can be removed.

## 6 Conclusions

With the development of science and technology, Chinese colleges and universities have begun to explore three-dimensional digital campus roaming. The three-dimensional digital campus roaming can fully display the actual geographical environment of the campus, and truly reproduce the campus environment, and has strong real-time interaction and dynamics. Users will have a real sense of experience in the virtual campus roaming system, as if walking around a real campus. The combination of virtual campus roaming and campus culture management not only allows the audience to feel the campus landscape during the roaming process, but also indirectly understands the campus culture. The popularity of the school has been enhanced in the process of roaming by the viewers, which has effectively promoted the modern management level of the campus, while at the same time providing a comprehensive and multi-perspective image for the school [4].

The production of the history system of the Tianjin University of Science and Technology has basically realized a variety of interactive functions. It plays an important role in displaying campus landscapes, enhancing campus image, introducing campus history, and constructing the profound cultural connotation of the school.

In the future, the development of a three-dimensional virtual campus system with comprehensive campus navigation, school appearance display, and campus information management functions is the trend of the times [5]. At the same time, the application of virtual roaming technology in the construction of campus culture is also an important step for schools to move towards digital management.

## References

1. Liu J (2012) Research and implementation of virtual reality tour guide training system based on Virtools. Master thesis, Xi'an University of Science and Technology, Xi'an, China
2. Ouyang P, Li Q, Lu X (2013) Research and implementation of virtual campus development based on Unity3D. Mod Electron Tech 36(04):19–22

3. Lanming J, Gaoming J, Honglian C (2016) Computer simulation and system realization of 3D weft knotted fabric. J Text Res 37(07):155–161
4. Ma Z, Dong G (2017) Research on virtual campus roaming design of 3DMAX. Educ Modern 4(06):190–192
5. Yanxia S (2015) Research and implementation of 3D virtual campus based on panorama. Master thesis, Northeast Normal University, Changchun, China

# Development of Multi-functional Intelligent Packaging for Skin Care Products Based on AR Technology

Shiyao Li[1] and Zhanjun Si[2(✉)]

[1] College of Light Industry Science and Engineering, Tianjin University
of Science and Technology, Tianjin, China
[2] College of Artificial Intelligence, Tianjin University of Science
and Technology, Tianjin, China
szj@tust.edu.cn

**Abstract.** Taking skin care products as an example, aiming at the disadvantage of single traditional packaging function of skin care products, this paper probes into the new idea of applying AR technology to the packaging of skin care products, and releases a multifunctional mobile phone program for smart packaging. Firstly, designing the structure and decoration of skin care package. Then, based on 3D Max, the model of skin care product is constructed, mapped, rendered. Editing the video of dismantling skin care package box and splicing it into receiving box. Using Visual Studio to write a real-time program to display the remaining shelf life and expiration reminder after opening. AR mobile phone application software is developed by Unity3D and Vuforia and interactive design is used to optimize the software. The software of smart packaged phone based on AR technology was released. AR technology endows skin care products with multi-functional packaging.

**Keywords:** AR technology · Skin care kit · Unity3D · Vuforia

## 1 Introduction

Augmented reality is a real-time direct or indirect observation of physical reality environment, enhanced or supplemented by computer generated sensory input (such as voice, video, graphics, or GPS data) [1]. It has been widely used in various industries. At present, many scholars have studied AR technology in packaging, such as Gaimei Zhang, Yue Cao, Lu Wang, Mingzhi Chen, Xiaoli Song scholars, have studied and developed intelligent packaging based on AR organic tomato [2]; Yanfei Chen scholars have studied the application trend of AR in packaging [3]; scholars Dong Liu and Junyan Wang have explored the topic of AR technology to make packaging more vivid [4]. However, the content of the information transmitted is same as the original packaging and the form of expression is single.

With the improvement on living standards, the visual perception, safety and functionality of products have become the focus of consumers' close attention [5]. At present, the packaging and decoration of skin care products carry too much information, leading to some products not beautiful; the shelf life of skin care packaging only

shows that it is not open and most people have no idea about the shelf life of skin care products after opening, this causing consumers to use expired products even causing skin problems; consumers will discard the outer boxes after using skin care products, resulting in environmental pollution and waste of resources [6].

Aiming at the existing problems of skin care packaging, this paper designs a multifunctional intelligent packaging program. The mobile program can not only get product information by a mobile phone scanning, click on video to learn about the second use of skin care products, but also real-time display of the remaining shelf life of skin care products after opening and expiration reminders.

## 2   AR Technology Principle

The AR system generally has four main features: feature matching, tracking registration, display technology, and human-computer interaction.

### 2.1   Feature Matching Technology

Feature matching technology recognizes matching objects of images according to their shape, color, texture and other characteristics [7]. It can be divided into two categories: local feature matching and global feature matching. At present, there are five main feature points matching algorithms: SIFT, SURF. FAST, BRIEF and ORB, all of which are based on local features. These five algorithms have their own advantages and disadvantages [8].

### 2.2   Tracking Registration Technology

AR technology is the key to realize the combination of virtual and real, and it is also the hot and difficult point of research [9]. This technology mainly recognizes the scene of the real world and tracks the object dynamically, calculates the position and pose of the camera in real time and accurately, so that the virtual object can be accurately superimposed on the real scene, and finally achieve seamless fusion.

### 2.3   Display Technology

Display module is a key part of user experience [10]. Computer showed technology is one of the key technologies in mobile AR technology. The ultimate goal of scene fusion is to output the registered virtual information and the target information in the real environment at the same time, and display it on the screen, so that users can obtain virtual images intuitively through human eyes. At present, showed technology is mainly divided into helmet type, projection type and hand-held type according to the different ways of carrying.

### 2.4    Human-Computer Interaction Technology

Human-computer interaction is one of the main branches of computer science, that is, to study the rational interaction between computers, robots and users, so as to achieve information exchange.

## 3    Skin Care Product Mart Packaging Development

In this paper, the development of multifunctional smart packaging mobile phone software based on AR technology is a trend of packaging industry. The current skin care products packaging have the function of information transmission, promotion of sales and protection of products. On this basis, this paper extends the function of packaging. The development ideas of this paper are as follows: (1) expand the secondary utilization of outer packaging of skin care products of the form of video. (2) to expand the lack of information on the shelf life of skin care products of the way of timing reminder.

### 3.1    Design and Manufacture of Packing Structure

**Table 1.**  Skin care package internal products

| Product | Type | Size (D × T)/mm | Number |
| --- | --- | --- | --- |
| Moisturizing water | Water | 250 × 40 | 1 |
| Moisturizer | Emulsion | 250 × 40 | 1 |
| Face cream | Cream | 230 × 40 | 1 |
| Facial cleanser | Cleaner | 250 × 40 | 1 |

Firstly, the type, quantity and size of skin care products in the package were determined (Table 1) and the outer packaging structure was drawn by Autodesk AutoCAD 2014 drawing software (Fig. 1). Then, investigating the products of the storage box, and adding the detachable module into skin care product box.

The storage box mechanism is composed of 6 parts (Fig. 2).

### 3.2    Design and Production of Packaging Drawings

The design contains four types: water cream and facial cleanser, and a new brand named "baby face" was created.

Product packaging is consumers' the first impression of the product, the design style of "baby face" chooses the Chinese style. After querying the data, the dimensions of the package of skin care products are 276 mm in length, 140 mm in width and 50 mm in height. The software used in the design of graphic drawings is CorelDraw and Photoshop.

(a) The upper box          (b) The lower box

**Fig. 1.** Upper and lower expansion of packaging box
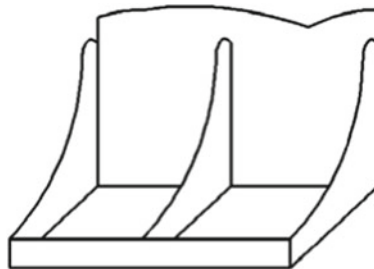


**Fig. 2.** Storage-box design

After determining the packaging style and collecting the corresponding materials, the materials and the cartons are imported into CorelDraw. Set the material as clip painting mode, and make fonts, refer to blue and white porcelain color, simple and generous blue background plus Chinese poetry, to attract consumers' attention (Fig. 3).

### 3.3    Material Collection and Production

Collect materials about "baby face" skin care kit: pictures, product information, etc., editing video of box picking and folding (Fig. 4). The three-dimensional model is an important content of realizing the augmented reality function. The model of this design is completed in 3DMAX (Fig. 5). The model is first made with the spline, and then the model is improved by using the modifier such as extrusion, turning, UVW mapping, UVW expansion, FFD cylinder, optimization and so on.

**Fig. 3.** Packing box decoration design
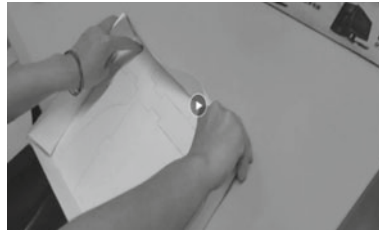


**Fig. 4.** The video of box picking and folding



**Fig. 5.** Skin care product model

## 3.4   APP Development

Pictures need to be validated before they can be recognized. Register vuforia official website and log out in. Get key in vuforia-development-liscense manager, import pictures in target manager for identification and verification. Star-high image to download generates a specific unit scan recognition package and imports unity. AR Recognition Production: Delete the original main camera in Unity, create AR camera and enter license, set parameters, import collected pictures and videos and models, and adjust camera position. APP Export: Add the code and plug-into realize human-computer interaction. After making, test it in the game panel of Unity. After the test is correct, export the APK file and install APP in Android mobile phone.

## 3.5    Partial Code Flow Chart

See Figs. 6 and 7.
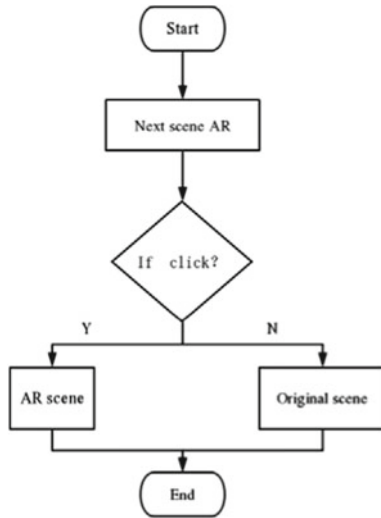


**Fig. 6.** Flow chart of scene jump
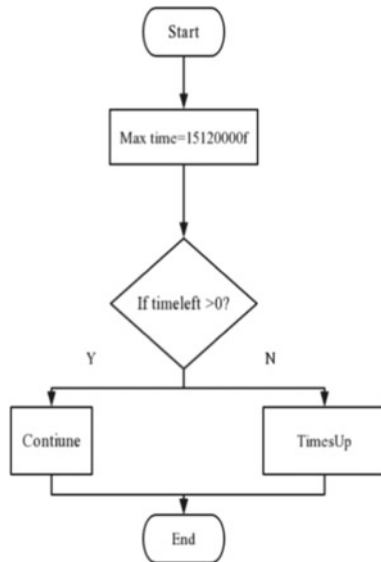


**Fig. 7.** To the time flow chart

# 4   Result

Use AR software to obtain product information, click and play video to reduce packaging waste and display skin care products open to time. The cover of the package of "Chuyan" skin care products (Fig. 8). A physical picture of the skin care kit disassembled and assembled (Fig. 9). Product information by scanning the upper left pattern (Fig. 10). The UI interface of AR-based skin care products and multi-functional intelligent packaging software (Fig. 11). The internal product model can be obtained by sweeping the package design (Fig. 12). The interface from opening to timing (Fig. 13).



**Fig. 8.**  Packaging and decoration design



**Fig. 9.**  Storage box



**Fig. 10.**  Introduction to product information

**Fig. 11.** UI interface



**Fig. 12.** Product model display



**Fig. 13.** To timing and video play

## 5   Conclusions

The function of packaging is not only to protect products, facilitate storage and transportation, promote sales, packaging is also the carrier of information transmission, intelligent packaging is the development trend of packaging industry. The AR technology transforms the packaging design into digital, provides more functionality for packaging, increases the interest in the package, and attracts the consumer's eyes. The future AR technology must be more visible in the packaging industry.

# References

1. Zhi G (2006) Application of mobile augmented reality technology in museum. MA thesis, Shenyang University of Technology, Shenyang, China
2. Gaimei Z, Yue C, Lu W, Mingzhi C, Xiaoli S, Jiandong L (2018) Research and development of organic tomato intelligent packaging based on augmented reality technology. Packag Eng 39(21):1–5. https://doi.org/10.19554/j.cnki.1001-3563.2018.21.001
3. Yanfei C (2018) Application trend of augmented reality in intelligent packaging. Packag Eng 39(07):27–30. https://doi.org/10.19554/j.cnki.1001-3563.2018.07.006
4. Dong L, Yan W (2017) AR technology makes packaging more vivid. Print Today 09:44–46. https://doi.org/10.16004/j.cnki.pt.2017.09.009
5. Tiantian H (2018) Packaging design and consumption psychology: taking cosmetic packaging design as an example. Chin Art 05:56–61
6. Denglin W, Ruiting W (2019) Discussion on green packaging of express industry in China. Logist Sci Tech 42(05):54–56. https://doi.org/10.13714/j.cnki.1002-3100.2019.05.018
7. Tao T, Kang Z, Liu J et al (2015) Small celestial body image feature matching method based on PCA-SIFT. Control Conf 4629–4634
8. Zongda Yue (2016) Research on image matching algorithm based on improved SIFT. MA thesis, Lanzhou University of Technology, Lanzhou, China
9. Xu Z (2010) Research on unknown environment reconstruction and camera posture estimation algorithms. MA thesis, Huazhong University of Science And Technology, Wuhan, China
10. Zhichao F, Chuming Y, Zhiyan M, Youping C (2017) Research on virtual registration technology in augmented reality NC machining. MA thesis, Huazhong University of Science and Technology, Wuhan, China

# Use Augmented Reality to Improve the Sales of Agricultural Products-Take Lemon as an Example

Shengnan Zhang[1] and Zhanjun Si[2(✉)]

[1] College of Light Industry Science and Engineering, Tianjin University
of Science and Technology, Tianjin, China
[2] College of Artificial Intelligence, Tianjin University of Science
and Technology, Tianjin, China
szj@tust.edu.cn

**Abstract.** The aim is to use AR technology to increase the sales of agricultural products. By analyzing the formation mechanism of consumer purchase behavior and problems in agricultural products industry, the utility and application strategy of Augmented Reality in purchasing behavior was studied. Taking lemon as an example, target customers is defined as online consumers aged 17–40 and according to the online marking strategy, AR bookmarks is designed to display multi-dimensional information of products. The development and production of paper bookmarks and mobile terminals are completed by using Unity 3D, Vuforia and other design software. The combination of AR and online sales of agricultural products greatly shortens time for the shopping impulse generated by consumers' purchasing perception, increases subsequent service experience, improves fruit branding and product competitiveness, and promotes online shopping and sales of agricultural products.

**Keywords:** Purchase behavior · Augmented reality · Service experience · Marketing means

## 1 Intrduction

With the arrival of the era of "Internet +", various traditional industries gradually integrate with the Internet, and e-commerce of agricultural products develops vigorously. The online sales mode greatly shortens the circulation channels of products and the circulation costs of middlemen, and enables consumers to obtain high-quality products with relatively low prices. Meanwhile, e-commerce is still facing the problems of low degree of branding, single service experience, backward marketing methods and so on. Augmented reality (AR) has a good interactive mode. The combination of agricultural products industry and AR conforms to the Internet trend and it is of great significance in promoting innovation for the brand development and the transformation and upgrading of the sales model.

## 2 Formation Mechanism of Purchasing Behavior and Problems in Agricultural Products Industry

Before people buy things in our daily life, they usually need to obtain information from various ways to preliminary recognize the function or application scope of products and determine whether they can meet their personal needs. On the premise of meeting the demand of personal or directly attracted to product appearance and other value-added services, the purchase intention or impulse is generated to promote the realization of the purchase behavior. The formation process of the purchase behavior is shown in Fig. 1.
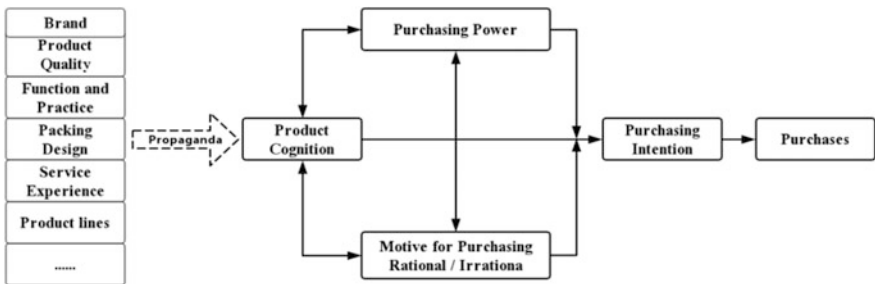


**Fig. 1.** Process of purchase behavior formation

The degree of product recognition will affect consumers' ecognition and purchase intention, which is the basis of purchase behavior and an indicator to measure whether consumers will produce further consumption behavior [1]. This will directly affect the actual purchase behavior. Meanwhile, it can be affected by many factors, such as personal actual demand, product quality, brand attraction, product efficacy and nutritional value, external packaging design, service experience, etc. By improving the service system, providing product additional services, optimizing packaging design and combining with various publicity ways, we can improve product awareness, promote the generation of purchase intention, and thus promote the emergence of shopping behavior. Research shows that [2], brand popularity, that is, the degree of cognitive of the brand will directly affect the purchase behavior, while the service mode, product quality, packaging design and trademark of enterprises will affect the continuous purchase of products. And product lines or shape will directly affect product purchase behavior.

Most of the online marketing models of agricultural products have similarities, and the main service contents are the same. They do not combine the characteristics of target customer groups and their main products to highlight their brand or characteristics business to consumers [3]. Hainan Province, Shandong Province, Taiwan and other regions are facing the problem of a low degree of marketization of most agricultural products [4, 5]. Enterprises and businessmen neglect non-price issues such as brand, service and quality, which caused weak product competition. In online retail brand promotion, the vicious competition of online merchants makes consumers lose confidence. Although excellent product quality and quality service can attract them, if

there is no additional service to surprise them, they cannot establish a very good impression [6]. It is found that the difficulty and low sales volume are mainly due to the lack of brand, backward marketing means and the inability to meet personalized needs, which results in consumers' inability to understand the specific information of product varieties, regions, functions, safety and quality parameters, so that they do not have a deep understanding of the product and service experience. Brand and consumers cannot be closely linked to obtain loyal customers, so that domestic agricultural products appear unsalable or low sales.

## 3    The Utility and Application Strategy of AR Technology in the Formation of Purchasing Behavior

Augmented Reality is a combination of computer technology, communication technology, multimedia technology and so on. It superimposes virtual information into the real environment, so that reality and virtual environment can be closely combined. It can realize real-time interaction with AR glasses or mobile phones, and make information more interesting. AR interactive mode breaks the traditional way of information carrying, brings digital information into the real world and changes the existing state and attributes of objects in the real world, and extends the information capacity, brand value and communication cycle of packaging. It is different from traditional interactive mode, which brings different experience and services to consumers.

### 3.1    Immersion in Multidimensional Interaction and Information Selection Autonomy

AR can realize multi-dimensional interaction and the autonomous transmission of product information [7]. In 2016, Sun Microsystems launched AR packaging of "Sun Brand Chocolate": when AR application scans the package, it will display the complete chocolate information to show the product; it can automatically tell the history of the product development to effectively publicize the brand culture; and it can obtain discount vouchers by scanning the products and carry out product promotion activities. The application of AR realizes the virtual interaction between products and consumers which enable consumers to freely access relevant product information.

Different kinds of products have different functions, effects and eating methods. Consumers are curious about unusual products. AR can provide all kinds of product functions and other related information through AR environment, and provide consumers with cognitive information stimulation or source, so that it can completely take them as the main body to selectively obtain information content that is effective and refuse mandatory information input [7]. Therefore, content planning and interaction design should be based on the needs and psychological characteristics of consumers to make them comfortable and efficient access to effective information.

## 3.2 Entertainment Promotion and Marketing to Enhance Cognitive Depth

The addition of AR technology can promote the shaping and development of brand. The three levels of advertising effect in traditional media are "cognition → influence → purchase behavior". AR advertising can compress the layers of effect in time and space [8, 9], shorten the time when shopping cognition promotes shopping intention and optimize shopping experience. Coca-Cola [10] launched AR Music Bottle app in 2013: Scanning the bottle to pick songs and listen to songs, and it launched the "Coca-Cola Magic" AR app at Christmas 2014 that you could take pictures with virtual Santa Claus in different poses. In 2016, Glico [11] launched AR joint marketing: 12 different AR packages correspond to different love stories. At the beginning of this marketing, it was only shared on the Internet in the form of private sharing by internal employees, because the interesting and continuity of the story makes it extremely topical. Glico's sales tripled in the current quarter, and its partner Kirin rise from third to first in the industry. In 2018, Olio launched AR Scanning App, which can unlock 18 games with a biscuit. Different forms or layouts can unlock AR games and get corresponding incentives. The content form of AR can be changed according to different design requirements. And it can be video, model, picture, text, game and even a combination of multiple content forms (Figs. 2 and 3).
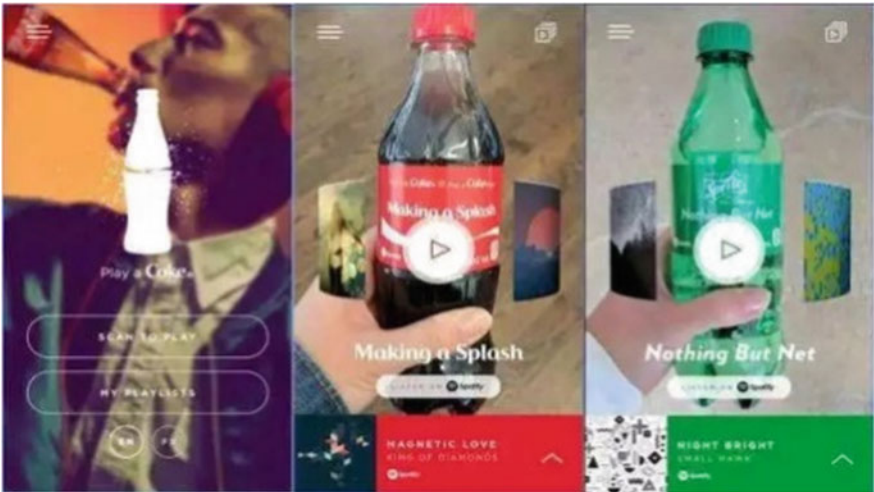


Fig. 2. AR music bottle app [10]

Therefore, reasonable AR application content can be designed according to the selling point and the information that consumers are interested in for example, in the way of storytelling, it introduces the origin and environment of the products to increase the trust; introduces smart ways to provide consumers with relevant knowledge of healthy life; displays the relevant quality indicators parameters of products, so that they

**Fig. 3.** Glico AR joint marketing [11]

can use or eat safely. Use reasonable methods to make dull life knowledge more interesting, fun and easy to be accepted.

### 3.3    Integrating Background Data to Provide Effective Information Services

AR virtual environment can carry Internet technology to provide relevant information such as sales purchases, access records, downloads and so on. According to relevant statistics [10], 75,000 users downloaded and used the Coca-Cola AR music bottle application for participation, which was 300% higher than the two-dimensional code promotional activities; the number of magic AR applications downloaded reached 50,000 times, and a total of 250,000 users searched for related words. According to SinaMicro Blog data, the related topics #Wang Yuan Olio Brand Ambassador # 810 million to read, 35.357 million to discuss, it triggered a large number of fan interaction and consumer secondary dissemination, also created a snack list sales of No. 1. Enterprises can integrate background data to obtain consumer preferences, consumption capacity and other relevant data, test the marketing effect of AR technology, and get effective and reliable information feedback, which is conducive to the next content design.

At the same time, the application embedded in the network social model, adding evaluation feedback and sharing links module, so that consumers can evaluate products and share product-related knowledge, but also to promote to friends. By interacting with friends, consumers can improve their memory and feelings, thereby increasing the rate of return visits and visits.

## 4    Take Lemon as an Example to Develop AR Bookmark APP

According to the utility and application strategy of Augmented Reality in purchasing behavior, the basic content of AR bookmarking mobile terminal is determined, and the target customer group is identified as online consumers aged 17–40 years old. The media resources related to lemon are integrated, and these resources are displayed to consumers in a reasonable storyline way. First, the lemon image and bookmarks are

designed by PhotoShop to make it have a high definition as shown in Fig. 4. The interactive behavior of AR content is realized through unity 3D and Vuforia plug-ins, and APK files are exported for installation and operation on the mobile side.



**Fig. 4.** AR bookmarks

The main page of AR app consists of two parts as shown in Fig. 5a: comprehensive information and AR scan. The comprehensive information can be accessed by clicking on different buttons (Fig. 5b, c) is one of the magical effect, and Fig. 5d is part of the content of introducing the origin of lemon. When the application scans the lemon bookmarks, the corresponding image will appear and double-click it will enter the interesting game as shown in Fig. 6.
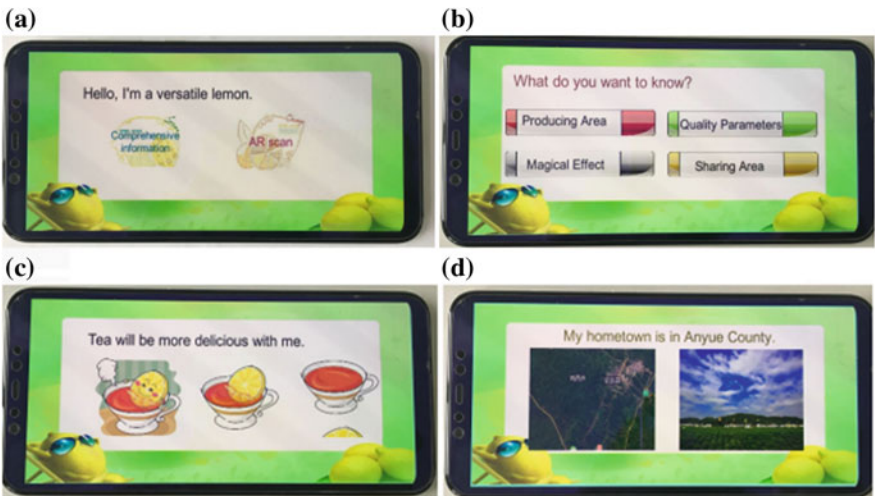


**Fig. 5.** AR application content
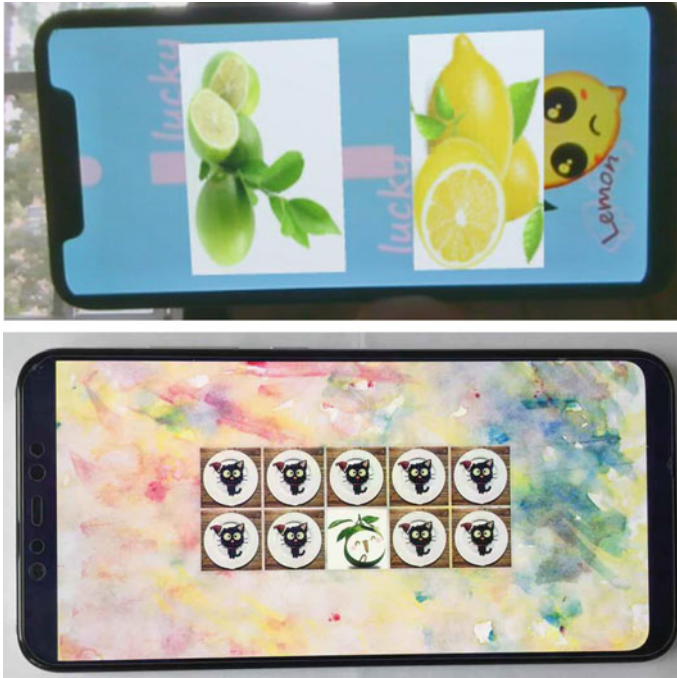
**Fig. 6.** AR image and game

## 5   Conclusions

According to the research of foreign Hayden research institutes [10], 45% of consumers will buy products after seeing 2D materials, while 74% of them will buy products after experiencing AR in products, and the purchase rate has increased by nearly 30%. AR packaging can provide enough information for consumers to make final shopping decisions. The combination of augmented reality technology and agricultural product sales can increase consumers' trust and cognitive depth, and greatly improve the sales of agricultural products.

## References

1. Jianying F, Weisong M (2006) A review of consumer's purchasing intention. J Mod Manage Sci
2. Yanqing C (2017) Research on influence of brand cognition to consumer behaviour. J Hum Post Telecommun Coll. https://doi.org/10.3969/j.issn.2095-7661.2017.01.030
3. Qunfang W (2017) Operational strategy of agricultural products online sales platform under the background of Internet. J Agric Econ 135–136. http://www.cnki.net. ISSN: 1001-6139
4. Shenglian C (2016) Marketing mode of "Internet + Hainan agricultural products". J Mod Bus. https://doi.org/10.14097/j.cnki.5392/2016.16.004

5. Chanteng N (2018) On the online sales strategy of agricultural products from the perspective of regional brand. J Taiwan Agric Res. https://doi.org/10.16006/j.cnki.twnt.2018.01.009
6. Guochun J (2018) Innovative thoughts on promotion strategies of online retail platform. J Taxpaying. http://www.cnki.net
7. Ying L, Ya S (2019) Interactive design of food packaging based on ar technology. J Packag Eng. https://doi.org/10.19554/j.cnki.1001-3563.2019.02.010
8. Qinchuan Z, Yang Z (2019) Research on the development of children's publications based on augmented reality technology. J View Publ. https://doi.org/10.16491/j.cnki.cn45-1216/g2.2019.03.011
9. Songlin Z, Jing W (2014) Application and development obstacles of augmented reality in paper publishing. J Sci Technol Publ. https://doi.org/10.16510/j.cnki.kjycb.2014.06.012
10. Fushuang A (2017) Coca-cola and pepsi all use packaging black technology. http://www.sohu.com/a/133671211_324615
11. Yan Z (2018) Realization of AR technology in packaging. J Print Technol. https://www.xianjichina.com/news/details_78033.html

# Printing Engineering Technology

# Preparation for Electrochromic Devices on PET Substrate Using Screen Printing

Guodong Liu[(⊠)], Yu Liu, Ningning Luo, Yameng Sun, and Xiao Li

College of Bioresources Chemical and Materials Engineering, National Demonstration Center for Experimental Light Chemistry Engineering Education, Key Laboratory of Paper-based Functional Materials of China National Light Industry, Shaanxi Provincial Key Laboratory of Papermaking Technology and Specialty Paper Development, Shaanxi University of Science & Technology, Xi'an, China
Lgdmax587@aliyun.com

**Abstract.** Poly(3,4-ethylenedioxythiophene) polystyrene sulfonate (PEDOT: PSS) as one of the organic electrochromic materials is frequently discussed in the development of Electrochromic Devices(ECDs) while it also can be as a potential electrode applied in the flexible electronic device. In this paper, we realized the ECDs through sceening printing and conductive polymer PEDOT: PSS, and the solution formulation of PEDOT:PSS was optimized by doping with organic solution including polyvinyl alcohol (PVA), methanol (Me), is opropanol (IPA) and dimethyl sulfoxide (DMSO). The conductivity of PEDOT: PSS films then is further improved by post-treatment of moderate acid, P-toluenesul fonic acid (PTSA). The performance of ECDs is valuated and compared at the different work voltage and the optimal voltage therefore is finally as certianed. The realized ECDs show the optimal color change in 3 s at 2.5 V with the chromatic aberration of 30.87. Meanwhile, the developed ECDs still works well after many times bending.

**Keywords:** Electrochromic · PEDOT:PSS · PET·flexible

## 1 Introduction

Electrochromic devices (ECDs) are light modulating devices inwhich the modulation of light is controlled by an electric potential [1]. The materials of electrochromic can undergo stable redox reaction applying a voltage. The color and transmittance of the electrochromic materials at oxidized and reduced states are different and this change is stably reversible. Generally, they are well known for many applications inthe areas of smart windows, sunglasses, displays, etc. [2]. The development of the ECDs relies on the chemical synthesis of the conjugated polymer materials. Since the discovery of the first conductive polymer polyacetylene in the late 1970s, various electroactive polymer materials have been synthesized. Polythiophene and its derivatives are a popular conductive polymers applied in the ECDs [3], in which Poly (3,4-ethylenedioxythiophene) polystyrene sulfonate (PEDOT:PSS) as one of the conductive polymers has been extensively explored in electronic applications, because of its

good solubility, processable ability and stability in air. Meanwhile, PEDOT:PSS also has different colors in oxidized and reduced state.

The conventional ECDs is achieved on the substrate coated previously by indium tin oxide (ITO) which is always as an electrodes in the ECDs due to the high conductivity and transparent properties of ITO. But it could be an issue to realize the ECDs on the flexible substrates as the mechanically brittle feature of ITO. The replacement for ITO has been concerned in the flexible ECDs and PEDOT:PSS is regarded as excellent candidates that have been discussed comprehensively [4]. The conductivity of pristine PEDOT:PSS, however, is quite as low as of less than $1 \, S \, cm^{-1}$. It is worth noting that the conductivity of PEDOT:PSS can be enhanced in terms of doping the alcohols solvent like ethylene glycol (EG), isopropanol (IPA), methanol (Me) [5] and acids post-treatments, such as strong acid $H_2SO_4$ [6]. Apart from the conductivity of PEDOT:PSS, the film forming for PEDOT:PSS on substrate also need to be noticeable. The screen printing is thought as the reasonable method to fabricate the ECDs, especially for the patterned ECDs device. But the viscosity of PEDOT:PSS still has distance to hit the requirement of film forming for screening printing. The adjustment of viscosity should be improved to reach the level for screen printing while maintaining the high conductivity. Liu N etc. [7] resorts topolyvinyl alcohol (PVA) to improve the viscosity and spin ability of PEDOT:PSS and the eligible film is successfully deposited on the substrate. In this paper, we realizes the ECDs using screen printing by considering critical factors such as the formula, conductivity enhancement, acid post-treatment of PEDOT:PSS film. The relevant properties of ECDs are accordingly analyzed and evaluated. The development of ECD shows the eligible ability and it suggests that it is quite reasonable to fabricate the ECDs based on the thickened viscosity of PEDOT:PSS solution and conductivity improvement for film forming using screen printing.

## 2    Experiment

### 2.1    Materials

PEDOT:PSS (Clevios PH1000, Heraeus, Germany, soild is 1.3wt%) is used to electrochromic and electrode materials. Me, IPA, acetone (Ac) and dimethyl sulfoxide (DMSO) are used to be as solvents, which are produced by DamaoChenical Reagent Factory. P-toluenesulfonic acid (PTSA, T823839, Shanghai Macklin Biochemical Co., Ltd) is used to post-treat for conductivity enhancement. Gel electrolyte in ECD sis composed of lithium chloride (LiCl, L812571, Shanghai Macklin Biochemical Co., Ltd), PVA (P119359, Shanghai Aladdin biochemical technology co., Ltd), and deionized water.

### 2.2    Preparation of the Film of PEDOT:PSS and Post-treatment

The screen printing was used to deposit the conductive polymer PEDOT:PSS on PET film. The pristine PEDOT:PSS suspension was diluted by Me with a ratio of 1:1 to lower the surface energy of the solution. And then the addition of gel substances, PVA was employed to improve the viscosity. It was added into PEDOT:PSS suspension with the ratio of 10 wt% to enhance the viscosity (Stirring at room temperature for 10 h to

dissolve PVA). Meanwhile, IPA and DMSO were used to improve the uniform film forming on the substrate with the ratio of 5 wt% respectively in the PEDOT:PSS solution. Then printed a film of PEDOT:PSS by screen printing was deposited on clean PET.

## 2.3 Preparation of ECDs

The lateral architecture is chosen to build the ECDs that do not need to laminate the top electrode as the required in the vertical structure. The parallel and adjacent electrodes are easy to form on the substrate at the same level as shown in Fig. 1.



**Fig. 1.** Two separate EC device structures

As PEDOT:PSS can be enquiped with high conductivity by doping withalcohol solventand post-treating with acids, it is eligible to be an electrode. Besides, it is also a well-known electrochromic material. Therefore, the lateral structure for ECDs can be simplified into the one as shown in Fig. 2. The device was fabricated in the following steps: First, PET was cleaned with Ac, IPA and Me ultrasonic cleaning for 15 min respectively, and dried in nitrogen atmosphere. Then, the prepared solution of PEDOT: PSS (PEDOT:PSS: Me: PVA: IPA: DMSO = 40 wt%: 40 wt%: 10 wt%: 5 wt%: 5 wt %) was printed on clean PET, dried for 10 min on a hot plate with 120°C. Films were then bathed in the solution of PTSA (0.9 mol/L PTSA solution in DMSO, it is called PTSA-DMSO) about 5 min, the extra PTSA then was washed with IPA. Finally, gel electrolyte was deposited top on PEDOT:PSS by drop-casting and dried for 24 h at room temperature. The gel electrolyte was composed with PVA, LiCl and DI by the ratio of, PVA: LiCl: DI = 10 wt%: 10 wt%: 80 wt% stirring with a magnetic stirrer for 30 min.



**Fig. 2.** The structure of ECDs

## 2.4 Characterization of Films and Devices

The surface of PEDOT:PSS films was observed using a 3D digital microscope (KH8700, HIROX, Japan). The four-probe tester (RTS-9, Guangzhou four probe technology co. LTD) was used to measure sheet resistance (SR) of samples, such as not mixed with DMSO (PEDOT:PSS: Me: PVA: IPA = 42.5 wt%: 42.5 wt%: 10 wt%: 5 wt%), blended with DMSO (PEDOT:PSS: Me: PVA: IPA: DMSO = 40 wt%: 40 wt%:

10 wt%: 5 wt%: 5 wt%) and post-treated with PTSA-DMSO. Portable color reflection spectrometer (x-rite 528, X-Rite, Inc.) was used to measure the color value ($L^*$, $a^*$, $b^*$) of ECDs, and calculated the chromatic aberration ($\Delta E^*$) of coloration and discoloration by formula (CIE 1976) is shown below:

$$\Delta E^* = (\Delta L^{*2} + \Delta a^{*2} + \Delta b^{*2})^{1/2} \tag{1}$$

The $\Delta L^* = L_1^* - L_2^*$, means contrast of luminance of coloration and discoloration of ECDs. The $\Delta a^* = a_1^* - a_2^*$ and $\Delta b^* = b_1^* - b_2^*$, mean the red-green color contrast and the yellow-blue color respectively between coloration and discoloration.

## 3    Result and Discuss

### 3.1    Films of PEDOT:PSS Based on PET

The edge of the film was observed with an ultra-deep field microscope (solution consists of PEDOT:PSS: Me: PVA: IPA: DMSO = 40 wt%: 40 wt%: 10 wt%: 5 wt%: 5 wt%), shown in Fig. 3. It can be seen a clear boundary, and there is not aggregation of solutes at the film edge. Therefore the solute distribution is relatively uniform and the evenness film is deposited successfully on PET.
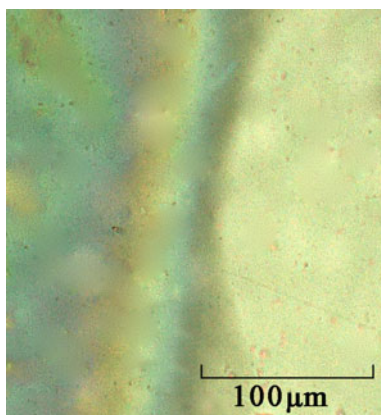


**Fig. 3.**  Edge of the film forming

### 3.2    SR of Films with Different Formulas and Post-treatment

PEDOT:PSS is used as the electrode for the design of ECDs. This requires that it should have an excellent in the high conductivity and low SR. The SR of sample films is shown in Fig. 4. As can be seen, that the film without DMSO shows the SR as high as $1.3 \times 10^5 \Omega/\square$. When doped with 5% DMSO, the SR ($875\Omega/\square$) is decreased obviously around three orders of magnitude. PTSA-DMSO poste-treated is used to further improve the conductivity of the film, which indicates the SR of sample is as low

as only 155 $\Omega/\square$. Therefore, the film is treated by PTSA-DMSO is expected to be qualified as an electrode for ECDs fabrication.
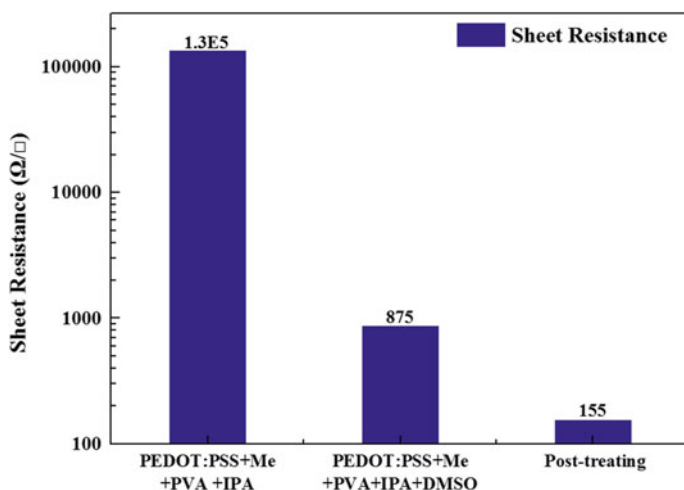


Fig. 4. SR of films with different formula

## 3.3 Properties of ECDs

The different voltages arranging from 0 V to 2.5 V with 0.5 V interval are applied on the fabricated ECDs as seen in Fig. 5. The ECD has no color change when the voltage is at 0.5 V (shown in Fig. 5(b)). When voltage increases at 1.0 V, the color change started to initiate (shown in Fig. 5(c)). The higher voltage applied, the color becomes more than before. However, when the voltage is higher than 2.5 V, the switch-color is no longer to continue becoming in blue. Therefore, the optimal voltage of color change is at 2.5 V. The calculated chromatic aberration and time of color change are measured at different voltages are shown in Fig. 6.
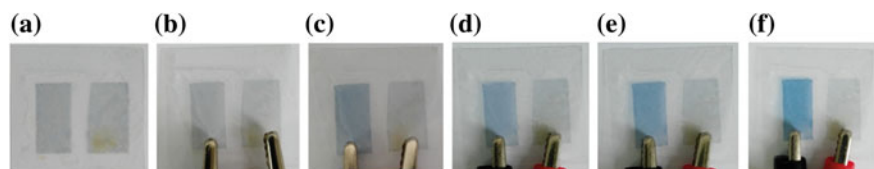


Fig. 5. Effects of ECDs at different voltages **a** 0 V. **b** 0.5 V. **c** 1.0 V. **d** 1.5 V. **e** 2.0 V. **f** 2.5 V

As shown in Fig. 6, $\Delta E^*$ of the device increases with increase of voltage. When the voltage of 2.5 V is on the ECDs, the $\Delta E^*$ is equal to 30.87. When the voltage above 2.5 V, the $\Delta E^*$ has a little change ($\Delta E^*$ is 29.66) and almost keeps a constant. Meanwhile, the time of color change is becoming shorter with increased voltage, and the minimum time around 3 s for color change is at 2.5 V work potential, which attributes to the reaction speed and is faster with the increase of voltage.
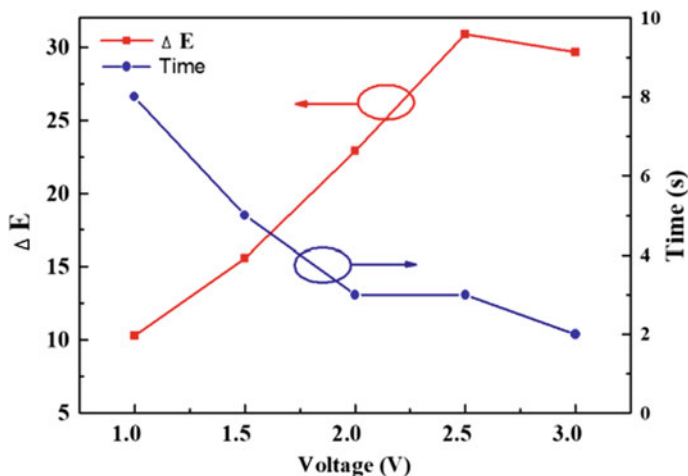
**Fig. 6.** $\triangle E^*$ and time of color change at different voltages

For testing the properties in the bending situation, the cyclic bended experiment reaching the 1000 times is carried on the ECDs, seen in Fig. 7. The ECDs keep the competent performance after bending to 100 times, the $\triangle E^*$ of the device nearly keeps the constant from 30.87 to 30.63. The bending cyclic after 600 and 1000 times, the $\triangle E^*$ of the device has somewhat decreased from 26.66 to 25.88, the changed $\triangle E^*$ trends to be leveled after 1000 times bending. Although the $\triangle E^*$ from 30.87 to 25.88 after as high as 1000 times bending, the extent of color change is quite acceptable that cannot cause the obvious visual observation.
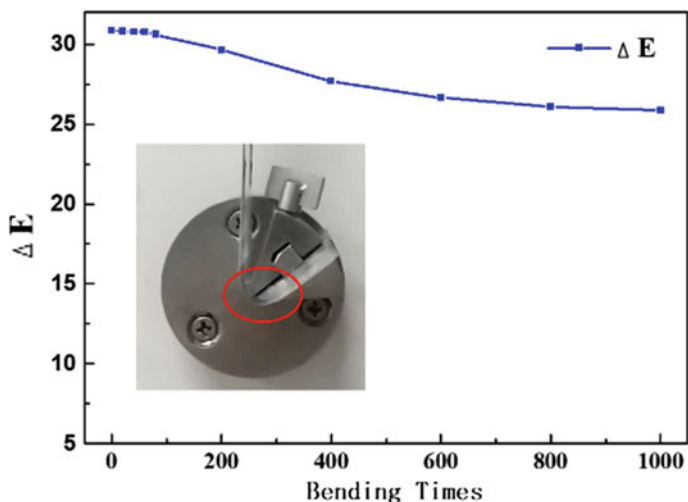


**Fig. 7.** Test the flexibility

# 4   Conclusions

In this paper, we have prepared the ECDs using screen printing based on the lateral configuration. The formula of PEDOT:PSS easy to be film forming is proposed to fabricate the ECDs, and the acid post-treatment of PTSA-DMSO is employed to enhance the conductivity reaching the electrode level. The ECDs prepared shows the property of switching color reaching 30.87 is at 2.5 voltages in 3 s and the keep the excellent performance in the cyclic bending measurements which enable these to be used in the flexible substrates and in the bending condition.

# References

1. Singh R, Tharion J et al (2017) ITO-free solution-processed flexible electrochromic devices based on PEDOT:PSS as transparent conducting electrode. ACS Appl Mater & Interfaces 9 (23):19427–19435
2. Chandrasekhar P, Zay BJ, Cai C et al (2015) Matched-dual-polymer electrochromic lenses, using new cathodically coloring conducting polymers, with exceptional performance and incorporated into automated sunglasses. J Appl Polym Sci 131(22): 547–557
3. Mortimer RJ (2011) Electrochromic materials. Annu Rev Mater Res 41: 241–268
4. Zhou L, Yu M, Chen X et al (2018) Screen-printed poly(3,4-Ethylenedioxythiophene): poly (Styrenesulfonate) grids as ITO-free anodes for flexible organic light-emitting diodes. Adv Funct Mater 28(11):1705955
5. Sun K, Zhang S, Li P et al (2015) Review on application of PEDOTs and PEDOT:PSS in energy conversion and storage devices. J Mater Sci: Mater Electron 26(7):4438–4462
6. Fan X, Xu B, Liu S et al (2016) Transfer-printed PEDOT:PSS electrodes using mild acids for high conductivity and improved stability with application to flexible organic solar cells. ACS Appl Mater & Interfaces 8(22):14029–14036
7. Liu N, Fang G, Wan J et al (2011) Electrospun PEDOT:PSS-PVA nanofiber based ultrahigh-strain sensors with controllable electrical conductivity. J Mater Chem 21(47):18962–18966

# Fabrication of Flexible Temperature Sensor Based on Printed Electronics

Ruping Liu[1], Xiaoyu Wang[1], Yue Shi[1], Zhicheng Sun[1], and Zhou Li[2(✉)]

[1] Beijing Institute of Graphic Communication, Institute of Printing and Packaging Engineering, Beijing Engineering Research Center of Printed Electronics, Beijing, China
[2] Chinese Academy of Sciences, Beijing Institute of Nanoenergy and Nanosystems, Beijing, China
zli@binn.cas.cn

**Abstract.** In this research, we developed a mass production method for the preparation of thermosensitive ink composite, followed by deposition of the composite on the flexible substrate via spray coating technology. Firstly, Ag micropattern was designed and deposited on flexible polyimide substrate by high-precision screen printing. The Ag interdigital electrodes with controlled spacing are realized by optimization of the sintering temperature, and the thermosensitive ink composed of polydimethylsiloxane (PDMS) mixed with graphite powder and graphene was coated on the surface of the electrodes. Effect of sintering temperature on the microstructure and electrical conductivity of Ag electrode is evaluated, and the sensitivity of the flexible temperature sensor in the large dynamic range of 15–40 °C is investigated. Finally, the sensing characteristics, response time, temperature hysteresis and effect of the spontaneous heating are tested, and the experimental results demonstrated a high-performance sensor with a higher sensitivity, a smaller hysteresis, a better linearity and a faster response.

**Keywords:** Temperature sensor · Flexible · Printed electronics · Ag interdigital electrodes · Hysteresis

## 1 Introduction

Fabrication of interdigital silver (Ag) electrodes by screen printing technology is applied for determining the electrical resistance change of composite subjected to ambient temperature variation [1, 2]. Development of the flexible temperature sensor is highly dependent on the sensing mechanism and large-area printing technique. Our preliminary study showed that a polymer dielectric filled with conductive particles could be a promising candidate to provide both flexibility and temperature sensitivity of the sensor. As the temperature increases, the resistance of the sensor dramatically increases. In principle, the interdigital Ag electrodes with appropriate aspect ratio and inter spacing will make the resistance of the composite sensitive to the temperature variation. In this study, we investigated the resistance-temperature relationship of the

thermosensitive ink. Also, the heating experiment is performed to verify the resistance response of the thermosensitive ink. For fabrication of positive temperature coefficient sensor based on PDMS/graphite powder/graphene composite, a mass production process is proposed, employing screen printing to fabricate Ag interdigital electrodes. Graphite powder and graphene are commonly applied as conducting fillers due to their low cost, high receivability and facile fabrication [3, 4]. Surface of Ag electrode is covered by the thermosensitive ink using an automatic dispensing system. We demonstrated that the sensor with thermosensitive ink displays the temperature dependent resistance, which allows us to realize the temperature sensor in the range of 15–40 °C.

## 2 Experimental

### 2.1 Materials

Sylgard® 184 silicone elastomer (PDMS) and curing agent are supplied by Dow Corning. Curing agent and PDMS with a weight ratio of 1:10 are mixed. Graphite powder, graphene, silver conductive paste and cyclohexane are purchased from Sigma-Aldrich.

### 2.2 Instruments

The automatic dispensing system (TS-300F, Shenzhen Tengsheng Industrial Equipment Co., Ltd) is employed. Morphology of the silver electrode is characterized by scanning electron microscope (SEM), and the temperature-control platform is utilized to keep the temperature at a desired set value.

### 2.3 Preparing of the Thermosensitive Ink

The thermosensitive ink was prepared in advance, which is essential for fabricating temperature sensor. Conductive fillers are graphite powder mixed with grapheme at a certain proportion. PDMS was added into 100 g cyclohexane and stirred for 30 min at stirring rate of 300 rpm. The thermosensitive ink was fabricated by interfusing 40 g conductive fillers into above mixture under ultrasonic stirring for 30 min. The mixture is then solidified by adding PDMS curing agent, followed by ultrasonic stirring for 30 min at room temperature to evaporate the volatile cyclohexane.

### 2.4 Fabrication of Flexible Temperature Sensor

The flexible temperature sensor consists of the printed interdigital Ag electrodes, the printed wiring, the pin plug of the electrode, the thermosensitive ink and the polyimide insulation layers. The schematic diagram of the proposed fabrication process is shown in Fig. 1. The interdigital electrodes were fabricated by screen-printing process upon polyimide insulation layers, and the thermosensitive ink is applied on these electrodes by spray coating process. Thermosensitive ink was dropped into a dispensing machine and be selectively applied on the designated interdigital Ag electrodes. Through

controlling the three-axis movement platform of the dispensing system, the thermosensitive ink is well aligned with the pattern of the sensing electrodes, forming the thermosensitive layers of sensor. Hence the diameter of the thermosensitive ink composite on each sensing electrode is 2.0 cm. The resistance of the sensing material has a fast response with the change of ambient temperature, therefore, the signals are detected by the pin plug of the electrode.
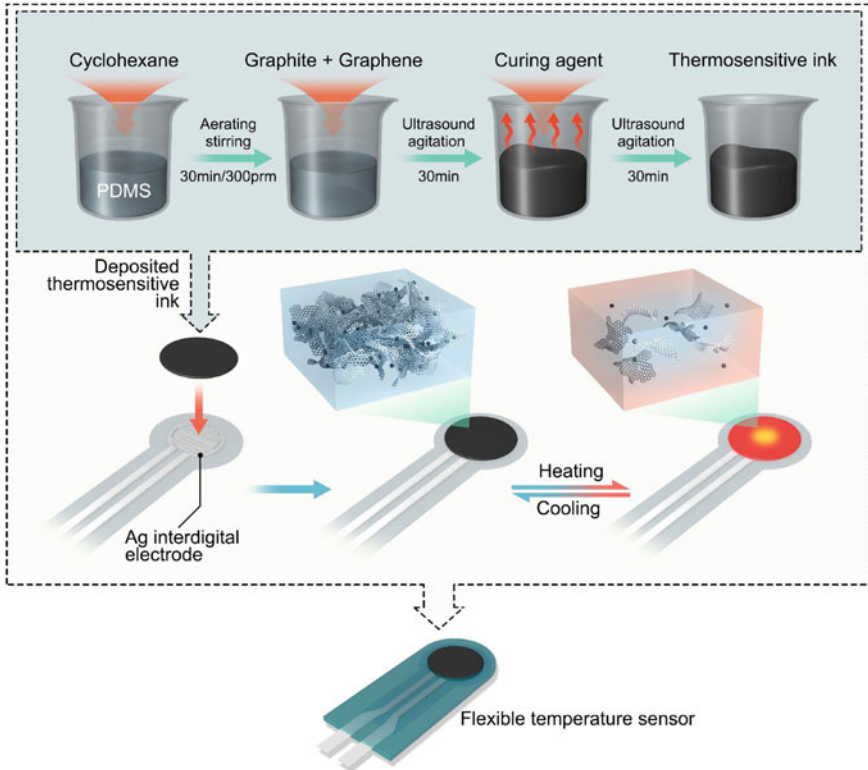


**Fig. 1.** Schematic illustration of fabrication process of flexible temperature sensor

## 3    Results and Discussion

### 3.1    Effect of Sintering Temperature on Microstructure and Electrical Conductivity of Ag Electrodesz

The effect of sintering temperature on resistivity of Ag electrodes was tested, and the results are shown in Fig. 2. The different sintering temperatures between 130 and 350 °C are applied. A decrease in the electrical resistivity of the Ag electrodes with sintering temperature increasing between 130 and 250 °C is demonstrated in Fig. 2, due to the formation of conductive network. As the treatment temperature increased further, the electrical resistivity of Ag film reached a minimum value at 250 °C ($4.7 \times 10^{-3}$ m$\Omega\cdot$cm)

and gradually increased when the sintering temperature above 250 °C due to that Ag coalescence aggregates into large particles and breaks up of the conductive paths. With the grain size exceeded the thickness of the Ag film, the Ag particles transformed to submicron-sized islands and the Ag film thereby possesses a lower electrical conductivity. The microstructure of Ag electrodes by sintering was further investigated. The SEM image (Fig. 3) indicates that the morphologies of Ag coalescence with irregular shape by sintering at 250 and 350 °C.
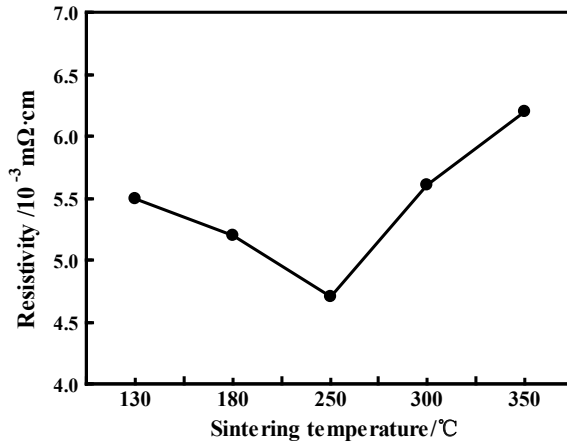


**Fig. 2.** Effect of sintering temperature on electrical resistivity of Ag films
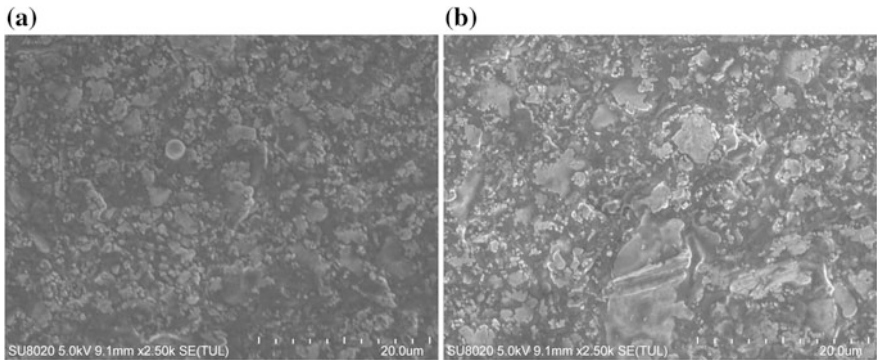


**Fig. 3.** SEM images of Ag electrodes sintered at **a** 250 °C and **b** 350 °C

## 3.2 Sensing Characteristics of Flexible Temperature Sensor

As shown in Fig. 4, a typical positive temperature-resistance coefficient of flexible temperature sensor is observed. The resistance is found to increase as the ambient environmental temperature increased in the temperature range of 15–40 °C. The expansion of thermosensitive coating caused by increasing the temperature implied that

the resistance of thermosensitive coating increases gradually with the increase of the distance between carbon black and graphene. By comparison, the resistance of the flexible temperature sensor increased from 134 to 180 Ω under temperature ranging from 15 to 40 °C.
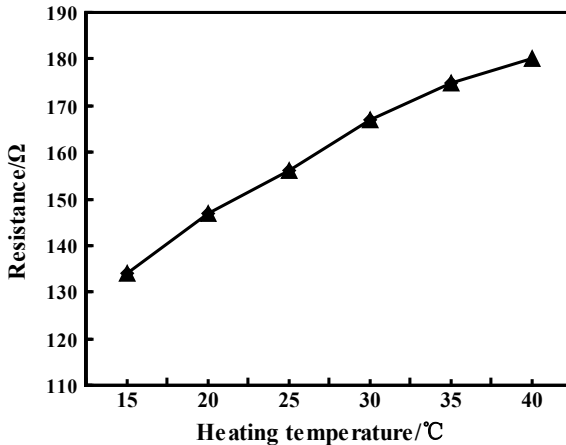


**Fig. 4.** Temperature sensitivity curve of flexible temperature sensor

## 3.3  Response Time of the Temperature Sensor

The response time is an important parameter of temperature sensor. Owing to its microstructure and thermoelectric sensing mechanism, the flexible temperature sensor displayed the response speed to an applied temperature signal. The flexible temperature sensor is placed on the heating plate at 40 °C, which makes the temperature of the sensor increased rapidly to 40 °C, then quickly cooled to room temperature, and its resistance variation is tested. The characterization results are shown in Fig. 5. The response time of the flexible temperature sensor is about 40 s and the recovery time is close to ∼20 s. The long response time is the bottleneck of the flexible device. It is necessary to further improve the thickness of the temperature sensitive layer, and to optimize the proportion of thermosensitive ink and forming method of thermosensitive film.

## 3.4  Hysteresis of Temperature Sensor Based on Printed Electronics

The initial temperature of the heating plate is 15 °C and the temperature range is 15–40 °C (Fig. 6). The temperature increases at a rate of 1.25 °C min$^{-1}$. In the cooling state, the temperature decreases at a rate of 2.5 °C min$^{-1}$. As shown in Fig. 6, the variation of resistance during the temperature cycle is irreversible. The reason is that the conductive network structure changes during the heating process, and the conductive network is not completely restored during the cooling process. However, during the whole heating and cooling processes, the resistance of the flexible temperature sensor changes with a positive temperature coefficient.
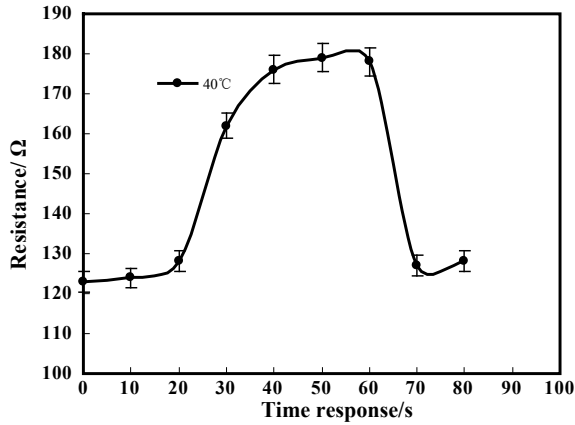
**Fig. 5.** Time response of the temperature sensor
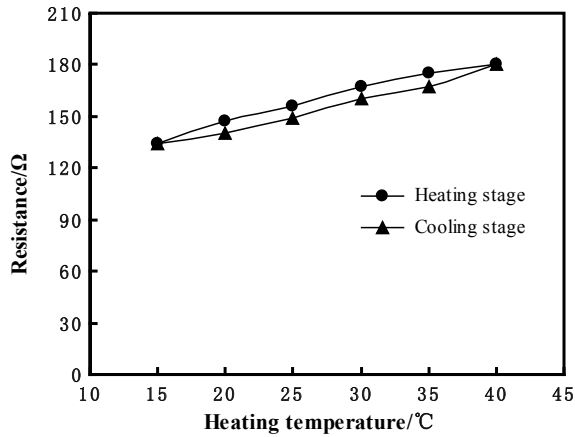


**Fig. 6.** Temperature hysteresis characteristic of the fabricated temperature sensor

## 3.5  Effect of the Spontaneous Heating of Temperature Sensor on Resistance

The voltage-ampere characteristics of the temperature sensor are evaluated at room temperature in air with a keithley parameter analyzer. Because the sensor will spontaneously be heated when employed in combination with the test circuit, and spontaneous heating causes error in temperature measurement. The experiment results about the voltage-ampere characteristic when the current is switched off in 5 min after the measurement, are demonstrated in Fig. 7. There is nearly no difference between the start of test and 5 min later for voltages at the same current. The voltage-ampere curve fluctuates slightly before and after electrification. When spontaneous heating occurs, it changes a little. It can be observed that the voltage-ampere characteristic curve of the flexible temperature sensor is stable.
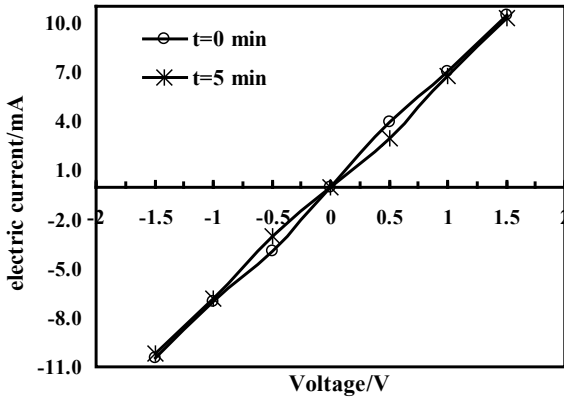
**Fig. 7.** Effect of the spontaneous heating of temperature sensor on resistance

## 4   Conclusions

We demonstrated a flexible temperature sensor based on the thermosensitive ink of PDMS/graphite powder/graphene. Within the temperature range of 15–40 °C, the resistance of the proposed sensor shows a linear temperature dependence. During the whole heating and cooling processes, the resistance of the flexible temperature sensor changes with a positive temperature coefficient. The volt-ampere characteristic curve shows that the temperature sensor is stable.

## References

1. Stempien Z, Rybicki E, Rybicki T, Lesnikowski J (2016) Inkjet-printing deposition of silver electro-conductive layers on textile substrates at low sintering temperature by using an aqueous silver ions-containing ink for textronic applications. Sens Actuators B: Chem 224 (3):714–725
2. Castro HF, Correia V, Pereira N, Costab P, Oliveira J, Lanceros-Méndez S (2018) Printed Wheatstone bridge with embedded polymer based piezoresistive sensors for strain sensing applications. Add Manuf 20:119–125
3. Alam A, Meng Q, Shi G, Arabi S, Ma J, Zhao N (2016) Electrically conductive, mechanically robust, pH-sensitive graphene/polymer composite hydrogels. Compos Sci Technol 127:119–126
4. Li X, Shao L, Song N, Shi L, Ding P (2016) Enhanced thermal-conductive and anti-dripping properties of polyamide composites by 3D graphene structures at low filler content. Compos Part A: Appl Sci Manuf 88:305–314

# Fabrication of Micro-Structure Electrode for Supercapacitor by Inkjet Printing

Chenghu Yun, Jiazhen Sun, Bo Cui, and Fuqiang Chu[✉]

Key Laboratory of Green Printing & Packaging Materials and Technology
in Universities of Shandong, School of Light Industry and Engineering,
Qilu University of Technology, Jinan, Shandong, China
fqchu@l26.com

**Abstract.** Supercapacitors are widely used in wearable electronic devices because of high power density, fast charge-discharge speed, and extremely long cycle life. However, low energy density is one of its shortcomings. In order to improve the energy density, in this paper, a flexible substrate having the micro-structure surface was fabricated by inkjet printing, which increased the specific surface of the electrode. Then the micro-structure surface was modified by plasma and promoted the deposition of graphene oxide(GO)/silver nitrate $(AgNO_3)$ solution on the micro-structure surface. For the micro-structure electrode prepared after vapor phase reduction of hydrated hydrazine, the area specific capacitance could reach 120 mF/cm$^2$ at the scanning rate of 0.05 v/s, which increased the specific capacitance.

**Keywords:** Inkjet printing · Micro-structure · Supercapacitor

## 1 Introduction

Advanced wearable electronic devices play a crucial role in artificial intelligence [1], lighting display [2], biological monitoring [3], etc., with the characteristic of integration, flexibility, wearable and so on. In order to support the use of the above devices, it is important to provide them with corresponding power supplies. Among various energy storage devices, supercapacitors have been favored due to their high power density, fast charge-discharge speed, and extremely long cycle life, becoming the most promising energy storage device [4–6]. At present, the method for preparing supercapacitors includes screen-printing [7], roll-to-roll processing [8] and so on. Although supercapacitors with good capacitance properties can be obtained in the above method, there are still some difficulties in preparing patterned supercapacitors. The inkjet printing method was more and more widely used due to its convenience, customization, and high resolution [9, 10].

Graphene (GP) material is an emerging material with excellent electrochemical performance and has been widely used in energy storage [11]. As an electrode material of a supercapacitor, it has a lot of advantages in capacitance storage due to its high specific surface area. Hyun et al. [12] prepared graphene-based micro-supercapacitor by capillary forces of micro-fluids. Diao et al. [13] prepared an all-solid-state

supercapacitor by inkjet printing the graphene/polyaniline composite material with a high specific capacitance.

Herein, the micro-structure was prepared by inkjet printing. After the micro-structure surface was modified by plasma, the GO/AgNO$_3$ solution was successfully deposited on the micro-structure surface. Then reduced by hydrazine hydrate in gas phase, the GP/Ag micro-structure electrode was fabricated. The micro-structure of inkjet printing was used to increase the specific surface area of the electrode and increase its specific capacitance. In addition, the modification of the micro-structure surface could effectively increase the adhesion of the active material to the micro-structure.

## 2    Experimental Section

### 2.1    Materials

Polydimethylsiloxane (PDMS, precursor and curing agent): (Sylgard 184, Dow Corning, USA), Polyethylene glycol terephthalate (PET): (Beijing Daxiang Plastic Co., Ltd.), Ethanol: (Beijing Chemical Co., Ltd.), Polyacrylic acid (PAA, Sigma-Aldrich, USA), Hydrated hydrazine: (Tianjin Fuyu Fine Chemical Co., Ltd.).

### 2.2    Equipment

Dimatix Materials Printer (2831): For manufacturing the micro-structure,
    PlasmaFlecto 30: For modifying the micro-structure surface.

### 2.3    Experimental Methods

#### 2.3.1    Preparation of GO/AgNO$_3$ Solution

The GO solution was prepared by modified Hummers method, then mixing the GO solution and AgNO$_3$ (mass ratio 1:3), magnetic stirring for 15 min, sonicating for 30 min, and leaving for use.

#### 2.3.2    Fabricated Micro-Structure Surface by Inkjet Printing

A layer of PDMS was spin coated (700 rpm for 30 s, then 2000 rpm for 10 s) on PET to a thickness about 60 μm and pre-cured in an oven at 70 °C. As the sacrificial ink, the polyacrylic acid solution having a mass fraction of 10% (volume ratio of deionized water to absolute ethanol of 40:60) was used. The inkjet printing pitch was 0.2 mm. After the printing was finished, the printed substrate was cured in an oven at 70 °C for 1 h. Then the micro-structure surface was washed several times with deionized water to remove the residual polyacrylic acid solvent, obtained the substrate with micro-structure surface.

#### 2.3.3    Deposition GO/AgNO$_3$ on Micro-Structure Surface

The micro-structure surface was modified by plasma for 30 s, and the GO/AgNO$_3$ solution was deposited on the micro-structure surface. After drying at room

temperature, it was placed in an oven at 90 °C, and the GO/AgNO$_3$ solution was reduced in the hydrazine hydrate vapor atmosphere to obtain a micro-structure electrode having GP/Ag.

## 2.4   Characterization

The surface morphology of the micro-structure was characterized using a polarizing microscope (NOVEL NP-800TRF); the modified micro-structure surface was characterized using a contact angle meter (KRUSS DSA100S); the electrochemical properties were tested using an electrochemical workstation (Metrohm PGSTAT 302 N).

# 3   Results and Analysis

The spin-coated substrate was pre-cured so that the surface of the substrate exhibited a viscoelastic state. As shown in Fig. 1(a) obtained by polarizing microscope, when the pre-cure time was 10 min, the sacrificial ink sunk on the surface after inkjet printing due to the low degree of pre-cure, and the desired micro-structure was not obtained after the complete curing. Extending the time to 15 min, the inkjet printed sacrificial ink could imprint the three-dimensional micro-groove on the surface (Fig. 1(b)). When the time was extended to 20 min, since the surface was completely cured, the sacrificial ink could not imprint the micro-groove on the surface, and no micro-structure was observed.
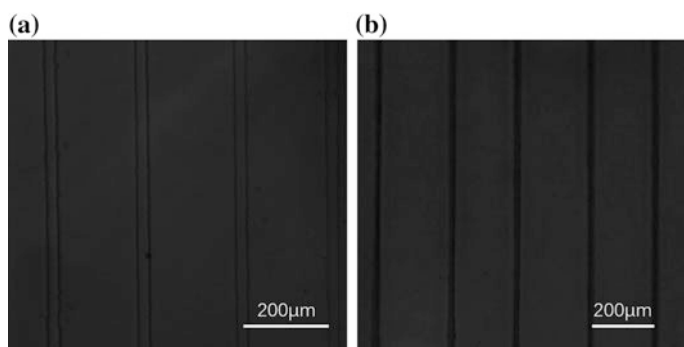


**Fig. 1.** The surface morphology of the micro-structure under the polarizing microscope. **a** micro-structure surface with pre-cure time of 10 min. **b** micro-structure surface with pre-cure time of 15 min

Since PDMS was a low surface energy object, in order to make the GO/AgNO$_3$ solution better spread on the micro-structure surface, the surface of the micro-structure was modified by plasma. As shown in Fig. 2(a), the surface of the micro-structure without modified exhibited a hydrophobic state to the aqueous solution, and the contact angle reached 120°, and the contact angle of the micro-structure surface after modified

was reduced to 14.6° (Fig. 2(b)), which was favorable for the GO/AgNO$_3$ solution deposited on the surface of the micro-structure to form a conductive layer that adhered well to the micro-structure surface.
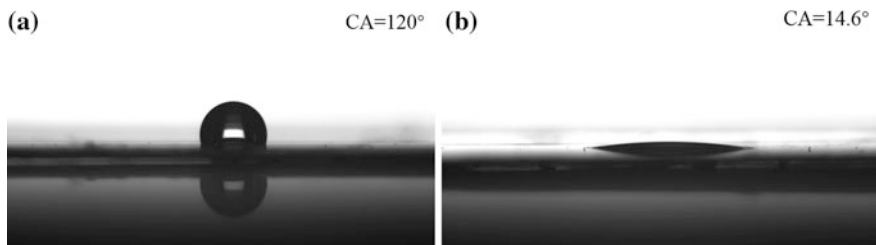


**Fig. 2.** Contact angle measurement. **a** contact angle of the micro-structure surface without modified with aqueous solution. **b** contact angle of micro-structure surface after modified with aqueous solution

Electrochemical performance tests were performed on the electrode fabricated by the paper's strategy. Firstly, cyclic voltammetry (CV) tests were performed on micro-structure electrode and non-micro-structure electrode fabricated under the same conditions. As shown in Fig. 3a, the electrode having the micro-structure exhibited good symmetry, which was significantly higher than that of the electrode having no micro-structure. That was due to the micro-structure on the surface increased the specific surface area of the electrode, allowing more functional material to deposit on the surface. The CV curves of the micro-structure electrode were tested at different scan rates and exhibited good electrochemical performance (Fig. 3b). The charge-discharge curve of Fig. 3c showed the micro-structure electrode had good charge and discharge cycle performance. And the area specific capacitance reached 120 mF/cm$^2$ at a scan rate of 0.05 v/s.

## 4   Conclusions

In order to increase the energy density of the supercapacitor, the micro-structure surface was fabricated by inkjet printing, and the micro-structure electrode greatly increased its specific surface area. The modified of the micro-structure surface promoted the deposition of GO/AgNO$_3$ solution on the micro-structure surface. For micro-structure electrode, the area specific capacitance could reach 120 mF/cm$^2$ at a scan rate of 0.05 v/s. Micro-structure electrode still exhibited good electrochemical performance at different scan rates. It was shown by the charge-discharge curve that it had good charge and discharge cycle performance.
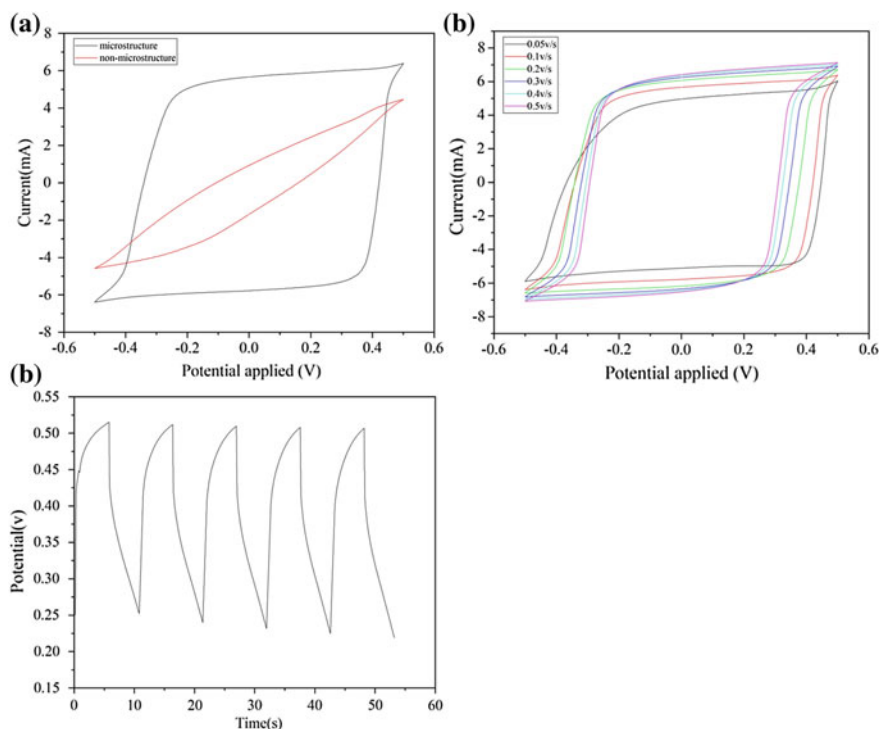
**Fig. 3.** Electrochemical performance tests. **a** CV curves of micro-structure and non-micro-structure electrode (scan rate of 0.1 v/s). **b** CV curves of micro-structure electrode at different scan rates (0.05 v/s, 0.1 v/s, 0.2 v/s, 0.3 v/s, 0.4 v/s, 0.5 v/s). **c** charge-discharge test of micro-structure electrode

# References

1. Gao M, Li L, Song Y (2017) Inkjet printing wearable electronic devices. J Mater Chem C 5 (12):2971–2993
2. Zhan Z, An J, Wei Y et al (2017) Inkjet-printed optoelectronics. Nanoscale 9(3):965–993
3. Kang DH, Han WB, Choi N et al (2018) Tightly sealed 3D lipid structure monolithically generated on transparent SU-8 microwell arrays for biosensor applications. ACS Appl Mater Interfaces 10(47):40401–40410
4. Sharma P, Bhatti TS (2010) A review on electrochemical double-layer capacitors. Energy Convers Manag 51(12):2901–2912
5. Yu G, Xie X, Pan L et al (2013) Hybrid nanostructured materials for high-performance electrochemical capacitors. Nano Energy 2(2):213–234
6. Wang G, Zhang L, Zhang J (2012) A review of electrode materials for electrochemical supercapacitors. Chem Soc Rev 41(2):797–828
7. Zhang H, Qiao Y, Lu Z (2016) Fully printed ultraflexible supercapacitor supported by a single-textile substrate. ACS Appl Mater Interfaces 8(47):32317–32323
8. Chen P, Chen H, Qiu J et al (2010) Inkjet printing of single-walled carbon nanotube/$RuO_2$ nanowire supercapacitors on cloth fabrics and flexible substrates. Nano Res 3(8):594–603

9. Sundriyal P, Bhattacharya S (2017) Inkjet-printed electrodes on A4 paper substrates for low-cost, disposable, and flexible asymmetric supercapacitors. ACS Appl Mater Interfaces 9 (44):38507–38521

10. Choi KH, Yoo JT, Lee CK et al (2016) All-inkjet-printed, solid-state flexible supercapacitors on paper. Energy Environ Sci 9(9):2812–2821

11. Stoller MD, Park S, Zhu Y et al (2008) Graphene-based ultracapacitors. Nano Lett 8 (10):3498–3502

12. Hyun WJ, Secor EB, Kim CH et al (2017) Scalable, self-aligned printing of flexible graphene micro-supercapacitors. Adv Energy Mater 7(17):1700285–1700294

13. Diao J, Yuan J, Ding A et al (2018) Flexible supercapacitor based on inkjet-printed graphene@polyaniline nanocomposites with ultrahigh capacitance. Macromol Mater Eng 303(6):1800092–1800098

# Study and Simulation on Forming Process
# of Ink Drops

Qiumin Wu$^{(\boxtimes)}$, Wenlong Guo, Lei Xu, and Fang Yuan

Faculty of Printing, Packing Engineering and Digital Medial Technology,
Xi'an University of Technology, Shaanxi, China

**Abstract.** Nowadays, piezoelectric inkjet printing technology has been widely used because of its unique advantages. It is of great significance to study the formation mechanism of ink droplets and the influence of various parameters on the ink-jet process. Therefore, a model of piezoelectric ink-jet system was established to simulate the formation process of ink droplets. Then numerical experiments were carried out to study the effects of frequency, driving speed, and ink properties (surface tension) on the formation of ink droplets. The results show that they have a great influence on the shape of ink droplets and the length of liquid column. They can also change the number of satellite droplets. The simulation results can provide preliminary data for the preparation, implementation, and application of the actual inkjet printing system.

**Keywords:** Piezoelectric inkjet printing · Droplet formation · Simulation

## 1 Introduction

Inkjet printing technology, as a non-contact, highly flexible, energy-saving, and environmental protection material distribution mode, greatly meets the requirements of miniaturization and automation of modern industrial production. Compared with other ink-jet printing technologies, piezoelectric ink-jet printing system of drop-on-demand (DOD) has gained more and more applications because of its advantages of stronger ink control ability and longer life of the nozzle, so the study of its droplet formation mechanism is of great significance [1].

## 2 Establishment of Droplet Formation Model

The behavior of droplets in piezoelectric inkjet mainly includes the formation and fracture of liquid column, the formation of satellite droplets, and the flight of main droplets and satellite droplets in the vapor phase region. Therefore, the geometric model should include not only the nozzle, but also the vapor phase region of droplet flight. In order to shorten the simulation time, it is necessary to establish the model including nozzle section and vapor phase region [2]. The geometric sketch of the cross section of the nozzle is established in Fig. 1. With the prtinthead of Epson 1930 printer, we set the specific parameters of the simulated area as shown in Table 1.

**Fig. 1.**  Geometric model diagram

**Table 1.**  Geometric parameters of simulation region

| Region | Dimensions (μm) | |
|---|---|---|
| | Radius | Length |
| Ink chamber | 150 | 500 |
| Nozzle | 90 | 500 |
| Vapor phase region | 300 | 2800 |

## 3    Results and Discussion

### 3.1    Droplet Formation Process

After completing the geometric model, the relevant physical parameters and boundary conditions need to be set. According to the parameters of Epson 1390 printer, the injection frequency of ink droplets is 2000 Hz. According to the literature, the pressure driving speed (i.e. amplitude) was preliminarily set to 3.5 m/s. The actual mass of micro-droplets is about 60 ng, so the effect of gravity on micro-droplets can be neglected. According to the ink of inkjet printer, the surface tension is 76.38 mN/m and the viscosity is $2.105 \times 10^{-3}$ N s m$^{-2}$.

As shown in Fig. 2, when the pressure was applied to the inkjet inlet, the ink was extruded from the inkjet head. During the continuous stage of pressure, the inkjet ink was in the shape of a liquid column. When the inlet pressure began to decrease, the diameter of the liquid column began to decrease. Until the pressure was zero, no ink was extruded. When the pressure was negative, the liquid column began to break under the action of gravity and the negative pressure of the ink chamber, forming a slender liquid column. When the liquid column was separated from the ink jet head, under the action of surface tension, the liquid column gradually became spherical, forming droplets. The air around the droplet exerts traction on the movement of the droplet. When the droplets became larger, the deceleration effect caused by air would be smaller. Therefore, if satellite droplets and main droplets were completely separated, they would not merge again. If the satellite droplet was close enough to the main droplet, the low pressure in the tail region of the main droplet would attract the satellite droplets and merge. This paper will discuss the influence of surface tension, pressure driving speed, and frequency [3] on ink droplet injection.
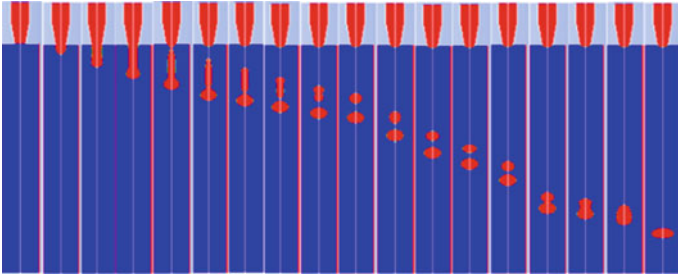
**Fig. 2.** Droplet formation process

## 3.2    Surface Tension Analysis

The surface tension of the ink determines the shape of the droplet when the ink is ejected from the nozzle. When the droplet travels in the vapor phase region, the shape of the droplet is determined by the surface free energy and the motion inertia of the droplet [4]. The surface tension of the ink of the inkjet printer is about 76.8 mN/m, and that of the general water-based ink is about 30–60 mN/m. In order to study the effect of surface tension on droplet formation under given pressure, the liquid with surface tension coefficients of 30, 40, 50, 60, and 70 mN/m was simulated.

As can be seen from Fig. 3, the longer the liquid column formed by the liquid with lower surface tension, the later the fracture time is. This was because the larger the surface tension was, the smaller the shrinkage radius of the liquid column was, which is conducive to the rapid fracture of the liquid column. In the multiple fragmentation stage of the tail, the smaller the surface tension, the more smaller satellite droplets formed by the tail fragmentation of droplets. It could be considered that the printing performance of 30 and 40 mN/m surface tension was poor. When the surface tension was 50 and 60 mN/m, although satellite droplets existed, the shape of droplets was relatively small. The satellite droplets didn't exist when the surface tension was 70 mN/m.



(a) 16ms                    (b) 20 ms
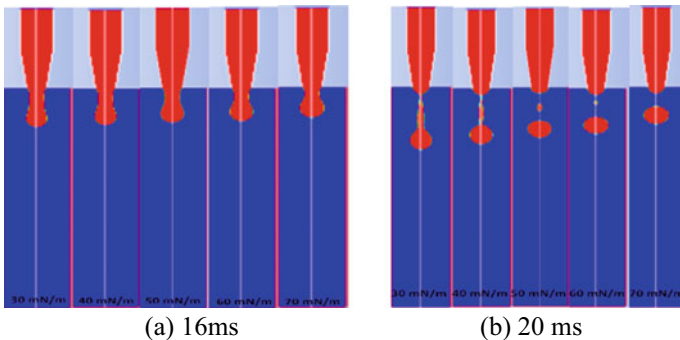
**Fig. 3.** Comparison of droplet formations of liquids with different surface tension

### 3.3    Frequency Analysis

The operating frequency is defined as the number of repetitive voltage pulse cycles in one second. The effect of operating frequency on droplet injection was discussed. The simulation results of droplets at different frequencies ranging from 3000 to 9000 Hz (spaced at 1000 Hz) were shown in Fig. 4. According to the droplet ejection pattern in Fig. 4, the droplets ejected at lower frequencies were less, and the time of ejecting a certain amount of droplets would be prolonged, thus the ejection efficiency would be reduced. More satellite ink droplets would be produced at higher frequency.



(a) 14 ms                      (b) 26 ms
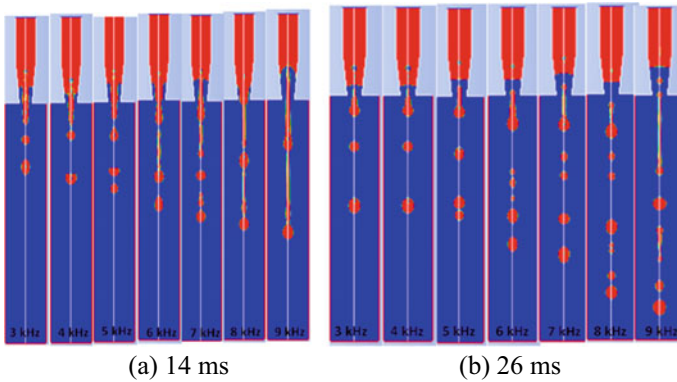
**Fig. 4.**  Comparison of droplet formations of liquids with different frequency

### 3.4    Entrance Drive Speed Analysis

The magnitude of the voltage determines the driving speed of the entrance [5]. The spray speed of most nozzles in the market ranges from 4 to 6 m/s. Converted to ink inlet speed, the spray speed is from 2 to 4.5 m/s. In order to study the influence of driving speed on droplet spraying process, 2, 2.5, 3, 3.5, 4 and 4.5 m/s were selected to simulate under the condition that the ink performance parameters were unchanged. Figure 5 showed that when the speed increased, the shape of the ink droplets did not change much, but the spray column became longer obviously. When the boundary moved at 2 m/s, no effective droplets were formed. This is because the ink droplets driven by piezoelectric crystals flowed out of the boundary outlet with the action of surface tension, but if there was not enough driving force, the droplets would return to the inkjet chamber. Therefore, it could be judged that when the driving speed of the ink-jet piezoelectric crystal was small enough, the ink droplets couldn't be formed. It could also be seen from Fig. 5 that with the increase of the inlet velocity, the jet liquid column became longer obviously, and the formed ink droplets were relatively large. Therefore, it can be considered that the boundary moving velocity is one of the factors affecting the size of the droplets. It could be concluded that the faster the inlet drive speed is, the larger the volume of the droplet so that the faster the droplet flight speed is.

(a) 12 ms        (b) 26 ms
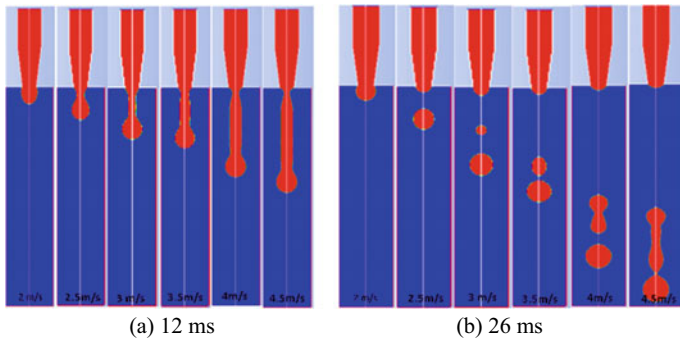
**Fig. 5.** Comparison of droplet formations of liquids with different inlet driving velocities

## 4 Conclusions

In order to study the effect of physical parameters and inlet driving speed of ink on ink-jet morphology, a model of droplet formation process was established, and the effects of surface tension of ink, frequency, and inlet driving speed on droplet formation characteristics were simulated numerically. The simulation results can provide initial data for the preparation of ink and the realization of actual ink-jet printing system and its application. The reasonable selection of process parameters lays a theoretical foundation.

## References

1. Ning B, Zhang R, Liu ZJ, Cheng GY (2018) Research status and development strategies of inkjet printing technology. Packaging Engineering 39(17):236–242
2. Wu H, Wang W, Lin H (2004) Development of a three-dimensional simulation system for micro-inkjet and its experimental verification. Mater Sci Eng 373(1):268–278
3. Zhu XJ (2015) Design of ink supply structure and control for ceramic inkjet printer. South China University of Technology
4. Wang YG, Zhang XL (2009) Freeform fabrication with micro-droplet jetting. Huazhong University of Science & Technology Press
5. Cheng M, Hua J, Lou J (2010) Simulation of bubble-bubble interaction using a lattice Boltzmann method. Comput Fluids 39(2):260–270

# Inkjet Printing of Water-Soluble Quantum Dots

Ying Pan, Wenguan Zhang, Shaohai Zhang, Zhaoxin Liu, Lulu Xue, Yu Gao, Jing Wang, Yinjie Chen[✉], and Luhai Li

Beijing Institute of Graphic Communication, Beijing, China
chenyinjie@bigc.edu.cn

**Abstract.** Quantum dots (QDs) have been widely applied in the fields of display, lighting and bioimaging due to their excellent optical properties, such as adjustable luminous color, high fluorescence efficiency and good color purity. Recently, inkjet printing of light emitting QDs has driven important advances in anti-counterfeiting technology. Here, we prepared a water-dispersible QDs inks and obtained a fluorescent pattern with high printing accuracy via inkjet printing. The coffee ring effect was avoided effectively by introducing a high boiling point ethylene glycol solvent in printing.

**Keywords:** Quantum dots · Inkjet printing · Coffee ring effect

## 1 Introduction

Quantum dots (QDs) are a kind of semiconductor particles, which have been used in emitting diodes [1, 2], biomedical imaging [3, 4] and fluorescent anti-counterfeiting technology [5, 6] owing to their distinctive electronic and luminescent properties.

Inkjet printing has emerged as a particularly attractive patterning technique for manufacture high performance devices with high printing accuracy and low materials loss. A few works have been acquired QDs patterns via inkjet printing. Junbiao Peng [7] engaged in the research of display materials and devices using CdSe QDs by means of inkjet printing technology. Ting Han [8] obtained fluorescent patterns using water dispersive QDs inks for inkjet printing that are invisible under ambient light.

One of the key problems in inkjet printing is the coffee ring effect. How to reduce the effect in inkjet printing of water-soluble QDs has been seldom studied. The low vapor pressure and high boiling point solvents such as chlorobenzene, ethylene glycol and the mixed solvents of toluene and 1,2-dichlorobenzene were employed to reduce coffee ring formation by Haverinen and Denneulin [9–11]. Liu et al. [12] achieved coffee ring-free and low-roughness quantum dot film using CdSe/ZnS QDs by adding cyclohexylbenzene and decane. Here, water-soluble CdSe/ZnS core-shell quantum dots with lower viscosity and less pollution to the environment are used as basic raw materials for the fabrication of functional inks, which is suitable for Jetlab4 micro-inkjet system. In addition, the coffee ring effect was modified by adding high boiling point solvent, ethylene glycol (EG). As a result, the optimum ink formulation was that the volume ratio of QD: deionized water (DI): EG was 1:30:20.

## 2 Materials and Methods

### 2.1 QDs Ink Preparation

Carboxyl water-soluble CdSe/ZnS quantum dots (QDs-COOH) were purchased from Wuhan Jiayuan Quantum Dot Co., Ltd. in this experiment. QDs-COOH were obtained by surface modification of oil-soluble quantum dots with polymers, which can be uniformly dispersed in aqueous solution. The maximum emission wavelength is $625 \pm 5$ nm, the molar concentration of QDs is 8 μmol/L, and the hydrodynamic size is 12–18 nm.

Carboxylic acid-functionalized water-soluble quantum dots inks were mixed with deionized water with volume ratios of 1:30, 1:60 and 1:90, respectively. The optimum ink formulation of the above (1:30) was selected to further reduce coffee ring effect by adding different content of EG. The proportion of specific addition was shown in Table 1. Silica glasses correspond to the substrate used for the majority of experiments. The treatment steps were as follows: the silica glasses were cleaned by ultrasonication in deionized water for 15 min, then washed with ethanol and dried by nitrogen stream for 2 min.

**Table 1.** Volume ratios of QDs-COOH, deionized water and ethylene glycol

| Component | QDs-COOH (μl) | Deionized water (μl) | Ethylene glycol (μl) |
|---|---|---|---|
| 1 | 5 | 150 | 10 |
| 2 | 5 | 150 | 50 |
| 3 | 5 | 150 | 100 |

## 3 Results and Discussions

### 3.1 Fluorescence Properties of QDs-COOH

As can be seen from Fig. 1, the QDs-COOH aqueous solution has a strong fluorescence emission. The QDs-COOH aqueous solution is red and then bright red before and upon UV irradiation at 365 nm, which is shown in the inset picture of Fig. 1. IR measurement was made on an FTIR spectrometer (NICOLET 6700) using KBr powder compression. Figure 2 shows the FTIR spectrum of CdSe/ZnS QDs-COOH. The bands at 3460 and 1640 $cm^{-1}$ are attributed to the O–H, C=O stretching vibrations of the carboxyl groups. The effect of different pH values on the fluorescence intensity of QDs-COOH dissolving in buffer solution (pH = 3.0–11.0) was also studied by FL spectrometer (RT-5301PC). As shown in Fig. 3, the fluorescence intensity of the solution varies slightly with different pH values, indicating that the QDs-COOH aqueous solution could have potential applications in complex environments.
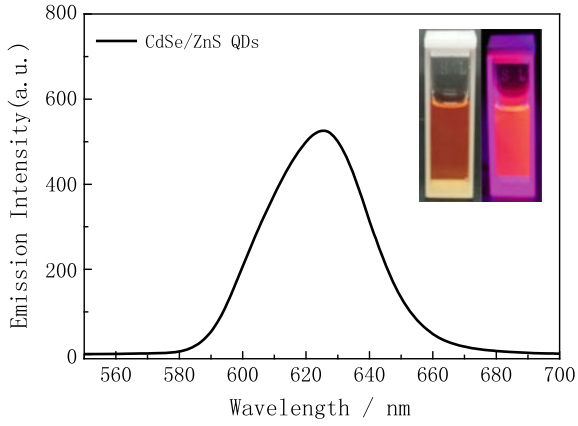
**Fig. 1.** Fluorescence spectrum of CdSe/ZnS QDs in deionized water
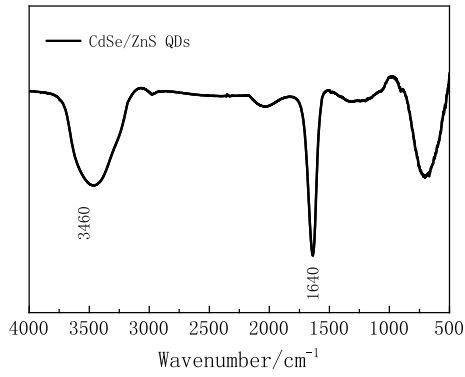


**Fig. 2.** FTIR of CdSe/ZnS QDs
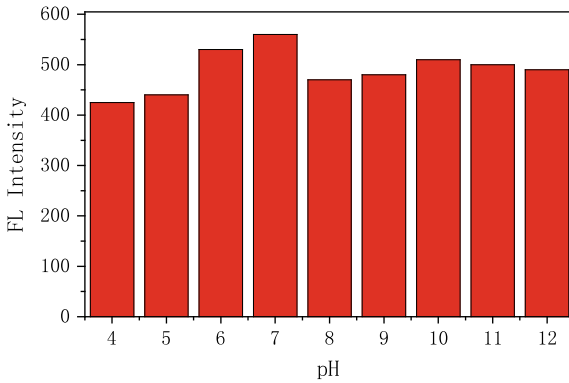


**Fig. 3.** Fluorescence intensity of CdSe/ZnS QDs at different pH values

### 3.2    Dimensionless Analysis

The developed QDs ink was in accordance with inkjet printing requirements is significant. Recent studies have shown that some dimensionless numbers can determine whether droplets are ejected or not and whether there are no satellite droplets, namely Weber number (We), Reynolds number (Re) and Z number (Z). This is described by the We number:

$$We = \frac{\rho d v^2}{\sigma} \tag{1}$$

and

$$Re = \frac{\rho d v}{\eta} \tag{2}$$

Where d is the feature length of the nozzle, v is its velocity, $\rho$ is the ink density, $\sigma$ is the surface tension of the liquid and $\eta$ is the dynamic viscosity of the ink.

Fromm [13] proposed the method of combining these two dimensionless numbers firstly, in which the fluid properties are described by Z number which is often used to predict ink printability, and the equation is shown below.

$$Z = \frac{Re}{\sqrt{We}} = \frac{\sqrt{\rho \sigma d}}{\eta} \tag{3}$$

The printable range is $1 < Z < 10$. Therefore, these numbers can be used to examine whether an ink can be processed with a given print head or not [14]. The viscosity of QDs ink is approximately equal to the solvents due to the low content of QDs in the solvents. The calculated dimensionless number is shown in Table 2. The optimized ink was selected to realize the stable printing of the inkjet printer in this study.

**Table 2** Physical characteristic parameters and Z value of ethylene glycol and QDs ink

| Solvent | Density | Surface tension | Viscosity | Nozzle diameter | Z value |
|---|---|---|---|---|---|
| | $\rho$ (g/cm$^3$) | $\sigma$ (dyn/cm) | $\eta$ (mPa·s) | d ($\mu$m) | |
| Ethylene glycol | 1.11 | 46.49 | 25.66 | 50 | 1.98 |
| QDs ink with EG | 1.05 | 67.47 | 11.56 | 50 | 5.15 |

### 3.3    Coffee-Ring Effect

When a drop of coffee evaporates on the table, it forms a dark ring at the edge of the drop. This uneven deposition phenomenon is called "coffee ring effect". In 1997, Deegan [15] and his colleagues described this phenomenon in Nature. The dot matrix

of QDs with different contents was printed on silica glass substrates and observed by laser microscope (vk-×200). As shown in Fig. 4, the obvious coffee rings of QD inks with different deionized water (v/v = 1:30, 1:60 and 1:90) were observed. While the point edge deposition of 1:30 ink is the least among them.

This phenomenon occurs because the water evaporation rate at the edge of the solution is the highest, resulting in the QDs flow to the edge of the pattern. One effective method to suppress the formation of the ring stain is altering the flow induced by the liquid evaporation from the drop edge. Addition of a high boiling point and low surface tension solvent such as ethylene glycol in the inks induce Marangoni flow [16], so that the droplets are evenly dispersed. As shown in Fig. 5a, there is still a weak coffee ring effect by adding a small amount of EG, while a better homogeneity was observed when increasing the content of EG in Fig. 5b and c. In addition, when the volume ratio of QD:DI:EG was 1:30:20 (Fig. 5c), a relatively small point was appeared which is beneficial for printing accuracy.
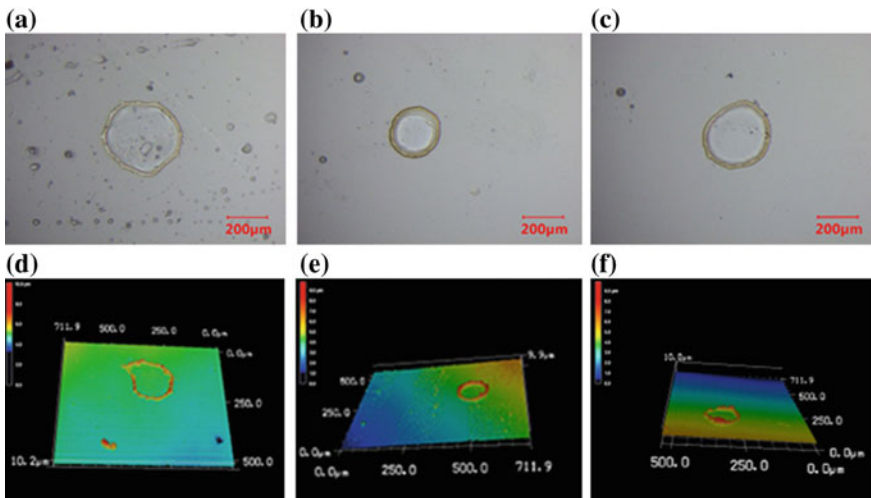


**Fig. 4** Morphology of QDs inks with different deionized water proportions under laser microscope. The volume ratios of **a–c** are 1:30, 1:60 and 1:90, **d–f** are their corresponding three-dimensional graphs

The minimum distance between two printed dots depends on the three-phase contact line (TCL) of the substrate and inks (Fig. 6a). When the distance between two droplets (center-to-center) is small, the two droplets will merge into one larger drop (Fig. 6b). Increasing contact angle can promote TCL sliding inward, resulting in smaller dots [17, 18]. Wu et al. [19] obtained the TFT arrays with smaller spacing via increasing the contact angle by hydrophobic treatment of substrates.

Figure 7 shows the contact angle of the inks on the silica glass substrate before and after adding EG. It can be seen that the contact angle increases significantly from 66 to 119° after adding EG, which is favor to reduce the spacing of printing point arrays.
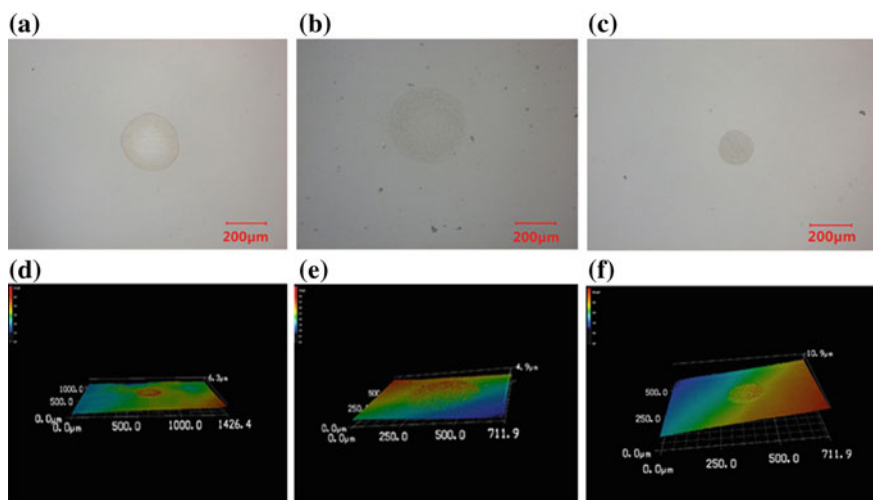
**Fig. 5** The morphology of QDs inks with different proportions of ethylene glycol under laser. microscope. The volume ratios of QD:DI:EG for **a–c** were 1:30:2, 1:30:10 and 1:30:20, **d–f** is their corresponding three-dimensional graph
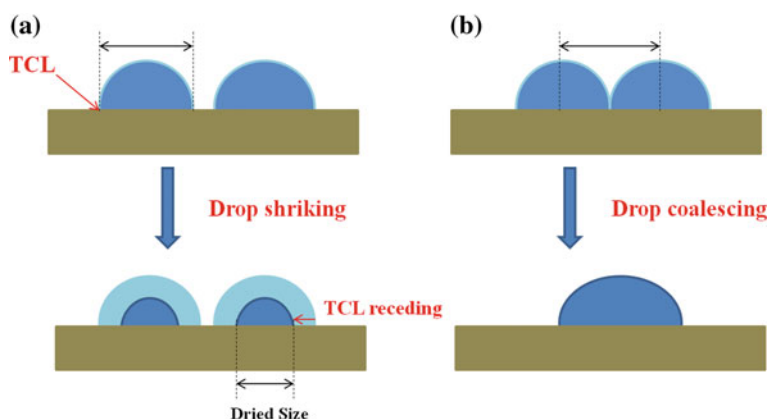


**Fig. 6 a** Drops spreading on a substrate shrink with solvent evaporation through receding of the three phase contact line until solidification; **b** When the distance between two droplets is small, the two droplets will merge into one larger drop [19]

## 3.4   Inkjet Printing of QDs Patterns

In order to reduce the interference of background ultraviolet fluorescence, a non-fluorescent paper was employed as printing paper. As shown in Fig. 8a, an image of the complex pattern was achieved by inkjet printing of modified QDs inks. This pattern is not visible in ambient light, while a bright color is displayed under 365 nm UV light, indicating a good optical property. Then the red color is nearly unchanged after two
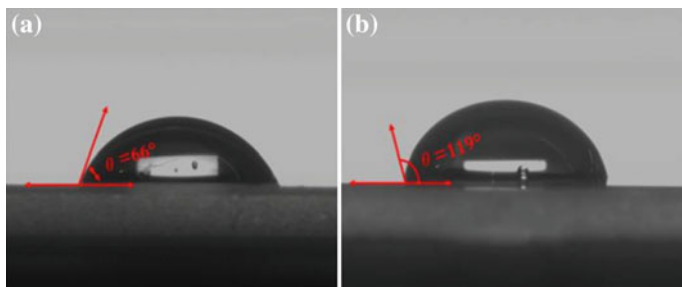
**Fig. 7** Contact angle without (**a**) and with (**b**) ethylene glycol in ink on silica glass

months and the pattern was still clearly visible and the brightness changed little in Fig. 8b. Then, the adhesion detection of the fluorescent image is carried out. It can be clearly seen from the Fig. 8c that there is a small area falling off at the intersection of the cross-cuts, but not more than 5%, indicating that the adhesion property is excellent. These results further confirm that the CdSe/ZnS QDs can be used as functional inks for inkjet printing, and are ideal for secure documents and encryption labels.
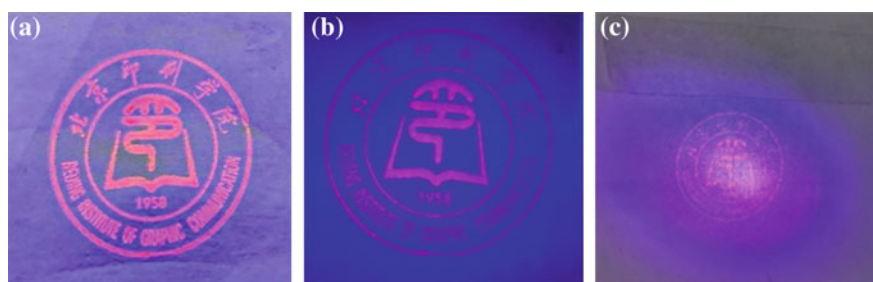


**Fig. 8 a** Image of the non-fluorescent inkjet paper with the logo printed with QDs inks; **b** Images two months later; **c** Image after tape sticking

## 4    Conclusions

In summary, ethylene glycol with high boiling point was used to disperse water-soluble QDs and inhibit coffee ring effect effectively, making it suitable for inkjet printing. The modified water-soluble QDs inks have been successfully used to print luminescent images and are an ideal choice for secure documents, encryption and labels.

# References

1. Li JS, Tang Y et al (2018) High efficiency solid–liquid hybrid-state quantum dot light-emitting diodes. Photonics Res 6(12):13–21
2. Kim BH et al (2015) High-resolution patterns of quantum dots formed by electrohydro-dynamic jet printing for light-emitting diodes. Nano Lett 15(2):969–973
3. Vu TQ, Lam WY, Hatch EW et al (2015) Quantum dots for quantitative imaging: from single molecules to tissue. Cell Tissue Res 360(1):71–86
4. Valizadeh A, Mikaeili H, Samiei M, Farkhani SM, Zarghami N et al (2012) Quantum dots: synthesis, bioapplications, and toxicity. Nanoscale Res Lett 7(1):480
5. Sun LW, Shi HQ, Li WN et al (2012) Lanthanum-doped zno quantum dots with greatly enhanced fluorescent quantum yield. J Mater Chem 22(17):8221–8227
6. Small AC, Johnston JH et al (2010) Inkjet printing of water 'soluble' doped zns quantum dots. Eur J Inorg Chem 2010(2):242–247
7. Peng JB (2018) Ink jet printing film and its display. Opt Optoelectron Technol 16(04):4–10
8. Han T et al (2017) Colloidal stable quantum dots modified by dual functional group polymers for inkjet printing. J Mater Chem C 5(19):4629–4635
9. Haverinen HM, Myllyla RA, Jabbour GE (2009) Inkjet printing of light emitting quantum dots. Appl Phys Lett. https://doi.org/10.1063/1.3085771
10. Han J, Ko D, Park M, Roh J, Jung H, Lee Y et al (2016) Toward high resolution inkjet-printed quantum dot light-emitting diodes for next generation display. SID Symp Dig Tech Pap 47(1):1354–1357
11. Denneulin A, Bras J, Carcone F, Neuman C, Blayo A (2011) Impact of ink formulation on carbon nanotube network organization within inkjet printed conductive films. Carbon 49 (8):2603–2614
12. Liu, Y., Li, F., Xu, Z., Zheng, C. (2017). Efficient all-solution processed quantum dot light emitting diodes based on inkjet printing technique. ACS Appl Mater Interfaces 9(30):25506–25512
13. Fromm JE (2010) Numerical calculation of the fluid dynamics of drop-on-demand jets. IBM J Res Dev 28(3):322–333
14. Meixner RM, Cibis D, Krueger K, Goebel H (2008) Characterization of polymer inks for drop-on-demand printing systems. Microsyst Technol 14(8):1137–1142
15. Deegan RD, Bakajin O, Dupont TF, Huber G, Witten TA (1997) Capillary flow as the cause of ring stains from dried liquid drops. Nature 389(6653):827–829
16. Hu H, Larson RG (2006) Marangoni effect reverses coffee-ring depositions. J Phys Chem B 110(14):7090–7094
17. Kuang MX, Wang JX, Bao B et al (2014) Photonic crystals: inkjet printing patterned photonic crystal domes for wide viewing-angle displays by controlling the sliding three phase contact line. Adv Opt Mater 2(1):102
18. Sun J, Bao B, He M, Zhou H (2015) Recent advances in controlling the depositing morphologies of inkjet droplets. ACS Appl Mater Interfaces 7(51):28086–28099
19. Wu SJ et al (2017) Inkjet printing of oxide thin film transistor arrays with small spacing with polymer-doped metal nitrate aqueous ink. J Mater Chem C 5(30):7495–7503

# Study on Grating Constant of Matte Light Pillar Holographic Materials

Yonghui Xi, Min Huang$^{(\boxtimes)}$, Yan Liu, Xueqing Yan, and Chunli Guo

School of Printing and Packaging Engineering, Beijing Institute of Graphic Communication, Beijing, China
huangmin@bigc.edu.cn

**Abstract.** In order to study the grating constant of the matte light pillar holographic materials, the X-Rite MA68 II multi-angle spectrophotometer was used to measure the spectral energies of the matte light pillar holographic materials. The reflective and diffractive spectral energies perpendicular to the direction of the light pillar and along the direction of the light pillar in the visible light range at five angles (15°, 25°, 45°, 75°, 110°) were analyzed with the grating equation. It was found that the grating constant of the matte light pillar holographic materials is in a range rather than that of the rainbow light pillar holographic materials which had fixed value, which will only cause the lightness variations significantly.

**Keywords:** Grating constant · Matte light pillar · Holographic material · Spectral energy information · Grating equation

## 1 Introduction

Holographic materials have been widely used in the field of packaging and printing because of high brightness or rainbow effect [1]. The existing researches were mainly focusing on the measurement of the color quality of the holographic materials, and there were few studies on the micro-structures, such as the direction of the grating, shape of the grating and grating constant of the holographic materials.

As for the micro-structure, high amplification microscopes are usually used to measure the microscopic parameters of holographic materials, but this kind of equipment is a high-precision optical instrument and cannot be widely used in the industry. In our previous study, it was found that the micro-parameters of the holographic materials can be measured by the spectrophotometer with the geometry of 45/0 [2]. However, this method can only be used to measure the materials with regular grating period and fixed grating constant, which can arouse the colors of the rainbow. Li Yang et al. [3] proposed that the grating constant of holographic materials can be measured by the scanning method, which needs to predict the illuminated and reflected optical parameters of scanning equipment in advance. Meanwhile, it is necessary to rotate the scanned samples many times to collect the RGB images at different rotation angles, which is inconvenient to operate. It is worth pointing out, all the materials used in the previous study are rainbow holographic materials. How about the matte light pillar holographic materials? There are few researches on these materials.

The matte light pillar holographic materials have a high lightness effect and an inconspicuous rainbow effect. In this study, the grating constant of the matte light pillar holographic materials will be computed with the spectral energies using the grating equation, and the results can also be compared with those from the optical amplification equipment.

## 2 Experiment

### 2.1 Holographic Materials

Holographic materials usually transferred from the master mask by a process of molding, aluminizing, compounding, coating, cutting, etc. In the processes, the materials will have the same grating structures and grating constants similar with those of the master masks [4]. Among them, the grating parameters are the key to the final appearance of the holographic materials. Figure 1 shows three different types of holographic materials, including matte light pillar holographic material (Fig. 1a), rainbow light pillar holographic material (Fig. 1b) and the uniform rainbow holographic material (Fig. 1c) respectively.
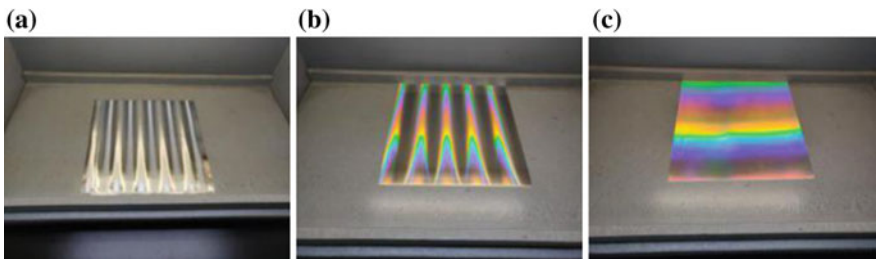


**Fig. 1.** Pictures of the holographic materials. **a** Matte light pillar holographic material; **b** rainbow light pillar holographic material; **c** uniform rainbow holographic material

As shown in Fig. 1, for the matte light pillar holographic material, only the lightness variations occurred when the viewing angle is changed. While for the rainbow holographic materials, we will have the colors of the rainbow in different viewing angles.

### 2.2 Spectral Measurement

Two matte light pillar holographic materials were selected as the experimental samples in this study, named as 1# and 2# respectively. The spectral energies of the materials in the positions of along and perpendicular to the light pillar were measured by the X-Rite MA68 II multi-angle spectrophotometer, with the measure conditions of D65 and 10° degree. The geometrical measurement conditions of the X-Rite MA68 II are shown in Fig. 2. As can be seen, the incident angle of the light source is 45° from the normal angle of the sample, and the photodetector is at the direction of 15°, 25°, 45°, 75°, 110°

to receive the reflected and diffracted light. The measured spectral range is from 400 nm to 700 nm and the sampling interval is 10 nm. Figures 3 and 4 illustrate the spectral energies of 1# and 2# holographic materials at five angles, respectively.
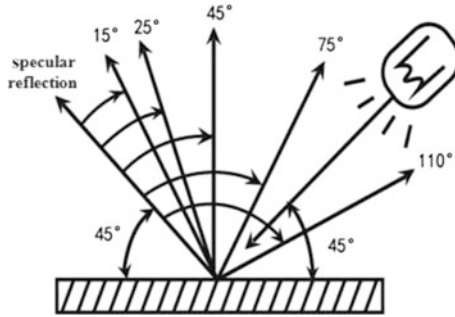


**Fig. 2.** Schematic diagram of geometric measurement conditions of X-Rite MA68 II multi-angle spectrophotometer
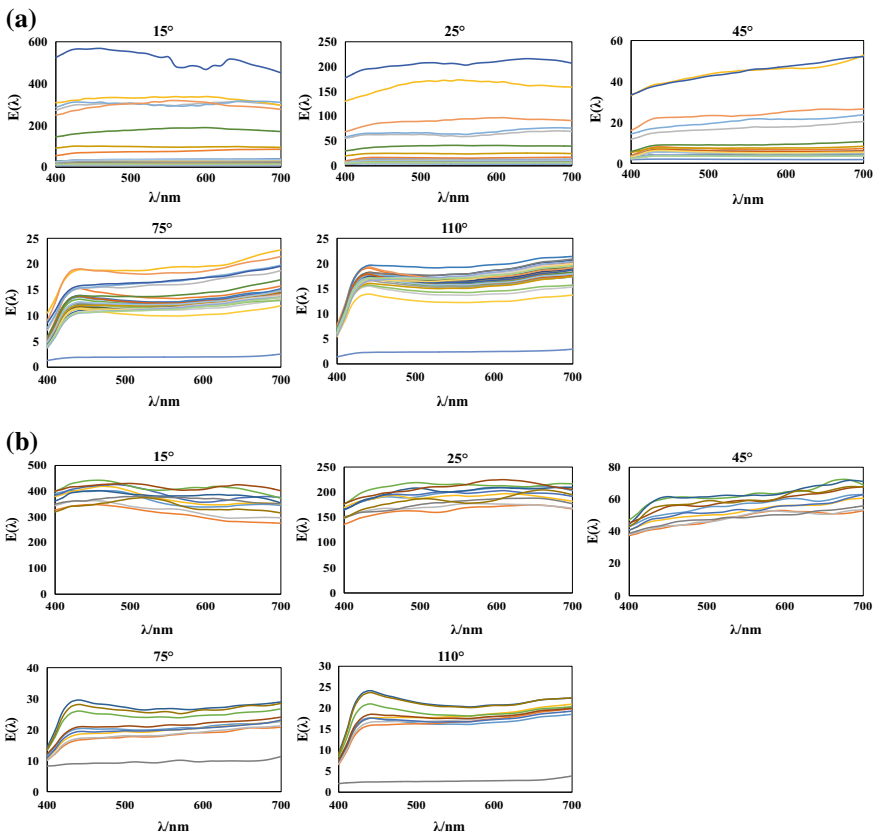


**Fig. 3.** Spectral energy curves of the matte light pillar holographic material 1#. **a** The direction of perpendicular to the light pillar; **b** the direction of along the light pillar

**(a)**



**(b)**
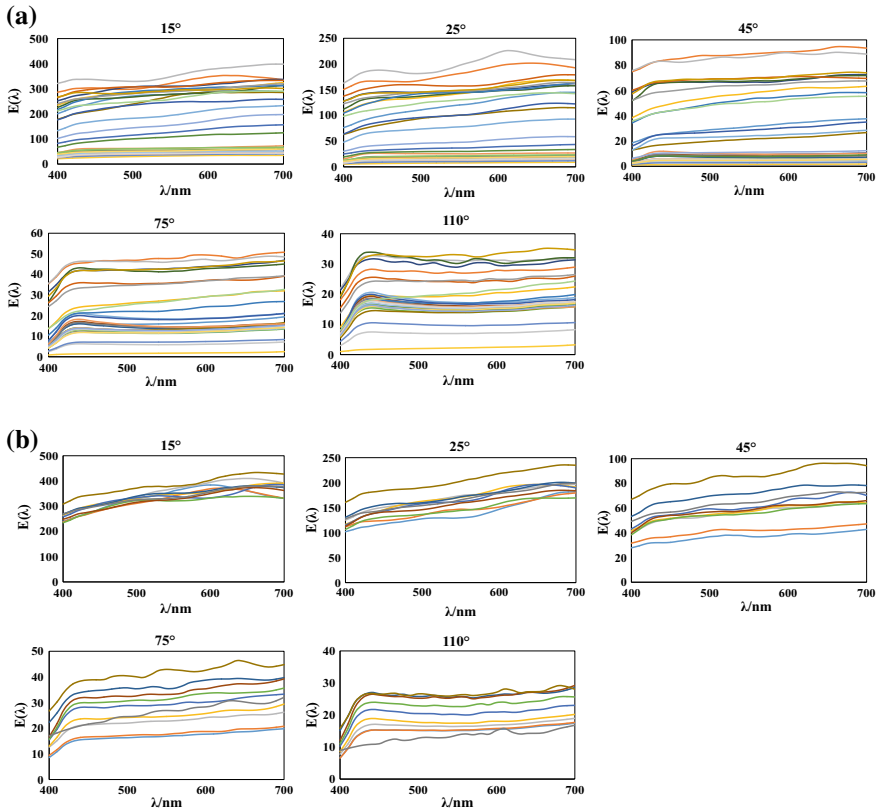


**Fig. 4.** Spectral energy curves of the matte light pillar holographic material 2#. **a** The direction of perpendicular to the light pillar; **b** the direction of along the light pillar

According to the spectral energies plotted in Figs. 3 and 4, it can be seen that the data measured along the light pillar is more stable than the data measured perpendicular to the light pillar. In addition, the spectral energies measured from 1# and 2# in the spectral range of 400 nm to 700 nm at 15° and 25° directions are beyond 100%, which may be caused by the diffraction phenomenon. And the differences between 1# and 2# are the intensity of the spectral curves, which may be caused by the micro-structure of the grating. The spectral energies measured from other angles in 400 nm to 700 nm are less than 100%, which means that in the angle of 45°, 75°, 110°, almost no diffracted energies or the energies diffracted from high order can be detected by the instrument.

The spectral energies in Figs. 3 and 4 are flatness in the visible range, as well as horizontal to the axis in the whole visible range compared with the rainbow holographic materials [5]. The spectral curves are basically, resulting in only lightness variation in different viewing angles, without obvious rainbow effect. According to our previous study [5], the spectral energy curves of the rainbow light pillar holographic materials have obvious peaks and valleys in the visible light range, which also have

different diffractive intensities in different wavelengths. Finally, we can see the continuous change of rainbow effect.

## 2.3   Grating Equation

The matte light pillar holographic material, the rainbow light pillar holographic material and the uniform rainbow holographic material were magnified 5000 times with the KEYENCE VK-X200K3D instrument. The grating constant range (defined by the thick line in the figure) of 1# and 2# was measured to be about 1.7 μm–2.5 μm and 3.0 μm–3.5 μm, respectively. For the rainbow light pillar and the uniform rainbow holographic materials, the grating constant of them are approximately about 1 μm. Their micro-structure was shown in Fig. 5.
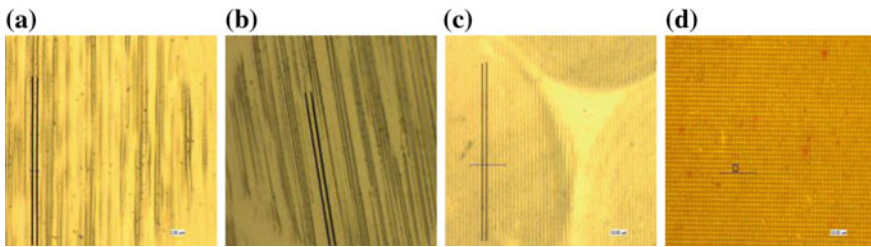


**Fig. 5.** The micro-structure of the holographic materials. **a** Matte light pillar holographic material 1#; **b** matte light pillar holographic material 2#; **c** rainbow light pillar holographic material; **d** uniform rainbow holographic material

It can be seen that the rainbow light pillar holographic material and the uniform rainbow holographic material have the regular grating periods, which can arouse a beautiful rainbow (continuous colorful phenomena) effect. However, the grating period of the matte light pillar holographic materials is irregular; there is only lightness variation in different viewing angle. For matte light pillar holographic materials 1# and 2#, the difference in micro-structure is that the grating stripes of 2# are more than those of 1#, which will result in a difference of the diffracted energies shown in Figs. 3 and 4.

The equation describing the relationship between the grating constant, the incident angle and diffraction angle of light is called grating equation [6], which is shown in Eq. (1):

$$d(\sin i + \sin j) = k\lambda \tag{1}$$

where, d is the grating constant or grating period, i is the incident angle, j is the diffractive angle, λ is the wavelength in the visible range is the diffraction order and its value can be ±1, ±2, ±3….

According to the grating equation and the spectral energy curves, the grating constant calculated for the 1# in the 15° diffraction direction is ranged from 1.93 μm to

3.38 μm (given i = 45°, j = −30°, k = 1). Similarly, the grating constant of 1# in the diffraction direction of 25° is calculated to be 2.19 μm to 3.84 μm (given i = 45°, j = −20°, k = 2). When the grating constant is calculated by the grating equation, the wavelength range, the diffraction order, the incident angle, and the diffraction angle of 1# and 2# are the same.

Considering the spectral energies measured from 15° and 25°, the grating constants of 1# and 2# materials computed from the grating equation are ranging from 1.93 to 3.84 μm, which are consistent with those measured by the instruments. In the measuring results, the grating constants of 1# and 2# were ranging from 1.7 μm to 2.5 μm, 3.0 μm to 3.5 μm, which were obtained by subjective judgment to seek the thick lines in the measurement shown in Fig. 5. The spectral measurement might be reliable than those from the instrumental measurement. In the future work, the equipment angular measurement can be built to measure the grating constant of the holographic materials precisely.

## 3    Conclusions

This study investigated the grating constant of matte light pillar holographic materials using the spectral measurement. Firstly, holographic materials were fixed and the spectral energies at the positions of along and perpendicular to the direction of the matte light pillar were measured using an X-Rite MA68II multi-angle spectrophotometer. Then, according to the spectral energies collected from different angles, the diffracted energies received by the photodetector can be determined. Finally, combining the grating equation and comparing the shape of the spectral energy curves, the grating constant of the matte light pillar holographic material is calculated to be a range rather than a fixed value.

## References

1. Wang Y (2013) From defect detection to quality control—a visual inspection scheme for the quality defects of cigarette package. Print Technol 16:60–61
2. Huang M, Xi YH, Li X et al (2019) A comparative study of grating constant measurement methods for plain rainbow holographic materials. Acta Optics Sinica 39(10):1033003
3. Yang L, Karlsson M (2017) Effective method for fast and detailed analysis of holographic patterns over a large area. Appl Opt 56(26):7491–7497
4. Ma HG (2015) The research and application of super laser paper. South China University of Technology, Guangzhou
5. Huang M, Wang LF, Liu Y et al (2014) Measurement and analysis of spectral and chromaticity values of pillars of light pattern holographic paper. Acta Optics Sinica 34 (6):0633002
6. Zhou HX, Cheng YF (2006) Holographic optics: design, manufacture and application. Chemical Industry Publishing House, Beijing, p 5

# Determination Method for Index Weight of RPMS Reconfigurable Scheme

Shisheng Zhou, Longfei Jiang, Huailin Li[(✉)], Rubai Luo[(✉)],
and Sheng Liu

Faculty of Printing, Packing Engineering and Digital Medial Technology,
Xi'an University of Technology, Shaanxi, China
lihuailin6666@sina.com, luorubai@xaut.edu.cn

**Abstract.** Reconfigurable printing manufacturing system (RPMS) can be reconfigured according to the changes of production tasks, which will produce multiple reconfiguration schemes. The determination method of index weight is of great significance to the optimization of schemes. In this paper, according to the actual production factors of printing manufacturing, a comprehensive evaluation model is established. The weight determination method of Analytic hierarchy process (AHP) and interval fuzzy number weight determination is introduced, and relative merits of the two methods are summarized. On this basis, a weight determination method based on triangular fuzzy number (TFN) is proposed, which provides a scientific basis for the scheme selection of RPMS.

**Keywords:** Reconfigurable printing manufacturing system · Comprehensive evaluation · Analytic hierarchy process · Triangular fuzzy number

## 1 Introduction

In order to meet the requirements of personalized and small-batch printing production, it is required that the RPMS can quickly adjust the function and productive capacity of the system by rapidly reorganizing and updating the system structure or component units to quickly respond to changes in market demand [1]. In actual printing production, there are often multiple reconfiguration schemes which require a comprehensive and effective method to optimize the scheme.

The selection of reconfiguration schemes must be based on scientific and objective methods, and there are few studies on the selection methods of RPMS. Literature [2] established an index evaluation system and used AHP to determine the index weight and optimize the scheme. In literature [3], interval fuzzy number is used to determine the weight of indexes and optimize schemes. The methods of the above is subjective, which leads to the lack of scientificity and objectivity in evaluation results and selection of schemes.

In this paper, according to the optimization problem of the RPMS, the multi-person evaluation method is adopted to determine the relative importance of the indexes. The triangular fuzzy number is used to represent the judgment result and the weight of the index is determined by defuzzification and standardization process to optimize reconfiguration schemes.

## 2 Construction of Comprehensive Evaluation Index System

The comprehensive evaluation index system includes target layer, criterion layer, and indicator layer, as shown in Fig. 1. The target layer comprehensively evaluates and optimizes the overall scheme; the criteria layer include the economic efficiency, reliability, reconfigure ability, the performance of production, human-machine relationship [4].
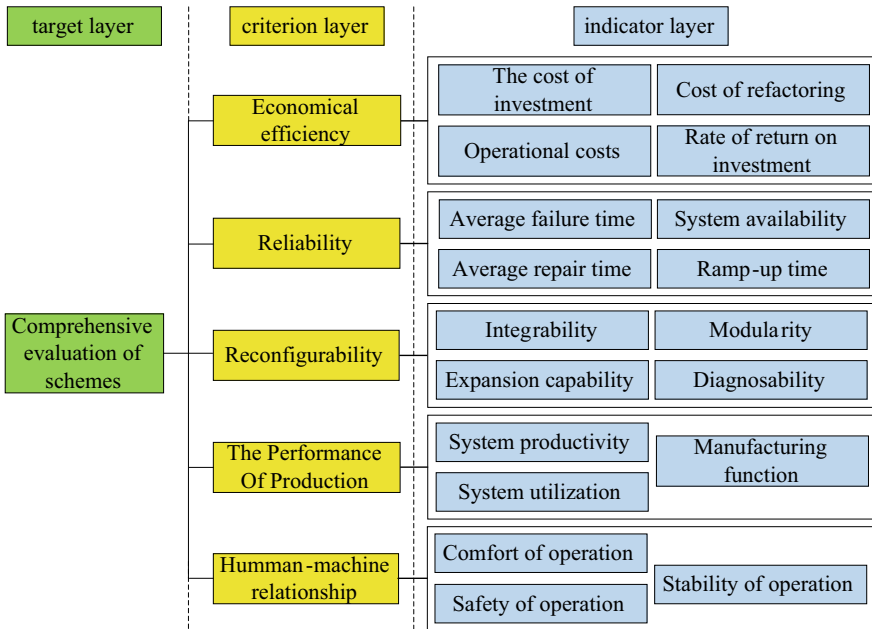


**Fig. 1.** Comprehensive evaluation model of reconfiguration scheme

**Economical efficiency**. Economy of system pursues the unification of inputs and benefits. Specific data can be determined by calculating actual print production data and quantitative evaluation methods.

**Reliability**. It is an important guarantee for enterprises to survive and develop in the fierce competition. The low frequency of system failure and the short repair time mean that the system is reliable [5]; System availability refers to the extent to which the system is ready for operation; Ramp-up time refers to the time required for RPMS to achieve a stable production level in terms of print yield and print quality.

**The performance of Production**. Analyzing the production performance of the system can help guide printing production. System productivity refers to the number of prints produced per unit time; Equipment utilization refers to the utilization degree of equipment during printing manufacturing; Manufacturing function measures the ability of a system to produce multiple types of prints.

**Reconfigurability**. It is an indicator of a system's ability to respond quickly to market changes. Integration refers to the ability of the system to integrate with other

printing production components and easily integrate new technologies [6]. Modularity means that the printing system reorganizes, updates and replaces the original modules to change their production functions and production as needed [7]; Scalability refers to the system's open system framework, which can accommodate multiple types of printing production units; Diagnostic capabilities refer to the system's ability to automatically detect product quality and system failure.

**Human-machine relationship**. It refers to the comfort and safety of working environment when operating the printing manufacturing system.

## 3 Analytic Hierarchy Process

AHP is a decision-making method that decomposes elements into target layer, criteria layer, and scenarios layer, and then uses the pairwise comparison method to determine the weight of each index. Specific steps are as follows:

**Step1:** Taking the criterion layer index as an example, the judgment matrix is constructed by the pairwise comparison method [9]. The meaning of the scale is shown in Table 1.

$$A = (a_{ij}) = \begin{bmatrix} a_{11} & \cdots & a_{12} \\ \vdots & \ddots & \vdots \\ a_{51} & \cdots & a_{55} \end{bmatrix} \tag{3.1}$$

with $a_{ii} = 1$, $a_{ij} = \frac{1}{a_{ji}}$, $a_{ij} > 0$.

**Table 1**  Compares the criteria scale

| Scale | Description |
|---|---|
| 1 | $i$ and $j$ indicators are equally important |
| 3 | The $i$ is slightly more important than $j$ |
| 5 | The $i$ is obviously more important than $j$ |
| 7 | The $i$ is more important than $j$ |
| 9 | The $i$ is extremely important than $j$ |
| 2, 4, 6, 8 | Intermediate value of two adjacent scales |

**Step2:** The root weight method is used to calculate the index weights, as shown in formula (3.2), and then the results are normalized.

$$\omega_i = \sqrt[n]{\prod_{j=1}^{n} a_{ij}}, \ i = 1, 2, \cdots, n \tag{3.2}$$

**Step3:** Consistency check can reduce errors caused by subjective factors.

$$CI = \frac{\lambda_{max} - n}{n - 1} \tag{3.3}$$

$$CR = \frac{CI}{RI} \tag{3.4}$$

where: $\lambda_{max}$—Maximum eigenvalue; $CR$—Random consistency ratio; $CI$—Consistency index; $RI$—Random consistency indicator.

When $CR < 0.1$, the consistency of the judgment matrix is good [8]. The average random consistency index is shown in Table 2.

**Table 2** Random consistency indicator value

| $n$ | 1 | 2 | 3 | 4 | 5 |
|---|---|---|---|---|---|
| $RI$ | 0 | 0 | 0.58 | 0.90 | 1.12 |

The AHP can systematically analyze the objectives, which is concise and practical. However, the AHP relies on the experience and knowledge of decision makers, and the objectivity of the results is insufficient.

## 4 Method of Interval Fuzzy Number

The judgment matrixis constructed by using interval fuzzy number to express the evaluation results, and then the weights of each index are calculated to make a comprehensive judgment. Specific steps are as follows:

**Step1:** Membership function scaled by interval fuzzy number is Established, as shown in Fig. 2.
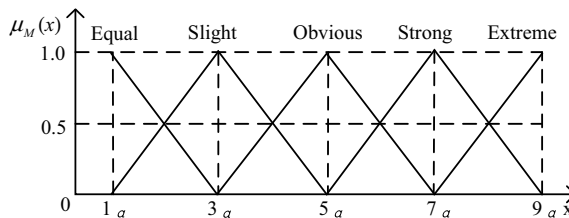


**Fig. 2.** Membership function scaled by interval fuzzy number

When the confidence level $\alpha$ of the interval number is defined, the Interval fuzzy number can be expressed as: $\forall \alpha \in [0, 1]$

$$\begin{cases} b_{ij} = \begin{bmatrix} b_{ijl}, b_{iju} \end{bmatrix} = \begin{bmatrix} l + (m-l)\alpha, u - (u-m)\alpha \end{bmatrix} \\ \left( b_{ij} \right)^{-1} = \begin{bmatrix} \frac{1}{u-(u-m)\alpha}, \frac{1}{l+(m-l)\alpha} \end{bmatrix} \end{cases} i = 1, 2, \cdots, n; j = 1, 2, \cdots, n$$

(4.1)

**Step2:** Fuzzy judgment matrix is established based on membership function.

$$B(b_{ij}) = \begin{bmatrix} 1 & \cdots & b_{15} \\ \vdots & \ddots & \vdots \\ b_{51} & \cdots & 1 \end{bmatrix}; b_{ij} = \begin{cases} 1 & i = j \\ 1, 3, 5, 7, 9, 1^{-1}, 3^{-1}, 5^{-1}, 7^{-1}, 9^{-1} & i \neq j \end{cases}$$

(4.2)

**Step3:** Calculate the maximum eigenvector of the matrix. The satisfaction of fuzzy judgment matrix can be expressed by the optimal index $\mu, \mu \in [0, 1]$, and the larger the $\mu$ value, the higher the satisfaction of the judgment matrix [9].

$$b_{ij}^{\alpha} = \mu b_{iju}^{\alpha} + (1 - \mu) b_{ijl}^{\alpha}$$

(4.3)

$$B\left(b_{ij}^{\alpha}\right) = \begin{bmatrix} 1 & \cdots & b_{15}^{\alpha} \\ \vdots & \ddots & \vdots \\ b_{51}^{\alpha} & \cdots & 1 \end{bmatrix}$$

(4.4)

The maximum eigenvector of the matrix is obtained by giving $\alpha$ and $\mu$, which is normalized to obtain the weight of the indexes.

Combining AHP with interval fuzzy number to express the evaluation results can better deal with uncertain information, but the selection of confidence level $\alpha$ and optimal index $\mu$ lacks objective basis.

## 5    Method of Triangular Fuzzy Number

Aiming at the problems existing in the AHP and the interval fuzzy number method in determining the weight of the index, the weight determination method is improved. By using the TFN to construct the judgment matrix and combining the multi-person evaluation method, the method of determining the weight of the index based on the TFN is proposed, which is applied to the selection of the reconfiguration schemes of the RPMS.

### 5.1    Constructing Fuzzy Judgment Matrix

Taking the criterion layer as an example, at least three professionals are selected to compare the importance of indexes to construct a fuzzy judgment matrix. The scale and meaning are shown in Fig. 2.

$$D_{ij} = \begin{bmatrix} d_{11} & \cdots & d_{12} \\ \vdots & \ddots & \vdots \\ d_{51} & \cdots & d_{55} \end{bmatrix} \tag{5.1}$$

With $d_{ij}$ is the average value of the evaluation results.

## 5.2    Calculating the Comprehensive Weight of Index

The comprehensive fuzzy value (initial weight) of the K-th index $i$ is calculated as formula (5.2), so that the initial fuzzy weight values $D_{c1}$, $D_{c2}$, $D_{c3}$, $D_{c4}$, $D_{c5}$ of the criterion layer index can be calculated.

$$D_i^k = \sum_{j=1}^{n} d_{ij}^k \div \left( \sum_{i=1}^{n} \sum_{j=1}^{n} d_{ij}^k \right), i = 1, 2, \cdots, n; j = 1, 2, \cdots, n \tag{5.2}$$

Then, the initial weights are defuzzified by formulas (5.3) and (5.4), and the initial weights are changed into general values to obtain the initial weights of the criterion layer.

**Definition 1** $M_1$ and $M_2$ are TFN, and the probability of $M_1 \geq M_2$ [10] is defined by the triangular fuzzy function as:

$$P(M_1 \geq M_2) = \begin{cases} 1 & m_1 \geq m_2 \\ \frac{l_2 - u_1}{(m_1 - u_1)(m_2 - l_2)} & m_1 \leq m_2 \ , \ u_1 \geq l_2 \\ 0 & otherwise \end{cases} \tag{5.3}$$

**Definition 2** The probability that a fuzzy number is greater than the other $k$ fuzzy numbers is defined as:

$$P(M \geq M_1, M_2 \cdots M_k) = minP(M \geq M_i), i = 1, 2, \cdots, k \tag{5.4}$$

Finally, the initial weight value is normalized by formula (5.5) to obtain the final weight of each index.

$$\bar{W}_{Cr} = \frac{W_{Cr}}{\sum_{r=1}^{5} W_{Cr}} r = 1, 2, \cdots, 5 \tag{5.5}$$

## 5.3    Determining Weights of Index at Different Levels

Assuming that $W$ is the weight of the evaluation index in the sub-system and $TW$ is the weight of the evaluation index in the whole evaluation system, the relationship between them is as follows:

$$TW_{ij} = \begin{cases} W_i & \textit{Indexes at criterion level} \\ W_{ij} & \textit{Between different indexes} \end{cases} \tag{5.6}$$

with $\sum\limits_{i=1}^{m}\sum\limits_{j=1}^{n} TW_{ij} = 1; \sum\limits_{i=1}^{m} W_i = 1; \sum\limits_{j=1}^{n} W_{ij} = 1; i = 1, 2, \cdots, m; j = 1, 2, \cdots, n.$

Evaluation results are represented by TFN and combine the method of multi-person evaluation to improve the objectivity of the evaluation results. Finally, the weight of indexes is determined by using the de-fuzzy method, so as to comprehensively evaluate the reconfiguration scheme.

## 6    Conclusions

In this paper, the index comprehensive evaluation model is established according to the optimization problem of reconfiguration scheme in actual printing production. Secondly, the AHP and the interval fuzzy number weight determination method are compared, and the advantages and disadvantages of the two methods are emphatically analyzed. On this basis, the TFN weight determination method is proposed, which is applied to the optimization of RPMS. The weight determination method of TFN uses triangular fuzzy number to represent evaluation results and combines the method of multi-person evaluation. It can not only evaluate the index objectively and truly, but also reduce the influence of subjective factors. This is an objective and reliable scientific method for the selection of reconstruction schemes of printing manufacturing.

## References

1. Li H, Luo R, Zhou S, Gao S (2018) Research on reconfigurable mechanism of manufacturing system for printing process based on ACP. Math Probl Eng 2018:1–7. https://doi.org/10.1155/2018/2323746
2. Qi J, Wang L, Ning S, Li J (2016) Comprehensive evaluation method for reconfiguration scheme of reconfigurable manufacturing systems. Mach Design Manuf 8:82–85
3. Gu Y, Wu L (2007) A fuzzy AHP approach to the determination of weights of evaluation factors in mechanism scheme evaluation process. Chin Mech Eng 18(9):1052–1067
4. Lou S (2002) Synthetic evaluation algorithm for manufacturing system's scheme selection. Modular Mach Tool Autom Manuf Tech 4:30–35
5. Sun L, Ning R-x, Zhang Z (2003) Research on comprehensive evaluation method of FMS planning. China Mech Eng 39(2):47–52

6. Wang G, Huang S et al (2017) Reconfiguration plan evaluation based on preference ranking of key characteristics in reconfigurable manufacturing system. Trans Beijing Inst Technol 37 (5):466–472
7. Koren Y, Heisel U, Jovane F et al (1999) Reconfigurable manufacturing systems. Ann CIRP 48(2):527–540
8. Li LJ, Dou K (2009) Research on the consistency of the judgment matrix in AHP. Comput Technol Devel (10):137–139
9. Yang C, Chen B (2004) Key quality performance evaluation using fuzzy AHP. J Chin Inst Ind Eng 21(6):543–550
10. Ran J (2011) The research of the rank of triangular fuzzy numbers. J Minzu Univ China (Nat Sci Ed) 20(4):37–42

# Research and Application on the Effect of Micro-Information Magnification Based on Human Visual System

Linghua Guo[1,2,3,4(✉)], Lei Wen[1,2,3,4], Lingyu Dang[1,2,3,4], Na Huo[1,2,3,4], and Rui Chen[1,2,3,4]

[1] College of Bioresources Chemical and Materials Engineering, Shaanxi University of Science and Technology, Xi'an, China
394889814@qq.com
[2] National Demonstration Center for Experimental Light Chemistry Engineering Education, Shaanxi University of Science and Technology, Xi'an, China
[3] Key Laboratory of Paper Based Functional Materials of China National Light Industry, Shaanxi University of Science and Technology, Xi'an, China
[4] Shaanxi Province Key Laboratory of Papermaking Technology and Specialty Paper Development, Shaanxi University of Science and Technology, Xi'an, China

**Abstract.** Printed matter is a kind of visual product. The magnification of micro-information based on human visual recognition is more in accordance with the requirements of the human eyes to observe and evaluate printed matter. In this paper, a method of magnifying the invisible micro-information to be visible is proposed based on the principle of moiré pattern. Firstly, the target information was set up according to moiré principle. And it was compressed and deformed based on human visual system. The basic micro-information layer to be magnified was obtained. Secondly, the parameters of the revealing grating were determined according to the relationship between the micro-information layer and the revealing grating, and the revealing grating matching with the micro-information layer was established. Finally, the magnification effect was obtained by superposing the revealing grating on the basic micro-information layer on the suitable position and angle. This method establishes the matching relationship between the basic micro-information layer and the revealing grating based on human visual system, which magnifies the micro-information invisible to the naked eye and achieves good results. It plays an anti-counterfeiting role in printing.

**Keywords:** Moiré pattern · Magnification · Human visual system · Micro-information

## 1 Introduction

Moirés are the visual results of interference between two objects at constant angles and frequencies. Moirés do not exist in any base layer and they change with the change of spatial position. Because moiré patterns are very sensitive to the micro-displacement,

transformation and distortion of the base layers [1, 2], moiré patterns are widely used in many fields, such as strain analysis, document anti-counterfeiting and protection, information encryption, information hiding and optical watermarking [3–7].

Munoz-Rodriguez proposed a specified moiré construction algorithm for image encryption [8]. The technique generates the reference layer, and then modulates its phase according to the secret image to get the deformed layer. When the reference layer and the deformed layer are superimposed, the secret image appears. In order to get a clearer secret image, it needs to be processed by low-pass filtering. Huang proposed a designated moiré construction algorithm based on phase modulation [9], which can be used for anti-counterfeiting optical watermarking of printed documents. This technique also superimposes the reference layer and the deformable layer to present the secret images. In order to avoid the problem of leakage of watermarking information in a single layer, Lu added random points to improve the hiding effect of watermarking information in the base layer [10]. The algorithm improved the hiding effect of watermarking information in the base layer, but there were random points in the overlapped moiré patterns, which reduced the quality of moiré patterns.

Amidror [11] proposed a method to construct the specified moiré patterns based on 2-D magnification effect. In their presented algorithm, the moiré pattern elements are arranged repeatedly in layer 1. Layer 2 is composed of transparent lattices with periodic repetition in black background. When the layer 2 is covered on the layer 1, the target moiré pattern with periodic repetition will appear. For the 2-D magnified moiré patterns, the whole image can only have one base element and cannot present rich image information. Hersch [12, 13] then proposed a designated moiré pattern construction algorithm based on 1-D magnification effect. The target moiré element is compressed vertically to compose a base layer, so it is also known as band moiré. The band moiré can only magnify elements in one dimension, unlike the 2-D magnified moiré pattern, which can magnify elements in two dimensions, but the band moiré can achieve better visual magnification effect with higher brightness.

Based on human visual system, the parameters of the base layer, the revealing grating and the magnified moiré pattern are determined according to moiré theory. By overlapping the base layer and the revealing grating, the invisible micro-information for human eyes can be amplified to be visible. In the meantime, the magnification effect of micro-information is achieved. Micro-information magnification technology can improve the anti-counterfeiting performance of printing and increase the added value of products.

## 2 Theories

### 2.1 Construction of Moiré Pattern

When two layers overlap, the black line grids intersect, which fall on each other in some areas and fall between each other in the other areas. There are less black pixels in the intersection region, so it is brighter than other regions. These bright and dark areas alternate to constitute moiré patterns [14].

where $p$ is the index of the parameter equation of the superimposed moiré, $m$ is the index of the parameter equation of the base layer, and $n$ is the index of the parameter equation of the revealing grating.

$$k_{1m} + k_{2n} = k \qquad (1)$$

The moiré pattern satisfying formula (1) is called $(k_1, k_2)$—moiré. In general, human eyes will automatically recognize the most prominent moiré pattern. The intersection of straight lines has the highest density, which forms $(1, -1)$—moiré, as shown in formula (2) (Fig. 1).

$$n - m = p \qquad (2)$$
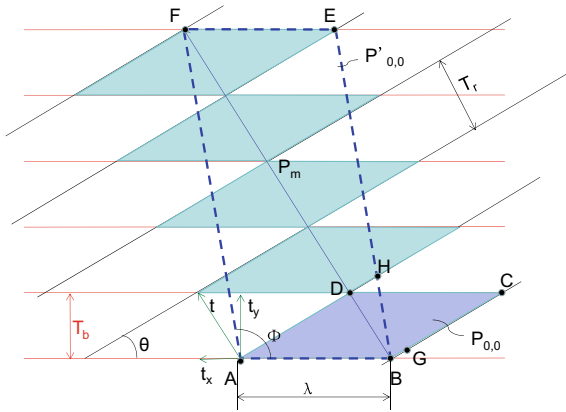


**Fig. 1.** Overlay diagram of 1-D magnified moiré pattern

The linear transformation of moiré has nothing to do with rotation $\theta$, but the trend of moiré is related to $\theta$. If the angle of moiré is $\varphi$, it satisfies formula (3).

$$\tan \phi = \frac{T_r \cdot \sin \theta}{T_r \cdot \cos \theta - T_b} \qquad (3)$$

where $T_b$ is the base layer period and $T_r$ is the revealing grating period.

The moiré repetitive vector $P_m$ is shown in formula (4).

$$P_m = \frac{T_r}{T_r - t_y} \cdot t \qquad (4)$$

where $t_y$ is the height of micro information.

The magnification factor of the moiré pattern is $s = T_r/(T_r - t_y)$, and the period of the moiré pattern is $T_m$, as shown in formula (5).

$$T_m = \frac{T_b \cdot T_r}{\sqrt{T_b^2 + T_r^2 - 2T_b \cdot T_r \cos \theta}} \qquad (5)$$

## 2.2   Rayleigh Criterion

The ability of human visual system to distinguish details depends on the change of relative brightness [15]. At the same time, the diffraction effect of light has an important influence on the human eyes resolution. Therefore, the minutiae of the object surface cannot be reflected in detail [16]. In the case of the simplest Fraunhofer circular hole, the range of the central bright spot is determined by the diffraction angle of the first dark ring radius $\theta_1$, $\theta_1 = 0.610\theta/R$. When the two points of light are imaged, some of their diffraction patterns fall on the same area of the screen. If the highlights of the two groups are far from each other and the central highlights are relatively small, then the *images* of the two points can still be separated into two highlights; if the two highlights are close and the range of each highlight is large, then the *images* will overlap and it is difficult to separate. In order to distinguish whether the two *images* can be distinguished, Rayleigh criterion is usually employed to judge.

According to the principle of geometrical optics, if there is no aberration, the imaging system can image perfectly [17]. The plane of the object is perpendicular to the optical principal axis of the relative imaging system. Each point on the surface will be imaged on the same plane in the image space perpendicular to the optical axis. And on the same image plane, the transverse magnification corresponding to each image point is equal. In fact, the diffraction of light exists objectively and will appear in the form of circular spots. According to the optical path of imaging, the image of the optical imaging system is first the diffraction pattern obtained by the circular aperture diffraction of the light emitted by the optical imaging system in the image space. Each point on the luminous object can be understood as a diffraction pattern diffracted by Fraunhofer circular aperture, and the central highlight of the diffraction pattern is Airy disk. When the distance between the two points is very small, the two diffraction points overlap after diffraction. When the two diffraction patterns overlap with maximum intensity, it is difficult to distinguish the two luminous points from their corresponding image points. Rayleigh gives a theory that can exactly distinguish the two image points, namely the Rayleigh criterion. As shown in Fig. 2, when the center of one Airy disk coincides with the edge of another, the two points are just distinguishable.

In optical imaging systems, the resolution power is the ability to distinguish the two adjacent points [18]. When the center of one Airy disk coincides with the first dark ring of another, the two images can just be distinguished. The angular resolution limit of the two images is

$$\Delta\theta = \frac{1.22\lambda}{D} \tag{6}$$

The distance between the centers of the two images is the resolution limit $\Delta L$.

$$\Delta L = \frac{D \times 1.22 \times \lambda}{d} \tag{7}$$

where $\lambda$ is the wavelength of light, $d$ is the diameter of the aperture of light, and $D$ is the distance between the object and the human eyes.
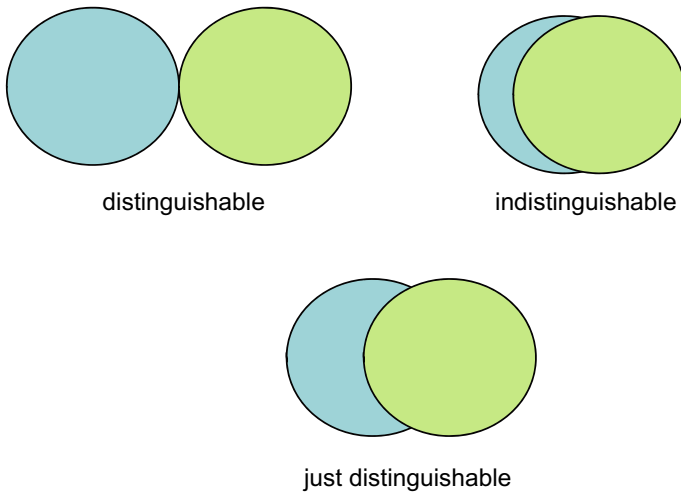
**Fig. 2.** Rayleigh criterion (diffraction resolution limit)

# 3    Micro-Information Magnification Experiments and the Results

## 3.1    Micro-Information Magnification Experiment

Considering human visual system, the most sensitive light wavelength for eyes is 550 nm, the distance between eyes and objects is 25 cm, and the diameter of the pupil is 3 mm in normal illumination condition. According to formulas (6) and (7), the minimum distance between micro-information that human eyes can distinguish is 0.056 mm. So the distance between the micro-information bands in this paper was all 0.056 mm.

According to moiré theory, the parameter relationship (i.e. period, frequency and angle) of the base layer, the revealing grating and the magnified moiré pattern is obtained. In this paper, the micro-information was selected as the letter *W* and the graphic *love*. The experimental steps are as follows:

1. The information *W* had a size of 33.261 mm × 25.253 mm, that was 100 pt. The size of information *love* was 35.979 mm × 35.979 mm. In CorelDraw, the messages of *W* and *love* were produced respectively.

2. The letter *W* and the graphic *love* were compressed vertically to form the micro-information, keeping their transverse width unchanged, that was 33.261 mm and 35.979 mm. Finally the vertical height of the micro-information of *W* and *love* were 2 mm and 4 mm respectively. The base layers were completed.

3. In this paper, the micro-information of *W* and *love* were magnified 13 times and 10 times respectively. According to formulas (4) and (5), the periods of the revealing gratings were 2.225 mm and 4.482 mm respectively. The revealing gratings matching with the base layers were completed in CorelDraw.

4. The matching revealing gratings were overlapped on the base layers to get the amplified moiré pattern information *W* and *love*. The magnification effect of micro-information is achieved.

## 3.2 Micro-Information Magnification Effect and Analysis

Figures 3 and 4 show the magnification effects of *W* and *love* respectively. The base layer was formed by compressing the target information vertically, as shown in Figs. 3 (a) and 4(a). The matching revealing gratings consisted of strip gratings, as shown in Figs. 3(b) and 4(b). By overlapping the revealing gratings on the base layers, the specified magnification effects of the micro-information can be obtained, as shown in Figs. 3(c) and 4(c).

Through observation, we can see that the base layer carries micro-information that is not recognizable for human eyes. After overlapping the matching revealing grating on the base layer, the pre-specified moiré pattern information can be magnified clearly. The information *W* with a height of 25.253 mm was compressed longitudinally, and the micro-information of 2 mm was obtained. Finally, the height of the moiré pattern *W* was amplified to 26.662 mm. In this process, the micro-information *W* was amplified



(a) *W* base layer          (b) *W* revealing grating          (c) *W* magnification effect
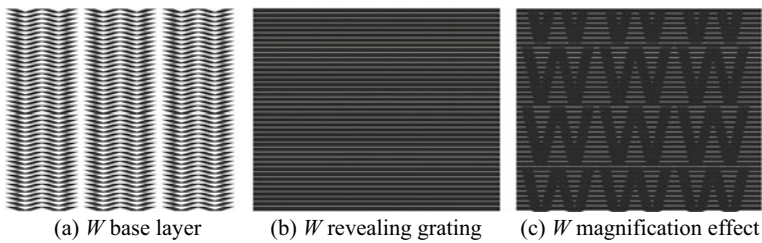
**Fig. 3.** The magnification effect of the micro-information of letter *W*



(a) *love* base layer          (b) *love* revealing grating          (c) *love* magnification effect
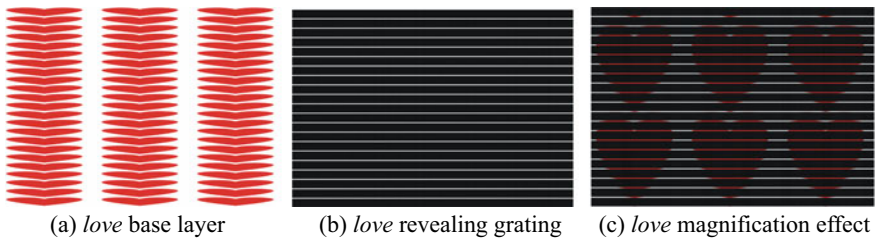
**Fig. 4.** The magnification effect of the micro-information of graphic *love*

13 times to obtain the enlarged moiré information that could be recognized by human eyes. After longitudinal compression, the information *love* of 35.979 mm was transformed to the micro-information with a height of 4 mm. Finally, the height of the amplified moiré pattern was 40.491 mm, and the *love* with a magnification of 10 times could be recognized by human eyes. Figure 3 is black text information, and Fig. 4 is

red graphic information. It proves that micro-information magnification technology is suitable for micro-information with different attributes, and the effect of information amplification is well.

The magnification of micro-information *W* and *love* is effective judged by human eyes subjectively. Next, we used objective evaluation method of cosine similarity to evaluate the two micro-information enlargement effect. Cosine similarity [19, 20] is the cosine value of the angle of two vectors in high-dimensional space, which is not affected by rotation, enlargement and reduction of reference coordinate system, and normalizes the length of vectors. The smaller the angle is, the greater the cosine value is. Its value has nothing to do with the length of the vector, but depends on the size difference of the components in each dimension. For two vectors *x* and *y*, the expressions of cosine similarity are

$$S(x, y) = \frac{(x, y)}{\|x\|\|y\|} = \frac{\sum\limits_{i=1} x_i y_i}{(\sum\limits_{i=1}^{n} x_i^2 \sum\limits_{i=1}^{n} y_i^2)^{1/2}} \tag{8}$$

Based on the target moiré pattern, the objective evaluation of the magnification of the micro-information *W* and *love* is shown in Table 1.

From Table 1, we can see that the cosine value of the micro-information *W* is 0.9994, the cosine angle is 1.9211°, the cosine value of micro-information *love* is 0.9580, and the cosine angle is 16.6624°. The cosine values of the amplification experiments of the two kinds of information are both close to 1, that is the micro-information magnification effect is very ideal. Compared with the target information, the magnification of the micro-information is perfect, which basically meets the

**Table 1.** Cosine similarity of micro-information magnification effect

|  | Cosine value | Cosine angle (°) |
|---|---|---|
| W | 0.9994 | 1.9211 |
| love | 0.9580 | 16.6624 |

amplification requirements. Although the cosine value of the graphic *love* is slightly smaller than that of the letter *W* because of the complexity of the figure is higher than that of the text, but the cosine value of *love* also reaches 0.9580, which magnification is very close to the target information. In this paper, the results of objective evaluation and subjective evaluation are consistent. For the micro-information of different attributes, the magnification is effective.

# 4  Conclusions

Based on moiré theory, this paper studies the relationship of the base layer, the revealing grating and the magnified moiré in micro-information magnification technology and introduces human visual system to application of this technology in printing field. Firstly, the target information is produced according to moiré theory. The target information is compressed vertically based on human visual system to get the micro-information to be enlarged, so that the base layer is obtained. Secondly, according to the relationship of the base layer and the revealing grating, the matching revealing grating is completed. The revealing grating in this paper is a band grating which is propitious to one-dimensional information amplification. Finally, by overlapping the revealing grating on the base layer, the magnified moiré pattern is presented and the magnification effect can be achieved. In this method, the attributes of magnified moiré pattern can be customized, and the micro-information can be enlarged from invisible to visible. Because of the customization of the magnified moiré pattern, the parameters of micro-information are difficult to leak, which resists the plagiarism and duplication of illegal elements and improves the anti-counterfeiting performance of printing. This technology increases the added value of printing products and will have a long-term development and application.

# References

1. Cadarso VJ, Chosson S, Sidler K et al (2013) High-resolution 1D moirés as counterfeit security features. *Light: Sci Appl 2*(7):e86
2. Cadarso VJ, Chosson S, Sidler K et al (2013) Micro-optical 1D moirés as anti-counterfeiting features. Solid-state sensors, actuators and microsystems (TRANSDUCERS & EURO-SENSORS XXVII), 2013 transducers & eurosensors XXVII: The 17th international conference on IEEE
3. Walger T, Hersch RD (2015) Hiding information in multiple level-line moirés. *Proc. ACM DocEng Conf*, pp 21–24. https://doi.org/10.1145/2682571.2797078
4. Wei WZ, Su S, Long YG et al (2017) Design methodology for moiré magnifier based on micro-focusing elements. Opt Express 25(25):31746–31757
5. Theocaris PS (2013) Moiré fringes in strain analysis. Thomas Nelson, London, pp 146–177. https://doi.org/10.1115/1.3423467
6. Wen XS, Ping XZ (2010) Application of moiré effect in anti-counterfeiting printing. Packag Eng 31(23):99–101
7. Ying HX, Zong CM, Qin HC (2006) Application of moiré fringes. J Nanjing Inst Eng: Nat Sci Ed 4(1):60–65
8. Munoz-Rodriguez JA, Rodriguez-Vera R (2004) Image encryption based on moiré pattern performed by computational algorithms. Opt Commun 236(4):295–301

9. Sheng H, Kang JW (2007) Optical watermarking for printed document authentication. IEEE Trans Inf Forensics Secur 2(2):164–173
10. Feng YL, Long XL, Fa WQ et al (2008) A further study on an optical watermarking scheme. In: 9th international conference on signal processing (ICSP), 2008, IEEE, pp 2213–2216. https://doi.org/10.1109/icosp.2008.4697588
11. Amidror I (2003) Glass patterns as moiré effects: new surprising results. Opt Lett 28(1):7–9
12. Hersch RD, Chosson S (2004) Band moiré images. ACM Trans Graph (TOG), ACM 23 (3):239–247
13. Chosson S, Hersch RD (2010) Model-based synthesis of band moiré images for authenticating security documents and valuable products. USA, U.S. Patent 7751608.2010-7-6, pp 1–40
14. Amidror I, Hersch RD (2010) Mathematical moiré models and their limitations. J Mod Opt 57(1):23–35
15. Yue ZC, Xia W, Feng XZ, Qi WJ (2012) Evaluation method of false color fusion image quality based on human visual system. J Photonics 41(4):451–455
16. Kui FZ (2008) The minimum resolution angle of human eye. J Tangshan Teach Coll 30 (5):67–69
17. Zhi ML (2013) Rayleigh criterion and the resolution ability of optical system. J Kaifeng Inst Educ 33(4):196–197
18. Xing F (2007) The applicable conditions of Rayleigh criterion. J Baoshan Teach Coll 26 (5):35–36
19. Mikolajczyk K, Schmid C (2005) A performance evaluation of local descriptors. IEEE Trans Pattern Anal Mach Intell 27(10):1615–1630
20. Yu Z, Dong YL, Zhao J (2009) Measurement of vector similarity. Acoust Technol 28 (4):532–536

# Research on Digital Watermarking Technology Based on MATLAB

Wenyu Li[✉] and Heng Zhang

College of Light Industry Science and Engineering, Shaanxi University
of Science and Technology, Shaanxi, China
liwenyu@sust.edu.cn

**Abstract.** With the rapid development of digital multimedia technology and Internet technology, the copyright protection of multimedia products has become a very important and challenging research topic at present. Digital watermarking technology is an effective method to realize the copyright protection of digital products, and it has become a hotspot in the field of information protection and information hiding. In this paper, DWT and LSB algorithm are adopted to realize the embedding and extraction of digital watermark through Matlab, after comparing the digital watermarking image under the Gaussian noise, salt and pepper noise, cutting and rotating attacks, the effect of two algorithms to extract digital watermarking image, the results show that: NC values (0.5067, 0.7584, 0.2301, 0.1330) and subjective ratings (3, 4, 2, 2) of DWT algorithm are superior to LSB algorithms (NC values are 0.0965, 0.7005, 0.5507, 0.0567, and subjective ratings are 1, 4, 3, 1). The DWT algorithm has better attack resistance and provides reference for the application of digital watermarking.

**Keywords:** Digital watermark · MATLAB · DWT · LSB

## 1 Introduction

With the development and popularization of network communication technology, more and more media content has been turned into digital. However the problem of information protection is becoming more and more prominent, and it is related to the progress of information [1]. Due to its invisible and safe features, digital watermarking technology has good application value in copyright protection and digital authentication, and has become an important method of anti-counterfeiting identification [2]. At present, the study of discrete cosine transformation algorithms [3, 4] (DCT) has matured, while the discrete wavelet transformation (DWT) algorithms [5] and the least significant bit (LSB) algorithm [6] has also been found. Therefore, in order to speed up the application of digital watermarking technology, it is necessary to provide more reference data for the digital watermark extraction effect of different algorithms. Based on the DWT and LSB algorithms, the embedding and extraction of watermark images is realized through MATLAB, and the anti-attack performance of the two algorithms is analyzed and compared in different ways by attacking the images embedded after watermarking in this study.

## 2    Digital Watermarking Algorithms and Evaluation

### 2.1    Digital Watermarking Algorithm

DWT algorithm is a method to achieve image watermarking based on discrete wavelet transformation domains. This algorithm makes full use of the characteristics of wavelet transformation. Firstly pyramid decomposition is applied to the original image. Then the watermark image is scrambled and pyramid decomposed through Arnold transformation. Thus the corresponding watermark information can be embedded in the medium and high frequency after multi-resolution decomposition. The algorithm can match the characteristics of human vision system well. It is easy to adjust the watermark embedding strength to adapt to the visual characteristics of the human eye, so as to better balance the contradiction between the watermark robustness and invisibility.

LSB algorithm is a typical hiding algorithm of the spatial domain information. The algorithm generates a random signal by using a certain key m sequence generator, then arranges the two-dimensional watermark signal according to certain rules, and inserts the corresponding minimum watermark signal into the original image pixel value according to certain rules. This algorithm is less robust, but as a method of hiding a lot of information data, LSB still occupies an important position in covert communication [7].

### 2.2    Realization and Evaluation of Digital Watermark

The MATLAB platform is used in this study. The host image is a standard Lena grayscale image (512 * 512), shown as Fig. 1, and the watermark image is a gray scale image of the emblem of Shaanxi University of Science and Technology (64 * 64), shown as Fig. 2.



**Fig. 1.** Host image



**Fig. 2.** Watermark image

In order to evaluate the hiddenness of the digital watermark algorithm and the robustness under attack, subjective and objective evaluation are adopted in this study. The subjective evaluation has 5 grades ranging from 1 (Poor) to 5 (Excellent) based on the ITU-R Rec.500 quality rating standard. Objective evaluation uses NC (Normalized correlation) coefficient (i.e. similarity measurement) to measure the degree of similarity between extracted watermark and original watermark.

### 2.3   Effect of Watermark Embedding and Extraction Without Attacks

The source files of DWT or LSB are created in MATLAB by encoding (The source file contains the calculation of NC value). Then run the source file and process the image. Figure 3 shows the effects of watermark embedding and extraction based on DWT and LSB.
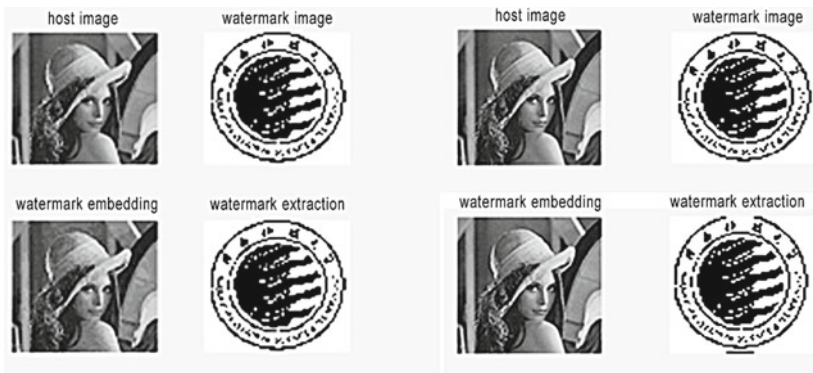


**Fig. 3.** Effects of digital watermark embedding and extraction based on two algorithms

As can be seen from Fig. 3, both DWT and LSB algorithms have good invisibility without outside interference or attack, and the images watermark embedded inside has almost no difference from the original images, while the watermark image extracted by the two algorithms is similar to the original watermark image.

### 2.4   Quality Evaluation Under Different Attack

In this study, the image containing watermark is attacked by gaussian noise (The overlay mean is 0.1 and the variance is 0.004), peppernoise (percentage is 0.04), cutting and rotation, and the extracted watermark is evaluated by subjective and objective.

Figure 4 shows the effects of digital watermark extraction after four attacks in DWT algorithm.

As can be seen from Fig. 4: there are some differences between the attacked image and the original image, and the watermark extracted from the images also has some distortion. The watermark extracted after pepper noise attacking is the best (NC = 0.7584), then the gaussian noise attacking's (NC = 0.5067), and the worst is the watermark image after rotating attack (NC = 0.1330).

**Fig. 4.** The effects of digital watermark extraction after four attacks in DWT algorithm. Among them, **a** is the watermark image and watermark extract image of the DWT algorithm, **b–e** are the results of the images containing watermarks after applying Gaussian noise attack, pepper noise attack, cutting attack, rotating attack and the corresponding images watermark extraction

Figure 5 shows the effects of digital watermark extraction after four attacks in LSB algorithm.
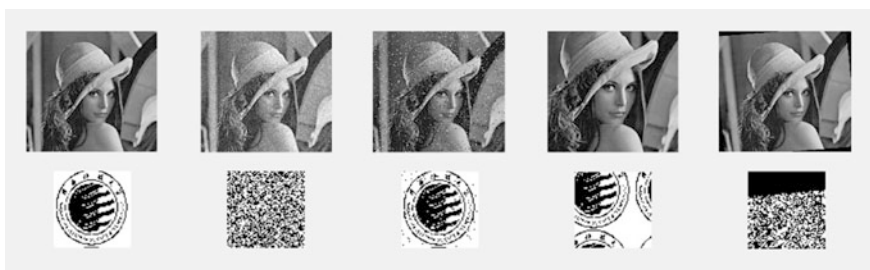


**Fig. 5.** The effects of digital watermark extraction after four attacks in LSB algorithm. Among them, **a** is the watermark image and watermark extract image of the LSB algorithm, **b–e** are the results of the images containing watermarks after applying Gaussian noise attack, pepper noise attack, cutting attack, rotating attack and the corresponding images watermark extraction

As can be seen from Fig. 5: there are some differences between the image with watermark under attack and the original image, and the watermark extracted will also have some distortion. The watermark extracted after pepper noise attacking is the best (NC = 0.7005), then the cutting attacking's (NC = 0.5507), and the worst is the watermark image after rotating attack (NC = 0.0567).

Figure 6 is a diagram showing the relationship between the NC value of watermark and the attack mode of the two algorithms, and Fig. 7 is a diagram showing the relationship between the subjective parameters of watermark and the attack mode of the two algorithms.

In this study, watermark embedding and extraction are implemented on MATLAB by two different algorithms, and the watermark extraction operation is carried out after attacking the embedded watermark image. As can be seen the results are different. Under the interference of Gaussian noise and pepper noise, the NC value of DWT
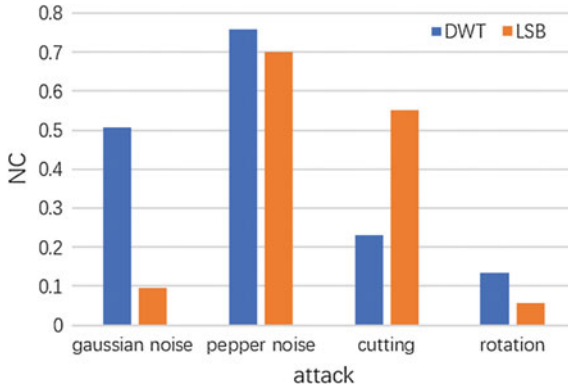
**Fig. 6.** Relationship between the NC value of watermark and the attack mode of the two algorithms
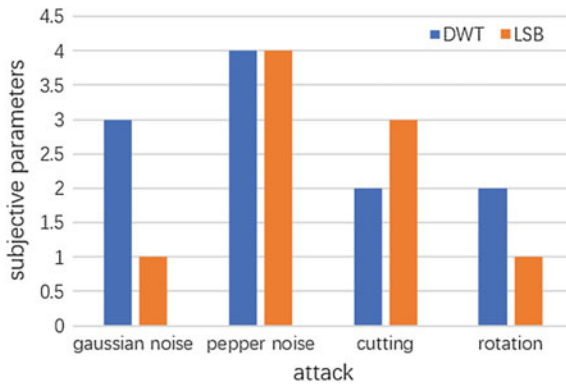


**Fig. 7.** Relationship between the subjective parameters of watermark and the attack mode of the two algorithms

algorithm is better than that of LSB algorithm, and the subjective evaluation level is higher. In terms of cutting and rotation, both algorithms are less practical, but DWT is still relatively easy to accept. In general, the DWT algorithm is superior to the LSB algorithm, and its resistance to noise attack is better than that of LSB algorithm.

## 3   Conclusions

In this study, a practice study is carried out on the still image digital watermarking technology based on the lowest effective bit (LSB) and discrete wavelet transformation (DWT), and the simulation of watermark embedding and extraction is realized by MATLAB, and robustness of these two algorithms are evaluated by Gaussian noise, pepper noise, cutting attack, and rotation attack. The experimental results can well reflect the advantages of DWT.

# References

1. Yu S (2009) Research status and development of digital watermarking technology. Popular Sci Technol 12:210
2. Zeng T, Yu Z (2019) Digital watermark detection method for portable device. Packag Eng 5:277–282
3. Zhang Y, He D, Li N (2018) Research on digital watermarking technology based on DCT algorithm. Precise Manufact Autom 4:14–16
4. Hu G, Wei J, Tang Y (2018) An improved frequency domain digital watermarking algorithm based on DCT transform. J Commun Univ Chin (Science and Technology) 6:19–27
5. Zhan H, Mao L (2018) Join digital watermarking algorithm based on NSCT-DCT-DWT-SVD. Comput Appl Softw 3:309–315
6. Qin L (2016) Digital watermark LSB algorithm with Delphi. Inf Commun 10:33–34
7. Ma J (2009) MATLAB implementation based on LSB information hiding algorithm. Guang xi J Light Ind 15:69

# A Summary of Thermosentive CTP Plate and Its Application and Research in China

Hongli Zhang, Zhongxiao Li[(✉)], Lu Wang, and Yuguang Feng

School of Printing and Packaging Engineering, Beijing Institute of Graphic
Communication, Beijing, China
lizhongxiao@bigc.edu.cn

**Abstract.** With the advent of the digital age, computer-to-plate (CTP) technology has become more and more important in printing technology. At present, CTP plates used in the industry are classified into photosensitive CTP plates and thermal CTP plates. The thermal CTP plate has the advantages of daylight operation, low price, fast plate-making speed, high quality printing and environmental friendliness, which has become the mainstream of CTP plate development. Processless thermal CTP plate is likely to be the direction and the focus of future research and development.

**Keywords:** CTP technology · Thermal CTP plate · Processless CTP plate

## 1 Introduction

Nowadays, CTP technology has become the mainstream of printing technology. CTP technology is a technology that directly outputs graphic information to a printing plate using a computer program [1]. Generally, CTP plates can be divided into two types, i.e., the photosensitive type and the thermal sensitive type. The thermal CTP plate is imaged by the heat generated by infrared laser exposure at 830 nm, which can be operated in a bright room. As a result, thermal CTP plate products have gotten the recognition and development of printing industry. With the continuous development of thermal CTP plate technology, the green (or environmentally-friendly) thermal CTP plate seems attracting more and more attention in the CTP plate industry. From a domestic prospective, the application of processless CTP plate in China started late. However, a series of environmental protection plans were recently issued by our country, which promoted the development and application of processless CTP plates. Domestic products mainly include TP-G and TD-W processless CTP plates of Lucky Huaguang Graphics, FIT eCO CTC processless plates of Chengdu Xintu and KTP-NP processless CTP plates of Zhejiang Konita New Materials [2, 3].

## 2    The Development of Thermal CTP Plates

### 2.1    Thermal CTP Plates

At Drupa 1995, the first thermal plate, Kodak Polyphoto 830 nm Infrared Light Sensitive Direct Imaging (DITP) thermal plate was introduced [4]. The combination of this plate and the Creo platesetter has driven a major transformation of the printing plate from visible light system to heat sensitive system. In 2000, the application of preheating type thermal CTP plate was started, and then there was a preheat-free CTP plate. Until the advent of the processless CTP plate in 2008, which made the thermal CTP plate occupied a dominant position in the offset plate market [5].

The imaging process of the thermal CTP plate involves physical or chemical changes in the imaging layer triggered by heat generated through an 830 nm infrared laser, such as thermal ablation, thermal polymerization, thermal cross-linking, and thermal dissolution [6]. When the plate is imaged by infrared laser irradiation, the exposed region of the heat-sensitive layer becomes either hardened or easily soluble to form a negative or positive pattern respectively. At present, infrared laser imaging devices have been widely used in commercial applications, and the commonly used imaging devices including inner drum imagesetters, outer drum imagesetters, and Flatbed imagesetters [7].

### 2.1.1    Thermal CTP Plate that Needs Heat-Treatment Before Development

The negative thermal crosslinking plate is a typical thermal CTP plate that needs to be heated for a period of time before development. The heat treatment process is helpful to further enhance the cross-linking degree of the exposed area of the plate. The plate consists of a roughened aluminum base and a thermal sensitive coating. The thermosensitive coating contains linear phenolic resin, hydroxyl-methyl resin, cross-linking agent, development promoter, stabilizer, infrared absorbing dye and photoluminescence acid agent. The imaging process is divided into three steps: exposure, heat-treatment and the development step [8].

Once the thermal coating is exposed, the infrared absorbing dye absorbs infrared light energy and converts light energy into heat energy, which raises the temperature. When the temperature reaches a certain threshold, the acid release agent is decomposed to generate acid, and the acid acts as a catalyst. The linear phenolic resin and the hydroxyl-methyl resin are cross-linked to a certain extent under the action of acid and heat, forming a latent image, and then applying high temperature (i.e., prebaking) to accelerate the cross-linking reaction of the resin layer at the exposed portion. When developing, the exposed portion is insoluble in the alkaline developing solution to form a graphic portion; and the unexposed portion is soluble in the alkaline developing solution, and is washed away to form a blank portion [9].

### 2.1.2    Thermal CTP Plate Without Prebaking Treatment

The positive-type thermal CTP plate based on heat-induced dissolving improvement is prebaking-free thermal CTP plate. The plate is composed of a roughened aluminum plate base and a heat sensitive layer, in which the heat sensitive layer includes film-

forming resin, infrared absorbing dye, dissolution inhibitors, photo-thermal acid generating source and surfactants. The imaging process only needs exposure and development through 830 nm infrared laser diode or 1064 nm FD-YAG laser [10].

Before exposure, a hydrogen bond between the molecules is formed between the dissolution-promoting compound and the film-forming resin in the composition, which has a resistance to the thermosensitive imaging system. When exposed, the infrared absorbing dye converts the infrared laser light energy into thermal energy, and the generated heat causes the photo-thermal acid source to release a large amount of proton acid. Under the action of proton acid, the dissolution-promoting solvent is decomposed and the hydrogen bond is rapidly destroyed. The phenolic hydroxyl group of the phenolic resin is released, so that the solubility difference between the exposed region and the non-exposed region is enlarged. This will facilitate the development of the plate and improve the imaging performance of the plate. Therefore, under the action of the infrared laser, the exposed part of the plate is decomposed and reacted with alkali. When developed with the alkaline developer, the aluminum plate base is exposed, and the hydrophilicity of the aluminum plate made it become the blank portion after development. The coating of the unexposed portion is not alkali-soluble and will become a graphic portion after development [11].

## 2.2 The Processless Thermal CTP Plate

### 2.2.1 General Classification of Processless Thermal CTP Plates

The processless CTP plate first appeared at Drupa 2004, and an official chemical-free CTP plate product was launched at Drupa 2008. Then, at Drupa 2016, processless CTP plate has gradually become practical and mature, and gradually entered the stage of large-scale application [12]. Broadly speaking, the processless thermal CTP plate refers to plate-making without any subsequent processing steps. After laser imaging, it can be directly used for printing without development, washing and other processes, which is the real sense of processless CTP plate. In the narrow sense, processless CTP plate means that the plate does not need to be chemically developed after exposure on the direct plate-making machine, but there are still some non-chemical treatment processes, such as water development, coating of protective adhesive, and removal of ablation disposal and other work.

According to the different imaging methods, processless CTP plate can be divided into: thermal-ablation-type, polarity-switching-type, thermal-melt-type and thermal-crosslinking-type [13].

(1) Thermal-ablation-type. When the plate is exposed, the exposed portion of the image coating is melted under the high infrared laser energy radiation, thereby exposing the plate base, so that the plate can exhibit hydrophilic and hydrophobic portions without developing process. The impurities produced after laser ablation can be removed by the action of water or fountain solution. The most representative product is the laser ablation CTP plate developed by Agfa. The plate has an oleophilic metal layer on the aluminum plate, and the exposed metal layer will melt into beads under higher exposure energy radiation, resulting in a decrease in

adhesion to the aluminum plate. Therefore, the development process is not required, and the aluminum plate base becomes the non-graphic part [14].

(2) Polarity-switching-type. Before exposure, the substrate is usually hydrophilic (or hydrophobic), and after being exposed by infrared laser scanning, the exposed portion has a physical or chemical polarity switching, so that the part is hydrophilic before exposure (or hydrophobic) becomes hydrophobic (or hydrophilic), forming a graphic part (or non-graphic part). Therefore, the exposed printing plate can be directly used without further processing.

We also prepared an amine oxide polymer through the modification reaction of epoxy phenolic resin. It is water soluble and thermo-sensitive. But it readily became completely water insoluble after heat-treatment at 170 °C for a short period of time. An image-recording layer was prepared with a coating solution consisting mainly of the amine oxide polymer and an infrared absorbing dye (830 nm). The layer can be exposed by an infrared laser. Due to the heat generated during the exposure step, heat-induced decomposition of the amine oxide polymer of the exposed areas (corresponding to the printing areas of the printing plate) will occur so as to form a hydrophobic phase. However, the non-exposed areas remain hydrophillic and can be easily removed from the support by water. The amine oxide polymer might be used for making a negative-working, heat-sensitive lithographic printing plate precursor [15].

(3) Thermal-melt-type. A coating (containing thermoplastic latex particles) is disposed on an aluminum plate substrate which is treated by graining (or roughening), anodizing and sealing processes. When exposed, the hydrophobic thermoplastic polymer particles may fuse or coagulate due to the heat generated during the exposure step, forming a hydrophobic phase which corresponds to the printing areas of the printing plate. Coagulation may result from heat-induced coalescence, softening or melting of the thermoplastic polymer particles. However, the latex particles in the unexposed area remain separated and can be washed away by water, forming the non-image area of the plate [5].

A typical chemistry-free CTP plate, Agfa Graphics' Azura TE, is based on the so-called ThermoFuseTM technology, which works with a single-layer water-based coating containing latex pearls. In our lab, narrowly distributed IR dye-containing polymer nanoparticles were prepared through miniemulsion polymerization and used for producing a latex coating. Negative image was obtained through imagewise exposure by IR laser radiation followed with water developing. This kind of coating based on the IR dye-containing polymer particles can be used for developing chemical-free thermal CTP plate [16].

(4) Thermal-crosslinking-type. This kind of lithographic printing plate is negative-working, which has a thermal cross-linking layer on a support. Generally, the imageable layer comprises free radical polymerizable compounds, free radical polymerization initiators, polymers having free radical polymerizable groups, infrared absorbing dye and other additives [17]. When exposed by infrared laser, the IR-absorbing dye converts IR-light energy into heat. As a result, crosslinking reaction of the precursor in the exposure area occurs and the exposed parts of the image-recording layer cannot be developed off press. Non-exposed parts of the

imageable layer of the plate precursor can be removed with a lithographic printing ink, a fountain solution, or both while the imaged precursor is on the printing press. So, this kind of CTP plate precursor is on-press developable and exhibits excellent printing performance [18].

### 2.2.2 Existing Problems and Application Experience of Processless CTP Plate

(1) Operation. In the process of plate-handling, plate-making and plate-mounting, the operator needs to wear gloves to avoid directly touching the surface of the plate and prevent fingerprints from being left on the plate surface. Otherwise, it will have adverse effects on printing quality [19]. Moreover, in order to reduce the damage to the plate, the lining paper should be taken out together with the plate

(2) Storage and transportation. After unsealing, the unused plates should be stored according to the requirements provided by the manufacturer. The plates should be kept away from light, especially natural light natural light. The recommended storage and transportation conditions are as follows: temperature 20–24 °C, humidity 30–60% RH [20].

(3) Scratch of plate. Scratches, white spots or dirty spots may occur due to improper operation. Therefore, the backing paper should be retained during use to reduce scratches. In the process of plate handling, due to the relative movement between the plates, the thermal coating may be rubbed, causing damages to the coating. For unavoidable scratches, it can be repaired using a cleaning solution or a developer, etc.

(4) Low printing press life. Low printing press life is the biggest problem with processless CTP plates. In the plate making process and printing process, due to the wrong operation of the operator, the influence of the external environment or improper adjustment of the instrument might reduce the printing durability. The first thing to do is to improve the sensitivity of the plate. In addition, the operator should make careful preparation prior to printing, regularly check and clean the equipment, and strictly control the age conditions to minimize the impact on the printing durability of the plate [21].

(5) On-press development. On-press development stability is affected by many factors, including temperature, pressure, ink, developer and so on. So, the printing process conditions should be optimized.

(6) The cost. Although the price of the processless CTP plate is about 15–20% higher than that of the traditional CTP plate, the advantages of environmental protection and easy operation offset the cost increase [22].

## 3  Conclusions

Thermal CTP plates have many advantages, including daylight operation which improves the safety of operation and reduces the harm to the operator, developing process-free which is beneficial to environmental protection and cost reduction, higher

print quality, faster plate making speed, more stable image quality, good printability and so on. Thermal CTP plate is the inevitable trend of plate technology. With the increasing demand for environmental protection, processless CTP plate is becoming the focus of CTP plate technology. Although processless CTP plate is still in the developing stage in China, it is expected to mature in 2–4 years and gradually replace the traditional CTP plates. It can be predicted that the processless CTP plate with many environmental advantages will be the ultimate development direction of CTP plate. Green plate making technology should be an important part of green printing.

# References

1. Jiang DS, Wu Y (2012) Based on image processing of CTP and CTF dot area coverage. Appl Mech Mater 200:645–648
2. Zhang BH, Cui HL, Xue XW, Shen PP et al (2013) Preparation and properties of thermo-sensitive resin for processless CTP plate. Adv Mater Res 666:123–129
3. Adamson JD, Bennett PAR, Potts RM (2017). U.S. Patent No. 9,586,392. U.S. Patent and Trademark Office, Washington, DC
4. King T (2010) CTP-trends and technology: part 2: computer-to-plate. Graphix 9(3):31–34
5. Xiong SZ, Quan ZY, Xian YS (2003) The progress of processless CTP plate. Photogr Sci Photochem 21(4):303–315
6. Cao J, Zhang WM, Pu JL (2012) Study on the double-layer structure thermal imaging system. Appl Mech Mater 262:440–443
7. Tamaki E, Hashimoto Y, Leung OS (2004) Computer-to-plate printing using the grating light valve (tm) device. Proc SPIE Int Soc Opt Eng 5348:89–97
8. Zhang Y, Zhang C, Zhang H (2005) The thermal cross-linking plate with high quality for CTP with laser. Proc SPIE Int Soc Opt Eng 5645:267–274
9. Zhao DD, Xue JA, Wang ZD et al (2009) Development and application of platform of process control system for plate heat-treatment. J Northeast Univ 30(10):1441–1444
10. Sha XZ, Pang YL, Zou YQ (2013) Synthesis of novel active ester ether resin and its effects on positive thermal CTP plates. Chin Sci Bull 58(13):1536–1542
11. Wang WW, Li ZX, Feng YG et al (2013) Preparation of an *in situ* crosslinked polymer coating and a double-layered thermal CTP plate. Adv Mater Res 781–784:458–462
12. Xing JF, Zhang J, He LJ (2012) The contact simulation of CTP imaging drum and plate on ansys. Appl Mech Mater 151:484–489
13. Oya T, Kunita K, Araki K et al (2016) Lithographic printing plate precursor and lithographic printing method. Oncol Rep 25(5):1271–1277
14. Leahy S, Lai Y (2015) Regenerating silicon biosensors through thermal ablation with a hot plate. Sens Bio-Sens Res 6:25–27
15. An L, Yu B, Pu J et al (2016) Synthesis and properties of a water-soluble thermo-sensitive resin with tertiary amine oxide substituent in the side chain. Polym Bull 73(1):53–64
16. An L, Cai Z, Wang W, Pu J et al (2014) A thermo-sensitive imaging coating derived from polymer nanoparticles containing infrared absorbing dye. Eur Polymer J 52:166–171

17. Taguchi Y, Yoshida S, Corporation F (2012) Process for making lithographic printing plate, developer for lithographic printing plate precursor, and replenisher for lithographic printing plate precursor development. Oncol Rep 25(5):1271–1277
18. Nguyen MT, Nguyen TS, Luu TD et al (2018) U.S. Patent Application. No. 15/701, 626
19. Wariishi K (2019) U.S. Patent Application. No. 10/166, 755
20. Fan C (2000) Phase change type CTP plate processless CTP technology. Beijing Inst Graph Commun 8(2):60–64
21. Tao T, Yung N, Ying Z et al (2019) U.S. Patent Application. No. 16/325, 584
22. Chen W, Li YM, Zhang XJ (2012) Determination of technical parameters in CTP process and its image quality. In Appl Mech Mater 197:462–466 (Trans Tech Publications)

# Data Control Method for Printing Quality Based on Polynomial Regression

Jinghuan Ge[✉], Enyin Fang, and Dongwen Tian

Department of Printing and Packaging Engineering, Shanghai Publishing and
Printing College, Shanghai, China
sytuprint@126.com

**Abstract.** With the progress of printing technology, the requirements for the
quality of prints have been continuously improved. The objective quality control
method based on measurement data is beginning to gradually replace the tra-
ditional subjective quality evaluation method. Now, the gray balance-based G7
printing quality control method and the TVI-based (tone value increase) PSO
printing quality control method are two mainstream technologies in the printing
industry, while both of them have advantages and disadvantages for the printing
enterprises. For example, the disadvantages include too many controlling
parameters and too complicated implementation processes. So through this
study, the polynomial regression is used to fit the printing dot gain curve, and
the coefficient of determination (R-Square) is introduced as an important eval-
uation parameter. The printing quality is controlled by the measurements from
the solid patches with process inks and the 50% gray balance patch as well as
the coefficient of determination. The experimental results show that the new
method can simplify the traditional quality control method and greatly improve
the printing production efficiency. It can also be the guidance in the actual
printing process.

**Keywords:** Printing quality · Data control · Polynomial regression ·
Coefficient of determination

## 1 Introduction

In recent years, due to the improvement of the printing technology and the use of
advanced printing equipment, printing manufacturers have realized that the process
control is more important than the final inspection of the products' quality. Therefore,
digitization and standardization have been put on the agenda. Also they become an
important topic for the scientific research, technology development and production
management [1].

Standardization of printing process control has become an effective way to improve
product quality and production efficiency in the printing industry. Based on ISO 12647
or ISO 15933 standards, many international and domestic organizations have intro-
duced specific implementation methods to help printers achieve ISO quality standards.
Among them, the G7 process control method of IDEAlliance from the United States
and the PSO (Process Standard Offset) method of FOGRA from Germany have been

promoted well. They also have been adopted and implemented by thousands of printing companies around the world [2]. However, all the above process control methods require many parameters to be controlled, and the implementation process is much more complicated. Many small and medium-sized printing enterprises have low production management levels and cannot fully implement professional printing quality process control methods.

## 2 The Data Control Method and Practice for Printing Quality

In this paper, a relatively simple and effective method for printing quality data control is proposed. The measured spectral data of the self-defined strip which includes the substrate and 9 color patches are used as the main target of quality monitoring, as shown in Fig. 1. Also the coefficient of determination ($R^2$) in the polynomial regression method is used as a monitoring parameter for evaluating whether the whole printing process is in a normal status [3]. The value of the coefficient of determination is calculated by the TVI (tone value increase) curve measured from the 4 color scales in the prints, as shown in Fig. 2. Therefore, the printing quality is reasonably controlled.



**Fig. 1.** The quality control strip with the substrate and 9 color patches
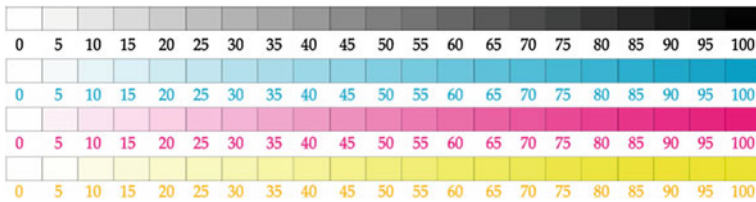


**Fig. 2.** The 4 color scales

In Fig. 1, there are 4 solid process color patches (C100, M100, Y100, K100), 4 process color patches with 50% dot coverage (C50, M50, Y50, K50), and 1 grey balance patch (C50, M40, Y40) in the control strip. In Fig. 2, there are different patches for the 4 process colors, and the dot coverage for each patch is written at the bottom.

The specific implementation of this method is as follows:

**Fig. 3.** The test printing sample

Firstly, after linearizing the CTP (computer to plate) equipment, the plates with lots of test targets is obtained, then we get the printed sheets as shown in Fig. 3.

Secondly, according to the measurements of the spectral data of the CMYK solid color patches from the control strip of Fig. 1 on the print sample, we can predict the four-color solid density corresponding to the ISO target value by the Beer–Lambert law [4]. The ISO target values for the different substrates are shown in Table 1. Then the CMYK solid color patches on the sheets are printed to the target value. It means the thickness of the ink film for the prints is just right.

**Table 1.** The ISO color target values for the different substrates

| CRPC | Substrate | | | Process Color (Solid) | | | | | | | | | | | |
|---|---|---|---|---|---|---|---|---|---|---|---|---|---|---|---|
| | | | | Cyan | | | Meganta | | | Yellow | | | Black | | |
| | $L^*$ | $a^*$ | $b^*$ | $L^*$ | $a^*$ | $b^*$ | $L^*$ | $a^*$ | $b^*$ | $L^*$ | $a^*$ | $b^*$ | $L^*$ | $a^*$ | $b^*$ |
| 1 | 85 | 1 | 5 | 59 | −24 | −26 | 56 | 48 | 0 | 80 | −2 | 60 | 37 | 1 | 4 |
| 2 | 87 | 0 | 3 | 57 | −28 | −34 | 52 | 58 | −2 | 82 | −2 | 72 | 30 | 1 | 2 |
| 3 | 96 | 1 | −4 | 60 | −26 | −44 | 56 | 61 | −2 | 89 | −3 | 76 | 32 | 1 | 1 |
| 4 | 89 | 0 | 3 | 55 | −36 | −38 | 47 | 66 | −3 | 83 | −3 | 83 | 23 | 1 | 2 |
| 5 | 92 | 0 | 0 | 57 | −37 | −44 | 48 | 71 | −4 | 87 | −4 | 88 | 19 | 0 | 1 |
| 6 | 95 | 1 | −4 | 56 | −37 | −50 | 48 | 75 | −4 | 89 | −4 | 93 | 16 | 0 | 0 |
| 7 | 97 | 1 | −4 | 54 | −42 | −54 | 47 | 79 | −10 | 90 | −4 | 103 | 14 | 0 | 0 |

Thirdly, Using the G7 or PSO printing process control method, the printing dot compensation curve is obtained and loaded into the RIP of the CTP plate making process, re-plated and printed on the machine, and the CMYK solid color patches on the new printing sample is printed to the target value [5].

Finally, the quality control software such as Curve or Pressign is used to evaluate the quality of the P2P (proof to print) test target or four-color scale area in the new

printed samples. If the target is not reached, repeat the previous steps until the desired goal is achieved.

All the above is a standardized plate making and printing correction process. It is also the necessary step to achieve standardization. In a printing company, it is more important to set the standardized printing process control method as the normal state of enterprise quality management.

Taking the G7 method as an example, in general, it is necessary to measure the quality of the prints by measuring hundreds of color patches on the P2P test target and using professional software [6]. However, in printing production, such an approach is not only inefficient, but also causes a large waste. Therefore, by directly evaluating the measurement of the nine patches in the control strip, the simple and effective printing quality data can be detected, so that the prints are monitored in real time. Among them, the first four solid color patches are mainly for monitoring the amount of ink for the prints. The middle 4patches are mainly to monitor the dot gain of the middle tone area, and the last 50% gray balance patch is the most important one which should be monitored. Also the standard data of this patch is calculated based on the measurement of the substrate.

In addition to the quality monitoring of the printed samples, it is necessary to periodically monitor the status of the printing equipment, especially when the measured data does not meet the standard, the status of the printing equipment needs to be analyzed in time. Since the monitoring data of this study is mainly based on the measurement of the print patches in the control strip of Fig. 1, only the 50% dot gain data is used as the monitoring parameter of the printing equipment, which does not fully reflect whether the dot gain of other tone meets the requirements. This study uses polynomial regression to fit the actual TVI curve of the prints, also the coefficient of determination ($R^2$) is selected as an evaluation parameter. An empirical threshold is introduced to determine whether the status of the printing device has changed. When $R^2$ is closer to 1, it means that all the dot gain value is close to the predicted points and the TVI curve is smooth. Therefore, in this condition, if the 50% dot gain value is in the reasonable range, all the other dot gain value will not deviate from the predicted smoothing curve. As long as 50% of the dot gain value meets the requirements, it means the print quality is quite well; conversely, the farther $R^2$ is from 1, the more unreliable of the 50% dot gain value to represent the overall print quality.

**Table 2.** The coefficient of determination of the different printing unit

| 1 | Color | C | M | Y | K |
|---|---|---|---|---|---|
| 2 | $R^2$ | 0.898 | 0.953 | 0.935 | 0.967 |
| 3 | $R^2$ | 0.976 | 0.978 | 0.963 | 0.974 |

By measuring the test strip of Fig. 2 on the printing plate and printed sample, we can obtain the dot coverage. Also the dot gain curve of the printing press can be calculated, as shown in Fig. 4a. Then polynomial regression is used for dot gain data,

and the coefficient of determination is obtained, as shown in Table 2 (see the data in row 2). Based on a large amount of experimental data, 0.95 is taken as the threshold value, that is, when $R^2$ is lower than 0.95, it is considered that the status of the printing unit is unstable, and it is necessary to keep the printing equipment in a good condition by replacing the blanket, checking the water-ink balance, adjusting the printing pressure and so on. According to the data in Table 2, the cyan and yellow printing units are in poor condition. At the same time, the measurements of the P2P test target are also shown that the Max wdCh does not meet the requirement, that is, the maximum hue angle error of the gray balance is out of range, as shown in Fig. 5a.



(A) Original                    (B) Revised
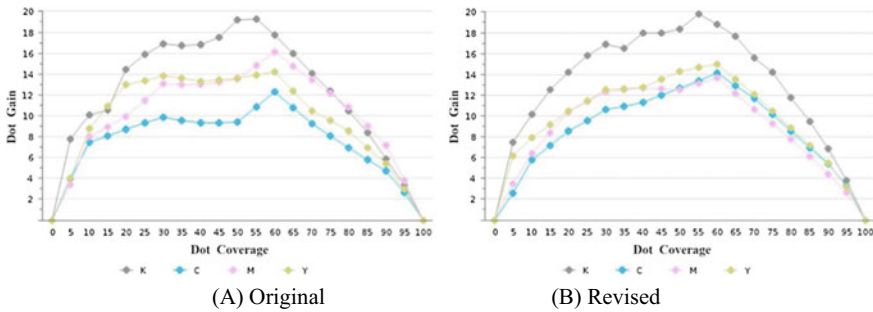
**Fig. 4.** The dot gain curve of the printing press

After checking the printing equipment, replacing the printing blanket, and cleaning dampening system, a new sample is printed, and new printing dot gain curves are drawn after the test, as shown in Fig. 4b. Visually, it was found that the dot gain curves of the green and yellow printing units are smoother. After calculation, the $R^2$ values of each unit are greatly improved and meet the requirements, as shown in Table 2 (see the data in row 3). By testing the P2P test target, it is proved that the new sample can pass the G7 certification test, as shown in Fig. 5b.



(A) Original                    (B) Revised
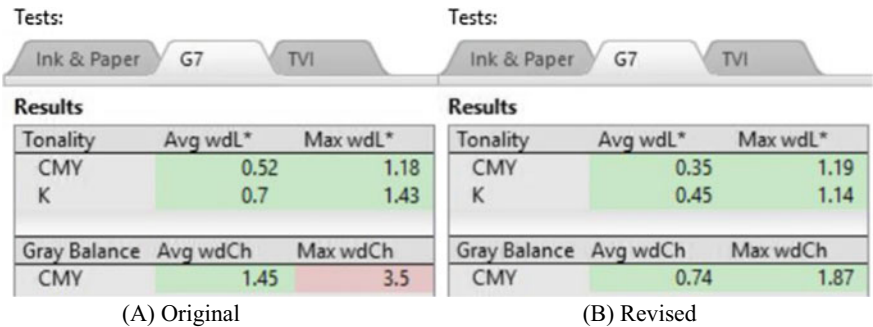
**Fig. 5.** The results of G7 analysis

# 3   Conclusions

In this paper, the simple quality control strip composed of 9 color patches is used to monitor the printing quality. The application of the new method can greatly reduce the inconvenience caused by measurements of too many patches in the original printing control method, and the efficiency of objective evaluation of the quality in the printing production process is greatly improved. At the same time, the coefficient of determination ($R^2$) is introduced as an important objective evaluation index of the status stability of the printing press. The practical conclusions show that the new method is simple and effective, and it can be used as a routine method for printing process control. It has certain guiding significance for the promotion of printing standardization and digitalization.

# References

1. Chen W (2005) New features and enlightenment of international standardization development. Commer Times 8(22):55–57
2. Li Y, Liu C (2016) Digitization, normalization and standardization of printing quality control system. China Print 19(07):62–64
3. Zong X (2016) Mathematical statistics and its application. China Machine Press, Beijing, China, pp 252–259
4. Hua D, Si C (2018) Analytical chemistry, 7th edn. Higher Education Press, Beijing, China, pp 324–325
5. Li X, Song Z (2011) Comparative study of PSO and G7. Print Qual Stand 12(6):20–23
6. Guide to Print Production 13.0. IDEAlliance Publishes. VA, USA, pp 48–52

# Study on the Application of G7 Process in Flexographic Printing

Enyin Fang[✉], Jinghuan Ge, and Zhangying Jin

Department of Printing and Packaging Engineering, Shanghai Publishing
and Printing College, Shanghai, China
`fensarying@163.com`

**Abstract.** G7 process is a new calibration method based on GRACOL7 standard. Unlike the traditional process, it is based on the technologies of Computer-to-Plate (CTP) imaging and spectrophotometer detection and the gray balance can be controlled better in offset printing process. G7 process is a revolutionary process from proofing to printing in offset. However, in flexographic printing, the problems of dot gain and small dots losing are more serious and ink layer is thicker than offset printing, which makes tone reproduction in flexographic printing quite different from offset printing. Therefore, the G7 process, which is usually used in offset printing, cannot achieve gray balance. By adjusting the plate making and compensation parameters through experiments, this paper gives a better solution to the color deviation in G7 process, which is used in flexographic printing.

**Keywords:** The process of G7 · Flexographic printing · Highlight dot technology

## 1 Introduction

Gray balance refers to the combination of the dots of CMY when visual neutral gray appeared. For example, the gray balance data defined in IS012647-2 standard is C-50, M-40, Y-40%. It is a key measure of appearance. The slight change of gray balance will result in a larger color shift of the image in the printing process [1, 2]. Therefore, gray balance has always been regarded as an important control parameter in printing. In traditional printing, the first concern is the field density, followed by TVI and grey balance. Densitometer is the most commonly used measuring tool, which is cheaper and more popular. However, densitometer cannot simulate the observation of human eyes and cannot reflect the objective attribute of specific colors (such as LAB value of color or XYZ value).

G7 process is a new calibration method based on GRACOL7 standard. Unlike the traditional process, it is based on the technologies of Computer-to-Plate (CTP) imaging and spectrophotometer detection. It uses spectrophotometer to measure and control the neutral gray balance on the printed sheet. Instead of focusing on the field density, dot enlargement (TVI) curve, relative contrast K value and the change of dark tone area, which are used as quality control methods in the traditional printing [3, 4]. The key control point in G7 process is HR (the highlight range). Through spectrophotometer,

the neutral gray balance on the printed sheet is measured and controlled. Then, a new NPDC curve (Neutral Print Density Curve) is used to match the visual effect of the image. Compared with the traditional printing process, the main difference between the G7 technology and the traditional printing process is that the reproduction of the original color is mainly focused on the highlight and mid-tone of the image. Rather than the controlling solid density and dot gain as the point in traditional process [5]. The control of the G7 gray balance is achieved by controlling the Lab value of the following three parameters, named the Highlight range, the Highlight contrast and the Shadow contrast.

## 2    Research Significance

In theory, G7 process can be applied to all printing methods, but in flexographic printing, the dot gain is more serious, small dots are easy to disappear and ink layer is thicker than offset printing, which makes the reproduction of color in flexographic printing quite different from offset printing [6]. In the Prepress process, the size of dots is reduced by adjusting the color separation curve of the flexographic plate to compensate for the dot gain. In flexographic printing production, the minimum dots on the plate must be controlled as far as possible, because there will be many variables affecting the dot gain in the process. Similar with G7 process using in offset, G7 process test in flexographic printing also needs to control the smallest highlight dots by adjusting the RIP curve. However, in the actual printing process, the highlights dots are easy to disappear in the process of plate making, furthermore, the HR is the key point of G7 process control. Therefore, the color deviation of highlights will result in the final failure of the Colorspace level.

At present, a large number of companies has not confirmed the application of G7 technology in flexographic printing. Therefore, this research mainly focuses on the practical testing of G7 technology in flexographic printing [7]. According to the specific production conditions, the requirements and test points of G7 technology are adopted, and the test conditions and pre-press preparation are summarized. By adjusting the plate making and compensation parameters through experiments, this paper gives a better solution to the color deviation in flexographic printing, which can help the enterprise easier to achieve the Colorspace level of G7 certification.

## 3    Test Conditions of the Printing

In order to better test the experimental results, the printing conditions are the following:

(1) Printing conditions: using the same CTP equipment, CTP flexographic plate. Before formal printing, it is necessary to calibrate and linearize CTP to ensure the accurate reproduction of dot. Detecting the state of the plate washer and controlling the pH value of the developer, it can ensure the stability and controllability of CTP plate making system in a good physical and chemical state.

(2)  Testing Printers: used the common flexographic press for testing. In order to better understand and control the status of printing press, necessary testing of printing press should be carried out. The main items to be tested are dry density decompression test, roller mark, printing registration test, etc. Adjust the printer according to the test results until the printer is in the best working condition.

(3)  Instruments: 100-fold magnifying glass, IC-Plate II plate tester, X-Rite 530, X-Rite i1io or Isis (T-density response mode, M1, CGATS format data format), D50 light source, 20 observation field.

(4)  Test software: Curve4, Excel 2010, etc. As shown in Table 1 In order to test the results, the printing conditions are shown in Table 1.

**Table 1.**  Test conditions of the printing

| Projects | Main test conditions | Brand and state |
|---|---|---|
| Inks | UV alcohol-based ink (cyan) | Meet the standard of ISO 2846-1 |
| Carriers | ISO Standard Coated Paper (128 gsm) Lab value of white paper with color tolerance less than or equal to 3 | Lab value of white point as following, L*(95 ± 3), a*(0 ± 2), b*(−2 ± 2) |
| Workshop environment | Constant temperature and humidity | temperature is about at 23 ± 5 °C, and the relative humidity is about at 50–75 |
| The pressure of the printing | As far as possible to take the minimum pressure printing, "zero pressure" | Generally speaking, the pressure is about l–3 kg/cm$^2$ |
| Analyze the project | Objectively evaluate, use i1io to test the samples and put the measured data into Curver4 for evaluation | |

(5)  The testing chart.

The TC1617 is a new CMYK printer characterization target combining the unique patch values in the standard IT8.7/4 target by removing 29 duplicate patches from the IT8.7/4 and replacing them with the 29 patches in columns 4 and 5 of the P2P51 that were absent in the IT8.7/4, as show in Fig. 1.



**Fig. 1.**  TC1617

# 4   Analysis and Evaluation of Measurement Results

The results of this experiment need to achieve the Colorspace level of G7 certification, so the color of blocks should matched the standard based on grayscale and targeted level of G7 certification. Grayscale level, which should meet the requirements of neutral grey, is the lowest level in the G7 certification, P2P will be measured during authentication and detection. On basis of Grayscale level, the color of C/M/Y/K and R/G/B must also meet the standard to reach the G7 Targeted level. Colorspace is the most difficult level in the G7 certification, which need the paper meet the ISO standard. Besides meeting the requirements of G7 Targeted, the IT8.7/4 data must also meet the requirements.

## 4.1   First Round Printing Based on Linearization of CTP

Output the TC1617 to record the dot information of the plate as CTP work at its original stated without loading any curve in it, so the plate-making process can be better controlled in the future. When printing using the test plate, the printing press must be in a stable state that meets the requirements after adjustment, using the spectrophotometer to find optimal solid density during printing. When the printing press was stable, the specific elements on the printing samples were measured. And then thorough using Curve4 software, results were processed, and new target values for RIP were assigned to complete the correction of CTP.

## 4.2   Second Round Printing of Certification Printing

After loading the calibration curve into the CTP system, print samples with optimal solid density mentioned above for the first time. In order to ensure the consistency of printing states, the entire job should be printed using the same machine and two rounds of printing should be done on the same day with the settings of the printing press unchanged. After printed, the samples are ready for measuring. The data acquired form the Samples using X-Rite i1io are tested and evaluated by Curve4 software, as shown in Fig. 2. The second round printing of certification printing has reached the target standard. Because the average tolerance of the color exceeded, the experimental results for Colors pace level of G7 certification are not passed.

As can be seen in Fig. 3, the ∇Ch belonged to the highlight area in TC1617 test draft have changed more intensely, The average value of color difference is larger, Ultimately, it affects the evaluation results. The reason is that the dots in the highlight area are so small, especially the yellow ink. So the problem is how to solve this kind of issue quickly through process improvement. In this experiment, combined with high-digital dot technology, the results of the experimental can be optimized.

High-digital dot technology is a comprehensive technology aimed at the problem of "hard port" in highlight area of flexographic products. The small dot reinforcement technology is realized through processing of documents in the stage of prepress. The principle is to add some smaller dots nearby the highlight dost on the plate, the small dots can protect the highlight dots from being washed out during the process of plate
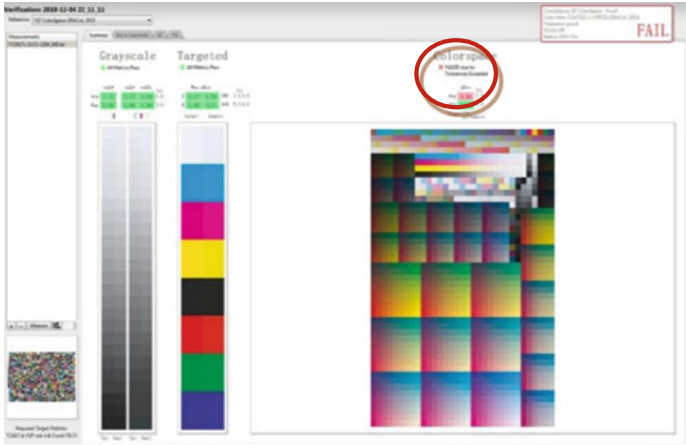
**Fig. 2.** Test failure for Colorspace level
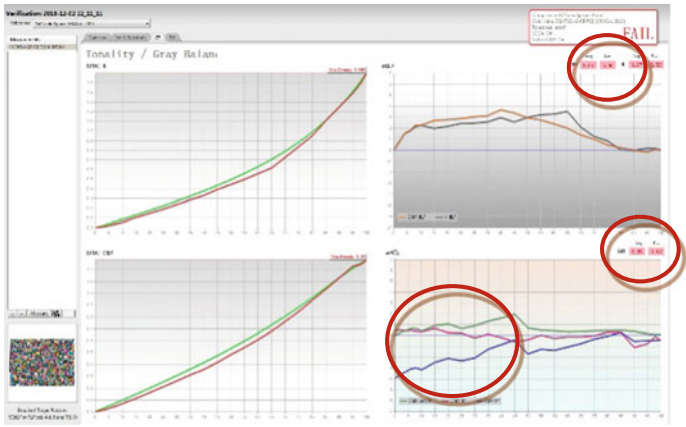


**Fig. 3.** Color expression of the highlight range

washing. Furthermore, this process can increase the resistance of the plate at the same time ensure that the highlight dots can be transferred to the substrate.

In order to verify the performance of High-digital dot technology in flexographic printing and reduce the cost of enterprise certification, this experiment was carried out during the internship of students in factories. Table 2 shows that the L*a*b*, C and H of neutral grey dots in highlight tone section are measured by X-Rite 530 after using non-highlight dot technology and highlight dot technology based on TC1617 test file.

From Fig. 4, it can be seen that the dots in the range of 0–20%, using high-digital dot technology are obviously superior to those of non-high-digital dot technology in terms of color difference, chroma and hue angle compared with theoretical values. Therefore, high-digital dot technology performs better in highlight range and can bring stronger color performance. On this basis, using high-digital dot technology for plate

**Table 2.** Color comparison of neutral grey dots in highlight area

| (%) | Initial L*a*b*, C, H values of neutral grey in test files | | | | | $L_1$*$a_1$*$b_1$*, $C_1$, $H_1$ values of neutral grey without high digital dot technology | | | | | $L_1$*$a_1$*$b_1$*, $C_1$, $H_1$ values of neutral grey with high digital dot technology | | | | |
|---|---|---|---|---|---|---|---|---|---|---|---|---|---|---|---|
| | L* | a* | b* | C | H | $L_1$* | $a_1$* | $b_1$* | $C_1$ | $H_1$ | $L_2$* | $a_2$* | $b_2$* | $C_2$ | $H_2$ |
| 2 | 92.41 | 0.73 | −4.97 | 5.02 | 278.32 | 94.53 | 0.93 | −6.47 | 7.22 | 282.32 | 93.86 | 0.88 | −5.90 | 6.35 | 289.62 |
| 4 | 91.62 | 0.63 | −4.71 | 4.75 | 277.57 | 93.89 | 0.80 | −6.21 | 6.85 | 280.97 | 92.55 | 0.76 | −5.81 | 5.98 | 279.17 |
| 6 | 90.02 | 0.69 | −4.41 | 4.46 | 278.84 | 92.57 | 0.83 | −6.08 | 6.66 | 281.24 | 91.68 | 0.84 | −5.33 | 5.65 | 279.64 |
| 8 | 88.73 | 0.57 | −4.28 | 4.32 | 277.59 | 90.83 | 0.76 | −5.89 | 6.52 | 280.59 | 89.53 | 0.69 | −5.10 | 5.32 | 278.32 |
| 10 | 87.11 | 0.53 | −4.43 | 4.46 | 276.81 | 89.54 | 0.73 | −5.98 | 6.79 | 279.43 | 88.34 | 0.64 | −5.34 | 5.26 | 277.95 |
| 15 | 83.64 | 0.83 | −3.63 | 3.73 | 282.86 | 85.74 | 0.99 | −5.23 | 5.83 | 286.94 | 84.26 | 0.95 | −4.43 | 4.53 | 283.66 |
| 20 | 79.71 | 0.42 | −3.21 | 3.24 | 277.38 | 81.91 | 0.64 | −5.93 | 5.34 | 279.98 | 80.53 | 0.53 | −4.35 | 4.64 | 278.58 |

making and the third round of certification can better optimize the results of demonstration. We put the measurement results into Curve4 software for evaluation, as shown in Figs. 5 and 6. The third round of certification printing has reached the Colorspace level of G7 certification, which is consistent with the previous experimental demonstration.
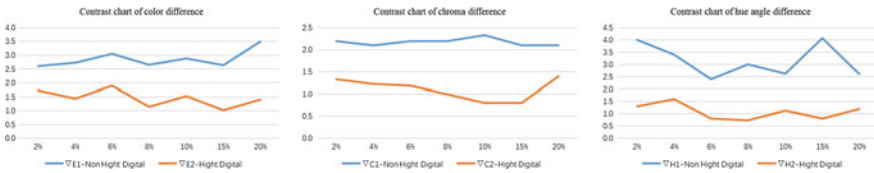


**Fig. 4.** Contrast chart of color difference, chroma difference, hue angle difference
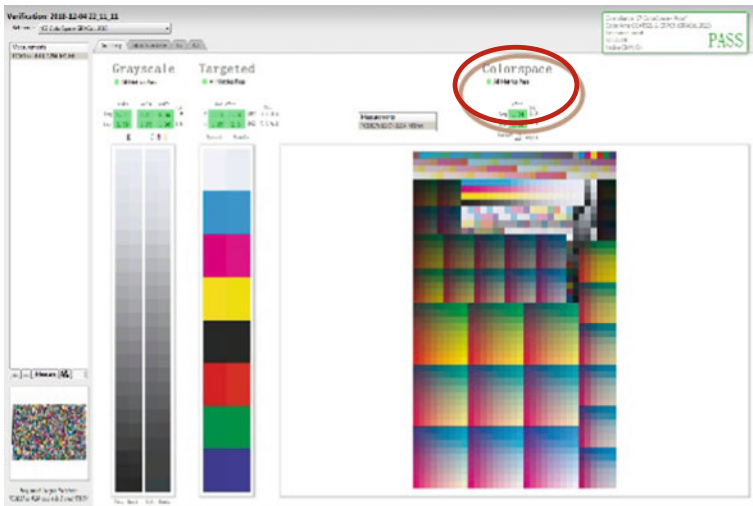


**Fig. 5.** Test pass for Colorspace level

## 5 Conclusions

In flexographic printing, the problems of dot gain and small dots losing are more serious and ink layer is thicker than offset printing, which makes tone reproduction in flexographic printing quite different from offset printing. Therefore, the G7 process, which is usually used in offset printing, cannot achieve gray balance. This paper focuses on flexographic printing and uses high-digital dot technology to adjust the plate making and compensation parameters in G7 process through experiments, to solve the
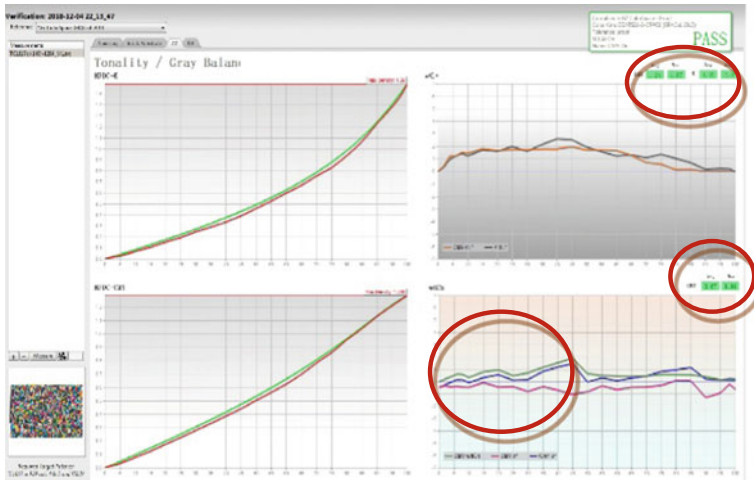
**Fig. 6.** Color expression of the highlight range

problem of color deviation of highlight area in G7 process for flexographic printing. It has certain guiding significance for enterprises to participate in Colorspace level of G7 certification.

# References

1. Huang PQ, Jin Y (2006) Tones and color reproduction of color flexography. Pack Eng 27 (6):9–11
2. Zhang H-M, Xu W-C (2008) Study on the dot Gain of Flexo printing. Pack Eng 18(1):41–42
3. Yang H-F (2016) Printing control in flexophotographic printing. Pack Eng 3:45–47
4. Hu Y (2011) Study on printing quality control method based on G7 process. Pack Eng 11:81–84
5. Yang M-N (2015) Applying G7 in Flexo. Qufu Normal University
6. Huang Y-W (2006) Analysis of tone and gradation reappearance performance in flexography printing. Pack Eng 24(5):297–298
7. Wang C-Y (2006) Testing principle and implementation steps of G7. Print Qual Stand 10:29–31

# Research on Improving Display Effect of Micro-lens 3D Printing

Linyi Chen and Guangxue Chen[✉]

State Key Laboratory of Pulp and Paper Engineering, South China University of
Technology, Guangzhou, People's Republic of China
chengx@scut.edu.cn

**Abstract.** Micro-lens 3D printing technology, which can achieve naked-eye
3D effect in 360° perspective without any special observation equipment or
skills, has gradually become a research hotspot in the field of 3D printing and
display. However, there are many problems in micro-lens 3D printing, such as
low resolution of 3D micro-image reproduction, image distortion. The process
flow of micro-lens 3D printing technology were studied and analyzed in this
paper from 3 aspects: micro-lens 3D micro-image design, micro-lens 3D optical
film preparation by nano-imprint technology, and micro-lens 3D printing pro-
cess control. The result showed that the problems which often exist in micro-
lens 3D printing, such as low reproduction clarity and image distortion were
effectively solved, which significantly improve the imaging and display effect of
micro-lens 3D printing.

**Keywords:** 3D printing · Micro-lens array · Naked-eye 3D effect

## 1 Introduction

The emergence of 3D printing technology makes the display mode of printed graphics
gradually change from 2D to 3D, which significantly improves the information display
level, interestingness and anti-counterfeiting performance of printing and packaging
products, and greatly increases the visual impact, sensory experience and added value
of products. Lenticular lens 3D printing technology has the comparative advantages of
larger imaging depth and better stereoscopic effect, but has the fatal defect of limited
viewing angle, that is, naked eye 3D effect can only be achieved in the horizontal
direction of lenticular lens arrangement instead of the vertical direction. Therefore,
micro-lens 3D printing technology, which can achieve naked eye 3D effect in 360° full
perspective (free viewing perspective with both horizontal and vertical parallax)
without any special observation equipment or skill, has gradually replaced the lentic-
ular lens 3D printing technology and become a research hotspot in academia and
industry.

## 1.1   Micro-lens Array and Its Research Status in 3D Printing

In recent years, a series of studies have been carried out on the fabrication technology, imaging characteristics and 3D printing and display of micro-lens arrays at home and abroad [1].

Wei [2] proposed a method for fabrication of micro-lens arrays using soft lithograph, which combined the traditional thermal reflow technology with the imprinting technology to fabricate micro-lens arrays. This method avoided the problem that the image effect was affected by the color interference of photoresist alone. Zhao [3] fabricated the micro-lens array with hexagonal aperture and buried in a glass substrate using photolithography and ion-exchange techniques, which enhanced the optical properties of plane micro-lens arrays by parameter optimization. The optical properties and imaging characteristics of the single plane micro-lens arrays and double plane micro-lens arrays were theoretically analyzed. Aymerich et al. [4] presented a laser based technique combined with the Talbot effect for micro-structuring surfaces, which was similar to the thermal reflow technology. The micro-cylindrical masks were fabricated by laser and then annealed to obtain micro-lens arrays. Nieto et al. [5] proposed a hybrid technique for fabricating micron scale micro-lens arrays on soda-lime glass substrates composed by a direct-laser write and a post thermal treatment. And the shape change of the micro-lens at different temperatures was characterized.

From the related research status at home and abroad, we can see that the research on micro-lens arrays focuses on the fabrication technology and imaging characteristics of micro-lens arrays. However, the research on micro-lens arrays in 3D printing is rare. Huang [6] studied the application of micro-lens arrays in stereo printing from the perspective of anti-counterfeiting, and analyzed the stereo printing process of micro-lens arrays. 540-line honeycomb micro-lens arrays anti-counterfeiting film was fabricated by roll-to-roll printing, but the 3D imaging display of honeycomb micro-lens arrays anti-counterfeiting film by printing was not achieved. Li [7] analyzed the imaging mechanism of micro-lens 3D printing, and improved the way of making the 3D image manuscript. The hemispherical micro-lens 3D printing sample based on UV offset printing was successfully fabricated. However, there were some existing problems such as low resolution and image distortion of 3D micrographics reproduction.

## 1.2   Proposal of Research Topic

The poor imaging and display effect of micro-lens 3D printing is generally caused by the matching of micro-lens array and 3D micrographics, the quality of micro-lens 3D printing materials and the process control of micro-lens 3D printing. Therefore, how to design 3D micrographics to match well with micro-lens arrays, how to fabricate high-quality micro-lens 3D printing materials, how to adjust the adaptability between micro-lens 3D printing materials, printing process and printing equipment, so as to improve the display effect of micro-lens 3D printing is a meaningful and valuable research topic. The process flow of micro-lens 3D printing technology were studied and analyzed in detail below from 3 aspects: how to design 3D micrographics combined with micro-lens array, how to fabricate micro-lens 3D optical films by nano-imprinting technology, and how to control micro-lens 3D printing technology process.

## 2    Research on Technological Process of Micro-Lens 3D Printing

### 2.1    Design of 3D Micrographics Combined with Micro-Lens Array

3D micrographics effect is a new periodic Moire pattern generated by the superposition of two arrays with similar periodicity and the double superposition of the visual depth of field effect of micro-lens, resulting in periodically magnified stereo depth of field pattern.

If a group of events or phenomena recur in the same order, the time or space interval to complete the group of events or phenomena is called period, which is expressed by "$T$". In acoustics, the interference of two sound waves with similar but different frequencies yields a frequency difference between the original two sound waves, which is called difference frequency. The period of 3D micrographics is, in short, the minimum distance between two opposing patterns in the generated periodic 3D micrographics.

As shown in Fig. 1, assuming that the period of sound wave 1 is $T1$, the frequency is $f1$, the period of sound wave 2 is $T2$, the frequency is $f2$, and the intervening period of two sound waves is $T$ and the frequency is $f$, then:

$$T = \frac{1}{f}; f = f1 - f2 = \frac{1}{T1} - \frac{1}{T2}$$

As a result, it can be concluded that:

$$T = \frac{T_1 * T_2}{|T_1 - T_2|}$$

According to the periodic formula, the closer $T1$ and $T2$ are, the larger the magnification of the 3D pattern of the micro-lens is. In particular, when $T1 = T2$, it's meaningless for mathematics, but meaningful for physical description.
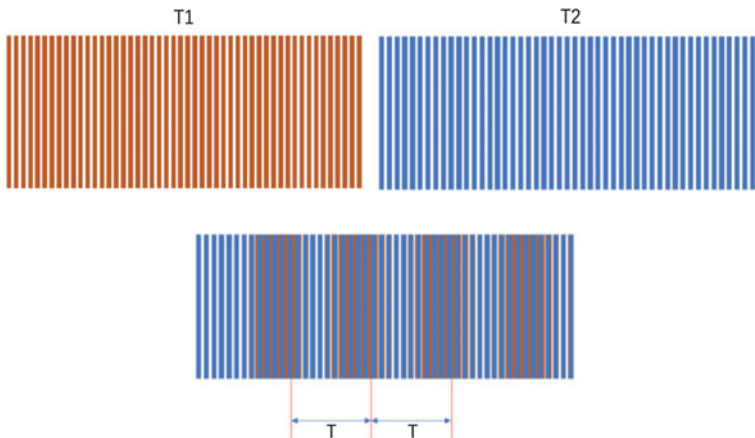


**Fig. 1.** Two sound wave and interference effects with different periods ($T1$, $T2$)

At this time, the period of the final 3D pattern is ∞, so we can not see the enlarged 3D pattern theoretically. However, due to the inevitable errors in the manufacturing process, we can finally see the enlarged 3D pattern.

We know that once the micro-lens 3D film is produced, the spacing distance between every two adjacent lenses has been fixed. Then how to control the cycle of designed 3D pattern in the design process to ensure that the design effect is consistent with the actual printing effect?

Taking micro-lens sheet with 0.4 mm thick as an example, the spacing distance between every two adjacent lenses of the sheet is $T1 = 0.18$ mm, the diameter of every lens is 0.13 mm, and the spacing distance between every two designed elements of 3D pattern is $T2$. Assuming that the distance $T$ of the final 3D pattern is 5 mm, according to the periodic formula of the micro-lens 3D pattern:

$$T = \frac{T_1 * T_2}{|T_1 - T_2|}$$

There are two values of the spacing between every two elements of the designed 3D pattern according to the above formula: $T2 = 0.174$ mm, the visual effect of 3D pattern is sinking. Or when $T2 = 0.184$ mm, the visual effect of the 3D pattern is floating. That is, when the element spacing of the designed 3D pattern is $T2 < T1$, the visual effect of the 3D pattern is sinking; when the element spacing of the designed 3D pattern is $T2 > T1$, the visual effect of the 3D pattern is floating.

As shown in Fig. 2 below, there are mainly three kinds of lens arrays for micro-lens 3D films, namely 45° orthogonal arrangement, honeycomb arrangement 1 and honeycomb arrangement 2.
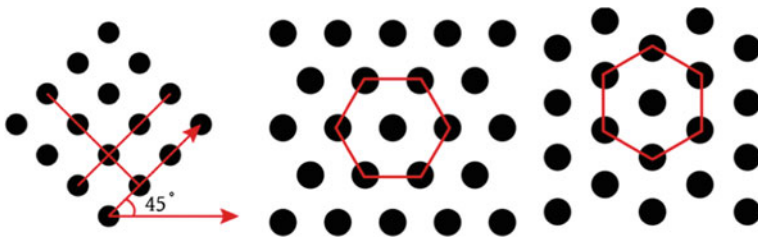


**Fig. 2.** Three common arrangement modes of micro-lens arrays

Taking a single channel, 45° orthogonal arrangement (0.4 mm micro-lens sheet) micro-lens 3D pattern as an example (we can know from the front discussed, the lens arrangement spacing of micro-lens sheet with 0.4 mm thick $T1 = 0.18$ mm, the spacing of every two designed 3D pattern elements $T2 = 0.178$ mm), the method of using Adobe Illustrator to design 3D micrographics for making printing plate and nano-precision optical mould was discussed in detail as follows. It mainly includes the following eight steps, which are shown in Fig. 3a, b, c, d, e correspondingly.

Step 1, determine the minimum repetitive unit (Fig. 3a).

Step 2, establish a minimum repetitive cell box, $a = 0.178 * \sqrt{2} = 0.252$ (Fig. 3b).

Step 3, the micro-lens 3D pattern elements are set to be in the center of the minimum repetitive unit block diagram.

Step 4, the micro-lens 3D pattern elements are copied and translated to the vertex of the minimum repetitive cell box (Fig. 3c).

Step 5, the path finder is used to cut the redundant parts and establish the minimum repetitive unit.

Step 6, drag the minimum repetitive unit into the color plate and rename it.

Step 7, establish filling area according to designed size (Fig. 3d).

Step 8, select the area to be filled and fill it with the smallest unit in the color plate (Fig. 3e).

After the above eight steps, the design of 3D micrographics for printing plate and nano-precision optical mould is completed.

Note: The edge length of the minimum repetitive cell frame and the arrangement spacing of the designed micrographics element $T2$ should satisfy $a = 2 * T2 = 1.414 * T2$. The calculation results are accurate to 3 decimal places.
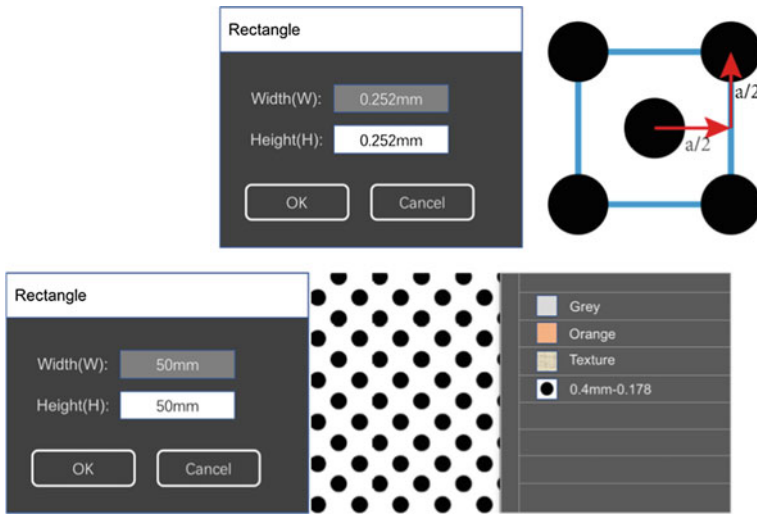


**Fig. 3.** The process of designing 3D micrographics in Adobe Illustrator (From left to right, from top to bottom, (**a**)–(**e**) successively)

## 2.2    Fabrication of Micro-lens 3D Optical Film

The micro-lens 3D optical films in this paper are fabricated by the 3D optical film fabrication machine based on nano-imprinting technology.
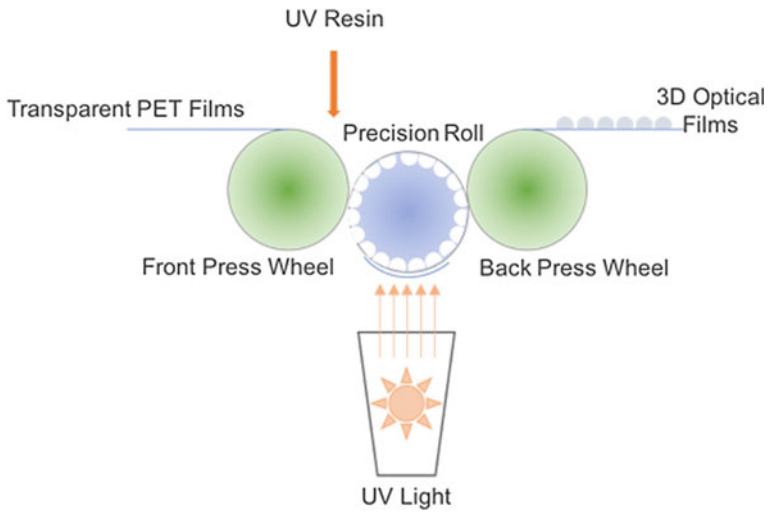
**Fig. 4.** Principle diagram of micro-lens 3D optical film fabrication machine

The film-made mechanism of micro-lens 3D optical film fabrication machine is as follows: UV resin flows into the micro-lens groove on the surface of nano-optical mould. The excess resin is extruded from the groove by pressing the front wheel. The surface of nano-optical mould and PET film are closely fitted with each other. The resin in the groove is solidified on the surface of PET film through UV lamp irradiation. The PET films with cured resin are peeled off from nano-optical mould after the back pressing wheel. The formed micro-lens layer is firmly attached to the surface of PET to form a transparent 3D optical film. The principle diagram of micro-lens 3D optical film fabrication machine is shown in Fig. 4.

The micro-lens 3D optical film fabrication machine can realize the development and manufacture of 3D optical films with 38–188 μm thick (the thickness of the micro-lens 3D optical film corresponds to the technical parameters of the precision optical mould. For instance, if micro-lens 3D optical film with 50 μm thick is expected, the precise optical mould with the corresponding parameters is needed).

The micro-lenses of 0.05 mm film are arranged by honeycomb (regular hexagonal arrangement), the distance between every two adjacent lenses is 0.046 mm, and the diameter of every lens is 0.03 mm. The micro-lenses of 0.075 mm film are arranged by honeycomb (regular hexagonal arrangement), the distance between every two adjacent lenses is 0.1 mm, the diameter of every lens is 0.08 mm. The micro-lenses of 0.4 mm sheet are arranged by orthogonal arrays, the distance between every two adjacent lenses is 0.18 mm, and the diameter of every lens is 0.13 mm. The micro-lenses of 0.3 mm sheet are arranged by honeycomb (regular hexagonal arrangement), and the distance between every two adjacent lenses is 0.12 mm, and the diameter of every lens is 0.08 mm.

## 2.3    Process Control of Micro-lens 3D Printing Technology

The process control of micro-lens 3D printing is crucial for the imaging and display effect of micro-lens 3D printing products. Usually, there are two printing methods for micro-lens 3D optical films: one is on the back of micro-lens 3D optical films, the other is on the double sides of micro-lens 3D optical films. However, the printing units of the UV offset press used are all 7 colors, including C, M, Y, K, 3D micrographics, white ink and wear-resistant OP varnish.

Technology process diagram of micro-lens 3D printing is shown in Fig. 5.

For back printing, the printing color sequence is: C, M, Y, K four-color printing for surface graphics, 3D micrographics, white ink, wear-resistant OP varnish.

For double-sided printing, the printing sequence is as follows: firstly, 3D micrographics, white ink and wear-resistant OP varnish are printed on the back of the micro-lens 3D optical films; secondly, C, M, Y, K four-color surface graphics and wear-resistant OP varnish are printed on the front of the micro-lens 3D optical films.

We have done a lot of research and testing on the micro-lens 3D printing process and found that:

On the one hand, unlike ordinary plane printing, micro-lens 3D printing requires very high resolution of CTP plate. Usually, in order to obtain clear naked eye 3D effect, the resolution of CTP plate should not be lower than 4000 *DPI*.
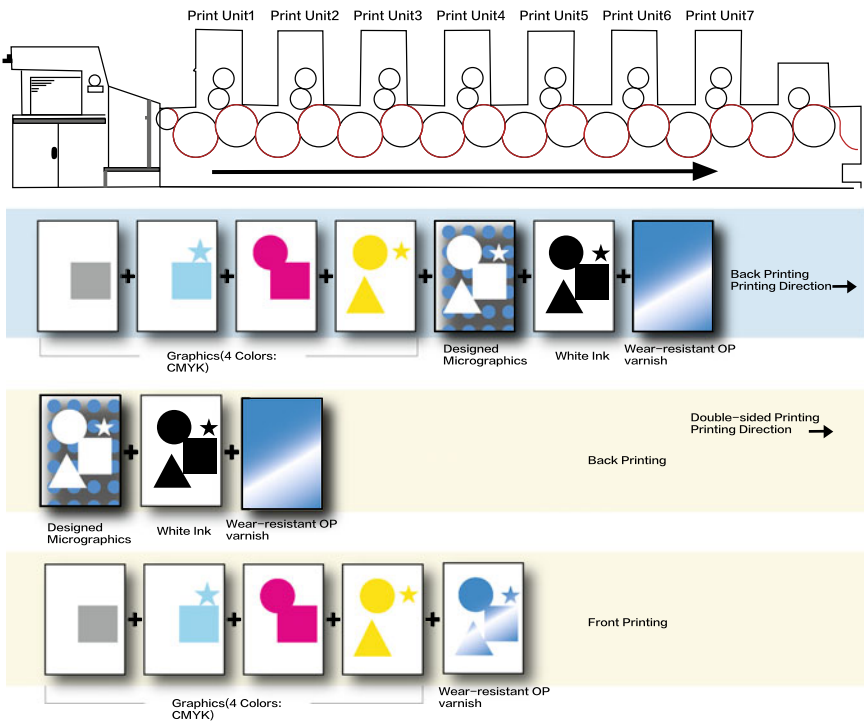


**Fig. 5.**  Technology process diagram of micro-lens 3D printing

On the other hand, like ordinary plane printing, in the process of micro-lens 3D printing, we need to flexibly adjust the corresponding printing speed, printing pressure and other production parameters according to the thickness and surface adhesion of micro-lens 3D optical films, so as to reach the best matching condition between micro-lens 3D printing materials, printing process and printing equipment, thus to achieve 3D printing effect beyond expectation.

## 3   Results and Discussion

Through the research on how to design 3D micrographics in Illustrator, how to fabricate micro-lens 3D optical films with nano-scale based on nano-imprint technology, how to set printing color sequence and printing parameters to realize the process control of micro-lens 3D printing process, we have successfully solved the existing problems on poor imaging and display effect in micro-lens 3D printing, for instance, low reproduction clarity of 3D micrographics, image deformation, etc. The research results related to micro-lens 3D printing have been successfully applied to packaging products in ICT, tobacco, alcohol, food, cosmetics and other fields, and have been recognized by customers and favored by the market. Figure 6 shows Structural diagram of micro-lens 3D printing product.
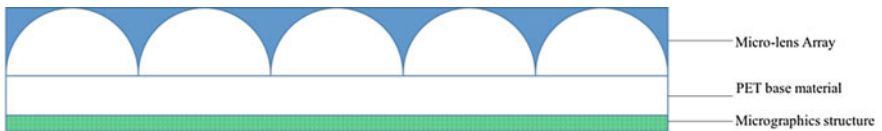


**Fig. 6.**  Structural diagram of micro-lens 3D printing product

## 4   Conclusions

In this paper, the technological process of micro-lens 3D printing was studied and analyzed from 3 aspects: the design of 3D micrographics, the fabrication of micro-lens 3D optical films based on nano-imprint technology and the process control of micro-lens 3D printing process. The problems, for instance, low resolution of micro-lens 3D printing and image distortion, were effectively solved. And the imaging and display effect of micro-lens 3D printing were improved. Related research achievements have specific reference significance for the technical research and product development in the field of micro-lens 3D printing.

# References

1. Liu D (2013) Micro optics and micro-lens array. Science Press
2. Wei W, Changhe Z (2009) New technology for fabrication of Polymer micro-lens arrays. Chin J Lasers 36(11)
3. Zhao Z (2012) Distribution-index and image properties of hexagon-aperture micro-lens arrays. Southwest University
4. Aymerich M, Nieto D, Flores-Arias MT (2015) Laser-based surface multistructuring using optical elements and the Talbot effect. Opt Express 23(19):24369
5. Nieto D, Arines J, Gomez-Reino C et al (2011) Fabrication and characterization of micro-lens arrays on soda-lime glass using a combination of laser direct-write and thermal reflow techniques. J Appl Phys 110(2):023108
6. Huang X (2014) Preparation of an anti-counterfeiting film with stereoscopic display different graphics at different viewing angles on the basis of surface micro-lens array. Beijing Institute of Graphic Communication
7. Li M (2015) Research on stereo image rendering based on micro-lens array. South China University of China

# Creative Visualization of Coin Classifier Design Based on 3D Modeling

Zhongmin Jiang[1] and Yingmei Zhou[2(✉)]

[1] Publishing and Printing College, University of Shanghai for Science
and Technology, Shanghai, China
[2] Printing and Packaging Department, Shanghai Publishing and Printing
College, Shanghai, China
471l31532@qq.com

**Abstract.** With the development of three dimensional printing, the personalization products are more and more welcomed by all kinds of industry fields. In daily life, creative application products are also wildly required. So the special design is very important for 3D application. This paper tells us an evolution solution on a coin classifier which used in the bank, home or on the bus to classify money for passengers. In this paper, two different structures of modeling are compared to get the optimization design for utility value. This study attempts to show the novel way on material and structure to help optimize ways to 3D application.

**Keywords:** 3D printing · Modeling · The optimization design · Coin classifier

## 1 Introduction

With the development of science and technology, We chat and alipay are well accepted by the people's daily life. The old and the child still use the coin or cash in buying breakfast, ice-creams, snacks after school. So one kind special coin box will meet our requirements to sort different coins for them. It is very convenient for the old to get certain coin number and for the kids to develop good habits of managing things by order. Recently, there are many types' coin classifier boxes in the market in Figs. 1 and 2. The functions focus on checking the false and clearing so that their price reaches on thousands of yuan which usually are used by banks and financial industry.

## 2 Modeling and Solution

In this paper, the creative visualization of coin classifier was designed with software 3D, the modeling process include the size, angle, part structure and the position.

Slope size, angle of inclination and whole size directly influence the other parts design. As the sole of the model, the size of the hole for coin dropping equals to the real coin size. The diameter output is considered as the reference to magnify the length, width and height of the slop. The material thickness of printing cause the diameter shrinks so that the coin cannot pass through smoothly. In addition, the slop angle is set

**Fig. 1.** Usual coin classifier
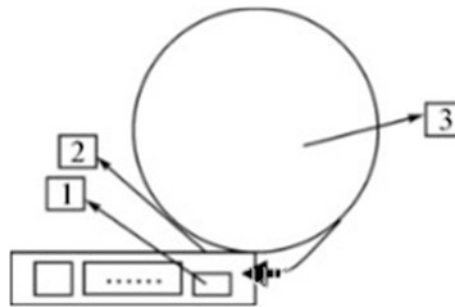


**Fig. 2.** The structure of the coin classifier

to be big enough to increase the speed of coin dropping which make the coin drop out of the slop surface.

According to 3D printing working time limit and workspace range, the slop size is set as 105 mm long, 3 mm high and 36 mm wide. In order to insure the coin pass through the hole, the hole shape was changed to square and large the length of side, setting the slope angle as 20° in Figs. 3 and 4.

Thinking of the handle of coin classifier, many tests should make insure handle size about 10 cm in Fig. 5 to hold for the children and the old. The guide plate is used to guide the coin pass. The original design is too small for the coin space so that the coin chocked rate is very high. The solution for this problem is to set one cylinder to stop the coin slide.
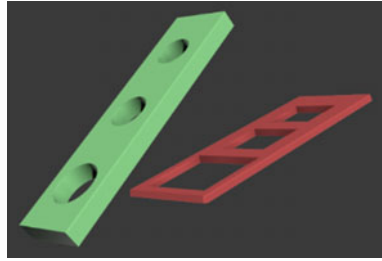
**Fig. 3.** Difference with different hole shape
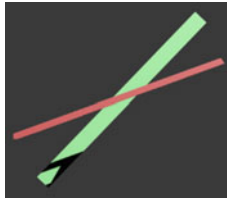


**Fig. 4.** Angle and degree selection



**Fig. 5.** Holding handle review

The important design is to set the structure as one high-heeled shoe in Figs. 6 and 7. In order to ensure the coin sliding component by its own gravity, and we cannot adjust Angle of slope, and three pieces of guiding direction of the guide plate can be modified, the article also explained the reason and the whole structure of the object position of aim is to ensure that the coin from the slot in the filtered from different guide plate after sliding into the corresponding new construct object structure in the collection box is the internal excavated slope of the guide plate, external three crescent on either side of the collector tray bending plate of a baffle the grip and hollow cylinder with slot constitute integral structure and structure in the shape of the reasons "beautification and convenience" of use in the safety to illustrate the translation.

**Fig. 6.** High-heeled shoe
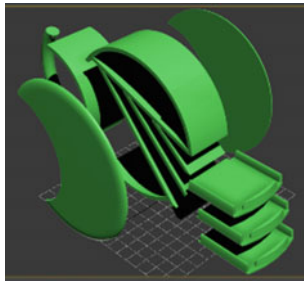


**Fig. 7.** Departs like high-heeled shoe

In addition, in the slot and the slope of the outlet was originally designed a trapezoidal cylinder (Figs. 8 and 9). Its purpose is to prevent coins from entrance to the slope without any rely on, and cause no rule of the coin, while the height difference is not large, but also affect the movement of the coin finally found after complete computer print $1 coin because its diameter problem, get stuck at the entrance solution can't achieve the desired effect: thought, finally decided to give trapezoidal cylinder support Connect the slope directly to the slot (Fig. 10) to avoid the uncontrollability of coin movement and save consumables and time for printing.
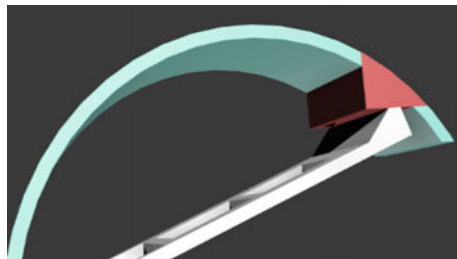


**Fig. 8.** Structure with trapezoidal cylinder
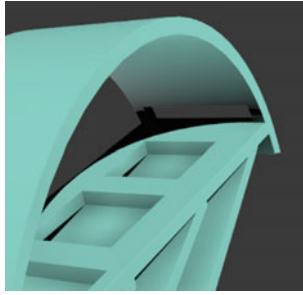
**Fig. 9.** Structure without trapezoidal cylinder
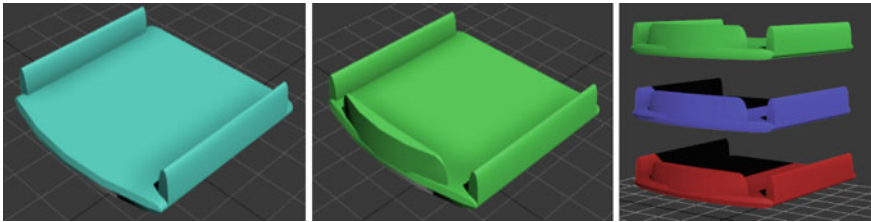


**Fig. 10.** Coin collection with guard

In order to prevent the slide to control a coin falling properly to the requirement place, the paper designed the both sides and collection guard in front. The original problem without guard will affect the use of objects for the shortcoming of the tray.

## 3    Output and Analyses

Use 3D software 3D-MAX to handle the model and parameter settings first is the file format of the import and export requirements after finish modeling in production. 3Dmax software need to export to the STL format, and do not check only when saved was selected for this option is selected by mistake and cause no save content again after processing through reviewing software which is saved as a GCO format, through a memory card or transmit the data line to the printer.

Coins go through the slope with different price, there is still a small probability of error whereabouts reason for this, but the slopes plus three fixed orbit (Fig. 11) limit the route of coins, forcing them from the specified channel through and to dig a hole size, and 1 yuan 1 angle is correct, but the 5 mao angle and the diameter of the angle is too close to 1. According to the center of gravity of the object, it exceeds the critical position which will produce rotating trend (Fig. 12) as a result, and can be shorten the length of the angle of digging hole, thus ensuring 5 mao angle not falling through the above two kinds of security, to avoid the happening of the error probability.

**Fig. 11.** Stable channel with white parts
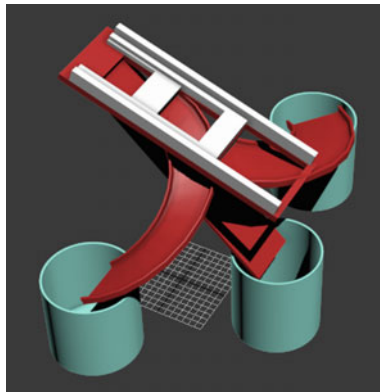


**Fig. 12.** Coin dropping theory

## 4   Conclusions

The personalization products are more and more welcomed by all kinds of industry fields. In daily life, creative application products are also wildly required. So the special design is very important for 3D application in this paper. An evolution solution on a coin classifier which used in the bank, home or on the bus to classify money for passengers. In this paper, two different structures of modeling are compared to get the optimization design for utility value. This study attempts to show the novel way on material and structure to help optimize ways to 3D application.

# References

1. Peng C (2016) Practical course of 3D printing technology. Electronic Industry Press, Beijing
2. Evans (2014) Analytical 3D printer: science and art of 3D printer. Machinery Industry Press, Beijing
3. Zhi L, Xiaofeng Q (2017) Chinese 3D max 2014 basic training course. People's Posts and Telecommunications Press, Beijing
4. Bo L, Yong Z (2017) 3D printing technology (Textbook for the 13th Five-Year Plan of National Colleges and Universities). China Light Industry Press, Beijing
5. Lipson H, Kurman M (2013) Fabricated: the new world Of 3D printing. Wiley, USA
6. Berman B (2012) 3-D printing: the new industrial revolution. Business Horizons

# Application and Surface Characterization of Braille Production Based on FDM 3D Printing

Chenfei Zhao[1(✉)], Siyuan Ruan[1], Jun Wang[1], and Yanli Su[2]

[1] School of Light Industry Science and Engineering, Shaanxi University
of Science and Technology, Shaanxi, China
20531919@qq.com
[2] Xi'an Guoli Automotive Services Co.,Ltd., Shaanxi, China

**Abstract.** At present, the cost of Braille printing on the market is high. The way of Braille printing can be gravure printing or screen printing and so on. The printing way will go through typesetting, plate-making, printing process, and that is a long period of time. Plate-making process causes great pollution to the environment. The using of 3D printers to print Braille can effectively shorten the printing time, and reduce environmental pollution, and reduce the cost of Braille printing. Firstly, using the three-dimensional software to design the text of Braille is necessary, designing corresponding parameters according to the characteristics and standards of Braille text, such as a little diameter, point distance, square distance, point height, line spacing and so on. The designed 3D text is then layered, and plastic wire and fused deposition 3D printers for printing are selected. The printed Braille is of strong touch and durability.

**Keywords:** Braille · 3D printing · FDM

## 1 Introduction

3D printing technology is a technology that constructs objects by printing layer by layer. Material is one of the main factors that restrict the development of 3D printing technology [1]. To some extent, the development of materials determines whether 3D printing can be more widely used. At present, 3D printing materials mainly include engineering plastics, photosensitive resins, rubber materials, metal materials, ceramic materials and so on.

So far, three types of Braille have appeared in the world [2]. At present the most commonly used Braille is the dot number composed of six points created by Blair in 1825. The six dots are arranged in different positions to form different dot numbers. The blind read them silently by touching the dot numbers with their fingers. The dot character number should be convex, and the size, pitch, font and line spacing of the convex should be designed in accordance with the standard requirements.

At present Braille can be produced by embossing, screen printing, etc. or by a 2.5D printer, which can form tiny convexities and concavities on the paper surface so as to

"float" the characters and graphics printed by ink jet. The printer can expand the thickness of any part up to about 2 mm by heating special paper.

It is of great significance to explore a method of printing Braille with printing filament and fused deposition 3D printer, which solves the problem that the traditional Braille printing process is complex and high cost.

## 2   Experiments

### 2.1   Braille Design

The Braille poem Red Bean is designed with Auto CAD software [3], and then is formed to the format of STL. The table shows the standard unit of parameters for Braille design (Table 1).

**Table 1.**   Standard unit of parameters for Braille design

| Parameter | Point diameter | Point height | Dot pitch | Square distance | Row spacing |
|-----------|----------------|--------------|-----------|-----------------|-------------|
| Size/mm | 1–1.6 | 0.2–0.5 | 2.2–2.8 | 3.5–4.0 | 5–6 |

Braille design's two-dimensional model is showed in Fig. 1a, and Braille design's three-dimensional model is shown in Fig. 1b.

### 2.2   Braille 3D Printing

Fused Deposition 3D Printer [4] is selected in this experiment. As one of the rapid prototyping technologies, fused deposition molding has many advantages, such as low cost, wide source of raw materials, small environmental pollution and small size of equipment, so it has been widely used. The 3D printer based on FDM technology includes mechanical structure and control system.
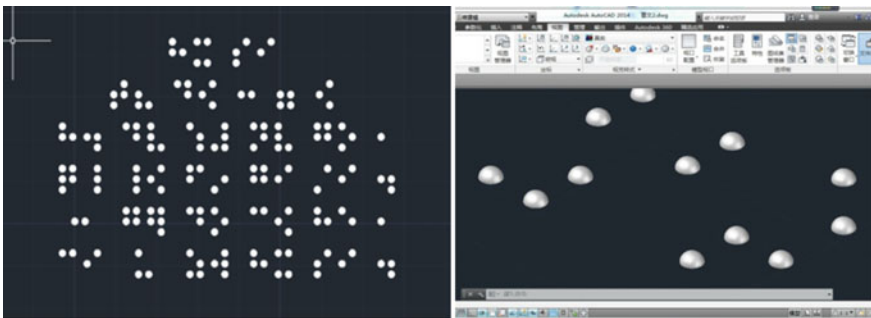


(a) Two-dimensional model                    (b) Three-dimensional model

**Fig. 1.**   Braille design's model

The selected wire is PLA. PLA, also known as polylactide [5], is a new type of bio-based and renewable biodegradable material. PLA raw materials come from a wide range of sources and are made from starch materials proposed by renewable plant resources (such as corn, cassava, etc.). The printing temperature is 160 °C, and the substrate is printed with pla material first, then braille dots are printed, as shown in Fig. 2.



(a) Braille's total graph                    (b) Braille's total graph
                                                 local micrograph
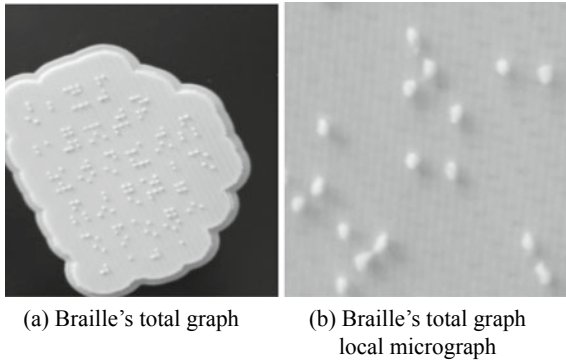
**Fig. 2.** Prints braille samples

## 3 Experimental Detection and Analysis

### 3.1 Detection of Size

According to Braille Point Standard, when Braille Points are printed, the height of Braille Points must be at least 0.5 mm, so as to ensure the fluent readability of the visually impaired and the blind (Table 2).

**Table 2.** Actual unit of Braille printed by 3D printer

| Parameter | 1 | 2 | 3 | Average value/mm |
|---|---|---|---|---|
| Point diameter | 1.12 | 1.10 | 1.06 | 1.09 |
| Point height | 0.5 | 0.5 | 0.5 | 0.5 |
| Dot pitch | 2.6 | 2.8 | 2.5 | 2.6 |
| Square distance | 3.0 | 3.2 | 3.1 | 3.1 |
| Row spacing | 5.2 | 5.4 | 5.2 | 5.3 |

Other parameters basically conform to the standard value, but the square distance is smaller than the standard value, mainly because the printing method of melt deposition has partial expansion between the two blind symbols, resulting in a smaller square distance.

## 3.2    Performance Testing

The Braille printed by 3D printer is hard but not brittle. Its deformation rate is small and stable. Its wear resistance and chemical resistance are higher than those of ordinary ink.

The method of firmness testing is using transparent tape to tear continuously to observe whether the Braille spot will fall off. If it falls off, record the number of times. Five Braille spots are randomly selected and torn with transparent tape. Each point has been torn more than 300 times and not fallen off, which indicates that the Braille spots has good firmness. Because this kind of Braille dot is printed on the PLA printed substrate, and the dot and the substrate is the same material, so the stickiness is better.

# 4    Conclusions

Braille is made by 3D printing, which has high strength, good friction resistance, and which saves time and reduces cost. It can be applied to Braille on plastic packaging boxes. However, the smoothness of Braille needs to be further strengthened.

# References

1. Didun L, Xiaoyong T, Yongxin W (2012) Development of additional materials manufacturing technology. Electr Process Mould 1:20–22
2. Cancai W (2014) Talking about Braille printing. Today Print (09):51–53
3. Chunji Z, Yue T (2016) Application of CAD/CAE technology in plastic mould design. Mod Plast Process Appl 16(1):34–35
4. Qiulin P (2018) Analysis and research of 3D printer control technology based on FDM technology. Internal Combust Engine Accessories 13:242–243
5. Liu W, Zhou J, Li Y, Wang J, Xu J (2017) ATBC on the preparation and properties of PLA/PCL wires for 3D printing. Funct Mater 48(11):11168–11173

# Research on the Printing Suitability of Alcohol-Free Fountain Solution Based on Green Printing

Jiasen Bai[1], Lujing Fu[1], Danfei Liu[2], and Yunfei Zhong[2(✉)]

[1] Hunan Yajia Color Printing Co. LTD, Hunan, China
l035627789@qq.com, kuaileangle04l5@l63.com
[2] School of Packaging and Materials Engineering, Hunan University of Technology, Zhuzhou, China
l5200405865@l63.com, yfzhong@hut.edu.cn

**Abstract.** Aiming at fountain liquor is the main source of VOCs in printing, this paper proposes a kind of alcohol-free fountain liquor by adjusting and optimizing the composition. Analyzed the basic theory of printing fountain solution and combined with the wetting principle, we realized the preparation of alcohol-free fountain solution by adjusted and optimized the composition of wetting agent, stabilizer and buffer in fountain solution. Then, the printing test experiment was used to verify the printing suitability of alcohol-free fountain solution. The experimental result shows that the printing suitability of alcohol-free fountain solution can met the printing requirements, it could be used to replace the traditional ethanol fountain solution, and reduce the VOCs emission in the printing effectively.

**Keywords:** Green printing · Printing VOCs · Education version fluid · Ethanol

## 1 Introduction

Fountain solution is an indispensable printing auxiliary material in offset lithography production, it forms a uniform water film in the blank part of a printing plate, and using the characteristics of oil and water do not melt to achieve selective adhesion. Then it forming graphic and non-graphic parts in plate to completing printing [1, 2]. The effect of fountain solution in printing is mainly reflected in the following aspects: form a uniform water film on the printing plate, reduce plate surface temperature; form stable water film equilibrium state and reduce the degree of emulsion ink [3–6]. Therefore, the key to ensure stable printing and efficient printing quality is to control fountain solution properly.

However, fountain liquor is mainly alcohol fountain liquor, which with low boiling point, high volatile characteristics, and produce volatile organic compounds VOCs [7, 8]. In particular, with the continuous promotion and demonstration of green printing, China has issued four green printing industry standards to reduce the emission of printing VOCs and further promote the implementation of green printing [9–12]. As an auxiliary material consumed in printing production, fountain liquor has become the

main source of VOCs in printing production. Therefore, it has become an important task for green printing to research new alcohol-free or low-alcohol fountain solution, reduce the alcohol content in fountain solution and reduce VOCs emission.

In this paper, we analyzed the basic theory of printing fountain solution, combined with the fountain solution composition and wetting principle, realized no alcohol fountain solution by adjusting and optimizing the composition of surfactant, stabilizer and buffer in fountain solution. Finally, through experiments to verify the printing suitability of alcohol-free fountain solution, a theoretical foundation was laid for the spread of alcohol-free fountain solution.

## 2   Basic Theory of Printing Fountain Solution

### 2.1   Fountain Liquid Fountain Principle

According to the basic theory of wetting, it can be known that the parameters to measure the wetting of a printing plate are contact angle $\theta$, and the smaller the contact theta angle $\theta$, the better the wetting effect. When the contact angle is 0°, complete wetting or spreading is indicated; When the contact angle is less than 90°, the theta appears to be wetting; When the contact angle is greater than 90°, it is not wetting. The specific principle of wetting is shown in Fig. 1.
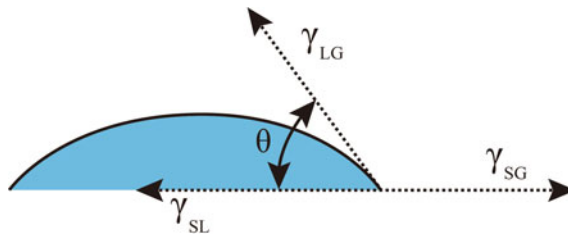


**Fig. 1.**  Wetting principle diagram

According to Fig. 1, the wetting equation is formed by the relationship between contact angle and solid-liquid-gas three-phase surface free energy, when the wetting of fountain solution reaches an equilibrium state.

$$\gamma_{SG} = \gamma_{SL} + \gamma_{LG} \cos \theta \tag{1}$$

$\gamma_{SG}$ is the gas-liquid surface tension, $\gamma_{SL}$ is the solid-liquid surface tension, $\gamma_{LG}$ is the gas-solid surface tension.

### 2.2   Analysis of Wetting Mechanism

Through the wetting theory analysis of fountain solution, it can be concluded that to reduce the VOCs emission of fountain solution, it is necessary to find a wetting agent

isopropyl alcohol substitute. In addition, the substitute has hydrophilic group, lipophilic group or ammonia bond structure between water molecules to reduce the surface tension of fountain solution.

# 3  Research on Preparation of Alcohol-Free Fountain Solution

## 3.1  Wetting Agent Selection

Through research we found that: 1,2-propylene glycol has the property of alcohol hydroxyl group, which can be mutually soluble with water and other organic solvents in any proportion. It has hydrophilic and oleophilic group, which can reduce the surface tension of liquid, and is not easy to volatilize. Its wetness mechanism is basically similar to propylene glycol. Therefore, it can be used as a wetting agent instead of propanediol in fountain solution.

## 3.2  Composition Analysis of Stabilizer

In order to ensure the stability of fountain solution and emulsion ink, it need to add a stabilizer in fountain solution. Through the experimental test, adding the appropriate proportion of glycerol and polyethylene glycol 400, can interact with the wet version solution to form a complex, by increasing the polar part of water and oil non-polar part of the interface of polymerization tendency, improve the oil and water interface film elasticity, so as to improve the stability of emulsion ink.

## 3.3  Buffer Solution Preparation

In order to ensure that the pH value of fountain solution remains within 4.5–5.5, we need to reconfigure the buffer solution according to the performance of 1,2-propylene glycol. Through experimental tests, we found that the buffer solution composed of oxalic acid and sodium oxalate mixed in a certain proportion, can well ensure that the pH value of fountain solution is stable between 5.0 and 5.5.

# 4  Test and Analysis of the Printing Suitability of Fountain Solution

According to the experimental test result, fountain solution composition and proportions shown in Table 1.

**Table 1.** Fountain solution composition and proportion

| Component | Content/g | Component | Content/g |
|---|---|---|---|
| water | 1000 | Polyethylene glycol 400 | 10 |
| 1,2 propanediol | 30 | Oxalic acid | 15 |
| Glycerin | 35 | Sodium oxalate | 60 |

At the same time, select 10% ethanol fountain solution as a comparative test, test the performance of the optimized fountain solution. The test conditions are as follows: Printing equipment: Komori folio four-color printing machine; Printing ink: HangHua four-color ink; Printing environment: temperature 26 °C, humidity 50%; Printing paper: 157 g coated paper; Testing content: dot expansion, field density, overprint rate and relative contrast; Testing instrument: X-Rite528 reflectometer.

## 4.1  Print Density Test Results Analysis

The field density values of different fountain solution are shown in Table 2.

**Table 2.**  Different fountain solution after printing the field density value

| Education version fluid | C | M | Y | K |
|---|---|---|---|---|
| Alcohol-free fountain solution | 1.23 | 1.35 | 0.92 | 1.63 |
| Ethanol fountain solution | 1.29 | 1.41 | 0.98 | 1.65 |

Magenta 1.25–1.50, Cyan 1.30–1.55, Yellow 0.85–1.10, Black 1.40–1.70. Improved fountain printing on the spot density to meet the requirements, but compared with ethanol fountain liquid phase, in fact, the density is low; there is still a certain gap in printing suitability.

## 4.2  Analysis of Dot Expansion Test Results

Dot expansion is measured based on the expansion value at 50% of the dot. Different fountain solution obtained dot expansion value as shown in Table 3.

**Table 3.**  Different fountain solution after printing dot expansion value (%)

| Education version fluid | C | M | Y | K |
|---|---|---|---|---|
| Alcohol-free fountain solution | 25.83 | 26.53 | 24.85 | 27.23 |
| Ethanol fountain solution | 22.13 | 21.45 | 20.54 | 24.53 |

50% of the outlets, the dot expansion value of fine prints is 10–20%, and that of general prints is 10–25%. The experimental results shows: the product dot expansion rate of alcohol-free fountain solution is basically more than 25%, suitable for general printing.

## 4.3  Comparative Contrast Test Results Analysis

The relative contrast is measured based on the relative contrast at 80% of the dot. The relative contrast value of different fountain solution is shown in Table 4.

**Table 4.** Different fountain printing relative contrast value

| Education version fluid | C | M | Y | K |
|---|---|---|---|---|
| Alcohol-free fountain solution | 0.312 | 0.341 | 0.239 | 0.372 |
| Ethanol fountain solution | 0.325 | 0.358 | 0.264 | 0.378 |

The K value of yellow ink general products is 0.2–0.3, then blue, magenta, black general products is 0.3–0.4, according to the experimental results, the relative contrast value of products obtained without alcohol fountain solution meets the requirements of general prints.

### 4.4    Comparative Contrast Test Results Analysis

Different fountain solution overprint rate as shown in Table 5.

**Table 5.** Different fountain printing after the overprint rate

| Education version fluid | C + Y | M + Y | C + M |
|---|---|---|---|
| Alcohol-free fountain solution | 84.37 | 78.63 | 76.93 |
| Ethanol fountain solution | 85.23 | 79.54 | 77.62 |

No alcohol fountain solution products overprint rate basically meet the requirements, but with ethanol fountain phase ratio, in the overprint rate is still a certain gap.

## 5    Conclusions

In this paper, we completed the preparation of alcohol-free fountain solution by using 1,2 propanediol as wetting agen. The results shows that alcohol-free fountain solution can replace traditional ethanol fountain solution, and its printing suitability can meet the requirements of general printing. The use of alcohol-free fountain solution can effectively reduce the VOCs emission in the printing process and promote the VOCs control of packaging and printing enterprises.

## References

1. Chen ZW (2005) Application of lubricating solution in high speed rotary offset press. Pack Eng 4(26):20–22
2. Yan G, Zhang HX (2012) Assessing and testing environmentally positive factors in eco-friendly printing. Pack Eng (5):150–153
3. Printing Industry Press (2012) Green printing manual, pp 53–54

 4. Wang Q, Hong L (2009) Control of wetting liquid performance for high-speed single sheet offset printing. Pack Eng 30(3):90–92
 5. Qi H, Wang YL (2012) Analysis of relation among fountain solution parameters. Pack Eng 33(6):101–103
 6. Chen SW (2008) Measurement and analysis of dampening solution in offset printing. Pack Eng 29(4):180–182
 7. Lee JY, Hildeman N, Lynn M (2013) Surface tension of solutions containing dicarboxylic acids with ammonium sulfate, D-glucose, or humic acid. J Aerosol Sci 64:94–102
 8. Karanikas EK, Nikolaidis NF, Tsatsaroni EG (2012) Synthesis characterization and application of hetarylazo disperse colorants: preparation and properties of ink-jet inks with active agents for polyester printing. J Appl Polym Sci 5:3396–3403
 9. China Books Publishing House (2015) Green printing terms. CY/T 129-2015
10. China Books Publishing House (2015) General technical requirements and evaluation methods for green printing—Part 1: Lithography. CY/T 130.1-2015
11. China Books Publishing House (2015) Green printing product sampling method and test site determination principle. CY/T 131-2015
12. China Books Publishing House (2015) Green printing product qualification criteria—Part 1: reading printed matter. CY/T 132.1-2015

# Review on the Research of Frontier Graphene Conducive Ink Printing Technology

Qingbin Cui[✉], Quanhui Tian, and Ping Gu

Department of Printing and Packaging Engineering, Shanghai Publishing and
Printing College, Shanghai, China
shpackcui@126.com

**Abstract.** Objective: with the premise of printability of graphene ink, the
printing technologies with graphene ink are applied in a large scale for printed
electronic products, realizing the extensive application of intelligent packaging.
Methods: in conjunction with characteristics of graphene ink, this article adopts
top-down and bottom-up preparation techniques and produces auxiliary dis-
persant by using n-methylpyrrolidone (NMP), dimethylformamide (DMF),
polyvinylpyrrolidone (PVP), and surfactants for observing the changes of
printability of graphene ink. Results: a technological breakthrough has been
made in graphic technologies, such as screen printing, gravure printing, flex-
ography, lithography, inkjet printing, and plate making methods in the appli-
cations of graphene inks, especially empirical research on micro-contact printing
based on flexography has been verified. Conclusion: the discovery of graphene
significantly promoted the development of flexible electronics. Green and sus-
tainable graphene ink with excellent conductivity can replace traditional metal
components in electronics industry, with promising prospect.

**Keywords:** Graphene conductive inks · Dispersion technology · Graphic
technology · Flexography · Micro-contact printing

## 1 Introduction

In 2004, a nanomaterial known as "black gold" that is graphene was successfully
exfoliated by researchers at the laboratory of the University of Manchester. Its
microscopic topology is featured with the thinnest, hardest, and minimal resistance,
excellent electric conductivity and heat conduction. The emerging of graphene has
aroused wide concerns of relevant industries. In recent years, the intelligent packaging
industry in China has developed rapidly, and excellent conductive graphene ink has
driven the fast reforming of the intelligent packaging industry cored on printed elec-
tronics. Currently, thin film transistors, conductive circuits, battery electrode materials
and other fields have realized scale applications. At the end of 2018, the researchers of
University of Manchester, UK has found that a dihydrogen oligomeric coca glucagon
material called Cyrene which is innoxious to produce high-concentration conductive
graphene inks at low cost. Their discovery will be widely applied in industries such as
radio frequency identification devices (RFID), supercapacitors, hydrogen storage
materials, and graphene batteries in the near future [1].

According to "2008–2013 China's Graphene Industry Investigation Analysis and Market Forecasting Report", China has the world's second largest graphite reserve that its basic graphite reserve accounts for 33% of the world's total graphite reserves. The identified graphite reserve is 260 million tons, and predicted potential reserve is 1.87 billion tons. China's affluent graphite resource has laid a solid foundation for the development of graphene ink industry.

Graphene is the two-dimensional sp2-bonded allotrope of carbon in the form of atomic-scale, honeycomb lattices in which one carbon atom provides an unbonded π electron that these π electrons can freely move on the lattice plane, giving graphene high conductivity, extremely high carrier mobility (250000 cm 2 $V^{-1}s^{-1}$), heat conductivity (5000 W $m^{-1}K^{-1}$) and force strength (1 TPa). In addition, graphene has a visible light transmission rate of 97.7% [2]. Because it has to consider the printability of graphene ink, the production of graphene ink has to take account of viscosity, surface tension, boiling point and density of graphene ink. In the preparation process, appropriate surfactants, rheological additives, and stabilizers are added to optimize the performance of graphene conductive ink. However, due to high specific surface rate, strong Van der Waals' force (VDW) between lattices, graphene lattices are extremely prone to agglomeration and precipitation at lower concentration. Therefore, how to select the best dispersion technology to obtain excellent conductivity and produce high concentration and non-agglomerative graphene ink is the prerequisite for wide application.

## 2  Preparation Methods of Graphene Ink

There are two preparation models of graphene: top-down and bottom-up. In top-down methods, graphite or carbon nano-tubes (CNTs) are exfoliated into single layer or a few layers of graphene through mechanical exfoliation, oxidation-reduction, solution-phase exfoliation; in bottom-up methods, carbon sources are dissociated into carbon atoms for in situ production of single layer or a few layers of graphene on the defined substrate through chemical vapor deposition, epitaxial growth, etc. [3]. In general, graphene flakes prepared by liquid phase method of top-down technique can be directly applied in typography, including gravure printing, flexography, inkjet printing. While graphene films prepared by bottom-up technique can be applied through transfer printing.

## 3  Primary Dispersion Methods and Difficulties

At present, auxiliary dispersants used mainly include n-methylpyrrolidone (NMP), dimethylformamide (DMF), polyvinylpyrrolidone (PVP), and surfactants. These solvents are equivalent to graphene surface energy and conducive to the stable dispersion of graphene after exfoliation. But NMP, DMF, PVP lead to degradation of single-layer graphene yield, which means that a large amount of unexfoliated graphene needs to be exfoliated through complex separation and purification, which has strong toxicity and destroys the sustainable utilization of graphene ink.

Surfactants have hypotoxicity, and can effectively change surface energy of solvents, making solvents match better to graphene surface and enabling more stable dispersion. Therefore, as a type of auxiliary dispersant, surfactants can improve dispersion stability of graphene in graphene conductive ink. In addition, surfactants form non-covalent modification on graphene flakes through Van der Waals force, hydrogen bonding, static electricity, and π-π interaction to improve stability of graphene dispersion. Lim et al. [4] used less toxic polyvinyl alcohol (PVA) as a dispersant to assist in exfoliation, dispersion and reduction-oxidation of graphene. Dua et al. [5] used ascorbic acid to reduce graphene, and used non-ionic surfactant polyethylene glycol octylphenol ether as a dispersant to produce stably dispersed graphene conductive ink.

In recent years, studies have verified the advantages of surfactants as auxiliary dispersants for graphene ink. However, surfactants can affect adhesion of graphene into the substrate, annealing treatment is necessary to remove surfactants, which complicate the procedures and greatly affect impede the scale application of graphene ink. Therefore, researchers have to make efforts devoted in developing the best dispersion method.

The biggest obstacle of using other dispersants is that a large amount of dispersants remain on the coating during the curing process after printing, which causes graphene to generate apertures in the contact of conductive ink, forming an air resistance effect and resulting in a degradation of conductivity in different proportions.

## 4    Main Printing Methods of Graphene Ink

Graphene ink is suitable for screen printing, gravure printing, flexography, lithography, inkjet printing, and can be applied in printed circuit boards (PCBs), radio frequency identification devices (RFID), display devices (such as OLED) and electrode sensors, as well as in organic solar cells, printed batteries, and supercapacitors. Therefore, graphene ink has a great potential application for next-generation of flexible electronic products, such as RFID tags, intelligent packaging, membrane switches, conductive circuits and sensors, which indicates a promising market prospect. The research progress of main graphene ink printing methods is introduced below.

### 4.1    Inkjet Printing

There are two types of inkjet printing: thermal inkjet and piezoelectric inkjet. Due to its high printing precision, piezoelectric inkjet is extensively applied in the graphene conductive ink researches. However, due to the physical properties of inkjet ink, the viscosity of ink has to be controlled at 10 cP [6], and the coffee-ring effect derived from the combination of ink and printing substrate affects the conductivity of graphene ink. With in-depth research, the influence of the surface state of printed silicon substrate on the typographical effects during the graphene inkjet printing process is studied. The research results show that when the alcohol-terpineol-dispersed graphene conductive ink is cured on the silicon substrate at room temperature (25 °C), due to bad infiltration of terpineol in silicon substrate and large difference of evaporation rates between alcohol and terpineol, cured graphene flakes cannot evenly dispersed, resulting in

coffee-ring effect. In a heating environment at 60 °C, the drying rate of terpineol accelerates and the contact angle increases, which effectively inhibit the coffee-ring effect and homogenize printing patterns. However, this method cannot be applied for the scale printing due to its slow operating rate, but only suitable for proofing or small batch printing.

## 4.2  Screen Printing

Screen printing has been applied for large-scale printed conductive lines as early as the end of 20th century. Compared to other three traditional printing methods, screen printing has properties of cheaper equipment and thick ink film, which ensures excellent conductivity. With the continuous development of technologies, screen printing has transformed from original flat-to-flat printing to the current roll-to-roll printing, therefore the printing rate and accuracy are greatly improved, and the fineness of printed lines is also upgraded from 100 to 50 μm. However, due to its slow printing rate, screen printing cannot be applied for large-scale and high efficiency printed flexible electronics.

Arapov et al. [7] exfoliated and dispersed expandable graphite from propylene glycol monomethyl ether, and added polyvinyl alcohol (PVA) and polyvinylpyrrolidone (PVP) as adhesives to produce graphene slurry used for screen printing through gelatinization. The width of printed lines is <40 μm. Hyun et al. used a graphene/EC composite to prepare high-viscosity ink with a mass concentration of $80 \text{ mg} \cdot \text{mL}^{-1}$ for high-precision screen printing. Their method is that 5 μm gaps are etched on a 90 μm thick silicon wafer as the high-precision stencil of screen printing, with a line accuracy of 40 μm. Since a large amount of EC is used, a sintering treatment at 300 °C is necessary after printing. Conductivity of lines prepared on flexible polyimide substrate is approximately $1.86 \times 10^4 \text{ sec} \cdot \text{m}^{-1}$ (as shown in Fig. 1). Figure 1 is the circuit diagram designed for measured conductivitity.
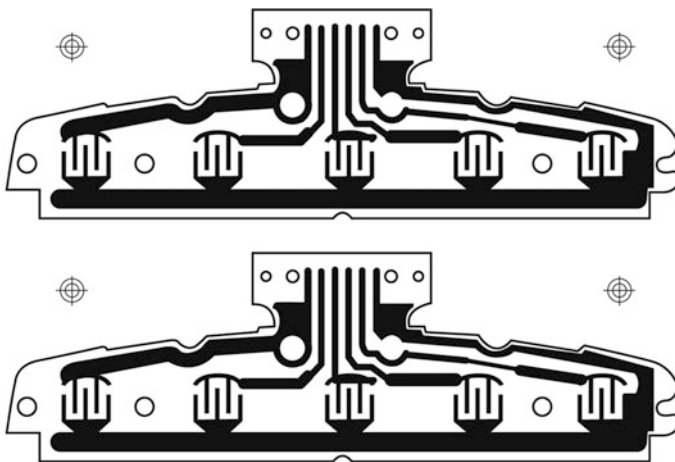


**Fig. 1.** Printed wiring via graphene/EC ink screen printing

## 4.3    Gravure Printing

During the printing process, low-viscosity ink is prone to diffusion in transfer printing, seriously reducing the printing resolution. In addition, printing that uses low-concentration graphene conductive ink needs several repetitive operations to obtain the desired electrical properties, which severely affects printing efficiency. Therefore, graphene ink used in gravure printing must have high viscosity and high concentration. Due to poor dispersibility in common solvents, graphene conductive ink is rarely applied in gravure printing.

Seeor et al. [8] prepared ink suitable for gravure printing by parameter optimization of graphene/EC composite system, and they applied the ink on flexible substrates to make large-area high-precision conductive patterns. The pattern accuracy is up to 30 μm, film thickness after sintering is <200 nm, and conductivity is $10,000 \ S \cdot m^{-1}$. Their work provides an effective strategy for large-scale high-efficiency graphene printed patterns.

## 4.4    Flexography

In printing industry, flexography is mainly used for the printing of flexible packaging, corrugated containers, and labels. Its advantages include roll-to-roll fast printing, low-cost plate making, and stable printing performance. Ink is transferred through micro grooves in anilox rollers that excess ink is scraped off by doctor blade and transferred to the printed substrate through the impression cylinder and the plate cylinder.

Due to small printing pressure, when using ultrathin graphene ink, flexography can effectively prevent destruction on the lower conductive layer by multilayer electronics during printing process. At present, flexography is a mature technique applied in the printing of solar cell substrates. In terms of research, however, there are few in-depth studies on graphene ink in flexography. Deganello et al. [9, 10] analyzed wireframes of various widths based on lines per inch of the anilox roller. The analysis results show that compared to other traditional printing methods, flexography uses more lines per inch of the anilox roller can reduce electrical resistivity. At same line width, the electrical resistivity of flexography is reduced 3–5 times. The analysis results show that based on the same printing method, changing the line angles has no impact on the electrical resistivity. Thinner lines have lower resistivity that compared to wider lines they are conducive to better conductivity of graphene molecules. Baker et al. [10, 11] analyzed graphene ink flexography that they dispersed graphene nanoflakes and bar-boxymethyl cellulose (CMC) in mixture of water and isopropyl alcohol to get the ink of a viscosity of $20 \ mPa \cdot s$ [11], which is printed on an ITO substrate at a rate of $0.4 \ m \cdot s^{-1}$ through roll-to-roll technique, resulting in a conductive membrane with good light permeability. Juliusz et al. [12] found that in the flexography the line direction has a great influence on the duplication quality. Critically, when then the angle is 90° to the printing direction, the width of correctly duplicated lines is at least two times of the lines parallel to the printing direction. The analysis results show that printing on flexography synchronously of 0°, 45°, 90°, the printing quality is stable when the line width exceeds 100 μm [13]. When the line width direction is not 0°, the unevenness of substrate and slight fluctuation of ink thickness are more easily detected.

Therefore, the flexography shall emphasize on the optimization of duplication rate of thin lines. When the line width exceeds 150 μm, seams are prone to coffee-ring effect, causing short circuit of electronic devices.

## 4.5    Micro-contact Flexography

Micro-contact printing is a printing technique used for mciro-nano patterns that compared to traditional flexography, it can produce finer lines. In Perl's previous studies, the results show that through optimization of flexographic plate the higher printing performance of flexography can be achieved, even with potential roughness of printed substrates, lines of width less than 1 μm can be printed. Maksud et al. [14] successfully printed patterns of 10-μm line width and 10 μm pitch by micro-contact printing technique, demonstrating that Perl's works are totally feasible. Suhaimi et al. [14] successfully printed patterns of 3 μm line width and 3 μm pitch by the same technique (as shown in Fig. 2). In ink field, Le et al. [15] used micro-contact printing technique to print graphene ink dots with a diameter of 50 μm through 20-min interval and 20 printing times, which demonstrates that graphene ink printing by micro-contact of 50 μm lateral resolution is feasible with hydrophilic graphene oxide dispersed in water.
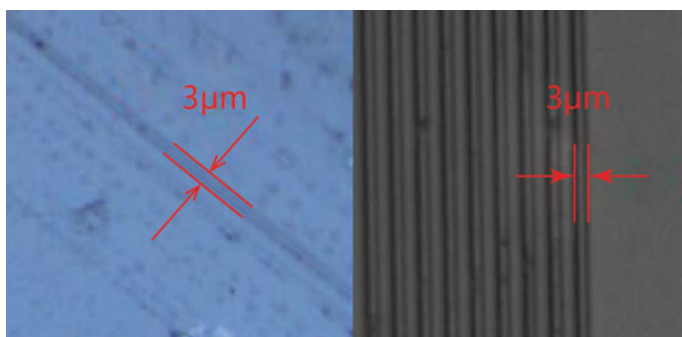


**Fig. 2.**  3 Pattern of μm line width and 3 μm spacing

After all, the combination of micro-contact and flexography printing is a revolutionary technique for the future scale graphene ink printing, manifesting clear industrial application prospects.

## 5    Conclusions

In recent years, with increasingly emerging of intelligent packaging and printed electronics, and continuous development of preparation technologies of graphene, a green and sustainable industrial application will be eventually achieved. Traditional printing techniques, especially the most environmental friendly and most promising flexography, will contribute to the development of flexible electronics and intelligent packaging

industries with the continuous optimization of ink dispersion technology, printing matching capability, flexographic plate innovation and plate making technique.

# References

1. Chang Q, Li L, Sai L, Shi W, Huang L (2018) Water-soluble hybrid graphene ink for gravure-printed planar supercapacitors. Adv Electron Mater 4(8):14–19
2. Tran T, Dutta N (2018) Graphene inks for printed flexible electronics: graphene dispersions, ink formulations, printing techniques and applications. Adv Colloid Interface Sci
3. Huang S, Shen R, Qian B, Li L, Wang W, Lin G, Zhang X, Li P, Xie Y (2018) Thermal bubble inkjet printing of water-based graphene oxide and graphene inks on heated substrate. J Phys D: Appl Phys 51(13)
4. Hassan S, Yusof M, Embong M, Ding S, Maksud M (2018) Surface study of graphene ink for fine solid lines printed on BOPP Substrate in micro-flexographic printing using XPS analysis technique. IOP conference series: materials science and engineering, vol 298, no 1
5. Xu C, Shi X, Lu G, Wang X, Wang X, Li J (2018) Optimization of graphene conductive ink with 73 wt% graphene contents. J Nanosci Nanotechnol 18(6)
6. Baker J, Deganello D, Gethin DT, Watson TM (2014) Flexographic printing of graphene nanoplatelet ink to replace platinum as counter electrode catalyst in flexible dye sensitised solar cell. Mater Res Innov 18(2)
7. Li P, Tao C, Wang B, Huang J, Wang J (2018) Preparation of graphene oxide-based ink for inkjet printing. J Nanosci Nanotechnol 18(1)
8. Lee C, Chen C, Chen C (2013) Graphene nanosheets as ink particles for inkjet printing on flexible board. Chem Eng J 230
9. Maksud M, Yusof M, Jamil M (2016) An investigation onto polydimethylsiloxane (PDMS) printing plate of multiple functional solid line by flexographic. Adv Mater Res 844:158–161
10. Hassan S, Yusof M, Embong Z, Maksud M (2016) Angle resolved x-ray photoelectron spectroscopy (ARXPS) analysis of lanthanum oxide for micro-flexography printing, AIP conference proceedings, vol 1704, p 040002
11. Hassan S, Yusof M, Maksud M, Nodin M, Rejab N, Mamat K (2015) A study of nanostructure by roll to roll imprint lithography. In: International symposium on technology management and emerging technologies (ISTMET), pp 132–135
12. Bould B, Claypole T, Bohan M (2014) An investigation into plate deformation in flexographic printing. Proc Inst Mech Eng Part B: J Eng Manuf 218:1499–1511
13. Tran T, Dutta N, Choudhury N (2018) Graphene inks for printed flexible electronics: graphene dispersions, ink formulations, printing techniques and applications. Adv Coll Interface Sci 12(6):20–23
14. Sang T, Dutta N, Roy C (2019) Graphene-based inks for printing of planar micro-supercapacitors. Rev Mater (Basel, Switzerland) 252–259
15. Luis B, Alfredo D, Escosura M, Marc B, Julio C, Arben M (2018) Production and printing of graphene oxide foam ink for electrocatalytic applications. Electrochem Commun 8 (22):65–67

# Review of Patented Technology of Magnetic Ink Anti-counterfeiting

Jiao Wu[(✉)] and Huilin Ge

Patent Examination Cooperation Guangdong Center of the Patent Office,
CNIPA, Guangzhou, China
`wujiao8l5@l63.com`

**Abstract.** Currently, the magnetic ink anti-counterfeiting technology has been widely used in the anti-counterfeiting manufacture of RMB, bank tickets, credit cards and other valuable tickets. However, the advantages and disadvantages of the anti-counterfeiting function are directly related to the vital interests of the state and the public. The intelligent manufacturing level of magnetic ink anti-counterfeiting technology is increasingly higher, with the improvement of modern technology. This paper firstly searches, counts and analyzes the domestic and foreign patents of magnetic ink anti-counterfeiting technology, summarizes the trend of patent application for magnetic ink anti-counterfeiting, and analyzes the patents of key nodes. Secondly, The development route of magnetic ink anti-counterfeiting patent technology from technical issues, patent application time, key technologies and other dimensions, and depicts the evolution map of magnetic ink anti-counterfeiting technology are summarized. Finally, the development trend of magnetic ink anti-counterfeiting technology is summarized and analyzed, and then the future development direction of patent technology and reference ideas for future technology development and patent application are provided in this paper, this contributes to the improvement of magnetic ink anti-counterfeiting technology.

**Keywords:** Anti-counterfeiting technology · Magnetic ink · Analysis of patent technology

## 1 Introduction

All kinds of counterfeit and shoddy products have flooded the market at an alarming rate, causing very serious economic losses. We must attach great importance to the development and application of the new anti-counterfeiting technologies [1, 2]. Anti-counterfeiting printing technology was originally applied to securities such as banknotes, checks, bonds, stocks, etc., and has been widely used in the trademark and packaging fields of commodities. The magnetic ink anti-counterfeiting technology involved in this paper belongs to the special ink anti-counterfeiting technology, and refers to the printing method using magnetic ink mixed with iron oxide powder [3, 4].

Magnetic anti-counterfeiting inks were first used in the anti-counterfeiting business of banks and postal services for automatic identification of analytical processing notes and automatic identification of sorted letters [5, 6]. Due to the excellent anti-

counterfeiting effect of magnetic anti-counterfeiting ink, it has been widely used in anti-counterfeiting of bills, certificates, banknotes and securities [7, 8]. Higher and higher requirements for the scientific and technological content and technical level of magnetic ink anti-counterfeiting technology were needed.

## 2   Patent Distribution of Magnetic Ink Anti-counterfeiting Technology

In order to study the development of magnetic ink anti-counterfeiting technology, the domestic and foreign patent documents related to magnetic ink anti-counterfeiting technology is obtained through patent search, and indexed the above documents [9, 10], and statistically analyzed the patent application data in the technical field according to the indexing results and analysis. The following is an analysis of the technical composition of the magnetic ink anti-counterfeiting technology.

Magnetic ink anti-counterfeiting technology can be divided into three aspects: magnetic ink material, magnetic ink anti-counterfeiting method and magnetic ink printing structure. Magnetic ink materials: magnetic pigment particles are the focus of patent applications; anti-counterfeiting methods: image combination and visual application of anti-counterfeiting technology patent application focus; magnetic ink printing structure: for magnetic orientation structure is the patent application focus.

The magnetic ink consists of a pigment, a binder, an auxiliary agent, etc., but the pigment used is not a pigment but a ferromagnetic material, and the so-called ferromagnetic material is magnetized by being inserted into a magnetic field. A functional special material that retains the magnetization value even if the magnetic field is removed [11, 12]. The main function of the binder and auxiliary agent is to ensure that the magnetic ink has comparable printing suitability to ordinary inks, and the magnetic material content of the magnetic pigment, the coercive force of the magnetic particles, the residual magnetic density and the like are all important factors affecting the performance of the magnetic ink. Factors have an important impact on the final anti-counterfeiting effect. Therefore, magnetic pigments have always been a material of concern to patent applicants, leading the number of patent applications in materials.

In order to pursue high-quality anti-counterfeiting effects, domestic and foreign applicants are constantly trying new anti-counterfeiting methods. The method of obtaining visually dynamic variable anti-counterfeiting patterns through magnetic field distribution characteristics has been the focus of research. In addition, anti-counterfeiting ink materials with different characteristics are used. Another research focus is printing different areas or printing at different levels to improve the level of anti-counterfeiting identification and which also belongs to the patent application center of gravity in the magnetic printing anti-counterfeiting method.

The characteristics of the magnetic field in which the magnetic particles are in the magnetic ink play an important role in the resulting anti-counterfeit image. Therefore, magnetic orientation structures are a research focus in magnetic ink printing.

## 3    3Development of Magnetic Ink Anti-counterfeiting Technology

### 3.1    Magnetic Ink Materials

The most commonly used magnetic pigments are $Fe_2O_3$ and $Fe_3O_4$. There are many proposals for improving the specific materials and components of magnetic ink binders, magnetic pigments and auxiliaries in various periods [13].

In the 1970s, optically variable magnetic materials were used in the anti-counterfeiting of magnetic inks, especially on banknotes. The United States has proposed a magnetic ink on the carrier in a low viscosity state, and changing the viscosity of the magnetic ink by heating; In the 1980s, a number of technologies for magnetic ink materials were proposed abroad, which respectively defined specific materials for magnetic ink binders, magnetic pigments, and auxiliaries. Specific materials can be seen in Fig. 1. In the 1990s, a magnetic color-changing ink containing a magnetic color-changing film powder in a colorless transparent ink was proposed.
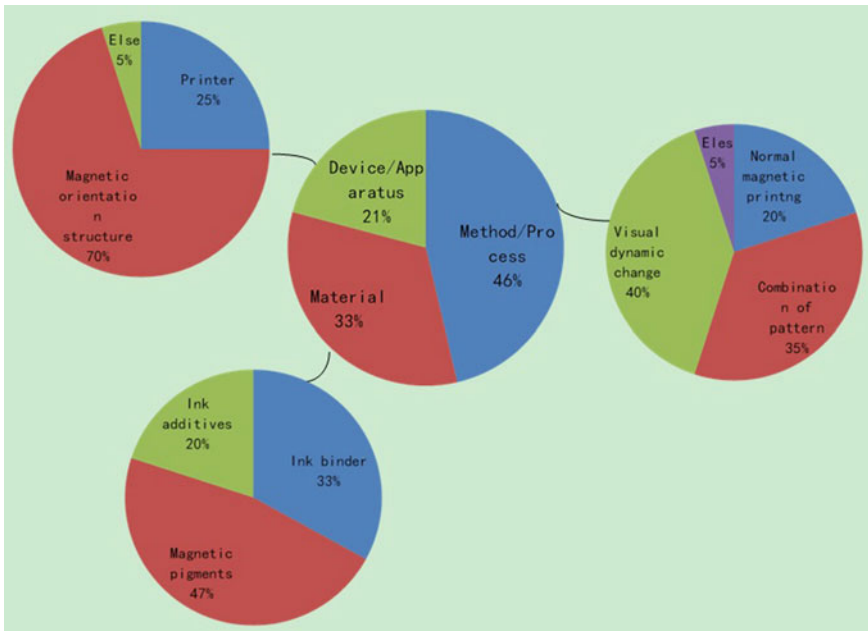


**Fig. 1.**  Analysis of the composition of magnetic ink anti-counterfeiting technology

In the 2000s, domestic applicants are committed to improving and innovating optical effects. At domestic and abroad, magnetic materials prepared by one or more selectively absorbed magnetic materials have been used to increase the anti-counterfeiting effect and increase the difficulty of imitation. Specific materials can be seen in Fig. 2. In addition, magnetically variable magnetic ink materials have emerged.

| Year of application | 1970s-1980s | 1990s | 2000s | 2010s |
|---|---|---|---|---|
| Key Technological Elements | Magnetic ink that can be heated by changing the viscosity; Adding selective absorbing materials; Polyester resin ues as ink binder; Add additives such as corrosion inhibitors; Multi-color magnetic ink。 | Color changeable magnetic ink; Oxidative drying reductase polymerization ink。 | Magnetic thin film interference pigment, interference coated metal pigment, interference coated non-metallic pigment, magnetic liquid crystal pigment | Nanoscale magnetic ink; The core of the magnetic material is coated with other materials on the outer periphery; Multifunctional magnetic ink; UV-LED magnetic anti-counterfeiting ink. |

**Fig. 2.** Analysis of domestic and foreign technical routes of magnetic ink materials

For example, when a certain temperature is exceeded, the ink is magnetically lost, and when the temperature returns to a certain temperature, the ink recovers magnetic properties. Magnetic ink with a memory code has also appeared, and password input and reading are realized by electromagnetic conversion. Magnetic thin film interference pigments, interference coated metal pigments, interference coated non-metallic pigments, magnetic liquid crystal pigments, and the like are also present, and the above pigments may be mixed to prepare magnetic ink materials [14].

In the past 10 years, there have been many improvements in the mixing of various magnetic pigments, such as magnetic optical pigments mixed with magnetic liquid crystal pigments to prepare magnetic inks; optical non-variable magnetic pigments mixed with optically variable magnetic pigments to prepare magnetic inks. Specific materials can be seen in Fig. 2. Techniques for coating other materials on the outer periphery of the core of the magnetic material to obtain a richer optical effect have also been improved, such as coating a highly reflective material, an interference material, and the like on the periphery of the magnetic core. Magnetic nano-ink materials have also appeared. Further, in terms of the drying efficiency of the magnetic ink, an oxidative drying type magnetic ink and an LED-UV magnetic anti-counterfeiting ink material have been proposed [15].

## 3.2    Magnetic Ink Anti-counterfeiting Process

Before 2000, there was a magnetic anti-counterfeiting printing method for forming a magnetic ink printing pattern in a specific region according to the distribution of magnets or magnetic poles. The magnetic particles in the magnetic ink would follow the electrode of the magnetic pole. The distribution or magnetic field direction exhibits directional movement and distribution, and the anti-counterfeiting effect of different patterns can be observed from different visual angles.

In 2000s, it was proposed at domestic and abroad to use a variety of printing methods to achieve magnetic ink printing, including inkjet printing, screen printing, stamping and multi-lamination. Specific methods can be seen in Fig. 3. There are improvements to the magnetic ink printing method for obtaining an optical pattern that can dynamically change the appearance by a magnetic field. There is also a composite anti-counterfeiting technology which uses a magnetic ink with different functions and features to form a metachromatic paired ink, and respectively prints a pattern which can be used as anti-counterfeiting information on the same substrate. In order to improve the level of anti-counterfeiting, a printing method in which a multi-layer magnetic ink pattern is used to form an anti-counterfeiting pattern is also proposed.

| Year of application | 1970s-1990s | 2000s | 2010s |
|---|---|---|---|
| Key Technological Elements | Optically variable transfer foil magnetic anti-counterfeiting. | Different patterns are presented at different angles; Multiple image combinations or stacks; A combination of images formed by a variety of functional inks. | Visually dynamic magnetic anti-counterfeiting. |

**Fig. 3.** Domestic and international technical route analysis of magnetic ink anti-counterfeiting method

In 2010s, it was proposed at domestic and abroad to prepare magnetic inks by adding materials with magnetic functional materials, specific methods can be seen in Fig. 3. In order to increase the diversity of anti-counterfeiting images, the level of anti-counterfeiting identification is improved to some extent. It is also proposed to improve the anti-counterfeiting pattern of the light-dark or color-symmetric change with the change of the viewing angle by adjusting the direction of the magnetic field so that the magnetic light-changing ink is arranged at different angles [16].

### 3.3 Magnetic Orientation Structure of Magnetic Ink Anti-counterfeiting Printing

Prior to 2000, both magnetic and magnetic structures that formed magnetic fields by conductive coils and magnetic-oriented structures of rollers were proposed in the word, in which magnets were distributed along the circumference of the drum to generate

magnetic force on the magnetic particles on the substrate on the outer surface of the cylinder. There are also arrangements for arranging rectangular magnets to create a magnetic field, the final magnetic printed image depending on the arrangement and shape of the rectangular magnet [17] (Figs. 4 and 5).
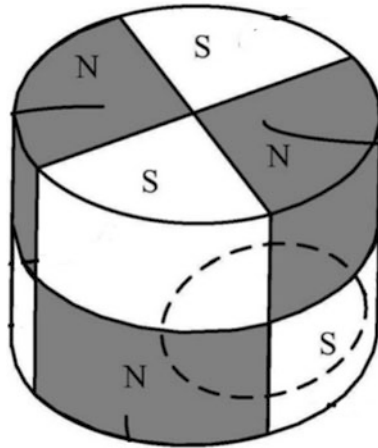


**Fig. 4.**  Schematic diagram of a magnet structure for magnetic orientation
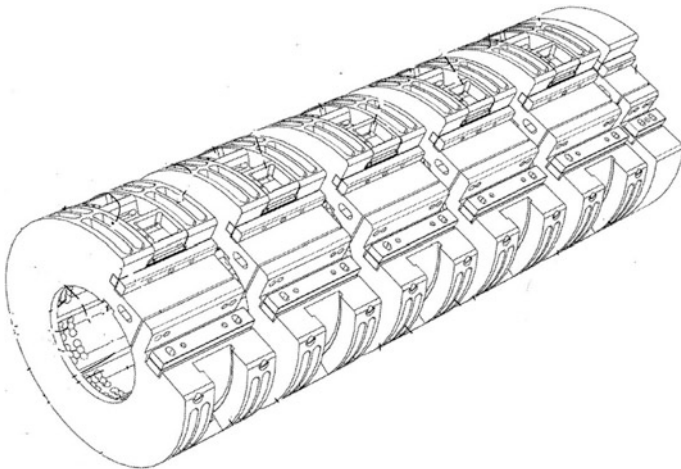


**Fig. 5.**  Schematic diagram of a drum type magnetic orientation structure

Subsequently, the surface structure of the seal with permanent magnet material was proposed in China. With the magnetic ink, the potential image of the magnetic distribution surface, shape and size can be obtained on the printing surface directly

through the stamping operation. Various magnetic printing drums have also been proposed, and the structural design of the drum has been improved.

In the past 10 years, there are magnetic orientation structures that arrange rectangular or other regular-shaped magnetic modules according to a certain regularity to generate magnetic force on the magnetic ink under the substrate, such as designing the magnet as a triangular ring, H-shaped, etc., or The N pole and the S pole are superimposed or alternately arranged according to a certain rule to form a regular magnetic field. There are also a variety of improved roller structures [18].

## 4 Prospect of Magnetic Ink Anti-counterfeiting Technology

The UV-LED magnetic anti-counterfeiting ink is mainly composed of a photoinitiator, a magnetic pigment, a binder and an auxiliary agent. UV-LED inks have the advantages of low VOC emissions, low energy consumption, and high drying efficiency. The use of UV-LED magnetic anti-counterfeiting inks is the research focus and mainstream direction in the field of magnetic anti-counterfeiting.

The design of the magnetic orientation structure directly determines the characteristics of the magnetic field in which the magnetic particles are located, and directly affects the effect of the final magnetic ink printing pattern. Research and development of magnetically oriented structures or magnetic ink printing structures containing magnetically oriented structures have been in existence at home and abroad.

In the future, magnetic ink anti-counterfeiting technology will introduce new performance materials or new applications of known materials in terms of materials. The structure direction will be developed in the direction of intelligence, refinement and automation, and will focus on the study of magnetic inks with rich layers and high discrimination difficulty.

## References

1. Jintao M (2015) Tracking new technology of anti-counterfeiting printing. China Printing 12:65–70
2. Xie Y, Zhao L, Lin Q (2017) Optically variable magnetic ink and its application in anti-counterfeiting. Pack Eng 21:174–179
3. Zhang Y (1999) Anti-counterfeiting printing. China Light Industry Press, Beijing, pp 1–86
4. Rui Y, Yuyong L (2017) Special inks and their USES. Guangdong Print 04:34–36
5. Mu B, Yin Z (2003) Magnetic ink printing. Chin Foreign Spec Print 31 005:31–34
6. Zhaoyuan S, Bingjun C, Guiliang Z (2015) Research on financial anti-counterfeiting magnetic detection head. Technol Wind 14:19–20
7. Yu Y (2018) UV-LED magnetic anti-counterfeiting ink research. Xi'an University of Technology, Xi'an, pp 1–4
8. Fei L (2015) Preparation of anti-counterfeiting magnetic ink. Print Today 06:60–62
9. Tianqi M et al (2015) Patent analysis—method, chart interpretation and intelligence. Intellectual Property Publishing House, Beijing, pp 1–36
10. Zegang Zhu (2015) Exploration of printing anti-counterfeiting ink and anti-counterfeiting technology. Print Qual Stand 03:8–15

11. Zhiwen G (2008) Special printing technology. China Light Industry Press, Beijing, pp 327–332
12. Haidong W, Junping D (2013) Talk about anti-counterfeiting ink anti-counterfeiting application. Guangdong Print 06:38–39
13. Bo Y (2016) Research on the preparation of nano $Fe_3O_4$ and its application to painting ink. Sci Educ Article Collect 05:180–181
14. Lei W (2009) Application and development of anti-counterfeiting inks in printing field. Chin Hi-tech Enterp 18:39–40
15. Yuchao W (2010) Anti-counterfeiting printing new technology and development trend. Print Qual Stand 04:8–12
16. Suojie W, Cancai W (2009) Application of magnetic ink and printing process. Screen Print 11:26–28
17. Zhong Z (2013) Brief introduction of printing ink anti-counterfeiting technology. Chin Brand Anti-counterfeiting 01:74–77
18. Jixuan C, Liangyou C (2012) Study on the matching characteristics of the anti-counterfeiting characteristics and the ability of the discriminator for RMB. Modern Bus Trade Ind 24 (01):160–161

# Critical Tension of Web Wrinkling

Li'e Ma[✉], Yi Guo, Bin Yang, Jimei Wu, Jiaqi Yang,
and Qipeng Long

Faculty of Printing, Packaging Engineering and Digital Media Technology,
Xi'an University of Technology, Xi'an, China
{malie,wujimei}@xaut.edu.cn, l03l904934@qq.com

**Abstract.** In recent years, roll-to-roll printing technology is considered as one of the most effective ways to realize large-scale manufacturing of flexible electronics. Due to some unstable factors, web wrinkling often occurs in the process of roll-to-roll printing, which will seriously affect the quality of printed products. In this paper, the stability of web transferring through roller is analyzed. Based on shell buckling theory, the theoretical model of web wrinkling is established. The analytical solutions of simple supports on four sides of open cylindrical shell are given and the critical stress and tension of web wrinkling are obtained. The maximum axial stress of the web is displayed, and the critical tension is obtained according to the critical stress. The results indicate that wider web with smaller elastic modulus is easy to wrinkle. The study provides theoretical basis for effective control of web wrinkle.

**Keywords:** Roll to roll printing · Wrinkle · Shell buckling · Critical tension

## 1 Introduction

Roll-to-roll printing is the most ideal production mode to manufacture the flexible electronic products [1, 2]. In roll to roll printing process, the thin flexible materials are called web such as paper, plastic web and so on. Web is a kind of flexible material with small bending stiffness and poor flexural compressive ability, which needs to be supported and guided by roller in the printing process. In this process, it is required that the web should run smoothly, without flutter, deviation or problems such as wrinkling, which will seriously affect the quality of flexible electronic products [3, 4]. Therefore, it is of great significance to study the web transferring stability especially when the web passing through the roller in the roll-to-roll printing process [5].

When the web is unstable, its ability to resist external forces is greatly reduced, which easily results in the web wrinkling. In this situation, the web stiffness in the wrinkling region will decrease or even disappear. Meanwhile, its mechanical properties are obviously different from those of the normal region. Therefore, it is necessary to determine the critical tension of the web and the relationship between stress and strain at one point in web [6, 7].

In this paper, the wrinkling problems of the web passing through the roller are studied.

## 2    Web Critical Tension Analysis

### 2.1    Theoretical Model of Web Wrinkling

Web wrinkling is a local buckling problem under compressive stress. In the roll-to-roll manufacturing process, compressive stress occurs in the web width direction due to the Poisson effect of the web structure when the web is transported through the roller, and then local buckling of the web follows [8]. This web instability is equivalent to the instability of thin shells with little bending stiffness. So the buckling of the web at the roller is analyzed based on the shell buckling theory. The model of the web and roller is shown in Fig. 1. $v$ is the web speed, $T$ is web tension, $\theta$ is the wrap angle and $R$ is radius of guide roller.
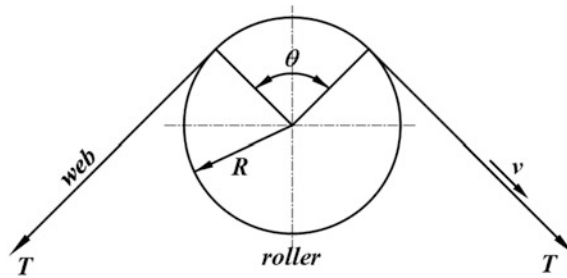


**Fig. 1.**  The web and roller

The orthogonal curvilinear coordinate system $(\alpha, \beta, \gamma)$ is shown in Fig. 2. Where $\alpha$ axis is the web width direction, $\beta$ axis is web moving direction, $\gamma$ axis is normal, $L$ is the web width, $R$ is the radius of guide roller, $\delta$ is the web thickness, and $d\theta$ is the wrap angle.

The internal force of the shell element is shown in Fig. 3.
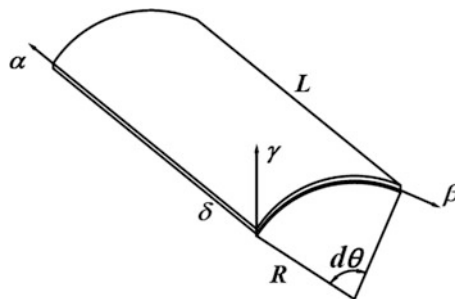


**Fig. 2.**  Cylindrical shell element model
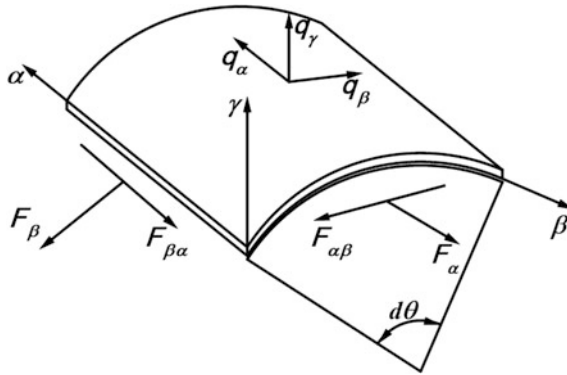
**Fig. 3.** The internal force of the shell element

The equilibrium equation of shell is obtained by the theory of flat shell [9].

$$\frac{D}{\delta}\nabla^4 w = \frac{\partial^2 \varphi}{\partial \beta^2}\frac{\partial^2 w}{\partial \alpha^2} + \frac{\partial^2 \varphi}{\partial \alpha^2}\frac{\partial^2 w}{\partial \beta^2} - 2\frac{\partial^2 \varphi}{\partial \alpha \partial \beta}\frac{\partial^2 w}{\partial \alpha \partial \beta} + \frac{1}{R_\alpha}\frac{\partial^2 \varphi}{\partial \beta^2} + \frac{1}{R_\beta}\frac{\partial^2 \varphi}{\partial \alpha^2} + \frac{q}{\delta} \quad (1)$$

where $D$ is the bending stiffness, $E$ is the elasticity modulus of web, $v$ is Poisson's ratio of web, $q$ is shell normal load, $\varphi$ is stress function and $w$ is the web deflection.

The relationship between stress and stress function is defined as follows:

$$\sigma_\alpha = \frac{F_\alpha}{\delta} = \frac{\partial^2 \varphi}{\partial \beta^2} \quad \sigma_\beta = \frac{F_\beta}{\delta} = \delta\frac{\partial^2 \varphi}{\partial \alpha^2} \quad \tau_{\alpha\beta} = \frac{F_{\alpha\beta}}{\delta} = -\delta\frac{\partial^2 \varphi}{\partial \alpha \partial \beta} \quad (2)$$

The deformation continuous equation of shell is calculated:

$$\frac{1}{E}\nabla^4\varphi = -\frac{1}{R_\alpha}\frac{\partial^2 w}{\partial \beta^2} - \frac{1}{R_\beta}\frac{\partial^2 w}{\partial \alpha^2} \quad (3)$$

The Eq. (1) is calculated using $\nabla^4$, the eighth order differential equation of deflection $w$ is obtained as follows:

$$\frac{D}{\delta}\nabla^8 w + \frac{E}{R_\alpha^2}\frac{\partial^4 w}{\partial \beta^4} + \frac{E}{R_\beta^2}\frac{\partial^4 w}{\partial \alpha^4} + 2\frac{E}{R_\alpha R_\beta}\frac{\partial^4 w}{\partial \alpha^4 \partial \beta^2} +$$
$$\frac{\partial^2 \varphi}{\partial \beta^2}\nabla^4\left(\frac{\partial^2 w}{\partial \alpha^2}\right) + \nabla^4\frac{\partial^2 \varphi}{\partial \alpha^2}\left(\frac{\partial^2 w}{\partial \beta^2}\right) - 2\frac{\partial^2 \varphi}{\partial \alpha \partial \beta}\nabla^4\left(\frac{\partial^2 w}{\partial \alpha \partial \beta}\right) = \frac{1}{\delta}\nabla^4 q \quad (4)$$

In the web and guide roller model, $R_\alpha = \infty$, $R_\beta = R$. Substituting Eq. (2) into Eq. (4), web equilibrium differential equation is obtained:

$$\frac{D}{\delta}\nabla^8 w + \frac{E}{R^2}\frac{\partial^4 w}{\partial\alpha^4} + \sigma_\alpha\nabla^4\left(\frac{\partial^2 w}{\partial\alpha^2}\right) + \sigma_\beta\nabla^4\left(\frac{\partial^2 w}{\partial\beta^2}\right) + 2\sigma_{\alpha\beta}\nabla^4\left(\frac{\partial^2 w}{\partial\alpha\partial\beta}\right) = \frac{1}{\delta}\nabla^4 q \quad (5)$$

## 2.2    Critical Tension

The wrinkling phenomenon of the web is attributed to the fact that the web cannot withstand compression stress. Therefore, in order to analyze the critical buckling condition of the web, it is necessary to consider the axial pressure of the web [10].

Assuming the web is under a free force moment, the normal load $q$ is zero.

$$\sigma_\alpha = \sigma, \ \sigma_{\alpha\beta} = 0, \ \sigma_\beta = 0 \quad (6)$$

Defining $\zeta = \alpha/R$, $\eta = \beta/R$, and substituting Eq. (6) into Eq. (5), the following expression is obtained:

$$\frac{D}{\delta}\nabla^8 w + \sigma R^2\nabla^4\left(\frac{\partial^2 w}{\partial\eta^2}\right) + ER^2\frac{\partial^4 w}{\partial\zeta^4} = 0 \quad (7)$$

The flexural function is defined as follows:

$$w(\zeta, \eta) = A\sin\frac{m\pi R}{L}\varsigma\sin\frac{n\pi}{\theta_0}\eta \quad (8)$$

Substituting Eq. (8) into Eq. (7), and defining $r = m\pi R/L$, $s = n\pi/\theta_0$.

$$\frac{D}{\delta}\left(r^2 + s^2\right)^4 + ER^2 r^4 + \sigma R^2 r^2\left(r^2 + s^2\right)^2 = 0 \quad (9)$$

Defining $P = (1 - v^2)\sigma/E$, $c = \delta^2/12R^2$, Eq. (9) becomes:

$$P = \frac{\left(r^2 + s^2\right)^2}{r^2}c + \frac{(1 - v^2)r^2}{\left(r^2 + s^2\right)^2} \quad (10)$$

Defining $t = \frac{\left(r^2 + s^2\right)^2}{r^2}$, $\frac{dP}{dt} = 0$, and substituting them into Eq. (10):

$$P = 2\left[c\left(1 - v^2\right)\right]^{1/2} \quad (11)$$

Substituting $P = (1 - v^2)\sigma/E$ and $c = \delta^2/12R^2$ into Eq. (11), the critical axial compression stress of the web is obtained:

$$\sigma_{cr} = \frac{E\delta}{R\sqrt{3(1 - v^2)}} \quad (12)$$

The maximum compressible stress between the web and the roller is defined as follows:

$$\sigma_\alpha = \mu \frac{TL}{2R\delta} \tag{13}$$

where $\mu$ is the static friction coefficient between the web and the roller, $T$ is the web tension.

Equating the Eqs. (12) and (13), the critical buckling tension of web is obtained:

$$T_{cr} = \frac{2E\delta^2}{\mu L \sqrt{3(1 - v^2)}} \tag{14}$$

When $T > T_{cr}$, the wrinkles will occur on the center line of the web wrapped over the roller.

## 3  Instance Analysis

In order to intuitively show the change law of critical tension and analyze the influencing factors, the critical web tension is calculated and analyzed based on the parameters of FR-400 gravure press of Beiren. The parameters of web and roller are displayed in Table 1.

**Table 1.**  Parameters of web and guide roller

| Parameters description | Parameters | Value | Unit |
|---|---|---|---|
| Static friction coefficient | $\mu$ | 0.3 | |
| Web Poisson's ratio | $v$ | 0.1 | |
| Elastic modulus of web | $E$ | 1.59, 2.1, 3.72, 5.32 | GPa |
| Web width | $L$ | 500–1500 | mm |
| Web thickness | $\delta$ | 0.025, 0.1, 0.175, 0.25 | mm |

When elastic modulus of web is 2.1 GPa, the relationships between the critical tension and the web width and web thickness are shown in Fig. 4. The critical tension decreases as the web width increases. The critical tension increases as the web thickness increases. Therefore, the smaller the web width and the thickness of web are not easy to cause wrinkle.

When web thickness is 0.1 mm, the relationships between critical tension and web width, web elastic modulus are shown in Fig. 5. The critical tension increases as the elastic modulus of web increases. Therefore, the web is difficult to wrinkle under the condition of large elastic modulus.
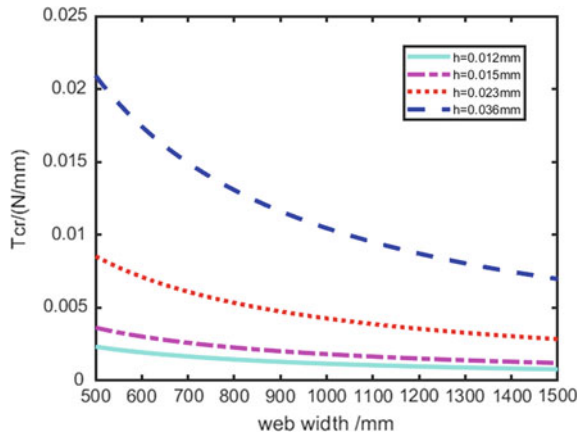
**Fig. 4.** The relationship between critical tension and web width and thickness
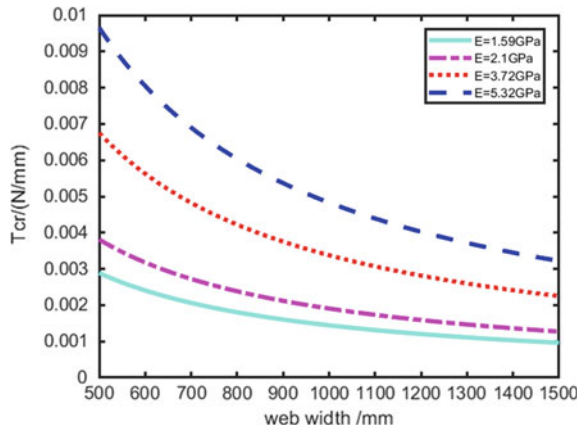


**Fig. 5.** The relationship between critical tension and elastic modulus of web

## 4    Conclusions

In this paper, the stability when web transferring through roller in the roll-to-roll printing process is analyzed. Based on shell buckling theory, the theoretical model of web wrinkling is established. The critical tension of web wrinkling is derived by combining the analytical solution of simple supports at four sides of open cylindrical shell under the critical instability state. The results indicate that the critical tension is related to the elastic modulus of web, web width and web thickness. When the width of the web is larger and the thickness and the modulus of elasticity are smaller, the web will be wrinkled easily. The above research provides an important theoretical basis for the control of web transferring stability.

# References

1. Abbel R, Galagan Y, Groen P (2018) Roll-to-roll fabrication of solution processed electronics. Adv Eng Mater 20(8):1701190
2. Mozumder MS, Mourad AH, Pervez H et al (2019) Recent developments in multifunctional coatings for solar panel applications: a review. Sol Energy Mater Sol Cells 189:75–102
3. Wu JM, Lei WJ, Wu QM (2014) Transverse vibration characteristics and stability of a moving membrane with elastic supports. J Low Freq Noise Vib Act Control 33(1):65–77
4. Chen SS, Chen WH, Liu JM (2018) Development of an aerostatic bearing system for roll-to-roll printed electronics. J Micromech Microeng 28(6):065002
5. Yin ZP, Ma L, Chen JK (2017) Advanced in transverse vibration of axially travelling web in roll to roll manufacturing. J Vib Meas Diagn 37(5):853–864
6. Tan F, Yang QS, Li ZW (2006) Wrinkling criteria and analysis method for membrane structures. J Beijing Jiaotong Univ 30(1):35–39
7. Zhang Y (2011) Finite element analysis of web structure wrinkling. Hebei University
8. Nukala V (2016) Buckling of isotropic and orthotropic webs. ProQuest dissertations and theses full-text search platform
9. He FB, Shen YP (1993) The of plates and shells theory. Xi'an Jiaotong University Press
10. Cheng XS (1989) Application of plate and shell theory. Shandong science and technology press, Jinan

# Packaging Engineering Technology

# Static Compression Experiment and Finite Element Simulation Analysis of Honeycomb Paperboard

Chenyu Liu, Wujie Zhang, Gaimei Zhang[(✉)], Xiaoli Song,
Jiandong Lu, Yue Cao, Jiazi Shi, Shasha Li, and Yanzhi Huang

Beijing Institute of Graphic Communication, Beijing, China
zhang_gaimei@163.com

**Abstract.** The work aims to study the mechanical properties of honeycomb paperboard during static compression. The finite element method was used to establish the honeycomb paperboard model, simulate the crushing process of honeycomb paperboard. Combining the real data obtained in the original experiment to verify the experimental conclusion and study the characteristics and the structural parameters (thickness) of honeycomb paper. The effect of the mechanical properties of honeycomb paperboard. The experiment result shows the quasi-static compression experiment and finite element simulation results of honeycomb paperboard consistently show that the quasi-static compression of honeycomb paperboard is divided into four stages: linear elastic phase, yield phase, platform phase and compaction phase. It is verified that the smaller the thickness of the honeycomb paperboard in the experimental range, the greater the maximum load force at the platform stage, and the better the energy absorption effect of the platform stage. This paper combines the actual test results of honeycomb paperboard static compression with the simulation results, and verifies the feasibility of finite element simulation analysis of the mechanical properties of honeycomb paperboard, and further explores the mechanical properties of honeycomb paperboard during static compression.

**Keywords:** Honeycomb paperboard · Static compression · Finite element method · Simulation analysis · Mechanical property test

## 1 Introduction

Honeycomb paperboard based on honeycomb structure has the characteristics of small density, high edgewise crush resistance, good cushioning performance, and environmental protection [1]. It is mainly used in heavy-duty cartons, trays and cushioning liners in packaging [2]. Honeycomb paperboard has great research value and has received extensive attention from academia. Wang et al. demonstrated the effects of different strength impacts on the cushioning properties of honeycomb paperboards [3]; Guo et al. evaluated the compression properties and buffer energy absorption of composite layered structures by static compression and drop impact compression tests [4]; Mou et al. established platform theory, the model studies the stress of honeycomb paperboard [5]; Yang et al. generated the relationship between damping characteristics

and structure of honeycomb paperboard [6]. The characteristics of the base paper in the current research simulation are not experimental data derived from practical applications. In this paper, the combination of honeycomb paperboard static compression testing and finite element simulation is used. We used the ABAQUS finite element analysis software to establish the honeycomb paperboard model, simulate the crushing process of honeycomb paperboard, and combine the experimental data of the base paper to study the structural parameters of honeycomb paperboard and the effect of on the mechanical properties (thickness) of honeycomb paperboard.

## 2  Mechanical Properties Test of Honeycomb Paperboard

**Experimental equipment**: Computer control electronic universal testing machine (Type: Shenzhen Xinsisi Material Testing Co., Ltd. SANS CMT4304).

Ten sets of tensile strain tests were carried out on110g/m$^2$ of inside liner and 200 g/m$^2$ of outer liner in longitudinal and transverse directions [7], and determine the elastic modulus and yield strength of the base paper [8]. The elastoplastic data of the longitudinal and transverse directions of the base paper are obtained by calculation [9], as well as the elastoplastic data in the ZD direction of the base paper, the shear modulus in the xyz direction, and Poisson's ratio [10, 11].

The data obtained in this experiment is substituted into the finite element simulation modeling to make the simulation realistic and ensure the accuracy of the model.

## 3  Quasi-static Compression Test of Honeycomb Paperboard

Set the compression rate to 12 mm/min, 90% of the thickness, that is, the compression specified strain is 90%, and gradually increase the load on the test sample along the thickness direction [12].

Since the honeycomb paperboard is subjected to a load in the vertical direction, the inside liner is mainly subjected to the force, and it can be considered that the cross-sectional dimension of the honeycomb paperboard sample remains unchanged during the compression process, which is 100 mm*100 mm. The external load-displacement curve of the honeycomb paper compression is changed into a nominal stress-strain curve by numerical calculation and unit transformation [13]. It can be known initially that without considering other factors, the greater the thickness of the honeycomb paperboard, the better the energy absorption effect.

## 4  Finite Element Simulation of Honeycomb Paperboard Quasi-static Compression

The finite element simulation analysis of the model studied by finite element software ABAQUS consists of three steps: pre-processing stage, simulation calculation (analytical calculation) and post-processing stage [14]. ABAQUS implements modular

operation, and builds a model based on the data obtained in the mechanical performance experiment [10]. The specific analysis process is as Fig. 1 (Fig. 2).
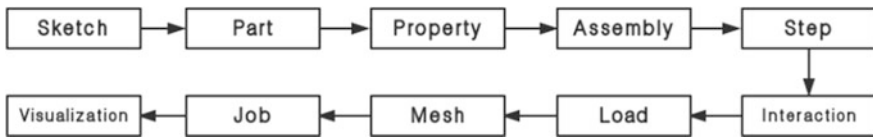


**Fig. 1.** Finite element simulation analysis process
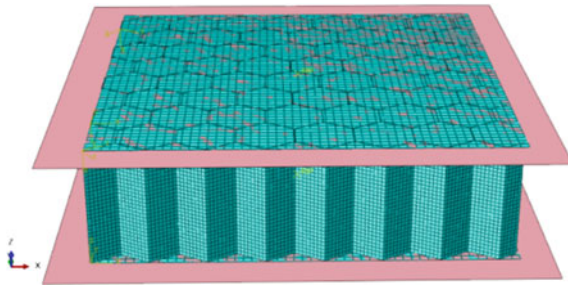


**Fig. 2.** Honeycomb cardboard model has been meshed

## 5   Comparing Simulation Results and the Experimental Results

Figure 3 is the deformation and crushing effect of the honeycomb paperboard in different stages of static compression in actual test and simulation test. Combined with the experimental results, the static compression of honeycomb paperboard can be divided into four stages: elastic stage, yield stage, plateau stage and densification stage.
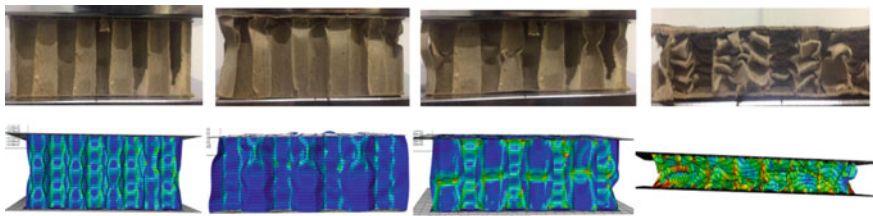


**Fig. 3.** Comparison chart of different compression quantities in actual test and simulation test

The following conclusions can be drawn from the comparison between the experimental diagram and simulation diagram of the above honeycomb board static compression at each stage:

(1) Under the premise of establishing the correct model and inputting the corre-
sponding properties of the base paper, the experimental process of the static
compression of honeycomb paperboard is basically consistent with the simulation
process.

(2) Both experiments and simulations indicate that the honeycomb paperboard ini-
tially yields from the position near the upper platen in the yield stage, rather than
yielding from the middle of the honeycomb board. And the fold form of the two
basically same as shown in Fig. 4.
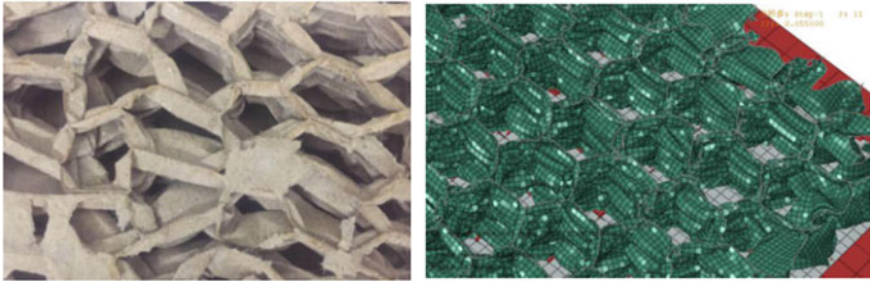


**Fig. 4.** Comparison of simulation results and experimental results in fold form

The following will analyze the difference between the finite element simulation
curves of honeycomb paperboard and the experimental curves from the stress-strain
curve angle, and compare the finite element simulation curves of honeycomb paper-
board with different thickness:
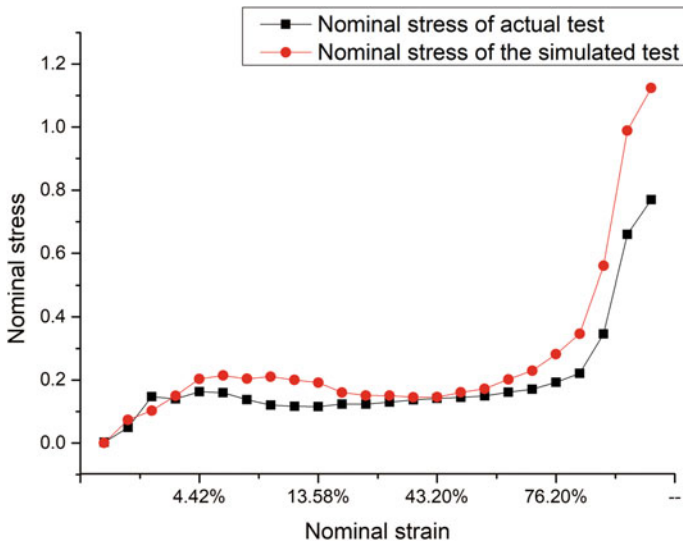


**Fig. 5.** The stress-strain curves of honeycomb paperboard with different thickness were obtained

By the result curve in the Fig. 5, it is found that:

(1) According to the data obtained by ABAQUS finite element simulation, the slope of the linear elastic phase is almost equal to the slope value of the stress-strain curve obtained by the experiment, but the stress value of the collapse point obtained by the simulation is slightly larger than that obtained by the experiment.

(2) The stress value obtained by ABAQUS finite element simulation during the plateau stage is higher than the real experimental value on average.

(3) The stress-strain curve trend of honeycomb paperboard with different thickness simulated by ABAQUS finite element method is consistent with the stress-strain curve in the laboratory.

# 6   Conclusions

In this paper, through the actual static compression test of honeycomb paperboard and finite element simulation test, it is verified that the quasi-static compression of honeycomb paperboard is divided into four stages: linear elastic phase, yield phase, platform phase, compaction phase, and honeycomb verification. The influence of structural parameters (thickness) of paperboard on its mechanical properties. By comparing the test results of the two, it is found that the experimental compression effect of the two is basically consistent with the stress-strain curve. It is verified that the static compression process of the honeycomb paperboard is simulated by the finite element model under the premise of establishing the correct model and inputting the corresponding original paper properties.

Although there are some factors that are uncontrollable in actual experiments, thus simplifying the model. These factors will more or less affect the simulation results, but from the results obtained, it is feasible to study the mechanical properties of honeycomb paperboard by using finite element simulation.

# References

1. Shengxiang L, Xingye W, Lili X, Su J, Wei S (2016) Application of honeycomb paperboard in the packaging of airdrop. Packag Eng 17:25–29
2. Junling Z, Zhongyan M (2004) Application of honeycomb paperboard in packaging. Mod Manuf 17:28–30
3. Wang ZW, Wang LJ, Xu CY et al (2016) Influence of low-intensity repeated impacts on energy absorption and vibration transmissibility of honeycomb paperboard. Packag Technol Sci 29(11):585–600
4. Guo Y, Ji M, Fu Y et al (2019) Cushioning energy absorption of composite layered structures including paper corrugation, paper honeycomb and expandable polyethylene. J Strain Anal Eng Des 54(3):176–191

5. Mou X, Lu L, Zhang W et al (2018) Characterization of in-plane load bearing of a honeycomb paperboard. Packag Technol Sci
6. Wang D, Yang R (2019) Study on damping characteristic of honeycomb paperboard and vibration reduction mechanism of packaging system. J Vib Control
7. JB/T 6544-1993, Plastic tensile and flexural modulus test method. SRIM, Shanghai
8. Yulong E, Longping L (2015) Method for determining elastic modulus and yield strength of base paper. Packag J 7(01):40–44
9. GB/T 1040.1-2006, Plastics - determination of tensile properties - part 1: general provisions. Standards Press of China, Beijing
10. Xiang H (2013) Theoretical and experimental research on nonlinear unitized packaging transport system by dynamic inverse sub-structuring method. Jiangnan University
11. Allansson A, Svärd B (2001) Stability and collapse of corrugated board. Struct Mech
12. GB/T 8168-2008. Static compression test method for cushioning materials of packaging. Standards Press of China, Beijing
13. Chunhu P (2011) Experiments and FEM analysis of cushioning property of molded pulp products. Jinan University
14. Zhihui Y (2012) Study on the characteristics of elastic wave propagation in honeycomb paperboard. Shanxi University of Science & Technology

# Experimental Study on Moisture-Proof Coating for Corrugated Boards and Boxes

Chenyang Liu, Lijiang Huo[✉], Yu Zhao, and Yin Shang

School of Light Industry and Chemical Engineering, Dalian Polytechnic
University, Liaoning, China
lijianghuo@163.com

**Abstract.** Moisture-proof coating on the surface of corrugated boards and corrugated board box is one of effective methods to satisfy a requirement of logistics distribution in damp environment. Moisture-proof coating mechanism of the corrugated board and related moisture-proof coating experimental study were discussed and carried out in this paper. Four-layer corrugated board (250 g/170 g/100 g/250 g, double C) and five-layer corrugated board (200 g/120 g/120 g/120 g/200 g, BA) were selected as experimental materials. The physical and mechanical properties of these two kinds of corrugated boards coated by damp-resistant material under different environment conditions were tested and analyzed. The optimum coating amount was determined under the conditions of temperature and humidity selected in the experiments. The results show that the combination performance of the corrugated boards and corrugated board box reached the best when the damp-resistant material consumption is 6 g/m$^2$ under RH65%.

**Keywords:** Moisture-proof coating · Corrugated board · Transport packaging · Protecting performance

## 1 Introduction

Corrugated board is one of important materials in the production system of paper transport packaging container. The physical and mechanical properties of the corrugated board and corrugated board box will be reduced once these paper materials and paper containers are stored or used in damp environment. So the corrugated board and corrugated board box need to be processed by moisture-proof coating to protect themselves to prevent or lessen the negative impact of humidification.

Most of moisture-proof coating used in the corrugated board and corrugated board box are made of hydrophobic grouping and grouping that is compatibility with paper fibre. One part of the moisture-proof coating will enter into inside of paper fibre to combine with the fibre, and the other part of the moisture-proof coating will stay on the surface of paper material, while the moisture-proof coating is used in the processing. After drying out, the coating film on the surface of the paper material will play the role of hydrophobicity. Moisture-proof coating mechanism of the corrugated board includes two kinds of types. They are the moisture proof mechanism of cationic moisture resistant coating and the moisture proof mechanism of anionic moisture resistant

coating respectively, as shown in Fig. 1a, b. Generally, the moisture resistant coating contains hydrophilic radical, like hydroxy etc. or amidogen etc., they can combine with paper fibre and play the role of hydrophobic interaction and moisture-proof [1].
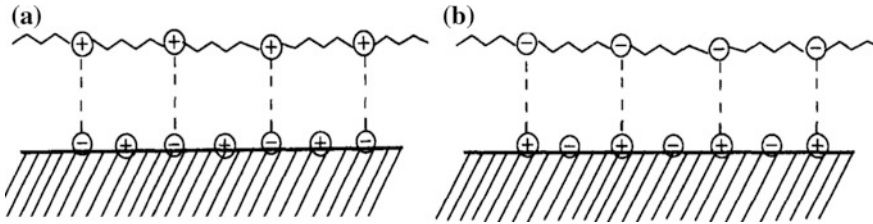


**Fig. 1.** The moisture proof mechanism

## 2 Moisture-Proof Coating Experiments

Four-layer corrugated board (250 g/170 g/100 g/250 g, double C) and five-layer corrugated board (200 g/120 g/120 g/120 g/200 g, BA) were selected as experimental materials in this study. X-300 moisture-proof coating was used to treat the corrugated boards by means of smooth roll gluing.

According to GB/T4857.2-2005 [2] and actual situation of transportation, three kinds of experimental conditions were design, such as 20 °C/RH65%, 30 °C/RH65%, 38 °C/RH65%. The samples were prepressed 72 h in climatic chamber, then performance testing were taken [3–7].

## 3 Results and Discussion

The testing results of compressive strength, edge compressive strength, breaking strength, puncture strength and rate of water content were shown in Figs. 2, 3, 4, 5, and 6. The signs of B47B and S555S respectively indicated two kinds of samples in the experiments.

The results show that the physical and mechanical properties of the two kinds of the corrugated boards costed by X-300 under the condition of RH65% all reached the performance of the corrugated boards under standard condition of 23 °C and RH50% when damp-resistant material consumption were 0–8 g/m$^2$. And the breaking strength and puncture strength of the samples reached the highest when damp-resistant material consumption were 8 g/m$^2$. However, the combination performance of the corrugated boards and boxes reached the best when the damp-resistant material consumption is 6 g/m$^2$. Also, it can be seen that the influence of ambient temperature on the physical and mechanical properties of the corrugated board and corrugated board box is relatively small under the same humidity condition.

Compressive
strength/N
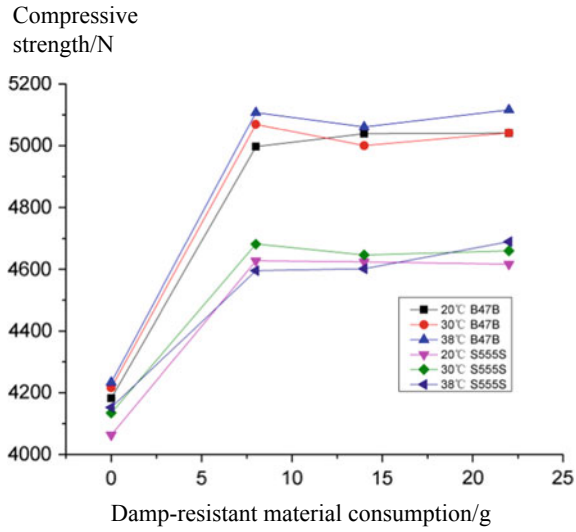


**Fig. 2.** The comparison of compressive strength

Edge compressive
strength/N/m
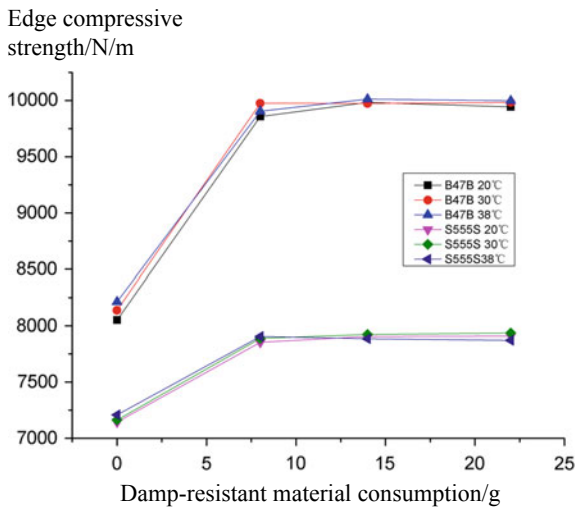


**Fig. 3.** The comparison of edge compressive strength

Breaking
strength/Kpa
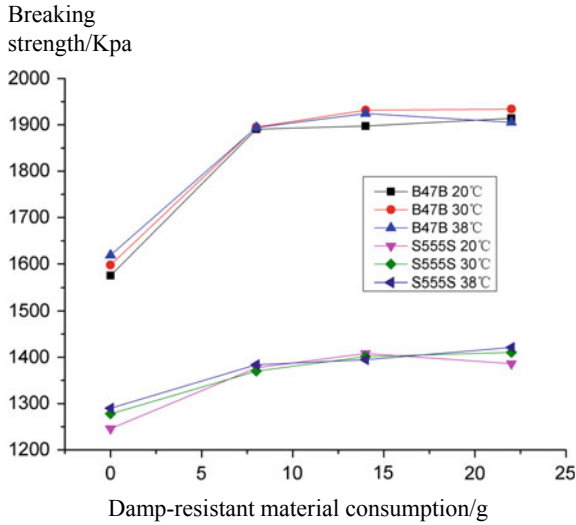


**Fig. 4.** The comparison of breaking strength

Puncturestrength/Ja
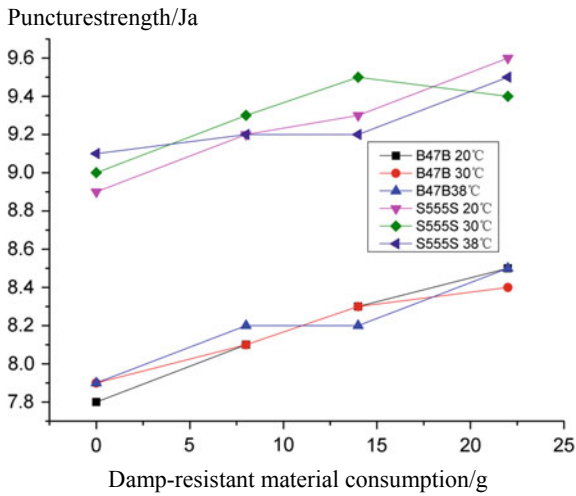


**Fig. 5.** The comparison of puncture strength

## 4   Conclusions

Be compare with temperature, humidity factor brings about more impact on the performance of corrugated boards and boxes. The paper materials and containers can be processed by moisture-proof coating method to prevent or lessen the negative impact.
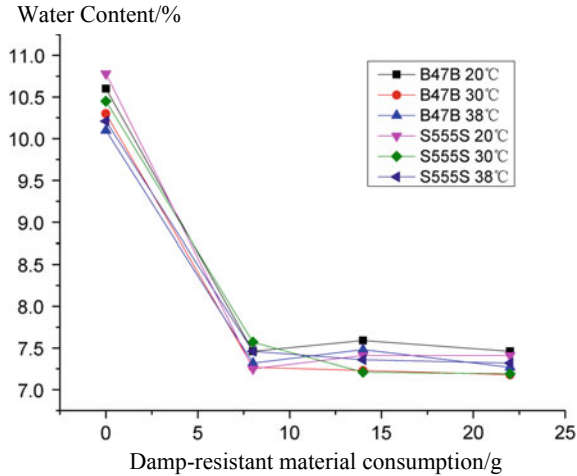
Water Content/%



**Fig. 6.** The comparison of rate of water content

With the development of the techniques, the corrugated boards would be used to design and produce more and more packaging container to satisfy special requirement of logistics distribution in damp environment.

## References

1. Zhan X, Zhu Y, Yan L et al (2006) Latest study progress of synthetic polymer cypres. East China Pap Ind 37(5):42–48
2. State Administration for Quality Supervision and Inspection and Quarantine of China, the National Standards Administration Commission of China, GB/T4857.2-2005, State Standard of the People's Republic of China, transport packaging test, the second part: Temperature and humidity control
3. State Administration for Quality Supervision and Inspection and Quarantine of China, the National Standards Administration Commission of China, GB/T 4857.4-2008, State Standard of the People's Republic of China
4. State Administration for Quality Supervision and Inspection and Quarantine of China, the National Standards Administration Commission of China, GB/T 6546-1998, State Standard of the People's Republic of China
5. State Administration for Quality Supervision and Inspection and Quarantine of China, the National Standards Administration Commission of China, GB/T 6545-1998, State Standard of the People's Republic of China
6. State Administration for Quality Supervision and Inspection and Quarantine of China, the National Standards Administration Commission of China, GB/T 2679.7-2005, State Standard of the People's Republic of China
7. State Administration for Quality Supervision and Inspection and Quarantine of China, the National Standards Administration Commission of China, GB/T 462-2003, State Standard of the People's Republic of China

# Research on Personalized Packaging Design Based on Double Gray Cardboard

Jinglin Ma$^{(\boxtimes)}$ and Qi Zeng

Shandong Communication & Media College, Jinan, China
`371725079@qq.com`

**Abstract.** The purpose of this paper is to design a personalized package using double gray cardboard. In the process of packaging design proofing and in some cases, personalized packaging production of small quantity, the use of high-density boards can cause disadvantages such as high cost and long production cycle due to the heavy reliance on mechanical equipment and complicated processes. This paper proposes the use of double-layer double-gray cardboard for the design of a unique packaging structure. By testing its compressive strength and tear strength, a complete and feasible personalized packaging design is obtained. The research method is by systematic experiments. By comparing the compressive strength increment of double-layer double-gray cardboard and single-layer double-gray paperboard, the compressive strength difference between the two materials of the same thickness is compared, and the practical feasibility is evaluated. The results indicate that the double-layer double-gray paperboard has twice the compressive strength and tear strength than the single-layer double-gray paperboard, which is close to the high-density board of the same thickness, and the process is simple and easy to operate. The important conclusion is that the use of double-gray cardboard for packaging design proofing and personalized packaging production of small quantity has important practical significance.

**Keywords:** Double gray cardboard · High density board · Compressive strength · Packaging structure design

## 1 Introduction

Among the materials used in packaging design and production, high-density fiberboard is commonly used, mainly for the skeleton lining of the gift box. It is characterized by being firm and flat, and has a certain waterproof and moisture-proof function and is not easily deformed. However, high-density fiberboard requires the use of mechanical equipment such as chainsaws and slotting machines in the production process, and generates a large amount of dust, which has a very adverse effect on environmental. Especially in the proofing process of packaging design works, the use of high-density fiberboard will complicate the process and raise the cost by a large portion due to the use of mechanical equipment, which will cause certain difficulties for proofing.

Double-gray paperboard is another material commonly used in packaging production. Compared with high-density fiberboard, double-gray paperboard of the same

thickness has a certain gap between stiffness and folding resistance. However, the use of white latex to cover the multi-layer double-gray paperboard can greatly improve its stiffness and folding resistance, and basically the strength of high-density fiberboard of the same thickness can be achieved. In addition, when the multi-layered double-gray paperboard is laminated, the processing problem of the splicing interface of the adjacent board can also be solved by using the multi-layer board of different length. Double-gray paperboard can be cut directly using a paper cutter. The operation is relatively simple, and it is suitable for individualized design of packaging and proofing of large-volume packaging products. From an environmental point of view, the raw materials used in the composite process of the double-gray paperboard are cardboard and corn starch binders, with zero harmful substances emitted during the production process, which is more conducive to environmental protection [1].

## 2 Strength Comparison Test of Double Gray Cardboard

### 2.1 Schematic Diagram of Strength Test

See Fig. 1.
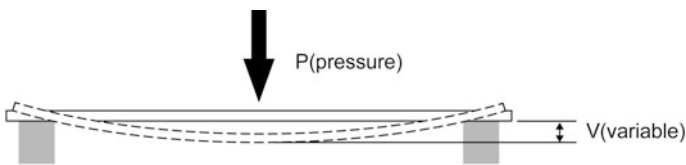


**Fig. 1.** Schematic diagram of strength test. P: pressure applied to double-gray cardboard or high-density fiberboard, V: sheet variable

### 2.2 Strength Test for Single Layer

By comparing the strength tests of high-density fiberboard and double-grey board of the same thickness, it is found that the compressive strength of the double-gray paperboard is much lower than that of the high-density fiberboard (Tables 1 and 2).

**Table 1.** 3mm comparison of strength test of high density fiberboard and double gray cardboard

|  | Thickness (mm) | Specification (mm) | Pressure (N) | Variable (mm) |
|---|---|---|---|---|
| High density fiberboard | 3 | 80 × 450 | 4.9 | 19 |
| Double gray cardboard | 3 | 80 × 450 | 4.9 | 28 |

**Table 2.** 2mm comparison of strength test of high density fiberboard and double gray cardboard

|  | Thickness (mm) | Specification (mm) | Pressure (N) | Variable (mm) |
|---|---|---|---|---|
| High density fiberboard | 2 | 80 × 450 | 4.9 | 23 |
| Double gray cardboard | 2 | 80 × 450 | 4.9 | 36 |

## 2.3   Strength Test for Double Layer Without Lamination

For the double-layer double-gray paperboard which is not covered with white latex, the compressive strength and the high-density fiberboard of the same thickness still have a large gap after being tested and tested (Table 3).

**Table 3.** 5mm comparison of strength test of high density fiberboard and double gray cardboard

|  | Thickness (mm) | Specification (mm) | Pressure (N) | Variable (mm) |
|---|---|---|---|---|
| High density fiberboard | 5 | 80 × 450 | 4.9 | 6 |
| Double gray cardboard | 5 | 80 × 450 | 4.9 | 15 |

## 2.4   Strength Test for Double Layer Cladding

Through experimental comparison, after the white latex is used to composite the double-layer double-gray paperboard and completely dried, the compressive strength of the white latex is greatly improved due to the adhesion and solidification of the white latex, and the high-density fiberboard of the same thickness has been basically Close (Table 4).

**Table 4.** 5mm comparison of strength test of high density fiberboard and double gray cardboard

|  | Thickness (mm) | Specification (mm) | Pressure (N) | Variable (mm) |
|---|---|---|---|---|
| High density fiberboard | 5 | 80 × 450 | 4.9 | 6 |
| Double gray cardboard | 5 | 80 × 450 | 4.9 | 8 |

## 2.5   Strength Test for Composite Layer

Through experimental comparison, after the white latex is used to compound and completely dry the double-gray paperboard of different layers, due to the adhesion and

solidification of the white latex, the increasing proportion of compressive strength is higher than the increasing proportion of the thickness, the multi-layer double gray board Paper lamination is conducive to the improvement of compressive strength (Tables 5 and 6).

**Table 5.** Comparison of incremental strength test of glueless laminate

|  | Thickness (mm) | Specification (mm) | Pressure (N) | Variable (mm) |
|---|---|---|---|---|
| 1- layer double gray cardboard | 2 | 80 × 450 | 4.9 | 36 |
| 2- layer double gray cardboard | 4 | 80 × 450 | 4.9 | 24 |
| 3- layer double gray cardboard | 6 | 80 × 450 | 4.9 | 12 |

**Table 6.** Comparison of incremental strength test with glue lamination

|  | Thickness (mm) | Specification (mm) | Pressure (N) | Variable (mm) |
|---|---|---|---|---|
| 1- layer double gray cardboard | 2 | 80 × 450 | 4.9 | 36 |
| 2- layer double gray cardboard | 4 | 80 × 450 | 4.9 | 17 |
| 3- layer double gray cardboard | 6 | 80 × 450 | 4.9 | 7 |

## 3 Double-Gray Cardboard Splicing Joint Design

Compared with the slotting process of high-density fiberboard, double-gray paperboard cannot be slotted by electric saw because of its soft texture, but it can be covered with different lengths of sheet metal to achieve the effect of slotting (Fig. 2).

The difference in length between the two layers of sheets is the thickness of the single-layer sheet. The step-wise splicing method is the same as the slotting of the high-density fiberboard, which can facilitate the flattening and positioning of the sheets while increasing the contact area.

### 3.1 Tear Strength Test of Adjacent Plate Joints

A tear test was performed on a high density fiberboard interface bonded with white latex and a double-gray cardboard interface of the same thickness. Both materials are joined using a stepped interface, and the detected value is the tensile value that can tear the sheet interface. The experimental results are as follows (Tables 7 and 8).

Through experimental comparison, because the adhesiveness of double-gray paperboard is better than that of high-density fiberboard, the tear strength of the
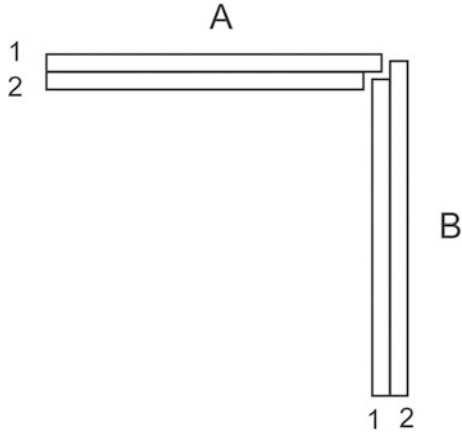
**Fig. 2.** Double gray cardboard splicing joint design

**Table 7.** Comparison of tear strength test of 5 mm sheet joint

|  | Thickness (mm) | Specification (mm) | Tear pull (N) |
|---|---|---|---|
| High density fiberboard | 5 | 80 × 200 | 18.6 |
| Double gray cardboard | 3 + 2 | 80 × 200 | 21.5 |

**Table 8.** Comparison of tear strength test of 6 mm sheet joint

|  | Thickness (mm) | Specification (mm) | Tear pull (N) |
|---|---|---|---|
| High density fiberboard | 6 | 80 × 200 | 24.1 |
| Double gray cardboard | 2 + 2 + 2 | 80 × 200 | 28.2 |

interface is better than that of high-density fiberboard. The firmness of the box made of multi-layer double-gray cardboard can meet the requirements, which promises future practical applications.

## 3.2    Double-Layer Double-Grey Board Packaging Structure Design

Due to the convenience and practicability of the double-layer double-gray paper in the cutting, laminating and splicing process, this material can be applied to the individual design and proofing of product packaging. Correct design of the board's flat structure is of great significance for the smooth completion of the finished product (Figs. 3 and 4).
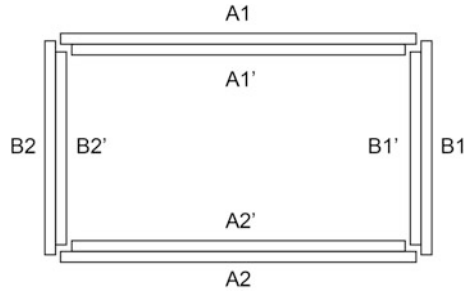
**Fig. 3.** Plane mosaic design of double gray cardboard. A1 = A2 = Design length-single layer sheet thickness $\times$ 2. A1' = A2' = design length-single layer sheet thickness $\times$ 4. B1 = B2 = Design Width. B1' = B2' = design width-single layer sheet thickness $\times$ 2
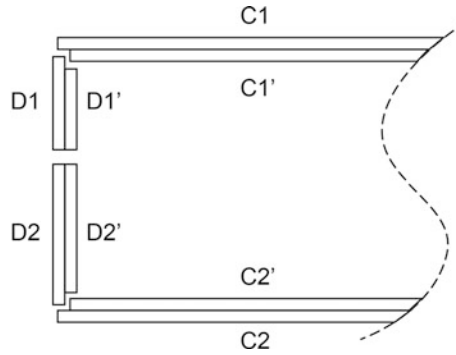


**Fig. 4.** Side splicing design of double gray cardboard. C1 = C2 = Design length. C1' = C2' = Design length-single layer sheet thickness $\times$ 2. D1 + D2 = Design height-single layer sheet thickness $\times$ 2. D1' + D2' = Design height-single layer sheet thickness $\times$ 4

## 4   Conclusion

Double-gray paperboard is double-layered or multi-layered with white latex. Due to the superior adhesiveness of double-gray paperboard, the compressive strength and tear strength are greatly improved, as well as the compressive strength. The high-density fiberboard of the thickness, the tear strength of the panel interface is better than the high-density fiberboard of the same thickness. Double-gray paperboard is easy to handle during processing, with no dust generated, and has less environmental pollution. In the design process of the packaging structure, the stepped interface is formed by using the difference in the length of the plate, which is suitable for the individualized design of the commodity packaging and the sample production of the large-volume packaging product. It is of positive significance for further promotion of personalized packaging design and environmental protection.

# Reference

1. Jing Q (2012) Energy saving, environmental protection, and efficiency improvement - new highlights of composite cardboard technology. Papermaking information, 5th edn, pp 54–55

# Integrated Testing System for Multiple Sensors in Intelligent Packaging

Haijun Zhang, Kunlin Gao, and Wei Wang[✉]

College of Information and Electrical Engineering, Zhengzhou University of
Light Industry, Henan, China
18900616029@189.cn

**Abstract.** With the huge growth of the diversified demand for the information about consumer goods, intelligent packaging plays a more and more important role. It is not only the main carrier of the process from the manufacturing end to the consumer end, but also a vital tool for information communication, and it becomes an important developing direction in package printing industry. There are many kinds of flexible sensor technologies, which can tell us the traceable information of humidity, impact, pressure, photosensitivity, route and so on in the transportation process, offering customized smart packaging service. It is essential to make an integrated testing system for these sensors, in this work, open source hardware and friendlier GUI is used by us to establish this testing system for various sensors using the updated sensor calibration algorithms, which can be compatible with Windows, Linux, Android and IOS platforms. The accuracy and efficiency of sensor testing for intelligent packaging have been greatly improved. This system can seamlessly connect with the cloud technology and the Internet of Things system through wireless communication technology, and will become the key test equipment in the field of intelligent packaging.

**Keywords:** Intelligent packaging · Integrated testing system · Flexible sensor · Generalization

## 1 Introduction

The integration of informatization and industrialization makes intelligent packaging enter a new stage of development. Intelligent packaging has become a new development direction of modern packaging industry in China [1].

For example, the application of printed electronic technology to prepare micro sensors in e-commerce intelligent packaging can help e-commerce achieve packaging informatization and visualization [2]. It can be seen that various micro sensors in intelligent packaging system play a vital role. Flexible pressure sensor is also an important part of wearable flexible equipment. It has attracted wide attention in the fields of real-time health monitoring, human motion detection, human-computer interaction and electronic skin [3–7]. However, there is no real-time testing system that can quickly measure the performance of flexible sensors in the field of intelligent packaging.

There are functional test systems in other fields according to different applications of sensors, but fewer test systems can judge the performance of sensors. For example, by comparing the duration and energy of waveform with the minimum values of sensors and instrument channels that are known to work normally on the same structure, the performance of the instrument, including coupling efficiency, can be determined. However, this method cannot measure multiple sensors simultaneously, and the effect is moderate [8]. In this study, we develop a testing system for sensors in intelligent packaging based on a new data acquisition and calibration system.

## 2   Construction of Sensor Testing System for Intelligent Packaging

The hardware part of the test system is realized by Arduino Mega2560 control board, and the communication protocol is defined to realize the data communication with the host computer software. The sensor part, flexible pressure sensor and array sensor $(4 * 4)$ reflect the pressure of the goods in the logistics process, and so on, are applied essentially to the physical information they are subject to. The number is converted to an analog signal that can be read by the controller. The software part uses the program written in Processing development environment to realize the post-processing of the sensor information. The structure block diagram is as follows (Fig. 1).
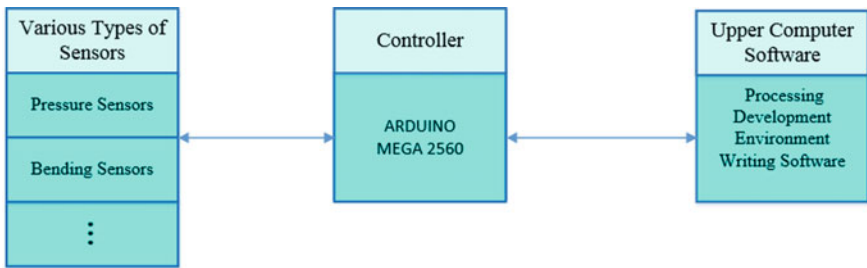


**Fig. 1.** The structure block diagram

## 3   Working Principle of Sensor Testing System for Intelligent Packaging

### 3.1   Data Acquisition

Arduino Mega2560 microcontroller board is used as the controller of this system. It can transmit data to computers and provide power for their work with USB cables. An optoelectronic isolator is added to the peripheral of the controller to improve the stability of the input and output ports, which makes the input analog more accurate. In addition, the microcontrollers with multiple communication ports provide various possibilities for future expansion, which can realize real-time communication between

cloud computing and Internet of Things system in the later stage, and provide more possibilities for subsequent development. Solidworks is used to build the 3D model and realize the data of the shape. According to the shape of the controller, the simulation platform is built, and the 3D model of the protective shell is designed to realize the digital twins. It can support the function of accurate testing of multi-channel sensors, so that the whole system has a high efficiency of testing and judging the performance of 16-point array sensors. Specific 16-point signal acquisition channel structure schematic diagram is as follows (Fig. 2).
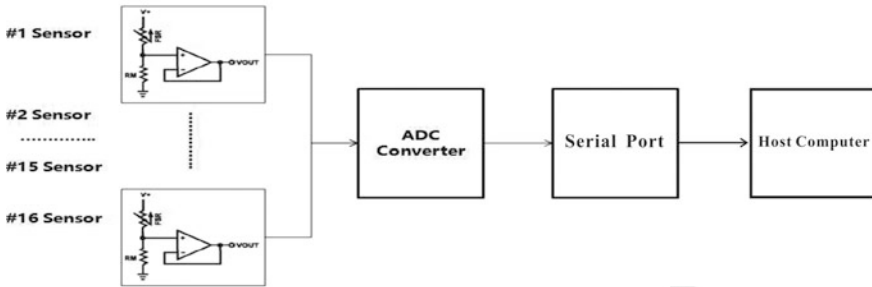


**Fig. 2.** 16-point signal acquisition channel structure schematic diagram

Using Processing development environment to design upper computer software, using CORTROLP5 library file and Serial library file in the language, data exchange with lower computer controller is realized by programming method, and the collected sensor information is processed and displayed. In order to avoid the collision and crash of multiple serial devices on the computer end, a serial port selection program is added. This development environment supports applications of multiple development platforms and can be compatible with multiple platforms at the same time, including Windows, Linux, Android and IOS, it can greatly improve the generalization and ease of use. The system realizes all-round control of sensor data. The specific functions can be divided into six functions: data transmission, data acquisition, data display, data processing, data preservation, data query and so on. It also has good interfaces for future development. Finally, through the integration of hardware and software, the data of lower computer and upper computer can be transmitted accurately and correctly, which provides a reliable platform for repeated testing.

## 3.2 Data Processing

In view of the irreplaceable role of sensors in intelligent packaging, the characteristic curve and application circuit of single-point film pressure sensor F − R are introduced emphatically. The principle of 16-point array sensor is the same. That is to say, following the formula:

$$F = K(1/R) \tag{3.1}$$

F is the force, R is the resistance value, and K is the conversion coefficient.

The production of any commodity has a certain rate of defective products, sensors are no exception. In the production process of sensors, there will be a variety of complex situations, which will lead to their performance deterioration. It is necessary to make an efficient judgment on the performance of this type of sensors. The test system we designed solves the above problems well. The K value and R value of a batch of sensors of the same type should be the same or the error should be within the range. This system is to judge the performance of the sensor by measuring the K value and R value. Firstly, it confirms whether the sensor is a universal product defined by the system. The universal product does not need to be studied and can be tested by preset parameters. Otherwise, the system needs to learn the parameters of the standard of such sensors, and save the parameters after learning, which can be used to judge the performance of such other sensors. In a simplified way, it can be described as: after learning, the sensor pressure values displayed on the computer end are compared with the sensor pressure values given by the standard pressure gauge, and the performance of the two values is better in the relevant range, otherwise they will be eliminated.

There are many noises after data acquisition, so it is necessary to filter the data to achieve results that are more accurate. Previous data acquisition systems mostly used average filtering method [9]. In this design, the method of using enhanced and linear Kalmanfiltering. It is to collect the data of the sensor in a period of time, to see the change of the value and the real value and the deviation of the data, and to establish a mathematical model of the current state. State $X(t)$ is the pressure value at the time t (the whole range is converted to 0-255 value) and t is the acquisition time of data. Since all aspects are not ideal state space, such as electromagnetic interference, vibration interference, etc., there will be many kinds of noise effects [10, 11]. Environmental impact is defined as process noise $W(t)$, whose system state equation is:

$$X(t) = X(t-1) + W(t) \tag{3.2}$$

When measuring the sensor, there are measurement errors, that is, the measurement noise is set to $V(t)$, such as the current acquisition of intensive reading of 8 bits, there are intensive reading errors. $Z(t)$ is the actual measurement value. So the equation for measurement is:

$$Z(t) = X(t) + V(t) \tag{3.3}$$

The state and observation equations of the system are as follows:

$$X(t) = AX(t-1) + \xi W(t) \tag{3.4}$$

$$Z(t) = HX(t) + V(t) \tag{3.5}$$

As a one-dimensional variable, $A = 1$; $\xi = 1$; $H = 1$ in the formula.

## 4  Working Performance of Sensor Testing System for Intelligent Packaging

According to the above model, data simulation shows that good results have been achieved. As shown in the Fig. 3.
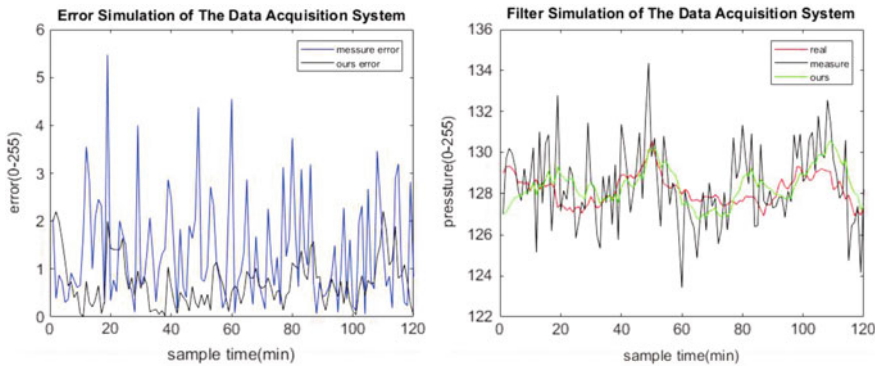


**Fig. 3.** Error simulation of the data acquisition system and filter simulation of the data acquisition system

At the same time, several groups of experiments were done to verify the accuracy of the simulation data and the collected data. We use a set of standard weights, including 100 g, 200 g. In the same environment, the above counterweights are correctly placed on the FSR Sensor in Intelligent Packaging in turn and transmitted to the host computer after AD conversion. These data are calculated once every 5 ms and averaged 30 times. The following data are obtained:

Table 1 shows that the accuracy of our acquisition system is better than that of the general system.

**Table 1.** Comparison of measurement accuracy

| Session number | 1 | 2 |
|---|---|---|
| Counterweight (g) | 100 | 200 |
| General measurement (g) | 103.2 | 203.8 |
| Ours (g) | 101.5 | 201.8 |

## 5  Conclusions

Aiming at the problem of sensor testing in the field of intelligent packaging, this study has proposed an integrated testing system for a variety of intelligent packaging sensors. It solves the problem of the previous work in that the array pressure sensor in the field of intelligent packaging can be used in a universal testing system across multiple

platforms accurately. Through the actual test experiment and the comparison with the data and simulation of the expensive manual precision instrument, the fast judgment of the sensor performance made by the system is sound and reliable, which shows the validity and feasibility of the test system for various sensors.

The sensor testing system can be further improved to meet the need of more sensor types, requirements that are more functional and more applications in intelligent packaging field. Thus, many kinds of sensors can be automatically identified; the data of sensors can be classified and saved; and the number of test sensors and test reports can be formed. Also, linking the testing system with the cloud computing will realize the remote operation of each sensor, which will be very important for intelligent packaging industry.

# References

1. Chen KF, Chen GX (2019) Intelligent packaging: development status, key technologies and application prospects. Packag J 11(1):1–17
2. Li WR, Li H, Sun JZ (2019) New development of intelligent packaging: manufacturing micro sensor based on printed electronics technology and its application in E-commerce packaging. Print Today 4:24–27
3. Wang X, Liu Z, Zhang T (2017) Flexible sensing electronics for wearable/attachable health monitoring. Small 13(25). https://doi.org/10.1002/smll.201770138
4. Zang Y, Zhang F, Di C, Zhu D (2015) Advances of flexible pressure sensors toward artificial intelligence and health care applications. Mater Horiz 2(2):140–156
5. Donati M, Vitiello N, Rossi SMMD, Lenzi T, Crea S, Persichetti A, Giovacchini F, Koopman B, Podobnik J, Munih M, Carrozza MC (2013) A flexible sensor technology for the distributed measurement of interaction pressure. Sensors 13(1):1021–1045
6. Lipomi DJ, Vosgueritchian M, Tee BC-K, Hellstrom SL, Lee JA, Fox CH, Bao Z (2011) Skin-like pressure and strain sensors based on transparent elastic films of carbon nanotubes. Nat Nanotechnol 6(12):788–792
7. Park J, Lee Y, Hong J, Ha M, Jung YD, Lim H, Kim SY, Ko H (2014) Giant tunneling piezoresistance of composite elastomers with interlocked microdome arrays for ultrasensitive and multimodal electronic skins. ACS Nano 8(5):4689–4697
8. Liu F, Jin L, Niu SH, Liu HP, Guo JC (2019) A for-low power MEMS piezoresistive sensor dynamic testing system. Trans Beijing Inst Technol 39(2):215–220
9. Li Q, Wang W, Peng DG (2016) Optimization of the filtering methods for process control measuring signals. Res Explor Lab 1006–7167. 04-0026-04
10. Lee SH, Lim KS (2018) Indoor positioning method using BITON and linear Kalman filter. Soft Comput 22(20):6741–6750
11. Wu C, Hu J (2018) Real-time pose estimation based on PnP and adaptive linear Kalman filter. Mot Control Appl 1673–6540. 07-0061-06

# Research Progress and Application of Flexible Humidity Sensors for Smart Packaging: A Review

Haowei He[1], Yabo Fu[1(✉)], Siqi Liu[2], Jinfu Cui[2], and Wencai Xu[1]

[1] Beijing Key Lab of Printing & Packaging Materials and Technology, Beijing Institute of Graphic Communication, Beijing, China
fuyabo@l26.com

[2] School of Printing and Packaging Engineering, Beijing Institute of Graphic Communication, Beijing, China

**Abstract.** This paper discussed the recent development of flexible resistive humidity sensors aiming for smart packaging applications. The research progress of flexible humidity sensor materials, such as graphene oxide, carbon nanotubes and other conductive materials, as well as sensor performance including measurement range, resistance change, sensitivity, response and recovery time, mechanics, sensing mechanism, etc., were extensively investigated in this work. Besides, the main challenges and development trend on flexible humidity sensor smart packaging were summarized to its future IOTs application.

**Keywords:** Flexible humidity sensor · Conductive materials · Smart packaging

## 1 Introduction

Packaging is closely related to people's lives, and the development of intelligent packaging will bring great convenience to people's daily life. Smart packaging can effectively ensure the quality of food from the production, transportation to the use of the consumers, and achieve protection, monitoring and traceability. It could save resources, reduces food waste, and achieves sustainable development. Within the food packaging, due to the breathing of vegetables and fruits, food spoilage and other factors, the gas components will change, and the content of $CO_2$, $O_2$, humidity, ethylene amines, etc. is essential for food quality. Among them, relative humidity is an important parameter to a successful MAP packaging. Accurate humidity monitoring is very crucial to the products quality within the package. Therefore, smart components were required to monitor the humidity environment in the package. It must be small, accurate, convenient, flexible, intelligent, and inexpensive. Flexible sensing tags made with flexible humidity sensing technology meet this requirement.

The flexible humidity sensor is mainly consisted of a substrate, an electrode and a sensitive layer. Common flexible substrates are polyethylene terephthalate (PET), polyimide (PI), polyvinyl alcohol (PVA), polyethylene naphthalate (PEN), polydimethylsiloxane (PDMS), polystyrene (PS), cellulose, textiles, etc. PET and PI are

substrates with excellent performance. The electrodes are generally made of conductive metals such as gold and silver. It is attached to the substrate by coating, printing, deposition, and the like. The electrodes are often in the form of interdigitated electrodes (IDEs) with variable dimensions, line widths, shapes and interdigitated pairs. A wide range of sensitive materials are available. Generally, conductive materials or semi-conductor materials can be used as sensitive materials which are sensitive to humidity, can produce significant electrical signal changes after moisture absorption, and are reversible and repeatable. The sensitive layer is bonded to the substrate with the electrode by coating, printing, self-assembly, etc.

In the 1930s, Dunmore first made a LiCl-based electrolyte resistance type humidity sensor [1]. Since then, humidity sensitive devices have been continuously explored and improved by many researchers for more than 80 years. Today, the trend of miniaturization and flexibility has emerged. Flexible humidity sensors can be divided into capacitive, resistive, surface acoustic wave (SAW), piezoelectric, fiber-optic, quartz crystal microbalance (QCM) according to the principle [1]. Capacitive humidity sensors can use power efficiently, but must be calibrated frequently based on changes in the dielectric constant of the sensor [2]. The resistive humidity sensor measures the impedance change of the sensor element in the light of changing in surrounding humidity, which is easier and more direct than using a capacitive sensor. Recently, various resistance type humidity sensors have been found using materials such as graphene oxide and carbon nanotubes. This review summarizes the relevant research results of flexible humidity sensors and briefly analyzes research and development directions in the future.

## 2   Classification of Flexible Humidity Sensors Based on Sensitive Materials

### 2.1   Graphene Oxide (GO)

Graphene oxide is a semi-conductor and includes graphene material that incorporated with functional groups of epoxy, carboxyl and hydroxyl [3]. The combination of water molecules with the functional groups of GO leads to a variation of the sensing material's conductivity. Su and Chiou [4] have been conducting research for many years to covalently bond GO to PET with gold electrodes and to fabricate flexible humidity sensors layer by layer. Peptide coupling reagents were introduced to firmly bond the sensitive layer to the substrate. Between the relative humidity of 30–90%RH, the sensor has acceptable linearity (0.995), negligible hysteresis, short responding and recovery time (28/48 s), as well as long-term stability of 42 days. Zhang et al. [5] also studied a humidity sensor with a rGO/poly (diallylimethyammonium chloride) (rGO/PDDA) composite film on PI by a LbL method. The resistance of the sensor increases with humidity changing (11–97% RH) and the largest hysteresis is only 2%.

Yao et al. [6] deposited chemically-derived GO as a moisture-sensitive coating on a QCM for moisture detection. The sensor showed excellent level of sensitivity and linear frequency responding (0.9718) in the range of 6.4–93.5% RH. By monitoring the dynamic resistance change, it can be found that: in the high humidity range (>54.3%),

the frequency response depends on the mass of adsorption/desorption on the water molecules and the effect of interlayer expansion; in the low humidity range, it only depends on the mass of adsorption/desorption.

## 2.2   Carbon Nanotubes

Carbon nanotubes (CNTs) have participated in many scientific research experiments thanks to the unique properties (electronic, optical, mechanical and thermal). It is appropriate for CNTs to be applied in flexible humidity sensors. Cao et al. [7] studied humidity sensors made of chemistry-treated and untreated MWCNTs, and the chemistry-treated MWCNTs has greater sensitivity than another. In the range of 11–98% RH, the resistance of the two types humidity sensors respectively increased by 120 and 28%. The former is almost three times than the latter. The adsorption of water molecules by MWCNTs causes a humidity sensing effect. MWCNTs have a p-type semiconductor behavior, and the adsorptive water molecules supply electrons to the electron band. So, the reducing of holes and growing the separation between the Fermi level and the valence band happened [8, 9]. This phenomenon resulted in resistance improving. The shorter carbon nanotubes, on account of chemistry-treatment, opens the ends, and increases defects. The adsorption sites of water molecules are located at the defects and open ends where numbers of hydroxyl groups are attached, which makes it easy for water molecules to adsorb the tubes. H in water molecules can form weak bonds with C atoms on the surface of CNTs, increasing charge transfer, and the humidity sensing effect is more prominent. In addition, defects existing after chemical treatment also reduce the MWCNT's electrical conductivity.

Lee et al. [2] claimed a resistive humidity sensor which was based on flexible MWCNTs and polyacrylic composite film based on PI (Fig. 1). Poly (4-styrenesulfonic acid) (PSS) wrapped MWCNT mixed with poly (acrylic acid) (PAA) as the sensing layer. The sensor is extremely sensitive to humidity (0.069/%RH according to $S = \frac{\Delta R/R_0}{\Delta (\%RH)}$) and shows suitable linearity (0.99). However, the responding and recovery z time are about 670/380 s. The MWCNT/PAA film is spiked with a small amount of PVA, which significantly reduces the responding time of the sensor. Based on the dispersibility of MWCNTs in graphene solution, MWCNTs/GO composite membranes were prepared on QCM by simple drop casting [10]. The QCM with GO/MWCNTs has showed a sensitivity of 9.8 Hz/% RH and a fast response to relative humidity changes (6, 12 s) in 10–80% RH.

Han et al. [11] studied a resistive type humidity sensor with SWCNTs on cellulose paper. Two electrodes were placed in parallel on the cellulose paper, and the intermediate area was coated with SWCNTs. On the cellulose, the conductance shift of the carboxylic acid functionalized nanotubes network entangled was measured in measurement range of 10–90% RH. With response and recovery time of 6/120 s, the sensor response exhibits linearity at 75% relative humidity with excellent repeatability and tiny hysteresis. Peng et al. [12] studied a resistance type humidity sensor based on KC-CNTs. Kappa-carrageenan (KC), MWCNTs and SWCNTs as main components to be used to prepare sensitive layer film. Four different proportions of the control group were set for the KC membrane, and the manufactured sensors all showed a downward
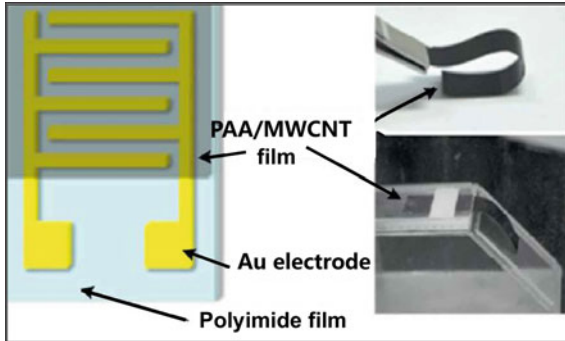
**Fig. 1.** Schematic diagram of humidity sensor [2]

trend with the increase of relative humidity. Long-term measurements of 40 days demonstrate good stability, repeatability and reversibility of the developed sensors.

## 2.3    Other Conductive Materials

Yang et al. [13] studied a humidity sensor consisting of an interdigitated electrode and a sensitive film. The sensitive layer is PANI doped polyvinyl alcohol. The film has nanofibers and porous structure and helps to enhance the response. When the PANI/PVA film absorbs and desorbs water vapor, some changes bas happened for sensor's electrical resistance. The resistance of the sensor is linearly reduced in half, and the sensitivity approximately is 12.6 k$\Omega$/% RH with almost no hysteresis in 25–85% RH. Zhang et al. [14] prepared a QCM type humidity sensor based on GO/PANI by LbL self-assembly. The response and recovery time of QCM sample 1–3 is 5 s–13 s, 7 s–2 s, respectively. Due to the hybrid nanostructure and hydrophilic group on GO and PANI, the PANI/GO film is yare to the adsorption of water molecules.

The PANI/GO film adsorbed water molecules by hydroxyl, carboxyl, epoxy functional, and amino groups on PANI. First, a chemically adsorbed aqueous layer is taken shape. Second, 1st layer of physical adsorption of $H_2O$ molecules is formed by the effect of a double hydrogen bond. At high humidity, next layer of physical adsorption is continued to form by hydrogen bonding. The water of free penetrates into the mezzanine of the films [15, 16].

Yuan et al. [17] prepared a sensor of testing humidity by LbL inkjet printing of GO and poly(3,4-ethylenedioxythiophene) (PEDOT) nano-particles. At 0–98% RH, the sensor exhibits excellent humidity sensing performance in terms of 0.13–68.46% RH, responding and recovery time (39/57 s), repeatability and flexibility. Kuberský et al. [18] manufacture chemically resistive humidity sensors by printing interdigital electrodes on flexible PET substrates. Poly(3,4-ethylenedioxythiophene): poly(4-styrenesulfonate) (PEDOT:PSS) film is used for the sensitive layer of the humidity sensor. In addition, the response and recovery time is less than 1.67 s/min and the hygroscopic hysteresis is about 15%.

Mahadeva et al. [19] made a cellulose-polypyrrole nanocomposite flexible capacitive humidity sensor. At different polymerization times, nano-sized polypyrrole (Ppy) as moisture sensing materials were applied to the cellulose film with interdigitated electrodes by in situ polymerization (Does not destroy the cellulose structure.). The capacitance of the sensor raises with the humidity growing. The flexible sensor with a polymerization time of 16 h has the excellent linearity and reversibility.

Su et al. [20] made a flexible transparent impedance humidity sensor based on PET. The sensor is fabricated with PAMPS, PDDA and ZnO (AZO) interdigital electrodes by self-assembly of LBL. The impedance of the sensor gradually decreases as the RH changes from 60% to 90%. The consistence of PAMPS improve, the impedance first decreases and then increases. At the same time, the impedance increases as the amount of PAMPS/PDDA double layers increases. That sensor has very high transmission (78%), better linearity, and faster responding recovery time (60/70 s).

Other sensors, composed of moisture sensitive polymers such as: poly (2-hydroxyethyl methacrylate) (pHEMA) [21], amine-terminated polyamide dendrimer-Au nanoparticles (G1-NH2-AuNPs) [22], PEDOT/PSS/MoS$_2$ [23], etc., has good sensitivity and acceptable linearity, response time and long-term stability in the medium range of RH 40–60%.

## 3    Conclusions

Smart packaging can improve the informationization and intelligence of packaging technology and meet the increasing consumer demand for food safety and better life [24]. The development of flexible humidity-sensitive smart packaging label technology provides a reliable guarantee for the quality and safety of food packaging, and has a wide market and application prospects. However, the technology is facing several challenges. First of all, the high cost of humidity packaging label has always been a constraint on the development of smart packaging, thus large scale and low-cost manufacture method is needed for fast-moving products. In addition, in the research of flexible humidity sensing technology, there are still many technical bottlenecks need to be solved, such as response time, stability, hygroscopic hysteresis, as well as repeatability, which are difficult to achieve balance at the same time, and need to be synergistically improved.

To advance with the industry 4.0 eras, intelligent packaging is the inevitable development of the times. In the future, bio-based degradable active packaging may be used to replace petroleum-based plastic packaging; packaging systems combining active packaging and smart labels have been widely developed. With the gradual popularization of the internet, cloud, big data and smart home, smart packaging has been given more information interaction functions, and bringing more convenience to our lives.

# References

1. Zhao Y, Wang Q (2012) Sensor sensitive materials and devices. Mechanical Technology Publishing House. 8 (in Chinese)
2. Lee J, Cho D, Jeong Y (2013) A resistive-type sensor based on flexible multi-walled carbon nanotubes and polyacrylic acid composite films. Solid-State Electron 87:80–84
3. Alrammouz R, Podlecki J, Abboud P et al (2018) A review on flexible gas sensors: from materials to devices. Sens Actuators A: Phys 284:209–231
4. Su PG, Chiou CF (2014) Electrical and humidity-sensing properties of reduced graphene oxide thin film fabricated by layer-by-layer with covalent anchoring on flexible substrate. Sens Actuators B: Chem 200:9–18
5. Zhang D, Tong J, Xia B (2014) Humidity-sensing properties of chemically reduced graphene oxide/polymer nanocomposite film sensor based on layer-by-layer nano self-assembly. Sens Actuators B: Chem 197:66–72
6. Yao Y, Chen X, Guo H et al (2011) Graphene oxide thin film coated quartz crystal microbalance for humidity detection. Appl Surf Sci 257(17):7778–7782
7. Cao CL, Hu CG, Fang L et al (2011) Humidity sensor based on multi-walled carbon nanotube thin films. J Nanomater 2011
8. Sun Y, Wang HH (2007) High-performance, flexible hydrogen sensors that use carbon nanotubes decorated with palladium nanoparticles. Adv Mater 19:2818–2823
9. Su PG, Wang CS (2007) Novel flexible resistive-type humidity sensor. Sens Actuators B: Chem 123(2):1071–1076
10. Li X, Chen X, Yao Y et al (2013) Multi-walled carbon nanotubes/graphene oxide composites for humidity sensing. IEEE Sens J 13(12):4749–4756
11. Han JW, Kim B, Li J, Meyyappan M (2012) Carbon nanotube based humidity sensor on cellulose paper. J Phys Chem C 116(41):22094–22097
12. Peng X, Chu J, Aldalbahi A et al (2016) A flexible humidity sensor based on KC-MWCNTs composites. Appl Surf Sci 387:149–154
13. Yang MZ, Dai CL, Lin WY (2011) Fabrication and characterization of polyaniline/PVA humidity microsensors. Sensors 11(8):8143–8151
14. Zhang D, Wang D, Li P et al (2018) Facile fabrication of high-performance QCM humidity sensor based on layer-by-layer self-assembled polyaniline/graphene oxide nanocomposite film. Sens Actuators B: Chem 255:1869–1877
15. Farahani H, Wagiran R, Hamidon MN (2014) Humidity sensors principle, mechanism, and fabrication technologies: a comprehensive review. Sensors 14:7881–7939
16. Zhang D, Liu J, Xia B (2016) Layer-by-layer self-assembly of zinc oxide/graphene oxide hybrid towards ultrasensitive humidity sensing. IEEE Electron Dev Lett 37:916–919
17. Yuan Y, Peng B, Chi H et al (2016) Layer-by-layer inkjet printing SPS: PEDOT NP/RGO. RSC Adv 114(6):113298–113306
18. Kuberský P, Syrový T, Hamacek A et al (2015) Printed flexible gas sensors based on organic materials. Procedia Eng 120:614–617
19. Mahadeva SK, Yun S, Kim J (2011) Flexible humidity and temperature sensor based on cellulose-polypyrrole nanocomposite. Sens Actuators A: Phys 165(2):194–199
20. Su PG, Li WC, Tseng JY, Ho CJ (2011) Fully transparent and flexible humidity sensors fabricated by layer-by-layer self-assembly of thin film of poly (2-acrylamido-2-methylpropane sulfonate) and its salt complex. Sens Actuators B: Chem 153(1):29–36
21. Reddy ASG, Narakathu BB, Atashbar MZ et al (2011) Fully printed flexible humidity sensor. Procedia Eng 25:120–123

22. Su PG, Shiu CC (2012) Electrical and sensing properties of a flexible humidity sensor made of polyamidoamine dendrimer-Au nanoparticles. Sens Actuators B: Chem 165(1):151–156
23. Siddiqui GU, Sajid M, Ali J et al (2018) Wide range highly sensitive relative humidity sensor based on series combination of MOS$_2$, and PEDOT: PSS sensors array. Sens Actuators B 266(2018):354–363
24. Guo P, He H, Fu Y, Xu W (2018) Research progress of gas sensitive smart packaging labels. Packag Eng 39(11):13–18 (in Chinese)

# Study on Paper Packaging Safety of Large Lithium Battery Based on ISTA 3E

Chenyang Liu, Lijiang Huo[✉], Yu Zhao, and Zhilin Huang

School of Light Industry and Chemical Engineering, Dalian Polytechnic
University, Liaoning, China
`lijianghuo@l63.com`

**Abstract.** A solution of whole paper packaging design for large lithium batteries and its material matching were proposed for meeting a requirement of modern logistics distribution. In this study, through simulating the common transportation environment, the protection performance of the transportation packaging for large lithium battery was analyzed. Based on ISTA 3E transportation safety inspection standards, the safety performance of the corrugated board box packaging was tested via related experiments. The results show that the whole paper packaging for large lithium batteries passed the impact test, pressure test, vibration test and rotary drop test experiment under detection conditions of the ISTA 3E standards. It can ensure the safety of the large lithium battery in process of actual transportation.

**Keywords:** Packaging for large lithium battery · Corrugated board box · Protective performance · ISTA test

## 1 Introduction

Lithium batteries are a kind of dangerous chemicals, it is easy to cause the damage of lithium batteries due to unqualified transportation packaging, and ultimately lead to irreparable consequences. In recent years, the regional circulation of the large lithium batteries has increased rapidly, which puts forward higher requirements for the safety performance of lithium battery transport packaging [1–3]. The purpose of this study is to explore a solution of paper packaging for the large lithium batteries, and then put forward scientific improvement measures and more reasonable lithium battery packaging scheme, and comprehensively improve its protective performance in transportation.

## 2 Paper Packaging Structure Design and Material Option

### 2.1 Structure Design

The VOLVO-NX11 automotive lithium battery net weight is 140 kg, maximum dimensions of the battery is $1300 \times 1050$ mm. The structure drawing of the lithium battery are shown in Fig. 1a, b.
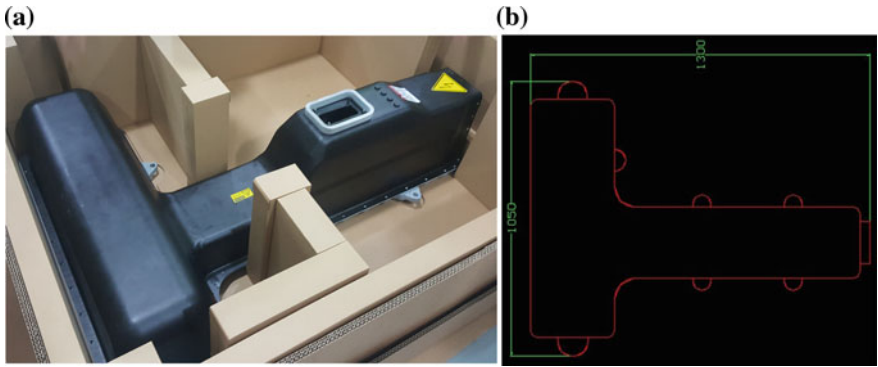
**Fig. 1.** The structure drawing of the lithium battery

According to GB/T 19451—2004 [4], the dimensional assembly drawing of large lithium battery transport package was design and shown in Fig. 2. The battery shape likes "T" and its centre-of-gravity position lays at the head of the "T", so cushion block was used in this structure. The cushion block is also made of corrugated boards.
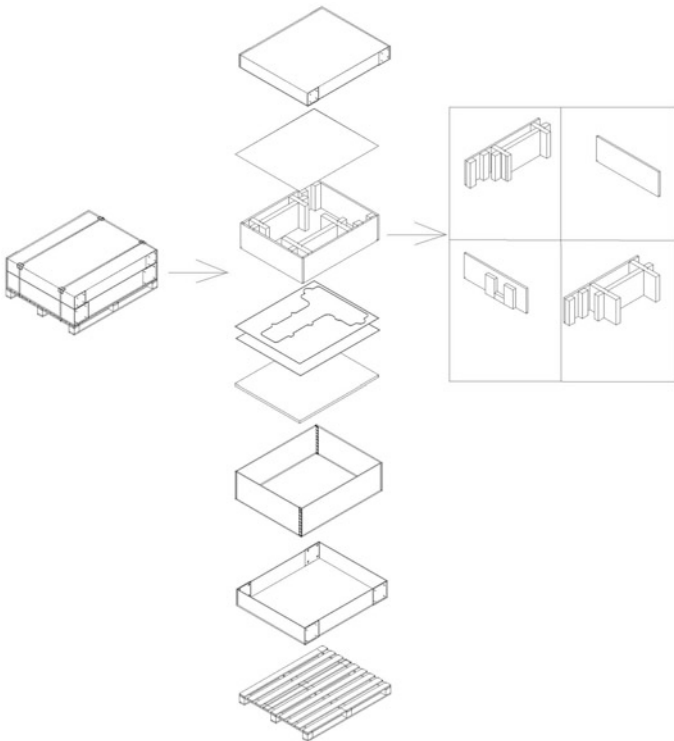


**Fig. 2.** The dimensional assembly drawing of large lithium battery transport package

## 2.2    Material Option

Materials used in the packaging design and their size and types are listed at Table 1.

**Table 1.** Transport packaging materials

| Name | Box type | Size (mm) | Material/corrugated type |
|---|---|---|---|
| Upper cover board | 0300 | 1431 × 1171 × 205 | G7S7G/AA |
| Bottom cover board | | 1431 × 1171 × 245 | |
| Inside frame | 0501 | 1404 × 1138 × 435 | G7S7S7G/AAA |
| Bottom cushion board | 0900 | 1379 × 1179 | K7S(55)J/BA |
| Six-layer fixed board | | | |
| Upper inside board | 0900 | 1379 × 1179 | Q5Q/B |
| Honeycomb paperboard | | 1379 × 1179 | Thickness 35 mm, hole diameter 10 mm |
| Cushion block | | | Inside block J547S/BA Outside block Q4Q/E |
| Tray | | 1500 × 1230 × 140 | Wood plate |

# 3    Packaging Safety Experiments

## 3.1    Experimental Materials and Equipment

Experimental materials and equipment used in the study are listed at Tables 2 and 3.

**Table 2.** Main paper materials of preparing large lithium battery transport packaging

| Materials | Code | Weight (g/m$^2$) |
|---|---|---|
| Corrugated boards | 4 | 100 |
| | 7 | 120 |
| | 5 | 175 |
| Honeycomb paperboard | | Thickness 35 mm, hole diameter 10 mm |

## 3.2    ISTA 3E Testing

The sample was labeled on every surface, such as 1–6. The sample was handled 72 h in the environment of 23 °C, RH60%, then performance testing was taken [5].

**Table 3.** Main equipment of preparing large lithium battery transport packaging

| Equipment name | Model number | Manufacturing location/measuring range |
|---|---|---|
| Vibration test system | DL-4000-50 | 1–220 Hz |
| Impact test system | SMJ-1000 | 3.1 m/s |
| Impact test equipment | DC-KYS50K | 0–50 KN |

**Table 4.** The test parameters

| Number | Speed (fps) | Position | |
|---|---|---|---|
| 1 | 1.36 | Face | 4 |
| 2 | 1.36 | Face | 2 |
| 3 | 1.36 | Face | 6 |
| 4 | 1.36 | Face | 5 |
| Rotational edge drop#1 | 200 mm | Edge | 3–4 |
| Rotational edge drop#2 | 200 mm | Edge | 3–5 |

### 3.2.1 Impact Testing

The impact test parameters are listed at Table 4. The impact test methods are shown in Figs. 3a, b and 4.

### 3.2.2 Compression Testing

The compression test method is shown in Fig. 5. The sample was placed at the center of experimental plate and pressed 1 h.

### 3.2.3 Vibration Testing

The experiment simulated long distance transportation (more than 2000 km), and vibration test time was 240 min. The vibration test method is shown in Fig. 6. Random vibration spectrum in the test are listed at Table 5.

### 3.2.4 Rotating Edge Drop Testing

The rotational edge drop test and parameters are shown in Fig. 7 and Table 6.

## 3.3 Result and Discussion

After above experiments, the sample and larger lithium battery inside were checked. The results showed that the surface of the sample and the larger lithium battery inside were not damaged at all. In above experiments, actual impact test result was 2269.36 kg. According to calculation, $M = Wt \times (S - 1) \times F \times 1.4$. Among the
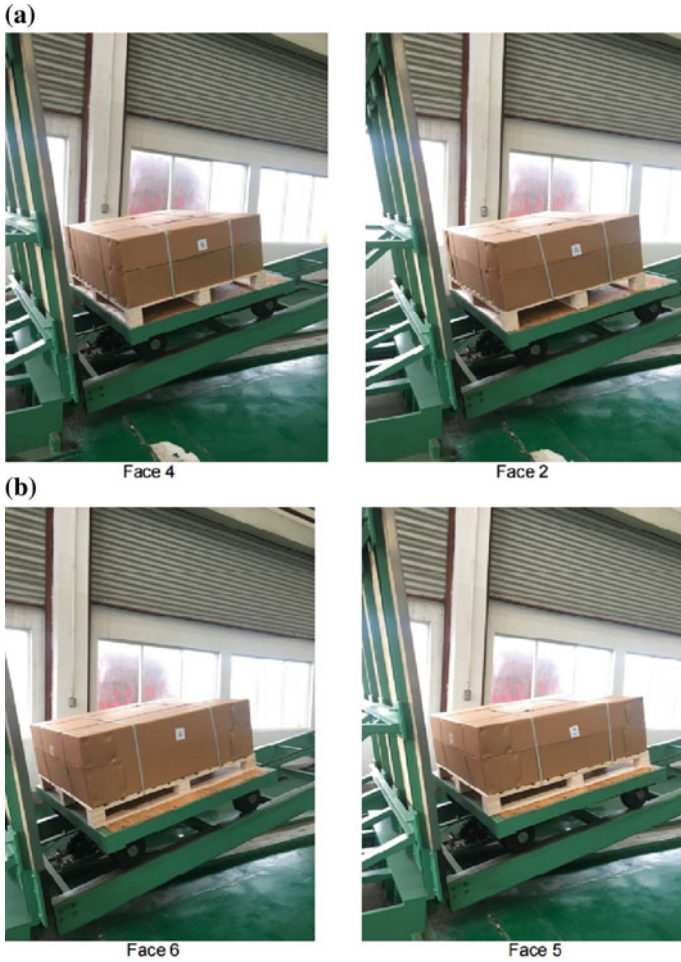
Fig. 3. Incline-impact

items, M is press forced (Kg), $W_t$ is sample gross weight (Kg), S equaled to 4, F was 3, compensation factor was 1.4 in this study. Through calculation, M was 2268 kg (less than actual test result). So the actual test result was valid. The vibration test result was also in line with standard, shown in Fig. 8. It can be seen the sample has strong adaptability under the vibration condition of experimental environment.

Edge 3-4                    Edge 3-5

**Fig. 4.** Rotational edge drop



**Fig. 5.** Compression test

**Fig. 6.** Vibration test

**Table 5.** Random vibration spectrum

| Vibration frequency (Hz) | PSD (g$^2$/Hz) |
|---|---|
| 1 | 0.00072 |
| 3 | 0.018 |
| 4 | 0.018 |
| 6 | 0.00072 |
| 16 | 0.0036 |
| 25 | 0.0036 |
| 30 | 0.00072 |
| 40 | 0.0036 |
| 80 | 0.0036 |
| 100 | 0.00036 |
| 200 | 0.000018 |
| Whole Grms | 0.54 |



Edge 3-2          Edge 3-6

**Fig. 7.** Rotational edge drop

**Table 6.** The test parameter of the rotating edge drop test

| Number | High (mm) | Rotating edge |
|--------|-----------|---------------|
| 2      | 200       | 3–6           |
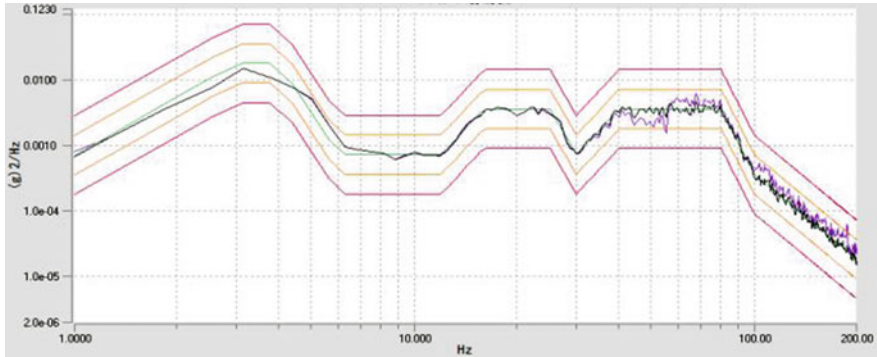


**Fig. 8.** Auto-spectral density

## 4  Conclusions

Through simulating the transportation environment, the protective performance of the paper transport packaging for large lithium battery were tested and analyzed. The results can meet the requirement of ISTA 3E transportation safety inspection standard. That is to say, the solution can ensure the safety of large lithium battery in actual transportation application. The packaging for large lithium battery can be designed and produced, with the corrugated board material instead of traditional plastic or metal materials.

## References

1. Song Y, Wang CJ, Wei HB et al (2009) Investigation of the appraisal technique in transportation of lithium battery. Chin Batter Ind
2. Tao HH, Chen X, Zhao YQ et al (2015) International transportation rules of large lithium cells and lithium batteries. Batter Bimon
3. Zhou YH, Huang YB, Liu Y et al (2009) Research on transportation package attribute evaluation method for lithium cell dangerous goods. Packag Eng
4. State Administration for Quality Supervision and Inspection and Quarantine of China, the National Standards Administration Commission of China, GB/T19451-2004, State Standard of the People's Republic of China, transport packaging design procedure
5. National Safety Transport association, Packaging Transport Standard ISTA 3E-CN

# Process and Quality Study of Cold Fresh Pork Under Low Temperature Plasma Treatment

Binglun Wang[1], Zheng Liu[2], Yunjin Sun[1(✉)], Tingjun Ma[1], and Jun Wu[1]

[1] Beijing Laboratory of Food Quality and Safety, Food Science and Engineering College, Beijing University of Agriculture, Beijing, China
aosdf2@163.com

[2] China National Pulp and Paper Research Institute Co., Ltd, Beijing, China

**Abstract.** As a novel green cold sterilization technology, low-temperature plasma has great potential application in food storage and preservation. In this paper, a low-temperature plasma discharge technology was adopted to treat the surface of cold fresh pork, and its bactericidal effect was observed by changing the discharge power and exposure durations, which indicated that the total number of colonies could be reduced by 2 log values under the optimized treatment process of (400 W, 30 s). The quality test showed that the volatile basic nitrogen (TVB-N) value of the treated group was significantly lower than that of the untreated group, reaching 7.38 mg/100 g after storage for 5 days compared with 9.67 mg/100 g for the untreated group. PH value and juice loss rate was decreased into a certain degree level after plasma treatment, indicating that plasma treatment inhibited the activity of endogenous enzymes to some extent and delayed the freshness reduction of cold fresh pork. It can be seen that, low-temperature plasma has an obvious inhibitory effect on microorganisms on the surface of fresh cold pork, and has no negative effect on pH and juice loss rate, which can prolong the storage and preservation period.

**Keywords:** Low temperature plasma · Storage preservation · Total number of colonies · Quality analysis

## 1 Introduction

In the traditional preservation and processing of meat and meat products, controlling and inhibiting the growth and reproduction of microorganisms are key technologies, generally including heating, reducing moisture activity, temperature reduction and preservatives addition. Traditional processing processes usually produce some undesirable chemical products or cause changes in sensory properties, and the by-products produced during processing cause changes in flavor or nutrients. Therefore, traditional processing techniques are often used for foods that are easy to handle, such as cooked products. With the progress of science and technology, consumers are pursuing higher and higher quality of life, so preserving the material characteristics of food itself becomes the key step to be processed, In particular, how fresh products can better retain

the quality of food itself such as cold fresh pork, brings new challenges to food processing methods [1].

As a new non-thermal food processing technology, low-temperature plasma technology has attracted more and more attention from scholars at home and abroad. Compared with food thermal processing technology, this technology has the advantages of safety, mildness, simple operation and low cost, and has been widely used in material processing [2], electronics [3], polymer processing, biological medical devices and biological materials and other fields [4]. The characteristics of low temperature plasma is able to produce a large amount of reactive oxygen species (reactive oxygen species, ROS) and reactive nitrogen (reactive nitrogen species, RNS) in the atmospheric conditions, of which ROS refers to oxygen atoms or groups with active chemical properties, including ozone, hydrogen peroxide, singlet oxygen molecules, superoxide anion radicals, hydroxyl radicals, etc. RNS refers to derivatives centered on nitric oxide (NO), including nitrogen oxides such as nitrogen dioxide (NO2), nitrogen trioxide (N2O3), and nitrogen tetroxide (N2O4) [5]. These active substances can inhibit or kill microorganisms by interacting with the surface of meat and its related products [6].

A large number of literature studies show that plasma has an obvious bacteriostatic effect. Dirks et al. [7] reported that dielectrically barrier discharge (DBD) can effectively inhibit the growth of microorganisms on the skin surface of skinless chicken breast and thigh, and reduce the total number of microorganisms by a logarithmic value. Ulbin-Figlewicz et al. [8] used He and argon plasma to treat the surface of pork, and found that He plasma treatment has a significant bacteriostatic effect, and the total number of microorganisms, yeast, mold and cold-loving microorganisms in pork are reduced by about 1.90, 1.14 and 1.60 (lg (CFU/g)) respectively, and the effect is more obvious with the extension of treatment time. In contrast, argon plasma has a lower inhibition effect on microbial growth. Zhang et al. [9] found that low-temperature plasma treatment of beef can enhance the surface brightness of beef during cold storage, reduce the red color, and have no significant negative impact on the pH and texture characteristics of beef. Therefore, low-temperature plasma technology, as a new non-thermal processing technology, has shown its advantages compared with traditional thermal technology, including safety, mild, non-destructive, simple operation and low cost.

According to the plasma generation system, low-temperature plasma discharge generally includes dielectric barrier discharge (DBD), atmospheric plasma jet (APPJ), gliding arc discharge [10] and corona discharge [11]. Compared with other low-temperature plasma technologies, the gliding arc discharge technology adopted in this paper has the characteristics of simple operation and large processing area, and the ionized gas generated by the discharge has strong active bactericidal characteristics, and has shown extensive bactericidal effect on various foodborne microorganisms [12]. Based on the good bactericidal effect of gliding arc discharge technology, this paper would explore its application in the cold sterilization of food, took cold fresh meat as the treatment object, studied the deactivation effect of this technology on the surface microorganisms of cold fresh pork, and evaluated the impact of gliding arc discharge treatment on the quality of cold fresh pork.

## 2    Materials and Methods

### 2.1    Materials and Reagents

Cold Fresh pork was bought at Beinong Supermarket, and PCA Plate Counting Medium from Beijing Oboxin Biotechnology Co., Ltd, and Aseptic Homogeneous Bag from Ningbo Scientz Biotechnology CO., Ltd, and Hydrochloric Acid Standard Solution from Shenzhen Bolinda Technology Co., Ltd.

### 2.2    Plasma Generating Device

The atmospheric plasma discharge device was mainly composed of a power source, a processing chamber, a gas flow test table, As shown in Fig. 1. There were two parallel copper electrodes in the reaction chamber (length 93 mm, thickness 3.6 mm, gas from the top of the reactor) The cold fresh meat sample was placed in the lower part of the reactor port. When the gas passed through the reactor, it was broken down by a voltage of 10 kV between the two copper sheets to generate a gliding arc discharge, and the raw meat sample at the lower end of the reactor was processed. Processing parameters for plasma discharge included sliding arc discharge power, gas flow rate, and processing time.
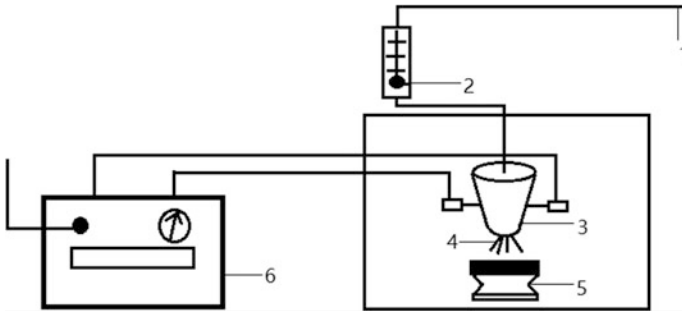


**Fig. 1.** Atmospheric plasma discharge equipment. 1. Gas source, 2. gas flow tester, 3. reaction chamber, 4. sliding arc discharge, 5. sample stage, 6. power supply

### 2.3    Method

#### 2.3.1    Raw Material Processing

Cold fresh pork was cut into pieces of uniform size, thin thickness and uniformity of $20 \pm 1$ g. The power was set as 450 W, the gas flow rate was 40 L/min, with atmospheric plasma (0, 15, 30, 60 s). When the treatment time was set to 30 s and the gas flow rate was 40 L/min, it was treated with atmospheric plasma (0, 300, 350, 400, 450, 500 W). The meat sample was placed in a homogenized bag, with addition of 180 mL of physiological saline, and was homogenized for 1–2 min. After gradient dilution, the plate was plated with appropriate dilution, and then cultured at 37 °C for 24 h to count the colony. The sterilization rate could be calculated as follows:

Sterilization rate = $\frac{No - Np}{No} \times 100$

Among them in the function: No: control group colony number, CFU/g,
$N_P$: treatment group colony number, CFU/g

### 2.3.2  TVB-N Value

Determination of TVB-N values by semi-micro distillation. By weighing 10 g ground
pork in a beaker, adding 100 mL distilled water, stirring evenly, for 30 min filtration.
5 mL of filtrate, and 5 mL magnesium oxide suspension (10 g/L) was mixed, and
distilled to be titrate with 0.01 mol/L standard hydrochloric acid solution, according to
the amount of hydrochloric acid calculated by the amount of TVB-N. Primary fresh-
ness: TVB-N value $\leq$ 15 mg/100 g; secondary freshness 15 mg/100 g, TVB-N
value $\leq$ 20 mg/100 g; metamorphic meat: TVB-N value > 20 mg/100 g. Following
equation:

TVB-N (mg/100 g) = $\frac{V_1 - V_2 \times C \times 14}{m \times 5/100} \times 100$

Where $V_1$ and $V_2$ represent the volumes of HCL required for titration of the mixture
with shrimps and the one without shrimps (ml); C is the concentration of HCL used in
this study (M); and m denotes the weight of shrimps sample (g).

### 2.3.3  pH Determination

The treated samples were stored under refrigeration at 4°. The samples taken at the
same time every day were measured with a pH meter. Each sample was recorded and
the pH meter was rinsed with distilled water. Three groups of samples were run in
parallel for five days.

### 2.3.4  Juice Loss Rate

The samples of cold fresh pork were measured after treatment; the samples were taken
at the same time every day (for five days), and the quality of the absorbent paper was
measured after the surface juice was removed. The difference between the quality of the
Nth day and the quality of the first day was the same as that of the first day. The quality
of cold fresh pork after one day of treatment is the rate of juice loss from cold pork.

## 3  Results and Discussion

### 3.1  Sterilization Effects

Cold fresh meat was just slaughtered pig carcass, rapid cooled at low temperature down
to 0–4 °C, during which the main effect of temperature is to inhibit the activity of
enzymes and the growth and reproduction of most microorganisms. However, in the
process steps of processing, storage, transportation and marketing steps, it was difficult
to avoid infecting microorganisms in the environment, which thus affected the hygienic
level of cold fresh pork. In this study, the effect of low-temperature plasma treatment
on the inactivation of microorganisms on the surface of cold fresh pork was first
studied. Figure 2 shows the influence of different plasma discharge powers on the total
number of colonies on the surface of cold fresh pork. In order to accelerate the test
effect, the storage temperature of cold fresh pork was set at room temperature.

Compared with the control group, there was no significant change in the total number of colonies on the surface of cold fresh pork treated with plasma. With the extension of storage duration time, the total number of colonies on the surface of cold fresh pork began to increase, and the total number of colonies on the surface of the control group exceeded 6 log values at day 2.2, reaching the standard of rotten pork. In contrast, the plasma-treated samples showed a reduced total number of colonies on their surfaces, all of which did not satisfy the criteria for putrefied meat until the third day. The higher the discharge power, the longer it will take for the cold fresh pork to reach the decay level, especially for discharge powers over 400 W. The storage time of cold fresh pork can reach 5 days, extending the shelf life by twice. This may be because the higher the power, the higher the gas ionization degree, the higher the electron density and ion density in the plasma, so as to improve the interaction degree between plasma and microorganisms from the pork surface, resulting in enhanced sterilization intensity. Among the active ingredients of low temperature plasma are hydroxyl radicals, which are strong oxidants and can exist for a long time. Choi et al. [13, 14] studied the effects of atmospheric plasma discharge on microorganisms in instant pickles by generation spectra and found that OH present in plasma is an important bactericidal component.
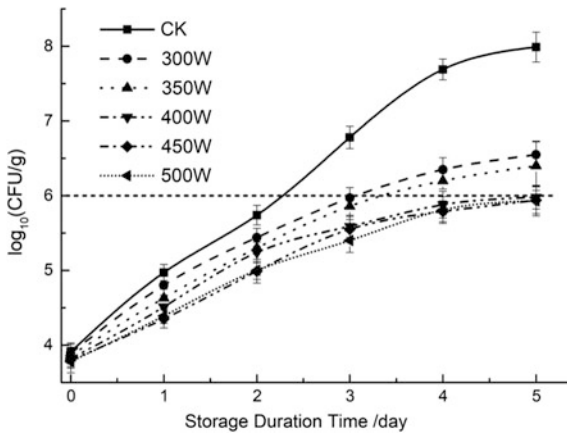


**Fig. 2.** Effects of discharge power on the sterilization rate of cold meat surface with plasma exposure duration time of 45 s and gas flow of 40 L/min

In order to study the influence of time accumulation effect on sterilization effect, the influence of different exposure time at the same power on the total number of bacterial colonies on the surface of cold fresh pork was studied as shown in Fig. 3. Although the active ingredients in the plasma have bactericidal effect, during the interaction between the plasma and microorganisms, the active ingredients in the plasma will also act on the surface of cold fresh pork, causing a certain degree of damage to the surface of chilled meat. Does this damage affect the quality of cold fresh pork? The following will be verified from TVB-N, pH and juice loss rate.
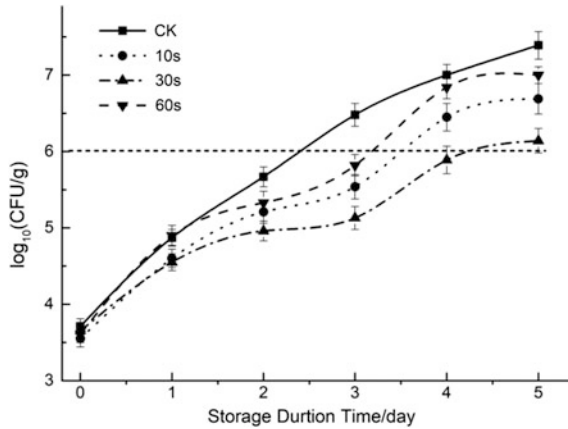
**Fig. 3.** Effects of plasma exposure duration time on the sterilization rate of cold meat surface with discharge power of 400 W and gas flow of 40 L/min

## 3.2 TVB-N Effects

TVB-N reflects the freshness level of cold fresh pork, and is an important indicator for evaluating the corruption and deterioration degree of meat products. The main principle of TVB-N value is to assess the freshness by measuring the alkaline nitrogenous volatile substances such as ammonia and amines produced by protein decomposition under the action of endogenous enzymes or bacteria. As shown in Fig. 4, the initial value of TVB-N of untreated samples is 4.97 mg/100 g, which gradually increased to about 11.09 mg/100 g with the storage time. TVB-N value of the treated samples was increased to 9.24 mg/100 g (day 5) with the storage time, which was lower than the original value, indicating that the cold fresh meat was still in a relatively fresh state. Since high level of TVB-N in cold fresh meat may be related to bacteria and endogenous enzymes to produce alkaline nitrogen compounds. After plasma treatment of cold fresh pork, TVB-N values has a relatively enormous reduction. In addition to the microbial inactivation of surface of cold fresh pork, TVB-N reduction is related to endogenous enzymes activity of cold fresh pork, which suggested the plasma treatment can inhibit the activity of endogenous enzymes in the cold fresh pork. Lackmann et al. has investigated the capabilities of nonthermal atmospheric-pressure plasmas to inactivate RNA, and found that direct plasma treatment with a DBD source caused permanent inactivation of RNA and continued plasma exposure led to over-oxidation of structural disulfide bonds. Ke et al. [15] has studied the effects of non-thermal plasma on horseradish peroxidase, and found that activity together with the contents of heme and iron in horseradish peroxidase decreased dramatically and on comitantly upon plasma treatment, since hydrogen peroxide from plasma broke the heme prosthetic group into fluorescent products, mainly dipyrroles and their derivatives [16]. Therefore, the inactivation of enzyme activity in the fresh meat may be the dominant factor to keep the storage circle, as its kinetic mechanism will be further instigated in next work.
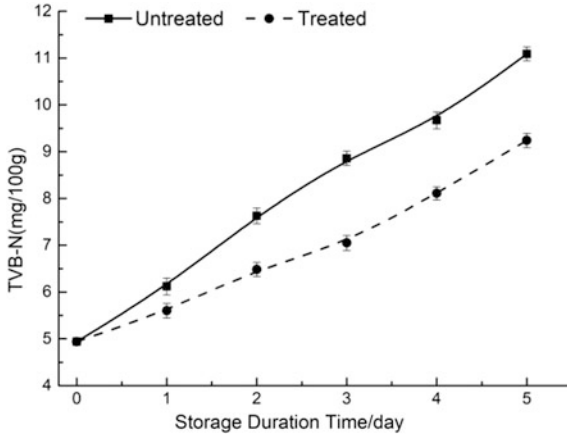
**Fig. 4.** Effect of atmospheric plasma treatment on TVB-N value of cold fresh pork

## 3.3 pH Effects

The pH value of pork is used as the detection index of meat products. The pH range of 5.8–6.2 is generally high in freshness, the range of 6.3–6.6 is secondary fresh pork, and the above 6.7 is rotten pork. The samples used in this study have high freshness, as shown in Fig. 5. As the storage time increases, the pH value gradually increases, indicating a decline in freshness. This is because some of the proteins inside cold fresh pork were broken down by bacterial enzymes into ammonia and amines, contributing to the increasing trend of pH. The freshness of the plasma treated samples showed the same change trend, and the pH value of the treated samples remained somewhat lower than that of the untreated samples. This further proved that plasma treatment was beneficial to inhibit the proliferation of bacteria on the surface of cold fresh pork and the decomposition of some proteins inside, and thus prolonged the storage and preservation period of cold fresh pork.
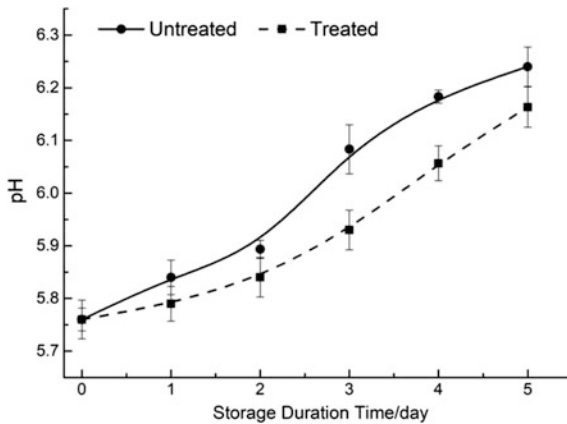


**Fig. 5.** Change trend of pH value as a function of storage duration time with untreated and treated samples

### 3.4    Juice Loss Rate Effects

Juice loss rate is an important index to evaluate the quality of cold fresh pork, reflecting the water retention of cold fresh pork, which will accelerate protein denaturation rate and muscle fiber structure changes. As shown in Fig. 6, the juice loss rate of cold fresh pork increased with the extension of storage period. After storage time of 5 days, the untreated group reached 3.42% with comparison of 2.56% for the treated group. The experimental results showed that low-temperature plasma treatment could not accelerate the increase of surface moisture of cold fresh pork, but was beneficial to reduce the rate of juice loss, which might be due to the fact that charged particles, groups and active substances generated during low-temperature plasma treatment could promote the ability of cold fresh meat to bind water molecules. The rate of juice loss was related to protein decomposition and muscle fiber structure changes during storage. It can be seen that low-temperature plasma treatment had no negative impact on the water holding capacity of cold fresh pork, indicating that the cold sterilization technology had certain advantages in the storage and preservation of fresh food.
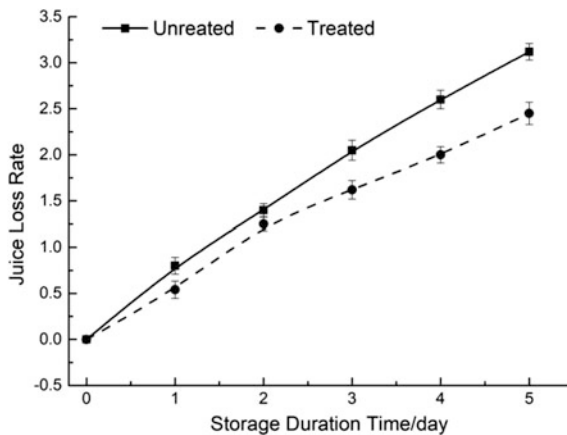


**Fig. 6.** Trend rate of juice loss rate as a function of storage duration time with untreated and treated samples

## 4    Conclusions

In this study, the surface of cold fresh pork was treated with atmospheric plasma discharge technology, and the results showed that atmospheric plasma treatment could effectively inhibit the growth of microorganisms in the surface of cold fresh meat, which was conducive to maintain the quality of cold fresh meat and extend the storage period. The discharge power and treatment time were obtained and optimized as follows: the treatment power was 450 W, and the treatment time was 30 s, when the total number of colonies on the surface of cold fresh pork was decreased the most, that was 2 log values. The quality test showed that the pH value and TVB-N value of cold fresh meat were decreased to a certain degrees under plasma treatment, which inhibited the

activity of endogenous enzymes to some extent, since the treated samples were still in the first-order freshness range when stored for five days. At the same time, the juice loss rate of the samples was reduced after treatment, which was beneficial to the storage and preservation of cold fresh pork. Therefore, it can be deduced that atmospheric plasma technology can significantly inhibit the growth of microorganisms on the surface of cold fresh pork, and has no negative impact on the quality of pork. The results of this study also indicated that atmospheric plasma technology, as a new cold sterilization technology, has the characteristics of green and pollution-free for food storage, and has great application potential.

# References

1. Pan Y, Sun D, Han Z (2017) Applications of electromagnetic fields for nonthermal inactivation of microorganisms in foods: an overview. Food Sci Technol 64:13–22. https://doi.org/10.1016/j.tifs.2017.02.014

2. Pankaj SK, Bueno-Ferrer C, Misra NN et al (2014) Applications of cold plasma technology in food packaging. Food Sci Technol 35(1):5–17. https://doi.org/10.1016/j.tifs.2013.10.009

3. Korner N, Beck E, Dommann A et al (1995) Hydrogen plasma chemical cleaning of metallic substrates and silicon wafers. Surf Coat Technol 76:731–737. https://doi.org/10.1016/02578972(95)02503-0

4. Miyamoto K, Ikehara S, Takei H et al (2016) Red blood cell coagulation induced by low-temperature plasma treatment. Arch Biochem Biophys 605:95–101. in-press. https://doi.org/10.1016/j.abb.2016.03.023

5. Misrann JOC (2017) Applications of cold plasma technology for microbiological safety in meat industry. Trends Food Sci Technol 64:74–86. https://doi.org/10.1016/j.tifs.2017.04.005

6. Nirmaly RV, Lavanya MN, Darsana K et al (2015) Application of cold plasma in food preservation discovery. Food Res Int 51:114–123

7. Dirks BP, Dobrynin D, Fridman G et al (2012) Treatment of raw poultry with nonthermal dielectric barrier discharge plasma to reduce Campylobacter jejuna and Salmonella enteria. J Food Prot 75(1):22–28. https://doi.org/10.4315/0362-028X.JFP-11-153

8. Ulbin-Figlewicz N, Jarmoluk A, Marycz K (2005) Antimicrobial activity of low-pressure plasma treatment against selected foodborne bacteria and meat microbiota. Ann Microbiol 65(3):1537–1546. https://doi.org/10.1007/s13213-014-0992-y

9. Zhang J, Qiao W, Huang M, Wang J (2018) Effect of low temperature plasma treatment on beef quality. Mod Food Technol 34(11):194–199 + 150

10. Kwon W-T, Lee W-S (2014) A study on combined processes of sliding arc plasma and corona dielectric barrier discharge for improve the efficiency treatment of harmful substance. Fire Sci Eng 28(6):108–113

11. Ehlbeck J, Schnabel U, Polak M et al (2011) Low temperature atmospheric pressure plasma sources for microbial decontamination. J Phys D-Appl Phys 44(1):013002

12. Moreau M, Feuilloley MGJ, Veron W, Meylheuc T, Chevalier S, Brisset J-L, Orange N (2007) Gliding arc discharge in the potato pathogen Erwinia carotovora subsp. atroseptica: mechanism of lethal action and effect on membrane-associated molecules. Appl Environ Microbiol 5904–5910

13. Choi EJ, Park HW, Kim SB, Ryu S, Lim J, Hong EJ, Byeon YS, Chuna HH (2019) Sequential application of plasma-activated water and mild heating improves microbiological quality of ready-to-use shredded salted kimchi cabbage (Brassica pekinensis L.). Food Control 98:501–509

14. Yang C, Zhao X, Chen G, Liang Z, Bai W, Yanping X (2018) Differences research on volatile basic nitrogen value and sensory quality of chilled pork. Food Ind 39(3):197–199

15. Lackmann JW, Baldus S, Steinborn E, Edengeiser E, Kogelheide F, Langklotz S, Schneider S, Leichert LI, Benedikt J, Awakowicz P, Bandow JE (2015) A dielectric barrier discharge terminally inactivates RNase A by oxidizing sulfur-containing amino acids and breaking structural disulfide bonds. J Phys D Appl Phys 48

16. Ke Z, Huang Q (2013) Inactivation and heme degradation of horseradish peroxidase induced by discharge plasma. Plasma Process Polym 10:731–739

# Mechanical Engineering Technology

# A Method of Fault Diagnosis for Rolling Bearing in Ink Rollers Based on Analysis of Sound Field

Zhuofei Xu[1(✉)], Rui Deng[1], Heping Hou[1], Shanhui Liu[1], and Qing Wen[2]

[1] Faculty of Printing Packaging Engineering and Digital Media Technology, Xi'an University of Technology, Xi'an, China
xuzhuofei@xaut.edu.cn

[2] North Industries Group Corporation, North Automatic Control Technology Institute, Taiyuan, China

**Abstract.** Aiming at the difficulty of direct measurement of rolling bearing signal in offset printing system, a method of diagnosis and locating for rolling bearings based on texture analysis of sound field is proposed. First, the sound field of area to be detected is reasonably divided into a series of small areas. The sound signal can be acquired from the sound test system. Second, the energy of sound signals in different areas during a certain time is calculated and it is used to express the status of each area. Take the values as some special points, therefore, an image can be obtained to describe the sound filed of printing press. Third, bi-dimensional empirical mode decomposition is introduced to analyze the image and high order signal of bi-intrinsic mode functions can be got. Finally, the proposed method is validated by the fault diagnosis and locating experiments of rolling bearings in ink system, and the classification is realized by using the acquisition features. The proposed method has strong recognition ability, it is also suitable for other complex mechanical systems.

**Keywords:** Sound fields · Bidimensional empirical mode decomposition · Fault diagnosis · Printing press

## 1 Introduction

The printing press is an integrated equipment with high precision, the master units usually have dozens of groups of ink roller system, which contains a large number of bearings [1]. The roller bearings are always in the harsh chemical environment which are strongly corroded and prone to malfunction, there are still some difficulties in the fault diagnosis of them, therefore, it is proposed that a method of fault diagnosis for rolling bearings in ink roller system based on the analysis of regional space sound signal [2].

## 2    Sound Field Construction of Multi-roller System

As Fig. 1 shows that this study is based on the sexto offset press YP1B3B of BEIREN. In this experiment, the detection area is divided into 60 squares as shown in Fig. 2, and the squares are numbered from 1 to 60 in turn. The sound sensor is placed in each square to acquire signal, and the sound field image will be composed of the 60 squares.
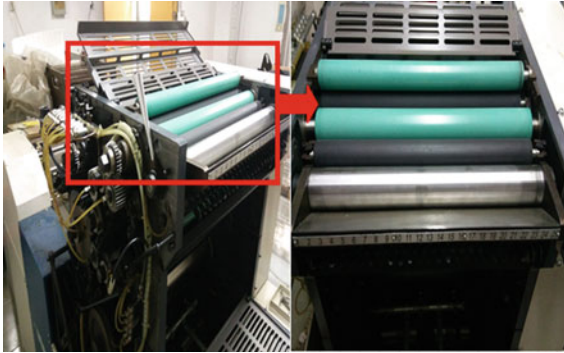


**Fig. 1.** YP1B3B offset press and multi-roll system
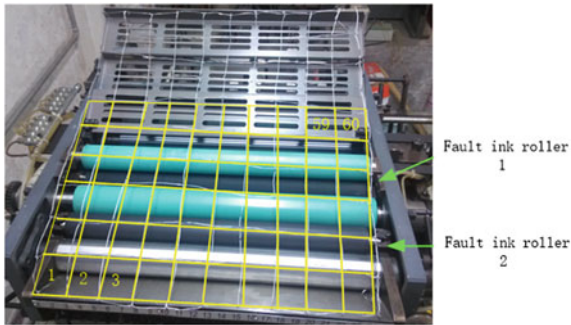


**Fig. 2.** The regional division in sound field

Figure 3 shows the sound field image of ink roller system under the normal state. The image is displayed in a contour map, the horizontal and vertical coordinates represent the positions of 60 points, corresponding to the position numbers in Fig. 2. It is necessary to suppress noise and low frequency components effectively.
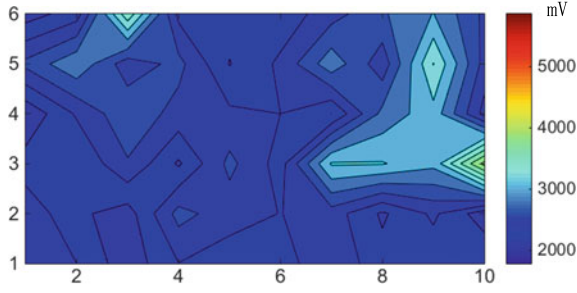
**Fig. 3.** The sound field image of ink rollers under normal state

## 3    Analysis of Sound Field Images Based on BEMD

Bidimensional empirical mode decomposition can transform an image into a series of bidimensional intrinsic mode functions (BIMF) and residuals [3]. The main calculation processes of BEMD are as follows: The original image is recorded as $f(x,y)$, the BIMF component is $BIMF_i(x,y)$, and the residual item after each decomposition is $R_i(x,y)$:

$$f(x,y) = R_0(x,y) \qquad (i=0)$$

Calculate the maximum envelope $h_{up}(x,y)$ and minimum envelope $h_{low}(x,y)$ of $R_i(x,y)$. Meanwhile calculate the mean surface of $R_i(x,y)$.

$$Mean(x,y) = \big(h_{up}(x,y) + h_{low}(x,y)\big)/2 \qquad (1)$$

Difference function $D_i(x,y)$ is calculated according to the mean surface and residual term.

$$D_i(x,y) = R_i(x,y) - mean(x,y) \qquad (2)$$

If the difference function satisfies the basic BIMF features, the $BIMF_i = D_i(x,y)$ is defined and the next BIMF continues to be calculated according to Eq. (3):

$$R_{i+1}(x,y) = R_i(x,y) - BIMF_i(x,y) \qquad (3)$$

Otherwise, the steps from (2)–(4) will be calculated repeatedly until the difference function meets the BIMF basic features. After completing the series decomposition, the data of original image can be expressed as the sum of BIMF components and the residual term. Formula for:

$$f(x,y) = \sum_{i=1}^{n} BIMF_i(x,y) + R_{n+1}(x,y) \qquad (4)$$

After the computation of BEMD, the BIMF1 components are selected for subsequent feature calculation as it always contains the main information of the original images [4].

# 4    Experiments and Results

The ink roller bearings are selected as fault bearings in this experiment, and the fault types include inner ring fault and outer ring fault [5]. The fault bearings are installed respectively as shown in Fig. 2. There are five types of equipment state in this experiment as shown in Table 1.

**Table 1.**  The types of device state

| Device state | Ink roller 1 | Ink roller 2 |
|---|---|---|
| Fault state A | Normal | Outer ring fault |
| Fault state B | Normal | Inner ring fault |
| Fault state C | Outer ring fault | Normal |
| Fault state D | Inner ring fault | Normal |
| Normal state | Normal | Normal |

The duration of the acquisition signal is one second, the data length of each test sample is 16640, and the rotation speed of the roller is 4 rad/s. Figure 4 are the sound field images of fault state A, B, C and D. It can be seen from Figs. 3 and 4 that the sound field distribution of the equipment varies greatly under different states, but it is difficult to directly find the fault law from the images because of the environmental noise.



(a) The fault state A            (b) The fault state B

(c) The fault state C            (d) The fault state D
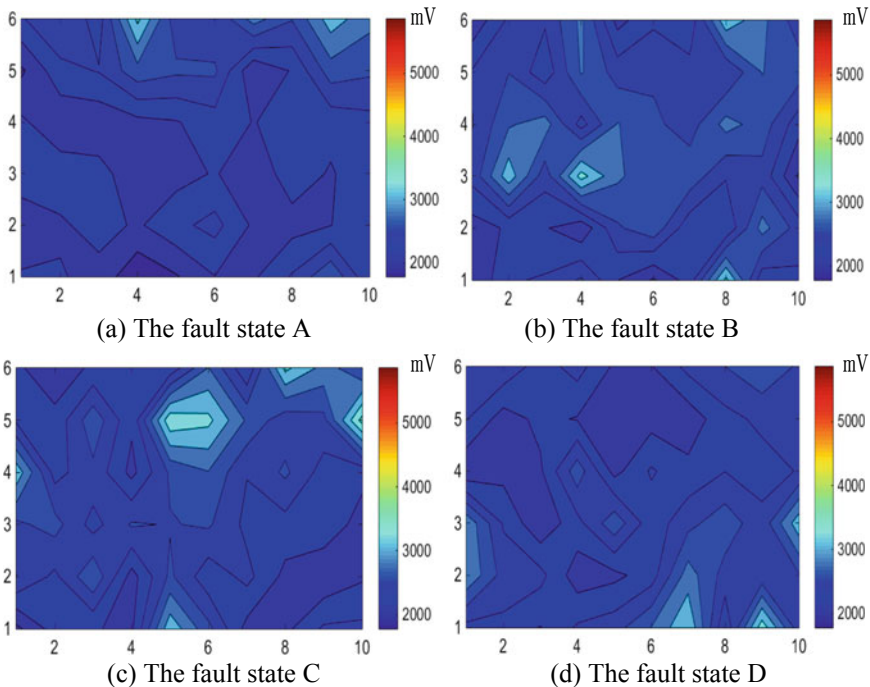
**Fig. 4.**  Ink rollers' sound field images in fault states

Through the BEMD operation of Fig. 3 and Fig. 4, the BIMF1 and BIMF2 are recorded in Fig. 5 and Fig. 6 respectively. The sound field energy under normal states is higher than other states, which also has disordered distribution and inconspicuous regularity from Figs. 3 and 4. By analyzing Figs. 5 and 6, it is clear that the BIMF components have strong regularity, which accords with the actual distribution of ink roller system [6]. Furthermore, compared the BIMF1-2 figures under fault state A and B, it finds that BIMF1-2 are sensitive to the fault types and locations.
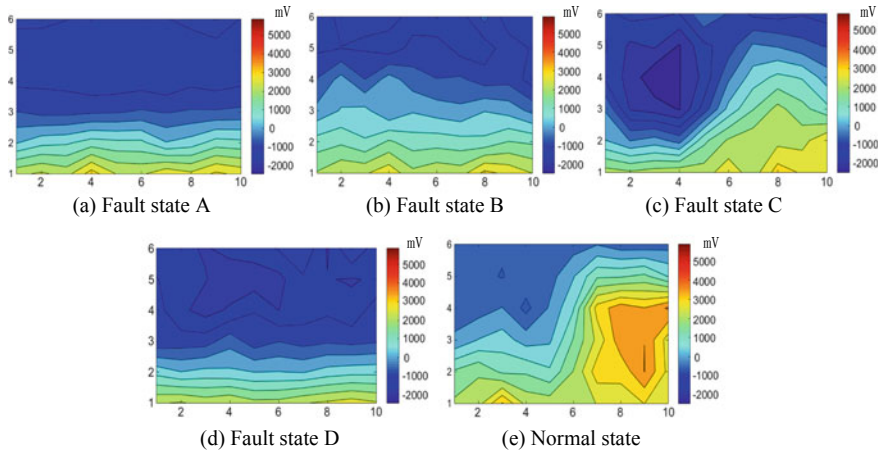


(a) Fault state A          (b) Fault state B          (c) Fault state C

(d) Fault state D          (e) Normal state

**Fig. 5.** BIMF1 component of ink rollers' sound field images in different states



(a) Fault state A          (b) Fault state B          (c) Fault state C

(d) Fault state D          (e) Normal state
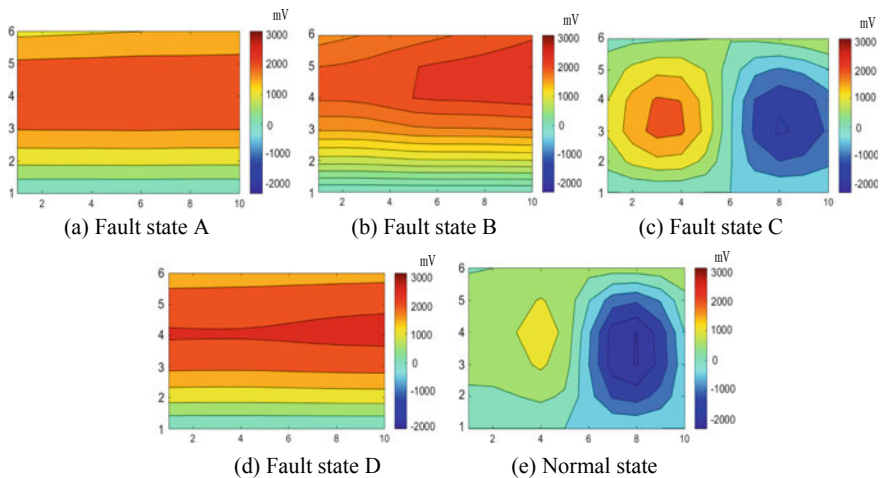
**Fig. 6.** The BIMF1 component of ink rollers' sound field images in different states

The fault locations can be preliminarily determined by the distribution state of BIMF, it is essential to extract effective features from the components in order to make a specific diagnosis. Thu time-domain features are selected. The mean, energy, maximum, minimum, extreme difference and value are chosen in experiment. Dimensionless features such as skewness, kurtosis, peak indicator, waveform indicator, pulse index and margin indicators are also used [7].

Figure 7 is the identification by the mean of BIMF1 component features, where the ordinate is the mean value, the transverse axis represents the sample number. 1–5 is the state A in Table 1. 6–10, 11–15, 16–20 represent B, C and D respectively. 21–25 is normal state. Fault A, fault C and the normal state get a good distinction with mean, but the distinction between the fault B and D is more difficult, this is because the inner ring fault signal is weak caused by interference of ink roller system [8].
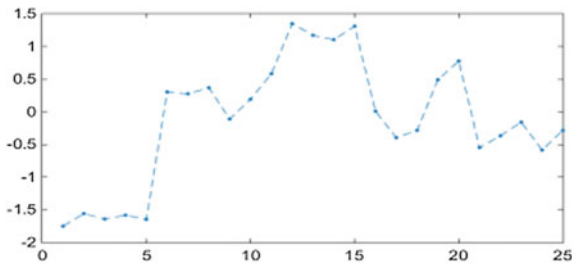


**Fig. 7.** The mean in four faults (ABCD)

Figure 8 shows the identification effect by the skewness of BIMF1 component. The abscissa is the same as that in Fig. 8, the ordinate is skewness. Fault A and B, fault C and D are well distinguished, but A, B, C and D cannot be further distinguished. So, the dimensionless features are more sensitive in the fault location and suitable for positioning. Combined with the comprehensive evaluation of statistical features and dimensionless features, the bearing faults of different positions and different bearings can be distinguished effectively.
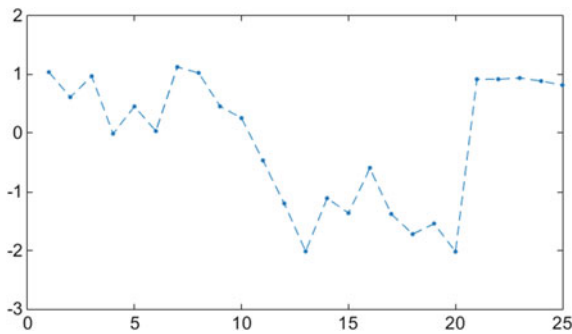


**Fig. 8.** The skewness in four faults

## 5 Conclusions

This paper proposes a fault diagnosis method of printing press bearings based on image analysis of sound field. It has a good effect on distinguishing in the ink roller bearing faults. Combining the comprehensive evaluation of statistical features and dimensionless features, the different positions and types of fault bearings are successfully distinguished. This method also provides a new method for the detection of complex faults in the printing press.

## References

1. Lundstrom J, Verikas A (2013) Assessing print quality by machine in offset color printing. Knowl Based Syst 37(2):70–79
2. Kang H, Lee C, Shin K (2013) Modeling and compensation of the machine directional register in roll-to-roll printing. Control Eng Pract 21(5):645–654
3. Zhao D, Li J, Cheng W (2016) Method for rolling element bearing fault diagnosis based on IDMM and EMD under time-varying rotational speed and gear noise. J Vib Shock 35 (10):101–107
4. Yan L, Guan L, Gengsheng H et al (2010) Real-time vibration monitoring and diagnosis of printing machine using discrete wavelet transform and probabilistic neural network. J Vib Meas Diagn 30(3):236–239
5. Yang J, Guan H (2004) Test and analysis of the vibration of printing press. J Beijing Polytech Univ 30(1):35–37+44
6. Hou H, Zhuofei X, Liu K (2016) Research on fault diagnosis method of rolling bear based on symbolic analysis of intrinsic mode function. J Mech Strength 38(5):916–921
7. Dilmaghani MS, Daneshvar S, Dousty M (2017) A new MRI and PET image fusion algorithm based on BEMD and IHS methods. In: Electrical engineering. IEEE, pp 118–121
8. Nunes JC, Bouaoune Y, Delechelle E et al (2003) Image analysis by bidimensional empirical mode decomposition. Image Vis Comput 21(12):1019–1026

# Study on the Structure Optimization of Oven Duct System in Gravure Press

Peng Liu[✉], Xiaofei Lei, Zhuofei Xu, and Kunhao Zhao

School of Printing Packaging and Digital Media, Xi'an University of
Technology, Shaanxi Province, China
`liupeng@xaut.edu.cn`

**Abstract.** In order to improve the uniformity of wind speed and save energy, the optimization method of duct system structure for the oven in gravure press is studied. The numerical model of oven duct system of gravure press is established. And the method of fluid simulation calculation is used to calculate and analyze the whole flow field. Then the components with obvious eddy current characteristics are selected to optimize their structures. An experimental platform of oven system was built to verify the results of structural optimization of duct system. The experimental data characteristics are consistent with those data of numerical simulation.

**Keywords:** Hot air oven · Duct system · Structure optimization · Fluid simulation calculation

## 1 Introduction

The hot air oven is mainly used for gravure press and coating machine. It is used for drying the printed or coated substrates. The main problem of hot air oven is that its thermal efficiency is very low, and there has been a huge pressure of energy saving. Therefore, the research on the main body of hot air oven has been carried out widely [1, 2].

As an integral part of the hot air oven system, the air intake duct has not attracted much attention and theoretical research is scarce. Because the oven air intake ducts are generally designed by experience, the general structure is unreasonable. There are defects such as large wind pressure loss and poor uniformity of wind speed, which directly causes energy loss and energy consumption. The research on hot air oven intake duct has not been consulted directly related research reports, but related research in other fields can be used for reference, such as pipeline research in gas transmission, oil transportation and heating and ventilation.

Sudok et al. carried out an experimental investigation on the flow field in the circular-sectioned 90° bend pipe and the square-sectioned 90° bend pipe [3, 4]. Jiangshan et al. also simulated the 90° bend pipebased on Fluent software [5]. Xiao Yimin et al. analyzed and the flow field of the Y-type pipe and proposed an optimized scheme to increase the cross-wind plate [6]. Don McGlinchey et al. studied the flow

field characteristics of stepped pipeline in pneumatic conveying systems [7]. Lanchang Xing et al. used fluid simulation to study the fluid behavior of gas-liquid two-phase flow in wavy pipes [8]. Gao Po et al. modeled the hot air duct of blast furnace and gave an optimized design to solve the problem of red drum kits on the duct wall [9]. Wang Yong et al. analyzed the influence of throat of square diffuser on the flow field with uniformity of air supply as the optimization objective [10]. Djunaedy et al. studied five different types of air supply diffuser modelling techniques on the micro level, and proposed a simple method to describe the diffuser without affecting the accuracy of the experimental result [11]. Ying Sun et al. developed a computational fluid dynamics model with radiant exchange between surfaces and examined the air flow characteristics of a room with square cone diffusers [12]. Ge Wentaoet al. designed a slit-shaped inner core structure in MD-82 airliner cabin to make the slit jet flow more uniform [13].

## 2    Oven Duct Structural Analysis

The structure of the oven air intake duct is shown in Fig. 1. Fresh air enters the duct system from the air inlet 2 to the heat exchanger 5 through the connecting pipe. The heat source medium heats the fresh air in the heat exchanger. Then the hot air passes through fan 6, funnel-shaped duct 7 and cavity duct 8. Finally, it enters the oven through inlet duct 1. A part of the exhaust gas from the oven is mixed with fresh air through the return air pipe 4 and then enters the heat exchanger again, so that the remaining heat is recycled. The other part of the exhaust gas enters the exhaust gas treatment system through the outlet duct 3. It can be seen from the structure of the oven duct that funnel-shaped shaped duct, wide box duct and elbows appear in the duct system, which are used to connect the fan or other components.
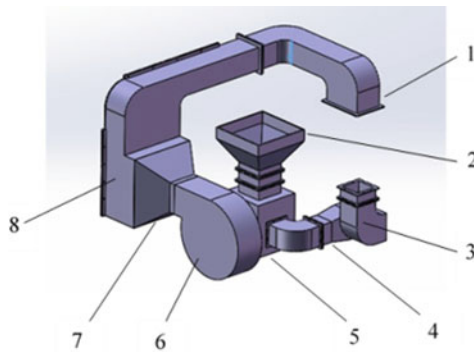


1 inlet duct 2 air inlet 3 outlet duct 4 return air pipe
5 heat exchanger 6 fan  7 funnel-shaped duct   8 cavity duct

**Fig. 1.**   The 3D model of oven air intake duct

## 3    Oven Duct System Modeling and Numerical Simulation

### 3.1    Hydrodynamic Equations

The air movement in the oven duct system obeys the hydrodynamic equations. The mass conservation equation is set up as follows

$$\frac{\partial \rho}{\partial t} + \frac{\partial (\rho u_x)}{\partial x} + \frac{\partial (\rho u_y)}{\partial y} + \frac{\partial (\rho u_z)}{\partial z} = 0 \tag{2.1}$$

where $u_x$, $u_y$ and $u_z$ are velocity components in x, y and Z directions of particles respectively, $\rho$ is the fluid density. The momentum conservation equations are as follows

$$\frac{\partial u_x}{\partial t} + u_x \frac{\partial u_x}{\partial x} + u_y \frac{\partial u_x}{\partial y} + u_z \frac{\partial u_x}{\partial z} = X - \frac{1}{\rho} \frac{\partial \rho}{\partial x} \tag{2.2}$$

$$\frac{\partial u_y}{\partial t} + u_x \frac{\partial u_y}{\partial x} + u_y \frac{\partial u_y}{\partial y} + u_z \frac{\partial u_y}{\partial z} = Y - \frac{1}{\rho} \frac{\partial \rho}{\partial y} \tag{2.3}$$

$$\frac{\partial u_z}{\partial t} + u_x \frac{\partial u_z}{\partial x} + u_y \frac{\partial u_z}{\partial y} + u_z \frac{\partial u_z}{\partial z} = Z - \frac{1}{\rho} \frac{\partial \rho}{\partial z} \tag{2.4}$$

The energy conservation equation is as follows

$$\rho c_p \left( \frac{\partial T}{\partial t} + u \frac{\partial T}{\partial x} + v \frac{\partial T}{\partial y} + w \frac{\partial T}{\partial z} \right) = \left( \frac{\partial \rho}{\partial t} + u \frac{\partial \rho}{\partial x} + v \frac{\partial \rho}{\partial y} + w \frac{\partial \rho}{\partial z} \right)$$
$$+ \left[ \frac{\partial}{\partial x} \left( \lambda \cdot \frac{\partial T}{\partial x} \right) + \frac{\partial}{\partial y} \left( \lambda \cdot \frac{\partial T}{\partial y} \right) + \frac{\partial}{\partial z} \left( \lambda \cdot \frac{\partial T}{\partial z} \right) \right] + \mu \cdot \Phi \tag{2.5}$$

where T is the fluid temperature, is the heat conduction coefficient, $\mu$ is the viscous coefficient, $C_P$ is the constant pressure ratio of the fluid, $\varphi$ is the viscous dissipation function.

### 3.2    Duct System Model

The three-dimensional model of oven duct is established by the software solidworks according to the ratio of 1:2 of the actual size of the equipment, as shown in Fig. 1. The fluid field is confined to the inside of the structure. On the premise of ensuring the accuracy, some relatively complex structures of the dry device are appropriately simplified. At the same time, the influence of duct wall resistance on the calculation results is ignored.

### 3.3   Solution Method

The Fluent software is used to simulate the velocity field and pressure field of hot air in the oven duct fluid domain. Then, the performance of the structural components of the oven duct system is evaluated to provide a corresponding theoretical basis for the optimization of the structure.

The unstructured grid is divided by the software Gambit for the previously established three-dimensional oven duct model. The total length, width and height of the computational fluid domain of the oven duct system are 980 mm, 892 mm and 480 mm respectively. The inlet boundary is a velocity inlet with an inlet velocity of 15 m/s. And the outlet boundary is a pressure outlet with a static pressure of 101 325 Pa. Adiabatic wall surface is adopted. Using the RNG k-ε turbulence model, the computational fluid domain is iteratively solved until a convergent solution is obtained. Then post-processing is performed using the software tecplot to display the results of the calculation.

### 3.4   Analysis of Numerical Simulation Results

As shown in Fig. 2, the velocity trace of the oven duct system is shown. The color change in the figure indicates the velocity value, and the density of the velocity trace represents the uniformity of the hot air flow.
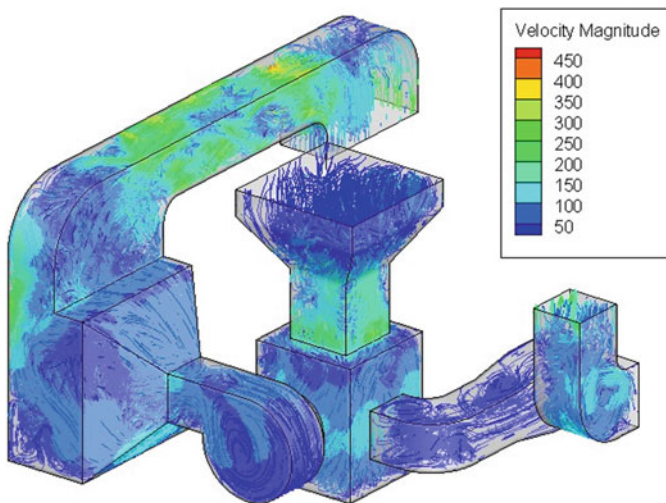


**Fig. 2.** The traces of oven air intake duct

In order to find the duct parts that need to be optimized, the velocity slice diagram of the duct structure is made. The three-dimensional model of the funnel-shaped duct and its connected cavity duct is shown in Fig. 3. The entrance of the funnel-shaped duct is connected with the fan, the outlet is connected with the entrance of the wide

box-shaped cavity duct, and the outlet of the box-shaped cavity duct is connected with the elbow, and then the hot air is fed into the oven body. The velocity slices of the funnel-shaped duct and the cavity duct behind are shown in Fig. 4. It is clear that the large eddy currents exist in the funnel-shaped duct and its connected box cavity duct. From the slice trace graph, it can be seen that most of the high-speed fluids blown out from the fan directly impact on the back of the cavity duct. The reflected air flows irregularly in the internal space of the cavity duct, thus forming a large number of eddies with large volume, resulting in extremely uneven fluid movement. A large number of eddy currents have resulted in a significant increase in energy consumption.
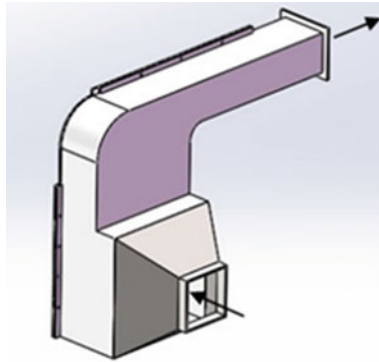


**Fig. 3.** The 3D model of funnel-shaped duct and cavity duct
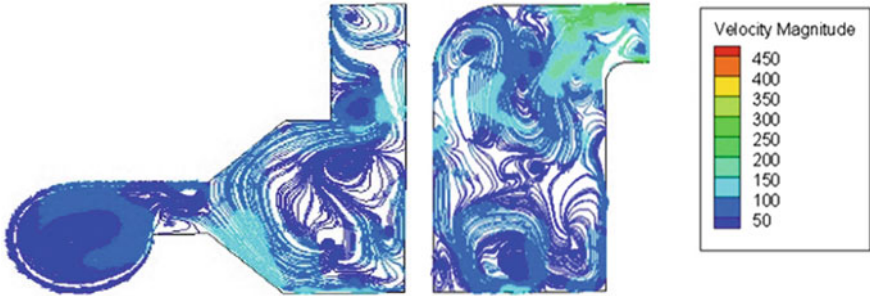


**Fig. 4.** The traces of funnel-shaped duct and cavity duct

## 4    Duct System Structure Optimizations

### 4.1    Structural Optimization of Funnel-Shaped Duct

The wind blows out from the fan and directly enters the funnel-shaped duct. At this time, the wind speed in the center of the duct is much higher than that in the edge, and directly impacts on the back of the cavity duct. After analyzing the structure of the

cavity duct separately, it is found that the eddy current in the cavity duct decreases obviously when the air intake is uniform at the entrance of the cavity duct. Therefore, the scheme of adding uniform air plate is proposed to make the wind velocity uniform at the outlet of the funnel-shaped duct.

The method of adding uniform wind structure is adopted to optimize funnel-shaped duct. The cross design of horizontal and vertical uniform air plates is adopted. If two uniform air plates are set up in both horizontal and vertical directions, the uniform air structure can be formed as shown in Fig. 5. This structure can be named as $2 \times 2$ structure, which divide the fluid area into nine parts.
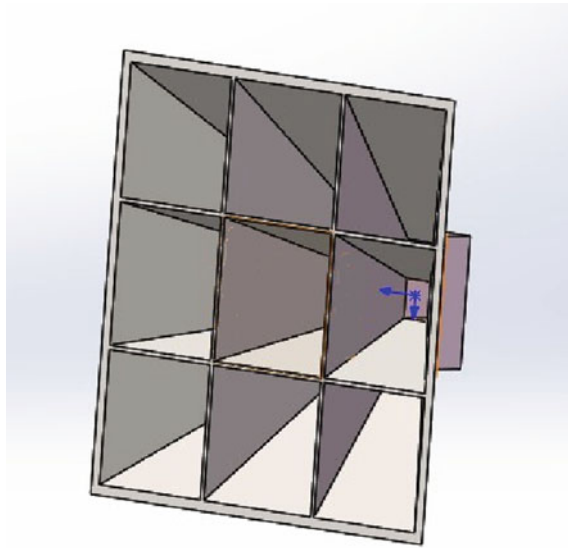


**Fig. 5.** The funnel-shaped duct with $2 \times 2$ structural improvement scheme

Fluid simulation of funnel-shaped ducts with $1 \times 1$ uniform wind structure, $2 \times 2$ uniform wind structure, $3 \times 3$ uniform wind structure and $4 \times 4$ uniform wind structure was carried out by using the fluid calculation method mentioned above. The velocity and pressure data of the funnel-shaped duct outlet of the above structure were extracted respectively, and the velocity standard deviation and pressure difference data are calculated as shown in Table 1. It was found that the uniformity of the overall velocity was improved with the addition of the uniform wind structure. By adding the uniform wind structure to the funnel-shaped duct, the uniformity of the flow field in the funnel-shaped duct was significantly improved. The optimum scheme is $3 \times 3$ uniform wind structure, with 1.41 (33.73%) reduction in wind speed difference and 14.84 pa (49.58%) reduction in pressure difference.

**Table 1.** The simulation results of the funnel-shaped duct with different improvement structure

| Structure name | Maximum speed (m/s) | Pressure difference (pa) | Average velocity (m/s) | Velocity difference (m/s) |
|---|---|---|---|---|
| Original | 16.23865 | 29.93 | 8.4557552 | 4.1762943 |
| 1 × 1 | 13.60235 | 18.56 | 8.1202410 | 3.4231624 |
| 2 × 2 | 14.75849 | 21.05 | 7.5732307 | 3.6423963 |
| 3 × 3 | 13.43950 | 15.09 | 6.8957806 | 2.7678123 |
| 4 × 4 | 14.64783 | 17.56 | 6.8184299 | 3.3463891 |

## 4.2    Structural Optimization of Box Duct

For the optimization of the cavity duct, the method is to add parallel straight plate-shaped uniform plate inside, whose shape is shown in Fig. 6. The circular holes of equal diameter are made on the rectangular uniform plate at equal distances. The total number of holes is 32 in the uniform plate, and the diameter of each circular hole is 30 mm. The structure of the cavity duct is optimized by setting the arrangement of the uniform plate. The uniform air plate is tilted in the interior of the cavity duct, and the upper edge is close to the outlet of the funnel-shaped duct, that is, the entrance of the cavity duct. Figure 7 shows the arrangement when four uniform plates are added.
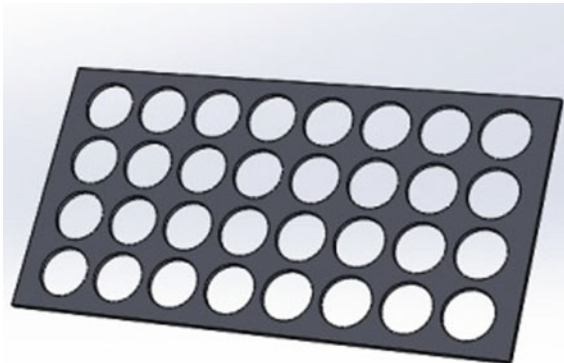


**Fig. 6.** The shape of the uniform plate

Considering that the cavity duct and the optimized funnel-shaped duct are assembled together, and the fluid state of the funnel-shaped duct will have a direct impact on the fluid analysis of the cavity duct. so, the optimization of the cavity duct is combined with the overall structure of the funnel-shaped duct after optimization. The fluid calculation method described above is used to simulate the optimization schemes of cavity ducts with one, two, three and four uniform plates respectively. The velocity and pressure data of the outlet of the cavity duct are extracted respectively in the numerical simulation of the above arrangement, and the standard deviation and
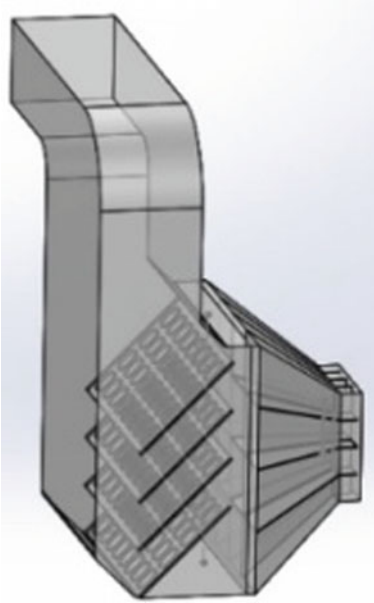
**Fig. 7.** The position of the uniform plate

pressure difference data of the outlet are calculated as shown in Table 2. It can be found that with the addition of uniform air plate, the uniformity of flow field velocity is obviously improved. The scheme with best optimization result is three uniform air plates, which reduces the velocity difference by 1.41 (29.01%) and the pressure difference by 14.84 Pa (65.36%). The addition of the uniform plate reduces the impact air flow on the back of the cavity duct and makes the large eddies disappear in the field.

**Table 2.** The simulation results of the cavity duct with different number uniform plate

| Structure name | Maximum speed (m/s) | Pressure difference (pa) | Average velocity (m/s) | Velocity difference (m/s) |
|---|---|---|---|---|
| Original | 16.32608 | 32.56 | 14.179035 | 1.5901245 |
| One-piece plate | 16.59702 | 21.47 | 14.197401 | 1.2208258 |
| Two-piece plate | 15.82904 | 16.34 | 14.22921 | 1.1973928 |
| Three-piece plate | 14.96022 | 11.28 | 14.227791 | 1.1287513 |
| Four-piece plate | 14.81036 | 14.60 | 14.238037 | 1.1461950 |

## 5    Experimental Verification

In order to verify the results of theoretical research and numerical simulation, the solid model of oven system was made and the air in take duct of oven was experimentally studied. The wind pressure loss and wind speed uniformity of the original duct structures and optimized duct structures were tested and compared with the results of numerical simulation. It can be verified that the uniformity of wind speed and wind pressure of the optimized duct structure is greatly improved, and the flow field distribution law obtained by the experiment is consistent with that of the numerical simulation.

## 6    Conclusions

The flow numerical simulation of the oven duct system is carried out to determine the structural parts that need to be optimized. Different types of air uniform plate are added to the funnel-shaped duct and the cavity duct respectively to reduce and suppress the eddy currents in the duct for improving the uniformity of the wind, reducing the total pressure and energy loss of the fluid. The validity of the optimized structure is verified by experiments.

The results show that the special-shaped ducts and large cavity ducts will produce a lot of eddy currents, which will lead to energy loss. And the fluid calculation method to optimize the oven duct system is effective.

## References

1. Jin L, Li Y, Wang Y-M, et al (2014) Energy efficiency analysis of Gravure press based on energy consumption test. Package Eng 35(23):94–99
2. Liu P, Xiang C, Hou H-P, et al (2017) The thermodynamic analysis on drying system of Gravure press. Package Eng 38(1):195–199
3. Sudo K, Sumida M, Hibara H (1998) Experimental investigation on turbulent flow in a circular-sectioned 90-degree bend. Exp Fluids 25:42–49
4. Sudo K, Sumida M, Hibara H (2001) Experimental investigation on turbulent flow in a square-sectioned 90-degree bend. Exp Fluids 30:246–252
5. Jiang S, Zhang J-W, Wu C-J, et al (2008) Numerical simulation of inner flow in 90° bending duct of circular-section based on fluent. Chin J Ship Res 3(1):37–41
6. Xiao Y-M, Liu B, Fan Y-C (2015) Analysis off low field in y-type pipe and optimization of its structure. Comput Simul 32(5):270–274
7. McGlinchey D, Cowell A, Crowe R, et al (2012) CFD investigation of dense phase pneumatic conveying at a pipeline enlargement. Particuology 10(2):176–183
8. Xing L, Yeung H, Shen J, et al (2013) Numerical study on mitigating severe slugging in pipeline/riser system with wavy pipe. Int J Multiph Flow 53:1–10

9. Gao P, Yang W-J, Wu Z-H, et al (2013) Study on the modeling of blast furnace hot air pipe structure and optimization design. Mach Des Manuf 32(7):63–66
10. Wang Y, Su K, Dai X-L, et al (2015) Analysis of the effect of square diffuser throat on the uniformity of air flow. J Hunan Univ (Natural Sciences) 42(5):126–133
11. Djunaedy E, Cheong KWD (2002) Development of a simplified technique of modeling four-way ceiling air supply diffuser. Build Environ 37(4):393–403
12. Sun Y, Smith TF (2005) Air flow characteristics of a room with square cone diffusers. Build Environ 40(5):589–600
13. Ge W-T, Guo Y, Shen D, et al (2015) Optimization design of inner-structure of the slot-jet in aircraft cabin based on investigation of multi-scale characteristics of slot turbulent jet flow. J Exp Fluid Mech 29(5):32–37

# Robot Hand Based on Multifunctional Tactile Sensor for Warehouse Application

Kunlin Gao, Haijun Zhang, and Wei Wang[✉]

College of Information and Electrical Engineering, Zhengzhou University
of Light Industry, Henan, China
18900616029@189.cn

**Abstract.** With the rapid development of e-commerce, the smart warehouse and delivery industry is increasing dramatically. Robot hand is the important equipment in this industry and its key technology is to improve the stability and accuracy of the manipulator in the process of sorting and handling process by using tactile sensor. In this work, we have developed new sensing materials and fabrication process to produce flexible multifunctional tactile sensors by using printed electronic technology. They are light and durable, and can test the pressure distribution and bending changes accurately during the grasping process. We have installed several sensors on the front and back of the robot hand, and designed a testing feedback system. It can monitor the dynamic process of grabbing in real time and send it to the control system, greatly improving grasping and object identification performance. It can be integrated with the artificial intelligence algorithms to provide intelligent sorting and handling process for smart warehouse application.

**Keywords:** Smart warehouse · Robot hand · Tactile sensor · Printed electronic technology

## 1 Introduction

With the development of industry 4.0 and intelligent manufacturing, smart warehouse has become a new direction for the development of delivery industry [1]. The intelligent car equipped with robot hand is the core equipment in the intelligent logistics industry. The image processing module of the car identifies the type of package, and then controls the robot hand to grasp and sort the package, which improves the efficiency of the operation of the smart warehouse. Through consulting the literature, we found that some robot hands don't use the flexible tactile sensor in the logistics industry, and they can only collect the pressure value of the robot hand through the upper computer, and can not collect the angle of the finger bending; some traditional robot hands can collect the bending action of the robot hand when grabbing the package, but the accuracy is not enough. They don't display the force and finger curvature of the robot hand synchronously and real-time, and can not realize real-time control of the force of the robot hand to grasp the package, so the grasping stability is not high [2]. In this paper, a flexible tactile sensor based on printed electronic technology is developed, which combines with a robot hand. The force and bend of the

finger are collected in real time by using a self-developed software for finger pressure and bend acquisition. By adjusting the control system of the manipulator, the accuracy and stability of the robot hand in grasping the package in smart warehouse are improved.

## 2    Material and Fabrication of Flexible Resistance Bending Sensor

By using laboratory equipment, we made some graphene layers and covered them on the flexible PET (Polyethylene terephthalate) substrate to prepare a simple flexible stress sensor. Before covering graphene, the interdigital electrodes (Fig. 1) should be printed on PET [3]. It can improve the sensitivity of flexible bending sensor, and is convenient for later testing and packaging.
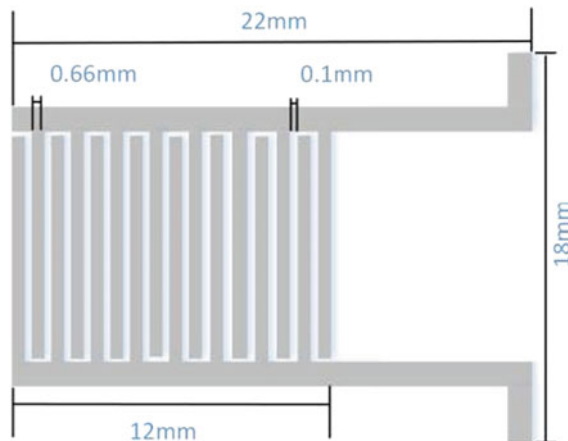


**Fig. 1.**  Interdigital electrode

Next, a flexible stress sensor is fabricated by using self-made graphene and interdigital electrodes, The specific steps are described below.

(1) Configuration of graphene solution

The graphene of 0.05 g was put into the test tube with electronic balance and 50 ml of absolute ethanol was added. The graphene powder was evenly dispersed in ethanol at room temperature for 5 min. The reason why ethanol is chosen as solvent is that ethanol is easy to volatilize and can promote graphene to cover PET rapidly.

(2) Covering of graphene

First, the two ends of the interdigital electrode are connected with the multimeter to observe the change of resistance value [4]. A little graphene solution was taken by dropping tube and dripped evenly to the interdigital part of the interdigital electrode until the ethanol was evaporated clean.

(3) According to steps (1) and (2), bending sensors with initial resistance of about 2.5 MΩ and 3.0 MΩ were fabricated respectively (Fig. 2).



**Fig. 2.** Flexible bending sensor

By testing the fabricated bending sensor, we get the characteristic curve of the flexible bending sensor (Fig. 3). Through the pressure test of the sensor's sensitive unit, we get that the linearity, hysteresis, repeatability and sensitivity of the sensor are 9.88%, 2.38%, 3.10% and 1150 mV/kPa respectively.
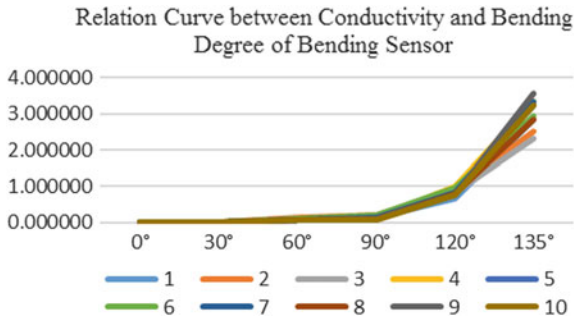


**Fig. 3.** The relation between conductivity and vending degree of bending sensor

## 3  Control of Robot Hand and Tactile Information Feedback System

### 3.1  Control of Robot Hand

In the experimental stage, we used a 3D printer to print components and assembled a robot hand (Fig. 4a). A pressure sensor was installed on the inside of each finger of the robot hand, and a bending sensor was installed on the outside of each finger, each finger is connected with a steering gear (Fig. 4b).
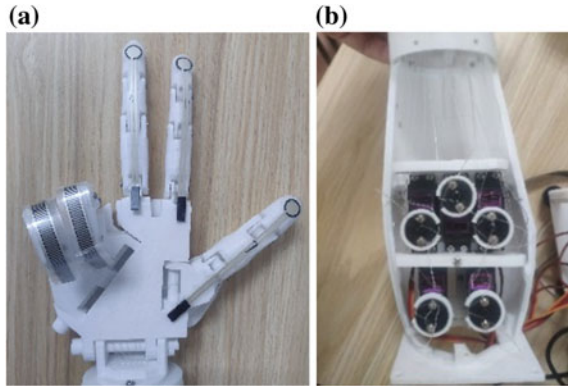
**Fig. 4.** Robot hand model

Robot hand is controlled by Arduino. We edit the program in the development environment, then the program is downloaded to the Arduino control board [5], connected to the power supply, and the extension board receives instructions to control steering gears to perform the operation. The servo myservo statement was used to define five actuators in the test [6]. The important procedures for controlling robot hand to grasp objects are shown in Fig. 5.



**Fig. 5.** **a** This statement initializes each steering gear to 0°; **b** this statement realizes the action of manipulator grasping object.

## 3.2 Tactile Information Acquisition System for Robot Hand Based on Flexible Tactile Sensor

In the design of the two acquisition systems, we use Arduino control board as the lower computer and Processing programming language to design the upper computer software [7].

(1) Pressure acquisition and testing system of robot hand

Lower computer design: The pressure sensor attached to the inside of the manip-ulator is connected with the A0, A1, A2, A3 and A4 ports of the Arduino control board in series with a resistance of 10 kΩ.

PC design: The following Fig. 6 is the designed pressure value acquisition inter-face. On the left side, there are start, stop, save and exit buttons to control the acqui-sition. The following are the preset and calibration modules of small force, medium force and strong force sensors. The middle part is the pressure value cylinder chart to visualize the pressure value collected; the right side is the pressure value acquisition table, which can display the pressure values collected by the sensors in real time.
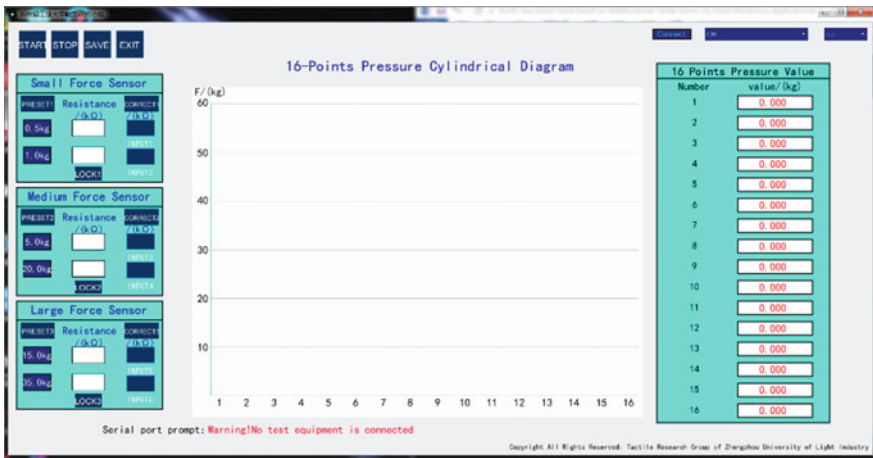


**Fig. 6.** Pressure value acquisition system

(2) Bending information acquisition system of robot hand

Lower computer design: The bending sensor attached to the inside of the robot hand is connected with the A5, A6, A7, A8 and A9 ports of the Arduino control board in series with a resistance of 10 kΩ.

PC design: The following Fig. 7 is the bending sensor information acquisition system designed by us. When the Arduino control board is successfully connected to PC, click the "Start" button, the real-time bending action of robot hand will be dis-played in the software. The bending angle of each finger will be displayed in real-time in the frame of the lower part of the software; the right side is the finger bending calibration module, in order to enable the sensor to collect more accurate bending value.
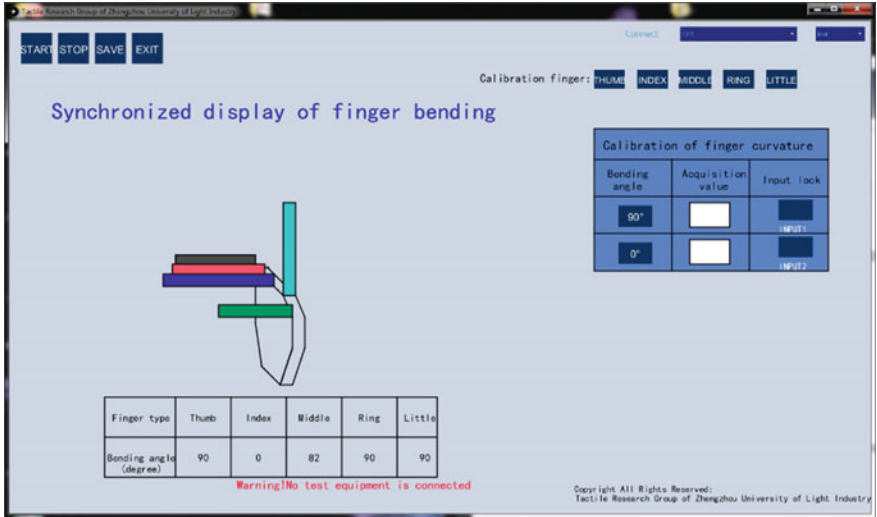
**Fig. 7.** Five-finger curvature testing system

Combining the above two acquisition systems, the flow chart of robot hand control and tactile information feedback is designed (Fig. 8).
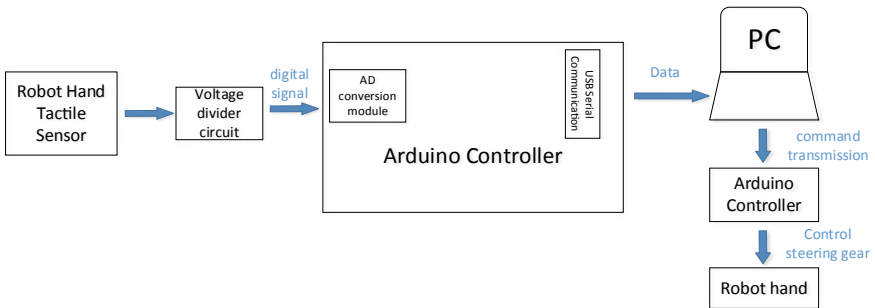


**Fig. 8.** General control diagram of the system

## 4 Conclusions

In this study, we have fabricated flexible resistance bending sensor by using new material and new method. We then applied these sensors to the robot hand in the logistics industry. By using the specifically designed control circuit, we have made the robot hand with tactile sensor for the intelligent grasping and sorting. At the same time, we designed a tactile information acquisition system of flexible tactile sensor. Through the collecting system, we could monitor the bending degree of the fingers and the pressure on each finger of the robot hand in real-time when grabbing the logistics

package. According to these results, we could adjust the grasping state of the manipulator in real time, which can avoid the problem of too little grip to make things fall off and too much grip to break down items. This improvement of the stability of handgrabbing logistics parcels is very important for smart warehouse application.

# References

1. Guo XH (2019) An intelligent automatic sorting and processing system for logistics industry. Logist Eng Manag 41(04):83–84
2. Wang HD, Xiong XQ, Chen S, Xiong Y, Du Y (2019) Intelligent logistics cart. Innov Appl Sci Technol (06):113–114
3. Janata J, Josowicz M (2003) Conducting polymers in electronic chemical sensors. Nat Mater 2(1):19–24
4. Leng MX, Song AG (2017) Design and calibration test of robot tactile sensor. J Electr Electr Teach 39(05):62–65
5. Liu JM (2019) Design of intelligent manipulator based on aduino infrared control. Sci Technol Wind (12):7–8
6. Deng Y, Liang FH, Cen J, Xing ZR (2004) Research on manipulator operation control with stress sensor. J Maoming Univ (04):45–48
7. Xiao NF, Chen XX (2018) Design and implementation of tactile sensor and joint drive and control system for humanoid manipulator. J Chongqing Univ Technol (Natural Science) 32(01):148–157

# Design of Rectifying Controller Based on Fuzzy PID Control Strategy

Xulan Chen[1(✉)], Heping Hou[1], Shanhui Liu[1], and Qing Wen[2]

[1] Faculty of Printing Packaging Engineering and Digital Media Technology,
Xi'an University of Technology, Xi'an, China
15529565716@163.com

[2] North Automatic Control Technology Institute, China North Industries Group
Corporation, Taiyuan, China

**Abstract.** Strip offset can cause registration errors, resulting in a large amount of waste during the printing process. In order to achieve precise control of the running track, this paper designs a correction system controller based on fuzzy PID control strategy. Firstly, the basic principle of the belt transmission is analyzed, and the dynamic model of the belt movement is established. Secondly, The ultrasonic sensor is used as the detection device, SCM is used as the control core and the stepping motor is used as the actuator. Thirdly, a correction system control method based on fuzzy PID control strategy is proposed, and the control system software is developed. Experiments show that the correction controller can realize rectifying control of various types of printing materials and is suitable for a variety of high-end printing equipment.

**Keywords:** Rectifying control · Fuzzy PID · Ultrasonic sensor

## 1 Introduction

Due to the tension and other factors in the printing process, the strip is offset, which results in the deviation of printing graphic in multi-color overprinter [1]. Therefore, precise control of the track is required by the external correcting controller [2]. In this paper, the basic principle of the belt transmission is analyzed, the dynamic model is established, and the correction control method based on fuzzy PID control is proposed. The ultrasonic sensor is used as the detection device, SCM is the control core and the stepping motor is used as an actuator, a type of belt rectification controller is designed, which is of great practical significance to ensure the normal printing process.

## 2 Dynamics Model of the Belt Movement

As shown in Fig. 1, $\theta_r$ is roller deflection angle. $\theta_L$ is paper tape offset angle. L is tape length between two rollers. $L_1$ is roller deflection center distance. Z is roller lateral offset distance. $y_L$ is paper tape lateral offset distance.
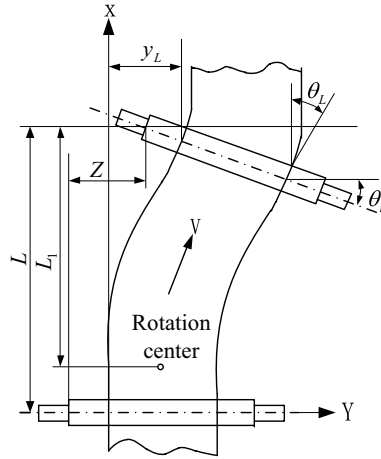
**Fig. 1.** Paper kinematics model

Assuming that the rollers are fixed, the initial offset of the tape entering the first roller is $y_0$, and the offset of the second roller is $y_L$, the lateral offset speed of the tape is shown in Formula (1).

$$\frac{dy_L}{dt} = V\frac{y_0 - y_L}{L} + \frac{dz}{dt} \tag{1}$$

In practice, the paper strip typically bends when it is laterally offset by the deflection roller, so the paper strip can be considered as an elastic Euler beam for analysis, according to the dynamic equation of Shelton and Reid [3], the equation of motion of the belt can be simplified as Formula (2).

$$\frac{\partial^4 y}{\partial x^4} - \frac{T}{EI}\frac{\partial^2 y}{\partial x^2} = 0 \tag{2}$$

The speed and acceleration of the lateral deviation of the paper strip are shown in Eqs. (3) and (4) by first-order and second-order derivatives.

$$\frac{dy_L}{dt} = V\left(\theta_r - \frac{\partial y}{\partial x}|_L\right) + \frac{dz}{dt} \tag{3}$$

$$\frac{d^2 y_L}{dt^2} = V^2\frac{\partial^2 y}{\partial x^2}|_L + \frac{d^2 z}{dt^2} \tag{4}$$

After the second differentiation of the x-axis by Eq. (3), the lateral displacement of the paper strip to the x-axis can be shown in Eq. (5).

$$\frac{\partial^2 y_L}{\partial x^2}\bigg|_L = \left(\frac{y_0 - y_L}{L^2}\right)f_1(KL) + \frac{1}{L}\frac{dy}{dx}\bigg|_L f_2(KL) \tag{5}$$

Combining the above formulas, the transverse motion of the strip can be shown in Eq. (6) [4].

$$\frac{d^2 y}{dt^2} = v^2\left[\frac{f_1(KL)}{L^2}(y_0 - y_L) + \frac{f_2(KL)}{L}\frac{dy_L}{dt}\right] + \frac{d^2 z}{dt^2} \tag{6}$$

## 3    Hardware Composition of the Correction Control System

The strip rectification control system includes the detection device, the central controller, the actuator and the feedback device [5].

### 3.1    Ultrasonic Sensor

The sensor is used to detect the position of the tape, and the ultrasonic wave is emitted through the transmitting probe. When the ultrasonic wave propagates in the air and hits the tape, it will be reflected back. However, when the tape is offset, the ultrasonic wave will be received. The lateral offset of strip can be determined according to the output voltage of sensor [6, 7]. The principle is shown in Fig. 2.
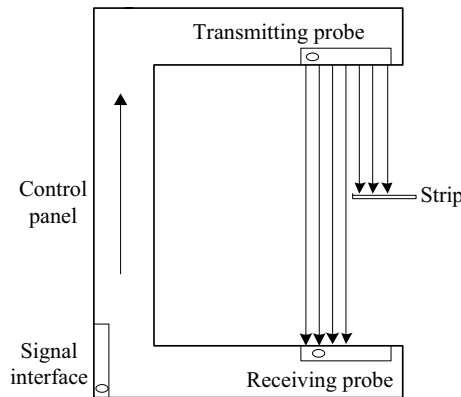


**Fig. 2.**  Principle diagram of the ultrasonic sensors

### 3.2    Correction Controller

The core of the tape rectification control system adopts the STC12C5A60S2 chip. SCM system and interface are shown in Fig. 3.
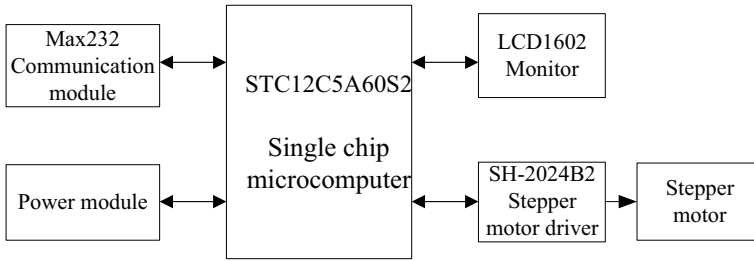
**Fig. 3.** The diagram of hardware circuit for single chip system

The LCD1602 liquid crystal displays the sensor output voltage value after A/D conversion [8]. The Max232 communication module connects the signal receiving and the transmitting end to the serial port of the computer through the serial port chip, which realizes the communication between the computer and the controller as well as between the controller and the host computer [9].

### 3.3    Correction Actuator

The correcting actuator is composed of a stepping motor and ball screw. The pulse frequency is used to control the speed and acceleration of the motor rotation, thereby achieving the purpose of speed regulation and accurate positioning [10].

## 4    Software Design of the Correction Control System

The working principle of the correcting controller is as follows. During the processing operation, the sensor detects the deviation signal and sends it to the controller. The deviation signal is obtained by comparing it with the set zero deviation value. The controller outputs the corresponding driving signal to the stepping motor driver, and finally drives the coil to complete the correcting. The software design mainly includes main program design, communication program, stepper motor and fuzzy PID control program, display module program [11].

### 4.1    Correction Controller Main Program Design

See Fig. 4.
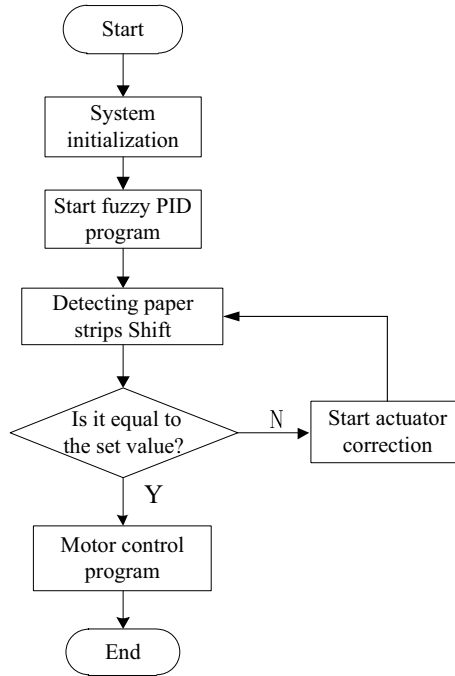
**Fig. 4.** Program flow chart

## 4.2 PC Software Preparation

In order to better realize the human-computer interaction performance, the upper computer software interface is designed, which mainly has three functions of communication, display and data storage. The upper computer receives data through the serial port. Click the open serial button to display the corresponding offset [12, 13].

## 5 Experimental Results and Analysis

The device is installed on the shaftless transmission experiment platform (Fig. 5).



**Fig. 5.** Experiment platform

In the effective working range, the offset correction effect at four different printing speeds was tested with offset printing paper, the average of 500 sets of experimental data were taken. The results are shown in Table 1.

**Table 1.** Data sheet of the rectification effect of different printing speed

| Printing speed (r/min) | Pre-correction (mm) | Correction offset (mm) | Value |
|---|---|---|---|
| 50 | 0.10 | 0.07 | 0.03 |
| 100 | 0.18 | 0.10 | 0.08 |
| 150 | 0.25 | 0.13 | 0.12 |
| 200 | 0.36 | 0.15 | 0.21 |

It can be seen from Table 1 that the correcting device can achieve higher precision, and the larger the value, the more significant the correcting effect is.

In order to test the corrective effect on different types of printed paper, the printing speed is 150 r/min. The results are shown in Table 2.

**Table 2.** Data sheet of the rectification effect of different types of strip

| Paper type | Pre-correction (mm) | Correction offset (mm) | Value |
|---|---|---|---|
| Newsprint | 0.32 | 0.15 | 0.17 |
| Offset printing paper | 0.25 | 0.10 | 0.15 |
| Coated paper | 0.19 | 0.09 | 0.10 |
| Printed film | 0.34 | 0.23 | 0.11 |

The value is less than 0.2 mm, it can be seen that the correcting device has a better correcting effect on different types of paper.

## 6    Conclusions

In this paper, the deviation in the strip during processing is studied. SCM is used as the control core, ultrasonic sensor, stepper motor and ball screw for detection and control. The fuzzy PID composite control algorithm is designed. The corrective effect on different printing speeds and different types of strips are verified. It is proved that the device can realize the strip rectification function well and is suitable for the detection of various types of strips, which is of great significance to actual production.

# References

1. Zhang P (2012) Tracking control of sinusoidal deviation during strip winding. Hangzhou University of Electronic Science and Technology, Hangzhou, China
2. Wang Y, Wang Y (2007) Fuzzy prediction control with strip correction. Mech Des Manuf 56 (3):113–115
3. Shelton JJ, Reid KN (1971) Lateral dynamics of a real moving web. J Dyn Syst Meas Contr 93(3):182
4. Wu J (2009) Research on dynamics and vibration control of moving paper tape. Xi'an University of Technology, Xi'an, China
5. Wang Y (2012) Design of automatic stripping control system for strip. Xi'an University of Technology, Xi'an, China
6. Heping Hou, Kai Liu, Haiyan Zhang et al (2012) Research and system development of new double sheet detection controller for printing machines. J Transduct Technol 25(4):552–556
7. Tian Z, Cao J, Liu X (2007) Application of ultrasonic sensors in electric wheelchairs. J Transduct Technol 20(3):719–722
8. Wu X, Ou Q (2009) Design of RS232 serial communication between PC and MCU. Foreign Electron Meas Technol 28(1):74–76
9. Jiang P, Zhang N (2015) Design and implementation of serial communication in data acquisition system. Electron Meas Technol 52(6):139–142
10. Liao P, Han W (2016) Design of drive control system based on STM32 multi-stepping motor. Instrum Technol Sens 33(4):71–73
11. Youfa Cai, Huiqun Zheng (2007) Design of high precision ultrasonic correction control system. Ind Instrum Autom 5:66–67
12. Mondal C, Azam MK, Ahmad M et al (2015) Design and implementation of a prototype electrooculography based data acquisition system. Int Conf Electr Eng Inf Commun Technol 25(2):1–6
13. Jiang T, Zhang J (2009) Design and implement for user-control software of data acquisition system. Electron Test 45(9):58–61

# Follow-up Property of Circumferentially Grooved Idle Roller in Roll-to-Roll Manufacturing

Li'e Ma[(✉)], Bin Yang, Yi Guo, Qipeng Long, Jimei Wu,
and Yonghui Lei

Faculty of Printing, Packaging Engineering and Digital Media Technology,
Xi'an University of Technology, 710048, Xi'an, China
malie@xaut.edu.cn, 1833725398@qq.com

**Abstract.** The web is supported and transported by using of many rollers in roll-to-roll manufacturing system. The idle roller plays a role in importing and changing the direction of the web movement and also in supporting the web transferring. The follow-up property of the idle roller is the moving synchronism between the roller and the web, and has an important impact on the web transferring accuracy and stability. In this paper, the follow-up time model of the circumferentially grooved roller is established. The effects of various parameters such as equivalent roughness, wrap angle, web tension, friction coefficient, web width, and groove parameters (groove number, groove width and groove depth) on the follow-up time of roller are analyzed. The results show that the follow-up property of the roller is better with the increasing of the equivalent roughness, the wrap angle, the friction coefficient and the web tension. Within a certain range, the follow-up property of the roller is worse with increasing the web width. The follow-up property of the roller can be improved by increasing the groove number, groove depth and groove width.

**Keywords:** Roll-to-roll manufacturing · Idle roller · Follow-up property · Friction

## 1 Introduction

Flexible electronic products are widely applied in information, energy sources, health care and the printing field. Roll-to-roll manufacturing technology is regarded as one of the most effective ways to realize flexible electronic mass manufacturing [1]. The follow-up property of the idle roller is the characteristic of the roller following the web synchronously. Poor follow-up property can cause web scratch, web wrinkles, lateral drift and directly affect the processing speed and accuracy of the web in printing process.

At present, the stability studies on the idle roller and web transferring mainly concentrated on installation and machining accuracy of the roller and mechanical properties of the roller [2–5]. Traction characteristics between web and roller were

discussed by several authors. Müftü [6] established the traction prediction model between a web and a smooth roller, and analyzed the effect of the web and roller speeds, roller radius, friction coefficient and web tension and thickness, et al. Mongkolwongrojn [7] investigated the traction characteristics of soft grooved roller and web considering the air entrainment and analyzed the effects of groove depth, web speed, permeability and curvature of idle roller on traction characteristics. Yang [8] studied the reduction of traction on magnetic tape during transmission and the correlation between lateral slip of magnetic tape and speed difference. Kasikci [9] investigated the contact mechanics between web and a circumferentially grooved cylindrical roller and described three distinct states of the interaction of the web with respect to the roller surface.

We don't find researches be involved in follow-up property of idle roller. In this paper, the follow-up time model of circumferentially grooved idle roller is established, and the effects of various parameters are analyzed.

## 2 Mathematical Model of Follow-up Time of the Circumferentially Grooved Roller

The model of the idle roller and the moving web is shown in Fig. 1. $v$ is the web velocity, $T$ is web tension at the roller enter side, $T + \Delta T$ is web tension at roller output side, $\omega(t)$ is the angular velocity and $\theta$ is the wrap angle. The rectangular cross section groove of roller is shown in Fig. 2. $w_g$ is groove width, $s_g$ is the cross-sectional area, $h_g$ is the groove depth and $L$ is the web width.
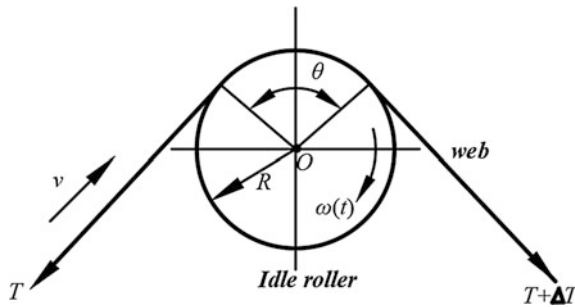


**Fig. 1.** The idle roller and the moving web

Idle roller torque balance equation:

$$J\dot{\omega}(t) = -\tau + RF \tag{1}$$

where $\tau$ is the bearing friction torque, $J$ is the moment of inertia of roller and $F$ is the traction force of the web for the roller.
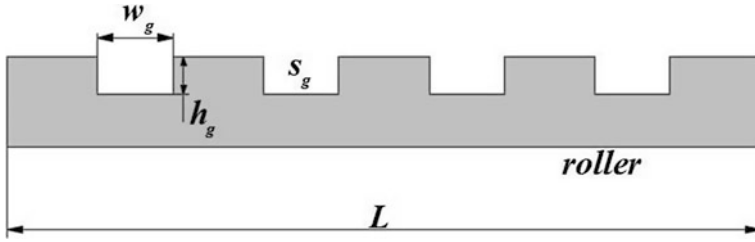
**Fig. 2.** The rectangular cross section of grooves

The roller circumferential velocity is defined as:

$$v_r(t) = \omega(t)R \tag{2}$$

There is no speed difference between web and roller, substituting Eq. (2) into Eq. (1) and integrating over the time $t$. The equation of the follow-up time $t$ is obtained:

$$t = \frac{vJ}{-\tau R + R^2 F} \tag{3}$$

The traction force equation of smooth roller (4) with the air entrainment is defined in reference [10]:

$$F = \left[ T - 3.094\eta(v_r + v)\left(\frac{R}{\alpha}\right)^{3/2} \right] \left(e^{\mu\theta} - 1\right) \tag{4}$$

where $\mu$, $\eta$, $v_r$ and $\alpha$ are the friction coefficient, the dynamic viscosity of air, the circumferential speed of the roller, and equivalent roughness respectively.

When roller is grooved, the air film thickness $h$ between the web and the circumferentially grooved roller is defined in reference [11]. Substituting $h$ for $\alpha$ into Eq. (4), the traction force equation of grooved roller is established.

$$h = 0.589R\left(\frac{6\eta U}{T}\right)^{\frac{2}{3}} - \frac{n_g s_g}{L} \tag{5}$$

where $n_g$ is the groove number, $s_g$ is the cross sectional area of the groove, $U$ is the sum of web velocity and roller surface velocity.

## 3    Idle Roller Follow-up Property Parameters

### 3.1    Bearing Load

The structure and mechanical structure of the idle roller are shown in Fig. 3.

The parameters of idle roller and web in Beiren FR-400 gravure printing machine are shown in Table 1.
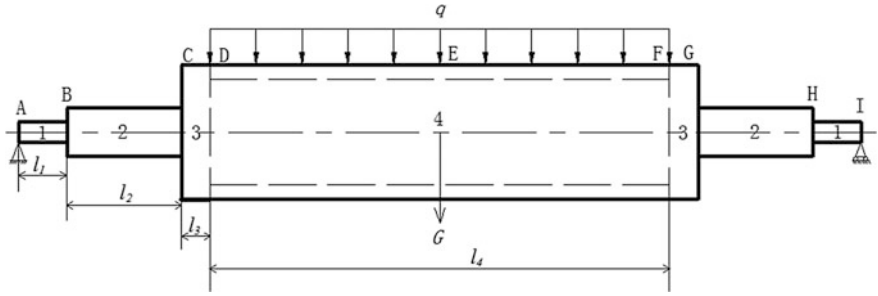
**Fig. 3.** Structure and mechanical structure of the idle roller

**Table 1.** The idle roller and web parameters

| Description | Value | Description | Value |
|---|---|---|---|
| Web Width $L$ (mm) | 1000 | Outer Diameter of Cylinder $d_4$ (mm) | 120 |
| Diameter of Journal $d_1$ (mm) | 21 | Inner Diameter of Cylinder $d_5$ (mm) | 111 |
| Length of Journal $l_1$ (mm) | 33 | Length of Cylinder $l_4$ (mm) | 1100 |
| Diameter of Shoulder $d_2$ (mm) | 40 | Density $\rho_1$ (kg/m³) | 7850 |
| Length of Shoulder $l_2$ (mm) | 160 | Density $\rho_2$ (kg/m³) | 7850 |
| Diameter of Plug $d_3$ (mm) | 120 | Density $\rho_3$ (kg/m³) | 2780 |
| Length of Plug $l_3$ (mm) | 60 | Density $\rho_4$ (kg/m³) | 2700 |

The pressure of the web acting on the idle roller is defined as follows:

$$q = 2TL \sin\frac{\theta}{2} \tag{6}$$

The bearing load can be obtained by the following formula:

$$P_1 = (q + G) \tag{7}$$

where $G$ is gravity of roller.

## 3.2 Bearing Friction Torque

The general calculation model of bearing friction torque is defined as follows [12]:

$$\tau = \tau_0 + \tau_1 \tag{8}$$

$$\tau_0 = 10^{-7} f_0 (\upsilon n)^{2/3} D_m^3 \tag{9}$$

$$\tau_1 = f_1 P_1 D_m \tag{10}$$

$$D_m = 0.05(d + D) \tag{11}$$

The coefficient of considering bearing structure and lubrication method $f_0$ is 0.05, which can be found in reference [13]. The $n$ is the bearing speed. The viscosity of the lubricant $v$ is 60 mm²/s. The inner diameter of the bearing $d$ is 15 mm, the outer diameter of the bearing $D$ is 35 mm, $D_m$ is the center pitch diameter of the bearing. The load factor $f_1$ is 1 by looking-up table in reference [14].

## 4    Discussions of Results

The effects of wrap angle and friction coefficient on follow-up time are shown in Fig. 4. The wrap angle is bigger, the follow-up time is smaller when wrap angle varies from $\pi/3$ to $\pi$, and the friction coefficient is bigger, the follow-up time is smaller when wrap angle is constant. The effects of equivalent roughness and web tension on follow-up time are shown in Fig. 5. The follow-up time reduces with the web tension increasing
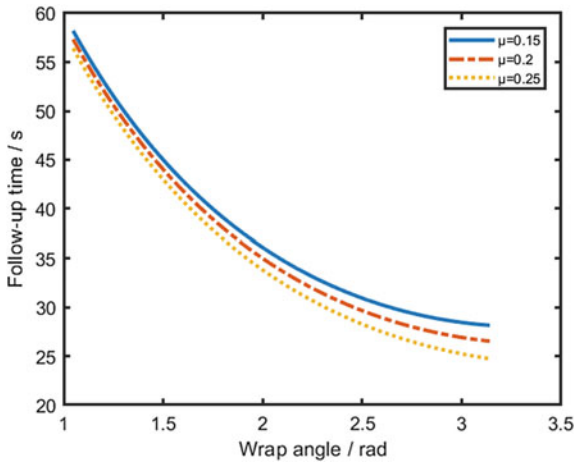


**Fig. 4.** Effects of wrap angle and friction coefficient on follow-up time

when the equivalent roughness varies from 5 to 25 μm. When web tension is constant, the follow-up time reduces with the equivalent roughness increasing.

A comparison between circumferential groove rollers with rectangular and triangular cross section is shown in Fig. 6. The roller with rectangular grooves has better follow-up property than triangular grooves. Therefore, the follow-up property of idle roller can be improved by selecting roller with larger surface roughness and increasing the web tension appropriately. The effects of groove depth and friction coefficient on
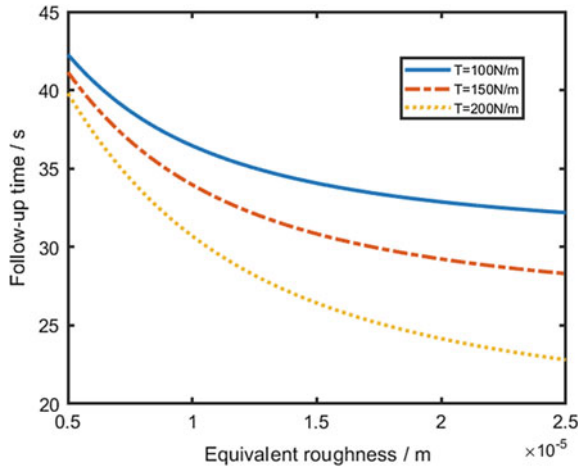
**Fig. 5.** Effects of equivalent roughness and web tension on follow-up time
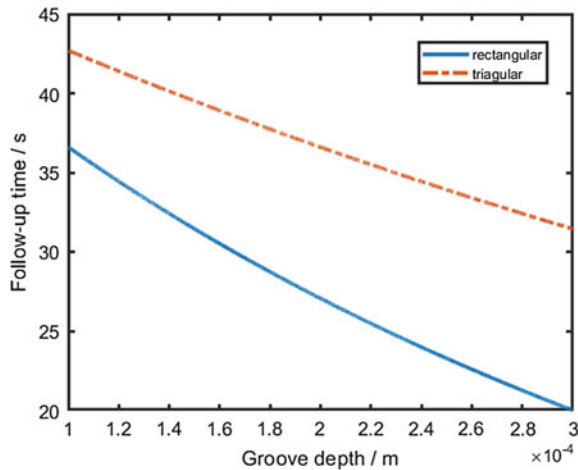


**Fig. 6.** Effects of groove depth and shape on follow-up time

follow-up time are shown in Fig. 7. It can be seen that the follow-up time can be significantly reduced by increasing the groove depth from 100 to 300 μm.

The effects of groove width and groove number on follow-up time are shown in Fig. 8. The follow-up time reduces with increasing the groove width from 100 to 550 μm. Similarly, the follow-up time obviously reduces with increasing the groove number from 200 to 400. As is shown in Fig. 9, the follow-up time increases as increasing the web width from 500 mm to 1000 mm. Therefore, the follow-up property of idle roller can be improved by increasing the groove depth, groove width, and groove number appropriately.
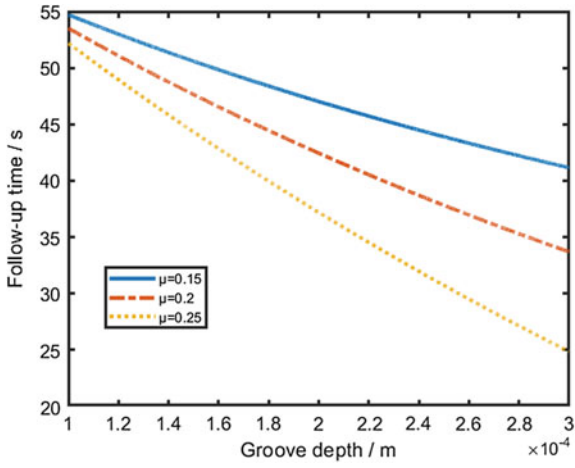
**Fig. 7.** Effects of groove depth and friction coefficient on follow-up time
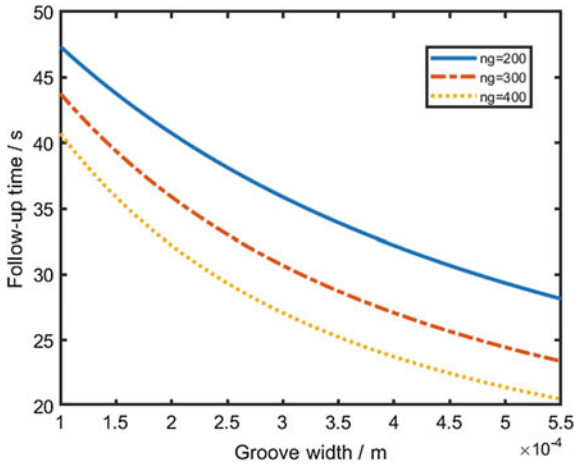


**Fig. 8.** Effects of groove width and groove number on follow-up time
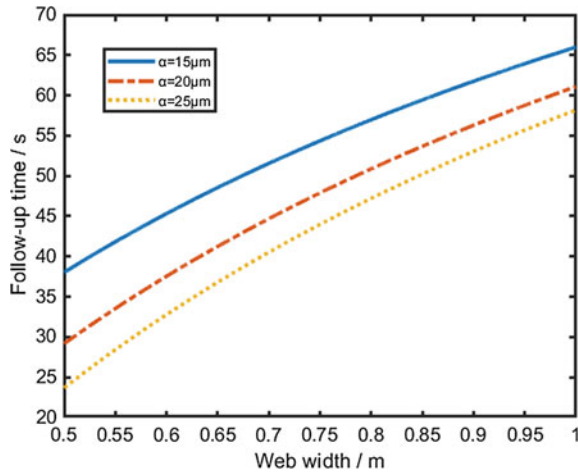
**Fig. 9.** Effects of web width and equivalent roughness on follow-up time

## 5    Conclusions

In this paper, the follow-up property of the circumferentially grooved roller is investigated. The follow-up time model of the circumferentially grooved roller is established and the influencing factors and varying rules of the follow-up time are analyzed. The results show that the follow-up property of the idle roller is better with the increasing of the wrap angle, the friction coefficient, the equivalent roughness and the web tension. Within a certain range, increasing the groove number, groove depth and groove width could improve the follow-up property of the roller. The follow-up time increases as the web width increasing. Therefore, the web transmission accuracy can be effectively improved by controlling the influence of the above parameters on the follow-up property of roller.

## References

1. Chen JK, Jin YW, Yin ZP (2019) Review of wound roll stress in roll-to-roll manufacturing of flexible electronics (in Chinese). Chin Sci Bull 64:555–565
2. Brake MR, Wickert JA (2010) Tilted guides with friction in web conveyance systems. Int J Solids Struct 47(21):2952–2957
3. Pagilla PR, Diao Y (2011) Resonant frequencies in web process lines due to idle roller s and spans. J Dyn Syst Meas Control Trans ASME 133(6):061018

4. Ma LE, Mei XS, Wu JM (2014) The modeling and simulation of the idle roller in web processing system. In: 2014 international conference on information science, electronics and electrical engineering, ISEEE, pp 1766–1769
5. Ma LE, Mei XS, Li YF (2014) Mechanical behaviors of guide roller in web transfer system. J Xi'an Jiaotong Univ 48(11):86–91
6. Müftü S, Jagodnik JJ (2004) Traction between a web and a smooth roller. J Tribol 126 (1):177–184
7. Mongkolwongrojn M, Jeenkour P (2013) Analysis of a flexible web on a grooved concave surface under soft EHL. Tribol Int 61:194–204
8. Yang HK, Engelen JBC, Pantazi A (2015) Mechanics of lateral positioning of a translating tape due to tilted rollers: theory and experiments. Int J Solids Struct 66:88–97
9. Kasikci T, Müftü S (2016) Wrap pressure between a flexible web and a circumferentially grooved cylindrical guide. Trans ASME 138(3):031101
10. Shao MY, Wu JM, Ma LE (2017) Traction characteristics of guide roller with the air entrainment. Lect Notes Electr Eng 417:759–766
11. Hikita S, Hashimoto H (2011) Improvement of slippage and wrinkling of transporting webs using micro-grooved rollers. Trans Jpn Soc Mech Eng Ser C 77(774):556–567
12. Zhu AH, Zhu CJ (2008) Analysis on calculation of friction torque of rolling bearings. Bearing 7:1–3
13. Qin DT, Xie LY (2011) Modern mechanical design handbook. Chemical Industry Press, Beijing
14. Yang KZ, Cheng GY, Li ZS (2006) Machine design foundation. Higher Education Press, Beijing

# The Motion Characteristics Analysis and Simulation of the Transverse Sealing Mechanism in a Pillow Bag Packaging Machine

Zhe Li, Guoping Yan[(✉)], Fei Zhong, and Qiancheng Wan

School of Mechanical Engineering, Hubei University of Technology,
Wuhan, China
iamygp@l63.com

**Abstract.** Aiming at the problem of realizing the high-speed continuous packaging of the pillow bag packaging machine, a double crank type transverse sealing mechanism was proposed, and its dynamic characteristics were analyzed. According to the technical requirements of the transverse sealing mechanism of the packaging machine, the driving law of the servo motor in the horizontal direction and the vertical direction were designed, and the driving speed and acceleration equations of the servo motor were obtained. The kinematics simulation of the transverse sealing device was carried out by using kinematics equations as some servo input in the dynamics software. The results show that it is a better way to accurately calculate the time of each phase of the transverse sealing mechanism during one cycle in order to meet the design requirements of the smooth and rapid operation, by means of obtaining the motion of the Z-direction which is determined the motion function of the X-direction of the transverse sealing mechanism. It can realize long-term stable high-speed continuous packaging. In view of the fact that the crank mechanism of the curve design can also be better applied to other transverse sealing mechanisms under the rush condition, the motion principle is worthy of promotion.

**Keywords:** Pillow bag packaging machine · Transverse sealing device · Motion characteristics · Dynamics simulation

## 1 Introduction

Transverse sealing is the key technology for the packaging in the pillow-shaped packaging machines, and its speed dominates the production efficiency of the entire packaging machine. Aiming at the problem of realizing the high-speed continuous packaging of the pillow bag packaging machine, Gong [1] designed a three-servo motor to drive the feeder conveyor, packaging film, and transverse sealing knife for improving the packaging quality and production efficiency. Liu [2] guaranteed the high-speed continuous packaging in the packaging machine through the eccentric sprocket mechanism. Masao Fukuda [3, 4] proposed a cross-sealing mechanism for the D-shaped trajectory, which could change the length of the straight portion according to the length of the packaged bag. Wang [5] mainly adopted the D-type inner cam

mechanism for designing a new type packaging machine, which could solve the problem of poor sealing in the thick film packaging. In this paper, a transverse sealing device in a pillow bag packaging machine is investigated. During the process of continuous transverse sealing, a transverse sealing device with servo motors which are driven double crank sliders was improved, compared to other mechanisms, the crank slider mechanism took up less space and had good stability. The horizontal sealing process was stable and could achieve better packaging quality. According to the control requirement. Finally, the working principle and motion characteristics were analyzed, and the simulation will be verified to provide some theoretical guidance for some similar mechanism design.

## 2    Working Principle and Motion Diagram of the Transverse Sealing Mechanism

The principle of the transverse sealing device [6] is shown in Fig. 1. The transverse sealing device has two direction movement in the X direction and the Z direction, respectively, motor 3 and 10 drive the crank slider to realize continuous sealing process.

Figure 1a shows a horizontal X-direction motion device diagram. The front transverse head 2 and the rear transverse head 1 are connected by two relatively moving crank sliders, and servo motor 3 drives the rotating shaft 4 through the synchronous pulley to realize reciprocating motion of the front and rear transverse heads in the X direction. The motion diagram is shown in Fig. 2a. Point A is the center point of the hinge. The rod BC is rotated around the point A by the servo motor. The rod BE is connected to the rear transverse head to reciprocate it in the horizontal direction. The rod CD surrounds the horizontal rod DF to cause the front cross head to reciprocate in the horizontal direction.

Figure 1b presents a vertical Z-direction motion device diagram. The servo motor 10 drives the crank 8 to move along Z direction, and the link 9 drives the overall movement in the X direction to realize continuous transverse packaging operation. The motion diagram is shown in Fig. 2b. Point O is the hinge center, the rod 1 is rotated around the point O by the servo motor, and the rod 2 is connected to the entire body 3 in the X direction so that body 3 makes a reciprocating motion in the vertical direction.

In order to achieve continuous transverse sealing, according to the principle of the X-direction and the Z-direction motion, a continuous transverse sealing step diagram is employed in a transverse sealing period t0 to t4 as shown in Fig. 3. Here, Fig. 3a indicates that the last transverse sealing has been completed at the time point of t0, and the transverse sealing head begins to escape outward, at the same time, the film bag starts to move downward in the Z-direction. Figure 3b indicates that the transverse sealing head is taken out of the film bag and kept at a certain distance from the film bag at the time point of t1, and the it is also ready to start the rapid movement. Figure 3c indicates that the transverse sealing head has completed the Z-direction rapid return movement at the time point of t2 and maintains the same distance with the film bag at the time point of t1 to be heat-sealed with the film bag. Figure 3d indicates that the film bag have been heat-sealed when the transverse seal head reaches the transverse sealing

position at time $t3$. Figure 3e indicates that the heat sealing and cutting of the film bag have been completed at the time point of $t4$, and working returns to the identical working state shown in Fig. 3a. Finally, a new working cycle will be performed as well. Therefore, the transverse sealing time is equal to $t4$ minus $t3$. In the Z direction, the transverse sealing head and the film bag are moved at the same speed and direction from (a) to (b) and from (c) to (e).
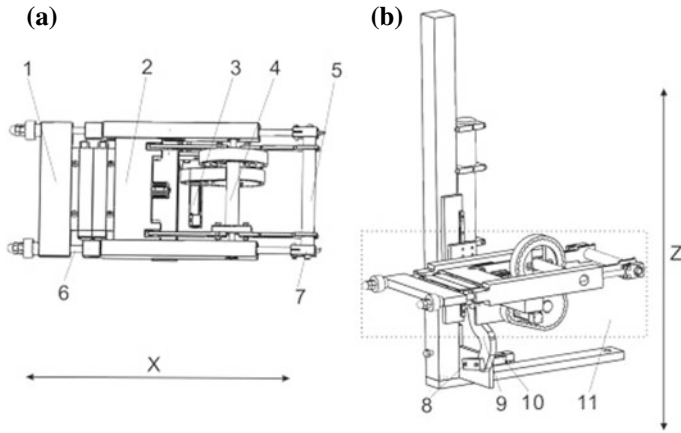


1-rear transverse sealing head; 2-front transverse sealing head; 3-X-direction servo motor;
4-turn shaft; 5--rotate rod; 6-rail rod 7-rear connection block; 8-Z-direction crank;
9-Z-Directional link; 10-Z-direction servo motor; 11-the whole X-direction

**Fig. 1.** Transverse device diagram



(a) X-directionmotiondiagram          (b) Y-directionmotiondiagram
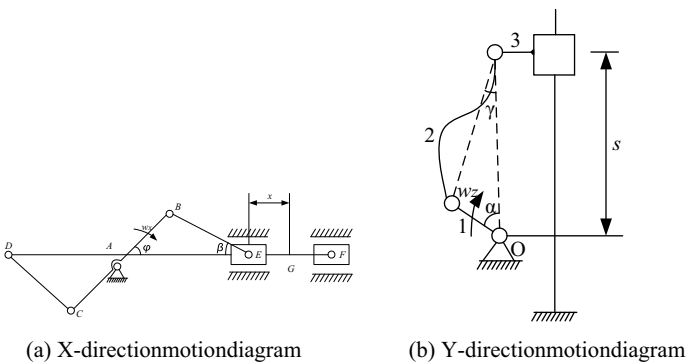
**Fig. 2.** Schematic diagram of the transverse sealing device
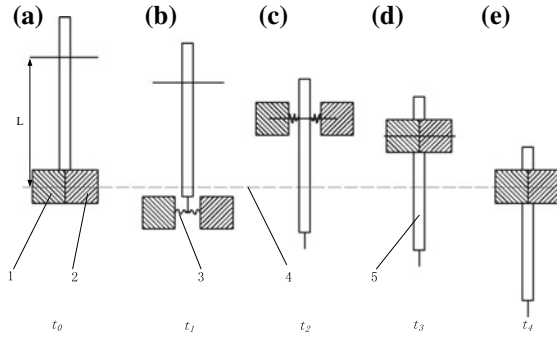
1 rear transverse sealing head; 2 front transverse sealing head; 3 heater;
4 transverse seal position; 5 film bag

**Fig. 3.** A periodic transverse sealing state diagram

## 3   Motion Analysis of Transverse Sealing Mechanism

As shown in Fig. 3, L represents the length of the bag of the finished package, and the film bag is vertically moved downward in the Z direction at a constant speed of $v_0$, so the time of one cycle is:

$$t_4 - t_0 = \frac{L}{v_0} \tag{1}$$

As shown in Fig. 2, The angle between the rod BA and the X direction is $\varphi$, the angle between the rod BE and the X direction is $\beta$, the length of the rod BA is $rx$, the length of the rod BE is $lx$. The displacement of the transverse sealing head moving distance is $x$. It is easy to know that the displacement equation is described as follows:

$$x = r_x(1 - \cos \phi) + l_x(1 - \cos \beta) \tag{2}$$

In case of no excessive impact during the operation of the servo motor, it would be thought that the speed and acceleration curves of the crank are smooth in the working cycle. According to the process requirements, the crank motion curve can be designed through the servo motor control. The cosine motion with the same magnitude and opposite direction at $t_0 - t_5$ and $(t_3 - t_0 + t_5)$ to $t_3$ can be satisfied the above requirements, so:

$$t_3 = t_2 + t_1 - t_0 \tag{3}$$

The initial angle of the crank is $\varphi_0$ at the time point of $t_0$, and the angle becomes $\varphi_1$ at the time point of $t_5$, it means that the X direction reaches the limit position at this moment. The equations of the angular velocity $w_x$ and the angular displacement $\Delta\varphi$ in the time period from $t_0$ to $t_5$ can be set as follows:

$$\omega_x = a\cos(\frac{2\pi t}{t_5 - t_0}) - b \tag{4}$$

$$\Delta\phi = \frac{a(t_5 - t_0)}{2\pi}\sin(\frac{2\pi t}{t_5 - t_0}) - bt \tag{5}$$

The temperature of the transverse sealing is too high when it is working, so it should be kept at the same speed as the film bag after the transverse sealing is completed. To prevent the film bag from heat deformation, the transverse sealing device should be kept a certain distance away from the film bag. The running distance of the transverse seal head may be set to $M_0$. During this period. The sealing position $M_0$, the equations for the movement angle $\varphi_2$ and the angular displacement $\Delta\varphi_2$ of rod AB are as follows respectively:

$$\phi_2 = \arccos\left[\frac{r_x^2 + (r_x + l_x - M_0)^2 - l_x^2}{2r(r_x + l_x - M_0)}\right] \tag{6}$$

$$\Delta\phi_2 = \frac{a(t_5 - t_0)}{2\pi}\sin(\frac{2\pi t_1}{t_5 - t_0}) - b(t_1 - t_0) \tag{7}$$

As shown in Fig. 2b, the angular velocity of the crank 1 controlled by the servo motor is $w_z$. the length of the crank 1 is $r_z$. the effective length of the rod 2 is $l_z$. and the speed of the slider 3 is $v_z$. In Fig. 3a, the angle between the crank 1 and the Z-direction is $\alpha_0$, and the angle between the rod 2 and the Z-direction is $\gamma_0$. According to the velocity projection method, $w_z$ can be obtained as follows:

$$w_z = \frac{v_z\cos\gamma}{r_z\sin(\alpha + \gamma)} \tag{8}$$

As shown in Fig. 2b, the distance between the center of the point $O$ and the body 3 is $s$, so its calculation equations in two intervals are as following:

$$s = \begin{cases} -v_0 t + \dfrac{l_z\sin(\alpha_0 + \gamma_0)}{\sin\alpha_0} & (t_0 \leq t \leq t_1) \\[3mm] -v_0(t + t_4 - t_0) + \dfrac{l_z\sin(\alpha_0 + \gamma_0)}{\sin\alpha_0} & (t_2 \leq t \leq t_4) \end{cases} \tag{9}$$

According to Eqs. (2–6) and Eqs. (2–7), the following equation for angular velocity $\omega_z$ can be obtained as follows:

$$w_z = \frac{v_0\left(s^2 + l_z^2 - {}_z^2\right)}{s\sqrt{4r_z^2 l_z^2 - \left(r_z^2 + l_z^2 - s^2\right)^2}} \quad (t_0 \leq t \leq t_1, t_2 \leq t \leq t_4) \tag{10}$$

According to Eqs. (2–8), the angular displacement equation of the crank in the process from Fig. 3b, c can be obtained by the fifth difference method [7].

## 4   Specific Study

Taking the pillow bag packaging machine as an example, the specific parameters are shown in Table 1 below.

**Table 1.** Parameters of pillow bag packaging machine

| Symbol | Parameter | Symbol | Parameter | Symbol | Parameter (mm) |
|--------|-----------|--------|-----------|--------|----------------|
| $v_0$ | 200 mm/s | $t_5$ | 0.2 s | $l_x$ | 200 |
| $L$ | 200 mm | $\varphi_0$ | 0° | $r_z$ | 80 |
| $M_0$ | 12.5 mm | $\varphi_1$ | 110° | $l_z$ | 260 |
| $t_0$ | 0 s | $\alpha_0$ | 80° | $r_x$ | 45 |

Based on the data in the Table 1, the motion analysis has been completed of the upper section transverse sealing mechanism. one cycle calculated time in this example is set to 1 s, the speed and acceleration curves of transverse sealing head are plotted in the X-direction at from 0 to 0.2 s as shown in Fig. 4a.



(a) X-direction velocity acceleration curve     (b) Z-direction velocity acceleration curve
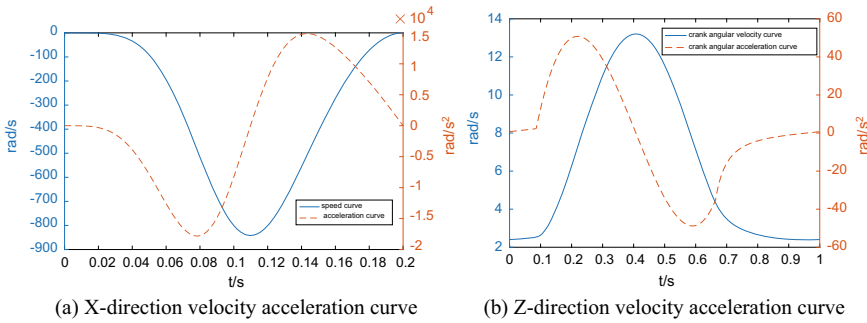
**Fig. 4.** The velocity acceleration image of the servo motor

The displacement equation in the process from Fig. 3b, c in the Z direction can be obtained by the fifth difference method as follows:

$$\theta = 196.37t^5 - 397.47t^4 + 254.53t^3 - 48.09t^2 + 6.11t + 1.30 \tag{8}$$

The angular velocity angular acceleration image of the Z-direction servo motor in one cycle are shown in Fig. 4b.

According to Figs. 4 and 5, the curve transitions smoothly, the maximum angular velocity of the servo motor for controlling the movement of the X-direction transverse sealing head is about 20 rad/s, and the maximum angular acceleration is about 300 rad/s$^2$. The maximum angular velocity of a servo motor for controlling the movement of the Z-direction transverse head is about 13 rad/s and the maximum

angular acceleration is about $50 \text{ rad/s}^2$. Compared with the rotary reciprocating transverse sealing mechanism [8], there is no significant difference in the demand for the servo system. Therefore, the transverse sealing mechanism is feasible in the servo and the feasible control angle can keep the mechanism work stably for a long time.

On the other hand, in order to verify the above mathematical model, one simulation by another dynamics software is performed as well. The cranks in the X and Z directions are set as the driving components, and the driven functions are implemented according to IF function mentioned in the reference [9].

The simulation time is set to 1 s and the number of steps is 500. As a result the X-direction and Z-direction velocity and acceleration curves of the transverse sealing head can be obtained, as shown in Fig. 5.
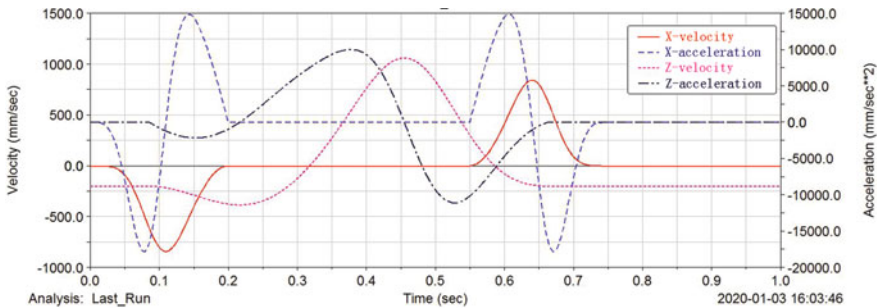


**Fig. 5.** X directions and Z directions speed and acceleration curves

Based on the above simulation results, the velocity and acceleration of the transverse sealing head are smooth in one cycle. Theoretically, the simulation results are highly consistent with the above mathematical model. As a result, the rotary reciprocating transverse seal mechanism basically meets the requirements of speed and acceleration during the transverse sealing. It indicates that it is a better way to apply the mathematical model and simulation method to analyze the transverse sealing mechanism.

## 5    Conclusions

(1) In the five processes involved in the transverse sealing mechanism, the curves transition from Fig. 3a, b and Fig. 3c–e, smoothly, and the curve transition from Fig. 3b, c is urgent, According to all the curves in the designed process, the design requirements can be better satisfied. In view of the fact that the crank mechanism designed by the curve can be better applied to other transverse sealing mechanisms under the urgent return condition, it is worth promoting.

(2) The improvement of the transverse sealing efficiency of the reciprocating transverse sealer depends on one good kinematics and smooth running state. X-directions and Z-directions parameters analysis will be a good way to deeply study the transverse sealing mechanism. On the other hand, it is very important to set well the time of each stroke for a better simulation. Combined with the characteristics of the process, the working time of each stage can be designed to significantly increase the efficiency of the horizontal seal and this will lay a certain theoretical foundation for the subsequent optimization of transverse sealing mechanism and high-speed stationary packaging.

# References

1. Gong F, Zhu X (2011) The design of three servo pillow packing machine control system based on PLC. J Hubei Univ Technol 51–53
2. Liu H, Zhang J, Li H, et al (2015) Improvement and simulation on transmission system and transverse sealing mechanism of automatic vertical packing machine. Food Mach 94–96
3. Masao Fukuda S (1994a) Apparatus for and method of transverse sealing for a form-fill-seal packaging machine: the United States, 5347795[P]
4. Masao Fukuda S (1994b) Transverse sealer for packaging machine: the United States, 5279098(l)
5. Wang A, Wang Q (2013) Automatic reciprocating transverse sealing packaging machine: Shan Dong, CN103010502A[P], 2013
6. Wan G (2018) Design and research of horizontal sealing device for high-speed vertical pillow bag packaging machine. Hubei University of Technology, 27–37
7. Sun Y (2015) Qnintic $G^2$ interpolating fair curves via curvature Variation Minimization. Zhejiang Gongshang University, 17–19
8. Duan N, Du W, Zhao H, et al (2014) Motion analysis of transverse sealing mechanism of pillow type packaging machine. Packag Eng 54–58
9. Jia C, Yin J, Xue W, et al (2008) MD ADAMS virtual prototype from entry to master. Mechanical Industry Press, Beijing, pp 95–105

# Numerical Simulation of Regenerative Thermal Oxidizer

Xulan Chen[1(✉)], Heping Hou[1], Shanhui Liu[1], and Qing Wen[2]

[1] Faculty of Printing Packaging Engineering and Digital Media Technology,
Xi'an University of Technology, Xi'an, China
15529565716@163.com
[2] North Automatic Control Technology Institute, China North Industries Group
Corporation, Taiyuan, China

**Abstract.** The emission of VOCs (Volatile Organic Compounds, VOCs) during packaging and printing production endangers human health and causes serious pollution to the environment. The regenerative thermal oxidizer is a widely used VOCs processing equipment. In order to fully grasp the law between its structural parameters and treatment effects, this paper numerically simulates the regenerative thermal oxidizer. Firstly, the working principle is analyzed, and the internal structure and 3D modeled are designed. Secondly, the simulation calculation of the regenerator is carried out, and the variation of temperature and pressure inside the regenerator is obtained. Thirdly, according to the simulation results and numerical analysis, the relationship between the pressure drop of the regenerator bed and the bed height, thermal efficiency and bed height under different mesh types is obtained. The results show that when the pore shape and flow rate are the same, the pressure drop is positively correlated with the bed height. The thermal efficiency increases with the increase of the bed height until the thermal efficiency reaches 100%. When the thermal efficiency meets the actual operation requirements, the bed height should be reduced as much as possible to improve equipment utilization.

**Keywords:** Thermal oxidizer regenerator bed · Performance study · Bed height · Pressure drop · Thermal efficiency

## 1 Introduction

Volatile organic compounds (VOCs) endanger human health and destroy the atmospheric ozone layer and form toxic photochemical smog, which is one of the important causes of haze weather [1–4]. At present, the effective management of VOCs has become a key factor restricting the development of the printing and packaging industry.

The VOCs treatment methods mainly include absorption and combustion. The adsorption has secondary pollution problems. The regenerative combustion method is widely used because of its high thermal efficiency, energy saving and environmental protection [5–8].

At present, in the design of regenerative thermal oxidizer, it is mainly to solve the shortcomings of low energy utilization and high cost. Therefore, it is of great

significance to study its key structural parameters and equipment performance. Researchers at home and abroad have focused on the performance of fillers such as thermal conductivity, wall thickness, and heat transfer and resistance properties of regenerators [9–12]. There are few studies on the effects between bed height and thermal efficiency. Based on this deficiency, this paper focuses on the influence of bed height on the pressure drop and thermal efficiency of the regenerator bed to improve equipment utilization efficiency and reduce costs.

## 2    Principle and Structure of Regenerative Thermal Oxidizer

Figure 1 depicts a schematic diagram of regenerative thermal oxidizer. Exhaust gas is preheated through the ceramic regenerator and then burning to purify gas, finally enters another ceramic regenerator and transfers the heat to it [13–15]. Figure 2 is a system model of a regenerative bed based on the principle of regenerative thermal oxidizer. We set up four kinds of regenerator with different pore densities in order to study the relationship between the pressure drop and bed height. The physical characteristics of the regenerator are shown in Table 1. The inner hole of ceramic honeycomb material is square, and Fig. 3 is a cross-sectional view of one of the ceramic honeycomb packing.
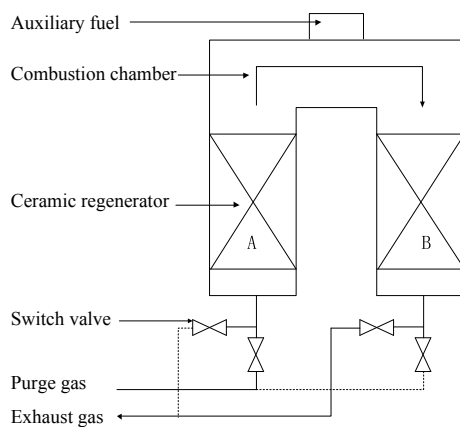


**Fig. 1.** Schematic diagram of regenerative thermal oxidizer

## 3    Regenerator Numerical Simulation

### 3.1    Establishment of Turbulence Model

The Reynolds number calculated by Formula (1) is 61613 > 2000, and the gas flow is in a turbulent state.
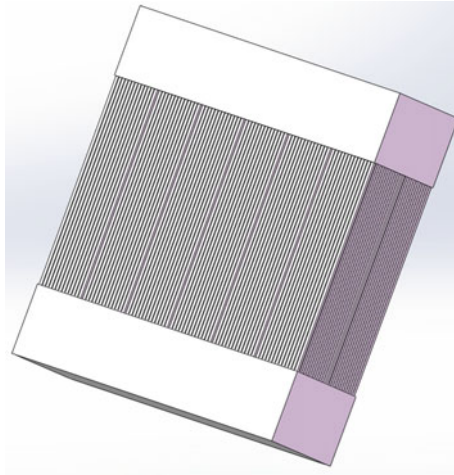
**Fig. 2.** Model diagram of regenerator bed

**Table 1.** Geometric characteristics of ceramic honeycomb fillers

| Channel hole (hole number) | Channel wide (mm) | Hole wall thickness (mm) | Specific surface area (m²/m³) | Porosity (%) |
|---|---|---|---|---|
| 13 × 13(169) | 9.2 | 2.0 | 278 | 64 |
| 20 × 20(400) | 6.4 | 1.0 | 455 | 73 |
| 25 × 25(625) | 4.9 | 0.9 | 540 | 67 |
| 32 × 32(1024) | 3.8 | 0.8 | 724 | 66 |
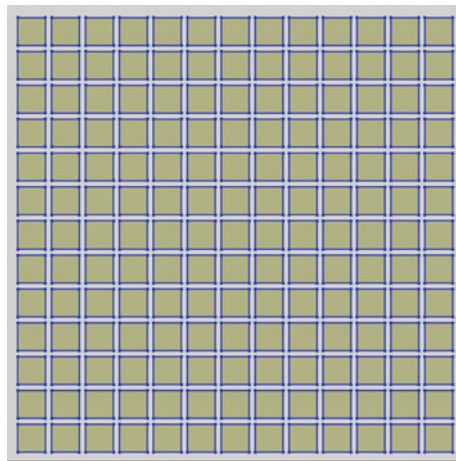


**Fig. 3.** Cross section of honeycomb packing

$$Re = \frac{\rho V L}{\mu} \tag{1}$$

In this formula, $\rho$ is the density of the fluid, the unit is kg/m$^3$. V is the average flow velocity of the fluid, the unit is m/s. L is the diameter of the round tube, if it is non-circular pipe, L is the equivalent diameter, the unit is m. $\mu$ is the fluid viscosity coefficient.

### 3.2    Boundary Condition Setting

Velocity_inlet, the velocity of the flow field at the inlet and the associated flow variable are used as the inlet boundary conditions. The velocity value is given and the inlet velocity is 3 m/s.

Pressure_outlet, the outlet type is pressure outlet, set to static pressure, and the outlet static pressure defaults to 101325 Pa.

## 4    Results and Discussion

### 4.1    Relationship Between Pressure Drop and Bed Height

The regenerative bed was numerically simulated, and the simulation results were post-processed. The pressure values were extracted from the inlet and outlet sections of the model. It can be seen from Fig. 4 that under the condition of certain pore shape, the pressure drop is positively correlated with the height of the bed. When the height of the bed is constant, the more the number of regenerator holes, the more obvious the pressure drop changes.
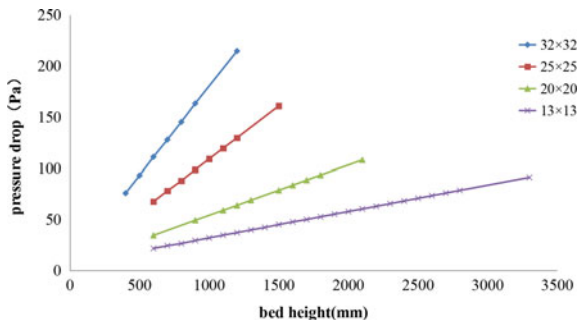


**Fig. 4.**  Relationship between pressure drop and bed height under different mesh types

### 4.2    Thermal Efficiency and Bed Height

The heat transfer simulation of the regenerator bed was carried out, and the simulation results were post-treated to obtain the average of the purge gas outlet temperature at different bed heights. Assuming that the gas mass flow of the inlet and outlet devices is

constant, the temperature efficiency is the thermal efficiency, the thermal efficiency of the regenerator bed is as shown in Eq. (2).

$$\eta_{RTO} = \frac{T - t_0}{T - t_i} \tag{2}$$

As shown in Fig. 5, the thermal efficiency of the regenerator bed increases with the increase of the bed height until it approaches 100%, because the increase of the bed height prolongs the residence time of the gas in the regenerator, and the gas energy and the solid energy is fully exchanged. The more the number of regenerator meshes, the higher the thermal efficiency. The reason is the larger the number of holes, the smaller the channel width of the holes, and the larger the specific surface area, the higher the thermal efficiency. When the holes are 32 × 32, 25 × 25, 20 × 20 and 13 × 13, and the corresponding bed heights are 600, 900, 1200 and 2500 mm, the thermal efficiency of the regenerative bed reaches 95%.
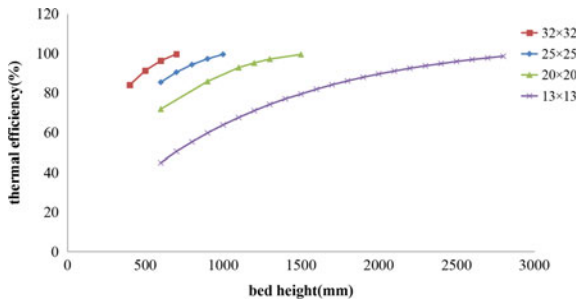


**Fig. 5.** Relationship between thermal efficiency of regenerator and bed height

## 5 Conclusions

In this paper, the regenerator of regenerative thermal oxidizer is taken as the research object, the influence of different pore types and different bed heights on the pressure drop and thermal efficiency is researched. The relationship between the pressure drop of the regenerative thermal oxidizer and the bed height, thermal efficiency and bed height is obtained. The conclusions are as follows.

(1) The pressure drop of the regenerator is positively correlated with the height of the bed. When the height of the bed is constant, the more the number of regenerator holes, the more obvious the pressure drop changes.
(2) The thermal efficiency of the regenerator bed increases with the height of the bed to nearly 100%. When the height of the bed is constant, the more the number of regenerator meshes, the higher the thermal efficiency.
(3) When the holes are 32 × 32, 25 × 25, 20 × 20 and 13 × 13, and the corresponding bed heights are 600, 900, 1200 and 2500 mm, the thermal efficiency of the regenerative bed reaches 95%.

These conclusions can provide important reference for different types of regenerator design. When the thermal efficiency meets the actual operation requirements, the bed height should be reduced as much as possible to improve the working efficiency and reduce VOCs pollution in the printing and packaging industry.

# References

1. Yang Y, Yang J, Yin SS, et al (2013) Speciated VOCs emission inventory and key species from printing industry in the pearl river delta region. Res Environ Sci
2. Farag MA, Paré PW (2002) C6-Green leaf volatiles trigger local and systemic VOCs emissions in tomato. Phytochemistry 61(5):545–554
3. Wang HL, Wang JH, Zhu CL et al (2014) Evaluation and selection of VOCs treatment technologies in packaging and printing industry. Environ Sci 35(7):2503–2507
4. Chen H, Zhang C, Cao G et al (2016) Development and research of integrated equipment for activated carbon adsorber + regenerative thermal oxidizer. Chem Ind 43(1):55–58
5. Oda T (2003) Non-thermal plasma processing for environmental protection decomposition of dilute VOCs in air. J Electrostat 57(3):293–311
6. Zuqiang Feng (2011) Regenerative high temperature air combustion technology. Liugang Sci Technol 4:62–62
7. Sugasawa M, Annadurai G, Futamura S (2005) Nonthermal plasma chemical processing of mixed VOCs. In: Fourtieth IAS meeting conference record of the industry applications conference
8. Liu H, Wen Z (2003) Regenerative high temperature air combustion technology. Metal World 6:10–12
9. Frigerio S (2007) Improve efficiency of thermal regenerators and VOCs abatement systems. Exp Thermal Fluid Sci 31(3):403–411
10. Carroni R, Griffin T, Mantzaras J, Reinke M (2003) High-pressure experiments and modeling of methane air catalytic combustion for power-generation applications. Catal Today 83(5):157–170
11. Baojie Yan (2011) Experimental study on resistance characteristics and heat transfer characteristics of honeycomb ceramic regenerator. Shandong University of Technology, Shandong, China
12. Xianglong Meng (2012) Study on heat transfer and resistance performance of ceramic regenerator. Wuhan University of Technology, Wuhan, China
13. Lu Z (2011) Purification technology of organic waste gas. Chem Ind Press 26(3):54–59
14. Choi BS, Yi J (2000) Simulation and optimization on the regenerative thermal oxidation of volatile organic compounds. Chem Eng J 76(2):103–114
15. Zhou HQ, Lan B, Chen B (2010) Numerical simulation of heat transfer in ceramic honeycomb of regenerative thermal oxidizer for ventilation air methane. Saf Coal Mines

# Study on Bubble Motion Characteristics Under the Effect of the Difference Stirring System

Luofan Liu, Hongwei Xu[✉], Weilai Li, and Wenhang Lu

College of Printing, Packaging and Digital Media, Xi'an University of
Technology, Xi'an, China
xuhongwei@xaut.edu.cn

**Abstract.** There are many small bubbles in the solvent-free compound adhesive, which directly affect the anti-stripping performance of the composite product. This paper studies the vacuum defoaming technology of solvent-free compound adhesive mixer. The gas-liquid two-phase flow theory and Fluent software were used to modeling and simulation of compound glue and bubble movement in the liquid holding tank under the stirring of the impeller. It was concluded that the bubbles under and near the impeller could not reach the liquid level. Then, a twin-screw belt stirring system is proposed and the same model is found and simulated. Simulation results show that each initial position of the bubble can reach the liquid level quickly under the effect of twin-screw belt stirring system. Finally, PIV experiments were made and the results verify the accuracy of simulation results.

**Keywords:** Solvent-free compound · Bubble motion characteristic · Gas-liquid two-phase flow · Simulation · PIV

## 1 Introduction

Solvent-free compound mixing machine is A and B material in a certain proportion of fully mixed, through the compound machine coating to the film surface. The bubbles in the mixed rubber reduce the quality of composite products and hinder the development of solvent-free composite technology. Among them, the method of stirring the liquid and vacuuming above the liquid surface is the best way to remove bubbles in the liquid with high viscosity [1, 2]. Xi'an university of technology has developed a solvent-free compound mixing machine with vacuum defoaming function, as shown in Fig. 1.

There are many studies on the flow characteristics of bubbles in liquid. Rabha et al. [3] used the VOF model to conduct numerical simulation on the movement of single bubbles in shear liquid, and obtained the influence relationship of lift force on the size, shape and movement of bubbles; Yamaguchi et al. [4] measured the motion path of a single small bubble in the rotating flow field with PIV technology, and proposed the empirical equation of period and amplitude of spiral motion, which indicate that PIV technology plays a good role in the experimental analysis of multiphase flow.

In this paper, the effects of vacuum defoaming system are simulated. And an optimization vacuum defoaming system will be improved.

**Fig. 1.** Solventless laminating machine with vacuum defoaming function

## 2    Impeller Agitator Simulation

### 2.1    Governing Equations

Continuity equation: for incompressible fluid, the density is constant, and the continuity equation is simplified as

$$\frac{\partial \rho}{\partial t} + \nabla \cdot (\rho u) = 0 \tag{1}$$

where $\rho$ is the density of liquid; u is the velocity vector.

Momentum equation: when considering the surface tension, the momentum equation can be expressed as

$$\frac{\partial (\rho v)}{\partial t} + \nabla(\rho v v) = -\nabla p + \mu\left(\nabla^2 v\right) + \rho f + F \tag{2}$$

where $\mu$, p, f and F are, respectively, the viscosity coefficient of liquid, pressure, unit mass force, the surface tension.

Function transport equation of VOF model [5]:

$$\frac{\partial C_q}{\partial t} + v \cdot \nabla\left(C_q\right) = 0 \tag{3}$$

where $C_q$ is the volume fraction of phase q; v is the $q$th phase velocity vector.

### 2.2    Original Impeller Modeling

The original impeller structure in the original vacuum defrosting system is found using fluent software, as shown in Fig. 2. The diameter of the feed cylinder is set at 90 mm, the height of the liquid is 70 mm, and the diameter of the impeller is 60 mm. The lower surface of the impeller is 20 mm from the bottom of the feed cylinder, and the blade size is 15 mm $\times$ 2 mm $\times$ 14 mm. The included radial Angle between the blade and the impeller is 45°.
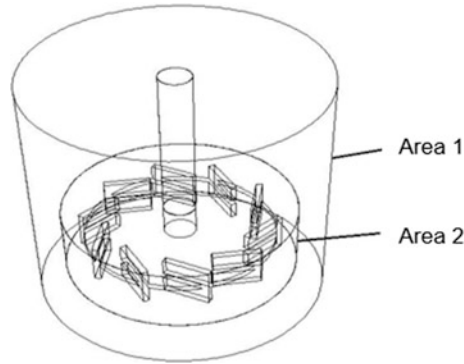
**Fig. 2.** Calculation domain of agitator in the liquid holding tank

In this study, WD8118A solvent-free composite adhesive was used as the analysis object. The initial position of a single bubble was set at (0, 0, 5), (0, 10, 5) for simulation, and the spatial position of the bubble was recorded at the same time interval. The result was drawn with Origin software, as shown in Fig. 3.
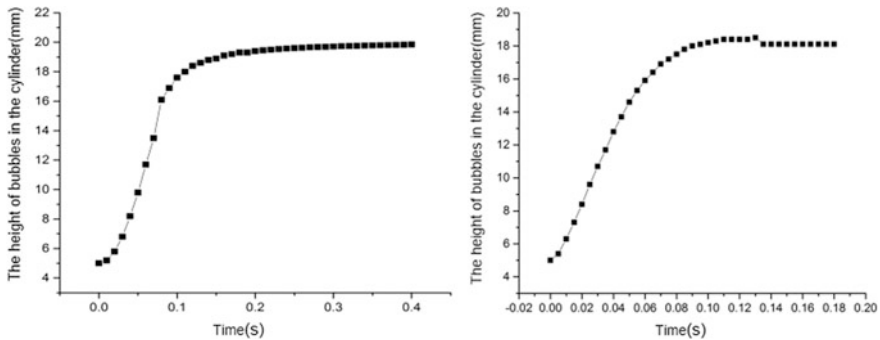


**Fig. 3.** The curve of bubble trajectory and height along the z-axis with time

As showed in Fig. 3, the height of bubbles does not increase after they rise near the bottom surface of the impeller. Through change the speed of the stirring impeller. The results are nearly same.

## 2.3 Twin-Screw Belt Structure Impeller Modeling

Through analysis and research, the impeller agitation was changed to twin screw belt type, as shown in Fig. 4. Set the diameter of the liquid holding tank to be 70 mm, the height to be 90 mm, the diameter of the screw belt to be 60 mm, the liquid level to be 65 mm, the pitch to be 60 mm, the width of the screw belt to be 7 mm, and the thickness to be 3 mm. Area 1 is the stationary domain and area 2 is the rotation domain, the rotating speed was 100 rpm.
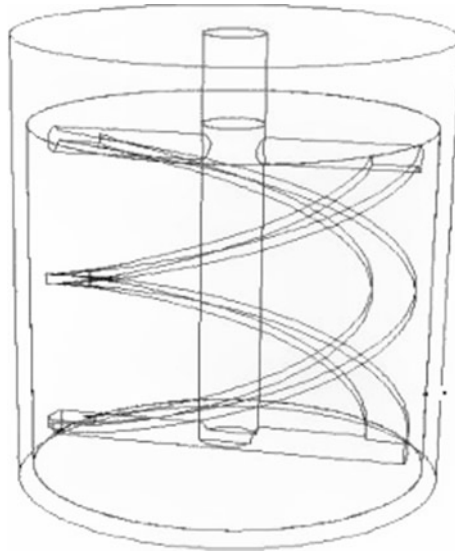
**Fig. 4.** Model of twin-screw belt type stirring system

The initial positions of a single bubble were set as (0, 7, 5), (15, 0, 3) respectively, and the simulation calculation was carried out. The processing results obtained the change curve of bubbles on the z-axis height.

As shown in Fig. 5, bubbles at different initial positions rapidly reach the liquid level under the agitation of the twin-screw belt structure, which proves that the twin-screw belt structure is conducive to the escape of bubbles in the glue.
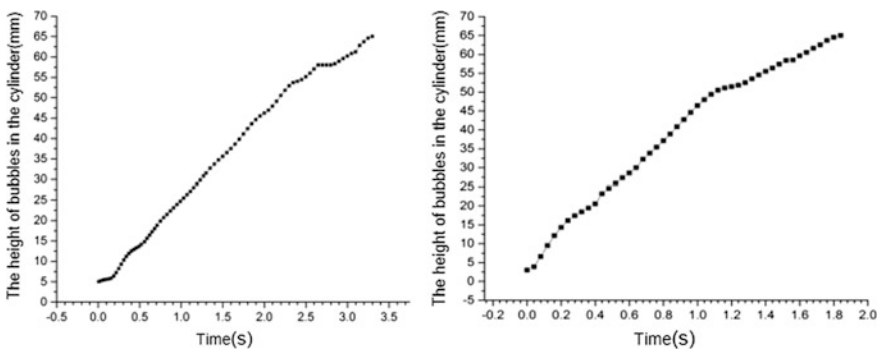


**Fig. 5.** Variation curve of bubble height along the z-axis with time

## 3   Experiment

In order to verify the effectiveness of the twin-screw belt structure, stirring systems with two structures and PIV imaging system were adopted to observe the bubble motion state, and the experimental platform was built as shown in Fig. 6.



**Fig. 6.**   Experimental device platform

The size of the impeller is about 2 times that of the simulation model, the size of the screw belt is about 3 times that of the simulation model, and the diameter of the cylinder is 200 mm. WD8118A solvent-free composite adhesive was used as the experimental object, bubbles are injected into the glue through a needle.

Similarly, the stirring experiment was conducted with the twin-screw belt structure, and the bubble motion curves at the initial position between the bottom of the cylinder wall and the screw belt, the bottom of the center, and the middle bottom of the cylinder were obtained, as shown in Fig. 7 successively.
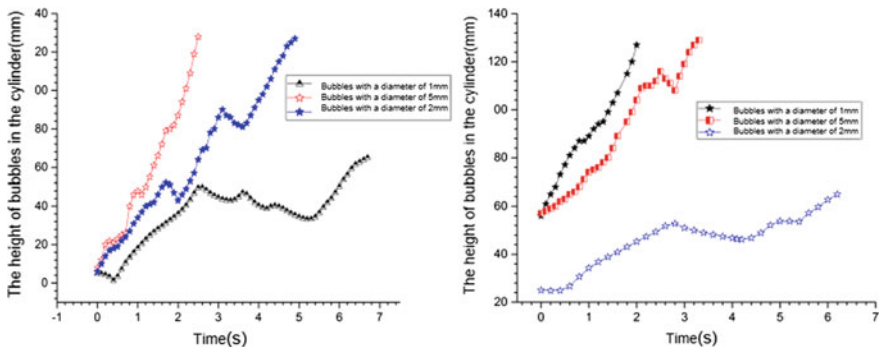


**Fig. 7.**   Height change curve of bubbles in the z-axis direction

The results show that three kinds of bubbles at different initial positions rise procession. All of this bubbles can eventually reach the top of the liquid surface under the effect of the twin-screw belt impeller.

## 4    Conclusions

The simulation results show that the bubbles in the impeller stirring system cannot reach the liquid level, while the bubbles in the twin-screw stirring system can reach the liquid level. The results of PIV experiment are basically consistent with the simulation data. The results of this study be used as the theoretical basis for the design of vacuum defoaming system of solvent-free compound mixer.

## References

1. Xu H, Wang X, Lei R, et al (2016) Experimental analysis of the effect of vacuum degassing technology on the solventless laminating adhesive performance. In: Lecture notes in electrical engineering—China Academic conference on printing & packaging and media technology. Springer, Singapore, pp 1123–1129
2. Spaulding M (2010) Solventless laminating adhesive runs cooler, cures rapidly. Convert Mag 28(4)
3. Rabha SS, Buwa VV (2010) Volume-of-fluid (VOF) simulations of rise of single/multiple bubbles in sheared liquids. Chem Eng Sci 65(1):527–537
4. Yamaguchi T, Iguchi M, Uemura T (2004) Behavior of a small single bubble rising in a rotating flow field. Exp Mech 44(5):533–540
5. Hirt CW, Nichols BD (1981) Volume of fluid (VOF) method for the dynamics of free boundaries. J Comput Phys 39(1):201–225

# A Review of FDM Nozzle System for Additional Materials Manufacturing Technology

Yanzhi Wu[1(✉)], Heping Hou[1], Shanhui Liu[1], and Qing Wen[2]

[1] Faculty of Printing Packaging Engineering and Digital Media Technology, Xi'an University of Technology, Xi'an, China
l6ll762578@qq.com

[2] North Automatic Control Technology Institute, China North Industries Group Corporation, Taiyuan, China

**Abstract.** Compared with the traditional material reduction manufacturing, additive manufacturing technology is a great change, which brings new opportunities for the production models. Fused Deposition Molding (FDM) equipment is one of the most widely used to additive manufacturing equipment. The nozzle system is the core component of FDM technology. Its performance directly affects the product forming accuracy and efficiency. Therefore, taking FDM nozzle system as the research object, this paper reviews the research process and development trends of the nozzle system at home and abroad in recent years from the aspects of its flow channel structure, heat sink, heating device and nozzle, points out the hotspots and challenges of nozzle system research, which provides important reference for the optimization design of nozzle system.

**Keywords:** Additive manufacturing technology · Fused deposition molding (FDM) · Nozzle system

## 1 Introduction

Additive manufacturing technology has great potential for development, it is to gradually form a complete product through the accumulation of layers of materials. At present, Fused Deposition Modeling (FDM) is one of the fastest developing manufacturing technologies. FDM technology in the superposition molding process, mainly relies on the computer control nozzle system to carry on the work. At present, FDM nozzle system has two working forms, namely screw type and plunger type. For the plunger type FDM nozzle system, it is mainly divided into three areas in the working process: (1) Filament feed zone; (2) fuse area; (3) additive zone. As show in Fig. 1. To sum up, the plunger type FDM nozzle system is one of the key components to realize rapid prototyping of products. However, During the printing process, it is easy to appear that the material blocks the nozzle and the printing precision is low. In this paper, the research status and progress of nozzle system including flow channel

structure, cooling device, heating device and nozzle structure at home and abroad are reviewed, and the challenges and future development trend of melt deposition molding technology in the present era are revealed.
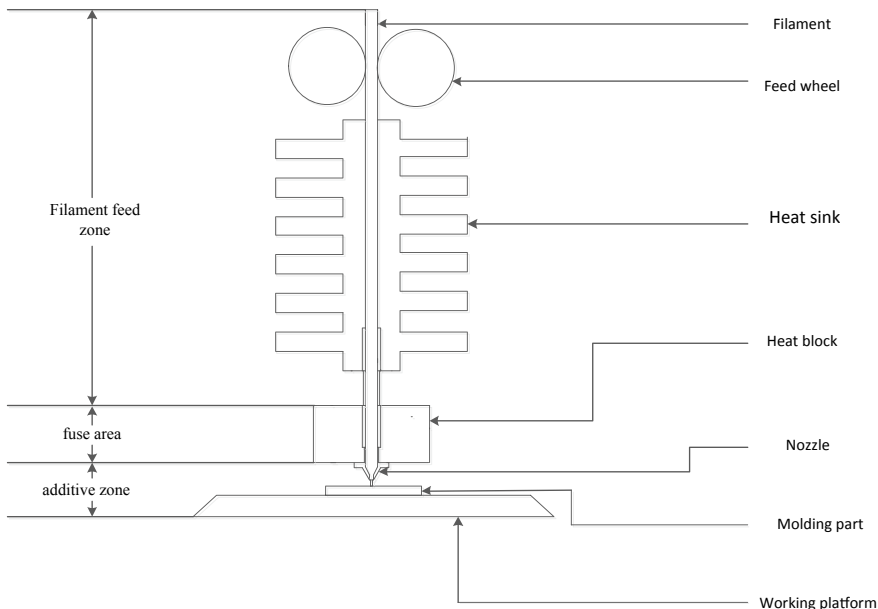


**Fig. 1.** Schematic diagram of plunger type FDM

# 2   Research Status at Home and Abroad

## 2.1   Advances in FDM Channel Research

Sukindar's [1] team used finite element software to analyze the pressure drop distribution of PMMA materials at tapered angles in different contraction sections. Sonsalla et al. [2] found that nozzle diameter would affect the printing accuracy of products. Patanwala et al. [3] discussed the effect of nozzle diameter on print flow. Ding et al. [4] studied the influence of inlet pressure, tapered Angle of contraction section of flow passage, length of molding section and diameter of nozzle on extrusion speed for energy-containing materials. Gao [5] points out that the convergence Angle, the radius of the transition arc, the length of the rectifier section and their interaction are important factors affecting the stability of the silk outlet velocity. Min [6] proposed to lengthen the most front end of the flow passage to increase the adhesive force of the melt on the inner wall by increasing the area of the inner wall, so as to prevent the printing material from dropping downward under the extrusion pressure when it stops printing. Han et al. [7] studied the flow situation of mixed color melt in Y-shaped flow passage, and the results showed that the melt had complex flow behavior in the flow passage and was prone to block at the intersection of the flow passage. As you can see, many scholars by

using simulation method analysis flow's influence on the melt flow behavior, guarantee the stability of the melt flow in the passage.

## 2.2    Research Progress of FDM Cooling Device

Wang et al. [8] sed fin-type heat dissipation mechanism for cooling treatment, assisted by fan to increase the flow rate, so that the temperature can be reduced to make the melted material solidified in reverse flow. Wang [9] on the basis of heat transfer analysis, combined with orthogonal test method, optimizes the height, spacing and thickness of the radiator, and reduces the space size of the radiator on the premise of guaranteeing its heat dissipation performance. Zhu et al. [10] designed a new cooling device to replace the radiator structure, which effectively solved the problem of softening printing materials ahead of time. Jin [11] Aiming at the problem of stack dislocation and collapse caused by poor heat dissipation of radiators in printing process, a power-adjustable semiconductor refrigeration system was designed and developed. According to the above research findings, the optimization and improvement of the cooling device can improve the cooling efficiency of heat sink to a certain extent, and preliminarily meet people's demand for the molding quality of printed products.

## 2.3    Research Progress of FDM Heating Device

Wang [12] analyzed the relationship between the temperature of the heating block and each physical field through ANSYS software simulation, which provided guidance for the improvement of subsequent equipment. Wang et al. [13] pointed out through simulation analysis that increasing the contact area between the heating rod and the heating block and reducing the volume of the heating block are conducive to improving the melt temperature and reducing the time for printing preparation. Sukindar [14] transformed the square structure design of the heating block into a cylindrical one, and then installed a high thermal insulation material on the heating block to maintain the heating temperature and reduce the temperature loss rate. It is found that scholars have achieved satisfactory results in the research of heating device, which greatly improved the molding quality of the molding products.

## 2.4    Research Progress of FDM Nozzle Structure

Wu et al. [15] proposed to add a heating hole and a temperature sensor at the nozzle, which could strictly control the temperature at the nozzle and enable the nozzle to output materials stably in the printing process. Jia [16] simulated analysis found that the sudden drop of temperature would cause the problem of nozzle blockage. Hu et al. [17] made multi-physical field coupling analysis of thermal field and stress field against different nozzle materials, providing references for their subsequent development and optimization of FDM nozzle. Liu [18] proposed to adopt the integrated nozzle and change the nozzle material from aluminum bronze to beryllium bronze, which could reduce the possibility of melt blocking the nozzle. Researchers of Xi'an Jiaotong university [19] carried out finite element simulation analysis and experimental verification of external nozzle and integrated nozzle respectively, and the results showed that

the integrated nozzle was better than external nozzle and could spin filament smoothly. Kłodowski [20] designed and developed an effective nozzle assembly method, which solved the problem of melt leakage. To sum up, the researchers' work solved the problems of melt blocking nozzle and melt leakage to some extent, and improved the molding precision of printing equipment.

## 3    Challenges of Nozzle System in the Future

However, with the rapid development of material technology, product design, manufacturing mode, computer theory and other technologies, it is necessary to dig deeply into the FDM technology's structure, technology and methods. Therefore, the existing nozzle system is facing new challenges.

(1) With the increasing automation of FDM devices, the relationship between their physical fields will become more complex. If the single physical field analysis is still carried out, the thinking of two-way analysis is lacking, and the effect of multiple physical field coupling is ignored, then the manufacturing accuracy of FDM technology will be far less than that of traditional machining methods.

(2) The equipment is less intelligent. In the era of high-speed operation, failure to solve the problem in time will reduce the production efficiency and directly damage the economic benefits of enterprises.

(3) In the current era, the rapid development of material technology and the increasing types of materials used by human beings force the FMD nozzle system to develop towards the direction of high precision and strong generalization ability.

(4) If the nozzle system wants to obtain high-precision products in the printing process, then it needs to reduce the printing speed. The molding precision is inversely proportional to the printing speed, which limits the development of FDM equipment. Therefore, it is a big challenge to optimize nozzle system to maximize these two parameters.

## 4    Potential Direction and Development Trend

(1) Diversified analytical thinking. We should consider not only the process of steady flow of melt, but also the change of transient flow behavior of melt. Only by combining qualitative and quantitative analysis, can we accurately control the flow behavior of melt.

(2) Intelligent printing process. The sensor can be used to monitor its working state in real time and establish a feedback control system. When a fault occurs in the working process, the problem can be compensated and corrected in time by information perception and analysis, autonomous decision-making and optimization.

(3) Visualization of printing process. In order to realize visual printing in the future, we need to study the materials of nozzle system vigorously, so that the materials have

the advantages of strong transparency, good sealing, high temperature resistance, wear resistance and impact resistance.

(4) Individualized operation mode. Direct to product manufacturing, through remote operation, you can control the sprinkler system to print products and realize personalized operation mode.

## 5  Conclusions

This paper expounds the characteristics and working principle of FDM technology, points out that the nozzle system is the core of FDM printing technology, and reveals the existing problems and challenges of the nozzle system.

It is considered that the future nozzle system should be deeply studied from the aspects of diversification of analytical thinking, intellectualization of printing process, visualization and individualization of operation mode, which is conducive to the improvement of the overall level of FDM nozzle system technology.

## References

1. Sukindar NA, Ariffin MKAM, Baharudin BTHT et al (2018) Effects of nozzle die angle on extruding polymethylmethacrylate in open-source 3D printing. J Comput Theor Nanosci 15 (2):663–665
2. Sonsalla T, Moore AL et al (2018) 3-D printer settings effect on the thermal conductivity of acrylonitrile butadiene styrene (ABS). Polym Test 70:389–395
3. Patanwala HS, Hong D, Vora SR et al (2018) The microstructure and mechanical properties of 3D printed carbon nanotube-polylactic acid composites. Polym Compos 39(S2):E1060–E1071
4. Ding XY, Li X, Lu XY et al (2018) Effect of nozzle parameters on extrusion speed of energetic material 3D printer. Mech Des Manuf 328(6):81–84
5. Gao Q, Zhou M, Zhu LL, et al (2018) Flow field analysis and structure optimization of the nozzle of FDM 3D printer. Comb Mach Tool Autom Process Technol 537(11):39–42+52
6. Min C, Li J, Shen XM et al (2017) Optimum design of fdm type 3D printer nozzle. Heilongjiang Sci 21:10–12
7. Han S, Xiao Y, Qi T, et al (2017) Design and analysis of fused deposition modeling 3D printer nozzle for color mixing. Adv Mater Sci Eng 2017(Article ID 2095137):12
8. Wang ZL, Zhang Y, Ren Y, et al (2018) Mprovement of heat dissipator in FDM process. Mech Des Manuf 332(10):89–91+95
9. Wang TF (2015) Thermal analysis and optimization design of radiator structure for 3D printing equipment. Guangxi University of Science and Technology, Guangxi, p 2015
10. Zhu LL, Zhou M, Gao Q et al (2018) Temperature field analysis and structure optimization of FDM_3D printer nozzle. Comb Mach Tool Autom Mach Technol 8:18–22

11. Jin YF, Wan Y, Zhang B et al (2016) Semiconductor refrigeration temperature control design and experimental study of FDM 3D printer. Mech Electr Eng 33(2):165–168

12. Wang Y (2017) Process analysis of FDM at different nozzle temperatures based on ANSYS simulation. Mod Manuf Technol Equip

13. Wang SB (2016) CFD analysis of FDM extrusion head and optimum design of mixed colour extrusion head. Harbin University of Technology, Harbin

14. Sukindar NA, Mohd Ariffin MKA, Bin Baharudin BTHT et al (2016) Comparison on dimensional accuracy using a newly developed nozzle for open-source 3D printer. Appl Mech Mater 859:15–19

15. Wu MX (2010) Rheological behavior analysis and screw optimum design of micro-extrusion melt. South China University of Technology, Guangzhou

16. Jia YZ, Liao DM, Chen T et al (2017) Fluent-based simulation analysis of melt heat flow in 3D printing ABS. Plastics 1:61–64

17. Hu B, Hu WL, Shi CC et al (2016) Thermal-stress simulation analysis of high temperature FDM nozzle based on multi-physical field coupling. J Nanchang Inst Eng 35(4):71–73

18. Liu XJ, Wang CS, Chi BH (2017) Optimum design of heat transfer structure for grained 3D printer head wood. Plastics 4:113–116

19. Wang YQ, Fang Y, Le G et al (2009) Finite element aided design of fused deposition rapid prototyping nozzle. Aeronaut Precis Manuf Technol 45(3):32–36

20. Kłodowski A, Harri E, Scott S (2015) Leakage-proof nozzle design for RepRap community 3D printer. Robotica 33(4):26

# Tooth Profile Optimization for Mixing Proportional Pump of Solvent-Free Laminating Mixer

Yihan Wei, Hongwei Xu[✉], Yu Han, and Shaoyuan Feng

College of Printing, Packaging and Digital Media,
Xi'an University of Technology, Xi'an, China
xuhongwei@xaut.edu.cn

**Abstract.** The accuracy and uniformity of mixing ratio directly affect the quality of solvent-free laminating products. In this paper, the gear pump as a proportional metering in the solvent-free laminating mixer is modeled and analyzed. The flow pulsation generated by the gear pump during the working process is studied. By establishing the formula of instantaneous flow at the outlet of the arc gear pump, the factors which affect the flow pulsation of arc gear pump are studied. An optimization model of the tooth profile parameters of the arc gear pump is constructed whose goal is to minimize the flow pulsation coefficient. Through the simulation, the results show that the optimized tooth profile parameter of arc gear pump can guarantee a more stability flow quantity. Finally, an arc gear pump flow experiment platform is found, and the experiment results verify the advantages of the optimized result.

**Keywords:** Solvent-free laminating · Gear pump · Flow pulsation · Tooth profile optimization

## 1 Introduction

Solvent-free laminating technology is widely used in flexible packaging industry for its unique advantages such as economy, safety and environmental protection. Solvent-free laminating mixing machine is the key equipment in the solvent-free laminating process. Solvent-free laminating mixing machine's role is to mix A and B two kinds of materials in certain proportion evenly. In Solvent-free laminating mixing machine, the mixing proportion pump is the core component, which generally composed of gear pump. The mixing proportional system consist two gear pumps. The gear pump outlet will produce a certain flow pulsation during the mixing process, which will directly lead to incorrect mixing ratio, thus affecting the quality of the solvent-free laminating products [1, 2]. Because gear pump is widely used in chemistry industry, a large number of scholars have studied its transmission performance. Chen et al. [3] proposed the envelope method to realize the design of spiral arc gear pump tooth profile; Liu et al. [4] proposed the laminating tooth profile with double arc gear pump arc and transition line; Huang et al. [5] adopts the fuzzy optimization method to optimize the geometric parameters of the helical gear pump.

In this paper, the gear proportional pump used in the newly developed solvent-free laminating mixer is taken as the research object. In order to reduce the mixing radio error of the two-component in the mixing process and improve the quality of the solvent-free laminating product.

## 2   Mathematical Model Analysis of Flow Calculation for Double Arc Gear Pump

### 2.1   Calculation Model of Instantaneous Flow Quantity of Double Arc Gear Pump

A pair of arc gears mesh is checked as shown as Fig. 1.
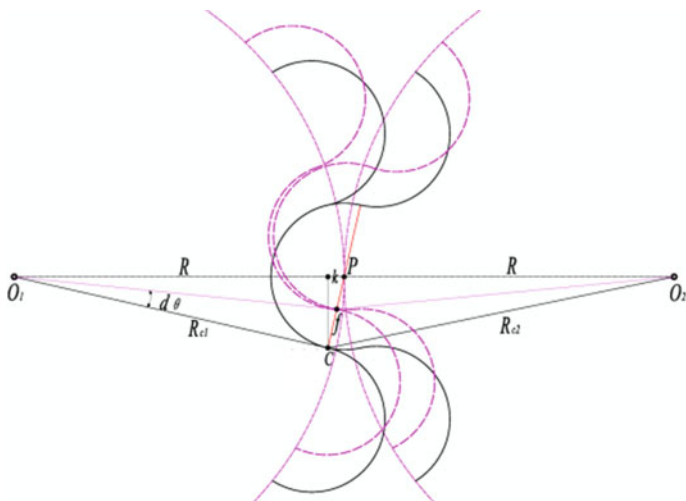


**Fig. 1.** Geometry of the meshing area

In Fig. 1, the gear center of the drive wheel I is $O_1$, and the gear center of the driven wheel II is $O_2$, and two gears form a sealed drain chamber at the initial meshing point $B_1$. After the β' angle is turned, the position of the meshing point forming the sealed drain chamber jump from $B_1$ to $B_2$. The end meshing line is a straight line passing through the node P, and f is the distance from the meshing point C to the node P.

The distance from meshing point C to node P is

$$f = \left| r - R\cos a \cdot \left( \theta - \frac{(n-1)\pi}{z} \right) \right|; \ \theta \in \left( \frac{(n-1)\pi}{z}, \frac{n\pi}{z} \right], \ n \in 1, 2, 3 \dots \quad (1)$$

where r is the radius of the tooth root, R is the radius of gear indexing circle. Take the derivative of S,

$$\frac{ds}{dt} = \left[ R^2 \cos^2 a \cdot \left( \theta - \frac{(n-1)\pi}{z} \right)^2 - 2Rr \cos a \cdot \left( \theta - \frac{(n-1)\pi}{z} \right) + R^2 + r^2 - R_f^2 \right] \frac{d\theta}{dt}$$

$$(2)$$

Then the formula of instantaneous flow quantity in gear pump sealed drain chamber is,

$$Q_S = \omega \left[ \frac{m^2 z^2}{4} \cos^2 a \cdot \left( \theta - \frac{(n-1)\pi}{z} \right)^2 - \frac{\pi m^2 z}{4} \cos^2 a \cdot \left( \theta - \frac{(n-1)\pi}{z} \right) + \frac{\pi m^2 z}{4} \cos a \right]$$

$$\theta \in \left[ \frac{(n-1]\pi}{z}, \frac{n\pi}{z} \right], \, n \in 1, 2, 3 \ldots \tag{3}$$

where m is module of rack, z is number of teeth of arc gear.

## 2.2 Analysis of Factors Affecting Flow Pulsation of Double Arc Gear Pumps

During the gear mesh process, the range of instantaneous flow pulsation is

$$\Delta Q_S = \max(Q_S) - \min(Q_S) \tag{4}$$

where $\max(Q_S)$ is the maximum value of the instantaneous flow quantity of the gear pump; $\min(Q_S)$ is the minimum value of the instantaneous flow quantity of the gear pump.

According to formulae (3) and (4) can be changed to,

$$\Delta Q_S = \frac{\omega \pi^2 m^2 \cos^2 a}{16} \tag{5}$$

The total liquid flow discharged by arc gear pump under a certain angular velocity rotating in a period is

$$Q_T = \int_{\frac{(n-1)\pi}{z}}^{\frac{n\pi}{z}} Q_S d\theta \tag{6}$$

The average flow quantity of gear pump is

$$\overline{Q} = \frac{Q_T}{\beta'} \tag{7}$$

The flow pulsation coefficient of arc gear is

$$\Delta Q = \frac{3\pi \cos \alpha}{12z - 2\pi \cos \alpha} \tag{8}$$

## 3   Tooth Profile Optimization Design of Double Arc Gear Pump

The optimization model is

$$\min \Delta Q(X) = \frac{3\pi \cos x_3}{12x_2 - 2\pi \cos x_3}; \, X \in D \tag{9}$$

D: $g_3(X) = 6 - x_2 \leq 0$;    $g_4(X) = x_2 - 12 \leq 0$;    $g_5(X) = 14.5° - x_3 \leq 0$; $g_6(X) = x_3 - 32.5° \leq 0$.

The points on each curve in the curve domain have equal objective function values, which constitute the objective function contour, the contour line equation is

$$\frac{3\pi \cos x_3}{12x_2 - 2\pi \cos x_3} = C_i \tag{10}$$

According to the optimization results, When the number of teeth of arc gear pump is 12, pressure angle is 32.5°, it will not only meet the requirements of arc gear meshing efficiency, but also can make the gear pump flow pulsation reach the optimal. At this point, the modulus of arc gear should meet 1.94 mm $\leq$ m $\leq$ 50 mm, to ensure the tooth root bending strength and easy processing.

## 4   Experimental

A experiment platform is found as shown as Fig. 2.
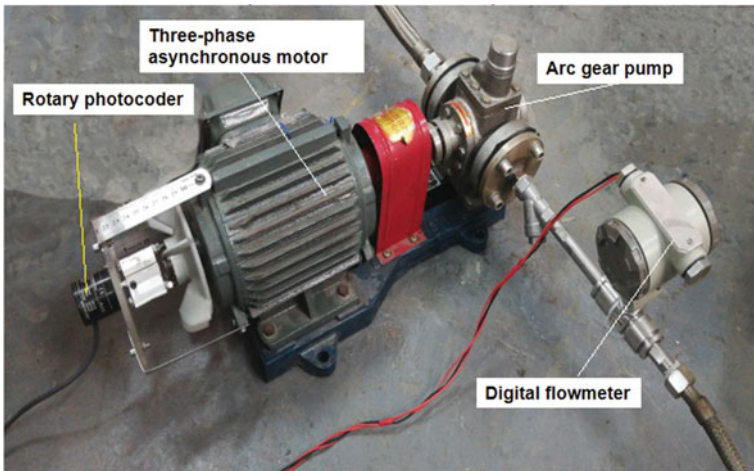


**Fig. 2.**  Experimental platform

The experimental platform includes a certain type of double arc gear pump, a digital flow-meter and a rotary photoelectric encoder. The upper computer software is used to collect and process flow data.

In order to monitor the output flow of gear pump at 300 rpm, the output frequency of the frequency converter was set to 10 Hz. Start the motor, and after the liquid flow at the gear pump outlet is stable, start to collect the digital flow-meter signal and photoelectric encoder signal respectively. Due to the inevitable noise in the system, the Signal Process toolbox is used to filter the collected data.

As shown in Fig. 3, in an encoder z-phase pulse signal, the output flow signal has 16 wave peaks. The relationship between the electrical signal value and the flow value is linear, therefore the arc gear pump rotate a cycle will produce 16 flow pulsations.
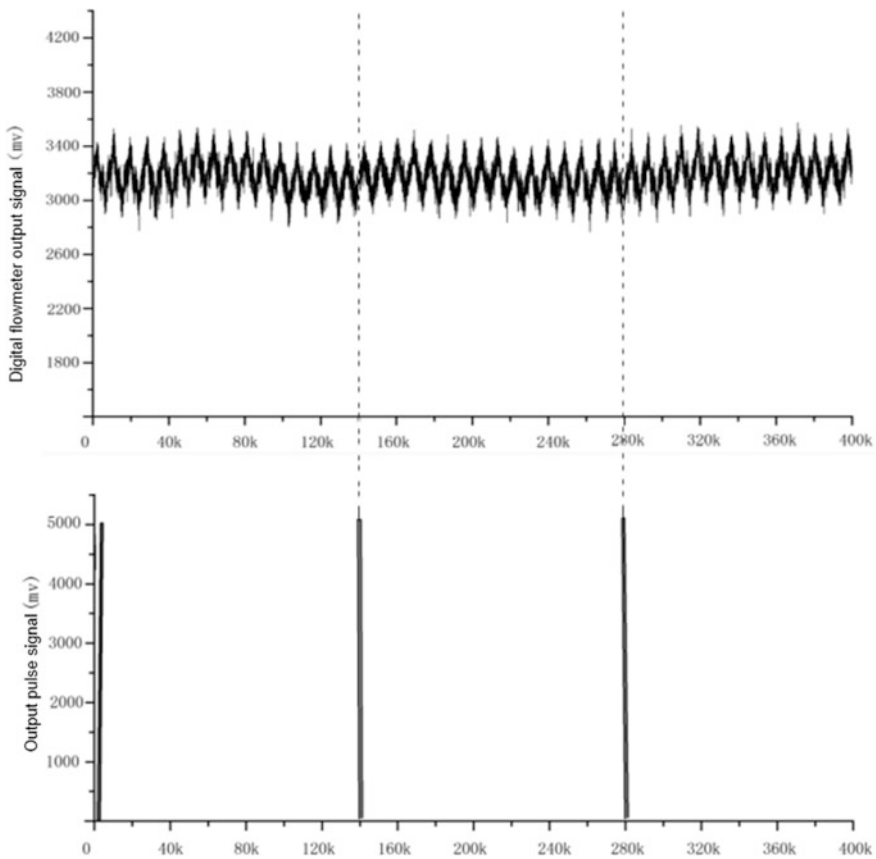


**Fig. 3.** Code pulse and gear pump flow pulsation correspondence

Using Matlab to graph instantaneous volume flow formula, and compare with the instantaneous flow pulsation curve of electric signal transformation of digital flow-meter. As shown in Fig. 4, for the flow pulsation curve of the theoretical model, the

flow pulsation interval is [299.8, 331.3](ml/s), and the range is 31.5 ml/s; for the flow pulsation curve obtained in the experiment, the flow pulsation interval is [294.8, 342.3] (ml/s).
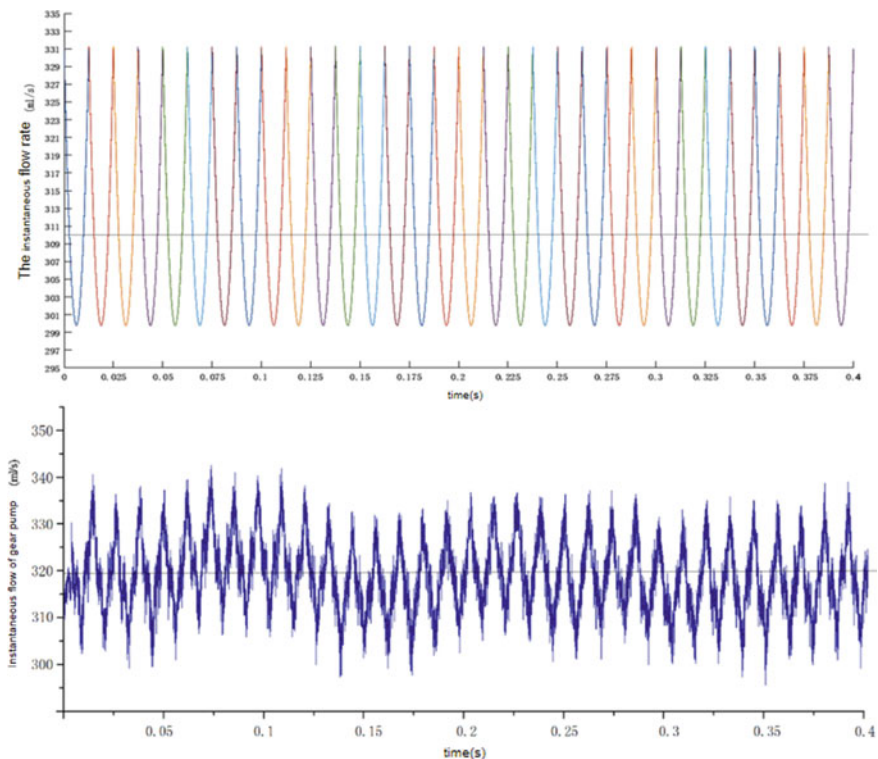


**Fig. 4.** Comparison of theoretical model instantaneous flow curve and experimental monitoring flow curve

Due to the interference of motor vibration, gear pump noise and other factors, the extreme value of instantaneous flow obtained by the experiment is not stable and fluctuates to some extent. In order to calculate the flow pulsation of a gear pump during a rotation period, sum all crest values and all trough values in a rotation period and then calculate the difference, and then calculate the mean value, and the mean value range is 36.4 ml/s.

For the instantaneous flow pulsation curve of the theoretical model, the average flow quantity of the gear pump in a rotation cycle is 310.12 ml/s. For the instantaneous flow data obtained in the experiment, using Matlab to average them, and the average flow quantity is 319.73 ml/s.

In summary, exclude the calculation error of theoretical model, systematic error and random error in experimental process, the theoretical model calculation method of the instantaneous flow quantity compared with the experiment, the arc gear pump of

instantaneous flow pulsation calculated relative accuracy is 13.5%, the gear pump of instantaneous flow calculated average relative accuracy is 3.0%.

## 5    Conclusions

In this paper, by deducing the formula of instantaneous flow at the outlet of arc gear pump the key factors affecting the flow pulsation of arc gear pump are the number of teeth and the pressure angle. By setting up the optimization model of gear structure parameters, the gear tooth profile is optimized theoretically, and it is obtained that when the number of teeth is 12 and the pressure angle is 32.5°, the meshing efficiency of arc gear is satisfied and the flow pulsation of gear pump is optimized. The correctness of the model is further illustrated by constructing an arc gear pump flow experiment platform.

## References

1. Xu H, Wang X, Lei R, et al (2016) Experimental analysis of the effect of vacuum degassing technology on the solventless laminating adhesive performance. In: China Academic conference on printing & packaging & media technology. Springer, Singapore
2. Xu H, Li W, Wang X, et al (2016) Study on the flow mixing results of revolving static mixer used in solventless laminator. In: China Academic conference on printing & packaging & media technology. Springer, Singapore
3. Chen CK, Yang SC (2000) Geometric modelling for cylindrical and helical gear pumps with circular arc teeth. Proc Inst Mech Eng Part C J Mech Eng Sci 214(4):599–607
4. Liu YW, Fan J (2010) Study of tooth profile design with asymmetric double circular arc gears for pumps. Appl Mech Mater 43:409–413
5. Huang KJ, Chen CC, Chang YY (2009) Geometric displacement optimization of external helical gear pumps. Proc Inst Mech Eng 223(C9)

# Information Engineering and Artificial Intelligence Technology

# Research Progress of Capacitive Flexible Pressure Sensors

Zhenxin Guo, Yu Ding, Xiangyou Meng, Di Wu, Lixin Mo[⊠], and Luhai Li

Beijing Engineering Research Center of Printed Electronics, Beijing Institute of Graphic Communication, Beijing, China
molixin@bigc.edu.cn

**Abstract.** The flexible pressure sensors which cover the human body can generate electric signal under pressure. Compared to other types of pressure sensors, the capacitive flexible pressure sensors have the advantages of low energy consumption, fast response time and low detection limit. In order to obtain high performance capacitive flexible pressure sensors, efforts have been done on the structures and materials of sensors. This chapter reviews the methods to improve the sensor performance, including the preparation of microstructures and composite dielectric layers. Moreover, the research progress of capacitive flexible pressure sensors in the fields of intelligent medical and robotics is summarized. Finally, the prospects and challenges are discussed for capacitive flexible pressure sensors.

**Keywords:** Capacitive flexible pressure sensors · Microstructures · Composite dielectric layer · Intelligent medical · Robot

## 1 Introduction

The flexible pressure sensors generate electrical signals under the pressure and work in the form of signal transmission [1]. Therefore, the flexible pressure sensor can simulate the human skins to transduce the important information about the specific needs between the human body and the external environment [2]. In recent years, with the rapid development of flexible sensing materials and sensor preparation technologies, flexible pressure sensors have made significant progress in applications such as electronic skin, flexible touch display, robotics, energy harvesting, medical diagnosis and self-reporting sensors [2–6]. Conventional pressure sensors are usually made of the rigid materials that are heavy and do not meet the requirements for flexible wearables, and they cannot be used to capture weak signal sources [7]. Flexible pressure sensors can be divided into four types according to the principle: piezoresistive sensors, piezocapacitive sensors, piezoelectric sensors and field effect transistors [8]. The piezoresistive sensors have a change in resistivity with adding pressure. They have the advantages of high sensitivity and the disadvantages of high energy consumption. Field effect transistors are limited in application due to high operating gate voltage and the

toxicity of organic semiconductors. Piezoelectric sensors rely on charge accumulation that is only sensitive to dynamic pressure. The capacitive sensors have the advantages of low energy consumption, fast response time, low detection limit and good sensing stability [9, 10], which has aroused great interest of researchers. The low detection limit, high sensitivity, wide range and good flexibility of the capacitive flexible pressure sensor are the hotspots pursued by researchers. In order to improve the performance of the sensors, it is the effective methods to prepare a micro structured electrode layer or a dielectric layer and to prepare composite dielectric layers. Furthermore, the flexible capacitive sensors have been prepared for different application fields. This reviews summarize the methods to improve the flexible sensor performance and their application in the fields of intelligent medical and robotics. Finally, the development of capacitive flexible pressure sensors is discussed.

## 2    Research Progress in Improving Sensor Performance

Sensitivity, range, response time and other factors are important technical parameters of sensor performance. To improve the performance of the sensor, the sensors will be designed with different processes and materials. The preparation of micro structured dielectric layers or electrode layers and the use of composite dielectric materials as dielectric layers are the most widely reported.

### 2.1    Micro-Nano Structures

Flexible sensors usually employ rubber elastomers such as polydimethylsiloxane (PDMS) as the elastic layers. The elastic layer without microstructures is less deformed under pressure, and the sensors with thin flat PDMS film have longer relaxation time [11]. The preparation of the micro/nano structures in the electrode layers or the dielectric layers can improve the sensitivity of the sensors and reduce the response time. Micro-nano structures are available in a variety of shapes, including pyramidal shapes, truncated pyramids, linear shapes, and microneedles. Bao et al. [11] prepared the pyramidal and linear dielectric layers using a silicon wafer as a template as shown in Fig. 1a. It is found that the sensor with the pyramidal dielectric layer possessed the higher sensitivity. Due to the existence of pyramidal microstructures, the response time and the detection limit of the sensor was greatly reduced and the maximum sensitivity of the sensor of 0.55 kPa$^{-1}$ was obtained. Bao et al. [12] prepared the dielectric layer using the PDMS soft mold as the template, improving the durability of the template and avoiding the template failure. It is found that the dielectric layer is more easily deformed under the same pressure as the sidewall angle of the dielectric layer was reduced, which is beneficial to improve the sensitivity. Pignanelli et al. [13] compared a dielectric layer prepared by the pyramidal inverse template, the replica template, the photolithographic template. The study found that the sensor using the dielectric layer prepared by photolithography wafer had the highest sensitivity (0.1851 kPa$^{-1}$) in the pressure range of less than 3 kPa.
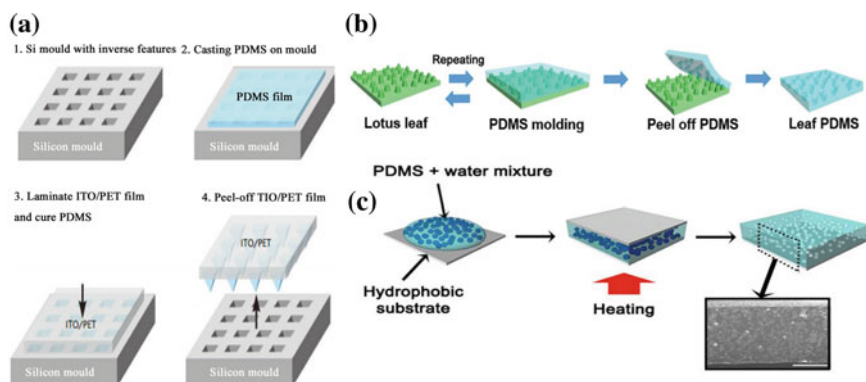
**Fig. 1.** **a** Schematic diagram of preparation process of microstructured dielectric layer using silicon wafer as template [11]; **b** schematic diagram of preparation process of PDMS soft template with lotus leaf as template [15]; **c** the fabrication process of an micro-pores elastomer film [19]

The preparation of silicon wafers often requires complicated processes such as photolithography or etching, which increases the cost and does harm to environment [14]. Therefore, researchers have begun to use low-cost templates to prepare microstructures. Li et al. [15] prepared the micro structured electrodes using lotus leaf as a template as shown in Fig. 1b. The flexible pressure sensor possessed the sensitivity of 0.815 kPa$^{-1}$, the response time of 38 ms and the range of 0–50 N. Yoon et al. [16] used the sandpapers with different roughness as templates to prepare dielectric layers. With increased roughness, the flexible sensor had the maximum sensitivity of 9.55 kPa$^{-1}$. However, the microstructures shape of the dielectric layers using sandpaper or lotus leaves as the template is irregular and the repeatability is poor, which is difficult to industrial production. Ma et al. [17] prepared the regular wavy microstructured dielectric layer by pre-stretching PDMS. The prepared sensor with wavy micro-structured dielectric layer also had good bending stability and repeatability.

Recently, porous elastomers have been used in flexible pressure sensors due to their light weight, easy deformation, and simple preparation methods [18]. The inorganic binder which is soluble in the solvent is filled in elastomers. Then, the porous elastomer is prepared by heating or washing with water. The mass fraction of the inorganic reagent and the particle size are the important factors of the porosity and elasticity of the porous elastomer. Lee et al. [19] mixed PDMS with water of different mass fractions to prepare microporous PDMS rubber as shown in Fig. 1c. As the mass fraction of deionized water increases, the pores increase and the sensitivity of the sensor based on the microporous elastic layer gradually increases. Ding et al. [20] immersed salt blocks with different pore sizes in Ecoflex prepolymers to prepare rubber elastics with pores of different particle sizes. The sensor with the microporous dielectric layer of smaller particle size (150–200 μm) has a higher sensitivity (1.096 kPa$^{-1}$) in the pressure range of 0–60 Pa. Chen et al. [21] smeared the PDMS and ammonium bicarbonate mixture on the ITO electrodes and prepared the microporous dielectric

layer after heating at 100 °C. The prepared sensor range of 0–1 MPa was greatly improved, and the sensitivity of 0.26 $kPa^{-1}$ was obtained.

## 2.2    Composite Dielectric Layers

Although the dielectric layer with microstructures greatly improves the sensor sensitivity in the high pressure region, the microstructures are compressed to saturation under high pressure and the sensitivity prepared by dispersing conductor fillers in insulating elastomers is reduced, which limits the application of the sensor [22]. When composites prepared by dispersing conductor fillers in insulating elastomers are employed in the sensor, the change of the dielectric constant under pressure and sensor sensitivity increase. Moreover, sensors with composite dielectric layers usually have the work range of up to hundreds kPa. Fang et al. [22, 23] prepared the dielectric layer by mixing nickel particles with different volume fractions and silicone rubber. The sensitivity of the prepared sensor was 19.3 times higher than that of the sensor with pure silicone rubber. The magnetic field is used to align the nickel particles in the silicone rubber along the magnetic field, which further improves the sensitivity of the sensor. When the elastomers are filled with conductive particles, the required conductive particles are more, which is harmful to the elasticity of the composites. When the dielectric layer is prepared by using one-dimensional or two-dimensional conductor fillers, the sensor sensitivity with conductive fills of low mass fraction possesses high sensitivity. Wang et al. [24] employed the silver nanowires/polyurethane composite dielectric layers. The sensor with the composites reached the highest sensitivity of 5.54 $kPa^{-1}$ when the mass fraction of silver nanowires was only 3wt%. Shi et al. [25] prepared the flexible sensor mixing silver nanowires with PDMS as shown in Fig. 2. When the mass fraction was 0.12 wt%, the sensor with 0.12 wt% silver nanowires possessed the highest sensitivity of 0.831 $kPa^{-1}$ and the detection limit was 1.4 Pa. Our group [26] prepared the sensor with high aspect ratio carbon nanotubes and PDMS, which demonstrated high sensitivity of 2.9 $kPa^{-1}$ (0–450 Pa).

Recently, some new type of composite dielectric layers have been applied to flexible pressure sensors, such as ion gels. Chen et al. [27] prepared the capacitive pressure sensors with zinc oxide nanowires and polymethyl methacrylate possessed high sensitivity ($9.95 \times 10^{-3}$ $cm^2\ gf^{-1}$) and low detection limit (0.01 $gf\ cm^{-2}$). When zinc oxide nanowires dispersed in an inorganic polymer, charge separation occurs under pressure, resulting in high sensitivity of the sensor. Choi et al. [28] prepared the sensor with pyramid-shaped ion gels composites, which can measure vertical pressure, shear and torsion forces. Qiu et al. [29] prepared a microstructured ion-gel dielectric layer using Calathea Zebrine Leaf as a template. The sensitivity was as high as 54.31 $kPa^{-1}$ in the range of 0–500 Pa and the sensitivity was always higher than 1 $kPa^{-1}$ in 0.1 Pa–115 kPa.
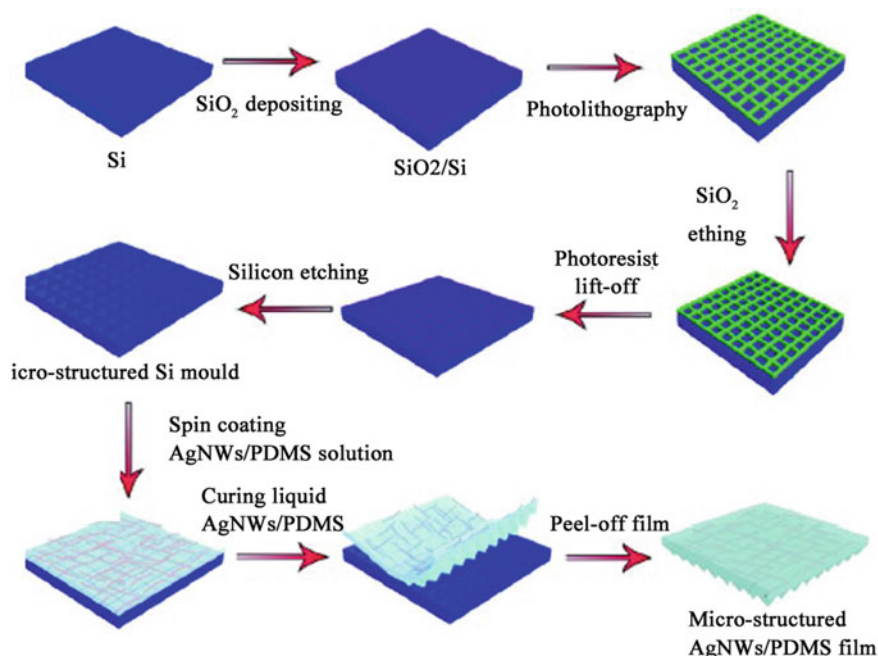
**Fig. 2.** Schematic illustration for the fabrication of the sensor with microstructured silver nanowires/PDMS composite dielectric film [25]

## 3   Applications of Capacitive Flexible Pressure Sensors

### 3.1   Intelligent Medical

Traditional medical services require patients to go to the hospital to receive services in person, and they cannot timely monitor the patient's condition in real time. Moreover, traditional medical equipments may cause secondary injury to the patients [30]. Nowadays, the flexible pressure sensor can be attached to the human body without harming the human body. It can measure blood pressure, pulse, vocal cord vibration, plantar pressure, grip strength and other body models in real time. Pruvost et al. [31] prepared sensors using porous carbon black particles/PDMS composites to measure the pulse, which can distinguish systolic and diastolic peaks of the arteries. And the sensor had good precision and repeatability. Liu et al. [32] prepared the self-healing pressure sensor which can be used to measure the force of the hand grabbing the basketball and the signal of the vocal cord vibration. Wen et al. [33] separately attached the flexible pressure sensor to the carotid artery and the heart, which can recognize the pulse rate and the heart rate at the same time in real time. Yoon et al. [16] prepared an ion gel capacitive pressure sensor that can be used not only for carotid beat measurement, but also for detecting dynamic forces such as finger slip. Also, they developed a microfluidic-based capacitive pressure sensor that can perform mechanical tests such as grip strength testing and finger sliding, as well as simultaneous force and temperature testing [34].

## 3.2    Robot

With the development of artificial intelligence and other technologies, robots can replace a large number of simple repetitive or dangerous work in the industrial field, home automation, military and other fields [35]. The visual and hearing capabilities of robots develop rapidly. With the rapid development of pressure sensors, pressure sensing expands the perception of robots and broadens the field of application of robots. Hua et al. [36] developed an electronic skin network in the robot hand to realize simultaneous detection of multiple signals such as pressure, temperature, humidity, and magnetic field. Maiolino et al. [37] mixed titanium dioxide and PMN-PT (lead magnesium niobate-lead titanat) into elastomers for the preparation of flexible pressure sensors, and covered the sensors on the robot body to detect the distribution of forces on the electronic skin and have better spatial recognition. Ji et al. [38] prepared a $4 \times 4$ flexible pressure sensor array on pet substrate. The sensor array is combined with the tactile feedback and signal acquisition system to realize the function of the robot to avoid obstacles. Larson [39] prepared a soft robot which can perceive the changes in robot shape to produce color changes.

## 4    Summary and Outlook

Capacitive flexible pressure sensors have received extensive attention from researchers due to their low power consumption and high sensitivity. The methods to increase sensor sensitivity and the applications of capacitive flexible pressure sensors are discussed. The flexible pressure sensors with various microstructures and new composite material shave been studied. The prepared microstructured dielectric layers or electrode layers and composite materials can greatly improve the performance of the sensor. The single improved method has limited performance improvement on the sensor. Therefore, more and more researchers will combine more strategies to enhance pressure sensors performance. These high-performance sensors are rapidly developing in the fields of smart medical and robotics. Though the rapid development of capacitive flexible pressure sensors, there are still some challenges with capacitive flexible pressure sensors. For example, it is difficult to maintain high sensitivity over a wide range of ranges; devices are prone to failure in extreme environments such as high temperatures; array sensors have poor uniformity and are difficult to large-scale applications. In order to realize the wider application of capacitive flexible pressure sensors, it is necessary to combine with the fields of micro-nano processing, composite materials, signal processing and promote the rapid development of capacitive flexible pressure sensors.

# References

1. Nam SH, Jeon PJ, Min SW, Lee YT, Park EY, Im S (2014) Highly sensitive non-classical strain gauge using organic Heptazole thin-film transistor circuit on a flexible substrate. Adv Func Mater 24(28):4413–4419

2. Li J, Bao R, Tao J, Peng Y, Pan C (2018) Recent progress in flexible pressure sensor arrays: from design to applications. J Mater Chem C 6(44):11878–11892

3. Li S, Peele BN, Larson CM, Zhao H, Shepherd RF (2016) A stretchable multicolor display and touch interface using photo patterning and transfer printing. Adv Mater 28(44):9770–9775

4. Jin X, Götz M, Wille S, Mishra YK, Adelung R, Zollfrank C (2013) A novel concept for self-reporting materials: stress sensitive photoluminescence in ZnO tetrapod filled elastomers. Adv Mater 25(9):1342–1347

5. Zhong LW, Chen J, Long L (2015) Progress in triboelectric nanogenerators as a new energy technology and self-powered sensors. Energy Environ Sci 8(8):2250–2282

6. Tee CK, Chortos A, Berndt A, Nguyen AK, Tom A, McGuire A et al (2015) A skin-inspired organic digital mechanoreceptor. Science 350(6258):313–316

7. Rodgers MM, Pai Vinay M, Conroy Richard S (2015) Recent advances in wearable sensors for health monitoring. Sens J IEEE 15(6):3119–3126

8. Qian X, Su M, Li F, Song Y (2016) Research progress of flexible wearable electronic sensors. Acta Chim Sinica 74(7):565–575

9. Cho SH, Lee SW, Yu S, Kim H, Chang S, Kang D et al (2017) Micropatterned pyramidal ionic gels for sensing broad-range pressures with high sensitivity. ACS Appl Mater Interfaces 9(11):10128–10135

10. Cai L, Song L, Luan P, Zhang Q, Zhang N, Gao Q et al (2013) Super-stretchable, transparent carbon nanotube-based capacitive strain sensors for human motion detection. Sci Rep 3(6157):3048

11. Mannsfeld SCB, Tee CK, Stoltenberg RM, Chen HH, Barman S, Muir BVO et al (2010) Highly sensitive flexible pressure sensors with microstructured rubber dielectric layers. Nat Mater 9(10):859–864

12. Tee CK, Chortos A, Dunn RR, Schwartz G, Eason E, Bao Z (2014) Tunable flexible pressure sensors using microstructured elastomer geometries for intuitive electronics. Adv Func Mater 24(34):5427–5434

13. Pignanelli J, Schlingman K, Carmichael TB, Rondeau-Gagné S, Ahamed MJ (2018) A comparative analysis of capacitive-based flexible PDMS pressure sensors. Sens Actuators, A 285:427–436

14. Nie B, Li X, Shao J, Li X, Tian H, Wang D et al (2017) Flexible and transparent strain sensors with embedded multiwalled-carbon-nanotubes meshes. ACS Appl Mater Interfaces 9(46):40681–40689

15. Li T, Luo H, Qin L, Wang X, Xiong Z, Ding H et al (2016) Flexible capacitive tactile sensor based on micropatterned dielectric layer. Small 12(36):5042–5048

16. Yoon SG, Park BJ, Chang ST (2017) Highly sensitive piezocapacitive sensor for detecting static and dynamic pressure using ion-gel thin films and conductive elastomeric composites. ACS Appl Mater Interfaces 9(41):36206–36219

17. Ma L, Shuai X, Hu Y, Liang X, Zhu P, Sun R et al (2018) A highly sensitive and flexible capacitive pressure sensor based on a micro-arrayed polydimethylsiloxane dielectric layer. J Mater Chem C 6(48):13232–13240

18. Ding Y, Xu T, Onyilagha O, Fong H, Zhu Z (2019) Recent advances in flexible and wearable pressure sensors based on piezoresistive 3D monolithic conductive sponges. ACS Appl Mater Interfaces 11(7):6685–6704

19. Lee BY, Kim J, Kim H, Kim C, Lee SD (2016) Low-cost flexible pressure sensor based on dielectric elastomer film with micro-pores. Sens Actuators, A 240:103–109

20. Ding H, Wen Z, Qin E, Yang Y, Zhang W, Yan B et al (2019) Influence of the pore size on the sensitivity of flexible and wearable pressure sensors based on porous Ecoflex dielectric layers. Mater Res Express 6(6):066304

21. Chen S, Zhuo B, Guo X (2016) Large area one-step facile processing of microstructured elastomeric dielectric film for high sensitivity and durable sensing over wide pressure range. ACS Appl Mater Interfaces 8(31):20364–20370

22. Fan Y, Liao C, Liao G, Tan R, Xie L (2017) Capacitive pressure-sensitive composites using nickel–silicone rubber: experiments and modeling. Smart Mater Struct 26(7):075003

23. Fan Y, Liao C, Xie L, Chen X (2018) Piezo-capacitive behavior of a magnetically structured particle-based conductive polymer with high sensitivity and a wide working range. J Mater Chem C 6(20):5401–5411

24. Wang J, Jiu J, Nogi M, Sugahara T, Nagao S, Koga H et al (2015) A highly sensitive and flexible pressure sensor with electrodes and elastomeric interlayer containing silver nanowires. Nanoscale 7(7):2926–2932

25. Shi R, Lou Z, Chen S, Shen G (2018) Flexible and transparent capacitive pressure sensor with patterned microstructured composite rubber dielectric for wearable touch keyboard application. Sci China Mater 61(12):1587–1595

26. Li Z (2017) Research on printing flexible pressure sensor based on composite dielectric material. Master's thesis, Beijing Institute of Graphic Communication

27. Chen YS, Hsieh GW, Chen SP, Tseng PY, Wang CW (2014) Zinc oxide nanowire-poly (methyl methacrylate) dielectric layers for polymer capacitive pressure sensors. ACS Appl Mater Interfaces 7(1):45–50

28. Choi D, Jang S, Kim JS, Kim HJ, Kim DH, Kwon JY (2019) A highly sensitive tactile sensor using a pyramid-plug structure for detecting pressure, shear force, and torsion. Advan Mater Technol 4(3):1800284

29. Qiu Z, Wan Y, Zhou W, Yang J, Yang J, Huang J et al (2018) Ionic skin with biomimetic dielectric layer templated from calathea zebrine leaf. Adv Func Mater 28(37):1802343

30. Wang X, Liu Z, Zhang T (2017) Flexible sensing electronics for wearable/attachable health monitoring. Small 13(25):1602790

31. Pruvost M, Smit WJ, Monteux C, Poulin P, Colin A (2019) Polymeric foams for flexible and highly sensitive low-pressure capacitive sensors. npj Flexible Electronics 3(1):7

32. Liu F, Han F, Ling L, Li J, Zhao S, Zhao T et al (2018) An omni-healable and highly sensitive capacitive pressure sensor with microarray structure. Chem–A European J 24 (63):16823–16832

33. Wen Z, Yang J, Ding H, Zhang W, Wu D, Xu J et al (2018) Ultra-highly sensitive, low hysteretic and flexible pressure sensor based on porous MWCNTs/ecoflex elastomer composites. J Mater Sci Mater Electron 29(24):20978–20983

34. Yoon SG, Chang ST (2017) Microfluidic capacitive sensors with ionic liquid electrodes and CNT/PDMS nanocomposites for simultaneous sensing of pressure and temperature. J Mater Chem C 5(8):1910–1919

35. Almassri AM, Wan Hasan WZ, Ahmad SA, Ishak AJ, Ghazali AM, Talib DN, Wada C (2015) Pressure sensor: state of the art, design, and application for robotic hand. J Sens 2015

36. Hua Q, Sun J, Liu H, Bao R, Wang ZL (2018) Skin-inspired highly stretchable and conformable matrix networks for multifunctional sensing. Nat Commun 9(1):244

37. Maiolino P, Galantini F, Mastrogiovanni F, Gallone G, Cannata G, Carpi F (2015) Soft dielectrics for capacitive sensing in robot skins: performance of different elastomer types. Sens Actuators, A 226:37–47
38. Ji Z, Zhu H, Liu H, Chen T, Sun L (2016) A flexible capacitive tactile sensor for robot skin. In: 2016 international conference on advanced robotics and mechatronics (ICARM). IEEE, pp 207–212
39. Larson C, Peele B, Li S, Robinson S, Totaro M, Beccai L et al (2016) Highly stretchable electroluminescent skin for optical signaling and tactile sensing. Science 351(6277):1071–1074

# Research on Face Recognition Based on Vertex Energy Minimum Patterns

Jinyi Qiao[1(✉)], Ping Yang[1], Yue Gao[2], Yuanzhuo Yuan[1],
Fenggen Guo[1], and Zizhao Wu[1]

[1] School of Digital Media and Design, Hangzhou Dianzi University, Hangzhou,
Zhejiang, China
1520362738@qq.com
[2] School of Data Science and Technology, North University of China, Taiyuan,
Shanxi, China

**Abstract.** Aiming at the loss of the geometric information of the three-dimensional surface caused by the existing three-dimensional face recognition algorithm in the process of dimension reduction, by studying the conformal geometry related knowledge, this chapter adopts the conformal mapping method based on Ricci curvature flow to reduce the three-dimensional face surfaces to two-dimensional planar disk. The geometric information in the 3D surface is not lost as much as possible thus improving the recognition efficiency in the subsequent recognition process. In this chapter, a three-dimensional face recognition method based on minimum vertex energy pattern is proposed. Each point on the surface will be given its unique energy value in the calculation process of conformal mapping through Ricci curvature flow. By counting the variation of the energy value of each vertex, the feature histogram is generated, which is used as the basis of recognition. The method achieves better recognition effect. The recognition rate has been increased to more than 95%.

**Keywords:** 3D face recognition · Ricci curvature flow · Energy characteristics

## 1 Introduction

Face recognition technology is a kind of biometric recognition technology, which extracts facial features of human face as a contrast standard. It has the advantages of nature, friendliness and accuracy. Although the recognition technology based on iris and fingerprint features has achieved very accurate results, but compared with face recognition, there are still some inherent defects which hinder the wider application. Under normal circumstances, the human face is exposed, and the acquisition of its related data does not require the permission of the collected object, so it has high concealment. The iris, fingerprint and other biological characteristics must be collected through the active cooperation of the object in order to complete the data acquisition. Therefore, compared with other recognition methods, face recognition has inherent advantages and its data acquisition is faster and more convenient. Face recognition technology has broad application prospects in the field of biometrics because of its huge advantages in data acquisition.

## 2   Theoretical Research of Face Recognition Algorithms Based on Ricci Curvature Flow

### 2.1   Discrete Ricci Curvature Flow

The essence of Ricci curvature flow is to measure the Riemann deformation of points on a surface. The degree of deformation is determined by the difference of the initial and final Gauss curvature of points on a surface. The Gauss curvature of points on a surface is uniformly transformed into points on a surface with time under the control of reaction-diffusion equation, so that the curvature of the final surface becomes a constant. In this algorithm, Ricci curvature flow can not only conformally map a three-dimensional face model to a two-dimensional plane, but also keep the local properties of the surface unchanged during the mapping process to achieve conformal mapping.

In the discrete case, the circle packing metric of a surface is $(\Gamma, I, M)$, M is a set of triangulation. In the discrete case, the Ricci curvature flow formula on the surface is shown in Formula 1.

$$\frac{du_i}{dt} = \left(\overline{K}_i - K_i\right) \tag{1}$$

It can be seen that the deformation process of Ricci curvature flow is a process of conformally changing the circle packing radius according to the difference between the set target curvature and the original curvature.

### 2.2   Constructing the Minimum Energy Model of Vertex

In triangular mesh generation, there may be n triangular facets adjacent to each vertex p, so the vertices adjacent to the original vertex P are 2n. The vertex energy unit is constructed by using the logarithmic form $u_0$ of the circle packing radius as the threshold value. The energy values of the adjacent 2n vertices are $u_1, u_2, \ldots, u_{2n}$. If the energy value of a vertex adjacent to the vertex is greater than the energy value of the central vertex, the energy value of the vertex is coded as 1, or less is coded as 0. The method of calculation is shown in Formula 2.

$$T \approx (S(u_1 - u_0), S(u_2 - u_0), \ldots, S(u_{2n} - u_0)) \tag{2}$$

After obtaining the energy values of the adjacent vertices of each vertex, all $S(u)$ links are generated into a binary vertex energy code. Each $S(u)$ links is assigned a weight of $2^i$. The binary code is converted into a decimal value, and its initial vertex energy pattern (VEP) is generated. The calculation formula is shown in Formula 3.

$$\text{VEP} = \sum_{i=0}^{2n} S(u_i - u_0)2^i \tag{3}$$

Considering that there are many vertices adjacent to triangular patches, different fixed-point energy codes will be generated if different coding order is adopted for the

energy values extracted from each vertex. Therefore, the binary codes generated by all energy values are calculated and their minimum values are taken as the final feature Vertex Energy Minimal Pattern (VEMP). The calculation formula is shown in Formula 4.

$$VEMP = \min\{VEP_i | i = 1, 2, \ldots, 2n\} \tag{4}$$

## 3    Face Recognition Based on Ricci Curvature Flow

### 3.1    Eigenvalue Extraction

Face recognition algorithm based on Ricci curvature flow first chooses the input three-dimensional face model, uses Ricci curvature flow to reduce dimension, then extracts VEMP eigenvalues, generates VEMP feature histogram, calculates similarity using chi-square statistics, and outputs matching model.

After completing the conformal mapping, using the VEMP algorithm proposed above, after extracting the energy values of each point on the face surface, the energy characteristic histogram of each point is calculated and generated. The horizontal axis of the histogram represents the magnitude of the energy value, and the vertical axis represents the frequency corresponding to the energy value. As shown in Fig. 1.



(a) Face model 1 histogram extraction



(b) Face model 2 histogram extraction
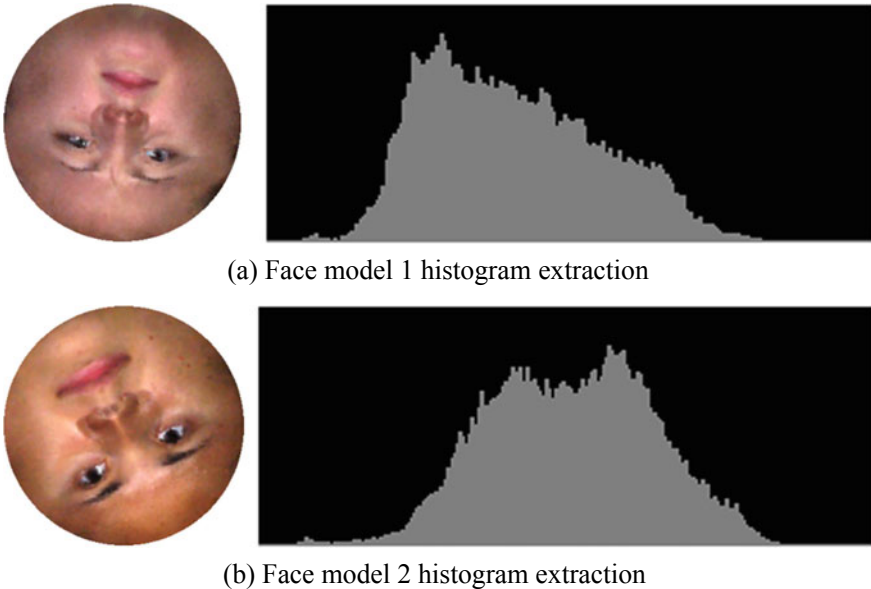
**Fig. 1.**  Extraction of VEMP histogram from different face models

As can be seen from the above figure, after completing the conformal mapping of different face models and extracting energy features through VEMP algorithm, the feature histograms produced by different models have obvious differences. At the same time, in order to simulate the influence of illumination on the system during operation, this chapter simulates the process by changing the color value of the three-dimensional face model. As shown in Fig. 2.



**Fig. 2.** Simulated illumination results and corresponding VEMP histogram

As can be seen from Fig. 2, when the color of the face model changes, compared with the histogram below Fig. 1, the VEMP feature histogram generated by the face model does not change significantly.

## 3.2  Method Comparison

In the experiment process of this chapter, the relative standard personal face model in BU-3DFE face model database is used as the standard database in the system operation process, and 1000 different face models are selected as the comparison model. Through chi-square statistics of VEMP features of the input model to be compared with those of the existing face features in the standard database, and output the model with the highest similarity, the process of comparative recognition is completed. Compared with the traditional three-dimensional face recognition algorithm, VEMP algorithm improves the recognition efficiency of face model without the influence of illumination, as shown in Table 1.

**Table 1.** Comparisons of different algorithms without illumination

| Method | Recognition rate (%) |
| --- | --- |
| LBP | 93 |
| PCA | 85 |
| VEMP | 97.6 |

By changing the color value of the face model surface to simulate the influence of illumination on the face, to test the robustness of the system to illumination conditions,

and further comparing with traditional face recognition algorithm, it can be found that the robustness of VEMP algorithm under illumination conditions is significantly higher than other algorithms, as shown in Table 2.

**Table 2.** Comparisons with traditional algorithms for illumination

| Method | Recognition rate (%) |
|--------|----------------------|
| LBP | 52 |
| PCA | 65 |
| VEMP | 97.6 |

## 4   Conclusion

In this chapter, by using the Ricci curvature flow based computational conformal geometry method, the 3D face model is conformally mapped to a two-dimensional plane disc, which ensures that the geometric data of the three-dimensional face model is well preserved while reducing the dimension. After the conformal mapping is completed, the geometric data of each triangle in the model are extracted by setting the energy disc, and the feature extraction is completed by generating the feature histogram. Finally, the recognition process of the face model in the matched face model and the standard face database is completed by using chi-square statistics. In the experiment, by comparing with the traditional three-dimensional to two-dimensional face recognition algorithm under normal conditions, it is proved that the VEMP algorithm proposed in this chapter has improved to a certain extent. After adding the simulated illumination effect, the recognition efficiency of the VEMP algorithm is compared. The VEMP algorithm proposed in this chapter has less impact and higher robustness to light.

## References

1. Yue M, Ruan Q (2012) Robust sparse bounding sphere for 3D face recognition. Butterworth-Heinemann
2. Al-Osaimi F, Bennamoun M, Mian A (2009) An expression deformation approach to non-rigid 3D face recognition. Int J Comput Vis 81(3):302–316
3. Llonch RS, Kokiopoulou E, Frossard P (2010) 3D face recognition with sparse spherical representations. Pattern Recogn 43(3):824–834
4. Elaiwat S, Bennamoun M, Boussaid F et al (2015) A curvelet-based approach for textured 3D face recognition. Pattern Recogn 48(4):1235–1246
5. Huang D, Ardabilian M, Wang Y et al (2012) 3-D face recognition using eLBP-based facial description and local feature hybrid matching. IEEE Trans Inf Forensics Secur 7(5):1551–1565

6. Berretti S, Bimbo AD, Pala P et al (2007) Geodesic distances for 3D-3D and 2D-3D face recognition. In: IEEE international conference on multimedia and expo. IEEE, pp 1515–1518
7. Hariri W, Tabia H, Farah N et al (2016) 3D face recognition using covariance based descriptors. Elsevier Science Inc.
8. Haar FBT, Veltkamp RC (2009) A 3D face matching framework for facial curves. Graph Models 71(2):77–91

# Transformer-Based Coattention: Neural Architecture for Reading Comprehension

Xinyu Wang, Ziwei Tang, Yaohua Yi$^{(\boxtimes)}$, and Chaohua Gan

School of Printing and Packing, Wuhan University, Wuhan, Hubei, PRC, China
yyh@whu.edu.cn

**Abstract.** Machine reading comprehension (MRC) is one of the primary challenges in natural language understanding (NLU), its objective is to give the correct answer based on the questions asked from the specified context. Nowadays, attention mechanisms have been widely used in reading comprehension tasks. In this chapter, based on the analysis of two state-of-the-art attention mechanisms, Coattention and Multi-head Attention, the Transformer-based Coattention (TBC) is proposed. Furthermore, a general hybrid scheme is proposed to incorporate the TBC into pretrained MRC models with little extra training cost. Our experiments on Stanford Question Answering Dataset (SQuAD) and Discrete Reasoning Over the content of Paragraphs (DROP) show that our hybrid scheme make models achieve better performance.

**Keywords:** Machine reading comprehension · Natural language understanding · Transformer-based coattention

## 1 Introduction

Most of the information generated and obtained by human beings is stored in the form of text. Nowadays, a large amount of text information is generated every day, so machine reading comprehension is among the most critical tasks in the field of NLU. Therefore, Machine reading comprehension (MRC), aiming to give the correct answer based contexts and questions, has gained significant popularity over the past few years. Attention mechanism, which is similar to human visual phenomena, has been firmly established as a state of the art approach to promote the development in various tasks. With the help of attention mechanism, some essential content within the context wins more attention, thus the most relevant information, without regard to their distance in the sequences, is extracted for answering the question.

In 2016, Hermann et al. [1] proposed an attentive reader and an impatient reader based on bidirectional RNN and attention mechanism, which are the essential basis of the latter machine reading comprehension models. Later, numerous efforts have since continued to improve the attention mechanism. For instance, the Attention Sum Reader [2] and the Stanford Attentive Reader [3] respectively use dot-product and bilinear attention between the question and context embeddings to select the answer. Furthermore, Bi-Directional Attention Flow (BiDAF) [4] computes bi-directional attention (context-to-question and question-to-context). Coattention mechanism is introduced by Dynamic Co-Attention network (DCN) [5] to attend to the question and document

simultaneously. Based on previous works, Hasan et al. [6] proposed a hybrid scheme combining BiDAF and DCN, and Double Cross Attention (DCA). The BERT [7], the state of the art transfer learning model, benefits from Transformer [8], which mainly consists of Scaled Dot-Product Attention and Multi-head Attention.

In this chapter we propose the Transformer-based Coattention (TBC), a model architecture attending to information in different representation subspaces between question and context. It can be easily incorporated into pretrained neural MRC models with nearly no additional computation via the proposed hybrid scheme.

## 2    Model

We start our study by analyzing Coattention and Multi-head Attention, both of which have been widely used in current neural MRC models. By combining the ideas of the two modules, we propose the TBC and a hybrid scheme incorporating the TBC to pretrained MRC models. In this section, we give a detailed description of each architecture.

### 2.1    Coattention

Xiong et al. [5] firstly introduced Coattention into MRC model called Dynamic Coattention Network (DCN). It fuses co-dependent representations of the question and context, in order to focus on relevant parts of both. Compared with the BiDAF [4], which combines the attention from question-to-context and context-to-question, this approach is more competitive. Assuming $P \in \mathbb{R}^{m \times d}$ and $Q \in \mathbb{R}^{n \times d}$ denote context and question. Firstly, dot product similarity matrix is computed by $S \in \mathbb{R}^{m \times n}$, then it computes column normalized and row normalized matrix, $S_{col}$ and $S_{row}$. Next, It computes context-to-question attention by $A = S_{col} \cdot Q$, question-to-context attention by $B = S_{row}^T \cdot P$, and context-to-context by $C = S_{col}^T \cdot B$. Finally, output is the concatenation of A and C.

### 2.2    Multi-head Attention

Transfer learning model BERT [7], the current state-of-the-art model of MRC, is designed to pre-train deep bidirectional representations, and then fine-tuned on MRC tasks with just one additional output layer. BERT's model architecture is a multi-layer bidirectional Transformer [8] encoder, which mainly consists of Multi-head Attention, Scaled Dot-Product Attention, point-wise fully connected feed-forward network, layer normalization [9] and residual connection [10].

After mapped by linear projection, origin sequence is transformed to $Q, K, V \in \mathbb{R}^{L \times d}$, these matrix will be divided into k parts and respectively passed into an attention head. In each head, it computes scaled dot-product attention as follows:

$$Attention(Q_i, K_i, V_i) = softmax\left(\frac{Q_i K_i^T}{\sqrt{d_k}}\right) V_i \qquad (1)$$

Finally, the output of each head is concatenated as follows:

$$\text{MultiHead}(Q, K, V) = \text{Concat}(head_1, head_2, \ldots, head_k) \tag{2}$$

In this method, different attention head attends to information in different representation subspaces, it's more effective than single-head attention with full dimensions. On the other hand, attention heads can compute in parallel, thus the computational cost is similar to single-head attention. However, Transformer, limited by inputting single sequence, is used as an architecture of self-attention.

## 2.3  Transformer-Based Coattention (TBC)

In this section, the Transformer-based Coattention (Fig. 1) is proposed by combining the ideas of the above two architectures. Coattention performs well when fusing co-dependent representations of context and question information, but it uses full dimension without considering the differences in feature subspaces. On the other hand, multi-head based Transformer is used to compute self-attention of a sequence. Obviously, their advantage is that they can complement each other. By combining the advantages of both, the TBC attends to information in different representation subspaces between question and context.

The overall structure of TBC is similar to Transformer, however, there is some changes. To be specific, in coattention layer, K and V are linearly projected from context, but Q is projected from question, among them are divided into $k \in \mathbb{R}^d$ parts. Instead of dot product, we compute similarity matrix by scaled dot product of the query with all keys, divided each by $\sqrt{d}$ as follows:

$$S = \frac{Q_i K_i^T}{\sqrt{d}} \tag{3}$$

After column and row normalization mentioned in 2.1, we compute context-to-question attention by $A = S_{col} \cdot Q$, question-to-context attention by $B = S_{row}^T \cdot V$, and context-to-context by $C = S_{col}^T \cdot B$. Ultimately, instead of concatenating A and C, we adopt the ensemble strategy similar to the BiDAF [4], thus the output is $[A; P \odot A; P \odot C]$, where $\odot$ is the element-wise multiplication. Just like Transformer, we add positional encoding to the input embeddings and employ residual connection, layer normalization and Drop [11] technique between layers.
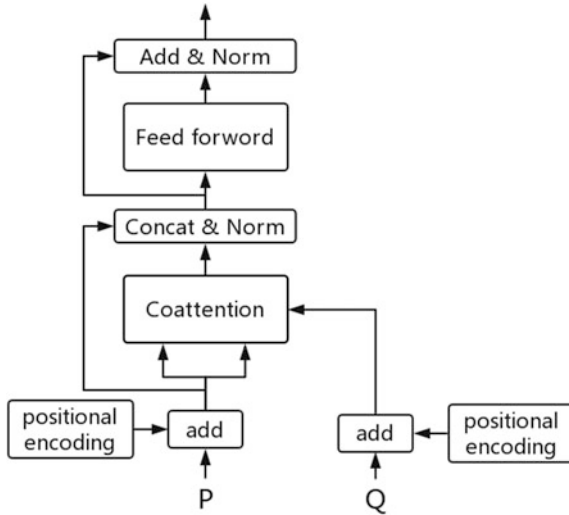
**Fig. 1.** Architecture of the TBC

## 2.4 Hybrid Scheme

In order to easily embed the TBC into the pretrained model and reduce training cost as much as possible, we propose a hybrid scheme for attention layer. Hasan et al. [6] proposed a scheme concatenating outputs from Bidirectional attention flow [4] and Coattention [5]. However, our method is to combine N layers TBC with pretrained attention layer, and to concatenate and pass their outputs to a two-layer Highway Network [12], which will control and fuse information flow from outputs of two modules. Finally, we linearly project the vector to origin output dimensions so that latter layers don't have to be changed. In general, this scheme makes the TBC easily applied to pretrained attention based models with little extra training cost and the TBC has tiny effect on model inference speed.

For instance, we can combine TBC with Coattention as Fig. 2 shows. Intuitively, Coattention and TBC respectively attends to overall and local dimensions between context and question, and the following Highway Network will effectively control information flow among them. In practice, we can easily add TBC to a pretrained model by this scheme and fine tune to get a better performance.
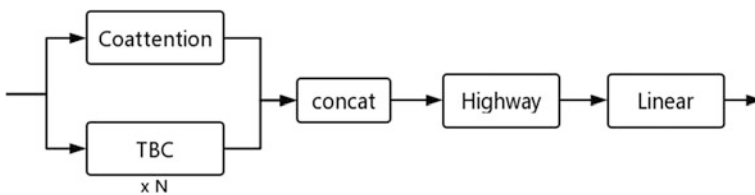


**Fig. 2.** Illustrations of the hybrid scheme

## 3    Experiments and Analysis

In this section, we first make an analysis of GloVe [13] vectors, which is an essential basis for the TBC. Furthermore, we evaluate three models with TBC on two datasets. The results indicate that models with TBC have higher prediction performance.

### 3.1    Word Representation Analysis

We first analyzed the pretrained word vectors, GloVe, which was trained on a large corpus of about 6 billion tokens and widely used in MRC models. Due to the ability to measure the similarity between words, the GloVe vectors have a good performance on
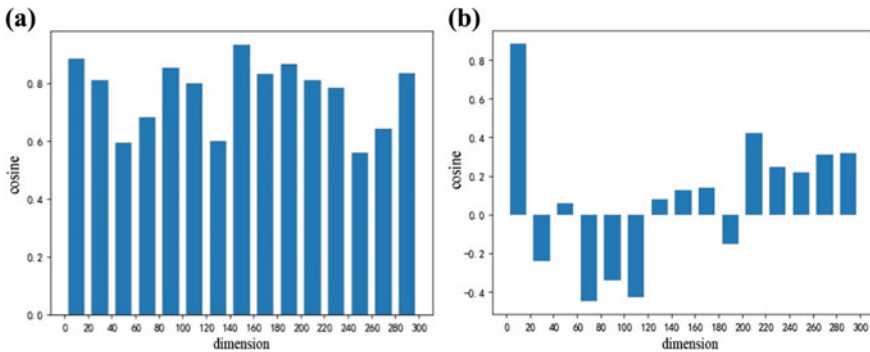


**Fig. 3.** Results of two experiments on 300 d GloVe vectors of the word "cat" and "dog". (**a**) and (**b**) respectively show the cosine similarity of the corresponding and non-corresponding vector segments

text representation. Previous researches usually analysed full dimension word vectors by visualization of dot product or cosine similarity matrix between two sequences. In this study, we used 300 d dimensions GloVe vectors of several words in experiment. We divided word vectors into 15 segments, in the first experiment, we visualized the cosine similarity between corresponding vector segments of two words. Furthermore, we used the first vector segment of a word to compute the cosine similarity in turn with all the vector segments of another word. The detailed results are shown in Fig. 3.

In Fig. 3a, for the two words of "cat" and "dog" with high similarity, cosine values calculated on different segments have subtle differences, this phenomenon indicates that the different semantic sub-features of the two words have different similarities. In addition, in Fig. 3b, the cosine similarity between first vector segment of a word and all non-corresponding segments of the other is small. From the results, we can draw a conclusion that word vector segments can well represent corresponding text semantic sub-features and different words have different similarity on semantic sub-features. Since the Coattention cannot attends to the difference of text semantic sub-features, we propose to combine it with the TBC to make up for this deficiency.

## 3.2   Hybrid Results

To verify the universality of our hybrid scheme, we evaluated the BiDAF and QANet model with TBC on Stanford Question Answering Dataset (SQuAD) [14], and the NAQANet [15] with TBC on Discrete Reasoning Over the content of Paragraphs (DROP) [15]. We started our experiment by re-implementing the three models with their default hyperparameters. Among them, Coattention was used by QANet and NAQANet and bi-directional attention flow was used by BiDAF, but we found that BiDAF worked better with Coattention. Then we introduced1 layer 8 heads TBC into these models by our hybrid scheme and fine tuned.

The performance of these models with TBC on dev set is reported in Table 1. In addition to the SQuAD and DROP evaluation metric F1 and EM, we tested inference time of these model by testing the average of ten inference times on the same sample. Inference times were measured on the same machine using an Intel E5-2620 v4 2.1 GHz*16 and a NVIDIA GeForce GTX 1080Ti GPU. Evaluation curves of BiDAF and QANet are shown in Fig. 4. Combining with the TBC, as Table 1 shows, the performance of the three models has improved. Moreover, there was almost no impact on the inference time, which indicates that this hybrid scheme and the TBC had feasibility for using in practical applications.
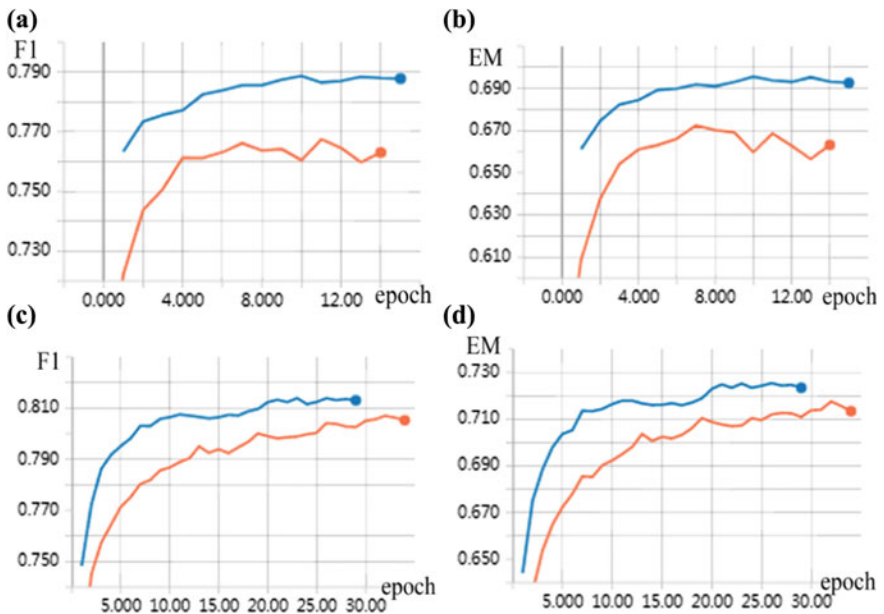


**Fig. 4.** Results of BiDAF and QANet on SQuAD dev set. Red and blue lines respectively denote origin models and models with TBC. **a** F1 of BiDAF, **b** EM of BiDAF, **c** F1 of QANet, **d** EM of QANet

**Table 1.** Results on dev set

| Model | Dataset | F1 | EM | Inference time (ms) |
|---|---|---|---|---|
| BiDAF | SQuAD | 76.61 | 67.25 | 28.63 |
| BiDAF + Coattention | SQuAD | 77.22 | 67.63 | 32.42 |
| BiDAF + Coattention + TBC | SQuAD | 78.86 | 69.56 | 33.74 |
| QANet | SQuAD | 80.7 | 71.75 | 24.18 |
| QANet + TBC | SQuAD | 81.41 | 72.84 | 24.39 |
| NAQANet | DROP | 50.52 | 46.89 | 24.81 |
| NAQANet + TBC | DROP | 51.49 | 47.85 | 25.14 |

Next, the QANet model was used to test different heads and layers TBC, in order to find the best settings. The result of different settings is reported in Table 2. Since 8 heads showed the best performance in one layer TBC, head numbers were set to 8 in layer number control experiments. Results indicate that the performance of the model had been improved by adding different number of heads and layers TBC. Among them, the 1 layer 8 heads TBC have the biggest improvement for QANet. This setup may not be the best choice for other MRC models based on attention mechanisms, and still needs to be determined via experiments.

**Table 2.** Results of different heads and layers TBC on QANet

| Layer number | Head number | F1 | EM |
|---|---|---|---|
| 1 | 4 | 80.94 | 72.13 |
| 1 | 8 | 81.41 | 72.84 |
| 1 | 16 | 81.15 | 72.27 |
| 2 | 8 | 81.15 | 72.19 |
| 4 | 8 | 81.08 | 72.27 |

## 4    Conclusions

In this chapter, we study the two widely used attention mechanisms called Coattention and Multi-head Attention. Combining their advantages, the TBC is proposed to attend to information in different representation subspaces between question and context. Moreover, a general hybrid scheme is proposed to introduce the TBC to pretrained models. Our experiment results show that the TBC improves the performance of the attention based models and has nearly no effect on the speed of inference. We believe that the TBC will also play a role in other fields of NLU, thus we will continue to validate it in future experiments.

# References

1. Hermann KM, Kocisky T, Grefenstette E et al (2015) Teaching machines to read and comprehend. In: Advances in neural information processing systems, pp 1693–1701
2. Kadlec R, Schmid M, Bajgar O et al (2016) Text understanding with the attention sum reader network. arXiv:1603.01547
3. Chen D, Bolton J, Manning CD (2016) A thorough examination of the cnn/daily mail reading comprehension task. arXiv:1606.02858
4. Seo M, Kembhavi A, Farhadi A et al (2016) Bidirectional attention flow for machine comprehension. arXiv:1611.01603
5. Xiong C, Zhong V, Socher R (2016) Dynamic coattention networks for question answering. arXiv:1611.01604
6. Hasan Z, Fischer S (2018) Pay more attention—neural architectures for question-answering
7. Devlin J, Chang MW, Lee K et al (2018) Bert: pre-training of deep bidirectional transformers for language understanding. arXiv:1810.04805
8. Vaswani A, Shazeer N, Parmar N et al (2017) Attention is all you need. In: Advances in neural information processing systems, pp 5998–6008
9. Ba JL, Kiros JR, Hinton GE (2016) Layer normalization
10. He K, Zhang X, Ren S et al (2015) Deep residual learning for image recognition
11. Srivastava N, Hinton G, Krizhevsky A et al (2014) Dropout: a simple way to prevent neural networks from overfitting. J Mach Learn Res 15(1):1929–1958
12. Srivastava RK, Greff K, Schmidhuber J (2015) Highway networks. Comput Sci
13. Pennington J, Socher R, Manning C (2014) Glove: global vectors for word representation. In: Proceedings of the 2014 conference on empirical methods in natural language processing (EMNLP), pp 1532–1543
14. Rajpurkar P, Zhang J, Lopyrev K et al (2016) SQuAD: 100,000+ questions for machine comprehension of text
15. Dua D, Wang Y, Dasigi P et al (2019) DROP: a reading comprehension benchmark requiring discrete reasoning over paragraphs. arXiv:1903.00161

# Game Comment Data Mining Based on Text Sentiment Analysis

Jiaxin Qian[(✉)] and Genfu Yang

School of Media and Design, Hangzhou Dianzi University, Hangzhou, Zhejiang,
China
`5439892811@qq.com`

**Abstract.** In order to understand the needs of the player, understand the
advantages and disadvantages of the game, this thesis proposes a way to eval-
uate the game by player comment content: (1) from the site to mine comment
information. (2) Calculate the importance and score of each attribute through the
neural network. (3) Analysis via importance-performance analysis (IPA) using
attribute importance and scoring. In this way, the advantages and disadvantages
of the game can be clearly demonstrated in the form of charts. This issues the
combination of dictionary and machine learning, the text vector of emotional
words, negative words, degree adverbs, punctuation and whole sentences is
characterized by the emotional analysis of sentences, and the evaluation and
analysis of the game in five dimensions by IPA method is used.

**Keywords:** Big data · Neural network · Text mining · Video game

## 1 Introduction

With the development of society and the advent of the era of pan-entertainment, the
game industry has developed rapidly, and more and more scholars have begun to study
and analyze the game industry. Amanda and others suggest that game reviews not only
have the role of guiding players to buy but can also be used to preserve the history of
the game. Raison et al. [1] extract user comments by clustering adjectives in game
reviews [2]. Guo Xin and others have constructed a model for evaluating the impor-
tance of player's needs and proposed an evaluation method based on fuzzy set and
entropy for the player's needs [3]. Few scholars analyze and evaluate games based on
game user data.

Text emotional classification has received wide attention in recent years and is one
of the hottest fields in natural language processing. Pang et al. first proposed ways to
use machine learning methods to classify text emotions [4]. Davidov and others used
the text and emoji of weibo as features, training a KNN-like classifier to classify text as
positive and negative by emotion, with a correct rate of up to 86% [5]. Huang Lei and
others have overcome the shortcomings of traditional text classification methods by
using the neural network model based on deep learning as the basic input unit of word
vector and retaining the semantic combination in the original text [6].

Therefore, this chapter proposes a method of using emotional analysis in evaluating
the game, taking user comment data as a sample, analyzing the emotional and

described properties of each sentence, using IPA to analyze the various attributes of the game, and evaluate the performance of the game in all aspects.

## 2    Methodology

### 2.1    Data Collection and Preprocessing

This article selected two popular games, *Subnautica* and *Gu Jian Qi Tan* from the Wegame platform, and crawled a total of 8,556 comments from the reviews of both games, which were the content of the player's comments and whether the game was recommended. Since a comment may involve a variety of attributes of the game, in order to be able to more thoroughly analyze the content of each comment, we need to divide the sentence into small sentences by punctuation, and in order to facilitate the later merge marks which long sentence this sentence originated from, and finally delete sentences less than four lengths.

### 2.2    Build Dictionaries

In order to analyze the game in more detail, this chapter scores the game from five dimensions according to the research done by the game media EEDAR. And create a property keyword dictionary for each dimension to identify the attributes involved in the sentence. These five dimensions, as well as their dictionaries, are as detailed as Table 1.

**Table 1.**  Each dimension attribute keyword and its quantity

| Category | Callout types | Amount |
|---|---|---|
| Gameplay | Controls, combat system, level design, etc. | 59 |
| Audio | Voice acting, soundtrack, sound effects, etc. | 12 |
| Graphics | Aesthetics, fidelity, animation, etc. | 47 |
| Narrative | Dialogue, plot, ending, etc. | 28 |
| Technical | Performance, bugs, physical, etc. | 52 |

After the dictionary is established, mark all small sentences, and mark the label of this property as 1 if the small sentence contains the property keyword.

This chapter has constructed three kinds of dictionaries for emotional analysis: emotional word dictionary, heavy adverb dictionary and negative word dictionary. The dictionary used in this thesis is based on the HowNet dictionary and is manually filtered and added. In the final dictionary, a total of 4,102 words representing positive emotion, a total of 3,956 words representing negative emotion, a total of 120 words for stronger adverbs, and 27 words for negative words.

### 2.3    Emotion Analysis

#### 2.3.1    Emotional Feature Selection

In a sentence, it is often the emotional words that determine the emotional tendency of a sentence. So, we use the established emotional word dictionary to mark each sentence and mark the number of positive and negative emotional words contained in each sentence. At the same time, negative words, heavy degree adverbs, exclamation points, and periods also affect the overall emotion of the sentence, so they are also marked out in the sentence, adding the emotional characteristics of the sentence. In addition, the text vector of the sentence is trained as a feature. This article uses Word2Vec to convert each sentence into a 300-dimensional vector.

#### 2.3.2    Training Model

In order to train the model, we need to manually rate the sentences emotionally, marking a total of 10,000 data.

In this chapter, the neural network is used to construct the model, combine the emotional characteristics of the sentence with the text vector of the sentence as input, and then put the fraction of the corresponding sentence of the manual label as output into the neural network for training. And use the cross-verification method to verify, the final accuracy rate of 90.8%, compared with only the sentence's text vector into the support vector machine for training, the accuracy is only 72%, so the method proposed in this chapter is more credible, in line with the expected requirements.

Finally, all the small sentences are predicted using trained models. Combine the scores of small sentences to get the final score for each comment (Table 2).

**Table 2.**  Input data

| Attribute | Input |
|---|---|
| F1 | Number of positive emotional words |
| F2 | Number of negative emotional words |
| F3 | Number of negative words |
| F4 | Whether it contains a degree of adverbs with a strong tone |
| F5 | Whether it contains an exclamation point or question mark |
| F6 $\sim$ F305 | Text vector |

### 2.4    Attribute Importance Analysis

This chapter takes the ensemble neural network-based model (ENNM) algorithm [7] to calculate the importance of each property. Use an entire comment as a single piece of data, with the score of the five attributes included in the comment as input, to whether the commenter recommends as the output data, for a total of 8,000. In this chapter, 8,000 data are divided into 40 groups, each group of 200, respectively, to calculate the weight of each attribute and the variance of the weight. These weights are divided into five groups by attribute, and several groups with large variances are sieved out. Finally, the weight of each attribute is obtained. The importance is shown in Table 3.

**Table 3.** Attribute importance and scores (only Gu Jian Qi Tan)

| Attribute | Importance | Score |
|-----------|-----------|-------|
| Gameplay | 0.24 | 3.05 |
| Narrative | 0.16 | 3.50 |
| Audio | 0.14 | 3.56 |
| Technical | 0.23 | 3.20 |
| Graphics | 0.22 | 3.20 |

## 2.5   Constructing the IPA Plot

After calculating the scores and importance of each attribute, we need to standardize the data before charting. After processing, we can use this data to draw an IPA plot. Figures 1 and 2 are the resulting IPA plots.
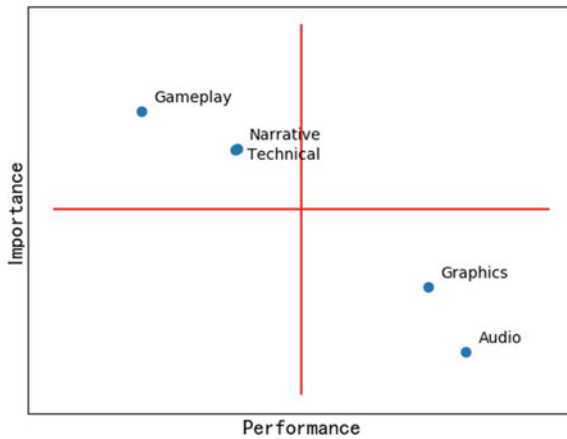


**Fig. 1.**  SIPA
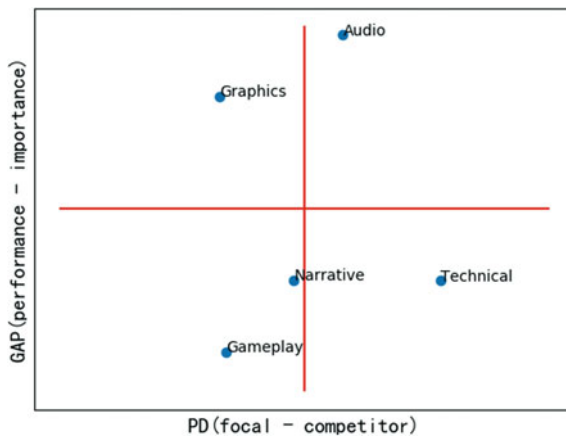


**Fig. 2.**  IPCA

### 2.5.1   SIPA

The horizontal coordinates of the SIPA chart are the performance scores for the attributes, the ordinates are the importance of the attributes, and the following figure is the chart of the *Gu Jian Qi Tan*. From this diagram, we can easily see the performance of the game in all aspects.

The importance and fraction of the attributes in the first quadrant of the graph are above the mean. Explain that these attributes are valued by the player, and the game is also very good in this regard, belongs to the absolute advantage of the game, need to continue to maintain. The lower score and high importance of the attribute in the second quadrant indicate that the attribute is the weakness of the game and needs to be focused and find a way to improve it in a timely manner. The third quadrant attribute score is low, the importance is also low, indicating that although the property is the weakness of the game, but the player is not very important to this, so do not need to spend a lot of energy to promote the property. The attribute score in the fourth quadrant is high, but not very important, is an overworked zone and does not require too much effort to sustain it.

### 2.5.2   IPCA

IPCA charts are mainly used to compare the gap between peers. Its horizontal coordinates are the difference between the score of the game and its competitors in a certain attribute, the ordinate is whether the game meets people's requirements in a certain attribute, and the value is the difference between the score and importance of the standardized property. Through IPCA, we can intuitively see the advantages and disadvantages of the game compared to other corporate games. The following image shows an IPCA chart of *Subnautica* and *Gu Jian Qi Tan.*

The above-average GAP and PD for the audio properties in the first quadrant in the graph show that the game is both better than its competitors and meets the needs of the player, and it is the game's advantage which should be firmly held. The image of the second quadrant has high GAP and lower PD, indicating that although it can meet the needs of the player, it is worse than the competitors and is area that need improvement but are not high priority. The PD and GAP values of the narrative and gameplay attributes in the third quadrant are very low, neither meet the requirements of the player nor better than other games, and they should be considered and improved in the first place. The technical attributes in the fourth quadrant, high PD but low GAP, are useless advantages, although better than their competitors but still cannot meet the needs of players.

## 3   Conclusion

This chapter proposes a method to evaluate the game by analyzing player's comments, evaluating the game through the process of emotion analysis, attribute importance analysis, chart making, etc., and the multi-featured emotion analysis model based on the emotion dictionary and neural network can accurately classify the text and ensure the reliability of the score. At the same time, IPA analysis will be all aspects of the game's disadvantages and advantages in the form of charts, the results are concise, so

that game companies do not have to do high-cost, inefficient and low-quality questionnaires to understand the player's ideas, so as to better manage and improve the game to meet the needs of players. And the analysis of attributes as needed to change the attribute keyword dictionary, this method can also be used in other areas (movies, hotel management, etc.), has a general use.

# References

1. Zagal JP, Ladd A, Johnson T (2009) Characterizing and understanding game reviews. In: International conference on foundations of digital games. ACM
2. Raison K, Tomuro N, Lytinen S et al (2012) Extraction of user opinions by adjective-context co-clustering for game review texts. In: International conference on advances in natural language processing
3. Xin G, Shugang L, Rui M (2008) Needs assessment method for online gamers. J Shanghai Jiaotong Univ 42(12):1983–1987
4. Pang B, Lee L, Vaithyanathan S (2002) Thumbs up? sentiment classification using machine learning techniques. In: Proceedings of EMNLP
5. Davidov D, Tsur O, Rappoport A (2010) Enhanced sentiment learning using twitter hashtags and smileys. In: COLING 2010, 23rd international conference on computational linguistics, posters, vol 23–27 August 2010. Association for Computational Linguistics, Beijing, China
6. Huang L, Du C (2017) Text classification based on recurrent neural network. J Beijing Univ Chem Technol (Natural Science Edition) 44(01):98–104
7. Bi JW, Liu Y, Fan ZP et al (2019) Wisdom of crowds: conducting importance-performance analysis (IPA) through online reviews. Tour Manag 70:460–478

# Negative Sentiment Analysis of MOOC Comments Based on Machine Learning

Shuhan Liu[(✉)] and Genfu Yang

School of Media and Design, Hangzhou Dianzi University, Hangzhou, Zhejiang, China
690083804@qq.com

**Abstract.** As the MOOC learning scenarios become more diverse, users also generate more unstructured text user data during use. This study takes the five computer courses of the Chinese University MOOC network as the experimental object, and mines a total of 20,176 comments, combined with the machine learning model and high-frequency lexical analysis method to analyze the negative comments. The study found that negative comments talked about the following five topics, course content, course difficulty, teacher attributes, supporting resources, and interaction design. And each topic has a more concentrated opinion. For example, the speed of the teacher, the amount of content, the course is difficult. Based on the above research results, both the course provider and the MOOC platform can be optimized to achieve better user evaluation and development.

**Keywords:** MOOC review · Machine learning · Word frequency statistical

## 1 Introduction

Since 2012, MOOC has grown rapidly with its diversity and openness. As a new way of learning in the Internet age, its development has attracted the attention of many scholars at home and abroad. Regarding the comments of MOOC, the research and analysis of domestic and foreign researchers mainly focused on four dimensions, learning social network, curriculum completion rate, participation rate and learning achievement [1]. Joksimovic et al. analyzed the relationship between social centripetality and learning achievement [2], Cao Chuandong and other found that the role of posters will affect the attention of the post [3]. Li et al. analyzed the curriculum participation and high dropout rate of MOOC learners [4]. Poquet et al. mainly focused on the relationship between the ability of learners to interact in the MOOC forum and the completion rate of MOOC [5]. Jonathan et al. analyzed how to guide the forum to maintain a warm atmosphere [6]. Sannian et al. used the course learning data in the edX platform as a sample to analyze the learner's participation and learning effectiveness from multiple dimensions [7]. By analyzing student participation and corresponding academic performance in the course discussion area, Gillani et al. found that students who participated more actively in the discussion had better grades [8]. Therefore, this study uses a machine learning model to conduct qualitative experiments, analyze and

predict the emotions of the comments, and take the comments with negative emotions in the MOOC comments as the starting point to analyze the factors affecting the development of MOOC.

## 2    Experimental Design

This study is designed to answer the following questions: What are the aspects of the MOOC users talking about when they are dissatisfied? So we designed the following experiment. The experimental framework is shown in Fig. 1.
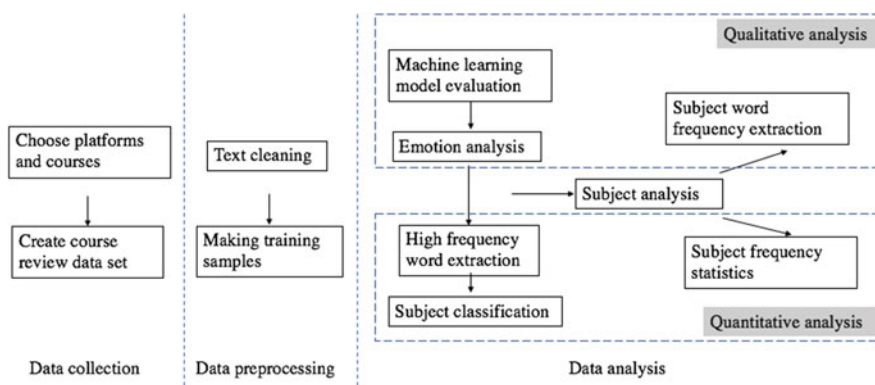


**Fig. 1.** Experimental framework

### 2.1    Data Collection

As a widely used platform in China, MOOC has been offering many free MOOC courses to the public since its launch in 2014. It is fully functional and well-established. The platform has supporting resources and an after-school interactive area for students to use, and each course has an assessment standard set by the teacher and also have an online answering assistant. Upon completion of the assessment, the student can obtain a certificate. With the advent of the era of universal programming, more and more people are trying to get in touch with computer language. Therefore, this experiment explored 20,176 comments on five computer courses of Chinese university MOOC platform, and processed and analyzed them.

### 2.2    Data Preprocessing

We first deleted the non-Chinese comments (including symbols or English only) from all the comments, and then randomly selected 3,000 of them as sample data for training. All comments and sample data were subjected to sentence segmentation, the results are shown in Table 1. The sample data is then manually labeled using a "non-negative is positive" labeling method. That is, comments with critical, suggestive, and

interrogative moods are marked as 0, and other positive or neutral comments are marked as 1. The result of the sample labeling is 617 negative and 6,264 positive, and the number of positive and negative labels differs greatly. In order to balance the sample data, 1,000 items are randomly selected in the comments marked positive, and the negative comments are used together as sample data.

**Table 1.** Sentence segmentation result

| All comments | | Training samples | |
|---|---|---|---|
| Total | 20,176 | Total | 3,000 |
| After the clause | 45,331 | After the clause | 6,863 |

We use the Python programming language to implement sample data preprocessing, first removing punctuation and stop words, and using the jieba library for word segmentation. Then use the Word2vec method to construct the word vector feature matrix. Word2vec is a shallow and double-layer neural network model used to generate word vectors. As shown in Fig. 2, it has two network structures. Finally, in order to make the model prediction results more accurate, the data of the constructed matrix is normalized.
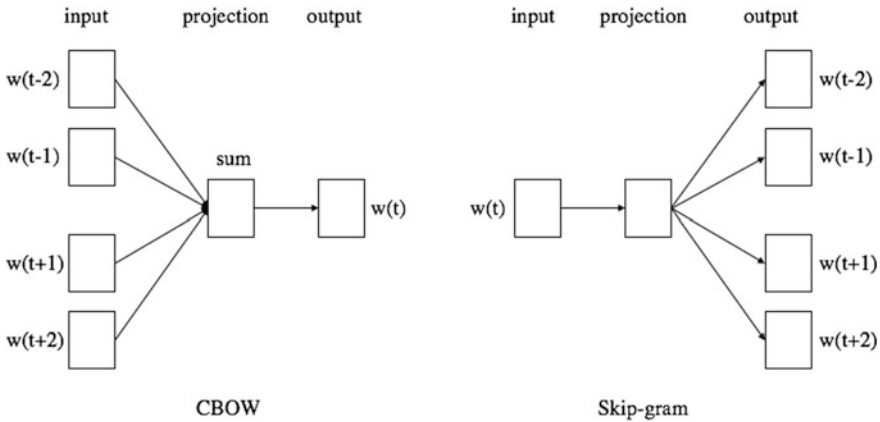


**Fig. 2.** Two structures of word2vec

### 2.3 Data Analysis

Since the performance of each classification model is different on different practical problems, the following five candidate models are prepared for training and comparison, KNN, GBT, SVM, LR, NB. In order to comprehensively evaluate the classification effect, the experiment used five indicators to evaluate the performance of the machine learning model. They are accuracy (1), precision (2), recall (3), F1 (4), and

Kappa. Of these indicators, the first four measurements were calculated from the confusion matrix (Table 2). The last indicator kappa value is used to measure the consistency between model predictions and manual annotations. Finally, the performance of the model on each metric is shown in Table 3. Therefore, we use the KNN model as a predictive model. The forecast classification results were 5,701 negative comments and 39,630 positive comments.

**Table 2.** Classification result confusion matrix

| True situation | Forecast result | |
|---|---|---|
| | Positive | Negative |
| Positive | TP | FN |
| Negative | FP | TN |

$$Accuracy\ (A) = \frac{TP + TN}{TP + FN + FP + TN} \tag{1}$$

$$Precision\ (P) = \frac{TP}{TP + FP} \tag{2}$$

$$Recall\ (R) = \frac{TP}{TP + FN} \tag{3}$$

$$\frac{1}{F1} = \frac{1}{2} \times \left(\frac{1}{P} + \frac{1}{R}\right) \tag{4}$$

**Table 3.** Machine learning model performance comparison

| | Accuracy | Precision | Recall | F1 | Kappa |
|---|---|---|---|---|---|
| KNN | 0.872 | 0.857 | 0.785 | 0.761 | 0.619 |
| SVM | 0.424 | 1.000 | 0.424 | 0.595 | 0 |
| GBT | 0.667 | 0.785 | 0.578 | 0.667 | 0.349 |
| LR | 0.772 | 0.714 | 0.740 | 0.727 | 0.532 |
| NB | 0.621 | 0.286 | 0.615 | 0.390 | 0.165 |

Then we conduct word frequency statistics on the negative comments predicted. In the existing research of Hew et al., the MOOC comments are divided into six themes for analysis [9], Therefore, this experiment is also based on the theory of participation, combined with this experiment, all negative comments are divided into the following five themes for analysis: course content, course difficulty, teacher attributes, supporting resources, and interaction design. Based on five topics, a user dictionary mandatory constraint was established to classify (Table 4). After the classification, qualitative and

quantitative analysis is performed based on the classification results. The word frequency statistics are performed on the negative comments under each attribute classification, and the results are analyzed according to the obtained results.

**Table 4.** Topic classification dictionary and topic classification quantity results

| Subject | Dictionary (number of dictionaries) | Result |
|---|---|---|
| Course content | content, key points, knowledge (16) | 1,639 |
| Course difficulty | difficulty, beginner, do not understand (8) | 365 |
| Teacher attributes | teacher, explain, speech rate (10) | 517 |
| Supporting resources | exercises, ppt, quizzes, handouts, (20) | 999 |
| Interaction design | Q&A, interaction, platform, MOOC (15) | 622 |

## 3   Results Analysis

Based on the distribution of negative comments on the number of different topics, and the results of the commentary frequency statistics under each topic, we obtained the following results.

The number of the theme of the course content is the highest. When referring to the content, the words *more* and *less* have higher frequency, *progress*, *update*, *fast* are also mentioned more, indicating that the amount of the content is the first thing students focus on and at the same time, they are also dissatisfied with the speed of content update. The number of negative evaluations on the curriculum supporting resources is second. But the aspects mentioned are many and average, such as courseware, videos, textbooks, etc. It is also important to show that in addition to the course, other factors that enhance the experience are equally important. When students consider the platform, they are more interested in the complete learning system. But at present, it seems that the platform is not perfect enough in this respect. Regarding teachers, most of them express suggestions for the speed of teachers. Since this study is only for negative comments, the result of mentioning that the teacher's comments are not much, also shows that the course teacher has been recognized by most students. Regarding platform interaction design, the most mentioned is the video, which is a problem that the video segmentation is too fragmented. The same is more of a problem that the platform start time is not flexible enough. The platform can be optimized based on this result. The number of references to the difficulty of the course is the smallest among all negative comments. This result is determined by the characteristics of the MOOC learning format. MOOC's courses are open to the public, mostly introductory courses, with a low difficulty setting.

# 4    Summary

The innovation of this research is to use a combination of machine learning model and text dictionary to conduct a comprehensive analysis of qualitative and quantitative. Taking negative comments as an analysis sample and exploring various topics, it provides an effective direction for the curriculum design of MOOC providers and the optimization of MOOC platform. The shortcoming is that due to the limitations of time and research funding, only the negative comments on the computer category MOOC are analyzed in detail, and there is no analysis of other categories and positive emotions. In the following work, we can continue to study in depth and improve it.

# References

1. Gu X, Hu B, Tingting H et al (2018) Analysis of learning behaviors in response to MOOC classroom feedback. J Huazhong Normal Univ (Natural Science) 52(180(04)):32–42
2. Dowell NMM, Oleksandra S, Joksimović S et al (2015) Modeling learners' social centrality and performance through language and discourse. Int Educ Data Min Soc
3. Chuandong C, Huaxin Z (2016) Case study of social interaction in MOOC course discussion area. China Distance Educ 3:39–44
4. Li M, Xu Y, Sun M (2015) Analysis of learning behavior of MOOC learners—taking the circuit principles as an example. Open Educ Res 21(2):63–69
5. Oleksandra P, Shane D (2016) Untangling MOOC learner networks. In: The sixth international conference. ACM Press, Edinburgh, United Kingdom, 25–29 April 2016; Proceedings of the sixth international conference on learning analytics and knowledge—LAK. ACM, pp 208–212
6. Huang J, Dasgupta A, Ghosh A et al (2014) Superposter behavior in MOOC forums. In: The first ACM conference. ACM Press, Atlanta, Georgia, USA, 4–5 March 2014; Proceedings of the first ACM conference on Learning @ scale conference—L@S, pp 117-126
7. Sannian L, Zhi L, Gao J et al (2016) An analysis of learners' learning behavior differences in the environment of MOOC. Res Audio-V Educ 10:57–63
8. Gillani N, Eynon R (2014) Communication patterns in massively open online courses. Internet High Educ 23:18–26
9. Foon HK, Chen Q, Ying T (2018) Understanding student engagement in large-scale open online courses: a machine learning facilitated analysis of student's reflections in 18 highly rated MOOCs. Int Rev Res Open Distrib Learn 19(3)

# Overview of the Reference Model for Printing Intelligent Factory

Yixue Xie[1], Linlin Liu[1(✉)], Yuling Zhang[2], Jianlong Xiang[3], and Hui Zhao[3]

[1] School of Printing, Packaging Engineering and Digital Media Technology, Xi'an University of Technology, Shanxi Province, China
369500983@qq.com
[2] China Academy of Press and Publication, Beijing Province, China
[3] Hangzhou Kelei Mechanical and Electrical Industry Co Ltd., Hangzhou Province, China

**Abstract.** In the 21st century, a new wave of technology represented by the Internet, cloud data, cloud computing, and Internet of Things has emerged around the world. In the era of high integration of information and industrialization, the concept of intelligent factory came into being. It has obvious economic benefit and technical prospect to study the intelligent factory model with the digitalization and intelligent characteristic as the core. Due to corporate resources, skills, team uneven level of each business intelligence process is unique, so this article by extensive research printing business intelligence development status quo, intelligent building printing plant of the present situation and future development trends, Established a smart printing factory reference model covering all printing companies' business direction (Li in Mach Des Manuf 4:162–164, 2006), and comprehensively expanded the content of this abstract model from 3 dimensions, 8 categories, 22 domains and 4 levels to help understanding and understanding. Printed intelligent manufacturing standardization of boundaries, objects, hierarchical relationships and internal connections of various parts, to support the development of standards related to printing intelligent manufacturing. Through the summary analysis of the company's existing production integration and management integration, as well as the future of intelligent trends, from the standardization, digital, network and intelligent four levels to guide the intelligent construction of enterprises. The ultimate goal is to establish by describing the scene of the macro from a different reference models, and based on the relevant business application case, verify the reasonableness of the model and guide.

**Keywords:** Printing intelligent factory · Reference model · Intelligent level

## 1 Introduction

The printing industry has three attributes of culture, industry and modern service industry [2]. It generally has typical order service and discrete processing manufacturing characteristics. In the process of continuous integration of information technology, the development of the printing industry presents more new models. The

printing intelligent factory is a new model developed in accordance with the requirements of the economy and the times. It is not only the execution center of printed matter production, but also the information connection center of the printing industry chain. The new printing factory based on intelligent production is the basis for realizing printing intelligent.

The construction of intelligent factory is a huge system analysis problem. Although there have been many researches on the theory and key technologies of intelligent factory construction in China, most of them are limited to partial analysis or one-sided understanding, and cannot constitute a complete intelligent factory framework. Whether it can be practically applied or not. China is only the title of manufacturing big country, not a manufacturing power. The modern processing industry is still mainly based on imitation; the product assembly business occupies a major share of the manufacturing industry, and functional innovation is the auxiliary; the automation related industry also mainly uses low-end system integration, as the main support technology and core infrastructure components are mainly imported, and the related basic support technologies are still relatively weak [3].

Based on the intelligent construction needs of printing enterprises with different development levels, this chapter establishes a general model of intelligent factories for most printing and packaging enterprises to solve the problem of missing models in the construction of intelligent factories, to help understand and knowledge the object, boundary, hierarchical relationship and internal relation of each part in printing intelligent manufacturing [4].

## 2  Reference Model for Printing Intelligent Factory

### 2.1  Reference Model

The printing intelligent factory reference model described in this chapter is a symbol of intelligent construction in the printing industry, which helps printing companies to understand and knowledge the concept and connotation of intelligent factories, so that each enterprise can find its own positioning in the reference model, and clarify the direction of intelligent development in the future. The reference model for printing intelligent factory is shown in Fig. 1. The model has certain rationality and reference.

Among them, the design, printing, storage, transportation and service of printed matter constitute the production integration dimension of the whole life cycle of printed matter.

The control, execution, management, and decision-making layers within the printing plant constitute Integrated dimension of management and control over the printing plant.

The standardization, digitization, networking and intelligence of the printing enterprise constitute the intelligent integration dimensions of printing enterprises.
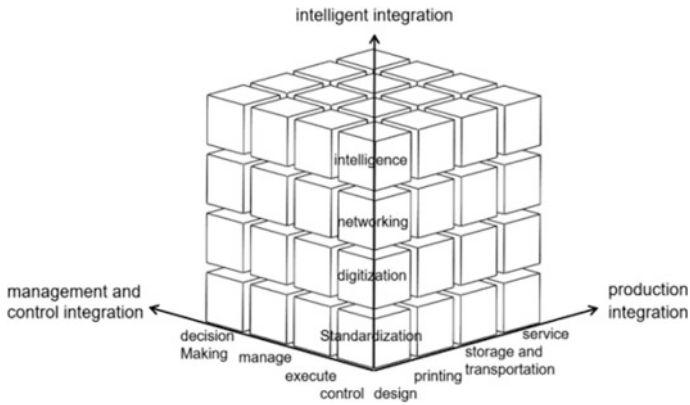
**Fig. 1.** The reference model for printing intelligent factory

## 2.2 Model Architecture

In this chapter, based on the research of China's intelligent manufacturing system architecture, industrial 4.0 reference architecture model (RAMI 4.0), the US industrial Internet reference architecture, and deepening the connotation of intelligent manufacturing [5], according to the two core dimensions of "production + control", it is decomposed into design, Printing, storage, transportation, service, control, execution, management, decision-making 8 categories of capabilities and refinement of 22 element domains, each domain is graded, each level corresponds to the corresponding requirements, constitutes a intelligent hierarchy matrix [6], model architecture and the relationship of the matrix is shown in Fig. 2.
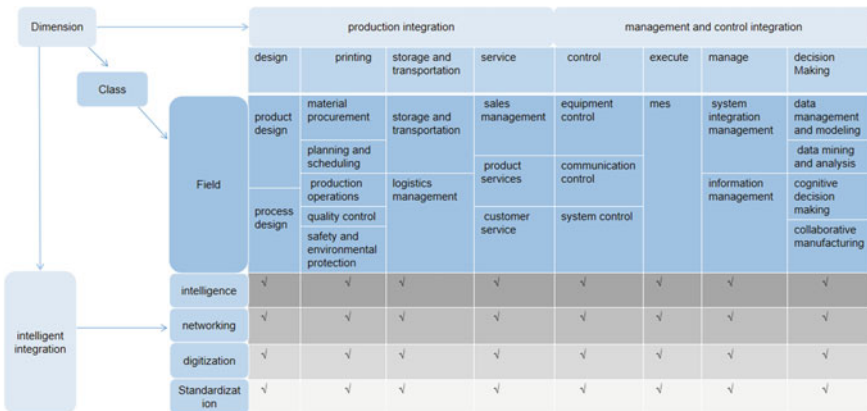


**Fig. 2.** Reference model architecture of printing intelligent factory

## 3   Model Application

### 3.1   Model Application Methodology

Depending on the company used, the intelligent printing factory reference model is divided into two manifestations—the overall model application and the single-capacity model application. The overall model application refers to the printing enterprise progressively upgrading the intelligent factory by improving some key domain sets. The construction level and the single-capacity model application refer to the printing company's ability to gradually and continuously improve the construction level of intelligent factories for a certain key category selected by the printing company [2].

### 3.2   Application of the Model

The printed intelligent factory reference model can be used for diagnostic evaluation, statistical analysis, and improvement [2]. It can be used by four major types of printing production enterprises, industry authorities, solution providers, and third-party organizations. It is suitable for all printing companies and is not restricted by enterprises.

Here is a case to explain in detail the application of the intelligent printing factory reference model.

As shown in Fig. 3, Company A's production integration dimension in the intelligent printing factory reference model covers the whole process of design, printing, storage, transportation and service; the control integration dimension covers the whole process of control, execution, management and decision-making; the intelligent level of 22 domains The level of the product varies (the product service has reached the level of intelligence, product design is still in the standardization level).
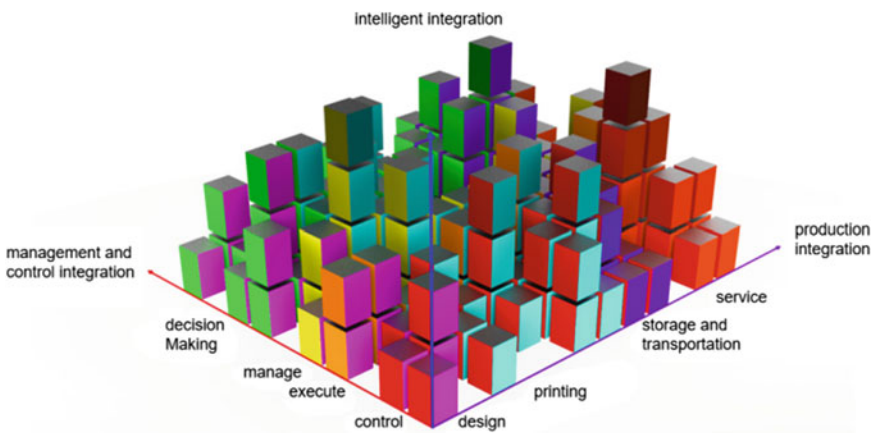


**Fig. 3.** A company reference model status

Compared with other companies, this case has established a model workshop at the production level [7], introducing advanced technologies such as lean production, APS advanced scheduling, and information management at the production site. At the management level, a lean core team has been established to achieve lean. Management, and the introduction of manufacturing execution systems, greatly improved the company's economic efficiency.

Through the analysis and comparison of the company's actual development status and the model proposed in this chapter, Company A is in the middle level of intelligent construction as a whole, Company A has realized the comprehensive coverage of Industrial Ethernet, and realized various systems by referring to industrial system software such as ERP and MES [8]. The integration management between the two, and the seamless integration between production and operation through the interconnection between the upstream and downstream systems of the enterprise. Most of the domains have reached the digital stage at the intelligent level. The next step is to upgrade all the domains of the company at the production integration level and the management integration level from the standardization level to the digital level.

## 4   Conclusion

The printing intelligent factory is the platform for the implementation of intelligent manufacturing technology in the printing industry [9]. It is the carrier of intelligent manufacturing development and the direction of current manufacturing efforts [10]. But for intelligent printing factories, there is no uniform definition, unified measurement standards, unified framework, and no solidified reference architecture [11]. Therefore, how to build a intelligent printing factory that is consistent with the strategic planning of the enterprise and meets the actual application needs of the enterprise needs to be considered. In short, the construction of intelligent factories in printing enterprises should be gradually carried out in stages and steps according to the actual situation, follow the basic ideas of intelligent manufacturing, coordinate the layout of intelligent manufacturing plans, determine the mode of intelligent manufacturing mode and the implementation path and implementation plan of intelligent factories, and comprehensively improve the manufacturing industry the overall level [12].

# References

1. Li C, Wang G, Zhou Y (2006) The research of enterprise reference model based on ontology. Mach Des Manuf 4:162–164 (in Chinese)
2. Smart Manufacturing Capability Maturity White Paper 1.0 (2016). http://wenku.baidu.com
3. Features of the Intelligent Manufacturing Pilot Demonstration Project in 2016, Ministry of Industry and Information Technology, 2016
4. National Intelligent Manufacturing Standard System Construction Guide, Ministry of Industry and Information Technology, National Standardization Management Committee
5. Institute of Software Engineering (SEI), Carnegie Mellon University (2016). www.sei.cmu.edu/cmmi
6. International Electrotechnical Commission. IEC 62264-3:2007 Enterprise-control system integration-part 3: activity models of manufacturing operations
7. Lindner, T&W, Manfred. Industrie 4.0 Readiness, Frankfurt: VDMA's IMPULS-Stiftung, 2015
8. Klett IJ (2007) Manufacturing execution system-MES. Springer, Berlin, Germany
9. Liu L, Cao C, Shang Y, Geng Z, Xuan D, China Printing Industry Intelligent Development Report (2018) Printing Technology
10. Berger R (2014) Industry 4.0 Era—How to Succeed in the Fourth Industrial Revolution
11. Smart Grid Maturity Model, NWPPS E&O Conference
12. Lu Y, Morris KC, Frechette S, Current standards landscape for smart manufacturing systems. National Institute of Standardization (NIST) Engineering

# Action Analysis of Carton Assembly Grab Robot

Peng Wang, Yuansheng Qi[✉], and Libo Dong

Beijing Institute of Graphic Communication, Beijing, China
Yuansheng-qi@bigc.edu.cn

**Abstract.** This chapter presents a method of laying a six-degree-of-freedom robot into the production line of paper printing and packaging products, and realizing the product transfer between the production lines of industrial units through the machine arm. In this chapter, Visual Components is used to simulate the grabbing action of SRA100, a six-degree-of-freedom manipulator, in the process of mobile packaging box production, and then to analyze the efficiency improvement of the manipulator in the production line. The experimental results show that the simulation manipulator can grasp the target accurately. Therefore, the author concludes that the participation of 6-DOF robots in the packaging process can save a lot of the human investment, and can ensure extremely high product qualification rate.

**Keywords:** Carton · Robot · Grab · Assembly

## 1 Introduction

Target Location and Grabbing of Robot Arm is the Core Problem in the Field of Industrial Robot Automation [1]. Currently, in the field of printing and packaging, there are few applications of mechanical arms in major enterprises, mainly relying on manual transfer of materials [2]. Robot system must determine the object it grasps and get the relative attitude of the object in order to carry out the next task [3]. When the target is within the operational range of the manipulator, target grabbing can be achieved. Experiments show the effectiveness of the proposed method [4].

## 2 Development in Carton Packaging

### 2.1 Mobile Phone Box

#### 2.1.1 Characteristic of Paper Packaging of Mobile Phone Box

Typical paper packaging design mainly refers to box design [5]. Firstly, the paper packaging mobile phone box has the advantages of light weight, low cost and simple manufacturing process also shown in Fig. 1, but due to its material types, it is more vulnerable to damage either processing or sales. Simple appearance and complex interior of mobile phone boxes cause many defects.
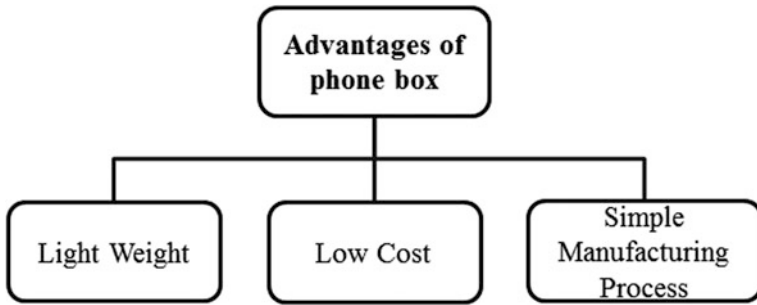
**Fig. 1.** Advantages of phone box

### 2.1.2 Physical Characteristics of Mobile Box

*Mechanical Properties*. Since the material of mobile phone box is usually paper therefore, its physical characteristics are same as paper. Paper is an orthotropic material. The micro-structure of paper fibers determines the specific mechanical properties of different aspects. It is worth noting that the fiber distribution is generally cross-network distribution and forward distribution. The base paper with cross-network distribution has high resistance to breakage, ring pressure and folding resistance; the corresponding index of the raw paper distributed in the forward direction is low. In general, the cardboard produced has a grain direction. It is assumed that the paper is an orthotropic linear elastic material, and its thickness is very thin, and the stress is equal in the thickness direction. The cardboard is composed of fibers. In the papermaking process, it is oriented along the machine direction, called the longitudinal or MD direction; the direction perpendicular to the fibers is called the transverse or CD direction. If we consider MD in x direction, the CD in y direction, and the thickness in z direction, a coordinate system formed at the center of the cardboard is shown in Fig. 2.
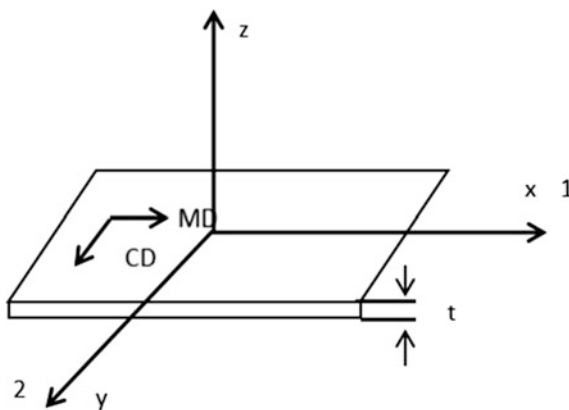


**Fig. 2.** Structure dimensions of paper

After analysis, most of the mobile phone boxes can withstand the grasp of the mechanical arm, and rarely cause damage to the appearance.

## 3   Grasping Analysis of Manipulator

### 3.1   Prospect and Present Situation of Grabbing Manipulator

Experiments are performed by using Visual Components software for reference, and one of the six-degree-of-freedom manipulators SRA100 is chosen, which simulates the process flow in packaging production and recognize the manipulator's grasping carton and carton assembly.

### 3.2   Grasping Accuracy Analysis of Manipulator

Since the rotational angle of the manipulator is limited, the rotation angles of 0 to 60 and −60 to 0 are selected for test. By successfully simulating the grabbing action of SRA100 manipulator on a brand mobile phone box, we can put forward the idea that this grabbing action can also transport materials between different machines.

### 3.3   Motion Analysis of Hand Grabbing Mobile Box

Position and posture requirements of manipulators. The main coordinate system must be calibrated or determined for the manipulator to grasp the target as shown in Fig. 3 (Fig. 4).
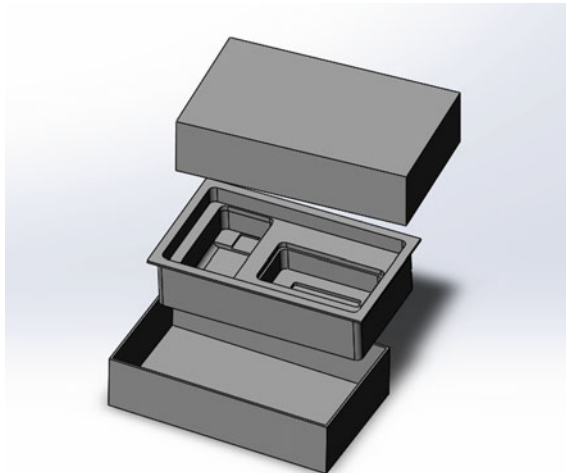


**Fig. 3.**   Mobile phone box
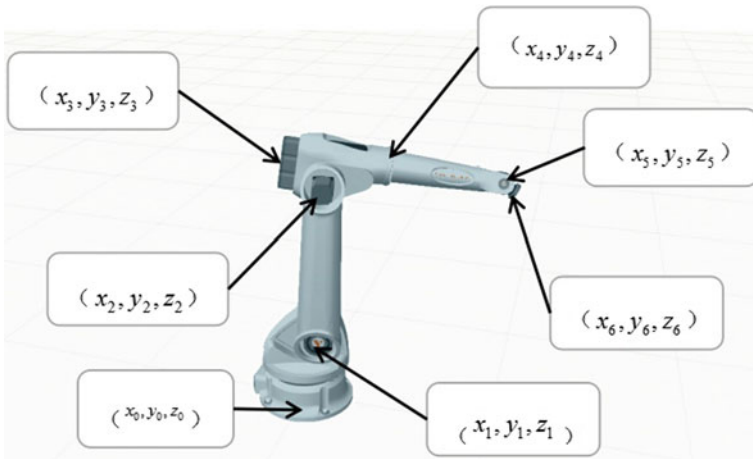
**Fig. 4.** Six node coordinates and basic coordinates of robot arm



**Fig. 5.** The manipulator is ready to grab according to the program instructions
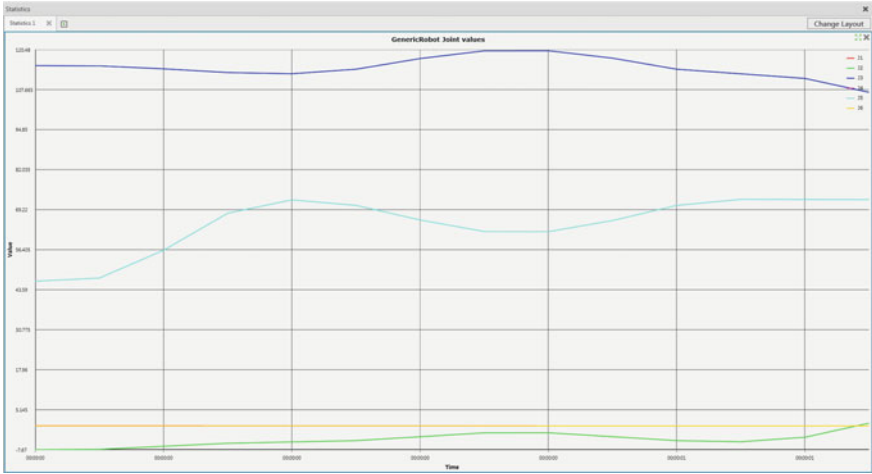
**Fig. 6.** Stress diagram of Fig. 5
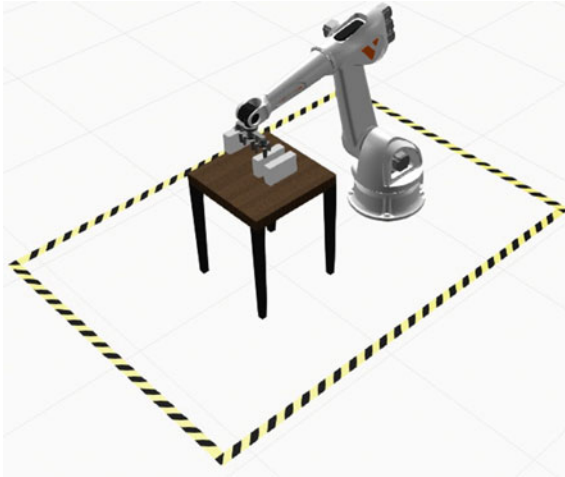


**Fig. 7.** Manipulator arm grabs cartons
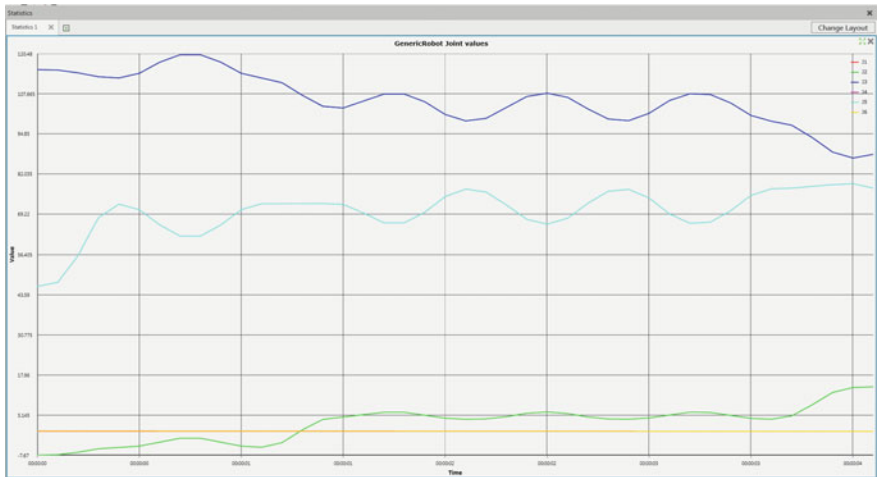
**Fig. 8.** Stress diagram of Fig. 7

# 4  Simulation of Carton Grabbing and Stress Diagram of Joints
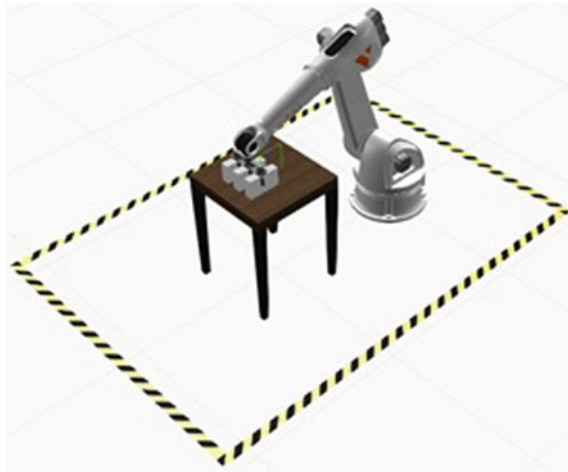


**Fig. 9.** Put down the mobile phone box with the manipulator arm
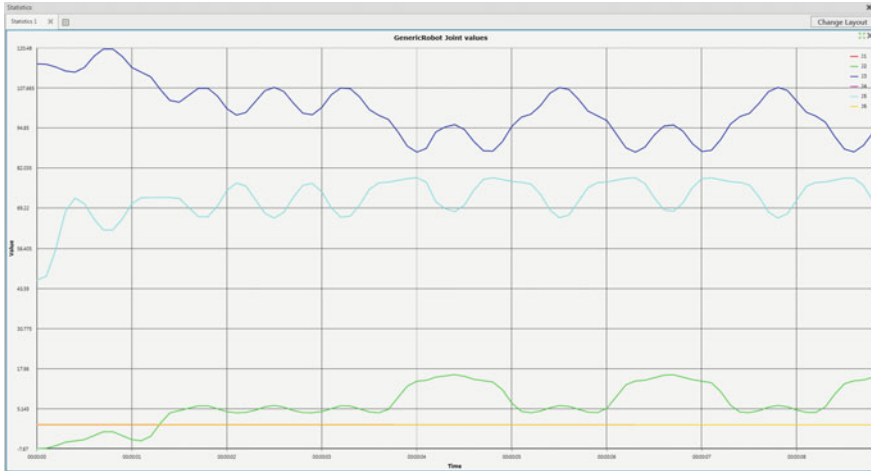
**Fig. 10.** Stress diagram of Fig. 9

Stage 1: The manipulator is ready to grab according to the program instructions, as shown in Figs. 5 and 6.

Stage 2: Manipulator arm grabs cartons, as shown in Figs. 7 and 8.

Stage 3: Put down the mobile phone box with the manipulator arm, as shown in Figs. 9 and 10.

## 5   Conclusions

This experiment mainly simulates the logistics applications of mechanical arm printing and packaging enterprises through Visual Components. The simulation results show that the manipulator can grasp and carry cartons directly in different production lines.

The manipulator moves to a specific position, judges the position coordinates of the grasping target, the six-degree-of-freedom manipulator starts to operate, activates the built-in drive of the top mechanical gripper, and moves the target to the specified position precisely after grasping the target, and repeats the grasping action. According to the node value in Figs. 6, 8 and 10, it can be seen that in the process of grasping cartons, the node J6 values remain unchanged, the node J5 values show periodic changes when grasping cartons, the node J2 reaches the peak value when the manipulator grasps cartons, and the node J3 reaches the peak value when the manipulator lowers the cartons. Therefore, it can be concluded that the six-degree-of-freedom manipulator only involves the movement of three nodes when grasping the carton.

The transfer and exchange of products between printing and packaging production lines are repetitive tasks, while the manipulator has the advantages of short working time, high efficiency, continuous and uninterrupted work to save the cost of enterprises.

# References

1. Guyu Z, Xu X, Zheng C, Multi-objective positioning and grasping of robotic arm based on CICP. Comput Eng Appl 1–9, 21 Jan 2019
2. Du X, Cai Y, Lu T, Wang S, Yan Z (2017) A manipulator grasping method based on deep learning. Robot 39(06):820–828 + 837
3. Li W, Zhang Y, Wang P, Xiong R, An iterative optimization method for mobile grasp planning. Robot 1–11, 21 Jan 2019
4. Han E, Liu H, Huang W, Sun F, Gao M (2013) Kinect-based manipulator target capture. J Intell Syst 8(02):149–155
5. Yang D (2005) Java solution of packaging carton CAD system. Xi'an University of Technology

# Printing Material and Related Technology

# Research on Analytical Method of Migratable Fluorescent Whitening Agent in Paper Products

Hui Wang[(✉)], Xianrui Zhang, Yuanmin Wang, Beiqing Huang, and Xianfu Wei[(✉)]

School of Printing and Packaging Engineering, Beijing Institute of Graphic Communication, Beijing, China
{wanghui,weixianfu}@bigc.edu.cn

**Abstract.** This research is focused on the quantitative analysis of migratable fluorescent whitening agent (FWA) VBL in paper products according to standards of GB/T 27741-2018 and CY/T 132.1-2015. Analytical method validation is carried out to investigate linearity, precision and accuracy. The analytical method validation results show that the relative standard deviation (RSD) is 1.52–2.02% and the recovery is 55.1–56.4% in the analysis of migratable VBL by ultraviolet visible (UV-Vis) spectrophotometer. Meanwhile, several factors affecting the quantitative determination result are discussed. Moreover, by using photoluminescence spectrophotometer and an optimal extraction method, the RSD is 3.24% and the accuracy has been improved significantly, which generates a recovery of 90.7%. This research is of great help for the development of the determination of migratable FWAs in paper products.

**Keywords:** Fluorescent whitening agent VBL · Analytical method validation · UV-Vis spectrophotometry · Photoluminescence spectrophotometry

## 1 Introduction

Fluorescent whitening agent (FWA) is a kind of organic compounds widely used in paper and printed reading products due to the ability of fluorescent emission at the wavelength of 400–500 nm, which has visually whitening effect by compensating for the yellowish shade of products [1]. However, abuse of FWAs in products may represent a health hazard to consumers; for instance, the migratable FWAs are suspected to have potential risks for human beings [2, 3].

In recent years, the government has enacted a series of standards that stipulate the limits and detection methods for migratable FWAs in products [4, 5]. VBL (C.I.85, CAS No. 12224-06-5) is one of the most widely used FWAs in paper and printed products. This research is focused on the quantitative analysis of migratable VBL in paper products according to standards of GB/T 27741-2018 "paper and board: determination of migratable fluorescent whitening agents" [4] and CY/T 132.1-2015 "green printing: the assessment criterion of products conformity, part 1: printed readings" [5]. Analysis method validation is carried out to investigate linearity, precision and

accuracy. Meanwhile, several operation procedures in the analysis method are discussed to optimize the quantitative determination result.

## 2    Experimental

### 2.1    Chemicals

VBL and ammonia (25–28%) were of AR grade and purchased from Macklin Biochemical Technology Co., Ltd (China). Ultra-pure water with resistivity of 18 MΩ cm was obtained with an Elix Advantage water purification system (Merck Millipore, USA).

### 2.2    Instrumentation

Samples were weight by an XS105DU analytical balance (Mettler Toledo, USA). THZ-82 water-bath oscillator (Changzhou Guohua Electric Co., Ltd, China) was used to extract migratable VBL from papers. Ultraviolet-visible (UV-Vis) absorption spectra were recorded by aLambda25 spectrophotometer (Perkin Elmer, USA). Photoluminescence (PL) spectra were characterized by a RF-5301PC spectrofluorophotometer (Shimadzu, Japan).

### 2.3    Sample Preparation

Offset printing paper was purchased from local markets in Beijing, China. Before analysis, samples were stored at 25 °C with a humidity of 60% RH for 48 h. The extraction of migratable VBL was performed according to GB/T 27741-2018 [4] and CY/T 132.1-2015 [5]. The extraction was analyzed by spectrophotometer and spectrofluorophotometer, respectively. All the operations were carried out in the dark at room temperature.

### 2.4    Preparation of VBL Standard Solutions

A series of standard solutions with the concentration of 1.0, 2.0, 5.0, 10.0, 15.0, 20.0, 25.0, 30.0 and 35.0 mg/L were prepared by diluting with ammonia solution (pH = 8.0–9.0) according to procedures described in GB/T 27741-2018 [4] and CY/T 132.1-2015 [5]. All the chemicals are used and stored under the condition protected from light.

### 2.5    Calibration and Statistics

#### 2.5.1    Calibration Method in UV-Vis Spectrophotometry

A typical procedure for the determination of migratable VBL by UV-Vis spectrophotometry was referred from GB/T 27741-2018 [4] and CY/T 132.1-2015 [5]. For standard GB/T 27741-2018, content of migratable VBL ($\omega$, mg/kg) in a sample was calculated from Eq. 1 [4]:

$$\omega = \frac{(c - c_0) \times V \times 1000}{m \times 1000} \tag{1}$$

where $m$ is the weight of sample and $V$ is the volume of extract, respectively. $c$ and $c_0$ are concentrations of VBL in extracts from sample and blank control, which are calculated from Eq. 2:

$$c = \frac{A - b}{k} \tag{2}$$

where $A$ is the absorbance at 348 nm while $k$ and $b$ are slop and intercept obtained from the linear regression equation, respectively.

According to standard CY/T 132.1-2015, content of migratable VBL ($\omega$, mg/kg) in a sample was calculated from Eq. 3 [5]:

$$\omega = \frac{[(1.2A_{348} - 0.5A_{305}) - b] \times V}{k \times m} \tag{3}$$

where $A_{348}$ and $A_{305}$ are absorbance at 348 nm and 305 nm, respectively.

### 2.5.2 Calibration Method in PL Spectrophotometry

Before the testing experiments, the excited spectrum of VBL standard solution (1 mg/L) was characterized to determine the maximum excitation wavelength. By employing the maximum excitation wavelength, PL spectra of standard solutions (1.0–35.0 mg/L) were characterized and values of PL intensity at the maximum emission wavelength were recorded to fit a linear regression equation. Then PL spectra of extracts and the control sample at the corresponding wavelength were characterized, and concentrations of migratable VBL in extracts were obtained by solving the linear regression equation. The content of VBL ($\omega$, mg/kg) in a sample was calculated from Eqs. 1 and 2, using PL intensity at the maximum emission wavelength instead of absorbance at 348 nm.

## 2.6 Quality Assessment of Quantitative Analysis Results

Precision of the method was given as relative standard deviation (RSD) of $\omega$. Recovery tests were carried out to evaluate the accuracy of the method.

# 3 Results and Discussion

## 3.1 Analytical Method Validation of Standard GB/T 27741-2018

### 3.1.1 Linearity of Calibration Curve

Figure 1 illustrates UV-Vis absorption spectra and the fitting curve of VBL standard solutions. According to the linear fitting result, the linear regression equation was $y = 0.0345x + 0.0074$ ($R^2 = 0.9998$), showing a good linearity relationship between absorbance and concentration of VBL ranged from 1 to 20 mg/L.
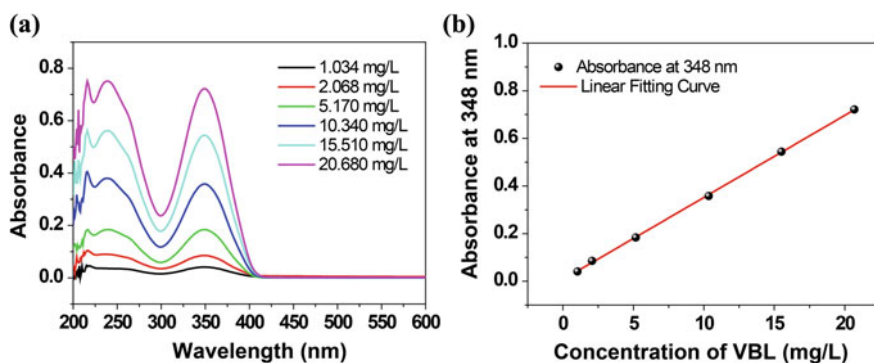
**Fig. 1.** **a** UV-Vis absorption spectra and **b** linear fitting result of VBL standard solutions with concentrations in range of 1.0–20.0 mg/L

### 3.1.2    Precision and Accuracy

The precision of the analytical method is evaluated by measuring homogenized samples for multiple times and calculating the RSD. In this experiment, 10 measurements were taken and the analytical results of migratable VBL are listed in Table 1. The RSD is 1.52% and able to meet the requirement of precision in quantitative determination.

**Table 1.**  Measurement results of migratable VBL according to GB/T 27741-2018

| No. | $m$ (g) | $A_{348}$ | $c$ (mg/L) | $\omega$ (mg/kg) | Average of $\omega$ (mg/kg) | RSD (%) |
|-----|---------|-----------|------------|------------------|------------------------------|---------|
| 1 | 1.0139 | 0.884666 | 25.4646 | 1255.7755 | 1285.5143 | 1.52 |
| 2 | 1.0212 | 0.899876 | 25.9061 | 1268.4158 | | |
| 3 | 1.0117 | 0.900639 | 25.9283 | 1281.4210 | | |
| 4 | 1.0164 | 0.902438 | 25.9805 | 1278.0644 | | |
| 5 | 1.0131 | 0.924060 | 26.6081 | 1313.2034 | | |
| 6 | 1.0167 | 0.910333 | 26.2097 | 1288.9577 | | |
| 7 | 1.0177 | 0.918255 | 26.4396 | 1298.9890 | | |
| 8 | 1.0143 | 0.922050 | 26.5498 | 1308.7737 | | |
| 9 | 1.0144 | 0.890223 | 25.6259 | 1263.1073 | | |
| 10 | 1.0180 | 0.918135 | 26.4361 | 1298.4351 | | |

Recovery tests were carried out to evaluate the accuracy of the method. Homogenized extracts containing known concentration of migratable VBL were prepared and a spike solution of VBL was added directly to each extract. The additional standards were of three concentration levels and 3 parallel tests were taken at each concentration level. Each sample was analyzed with the described overall method. As listed in Table 2, the recovery from the spiked solution is no more than 55.1%. The results are not satisfactory and the possible influencing factors will be analyzed in detail later.

**Table 2.**  Results of recovery tests according to GB/T 27741-2018

| Standard addition (mg/kg) | Average of recovery (%) | RSD (%) |
|---|---|---|
| 550 | 25.9 | 5.31 |
| 1100 | 30.6 | 5.44 |
| 1650 | 55.1 | 4.57 |

## 3.2    Analytical Method Validation of Standard CY/T 132.1-2015

The quantitative analysis method of migratable VBL based on UV-Vis spectropho-tometry described in CY/T 132.1-2015 is extremely similar with GB/T 27741-2018. Procedures for evaluating precision and accuracy are as the same as those which are described in Sect. 3.1.2. According to the results of analytical method validation, the precision is 2.02% and the recovery from the spiked solution is no more than 56.4%, respectively. The experimental results are listed in Tables 3 and 4. Potential influencing factors on the accuracy will be discussed in the next chapter.

**Table 3.**  Measurement results of migratable VBL according to CY/T 132.1-2015

| No. | $m$ (g) | $A_{348}$ | $A_{305}$ | $\omega$ (mg/kg) | Average of $\omega$ (mg/kg) | RSD (%) |
|---|---|---|---|---|---|---|
| 1 | 1.0139 | 0.884666 | 0.553304 | 1113.0442 | 1150.4013 | 2.02 |
| 2 | 1.0212 | 0.899876 | 0.557678 | 1127.9200 | | |
| 3 | 1.0117 | 0.900639 | 0.551546 | 1144.2233 | | |
| 4 | 1.0164 | 0.902438 | 0.551360 | 1142.1477 | | |
| 5 | 1.0131 | 0.92406 | 0.547516 | 1185.7927 | | |
| 6 | 1.0167 | 0.910333 | 0.543905 | 1160.6564 | | |
| 7 | 1.0177 | 0.918255 | 0.562461 | 1159.8416 | | |
| 8 | 1.0143 | 0.92205 | 0.554423 | 1175.9967 | | |
| 9 | 1.0144 | 0.890223 | 0.545000 | 1127.9772 | | |
| 10 | 1.0180 | 0.918135 | 0.552475 | 1166.4131 | | |

**Table 4.**  Results of recovery tests according to CY/T 132.1-2015

| Standard addition (mg/kg) | Average of recovery (%) | RSD (%) |
|---|---|---|
| 550 | 27.9 | 5.42 |
| 1100 | 31.2 | 5.22 |
| 1650 | 56.4 | 3.92 |

### 3.3 Influence Factors in the Determination of Migratable VBL by UV-Vis Spectrophotometry

In summary, rather precise results could be obtained from multiple parallel experiments. However, the poor recovery reveals that the accuracy is not satisfactory. Herein, several potential influence factors in the determination of migratable VBL by the means of UV-Vis spectrophotometry are discussed.

#### 3.3.1 Spectral Interference

One of the factors that may affect the accuracy of the analytical results is the spectral interference from impurities present in the sample, for instance, lignin, dyes, pigments, additives or other compounds. In order to study the spectral interference of impurities, UV-Vis spectra of a VBL standard solution, an extract of off-set printing papers and an extract of blank sample were characterized, as shown in Fig. 2. It is obvious that there is a significant absorption around 300–330 nm in the extract of offset printing paper, which may interfere with the quantitative wavelength at 348 nm [4–7]. It is noted that the determination equation (Eq. 3) proposed by CY/T 132.1-2015 takes the method of correcting the absorption at 308 nm to improve the accuracy, however, considering the diversity and complexity of impurities, this simple processing method might be not universal and difficult to completely eliminate the interference.
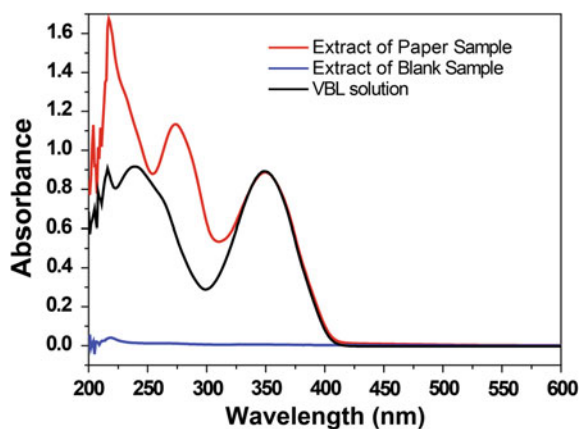


**Fig. 2.** UV-Vis absorption spectra of a VBL solution, a sample extracted from offset printing papers and a blank sample as control

#### 3.3.2 Photoisomerization of VBL

VBL is a kind of stilbene compounds which contain *trans* and *cis* isomers. With the irradiation of UV light, *trans* isomers of absorb photons and transform into *cis* isomers, which is represented in the UV-Vis absorption spectrum as a change in both intensity and wavelength of the maximum absorbance. In order to confirm the interference caused by sunlight during the experimental process, VBL was soluted in diluted ammonia (pH = 8.0–9.0) and its UV-Vis absorption spectrum was characterized before and after irradiation in sunlight for 15 min.

As shown in Fig. 3, with the influence of sunlight, the absorbance at 348 nm obviously decreases and a significant blue shift occurs, while the absorbance at shorter wavelength increase, indicating the occurring of photoisomerization. Therefore, it is important to avoid light during the use and storage of both standard materials and samples to be tested.
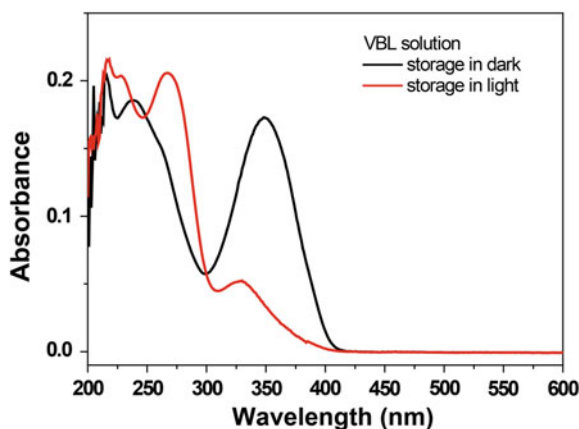


**Fig. 3.** UV-Vis absorption spectra of VBL solutions stored in dark and light

### 3.3.3   Volume of Extract

According to the experimental procedure described in GB/T 27741-2018 and CY/T 132.1-2015, migratable VBL in the sample was extracted by 50 mL ammonia solution. The concentration of VBL in the extract and sample ideally reached dynamic equilibrium after stirring for 1 h at 80 °C. However, for the sample with high content of VBL, 50 mL of ammonia solution is easily saturated by migratable VBL, resulting in a large error in recovery test.

In order to verify this hypothesis, measurements were taken by preparing extracts using different volumes of ammonia solution (pH = 8.0–9.0). The calibration method was referred to GB/T 27741-2018, using Eqs. 1 and 2.

Table 5 illustrates the measurement results of migratable VBL in different volumes of extracts. Compared with data in Table 1, when the volume of the extract is increased from 25 to 75 mL, the determination result of VBL is continuously increased, while

**Table 5.** Measurement results of migratable VBL using different volumes of extracts

| Volume of extract (mL) | $\omega$ (mg/kg) | Average of $\omega$ (mg/kg) | RSD (%) | Standard addition (mg/kg) | Recovery (%) |
|---|---|---|---|---|---|
| 25 | 1169.7699 | 1167.7716 | 0.24 | – | – |
|  | 1165.7732 |  |  |  |  |
| 75 | 1383.1672 | 1382.3320 | 0.09 | – | – |
|  | 1381.4968 |  |  |  |  |
| 100 | 1378.1825 | 1389.5347 | 1.16 | 1100 | 47.6 |
|  | 1400.8869 |  |  |  |  |

when the volume of the extract continues to increase to 100 mL, the determination result of VBL is almost constant. This experiment confirms the previous hypothesis, indicating that the volume of the extract has a greater impact on the measurement results. Furthermore, a recovery test was taken using 100 mL of the extract and repeated three times. The average recovery from the spike solutionis 47.6% at the standard addition level of 1100 mg/kg, which is promoted compared with the result in Table 2.

### 3.4     Analytical Method Based on PL Spectrophotometry

### 3.4.1     Selection of Excitation Wavelength

First of all, excitation and emission spectra of VBL standard solution was characterized to determine the appropriate test conditions. As illustrated in Fig. 4, the maximum emission intensity could be obtained by employing the excitation wavelength at 348 nm. Subsequently, emission spectrum was characterized using an excitation wavelength of 348 nm and the corresponding maximum emission was 435 nm. Therefore, in the subsequent experimental procedures, PL spectra of VBL standard solutions and extracted samples were measured at an excitation wavelength of 348 nm, and corresponding PL intensities at 435 nm were recorded in the calibration and quantitation.
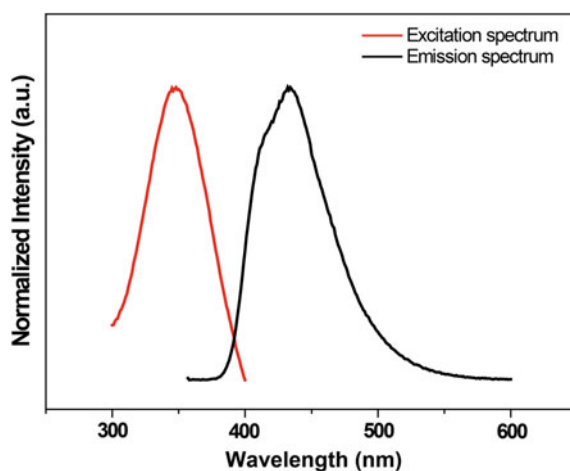


**Fig. 4.**  Excitation and emission spectra of VBL standard solution (1 mg/L)

### 3.4.2     Linearity of Calibration Curve

PL spectra of 9 VBL standard solutions were characterized and illustrated in Fig. 5a. It is indicated that as the concentration of VBL increases from 1.0 to 35.0 mg/L, the PL emission intensity increases. Linear regression equation was obtained by fitting PL emission intensity at 435 nm to the concentration of VBL. It is worth noting that there is a good linearity relationship ($R^2 > 0.999$) in any of the five concentration ranges. As illustrated in Fig. 5b, the linear fitting result from all of the 9 concentrations was

$y = 26.0118x + 10.7014$ with $R^2$ of 0.9996, showing a significantly expanded linear range than spectrophotometry. This indicates that PL spectroscopy could have better applicability for samples with high VBL migration without additional dilution procedures.
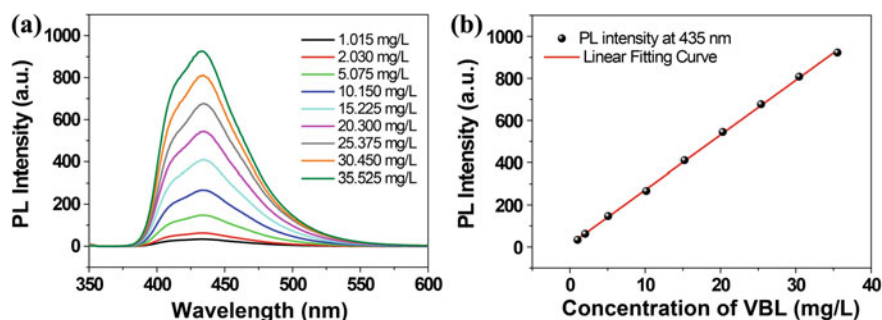


**Fig. 5.** **a** PL spectra and **b** linear fitting result of VBL standard solutions with concentrations in range of 1.0–35.0 mg/L

### 3.4.3    Precision and Accuracy

As shown in Table 6, multiple parallel measurements were taken to examine the precision of the analytical method. By the means of PL spectrophotometry, the quantitative detection result of migratable VBL is 1957.5187 mg/kg, which is higher than that resulted from UV-Vis spectrophotometry. One possible reason is that PL spectra could avoid the interference of lignin and other impurities on absorption spectra. Besides, attenuation and blue shift of absorbance ascribed to illumination exposure could also be avoided. The RSD of measurement results is 3.24%, which means a slightly reduced precision compared to analytical methods based on UV-Vis spectrophotometry; however, it is still acceptable in practical applications.

**Table 6.** Measurement results of migratable VBL according to analytical method based on PL spectrophotometry

| $m$ (g) | PL intensity at 435 nm | $\omega$ (mg/kg) | Average of $\omega$ (mg/kg) | RSD (%) | Standard addition (mg/kg) | Recovery (%) |
|---|---|---|---|---|---|---|
| 1.0013 | 519.475 | 1953.3809 | 1957.5187 | 3.24 | 1100 | 90.7 |
| 1.0017 | 490.116 | 1839.9253 | | | | |
| 1.0019 | 522.396 | 1963.4193 | | | | |
| 1.0021 | 528.247 | 1985.4737 | | | | |
| 1.0012 | 524.617 | 1973.3202 | | | | |
| 1.0013 | 539.325 | 2029.5928 | | | | |

To evaluate the accuracy of the analytical method based on PL spectrophotometry, the recovery test was executed with a standard additional level of 1100 mg/kg and repeated twice. The recovery from the spiked solution was 90.7%, which is significantly improved compared to the analytical method validation results of GB/T 27741-2018 and CY/T 132.1-2015. The experimental results show that the accuracy of analysis results of migratable VBL has been greatly promoted with the method of PL spectrophotometry.

## 4    Conclusions

This research is focused on the determination of migratable FWA VBL in offset printing paper products. According to determination methods based on UV-Vis spectrophotometry described in GB/T 27741-2018 and CY/T 132.1-2015, analytical method validation is taken by the investigation of linearity, precision and accuracy. Spectral interference and several experimental processes are discussed. PL spectrophotometry is demonstrated to improve the reliability of the analytical method and the validation is implemented. Experimental results show that the analytical method of migratable VBL based on PL spectrophotometry has excellent linearity in the range of 1.0–35.0 mg/kg with good precision and a recovery of 90.7%, which is a significant promotion of accuracy. This research is of great help for the development of standards for the determination of migratable FWAs in paper products.

## References

1. Jiang DG, Chen LS, Fu WS et al (2015) Simultaneous determination of 11 fluorescent whitening agents in food-contact paper and board by ion-pairing high-performance liquid chromatography with fluorescence detection. J Sep Sci 38(4):605–611
2. Escabasse JY, Ottenio D (2002) Food-contact paper and board based on recycled fibres: regulatory aspects—new rules and guidelines. Food Addit Contam 19(4):79–92
3. Yu Y, Wang XH, Fei Q et al (2017) On-site determination of the migration amount of fluorescent whitening agents from paper to finger by fluorescence spectrophotometry. Anal Methods 9(3):465–472
4. State Administration for Market Regulation, Standardization Administration of People's Republic of China (2018) GB/T 27741-2018 paper and board—determination of migratable fluorescent whitening agents. Standards Press of China, Beijing
5. State Administration of Press, Publication, Radio, Film and Television of The People's Republic of China (2015) CY/T 132.1-2015 green printing—the assessment criterion of products conformity—part 1: printed readings. Standards Press of China, Beijing

6. Li LL (2016) Application of multivariate spectral analysis on the testing of paper-related materials. Dissertation submitted for the degree of master, South China University of technology, Guangzhou

7. Shi H (2013) Study on the interaction between lignin and optical brightening agent. Dissertation submitted for the degree of master, Tianjin University of science and technology, Tianjin

# Luminescent Properties of BisBenzimide H Doped with DNA-CTMA and Its Application in Fluorescent Ink

Rong Cao, Beiqing Huang, Xianfu Wei, and Lijuan Liang$^{(\boxtimes)}$

Beijing Institute of Graphic Communication, Beijing, China
`lianglijuan@bigc.edu.cn`

**Abstract.** In recent years, fluorescent dyes have attracted more and more attention in the field of packaging anti-counterfeiting because of their good concealment and convenient color detection. The luminescent properties of the fluorescent dye bisBenzimide H doped with DNA lipid complex (DNA-CTMA) are discussed. The maximum luminescence intensity of the bisBenzimide H solution was found to be 320 by testing the absorption spectrum and the fluorescence spectrum. After doping DNA-CTMA, the luminescence intensity of the solution is reduced but the luminescence intensity of the film is increased. This study laid solid foundation for the new packaging anti-counterfeiting technology.

**Keywords:** Biomaterials · DNA-CTMA · BisBenzimide H · Fluorescent ink

## 1 Introduction

Anti-counterfeiting technology is a cross-disciplinary subject involving many fields such as optics, chemistry, physics, printing technology, and packaging technology [1]. BisBenzimide H is a benzimidazole dye, which is a common dye for DNA, chromosomes and nucleus. It has membrane permeability, fluorescence stability and non-toxicity [2, 3]. DNA is a double-helical molecular structure that is hereditary and can guide the biological development and life function. There are four bases in the double helix structure, which are connected by hydrogen bonds and are p–p electron overlapping structures [4, 5]. At the same time, there are some main grooves and narrow small grooves in the DNA, so that many dyes such as bisBenzimide H, rare earth ions can be easily embedded in the grooves. The binding constant is high, which can enhance the fluorescence emission intensity. Based on this, this chapter develops a fluorescent complex-bisBenzimide H/DNA-CTMA for anti-counterfeiting printing, which can be used to formulate new anti-counterfeiting inks for packaging anti-counterfeiting.

In this chapter, we discuss the luminescence properties of bisBenzimide H. The DNA-CTMA lipid complex is prepared and mixed with bisBenzimide H to investigate its effect on the luminescence properties.At the same time, the interaction between DNA-CTMA and fluorescent dyes is analyzed based on molecular structure in solution and film state.

## 2  Experimental

### 2.1  Materials

DNA, derived from salmon fish was purchased from Japan. Cexadecyltrimethyl-ammonium bromide (CTMA) was purchased from TCI. BisBenzimide H was purchased from Sigma-Aldrich.

### 2.2  Instruments

The solution was prepared by using the MS-H magnetic stirrer. The DNA-CTMA complex was dried using a vacuum oven. The UV-Vis absorption of the solution was measured using the 2501 PC UV-Vis spectrophotometer. The solution emission spectrum and excitation spectrum were measured using the RF-5301PC fluorescence spectrometer.

### 2.3  Preparation of DNA-CTMA

DNA and CTMA were dissolved in ultrapure water and stirred about 30 min through using magnetic stirrer, respectively. Then both the solutions were mixed and stirred for about 20–30 min, and the resulting solid was filtered and dried for at least 24 h to obtain the DNA-CTMA compound. The compound was dissolved in the n-butyl alcohol, and then the DNA-CTMA solution was obtained [6].

### 2.4  Preparation of BisBenzimide H/DNA-CTMA

Weighing 0.001, 0.003, 0.004, 0.005, 0.007, 0.009 g of bisBenzimide H powder. It was dissolved in 2 ml of butanol solution to prepare bisBenzimide H solution. Taking 2 ml of different concentrations of bisBenzimide H solution and 10 mmol/L of DNA-CTMA solution respectively, then mix.

## 3  Results and Discussion

### 3.1  Luminescence Properties of Different Concentrations of Bisbenzimide H Solution

In order to study the luminescence properties of $Eu(TTA)_3(H_2O)_2$ complexes, $Eu(TTA)_3(H_2O)_2$ solutions with concentrations ranging from 1 to 9 mmol/L were prepared. The absorption spectra were tested as shown in Fig. 1. There are two absorption bands at the wavelengths of 260 and 340 nm, respectively, and the absorbance increases with increasing concentration. By analysis, the electronic transition of the conjugated system in the benzene ring of bisBenzimide caused an absorption peak at 260 nm, and the peak at 340 nm was attributed to the $\pi$–$\pi^*$ transition of the TTA ligand.
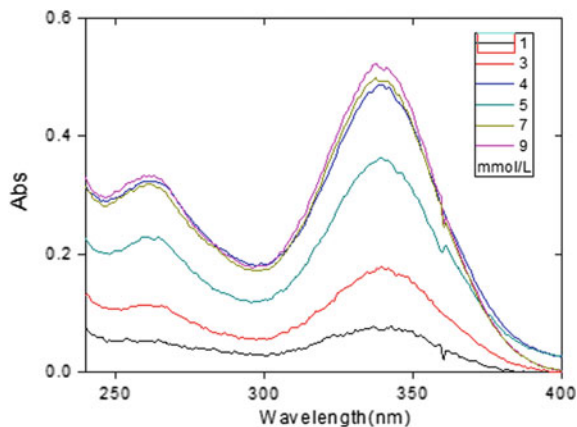
**Fig. 1.** UV spectra of different concentrations of bisBenzimide H solution

As can be seen from Fig. 2a, the maximum emission wavelength of the bisBenzimide H at 340 nm excitation wavelength is 496 nm, so the bisBenzimide H shows bright yellow-green light. As shown in Fig. 2b, as the concentration of the solution gradually increases, the fluorescence intensity of the bisBenzimide H increases first and then decreases. This is because the increase in concentration causes an increase in the number of luminescent groups in the solution, and the luminescence intensity increases. When the concentration exceeds 4 mmol/L, the concentration of the luminescent group is too high, and self-quenching occurs, and the luminescence intensity of the solution is lowered.
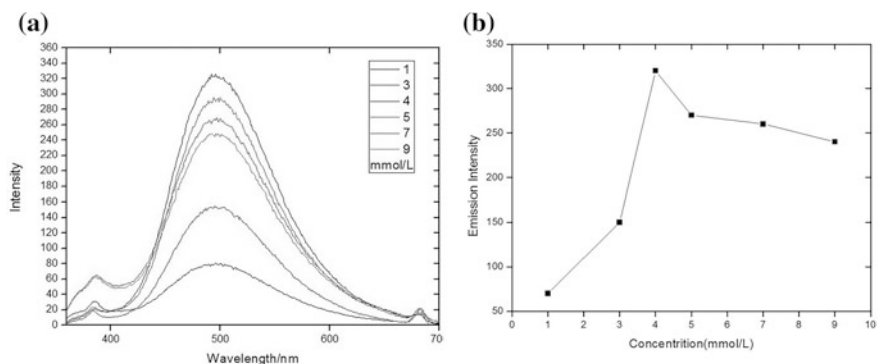


**Fig. 2. a** Emission spectrum of different bisBenzimide H solution concentrations (emission wavelength 340 nm); **b** peak plot of fluorescence intensity of different bisBenzimide H solutions

### 3.2  Luminescence Properties of Bisbenzimide H and DNA-CTMA Doped Solution

From Fig. 3a, the absorption wavelength of the mixed solutions are at 260 nm and 340 nm, indicating that the addition of DNA-CTMA does not affect the absorption wavelength range of the bisBenzimide H. At the same time, as the concentration of the bisBenzimide H solutions increase, the absorption rate of the mixed solutions also gradually increase. Subsequently, we mix the 4 mmol/L bisBenzimide H solution with the highest luminescence intensity with DNA-CTMA to compare its absorption property. As shown in Fig. 3b, when the DNA-CTMA is added to the bisBenzimide H solution, the absorbance of the solution is greatly reduced, which is because the bisBenzimide H molecule is embedded or semi-embedded in the size of the double-stranded structure of the double-stranded DNA, so that reduce the luminous intensity of the fluorescent dye and decrease the absorbance.
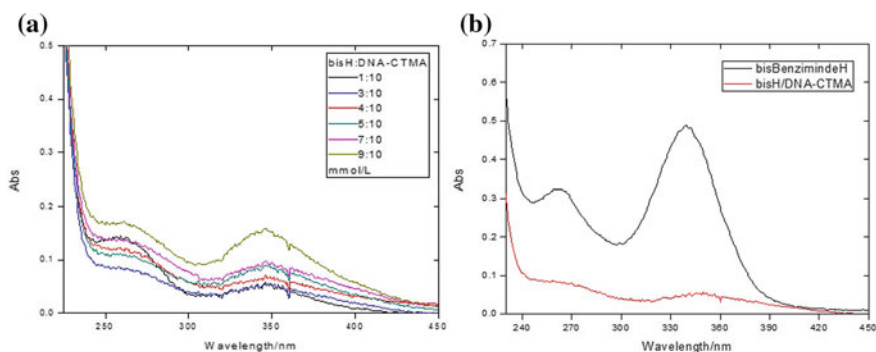


**Fig. 3.  a** UV spectra of different concentrations of bisBenzimide H solution and a certain amount of DNA-CTMA doping; **b** UV spectrum of bisBenzimide H solution and mixed solution of bisBenzimide H added with DNA-CTMA

As shown in Fig. 4, the fluorescence intensity of the bisBenzimide H solution is significantly reduced after the addition of DNA-CTMA, which is consistent with the absorption spectrum. The reduced fluorescence intensity by analysis is attributed to the incorporation of the bisBenzimide H molecule into the DNA-CTMA complex such that the electron energy of its excited state changes. In order to further study the interaction between the bisBenzimide H and the DNA-CTMA complex, different films were prepared by spin coating at the same concentration in solution, and the luminescent properties of the film were investigated.

Inking different ratios of bisBenzimide H/DNA-CTMA solution, and the film is prepared by spin coating process. Figure 5 shows the fluorescence spectrum emission of the bisBenzimide H film before and after DNA-CTMA doping. As shown in the Fig. 5, the fluorescence intensity of the film increases significantly after adding DNA-CTMA. On the one hand, in the state of the film, the fluorescent dye molecules can be embedded in the grooves of the DNA-CTMA molecules, and the exciton energy
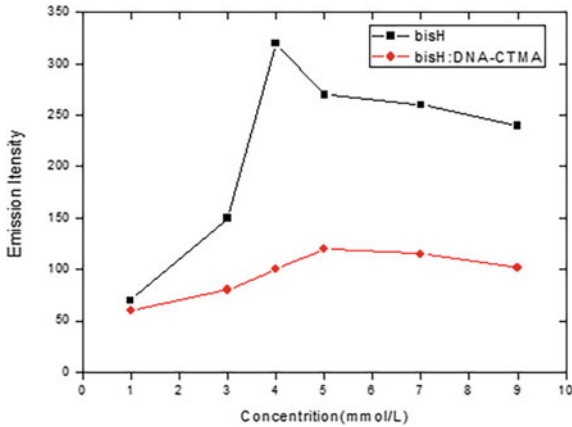
**Fig. 4.** Peak fluorescence intensity of bisBenzimide H itself and peak fluorescence intensity of solution after doping DNA-CTMA
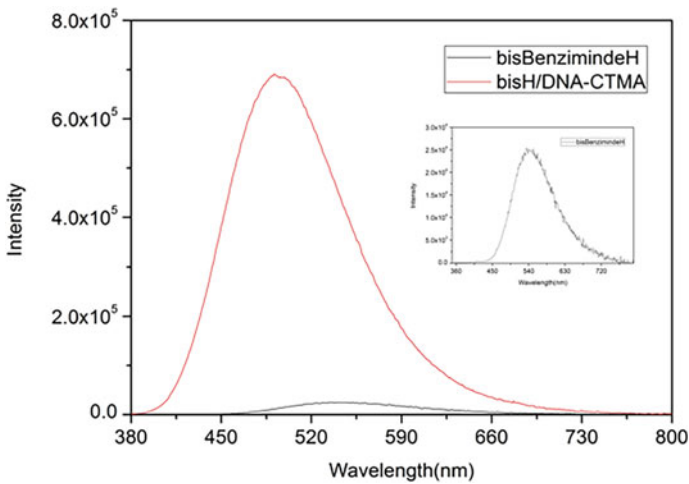


**Fig. 5.** Fluorescence emission diagram of bisBenzimide H film and doped bisBenzimide H film doped with DNA-CTMA

transfer of $Eu^{3+}$ in the DNA-CTMA after drying and film formation improves the luminescence intensity of the film. On the other hand, the volatilization of the solvent during drying causes the non-radiative conversion of the bisBenzimide H to be effectively reduced, which also increases the luminescence intensity.

Figure 6 is a view showing the luminescence of the observation film under irradiation with an ultraviolet lamp. It can be seen that when the concentration ratio of the bisBenzimide H/DNA-CTMA is equal to 1:0 in the film state, the fluorescence intensity is too weak to be observed. As the concentration of the bisBenzimide complex increases, the film exhibits intense yellow-green light.
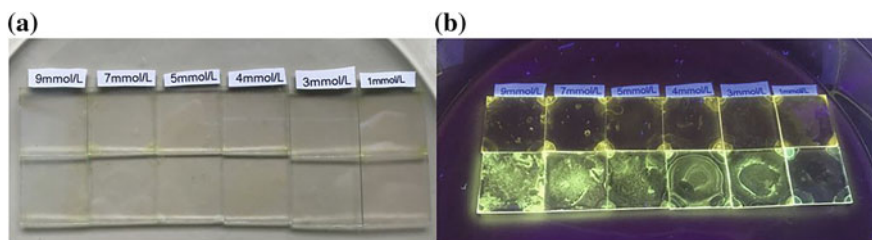
**Fig. 6.** Film under the **a** common light source and **b** UV lamp

## 4 Conclusion

In this chapter, we explore the luminescence properties of different concentrations of bisBenzimide H doped DNA-CTMA. From the absorption spectra, the absorption wavelengths of the bisBenzimide H are 260 nm and 340 nm, respectively. It can be seen from the emission spectrum that the bisBenzimide H has an emission wavelength of 500 nm and emits intense yellow-green light under ultraviolet light. In addition, we discuss the interaction between bisBenzimide H and DNA-CTMA molecules in solution and film state. In the future, it will be applied to inks to prepare new inks with anti-counterfeiting effects, and applied to pharmaceutical packaging, food packaging and other industries, laying a good foundation for new packaging anti-counterfeiting technology.

## References

1. Zhou L et al (2015) Ionic liquid-assisted synthesis of multicolor luminescent Silica Nanodots and their use as Anticounterfeiting Ink. ACS Appl Mater Interfaces 7(4):2905–2911
2. Weisblum B, Haenssler E (1974) Fluorometric properties of the bibenzimidazole derivative hoechst 33258, a fluorescent probe specific for AT concentration in chromosomal DNA. Chromosoma 46(3):255–260
3. Kim YJ et al (1988) Fluorometric assay of DNA in cartilage explants using Hoechst 33258. Anal Biochem 174(1):168–176
4. Turro C et al (1995) Proton transfer quenching of the MLCT excited state of Ru(phen)2d ppz2 + in homogeneous solution and bound to DNA. J Am Chem Soc 117(35):9026–9032
5. Yang X, Shen G-L, Yu R-Q (1999) Studies on intramolecular charge transfer fluorescence probe and DNA binding characteristics. Microchem J 62(3):394–404
6. Liang L et al (2018) Layer-by-layer printing non-volatile organic thin-film transistor memory with a planarly-oriented DNA-complex dielectric. Org Electron 55:75–81

# Preparation and the Properties of Epoxy Acrylic Resin for Inkjet Printing Ink

Jilei Chao[1,2,3], Ruizhi Shi[1(✉)], Fuqiang Chu[2(✉)], Yanling Guo[2], Qian Deng[1], and Siyang Liu[1]

[1] Information Engineering University, Henan, China
`chaojilei@l26.com`, `ruizhishi@sina.com`
[2] School of Light Industry and Engineering, Qilu University of Technology
(Shandong Academy of Sciences), Shandong, China
`{chaojilei,fqchu}@l26.com`
[3] Key Laboratory of Green Printing & Packaging Materials and Technology in
Universities of Shandong, Qilu University of Technology (Shandong Academy
of Sciences), Shandong, China

**Abstract.** In order to improve the flexibility, water solubility and viscosity of epoxy acrylic resin and obtain the linking material for inkjet ink, epoxy acrylic resin was prepared and its properties were studied. Ring opening esterification of acrylic acid (AA) withepoxy diluent (ED) and epoxy resin (E-51) was carried out. The modified epoxy acrylic resin was prepared by esterification and neutralization of trimellitic anhydride (TMA) and maleic anhydride (MA), 2-(Dimethylamino) ethyl methacrylate (DMAEMA) and triethylamine (TEA) respectively. The results showed that when the mole ratio of reaction groups ED:E-51 = 2:1, TMA: MA = 1:4 and DMAEMA:TEA = 1:3, the synthetic properties of epoxy acrylic resin were the best. The test results of the properties of the synthetic resin showed that the viscosity value was 15 mPa · s, the average particle size was less than 0.2 micron, the surface tension was 35 mN/m, the water solubility, stability and mechanical properties of the paint film were good. The prepared epoxy acrylic resin can be used in inkjet printing ink system.

**Keywords:** Inkjet · Epoxy acrylic resin · Particle size · Surface tension

## 1 Introduction

According to the properties of liquid carriers, Inks could be divided into water-based ink, solvent-based ink and reactive ink. Water-based ink, as a "green" printing material, had attracted more and more attention due to its low volatile organic compounds (VOCs) [1–3]. Inkjet printing ink components included binders, pigments, auxiliaries, etc., wherein the binder was an important component of the ink. The binder not only adjusted the viscosity of the ink, but also had an important influence on the mechanical properties such as flexibility and adhesion of the system.

The oligomers, which were used for inkjet inks, commonly included epoxy acrylate, urethane acrylate, polyester acrylate and so on. Among them, epoxy acrylate had hydroxyl groups on the molecular chain, which made the resin have better polarity and

excellent wettability of pigment. Due to the relatively stable C-C bond and ether bond on the molecular chain, epoxy acrylate had excellent chemical resistance. Because of the benzene ring in the main chain of the molecule, it had high stability [4–6]. Because of the excellent properties described above, epoxy acrylates had been used as pre-polymerswidely. However, due to the disadvantages of high viscosity and high brittleness of epoxy acrylate, its applications in inkjet ink formulations had been limited [4].

Based on the preliminary work [2, 7], the effects of raw materials and their ratios on the performance of the systemwere studied in this paper. The test results showed that the epoxy resin prepared by the new formulation and process had good properties and could be used as the binder for preparing inkjet printing inks.

## 2    Experimental

### 2.1    Equipments

The surface tension of the reactants was tested by a quality control surface tension meter. And the instrument model was K100, which was purchased from TA Instruments, USA. The particle size of the resin was tested by a particle size analyzer, model number Nano-ZS90, purchased from Malvern, UK. The viscosity of the reactant system was tested by a viscometer, the model of which was DVS and the brand was Brookfield.

The mechanical properties of the resin were measured by the paint film flexibility tester and the paint film adhesion tester. And the models of the two instruments were QTX and QFH-HG600, respectively, which were purchased from Shanghai Jingyu Instrument Equipment Co., Ltd. and Dongguan Huaguo Precision Instrument Co., Ltd, China.

### 2.2    Materials

The main raw materials used in this experiment includedbisphenol A epoxy resin (E-51), industrial grade, purchased from Nantong Xingchen Synthetic Material Co., Ltd, China. Polyethylene glycol diglycidyl ether (E-400) and polypropylene glycol diglycidyl ether (P-400), both of which were industrial grade and purchased from Shanghai Rufa Chemical Technology Co., Ltd, China. Acrylic acid (AA) and triethylamine (TEA), both of which belonged to analytical reagent, were purchased from Damao Chemical Reagent Factory in Tianjin, China. Trimellitic anhydride (TMA), industrial grade, purchased from Guangzhou Susong Chemical Co., Ltd., China. Maleic anhydride (MA), AR, was purchased from Chemio Chemical Reagent Co., Ltd, China. Dimethylaminoethyl methacrylate (DMAEMA), industrial grade, was purchased from Guangzhou Boshun Chemical Co., Ltd., China.

## 2.3    Sample Preparation

Firstly, a certain proportion of bisphenol A epoxy resin (E-51), polyethylene glycol diglycidyl ether (E-400) and polypropylene glycol diglycidyl ether (P-400) were esterified with acrylic acid (AA) by ring-opening esterification reaction.

Secondly, when the acid value of the system was reduced to a certain value, the esterification reaction would be further carried out by adding TMA and MA in a certain ratio.

Finally, the modified epoxy acrylic resin was obtained by introducing a certain proportion of organic amine dimethylaminoethyl methacrylate (DMAEMA) and tri-ethylamine (TEA) to neutralize the system and adding deionized water to adjust the solid content.

## 2.4    Performance Tests

### 2.4.1    Viscosity

Viscosity of resin system was tested by DVS digital viscometer. Rotor and rotating speed were selected for testing at 23 + 0.5 °C. Each sample was measured at least twice at the same temperature, and the average value was calculated as the final viscosity value of the system.

### 2.4.2    Surface Tension

The surface tension of the resin was measured at room temperature using the surface tension measuring instrument, and each sample was measured 3 times. The average value was calculated as the final surface tension value of the resin.

### 2.4.3    Particle Size

The prepared sample was diluted with deionized water to 0.5% solution. The particle size was measured by particle size analyzer at room temperature. When the measurement was performed 3 times and the obtained values were close, the average value would be taken as the final particle diameter value of the sample.

### 2.4.4    Water Solubility

Firstly, the quality of the conical bottle was called $m_1$, and a certain quality of the resin was put into the bottle, when the total mass of the bottle and sample was called $m_2$.

Then deionized water would be added to the bottle until the resin was just turbid, and the total mass $m_3$ wasweighed at that time.The water content was W%, and the value was calculated according to formula (1.1).

$$W\% = (m_3 - m_2) \div (m_3 - m_1) \times 100\% \qquad (1.1)$$

### 2.4.5    Adhesion and Flexibility

Adhesion of resin was tested by adhesivity tester according to Chinese standard GB 1720–79. The flexibility of the resin was measured using a paint film flexibility tester according to Chinese standard GB/T 1731–1993.

## 3   Results and Discussion

### 3.1   Factors Affecting the Preparation of Epoxy Acrylic Resin

#### 3.1.1   Ratio of Epoxy Resin (E-51) To Epoxy Diluent (ED)

In this experiment, polyethylene glycol diglycidyl ether (E-400) and polypropylene glycol diglycidyl ether (P-400) were selected as epoxy diluent (ED), which was combined with epoxy resin (E-51) in a certain ratio. Under the premise of ensuring the mechanical properties of the prepolymer system, it was attempted to reduce the viscosity of the epoxy resin system. The resin system prepared by simply using E-51 as a matrix had a large viscosity and it was difficult to be used in an inkjet ink system, which had a relatively low viscosity requirement.

In this experiment, the effect of the diluent on the viscosity of the initial reaction system of the epoxy resin was tested firstly. The ED was mixed with E-51 at the molar ratios of 1:3, 1:2, 1:1, 2:1 and 3:1, respectively, to reduce the viscosity of the initial resin system. The moderate viscosity facilitatedthe smooth reaction.

From Fig. 1, it can be seen that the viscosity of the initial resin system became smaller and smallerwith the increase ofED content. When the epoxy molar ratio of E-51 to ED was 1:2, the initial viscosity of the resin system decreased from 8325.80 mPa · s to 157.06 mPa · s, and the viscosity reduction rate reached 98.11%.
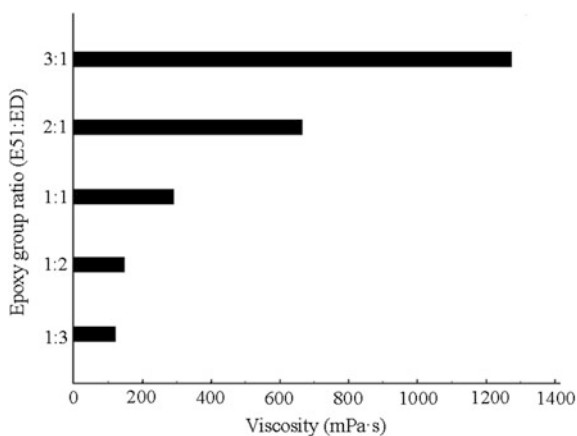


**Fig. 1.** Relations betweenthe viscosity of initial reaction system and the ratio of E-51and ED

In combination with the previous works, in this experiment, a series of epoxy acrylates with solid content of 10–80% were prepared by mixing ED and E-51at the molar ratio of 1:3, 1:2, 1:1, 2:1 and 3:1. Their viscosity was tested and the effect of diluent on the viscosity of epoxy acrylate was examined.

It can be seen from Fig. 2 that when the solid content of epoxy acrylates prepared increased from 10% to 80%, the viscosity increased accordingly. The viscosities of E-51 and ED epoxy prepolymer systems with molar ratios of 3:1, 2:1 and 1:1 increased rapidly, and most of the solid prepolymer systems could not meet the requirements of

ink-jet ink. The viscosities of the two prepolymers with ratios of 1:2 and 1:3 changed slightly, and could also meet the requirements of low viscosities even when the solid content was high.
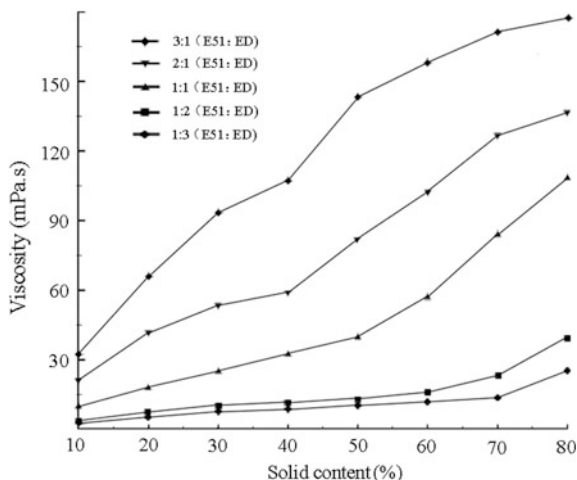


**Fig. 2.** Effect of the ratio of E-51 and ED on the viscosity of epoxy acrylate with different solid contents

### 3.1.2    Ratio of Trimellitic Anhydride (TMA) to Maleic Anhydride (MA)

Because of having three carboxylic acid functional groups, which can react with hydroxyl groups to produce more carboxyl groups, TMA can increase the water solubility of the resin system. In combination with previous work, epoxy acrylate resins were prepared according to different proportions of TMA and MA. Their water solubility was tested, and the influence of the ratio of TMA to MA on the hydrophilicity of the prepolymer epoxy acrylate was examined.

Due to the large molecular mass of TMA, the viscosity of the reactants increases with the increase of TMA content, which affects the progress of the reaction. As shown in Fig. 3, when TMA: MA < 1:4, the water solubility of the resin system increased linearly. However, when the ratio of TMA to MA continued to increase, the water solubility of the resin system presented a declining trend. Itwas because the increase of TMA led to the increase of the viscosity of reactants, and some anhydrides did not react, which ultimately made the reaction incomplete and reduced the water solubility of resin system.

### 3.1.3    Proportion of Triethylamine (TEA) and Dimethylethylamine
###             Methacrylate (DMAEMA)

In the previous work, it was found that the mechanical properties of epoxy acrylate system, whichafter film formation, decreased in varying degrees with the increase of the amount of ED. The chemical structure of DMAEMA contains acryloxy groups, which can increase the number of active groups, improve the crosslinking density of
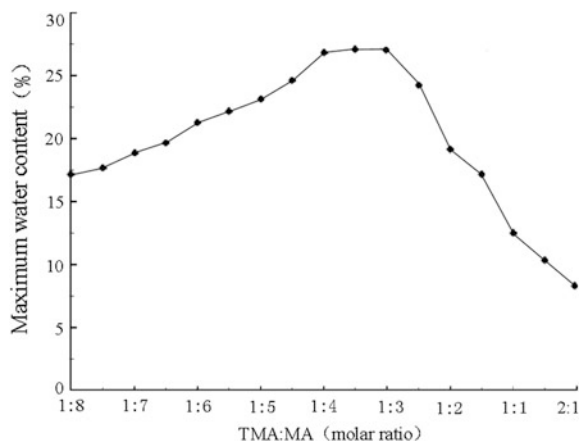
**Fig. 3.** Relations between TMA: MA ratio and water solubility of epoxy acrylate

resin system, and improve the comprehensive mechanical properties of resin filmfinally. Based on the molar ratio ED: E-51 = 2:1 and TMA: MA = 1:4, epoxy acrylates with different molar ratios of TEA to DMAEMA were prepared in this experiment. Their mechanical properties were tested and the effect of the ratio of TEA to DMAEMA on the mechanical properties of the resin system was examined. The experimental results were shown in Table 1.

**Table 1.** Effect of compounding ratio of TEA and DMAEMA on mechanical properties of resin system

| TEA:DMAEMA (molar ratio) | Flexibility (mm) | Adhesion (level) |
|---|---|---|
| 1:1 | 4 | 1 |
| 2:1 | 4 | 1 |
| 3:1 | 3 | 1 |
| 4:1 | 2 | 2 |
| 5:1 | 2 | 2 |

As can be seen from Table 1, with the increase of the ratio of DMAEMA and TEA, the flexibility of the resin systemgenerated by the reaction increased and the adhesion also showed an improvement trend. When molar ratio TEA: DMAEMA = 3:1, the mechanical properties of epoxy acrylates prepared by the reaction could meet the requirements of ink linker for inkjet.

## 3.2   Performance Test of Modified Epoxy Acrylic Resin System

The binder for inkjet ink has a great influence on the performance of the ink. The surface tension affects the shape of ink droplets in the printing process, and has a great influence on the printability match between ink and substrate. Good surface tension is

the key to ensure the quality of inkjet printing. Particle size is an important evaluation index of inkjet ink. Appropriate particle size has a great influence on the use range and printability of inkjet ink.

On the basis of synthesizing epoxy acrylic resin with new formulation, in this experiment, the surface tension, particle size and stability of epoxy acrylic resin were tested to verify whether the synthesized prepolymer was suitable for the preparation of ink for inkjet printing.

The experimental results in Table 2 showed that the prepared epoxy acrylate had good surface tension, small particle size and good stability, and could be used as a binder for preparing ink for inkjet printing.

**Table 2.** Performance tests of epoxy acrylic resin systems synthesized with new formula

| Test performance | Surface tension (mN/m) | Particle size (μm) | Stability |
|---|---|---|---|
| Value/Phenomenon | 35 | <0.2 | No gelation or delamination |

## 4   Conclusions

The results of the synthesis experiment showed thatthe epoxy acrylic resin system had the best performancewhen the molar ratio of epoxy group ED: E-51 = 2:1, TMA: MA = 1:4 and DMAEMA: TEA = 1:3. The performance test results of the synthesized resin showed that the viscosity value was 15 mPa·s, the average particle size was <0.2 μm, the surface tension was 35 mN/m, and the water solubility, stability and mechanical properties of the paint film were all good. It could be used in the inkjet printing ink system.

## References

1. Clay K, Gardner I, Bresler E, Seal M et al (2004) Direct legend printing (DLP) on printed circuit boards using piezoelectric inkjet technology. Circuit Word 28:24–31. https://doi.org/10.1108/03056120210412526
2. Zhang Z, Chao J, Chu F (2016) Study on the synthesis and property of water-based UV-curable epoxy acrylate with low viscosity. Lect Notes Electr Eng 369:941–947. https://doi.org/10.1007/978-981-10-0072-0_116
3. Sun Z, Zhang P, Liu X (2018) Application status and development of water-based ink and EB ink. Print Technol 10:102–104
4. Shlomo M (2009) The chemistry of inkjet inks. World Scientific Publishing Co. Pte. Ltd., Singapore. https://doi.org/10.1142/6869
5. Ma Y (2017) Preparation and properties of polyaniline modified waterborne epoxy anticorrosive coatings. Shenyang Ligong University, Shenyang, China

6. Ju Z, Liu X, Cao J et al (2018) Research progress in the waterborne and modification of UV-curable epoxy acrylate resin. China Plast Ind 46(9):26–29
7. Chao J (2014) Study on waterborne UV-curable INK BASED on UV LED light source. Master's thesis. Qilu University of Technology, Jinan, China

# Preparation and Performance of Inkjet Ink Based on Biopolymers DNA-Lau

Rong Cao, Beiqing Huang, Xianfu Wei, and Lijuan Liang[(✉)]

Beijing Institute of Graphic Communication, Beijing, China
lianglijuan@bigc.edu.cn

**Abstract.** In recent years, fluorescent dyes have received more and more attention in the field of packaging anti-counterfeiting due to their good concealment, bright colors and convenient inspection. At the same time, research on new fluorescent inkjet inks based on the interaction between biopolymer DNA and fluorescent dyes has attracted wide attention. In this paper, the $Eu(TTA)_3(H_2O)_2$ complex was synthesized and the luminescence property was analyzed. It is found that when the $Eu(TTA)_3(H_2O)_2$ content was 0.7% and the ratio of DNA-Lau to $Eu(TTA)_3(H_2O)_2$ was 1:20, the luminescent dye had the highest luminescence intensity. The fluorescent ink was prepared as a pigment, the results showed that the resin content was 15%, the mixing ratio of propylene glycol methyl ether to propylene glycol methyl ether propionate was 0.61:0.39, and the luminous intensity, surface tension and viscosity of the fluorescent ink were optimized, which laid a solid foundation for the development of new fluorescent inkjet inks.

**Keywords:** DNA-Lau · Eu(TTA)3(H2O)$_2$ · Inkjet inks · Anti-counterfeit printing

## 1 Introduction

Fluorescent materials have been widely applied in the fields of information, medicine, display, and new energy in the new century [1–3]. The rare earth lanthanum complex is a red fluorescent material with high luminescent properties of organic compounds and good stability of inorganic compounds [4, 5]. DNA is a double helix molecular structure, which possesses genetic instructions could guide biological development and the operation of vital functions [6]. In the previous research work, Liang et al. [7, 8] found that the addition of DNA lipid complex can effectively improve the luminescence intensity of fluorescent dyes. This may be ascribable to the presence of some major channels and narrow minor grooves in DNA, so that many of the dyes such as Rhodamine, rare earth ions can be well implanted into the groove to strengthen the fluorescence emission intensity [9]. Inspired by the idea, this paper aimed to study the effect of DNA lipid complexes on the luminescence intensity of $Eu(TTA)_3(H_2O)_2$.

The effect of different DNA-lauroylcholine hydrate (DNA-Lau) concentration on the luminescence properties of $Eu(TTA)_3(H_2O)_2$ was discussed. Fluorescent inkjet ink was made by using $Eu(TTA)_3(H_2O)_2$ as pigment. The effects of resin, solvent and DNA-Lau on the viscosity, surface tension and the luminescence intensity of

fluorescent inkjet ink were studied, which laid a solid foundation for new packaging anti-counterfeiting technology.

## 2    Experimental

### 2.1    Materials

Solvent: propylene glycol methyl ether, propylene glycol methyl ether propionate, and ethanol; Resin: AZ-5391; Fluorescent dyes: $Eu(TTA)_3(H_2O)_2$was purchased from TCI; Other additives: DNA-Lau.

### 2.2    Instruments

Fluorescence spectrum (RF-5301PC, Shimadzu, Japan), UV spectrophotometer (UV-2501PC, Shimadzu, Japan), Rheometer (AR2000, TA Company, USA), Static interface tension meter (k-100, Germany).

### 2.3    Preparation of DNA-CTMA

The thiophene trifluoroacetone (TTA) was mixed with absolute ethanol and aqueous ammonia until completely dissolved. At the same time, the Eu(III) complex was dissolved in water and allowed to stand for a while until completely dissolved. The two solutions were mixed, stirred, filtered, and dried to obtain a precipitate. The precipitate was dissolved in acetone and water, filtered, dried, and treated with mineral spirits at a certain temperature to obtain $Eu(TTA)_3(H_2O)_2$.

### 2.4    Preparation of Fluorescent Inkjet Ink

First, the resin was dissolved in a solvent, and the mixture was completely dissolved using a stirrer. Then, a fluorescent dye was added to the solution, stirred to make a uniform distribution, and then filtered using a 0.24 μm diameter filter rotor to obtain a fluorescent inkjet ink sample.

## 3    Results and Discussion

### 3.1    Luminescence Properties of Eu $(TTA)_3(H_2O)_2$

In order to study the luminescence properties of $Eu(TTA)_3(H_2O)_2$ complex, thesolution of $Eu(TTA)_3(H_2O)_2$ with different concentration had been prepared, and the absorption spectrum was tested, shown as Fig. 1. From Fig. 1, it is shown that $Eu(TTA)_3(H_2O)_2$ complex has an absorption peak at the wavelength of 340 nm, which is attributed to the n-π* transition of the TTA ligands. With the increasing of the concentration of Eu $(TTA)_3(H_2O)_2$ complex,the absorption band also increases.

　　As shown in the Fig. 2a, the main excitation wavelength was 400 nm, which is due to the charge transfer transition band, where electrons are transferred from the orbit of
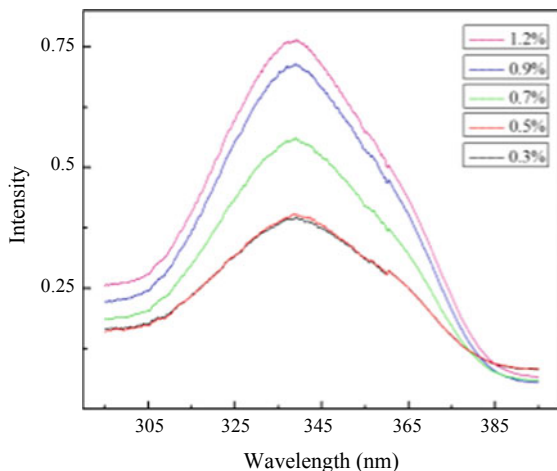
**Fig. 1.** UV spectrum of Eu(TTA)$_3$(H$_2$O)$_2$ with different concentrations

the ligand to the 4f6 empty orbit of Eu$^{3+}$. As shown in the Fig. 2b, Since the triplet energy level of thiophene trifluoroacetone (TTA) matches the excited state energy level of Eu$^{3+}$, Therefore, with the gradual increase of the concentration of the solution, the fluorescence intensity of Eu(TTA)$_3$(H$_2$O)$_2$ first increases to the maximum value and then gradually decreases due to exciton quenching, reaching the maximum of 0.7%.
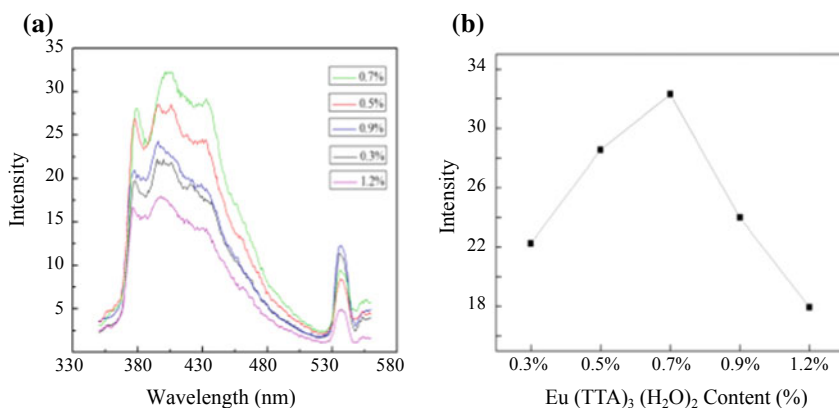


**Fig. 2. a** Excitation spectra of different concentrations of Eu(TTA)$_3$ (H$_2$O)$_2$; **b** Peak intensity spectrum of different concentrations of Eu(TTA)$_3$ (H$_2$O)$_2$

In order to further clarify the fluorescence intensity of fluorescent dyes, it is of practical research significance to explore the effect of DNA complexes on the performance of fluorescent dyes. In this experiment, the concentration of Eu(TTA)$_3$(H$_2$O)$_2$ (0.3%) was fixed, and the effect of different DNA-Lau concentrations on the

luminescence intensity of Eu(TTA)$_3$(H$_2$O)$_2$ was investigated. It can be seen from Fig. 3 that the optimum excitation wavelength is 402 nm, indicating that the molecules in the excited state are the most at the excitation wavelength, so that the fluorescence intensity is the highest. According to theexcitation spectra, with the growth in the ratio of DNA-Lau compound, the fluorescence intensity also enhanced, and the fluorescence intensity was the highest at a concentration ratio of 1:20, indicating that DNA-Lau can enhance the luminescence properties of Eu(TTA)$_3$(H$_2$O)$_2$.
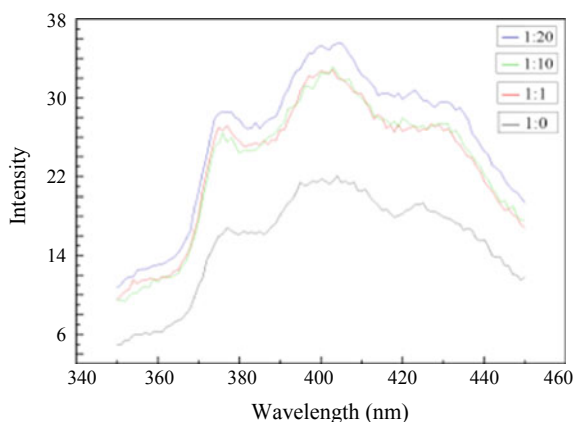


**Fig. 3.** Excitation spectrum of different Eu(TTA)$_3$(H$_2$O)$_2$/DNA-Lau concentration

The effects of different DNA-Lau contents of the ink properties are presented in Table 1. It can be determined from Table 1 that as the DNA-Lau content increases, the luminous intensity, viscosity and drying time of the fluorescent ink gradually increase, but the surface tension does not vary a great deal.

**Table 1.** Effect of different Eu(TTA)$_3$(H$_2$O)$_2$/DNA-Lau concentration of ink properties

| Concentration ratio | Fluorescent intensity | Surface tension (mN/m) | Viscosity (mPa■s) | Drying time (s) |
|---|---|---|---|---|
| (1:0) | 23.313 | 27.74 | 9.810 | 478.76 |
| (1:1) | 32.850 | 27.24 | 8.585 | 597.69 |
| (1:10) | 33.111 | 27.46 | 10.940 | >900 |
| (1:20) | 35.558 | 27.25 | 14.430 | >900 |

## 3.2   Optimal Solvent Selection

In this experiment, the simple mass center design method was utilized to define the best mass fraction of the solvent, and the three-component simple center of gravity design (m = 3) was used. The ratio of propylene glycol methyl ether, propylene glycol methyl ether propionate, and ethanol in the mixed solvent was X1, X2, and X3, respectively.

Seven sets of experiments were designed to prepare fluorescent inkjet inks and test their operations. The ratio of luminescence intensity, surface tension, viscosity, and drying time in the ink was set to 0.25, 0.3, 0.15, and 0.3, respectively. Through the data processing, the regression equation of the comprehensive performance of the fluorescent inkjet ink is obtained:

$$Y = 0.681X1 + 0.525X2 + 0.440X3 + 0.702X1X2 - 0.474X1X3 + 0.508X2X3 - 0.100X1X2X3$$

Through the solution, the optimal experimental scheme was held. When X1:X2:X3 = 0.61:0.39:0, the performance of the fluorescent inkjet ink is the best. Table 2 is the comprehensive performance test result of the best component content of fluorescent inkjet ink obtained by the above discussion.

**Table 2.** Fluorescent ink best performance test results

| Fluorescent intensity | Surface tension (mN/m) | Viscosity (mPa•s) | Drying time (s) |
| --- | --- | --- | --- |
| 43.173 | 27.74 | 9.810 | 478.76 |

### 3.3   Determination of Resin Content

In this experiment, AZ-5391 was used as the resin component, and the influence of the content of the resin on the properties of the ink was measured. As shown in Table 3, the viscosity of the ink increases as the resin content increases. At the same time, the surface tension of the ink does not change much. In combination with various influencing factors, when the resin content is 15% in this experiment, the viscosity and surface tension are within the ideal range of the inkjet ink.

**Table 3** Effect of different resin content changes on the viscosity and surface tension of fluorescent inks

| AZ-5391 resin content (%) | Viscosity (mPa•S) | | Surface tension (mN/m) | |
| --- | --- | --- | --- | --- |
| | Propylene glycol monomethyl ether | Propylene glycol methyl ether propionate | Propylene glycol monomethyl ether | Propylene glycol methyl ether propionate |
| 3 | 2.084 | 2.093 | 28.17 | 27.86 |
| 6 | 3.624 | 2.929 | 28.26 | 28.00 |
| 9 | 5.902 | 5.575 | 28.31 | 27.96 |
| 12 | 6.778 | 6.841 | 28.25 | 27.95 |
| 15 | 9.976 | 12.520 | 28.00 | 27.96 |

Using the optimal composition ratio obtained above, the new fluorescent inkjet ink with good luminous intensity, surface tension, viscosity and other properties can be developed in the future. The new fluorescent inkjet ink also has good printability and anti-counterfeiting effects.

## 4   Conclusions

This experiment mainly discussed the influence of the composition of red fluorescent inkjet ink on its operation. It is experimentally found that adding DNA-Lau can effectively improve the luminous intensity, When the $Eu(TTA)_3(H_2O)_2$ content is 0.7% and the DNA-Lau and $Eu(TTA)_3(H_2O)_2$ concentration ratio is 1:20, the fluorescent inkjet ink has the maximum luminescence intensity. When the resin percent is 15%, the mixing ratio of propylene glycol methyl ether and propylene glycol methyl ether propionate is 0.61:0.39, the luminous intensity, surface tension and viscosity of the fluorescent ink are optimized. The results of this research will drive the development of new fluorescent inkjet inks.

## References

1. Blasse G, Grabmaier BC (1950) Luminescent materials. Manuf Chem Aerosol News. 21(8):335
2. Jüstel T, Nikol H, Ronda C (2010) New developments in the field of luminescent materials for lighting and displays (pp 3084–3103). Angewandte Chemie 37(22):3084–3103
3. Forster PL et al (2009) Calorimetric investigations of luminescent films polycarbonate (PC) doped with europium complex [Eu(TTA) $_3$ (H$_2$O)$_2$]. J Thermal Anal Calorim 97(2):497
4. Lourenço AVS et al (2013) Luminescent material based on the [Eu(TTA)$_3$(H$_2$O)$_2$] complex incorporated into modified silica particles for biological applications. J Inorg Biochem 123(6): 11–17
5. Liu et al (2005) Influences of matrices and concentrations on luminescent characteristics of Eu (TTA)$_3$(H$_2$O)$_2$/polymer composites. J Lumin 114(3):187–196
6. Singh TB, Sariciftci NS, Grote JG (2009) Bio-organic optoelectronic devices using DNA
7. Zhao T et al (2017) Luminescence properties of Eu(TTA)$_3$(H$_2$O)$_2$ doped with DNA-CTMA and its application in fluorescent inkjet ink. Springer, Singapore
8. Hao H et al (2017) Luminescent properties of rhodamine 6G doped with DNA-CTMA and its application in fluorescent ink-jet ink. Springer, Singapore
9. Moreira BG et al (2005) Effects of fluorescent dyes, quenchers, and dangling ends on DNA duplex stability. Biochem Biophys Res Commun 327(2):473–484

# Preparation and Application of Photographic Reflective Ink

Zijie Cui[1], Danfei Liu[1], Mi Shang[1], and Yunfei Zhong[1,2(✉)]

[1] School of Packaging and Materials Engineering, Hunan University of Technology, Hunan, China
yfzhong@hut.edu.cn
[2] Hunan Furui Printing Co., Ltd., Hunan, China

**Abstract.** Fake and inferior products appear frequently in the market, seriously disturbing the normal social and economic order. In order to make the invisible anti-counterfeiting technology has more convenient and effective anti-counterfeiting effect, using the retro-reflection properties of glass micro-beads, prepared a kind of photographic reflective ink, and initially used in screen printing. The photographic reflective ink is prepared by using water and ethanol as solvent, waterborne polyurethane as binder, glass micro-beads as light reflection material, adding dispersant, anti-settle agent and other additives. The printed is usually invisible, and visible in the mobile phone by flash photography, possess the characteristics of photographic reflection. The photographic reflective ink could be used as anti-counterfeiting printing ink to meet various anti-counterfeiting requirements.

**Keywords:** Printing Anti-counterfeiting technology · Anti-counterfeiting ink · Transparent ink · Glass micro-beads

## 1 Introduction

With the imitation technology develops continuously, which leads to the flow of fake and shoddy products into the market, and seriously damaging the order of market economy. Most of the fake items cannot be judged by appearance, thus prompting us to improve the means of anti-counterfeiting. The key to anti-counterfeiting technology is to extend the time length and uniqueness of anti-counterfeiting technology [1], and the improvement of anti-counterfeiting technology is inseparable from the functional development and application of various emerging materials [2, 3]. Therefore, it is necessary to actively study the application of various emerging materials in the anti-counterfeiting technology of printing, and make the anti-counterfeiting technology of printing more mature and reliable. Among anti-counterfeiting techniques, invisible anti-counterfeiting technology is good concealment and wide application, mainly including infrared invisible anti-counterfeiting, ultraviolet invisible anti-counterfeiting and so on.

In this paper, a kind of photographic reflective ink was prepared by using glass micro-beads as the main reflective material. This ink will be used in screen printing. The printing effect is to achieve invisibility under the ordinary light, in mobile phone

flash photography display graphic and text information, so as to achieve a certain anti-counterfeiting effect.

## 2 Experimental Section

### 2.1 Materials

Waterborne polyurethane,dispersant and defoamer were purchased from Shenzhen Jitian Chemical Co., Ltd. (Shenzhen, China). Glass micro-beads obtained from Lanxin Chemical Co., Ltd. (Guangdong, China). Ethanol (99.7%) and Fumed silica (Anti-settling agent) were purchased from Sinopharm Chemical Reagent Co., Ltd. (Shanghai, China). All other reagents were of analytical grade.

### 2.2 Principle of Reflective

Glass micro-beads for optics purposes have unique light reflection properties and good refractive properties for all kinds of incident light [4]. When the diameter of glass micro-beads is less than 0.8 mm and the refractive index is between 1.9 and 2.1, the glass micro-beads exhibit a regressive reflection characteristic [5]. That is, when a beam of light shines on the surface of micro-beads at any angle within a certain range, the high refraction of the beads concentrates the light on the special reflective layer of the focus of micro-beads, and the reflective layer reflect the light back parallel to the direction of the source, as shown in Fig. 1.
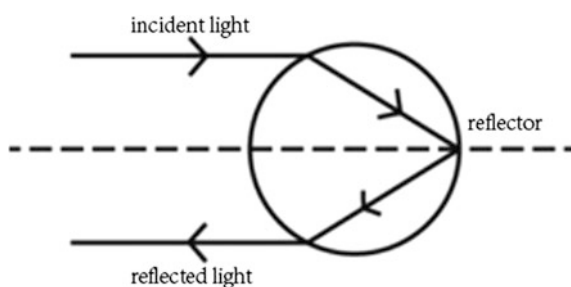


**Fig. 1.** Graphics of glass micro-bead regression reflection

Because of the reflective properties of glass micro-beads for optical purposes, they have been used in the preparation of various reflective coatings [6–9]. The best refractive index for reflecting glass micro-beads is 1.93, under which parallel light can be perfectly refracted, the maximum reflective intensity occurs when the diameter of glass micro-beads is 50–60 microns.

The basic principles of applying optical glass beads to photographic reflective inks are as follows: The ink is printed on ordinary substrate without reflective coating. The substrate surface is not completely flat, it will absorb most of the incident light under normal light. Then if the prepared ink is transparent, the printed pictures and texts

should be basically invisible under normal light. When the amount of incident light increase greatly, such as under the photography of mobile phone flash, the reflected light of glass micro-beads increases, and the printed texts and pictures will be presented due to the reflective effect.

## 2.3   Ink Preparation and Printing

The photographic reflective ink prepared in this experiment was transparent ink. According to the environmental protection performance, transparency requirements, glass bead characteristics and laboratory equipment, water-based ink was selected as the best solution [10–12].

### 2.3.1   Ink Formulations

The preparation experiment of photographic reflective ink was divided into three groups, and the formula was shown in Table 1.

**Table 1.**  Ink formulations

| Components | Experiment 1 | Experiment 2 | Experiment 3 |
|---|---|---|---|
| Waterborne polyurethane | 60% | 40% | 36% |
| Water | 10% | 10% | 6% |
| Ethanol | 10% | 40% | 40% |
| Glass micro-beads | 18% (350 meshes) | 6% (350 meshes) | 6% (500 meshes) |
| Dispersant | 0% | 6% | 5% |
| Defoamer | 2% | 2% | 3% |
| Anti-settling agent | 0% | 0% | 3% |

### 2.3.2   Preparation Step of Ink

The experimental steps are as follows.

1. Check the experimental equipment.
2. Weighing. Quantitative weighing of each component in the ink formulation was carried out according to the percentage. The total quality of the prepared ink was 100 g;
3. The solvent was obtained by mixing water with absolute ethanol, and the waterborne polyurethane was added to mix;
4. Add glass micro-beads and use DW-3 digital display electric stirrer to mix. The speed is optimized at 600 r/min and the stirring time is 30 min to obtain the first solution.
5. Add defoamer [13], dispersant and anti-sedimentation agent to the first solution, and use jj-3 digital display electric agitator to stir it, with the optimal speed of 800–1000 r/min and the stirring time of 30 min, so as to evenly mix all components and obtain photographic reflective ink [8].

The glass micro-beads in group 1 could not be dispersed, and most of them were deposited at the bottom of the beaker, so the preparation failed.

### 2.3.3 Basic Performance Test of Ink

Because of the failure of the experiment group 1, the basic performance of the experiment group 2 and the experiment group 3 were tested. The basic properties of ink include fineness, viscosity, dryness and so on. The test results are shown in Table 2.

**Table 2** Test results of basic properties of ink

| Basic performance | Group 2 | Group 3 |
|---|---|---|
| Fineness test (μm) | 38 | 18 |
| Initial dryness test (mm/30 s) | 28 | 20 |
| Viscosity test (P) | 48.3 | 102.1 |

### 2.3.4 Ink Printing

Screen printing can use water-based ink, and has the advantages of simple process, low cost and low printing pressure. This experiment used different mesh count to print the prepared ink, to detect whether it has the effect of invisible under normal light and visible under mobile phone flash photography. Printing was performed at room temperature, 25°.

## 2.4 Characterization

Experimental materials were weighed by an AR1140 electronic analysis balance weighing from Ohauscorp (USA) Co.LTD. Ink was stirred by Gongyi Yuhua Instrument Co., Ltd. DW-3 digital display electric mixer (Beijing, China). The stretching network used Dongguan Yongqi Mechanical Equipment Co., Ltd. RD117 pneumatic stretching machine (Guangdong, China). Manual platform screen printing machine and vacuum screen exposure machine were both from Linxin Xinfeng Screen Printing Machinery Factory (Liaocheng, China). Diazo photosensitive adhesive comes from Taipingqiao Jingfeng Screen Printing Material Co., Ltd. (Beijing, China).

## 3 Results and Discussion

### 3.1 Analysis of Ink Formulation

According to the ink formula in Table 1, three sets of inks were obtained. The glass micro-beads in group 1 could not be dispersed, and most of them were deposited at the bottom of the beaker, so the preparation failed. The glass micro-beads in group 2 settled after standing for 2 h. The glass micro-beads in group 3 have good dispersibility and not easy to settle.

According to the experiment, we can know that the dispersant can improve the dispersion of glass beads in ink, and gas-phase silica anti-settling agent has a good

effect on the precipitation of glass micro-beads. But a part of glass micro-beads will still precipitate after a long period of standing.

## 3.2    Analysis of Printing Results

The printing results are shown in the figure below.

The experimental results showed that the group 3 of ink transparency than the group 2 of ink under the same printing conditions, as shown in Figs. 2 and 3. The reason is that the larger the mesh number of glass micro-beads is, the smaller the particle size is, and the reflective effect will be correspondingly weakened. The 300 mesh screen printing effect was better than 100 mesh screen printing effect by used the same formula of ink printing, as shown in Figs. 3 and 4. It showed that higher meshcount could make the photographic reflective ink transparency better in normal light.



| (a) Shooting under normal light | (b) Shooting under flash |
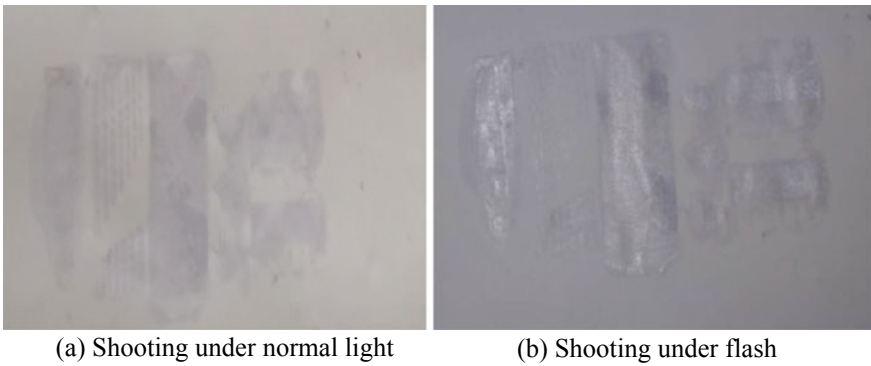
**Fig. 2.** Experimental group 2 printing effect by using 100 mesh screen printing



| (a) Shooting under normal light | (b) Shooting under flash |
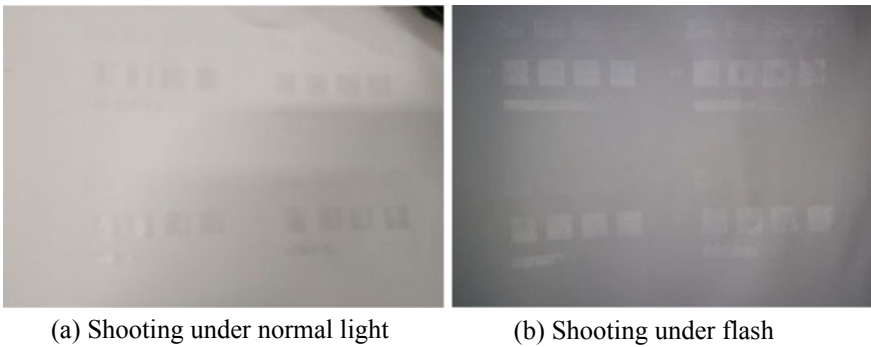
**Fig. 3.** Experimental group 3 inks effect by using 100 mesh screen printing

(a) Shooting under normal light          (b) Shooting under flash
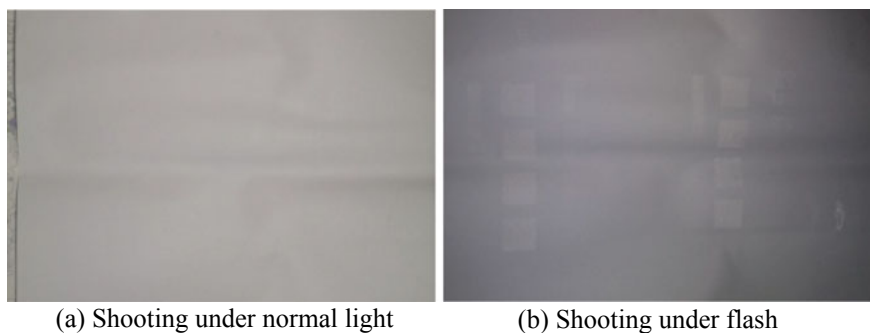
**Fig. 4.** Experimental group 3 inks effect by using 300 mesh screen printing

The experimental results showed that the selection of 500 mesh glass micro-beads to prepare ink, 300 mesh screen printing effect was the best. The prepared ink was used in screen printing. The prepared ink can be used in anti-counterfeiting packaging by screen printing, but also can further test the applicability of the ink in other printing methods.

According to the experimental results, the photographic reflective ink prepared in this paper can be used in screen printing, and has the characteristics of invisible under normal light and visible under flash photography. It has the anti-counterfeiting effect initially.

## 4   Conclusions

In order to make ink anti-counterfeiting technology more convenient and effective, and more interactive, glass micro-beads were selected as reflective materials in this paper. A transparent photographic reflective ink was prepared by using glass beads, waterborne polyurethane resin, water, ethanol and some ink additives based on the regressive reflective properties of glass micro-beads, and the basic properties of the ink were tested. According to the research, the optimal formula of photographic reflective ink is 6% glass micro-beads, 36% waterborne polyurethane, 6% pure water, 40% anhydrous ethanol, 5% dispersant, 3% defoamer, 3% anti-sink agent, and the sum of the mass percentage of the above components is 100%.

The prepared photographic reflective ink is applied to screen printing. The observation and analysis of the printed products show that the ink is basically invisible under normal light, visible under flash photography, and has a preliminary anti-counterfeiting effect.

# References

1. Zhu ZG (2014) Probing into the secret printing security ink and its security technology. Hunan Packag 4:15–18
2. Xie SW, Gong G, Song Y et al (2019) Design of novel lanthanide-doped core-shell nanocrystals with dual up-conversion and down-conversion luminescence for anti-counterfeiting printing. Dalton Trans 48(20):6971–6983. https://doi.org/10.1039/c9dt01298b
3. Alaman J, Lopez-Valdeolivas M, Alicante R et al (2019) Digital luminescence patterning via inkjet printing of a photoacidcatalysed organic-inorganic hybrid formulation. Polymers 11 (3):1–16. https://doi.org/10.3390/polym11030430
4. Peng S (2015) Spherical vitreous material, 1st edn. Higher Education Press, Beijing, China
5. Huang C, OuYang YD, Zhou XP (2004) Reflective properties of beaded materials. J. Shantou Univ 19(2):23–27
6. Yuan JS (1998) Glass beads and road sign reflective paint. Build Mater Prod Appl 3:42–43
7. Wang XM, Chen GR (1998) Synthesis of glass bead emulsion coatings. Green Build (4):17–18
8. Xu SS, Guo F (2019) Reflective ink and its preparation method, paper for tobacco and its preparation method. ZL201811407550.X, 2019-04-19
9. Li HN (2019) Study on the divergence characteristics of glass bead originally reflecting screen. Sens Microsyst 38(3):14–16
10. Du XY, Chen QF, Chen GX (2018) Development of water- based UV inks based on wood-based panel printing. Appl Sci Graph Commun Packag 477:677–688. https://doi.org/10.1007/978-981-10-7629-9_84
11. Jin ZH (2002) Development and market prospect of environmental-friendly water-based ink. Res Print Packag China 19(1):35–38
12. Liu XT (2011) Green printing is imperative. GuangDong Packag 1:7–10
13. Liu XL, Ouyang Y, Wang XF et al (2017) Effect of defoamer on the performance of plastic water-based flexographic ink. Adv Graphic Commun Media Technol 417:967–974

# Preparation and Application of Carbon-Based Conductive Ink Based on Graphene

Zhihui Xie[1], Li Liu[1,2], Ningyu Xiao[1], Yunfei Zhong[1(✉)], and Xin Jing[1]

[1] School of Packaging and Materials Engineering, Hunan University of Technology, Zhuzhou, China
`maczone@l63.com`
[2] College of Communication and Art Design, University of Shanghai for Science and Technology, Shanghai, China

**Abstract.** The rapid development of the printing electronics industry had promoted the development of conductive inks. The conductive fillers of carbon-based conductive inks had the characteristics of wide source, low price and good stability, and had great application value. This paper analyzed the performance of carbon-based conductive inks with different raw material ratios. The conductive inks having a graphene content of 16%, 18%, 20%, and 22% were numbered A, B, C, and D, the resistivity and fineness of the four sets of inks were measured, and the printability of the carbon-based conductive ink in the practical application of the screen printing circuit was investigated. The experimental results showed that the resistivity decreases with the increase of graphene content, and the resistivity of conductive ink D was the smallest, which was 10.26 $\Omega$ cm; the fineness increases with the increase of graphene content, and the value was within the range of screen printing ink fineness. When the graphene content was 22%, the conductivity was better, and the quality of the screen printing sample wasalso higher.

**Keywords:** Graphene · Conductive ink · Conductive properties · Screen printing

## 1 Introduction

Conductive ink is a functional composite composed of conductive filler, binder, solvent and additives, conductive filler plays a key role in this [1, 2]. Conductive fillers are mainly divided into three major systems: metal, carbon and organic polymer [3]. Among the carbon-based conductive fillers are graphene, conductive carbon black, carbon nanotubes, etc., carbon-based conductive inks have excellent properties such as high electrical conductivity, excellent mechanical strength, light weight and low cost, but its adhesion is poor, the coating structure is unstable, and quality problems are prone to occur in practical applications. Therefore, the development of a new type of conductive ink with low cost and high performance has become a hot topic [4, 5]. Among carbon materials, graphene is a new energy material, which is a single-layer sheet composed of carbon atoms. It has high specific surface area, low resistivity and extremely fast electron

migration velocity [6–10]. It is widely used in electronic label printing, printed circuit boards, electronic switches, membrane switches, etc., and has broader research prospects and market value compared with other conductive inks [11, 12].

Therefore, based on the fixed polyurethane resin system, the effects of different raw material ratios on the performance of carbon-based conductive inks were studied. The best carbon-based conductive inks were obtained by analysis.

## 2 Experimental

### 2.1 Experimental Materials and Instruments

The raw materials of the experimental materials used in the research process are polyurethane resin, absolute ethanol (analytical grade), glycerol (analytical grade), polyethylene wax (analytical grade), graphene (high purity), conductive carbon black (LZ80-85), deionized water, defoamer (J0401).

The experimental Instruments used in the experiment were an electronic balance (JY5002), a digital display electric stirrer (JJ-3), a collector type magnetic heating stirrer (DF-2), and a scraper fineness meter (QXP), screen drying box (WJ-HG9010), vacuum screen printing machine (WJ-VS9010), manual screen printing machine (6080), digital multi-meter (DT-9205A), ink adjustment knife (GH-02), Anton Star digital electronic magnifying glass (A7).

### 2.2 Preparation and Proofing of Carbon-Based Conductive Inks

  (I) First use the electronic balance to weigh the polyurethane resin with 16% mass fraction, 11% glycerol, 2% polyethylene wax, 18% deionized water, 2% conductive carbon powder, 1% defoamer. Further, 16, 18, 20, 22% graphene and 34, 32, 30, 28% absolute ethanol.
 (II) A certain amount ofacrylic resin, solvent and auxiliary agent are placed in the reaction vessel to be fully dissolved, and then stirred by a collecting magnetic heating stirrer to obtain an ink binder. The filler is further dissolved, and then uniformly stirred by a collecting magnetic stirrer to obtain a conductive ink.
(III) The graphene mass fraction is 16%, the ink number A; 18%, ink number B; 20%, ink number C; and 22%, ink number D.
 IV) Designing the proofing rectangular strip:1st is 6 cm × 3 cm, 2 nd is 8 cm × 3 c m, and 3rd is 8 cm × 4 cm, the total area of the proofing strip is 74 cm$^2$.
  (V) Make a screen printing plate.
 (VI) Sample proofing: conductive inks A, B, C, and D were proofed by screen printing to obtain proof samples a, b, c, and d.

### 2.3 Carbon-Based Conductive Ink Performance Testing

#### 2.3.1 Measure the Density of Carbon-Based Conductive Inks

The prepared four sets of conductive inks were respectively taken into 10 ml in a measuring cylinder, and each set of conductive ink was subjected to three experiments,

and the average value of the three groups was used as the fixed value of the density, and the measurement results are shown in Table 1, the prepared ink density values are not much different.

**Table 1.** The results of conductive ink density measurement

| Ink | Quality (g) | Density (g/cm$^3$) |
|-----|-------------|--------------------|
| A | 7.94 | 0.79 |
| B | 8.31 | 0.83 |
| C | 8.77 | 0.88 |
| D | 9.12 | 0.91 |

### 2.3.2 Measure the Ink Layer Thickness of Carbon-Based Conductive Inks

The weight of the coated paper to be printed and proofed by the electronic balance is m; the total weight of the coated paper and the transferred ink after screen printing is M; according to the transferred ink quality, the total area of the rectangular strip to be proofed, and the prepared The density of the conductive ink is obtained, and the thickness of the ink layer of each sample is obtained. The measurement results are shown in Table 2, the thickness of the ink layer to be proofed is within the allowable range of the screen print.

**Table 2.** The results of conductive ink layer thickness measurement

| Sample | h (μm) |
|--------|--------|
| a | 8.55 |
| b | 8.63 |
| c | 7.52 |
| d | 8.76 |

### 2.3.3 Measure and Calculate the Resistivity Of Carbon-Based Conductive Inks

Take each set of experimental samples, measure the resistance value of each rectangular strip with a multimeter; calculate the resistivity of the prepared conductive ink by the formula (2.1), and the data is recorded in Table 3.

$$\rho = \frac{RS}{L} = \frac{Rhd}{L} (2.1)$$

It can be seen from Table 3 that as the mass fraction of graphene increases, the resistivity of the conductive ink gradually decreases, and the electrical conductivity gradually increases.

**Table 3.** The results of conductive ink resistivity measurement

| Ink | Resistivity ($\Omega$ cm) |
|-----|---------------------------|
| A | 15.17 |
| B | 13.58 |
| C | 10.69 |
| D | 10.26 |

### 2.3.4    Measurethe Fineness of Carbon-Based Conductive Inks

In this experiment, the prepared conductive ink was measured for fineness using a QXP type scraper fineness meter. Each group was measured 3 times, and the average value of three times was the value of ink fineness. The measurement results are shown in Table 4. As can be seen from Table 4, the fineness of the ink is within the range of screen printing fineness [13]. However, the ink particles are too large to cause blockage, resulting in low screen printing quality and even reduced mechanical properties of the printing plate [14].

**Table 4.** The results of conductive fineness measurement

| Ink | Fineness ($\mu$m) |
|-----|-------------------|
| A | 12 |
| B | 12 |
| C | 13 |
| D | 14 |

### 2.4    Application of Carbon-Based Conductive Inks

According to the designed RFID antenna, the screen required for the experiment was prepared by the direct plate making method; the prepared four sets of different graphene content inks were selected as experimental samples; the coated paper was selected as the printing material; and the printing was performed by a manual screen printing machine. The quality of the print was analyzed after thorough drying at room temperature.

### 2.4.1    Partial Enlargement Analysis of Printed Samples

The printed sample is shown in Fig. 1, and the partial enlarged view is shown in Fig. 2. Among them, (a) graphene is used in an amount of 16%, (b) graphene is used in an amount of 18%, (c) graphene is used in an amount of 20%, and (d) graphene is used in an amount of 22%. When the graphene content is 16%, the viscosity is small, the fluidity is good, and the boundary of the printed product has a side leakage phenomenon; When the graphene content is 18 and 20%, the fluidity and uniformity are generally the same, and the edge seepage is also small; When the graphene content is 22%, compared with the other three groups of conductive inks, the ink has moderate viscosity, good printing adaptability, good fluidity and uniformity, and the printed corners and boundaries of the printed products are clear.
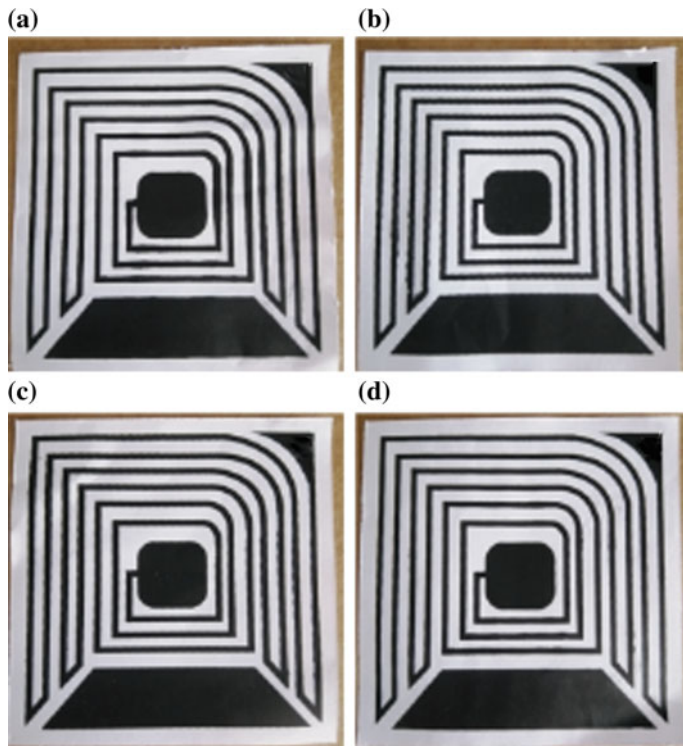
**Fig. 1.** The print sample

### 2.4.2 Abrasion Resistance Analysis of Printed Samples

The abrasion resistance test was performed on the printed product using a friction tester. The abrasion resistance of the printed product was calculated by the formula (2.2), and each group was measured 3 times, and the average value of three times was used as the value of the abrasion resistance, and the data is recorded in Table 5.

$$A_s = \frac{D}{D_0} \times 100\% (2.1)$$

It can be seen from Table 5 that the wear resistance of the inks produced meets the requirements for screen printing on the screen [15].
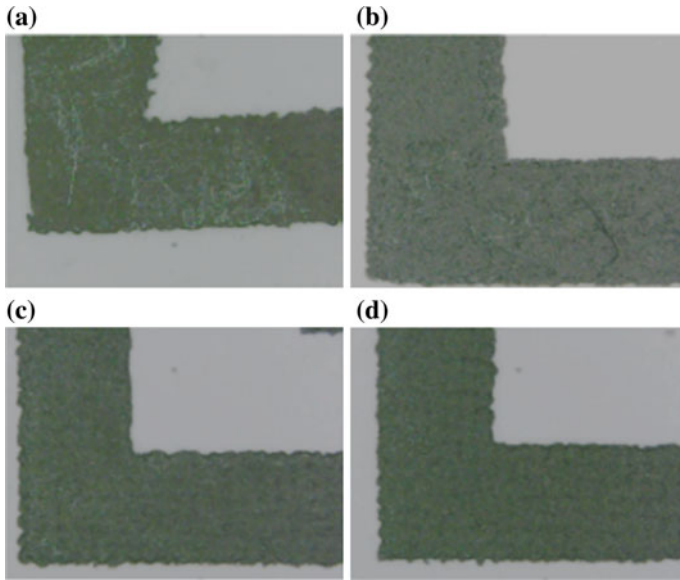
**Fig. 2.** The partial enlargement

**Table 5.** The results of abrasion resistance of printed samples

| Printed samples | $A_s$ (%) |
|---|---|
| a | 88.06 |
| b | 88.15 |
| c | 92.09 |
| d | 92.75 |

## 3 Conclusions

Conductive inks are the key materials for electronic product printing. A good conductive ink formulation has good printability, and the printed ink layer has the characteristics of low resistivity, low curing temperature, and stable electrical conductivity. Therefore, the subject of the study on the preparation and application of graphene-based carbon-based conductive inks, the experimental results show that:

As the graphene content increases, the resistivity of the conductive ink gradually decreases; the resistivity of the conductive ink D is at least 10.26 $\Omega$ cm.The fineness of the conductive ink becomes larger as the graphene content increases, and the fineness values are within the allowable range of the screen printing ink.When the added mass fraction of graphene is 22%, the printing suitability and uniformity of the conductive

ink are better than those of the other three sets of inks, and the printed matter boundaries and corners of the printed product d are clear and uniform.The best ratio of carbon-based conductive ink is: polyurethane resin, glycerol, polyethylene wax, deionized water, conductive carbon powder, defoamer, absolute ethanol, graphene added mass fraction of 16%, 11%, 2%, 18%, 2%, 1%, 28%, 22%. Carbon-based conductive inks are widely used in many fields and will be the focus of research in the field of materials in the future.

# References

1. Li L, Mo L, Ran J,Xin Z (2014) Conductive ink and its application technology progress. Imaging Sci Photochem 32(4):393–401
2. Lee CL, Chen CH, Chen CW (2013) Graphene nanosheets as ink particles for inkjet printing on flexible board. Chem Eng J 230(16):296–302
3. Ye Li (2015) Conductive ink application status and future application prospects. Technol Innov Appl 5(19):286
4. Wang Z, Li Y, Yin J (2018) Preparation of graphene-carbon nanotube conductive ink and its electrical conductivity. J Heilongjiang Univ Sci Technol 28(5):514–518
5. Xiao S, Du Y, Liu Q, Wang H, Yang C (2013) The effect of function on ink properties in carbon-based conductive inks. Electr Mater 5(1):27–31
6. Tobjork D, Osterbacka R (2011) Paper electronics. Adv Mater 23(17):1935–1961
7. Gao Y, Wen S, Wang W, Leng Y, Zhao Y (2014) Inkjet printing patterns of highly conductive pristine graphene on flexible substrates. Ind Eng Chem Res 53(43):16777–16784
8. Arapov K, Rubingh E, Abbel R, Laven J, De With G, Friedrich H (2016) Conductive screen printing inks by gelation of graphene dispersions. Adv Funct Mater 26(4):586–593
9. Overgaard MH, Kuhnel M, Hvidsten R, Petersen SV, Vosch T, Nørgaard K et al (2017) Highly conductive semitransparent graphene circuits screen-printed from water-based graphene oxide ink. Adv Mater Technol 2(7):1700011
10. Li J, Zhao X (2017) Recent developments in graphene conductive ink: Preparation, printing technology and application. Chin Sci Bull 62(27):3217–3235
11. Wang W, Guo Y, Sun Z (2015) Research progress of carbon-based conductive ink fillers. Chem Ind Eng Prog 34(12):4259–4264
12. Lu X, Liang Y, Zhong Y, Chen H (2017). Optimized formulation design of graphene-based condnctiveink. Packag J 9(3):89–94
13. QB/T 4753–2014 (2014) General technical conditions for screen printing inks. China Light Industry Press, Beijing
14. Wang R (2016) Development of printed electronics and conductive materials technology. Inf Rec Mater 17(2):22–24
15. GB/T 7706–2008 (2008) Letterpress decoration printed matter. China Standard Press, Beijing

# Research on Curing Performance and Printability of Magenta UV-LED Gravure Ink

Beiqing Huang, Bin Wang, Le Ma, Hui Wang[✉], and Xianfu Wei[✉]

School of Printing and Packaging Engineering, Beijing Institute of Graphic Communication, Beijing, China
{wanghui,weixianfu}@bigc.edu.cn

**Abstract.** At present, gravure ink has become the most widely used ink in China due to its extensive application in packaging and printing. However, conventional gravure ink contains a large amount of organic solvents, which are harmful to the environment. Therefore, it is extremely urgent to develop environmental-friendly gravure ink. UV-LED gravure ink is a kind of solvent-free ink which can be cured by low-energy UV-LED light source. Due to the advantages of low energy consumption, no pollution and good printing quality, UV-LED gravure ink is realized as environmental-friendly ink with high-quality and leading the development direction of gravure ink. In order to develop high-quality UV-LED gravure ink, this research reports the preparation of magenta UV-LED gravure ink and its important properties, such as curing rate and printability. Prepolymers, monomers, photoinitiators and laboratory-made magenta ink paste are employed to prepare a series of UV-LED gravure ink. Curing rate, viscosity, surface tension and color density are characterized to investigate the effect of reactive components on curing performance and printability. Meanwhile, the optimal ink formulation is determined by design of experiments. The results show that the prepared magenta UV-LED gravure ink exhibits good curing performance and printability to achieve excellent printing quality.

**Keywords:** UV-LED gravure ink · Curing rate · Printability

## 1 Introduction

In the past decades, gravure ink has become the most widely used ink in package printing products due to the advantages of rich color-tone, high color saturation and high press-run [1]. Currently, the most widely used gravure ink on the market issolvent-based ink containing a large amount of volatile organic compounds (VOCs), which are harmful to the environment. Therefore, it is extremely urgent to develop environmental-friendly gravure ink.

Recently, UV-LED ink has become the focus of printing and packaging industry due to the advantages of efficient, energy-savingand environmental-friendliness. The solvent-free UV-LED ink can be rapidly cured by low-energy UV-LED irradiation, making it suitable for a wide range of substrates, especially materials with poor solvent

or heat resistance. Most importantly, almost no VOC is released during the manufacturing and applying of UV-LED ink, meeting the requirements of environmental protection laws and regulations.

At present, although UV-LED inks have been widely applied in off-set printing [2, 3], screen-printing [4], flexo-printing [5] and ink-jet printing [6–8], rarely research or application in gravure printing process is reported. In this research, preparation and performance of magenta UV-LED gravure ink are reported. This research will promote the application of high-quality UV-LED gravure ink, which is of great helpful for the sustainable development of printing and packaging industry.

## 2 Experimental

### 2.1 Materials

Hyper branched polyester acrylateresins EB150, EB151, EB152, LED01 and aliphaticpolyurethane acrylateresins EB270 and EB870were purchased from Allnex and employed as prepolymers. 4-acryloylmorpholine (ACMO), 2-(2-ethoxyethoxy) ethyl acrylate (EOEOEA), dipropylene glycol diacrylate (DPGDA), neopentyl glycol diacrylate (NPGDA), tri (propylene glycol) diacrylate (TPGDA) and trimethylolpropanetriacrylate (TMPTA) werepurchased from Tianjin Tianjiao Radiation Curable Materials Co., Ltd and employed as monomers. Photoinitiatorsbis (2,4,6-Trimethylbenzoyl) phenyl phosphine oxide (819) and 1508 were purchased from Tianjin Jiuri New Materials Co., Ltd. Photoinitiators diphenyl (2,4,6-trimethylbenzoyl) phosphine oxide(TPO), 2-isopropylthioxanthone (ITX), 2,4-diethyl-9H-thioxanthen-9-one (DETX) andamine-assisted initiator EHA were purchased from Beijing Yingli Science and Technology Development Co., Ltd. Additive TEGORad 2100 was purchased from Degussa.

### 2.2 Equipments

Electronic balance (Ohaus CP153, USA) and mechanical agitator (JJ-I, Changzhou Guohua Electric Appliance Co., Ltd., China) were used to prepare ink. Gravure printing proofer (RK Printcoat Instruments, UK) and UV-LED curing illuminator (Heraeus Semray UV4003, Germany) with tunable power density at the wavelength of 395 nmwere employed to prepare gravure printing sheets and evaluate curing performance. Surface tensiometer (Krüss K100, Germany) and rheometer (TA AR2000ex, USA) were used to test surface tension and viscosity of ink samples, respectively. Spectral photometer (GretagMacbeth SpectroEye, Switzerland) was used to characterize color density of ink films.

### 2.3 Preparation of Magenta UV-LED Gravure Ink

Laboratory-made magenta color paste, prepolymers, monomers, photoinitiators and additives were mixed and stirred until a homogeneous liquid was formed. Then the sample was used for gravure proofing and other tests.

## 2.4   Preparation of Gravure Printing Sheet

Printing sheets were prepared on coated papers using the gravure printing proofer with a medium printing speed. The gravure printing area with an ink film thickness of 36 μm was then used to test UV-LED curing performance and color density.

## 2.5   Performance Characterization of Magenta UV-LED Gravure Ink

### 2.5.1   Viscosity

Viscosity was tested by the rheometer with a 60 mm aluminum rotor plate at 25 °C and the value of viscosity with the shear rate of 1 s$^{-1}$ was recorded.

### 2.5.2   UV-LED Curing Performance

UV-LED curing performance of ink was checked by the following steps. First of all, a printing sheet was prepared by the gravure printing proofer. Then power density of the curing illuminator was set as a maintained value and the conveyor speed was adjusted to make the ink to be cured. The score of UV-LED curing performance (*CP*) was defined by Eq. 1:

$$CP = \left( 0.3 \times \frac{R}{50} + 0.7 \times \frac{1}{T} \right) \times 100 \tag{1}$$

where *R* was the curing rate represented by the maximum speed (m/min) of conveyor, and *T* was the minimum numbers of passes through the UV-LED illuminatorto dry the printing sheet with the corresponding conveyor speed.

### 2.5.3   Surface Tension

Surface tensiometer was employed to characterize surface tension of the ink with pull-out method using a platinum plate at 25 °C.

### 2.5.4   Color Density

After being cured in the UV-LED irradiation, color density of the printing area with an ink film thickness of 36 μm was measured by a spectral photometer.

### 2.5.5   Surface Condition of Ink Films

Surface condition of an ink film was checked by observation in various viewing angles and light sources. According to the different wetting and flowing conditions, sampleswere divided into five levels. For instance, samples without void, speckle, blister or streak were ranked as level 5; meanwhile, samples with multiple visible problems were ranked as level 1.

# 3    Results and Discussion

## 3.1    Effect of Monomers on Performance of Magenta UV-LED Gravure Ink

### 3.1.1    Species of Monomers

As one of the most important components of UV-LED curable ink, monomer not only participates in the photopolymerization, but also acts as a dilution, affecting the curing performanceand various properties of cured ink films. UV-LED gravure ink prepared with different monomers and the corresponding performances are illustrated in Fig. 1.
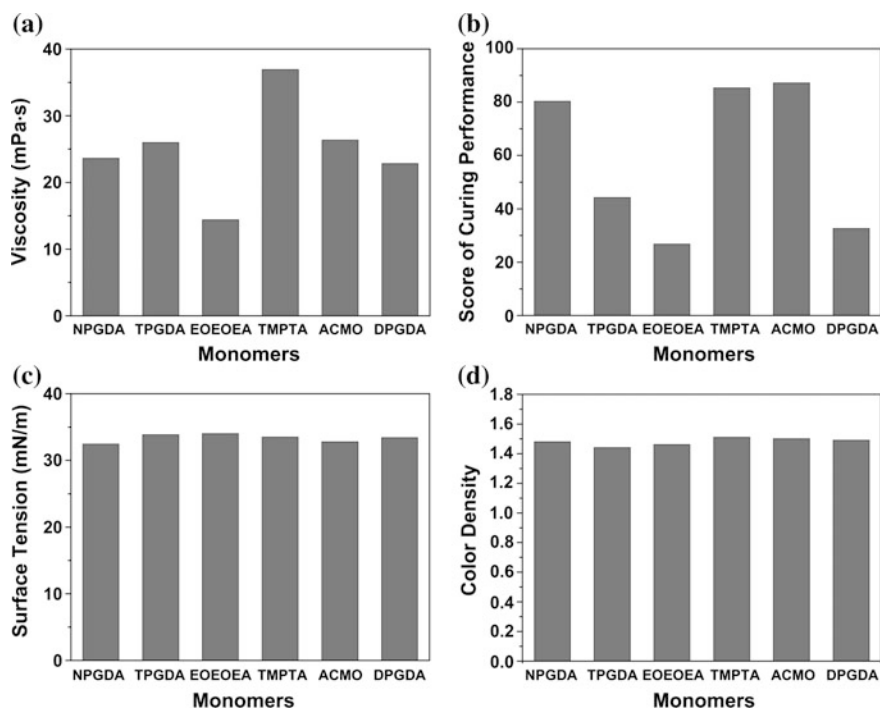


**Fig. 1.** **a** Viscosity, **b** score of curing performance in the UV-LED irradiation with a power density of 14 W/cm², **c** surface tension and **d** color density of magenta UV-LED gravure ink prepared with different monomers

As shown in Fig. 1a, the viscosity of magenta UV-LED gravure ink varies from 14 to 37 mPa s. The viscosity of ink is related to the viscosity of the monomer itself. Since the viscosity of the monomer has a great correlation with the functionality [9], ink prepared with tri-functional monomer TMPTA has the largest viscosity, while the mono-functional monomer EOEOEA brings out the lowest viscosity.

As shown in Fig. 1b, ink prepared with different monomers exhibits different curing performances. Following the mechanism of free-radical photopolymerization, the curing performance depends not only on the chemical reactivity of active materials, but also partially on the viscosity. Generally, higher functionality leads to larger viscosity and faster curing rate, for instance, ink prepared with TMPTA has significantly better curing performance than that prepared with EOEOEA. Specially, mono-functional monomer ACMO produces better curing performance than any other monomers due to the extremely high chemical reactivity provided by the tertiary amine group.

As shown in Fig. 1c, surface tension of ink was in the range of 32–34 mN/m. As all of the monomers are acrylate compounds, and the rather small structural difference has almost no influence on the surface tension of ink.

As shown in Fig. 1d, color densities of ink prepared by different monomers are all about 1.5, which meets the requirements of gravure printing process.

### 3.1.2 Design of Experiments for Mixed Monomers

By investigating the influence of monomers on the performances of magenta UV-LED gravure ink, it is known that different monomers have different effects on properties of ink. EOEAEA is helpful to reduce the viscosity of ink, and ACMO and TMPTA are beneficial to improve curing rate. However, none of the monomers can meet all aspects of technical requirements. In order to solve this problem, it could be an efficient process to prepare UV-LED gravure ink with mixed monomers to improve each performance. According to the experimental results described above, a simplex centroiddesign of experiment (DOE) was carried out for the development of mixed monomers, in which $X_1$, $X_2$, $X_3$ and $X_4$ represented the weight fraction of EOEOEA, ACMO, NPGDA and TMPTA, respectively [10], as shown in Table 1. Magenta UV-LED gravure ink was prepared according to the design in Table 1 and the properties were determined, as listed in Table 2.

Considering the importance of each technical indicator on UV-LED gravure ink, the weight of viscosity, curing performance, surface tension and color density was respectively valued as 0.25, 0.35, 0.20 and 0.20 to calculate memberships and comprehensive scores. According to the result of solution programming, the regression equation has a maximum value of 76.00 when $X_1 = 0.3$, $X_2 = 0.7$, $X_3 = 0$ and $X_4 = 0$. Therefore, the best comprehensive performance could be achieved from an optimal-formulation with mixed monomers, in which the mass ratio of EOEOEA and ACMO is 30:70. Subsequently, a sample was prepared with this formulation and the performances were tested, as listed in Table 3.

**Table 1.** Experimental design of ink formulation with mixed monomers

| No. | $X_1$ (EOEOEA) | $X_2$ (ACMO) | $X_3$ (NPGDA) | $X_4$ (TMPTA) |
|-----|------|------|------|------|
| 1 | 1 | 0 | 0 | 0 |
| 2 | 0 | 1 | 0 | 0 |
| 3 | 0 | 0 | 1 | 0 |
| 4 | 0 | 0 | 0 | 1 |
| 5 | 1/2 | 1/2 | 0 | 0 |
| 6 | 1/2 | 0 | 1/2 | 0 |
| 7 | 1/2 | 0 | 0 | 1/2 |
| 8 | 0 | 1/2 | 1/2 | 0 |
| 9 | 0 | 1/2 | 0 | 1/2 |
| 10 | 0 | 0 | 1/2 | 1/2 |
| 11 | 1/3 | 1/3 | 1/3 | 0 |
| 12 | 1/3 | 1/3 | 0 | 1/3 |
| 13 | 1/3 | 0 | 1/3 | 1/3 |
| 14 | 0 | 1/3 | 1/3 | 1/3 |
| 15 | 1/4 | 1/4 | 1/4 | 1/4 |

**Table 2.** Data of performances in design of experiments for mixed monomers

| No. | Viscosity (mPa s) | $CP^a$ | Surface tension (mN/m) | Color density |
|-----|------|------|------|------|
| 1 | 14.37 | 27 | 34.00 | 1.46 |
| 2 | 26.35 | 87 | 32.77 | 1.50 |
| 3 | 23.61 | 80 | 32.45 | 1.48 |
| 4 | 36.90 | 85 | 33.49 | 1.51 |
| 5 | 20.56 | 80 | 34.41 | 1.55 |
| 6 | 17.03 | 38 | 32.57 | 1.58 |
| 7 | 21.31 | 47 | 32.82 | 1.62 |
| 8 | 24.69 | 81 | 33.95 | 1.53 |
| 9 | 32.17 | 85 | 34.31 | 1.46 |
| 10 | 31.03 | 41 | 32.28 | 1.56 |
| 11 | 21.04 | 53 | 33.30 | 1.51 |
| 12 | 24.67 | 50 | 33.49 | 1.53 |
| 13 | 23.49 | 44 | 30.02 | 1.61 |
| 14 | 24.59 | 51 | 33.48 | 1.52 |
| 15 | 21.12 | 47 | 33.22 | 1.55 |

[a]The value of CP was calculated by Eq. 1. The power density of UV-LED irradiationwas 14 W/cm$^2$

**Table 3.** Performances of magenta UV-LED gravure ink prepared with the optimal ratio of mixed monomers (EOEOEA:ACMO = 30:70)

| Viscosity (mPa·s) | $R^a$ (m/min) | $T$ | Surface tension (mN/m) | Color density |
|---|---|---|---|---|
| 22.37 | 24 | 1 | 32.55 | 1.52 |

[a]The power density of UV-LED irradiation was 14 W/cm$^2$

## 3.2  Effect of Prepolymers on Performance of Magenta UV-LED Gravure Ink

Besides the monomer, the prepolymer is another important constituent of UV-LED gravure ink. In order to investigate the effect of the prepolymer on properties of magenta UV-LED gravure ink, samples were prepared with different prepolymers and the corresponding performances were tested, as shown in Fig. 2.
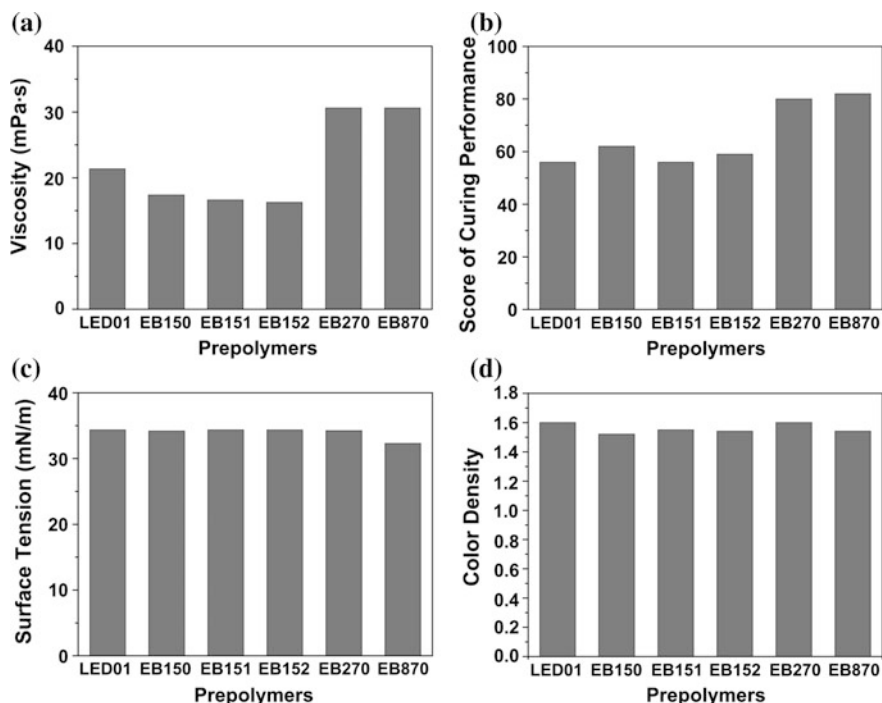


**Fig. 2.** **a** Viscosity, **b** score of curing performance in the UV-LED irradiation with a power density of 14 W/cm$^2$, **c** surface tension and **d** color density of magenta UV-LED gravure ink prepared with different prepolymers

As shown in Fig. 2a, there exist significant differences among viscosities of samples prepared with different prepolymers. Hyper branched polyester acrylate resin LED01, EB150, EB151and EB152 have lower viscosity than aliphatic polyurethane

acrylate EB270 and EB870. The reason is hyper branched polymer could effectively hinder the entangling of chain segments among molecules due to the spherical molecular structure [11]. Similar to the research of monomers, viscosity, functionality and curing performance are quite correlated; moreover, with the presence of hyper branched prepolymers, polymerization could be accelerated due to the high functionality and the rare occurrence of chain-transfer reaction. For this reason, EB270 and EB870 with both higher viscosity and functionality are easier to participate the polymerization to form solid ink films than other kind of prepolymers, as illustrated in Fig. 2b.

Figure 2c shows that surface tension of samples prepared from different prepolymers is extremely close, the value of which is about 32–35 mN/m. Figure 2d illustrates that the magenta UV-LED gravure ink prepared with any kind of prepolymer generates a color density with a value of 1.5–1.6, showing excellent color performance.

Similarly with the strategy of making use of mixed monomers, mixed prepolymers were utilized to prepare magenta UV-LED gravure inkto generate excellent comprehensive performances. EB152, EB270 and EB870 were used in the DOE. According to the result, a mixture of EB152 and EB870 with the mass ratio of 21:29 could have the best comprehensive performances. Thus, as shown in Table 4, a favorable comprehensive performanceis achieved by applying the optimal proportion of mixed prepolymers.

**Table 4.** Performances of magenta UV-LED gravure ink prepared with the optimal ratio of mixed prepolymers (EB152:EB870 = 21:29)

| Viscosity (mPa s) | $R_a$ (m/min) | $T$ | Surface tension (mN/m) | Color density |
|---|---|---|---|---|
| 23.57 | 25 | 1 | 34.04 | 1.54 |

[a]The power density of UV-LED irradiation was 14 W/cm$^2$

## 3.3 Effect of Photoinitiators on Curing Rate of Magenta UV-LED Gravure Ink

As the key performance of UV-curable materials, the reaction rate of photo-induced polymerization is related to theabsorption spectrum of photoinitiator and the mechanism of chemical active intermediates (free-radicals or ions) generation [12]. In this research, several free-radical photoinitiators are used to investigate the curing performance in the UV-LED irradiation at the wavelength of 395 nm. Figure 3 illustrates the curing rate of UV-LED gravure ink prepared with different free-radical photoinitiators. As a kind of acryl phosphine oxide compounds, photoinitiator 819 generates a curing rate of 50 m/min, which is much higher than TPO. It could be attributed tothe larger molar extinction coefficient of photoinitiatorat 395 nm [11]. The most essential reason is that the photodecomposition products of one 819 molecule include two trimethylbenzoylradicals and one phenylphos phonoacetate radical, which is higher in number
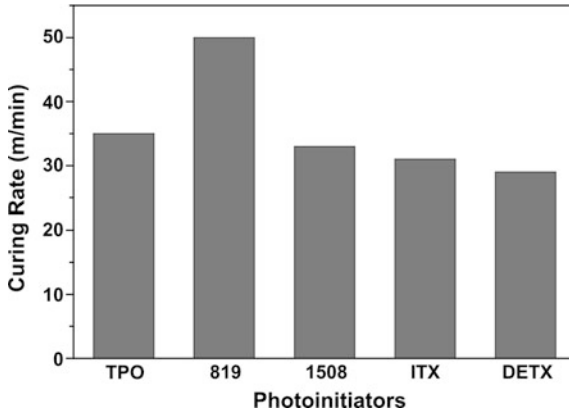
**Fig. 3.** Curing rate of magenta UV-LED gravure ink prepared with different photoinitiators in the UV-LED irradiation with a power density of 14 W/cm$^2$

than the photodecomposition products of TPO. Photoinitiator 1508 is a kind of thioxanthone macromolecules which could also provide excellent photo-induced curing performance. To further improve the curing rate, a mixture of 819 and 1508 were developed through a simplex centroid DOE. By the means of programming solution, the highest curing rate could be achieved when the mass ratio of 819 and 1508 is 14:11. Prepared with mixed photoinitiators of this proportion, the magenta UV-LED gravure ink is determined to have a curing rate higher than 76 m/min in the UV-LED irradiation with a power density of 14 W/cm$^2$ at 395 nm, which is able to meet the requirement of gravure printing production.

Further more, the concentration of photoinitiator also plays a key role on the curing performance of ink, as it directly determines the amount of chemical active intermediates (free-radicals or ions) produced in the process of photo-initiating. In order to explore the appropriate concentration of photoinitiator, samples with different concentrations of mixed photoinitiators were prepared and the corresponding curing rates were tested. As shown in Fig. 4, the curing rate accelerates along with the increase of photoinitiator concentration. By using UV-LED irradiation with a power density of 7 W/cm$^2$, when the concentration of photoinitiator reaches 9% or more, a curing rate of higher than 50 m/min is obtained.

## 3.4    Effect of Color Paste Concentration on Color Density of Magenta UV-LED Gravure Ink

The concentration of color paste in ink determines the color density of printing area. Samples with different concentrations of magenta color paste were prepared and used to proof. Color densities of ink films with a thickness of 36 μm on proofing sheets were characterized after UV-LED curing, which are illustrated in Fig. 5. Obviously, as the concentration of color paste in the ink increases from 40–60%, the color density of printing area increases from 1.38 to 1.63. However, when the concentration of color
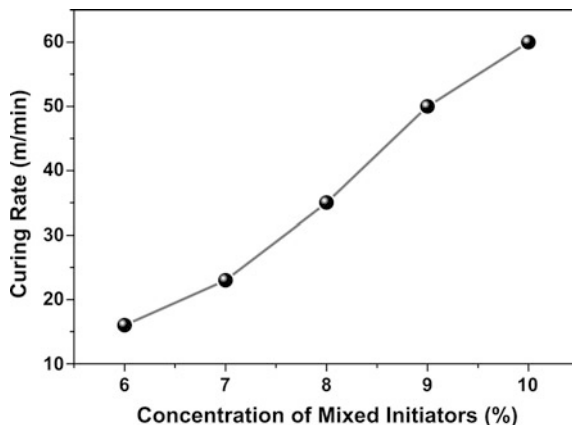
**Fig. 4.** Curing rate of magenta UV-LED gravure ink prepared with different concentrations of mixed photoinitiators in the UV-LED irradiation with a power density of 7 W/cm$^2$
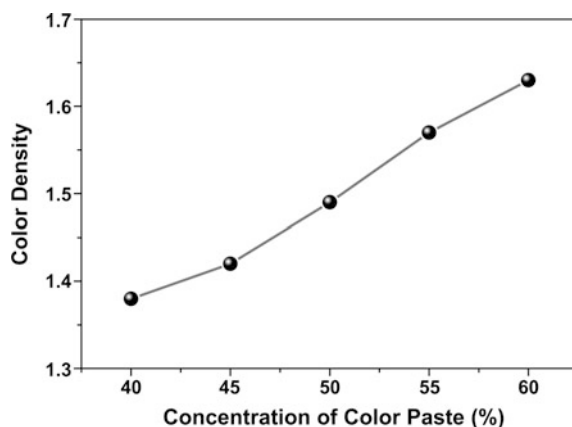


**Fig. 5.** Color densities of printing areas prepared by ink with different concentrations of magenta color paste

paste is too high, the viscosity of ink is too large to satisfy the printability. Therefore, it is necessary to use an appropriate concentration of color paste according to actual requirements.

## 3.5   Comprehensive Performance of Magenta UV-LED Gravure Ink

According to the experimental results above, an optimal formulation of UV-LED gravure ink was achieved by DOE. Based on this formulation, magenta UV-LED gravure ink was prepared by using monomers, prepolymers, photoinitiators and 50% magenta color paste. In addition, 0.5% TEGORad 2100 was used to improve the wetting and flowing properties. Proofing sheets were prepared and cured in UV-LED

irradiation with a power density of 7 W/cm$^2$ at 395 nm. Characterization results of ink prepared with optimal formulation are listed in Table 5. The prepared magenta UV-LED gravure ink provides excellent comprehensive performances, which guarantees the production efficiency and printability.

**Table 5.** Performance of magenta UV-LED gravure ink prepared with the optimal formulation

| Viscosity (mPa s) | Surface tension (mN/m) | $R^a$ (m/min) | $T$ | Color density | Surface condition |
|---|---|---|---|---|---|
| 41.27 | 25.41 | 55 | 1 | 1.60 | 5 |

$^a$The power density of UV-LED irradiation was 7 W/cm$^2$

## 4    Conclusions

In this research, we report the preparation and performance of magenta UV-LED gravure ink consisted of laboratory-made magenta color paste, monomers, prepolymers, photoinitiators and additives. Experimental results show that species and concentration of monomers, prepolymers and photoinitiators greatly affect UV-LED curing performance, and printability is strongly depended on monomers and prepolymers. By the means of DOE for the formulation, the optimal viscosity, curing rate and surface tension are obtained with mixed monomers consisted of EOEOEA and ACMO (3:7), mixed prepolymers consisted of EB152 and EB870 (21:29) and mixed photoinitiator consisted of 819 and 1508 (14:11). Besides, color density of printing area and concentration of color paste appear a positive correlation. The prepared magenta UV-LED gravure ink is of excellent comprehensive performances and expected to be applied as novel environmental-friendly printing materials.

## References

1. Leach RH, Pierce RJ, Hickman EP, Mackenzie MJ, SmithH G (1993) The printing ink manual. Springer, Dordrecht
2. Feng LT, Zheng JY, Wu XF et al (2017) UV-LED offset printing ink and preparation method there of. Chinese Patent: CN107286740A
3. Mendoza KL, Ortega A, Kim NS (2015) Optimization of UV LED-curable ink for reverse-offset roll-to-plate (RO-R2P) printing. J Electron Mater 44(3):784–791
4. Song C (2012) Application analysis of LED UV curing technology in screen printing. Screen Print Ind 12(1):50–53
5. Wang DF (2018) The preparation of UV-LED flexo ink. Master Dissertation, Xi'an University of Technology, Xi'an
6. Zapka W (2017) Handbook of industrial inkjet printing: a full system approach. Wiley, Weinheim

7. Nakane H, Kumai M, Hagi M et al (2015) Advanced LED UV inks for industrial applications. NIP and digital fabrication conference, vol 1, pp 448–451
8. Huang B, Lü Y, Ma L, Wei X, Wang H (2019) Research on printing and prototyping performance of three-dimensional printing materials for UV-curing ink-jet. In: Zhao P, Ouyang Y, Xu M, Yang L, Ren Y (eds) Advances in graphic communication, printing and packaging. Lecture notes in electrical engineering, vol 543. Springer, Singapore
9. Jin YZ (2018) Photo curing inks. Chemical Industry Press, Beijing
10. Li YY, Hu CR (2005) Experiment design and data processing. Chemical Industry Press, Beijing
11. Jin YZ (2010) Photo curing material performance and application manual. Chemical Industry Press, Beijing
12. Liu XX, Liao ZF, Cui YY et al (2019) Principle of polymeric photochemistry and technology of photo curing. Science Press, Beijing

# Effect of Reactivee Mulsifier on Properties of Acrylate Microemulsion

Chunxu Zheng, Xiulan Xin[✉], and Yingying Li

Beijing Technology and Business University, Beijing, China
xinxl2007@l26.com

**Abstract.** The polymerizable surfactant will form a covalent bond with the monomer in the reaction system, and will not migrate during the film-forming process. This will help to improve the water resistance and the stability of the emulsion. In this paper, an acrylate microemulsion with an average particle size of 55 nm and solid content of 40% was synthesized by non-pre-emulsion polymerization. The reactive surfactant NR-1 on the properties of acrylate emulsion was systematically studied. The emulsion resistance was increased, the stability was increased, and the shear resistance of the emulsion was enhanced effectively with the increase of the amount of reactive emulsifier NR-1. It was found that when the amount of NR-1 was 1%, the emulsion had the best comprehensive properties.

**Keywords:** Polymerizable surfactant · Comprehensive properties · Acrylate microemulsion

## 1 Introduction

Microemulsion and emulsion are all oil-water mixtures formed under the action of emulsifier, but there is a significant difference between them. Emulsion is a turbid unstable system, and microemulsion is a transparent system of thermodynamics and stability [1]. The size of the dispersed phase in the emulsion is large, while the dispersed phase in the microemulsion is small. This is because the surface of the microemulsion is coated with emulsifier or cosurfactant, and has good stability [2, 3]. It has certain application prospects in social production and industrial production [4]. Because of the large demand for emulsifiers and the small amount of monomers, the production and application of microemulsions are limited [5]. We used the APS as initiator to prepare acrylate microemulsion with average particle size of 55 nm and the solid content 40%. The addition of reactive surfactant (NR-1) can effectively improve the alcohol resistance and shear resistance of acrylate microemulsion. The core-shell latex particles were successfully polymerized. It had the characteristics of small particle size and high stability of microemulsion. On the premise of maintaining good emulsion properties, the optimum initiator content, the content of reactive emulsifier and the best kind of non ionic emulsifier were determined materiel.

# 2 Experiment

## 2.1 Materials

Methyl Methacrylate (MMA), n-Butyl; Acrylate (BA): Chemically pure, Sinopharm Group Chemical Reagent Co., Ltd.; Sodium Dodecyl Sulfate (SDS): Chemically pure, Tianjin Chemical Reagent Factory No. 6; Polyphenol Ethers (OP-10): Chemically pure, Tianjin Institute of Chemical Reagents; Reactive Emulsifier (NR-1), Industrial Grade, Hangzhou Shipeng Co., Ltd.

## 2.2 Preparation

Nonpreemulsifying: All emulsifiers and part of water was stirred and dissolved at a certain temperature and speed to form an emulsifier aqueous solution. After adding a certain amount of initiator aqueous solution, the reaction temperature was raised to the reaction temperature, the monomer was added, and the remaining initiator aqueous solution was added. After finished dropping monomer, the aging reaction continued for 1 h. after cooling to 50–55 °C, adjust pH to 7–8 with ammonia water.

Preemulsification: All monomers, part of water and emulsifier were prepared into preemulsifier, and then the residual emulsifier was stirred with residual deionized water to form an emulsifier aqueous solution. After adding a certain amount of initiator aqueous solution, the temperature began to rise to the reaction temperature. The prepared emulsion was added to it. After the pre-emulsion was finished, it continued to grow 1 h. adjust pH to 7–8 with ammonia water after cooling to 50–55 °C.

## 2.3 Characterization

The rheometer used in rheology test is the HAKEMARS rheometer produced by t thermo scientific. The temperature is 25 °C degrees. The rotor and the corresponding sample cup are selected according to the viscosity of the emulsion. The shear rate range is in 1–1000 $s^{-1}$.

Dynamic stability analyzer was used to test the stability of the microemulsion.

TEM measurement (JEM-2100) was taken to observe the morphology of acrylate microemulsion. In sample preparation, the sample was stained with 2% phosphotungstic acid (PTA) solution after it was diluted to a certain concentration.

Nano-ZS dynamic light scattering particle size (DLS) was used to test the size of the latex.

A certain amount of samples were placed in a known weight aluminium box and dried at 55 °C for 24 h to form a dry film. The m was white and soft.

# 3 Results and Discussion

## 3.1 Polymerization Process

In this study, anionic emulsifier SDS and nonionic emulsifier OP-10 were used to compounded the size of acrylate microemulsions prepared by pre-emulsification and

non-pre-emulsification under the same formulation conditions. The experimental results are shown in Table 1. According to the experimental results, the size of the acrylate microemulsion prepared by non-pre-emulsificatfilm was immersed in 50% ethanol solution for 12 h to observe whether the filion method is smaller than that of the acrylate microemulsion prepared by pre-emulsification. It can be determined that the preparation of acrylate microemulsion by non-pre-emulsification is the best method. The reason is that the content of emulsifier in pre-emulsifying base liquor is less than that in non-pre-emulsifying base liquor, and the number of micelles formed in aqueous solution is also less, which leads to the inability to provide enough micelles to maintain the stability of the further polymerization of latex particles in the late stage of reaction. The synthesis results are larger than that of non-pre-emulsifying.

**Table 1.** Effect of preparation process of acrylate microemulsion on average particle size

| Solid content (%) | Average particle size (nm)/Pre-emulsification | Average particle size (nm)/Non-pre-emulsifying |
|---|---|---|
| 41.5 | 96.97 | 67.54 |
| 42.1 | 90.45 | 70.25 |
| 43.6 | 90.01 | 73.64 |

The stability, dryness and water absorption of the emulsion are related to the emulsifier. In order to improve the appearance transparency, alcohol resistance and shear strength of the acrylate microemulsion, NR-1 surfactant was added into the emulsifier system. A series of characterizations of acrylate microemulsion with solid content of 40% were also carried out. Firstly, the influence of the amount of reactive surfactant NR-1 on the particle size of acrylate microemulsion was studied. When the amount of active surfactant NR-1 was 0.5–1% of the total monomer, the average particle size can be effectively reduced to about 55 nm. The increased of the amount of active surfactant will lead to the increase of particle size. The results showed that NR-1 can contain both polymeric and emulsifying groups. Reactive emulsifier NR-1 can form micelles or solubilizing micelles during the polymerization process. It can also participate in the polymerization reaction. The particle size of the prepared microemulsion was small. However, when the total amount of emulsifier remains unchanged, the increase of NR-1 will reduce the amount of traditional anionic emulsifier, resulting in the decrease of the total charge of anionic emulsifier, and ultimately the stability of the polymer is difficult to maintain. With the increase of particle size, milky white appears. The experimental results showed that the optimum dosage of reactive emulsifier NR-1 is 1% (Fig. 1).
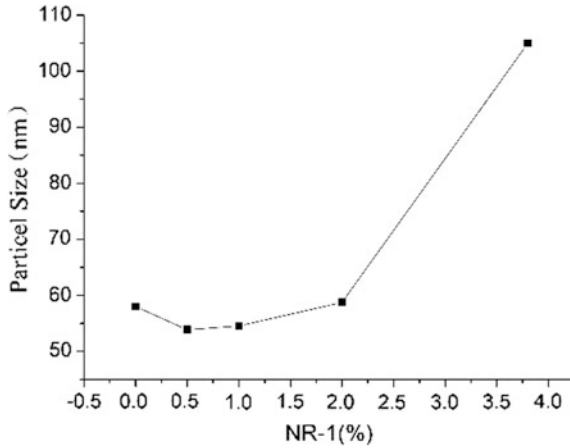
**Fig. 1.** Particle size of acrylate microemulsion latexes varied with theincrease of reactive emulsifier

Figure 2 showed the particle morphology of acrylate microemulsion samples with different content of reactive emulsifier NR-1. It can be seen from the figure that the shape of the particle is a uniform spherical structure, and the size of the particle was consistent with the experimental results. The core-shell structure may be due to the different reactivity of monomers in the process of polymerization.
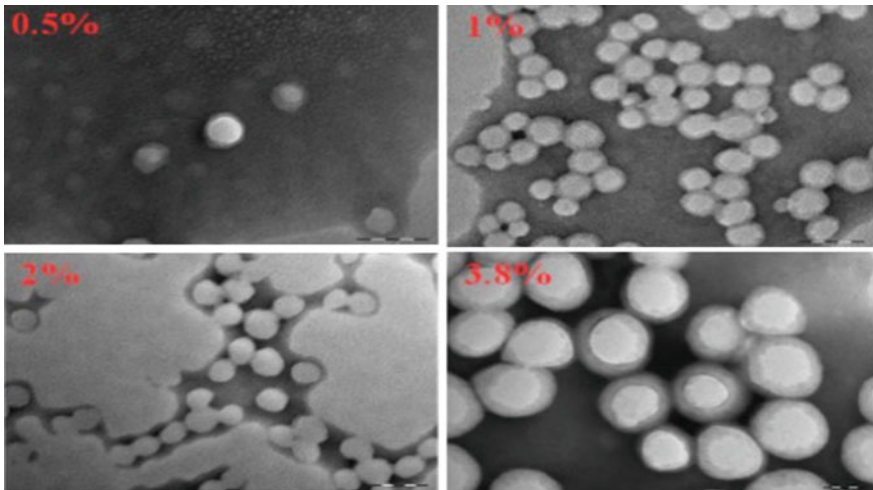


**Fig. 2.** TEM image of acrylatelatex particles

## 3.2    Polymerizable Emulsifier NR-1 Dosage on the Rheology

Figure 3 is the effect of NR-1 dosage on the rheological properties of acrylate microemulsion. The viscosity of emulsion with 0.5% reactive emulsifier NR-1 is higher than that without NR-1. The reason is that reactive emulsifier participates in the polymerization and increases molecular weight, molecular volume, intermolecular entanglement and viscosity. However, with the increase of NR-1 dosage, the shear viscosity of emulsion decreased. This is due to the excessive amount of emulsifiers wrapped on the polymer surface, the decrease of the total specific surface area of the polymer particles, the decrease of the total amount of hydrated water on the surface of the polymer particles, and the increase of the free water content. So the viscosity decreases. In conclusion, the optimum addition of NR-1 is 1%.
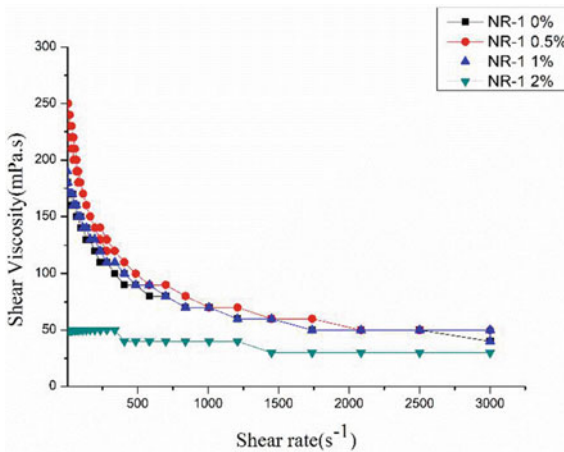


**Fig. 3.**  Effect of reactive emulsifier NR-1 on rheological properties of acrylate microemulsion

## 3.3    Effect of Polymerizable Emulsifier on TSIandalcohol Resistance

Figure 4 is the effect of the amount of reactive emulsion on the stability of emulsion. The addition of active surfactants effectively reduced the TSI exponent and range of the microemulsion, indicating that the surfactant NR-1 improved the stability of the microemulsion effectively.

The alcohol resistance of acrylic acid microemulsion with different NR-1 content was tested. The experimental results are shown in Fig. 5. The addition of reactive emulsifier can effectively improve the alcohol resistance of acrylate microemulsion.
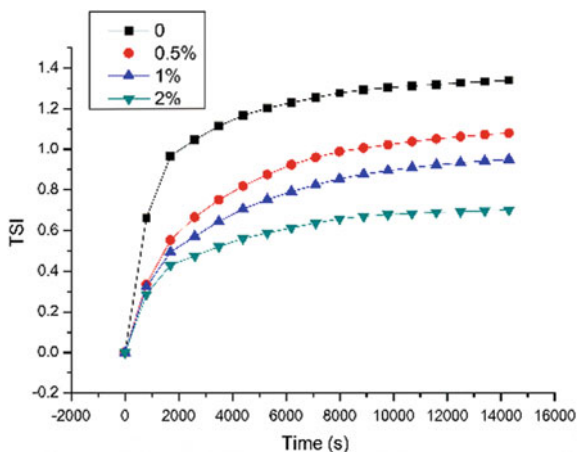
**Fig. 4.** Effect of reactive emulsifier NR-1 on TSI index of acrylate microemulsion
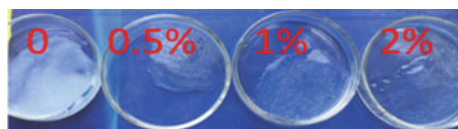


**Fig. 5.** Experimental results of alcohol tolerance of NR-1 with different additions

## 4   Conclusions

A series of acrylate microemulsions were prepared in this study. The addition of reactive emulsifier NR-1 effectively improved the durability, alcohol resistance and emulsion stability of acrylate microemulsion. The results showed that when the amount of NR-1 was 1%, the synthesized acrylate microemulsion had good comprehensive properties.

## References

1. Xianglin X, Yadong Y, Ge X et al (2016) Research progress in microemulsion polymerization. J Chem Coll Univ 20(03):478–485
2. Cao T, Liu P, Hu J (2007) Polymer emulsion synthesis principle, performance and application. Chemical Industry Press, Beijing
3. Smeets NMB, Mckenna TFL (2012) The synthesis of translucent polymer nanolatexes viamicroemulsion polymerization. J Colloid Interface Sci 383(1):28–35

4. Pham QT, Hsu MC, Chern CS (2016) Kinetics of isothermal miniemulsion polymerization of1,6-hexanediol diacrylate. Thermochim Acta 634:31–37
5. Yi M, Qiu T, Okubo M et al (2018) Innovative on-line Near-Infrared (NIR) spectroscopy to estimate content of each phase in composite polymer particles prepared by seededemulsion polymerization. Vib Spectrosc S0924203117302801

# Study on the Effect of Additive Content on the Performance of Waterborne Flexible Printing Ink Used on Films

Shu Yan[1,2], Pingping Zhang[1,2], Kai Huang[1,2], Jiaqi Ren[1,2], Pengfei Zhao[1,2], Zhuangzhi Ye[1,2], and Ya'nan Liu[1,2(✉)]

[1] Key Laboratory of Environmental Protection Technology for Printing Industry, Academy of Printing Technology, Beijing, China
{yanshu, liuyanan}@keyin.cn

[2] Beijing Key Laboratory of New Technology of Packaging & Printing, China Academy of Printing Technology, Beijing, China

**Abstract.** Under the trend of environmental protection, as a kind of environmentally friendly printing ink, research printability of flexible printing ink used on films has been paid more and more attention by enterprises and the market. In order to, effect of the content sofwetting agent W1 and mixing wetting agent on waterborne ink were researched to improve the printability effectively. Wettability of waterborne ink was increased firstly and then decreased with the increase of wetting agent W1content. The optimum amount of W1 is 0.4wt% W1, W2 after the combination of flexographic waterborne ink wettability is better than simply adding W1 wettability, its complex ratio of 1:1, the wettability of waterborne ink is the best. The printability of water-based flexible printingink used on films was improved by adjusting the appropriate content of wetting agent and thickener.

**Keywords:** Flexible printing ink · Waterborne ink · Wetting agent

## 1 Introduction

In developed countries, Flexographic printing technology is widely used in printingon traditional plastic films used as packaging materials. Flexographic printing technology started late in China, but under the trend of environmental protection, the research and development and application of water-based flexographic ink are gradually valued by enterprises and markets [1]. In recent years, flexographic waterborne ink has been advancing along the direction of low VOCs content, high performance and low cost [2]. Waterborne ink is mainly composed of four parts: binder, pigments, additives and solvents [3–5]. Among them, although the proportion of additives in the ink system is small, it has a greater impact on the printability [6]. Among them, there are many kinds of auxiliaries in water-based ink, and their mechanisms are different, such as wetting agent, defoamer, thickening agent, leveling agent and quick drying agent, etc. [7, 8] to increase the printability of water-based ink.

The wettability of flexible printing ink on plastic film is an important indicator of its application. The main solvent of water-based ink is water (72.8 mN M$^{-1}$ at 20 °C) [9]. The surface tension of water-based flexographic ink is higher than that of solvent-based ink, and the wetting effect on non-absorbable plastic film materials (such as BOPP and BOPET) is not ideal. Therefore, suitable and appropriate wetting agent should be added to reduce the surface tension of water-based ink and improve the wetting effect on plastic film [10].

In order to effectively improve the wetting effect of the ink on the film, we investigated the single wetting agent and the combination of wetting agent.

## 2  Experiments

### 2.1  Experimental Materials and Instruments

#### 2.1.1  Experimental Materials

Waterborne resin 201 were provided by Guangzhou Hengjike New Materials Co., Ltd. Wetting agent W1 was provided by Guangzhou Ruiju Chemical Technology Co., Ltd. which is Polyether Modified Silicone Oil. Wetting agent W1 was provided by Guangzhou Ruiju Chemical Technology Co., Ltd. which is Polyether Modified Silicone Oil. Wetting agent W2 was provided by Guangzhou Zengmao Chemical Technology Co., Ltd., which is sodium diisooctyl succinate. Color paste was provided by Shanghai Caisheng Pigment Chemistry Co., Ltd.

#### 2.1.2  Experimental Instruments

Densitometer (X-Rite) was provided by U.S.A. Surface tension meter (BZY-1) was provided by Shanghai Pingxuan Scientific Instruments Co., Ltd. Vibrator (HT-30C) was provided by Shanghai Modern Environmental Engineering Technology Co., Ltd. Scraper fineness meter (QXD) was provided by pushen testing instruments (Shanghai) Co., Ltd. Disc peel tester was provided by Labthink.

### 2.2  Characterization

1. Adhesion. Inkjet ink was coated on the substrate with No. 0 wire rod, and then the ink layer was dried under hot air. 3 M tape was affixed on the surface of the printed sample and then the tape was peeled off. It was evaluated from level 0 to level 5, according to the desquamate degree of ink on the surface of printed substrate. The level 0 represents the maximum value of adhesion, and the level 5 represents the minimum value of adhesion.
2. Leveling. The IGT proofing machine was used to proof, and the 60-fold magnifying glass was used to measure the leveling wettability of the sample. magnifier.
3. Viscosity. Zahn 4# was used to test the rotational viscosity of ink.
4. Fineness: According to GB/T 13217.3-2008 "Test Method for Fineness of Liquid Ink", the scraper fineness meter was used to measure the fineness.
5. Surface tension. BZY-1 automatic interface tension meter is used to measure and record data.

6. Stability of the water-based inkjet ink. Water-based inkjet ink is placed in an electricity heat drum wind drying oven at 50 °C. Test the performance of the waterbased inkjet ink two days later.

## 3   Results and Discussions

### 3.1   Effect of Wetting Agent W1 on Waterborne Ink

In order to improve the wetting effect of water-based ink, a suitable amount of wetting agent matching the system is needed. The effects of different contents of wetting agent W1 (see Table 1) on the surface tension and thermal stability of water-based ink system were studied as shown in Table 2.

**Table 1.**  Formulas of waterborne ink with different wetting agent W1 proportions

| NO | Water-borne resin201/% | Pastes C/% | Wetting agent W1/% | Other auxiliaries/% |
|---|---|---|---|---|
| CW0 | 51 | 45 | 0 | 4.0 |
| CW1 | 50.8 | 45 | 0.2 | 4.0 |
| CW2 | 50.6 | 45 | 0.4 | 4.0 |
| CW3 | 50.4 | 45 | 0.6 | 4.0 |
| CW4 | 50.2 | 45 | 0.8 | 4.0 |
| CW5 | 50.0 | 45 | 1.0 | 4.0 |

It can be seen from Table 2 that the wetting agent W1 has little effect on the fineness of water-based ink. In order to more intuitively see the effect of wetting agent content on the viscosity of water-based ink, Fig. 1 is drawn. Figure 1 shows that when the mass fraction of water-based ink wetting agent increases from 0% to 1.0%, the instant viscosity of water-based ink does not change significantly, and the viscosity is 12–13 s. The thermal stability of water-based ink was tested after 48 h in an oven at 50 °C. When the content of wetting agent was 0–0.4%, the viscosity did not increase

**Table 2.**  Performance test of waterborne ink with different wetting agent W1 contents

| NO | Surface tension/mN*m$^{-1}$ (20 °C) | Viscosity/s (original 24 h) | Fineness/μm (original 24h) | Viscosity/s (50 °C, 48 h) | Fineness/μm (50 °C, 48 h) |
|---|---|---|---|---|---|
| CW0 | 31.4 | 12.85 | 10–15 | 12.87 | 10–15 |
| CW1 | 30.2 | 12.96 | 10–15 | 13.13 | 10–15 |
| CW2 | 29.0 | 13.00 | 10–15 | 13.29 | 10–15 |
| CW3 | 28.7 | 13.10 | 10–15 | 16.86 | 15–20 |
| CW4 | 28.4 | 13.15 | 15–20 | 23.37 | 20–25 |
| CW5 | 28.1 | 13.21 | 20–25 | 51.70 | 25–30 |
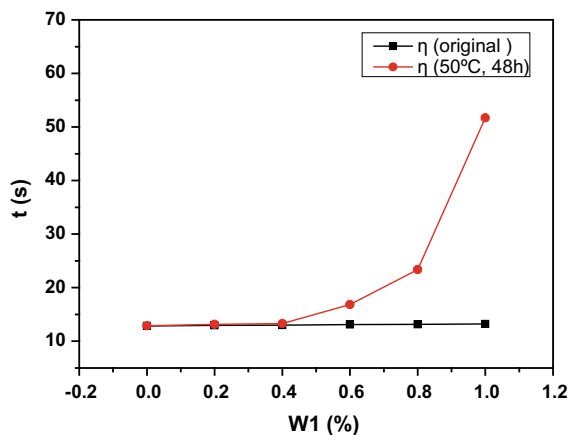
**Fig. 1.** Effect of wetting agent W1 on viscosity of waterborne ink

significantly and the thermal stability was good. But when the content of wetting agent was more than 0.4%, the viscosity of water-based ink system increased and the thermal stability became worse. This is because excessive wetting agent affects the balance of water-based ink, makes the molecules combine rapidly, and eventually agglomerates, making the viscosity of the system rise.

The addition of wetting agent reduces the surface tension of flexographic water-based ink and makes it easier to spread on the base material BOPP [11]. The wetting effect of ink on BOPP film was tested by IGT proofing. As shown in Fig. 2, the wetting effect of flexographic ink on BOPP was poor when no wetting agent was added (Fig. 2a). With the increase of the content of wetting agent W1, the leveling effect of flexographic ink was gradually improved. When the mass fraction of the wetting agent is 0.4%, the wetting effect is shown in Fig. 2b. When the content of the wetting agent is 1%, the wetting effect is shown in Fig. 2c. The optimum addition of W1 was determined to be 0.4% in combination with stability and wetting effect.



**Fig. 2.** The influence of different content of wetting agent on the leveling effect of flexographic ink is shown in **a–c**. The mass fractions of wetting agent are 0, 0.4 and 1.0% respectively.

### 3.2 Influence of Different Compounding Ratios Wetting Agents on Waterborne Ink

Only suitable for a single wetting agent can not improve the wetting effect of water-based ink, which requires us to mix two or more to improve the wettability of water-based ink. But water—based ink adding a variety of wetting agents may lead to its stability and other basic performance. This requires us to explore the compounding proportion and total content. The influence of wetting agent W1.W2 (formula is shown in Table 3) on surface tension and thermal stability of water-based ink system under different compounding ratios is discussed, as shown in Table 4.

**Table 3.** Formulas of waterborne ink with different mixture proportion of wetting agent

| NO | Water-borne resin 201/% | Pastes C/% | Wetting agent W1/% | Wetting agent W2/% | Other auxiliaries/% |
|----|----|----|----|----|----|
| CW0 | 50.6 | 45 | 0.4 | 0 | 4.0 |
| CW1 | 50.6 | 45 | 0 | 0.4 | 4.0 |
| CW2 | 50.6 | 45 | 0.3 | 0.1 | 4.0 |
| CW3 | 50.6 | 45 | 0.2 | 0.2 | 4.0 |
| CW4 | 50.6 | 45 | 0.1 | 0.3 | 4.0 |

From Table 4, we can see that different mixing ratio on the fineness of water-based ink has no significant impact. In order to more directly see the different proportion of wetting agent on the viscosity of water-based ink drawing Fig. 2. Figure 3 shows that the proportion of water-based ink wetting agent in each proportion, the instant viscosity of water-based ink did not change significantly, viscosity in 13–14 s. The water-based ink was placed in a oven at a temperature of 50 °C and its thermal stability was tested after 48 h. As the proportion of wetting agent W2 increased, the stability became worse. When the wetting agent ratio is 1:3, the viscosity increases from 13.25 to 28.37 s.

IGT proofing was used to test the wetting effect of ink on BOPP film, as shown in Fig. 4. Figure 4a shows the wetting effect of wetting agent W2 with a mass fraction of 0.4%. It can be seen that the wetting effect of pure wetting agent W2 on water-based

**Table 4.** Performance test of waterborne ink with different mixture proportion of wetting agent

| NO | Surface tension/mN*m$^{-1}$ (20 °C) | Viscosity/s (original 4 h) | Fineness/μ (original 24 h) | Viscosity/s (50 °C, 48 h) | Fineness/μm (50 °C, 48 h) |
|----|----|----|----|----|----|
| CW0 | 29.0 | 13.00 | 10–15 | 13.29 | 10–15 |
| CW1 | 31.2 | 13.96 | 10–15 | 18.33 | 20–25 |
| CW2 | 29.6 | 13.50 | 10–15 | 13.89 | 10–15 |
| CW3 | 29.2 | 13.20 | 10–15 | 13.60 | 10–15 |
| CW4 | 29.4 | 13.25 | 15–20 | 28.37 | 20–25 |
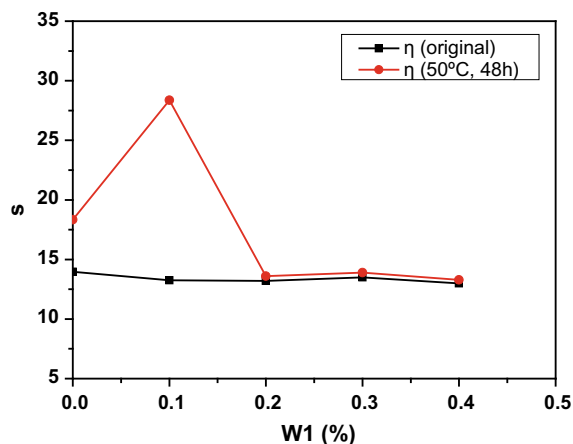
**Fig. 3.** Effect of the different compounding ratios wetting agent on viscosity of waterborne ink
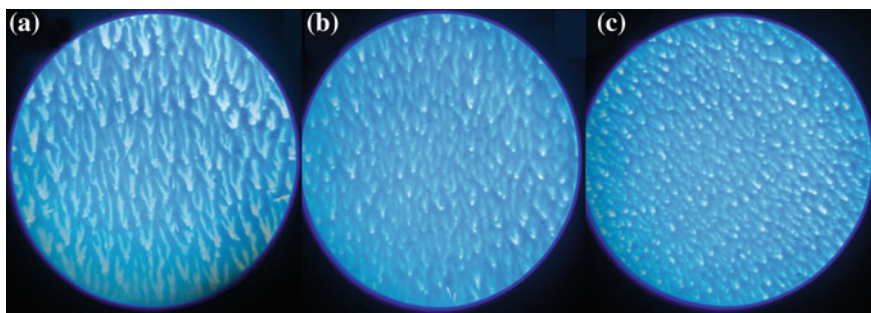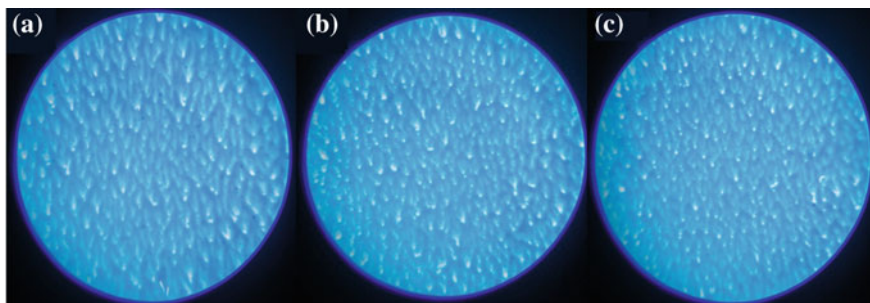


**Fig. 4.** The influence of different content of wetting agent on the leveling effect of flexographic ink is shown in **a–c**. The mass fractions of wetting agent W2 are 0.4, 0.1 and 0.2% respectively.

ink with the same content was better than that of W1. From the wetting effect pictures (b) and (c) of W1: W2 = 3:1 and 1:1 respectively, it can be seen from the figure that the wetting effect of water-based ink gradually improves with the increase of wetting agent W2 content. According to the stability of water-based ink and wetting effect, determine the wetting agent ratio of W1:W2 = 1:1.

## 4   Conclusions

In this paper, the wetting agent W1 and wetting agent of W1 and W2 compound in the process of preparing ink and different adding quantity and the impact of different proportion and its optimal value has carried on the exploration, the results show that with the increase of wetting agent content of W1, flexo water-based ink wettability first increase then decrease, determine the optimum wetting agent W1 added mass fraction is 0.4%; W1, W2 after the combination of flexographic waterborne ink wettability is

better than simply adding W1 wettability, its complex ratio of 1:1, the wettability of waterborne ink is the best.

# References

1. Xiu-lan X (2011) Research progress in water-based inks. China Print Packag Study 3(3):1–8
2. Zhao P-F, Feng W-G, Liu Y-N et al (2018) Film flexographic ink the future is promising. Print Technol 09:35–39
3. Peng XJ, Zhang Q, Cheng JS et al (2017) Preparation and characterization of a stable nano-sized $Zn_xCo_1$-$xAl_2O_4$, ink for glass decoration by ink-jet printing. Glass Phys Chem 43 (3):246–256
4. Xing Z, Yan L, Fang C et al (2015) Recent advances in synthesis of waterborne polyurethane and their application in water-based ink: a review. J Mater Sci Technol 31 (7):708–722
5. Fang C, Xing Z, Qian Y et al (2014) Synthesis and characterization of low crystalline waterborne polyurethane for potential application in water-based ink binder. Prog Org Coat 77(1):61–71
6. Ramirez JCC, Tumolva TP (2018) Analysis and optimization of water-based printing ink formulations for polyethylene films. Appl Adhes Sci 6(1):1–21
7. Ouyang Y, Feng WG, Sun ZY et al (2018) Research of wax additives in the water-based ink for flexographic printing, vol 477. Springer, Berlin, pp 737–744
8. Xu YJ, Wei XF, Huang BQ (2013) Study on temperature control microcapsule drying agent applies to water-based gravure ink. Appl Mech Mater 469:46–50
9. Huang QJ, Zhu Y (2018) Gravure printing of water-based silver nanowire ink on plastic substrate for flexible electronics. Sci Rep 8(1):1–10
10. Li JY, Wang XF, Ouyang Y et al (2016) Impact of leveling agents on the film-forming performance of water-based inks. In: Advanced graphic communications, packaging technology and materials, vol 369. Springer, Singapore, pp 985–990
11. Xiao-Li L (2016) Effect of auxiliaries on the properties of film flexographic ink. Print Technol 13:45–47

# Simulated Analysis of Electronic Performance of Copper Nanowires-Based Conductive Ink

Rong Xue[✉] and Guodong Liu

National Demonstration Center for Experimental Light Chemistry Engineering
Education, College of Bioresources Chemical and Materials Engineering,
Shaanxi University of Science & Technology, Xi'an, China
alveycc@163.com

**Abstract.** Copper nanowires offered many new ways for fabricating high-performance flexible electronics in a variety of applications. Mass production of these new-generation electronics with the printing technology may be the best way. However, the effect of physical dimension of copper nanowires on materials' photoelectric property still needs further studies. Herein, 3D and 1D model of copper nanowires with different physical dimensions and distribution in circuit were simulated by Comsol Multiphysics. The results showed that more multiple circuits were built with high aspect ratio of copper nanowires which was the key for improving photoelectric property and indicated the ways of fabricating high performance copper nanowires-based composites materials in the future.

**Keywords:** Copper nanowires · Comsol multiphysics · Simulation

## 1 Introduction

With fast development of new emergence of flexible electronics, there is no doubt that these electronics would have a great effect on people's lives [1–6]. Printing the flexible electronics is also the most promising way of producing them, so the conductive ink is the core part in order to realize the mass production. Compared with carbon based materials [7, 8] like carbon nanotubes (CNT) or graphene, metallic nanowires are obviously the most ideal candidate for being used as conductive ink, especially for producing transparent flexible electronics, because of the excellent photoelectric properties. To date, many noble metal based nano materials have arised in the printed electronics fields especially because of the excellent properties [9–12]. Copper nanowires (CuNW) seems more proper because of the abundant number and the lower price of copper than novel metal like silver or gold. People have also studied many methods to increase the aspect ratios of CuNW in order to improve the photoelectric properties [13–15]. Although those methods showed great improvements, the interesting part was that the phenomenon conflicted with the formula for calculating resistance of wires, because the longer length or thinner radius meant longer or more narrow way for electron transportation which would result in increasing resistance of materials. In this article, two dimensions of CuNW were simulated with Comsol Multiphysics by building 1D and 3D model and it was also considered the distribution of CuNW in the

matrix in order to investigate the impact factors of improving photoelectric properties. (for better visual effect, the simulated picture was made by setting CuNW with shorter length and larger radius, but the simulated calculation was simulated by real dimension of CuNW in this article and the typical length and radius of CuNW was 40 µm and 35 nm, respectively). Our simulation method may open up a new avenue to evaluate the potential ability of the similar nano materials applied in the printed electronics industry.

## 2   Characterization

For investigating the effect of physical dimension of copper nanowires on composites' performance, Comsol Multiphysics (COMSOL, Inc. Sweden) was applied. The simulation theory is based on solving partial differential equations.

   For better accurate simulated results, the other components in conductive ink were not considered in this article.

## 3   Results and Discussion

Figure 1a showed the changes in electric potential of the CuNW under input DC voltage. Obviously, the electric potential changed along the length direction of CuNW, but the overlap between CuNW may cause junction resistance existed in the junction area. Our original hypothesis of the simulation was that this point was the only contact area between CuNW, which meant that the conductive path was limited causing the limited path for electron transportation. As can be seen in Fig. 1b, the highest density of electrons located in the middle of the point this is because the narrow conductive path which resulted in this phenomenon, indicating the high junction resistance at this area. Junction resistance has a great influence on electronic properties of CuNW-based materials and many researchers have studied to eliminate or reduce this impact [16]. In Fig. 1a, b, the electrons moved along the CuNW ignoring the junction because of high resistance of this area leading to limited number of electrons passing this area,which meant this circuit was a typical series circuit. Figure 1c, d showed the change in resistance of the circuit gradually increased with longer length and decreased with thinner radius of CuNW. However, the radius value had nonlinear effect on resistance of the circuit which indicating better effect on improving the electric property. The resistance of this circuit was 68.68 Ω.

   Actually, the morphology of conductive path made by CuNW was a little different from Fig. 2, especially when the contents of CuNW existed in composite matrix was low, which meant not all CuNW could connect to the input and terminal of the voltage at the same time.In Fig. 2a, circuit made by four CuNW with three CuNW connected to the terminal was simulated, the resistance was 41.82 Ω. It can be seen that one CuNW was equipotential, so the resistance was lower than the previous. When the parameters of the CuNW was set to other value, the results showed that the disparity of resistance could become obvious in Fig. 2c, d. Although the tendency of the four curves were similar, the value of the two were different, thus that meant the distribution of
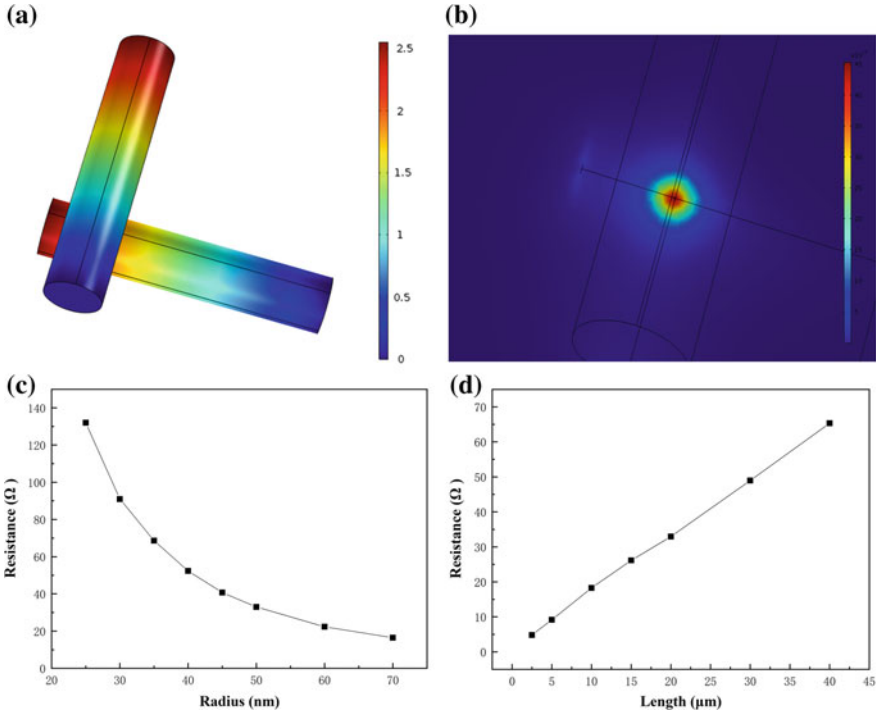
**Fig. 1.**  **a** Image of electric potential for two CuNW. **b** simulation of electric current density at CuNW junction. the resistance of two CuNW as a function of (**c**) different length. **d** different radius

conductive CuNW in circuit would have an obvious impact on the resistance. The more number of CuNW connected to the input and terminal port of voltage at the same time, the lower resistance of the circuit would get because of less equipotential CuNW formed. On the other hand, the formed multiple circuit was the key to make the difference of the resistance.

Actually the junction resistance is usually very large because of narrow path for electrons between nanowires, so many methods have been applied. The key to solve the problem is to form bigger areas and strong contact at junction area. In Fig. 3a, we assumed the formed shape was hexahedron after post treatment between nanowires. As it can be seen in Fig. 3b, the conductive path for electron was much wider and the electron didn't pass the whole area because the electron would choose the shortest way. Some papers have also reported that the longer CuNW meant the less number of junction existed, so longer CuNW and post treatment of CuNW were necessary for CuNW materials.

The 1D model of CuNW was applied and the simulated pictures could be seen in Fig. 4 in order to test our previous hypothesis. When only one CuNW was connected with the terminal in Fig. 4a, d, the resistance was $10^{-6}$ $\Omega$, whereas the value was $10^{-7}$ $\Omega$ with two CuNW connected with the terminal in Fig. 4b, e. The results meant if the
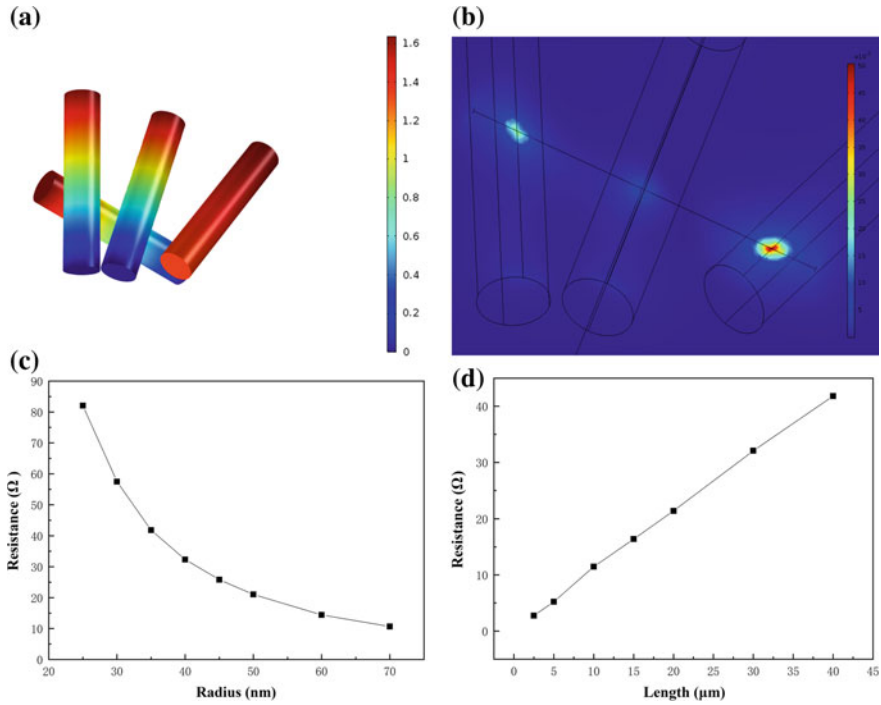
**Fig. 2.** **a** Image of electric potential for four CuNW with four ends as voltage input and three ends as terminal. **b** simulation of electric current density at CuNW junction. the resistance of CuNW as a function of (**c**) different length. **d** different radius
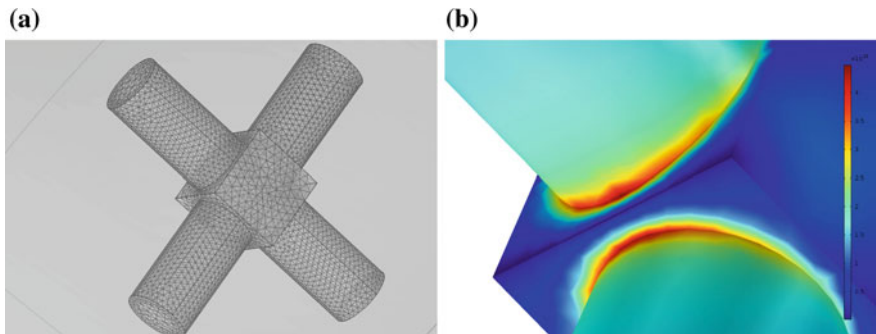


**Fig. 3.** Simulation of electric current density of annealed CuNW with hexahedron shape-like at junction **a** overall picture. **b** detail at junction

CuNW could own longer length that meant the more series circuit would form resulting in the decreasing of resistance. (the distance between voltage input and terminal was set to 8 μm in this picture)
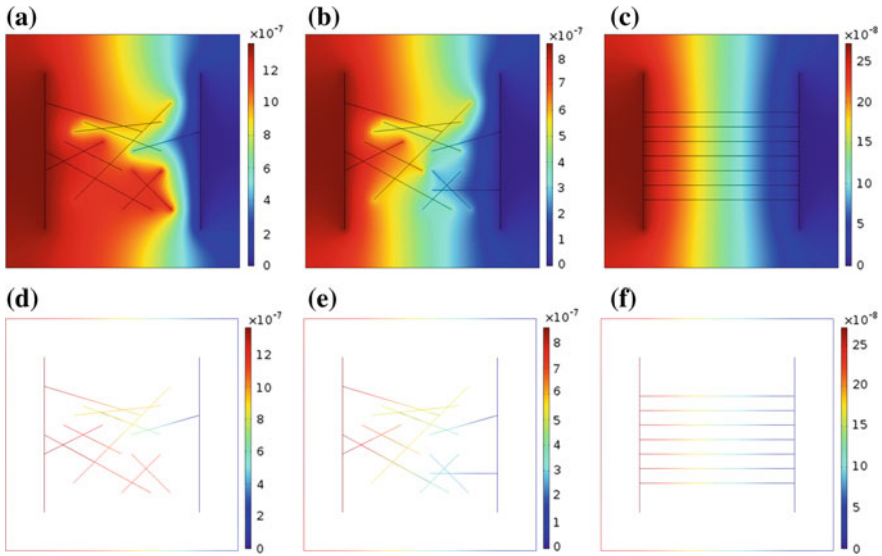
**Fig. 4.** Simulation of electric potential of CuNW contacted with terminal **a** one. **b** two. **c** simulation of electric potential of aligned CuNW network. simulation of line-shape electric potential of CuNW contacted with terminal **d** one. **e** two. **f** aligned CuNW network

Fabrication of aligned metallic nanowires network was an advanced technology which was applied to product materials with ultra high performance. In Fig. 4c, f, the 1D aligned CuNW network was simulated. As we can see, more series circuit was formed with less number of CuNW and the transparency must be extremely high because of the limited amount of CuNW when all the aligned CuNW were connected the circuit directly. However, this new technology was usually too complicated with high cost to be applied in industrial fields. Further research is needed, especially in printing field. The distribution of CuNW printed on substrates is usually random which means that more CuNW is needed which would have a negative on transparency of products.

## 4   Conclusions

To conclude, the physical dimension of CuNW has an important impact on performance of CuNW based materials. The performance is obviously higher for CuNW with high aspect ratio or aligned distribution of CuNW network by creating more multiple circuits, so the transparency would also increase because of less CuNW used. Thus, our results offered a new way for analyzing performance of printed electronics with CuNW based ink.

**Conflict of Interest.** The authors declare that they have no conflict of interest.

# References

1. Song TB, Rim YS, Liu F et al (2015) Highly robust silver nanowire network for transparent electrode. ACS Appl Mater Interfaces 7(44):24601–24607
2. Chen L, Weng M, Zhou Z et al (2015) Large-deformation curling actuators based on carbon nanotube composite: advanced-structure design and biomimetic application. ACS Nano 9 (12):12189–12196
3. Qingwei L, Changhong L, Yuan-Hua L et al (2015) Large-strain, multiform movements from designable electrothermal actuators based on large highly anisotropic carbon nanotube sheets. ACS Nano 9(1):409–418
4. Erb RM, Sander JS, Grisch R et al (2013) Self-shaping composites with programmable bioinspired microstructures. Nat Commun 4(2):1712
5. Lan W, Chen Y, Yang Z et al (2017) Ultraflexible transparent film-heater made of Ag nanowire/PVA composite for rapid-response thermotherapy pads. ACS Appl Mater Interfaces 9(7):6644–6649
6. Kim TY, Kim YW, Lee HS et al (2013) Uniformly interconnected silver-nanowire networks for transparent film heaters. Adv Func Mater 23(10):1225
7. Hu Y, Wu G, Lan T et al (2016) A graphene-based bimorph structure for design of high performance photoactuators. Adv Mater 27(47):7867–7873
8. Han DD, Zhang YL, Liu Y et al (2015) Bioinspired graphene actuators prepared by unilateral UV irradiation of graphene oxide papers. Adv Func Mater 25(28):4548–4557
9. Hwang HJ, Oh KH, Kim HS (2016) All-photonic drying and sintering process via flash white light combined with deep-UV and near-infrared irradiation for highly conductive copper nano-ink. Sci Rep 6:19696
10. Chung WH, Hwang YT, Lee SH et al (2016) Electrical wire explosion process of copper/silver hybrid nano-particle ink and its sintering via flash white light to achieve high electrical conductivity. Nanotechnology 27(20):205704
11. Chen X, Wu X, Shao S et al (2017) Hybrid printing metal-mesh transparent conductive films with lower energy photonically sintered copper/tin ink. Sci Rep 7(1):13239
12. Patil SA, Ryu CH, Kim HS (2018) Synthesis and characterization of copper nanoparticles (Cu-Nps) using rongalite as reducing agent and photonic sintering of Cu-Nps ink for printed electronics. Int J Precis Eng Manuf-Green Technol 5(2):239–245
13. Jason NN, Shen W, Cheng W (2015) Copper nanowires as conductive ink for low-cost draw-on electronics. ACS Appl Mater Interfaces 7(30):16760–16766
14. Wei-Hong X, Lei W, Zheng G et al (2015) Copper nanowires as nanoscale interconnects: their stability, electrical transport, and mechanical properties. ACS Nano 9(1):241–250
15. Seungyong H, Sukjoon H, Jooyeun H et al (2014) Fast plasmonic laser nanowelding for a Cu-nanowire percolation network for flexible transparent conductors and stretchable electronics. Adv Mater 6(33):5808–5814
16. An S, Jo HS, Kim DY et al (2016) Self-junctioned copper nanofiber transparent flexible conducting film via electrospinning and electroplating. Adv Mater 28(33):7149–7154

# Effect of Modification Methods of Polyurethane Latexes on Its Properties and Adhesion to BOPP Film of the Inks

Mingguang Zhang, Xiuye Lian, Xiaoyu Li[(⌐)], and Haiqiao Wang[(⌐)]

Key Laboratory of Carbon Fiber and Functional Polymers, Ministry of
Education, Beijing University of Chemical Technology, Beijing, China
{lixy,wanghaiqiao}@mail.buct.edu.cn

**Abstract.** Polyurethane (PU) latexes are difficult to be applied in PE or PP thin film inks because of their weak adhesion, and low polarity and low surface tension of PE and PP thin films. In this paper, two kind of different polyurethane latexes were prepared by modifying their hard and soft segments, respectively. The effects of modification methods on the properties of the polyurethane latexes and the adhesion fastness of the corresponding inks on BOPP were studied. The as prepared PU latexes by using both modification methods have good stability and improved adhesion on the BOPP films. However, using glycerol monooleate (GMO) to modify hard segments of PU increases the proportion of the hard segment with higher polarity in the whole molecule, and in turn increases the glass transition temperature (Tg) of PU, so a slight excess use of GMO demonstrates significant effect on the adhesion and low temperature performance of the ink. The maximum adhesion on BOPP of the corresponding ink is only 35%. The modification on the soft segments using polyester polyol (BY3003) nearly do not affect the Tg and the low temperature performance of PU, therefore the maximum adhesion of the ink reaches 97%.

**Keywords:** Waterborne polyurethane · Hard segment modification · Soft segment modification · BOPP thin films · Adhesion

## 1 Introduction

Recently, waterborne polyurethane materials have received extensive attention in the ink industry due to their excellent abrasion resistance, chemical resistance and flexibility [1–3].

Owing to the unique two-phase structure, polyurethane materials have a wide temperature range of adaptation, which makes the aqueous PU inks have better high and low temperature resistance performance. There are a large number of highly polar ester bonds and urethane bonds in the molecular chain of polyurethane, so polyurethane inks usually exhibit good adhesion on PA and PET, but poor adhesion on low polarity BOPP and PE thin films. In order to improve the performance of polyurethane inks, structural modification on the hard or soft segment of polyurethane were widely studied. For example, trimethylolpropane monooleate (TMPM) was used as a hard segment modifier to produce polyurethane, and the adhesion fastness on BOPP film

reached 96% [4]; Wang Zhen et al. [5] using homemade phthalic anhydride polyester polyol as a soft segment to synthesize a waterborne polyurethane, and found that the aqueous ink prepared by using this polyurethane as a binder has good adhesion and retort resistance. Therefore, modification whether on the hard or the soft segments of the polyurethane all can improve adhesion fastness on low-polar substrates of the corresponding inks. Obviously, these two different modification strategies not only have influences on the adhesion to non-polar substrates of the prepared polyurethane latexes, but have influences on the glass transition temperature (Tg), particle size and particle size distribution, and viscosity of the latexes, which are directly related to the practical performance of polyurethane. However, these two modification methods were compared in few literatures.

Herein, two different waterborne polyurethanes with GMO as a hard-segment modifier or BY3003 as a soft-segment modifier were prepared respectively. The effects of modification methods on the properties of polyurethane latexes and the adhesion on BOPP film of the corresponding ink were comparative studied.

## 2    Experimental

### 2.1    Materials

Isophorone diisocyanate (IPDI), polybutylene adipate diol (PBAD, Mw = 2000), BY3003 (Mw = 1360), GMO, dimethylol butyric acid (DMBA), 1,4-butanediol (BDO), dibutyltin dilaurate (DBTDL) were used as received.

### 2.2    Methods

(1) Preparation of waterborne polyurethane latex (GPU) through hard-segment modification: metered IPDI, PBAD, GMO and DBTDL were added to a 250 ml four-necked flask. The reaction was carried out under a nitrogen atmosphere at 80 °C. Then cooled to 50 °C, DMBA and BDO were added, and reacted for 1 h, and then heated up to 80 °C for a certain period of time. Finally, metered triethylamine and sodium hydroxide aqueous solution were added, waterborne polyurethane latex was obtained by high-speed stirring at 1500 r/min.

(2) Preparation of waterborne polyurethane latex (BPU) through soft-segment modification: The steps are the same as the GPU preparation method besides metered BY3003 was added in the first step.

(3) Preparation of water-based ink: a certain proportion of blue color paste was added to the polyurethane latex, and mixed for 30 min at a certain rotation speed to prepare a polyurethane original ink.

### 2.3    Characteristic

(1) Latex particle size test: The latexes particle size was tested by a ZETA-ZS type particle size analyzer.

(2) Film thermal performance test: The glass transition temperature (Tg) of the polyurethane latex films was tested by differential scanning calorimeter Mettler Toledo DSC, the heating rate was 10 °C min$^{-1}$, the nitrogen flow rate was 10 mL·min$^{-1}$, and the test temperature range was—50–150 °C.
(3) Adhesion fastness: Cover the ink strip with 3 M tape, put a 10 mm × 10 mm squared paper under the sample strip. After sticking, remove the tape from the plastic surface at 90° quickly, and calculate the grid of the remaining ink film.

# 3   Results and Discussion

## 3.1   Effect of Modified Monomers on Properties of the Polyurethane Latexes

The basic properties of the polyurethane latexes modified with different amount of GMO or BY3003 were shown in Table 1.

**Table 1.** Basic properties of the polyurethane latexes modified with GMO and BY3003

|  | GMO content (%) | | | | | BY3003 content in soft segment (%) | | | | |
|---|---|---|---|---|---|---|---|---|---|---|
|  | 0 | 2 | 4 | 6 | 8 | 18 | 26 | 40 | 57 | 67 |
| Partical size (nm) | 40.3 | 47.6 | 60.5 | 60.4 | 75.6 | 66.4 | 66.3 | 60.8 | 54.4 | 50.7 |
| Viscosity (mpa s) | 15 | 45 | 30 | 25 | 23 | 23 | 29 | 29 | 58 | 73 |
| Storage stability | >6 | >6 | >6 | >6 | >6 | >6 | >6 | >6 | >6 | >6 |

It can be seen from Table 1 that as the GMO content increased, the particle sizes of the latexes tended to increase gradually. Because increasing the amount of GMO increases the number of long alkyl hydrophobic side chains on the polyurethane molecular chain, which weakens the hydrophilicity of the polyurethane micelles.

In addition, with the increase of the GMO content, the latexes' viscosity first increased and then decreased. The main reason is that when the content of GMO was low, association of the hydrophobic side chain formed slight mesh structures [6], which increases the viscosity of polyurethane latexes. However, when the content of GMO exceeded 4wt%, serious entanglement between alkyl chains occurred, which would weak motility of the molecular chains thus result in reduced latex viscosity.

The particle sizes of the latexes decreased with the increase of BY3003 content. Since BY3003 molecular chain contains a secondary hydroxyl group with strong hydrophilicity, the hydrophilicity and self-emulsifying ability of polyurethane were improved as the increase content of BY3003, which made the particle sizes of latex particles decrease gradually. In addition, the viscosity of the latexes gradually increased with the increase of the amount of BY3003 for the decrease of latex particle sizes and

the increase of the number of hydrogen bonds formed between secondary hydroxyl groups on the surface of latex particles and water.

Obviously, both the latexes prepared by two different modification methods exhibit good stability and low viscosity. Especially, the latexes modified by BY3003 possesses small particle sizes even in the case of relatively large amount of BY3003, which means that modification method on the soft segment has more flexible adjustability. In addition, the smaller the particle size is, the easier it is for the latexes to form a film, and the higher the film density, the better the performance for the latex films.

## 3.2 Effect of Modification Methods on the Thermal Properties of Polyurethane Film

In the experiment, DSC was used to test the glass transition temperature (Tg) of the above-prepared latexes. The DSC test results of the GPU and BPU latexes are shown in Figs. 1 and 2, respectively.
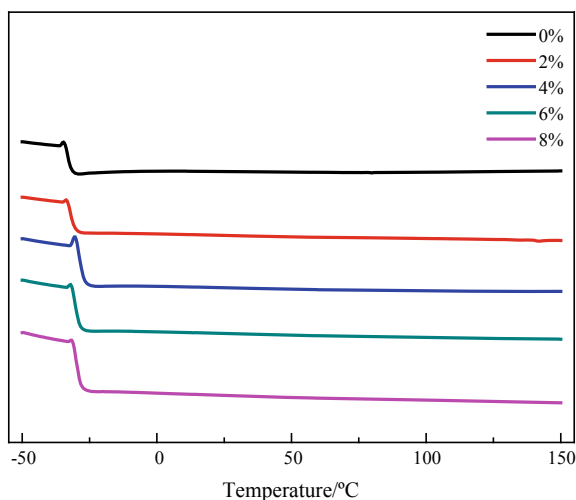


**Fig. 1.** DSC curve of GPU

In the DSC curves of GPU, only one glass transition temperature attributed to the soft segments can be observed for the all polyurethane latexes modified with GMO, indicating good compatibility between the soft with the hard segments in the corresponding polyurethane molecules. The glass transition temperature of the polyurethane gradually increased from –33 °C to –28 °C with the increase of GMO content from 0 to 8wt%. That is possibly because that, in the polyurethane with good compatibility between soft and hard segments, the Tg of the soft segments usually moves gradually to the high temperature region as the proportion of the hard segment increases. The increasing amount of GMO made the proportion of hard segment in GPU increased correspondingly, in turn made the Tg of soft segment increased gradually. In addition,
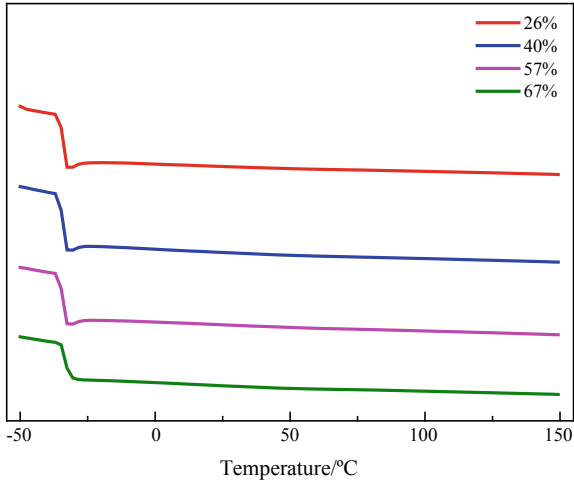
**Fig. 2.** DSC curve of BPU

the long alkyl side chain in the GMO molecular chain caused entanglement between the polyurethane molecular chains, which hindered the movement of the polyurethane molecular chains and reduced the phase separation degree of the hard and soft segments, which maybe also contribute to the increase of the glass transition temperature of the soft segments.

From the DSC curves of the BY3003 modified polyurethane, only Tgs (Tg of the soft segments) can be seen, while Tgh (Tg of the hard segments) cannot be measured, which also indicates that the soft and hard segments of this series of polyurethane materials have good compatibility. As the proportion of BY3003 in the polyurethane soft segment increased, the BY3003 soft segment modifier has little influence on the Tgs of polyurethane, and did not affect its low temperature resistance. The reason is that a certain amount of BY3003 was used to replace PBAD in the original formula, which did not cause significant change in the structure of polyurethane. In addition, the difference in the glass transition temperature of the soft segment between BY3003 and PBAD is small, so changing the amount of BY3003 did not affect the glass transition temperature of the soft segment of the whole molecule. It is obvious that the modification method on soft segment is more beneficial to maintain the good low temperature resistance.

## 3.3  Effect of Modified Methods on the Adhesion on BOPP Films of Polyurethane Inks

GPU and BPU were mixed with a blue color paste to prepare water-based inks respectively, and the inks were coated on the corona treated BOPP films by using wire rod coating device with wet film thickness of 25 μm. After standing in an oven at 50 °C for 30 min, the adhesion of the ink was tested and the test results are shown in the Figs. 3 and 4, respectively.

From Fig. 3 we observed that, with the increase of GMO content, the adhesion fastness on BOPP films of the corresponding ink first increased and then decreased. Obviously, the long alkyl side chain with low polarity on glycerol monooleate played a key role in improving the adhesion on BOPP films of the inks, which reduced the polarity of PU molecular chain, therefore improved its wettability and adhesion on low polarity materials. However, when the amount of GMO exceeded 4wt%, on the one hand, it significantly increased the proportion of hard segment with large polarity in polymer molecules, on the other hand, it increased the glass transition temperature of PU, both of which reduced the adhesion on BOPP of the inks.
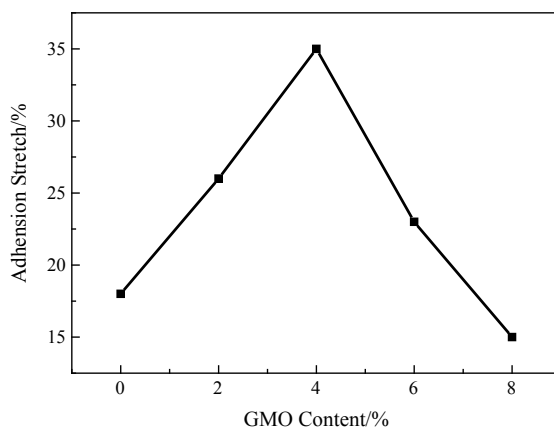


**Fig. 3.** Adhesion fastness of GPU

Figure 4 is adhesion fastness on BOPP thin films of the inks made from the latexes with different BY 3003 contents. With the increase of BY3003 content, the adhesion fastness on BOPP film of the polyurethane inks was obviously improved. When BY3003 accounted for 67% of the soft segment quality, the adhesion fastness on the BOPP film of the ink was as high as 97%. While the adhesion fastness of the ink using GMO modified polyurethane as the binder was only 35%. Therefore, the modification method on soft segment is more effective for improving the adhesion on low polarity BOPP films of the polyurethane inks. However, considering the cost factor and the influence on latex viscosity, BY3003 should not be used more.

## 4   Conclusions

Two kinds of waterborne polyurethanes latexes were prepared through modification on hard-segment with GMO or on soft-segment with BY3003, respectively. Both latexes exhibited good storage stability over 6 months. Modification on the hard-segment improved the glass transition temperature of the polyurethane latexes, and affected the low temperature performance of PU, while modification on the soft-segment had no obvious effect on the glass transition temperature and low temperature properties of
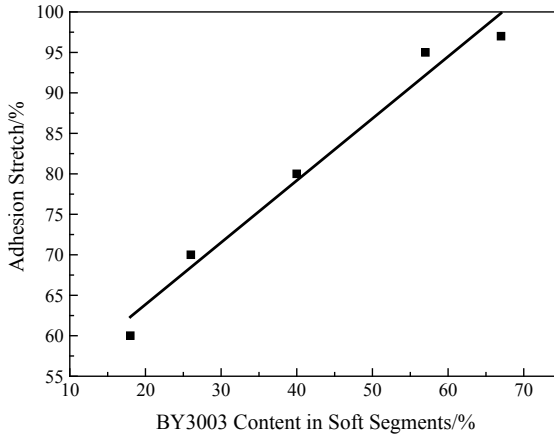
**Fig. 4.** Adhesion fastness of BPU

PU. Only a small amount of GMO could be introduced into the latexes, which improved adhesion on the BOPP film of the corresponding inks, but the maximum adhesion was only 35%. As contrast, the maximum adhesion of BY3003 modified PU inks on the BOPP film is much higher, even reach to 97%.

# References

1. Wang Z, Yang JJ, Wu MY et al (2008) Research progress of polyurethane inks. Polyurethane Ind 23(1):5–8
2. Wang ZX, Ran L, Chen H (2011) Research on polyester waterborne polyurethane ink binder. China Adhes (2):34–38
3. Wang JL, Wang ZX (2013) Preparation and properties of mixed polyester waterborne polyurethane ink binder. Adhes China 8:53–55
4. Liang L (2015) Preparation and properties of water-based polyurethane ink binder for plastic film printing. South China University of Technology, Guangzhou
5. Zhen W (2008) Synthesis and properties of silane-modified polyurethane binders for one-component retort inks. Anhui University, Hefei
6. Winnik MA, Yekta A (1997) Associative polymers in aqueous solution[J]. Curr Opin Colloid Interface Sci 2(4):424–436

# Relationship Between Ink Quantity and Density Based on Nonlinear Regression Analysis

Xuan Zuo[(✉)] and Qian Chen

School of Printing and Packaging Engineering, Beijing Institute of Graphic Communication, Beijing, China
zuodxuan@163.com

**Abstract.** Whether the amount of ink is suitable or not greatly affects the color reproduction of printed matter. In order to improve the quality of the printed matter, the mathematical relationship between the ink thickness and field density is obtained by Lambert-Beer law and a mathematical model is established accordingly. The traditional offset printing process is simulated by a printability tester, and nonlinear regression method and least square method are used to solve the parameters $D_{\infty}$ and m to get the fitting curve. Finally, the effect of the fitted curve is evaluated according to the size of the coefficient of determination $R^2$. That is the closer $R^2$ is to 1, the better the fitting effect.

**Keywords:** Ink layer thickness · Nonlinear regression analysis · The least square method

## 1 Introduction

In offset printing, the amount of ink has a great influence on the color reproduction process of the printed matter. When the amount of ink changes (the thickness of the ink layer changes), the color of the printed matter will change accordingly. The ink layer thickness refers to the average thickness of the ink layer attached to the paper surface in the vertical direction with the ink layer paper [1]. Low ink supply, thin ink layer, dim ink gloss, printing quality is not good. More ink supply, thicker ink layer and longer drying time will result in serious dot enlargement, dirty back, ink bar, paste and other phenomena, which will affect the quality of printed matter [2, 3]. Therefore, the control of the amount of ink is particularly important. In practice, by measuring the density of the ground, the amount of ink is determined, and then the amount of ink is adjusted to ensure the ideal reproduction of the image color and the quality of the print.

In this paper, the corresponding values of ink layer thickness and field density are obtained through experiments, and then their mathematical expressions are obtained. Then, the accuracy of the mathematical model established by MATLAB curve fitting analysis is used to guide production practice.

## 2    Analysis of the Relation Between Ink Thickness and Field Density

Practice has shown that within a certain range, the printed solid density increases with the increase of the thickness of the ink layer. When the thickness of the ink layer increases to a certain value, the solid density does not continue to increase, and a maximum density value, that is, the saturation density value is generated [4], as shown in Fig. 1. It can be seen from the figure that when the amount of ink is low, the ink layer is thin, the color is light, and the absorption light is less, so the reflectance is high and the density value is small; when the amount of ink is high, the ink layer is thick, the color is deep, and the amount of absorbed light is large. Therefore, the reflectance is low and the density value is large [5, 6]. The Lambert-Beer's law is usually used to describe the relationship between the density of the field and the thickness of the ink layer. The expression is as follows:
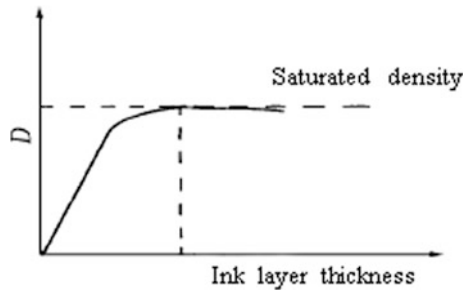


**Fig. 1.**   Relationship between ink layer thickness and field density

$$D = D_\infty(1 - e^{-m \cdot l}) \tag{1}$$

D is the solid density, $D_\infty$ is the saturation density, m is the parameter related to the printing paper, and l is the thickness of the ink layer. Among them, $D_\infty$ and m are obtained by experimental methods.

## 3    Experimental Part

### 3.1    Experimental Materials and Instruments

Printing material: SKYEYLION offset light fast dry blue ink 128 g double-sided coated paper. Printing instrument: ACT2-5IGT Printability meter Electronic balance Precision ink injector X-Rite Spectrodensitometer.

## 3.2    Experimental Procedure

(1)  Calculating Ink Density

The uniform ink was injected into the ink injector, the ink quality $M_1$ was measured with an electronic balance, and then the ink amount of 0.01 ml was extruded, and the mass at this time $M_2$ was measured. It is known that the ink quality is $\Delta M = M_1 - M_2$ and the ink volume is $V = 0.01$ ml, so the ink density $\rho = 0.95$ g/cm$^3$ is calculated by the formula $\rho = \Delta M / V$.

(2)  Uniform Ink and Proofing

In this experiment, 18 groups of numerical values were selected in the range of 0.01–0.3 ml to homogenize the ink. After homogenization, color samples were printed at 625 N printing pressure and 0.2 m/s printing speed on the printability tester.

(3)  Calculating Ink Thickness

Measuring the quality $m_1$ of ink roll after inking with electronic balance and the quality $m_2$ of ink roll after printing, the ink consumption transferred to paper is $\Delta m = m_1 - m_2$. The length and width of ink imprint on paper were measured and the imprint area $s$ was calculated. Then, the ink thickness $L_C$ was calculated by formula $d = \Delta m / (\rho \cdot s)$.

(4)  Measuring Field Density

After the ink on the spline is dried, the solid density value $D_C$ is measured by a spectrodensitometer in a portion where the amount of ink is uniform. Then establish the one-to-one relationship between the two, and select some data to form a table, such as Table 1, and finally draw a scatter map using 18 sets of data. As shown in Fig. 2.

**Table 1.**  Some data of $D_c$ and $l_c$

| Ink injection quantity | $l_c$ | $D_c$ |
| --- | --- | --- |
| 0.03 | 0.2039 | 0.52 |
| 0.04 | 0.7139 | 0.64 |
| 0.06 | 0.6119 | 0.79 |
| … | … | … |
| 0.23 | 2.6520 | 2.34 |
| 0.24 | 2.9579 | 2.36 |
| 0.25 | 3.1619 | 2.38 |
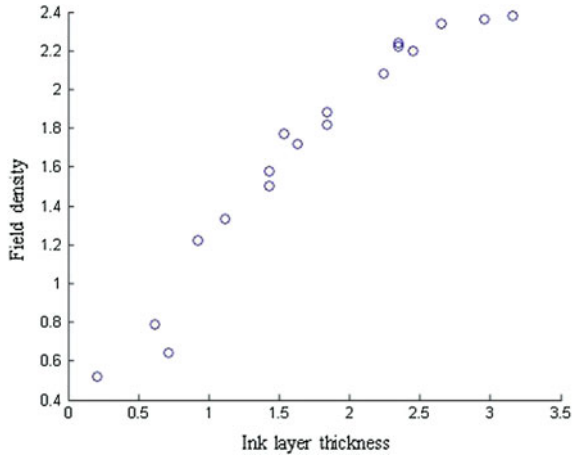
**Fig. 2.**  Scatter plot of field density as a function of ink layer thickness

The regression analysis was performed using the data in the table to determine $D_\infty$ and m in this experimental environment. And the relationship between ink layer thickness and field density is plotted by MATLAB, as shown in Fig. 3. From this, the relationship of the model is obtained.

$$D = 2.0689 \left(1 - e^{(-1.0723 \cdot l)}\right) \tag{2}$$
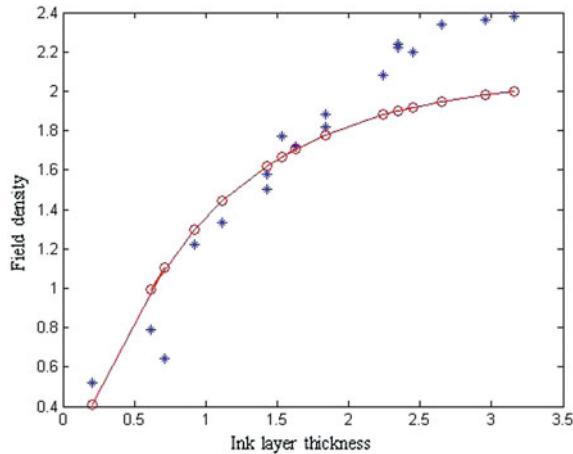


**Fig. 3.**  Relationship between ink layer thickness and field density and fitting curve

### 3.3  Model Checking

The coefficient of determination $R^2$ is also called the goodness of fit or the correlation index, and the closer to 1 indicates the better the fitting effect. The calculation formula is:

$$R^2 = 1 - \frac{\sum_{i=1}^{18}\left(D_i - \overline{D_i}\right)^2}{\sum_{i=1}^{18}\left(D_i - \overline{D_i}\right)^2} \tag{3}$$

According to the data in the table and the fitting curve, $R^2 = 0.8184$ is calculated, which approaches 1. This shows that the fitting curve and the sample value have higher goodness of fit, and the model is more accurate, which accords with the relationship between ink layer thickness and field density under this condition. However, the mathematical model with high accuracy will also have errors. We analyze the reasons for the errors. There are the following points.

1. The acquisition of the experimental data is obtained by simulating the actual printing process on the printing suitability meter, and the printing suitability meter does not represent the actual working condition of the printing machine, which is the main cause of the errors.
2. The measurement of ink volume is not accurate due to air bubbles in ink injector when calculating ink density, and the quality of ink is measured by electronic balance, so there are inevitable errors in the measurement process.
3. There are human errors in density measurement and other calculations.

## 4  Conclusions

Since there are many factors affecting the ink density in the actual printing process, a mathematical model is established as much as possible for the specific printing conditions, so that it can better reflect the relationship between the amount of ink and the density. In this paper, the mathematical model established obtains the density law equation of the ink used in the laboratory, and through verification, the fitting value is in good agreement with the experimental value, which provides theoretical guidance for production practice. Therefore, the effective reduction of the color and the level can be achieved by effectively controlling the amount of ink to ensure the stability of the print quality. In the actual printing process, we can change the mathematical model according to the specific printing conditions, as long as the model is generated, the amount of ink can be effectively controlled.

## References

1. Hu C (1993) Printing color and colorimetry. Printing Industry Press, Beijing
2. Zhou M, Lu L (2008) Technical analysis and quality control of offset printing ink layer thickness. Packag Eng 66–68

3. Zheng Y (2010) Printing quality detection and control technology, vol 34. Chemical Industry Press, Beijing
4. Wang X, Tang W, Cheng J (2009) Study on the relation between ink layer thickness and field density. Packag Eng 93–95
5. Ren L (2004) An improved study on the accuracy of the Lambert-Beer equation. Mag Print 11:77–79
6. Ren L, Cheng G (2004) The effect of ink quantity on ink density. Print Today 30(12):80–81

# Study on the Printability of Chemical and Physical Foaming Inks

Furong Li, Zhicheng Sun[✉], Shouzheng Jiao, Zixiong Que, Xiaoyang Du, Ruping Liu, Siyu He, Shiyi Wang, and Luhai Li

Beijing Engineering Research Center of Printed Electronics, Beijing Institute of Graphic Communication, 102600, Beijing, China
sunzhicheng@bigc.edu.cn

**Abstract.** Foaming inks have a wide range of applications in the light industry, mainly including chemical foaming inks and physical foaming inks. The chemical foaming ink was obtained by chemical reaction of a chemical foaming agent to form gas, and the physical foaming ink was obtained by vaporizing the liquid core material in the microcapsule at a certain temperature to generate internal pressure. In this paper, chemical foaming agents and physical foaming microcapsules were used as functional materials. The corresponding foaming ink was obtained by formula design. Meanwhile, the chemical and physical foaming inks were printed by screen, flexo and gravure printing processes, and the printing law was systematically studied. The print abilities of products, including foam height, color and ink adhesion were mainly investigated by different printing methods. The ultimate aim was to provide practical guidance for the foaming ink in the application process of lightweight technology.

**Keywords:** Physical foaming · Chemical foaming · Screen printing · Flexographic printing · Gravure printing

## 1 Introduction

The foaming agents are divided into a physical and a chemical foaming agent, and the mechanisms of the above two foaming agents are different. The physical foaming agent refers to a thermally expandable microcapsule. This causes the core material to change from a solid to a liquid state or a liquid state to a gaseous state when the temperature is raised. When the temperature raised, the core material expanded into a large-diameter sphere, and the volume was several tens of times larger than that of the original microcapsule. The shell materials were commonly made of acrylonitrile [1], methacrylic acid [2] and methyl methacrylate [3]. The core materials include alkanes [4, 5], petroleum ether [6] and paraffin [7]. The chemical foaming agent means that a chemical substance such as azodicarbonamide is decomposed to generate a large amount of gas and expand in the case of heat or high temperature. Common chemical foaming agents are azodicarbonamide [8], sodium hydrogencarbonate, 4,4-oxobisbenzenesulfonyl hydrazide [9], tosyl hydrazide [10] and the like.

Nowadays, the development and application of these two kinds of foaming inks are very extensive, such as textile, leather, wallpaper, buffer coating and so on. However, there is no comparison between the two foaming agents in terms of printing technology and lack of knowledge in this area. The focus of this paper was to study the printing suitability of products such as foam height, color and ink adhesion obtained by different printing methods, so as to provide a practical guidance for the foaming ink in the technical application process.

## 2   Experiment

### 2.1   Materials and Instruments

Main materials: thermal expansion microcapsules (self-prepared); 4,4-oxobisbenzenesulfonyl hydrazide foaming agent, Owen New Materials Co., Ltd.; acrylic film-forming resin, Qingdao Linke Industry and Trade Co., Ltd.; color paste, Tianjin Xinmei Coating Technology Co., Ltd.; transparent pulp, Jiangshan Weir Fine Chemical Co., Ltd.; defoamer BYC-6381, Hefei Xinwancheng Environmental Protection Technology Co., Ltd.; leveling agent BYK-300, Germany BYK company.

Main instruments: automatic constant speed mixer D2004, Shanghai Zhiwei Electric Co.,Ltd.; electric heating plate PB-3, Changzhou Guohua Electric Co., Ltd.; 3D laser confocal microscope VK-X200K, Japan KEYENCE; screen printing 100 mesh, Beijing Ingram Micro Printing Machinery Co., Ltd.; gravure printing proofing machine, flexographic printing proofing machine, Shanghai Modern Environmental Engineering Technology Co., Ltd.

### 2.2   Preparation of Foaming Agent Ink

(1)  Preparation of ink

Preparation of Screen Printing Ink: 50 g of clear paste and 9 g of color paste were placed in a beaker and mechanically stirred for a while. Then, 25 g of an acrylic film-forming resin, 5 g of water, 10 g of a foaming agent, 0.2 g of an antifoaming agent and 0.8 g of a leveling agent were placed in a beaker and mechanically stirred for 20 min. The ink was transfered on a screen printing plate at 45° to obtain a printed product.

Preparation of gravure ink: 70 g of a transparent paste and 12 g of a color paste were placed in a beaker and mechanically stirred for a while. Then 5 g of water, 12 g of blowing agent, 0.2 g of defoamer and 0.8 g of leveling agent were added to the beaker and mechanically stirred for 20 min. The ink is then printed onto the substrate by a gravure press to obtain a printed product.

Preparation of flexographic ink: 67 g of a clear paste and 15 g of paste were placed in a beaker and mechanically stirred for a while. Then 5 g of water, 12 g of blowing agent, 0.2 g of defoamerand 0.8 g of leveling agent were added to the beaker and mechanically stirred for 20 min. The ink is then applied to the printed material by a flexographic printing press to obtain a printed product.

(2)  Post processing

After the printed sample ink was dried, it was heated at 120 °C for 1 min to obtain a sample having a stereoscopic effect.

## 3  Results and Discussion

### 3.1  Microscopic Characterization of Printed Samples

According to the ISO 12944 international standard classification, the test results are shown in Table 1. In the domestic standard, it is qualified that the adhesion is 1 to 2. It can be concluded from the table that the foaming height of the physical foaming ink is significantly lower than that of the chemical foaming agent. Because the chemical foaming agent foam is highly unstable, it is difficult to control by humans. However, the physical foaming agent is the outer shell layer protection and control of the thermal expansion microcapsule, which can better control the foaming height. The foaming height of the offset paper is lower than the foaming height of the kraft paper, because the roughness of the offset paper is lower than that of the kraft paper. There are more holes in the kraft paper to hold more ink.

Printing standards: clear patterns, clear fonts, no burrs, drag, misplacement, overlap, etc. Screen printing products have a thick ink layer and no missing patterns. The gravure printing product has a uniform ink layer, no water marks, no deformation, and no defects. Flexographic printing products have a uniform ink layer and a bright ink color. As can be seen from the picture of the laser confocal microscope of Fig. 1, the foamed ink is suitable for screen printing and the printed sample is very uniform. Because the screen printed mesh is large, the blowing agent can pass through the screen. Comparing the two blowing agents, it can be seen that the ink of the physical foaming agent is very uniform after foaming, and the pattern is a soap bubble type, which has a fluffy visual sense and a smooth touch. The foam of the chemical foaming agent is relatively uniform but not as good as the physical foaming agent, and the pattern exhibits a bee-like style with an embossed visual impression. It can be seen from the figure that the gravure and flexographic printing samples have large fluctuations, and some parts are obviously free of foaming agent, but the gravure printing effect is better than the flexographic printing. In flexo and gravure printing technologies, the height of chemical blowing agents precedes the printed products of physical blowing agents.

### 3.2  Ink Performance Analysis of Printed Samples

The L*, a*, and b* values of the physical foaming ink and the chemical foaming ink were measured using an X-Rite Swatchbook spectrophotometer. According to the International Lighting Association (CIE) standard chromatic aberration and chroma formula:

$$\Delta E^* = \sqrt{(\Delta L^*)^2 + (\Delta a^*)^2 + (\Delta b^*)^2}$$

**Table 1.** Adhesion and foaming height difference of different foaming inks

| Printing material | Offset paper | | | | | | Kraft paper | | | | | |
|---|---|---|---|---|---|---|---|---|---|---|---|---|
| Ink type | Physical foaming ink | | | Chemical foaming ink | | | Physical foaming ink | | | Chemical foaming ink | | |
| Printing method | Silk screen | Gravure | Flexo | Silk screen | Gravure | Flexo | Silk screen | Gravure | Flexo | Silk screen | Gravure | Flexo |
| Adhesion | 0 | 1 | 3 | 1 | 3 | 4 | 0 | 1 | 4 | 1 | 3 | 3 |
| Height difference/um | 15.82 | 40.83 | 13.25 | 45.34 | 65.47 | 56.63 | 77.85 | 37.06 | 138.68 | 99.86 | 170.71 | 181.95 |
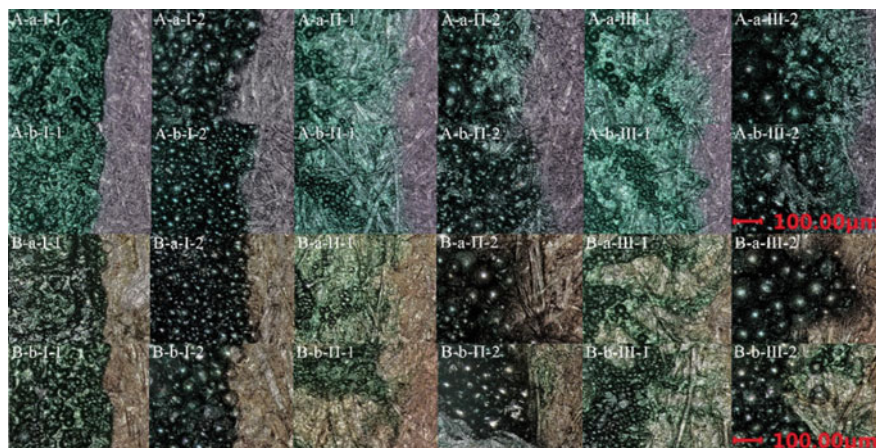
**Fig. 1.** Foamed ink sample under laser copolymerization microscope *Note* A/B is offset paper/kraft paper, a/b is chemical/physical foaming agent, I/II/III is screen/flexo/gravure, 1/2 is unfoamed/foamed

$$\Delta C^* = \sqrt{(a^*)^2 + (b^*)^2}$$

The $\Delta L^*$, $\Delta a^*$, and $\Delta b^*$ were obtained by using $L^*$, $a^*$, and $b^*$ before and after foaming as shown in Table 2.

By comparing the physical foaming inks printed on different substrates through the same printing method, it was found that, in addition to the flexographic printing method, the kraft paper has a smaller color difference and chroma than the offset paper. However, in addition to the gravure method, the kraft paper in the chemical foaming ink sample has a smaller color difference and chroma than the offset paper. Therefore, kraft paper is generally smaller in color and chroma than offset paper. This is because kraft paper is more rough than offset paper, which results in a higher degree of adhesion of the foamed ink. Therefore, if the paper has a large roughness, the chromatic aberration and chroma before and after the foaming of the sample are smaller. The same substrate and printing method are printed with different foaming inks. It has been found that physical foaming inks have smaller color and chroma than chemical foaming inks because of the unstable foaming process of chemical foaming ink. Therefore, it is extremely easy to cause uneven foaming height and larger difference between chromatic aberration and chroma. By changing the different printing methods, it was found that the chromatic aberration and chroma change of the gravure printing were smaller.

**Table 2.** Color difference between physical foaming ink and chemical foaming ink

| Printing material | Offset paper | | | | | | Kraft paper | | | | | |
|---|---|---|---|---|---|---|---|---|---|---|---|---|
| Ink type | Physical foaming ink | | | Chemical foaming ink | | | Physical foaming ink | | | Chemical foaming ink | | |
| Printing method | Silk screen | Gravure | Flexo | Silk screen | Gravure | Flexo | Silk screen | Gravure | Flexo | Silk screen | Gravure | Flexo |
| $\Delta L^*$ | −0.93 | 1.32 | 2.19 | −0.03 | 1.07 | 3.81 | 6.35 | 4.34 | 5.15 | 10.78 | 8.91 | 10.52 |
| $\Delta a^*$ | 15.42 | 8.79 | 9.07 | 23.58 | 7.69 | 16.18 | 3.83 | 5.91 | 5.18 | 8.89 | 1.40 | 0.09 |
| $\Delta b^*$ | −1.31 | −0.22 | 0.02 | −2.66 | −0.01 | −1.26 | −4.28 | −4.19 | −13.06 | −5.65 | −10.10 | −11.45 |
| $\Delta E^*$ | 15.51 | 8.89 | 9.33 | 23.73 | 7.76 | 16.67 | 8.57 | 8.44 | 14.97 | 15.08 | 13.54 | 15.55 |
| $\Delta C^*$ | 15.48 | 8.80 | 9.07 | 23.73 | 7.69 | 16.23 | 5.75 | 7.24 | 14.05 | 10.54 | 10.20 | 11.45 |

# 4    Conclusion

For the two foaming inks, the physical foaming ink exhibits a soapy-like feel with a soap bubble type, but the chemical foaming ink exhibits a bee-like style with a relief feeling. The physical foaming ink has a better printing effect than the chemical foaming ink. For the printing method, the finished product printed by screen printing was better in terms of adhesion, chromatic aberration and chroma. However, gravure and flexo were not very suitable for two foaming inks. For different papers, if the paper has a large roughness, the more the amount of ink adheres, the smaller the chromatic aberration and chroma will become before and after foaming.

# References

1. Aoki Y, Arendt O (2001) Melt rheology of poly (epsilon-caprolactone)/poly(styrene-co-acrylonitrile) blends. J Appl Polym Sci 82(8):2037–2041
2. Han N, Gao X et al (2013) Structures and properties of thermoregulated acrylonitrile-methyl acrylate sheet containing microphase change materials. Polym. Compos. 34(5):641–649
3. Huang C, Gao J, Yu, W et al (2012) Phase separation of Poly(methyl methacrylate)/Poly (styrene-co-acrylonitrile) blends with controlled distribution of silica nanoparticles. Macromolecules 45(20):8420–8429
4. Fu H, Gong W, Chen Y et al (2019) Influence of electrolytes on thermal expansion microcapsules. J Macromol Sci Part A Pure Appl Chem 56(1):104–114
5. Hou Z, Kan C (2014) Preparation and properties of thermoexpandable polymeric microspheres. Chin Chem Lett 25(9):1279–1281
6. Hosseinzadeh L, Shokoohinia Y, et al (2019) Cytotoxic and Apoptogenic Sesquiterpenoids from the Petroleum Ether Extract of Artemisia aucheri Aerial Parts. Iran J Pharm Res 18 (1):391–399
7. Han S, Lyu S et al (2019) Fabrication of melamine-urea-formaldehyde/paraffin microcapsules modified with cellulose nanocrystals via in situ polymerization. J Appl Polym Sci 54 (9):7383–7396
8. Lopez-Gonzalez E, Salmazo LO et al (2019) Study of the effect of different electron irradiation doses on the decomposition temperature of azodicarbonamide. Polym Eng Sci 59 (4):791–798
9. Li S, Cai L (2004) Synthesis and application of Universal foaming agent OBSH. Chem Ind J
10. Cui W, Wu H (2000) Synthesis mechanism of 4,4'-Oxobisbenzenesulfonyl chloride and its application in industry. Hubei Chem Ind

# Stable Dispersion Technology of Ultrafine Nickel Powder

Lihong Cao, Fan Su, Aijing Gao, and Luhai Li[✉]

Beijing Engineering Research Center of Printed Electronics,
Beijing Institute of Graphic Communication, Beijing, China
`liluhai@bigc.edu.cn`

**Abstract.** Nickel powder has shown great advantages in printing electronically conductive pastes due to its excellent properties. Thus, it is of great significance to study the secondary dispersion performance of nickel powder. To this end, the effects of dispersant PVP or triethanolamine on the dispersion properties of nickel powder in anhydrous ethanol or terpineol were investigated. In the experiment, the nickel powder was sufficiently chemically bonded to the dispersant in a solvent by a mechanical stirring method. Observed by the laser scanning confocal microscope and comparing $D_{90}$ and zeta potential, the result shows that when the dispersant PVP is used in terpineol, the greatest dispersion performance of nickle powder was shown.

**Keywords:** Nickel powder · Dispersant · Solvent · Dispersion stability

## 1 Introduction

As an emerging technology, printed electronics has attracted the attention of researchers at home and abroad. The ultimate goal of research of printed electronics is to achieve a wide range of flexible, low-cost electronic or optoelectronic products by printing. To achieve these goals, the production of conductive paste is one of the most essential aspects. But nowadays precious metals are expensive, the use of base metals instead of precious metals to prepare conductive pastes and conductive coatings is the future trend.

Ultrafine nickel powder, owing to its high chemical activity, great electrical conductivities, low resistance, has widely potential applications in various fields, such as, electrically conductive polymers, electrode material and nickel-ceramics complex [1–3]. For the nickel powder for the conductive paste, the particle size is required to be uniform and disperse well, and the particles are spherical. Currently, with the rapid development of the electronics industry, the demand for ultra-fine nickel powder has increased year by year. It tends to be highly pure, highly dispersed and ultra-fine. There are various methods for preparing ultrafine nickel powder, such as chemical vapor deposition methods, thermal decomposition reducing methods, electrochemical deposition method [4, 5]. But there is little concern about the secondary agglomeration of the obtained nickel powder. Based on this, it is practical and meaningful to study the effect of different dispersants on the dispersion properties of nickel in different solvents.

## 2 Experiment

### 2.1 Materials and Reagents

All reagents were analytical grade. Nickel powder has a particle size of 300–400 nm and is produced by Guangdong Fenghua Company. The solvents are ethyl alcohol absolute ($C_2H_6O$, $Mr = 46.07$, Beijing Chemical Works) and terpineol ($C_{10}H_{18}O$, $Mw = 154.25$, Aladdin Industrial Corporation). The dispersant is PVP (($C6H9NO)_n$, $Mw = 40,000$, Tianjin Guangfu Fine Chemical Research Institute), and triethanolamine ($C_6H_{15}NO_3$, $Mw = 149.19$, Tianjin Fuchen Chemical Reagents Factory). Observation of dispersion properties of nickel powder by laser confocal microscopy (KEYENCE, VK-X210), $D_{90}$ and zeta were tested by nanosizer (MALVERN, Nano-ZS), IR spectrum was tested by infrared spectrometer (Thermo Fisher Scientific, Nicolet iS50).

### 2.2 Secondary Dispersion of Nickel Powder

The experiment was run in a room temperature laboratory. Reaction parameters and dosage of chemical reagents are fixed. Dosage of each nickel powder is 2 g and dispersant is 1 g. The specific experimental details are as follows: 2 g of nickel powder and 1 g of PVP or triethanolamine were added to a 100 ml beaker, and then ethyl alcohol absolute was poured to make the solution close to 70 ml. According to the paper [6], the ultrafine nickel powder had the best wettability of the powder at pH 4. In the experiment, the pH of the solution was adjusted to about 4 with hydrochloric acid. The beaker was sealed and stirred using a mechanical stirrer for 5 h at 300 rpm. During stirring, samples were taken every hour, and five samples were taken. The dispersion of nickel powder was observed under a laser confocal microscope with a 200-fold microscope, and the $D_{90}$ and zeta potenial were tested. The same experimental conditions were controlled, the solvent was replaced with terpineol, and two sets of samples were obtained.

## 3 Results and Discussion

Now name the sample as follows: the solvent is anhydrous ethanol, the dispersing agent is PVP and triethanolamine respectively corresponding to sample A and sample B; the solvent is terpineol, the dispersing agent is PVP and triethanolamine are sample C and sample D, respectively. In the experiment, the dispersion of the nickel powder was observed under a laser confocal microscope of a 200-fold mirror as shown in the Fig. 1. The $D_{90}$ and zeta potential of the dispersed sample are provided in Fig. 2.
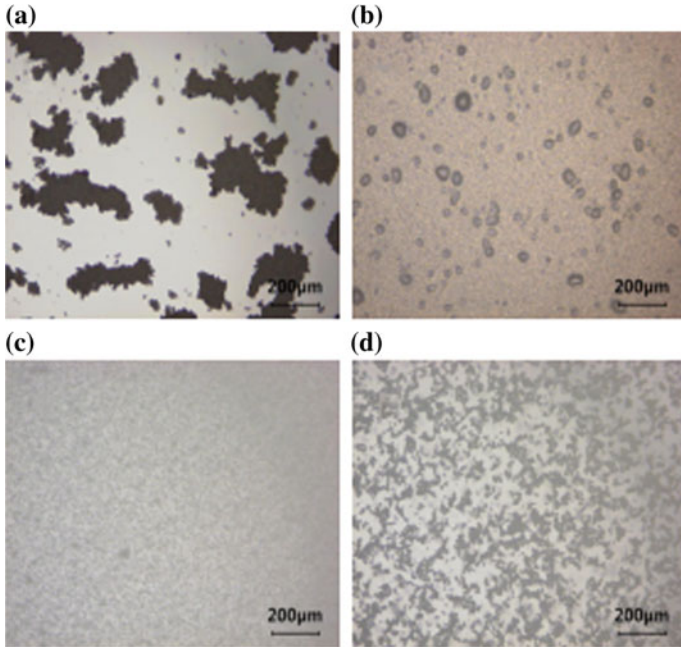
**Fig. 1.** Laser confocal microscope image of nickel powder dispersion: **a** sample A; **b** sample B; **c** sample C; **d** sample D
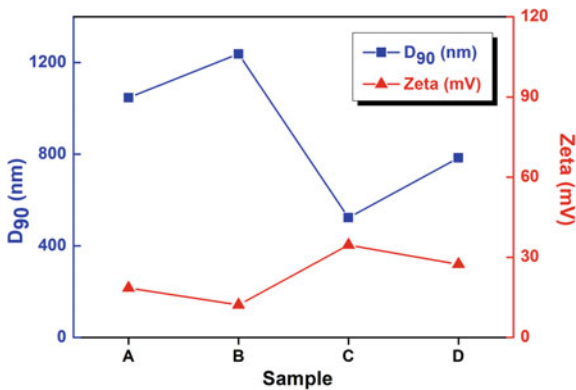


**Fig. 2.** The $D_{90}$ and zeta potenial of samples

## 3.1    Effect of Different Types of Solvents

After sampling, the sample was observed under a microscope and it was observed that the nickel powder rapidly aggregated in anhydrous ethanol. The difference is that, as shown in Fig. 1, the dispersion performance of sample C and D is significantly better than that of samples A and B, especially sample C. According to Fig. 2, the $D_{90}$ of

sample C and D is much smaller than A and B, it indicates that the sample is more dispersed in terpineol. At the same time, the zeta potentials of samples C and D were also much higher, further confirming that terpineol is more suitable as a solvent for nickel powder dispersion than anhydrous ethanol.

We see that the biggest cause of this phenomenon is viscosity. Viscosity is a physicochemical property of a fluid that reflects the frictional resistance of a substance as it moves through a fluid. The viscosity of terpineol(approximately 32.30 cP at 25 °C) is much larger than that of anhydrous ethanol(approximately 1.10 cP at 25 °C). Due to the viscosity, the flow resistance of nickel powder in terpineol is much greater than that of nickel powder in absolute ethanol. Thus, the nickel powder dispersed in terpineol is not easily agglomerated.

## 3.2  Effect of Different Types of Dispersants

Comparing the laser confocal microscopy images of samples, whether in solvent anhydrous ethanol or terpineol, the nickle in solvents of using the dispersant PVP is more uniformly dispersed than the dispersant triethanolamine and the particle agglomeration is more slight. This conclusion is also verified by the $D_{90}$ and zata potentials of samples. It indicates that the Van Der Waals force and magnetic force between the molecules after the nickel powder is combined with PVP is greater than the intermolecular force after the nickel powder and triethanolamine are combined.

The structure of PVP and triethanolamine molecule is as shown in Fig. 3 According to this paper [7], the C=O bond of dispersant molecules could coordinate with Ni to form Ni-PVP or Ni-triethanolamine complex. Taking PVP as an example, it's bonding with nickel powder is shown in Figs. 3 and 4. The pyrrole group end is chemically bonded directly to the nickel powder, and the long chain end will present extended status on the surface of nickel particles. This results in a steric hindrance effect which increases the barrier and reduces the contact between the nickel particles. IR spectra of nickel powders synthesized with Ni-PVP and pure PVP are shown in Figs. 3 and 5. For pure PVP, the absorption peak of the C=O bond at 1701 cm$^{-1}$ was shifted to 1607 cm$^{-1}$ of the nickel powder. The change in the spectrum indicates that the PVP molecule containing C=O can coordinate with nickel to form a PVP-Ni complex. It is obvious that the chain length of triethanolamine is not enough to against aggregation of nickel particles. As a result, nickel particles synthesized with PVP showed excellent dispersion properties [7].
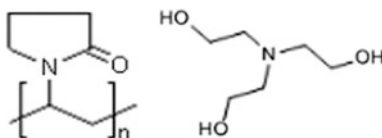


**Fig. 3.** The structure of PVP (left) and triethanolamine (right) molecule
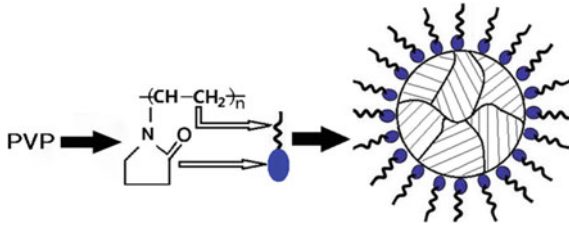
**Fig. 4.** Schematic diagram of bonding of PVP and nickel particles
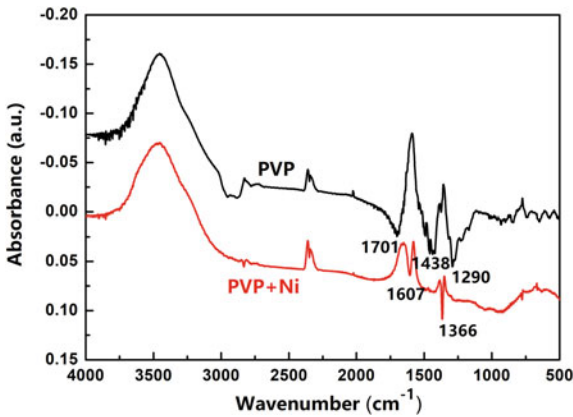


**Fig. 5.** IR of nickel powders synthesized with PVP as dispersant

## 4   Conclusion

Two different dispersants and two different solvents were employed for the investigation of the effect on the dispersion of the nickel powder. Among them, because terpineol has a much higher viscosity than anhydrous ethanol, the dynamic resistance of nickel powder increases, resulting in better dispersion of nickel powder. At the same time, when PVP was used as dispersant, since the molecular chain length is longer than that of triethanolamine, it is better able to prevent nickel powder from agglomerating. Based on this, studying the dispersion properties of nickel powder will help to study the preparation of conductive nickel paste in the future.

# References

1. Park J, Kang E, Son SU, Park HM, Lee MK, Kim J, Kim KW, Noh HJ, Park JH, Bae CJ, Park JG, Hyeon T (2005) Monodisperse nanoparticles of Ni and NiO: synthesis, characterization, self-assembled superlattices, and catalytic applications in the Suzuki coupling reaction. Adv Mater 17(4):429–434
2. Phetsinorath S, Jian-xin Z, Xiao-qin Z, Hai-quan S, Wen-jiang D (2012) Preparation and hydrogen storage properties of ultrafine pure Mg and Mg−Ti particles. Trans Nonferrous Metals Soc China 22:1849–1854
3. Xia XH, Wang XL, Mai YJ, Shi SJ, Tang YY, Gu CG, Tu JP, Zhang YQ (2012) Three-dimensional porous nano-Ni supported silicon composite film for high-performance lithium-ion batteries. J Power Sources 213:106–111
4. Singjai P, Wongwigkarn K, Laosiritaworn K, Yimnirun R, Maensiri S (2007) Carbon encapsulated nickel nanoparticles synthesized by a modified alcohol catalytic chemical vapor deposition method. Curr Appl Phys 7:662–666
5. Pan H, Liu BH, Yi JB et al (2005) Growth of single-crystalline Ni and Co nanowires via electrochemical deposition and their magnetic properties. J Phys Chem B 109:3094–3098
6. Li Q, Huang H et al (2007) Study on dispersion behavior of ultrafine nickel powder in liquid phase. Hydrometallurgy China 26(104):188–192
7. Liu D, Lin L, Ren S, Fu S (2015) Effect of polyvinyl pyrrolidone (PVP) molecular weights on dispersion of sub-micron nickel particles by chemical reduction process. J Mater Sci 51 (6):3111–3117

# Large-Scale Preparation of Nano-Copper Particles for Conductive Ink

Xinjie Lei, Dawa Lamu, and Yi Fang[✉]

Beijing Engineering Research Center of Printed Electronics, School of Printing and Packaging Engineering, Beijing Institute of Graphic Communication, Beijing, China
fangyi@bigc.edu.cn

**Abstract.** Nano-metal conductive ink is the key material to realize the industrialization of printed electronics. Compared with silver, copper has the advantages of low cost and good conductivity. If large-scale preparation of nano-copper particles can be realized, it is expected to greatly reduce the production cost of printed electronics. In this work, an aqueous solution of copper sulphate, polyvinylpyrrolidone (PVP) and hydrazine hydrate were used as reactants. Firstly, nano-copper particles were prepared in a 10 L volume reactor by liquid phase chemical reduction method. Then the prepared nano-copper particles dispersion was concentrated. After removing impurities, a concentrated solution of nano-copper particles is obtained. Further, the morphology and size of the nano-copper particles are characterized by scanning electron microscopy. Combined with factors such as pH and reactant concentration, the best reactant ratio is obtained. Finally, about 20 g of nano-copper particles can be prepared from the reactor. According to different reaction conditions, the prepared nano-copper particles are well dispersed without aggregation, and the average particle size is between 50–300 nm. The results of this research can provide low-cost conductive materials for printed electronics.

**Keywords:** Nano-copper · Large-scale · Conductive ink

## 1 Background

As an emerging technology, printed electronics has obtainedhuge researching interest due to its simple process, environmental protection, large area and flexibility [1, 2]. At present, printed electronic technology has been applied in many fields such as printed circuit boards, printed RFID antennas, printed thin film transistors, printed organic solar cells, and printed organic light-emitting devices [3–6]. Nano-metal conductive ink is an indispensable raw material for printed electrons. Nano-particles have special effects such as quantum size effect, surface effect, small size effect and macroscopic quantum tunneling effect, which can exhibit unique optical, electrical, magnetic, mechanical and chemical properties [7]. As an inorganic functional material, nano-metal conductive inks have quickly attracted researchers' attention. The early researches were on conductive inks which represented by nano-silver [8–10]. However, the relatively high price of silver and the susceptibility to ion migration or electro-

migration in humid environments have limited its use in mid-end to low-end products. Currently, there is an urgent demand to select a metal which is electrically conductive and inexpensive to replace silver. The low price and good electrical conductivity enables nano-copper conductive inks to be a substitute for nano-silver conductive inks.

There are chemical methods and physical methods for preparing nano-copper particles. The physical methods include conventional electrolysis method, ball milling method, vapor phase vaporing method, gamma ray irradiation-hydrothermal crystallization method, plasma method, supercritical fluid drying method, ultrasonic electrolysis method and so on [11]. Due to the expensive equipment and multi-steps process of physical preparation, chemical methods were more attractive [12]. Among them, the liquid phase chemical reduction is the most commonly used method for preparing nano-copper particles in laboratory. The reduction reaction occurs in the aqueous phase or solvent with the copper salt precursor and the reducing agent. The $Cu^{2+}$ ions are reduced to different sizes and shapes of copper particles. However, the large-scale preparation of nano-copper particles is one of the bottlenecks restricting the application of nano-metal conductive inks.

In this work, a 10 L-scale reactor was used to prepare large-scale nano-copper by liquid phase chemical reduction. In addition, the morphology and particle size of the synthesized nano-copper were characterized by a scanning electron microscopy (SEM) and a zeta potentiometer. The synthesized nano-copper particles can be used as fundamental materials for printed electronics.

## 2   Experimental

In this work, copper sulfate pentahydrate ($CuSO_4 \cdot 5H_2O$) was selected as the precursor of copper salt. Polyvinylpyrrolidone (PVP K30) was used as a protective agent. Hydrazine hydrate ($N_2H_4 \cdot H_2O$) was used as a reducing agent to prepare nano-copper particles. The preparation was carried out by optimizing the conditions. The chemical reagents used in this experiment and their main chemical properties are as follows (Table 1).

**Table 1.**  Chemical parameters

| Category of chemicals | Purity (%) | Manufacturer |
|---|---|---|
| Copper sulfate pentahydrate ($CuSO_4 \cdot 5H_2O$) | $\geq 99.0$ | Alfa Aesar (China) Chemical Co., Ltd |
| Polyvinylpyrrolidone (K30) | $\geq 98.0$ | Sinopharm Chemical Co., Ltd |
| Hydrazine hydrate ($N_2H_4 \cdot H_2O$) | $\geq 80$ | Tianjin Guangfu Technology Development Co., Ltd |
| Sodium hydroxide (NaOH) | $\geq 95.0$ | Beijing Chemical Plant |

# 3   Results and Discussion

During the synthesis, the parameters such as the concentration of copper sulfate, the concentration of hydrazine hydrate, the concentration of the protective agent, and the pH value are variable. Depending on the parameters, nano-copper particles with different sizes were tested by azeta potentiometer. The results of the small-scale preparation are shown in Fig. 1.
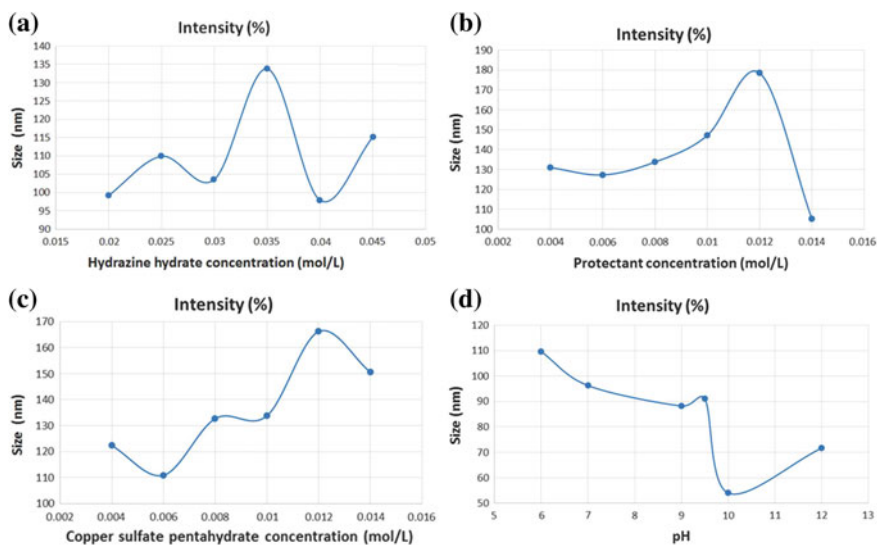


**Fig. 1.** Relationship between reaction parameters and nano-copper particles average size. (**a** the relationship between hydrazine hydrate concentration and nano-copper particles average size; **b** the relationship between protective agent concentration and nano-copper particles average size; **c** the relationship between concentration of copper sulfate pentahydrate and nano-copper particles average size; **d** the relationship between pH and nano-copper particles average size)

After the small-scale experiment, the best experimental parameters were determined and a large-scale of experiment was started. A reactor with a volume of 10 L was used. First, the inner and outer surfaces of the double-layer glass reactor were cleaned with water and detergent. The inner wall of the reactor was rinsed with deionization. 100 g of polyvinylpyrrolidone was poured into the reaction vessel, and then 4 L of deionized water was added to the reaction vessel. Then, Plug in the power, turn on the constant speed mixer and modulate the rotation speed for 120 rpm. The mixture was slowly spun to dissolve for 1 h. Further, 80 g of anhydrous copper sulfate was added to the reaction vessel, and the color of the solution changed from transparent to light blue. 50 ml of hydrazine hydrate was placed in a beaker. Then, the 50 ml of hydrazine hydrate in the beaker was quickly poured into 5 L of deionized water for dilution. The diluted dosing solution was slowly poured into the reaction vessel and stirred at a speed

of 200 rpm. The reaction solution undergoes a distinct color change during the pouring process, from light blue to dark blue, then yellow-green, and finally to brown-red, as shown in Fig. 2.
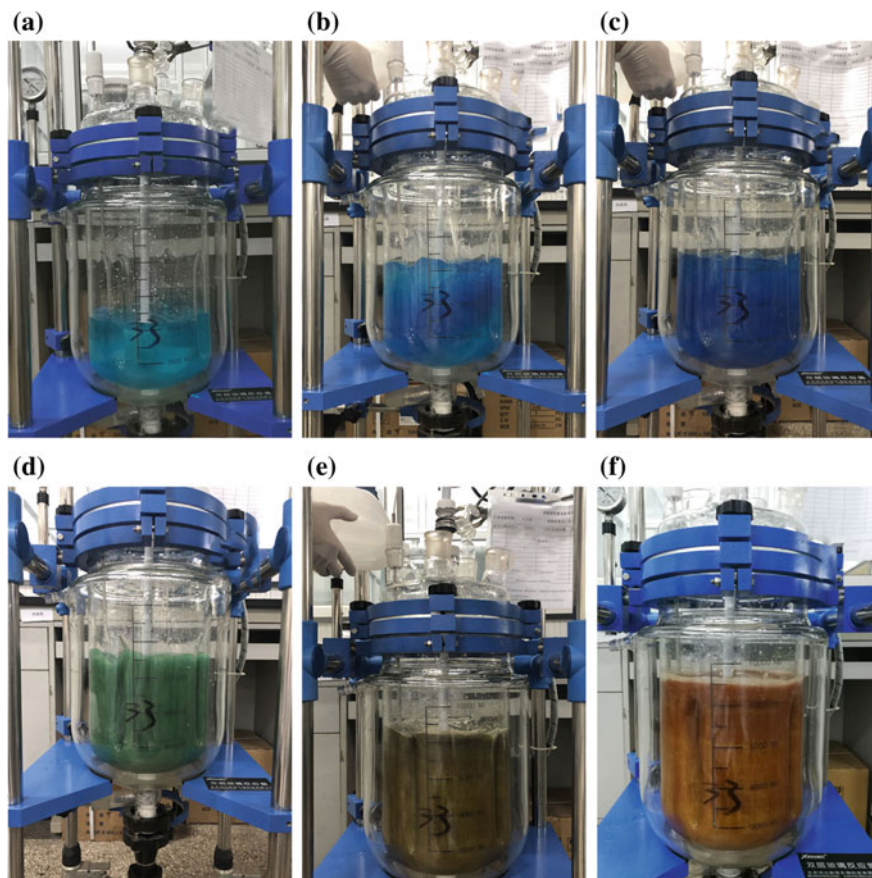


**Fig. 2.** The reacting phenomenon of the solution in the reactor. (**a** before the reaction, t = 0 min; **b** start adding hydrazine, t = 0.5 min; **c** continue to add hydrazine, t = 1 min; **d** continue to add hydrazine, t = 5 min; **e** continue to add hydrazine, t = 10 min; **f** end of the reaction, t = 20 min)

After the reaction was completed, the reaction solution was placed and settled for 12 h. In order to collect the precipitate in the reactor, the bottom drain of the reactor in the opposite direction was slowly rotated. When all the precipitates have flowed out, the bottom drain of the reactor can be turned off. The precipitated nano-copper particles were poured into several centrifuge tubes and concentrated by centrifugation. The centrifugation speed is 5000 rpm, the centrifugation time is 5 min. Finally, the pure nano-copper particles concentrate is obtained (Figs. 3 and 4).
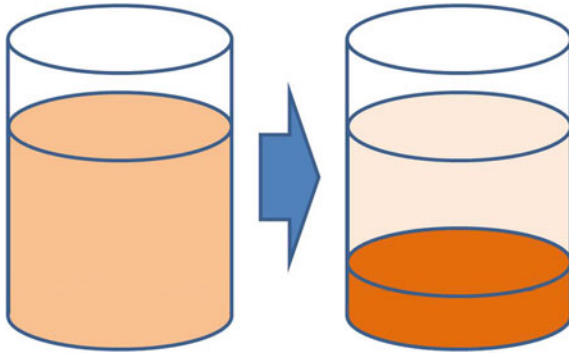
**Fig. 3.** Schematic diagram of sedimentation and concentration of nano copper dispersion
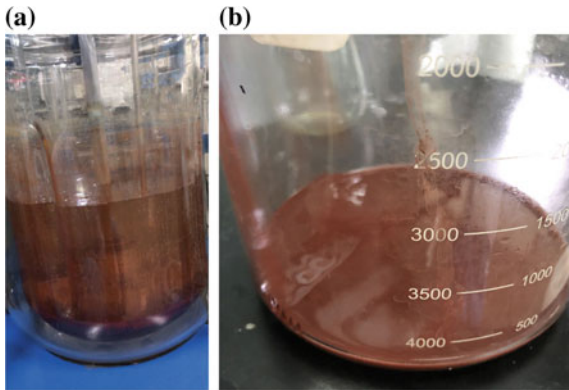


**Fig. 4.** Nano-copper dispersion before (**a**) and after (**b**) concentration

Figure 5 is the captured pictures of the prepared nano-copper particles selected from different reaction conditions by SEM. It can be found that the size distribution of nano-copper particles is uniform in the pictures. The shape of the nano-copper particles is ellipsoidal. The dispersion is good and only a small part of the nano-copper particles is agglomerated. It can be seen that the size of nano-copper particles is between 50–300 nm.
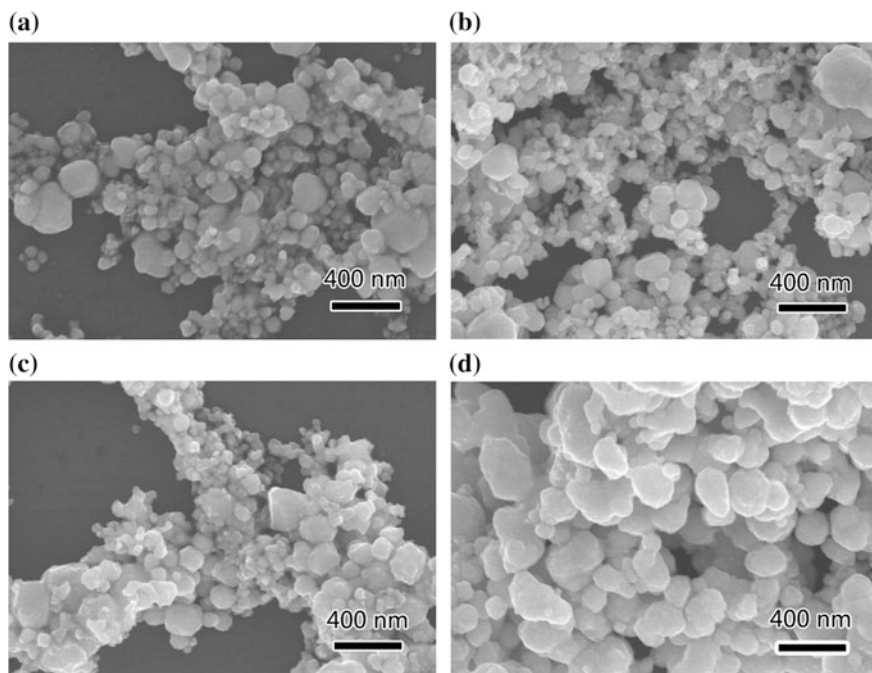
**Fig. 5.** Nano-copper SEM-picture under different reaction conditions

## 4    Conclusions

In this work, nano-copper particles were prepared by liquid phase reduction. In a 10 L volume reactor, about 20 g of nano-copper particles can be prepared at room temperature. According to different reaction conditions, the prepared nano-copper particles were well dispersed without aggregation, and the particles size is between 50-300 nm. The preparation method can provide a low-cost conductive material for printed electronics.

## References

1. Aleeva Y, Pignataro B (2014) Recent advances in upscalable wet methods and ink formulations for printed electronics. J. Mater. Chem. C 2:6436–6453
2. Allen M, Leppaniemi J, Vilkman M, Alastalo A, Mattila T (2010) Substrate-facilitated nanoparticle sintering and component interconnection procedure. Nanotechnology 21:475204

3. Mo L, Guo Z, Yang L, Zhang Q, Fang Y, Xin Z, Chen Z, Hu K, Han L, Li L (2019) Silver nanoparticles based ink with moderate sintering in flexible and printed electronics. Int J Mol Sci 20:2124

4. Huang Q, Zhu Y (2019) Printing conductive nanomaterials for flexible and stretchable electronics: a review of materials, processes, and applications. Adv Mater Technol 5

5. Allen ML, Jaakkola K, Nummila K et al (2009) Applicability of metallic nanoparticle inks in RFID applications. IEEE Trans Comp Packag Technol 2(32):325–332

6. Liu L, Feng Y, Liang J, Li S, Tian B, Yao W, Wu W (2019) Structure-designed fabrication of all-printed flexible in-plane solid-state supercapacitors for wearable electronics. J Power Sources 425:195–203

7. Kubo R (1962) Electronic properties of metallic fine particles. J Phys Soc of Jpn 17:975–986

8. Kamyshny A, Steinke J, Magdassi S (2011) Metal-based inkjet inks for printed electronics. Open Appl Phys J 4:19–36

9. Karthik PS, Singh SP (2015) Conductive silver inks and their applications in printed and flexible electronics. RSC Adv 5:77760–77790

10. Raut NC, Al-Shamery K (2018) Inkjet printing metals on flexible materials for plastic and paper electronics. J Mater Chem C 6:1618–1641

11. Dadgostar N, Ferdous S, Henneke D (2010) Colloidal synthesis of copper nanoparticles in a two-phase liquid-liquid system. Mater Lett 64(1):45–48

12. Wu SH, Chen DH (2004) Synthesis of high-concentration Cu nanoparticles in aqueous CTAB solutions. J Colloid Interface Sci 273:165–169

# Performance Study of Flexible Temperature Sensor Based on Carbon Sensitive Material

Yue Shi, Shilin Huang, Zhicheng Sun, Wei Wang, and Ruping Liu[✉]

Institute of Printing and Packaging Engineering, Beijing Institute of Graphic
Communication, Beijing, China
liuruping@bigc.edu.cn

**Abstract.** In this study, a flexible film temperature sensor was fabricated by
screen printing technology. The temperature sensor was fabricated by firstly
printing nano-silver conductive ink and sequentially carbon temperature sensi-
tive ink onto a flexible polyethylene terephthalate (PET) substrate. By changing
the proportion of nano-carbon black in the temperature sensitive ink and the
sintering temperature of the nano-silver conductive ink, the effects on the
conductivity and temperature sensitivity of the flexible film sensor were
investigated, and the linearity, hysteresis and stability of the prepared sensor
were verified. When the sintering temperature of silver electrode based on PET
film was 130 °C, the electrode square resistance was 10.2 m$\Omega$/□. When the
ambient temperature varies between 25 and 75 °C, the resistance of the tem-
perature sensor decreases as the amount of nano-carbon black added increases.
Besides, the flexible temperature sensor shows high linearity and good stability.
By virtue of the flexibility, simple preparation process and low cost, this flexible
temperature sensor that can be found useful in a certain range of applications,
including wearable devices, biomedical devices, smart packaging and smart
house.

**Keywords:** Temperature sensor · Nano-silver conductive ink · Carbon
system · Flexible

## 1 Introduction

Temperature is a physical quantity that characterizes the degree of heat and cold of an
object. The measurement of temperature plays an essential role in ensuring product
quality and industrial production safety. Therefore, temperature sensors are widely used
due to the importance of temperature measurement [1, 2].

With the continuous development of microelectro mechanical systems (MEMS),
four main types of commercial temperature sensors occupy the market, including the
resistive temperature detectors, thermocouples, thermistors, and integrated circuit
sensors with digital and analog interfaces [3]. However, since these temperature sensors
mainly use relatively rigid silicon as the substrate material, which limits their appli-
cations and increases the manufacturing cost [4]. Moreover, the conventional MEMS
sensor needs to perform operations such as photolithography and etching in the

preparation process, which has high requirements on the processing equipment and the processing environment, and further increases the manufacturing cost [5].

With the development of printed electronics and the increasing demand for flexible microcircuits, flexible polymers such as PET, polyimide (PI), and polydimethylsiloxane (PDMS) are used as substrates to prepare flexible temperature sensors using a printing process [6]. The preparation has been widely concerned because of its advantages of good flexibility, strong adhesion, simple preparation process, low cost and mass production [7]. In this study, we prepared a flexible temperature sensor by screen printing, in which PET film as the substrate, nano-silver conductive ink as the electrode material and temperature sensitive ink added into nano-carbon black as the temperature sensitive coating. Finally, a positive temperature coefficient (PTC) resistance type flexible temperature sensor was constructed, and the performance of temperature sensor was tested.

## 2   Experimental

### 2.1   Preparation of Flexible Temperature Sensor

Firstly, we used screen printing to prepare an electrode of the sensor. The PET substrate was first cleaned with acetone, alcohol, and deionized water, and then the nano-silver conductive ink (Yingshang Electronic Materials Co., Ltd, China) was printed on the PET film by a screen printing machine (0S-300 FV, OLAT Printing Machinery Industry Co., LTD, China), and dried in an oven at 130 °C for 1 h. Then, the preparation of nano-carbon black added temperature sensitive ink is a key step in the experiment. In the preparation of the temperature sensitive ink added into nano-carbon black (particle size 10–20 nm, Cabot, America), the epoxy resin (Zhifan, China) was first divided into three parts and added to the solvent of ethylene glycol monobutyl ether acetate (BGA, J&K, China) in three times, and completely dissolved by continuous stirring by a mechanical stirrer, and then the nano-carbon black was added. The above components were mixed for 20 min by using D-2004 type mechanical stirrer and the stirring paddle rotation speed was stirred at 200 r/min. Finally, under the rolling action of the three-roll mill, the nano-carbon black particles were further dispersed and dispersed more uniformly, and the volume ratio of nano-carbon black in temperature sensitive resin was 20, 25 and 30%, and naming them as Formula 1, Formula 2 and Formula 3, separately. After preparing the temperature sensitive ink added into nano-carbon black, it was printed on the interdigitated electrode of the previously printed silver electrode by a screen printer, and dried by in oven at 120 °C. The structure of the obtained finished product was shown in Fig. 1, wherein Fig. 1a is a structure of the interdigitated electrode, and Fig. 1b is a sectional view of the sensor.

### 2.2   Measuring Instrument

During the test, the effect of the sintering temperature of the nano-silver conductive ink on the square resistance of the interdigitated silver electrode was investigated by an RTS-9 type double electrical test four probe tester. The surface morphology of the
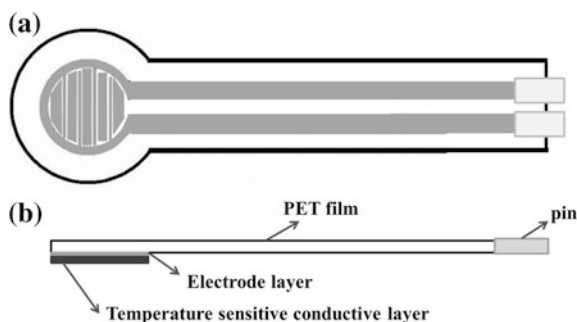
**Fig. 1.** Structure diagram of flexible temperature sensor: **a** Structure diagram of interdigital electrode; **b** sectional configuration

silver electrode was observed using Hitachi SU8000 cold field emission scanning electron microscopy (SEM). Moreover, the influence of the adding ratio of different nano-carbon black on the temperature-sensitive characteristics of flexible sensor was investigated by the temperature-control platform in the CGS-1TP intelligent gas sensitivity analysis system, and the prepared sensor was tested for linearity, hysteresis and stability.

## 3   Results and Discussion

### 3.1   Silver Electrode Conductivity Test

Since the optimum sintering temperature of nano-silver conductive ink used in this experiment was uncertain, the overall conductivity of the nano-silver conductive ink used in the sintering process was examined in a large temperature range (100–400 °C). In view of the high temperature resistance of the substrate used in the temperature range of 100–400 °C, the glass was selected as a substrate for sintering of the nano-silver conductive ink. The square resistance of the silver film with different sintering temperatures by RTS-9 type double electrical test four probe tester was tested. As shown in Fig. 2, as the temperature increases, the connecting material in the silver paste gradually volatilizes. The square resistance of the silver electrode was gradually reduced, which shows a decrease in the on-resistance. Moreover, as the temperature rises, the sintering of the conductive silver paste is more sufficient, and a dense conductive network is formed between the silver particles. When the sintering temperature is 250 °C, the minimum square resistance is 8.3 mΩ/□. However, as the temperature further increases, the square resistance of the silver electrode begins to increase gradually. It shows that at the sintering temperature of 250 °C, silver electrode has excellent conductivity. The surface microstructure of the silver electrode was observed by SEM, and the image shows that the silver film formed a dense conductive network, as shown in Fig. 3. When the square resistance is in the range of 8.3–10.7 mΩ/□, the square resistance of the silver electrode can be satisfied. However, considering that the PET film can be used for a long time at 130 °C, PET can withstand 150 °C for a short

time. At the same time, considering the energy consumption problem, the sintering temperature of the nano-silver conductive ink was chosen to be 130 °C.
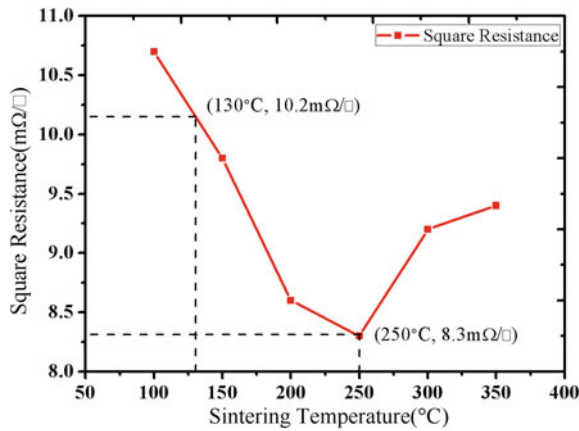


**Fig. 2.** Effect of sintering temperature on the sheet resistance
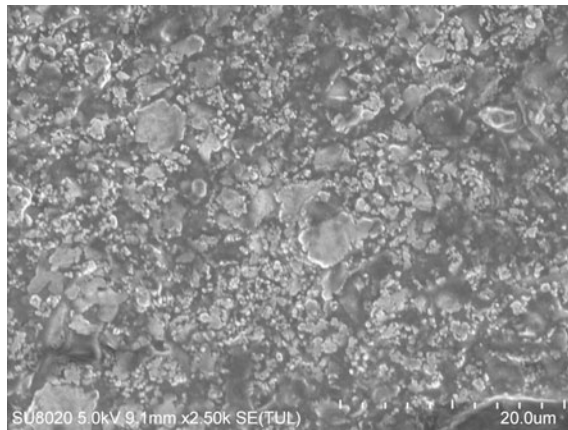


**Fig. 3.** SEM image of silver electrode

In order to verify the stability of the silver conductive electrode, a series of tests were conducted. First, in order to test its environmental adaptability, two pieces of PET printed with silver electrodes were placed in an aqueous solution and an ethanol solution for 48 h, and no electrode peeling occurred. What's more, peeling experiments were carried out using 3 M tape, and it was found that the silver electrode had good adhesion and no significant change. In addition, the results showed that after 50 bends, no obvious cracks appeared, and the resistance was tested without major changes.

## 3.2    Temperature Sensor Performance Test

We used the temperature control platform in the CGS-1TP intelligent gas sensitivity analysis system to test the relationship between temperature and resistance in the temperature sensors of Formula 1, Formula 2 and Formula 3, as shown in Fig. 4. The result shows that as the content of nano-carbon black increases, the higher the nano-carbon black content, the lower the resistance can be measured in the same temperature range (25–75 °C). And the three formulations' resistance all increased with the temperature rose, because the temperature sensitive ink expands to dilute the conductive network formed by the nano-carbon black filler, resulting in the rise of the temperature sensor resistance. Moreover, we can see from the curve of Fig. 4 that the linearity of the temperature sensor is good. And the more nano-carbon black is added, the smaller the change of resistance.
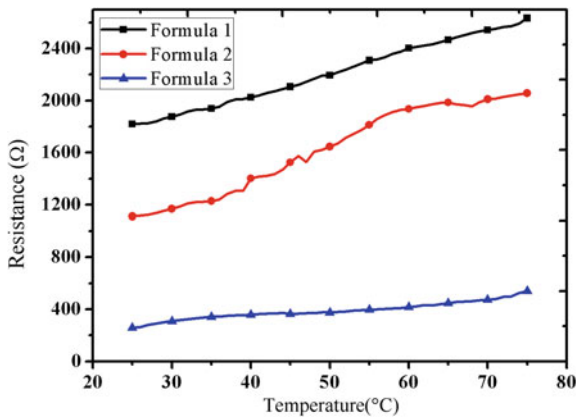


**Fig. 4.** The relationship between resistance and temperature of temperature sensor

Next, for Formula 3, we further conducted hysteresis testing and stability testing, as shown in Fig. 5. Figure 5a shows the temperature sensor in the temperature range of 25–75 °C positive (increase in input) reverse (input reduction) travel curve. Through the curve change, the forward and reverse travel curve coincidence rate not high, the maximum difference between the forward and reverse travel output values is 60 $\Omega$, so a series of improvements are needed in the next experiment to minimize the hysteresis error. Figure 5b shows the change in resistance within 60 s of the temperature sensor at 50 °C. The result shows that the resistance value fluctuates up and down only 1 $\Omega$ in the case of continuous measurement for one minute, which proves that the device has better stability.
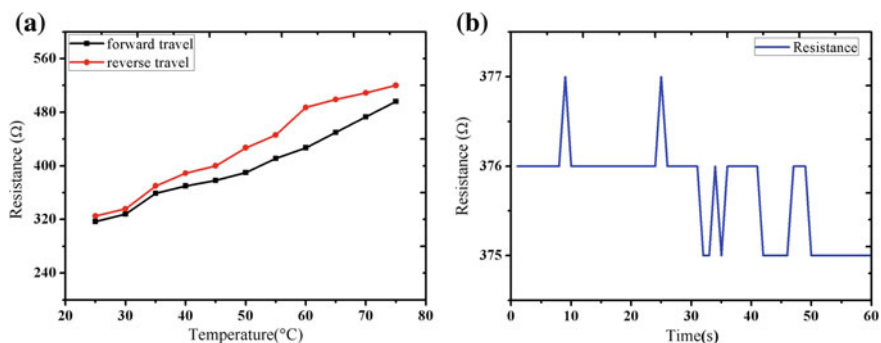
**Fig. 5.** Hysteresis and stability test of formula 3

## 4   Conclusion

In this study, we designed a flexible temperature sensor with an interdigitated silver electrode and a temperature-sensitive coating. We systematically studied the effect of sintering temperature on the conductivity of silver electrode and the effect of different nano-carbon black adding into the temperature sensitivity of the sensor. The result shows that at a sintering temperature of 250 °C, the silver electrode has the lowest square resistance and exhibits the best conductivity. The temperature-sensitive coating printed on the silver electrode reflects that the nano-carbon black-added temperature sensitive ink has PTC characteristics in a certain temperature range (25–75 °C). As the amount of adding increases, the range of resistance change decreases in the same temperature range, indicating that the device has excellent thermal stability. However, the hysteresis error of the sensor is large. Therefore, it is important to select a suitable sintering temperature and nano-carbon black adding amount to obtain good performance. Due to its advantages, the proposed sensor can be widely used in the fields of wearable devices, biomedical devices, smart packaging and smart house.

## References

1. Qin YH, Alam AU, Pan S, Howlader MMR, Ghosh R, Hu NX, Jin H, Dong SR, Chen CH, Deen MJ (2018) Integrated water quality monitoring system with pH, free chlorine, and temperature sensors. Sens Actuators B 255(1):781–790
2. Oh JH, Hong SY, Park H, Sang WJ, Jeong YR, Oh SY, Yun J, Lee H, Kim JW, Ha JS (2018) Fabrication of high-sensitivity skin-attachable temperature sensors with bioinspired microstructured adhesive. ACS Appl Mater Interfaces 10(8):7263–7270

3. Meijer GCM, Wang G, Heidary A (2018) Smart temperature sensors and temperature sensor systems. Smart Sens MEMs (Second Edition) 57–85
4. Liu GY, Tan QL, Kou HR, Zhang L, Wang JQ, Lv W, Dong HL, Xiong JJ (2018) A flexible temperature sensor based on reduced graphene oxide for robot skin used in internet of things. Sensors 18(5):1400
5. Spearing SM (2000) Materials issues in microelectromechanical systems (MEMS). Acta Mater 48(1):179–196
6. Maslik J, Andersson H, Forsberg V, Engholm M, Zhang R, Olin H (2018) PEDOT:PSS temperature sensor ink-jet printed on paper substrate. J Instrum 13:C12010
7. Khan S, Lorenzelli L, Dahiya RS. Technologies for printing sensors and electronics over large flexible substrates: a review. IEEE Sens J 15(6):3164–3185

# Application of Stretchable Conductive Ink in the Field of Flexible Electronic Devices

Yu Ding, Xiaoyu Wang, Zhenxin Guo, Lixin Mo, Wei Wang[(✉)],
and Luhai Li

Beijing Engineering Research Center of Printed Electronics, Beijing Institute
of Graphic Communication, Beijing, China
18900616029@189.cn

**Abstract.** The stretchable conductive ink is a functional material which enables the ink film to have better electrical conductivity after stretching and folding. It has broad application prospects in the field of flexible electronic devices. From the perspective of realizing the stretchability and electrical properties of ink films, this paper introduces the most research progress of nanometal-based stretchable conductive inks. The definition and characteristics of flexible electronics are introduced, and several methods for flexible electronic devices are mainly summarized. The mechanism and realization of stretchable conductive inks are reviewed. Then the applications of stretchable conductive inks based on these methods are introduced. Finally, the problems and technical shortcomings of the stretchable conductive ink in the development of flexible electronic devices are analyzed and the prospect of this new functional ink is predicted. The application of this ink can simplify and optimize the production process of stretchable conductor and make important impacts to flexible electronics.

**Keywords:** Stretchable conductive ink · Flexible electrons · Conductive ink

## 1 Introduction

Traditional electronic devices integrate electronic components on rigid substrates, and the devices themselves are difficult or unable to withstand deformations such as stretching, bending, and distortion [1]. Flexible electronic devices improve their structure on the basis of rigid electronic devices, enabling the device to withstand a certain degree of deformation [2]. With the development and advancement of mechanics, materials science, and manufacturing processes, the performance of flexible electronic devices has also increased. A certain degree of stretching, folding and bending can still maintain a certain conductivity and the device has high reliability and durability. Flexible electronic devices have been widely used in smart clothing, foldable displays, robot skins, stretchable solar cells, flexible electronic labels [3], etc. The research and application of flexible electronic devices will definitely change the lives of human beings.

The research and application of flexible electronic devices will definitely change the lives of human beings [3]. Previous research focused on improving the thickness and brittleness of silicon chips, mainly by replacing the rigid substrate with a soft elastic

substrate and integrating the microstructure on the elastic substrate, thereby making the electronic device flexible and light and shock resistant. In 2006, Professor Rogers of the University of Illinois and Professor Huang Yonggang successfully prepared wavy monocrystalline silicon strips on PDMS substrates by pre-strain control method [4]. This silicon film can withstand tensile strain of about 20%, which significantly improves the ductility of silicon. As shown in Fig. 1. This work provides an idea for the flexibility of electronic devices, and other structures are proposed around the mechanical structure design. Such as mesh structures, two-dimensional serpentine structures and three-dimensional coil structures and composite structures, such stretchable structures still use traditional conductive metals (mainly including Cu, Au and Ag) [5]. Therefore, the electrical conductivity of the device can be ensured, and the buckling structure is designed on the basis of which the device has flexibility.
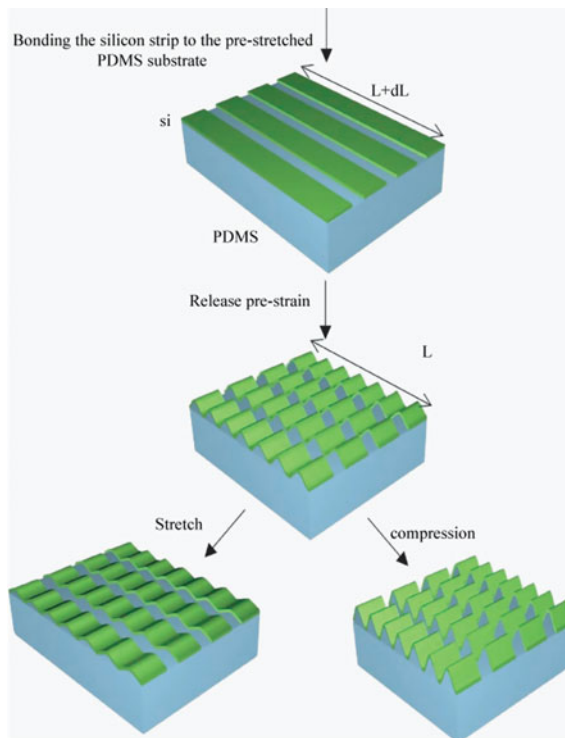


**Fig. 1.** Schematic illustration of process for fabricating buckled Si ribbons on a PDMS substrate [6]

The wavy structure is the simplest and commonest structure in a stretchable device. As shown in Fig. 2 [7], the method simply deposits or coats a conductive material onto the surface of a pre-strained elastomeric polymer substrate and then releases the pre-strain. After the pre-strain release, the surface of the substrate on which the conductive material is deposited spontaneously forms a periodic wave structure having a certain

wavelength and amplitude, which involves some mechanical models [7]. When strain is applied, the wavelength and amplitude of the wavy structure change as the strain changes. Thereby, relatively obvious stretchability is produced, and at the same time, it has high conductivity. The tensile properties of the device are mainly determined by the Young's modulus and Poisson's ratio of the elastic substrate, and have little to do with the material deposited on the surface of the substrate. The surface of the film obtained by this method is relatively rough, and the conductive layer and the flexible substrate have poor adhesion, and the layer of the functional layer and the substrate may be formed after stretching for a certain number of times.
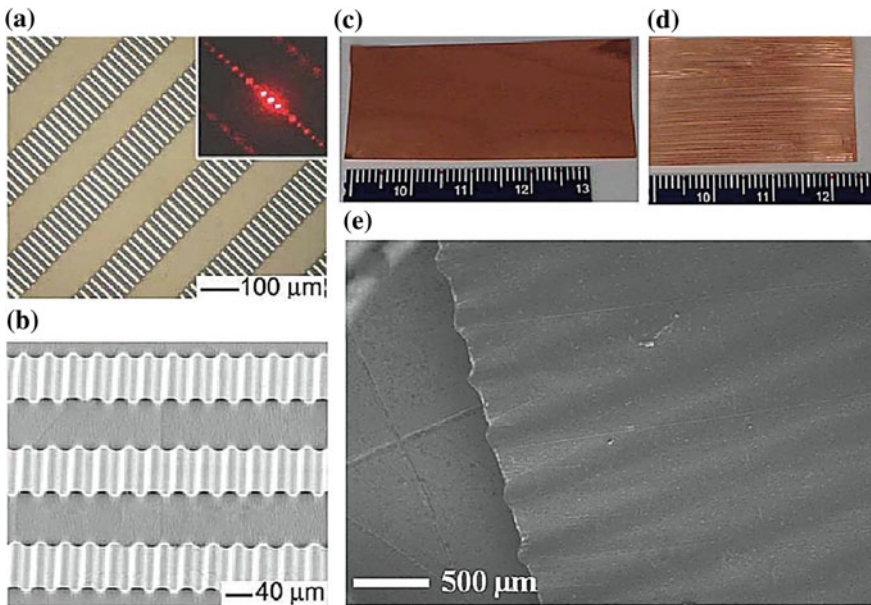


**Fig. 2.** Structural characterization of wavy GaAs nanoribbons: **a** Optical micrographs and **b** SEM photographs; structural characterization of wavy graphene sheets: **c, d** Digital photographs of copper foil (**c**) before making a wave shape; **d** after making a wave shape; **e** SEM photo of the surface of a wave-shaped graphene sheet on a PDMS substrate [8]

The network structure is distributed on the elastic substrate by nanowires or the fiber structure of the nanomaterials [9]. When stretched, the randomly distributed nanowires form an overlap with each other to ensure the integrity of the conductive network. As shown in Fig. 3 [10], the nano silver wire is taken as an example. The nano silver wire solution was dropped on a glass plate, and liquid PDMS was dispensed. After drying, silver wire was partially embedded in the PDMS. The formed stretchable structure is more stable than the wavy structure, and the surface roughness is low, and can be further compounded with other materials.

A two-dimensional serpentine structure is the formation of an ordered curved structure of material within an elastic substrate [11]. As shown in Fig. 4, the stretching
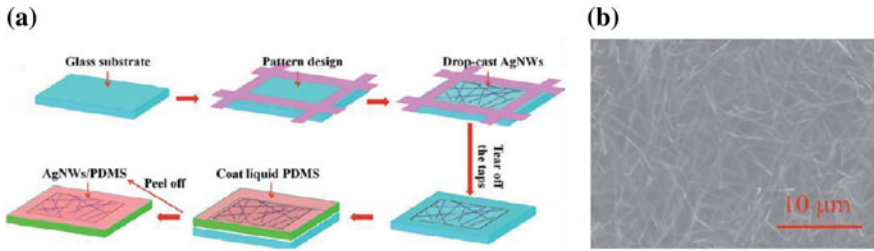
Fig. 3. **a** Schematic illustration of the fabrication process of percolating networks. **b** Scanning electron microscopy image of the AgNW percolating network [10]

ability of the serpentine structure is determined by the amplitude-wavelength ratio, and the larger the ratio, the stronger the stretchability. The direction of the force when being stretched is different from the wave structure. The direction of the force of the wave structure is a vertical elastic base, and the direction of the bend in the serpentine structure is parallel to the elastic base. Compared with the grid structure, the serpentine structure only changes the amplitude and wavelength under strain, and the force and relative position between the conductive materials does not change much, and the resistance changes less under the same tensile degree.
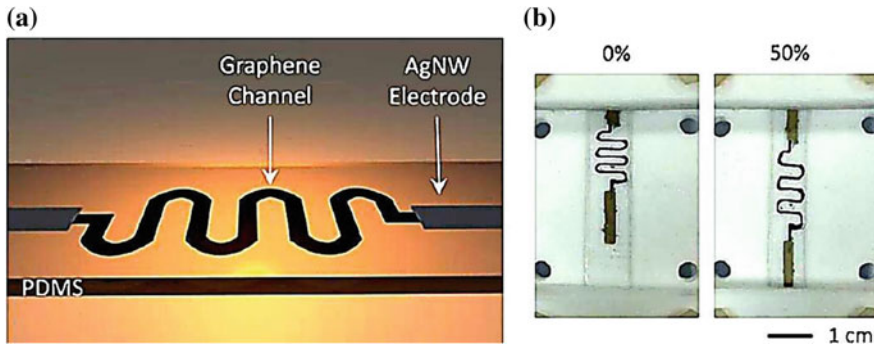


Fig. 4. **a** Schematic diagram of the relaxed state of the stretchable serpentine graphene thermistor; **b** digital photo of the serpentine graphene thermistor at 0 and 50% strain [11]

The three-dimensional coil structure is formed by coating a conductive material on a three-dimensional polymer network, and forming a conductive network by means of a polymer skeleton [12, 13]. This structure is basically an improved version of the two-dimensional structure, which is capable of transferring the stress portion into the polymer structure when stretched, greatly increasing the stress tolerance limit of the device (Fig. 5). The tensile properties are significantly better than the two-dimensional serpentine structure, but the complicated fabrication process and high cost of such structures are not conducive to commercialization.
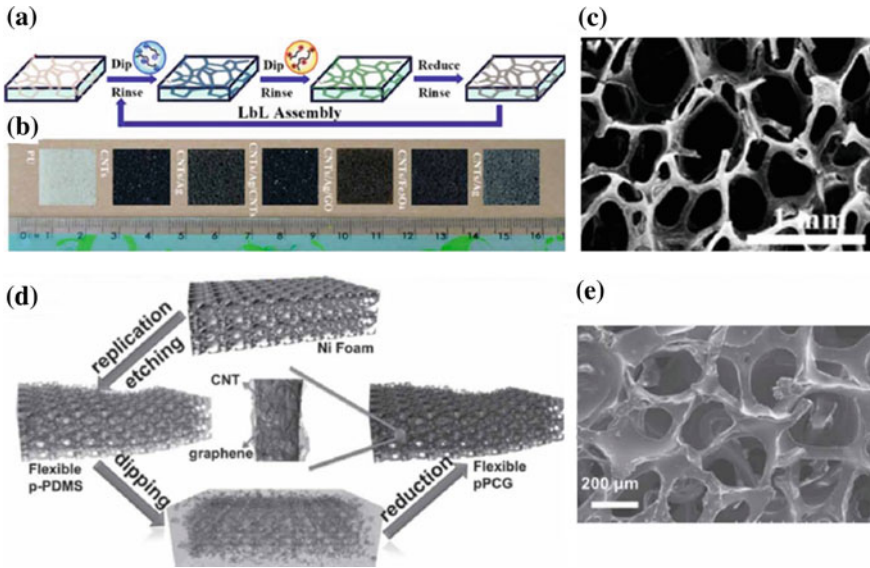
**Fig. 5. a** Schematic diagram of preparation method of carbon nanotube/polyurethane network structure; **b** digital photograph of carbon nanotube/polyurethane network structure and **c** SEM photograph [14]; **d** preparation of graphene/PDMS network structure Schematic diagram of the method; **e** SEM photo of graphene/PDMS network structure [15]

Considering the advantages and disadvantages of the above structures, we combine the above two or more structures, which is called a composite structure. Since the composite structure is composed of a plurality of structures, the stretchability which is not possessed by a single structure can accommodate a wider range of deformation. In the study of stretchable structures, composite structures are also the structures we often consider.

With the development and application of flexible electronic technology, more flexible solutions have been proposed. The mechanical buckling structure is flexible in a single way, and the tensile properties of the fabricated device need to be improved. This article focuses on one of the flexible conductive inks that can be stretched. The research trends of stretchable conductive inks are reviewed.

## 2    Stretchable Conductive Ink

### 2.1    Conductive Ink

Conductive inks are currently the most widely used functional materials in printed electronics [16]. It means that it can be printed on the substrate, and the substrate can conduct current and eliminate the accumulation of static charge [17]. Conductive inks are mainly composed of conductive fillers, binders, solvents and auxiliaries [18]. The binder is generally composed of a resin (synthetic resin, carbon powder resin, etc.).

And mainly functions are to connect the ink film and the substrate. The additives mainly include leveling agents, dispersing agents, inhibitors and thickeners, etc., which can improve the printability of the ink and can increase the adhesion to the substrate, dissolve the resin, and disperse the filler. The conductive filler is the core component of the conductive ink, which determines the conductivity of the ink. The conductive filler is mainly divided into inorganic nonmetal, metal and metal oxides and organic polymers. The development of the printing and electrical electronics industry and new applications has put forward more and higher requirements for the performance of conductive inks. This makes conductive inks more suitable for the application of nanotechnology, and also represents the development trend of conductive inks. With the rise of artificial intelligence, people's expectations for flexible electronic devices have gradually increased. The stretchable conductive ink is based on the nano metal conductive ink, and the ink film printed on the substrate is made flexible by changing the connecting material or adding a functional auxiliary. Stretchable conductive inks are a direction in the development of conductive inks.

## 2.2    Mechanism of Stretchable Conductive Ink

The composition of the stretchable conductive ink is substantially the same as that of the conductive ink, and the mechanism is similar to that of the conductive ink, which belongs to the particle-filled conductive composite material. The mechanism involves the formation of a conductive network and the migration of carriers, wherein the formation of the conductive network is explained by the seepage theory, and the migration of carriers is explained by the theory of tunnel conduction and the theory of electric field emission [19].

The seepage theory explains the effect of the volume fraction of the conductive filler on the electrical conductivity of the composite [20]. When the volume fraction of the conductive filler is small, the conductive fillers are mutually dispersed in the system, and the conductivity of the composite material is low at this time; when the volume fraction of the filler exceeds a certain critical value, the filler particles come into contact to form a conductive network in the system, and the electrical conductivity of the composite material is greatly improved. This threshold is called the percolation threshold. The size of the percolation threshold depends not only on the type of conductive filler and matrix, but also on the dispersion of the conductive filler in the matrix and the morphology of the matrix. The percolation theory considers that the conductive particles are in contact with each other or the particle gap is less than 1 nm to form a conductive network.

The tunnel theory believes that the material has the problem of conductive network formation, but it is not caused by the direct contact of the conductive particles, but the thermal vibration causes the electrons to transition between the particles. When the volume fraction of the conductive filler is less than the percolation threshold, the tunneling effect on the conductivity of the material is particularly significant. The tunneling current is an exponential function of the gap width, so tunneling occurs only between conductive particles that are close together, and there is no current conduction between the conductive particles with excessive gaps [21].

Van Beek and Van Pul [22] believe that the conductive behavior of conductive composites is caused by tunneling and is a special case of electric field emission inside conductive particles. They pointed out that although there are insulators (or poor conductors) between the conductive particles, when the distance between the conductive particles is less than 10 nm, under the applied electric field, the strong electric field between the particles can induce the generation of the emission electric field, resulting in the generation of current, that is, the theory of electric field emission.

## 2.3    Stretchable Conductive Ink Type

The conductive conductive ink based on the above theory can meet the working requirements of the flexible device. With the deepening of research on nanomaterials in recent years, nanomaterials can be synthesized, purified and analyzed in a controlled manner [23]. This gives us a better understanding of nanomaterials and their optical, electrical, thermal and mechanical properties. Due to their small size, these nanomaterials can be effectively dissolved or uniformly dispersed in common solvents by relatively simple and low cost techniques [5]. In the stretchable conductive ink, we use nano-metal (Ag or Au) as the conductive filler, which is the result of considering the conductivity of the system and the feasibility of the technology. In the already reported literature, some of the ink films are stretched by adjusting the function of the binder in the conductive ink, and some are partially enriched in the ink film by adding some auxiliaries such as surfactants. A local conductive network can be maintained when stretched. The stretchable conductive ink is divided into two types according to different components of the ink, and the stretchable conductive ink is divided into a binder type ink and a functional additive type ink.

### 2.3.1    Binder Type Stretchable Conductive Ink

The tie-type stretchable conductive ink is a major factor in guiding the binder in the electrical ink to provide stretchability of the overall system. Mohammed and Pecht [24] reported in 2016 a stretchable conductive ink that can be used for the screen printing, which can circulate more than 500 times under 20% strain, and meanwhile ensure the conductivity and mechanical properties of ink film. The conductive filler of the ink is nano silver powder, the powder is small but large diameter silver flakes. The nano-scale metal is used to lower the sintering temperature of the ink, and the nano-powder can be dispersed in the solvent by simply stirring. Nano silver sheets of different diameters are used to increase the contact points of the silver sheets in the film layer (Fig. 6), and the contact between adjacent particles of the large diameter silver sheets is in surface contact, the contact surface is large and the contact resistance is much smaller than the spherical silver particles; smaller diameter silver flakes can increase the electrical conductivity of the system and lower the sintering temperature.

The binder plays a major role in providing stretchability to the ink, and the silver sheet itself is not stretchable but is included in the stretchable binder system. An elastomeric binder is added to the conventional ink vehicle, one binder provides the adhesion required for the ink film to adhere to the substrate, and the other binder provides the ink film with stretchability. The optimum ratio between the general binder and the elastic binder is determined experimentally, so that the overall performance of
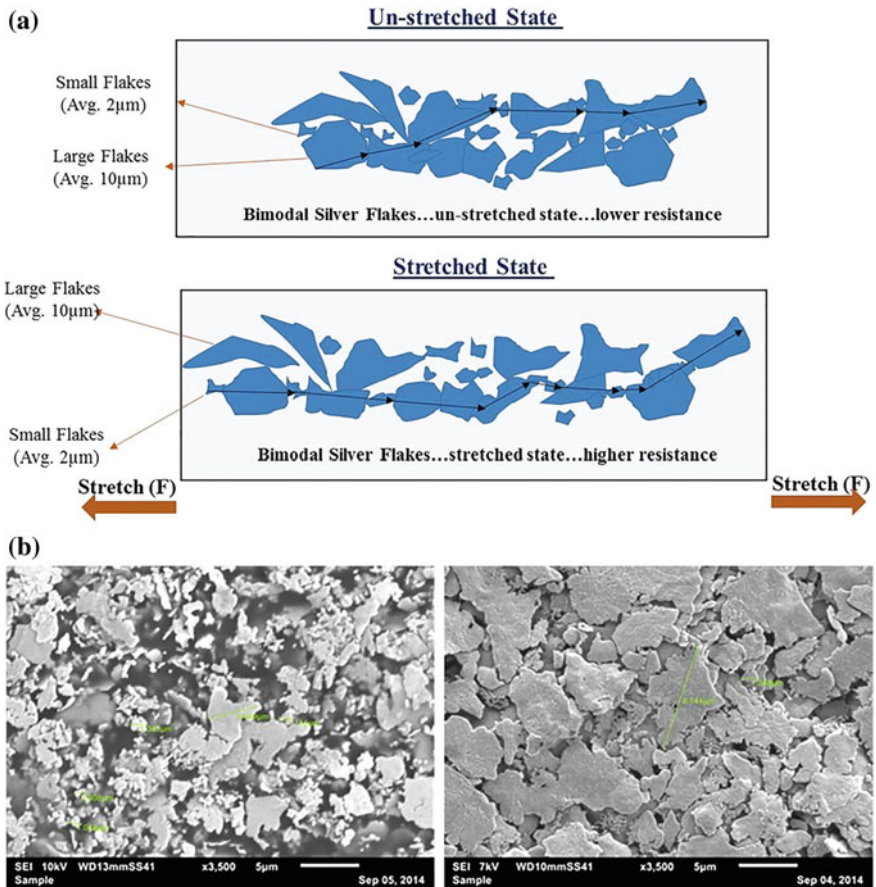
**Fig. 6. a** Bi-modal flake distribution maintaining ohmic connectivity during stretching—a conceptual approach; **b** uni-modal (left) compared to bi-modal (right) flake distribution at 0 cycles and no strain [24]

the stretchable conductive ink is optimized. Conventional binder inks and two-component binder inks using stretchable binders obtained SEM photographs of 2500-fold amplified conductive inks after 500 cycles at 20% strain (Fig. 7). The latter exhibits better ohmic contact and lower resistivity.

### 2.3.2 Functional Additive Type Stretchable Conductive Ink

The functional auxiliaries referred to herein mainly refer to surfactants. The surfactant modifies the surface of the conductive filler and cooperates with other components in the ink to drive the self-assembly of the conductive filler by phase separation. Matsuhisa et al. [25] reported a stretchable conductive ink in 2015. The nano silver plate is used as the conductive filler, the fluorine rubber is the elastic connecting material, the 4-methyl-2-pentanone is used as the organic solvent, and the surfactant is used as the auxiliary agent to prepare the stretchable conductive ink. The surfactant
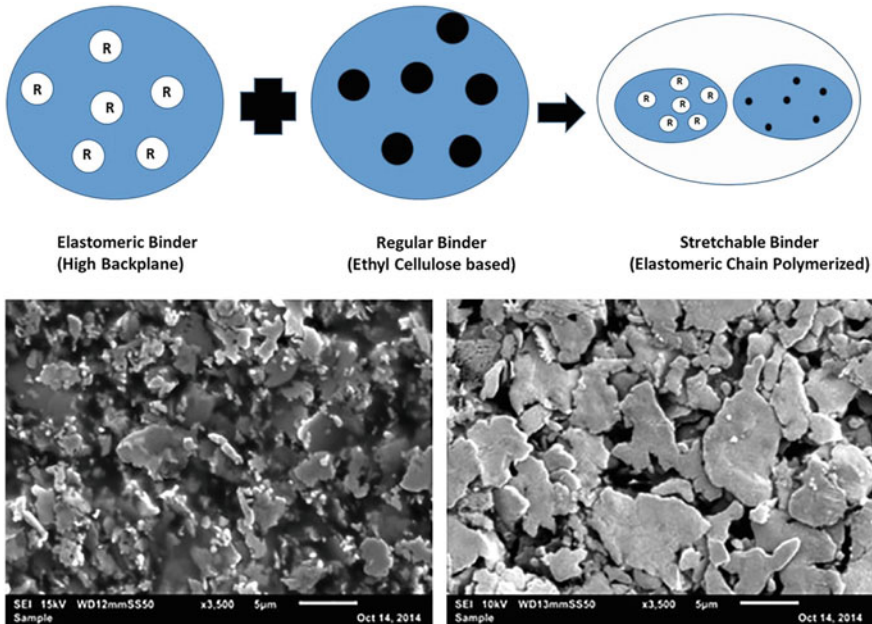
**Fig. 7.** Conceptual description of a two-component adhesive system for stretchable inks and the ink with the conventional binder system (left) was compared to the ink with the stretchable binder system (right) after 500 cycles at 20% strain [24]

is added to the conductive ink system in order to adjust the interfacial energy between the conductive filler and the solvent so that the conductive filler can spontaneously accumulate in the upper portion of the ink film during sintering and solidification, thereby forming a locally highly enriched conductive filler. As shown in Fig. 8. The ink film can still ensure the integrity of the surface conduction network after being stretched. The ink film as a whole can exhibit high electrical conductivity and high stretchability. It has a high initial conductivity of 738 S cm$^{-1}$ and a high electrical conductivity of 182 S cm$^{-1}$ when stretched to 215% strain. The conductive filler selected is a nano silver sheet, which can reduce the sintering temperature of the ink. This makes it possible to expand the selection of the substrate and even consider paper and plastic films with lower ignition points.

Based on this system, in 2017 Matsuhisa reported an improved version of the stretchable conductive ink [26], adjusting the sintering temperature and the amount of surfactant (Fig. 9). Nano silver particles are formed in situ on the silver flakes, greatly improving the electrical conductivity of the system. When the ink film is stretched, on the basis of the misalignment of the silver flakes, the nano silver particles are filled into the voids to further improve the conductive network in the ink film, so that the tensile properties of the ink film as a whole are improved. The improved stretchable conductive ink has an initial conductivity of 6,168 S cm$^{-1}$ and a conductivity of up to 935 S cm$^{-1}$ at 400% strain.
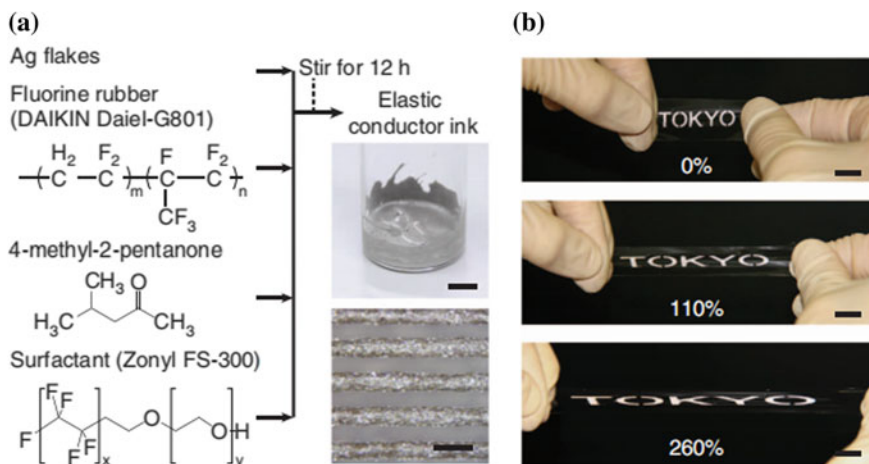
**Fig. 8.** **a** A process for producing an elastic conductor ink. Above, elastic conductor ink. Scale bar, 10 mm. The picture below shows the printed elastic conductor with high resolution. Scale bar, 100 mm. **b** Printing the elastic conductor and exhibiting stretchability. Scale bar, 10 mm [25]
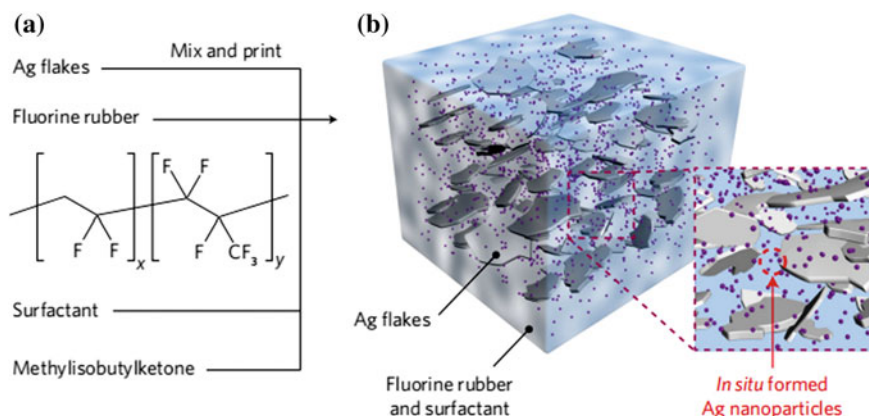


**Fig. 9.** **a** The manufacturing process. **b** AgNP is synthesized in situ only by mixing the four components and printing. They form a conductive path with micron-sized Ag flakes [26]

## 3   Application of Stretchable Conductive Ink in Flexible Devices

The manufacture of large-area stretchable electronic devices has a wide range of applications in the fields of healthcare, wearable devices and robotic skin [27]. One application of stretchable conductive inks are the printing of stretchable wires which are required to withstand a substantial degree of stretching and the overall electrical resistance of the wires hardly change. The use of stretchable conductive inks to print

the wires is compared to conventional wire fabrication methods [28]. This method is cheaper, more environmentally friendly, and simpler. Applying such a stretchable wire to a stretchable device can greatly increase the overall flexibility of the device. When the device is stretched, the wire portion can share some stress to reduce the stress accumulation at critical functional sites and thereby increase the overall stress tolerance of the device. A common design today is in combination with a stretchable structure, such as designing a wire shape into a diamond shape or a serpentine shape while printing with a stretchable conductive ink. The resulting wire structure and the wire itself can withstand a certain tensile strain, and the stress tolerance of the wire under this design is higher than any single flexible solution.

With the deepening of the research on the mechanism of stretchable conductive ink, the working principle is becoming more and more clear [2]. It also provides the basis for our better application of stretchable conductive inks. Among them, the tensile sensor is a relatively mature application. Conventional stress-strain sensors require a linear change in the overall resistance of the device under stress or strain, which can reflect stress or strain through linear changes in the electrical signal. However, such sensors are generally only capable of withstanding strain perpendicular to the functional layer of the device and are insensitive to strain parallel to the functional layer of the device. Stretch sensors made from stretchable conductive inks are a good solution to this type of problem. This type of sensor can be combined with artificial skin and motion detection to solve the problem that it is difficult to maintain the stability of the device when the flexible electronic device is deformed (stretched, bent, twisted).

Another application for stretchable conductive inks is a tensile strain sensor. This sensor is sensitive to small strains and can convert small strains acting on the sensor into larger current model outputs. This requires the strain sensor to have higher sensitivity. It is generally considered that the mass fraction of the conductive filler in the system is infinitely close or reaches the percolation threshold to achieve high sensitivity of the sensor. For example, a cardiac monitoring sensor, the sensor is a film structure that can be seamlessly attached to the heart. When the heart beats, the device is squeezed and deformed. The film is elongated in plane, the cross section is compressed, and the conductive network is compressed by the local conductive filler mass fraction and reaches the percolation threshold. At this time, the resistance is drastically lowered, and a large current can be generated. The heart pacing signal is converted into a distinct electrical signal output for the purpose of monitoring the heart.

## 4   Challenges and Prospects

Currently, flexible devices made of stretchable conductive inks are used to meet the needs of the application. As the number of times of stretching of the device increases, the wrinkles of the ink film increase and become larger so that the conductive connection in the ink film is reduced, and the conductive network is gradually broken to cause device failure [27]. The durability of the device has become a difficult point that restricts the wide application of stretchable conductive inks, and the conductivity of the device still needs to be further improved. As an important manufacturing method for flexible devices, the performance of stretchable conductive inks has a great influence

on the overall performance of flexible devices. Compared with the conventional method of fabricating a flexible device, a flexible device fabricated using a stretchable conductive ink is more advantageous in reducing cost and achieving mass production, which will facilitate large-scale commercialization of the flexible device. In this review we present several unconventional structures for making flexible devices today, making the device flexible by making a buckling structure. The mechanism of stretchable conductive ink and the reasons for achieving stretchability are highlighted. Conductive networks based on the seepage theory, tunneling theory and electric field emission theory can ensure the overall electrical conductivity of the device. And due to the multi-layer bonding of the conductive filler, the device can always ensure the integrity of the conductive network when being stretched, thereby ensuring the stretchability of the device. Flexible devices made based on stretchable conductive inks are of great importance in the fields of smart clothing, foldable displays, robot skins, and the like. For the upcoming artificial intelligence, it provides a more convenient and effective means of hardware manufacturing. The application of stretchable conductive inks will greatly increase the capacity of the flexible industry and expand the scale of the flexible industry. Stretchable conductive inks will certainly occupy a large market share due to their lower cost, and thus change people's lives like the Internet.

# References

1. Yichen C, Wei H, Xiaochen D (2017) Wearable flexible electronic strain sensor. Sci Bull 07:23–37
2. Wu W (2019) Stretchable electronics: functional materials, fabrication strategies and applications. Sci Technol Adv Mater 20(1):187–224
3. Xu L, Yanjun L, Longfei W, Yinyan Z (2015) Research progress in ductile flexible electronic technology. Semicond Technol 40(3)
4. Ryu SY et al (2009) Lateral buckling mechanics in silicon nanowires on elastomeric substrates. Nano Lett 9(9):3214–3219
5. Cheng T et al (2015) Stretchable thin-film electrodes for flexible electronics with high deformability and stretchability. Adv Mater 27(22):3349–3376
6. Song J et al (2009) Mechanics of stretchable inorganic electronic materials. J Vac Sci Technol Vac Surf Films 27(5):1107–1125
7. Rogers JA, Takao S, Yonggang H (2010) Materials and mechanics for stretchable electronics. Science 327(5973):1603–1607
8. Feng X et al (2010) Mechanical properties of ZnO nanowires under different loading modes. Nano Res 3(4):271–280
9. Wassei JK, Kaner RB (2010) Graphene, a promising transparent conductor. Mater Today 13 (3):52–59
10. Yu C, Ling LM, Chun ZH (2005) Large-scale synthesis of high-quality ultralong copper nanowires. Langmuir ACS J Surf Colloids 21(9):3746–3748
11. Hu W et al (2013) Elastomeric transparent capacitive sensors based on an interpenetrating composite of silver nanowires and polyurethane. Appl Phys Lett 102(8):38–1487
12. Yu Z et al (2011) Intrinsically stretchable polymer light-emitting devices using carbon nanotube-polymer composite electrodes. Adv Mater 23(34):3989–3994
13. Yu Z et al (2011) Highly flexible silver nanowire electrodes for shape-memory polymer light-emitting diodes. Adv Mater 23(5):664–668

14. Zhao S et al (2015) Layer-by-layer assembly of multifunctional porous N-doped carbon nanotube hybrid architectures for flexible conductors and beyond. ACS Appl Mater Interfaces 7(12):6716–6723
15. Chen M et al (2015) Highly stretchable conductors integrated with a conductive carbon nanotube/graphene network and 3D porous poly(dimethylsiloxane). Adv Func Mater 24 (47):7548–7556
16. Yuan Z (2015) Research progress in conductive inks for printing electronics. New Chem Mater 7:9–11
17. Jinhuan L, Jianhui L, Yufeng W, Jun X (2014) Progress in the application of conductive inks and nano-conductive particles. Electron Comp Mater 33(5):12–16
18. Xiufeng M, Fei L (2010) Conductive ink technology and its research direction. China Print Packag Res 2(6)
19. Jing Z, Haibin S, Wei Z, Juncheng L (2009) Conducting mechanism of particle-filled conductive composites. J Ceram 30(3):15–19
20. Fish D, Khan IM, Smid J (2011) Anionic ring opening polymerization of cyclotetrasiloxanes with large substituents. Macromol Symp 32(1):241–253
21. Shklovskiĭ BI, Efros AL (1984) Electronic properties of doped semiconductors
22. Van Beek LKH, Van Pul BICF (1963) Internal field emission in carbon black-loaded natural rubber vulcanizates. Rubber Chem Technol 36(3):740–746
23. Mo LX et al (2019) Silver nanoparticles based ink with moderate sintering in flexible and printed electronics. Int J Mol Sci 20(9):28
24. Mohammed A, Pecht M (2016) A stretchable and screen-printable conductive ink for stretchable electronics. Appl Phys Lett 109(18):1603–1607
25. Matsuhisa N et al (2015) Printable elastic conductors with a high conductivity for electronic textile applications. Nat Commun 6:7461
26. Matsuhisa N et al (2017) Printable elastic conductors by in situ formation of silver nanoparticles from silver flakes. Nat Mater 16(8):834–840
27. Liu Y, Pharr M, Salvatore GA (2017) Lab-on-skin: a review of flexible and stretchable electronics for wearable health monitoring. ACS Nano 11(10):9614–9635
28. Ramli MR (2019) Stretchable conductive ink based on polysiloxane-silver composite and its application as a frequency reconfigurable patch antenna for wearable electronics. ACS Appl Mater Interfaces 11(31):28033–28042

# Study on Volume Shrinkage Performance of 3D Printing Materials

Le Ma, Beiqing Huang, Chenhui Wei, Yongjian Wu,
and Xianfu Wei[(⊠)]

Beijing Institute of Graphic Communication, Beijing, China
`25ll8l2756@qq.com`, {`huangpeiqing`, `weixianfu`}`@bigc.edu.cn`

**Abstract.** Studies have found that 3D printed materials have stringent requirements for volumetric shrinkage. For the 3D printing materials of the UV inkjet method, materials of different structures have different effects on them. In order to reduce the volume shrinkage of 3D printed materials, the effects of prepolymers and monomers of free radical systems, prepolymers and monomers of cationic systems on the volume shrinkage of 3D printed materials were investigated, and 3D printing was prepared by controlled variable method. Material and performance test analysis of volume shrinkage. The conclusion is that the structure of prepolymer and monomer has a great influence on the volume shrinkage, the volume shrinkage of the radical curing system is large, and the volume shrinkage of the cationic curing system is small.

**Keywords:** Free radical curing system · Cationic curing system · Volume shrinkage · 3D printing

## 1 Introduction

With the advancement and development of science and technology, 3D printing technology has been greatly developed and promoted. Nowadays, the main technologies are selective laser sintering, fused deposition, stereolithography, layered solid manufacturing, etc., and UV inkjet curing technology used in 3D printing is also a common technology, which has been carried out since the early 1990s in China. Technology development [1, 2]. UV photo polymerization technology is fast, efficient, and environmentally friendly, and is widely used in the curing of various inks. However, for photocuring, especially for the widespread application of free radical photocuring, the shrinkage caused by polymerization has always been a major problem that restricts the use of photocurable materials in the production of shaped products [3, 4]. This paper mainly studies the matching of different material properties to achieve the purpose of reducing the shrinkage of the entire material system.

In the 3D printing photocurable material system, the prepolymer and the monomer are the main components, which directly affect the film forming properties after curing, and have an important influence on the volume shrinkage of the 3D printing material. Therefore, the prepolymers of different structures are studied. The effect of the volume on the volume shrinkage of 3D printed materials provides a theoretical basis for the

preparation of 3D printed materials with good performance in order to reduce the volume shrinkage of 3D printed materials.

## 2    Experimental Materials and Instruments

### 2.1    Experimental Materials

Prepolymer: EB151, EB152 hyperbranched acrylate (American Cytec), EB270 aliphatic urethane acrylate (Guangdong, China), EB870 hyperbranched polyester acrylate (Zhanxin Resin Shanghai Co., Ltd.), LED01 polyhydroxy acrylic resin and Mixture of sulfur-based derivatives (Zhanxin Resin Shanghai Co., Ltd.); free radical active monomer: (1) mono-functional monomer: EOEOEA ethoxyethyl acrylate, ACMO acryloyl morpholine, (2) difunctional monomer: HDDA 1,6-hexanediol diacrylate, DPGDA dipropylene glycol diacrylate, TPGDA tripropylene glycol diacrylate, (3) trifunctional monomer: TMPTA trimethylolpropane triacrylate (Tianjin Tianjiao Chemical); Cationic prepolymer: E-44 bisphenol A epoxy resin (Shandong Tianmao); cationic monomer: TTA-15 3,4-epoxycyclohexylmethyl methacrylate, TTA-21P 3,4-Epoxycyclohexylmethyl- 3′,4′-Epoxycyclohexane Carboxylate, TTA-26 Bis (3,4-Epoxycyclohexylmethyl) Adipate, TTA22 1,2-Epoxy-4-epoxyethylcyclohexane, OXT-1 3-Oxetanemethanol, 3-ethyl-, OXT-3Oxetane,3,3′-[oxybis(methylene)]bis[3-ethyl- (Hubei Gurun Technology Co., Ltd.), EHMO 3-ethyl-3 carboxymethyl oxetane; free radical photoinitiator DETX (Beijing Yingli Technology Development Co., Ltd.), cationic photoinitiation Agent PAG-2, IK-1 (Nanjing Hengqiao Chemical Technology Materials Co., Ltd.), EHA Active Amine (Beijing Yingli Technology Development Co., Ltd.).

### 2.2    Experimental Instruments

SARTORIUS JA5003 electronic balance; thermostatic magnetic stirrer, Jiangsu Ronghua instrument; curing machine (UV-LED) main performance parameters are as follows: main wavelength: 395 nm, output power: 14 mW/cm, power 100%, radiation distance: 20 mm; 10 ml pycnometer.

## 3    Sample Preparation

According to the content of each component in the formula, first adding prepolymer, monomer, photoinitiator, etc. in the beaker, and then stirring evenly with a glass rod, end to stir for 30 min on a HJ-6 multi-head magnetic heating stirrer.

## 4    Volume Shrinkage Performance Test

### 4.1    Preparation Method of Solid

The prepared liquid sample is placed in a PE mold and fixed in a curing machine at a wavelength of 395 nm for a certain period of time, and the fracture is removed to see if

it can be brittle and can be brittle to indicate that the curing is complete. Otherwise continue to cure.

## 4.2    Test Method of Volume Shrinkage

The method for measuring the volume shrinkage of this experiment is carried out in accordance with the relevant provisions of the international standard ISO 3521, namely the pycnometer method. The density of the sample liquid and the density of the solid after solidification were measured using a pycnometer, and the measured solid shrinkage rate was calculated from the density before and after the sample was cured.

# 5    Test Results Analysis

## 5.1    Effect of the Type of Free Radical Prepolymer on the Volume Shrinkage of 3D Printed Materials

Prepolymer is the basic skeleton of 3D printed photocurable materials. In order to explore the effect of the type of prepolymer on the volume shrinkage of the material [3], the type of fixed active monomer, the type and content of photoinitiator, change the prepolymerization For the kind of the object, a 3D printed material was prepared and tested for volume shrinkage. The experimental results are shown in Fig. 1.
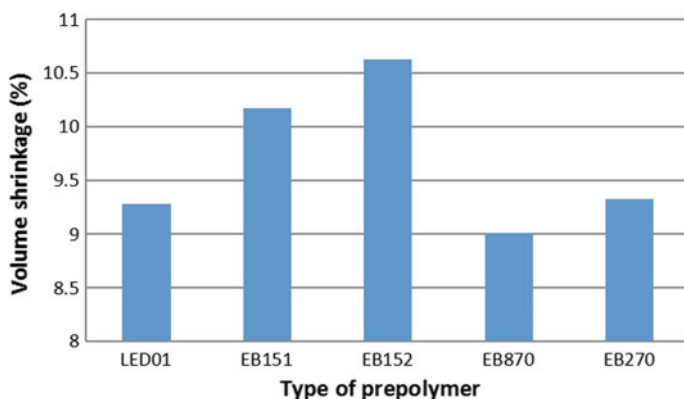


**Fig. 1.**  Effect of different kinds of prepolymers on volume shrinkage of 3D printing materials

The experimental results show that the volume shrinkage of hyperbranched polyester acrylates EB151 and EB152 is relatively large, because the hyperbranched polymer has a very strong terminal function and the end group is a reactive group, so the reactivity is extremely high. The curing speed is fast, the hardness is very high, and the volume shrinkage is serious. Both EB270 and LED01 belong to urethane acrylate. EB270 is an aliphatic acrylate. Because of the presence of benzene ring, the volume shrinkage after curing is small. LED01 is a polyhydroxy acrylate which belongs to

branched polyurethane propionate and has multiple functional groups. Faster, the photocuring shrinkage rate is lower. EB870 is a hexafunctional polyester acrylate with more reactive functional groups, but has an oxygen inhibition effect, so the double bond conversion rate is lower and the cure shrinkage rate is reduced [3, 4].

## 5.2    Effect of the Type of Free Radical Reactive Monomer on the Volume Shrinkage of 3D Printing Materials

In the ink jet system, the viscosity of the material is highly demanded, so that the main component is the active monomer. It has been found that the double bond concentration and double bond conversion rate of various acrylic monomers are important factors affecting shrinkage, so monomer is an important source of shrinkage of photopolymerization system compared with oligomers [4].. However, whether the mixed monomer has a synergistic gain or a subtractive effect requires experimental research. Therefore, the type of prepolymer, photoinitiator and content in the fixed material, change the type of monomer, prepare samples, and test the volume shrinkage rate. The test results are shown in Fig. 2.



**Fig. 2.** Effect of different kinds of free radical monomers on volume shrinkage of 3D printing materials

It is known from the experimental results that the volume shrinkage of the trifunctional monomer is relatively minimal, and the volume shrinkage of the monofunctional acryloylmorpholine monomer ACMO and the acrylate EEOEOEA are relatively small, and the volume shrinkage ratio of the bifunctional monomer is relatively maximum. This is because the monofunctional monomer has only one reactive group, which is not easy to crosslink when photocured, and because of its small molecular weight, small viscosity, relatively easy to cure, so the volume shrinkage rate is high; the bifunctional monomer contains two The reactive group of the photocuring reaction has an improved degree of solidification and a large volume shrinkage ratio; the trifunctional monomer has a relatively large molecular mass and a large viscosity,

and does not easily move the molecules in the late stage of solidification, thereby affecting further solidification, thus Volume shrinkage is small [3, 4].

## 5.3 Effect of Types of Cationic Monomers on Volume Shrinkage of 3D Printing Materials

The cationic curing system has a process of low volume shrinkage or expansion curing [5–7], so this experiment investigated the volume shrinkage of cationic monomers and their compounding. The cationic system is difficult to cure, and the free radical system has a faster degree of solidification. Therefore, the monomer test of the cation is carried out on the basis of the free radical system, and the ratio of the radical system to the cationic system is 5:1. The amount of the immobilized radical system, the type and content of the cationic prepolymer, and the type and content of the cationic photoinitiator change only the type of the cationic monomer. The experimental results are as follows (Fig. 3).
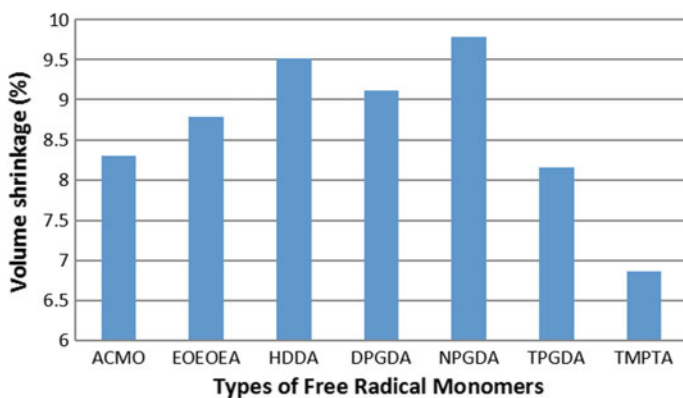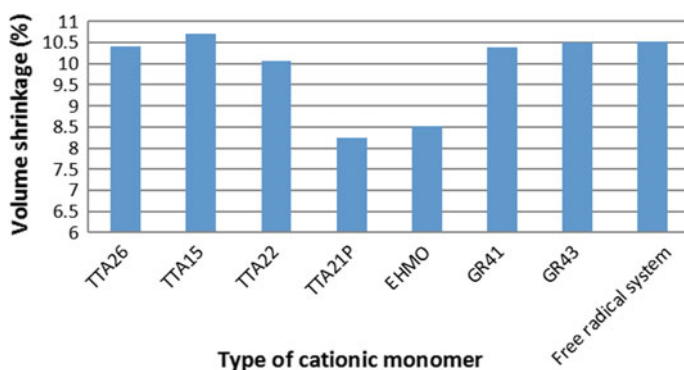


**Fig. 3.** Effect of different kinds of cationic monomers on volume shrinkage of 3D printing materials

It is found from the experimental results that not all cationic monomers can significantly reduce the volume shrinkage of the free radical system, wherein the volume shrinkage of the ester monomer TTA-21P and the cyclobutane monomer EHMO is small. This is because TTA21P is a bifunctional alicyclic epoxy monomer with two epoxy groups and a short chain length. Although EHMO has only one epoxy group but a short alkyl chain, ring-opening polymerization expands the volume. The chain is not easy to crosslink [7, 8], and the density of the 3D printed material after curing is small, so the volume shrinkage rate is significantly reduced. On the contrary, the volume shrinkage rate is high.

## 5.4 Effect of Different Content of Prepolymer on Volume Shrinkage

Through the above experiments, it was found that in the curing system, the type of the prepolymer and the type of the monomer have different effects on the volume shrinkage rate. Whether the content of the component also has a great influence on the volume

shrinkage rate, so the following is a ratio experiment of the first, second and third functional groups ACMO, TPGDA, TMPTA monomer and EB152 prepolymer, and the cationic monomers TTA21P and E-44. Experimental study of prepolymers. The experimental results are as follows (Figs. 4 and 5).

It is known from the experimental results that both the free radical system and the cationic system increase first and then decrease as the prepolymer content increases. This is because the pure monomer system is a small molecule, and it is difficult to diffuse the molecule to a certain extent, hindering further curing, so the volume shrinkage of the monomer is small. The relative molecular mass of the pure prepolymer is larger than that



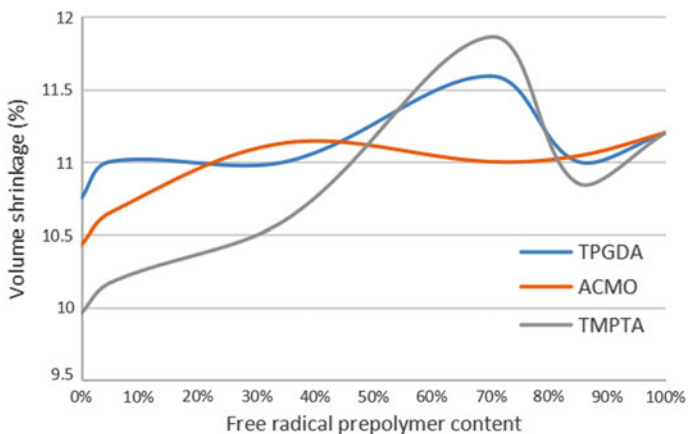**Fig. 4.** Effect of different content of free radical prepolymer on volume shrinkage of 3D printing materials
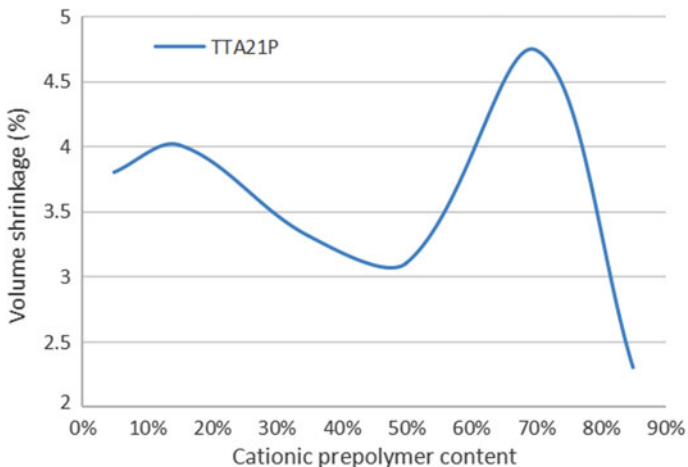


**Fig. 5.** Effect of different contents of cationic prepolymer on volume shrinkage of 3D printing materials

of the monomer, and the content of the polymerizable functional group is high, which tends to cause a large volume shrinkage. However, when the content of the prepolymer is at a certain point, the degree of curing of the entire system is promoted, thereby making the volume shrinkage ratio of the 3D printed material large [4].

## 6    Conclusion

Through the study of the volume shrinkage performance of 3D printing materials, it is possible to better grasp the changes in the structure of each component of the material formulation, and the changes caused by the volume shrinkage performance. It is concluded that the volume shrinkage is related not only to the functionality and molecular weight of the 3D printed material, but also to the double bond concentration and conversion of the material. The functional volume shrinkage of the EB870 and trifunctional monomer TMPTA of the prepolymer hexafunctional polyester polyacrylate in the free radical system is relatively minimal; the volume shrinkage of the cationic monomers TTA2P and EHMO is relatively small. In the prepolymer content experiment, both the free radical system and the cation system first increase and then decrease as the prepolymer content increases.

## References

1. Shi Y, Zhang L, Bai Y, Zhao Z (2015) Development of 3D printing technology and its software implementation. China Sci Mag 45(2):197–198
2. Guo C (2015) Research on UV-curable molding materials for flexographic plates suitable for 3D printing materials. Beijing Inst Graph Commun
3. Chen Y, Zeng Z, Yang J (2003) Radiation curing materials and their applications. Chem Ind Press 10
4. Jin Y (2018) Light curing ink. Chemical Industry Press
5. Duan Y, Wang S, Lu B (2000) Study on shrinkage of photocurable resin used in stereoscopic modeling. J Xi'an Jiaotong Univ 3(34):45–48
6. Han Y (2013) Research on photopolymerization shrinkage. PhD thesis, Beijing University of Chemical Technology
7. Hong Z (2013) Research and application of cationic and hybrid photocurable resin systems, vol 6. Master thesis, South China University of Technology pp 68–69
8. Zou Y (2017) Cationic photocuring monomer. In: 2017 the 18th China radiation curing annual conference. Beijing Normal University

# Film and Related Material Technology

# Preparation of Super-Hydrophobic Surface via Fluorinated Epoxy Resin and Nano-SiO$_2$

Chengmin Hou[✉], Yanping Kou, and Congjun Cao

Shaanxi Provincial Key Laboratory of Printing and Packaging, Xi'an University
of Technology, Xi'an, China
1042067175@qq.com

**Abstract.** The super-hydrophobic surface has been widely studied for its self-cleaning effect, but most of its preparation methods have disadvantages, such as low cross-linking degree and the need to use an organic solvent. In this paper, aqueous fluorinated epoxy polymers P(GMA-*r*-HEMA-*r*-St) (PGHS)-*g*-TFA was prepared by conventional radical polymerization method, which have low surface energy chains and cross-linked chains, was hybridized with nano-SiO$_2$ modified by KH550, to prepare the super-hydrophobic coatings on cotton. The water contact angle (CA) and the durability of the super-hydrophobic surface were tested. The CA can reach 160° and the durability can also reach 80 min. The introduction of HEMA makes the obtained polymers can be dissolved in water, which reduced the use of organic solvents.

**Keywords:** Super-hydrophobic · Water soluble · Contact angle · Nano-SiO$_2$

## 1   Introduction

When the water contact angle (CA) was greater than 150° and the rolling angle was less than 10°, the surface was defined as super-hydrophobic [1]. Recently, super-hydrophobic surfaces [2] become important, due to their self-cleaning, corrosion resistance, and anti-icing performances. The fluorine-containing materials [3] were widely applied. However, the fluorine-containing materials have disadvantages, such as the poor cross-linking effect with the substrates and the insolubility in water solvent.

Presently, the main methods [4–7] constructing super-hydrophobic surface contain sol-gel, layer-by-layer self-assembly (SA), etching method and organic-inorganic composite method. Among them, the polymer/inorganic nanoparticle composite method [8] refers to a method adding micro/nanoparticles to a polymer system [9–11]. Different inorganic materials were blended with polyurethane, polytetrafluoroethylene emulsion, polymethyl methacrylate powder, to obtain the super-hydrophobic coatings. However, environmentally harmful organic solvents are used in the preparation process, such as trifluorotoluene.

This paper adopted the organic-inorganic composite method to prepare the super-hydrophobic surfaces by introducing a water-soluble chain into the polymer molecule. Aqueous fluorinated epoxy polymers P(GMA-*r*-HEMA-*r*-St) (PGHS)-*g*-TFA was synthesized by conventional free radical polymerization. PGHS-*g*-TFA was hybridized with modified nano-SiO$_2$, and the super-hydrophobic coatings on cotton was

constructed. The water CA and the durability of super-hydrophobic cotton surface constructed were investigated.

## 2    Experimental Part

### 2.1    Reagents

Nano-SiO$_2$ (10 nm), glycidyl methacrylate (GMA), hydroxyethyl methacrylate (HEMA) and styrene (St), which are analytically pure, were purchased from Aladdin Technology Company. KH-550, which is analytically pure, was purchased from Nanjing Liangui Chemical Company. Azobisisobutyronitrile (AIBN) was purchased from Tianjin Zhiyuan Chemical Reagent Company.

### 2.2    Preparation of Modified SiO$_2$ and PGHS-$g$-TFA Composite

1 g nano-SiO$_2$ was dispersed in 50 mL of 97% ethanol. Triethylamine was added to adjust pH value to 9. 2 g KH-550 was added and refluxed for 5 h. After the reaction, the mixture was filtered, washed, and dried. The structure was analyzed by FTIR (IR Prestige-21) and TG (TG209, NETZSCH, Germany).

GMA, St, HEMA, AIBN, THF and NaHSO$_3$ were added to the reaction flask. The solution was deoxidized for 30 min, and then stirred for 2 h at 70 °C. After the reaction, the mixture was precipitated and dried to obtain the product PGHS. 1 g PGHS was added into the mixture of 5 mL dichloromethane and 5 mL THF. 1.15 g TFA, 0.019 g triethanolamine and 1.15 g CTAB were added at 60 °C for 3 h. The mixture was concentrated, precipitated and dried to obtain the PGHS-$g$-TFA. The structure was measured by FTIR. The structure diagram is shown in Fig. 1.
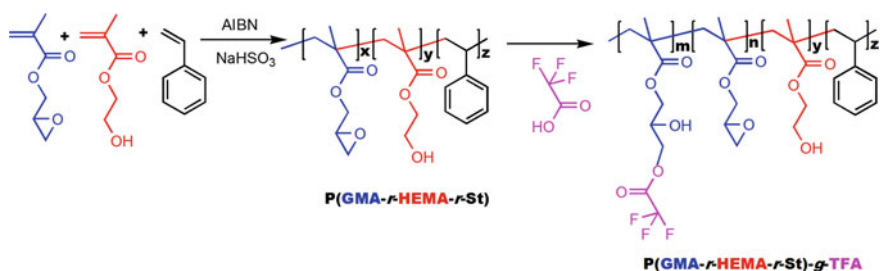


**Fig. 1.**  Synthesis of water-based fluorine-containing epoxy polymer PGHS-$g$-TFA

### 2.3    Construction and Characterization of Super-Hydrophobic Cotton

0.81 g PGHS-$g$-TFA was dissolved in 40 mL THF. The solution was dialysis by water for 7 days to remove THF. 0.05 g modified nano-SiO$_2$ and 0.5 mL triethylamine were added. Then the mixture was stirred at 70 °C for 10 h. The clean cotton was placed into the solution and kept stirring. Every 3 h, one of samples was taken off, washed and

dried. CA were tested with 10 μL water. The morphological characteristics were observed by SEM (Merlin Compact).

The obtained cotton cloth was treated with water, 1% $Na_2CO_3$ solution, 1% NaOH solution, 1% hydrochloric acid, THF soaking, and water sonication respectively to explore the durability of the super-hydrophobic surfaces. The damage of the surface after different treated time (1–5 min) was measured by CA (JC2000A).

# 3   Results and Discussion

## 3.1   Characterization of Modified Nano-SiO$_2$ and Fluorine-Containing Epoxy Polymers

The modified nano-SiO$_2$ was characterized by FTIR and TG (Fig. 2). In Fig. 2a, the peak at 3440 cm$^{-1}$, which was the -OH stretching vibration peak of nano-SiO$_2$, decreased and moved to 3565 cm$^{-1}$ after modification. A new peak at 2956 cm$^{-1}$ was the Si–O–C absorption peak for modified nano-SiO$_2$. The peak at 1545 cm$^{-1}$ was vibration peak of –NH$_2$, and the peaks at 696 cm$^{-1}$ and 1738 cm$^{-1}$ were the bending vibration peak of N–H. The above peak information indicated that KH-550 was successfully grafted onto the surface of nano-SiO$_2$. In Fig. 2b. the unmodified nano-SiO$_2$ only degraded about 8% of the mass, while the modified nano-SiO$_2$ pyrolyzed 30% of the mass indicating that the nano-SiO$_2$ grafted a large number of KH-550.
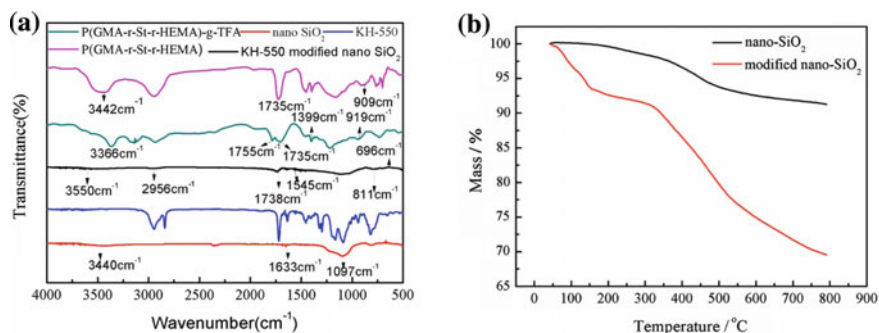


Fig. 2.  Characterization of modified nano-SiO$_2$ and PGHS-$g$-TFA

The structure of PGHS and PGHS-$g$-TFA were characterized by FTIR as shown in Fig. 2a. The absorption peak at 1735 cm$^{-1}$ was the –C=O carbonyl groups of HEMA and GMA units. After TFA modification, another peak at 1755 cm$^{-1}$ was contributed to the –C=O of TFA. There is also a peak at 1399 cm$^{-1}$ which was the stretching vibration peak of –C–F bonds of TFA. In addition, there is a big absorption peaks at 3442 cm$^{-1}$ for the –OH groups of PGHS before TFA modification, while this peak decreased after TFA modification. These information means that the polymer PGHS has been successfully grafted with TFA.

## 3.2    Preparation and Characterization of Super-Hydrophobic Surface of Cotton Fabric

The micro structure of the cotton fabric surface was observed by SEM as shown in Fig. 3. The unmodified fiber surface was basically smooth. The structure of the modified fiber fabric is not glued. At the same time, the surface of the modified cotton fiber has a rough $SiO_2$/polymer coating, and there are many irregularities.
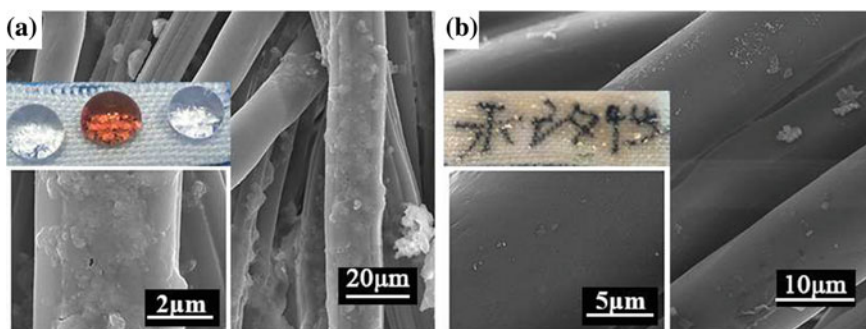


**Fig. 3.** SEM image of cotton fabric before and after modification with PGHS-$g$-TFA/modified nano-$SiO_2$

## 3.3    Performance of Super-Hydrophobic Cotton Cloth

The effect of soaking time on the super-hydrophobic performance was tested and the result was shown in Fig. 4a. The change in soaking time has little effect on the hydrophobic properties within a certain range. The water have a CA of up to 160° and the duration of up to 80 min. Super-hydrophobic cotton fabrics samples were soaked in different solutions to study the effects of different conditions on the hydrophobic properties and the results were shown in Fig. 4b. It can be found that these damage conditions had little effect on the hydrophobic properties, indicating that the surface of the fluoropolymer and cotton cloth is chemically cross-linked and not easily destroyed.
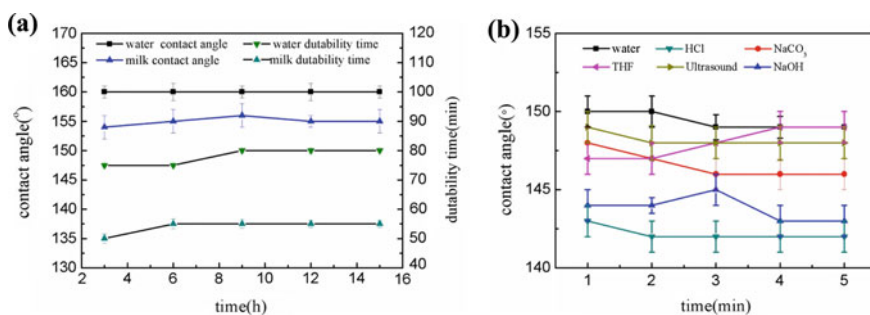


**Fig. 4.** The effect of soaking time and different solution soaking conditions on the super-hydrophobic performance of modified cotton fabric

# 4   Conclusion

A water-soluble fluoropolymer PGHS-*g*-TFA was synthesized by free radical poly-merization and TFA modification. Then PGHS-*g*-TFA was hybrid assembled with modified nano-$SiO_2$ to construct super-hydrophobic surfaces on cotton cloth. The results showed that the CA of cotton cloth was up to $160°$ and the residence time was up to 80 min. The durability performance of cotton cloth surfaces was very well and tolerative for various conditions. However, due to the introduction of TFA, the obtained cotton fabrics s are poorly resistant to acid and alkali. In next study, some functional blocks can be introduced to improve the acid and alkali resistance of the hydrophobic cotton fabric while giving it better performance.

# References

1. Manatunga DC, Silva RMD, Silva KMND (2016) Double layer approach to create durable superhydrophobicity on cotton fabric using nano silica and auxiliary non fluorinated materials. Appl Surf Sci 360:777–788
2. Ueda E, Levkin PA (2013) Emerging applications of superhydrophilic superhydrophobic micropatterns. Adv Mater 25(9):1234–1247
3. Liu B, He Y, Fan Y et al (2006) Fabricating super-hydrophobic lotus-leaf-like surfaces through soft-lithographic imprinting. Macromol Rapid Commun 27(21):1859–1864
4. Lopez-Torres D, Elosua C, Hernaez M (2015) From superhydrophilic to superhydrophobic surfaces by means of polymeric Layer-by-Layer films. Appl Surf Sci 351:1081–1086
5. Jiang Z, Fang S, Wang C et al (2016) Durable polyorganosiloxane superhydrophobic films with a hierarchical structure by solgel and heat treatment method[J]. Appl Surf Sci 390:993–1001
6. Shang Q, Zhou Y (2016) Fabrication of transparent superhydrophobic porous silica coating for self-cleaning and anti-fogging. Ceram Int 42(7):8706–8712
7. Cho SW, Kim JH, Lee HM et al (2016) Superhydrophobic Si surfaces having microscale rod structures prepared in a plasma etching system. Surf Coat Technol 306:82–86
8. Xue ZX, Liu MJ, Jiang L (2012) Recent developments in polymeric superoleophobic surfaces. J Polym Sci Polym Phys 50(17):1209–1224
9. Steele A, Bayer I, Loth E (2012) Adhesion strength and superhydrophobicity of polyurethane/organoclay nanocomposite coatings. J Appl Polym Sci 125(S1):E445–E452
10. Zheng Y, He Y, Qing Y et al (2012) Formation of $SiO_2$/polytetrafluoroethylene hybrid superhydrophobic coating [J]. Appl Surf Sci 258(24):9859–9863
11. Zhu X, Zhang Z, Ren G et al (2012) A novel superhydrophobic bulk material. J Mater Chem 22(38):20146–20148

# Preparation and Characteristic Analysis of Ultra-Low Dielectric Constant Nano-Porous Silicon Oxide Films

Gaimei Zhang[✉], Yue Cao, Yinglu Zhang, Xiaoli Song,
Jiandong Lu, and Shasha Li

Institute of Printing and Packaging Engineer, Beijing Institute of Graphic
Communication, Beijing, China
zhang_gaimei@163.com

**Abstract.** In order to reduce the dielectric constant of nano-silicon oxide films, the effects of preparation and post-treatment methods on the structure of nano-porous silicon oxide materials are investigated. Herein, using plasma enhanced chemical vapor deposition (PECVD) method, hexamethyldisiloxane (HMDSO) is as monomer and dimethoxyethane (DME) as porogen. The silicon oxide film is deposited on the glass substrate surface, and then it is heat-treated at a high temperature, so organic components such as carbon-hydrogen bonds are removed and the pores are formed to reduce the dielectric constant. At the same time, the skeleton of the nano-porous silicon oxide film is cured by ultraviolet irradiation. The surface morphology of the film is observed by scanning electron microscope (SEM). Fourier transform infrared spectroscopy (FTIR) is used to investigate the effects of ultraviolet irradiation with different wave numbers on the composition of it. Also, using ellipsometer, the refractive index of it is tested, and its dielectric constant is calculated. The effect of poroge on the microstructure and properties of it is investigated by adjusting the dosage of porogen and post-treatment methods. The results show that the method is effective. When the ratio of porogen and monomer is 1:5, the dielectric constant of the prepared nano-porous silicon oxide film is the lowest. The short wavelength ($\lambda = 185$ nm) cures modified the chemical structure and obtained higher Young's moduli. While the higher wavelength ($\lambda > 300$ nm) cures resulted in less modification of it and more elimination of the porogen.

**Keywords:** Plasma enhanced chemical vapor deposition (PECVD) · Porous silicon oxide film · Dielectric constant · UV-cure

## 1 Introduction

As large-scale integrated circuits develop toward high density, large capacity and high operating speed, the feature sizes of devices are getting smaller. This requires the insulated film with ultra-low dielectric constant to replace the traditional silicon oxide film, so as to reduce crosstalk between lines and power consumption [1–3]. It has been proved that introducing porosity into the film can decrease its dielectric constant(k) by reducing the proportion of polarized molecules in it [4]. At present, the commonly used

porogen approach is to co-deposit the porogen and the matrix to prepare the silicon oxide film, firstly. Then, using an appropriate thermal annealing treatment or other methods to remove the porogen, so as to form a porous structure [5]. But the introduction of pores in the film leads to the decrease of some important properties, such as mechanical properties [6]. Therefore, the latest developments in microelectronic have mainly focused on this issue. The introduction of UV-cure is an important advance in the preparation of porous silicon oxide films [7–9]. This treatment was used to improve mechanical properties of low-k films by improving the skeleton crosslinking [10, 11] and can decrease the thermal annealing time down to few minutes when in porogen approach [12]. Chang [13] compared the difference between the annealing treatment and UV-cure in porogen approach. The annealing temperature above 500 °C has a decomposing effect similar to UV-cure for 10 min. Cheng et al. [14] found that UV-cure with 200–450 nm wavelength caused a severely shrinkage in the thickness of the low-k film with $C_8H_{16}$ precursor. However, the effect of UV-cure with different wavelengths on the properties of the film is not perfect in porogen approach.

In this paper, the silicon oxide film is deposited by PECVD with the precursor of Hexamethyldisiloxane (HMDSO) and the porogen of Dimethoxyethane (DME), firstly. Then it is heat-treated at a high temperature, so organic components such as carbon-hydrogen bonds are removed and the pores are formed to reduce the dielectric constant. Thirdly, the skeleton of the nano-porous silicon oxide film is cured by ultraviolet irradiation. The main purpose of this paper is to discuss the effect of DME dosage, UV-cure wavelength and time on the structure of the film.

## 2 Experimental

### 2.1 Preparation of the Nano-Porous Silicon Oxide Film

The silicon oxide film was prepared by PECVD mixing of the matrix precursor (HMDSO) and the porogen precursor (DME) as described in our previous report with some modification [15, 16], the schematic diagram and photo of the experimental apparatus are shown in Fig. 1. The radio frequency power was 100 W with discharge time of 10 min. The flow rate of the matrix precursor to oxygen was set to 2:1 to obtain samples. After deposited, the film was heated at 450 °C in a vacuum heating furnace to volatilize the organic components, solidify the skeleton and form nano-pores. Further, either a 185 nm narrow band (NB) or a 300 nm broadband (BB) UV cure was applied. Under this condition, the residual porogen decomposes, so that the nano-porous silicon oxide film with low dielectric constant can be obtained. This process will be referred to as the UV-cure.

### 2.2 Characterization

Thickness and refractive indices of the processed films are measured by spectroscopic ellipsometry. Chemical bonding type of the film was investigated by FT-IR. The surface morphology of the nano-porous silicon oxide film was characterized with scanning electron microscopy (SEM).
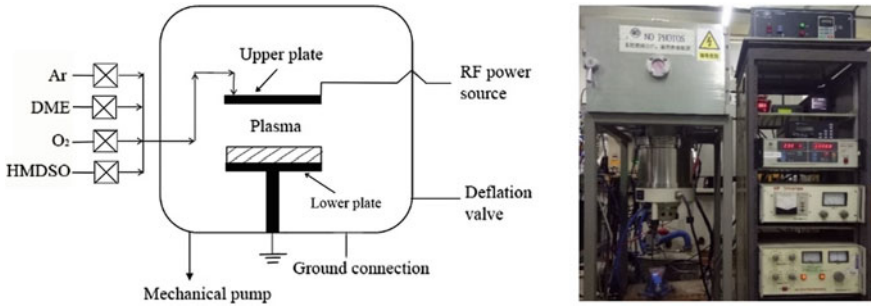
**Fig. 1.** Devices for deposition of silicon oxide film by PECVD **a** the schematic diagram **b** the photo of PECVD devices

## 3   Result and Discussion

### 3.1   Effect of DME Dosage on the Structure of Films

In order to investigate the effect of DME dosage on the structure of films, three different samples were prepared separately. Under the same other conditions, the ratio of porogen used in the three groups of samples was 1:2:3, named DME-1, DME-2, DME-3. The thickness of the film are shown in Table 1. It can be seen that with the increase of DME dosage, the thickness of the films increase and it decreases more after thermal annealing. It can be inferred that with the increase of DME dosage, the proportion of organic content in the films increases.

**Table 1.** The thickness of silicon oxide films with different DME dosages

| Dosage of DME | Thickness before thermal annealing (nm) | Thickness after thermal annealing (nm) |
|---|---|---|
| DME-1 | 137.28 | 72.03 |
| DME-2 | 164.32 | 89.05 |
| DME-3 | 222.07 | 98.29 |

Porosity is an important factor influencing the performance of porous silicon oxide films as interlayer materials [16]. To further investigate the effect of DME dosage on the structure and properties of films, the refractive index of thin films was measured by ellipsometer in this experiment. Then the porosity of porous thin films was calculated by Lorentz-Lorenz formula [17]. The formula is as follows:

$$\frac{n_0^2 - 1}{n_0^2 + 2}(1 - p) = \frac{n^2 - 1}{n^2 + 2} \tag{1}$$

where, $n_0$ is the refractive index of the glass slide, and $n_0 = 4.340$; $n$ is the refractive index of film; and $p$ is the porosity of film.

The dielectric constant of film is calculated by Maxwell-Garnette formula [18].

$$k = n^2 \tag{2}$$

where, $k$ is the dielectric constant of film, and $n$ is there fractive index of film. The dielectric constant and porosity of the films are calculated as shown in Table 2.

**Table 2.** The dielectric constant and porosity of the film

| Dosage of DME | Refractive index before thermal annealing/A° | Refractive index after thermal annealing/A° | Dielectric constant after thermal annealing | Porosity after thermal annealing (%) |
|---|---|---|---|---|
| DME-1 | 1.371 | 1.356 | 1.839 | 74.474 |
| DME-2 | 1.394 | 1.371 | 1.879 | 73.513 |
| DME-3 | 1.429 | 1.373 | 1.885 | 73.385 |

It can be seen from Table 2 that the refractive index of the film decreases after thermal annealing, and the dielectric constant of it increases with the increase of DME dosage. This is due to the removal of the organic components such as -CH$_3$, resulting in the formation of porous structure with stable inorganic components such as Si-O-Si as the skeleton, which reduces the refractive index of the film. The increase in the dosage of porogen generally increases the content of organic components in the film, leading to an increase in the porosity of it after annealing in turn.

## 3.2 Effect of UV-Cure with Different Wavelengths on Bonding State of Porous Silicon Oxide Films

It has been described in our previous report [15] that the change in the bonding state of the silicon oxide film after annealing. Figure 2 shows the FT-IR absorption spectra of sample DME-1 after annealing and UV-cure.

It can be found that within the scope of the study, there are four distinct absorption peaks: 1382, 1140, 1060 and 902 cm$^{-1}$. The absorption peak at 1060 cm$^{-1}$ and 1140 cm$^{-1}$ belongs to the stretching vibration peak [15] of network Si-O-Si and cage-like Si-O-Si [19], respectively. The absorption peak at 902 cm$^{-1}$ belongs to the bending vibration of Si-H in O$_3$-Si-H [20]. It can be seen that UV-cure with different wavenumbers has different effects on the film. It has been reported [21] that the bond intension of the Si-O and C-C bonds is large, and the bond breakage may occur under the condition in which the wavelength of UV-cure is lower than 200 nm. Therefore, it is considered that after the NB-cure, the Si–H bond is broken, generating a highly active Si dangling bond, which can be incorporated into the film skeleton again to form a Si-O-Si bond, and it is the main skeleton of the film, the main source of mechanical strength of the film. This indicates that the NB-cure makes a certain adjustment of the skeleton structure of the film, making its skeleton more stable. The BB-cure can break
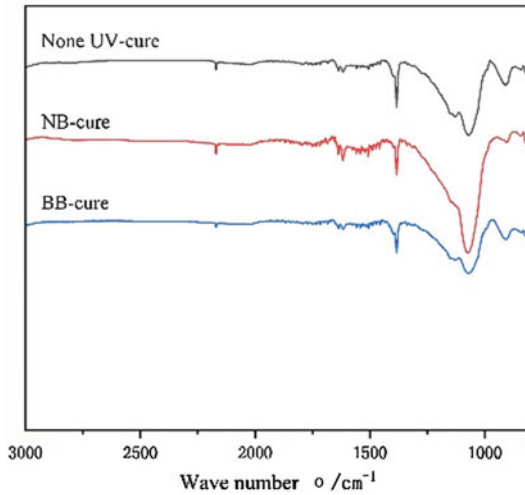
**Fig. 2.** FTIR spectra of low-k films with different UV-cures after thermal annealing

the bond with weak intension in the film, like the C-H absorption peak [22] corresponding at 1382 cm$^{-1}$, but it has little effect on the structure of the film.

## 3.3    Effect of Different Experimental Conditions on Surface Morphology of Films

The surface morphology of sample DME-3 after annealing and UV-cure is shown in Fig. 3. It can be seen that after annealing, pore is formed on the surface of the film, but its distribution is not uniform. After NB-cure, its distribution becomes better, indicating that NB-cure not only changes the structure of films, but also plays a role in further removing the porogen.



(a) After annealing                    (b) After annealing and UV-cure
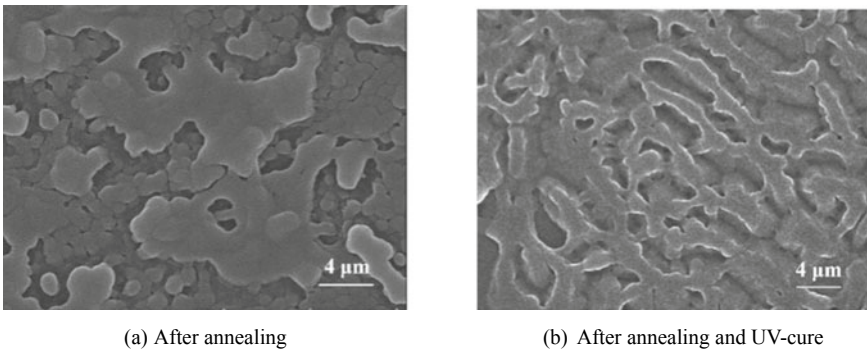
**Fig. 3.** The SEM topographies of the surface of silicon oxide film before and after UV-cure

# 4   Conclusion

In this paper, nano-porous silicon oxide films were deposited by PECVD under various experimental conditions, such as adjusting the dosage of pogogen and UV-cure with different wavelength. The thickness, refractive index, bond structure and surface morphology of the films were characterized and analyzed. When the dosage of porogen is increased, the content of organic components in the film is increased, and the collapse of the pores occurs during annealing, resulting in a decrease in porosity and an increase in k value. UV-cure with narrow wavelength can make the skeleton of films more stable and help to improve the mechanical strength. While UV-cure with wavelength over 200 nm is helpful to further remove the porogens in the films, but has little effect on the structure of the films.

# References

1. Ning Z, Ye C (2004) Ultra-low dielectric constant materials and porous SiOCH films. World Sci-Tech R&D 6:19–23
2. Ye C, Ning Z (2006) Ultra-low dielectric constant materials and porous SiCOH film for nano-electronic devices. Physics 35(4):322–329
3. Fu Z (2011) Preparation of porous materials with low dielectric constant. Nanjing University of Technology, Nanjing
4. Favennec L, Jousseaume V et al (2004) Porous extreme low k (EL k) dielectrics using a PECVD porogen approach. Mater Sci Semicond Process 7(4)
5. Jousseaume V, Zenasni A et al (2012) Ultra-low-k by CVD: deposition and curing. Advanced Interconnects for ULSI Technology. Wiley, New York, pp 35–77
6. Jousseaume V, Sabahy J et al (2017) SiOCH thin films deposited by chemical vapor deposition: From low-k to chemical and biochemical sensors. Microelectron Eng 167:69–79
7. Zenasni A, Jousseaume V et al (2007) The role of ultraviolet radiation during ultralow k films curing: strengthening mechanisms and sacrificial porogen removal. J Appl Phys 102 (9):094107
8. Prager L, Marsik P et al (2008) Effect of pressure on efficiency of UV curing of CVD-derived low-k material at different wavelengths. Microelectron Eng 85(10):2094–2097
9. Ito F, Takeuchi T et al (2004) Improvement of mechanical properties of porous SiOCH films by post-cure treatments. Proceedings of the Advanced Metallization Conference, pp 32–33
10. Fu S, Hu L et al (2011) The effect of ultraviolet irradiation on composition and mechanical properties of ultra-low dielectric constant SiCOH films. J Funct Mater 42(09):1657–1659 +1662
11. Iacopi F, Travaly Y et al (2006) Short-ranged structural rearrangement and enhancement of mechanical properties of organosilicate glasses induced by ultraviolet radiation. J Appl Phys 99(5):053511
12. Zenasni A, Remiat B et al (2007) Thermal furnace and ultraviolet assisted curing impact on SiOCH spin-on ultra low dielectric constant materials. Thin Solid Films 1097–1103

13. Chang Y, Chang W et al (2013) Effect of thermal treatment on physical, electrical properties and reliability of porogen-containing and porogen-free ultralow-k dielectrics. Thin Solid Films 528:67–71
14. Cheng Y, Lee C et al (2018) Comparison of various low dielectric constant materials. Thin Solid Films 660
15. Cao Y, Wang C, Zhang G et al (2017) Preparation of nano-porous SiOx films by PECVD method. Packag Eng 19:41–46
16. Zhang G, Wang C et al (2018) Characterization and measurement of elastic modulus based on ultrasonic atomic force microscopy for nano-porous silicon oxide film. J Mech Eng 54 (12):109–114
17. Chen H, Fu M (2007) Core-shell-shaped organic-inorganic hybrid as pore generator for imprinting nanopores in organosilicate dielectric films. Macromolecules 40(6):2079–2085
18. Yao Q (1989) Optical tutorial. Higher Education Press, Beijing
19. Tan Z, Wu X et al (2015) The effect of thermal annealing on structure and properties of plasma enhanced chemical vapor deposition of SiCOH films. Acta PhysicaSinica 64 (10):263–269
20. Grill A, Neumayer D (2003) Structure of low dielectric constant to extreme low dielectric constant sicoh films: fourier transform infrared spectroscopy characterization. J Appl Phys 94(10):6697
21. Shioya Y, Ohdaira T et al (2008) Effect of UV anneal on plasma CVD low-k film. J Non-Cryst Solids 354(26):2973–2982
22. Redzheb M, Prager L et al (2016) UV cure of oxycarbosilane low-k films. Microelectron Eng

# Research Progress in Modification of Polyvinyl Alcohol Films for Packaging

Hui Liu[1,2(✉)], Dongli Li[2], Wencai Xu[1,2], and Yunzhi Chen[1]

[1] Institute of Packaging and Printing Engineering, Tianjin University of Science and Technology, Tianjin, China
liuhui1022@126.com

[2] Beijing Key Laboratory of Printing and Packaging Materials and Technology, Beijing Institute of Graphic Communication, Beijing, China

**Abstract.** Polyvinyl alcohol film can be soluble and degradable under certain conditions, and has many applications in packaging field. However, there are still many shortcomings (for example, insufficient mechanical properties and poor water resistance) in its performance, so how to improve the performance of polyvinyl alcohol film for packaging has become a research hotspot. The modification methods of polyvinyl alcohol film for packaging were studied, and the main research results at home and abroad were discussed in detail. At present, the most commonly used modification methods of Polyvinyl alcohol films are polymer blending, inorganic nanomaterials composite, physical crosslinking and so on. It is found that some modification methods can not only improve the properties of polyvinyl alcohol films, but also have the advantages of non-toxic and harmless, easy processing and low cost. They can be widely used in the modification of films.

**Keywords:** Polyvinyl alcohol · Film · Modification · Packaging

## 1 Introduction

Polyvinyl alcohol (PVA) has water solubility and biodegradability. It is a kind of high molecular polymer with excellent performance and wide application. PVA film has excellent barrier property, wear resistance, tear resistance, transparency, antistatic property, printability, chemical corrosion resistance and so on. It is water-soluble and biodegradable under certain conditions. It occupies a unique and very important position in film materials and is widely used in the field of industrial, pharmaceutical and food contact packaging materials [1].

Polyvinyl alcohol is a kind of polymer containing a lot of hydroxyl groups. Because of its small volume of side groups –H and –OH, which can enter the crystallization point without causing stress, so it made the film has high crystallinity and high barrier properties. At the same time, due to the existence of hydroxyl groups, PVA has a high water absorption [2]. Therefore, in the dry environment, PVA film has good oxygen barrier and water vapor barrier. It is an excellent high barrier film, which can protect packaged products, especially food. However, pure PVA film is easy to absorb water in high humidity (RH 60–90%) environment, and its barrier property is greatly reduced or

even disappeared, which seriously affects the application of PVA film in packaging. In the actual production and use process, it must be taken into account that the material can be used under various temperature and humidity conditions. Therefore, how to improve the performance of thin films has become an important research topic. At present, the main methods to improve the properties of PVA films are polymer blending, inorganic nanomaterials composite, physical crosslinking and chemical crosslinking. Firstly, modification of PVA film by citric acid, boric acid, polysaccharides and nano-materials (nano-$SiO_2$, nano-montmorillonite, nano-cellulose, etc.) [3–6] can improve the mechanical properties, hydrophobic properties, thermal stability and barrier properties of PVA film. Secondly, physical cross-linking (heat treatment, irradiation treatment, etc.) is used to modify the PVA film in order to improve the performance of the film material. On the basis of improving the properties of PVA film materials, these modification methods are non-toxic, harmless, easy to process and low cost.

## 2 Study on Modification of Polyvinyl Alcohol Film

### 2.1 Polymer Blend Method

In the polymer blending method, the preparation process of polyvinyl alcohol film with polysaccharides as additives has been studied extensively in order to improve its properties. The mechanical properties of the films could be significantly improved by polymer blending. The preparation process was simple, the raw material was cheap and easy to obtain, and the added polymer was non-toxic and harmless.

Zhang et al. [7] studied the effect of maize amylose on the properties of PVA film. The results showed that with the increase of amylose content, the mechanical properties and water resistance of the composite film increased, and the comprehensive properties were better than those of pure PVA film. Gao et al. [8] modified corn starch with glycerol and citric acid. The compatibility of modified starch with PVA was improved, the crystallinity of the composite film was decreased, and the mechanical properties, water resistance and thermal stability were improved significantly. Li and Wang [9, 10] respectively studied the effect of the content and structure of chitosan on the chitosan/PVA composite membrane. The results showed that the addition of chitosan changed the crystallinity of the films, and improved the mechanical properties and barrier properties of the PVA films. Li et al. [11] prepared PVA/modified NCC nanocomposite films, and further heat treatment prepared crosslinked PVA/modified NCC nanocomposite films. The results showed that the initial decomposition temperature of the film increases, the crystallization peak moved towards high temperature, the water absorption was basically unchanged, and the mechanical properties were sensitive to environmental humidity. After heat treatment and crosslinking, the initial decomposition temperature of the film continues to rise, the crystallization peak moved to high temperature, the water absorption decreased significantly, and the mechanical properties did not change with environmental humidity. PVA films with different MCC mass fraction were prepared by blending solution tape casting method by Chen et al. [12]. The effects of MCC content on the color, optical properties, mechanical

properties, barrier properties, thermal stability and surface morphology of PVA films were measured and analyzed. The experimental results show that the addition of MCC improves the mechanical properties, hydrophobicity, barrier and thermal stability of PVA films. The properties of PVA films can be effectively improved by controlling the amount of PVA films. Ali et al. [13] studied the distribution, compatibility and mechanical properties of kenaf fibers treated by single-stage treatment and two-stage treatment in PVA. The results showed that the tensile strength, Young's modulus and bending strength of the films were improved. The mechanical properties and water resistance of PVA film modified by two-stage kenaf fiber were better. Further studies [14] showed that the strength and stiffness of starch/PVA membranes enhanced by nanofibers depended on storage conditions. Sarwar et al. [15] found that when the content of nanofibers was 8% in PVA/nanofibers/Ag nanocomposite films, the strength of the films increased, and the composite films showed strong inhibition on Escherichia coli and Staphylococcus aureus.

## 2.2　Inorganic Nanomaterials Composite Method

Another widely used modification method of polyvinyl alcohol film is blending modification with inorganic particles. There are a lot of hydroxyl groups in PVA. The hydrogen bond interaction between these hydroxyl groups makes the thermoplasticity of PVA worse. It is often necessary to add a certain amount of plasticizer to modify PVA. Commonly used plasticizers are polyols, urea and other small organic molecules. However, compared with inorganic particles, these organic plasticizers have some shortcomings, such as limited plasticizing efficiency and poor compatibility with film-forming matrix. Therefore, some inorganic particles have been explored as plasticizers to modify the PVA film matrix, mainly nano-silica, nano-titanium dioxide, montmorillonite and so on. Inorganic nanoparticles can improve the mechanical properties, barrier properties, thermal stability, antimicrobial properties and water resistance of polyvinyl alcohol films to varying degrees. Polyvinyl alcohol film modified by inorganic nanoparticles is an excellent modification process because of its simple preparation process, easy availability of raw materials and low price.

Liu and others [16] prepared thermoplastic cassava starch/polyvinyl alcohol/silica composites by melting method. The experimental results show that the surface modified $SiO_2$ was beneficial to improve the tensile strength of the composites. With the increase of $SiO_2$ content, the plasticizing time of the composites was shortened, and the plasticizing torque and equilibrium torque were increased. The addition of PVA-1788 and surface treated $SiO_2$ could improve the plasticizing properties of TPS/PVA/$SiO_2$ composites. Lei et al. [17] modified polyvinyl alcohol composite film packaging materials by nano-$SiO_2$. The results showed that the moisture permeability of modified PVA composite membrane was 31.43% lower than that of unmodified PVA composite membrane, the water absorption was 35.34%, the oxygen permeability and $CO_2$ permeability were 17.91% and 18.31% lower respectively, and the bacteriostasis of the composite membrane was also improved. Modification of nano-$SiO_2$ could significantly improve the barrier property of PVA composite film and the application effect of its food preservation packaging. Sun et al. [18] prepared polyvinyl alcohol/titanium dioxide composite nanofiber membranes by electrospinning technology. The results

show that the surface roughness of the films increased with the increase of titanium dioxide content. The results show that the surface roughness of the films increases with the increase of titanium dioxide content. After modification, the morphology of the fibers remained unchanged, the bonding between the fibers occurred, and the aldol condensation reaction took place on the surface of the material. The water resistance of the composite nanofibers membrane was significantly improved, and the melting peak disappeared at 190 °C. Cano et al. [19] studied the effect of antibiotic neem oil, oregano essential oil and silver nanoparticles on the degradation of starch/PVA film. The results showed that the addition of 9.8% silver nanoparticles had a significant effect on the degradation, and it was an ideal additive. Zhou and Tang [20] modified natural montmorillonite with soybean protein and added it into PVA film. The results showed that the intermolecular force of montmorillonite was decreased and the compatibility of starch, polyvinyl alcohol and clay layers was increased when montmorillonite modified by soybean protein. This resulted in better dispersion of clay layers in polymer matrix and formation of nanostructures with high degree of peeling. The water vapor permeability and tensile strength of starch/polyvinyl alcohol films decreased significantly due to the formation of nanostructures.

## 2.3    Physical Crosslinking Method

In addition to the modification of PVA films with polysaccharides and inorganic nanoparticles, physical cross-linking is also the simplest and most effective method in the post-treatment process of PVA films, especially the heat treatment method. The structure and properties of PVA films will be affected by different treatment temperature and time. High temperature treatment could increase the crystallinity of the molecule, thereby enhancing the mechanical properties and water resistance of the film [21].

Wang et al. [22] improved the processing stability of modified polyvinyl alcohol by micro-crosslinking. The results showed that heat treatment could adjust the residual water content of modified PVA system, improve the crystalline structure of PVA and its mechanical properties. Wang et al. [23] found that the crystallinity of PVA films increased and the stability of PVA films increased after heat treatment for 1–3 h at 120 °C. Liu et al. [24] studied the effect of high temperature treatment on the film-forming properties of corn starch/PVA. The results showed that the film-forming properties of the composite films were different when the treatment temperature was between 90 and 150 °C. The compactness of corn starch/PVA film treated at 110 °C was improved, the compatibility of starch and PVA was improved, the crystal area of composite film was reduced, the thermal stability was enhanced, and the comprehensive performance was better. Hao et al. [25] found that the combination of heat treatment and boric acid crosslinking improved the water resistance of PVA films significantly. Ciela and Abramowska [26] studied the effects of radiation treatment with cobalt 60 in nitrogen atmosphere on PVA with different molecular weight and electron irradiation in air atmosphere on starch/PVA film. The results showed that the physicochemical properties and irradiation sensitivity of the composite film depend on the type of matrix PVA. PVA with high molecular weight was better than that with low molecular weight. The properties of the films were not affected by irradiation.

# 3   Conclusions

In summary, the commonly used modification methods of polyvinyl alcohol film for packing at this stage are polymer blending, inorganic nanomaterials composite, physical cross-linking and so on. These modification methods can improve the properties of PVA films for packing to varying degrees. Moreover, the modification methods have the advantages of simple process and low cost of raw materials, which can expand the application range of PVA films. Polyvinyl alcohol film has good mechanical properties and barrier properties. Under certain conditions, it has water solubility and biodegradability. At the same time, its water resistance is poor and its application conditions are limited. Therefore, the study of water resistance should be the focus of the next research. On the premise of ensuring that the film can dissolve in water, the water resistance of the material can be improved by increasing the water-soluble temperature of the film.

# References

1. Liu G, Ye S, Wang J et al (2014) Effects of nanoclay type on the physical and antimicrobial properties of PVOH-based nanocomposite films. LWT-Food Sci Technol 57(2):562–568
2. Li S, Lei Y, Wang J (2018) Research progress of polyvinyl alcohol film. Coat Prot 39(8):44–49
3. Zhang Y, Yang F, Jiang S et al (2014) Study on the properties of citric acid/PVA antibacterial films. Packag Eng 35(21):10–14
4. Xu W, Yang R, Tao J (2012) Preparation and properties of boric acid modified polyvinyl alcohol films. Colloids Polym 30(3):109–111
5. Johansson C, Clegg F (2014) Hydrophobically modified poly(vinyl alcohol) and bentonite nanocomposites there of barrier, mechanical, and aesthetic properties. J Appl Polym Sci 132 (13):55–58
6. Pereira AL, Nascimento DM, Filho MS et al (2014) Improvement of polyvinyl alcohol properties by adding nanocrystalline cellulose isolated from banana pseudostems. Carbohyd Polym 112(1):165–172
7. Zhang Q, Chen Z, Sun Y (2014) Study on the preparation of starch-polyvinyl alcohol biodegradable films. Sci-Tech Horizon 35:166–167
8. Gao C, Sun W, Yuan H et al (2012) Study on preparation and properties of modified starch/polyvinyl alcohol composite film. Anhui Agric Sci 40(7):3989–3991
9. Li X, Fang J, Zhou Y (2017) Effects of chitosan and nano-chitosan on the structure and properties of polyvinyl alcohol membranes. Food Sci 38(17):132–137
10. Wang S, Lu R, Lan W et al (2017) Study on the influence of different chitosan content on the properties of chitosan/polyvinyl alcohol composite plastic film. Plast Ind 45(7):94–97

11. Li B, Cao X, Xia T et al (2013) Preparation and properties of polyvinyl alcohol/modified nanocellulose crystal nanocomposite films. Polym Mater Sci Eng 29(7):152–157
12. Chen C, Chen S, Xu Z et al (2017) Effect of microcrystalline cellulose modification on the properties of polyvinyl alcohol film. Packag Eng 38(9):85–90
13. Ali ME, Yong CK, Ching YC et al (2014) Effect of single and double stage chemically treated kenaf fibers on mechanical properties of polyvinyl alcohol film. Bioresources 10 (1):822–838
14. Panaitescu DM, Frone AN, Ghiurea M et al (2015) Influence of storage conditions on starch/PVA films containing cellulose nanofibers. Ind Crops Prod 70:170–177
15. Sarwar MS, Niazi M, Jahan Z et al (2018) Preparation and characterization of PVA/nanocellulose/Ag nanocomposite films for antimicrobial food packaging. Carbohydr Polym 184:453–464
16. Liu Y, Fan L, Wu A et al (2017) Processing behavior and mechanical properties of thermoplastic cassava starch/PVA/SiO$_2$ composites. Plast Ind 45(8):109–112
17. Lei Y, Yin Y, Wang J et al (2012) Effects of nano-SiO$_2$ modification of polyvinyl alcohol-based coating materials on their film-forming packaging performance. Food Sci 33(6):232–238
18. Sun F, Yan B, Wang X et al (2016) Preparation and modification of polyvinyl alcohol/titanium dioxide composite nanofiber membranes. Mater Sci Eng 34(1):54–59
19. Cano AI, Chfer M, Chirala A et al (2016) Biodegradationbehavior of starch-PVA films as affected by the incorporation of different antimicrobials. Polym Degrad Stab 132:11–20
20. Zhou J, Tang X (2015) Structure and properties of starch-polyvinyl alcohol-soybean protein modified montmorillonite composite films. Chin J Cereals Oils 30(5):29–35
21. Hao J, Dai C, Wu L (2017) Progress in cross-linking modification and application of polyvinyl alcohol membranes. New Chem Mater 45(1):41–43
22. Wang N, Zhao L, Li L (2015) Effects of heat treatment on the structure and properties of boric acid modified polyvinyl alcohol. Plastics 44(5):40–44
23. Wang Y, Yang H, Xu Z (2006) Effects of chemical crosslinking and heat treatment on the properties of polyvinyl alcohol membranes. Chem Eng 34(8):36–39
24. Liu S, Chen P, Zhu S (2010) The effect of high temperature treatment on the film-forming properties of corn starch/polyvinyl alcohol composite film. China J Cereals Oil 25(2):57–61
25. Hao X, Tao F, Wei H (2016) Study on water resistance of fully alcoholized PVA packaging film. Packag Eng 3:40–45
26. Ciela K, Abramowska A et al (2017) The effect of poly (vinyl alcohol) type and radiation treatment on the properties of starch-poly (vinyl alcohol) films. Radiat Phys Chem 141 (1):2297–2301

# Study on Preparation and Properties of Starch/Gelatin/Polyvinyl Alcohol Biodegradable Composite Films

Lin Wang[(✉)] and Fei Li

School of Packaging and Printing Engineering, Henan University of Animal Husbandry and Economy, Zhengzhou, China
xingyang20ll@l63.com

**Abstract.** As one of the four major materials in packaging industry, plastic packaging has been widely used in many industries. However, the traditional plastics have caused serious pollution and damaged the ecological environment. At present, the most effective method is to develop biodegradable packaging materials. In this study, using starch and gelatin as fillers and PVA as matrix, we prepared a new type of biodegradable composite films and studied their properties. When the mass fraction of starch and gelatin are 25% and 12.5% respectively, the mechanical properties, optical properties and water vapor barrier properties of the composite film are the best. The composite films exhibit excellent ability to block ultraviolet radiation and biodegradability, which can be used not only for light-sensitive food packaging, but also for green package.

**Keywords:** Polyvinyl alcohol · Starch · Gelatin · Composite films · Biodegradability

## 1 Introduction

As one of the four major materials in packaging industry, plastics packaging has been widely used in various fields, and brought great convenience to people's lives. However, the raw materials of traditional plastics are non-degradable and non-renewable, which will seriously pollute the environment and endanger sustainable development. Therefore, exploring and researching biodegradable packaging materials based on renewable animal and plant resources has became an important issue to the life and development of people [1–3].

Starch is a renewable, biodegradable natural macromolecule material, which polymerized from glucose molecules. The degradation products of starch, $CO_2$ and $H_2O$, can be recycled by photosynthesis and are environment-friendly [4, 5]. Gelatin is a protein formed by partial hydrolysis of collagen. It has a wide range of sources, low cost, good biocompatibility and biodegradability [6, 7]. However, pure starch or gelatin films have many disadvantages, such as low strength, poor toughness, and poor water resistance, which make them unable to meet the application requirements. Therefore, it is necessary to add synthetic polymer to modify them [8–10]. Polyvinyl alcohol (PVA) is a water-soluble polymer, and PVA films can completely degrade by

microorganisms in nature. It can be used as an auxiliary film-forming material and added to natural macromolecule materials to prepare composite packaging films, thus improving the performance of natural macromolecule packaging materials [11].

In this paper, two-component and three-component composite biodegradable PVA-based composite films were prepared by solution casting method with starch and gelatin as fillers and polyvinyl alcohol as matrix. Their optical properties, mechanical properties and degradation properties were studied.

## 2   Experiment

### 2.1   Materials and Equipment

Polyvinyl alcohol (PVA), AR, is produced by Kuraray Co., Ltd., Shanghai. Soluble starch, AR, is produced by Aladdi chemical reagent Co., Ltd., Shanghai. Gelatin, CP, is produced by Yongda chemical reagent Co., Ltd., Tianjin. Ethanol, AR, is produced by Guangfu chemical reagent Co., Ltd., Tianjin.

Thickness gauge, CHY-CZA, Labthink Co., Ltd., Shandong. Intelligent electronic tension tester, XLW, Labthink Co., Ltd., Shandong. Light transmittance/ haze tester, WAT-S, Shenguang instruments Co., Ltd., Shanghai. Water vapor transmission tester, W3/031, Labthink Co., Ltd., Shandong. UV-vis spectrophotometer, TU-1901, Purkinje general instruments Co., Ltd., Beijing. FT-IR spectrometer, Nicoletis10, Thermo fisher scientific Co., Ltd., Shanghai.

### 2.2   Preparation of Starch/PVA Composite Films

Six kinds of starch/PVA composite films were prepared according to the solid-liquid ratio of 1:10 and the mass fraction of soluble starch in the solid ratio of 0, 10%, 15%, 20%, 25% and 30% respectively. The mixture solution of starch and polyvinyl alcohol was heated at 90 °C for 2 h. Then the solution was coated on clean and flat glass plates. After 24 h, the films were peeled off, dried, and reserved in a drying cabinet. The thickness of the films was about 12–25 μm.

### 2.3   Preparation of Starch/Gelatin/PVA Composite Films

Gelatin was added to the starch and PVA solution, and the mass fraction of gelatin in total solids was 5%, 7.5%, 10%, 12.5% and 15% respectively. The mixture solution was heated and stirred at 50 °C for 2 h. After defoaming, the casting solution was coated on the glass plates. Then the films were peeled off, dried, and reserved in the drying cabinet. The thickness of the films was about 15–31 μm.

### 2.4   Mechanical Property Test

According to GB/T 1040-2006, the films were cut into 10 × 1.5 cm and balanced at 25 °C with relative humidity of 50% for 48 h. Tensile strength and maximum breaking elongation of the films were measured. Each sample was measured 10 times in parallel and the average value was obtained.

## 2.5  Optical Property Test

According to GB/T 2410-2008, the films were cut into 50 × 50 mm. The transmittance and haze were measured. Each sample was measured 5 times in parallel and the average value was obtained.

## 2.6  Water Vapor Permeability Test

According to GB/T 16928-1997, the films were cut into circles with diameter of about 76 mm. Under the standard mode, the experimental temperature was 38 °C, and the relative humidity difference between the two sides of the film was 90%. Each sample was measured 3 times and the average value was obtained.

## 2.7  FT-IR Spectroscopy

The measurement was carried out using the ATR mode with test range of 500 to 4000 cm$^{-1}$ and resolution of 4 cm$^{-1}$. The scanning times were 32 times.

## 2.8  UV-vis Spectroscopy

The thin film spline with 0.6 × 4 cm was placed into the cuvette, and light transmittance of the film was measured with air as the reference. The wavelength range was 200–700 nm, and the sampling interval was 1 nm.

## 2.9  Soil Degradation Test of Starch/Gelatin/PVA Composite Films

The degradation of the composite films was characterized under indoor humidity chamber and outdoor natural conditions respectively, and the degradation performance was expressed by weight loss percentage. The relative humidity of indoor was 60%, and the temperature was 25 °C. The soil was common horticultural soil, which was transferred into containers after debris removal. Outdoor conditions were natural and rainy in summer. After drying the films with 10×10 cm to constant weight ($w_0$), they were buried in the soil below 10 cm and taken out periodically. After cleaning, the samples were dried in the oven at 65 °C to constant weight ($w_1$). The weight loss rate (RWL) was calculated as follows.

$$\text{RWL}(\%) = \frac{w_0 - w_1}{w_0} \times 100\%$$

# 3  Results and Discussion

In this section, we first prepared starch/PVA composite films, and determined the optimal starch and PVA mass ratio according to optical properties and mechanical properties. Then, starch/gelatin/PVA composite films were prepared, and studied their properties in order to develop new biodegradable composite materials.

## 3.1    Characterization of Starch/PVA Composite Films

Table 1 shows mechanical and optical properties of the starch/PVA films with different starch contents. The results shows the tensile strength and elongation of the films initially rised and then decreased gradually with the increase of starch content. This is because starch and PVA both contain much hydroxyl groups, which can interact with each other by hydrogen bonds, so that the mechanical properties of the composite films are gradually improved. When the starch content is too high, starch are cross-linked excessively with PVA, which limited's the extension of molecular chains and increases the brittleness of the films, resulting in the decrease in tensile strength and elongation of the films. When the mass fraction of starch is 20%, the mechanical properties of the starch/PVA composite films are the best, with tensile strength of 110.96 MPa and elongation of 2.86%.

**Table 1.** Mechanical and optical properties of the starch/PVA films with different starch contents

| The mass fraction of starch (%) | Tensile strength (MPa) | Elongation (%) | Transmittance (%) | Haze (%) |
|---|---|---|---|---|
| 0 | 101.49 ± 4.52 | 2.32 ± 0.21 | 92.48 ± 3.12 | 0.25 ± 0.04 |
| 10 | 103.21 ± 3.34 | 2.65 ± 0.19 | 92.21 ± 2.57 | 1.62 ± 0.13 |
| 15 | 104.97 ± 2.67 | 2.74 ± 0.26 | 92.08 ± 2.21 | 2.36 ± 0.19 |
| 20 | 110.96 ± 3.45 | 2.86 ± 0.31 | 91.50 ± 2.49 | 3.55 ± 0.21 |
| 25 | 93.18 ± 3.01 | 2.44 ± 0.23 | 91.26 ± 2.86 | 4.47 ± 0.27 |
| 30 | 87.83 ± 2.87 | 2.08 ± 0.20 | 91.20 ± 3.01 | 6.23 ± 0.31 |

From the results of transmittance and haze of the composite films, it can be seen that with the increase of starch, the transmittance of the films decreased slightly, but all of them were above 90%, and the haze gradually increases. This indicates that the blend membranes have good compatibility with each other, but as the starch increases, the thickness of the film increases, the more light is absorbed, resulting in a decrease in transmittance. At the same time, the increase in thickness increases the scattering of light, resulting in an increase in haze.

Through synthetical consideration, the composite film with starch of 20% was selected for further research, that is, the ratio of starch to PVA in the composite film was 1:4.

## 3.2    Characterization of Starch/Gelatin/PVA Composite Films

### 3.2.1    FT-IR Spectroscopy

The FT-IR spectra of PVA, starch/PVA film and starch/gelatin/PVA composite films with different gelatin contents are shown in Fig. 1. The broad and strong absorption peaks of pure PVA film at 3342 cm$^{-1}$ are O–H stretching vibration peaks, the double peaks at 2939 cm$^{-1}$ and 2912 cm$^{-1}$ are C–H stretching vibration peaks at –CH$_3$ and –CH$_2$ respectively, the peak at 1332 cm$^{-1}$ is the bending vibration peak of

CH–OH, the peak at 1140 cm$^{-1}$ is the C–O stretching vibration peak, and the stretching vibration peaks at 1710 cm$^{-1}$ of C=O bonds on the PVA branch are also observed. The stretching vibration peak of O–H in the starch/PVA film was narrowed, indicating hydrogen bonding interaction occurred between starch and PVA. After adding gelatin, the O–H stretching vibration peak narrowed further with the increase of gelatin, and a new peak appeared at 1662 cm$^{-1}$, which corresponds to the stretching vibration peak of C=O in gelatin. This fully indicated gelatin entered the starch/PVA films and formed strong hydrogen bonds.
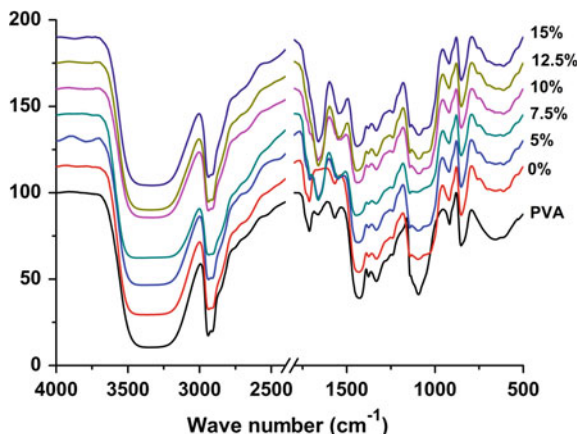


**Fig. 1.** FT-IR spectra of PVA and starch/gelatin/PVA composite films

### 3.2.2 Tensile Strength and Elongation at Break

The tensile strength and elongation of starch/gelatin/PVA films with different gelatin contents are shown in Fig. 2. With the increase of gelatin content, the tensile strength
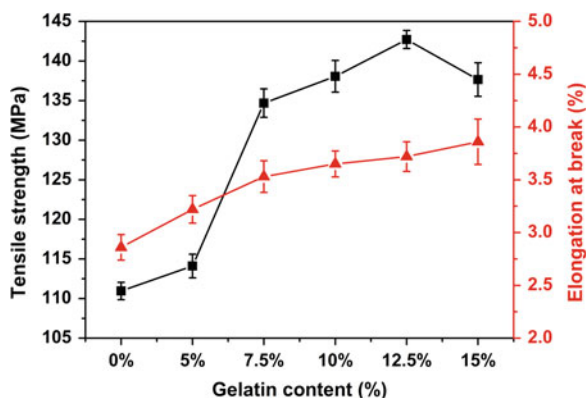


**Fig. 2.** Mechanical property of starch/gelatin/PVA composite films

of the composite films increases rapidly and then decreases, while the elongation increases gradually. This is because the interaction between gelatin and PVA enhanced, resulting in a denser network structure. Simultaneously, the interaction between gelatin and PVA destroys the interaction between starch and PVA, which increases the flexibility of the films. However, when the gelatin content reaches the certain value, the film-forming property of the solution is deteriorated, gelatin agglomerated and stress concentration formed, which reduces the tensile strength of the films, but has little effect on the toughness. When the percentage of gelatin was 12.5%, the tensile strength reached maximum value of 143.52 Mpa, and the elongation was 3.72%.

### 3.2.3    Transmittance and Haze

Figure 3 shows the optical properties of starch/gelatin/PVA films. With the increase of gelatin content, the transmittance of the films changed less, indicating that the compatibility between starch, gelatin and PVA was good. The haze of the films gradually increased, which was mainly caused by the thickness of the films. The addition of gelatin increases the thickness of the films, causes serious light scattering, and leads to an increase in haze.
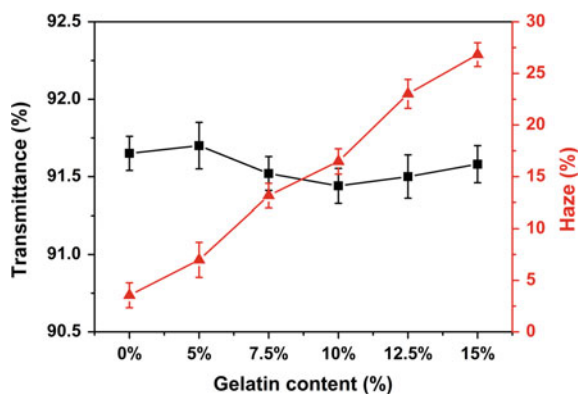


**Fig. 3.**  Optical property of starch/gelatin/PVA composite films

### 3.2.4    Water Vapor Permeability Test

Figure 4 shows the effect of gelatin on water vapor permeability (WVP) of starch/gelatin/PVA films. As the gelatin content increases, the WVP of the films firstly decreased and then increased. This is because the functional groups in gelatin can interact with the hydroxyl groups in starch and PVA. This interaction reduce the exposed hydrophilic groups, thereby decrease the water absorption of the films. When the gelatin is too high, not only the network structure has been destroyed, but also the hydrophilic group has been directly introduced, and the water absorption of the film increased.
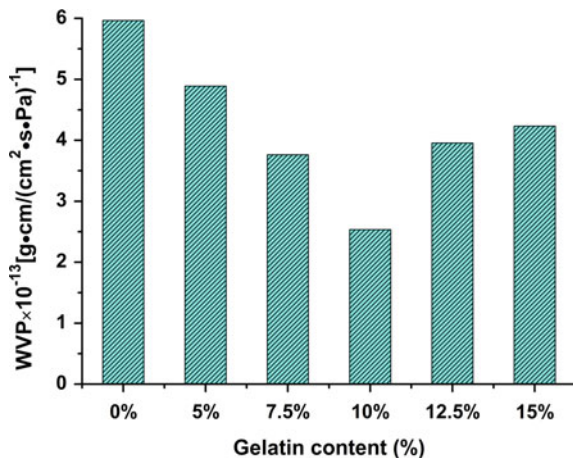
**Fig. 4.** Water vapor permeability of starch/gelatin/PVA composite films

### 3.2.5 UV-vis Spectroscopy

Figure 5 shows the UV-vis spectra of pure PVA and starch/gelatin/PVA composite films. In the regions of 300–700 nm, the transmittance of pure PVA film is about 80%, and only partial ultraviolet absorption is exhibited below 300 nm, which indicates the ability to block ultraviolet radiation of PVA film is very poor. After adding gelatin, the transmittance of starch/gelatin/PVA composite films both decreases in the range of 300–700 nm and 200–300 nm, showing obvious ability to block ultraviolet radiation. With the increase of gelatin content, the ability to block ultraviolet radiation increases continuously. Since the composite films are effective in blocking UV radiation, they will have potential applications in light-sensitive food packaging.



**Fig. 5.** UV-vis spectra of PVA and starch/gelatin/PVA composite films

### 3.2.6  Biodegradability Test in Soil

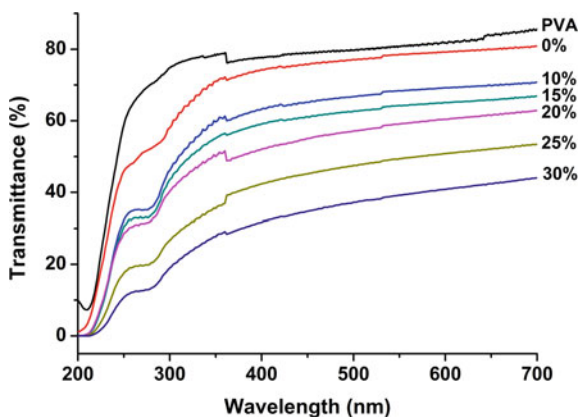From the films degradation diagram (Fig. 6a) under indoor conditions, it can be seen the degradation rate of PVA film is slow in a short time. The weight loss rate (RWL) is only 7.18% in 52 days, and the degradation rate is almost zero in the first 24 days. After adding starch and gelatin, the degradability of the composite films increased rapidly. The RWL is high in the first seven days, then slowed down, and it increased with the increase of gelatin content. On the 52th day, the RWL of the composite films was all above 26%. This is because in the initial stage, the microorganisms in the soil are abundant, the starch and gelatin in the films can be used as nutrient matrix of microorganisms, the RWL of the films increased. Then the microbial nutrients in soil decrease, leading to a slower rate of RWL.
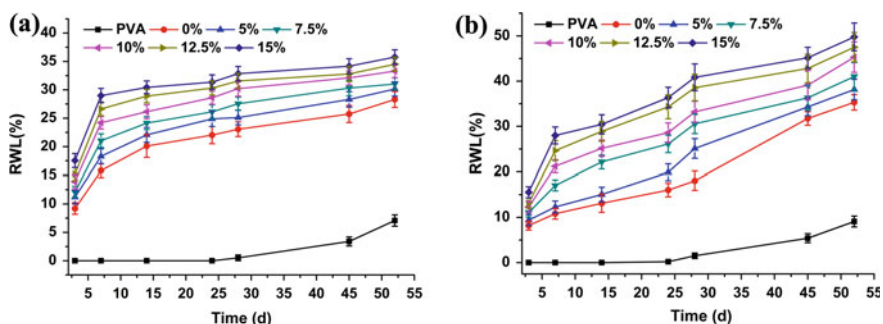


**Fig. 6.**  Weight loss of films in soil **a** indoor; **b** outdoor

The weight loss of the films under outdoor conditions was shown in Fig. 6b. Compared with the PVA film, the degradation rate of the composite films increased significantly. The RWL was proportional to gelatin content in 52 days. The outdoor temperature is high and rainy, the humus is more, and the quantities of microorganisms increase. Starch and gelatin can be used as nutrients for microorganisms, therefore the RWL of the films is always fast, and the weight loss exceeds the weight loss of the films under indoor conditions.

## 4   Conclusions

In this study, biodegradable PVA-based composite films were prepared by solution casting method with starch and gelatin as fillers and PVA as matrix, and their properties were studied. (1) Using starch as the filler, the mechanical and optical properties of the composite films depended on the change in the starch content. When the starch content was 20%, the performance of the film was the best. (2) Using both starch and gelatin as the fillers, the mechanical properties and biodegradability of the composite films were significantly improved. When the mass fractions of starch and gelatin are 20% and 12.5% respectively, ultraviolet barrier and degradation properties of the film are the best. After 52 days in soil, the degradation rate of the film reached 35% indoor and

50% outdoor. Starch, gelatin and PVA have good compatibility, and adding starch and gelatin to PVA film can significantly improve the properties of PVA-based composite films, which make them suitable for light-sensitive food packaging and green package.

# References

1. Richard AG, Bhanu K (2002) Biodegradable polymers for the environment. Science 297 (5582):803–807
2. Khalil HPS, Tye YY, Saurabh CK, Leh CP (2017) Biodegradable polymer films from seaweed polysaccharides: A review on cellulose as a reinforcement material. Express Polym Lett 11(4):244–265
3. Zarina S, Ahmad I (2015) Biodegradable composite films based on κ-carrageenan reinforced by cellulose nanocrystal from kenaf fibers. BioResources 10(1):256–271
4. Wang S, Li C, Niu Q, Wang S (2015) Starch retrogradation: A comprehensive review. Compr Rev Food Sci Food Saf 14:1541–4337
5. Rahman WAWA, Sin LT, Rahmat AR (2010) Thermal behavior and interactions of cassava starch filled with glycerol plasticized polyvinyl alcohol blends. Carbohydr Polym 81(4):805–810
6. Russo MAL, Truss R, Halley PJ (2009) The enzymatic hydrolysis of starch-based polyvinyl alcohol plastics blends. Carbohydr Polym 77(3):442–448
7. Liu D, Nikoo M, Boran G, Zhou P, Regenstein JM (2015) Collagen and gelatin. Annu Rev Food Sci Technol 6:527–557
8. Zhao X, Lang Q, Yildirimer L (2016) Photocrosslinkable gelatin hydrogel for epidermal tissue engineering. Adv Health Mater 7:108–118
9. Farayde MF, Daryne C, Fábio Y (2012) Comparative study of processing methods for starch/gelatin films. Carbohydr Polym 95(2):681–689
10. Olga M, Julián C (2017) Influence of starch oxidation on the functionality of starch-gelatin based active films. Carbohydr Polym 178(15):147–158
11. Yang T (2006) Using water-soluble PVA bag packaging is solutions for the harm of pesticide packaging. Plast Packag 25(3):22–25

# Investigation of Coated Indium Tin Oxide Conductive Film

Fan Su, Lihong Cao, Aijing Gao, and Luhai Li[✉]

Beijing Engineering Research Center of Printed Electronics, Beijing Institute of
Graphic Communication, Beijing, China
liluhai@bigc.edu.cn

**Abstract.** Flexible indium tin oxide (ITO) film has good optical and electrical properties, and is lightweight and flexible, which is why it has become the focus of research into flexible electronic devices. Coating methods for preparing flexible ITO film can help cut costs but ITO film manufacturing technology needs to be optimized as well. To solve this issue, we tested a series of experiment parameters. The results indicate that well-performing ITO films can be prepared by heating them for two minutes at 100 °C with Mayer rod of RDS No. 20. The sheet resistance of the ITO film can reach up to 578 Ω/sq and keep a transmittance of 70%.

**Keywords:** Coating · Sheet resistance · Transmittance

## 1 Introduction

The visible light of the ITO transparent conductive film ($\lambda = 400 - 800$ nm) has an average transmission rate of more than 80% and the resistivity is less than $10^{-3}$ Ω cm, so it is widely used in electrode materials found in things such as flat panel displays, solar cell, etc. [1]. ITO and glass substrate has a strong adhesion, high hardness, and good chemical resistance [2], so ITO transparent conductive film mostly uses glass as the substrate. However, with the development of flexible electronic devices, glass-based material no longer meets people's needs because it is brittle, not easy to bend, and so it limits the application of ITO transparent conductive film. Flexible substrate has become a new research hotspot because it is bendable, lightweight, and difficult to break. The commonly used preparation method of flexible ITO transparent conductive film is magnetically controlled sputtering, which requires a vacuum environment and complex equipment, resulting in high cost. Coating preparation for flexible ITO transparent conductive film can be done using relatively simple coating, printing, and other ways to roll on to the continuous production and improved efficiency, thus reducing costs [3]. However, at present, the substrate used in the coating method is mostly glass, such as when Liu et al. [4] prepared ITO transparent conductive film with glass as the substrate, the resulting film resistance rate was $1.5 \times 10^{-2}$ Ω cm, and the light transmission rate was up to 87%. Yang [5] prepared ITO transparent conductive film on the glass substrate, the resulting film block resistance minimum was 258 Ω/sq, its transmission rate was at a wavelength of 550 nm and reached 89.6%. There are a

few studies on the preparation of flexible ITO transparent conductive film by coating and the preparation conditions are unstable, which is not conducive to the industrial production of flexible ITO transparent conductive film. Therefore, this study used polyethylene terephthalate (PET) as a substrate to prepare flexible ITO films of different thicknesses. The results show that different film thicknesses and different heat treatment conditions had a great impact on the performance of the ITO film. Well-performing ITO films can be prepared by heating for two minutes at 100 °C with Mayer rods of RDS No. 20. The sheet resistance of the ITO film can reach up to 578 Ω/sq and keep a transmittance of 70%.

## 2    Experiment

### 2.1    Materials

ITO coating slurry (PTT-023) was purchased from Shanghai Huzheng Nano Technology Co., Ltd.; Absolute ethanol was purchased from Suzhou Yihao Chemical Co., Ltd.

### 2.2    Preparation of ITO Film

The ITO slurry dispersed was coated on PET with a Mayer rod. The ITO film was prepared at different thicknesses, different heat treatment temperatures and time, and was subjected to an orthogonal test. Specific film preparation conditions are shown in Table 1.

**Table 1.**  Experimental conditions for preparation of ITO film by coating

| Number variable | Mayer rod model | Heat treatment temperature (°C) | Heat treatment time (min) |
| --- | --- | --- | --- |
| 1 |    | 80 | 1 |
| 2 | 10 | 90 | 2 |
| 3 | 20 | 100 | 3 |
| 4 | 30 | 110 | 4 |
| 5 |    | 120 |    |
| 6 |    | 130 |    |

### 2.3    Equipment and Characterization

Granularity of ITO was characterized by nanosizer (MALVERN, Nano-ZS). Light transmittance and conductivity of ITO films were characterized by UV-Vis spectrophotometer (UV-2501PC) and Double electric test four probe tester (RTS-9).

## 3   Results and Discussion

### 3.1   Dispersion of ITO Paste

Due to the high surface energy of ITO nanoparticles, agglomeration between particles can occur easily during the preparation of the slurry, resulting in uneven dispersion of particles in the slurry system or even sedimentation [1], thereby affecting the electro-optical properties of the transparent conductive film, so preparing to coat an ITO transparent conductive film via a cloth method first requires obtaining an ITO paste that has good dispersion properties. The particle size of the ITO slurry was measured with a particle size ZETA point resistance tester as showed in Fig. 1.
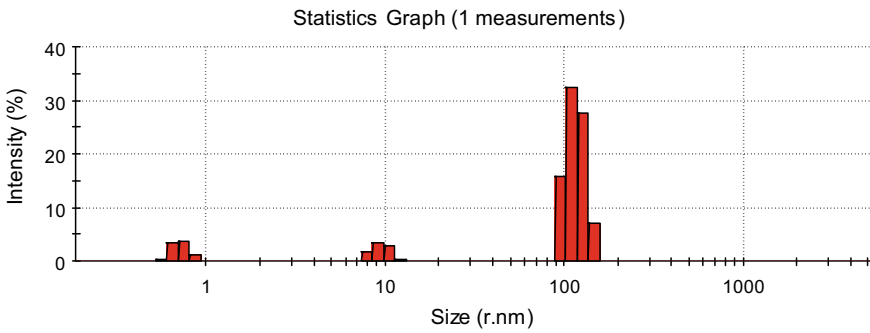


**Fig. 1.**  Particle size distribution of ITO slurry

   Figure 1 shows that the particle size of the ITO paste is concentrated at about 100 nm, and has both a narrow size and uniform distribution. The ITO slurry was left alone for 2 weeks without obvious sedimentation and delamination, indicating that the dispersibility was good.

### 3.2   Electrical Properties of ITO Film

It can be seen from Fig. 2a that when the heat treatment temperature is at 100 °C, the sheet resistance of the ITO film is at its lowest and the conductivity at its best. When the heat treatment temperature is lower than 100 °C, the sheet resistance of the film is higher and then decreases linearly with the increase of the heat treatment temperature. There may be two reasons for this phenomenon: First, as the heat treatment temperature increases, the crystallization characteristics are more and more obvious. As the crystallinity of the film and the mobility of the film carriers increase, the sheet resistance of the film decreases. Second, as the temperature of the heat treatment increases, the oxygen atoms in the film appear to leave the original lattice to form oxygen vacancies,

and the carrier concentration in the film increases with the increased oxygen vacancy solubility, therefore lowering the sheet resistance of the film. However, when the heat treatment temperature is higher than 110 °C, the film resistance gradually increases, rather than decreasing. This may be due to the increase in temperature, which causes cracks to appear on the surface of the film, voids in-between particles, and lower density, resulting in an increase in the sheet resistance of the film.
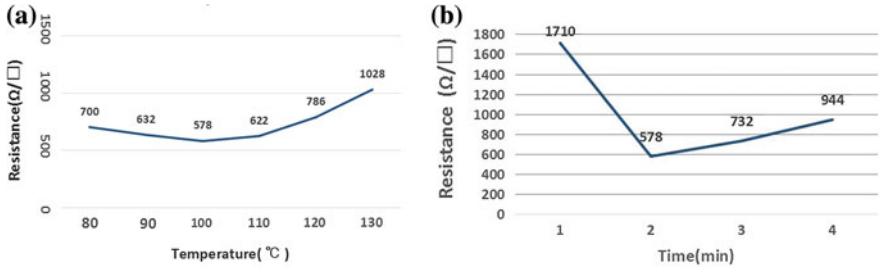


**Fig. 2.** Sheet resistance of ITO film under different temperatures (a) and heating time (b)

It can be seen from Fig. 2b that the ITO film has the lowest sheet resistance and the best conductivity when the heat treatment time is 2 min. When the heat treatment time is 1 min, the sheet resistance of the film is higher, likely because there is no adhesion between the particles, there are many voids and vacancies between the particles, and there is poor compactness. After 2 min of heat treatment, the sheet resistance of the film decreases to 578 $\Omega/sq$, indicating that the particles were bonded while at the same time, the inter-particle voids were reduced, and the electrical conductivity was greatly increased. After 2 min, the sheet resistance of the film gradually increased. The longer heat treatment time caused the surface of the film to gradually crack [2], resulting in a serious deterioration of the film properties.

## 3.3   Optical Properties of ITO Film

The thickness of the coating of different types of Mayer rods is different, and the thickness of RDS No. 10–No. 30 increases sequentially. As can be seen from Fig. 3, the ITO film coated with No. 20 Mayer rod has the best transmittance in the visible light range, the highest is 70%, the ITO film coated with No. 20 Mayer rod has the worst light transmittance. Theoretically, the thicker the film, the more particles of ITO there will be, thereby reducing the light transmittance of the film. However, the ITO film coated with No. 20 Mayer rod has a higher light transmittance than the ITO film coated with No. 10 Mayer rod. The reason may be that while the heat treatment is the same duration, the thin interior of the film layer is more susceptible to heat, and the particle agglomeration is more intense, thus hindering the transmission of light.
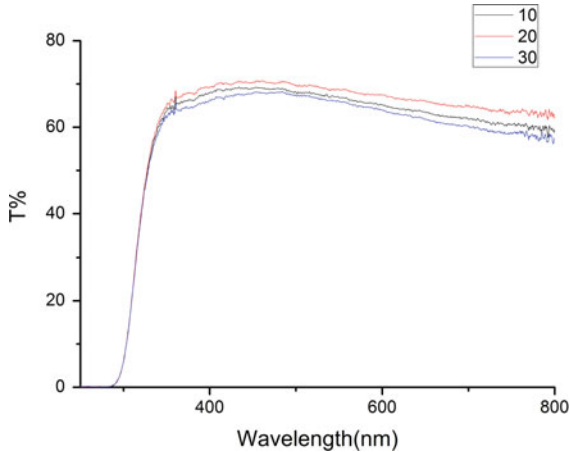
**Fig. 3.** Light transmittance of ITO film with different thickness (2 min, 100 °C)

## 4 Conclusions

The ITO [6] film prepared by the above experimental coating method was coated with RDS No. 20 at a heat treatment temperature of 100 °C and a heat treatment time of 2 min obtained high conductivity and light transmittance. The sheet resistance is 578 Ω/sq, and the light transmittance is 70%. Compared with other preparation methods, although the coating method can reduce preparation costs to some extent, the prepared film has insufficient performance, low quality, and narrow application range. Thus, further research is needed to further improve the photoelectric performance of the film.

## References

1. Gao M, Xin K, Zhang F et al (2009) Effect of heat treatment time on the structure, morphology and properties of ITO films prepared by sol-gel method. Mater Rev 23(1):87–90
2. Yang X (2015) Study on wet preparation and properties of ITO transparent conductive film. New Chem Mater 43(4):76–85
3. Hong SJ, Kim JW, Lim JW et al (2010) Characteristics of printed thin films using indium tin oxide (ITO) Ink. Mater Trans 51(10):1905–1908
4. Liu J, Gan Y, Shengjie P (2005) A transparent conductive ITO film was prepared by a colloid method. Rare Metal Mater Eng 34(7):1169–1172
5. Yang X (2014) Preparation and properties of ITO transparent conductive film. Tianjin University, Tianjin
6. Lan J (2017) Study on preparation of ITO transparent conductive film by ultrasonic spray-microwave pyrolysis. Kunming University of Science and Technology, Kunming

# Effect of Ambient environment on Mechanical Properties of PBAT/PLA Fully-Degradable Packaging Films

Guocheng Han[1], Zhaohui Yu[1], Rui Guo[1], and Guangxue Chen[1,2(✉)]

[1] Shenzhen YUTO Packaging Technology Co., Ltd., Shenzhen, People's Republic of China
chengx@scut.edu.cn

[2] State Key Laboratory of Pulp & Paper Engineering, South China University of Technology, Guangzhou, People's Republic of China

**Abstract.** In order to study the change of mechanical properties of commercial fully-degradable packaging bags under ambient environment, and to provide reference and guidance for the development, the mechanical properties of PBAT/PLA fully-degradable packaging films were test under ambient environment prolonged time. The results show that with the increase of the standing time, the ambient environment has a significant negative impact on the mechanical properties of PBAT/PLA fully-degradable bags: before and after the aging test, the tensile strength of PBAT/PLA fully-degradable films with thickness of 0.015 mm is better than those with thickness of 0.04 mm; in terms of elongation at break and heat seal strength, fully-degradable bags with a thickness of 0.04 mm are superior to those with thickness of 0.015 mm. Furthermore, degradation test in cultivated soil shows that PLA/PBAT film has remarkable higher biodegradation degree than other commercial degradable or non-degradable films, which is completely disintegrated after 6 months. This study provides guidance for the commercial use and handling of fully-degradable packaging films.

**Keywords:** Fully-degradable · Packaging · Ambient environment · Mechanical property · Soil burial

## 1 Introduction

With the increasing environmental protection concerns of governments and ordinary consumers, the researches on biodegradable and recyclable green packaging materials has become a research hotspot in the field of packaging. In particular, traditional disposable plastic packaging materials are gradually being listed to be banned list in developed countries. Fully-degradable packaging materials are meeting unprecedented development opportunities as an important category of packaging solutions in the modern consumer area. Many enterprises and institutions in China and abroad have developed fully-degradable packaging materials and products for different application scenarios, such as food packaging materials [1], foam cushioning materials [2], pulp molded material [3] and so on.

In the process of transportation, storage, shelf placement, etc., packaging materials tend to age, affecting the usage and consumers' impressions. Therefore, it is necessary to test the weatherability of packaging materials. Currently, laboratory-prepared materials and experimental equipment are often used to evaluate and predict the long-term service life of materials from short-term experimental results [4]. However, test in real environment is the most reliable method for determining the weatherability of packaging materials for long-term usage [5]. In this study, we evaluate the changes of mechanical properties of poly (butyleneadipate-co-terephthalate)/polylactic acid (PBAT/PLA) fully-degradable packaging films under real environmental conditions and analyzes the degradation properties of different commercial packaging films, providing reference and guidance for the development of fully-degradable packaging materials, and further promotes environmental-friendly packaging materials.

## 2 Experimental

### 2.1 Reagents and Instruments

Fully-degradable blended modified resin, film grade, is self-made, mainly composed of PBAT, PLA. The three-layer co-extrusion blown film machine, FM3-1700, is produced by Shunde Xiongqi Plastic Machinery Co., Ltd., Foshan. Microcomputer controlled electronic universal testing machine, model E43.104, produced by MTS Industrial Systems (China) Co., Ltd.

### 2.2 Experiment Procedure

The blended modified resin was dried at 60 °C for 24 h before processing. The dryresin was prepared by a three-layer co-extrusion blown film machine to prepare the three-layer co-extruded film. The heating temperature of outer zone 1–5 was 120 °C, 125 °C, 127 °C, 128 °C, 130 °C, and the heating temperature of middle layer was 120 °C, 125 °C, 125 °C, 125 °C, 125 °C, and the heating temperature of inner zone was 120 °C, 125 °C, 125 °C, 130 °C, 130 °C, respectively. The temperature of the splitter zone and the body region was 130 °C. Two different thickness films were obtained by controlling the blown film speed, which were 0.015 mm and 0.04 mm, respectively.

### 2.3 Characterization and Test

Mechanical properties test: tensile strength and elongation at break according to GB/T 1040-2006 standard, tensile speed was 50 mm/min; heat sealing strength according to QB/T 2358-1998 standard. Before the test, all the strips were placed under constant temperature and humidity (23 ± 1 °C, 50 ± 2% RH) for 24 h, and 3 tests were conducted for each test condition. The surface morphology of the PBAT/PLA film was observed using a Pro-X scanning electron microscope (SEM) (Phenom, Netherlands) with accelerating voltage of 5 kV.

Ambient environment aging test: the PBAT/PLA fully-degradable packaging bag samples of different thickness prepared above were placed in a light-shielding

packaging box and placed in ambient environment. The test period was 0, 30, 60, 90, 180, 240 days specifically, from November 2018 to July 2019.

Soil burial test: samples of 10 cm * 10 cm self-made PBAT/PLA degradable film (referred to as "YT film"), ordinary PE film (referred to as "SF film"), and commercial PBAT/PLA/starch film (referred to as "CN film"), commercial PLA film (referred to as "PLA film"), and commercial PBAT film (referred to as "PBAT film"), which were buried in a container of cultivated soil with bury depth of 10 cm. Samples were picked up and observed every 2 months for evaluation.

## 3 Results and Discussions

### 3.1 Tensile Strength Changes of PBAT/PLA Film

Tensile strength is one of the most important mechanical properties and quality evaluation indicators for packaging films. Figure 1 shows the change of tensile strength of PBAT/PLA films under ambient environment. It can be seen from Fig. 1 that with the increase of aging time, the tensile strength of fully-degraded films with different thicknesses shows a downward trend, indicating that with longer exposure time, the aging of the materials and damage of internal structure were deeper. Specifically, comparing Fig. 1a, b, it can be seen that after 240 days of aging, the transverse tensile strength of 0.04 mm-thick film decreased from 18.2 to 11.0 MPa, with a decrease of 39.6%. The longitudinal tensile strength decreased from 20.8 to 12.4 MPa, with a decrease of 40.4%; the transverse tensile strength of the 0.015 mm-thick film decreased from 23.1 to 11.8 MPa, with a decrease of 48.9%, longitudinal tensile strength decreased from 39.3 to 30.6 MPa, with a decrease of 22.1%. It can be seen from the results that the initial and final tensile strength of the 0.015 mm-thick film are higher than thatof0.04 mm-thick film. The aging process is essentially thermal oxygen degradation process. In the early stage of aging, part of the carbonyl group of the polymer resin is oxidized to generate free radicals, which accelerates the degradation of the resin [6]. Microscopically, it results in molecular chain scission of the film, the
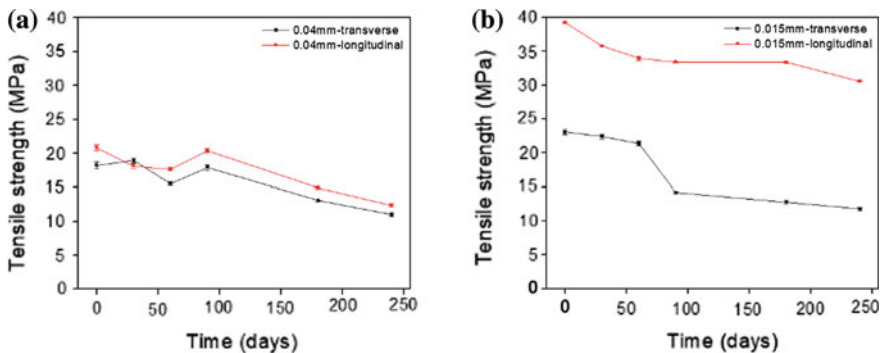


**Fig. 1.** Tensile strength change of PBAT/PLA fully-degradable films prolonged time

destruction of the crystallization zone and the molecule, and the weakening of inter-chain force, illustrating decrease of mechanical strength of the film.

## 3.2    Change in Elongation at Break of PBAT/PLA Film

In general, the greater the elongation at break, the better the toughness of the material, and the smaller the elongation at break, indicating that the material is more brittle. Figure 2 shows the change of elongation at break of PBAT/PLA fully-degradable packaging films under ambient environment. It can be seen from Fig. 2 that with the increase of aging time, the elongation at break of fully-degraded films with different thicknesses shows a downward trend, indicating that with longer aging time, the damage of internal structure of the material was more serious, and the elongation at break worse. Specifically, comparing Fig. 2a, b, it can be seen that after 240 days of aging, the transverse elongation at break of 0.04 mm-thick fully-degradable film is reduced from 597 to 450%, with a decrease of 24.6%, the longitudinal elongation at break decreased from 562 to 284%, with a decrease of 49.5%; the transverse elongation at break of 0.015 mm-thick fully-degradable film decreased from 443 to 129%, with a decrease of 70.9%, and the longitudinal elongation at break decreased from 144 to 82%, with a decrease of 43.1%. It can be seen from the results that the elongation at break of 0.04 mm-thick fully-degradable film is higher than thoseof0.015 mm-thick film during the test. Comparing Figs. 1 and 2, it can be seen that the elongation at break of the film packaging material decreases more than the tensile strength, indicating that the aging leads to a decrease in the flexibility of the material, an increase in brittleness, and may interact with the oxygen radicals present in the air. The chemical bond of the molecular chain leads to the oxidation chain scission of the molecular side chain and the decrease of the stability of the macromolecular network structure [7].
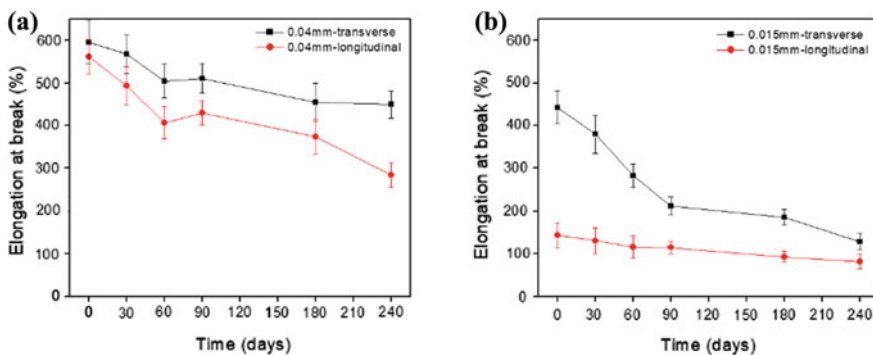


**Fig. 2.**  Change in elongation at break of PBAT/PLA fully-degradable films prolonged time

## 3.3    Morphology of PBAT/PLA Film

Figure 3 is scanning electron micrograph of the microscopic morphology of the PBAT/PLA films before and after aging. Comparing Fig. 3a, b, it can be seen that the
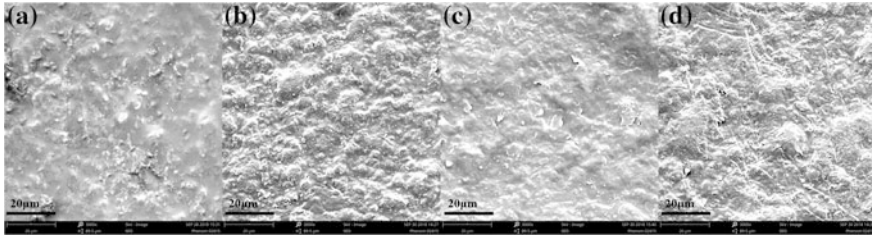
**Fig. 3.** SEM images of 0.04 mm PBAT/PLA films **a** before and **b** after aging, and 0.015 mm PBAT/PLA films **c** before and **d** after aging

newly prepared 0.04 mm-thick PBAT/PLA film has a flat topography, and after 240 days of aging in ambient environment, the microscopic morphology of PBAT/PLA film changed a lot, and there are many protrusions and grooves, and the surface is very uneven. Similar morphology is found in 0.015 mm-thick film, as seen in Fig. 3c, d. It can be speculated that after prolonged aging, the surface of the fully-degraded film is gradually "eroded" by moisture and oxygen in the air, and some depressions may be locally generated. The depressions have a larger specific surface area, which is further oxidized and degraded, and gradually spread, so that the surface of the fully-degradable film is rough, and the pores gradually appear inside, leading to the decrease of mechanical properties such as tensile strength and elongation at break [8].

### 3.4 Morphology of Films in Cultivated Soil Burial Test

Figure 4 shows the appearance changes of various films buried in a cultivating soil environment. It can be seen from Fig. 4a–c that with the increase of the burying time, the SF film made of PE material has no obvious change after 6 months, and the sample is intact. And after two-months' burial, the CN film made of PBAT/PLA/starch shows black plaques of different sizes on the surface, but when the burying time increased there was no significant change in appearance from the outside. However, the YT film made of PBAT/PLA material, whether printed or not, has contracted and disintegrated after degradation for 2 months, and the disintegration degree is gradually higher as the burying time increases. After burying for 6 months, the sample has become a fragment with diameter of less than 5 mm. It can be seen from Fig. 4d, e that the PLA film and the PBAT film have a small range of rupture after 2 months of burying, and the rupture degree increases with prolonged time, but the granules are generally larger and those of YT film, and the degradation effect is not as remarkable as YT film.

## 4 Conclusions

In conclusion, the ambient environment has significant negative impact on the mechanical properties of PBAT/PLA fully-degradable film. Specifically, after the 240 days of aging, the tensile strength of PBAT/PLA films with thickness of 0.015 mm is better than those with thickness of 0.04 mm; in terms of elongation at break, the
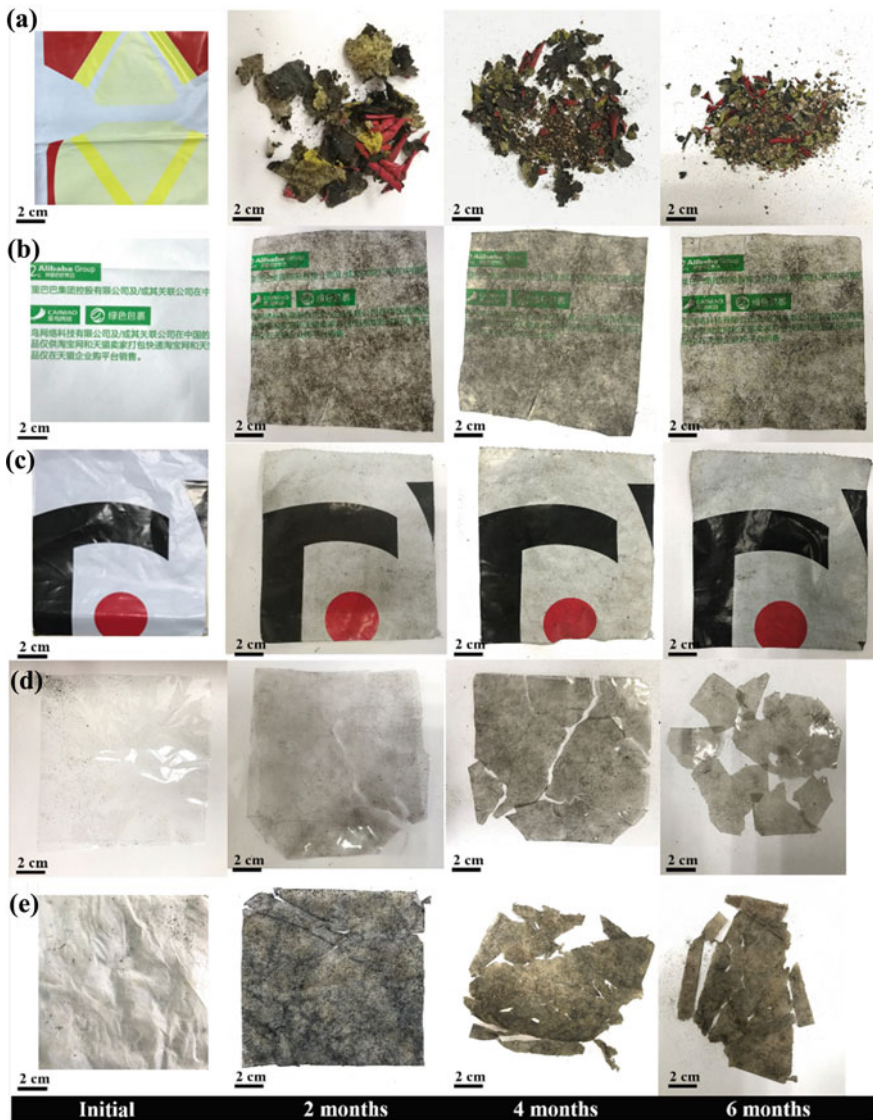
**Fig. 4.** Morphology of **a** YT film, **b** CN film, **c** SF film, **d** PLA film and **e** PBAT film in cultivated soil burial test prolonged time

fully-degradable film with thickness of 0.04 mm is preferred than those with thickness of 0.015 mm. And the PBAT/PLA film has higher biodegradation degree in the soil, with obvious degradation effect, which is completely disintegrated. In contrast, commercial non-degradable PE films and degradable films did not show significant degradation. In summary, for different applications and environmental conditions, attention shall be paid to avoid direct sunlight and high humidity.

# References

1. Panseri S, Martino PA, Cagnardi P et al (2018) Feasibility of biodegradable based packaging used for red meat storage during shelf-life: A pilot study. Food Chem 249:22–29
2. Wang WJ (2013) Cellulose-based biodegradable cushioning packaging material. Appl Mech Mater 446–447:1570–1573
3. Curling SF, Laflin N, Davies GM et al (2017) Feasibility of using straw in a strong, thin, pulp moulded packaging material. Ind Crops Prod 97:395–400
4. Muthuraj R, Misra M, Mohanty AK (2015) Hydrolytic degradation of biodegradable polyesters under simulated environmental conditions. J Appl Polym Sci. https://doi.org/10.1002/APP.42189
5. Emadian SM, Onay TT, Demirel B (2017) Biodegradation of bioplastics in natural environments. Waste Manag 59:526–536
6. Oliveira M, Santos E, Araújo A et al (2016) The role of shear and stabilizer on PLA degradation. Polym Test 51:109–116
7. Patil SS, Misra RDK (2018) The significance of macromolecular architecture in governing structure-property relationship for biomaterial applications: an overview. Mater Technol 33 (5):364–386. https://doi.org/10.1080/10667857.2018.1447266
8. Chinaglia S, Tosin M, Degli-Innocenti F (2018) Biodegradation rate of biodegradable plastics at molecular level. Polym Degrad Stab 147:237–244

# Study on Preparation and Properties of PVA Coating Film Products

Yafang Feng[1], Guorong Cao[1(✉)], Kewen Liu[2], Yun Zhang[3],
Mengke Feng[3], and Ziyao Tang[1]

[1] School of Printing and Packaging Engineering, Beijing Institute of Graphic
Communication, Beijing, China
caoguorong@bigc.edu.cn

[2] Shanxi Yuncheng Plate Making Group Co., Ltd., Yuncheng, Shanxi, China
[3] China Printing Technology Association, Beijing, China

**Abstract.** The water-soluble intermediate temperature PVA film replaces the BOPP film, and the PVA adhesive replaces the EVA hot melt adhesive to prepare a film product based on paper printed matter. PVA adhesive and PVA coating film products were prepared and tested for performance. PVA adhesives and PVA coating film products have excellent performance and meet the requirements of national standard film products.

**Keywords:** PVA adhesive · PVA film products

## 1 Introduction

The paper-plastic coating film process uniformly coats a certain thickness of the adhesive on the film, and then heat-presses with the paper printed matter to form a high value-added printed packaging product with waterproof, wear-resistant and beautifully decorated, mainly used in Paper products such as book publications, folding cartons, paper bags, labels, corrugated boxes, etc. At present, the film used is PE, PVC, PP, PET, etc. These materials have the advantages of good quality, easy processing, low cost, etc., but they cannot be degraded, so that the paper-based printed matter of the film needs pulp separation after pulp separation. This leads to high recycling costs, loss of commercial value and recycling value, resulting in waste of paper resources, formation of large amounts of solid waste, and environmental pollution problems. Commonly used laminating adhesives include EVA hot melt adhesive, Acrylate adhesive, Styrene butadiene rubber adhesive, etc. These adhesives are harmful and not water soluble [1]. PVA film is non-toxic, non-polluting, optical, mechanical and corrosion resistant, water soluble and biodegradable [2]. Therefore, it is imperative to prepare a water-soluble PVA binder and a PVA coating film product using a medium temperature PVA film.

## 2   Experiment and Performance Test

### 2.1   Materials and Instruments

The test materials were medium temperature PVA film, PVA pellet (polyvinyl alcohol 24-99), OP-10, HDI and boric acid. The test equipment: Electric blast drying oven, Shanghai Yiheng Scientific Instrument Co., Ltd.; WGT-S transmittance/haze meter, Shanghai Precision Science Instrument Co., Ltd.; INSTRON high and low temperature environment electronic tensile machine,Instron (Shanghai) Test Equipment Trading Company;Electric thermostatic water bath, Beijing Yongguangming Medical Instrument Co., Ltd.; Electronic balance, Shanghai Huachao Electric Company; Constant temperature and humidity test chamber, Jinan Derrick Instrument Co., Ltd.; Semi-automatic laminating machine; Surface tension value test pen, Shanghai Cuiyuan Electronic Instrument Co., Ltd.

### 2.2   Preparation and Performance Testing of PVA Adhesives

The technical route for preparing PVA adhesive is shown in Fig. 1.
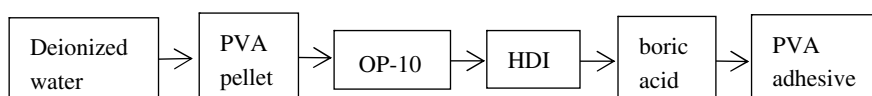


**Fig. 1.**  PVA adhesive preparation technology route

Each group of experiments was added with 2‰ of OP-10 as a surfactant for smooth wetting, boric acid to increase the viscosity of PVA, thickening effect, and HDI as a crosslinking agent. According to the influence factors of PVA adhesive, PVA concentration, HDI concentration and boric acid concentration, the peeling strength of the film product was used as the evaluation index, and the orthogonal test L9 ($3^3$) orthogonal table was designed to test, see Table 1.

**Table 1.**  PVA adhesive orthogonal factor—level table

| Levels | Factors | | |
|---|---|---|---|
| | PVA (%) | HDI (%) | Boric acid (%) |
| 1 | 4 | 0.20 | 0.10 |
| 2 | 5 | 0.25 | 0.20 |
| 3 | 6 | 0.30 | 0.30 |

The lamination test was carried out according to the orthogonal experimental table. The design group and the results are shown in Table 2.

Table 2 shows that the primary and secondary factors affecting the peel strength of PVA adhesive film products are: PVA concentration > boric acid concentration > HDI

**Table 2.** Orthogonal test and result of PVA adhesives

| Number | PVA (%) | HDI (%) | Boric acid (%) | Peel strength (N/cm) |
|---|---|---|---|---|
| 1 | 1 (4) | 1 (0.20) | 1 (0.10) | 0.44 |
| 2 | 1 | 2 (0.25) | 2 (0.20) | 0.39 |
| 3 | 1 | 3 (0.30) | 3 (0.30) | 0.38 |
| 4 | 2 (5) | 3 | 2 | 0.46 |
| 5 | 2 | 1 | 3 | 0.52 |
| 6 | 2 | 2 | 1 | 0.52 |
| 7 | 3 (6) | 1 | 3 | 0.49 |
| 8 | 3 | 2 | 1 | 0.48 |
| 9 | 3 | 3 | 2 | 0.54 |
| $K_{1j}$ | 0.403 | 0.463 | 0.480 | |
| $K_{2j}$ | 0.500 | 0.463 | 0.463 | |
| $K_{3j}$ | 0.503 | 0.480 | 0.440 | |
| R | 0.100 | 0.017 | 0.060 | |

concentration through visual analysis of orthogonal design test results. In the scope of the orthogonal test design, the optimal test protocol for preparing PVA binders meeting the peel strength requirements is PVA concentration of 6%, HDI concentration of 0.3%, and boric acid concentration of 0.1%.

The test verified that the best solution was compared with the best test 9 in the orthogonal table to test the peel strength of the sample. The average peel strength of the optimal group was 0.85 N/cm, which met the standard requirements and was higher than the test group 9. As a result, it is therefore the optimal test protocol.

## 2.3    Preparation of PVA Coating Film Product

The PVA adhesive prepared by the optimal test scheme will show obvious swelling effect on the surface of PVA film at normal temperature and medium temperature. The test uses the biaxial stretching middle temperature (water soluble temperature above 90 °C) PVA film material for film thickness12μm, surface tension 43 dyn/cm$^2$, haze 1.21%, transverse longitudinal heat shrinkage rate 0%, tensile strength 135 MPa. PVA is the coating film process parameters: the film temperature is 85 °C, the film speed is 9 m/min, the film pressure is 10 MPa/cm$^2$, the amount of glue is about 6 g/m$^2$. The printed materials for different formulations of PVA adhesive film were all made of the same type of paper, 5 sheets of coated film prepared for each adhesive, The coated samples were placed for 24 h for performance testing.

## 2.4    PVA Is the Performance Test of Coated Film Products

According to GB/T 27934.1-2011, the performance of PVA coating film products is tested.

- Appearance, the surface of the coated product is smooth and flat, no air bubbles appear between the printed matter and the PVA film, and after being placed at room temperature for 24 h, the curl appears in the direction of the sizing, which may be caused by the film under heating and pressure conditions. The internal stress is greater than the internal stress caused by the paper.
- The heat shrinkage rate and the heat shrinkage rate of the coated product are 0.01%. Due to the large moisture content fraction in the PVA adhesive, the PVA film and the printed matter have moisture absorption during the film coating process.
- Stability, the film product is placed in a constant temperature and humidity test chamber (temperature is 23 °C, relative humidity is 50%) for 24 h, no quality problems such as foaming, peeling, swelling, chromatic aberration and bonding The strength is in line with the relevant requirements of the national standard.
- Water-soluble, the film-coated products are placed in an aqueous solution of 90 °C, and the PVA film and the PVA binder and the paper printed matter have better dissolution effects, thereby reducing the recycling cost of the paper product caused by the traditional paper-plastic separation. At normal temperature, the high-temperature PVA film is almost insoluble in water, and thus, the PVA film-coated product has excellent performance in a normal temperature environment.

## 3   Conclusions

Preparation of PVA adhesive and PVA coating film products, and tested their properties. The results show that the PVA binder ratio is PVA concentration of 6%, HDI concentration is 0.3%, boric acid concentration is 0.1%, that is, the peel strength of the coated film product reaches 0.85 N/cm; The appearance, heat shrinkage, stability and water solubility of PVA coating film products can meet the performance requirements of national standards. Therefore, A medium temperature PVA film and a prepared PVA binder can be used as a substrate for a paper print.

## References

1. Meiqi Y, Preparation and properties of PVA based film products
2. Fayong L, Dong X, Mingzhou C et al (2018) Review of water-soluble polyvinyl alcohol films. Guangdong Chem Ind

# Preparation and Property Analysis of Natural Antibacterial Agents-Magnolol and Chitosan-Based Antibacterial Wrapping Paper

Yan Zhang[1,2], Deshui Li[1], and Qingbao Wei[1(✉)]

[1] Henan University of Animal Husbandry and Economy, Zhengzhou, China
yanzhang12@yeah.net, zzmzwqb@163.com
[2] Zhengzhou Sanquan Foods Co., Ltd., Zhengzhou, China

**Abstract.** In this paper, chitosan and magnolol and their compound were used as antibacterial agents, and the antibacterial wrapping paper was prepared by coating these on paper surface to compare the antibacterial effects of chitosan and magnolol, The preservation effect of antibacterial wrapping paper on strawberry is studied too. The results showed that when the compound ratio of magnolol and chitosan was 2:1, the antibacterial wrapping paper functions the best preservation effect on strawberry.

**Keywords:** Magnolol · Chitosan · Antibacterial wrapping paper

## 1 Introduction

Natural antibacterial agent refers to antimicrobial active substances isolated from natural organisms, including among others chitosan, plant essential oil and magnolol. Wrapping paper made of natural antibacterial agents boasts advantages of low cost and environmental protection [1]. The development and application of wrapping paper has become a hotspot in the field of food packaging.

## 2 Material and Method

### 2.1 Instruments and Materials

The selected small coating machine was ZY-TB-B from Shandong Zhongyi Instrument Co., Ltd.; the used texture analyzer was CT-3 from Brookfield Ltd., USA.

Chitosan was purchased from Shandong Luhai LanSheng Biotechnology Co.,Ltd; magnolol bought from Zhang Zhongjing Pharmacy; coated paper (300 g/m2) provided by zhengzhou Chenghui Paper Products Co., Ltd.; PDA culture medium was purchased from Beijing Aoboxing Biotech Co., Ltd.

## 2.2 Experimental Method

### 2.2.1 Preparation of Magnolia Officinalis Extract

Bacteriostatic substances in magnolia officinalis were extracted by ultrasound-assisted method. Weigh 40 g filtered magnolia officinalis powder and place them in a conical flask, then add 100 mL 90% (by volume) ethyl alcohol, then expose the solution to 40 min of ultrasound, by centrifugation extract the supernatant, and concentrate the same to 40 mL magnolia officinalis extract by rotary evaporation.

### 2.2.2 Preparation of Antibacterial Wrapping Paper

Add magnolia officinalis extract to 10% PVA solution, with a mass ratio of 8%. A certain mass of chitosan was weighed and added to acetic acid solution, and then the solution was stirred in a water bath at 60 °C until chitosan was completely dissolved. The mass fraction of chitosan in coating solution was 4%. Chitosan powder of certain mass and magnolia officinalis extract of certain volume were added into 10% PVA aqueous solution, and the coating solution was stirred in a water bath at 60 °C until chitosan powder and magnolia officinalis extract were completely dissolved. The proportions of chitosan and magnolia officinalis extract were respectively of 1:1, 1:2 and 2:1.

The coating machine is used to respectively apply thickness 0.02 mm the said coating solution onto the original paper, then place the coated paper in the oven at 102 °C for 1 min, take the paper out, and spread it on the table for natural dry by air [2]. The number and the corresponding antibacterial coating mix proportion of antibacterial wrapping paper are as shown in Table 1.

**Table 1.** Coated antibacterial wrapping paper

| Type of antibacterial wrapping paper | Coating parameters |
|---|---|
| Blank control | No |
| No. 1 | 4% chitosan antibacterial wrapping paper |
| No. 2 | 8% magnolol antibacterial wrapping paper |
| No. 3 | Antibacterial wrapping paper with 1:1 ratio of magnolia officinalis extract to chitosan |
| No. 4 | Antibacterial wrapping paper with 1:2 ratio of magnolia officinalis extract to chitosan |
| No. 5 | Antibacterial wrapping paper with 2:1 ratio of magnolia officinalis extract to chitosan |

### 2.2.3 Test of the Bacteriostasis of Antibacterial Agent

With forceps clip a small amount of penicillium to the center of the agar culture dish, then around the penicillium place three sterile filter paper pieces, prepare three such culture dishes, drip chitosan onto sterile filter paper pieces in the first dish, magnolia officinalis extract onto sterile filter paper pieces in the second dish, and use the third

culture as black control group, after a certain period of time observe the bacteriostatic circle size to determine the bacteriostasis effect.

### 2.2.4 Study on the Preservation Effect of Antibacterial Wrapping Paper on Strawberry

Make the antibacterial paper into a carton and place strawberry into the carton, then put the carton into a 25 °C incubator and test the weight loss and hardness change of strawberries.

The weight loss ratio is calculated as follows:

$$Weightloss\ ratio = \frac{weightloss\ during\ storage}{weight\ before\ storage} \times 100\% \tag{1}$$

Texture analyzer, TA39 probe and TA-MTP fixture were used to measure the hardness of strawberry, with load at the trigger point set as 4 g, the measuring speed being 2 mm/s, and the number of cycles being 2. The same group of samples was measured 6 times, and the average value of data was calculated and taken as the hardness value of strawberry.

## 3 Results and Discussion

### 3.1 Bacteriostasis Effect of Antibacterial Agent

As shown in Fig. 1, the filter papers of the blank control group were covered with penicillium; the filter papers with 4% chitosan and those with 8% magnolia officinalis extract had no penicillium on the surface, and there was a certain range of bacteriostatic circle around them, indicating that the two kinds of liquid both had certain inhibitory effects on penicillium.
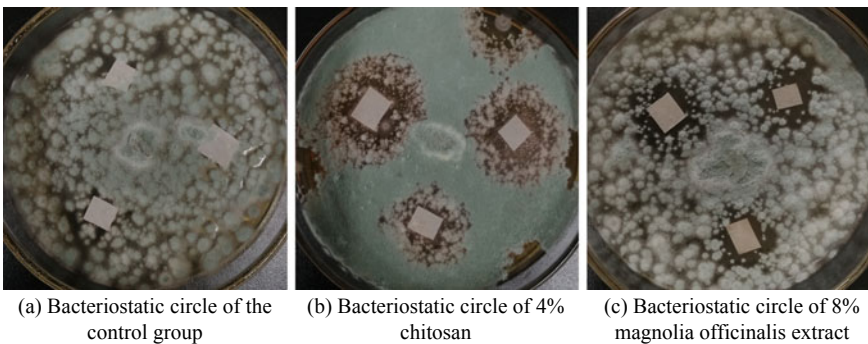


| (a) Bacteriostatic circle of the control group | (b) Bacteriostatic circle of 4% chitosan | (c) Bacteriostatic circle of 8% magnolia officinalis extract |

**Fig. 1.** Bacteriostatic circle contrast

## 3.2  Preservative Effect of Antibacterial Wrapping Paper on Strawberry

### 3.2.1  Effect of Antibacterial Wrapping Paper on Weight Loss Ratio of Strawberry

Figure 2 shows that the weight loss ratio of strawberries in different cartons all increase with the storage time; the weight loss ratios of strawberries packed in cartons with antibacterial coating are all less than those packed in carton made of blank control paper [3]; the weight loss ratio of strawberries in No. 5 antibacterial wrapping paper carton is the lowest, that of strawberries in No. 3 antibacterial wrapping paper carton and that of strawberries in No. 4 antibacterial wrapping paper carton are both higher than the same of strawberries respectively in No. 1 and No. 2 antibacterial wrapping paper cartons, this suggests that when antibacterial compound is used, after the concentration of chitosan reaching a certain value, continued increase of chitosan does not improve strawberry preservation effect [4], therefore, the concentration of chitosan shall draw due consideration in compound mix proportion.
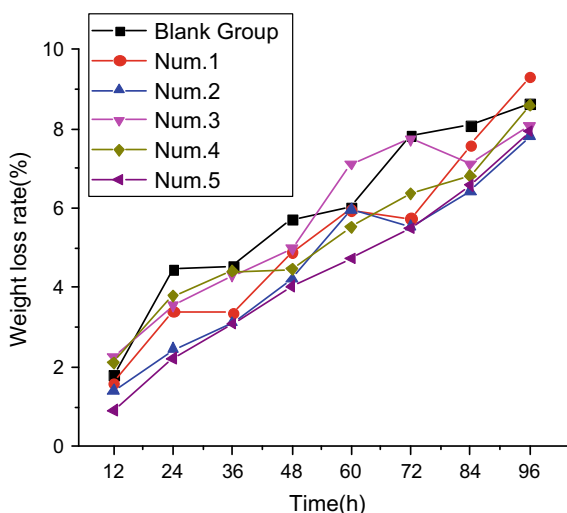


**Fig. 2.**  Strawberry weight loss rate

### 3.2.2  Effect of Antibacterial Wrapping Paper on the Hardness of Strawberry

As can be seen from Fig. 3, the hardness of strawberries in the blank control group was the lowest, while the hardness of strawberries in No. 5 antibacterial wrapping paper decreased slowly during storage, slightly higher than that of strawberries in other groups. It can also be seen that the hardness of strawberries preserved respectively by No. 3 and No. 4 packaging papers is lower than that of strawberries separately in No. 1 and No. 2 packaging papers, which indicates that when the antibacterial compound is used, there are certain requirements on the concentration of chitosan [5], and continued increase of chitosan concentration will not always improve the preservation effect on strawberry.
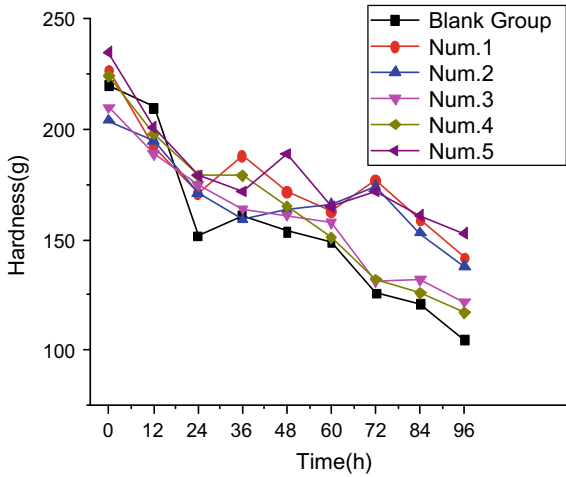
**Fig. 3.** Strawberry hardness

## 4   Conclusions

In this paper, chitosan and magnolol and their compound were used as antibacterial agents, and the bacteriostasis effects of chitosan and magnolol as well as the preservation effect on strawberry of five kinds of antibacterial wrapping papers were compared and analyzed. Compared with the blank control group, both chitosan and magnolia officinalis extract had obvious bacteriostatic effects. Functional cartons prepared by using the two alone or together all extended the shelf life of strawberries to some extent, and the preservation effect was best when the compound ratio of magnolia officinalis to chitosan was 2:1.

## References

1. Yazhu Z, Xiaoxiu H, Jie M et al (2018) Research status and development trend of antibacterial food packaging paper. Packag Eng 39(381)(15):98–104
2. Fang Hu, Xuying Li, Zeng Xu (2015) Preparation and property study of chitosan-montmorillonite composite antibacterial coated paper. China Paper Ind 34(6):1–5
3. Guangfa L, Zhengjian Z, Liying Y et al (2018) Effects of antibacterial wrapping paper of magnolia officinalis extract on shelf life of cheese. Packag Eng 31–33
4. Xihong Liu, Jiuyin Pang (2017) Study on antibacterial properties of chitosan treated food wrapping paper. Forest Prod Ind 6:22–24
5. Rollinim M, Caprettig G, et al (2017) Propolis and chitosan as antimicrobial and polyphenols retainer for the Development of paper based active packaging materials. Food Packag Shelf Life 14:75–82

# Novel Functional Material Technology

# Superhydrophobic Materials Constructed by Modified Nano-SiO₂ Hybrid Low-fluorine Epoxy Polymer and Their Properties

Chengmin Hou[✉], Na Li, and Xiaolin Zhang

School of Printing Packaging Engineering and Digital Media Technology,
Xi'an University of Technology, Xi'an, China
`1042067175@qq.com`

**Abstract.** Most of the preparation procedures for super-hydrophobic materials are complicated, and the durabilities are poor. In this paper, a low-fluorinated epoxy polymer poly(glycidyl methacrylate-random-trifluoroethyl methacrylate) (P(GMA-$r$-TFEMA)) was prepared by conventional radical polymerization method, and hybridized with amino-modified nano-SiO₂ particles. This solution was used to construct super-hydrophobic surface on cotton cloth. The optimum construction conditions were investigated by changing the P(GMA-$r$-TFEMA) concentration, the immersion time, and the drying time. The performance were characterized by static contact angle (CA). The water contact angle is up to $153^{\circ} \pm 3^{\circ}$, rolling angle is low to $35^{\circ} \pm 3^{\circ}$, and resistance of anti-abrasion, acid and alkali are high.

**Keywords:** Low-fluorine epoxy · Modified nano-SiO₂ particles · Super-hydrophobic · Cotton · Solution impregnation

## 1 Introduction

According to the spreading degree of the liquid on the solid surface, the solid surface of the material is divided into hydrophilic, hydrophobic, oleophobic, super-hydrophobic and super-oleophobic [1]. If the contact angle (CA) is generally greater than 150°, and the rolling angle is less than 10°, the surface is super-hydrophobic [2]. This surface has pollution resistance, corrosion resistance, anti-ice reduction, and anti-fog performance. And it plays an important role in the fields of chemical engineering, biology, medicine and environment.

At present, there are many methods for preparing super-hydrophobic materials, such as phase separation method [3], electrospinning method [4], sol-gel method [5], surface micromachining method, self-assembly method [6], nanospheres and organic polymer hybrid method [7], plasma method [8], and impregnation method [9]. However most of the preparation procedures are complicated, and the durabilities are poor.

This study used traditional free radical polymerization to synthesize low-fluorine epoxy polymer P(TFEMA-$r$-GMA), and hybridized with KH550 modified nano-SiO₂ to synthesize hydrophobic materials. Cotton fabrics were used as substrates to explore the optimal construction conditions of the hydrophobic materials. The chemical

stability, abrasion resistance and self-cleaning of the hydrophobic cotton fabric prepared under optimal construction conditions were characterized.

## 2   Experimental

### 2.1   Materials and Experimental Instruments

Sodium sulfite ($NaHSO_3$), tetrahydrofuran (THF), $\gamma$-aminopropyltriethoxysilane (KH550), and triethylamine (TEA), were purchased from Tianjin Fuchen Chemical Reagent Factory. Glycidyl methacrylate (GMA), trifluoroethyl methacrylate (TFEMA), azobisisobutyronitrile (AIBN) and nano-$SiO_2$ (approximately 20–30 nm) were purchased from Aladdin Technology Co., Ltd.

### 2.2   Preparation of Super-Hydrophobic Materials via Modified Nano-$SiO_2$ and P(TFEMA-$r$-GMA)

1 g of nano-$SiO_2$ was dispersed in 50 mL 75% ethanol. 1 g of KH550 was added dropwise and reacted for 5 h with reflux phenomenon. The modified nano-$SiO_2$ was washed and centrifuged in ethanol, and dried at 130 °C for 3 h.

GMA (3.116 g, 21.9 mmol), TFEMA (0.986 g, 5.9 mmol), initiator AIBN (0.2282 g, 1.4 mmol) and catalyst $NaHSO_3$ (0.1446 g, 1.4 mmol) were added into 5 mL THF in a flask and then sealed. The mixture was purged with nitrogen for 30 min and then reacted at 65 °C for 2 h. The P(TFEMA-$r$-GMA) was purified by $n$-hexane purification, and dried at 50 °C. The FTIR (FTIR-8400S, Japan Shimadzu) was used to analyze the structure of modified nano-$SiO_2$ and polymer P(TFEMA-$r$-GMA).

Different amounts of polymer P(TFEMA-$r$-GMA) (10 mg, 20 mg, 30 mg, 50 mg, 100 mg) was dissolved in 10 mL THF. 1 mg modified nano-$SiO_2$ was added and magnetically stirred for 10 h to prepare hydrophobic solution. The 2 cm * 2 cm substrates were immersed in the hydrophobic solutions with different polymer concentration. Different construction factors were used to prepare hydrophobic surfaces on cotton, such as polymer concentration (0.1%-1%), impregnation time (3–11 h), drying time (2–10 h) and drying temperature (80–130 °C). 5–10 μL deionized water droplets were used to measure the contact angles on the Static Drop Contact Angle/Interface Tension Tester (JC2000A, Shanghai Zhongchen).

### 2.3   Performance Characterization of Super-Hydrophobic Cotton

The resistance of obtained cotton for acid and alkali conditions were measured by 0.5 mg/mL citric acid solution, 0.5 mg/mL sodium chloride solution and 0.5 mg/mL sodium citrate solution. Additionally, 0.5 mg/mL detergent aqueous solution was used to test the washing durability. The morphology of cotton was studied on the Scanning Electron Microscope (SU800 type, Hitachi, Japan).

# 3 Results and Discussion

## 3.1 Characterization of KH550 Modified Nano-SiO$_2$ and P(TFEMA-*r*-GMA)

The structure of KH550 modified nano-SiO$_2$ was characterized by FTIR and TGA, shown in Fig. 1. The peaks at 3444 cm$^{-1}$ represented the stretching vibration peaks of nano-SiO$_2$. After modification by KH550, the –OH stretching vibration peak near 3527 cm$^{-1}$ decreased. The peaks at 1557 and 696 cm$^{-1}$ were the deformation vibration peak of –NH$_2$ group. It indicates that KH550 was successfully grafted onto the nano-SiO$_2$. From Fig. 1b, nano-SiO$_2$ only degrades about 8%, and KH550 modified nano-SiO$_2$ degraded about 50%. They showed that a large amount of KH550 grafted on the nano-SiO$_2$.
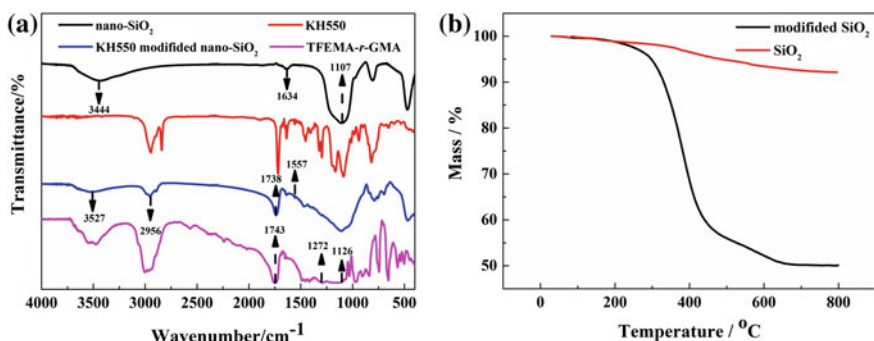


**Fig. 1.** FTIR spectra and TGA curves of KH550 modified nano-SiO$_2$ and P (TFEMA-*r*-GMA)

The structure of polymer P(TFEMA-*r*-GMA) was characterized by FTIR. The peak near 945 cm$^{-1}$ was the absorption vibration peak of the epoxy group of P(TFEMA-*r*-GMA). The spectral bands at 1160 and 1760 cm$^{-1}$ represented the stretching vibration peaks of C–O and C=O groups. The peaks at 1126 and 1272 cm$^{-1}$ were a characteristic peak of –CF$_3$.

## 3.2 Construction of Super-Hydrophobic Cotton Surface

The super-hydrophobic surfaces on cotton were constructed using P(TFEMA-*r*-GMA) and aminated nano-SiO$_2$ under different conditions and the results were shown in Fig. 2a. It showed that all the water contact angles can reach 130° ± 2°, and some of them were up to 152° ± 2°, and the water rolling angle was at least 35° ± 3°. The best preparation conditions for super-hydrophobic cotton fabric surface were as follows: polymer concentration was 2 mg/mL, the impregnation time was 7 h and the drying time was 6 h. As shown in the Fig. 2b, the surface of the hydrophobic material compared with pristine cotton had a bright water film due to the reflection and refraction of light in water. It was called the "silver mirror phenomenon" [10].
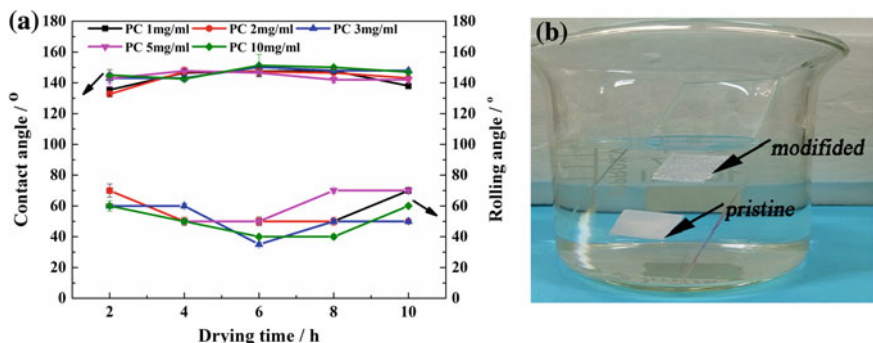
**Fig. 2.** The effect of different construction conditions on the super-hydrophobic surface of cotton cloth and silver mirror phenomenon

### 3.3    Super-Hydropboic Properties of Super-Hydrophobic Cotton

The load-bearing abrasion resistance of the hydrophobic modified cotton surface was explored and the results were shown in Fig. 3a. As the abrasion cycle increases, the water contact angles showed a downward trend. After 15 abrasion cycles, the water contact angle decreased from $150° \pm 2°$ to $100° \pm 2°$, and the water rolling angle increased from $16° \pm 2°$ to $90° \pm 3°$.

The chemical resistances were investigated by immersing in different pH solutions as shown in Fig. 3b. The cotton fabric surface has a good super-hydrophobic effect and the resistance of acid and alkali. However, the water contact angle decreased from $152° \pm 2°$ to $140° \pm 2°$, and the water rolling angle increased from $8° \pm 2°$ to $14° \pm 2°$ after detergent washing.

The self-cleaning effect of the hydrophobic and native cotton cloth were shown in Fig. 3c. The surface of hydrophobic modified cotton fabric was cleaned gradually with the addition of deionized water. But the nano-carbon powder can not be removed by water and adhered to the surface of native cotton.
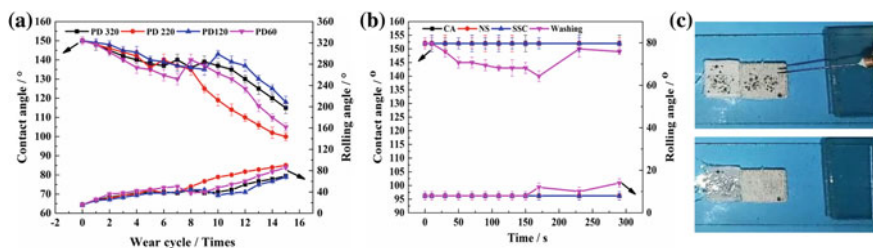


**Fig. 3.** Load-bearing abrasion, chemical stability, and self-cleaning properties of super-hydrophobic modified cotton

### 3.4 SEM of Super-Hydrophobic Materials

The super-hydrophobic cotton fabric surface was investigated by SEM and the results were shown in Fig. 4. As shown in the Fig. 4a, the fiber surfaces of the pristine cotton fabric were smooth. But the super-hydrophobic modified cotton fabric surfaced were piled up with particles and overlapped with each other, and there were wrinkles, pits and protrusions as shown in Fig. 4b. The surface was similar to "island" or "tree Raspberry-like" structure.
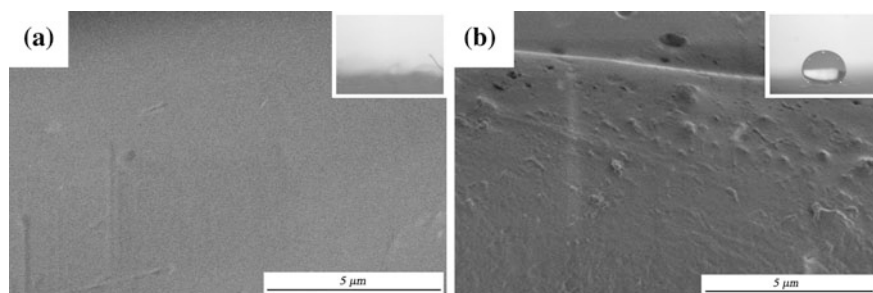


**Fig. 4.** SEM image of cotton fabric before and after super-hydrophobic treatment

## 4 Conclusion

In this study, a low-fluorescence epoxy polymer P(TFEMA-$r$-GMA) was prepared by conventional radical polymerization. KH550 modified nano-SiO$_2$ was mixed with the polymer to prepare hydrophobic materials. The optimum construction conditions for super-hydrophobic cotton fabrics were polymer concentration of 2 mg/mL, immersion time of 7 h, and drying time of 6 h. The water contact angle of the hydrophobic cotton surface was $152° \pm 2°$ at the maximum, and the water rolling angle was at least $35° \pm 3°$. The surface of the cotton fabric had good self-cleaning effect, good hydrophobic effect and a certain acid and alkali resistance.

## References

1. Ellinas K, Tserepi A, Gogolides E (2017) Durable superhydrophobic and superamphiphobic polymeric surfaces and their applications: a review. Adv Coll Interface Sci 250:132–157
2. Wang J, Wang K, Zheng Y, Jiang L (2010) Relationship between surface nanostructure and wettability of lotus leaves. J Chem 31(8):1596–1599
3. Gao S, Dong X, Huang J, Li S, Li Y, Zhong C et al (2018) Rational construction of highly transparent superhydrophobic coatings based on a non-particle, fluorine-free and water-rich system for versatile oil-water separation. Chem Eng J 333:621–629

4. Ganesh VA, Dinachali SS, Nair AS, Ramakrishna S (2013) Robust superamphiphobic film from electrospun tio2 nanostructures. ACS Appl Mater Interfaces 5(5):1527–1532
5. Shanshan J, Haibo C, Sha L, Yan Q, Songlin D, Ning Y et al (2018) One-step approach to prepare superhydrophobic wood with enhanced mechanical and chemical durability: driving of alkali. Appl Surf Sci 455:115–122
6. Chen FF, Zhu YJ, Xiong ZC, Sun TW, Shen YQ (2016) Highly flexible superhydrophobic and fire-resistant layered inorganic paper. ACS Appl Mater Interfaces 8(50):34715–34724
7. Xiong D, Liu G, Duncan EJS (2012) Diblock-copolymer-coated water- and oil-repellent cotton fabrics. Langmuir 28(17):6911–6918
8. Yang J, Pu Y, Miao D, Ning X (2018) Fabrication of durably super-hydrophobic cotton fabrics by atmospheric pressure plasma treatment with a siloxane precursor. Polymers 10(4): 460
9. Yang M, Chen X, Lin H, Han C, Zhang S (2018) A simple fabrication of superhydrophobic wood surface by natural rosin based compound via impregnation at room temperature. Eur J Wood Wood Prod 76(5):1417–1425
10. Zou H, Lin S, Tu Y, Li F, Hu J, Liu G et al (2016) An aqueous process for durable superamphiphobic diblock copolymer coatings on fabrics. Adv Mater Interfaces 3(8): 1500693

# Synthesis and Characterization of Silver Nanowires Prepared by Polyol Method

Qiankun Zhang, Linjuan Yan, Guangxue Chen[(✉)], and Qing Wang

Key Laboratory of Pulp and Paper, South China University of Technology,
Guangdong, China
chengx@scut.edu.cn

**Abstract.** Uniform silver nanowires (AgNWs) were synthesized by polyol method, and the effects of different reaction conditions on the growth of AgNWs were discussed. Specifically, uniform AgNWs were prepared using glycerol and diethylene glycol (DG) as alcohol solution, sodium chloride (NaCl) as metal salt and poly(vinyl pyrrolidine) (PVP) as inducer. The effects of alcohol solution with different volume ratios, molar ratio of PVP to $AgNO_3$ and average molecular weight of PVP on the preparation of AgNWs were discussed in detail. The as-synthesized AgNWs are characterized by scanning electron microscopy (SEM). The results show that AgNWs with good aspect ratio can be prepared by changing the volume of glycerol and DG, the molar ratio of PVP to $AgNO_3$ and the average molecular weight of PVP. The optimal process parameters are as follows: the volume ratio of glycerol to DG is 1:1, the molar ratio of PVP to $AgNO_3$ is 4:1 and the average molecular weight of PVP is 40 000.

**Keywords:** Polyol method · Silver nanowires · Preparation parameters

## 1 Introduction

Considering excellent optical and electrical properties, uniform AgNWs have great application prospects in the field of printing electronics [1]. The morphology and structure of AgNWs are related to the preparation methods which mainly divided into template [2], wet chemical [3], electrochemical [4], and polyol process [5]. In terms of cost, environmental protection and simple process, polyol process has gradually become a promising method to prepare uniform AgNWs [6]. In the presence of ethylene glycol and PVP, the strategy and growth mechanism of large-scale synthesis of AgNWs by polyol method were first reported by Sun et al. [7]. Jia et al. explored a method for large-scale synthesis of polycrystalline AgNWs with glycerol and ethylene glycol as co-solvents [8]. Li et al. reported a synthesis of AgNWs through glycerol mediated polyol process with the assistance of PVP and NaCl [9]. Meanwhile, PVP can passivate the {100} planes of multiply-twinned particles (MTPs) and prevent the silver atoms from nucleating at these locations [10]. Ran et al. report the synthesis of AgNWs of high aspect ratio with a mixture of PVP molecules of different molecular weight [11]. However, there is a lack of research on the process parameters of synthesizing uniform AgNWs based on glycerol and DG with a certain volume ratio.

In this work, uniform AgNWs were synthesized in the presence of PVP and NaCl using glycerol and DG as mixed reductants and solvent. We explore the effects of glycerol and DG with different volume ratios on the morphology and structure of AgNWs. After that, based on the optimal volume ratio, we examined effects of the molar ratio of PVP to AgNO$_3$ and the average molecular weight of different PVP.

## 2    Experimental

### 2.1    Materials

Poly(vinyl pyrrolidone) (PVP, Mw: 10 000, 40 000, 58 000, 130 000) was obtained from Boao Biotechnology Co, Ltd. Silver nitrate (AgNO$_3$, AR) was purchased from Sinopharm Chemical Reagent Co., Ltd. Glycerol (impurity > 99%) was acquired from Aladdin Chemistry Co, Ltd. Diethylene glycol (DG, AR) was gained from China Pharmaceutical Group Chemical Reagents Co., Ltd. Sodium chloride (NaCl, AR) was obtained from Aladdin Chemistry Co. Ltd. All the water used was deionized water. All the above reagents were pure analyzers and were not further treated before use.

### 2.2    Preparation and Characterization

In the typical synthesis, a certain amount of glycerol and DG was added to a round-bottom flask and stirred evenly at room temperature. Subsequently, the homogeneous mixture is transferred to the oil bath pan. Appropriate amount PVP (0.103 ∼ 0.619 g) was dissolved in the mixed solution and stirred gently at 80 °C to form a homogeneous solution. After cooling to room temperature, 0.158 g AgNO$_3$ powder was added to the solution. Meanwhile, a mixed solution containing 0.0059 g NaCl, 0.05 mL of deionized water and 1 mL of glycerin (or DG) was gently stirred and heated. When the solution temperature goes from room temperature to 210 °C, stop heating immediately and return to room temperature. The prepared samples were diluted with deionized water (ρ ∼ 18 MΩ cm) and centrifuged three times at 5000 rpm for 3 min to remove excess PVP and polyols residue. The final samples were redispersed in deionized water for further characterization. The morphology and distribution of AgNWs were observed by scanning electron microscopy (SEM, Zeiss Merline, Germany).

For convenience, the volume of glycerol and DG are simplified as V$_1$ and V$_2$, respectively. The total volume remains constant, increasing the volume of DG while reducing the same volume of glycerol at the same time. The preparation conditions of samples are shown in Table 1.

**Table 1.** Preparation conditions of AgNWs

| Sample | AgNO3 (g) | PVP (g) | PVP (Mw) | NaCl (g) | Glycerl (ml) | DG (ml) | Temperature (°C) |
|--------|-----------|---------|----------|----------|--------------|---------|------------------|
| 1 | 0.158 | 0.586 | 58 000 | 0.0059 | 20 | 0 | 210 |
| 2 | 0.158 | 0.586 | 58 000 | 0.0059 | 15 | 5 | 210 |
| 3 | 0.158 | 0.586 | 58 000 | 0.0059 | 10 | 10 | 210 |
| 4 | 0.158 | 0.586 | 58 000 | 0.0059 | 5 | 15 | 210 |
| 5 | 0.158 | 0.586 | 58 000 | 0.0059 | 0 | 20 | 210 |
| 6 | 0.158 | 0.103 | 58 000 | 0.0059 | 10 | 10 | 210 |
| 7 | 0.158 | 0.206 | 58 000 | 0.0059 | 10 | 10 | 210 |
| 8 | 0.158 | 0.413 | 58 000 | 0.0059 | 10 | 10 | 210 |
| 9 | 0.158 | 0.619 | 58 000 | 0.0059 | 10 | 10 | 210 |
| 10 | 0.158 | 0.413 | 10 000 | 0.0059 | 10 | 10 | 210 |
| 11 | 0.158 | 0.413 | 40 000 | 0.0059 | 10 | 10 | 210 |
| 12 | 0.158 | 0.413 | 58 000 | 0.0059 | 10 | 10 | 210 |
| 13 | 0.158 | 0.413 | 130 000 | 0.0059 | 10 | 10 | 210 |

## 3 Results and Discussion

### 3.1 Effects of Different Volume Ratios of Glycerol and DG

Figure 1 shows the SEM images of AgNWs prepared with different volume ratios of glycerol to DG. More AgNWs and silver nanoparticles with different sizes ($V_1$: $V_2$ = 20:0) were obtained when only glycerol was present in Fig. 1a. When a certain volume of DG was added in the reaction system to replace glycerol, the content of AgNWs increased significantly, as shown in Fig. 1b ($V_1$:$V_2$ = 5:15). Uniform AgNWs were obtained when the volume of DG increased to 10 ml (Fig. 1c, $V_1$:$V_2$ = 10:10). However, in the case of the volume of DG add to 15 mL, as shown in Fig. 1d
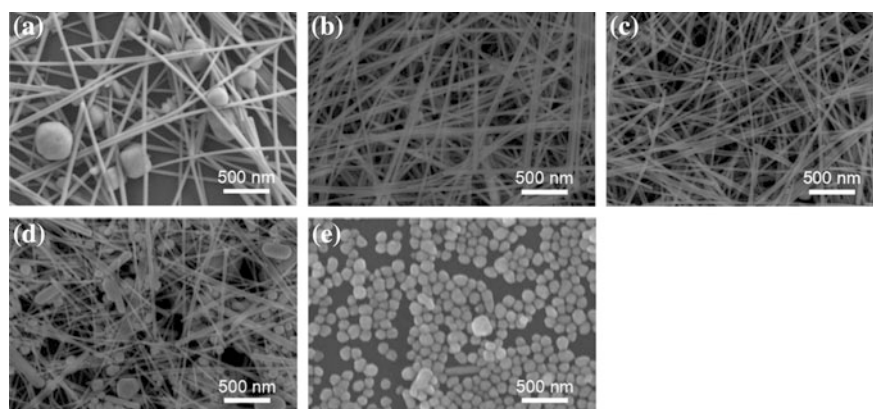


**Fig. 1.** SEM images of AgNWs prepared with different volume ratios of Glycerol to DG, **a** 20:0, **b** 15:5, **c** 10:10, **d** 5:15, **e** 0:20

(V$_1$:V$_2$ = 15:5), many silver nanoparticles and AgNWs are created. Under the condition of DG as reductant without glycerol, almost all the products are silver nanoparticles as shown in Fig. 1e (V1:V2 = 0:20).

Therefore, glycerol and DG with different volume ratios have important effects on the morphology of AgNWs. Compared with DG, glycerol has more hydroxyl groups and stronger reduction ability at high temperature. In addition, glycerol has a higher viscosity (945 mPa s at 25 °C) than DG (30 mPa s at 25 °C). The solubility and viscosity of AgNO$_3$ and PVP in glycerol or DG affects the formation of multiply twinned particles (MTPs) with a decahedral shape consisted of ten {111} facets. The growth mechanism of AgNWs can be explained by Sun et al. [12]. Since {100} facets of MTP are completely passivated by PVP, silver atoms can only selectively grow on {111} facets, producing one-dimensional nanostructures such as nanowire or nanorods. Different volume ratios of glycerol and DG affect the passivation degree of PVP on {100} and {111} facets, thus forming various silver nanostructures.

## 3.2 Effect of Molar Ratio of PVP to AgNO$_3$

The molar ratio of PVP to AgNO$_3$ determines the number of silver sources and the formation of AgNWs seed crystal when the volume ratio of solvent in the reaction system is kept at an appropriate value. Based on the optimal volume ratio, the experiments are carried out by changing the molar ratio of PVP to AgNO$_3$ of 1:1, 2:1, 4:1 and 6:1, respectively.

Figure 2 shows the SEM images of the samples fabricated using different molar ratios of PVP to AgNO$_3$. Irregular silver nanostructures, including linear, short rod and granular structures, were obtained with the same molar amount of PVP to AgNO$_3$ as shown in Fig. 2a. This is because the concentration of PVP in the system is not enough to cover the {111} facets, and the higher energy on the surface of the nuclei results in the more complex products. When the molar ratio was set at 2:1, the short rods and particles still exist, but obviously the diameter of the short rods becomes finer (Fig. 2b). As the molar ratio of PVP to AgNO$_3$ increases from 2 to 4, the silver nanoparticles and short rods almost disappear, and the diameter and length of AgNWs become more uniform (Fig. 2c). This phenomenon is attributed to the selective adsorption of PVP on {100} facets rather than the {111} facets via O-Ag bond [13]. With the increase of the amount of PVP, the {100} facets of the crystal nuclei is partially or completely surrounded, promoting deposition of silver atoms on {111} facets and subsequent linear growth. However, when the ratio was adjusted to 6, more silver nanoparticles and short rods appeared again (Fig. 2d). Excessive PVP easily covers {111} facets, resulting in many silver nanoparticles and short nanorods. Therefore, the appropriate molar ratio of PVP to AgNO$_3$ is beneficial to the growth of AgNWs and the optimal molar ratio is 4:1.
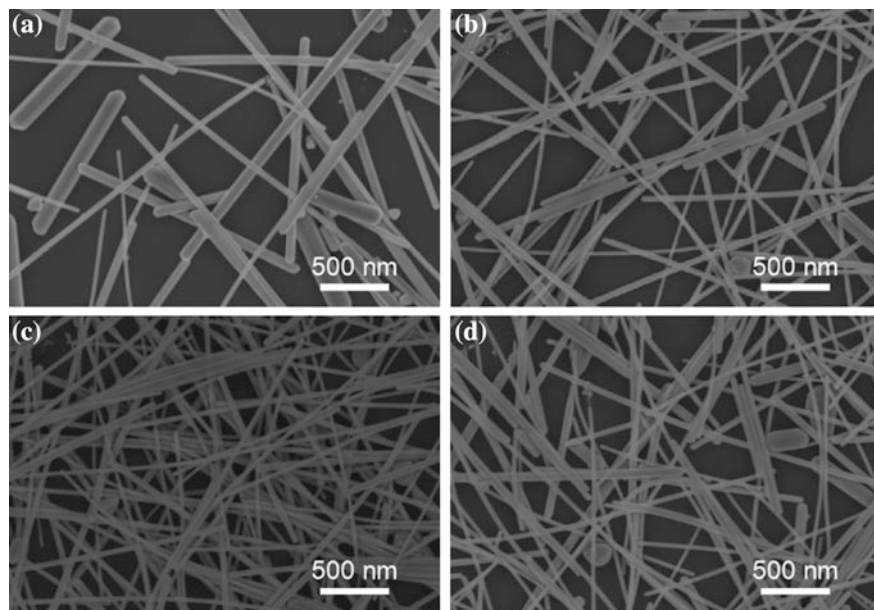
**Fig. 2.** SEM images of AgNWs synthesized at various PVP: AgNO$_3$ molar ratios of **a** 1:1, **b** 2:1, **c** 4:1, and **d** 6:1

## 3.3    Effect of PVP Average Molecular Weights(MWs)

The structure of AgNWs also depends on PVP's chain length, corresponding to the average molecular weight [14]. Based on the optimal volume ratio and molar ratio discussed above, the influences of different PVP average molecular weights on the morphology of AgNWs are further explored. For convenience, the average molecular weight of PVP was abbreviated to PVP-10 k, PVP-40 k, PVP-58 and PVP-130 k, respectively.

Figure 3 shows the SEM images fabricated using different average molecular weight of PVP. There are only silver particles with different morphologies and short nanorods (Fig. 3a) were entangled with each other when PVP-10 k was used. The short chain, produced from the PVP with lower average molecular weight, is not conducive to the selective adsorption of PVP and the growth of AgNWs, resulting to the aggregation of silver atoms and the appearance of silver nanorods. In contrast, when the PVP-k40 was adopted, uniform AgNWs with sporadic particles were produced as shown in Fig. 3b. Meanwhile, the similar morphologies were formed when the average molecular weight increase to 58 000 in Fig. 3c, since PVP can effectively cover the {100} facets. However, short nanorods with irregular shape were obtained again when the average molecular weights further increased from 58 000 to 130 000 in Fig. 3d. Therefore, we believe the critical average molecular weight of PVP that can produce AgNWs in this reaction system is between 40 000 and 58 000. But in order to make it easier to remove excessive PVP and its derivatives before characterization, we chose a molecular weight of 40 000.
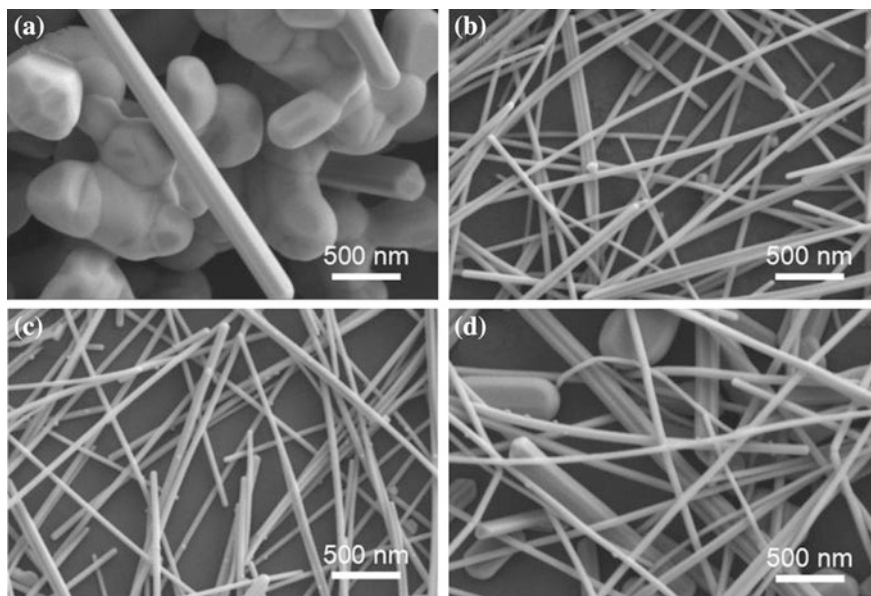
**Fig. 3.** SEM images of AgNWs prepared with different average molecular weights of PVP: **a** 10 000, **b** 40 000, **c** 58 000 **d** 130 000

## 4    Conclusions

Uniform silver nanowires (AgNWs) were synthesized in the presence of poly(vinyl pyrrolidine) (PVP) and sodium chloride (NaCl) using glycerol and diethylene glycol (DG) as mixed reductants and solvent. The parameters of uniform AgNWs prepared by polyol method were studied in detail, including the volume ratio of glycerol to DG, the molar ratio of PVP to $AgNO_3$, and the average molecular weight of PVP. The appropriate volume ratio of glycerol to DG can well regulate the length and uniformity of AgNWs effectively. Based on the optimal volume ratio, the effects of the molar ratio of PVP to $AgNO_3$ and the average molecular weight of PVP on the morphology were further discussed. Uniform AgNWs can be appeared at a special value of the molar ratio, while increasing or decreasing this ratio will produces particles. Moreover, both lower and higher average molecular weight result in the formation of Ag nanorods in addition to AgNWs. Finally, the optimal process parameters for uniform AgNWs are as follows: the volume ratio of glycerol to DG is 1:1, the molar ratio of PVP to $AgNO_3$ is 4:1, and the average molecular weight of PVP is 40 000. These results provide some references for the synthesis and application of uniform AgNWs.

# References

1. Zhang P, Wyman I, Hu J et al (2017) Silver nanowires: synthesis technologies, growth mechanism and multifunctional applications. Mater Sci Eng B 223:1–23
2. Yang R, Sui C, Gong J et al (2007) Silver nanowires prepared by modified AAO template method. Mater Lett 61(3):900–903
3. Zhang D, Qi L, Yang J et al (2004) Wet chemical synthesis of silver nanowire thin films at ambient temperature. Chem Mater 16(5):872–876
4. Zheng XJ, Jiang ZY, Xie ZX et al (2007) Growth of silver nanowires by an unconventional electrodeposition without template. Electrochem Commun 9(4):629–632
5. Zhang K, Du Y, Chen S (2015) Sub 30 nm silver nanowire synthesized using KBr as co-nucleant through one-pot polyol method for optoelectronic applications. Org Electron 26:380–385
6. Coskun S, Aksoy B, Unalan HE (2011) Polyol synthesis of silver nanowires: an extensive parametric study. Cryst Growth Des 11(11):4963–4969
7. Sun YG, Gates B, Mayers B et al (2002) Crystalline silver nanowires by soft solution processing. Nano Lett 2(2):165–168
8. Jia C, Yang P, Zhang A (2014) Glycerol and ethylene glycol co-mediated synthesis of uniform multiple crystalline silver nanowires. Mater Chem Phys 143(2):794–800
9. Nghia NV, Truong NNK, Thong NM et al (2012) Synthesis of nanowire-shaped silver by polyol process of sodium chloride. Int J Mater Chem 2(2):75–78
10. Murshid N, Kitaev V (2014) Role of poly(vinyl pyrrolidone) (PVP) and other sterically protecting polymers in selective stabilization of 111 and 100 facets in pentagonally twinned silver nanoparticles. Chem Commun 50(10):1247–1249
11. Ran Y, He W, Wang K et al (2014) A one-step route to Ag nanowires with a diameter below 40 nm and an aspect ratio above 1000. Chem Commun 50(94):14877–14880
12. Sun Y, Mayers B, Herricks T et al (2003) Polyol synthesis of uniform silver nanowires: a plausible growth mechanism and the supporting evidence. Nano Lett 3(7):955–960
13. Huang HH, Ni XP, Loy GL et al (1996) Photochemical formation of silver nanoparticles in poly (N-vinylpyrrolidone). Langmuir 12(4):909–912
14. Zeng X, Zhou B, Gao Y et al (2014) Structural dependence of silver nanowires on polyvinyl pyrrolidone (PVP) chain length. Nanotechnology 25(49):495601

# Preparation of Flowerlike Calcium Vanadate Microspheres by Binary Solvent Method

Congcong Chi[(✉)], Zhao Wang, Liang Xia, and Meng Zhang

College of Bioresources Chemical and Materials Engineering, Shaanxi University of Science & Technology, Xi'an, China
congcongchi@163.com

**Abstract.** Using sodium metavanadate and calcium acetate as raw materials, citric acid and Polyvinylpyrrolidone (PVP) as morphological control agents, the flowerlike calcium vanadate microspheres were prepared by ethylene glycol (EG)-water binary solvent thermal method. The effects of solvent ratio, reaction temperature and time on the morphology were investigated, and the growth mechanism of the flowerlike calcium vanadate microspheres was elucidated. The microspheres had the most complete morphology at the EG/$H_2O$ ratio of 4:3. More obvious and better growth of flower clusters was shown for longer reaction time. With the increase of temperature, the crystallinity of the product gradually increased.

**Keywords:** Flowerlike · Calcium vanadate · Binary solvent method

## 1 Introduction

In recent years, vanadate-based micro-nano semiconductor materials have gained more and more attention due to their excellent electrochemical [1], optical [2–5], and catalytic properties [5, 6]. Vanadate can be used for electrochemical sensors, lithium ion batteries, optical instruments, and in the catalytic fields.

As one of the important ternary semiconductor materials, the performance of vanadate is different from that of the general binary semiconductors. In MVO (M stands for a metal element, V is vanadium, and O is oxygen), the vanadium oxide polyhedron and the MO polyhedron are nested with each other to form different crystal phases, thereby endowing vanadate different properties. Calcium vanadate has shown excellent performance and attracted widespread attention.

Wei et al. [7] used hydrothermal method to synthesize calcium vanadate ($Ca_{10}V_6O_{25}$) nanorods, which were applied as glassy carbon electrode modification materials. Zhang et al. [8] prepared nano-calcium vanadate ($CaVO_3$) for the transparent conductive film by atomic deposition technology. Chen et al. [9] synthesized calcium vanadate gel by sol-gel method, the $CaVO_3$ powder obtained after calcination in argon atmosphere can be used in the field of catalytic oxidation. Zhang and Wei [10] produced $Ca_2V_2O_7$ nanospheres by hydrothermal method, and it has great potential for the lithium-ion batteries as a negative electrode material.

The size, morphology, crystal orientation and crystallinity are the main factors affecting the performance of calcium vanadate. It is necessary to develop micro-nano

materials of calcium vanadate with uniform size and high crystallinity. The flowerlike structure has large specific surface area and a large number of reactive sites, which has attracted great attention of researchers in related fields. So far, studies on the preparation of flowerlike calcium vanadate microspheres ($CaV_3O_7$) and their UV absorption properties have not been reported.

In this paper, binary solvothermal method is used to synthesize flowerlike calcium vanadate microspheres, which have larger specific surface area than that of the traditional single solvothermal method. The effect of temperature, reaction time and $EG/H_2O$ ratio on its morphology were investigated, and the UV absorption performance of the microspheres were studied. The results can provide reference for the controllable synthesis of flowerlike calcium vanadate microspheres by binary solvent method, which has great significance for expanding the application of micro-nano vanadate calcium materials in the field of UV shielding.

## 2  Experimental

### 2.1  Materials

Calcium acetate and ethylene glycol (Tianjin Damao Co., Ltd.), sodium metavanadate (Aladdin), citric acid (Tianjin Yongsheng Chemical Co., Ltd.), polyvinylpyrrolidone (PVP, Aladdin) are all analytically pure reagents. The deionized water is made by an ultrapure water machine (Milli-Integral 15, Germany).

### 2.2  Preparation of Calcium Vanadate

Calcium acetate, sodium metavanadate and PVP were weighed based on certain molar ratio. The sodium metavanadate was dissolved in deionized water, while the calcium acetate and PVP were dissolved in EG. The solution of calcium acetate and sodium metavanadate was mixed together after being magnetically stirred, then PVP was slowly added. After being stirred for certain time, the mixture was transferred to the reaction vessel, which was then put in an oven at certain temperature for certain time. After reaction, the pot was taken out of the oven and cooled down, then it was centrifuged and oven dried at 60 °C for 12 h, finally the white powder sample was obtained.

### 2.3  Scanning Electron Microscope (SEM)

The sample suspension was ultrasonically dispersed in ethanol for 15 min, then a drop was transferred onto a piece of tin foil with a disposable pipette and dried at room temperature for 1 h. Finally, the microstructure analysis was conducted using a VEGA-3-SBH scanning electron microscope at an accelerating voltage of 10 kV.

### 2.4  X-Ray Diffraction (XRD)

The XRD analysis was done by German Bruker D8-Advance XRD diffractometer. The diffraction angle of 2θ ranged from 10° to 70°, and the scanning speed was 0.1°/s.

# 3   Results and Discussion

## 3.1   Effect of EG/H₂O Ratio on the Calcium Vanadate Microspheres

Figure 1 shows the SEM images of calcium vanadate microspheres obtained at different EG/H$_2$Ovolume ratios. It can be seen that when the volume ratio of EG to H$_2$Ois 1:6, both spherical and semi-flowered calcium vanadate exist simultaneously. At the solvent ratio of 2:5, both spherical and rod-like structures exist. While the solvent ratio is 3:4, flowerlike calcium vanadate appears with some rod-like structures. Figure 1d, e show that when the solvent ratio rises to 4:3, complete flowerlike structure of uniform calcium vanadate microspheres is shown without any rod structures. The flowerlike structure is not obvious at the EG/H$_2$O ratio of 5:2. It can be seen that the solvent ratio has great influence on the morphology of calcium vanadate. In summary, when the EG/H$_2$O ratio is 4:3,calcium vanadate has tufted microsphere structure and uniform morphology without any other structures, and the diameter ranges from 1 to 5 μm.
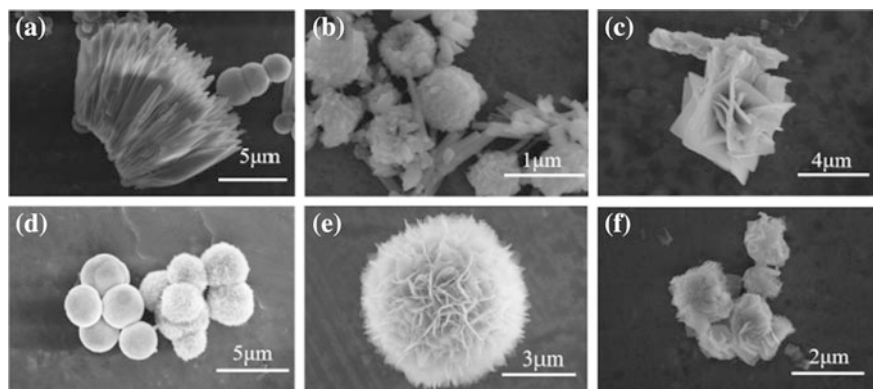


**Fig. 1.** SEM images of microspheres obtained at different solvent ratios **a** 1:6, **b** 2:5, **c** 3:4, **d**, **e** 4:3, **f** 5:2. Other same conditions: 180 °C, 24 h, which is the same for Fig. 2

Figure 2 shows the effect of solvent ratio on the X-ray diffraction of calcium vanadate. When the volume ratio is 1:6, or 2:5, or 3:4, the obtained product is mixed crystal phase of CaV$_3$O$_7$ and CaV$_6$O$_{16}$ (JCPDS-37-0177). CaV$_3$O$_7$ crystal phase is shown at the solvent ratio of 4:3, while the Ca$_2$V$_2$O$_7$ (JCPDS-72-2312) crystal phase presents at the solvent ratio of 5:2. Based on the above results, we can see that the particles gradually change from mixed crystal phase of CaV$_3$O$_7$ and CaV$_6$O$_{16}$ to single crystal phase of CaV$_3$O$_7$, when the solvent ratio increases from 1:6 to 4:3. As is shown in Fig. 1, the morphology gradually transforms from a mixture of spheres and rods to single flowerlike microspheres.
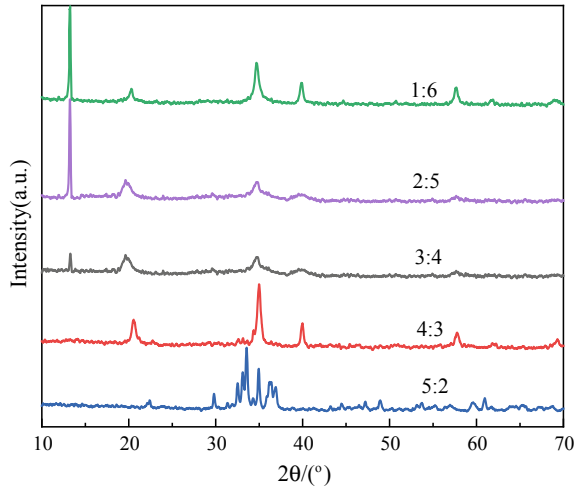
**Fig. 2.** Effect of solvent ratio on the XRD spectra of calcium vanadate microspheres

## 3.2 Effect of Temperature on the Calcium Vanadate Microspheres

Figure 3 shows the effect of temperature on the microstructure of calcium vanadate. Seen from Fig. 3a, no flowerlike calcium vanadate microspheres appear at 120 °C. As the temperature increases, the surface of the microspheres begins to differentiate, and flowerlike structure gradually forms. The calcium vanadate changes from solid spheres to flowerlike structure with the rise of temperature, and the flowerlike microspheres have a diameter of around 4 μm. Maybe due to the increase of temperature, the combination of $V_3O_7^{2-}$ and $Ca^{2+}$ in the solvent is accelerated. Some particles rapidly enter the PVP micelles, others not entering the micelles differentiate on the surface to minimize energy and achieve stable structures, which conforms to the Ostwald ripening theorem [11].
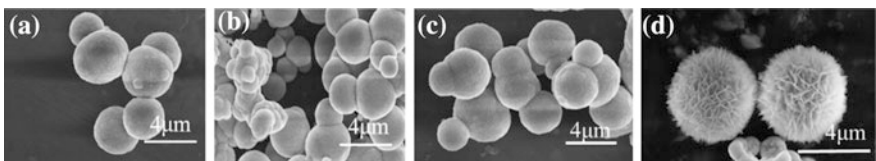


**Fig. 3.** SEM images of microspheres obtained at different temperature **a** 120 °C, **b** 140 °C, **c** 160 °C, **d** 180 °C. Other conditions: 24 h, EG:H$_2$O = 4:3, which is the same for Fig. 4

Figure 4 shows the X-ray diffraction patterns of calcium vanadate prepared at different temperature. Obviously, there are mixed crystal of $CaV_4O_9$ (JCPDS-70-1325) and $CaV_3O_7$ at lower temperature. With the rise of temperature, the intensity of diffraction peak at $2\theta = 34.4°$ significantly increases. The results show that increasing

temperature can help convert the calcium vanadate microspheres from $CaV_4O_9$ crystal phase into $CaV_3O_7$ crystal phase.
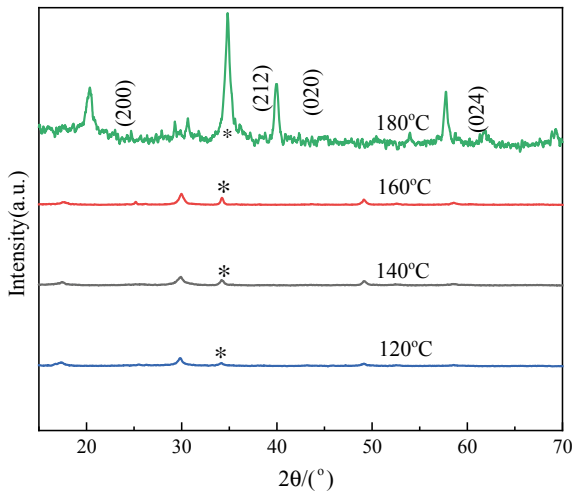


**Fig. 4.** XRD spectra of calcium vanadate microspheres at different reaction temperatures

## 3.3    Effect of Retention Time on the Calcium Vanadate Microspheres

The effect of retention time on the microstructure of calcium vanadate is shown in Fig. 5. As is shown, the surface of the microspheres is smooth, and no flowerlike microspheres are present at the beginning of reaction. With the extension of retention time, the surface of the microspheres begins to differentiate, and the flowerlike structure becomes more and more obvious. It is probably that more small particles will be deposited and grow along the (212) and (020) crystal planes on the surface of microspheres with the extension of time, which will result in more and more dense flowerlike structures. The size of the microspheres is approximately 5 μm in diameter. It can be concluded that the flowerlike structure will be more obvious and denser as the time extends.

The X-ray diffraction patterns of calcium vanadate for different retention time are shown in Fig. 6. Obviously, four distinct diffraction peaks can be seen, and they are consistent with the XRD standard spectrum JCPDS card of $CaV_3O_7$. The diffractions at $2\theta = 19.62$, 34.42, 39.43 and 57.69, correspond to the crystal planes of (200), (212), (020) and (024). As the retention time extends, the crystal phase of $CaV_3O_7$ (JCPDS-26-0337) shows a significant increase in the intensity of the diffraction peak at $2\theta = 19.6°$ and 34.4°, and the diffraction peak becomes more sharpened. Therefore, the elongation of reaction time contributes to increased crystallinity of the microspheres and promotes the growth of calcium vanadate along the (212) and (200) planes.
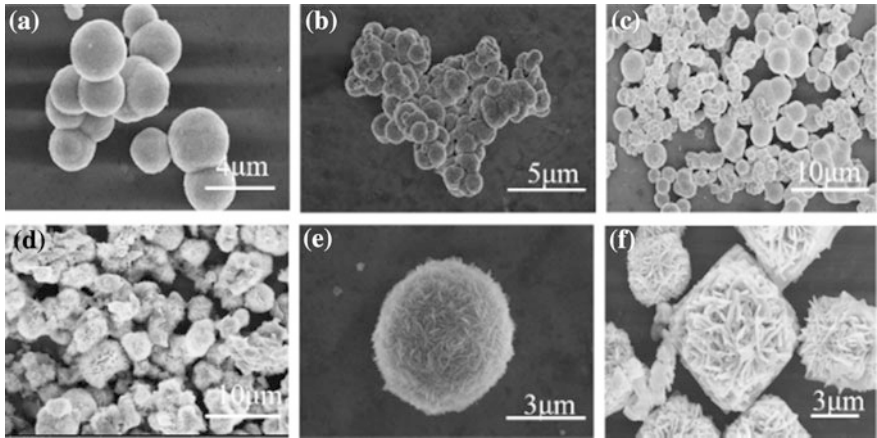
**Fig. 5.** SEM images of calcium vanadate at different retention time **a** 12 h, **b** 16 h, **c** 20 h, **d** 24 h, **e** 32 h, **f** 36 h. Otherconditions: 180 °C, EG:H$_2$O = 4:3. It is the same for Fig. 6
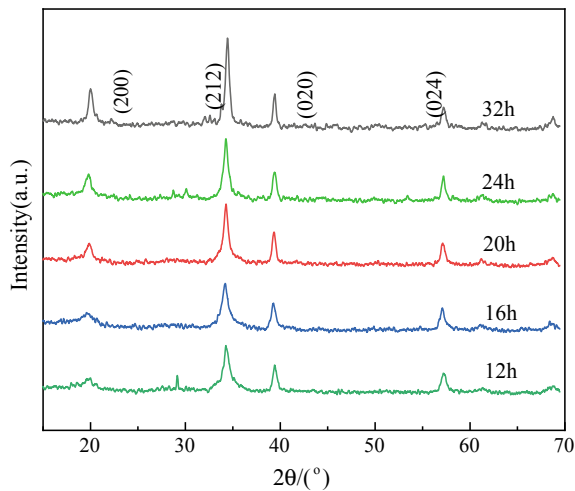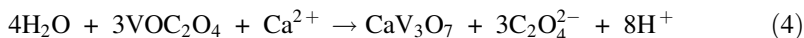


**Fig. 6.** XRD spectra of calcium vanadate microspheres at different retention time

## 3.4 Growth Mechanism

Based on the above results, the formation mechanism of the flowerlike calcium vanadate microspheres is probably as follows. Firstly, ethylene glycol reacts with oxygen to form glyoxal, which is then oxidized to form oxalic acid. Secondly, the vanadyl oxalate is formed through the reaction between oxalic acid and calcium vanadate [9]. Finally, vanadyl oxalate react with calcium ion to obtain calcium vanadate (CaV$_3$O$_7$ CaV$_6$O$_{16}$, CaV$_4$O$_9$, Ca$_2$V$_2$O$_7$). The reaction is as follows:

$$HOCH_2CH_2OH + O_2 \rightarrow HOCCHO + 2H_2O \tag{1}$$

$$HOCCHO + O_2 \rightarrow H_2C_2O_4 \tag{2}$$

$$2H^+ + 3H_2C_2O_2 + 2VO_3^- \rightarrow 2VOC_2O_4 + 4H_2O + 2CO_2 \tag{3}$$

$$4H_2O + 3VOC_2O_4 + Ca^{2+} \rightarrow CaV_3O_7 + 3C_2O_4^{2-} + 8H^+ \tag{4}$$
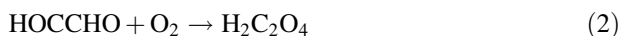
In the glycol/PVP reaction system, PVP molecules are dissolved in the ethylene glycol phase. When the concentration is higher than the critical micelle concentration, PVP forms spherical micelles in ethylene glycol solution [12]. The hydrophilic groups of Amido groupin PVP molecules are linked to water phase, while the hydrophobic alkyl groups are linked to ethylene glycol molecules. In the beginning, large amount of Vanadium oxalate and $Ca^{2+}$ dispersed in the solution enters the PVP micelles due to the ion-dipole interaction to form $CaV_3O_7$ crystal nucleuses. Then the crystal nuclei continue to grow and accumulate together to form spherical $CaV_3O_7$ microspheres. With the extension of reaction time, large number of small particles are deposited on the surface of large spheres, and they will grow along the crystal planes and differentiate into sheets to achieve stable structures. The flower cluster calcium vanadate formation mechanism is shown in Fig. 7.
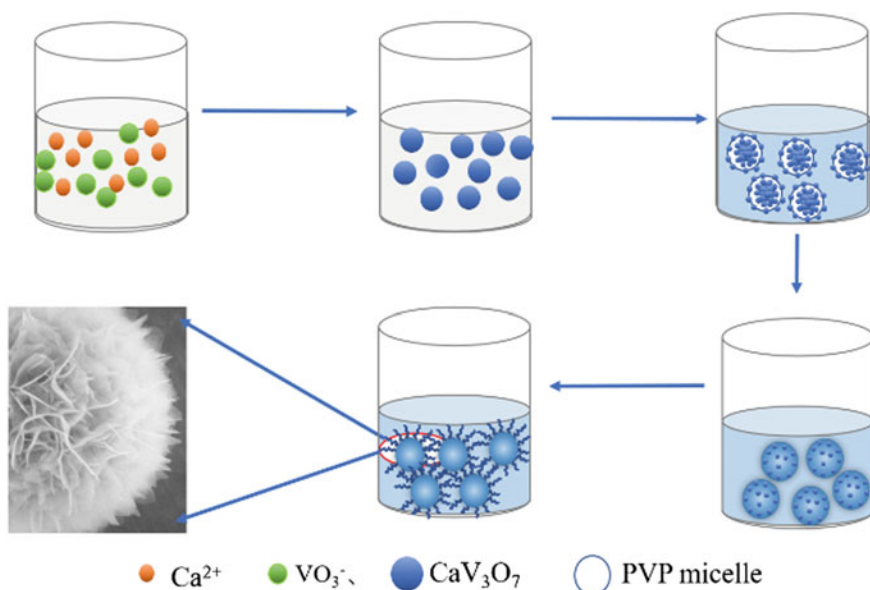


● $Ca^{2+}$     ● $VO_3^-$、     ● $CaV_3O_7$     ○ PVP micelle

Fig. 7. Growth mechanism of flowerlike calcium vanadate microspheres

# 4   Conclusions

The polycrystalline flowerlike calcium vanadate microspheres were synthesized by binary solvent hydrothermal process, and the average diameter is approximately 4 μm. The sodium metavanadate and calcium acetate were raw materials, and the dispersant of PVP was added. The volume ratio of EG to $H_2O$, hydrothermal temperature and retention time have great influence on the formation and growth of flowerlike calcium vanadate microspheres. It is found that higher temperature or longer reaction time helps to increase the crystallinity of calcium vanadate microspheres, and leads to more dense flowerlike particles.

# References

1. Wang J, Pei J, Hua K, Chen DH, Jiao Y, Hu YY, Chen G (2018) Synthesis of $Co_2V_2O_7$ hollow cylinders with enhanced lithium storage properties using $H_2O_2$ as an etching agent. ChemElectroChem 5(5):737–742

2. Wang J, Huang H, Zhang D et al (2015) Synthesis of gold/rare-earth-vanadate core/shell nanorods for integrating plasmon resonance and fluorescence. Nano Res 8(8):2548–2561

3. Niu P, Liu X, Wang Y, Zhao WR (2018) Photoluminescence properties of a novel red-emitting phosphor $Ba_2LaV_3O_{11}$:$Eu^{3+}$. J Mater Sci: Mater Electron 29(1):124–129

4. Yang Z, Xu X, Liang X, Lei C, Cui YH, Wu WH, Yang YX, Zhang Z, Lei ZQ (2017) Construction of heterostructured MIL-125/Ag/g-$C_3N_4$, nanocomposite as an efficient bifunctional visible light photocatalyst for the organic oxidation and reduction reactions. Appl Catal B 205:42–54

5. Zhao XX, Huang JF, Feng LL, Cao LY, Li JY, Zhou L (2017) Facile synthesis of α-$Ag_3VO_4$ hollow nanospheres with improved photocatalytic activities. J Alloy Compd 718:7–14

6. Ge L, Zhang XH (2009) Synthesis of novel visible light photocatalyst $BiVO_4$ by microemulsion method and its photocatalytic activity. J Inorg Mater 24(3):453–456

7. Wei T, Ma J, Yu SC, Pei YQ, Pei LZ (2014) Growth regulation and electrochemical characteristics of calcium vanadate nanorods. Bronze Eng 6:38–43

8. Zhang L, Zhou Y, Guo L et al (2015) Correlated metals as transparent conductors. Nat Mater 15(2):204–210

9. Chen FY, Xiao L, Yang CX, Zhang L (2015) Preparation of perovskite-type composite oxide $CaVO_3$ and its electrocatalytic performance for oxygen reduction. Acta Phys Sin 31(12):2310–2315

10. Zhang S, Wei M (2016) Fabrication of $Ca_2V_2O_7$ microspheres and its application in lithium-ion batteries. Mater Lett 183:311–314

11. Kim K, Voorhees PW (2018) Ostwald ripening of spheroidal particles in multicomponent alloys. Acta Mater 152:327–337

12. Lei C (2011) Preparation and fluorescence properties of flower clustered ZnS:Mn microspheres. Guangzhou Chem 39(13):70–73

# Preparation of Amphipathic and Thermo-Sensitive Poly(tertiary amine oxide)

Lu Wang[1], Li An[1], Hongli Zhang[1], and Zhongxiao Li[2(✉)]

[1] Lab of Printing & Packaging Material and Technology, Beijing Institute of Graphic Communication, Beijing, China
{503502429,286081844}@qq.com, anli@bigc.edu.cn
[2] Beijing Institute of Graphic Communication, Beijing, China
lizhongxiao@bigc.edu.cn

**Abstract.** Water-based thermo-sensitive polymers are probably more important for developing new processless CTP plates. Tertiary amine oxide-based polymers exhibit good aqueous solubility (or dispersibility) and unique thermal behaviors, which are worth of further investigation. In this paper, water-soluble poly(tertiary amine) (PDMAPMA) was prepared through redox-initiated RAFT polymerization of DMAPMA at ambient temperature. Poly(tertiary amine oxide), O-PDMAPMA, was obtained through the oxidization of PDMAPMA with hydrogen peroxide. O-PDMAPMA exhibited thermal- induced decomposition around 160 °C, leading to great changes in solubility. O-PDMAPMA was used as a reactive emulsifier and used in soapless radical emulsion polymerization of MMA without using co-emulsifier. The emulsion was quite stable, having a solid content of 33.7 wt% and average particle size of 110 nm. A coating solution for IR-sensitive layer was prepared with polymethyl methacrylate (PMMA) emulsion, a water-soluble infrared-absorbing dye and a hydrophilic binder. A negative-working heat-sensitive lithographic printing plate precursor was prepared by spin-coating of the solution on an aluminum sheet-like support, which had been grained by electrochemical graining and anodized by means of anodizing technique. The imageable layer of the printing plate precursor is exposed imagewise using infrared laser radiation (830 nm) to produce an imaged layer. The energy density was up to 180 mJ/cm$^2$. After exposure, the material can be developed by neutral water whereby the non-image areas of the layer are removed. Thus, a printing plate based on the prepared PMMA emulsion was obtained.

**Keywords:** Amine oxide · Soapless emulsion polymerization · Thermal-induced decomposition · Printing plate precursor

## 1 Introduction

Amine oxide is characterized by a direct combination of nitrogen atom and oxygen atom in tertiary amine molecule Amine oxides containing long chain alkyl groups are very typical surfactants, and their surface activity is better than that of quaternary ammonium salts, and have excellent emulsifying properties in a wide range of pH value

[1, 2]. In addition, amine oxides not only have general surface activity, but also have unique low physiological toxicity [3, 4].

There have been some studies on the syntheses, properties and applications of amine oxides, but few studies have been reported on amine oxide-containing polymers [5, 6]. This might be due to the lack of effective synthesis method. However, amine oxide-containing polymers should have the combined performance of amine oxides and polymers. Duan et al. prepared macroporous cross-linked amine oxide resin, and studied the adsorption of phenol [7]. It was found that the interaction between tertiary amine resin and phenol and the spontaneous tendency of hydrogen bond adsorption increased after oxidation of tertiary amine resin. A water-soluble polymer containing tertiary amine oxide was also prepared in our lab and the water solubility and thermal properties were studied. Results showed that the introduction of amine oxide made the polymer have both water solubility and thermal sensitivity (i.e. thermal-induced decomposition) [8]. In this study, an amphipathic and thermo-sensitive poly(tertiary amine oxide) was prepared through soapless emulsion polymerization. The prepared poly(tertiary amine oxide) was characterized and used in developing laser thermo-sensitive composition.

## 2   Experimental

### 2.1   Materials and Methods

Dimethyl aminopropyl methacrylamide (DMAPMA), methyl methacrylate (MMA), sodium persulfate (APS), trifluoroacetic acid and 2,2′-azobis-(2,4-dimethylvaleronitrile) (ABVN) were commercial products from Beijing Chemicals Co. 2-(((Dodecylthio) carbonothioyl)thio)propanoic acid (DTCTPA), poly(acrylic acid) (PAA) aqueous solution (20 wt%) and water soluble IR dye (IR-830, maximum absorption at 830 nm) were prepared in our lab. All solvents were used as received.

FTIR spectra were obtained with a Shimadzu FTIR-8400 infrared spectrophotometer. The particle size and distribution were determined using a Malvern Mastersizer 2000 (Malvern, UK). Differential scanning calorimetry (DSC) was recorded on a Netzsch DSC200PC analysis apparatus. Laser exposure was performed with a TP-46XX image-setter (Hangzhou CRON Machinery & Electronics Co., Ltd). The morphology of the printing plate was recorded by light microscope (DMI3000M).

### 2.2   Preparation of PDMAPMA

DMAPMA (20 g), DTCTPA(1.0 g) and $H_2O$ (20 g) were placed in a 100 mL single-necked round-bottom flask. The mixture was stirred for 3 h at ambient temperature to obtain a clear solution. Then, the aqueous APS solution (0.12 g of APS in 10 g of deionized water) was added dropwise with stirring, the temperature increased dramatically (up to approximately 60 °C) in a short period of time, and the mixture became viscous due to the polymerization of DMAEMA. After the addition, the reaction mixture was stirred for another 2 h, which gradually cooled to room temperature. The water-soluble PDMAEMA was prepared by radical polymerization and poured into

200 mL isopropanol under rapid agitation. Yellowish PDMAPMA was then precipitated from the solvent. Finally, the obtained solid was collected and dried in 70–80 °C, respectively.

## 2.3    Oxidation of PDMAPMA

PDMAPMA (15 g), dimethyl carbonate (0.5 g), deionized water (15 g) and ethanol (15 g) were added to a 250 mL flask equipped with mechanical stirring, condensation tube and thermometer. The mixture was stirred and heated to 70–75 °C. Hydrogen peroxide (15 g, 30 wt%) was added dropwise, and the temperature is controlled between 75 and 80 °C. The addition is completed in about 2 h. The reaction was continued for 6 h at 75–80 °C. Then, the reaction was stopped. Most of the solvents were removed by vacuum distillation. The solid product was treated by soaking in 100 ml isopropanol. The precipitation was collected and dried under vacuum at 60 °C for 10 h. The oxidized PDMAPMA is denoted as O-PDMAPMA.

## 2.4    Emulsion Polymerization of MMA Using O-PDMAPMA as the Reactive Emulsifier

5.0 g O-PDMAPMA was dissolved in 30 g of deionized water in advance. A mixture consisting of 0.25 g of AVBN and 10 g of MMA was added to the aqueous solution of O-PDMAPMA and stirred at room temperature for 30 min, and this was followed by high speed homogenization for 10 min. The obtained mini-emulsion was placed in a four-necked flask and mechanically stirred for 20 min at ambient temperature. Then, the bath was heated at 75 °C, and the mixture was stirred at a speed of 350 r/min for 5 h. Finally, the yielded polymethyl methacrylate (PMMA) emulsion was filtered with a Buchner funnel. The solid content of the obtained emulsion was 33.7 wt%.

## 2.5    Preparation of a Laser-Imageable Layer with the Polymer Emulsion

First, a coating solution for an image forming layer was prepared. In a typical experiment, PMMA emulsion (23.7 g), PAA aqueous solution (4.0 g, 20 wt%), IR-830 (0.8 g) and a small amount of defoamer were added in turn to 68 mL of deionized water, and the aqueous mixture was stirred with a magnetic stirrer for 2–3 h to give a stable solution. The image forming layer was prepared by spreading the coating solution directly on a clean anodized aluminium plate, and this was followed by drying at 90 °C for 10 min. The thickness of the layer was about 1 μm.

# 3    Results and Discussion

## 3.1    Preparation and Oxidization of PDMAPMA

The synthesis of PDMAPMA and O-PDMAPMA was shown in Scheme 1. DMAPMA contains both aliphatic tertiary amine and polymerizable double bonds. A redox initiator system formed by DMAPMA and persulfate produced free radicals (aminoalkyl radicals) and initiated self-polymerization. DTCTPA was used as an addition-

fragmentation chain transfer (RAFT) agent. The polymerization proceeded in the presence of the RAFT agent yielded a macro RAFT agent (PDMAPMA). It should be noted that the role of DTCTPA is to prevent cross-linking. In fact, a gel product will be obtained without the use of DTCTPA. PDMAPMA was characterized by gel permeation chromatography (GPC) (relative to styrene standards). The GPC analysis of PDMAPMA (Fig. 1) presented an average molecular weight (Mn) of 12825 and a polydispersion index (PDI) of 2.09. The Mn and PDI values are higher than those of a typical live radical polymerization. This may be caused by the high speed polymerization and the inter-molecular hydrogen bonding between the carboxylic acid group of the RAFT agent and the tertiary amine group.
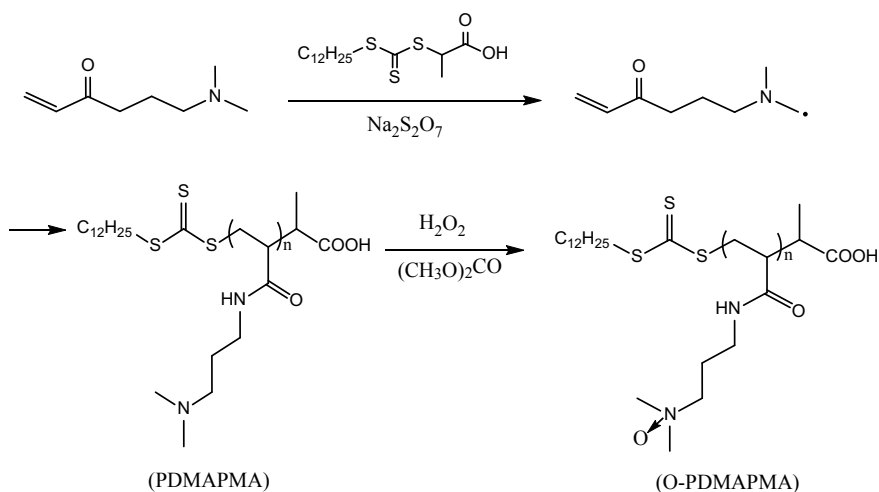


**Scheme 1.** Synthesis of PDMAPMA and O-PDMAPMA

Oxidization of PDMAPMA to O-PDMAPMA was carried out by using hydrogen peroxide aqueous solution and dimethyl carbonate as the oxidizer and the catalyst, respectively. Figure 2 compares the FTIR spectra of PDMAPMA and O-PDMAPMA. Both have absorption bands at 1600–1700 $cm^{-1}$ arising from the amide moiety. The weak absorption band around 1065 $cm^{-1}$ is assigned to the trithiocarbonate group of the RAFT agent. The difference is that there appears a weak absorption band at 968 $cm^{-1}$ for O-PDMAPMA. It is the characteristic absorption peak of N-O stretching vibration arising from the amine oxide group of O-PDMAPMA, implying that tertiary amines were oxidized.

## 3.2 Mini-Emulsion Polymerization of MMA

High-speed shearing homogenization of the mixture is necessary to produce a stable emulsion. The PMMA emulsion was prepared through mini-emulsion polymerization of MMA in the presence of O-PDMAPMA, which had the "reactive trithiocarbonate group" grafted at the end of the polymer chain. Therefore, the O-PDMAPMA polymer
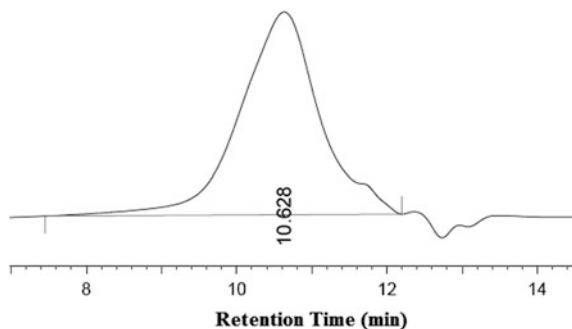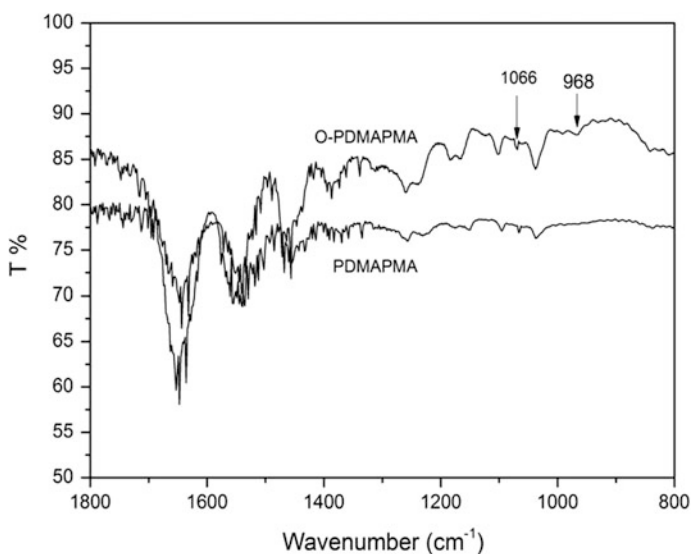
**Fig. 1.** GPC trace of PDMAPMA



**Fig. 2.** FTIR spectra of PDMAPMA and O-PDMAPMA

chains should be chemically bonded with the molecular chains of PMMA as the emulsion polymerization proceeded. Furthermore, the hydrophilic moieties of O-PDMAPMA, namely amine oxides, should be located on the surface of the polymer particles, forming a stable hydrophilic layer around the surface. Results showed that O-PDMAPMA could enhance the effect of emulsification and prevent coagulation. Little coagulation occurred during the emulsion polymerization. The polymer emulsion was measured with DLS (Fig. 3). It is found that the mean diameter was around 110 nm and the particle size distribution is normal (polydispersity 11%).
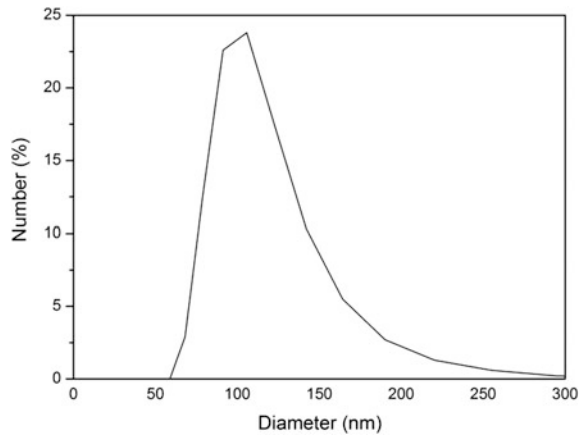
**Fig. 3.** DLS results of the PMMA emulsion

### 3.3 DSC Analysis of O-PDMAPMA

Figure 4 is a DSC curve of O-PDMAPMA. An evidently exothermic peak with the maximum appeared at 160 °C, which is due to the thermal decomposition of the amine oxide [8]. This is also confirmed by the solubility change after high temperature treatment. O-PDMAPMA was easily soluble in water and non-proton strong polar solvents such as DMF, DMAc and NMP. However, the O-PDMAPMA sample readily became water-insoluble when it is heated to 150°C or above. According to the mechanism of Cope elimination reaction, thermal decomposition of amine oxide yields hydroxylamine and olefin, which are oleophilic products.
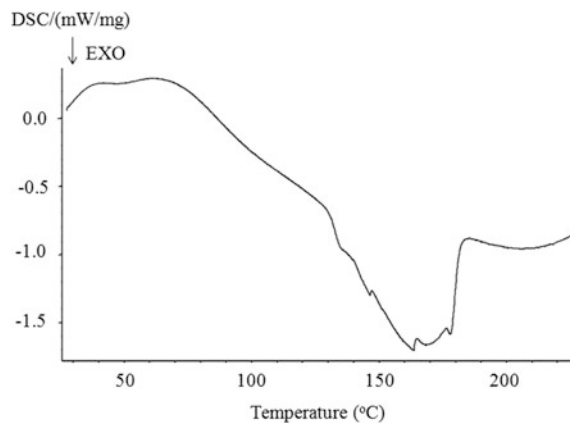


**Fig. 4.** DSC analysis of O-PDMAPMA

### 3.4    A Negative-Working Lithographic Printing Plate Precursor and Imagewise Exposure

An image recording layer of the lithographic printing plate precursor mainly consists of the following three components: the PMMA emulsion, IR-830 and PAA. PAA is employed as a film-forming binder for the image recording layer. The addition of a small amount of defoamer is helpful to get a uniform coating. The prepared lithographic printing plate precursor was image-wise exposed at a rate of 180 mJ/cm$^2$, using a image-setter (CRON) with a laser which can emit a IR rays and a wavelength of 830 nm. IR laser scanning caused an instantaneous temperature rise (nearly up to 300 °C) of the exposed area [9]. Infrared dyes play an important role in this process, which could convert the lase energy into heat efficiently. Due to the heat generated during the exposure step, two changes took place in the exposed parts: (1) physical change, i.e. the fuse and coagulation of PMMA polymer particles; (2) chemical change, i.e. the decomposition of the hydrophilic amine oxide. The two changes contributed to form a hydrophobic phase, which could not be removed by water development. As a result, the exposed parts of the layer became the printing areas of the printing plate. However, the unexposed parts of the layer could still be developed with water, which corresponds to the non-graphic area of the printing plate. Finally, a negative image was obtained successfully (Fig. 5).
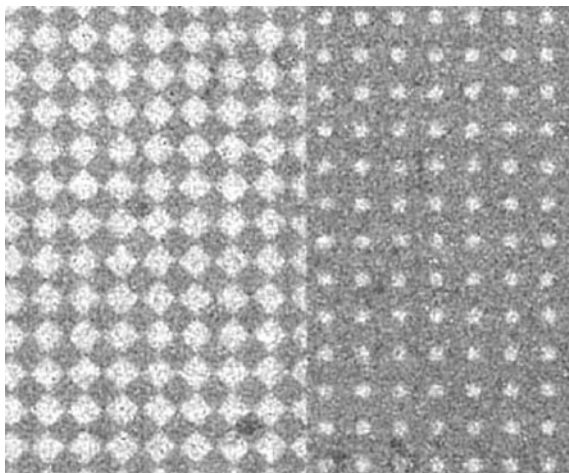


**Fig. 5.** Micrograph of the imageable layer after laser exposure and developing with water (40 times).

## 4    Conclusions

Soapless emulsion of methyl methacrylate was carried out using a reactive emulsifier, poly(tertiary amine oxide) (O-PDMAPMA), which was obtained through the oxidization of a poly(tertiary amine) (PDMAPMA) prepared by reversible addition-

fragmentation chain transfer (RAFT) radical polymerization of N-(2-dimethylaminopropyl) acrylamide. The radical emulsion polymerization of MMA proceeded smoothly in the presence of O-PDMAPMA, resulting in a stable PMMA emulsion with regular size and distribution. A negative working and laser-imageable layer was prepared through the combination of the polymer emulsion, PAA and IR-830. Clear images can be obtained after IR laser imaging and water development. This work may contribute to the development of new negative working lithographic printing plate precursor.

# References

1. Majhi PR, Dubin PL, Feng XH et al (2004) Coexistence of spheres and rods in micellar solution of dodecyldimethylamine oxide. J Phys Chem B 108(19):5980–5988
2. Brinchi L, Germani R, Di Profio P et al (2010) Viscoelastic solutions formed by worm-like micelles of amine oxide surfactant. J Colloid Interface Sci 346(1):100–106
3. McDonough K, Itrich N, Menzies J, Casteel K et al (2018) Sci Total Environ 616–617:164–171
4. Lim JC, Han DS (2011) Synthesis of dialkylamido amine oxide surfactant and characterization of its dual function detergency and softness. Coll Surf A Physicochem Eng Asp 389 (1):166–174
5. Kumar SS, Bajpai M, Tyagi VK (2006) Amine oxides: a review. J Oleo Sci 55(3):99–119
6. Mercedes FS, Encarnacion J, Alejandro FA et al (2014) Ecotoxicological assessment of mixtures of ether carboxylic derivative and amine-oxide-based non-ionic surfactants on the aquatic environment. J Surfactants Deterg 17(6):1161–1168
7. Duan JT, Xu MC, Li HT, Shi ZQ, He BL (2004) Synthesis of oxidized tertiary amine resin and its adsorption property for phenol. Ion Exch Adsorpt [Chin] 20(1):40–45
8. An L, Yu BB, Pu JL, Li ZX (2016) Synthesis and properties of water soluble thermo-sensitive resin with tertiary amine oxide substituents in the side chain. Polym Bull 73(1):53–64
9. Celin S, Ken-ichi S, Hans-Joachim T, et al. (2003) Thermal digital litho-graphic printing plate. US Patent. US6534238

# Synthesis and Photophysical Properties of 9,10-Diarylanthracene

Wan Zhang[1(✉)], Yuke Wu[1], Xing Feng[2], Yingjie Xu[1], Le Ma[1], and Xianfu Wei[1]

[1] School of Printing and Packaging Engineering, Beijing Institute of Graphic Communication, Beijing, China
22722234@qq.com
[2] School of Materials and Energy GDUT, Guangdong University of Technology, Guangdong, China

**Abstract.** 9,10-Bis(4-methoxyphenyl) anthracene(**2a**) and 9,10-bis(4-formylphenyl) anthracene(**2b**) were synthesized by Suzuki coupling reaction. The target molecular structure was fully characterized by ^{1}H NMR and mass spectra. The photophysical properties of two compounds in diluted $CH_2Cl_2$ solutions were obtained by using UV-vis and FL spectra and the thermal stability were researched by TGA and DSC. At the same time, the aided verification was operating by DFT calculations. The results show that two compounds have excellent thermal stability because of the increase of substituents which can benefit to improve thermal stability. The decomposition temperatures ($T_d$) of 9,10-bis(4-methoxyphenyl) anthracene can reach to 307 °C. All these molecules show highly blue emissions ($\lambda_{max}FL < 477$ nm) with excellent quantum yields ($\Phi_f > 0.52$) in solution and with the increase of π-conjugation, the emission peak maximum exhibits the red Stokes shift (40 nm). The UV-vis absorption and FL emission spectra of compound **2a** have almost no change depending on the solvent polarity, moreover, the FL emission spectra of compound **2b** has the obvious red Stokes shift on moving from non-polar solvent(cyclohexane) to strong-polar solvent(DMF). That can be utilized as promising potential blue emitters in organic light-emitting devices (OLEDs) applications.

**Keywords:** Anthracene · OLED · Blue emitter · Photophysical · DFT calculations

## 1 Introduction

At present, the Organic Light-Emitting Diodes (OLEDs) devices are showing significant commercial application prospect in communications, information, display, lighting, Full-Color Flat-Panel Displays and other high-tech areas [1, 2], which has become a research hotspot at present stage. Many scientists committed to the research of OLED, and achieved good results [3–8]. In the process of the development of OLED, in order to realize Full-Color Flat Panel Displays, the development of blue light emitting materials is very important. Blue material not only can realize high efficient

and stable blue light emission, meet the requirements of Full-Color display, and because of its wide energy gap, you can get the corresponding red light and green light materials by using chemical modification methods or methods of energy transfer.

Anthracene belongs to a family of PAHs compounds, that possesses excellent photoluminescence (PL) quantum yields and EL properties, as well as high thermal stabilities, which has become a very important kind of light-emitting materials [9–12]. Since Pope [13] first determined that a single crystal of anthracene exhibits the phenomenon of organic electroluminescence under a high voltage, the synthesis of anthracene compounds and its application in luminescence devices received widespread attention, and the photophysical properties of anthracene derivatives were systematically studied. 9,10-diarylanthracene as a kind of classic blue light material, widely used in OLED devices, shows a good application prospect. However, the reports about the influences of substituent on the photophysical properties and thermal stability of 9,10-diarylanthracene are rarely. This work adopt 9,10-diarylanthracene as raw material and prepared 9,10-bis(4-methoxyphenyl) anthracene (**2a**) and 9,10-bis(4-formylphenyl) anthracene (**2b**) by using the Suzuki coupling reaction. The structures were characterized by $^1$H NMR and mass spectrometry and the luminescence property was studied by ultraviolet and fluorescence spectrum.

## 2 Experimental

### 2.1 Materials

Toluene (A.R.), dichloromethane (A.R./S.P.), ethanol (A.R.), acetone (A.R.) and Dimethyl Formamide (DMF) (S.P.) were purchased from Beijing chemical reagent factory; Tetrahydrofuran (THF) (S.P.), cyclohexane (S.P.), acetonitrile (S.P.), 1,4-dioxane (S.P.), 9-bromoanthracene (98%), 9,10-bis-bromoanthracene (98%), 4-methoxyphenylboronic acid (98%), 4-formylphenylboronic acid (98%), $K_2CO_3$ (98%), NaCl (98%) and $MgSO_4$ (98%) were purchased from Beijing guoyao; Pd $(PPh_3)_4$ (98%) was purchased from Aladdin.

### 2.2 Instruments

$^1$HNMR spectra was recorded at 400 and 100 MHz, respectively, on a Bruker AV-400 NMR spectrometer using DMSO as an internal reference. Mass spectra were obtained by using a Bruker (MALDI-TOF/TOF) ultrahigh performance mass spectrometer. Elemental analysis was performed using a Yanaco MT-5 instrument. Thermogravimetric analysis (TGA) was carried out under a nitrogen atmosphere at a heating rate of 10 °C min$^{-1}$ using a NETZSCH TASC414/4 instrument. Differential scanning calorimetry (DSC) was performed under a nitrogen atmosphere at a heating rate of 10 °C min$^{-1}$ using a NETZSCH DSC-200PC instrument. UV-vis spectra were obtained by using a Shimadzu UV-2501PC UV/Vis/NIR spectrophotometer. FL spectra were recorded on a Shimadzu RF-5301PC FL spectrophotometer. The FL lifetimes of the compounds were determined using an Edinburgh FL920 spectrophotometer.

## 2.3    Synthesis of Anthracene Derivatives

The synthesis of 9,10-bis(4-methoxyphenyl) anthracene (**2a**): A mixture of 9, 10-bromoanthracene (588 mg, 1.55 mmol), 4-methoxyphenylboronic acid (588 mg, 3.87 mmol), $K_2CO_3$ (200 mg, 1.45 mmol), toluene (30 mL), a mixed solution of ethanol and $H_2O$ [10 mL, V(ethanol):V($H_2O$) = 1:1] and Pd(PPh$_3$)$_4$ (45 mg, 0.03 mmol) was heated from room temperature to 90 °C and then maintained at this temperature for 24 h with stirring under argon. After cooling to room temperature, the mixture was quenched with water, extracted with $CH_2Cl_2$ [V($CH_2Cl_2$) = 3 × 100 mL], and washed with water and brine. A yellow solid (500 mg) was obtained that could be dissolved in $CH_2Cl_2$ and $CHCl_3$ easily but with some difficulty in methanol, ethanol and acetone and other commonly used solvents. Recrystallization from a mixed solution of $CH_2Cl_2$ and $CHCl_3$ (2:1 V/V) gave **2a** (288 mg, 63%) as a white crystal (Fig. 1).
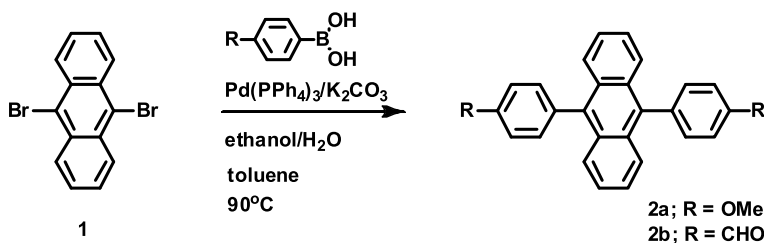


**Fig. 1.**  The synthesis of 9,10-diarylanthracene **2**

The synthesis of 9,10-bis(4-formylphenyl) anthracene (**2b**): A mixture of 9, 10-bromoanthracene (588 mg, 1.55 mmol), 4-formylphenylboronic acid (588 mg, 3.87 mmol), $K_2CO_3$ (200 mg, 1.45 mmol), toluene (30 mL), a mixed solution of ethanol and $H_2O$ [10 mL, V(ethanol):V($H_2O$) = 1:1] and Pd(PPh$_3$)$_4$ (30 mg, 0.03 mmol) was heated from room temperature to 90 °C and then maintained at this temperature for 24 h with stirring under argon. After cooling to room temperature, the mixture was quenched with water, extracted with $CH_2Cl_2$ [V($CH_2Cl_2$) = 3 × 100 mL], and washed with water and brine. A yellow solid (500 mg) was obtained that could be dissolved in $CH_2Cl_2$ and $CHCl_3$ easily but with some difficulty in methanol, ethanol and acetone and other commonly used solvents. Recrystallization from a mixed solution of $CH_2Cl_2$ and $CHCl_3$ (2:1 V/V) gave **2b** (255 mg, 53%) as a yellow crystal.

## 3    Result and Discussion

### 3.1    Structural Characterization

The molecular structure of **2a** and **2b** were characterized by [1] HNMR, MS and elemental analysis, as shown in Figs. 2, 3 and Table 1. The peaks in the $\delta_H$ = 7.21 ppm and 7.36 ppm respectively represent four hydrogen atoms on two phenyl of compound **2a**, $\delta_H$ = 7.40 ppm and 7.62 ppm respectively represent four hydrogen atoms on anthracene ring, and the single peak in the $\delta_H$ = 3.91 ppm represents six hydrogen

atoms on methoxy. Because of the electron-donating conjugation effect of methoxy group, its chemical shift has larger shift compared to the hydrogen atom on anthracene ring and phenyl. It is obvious to see one of the biggest mass peak 390.1621 $m/z$ on the mass spectrogram, which is in accordance with the molecular weight of **2a** $C_{28}H_{22}O_2$ (390.16).
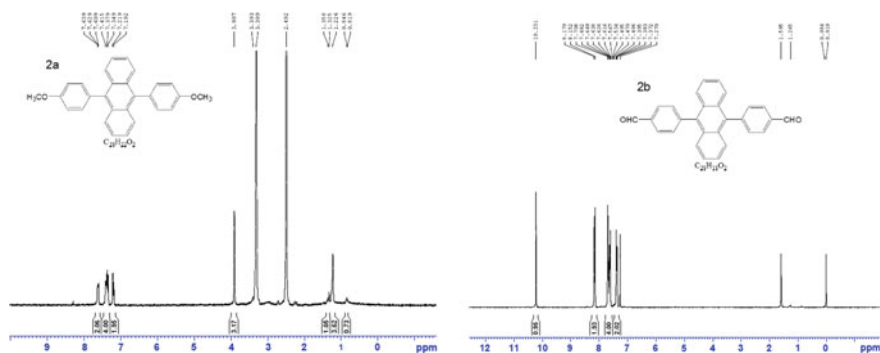


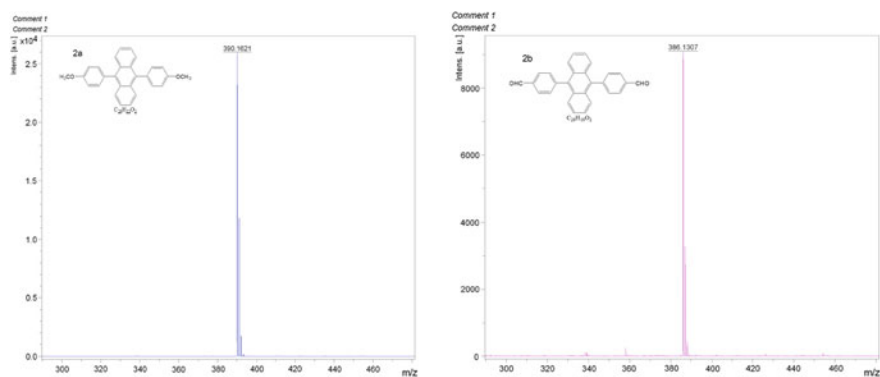**Fig. 2.** The $^1H$ NMR of compounds **2a** and **2b**



**Fig. 3.** The mass spectra of compounds **2a** and **2b**

The peaks in the $\delta_H = 7.38$ ppm and 7.48 ppm respectively represent four hydrogen atoms on two phenyl of compound **2b**, $\delta_H = 7.66$ ppm and 8.16 ppm respectively represent four hydrogen atoms on anthracene ring, and the single peak in the $\delta_H = 10.23$ ppm represents two hydrogen atoms on formyl. Because of the strong electron-withdrawing of formyl group, its chemical shift moves to low field compared to the hydrogen atom on anthracene ring and phenyl. It is obvious to see one of the biggest mass peak 386.1307 $m/z$ on the mass spectrogram, which is in accordance with the molecular weight of **2b** $C_{28}H_{18}O_2$ (386.13).

The elemental analysis values in Table 1 show the elemental theoretical values are in accordance with the measured values.

**Table 1.** Relevant data of compounds **2a** and **2b**

| Comds. | Chemical structure | Elemental analysis: theoretical value (measured value) | ^{1}H NMR (300 MHz, DMSO), δ (ppm) |
|---|---|---|---|
| **2a** | | C:86.13 (86.27), H:5.68 (5.71), O:8.19 (8.16) | 3.91 (s, 6H, OMe-*H*), 7.21(d, *J* = 10.8 Hz, 4H, Ar-*H*), 7.36 (d, *J* = 12 Hz, 4H, Ar-*H*), 7.40 (d, *J* = 14.4 Hz, 4H, Antracene-*H*), 7.62 (d, *J* = 12 Hz, 4H, Antracene-*H*) |
| **2b** | | C:87.02 (87.13), H:4.69 (4.85), O:8.28 (8.16) | 7.38 (d, *J* = 10.8 Hz, 4H, Ar-*H*), 7.48 (d, *J* = 10.8 Hz, 4H, Ar-*H*), 7.66 (d, *J* = 14.4 Hz, 4H, Antracene-*H*), 8.16 (d, *J* = 12 Hz, 4H, Antracene-*H*), 10.23 (s, 2H, CHO-*H*) |

## 3.2  Stability Analysis

The high melting point ($T_m$) and decomposition temperature ($T_d$) are essential properties for preparing long-life practical devices. In this part, the thermal stability of the synthetic luminescent materials was studied.

The thermal weight loss (Tg) curves of compounds **2a** and **2b** are shown in Fig. 4. The Tg curve of compound **2a** has two weight-loss platforms. One occurs in about 100 °C and the weight loss ratio is about 20%, which is possibly corresponding to the weight loss caused by the volatilization of moisture or small organic molecule in compound **2a**. The second weight loss occurs after 270 °C, which shows a bigger weight-loss curve corresponding to the fracture of molecular skeleton in compound. Compound **2b** has a 5% weight-loss in about 307 °C, which illustrates compound **2b** starts to break down in this temperature, along with the molecular skeleton of the collapse. Two compounds as temperatures continue to rise, TG curves gradually become level, the quality of the final residue number of molecules of 15% or less.
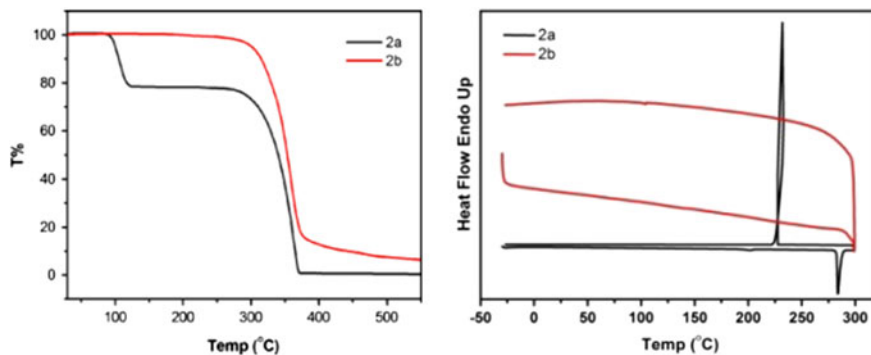


**Fig. 4.** The TG and DSC curve of 9,10-diarylanthracene **2**

Compared with the previously reported single substituent anthracene compounds at the 9-position, the decomposition temperature of 9-(4-methoxyphenyl) anthracene is 247 °C, 9-(4-formylphenyl) anthracene is 221 °C [14], the bis-substitution compounds **2a** and **2b** at the 9- and 10-positions significantly have higher decomposition temperature than single substituent anthracene compounds at the 9-position, this shows that with the increase of replacing groups, anthracene compounds will also further enhance the thermal stability. In addition, it also shows that due to the substituent –CHO with strong electron-withdrawing and larger molecular conjugate degree than –OMe, therefore, different substituents will also further influence of the thermal stability of anthracene luminescent material. The glass transition temperatures ($T_g$) were not observed for these compounds by DSC, as shown in Fig. 4 (right).

## 4 Photophysical Properties

At room temperature, using dichloromethane as solvent, the ultraviolet absorption spectrum and fluorescence spectrum of compounds **2a** and **2b** respectively tested. As shown in Fig. 5 (left), the UV-vis absorption spectra of compounds **2a** and **2b** in 325–400 nm appears obvious three sharp peaks, belongs to the characteristic absorption peak of anthracene ring. Obviously, the ultraviolet absorption curves of **2a** and **2b** are almost the same, which exhibits the small volume of replacing groups such as methoxyl, formylin this system, has little impact on the ultraviolet absorption spectrum of the whole molecule. The maximum absorption wavelength of 376 nm is corresponding to the electronic π-π* transition. Figure 5 (right) are the fluorescence spectrums of compounds **2a** and **2b** in methylene chloride solution at room temperature. It can be seen by the fluorescence spectra, compound **2a** shows a narrow bandwidth, and the fluorescence spectrum of **2b** is wide, which shows that due to the introduction of the group –CHO, the interaction between the molecules increase. The maximum emission wavelength of compounds **2a** and **2b** are 430 nm and 477 nm.
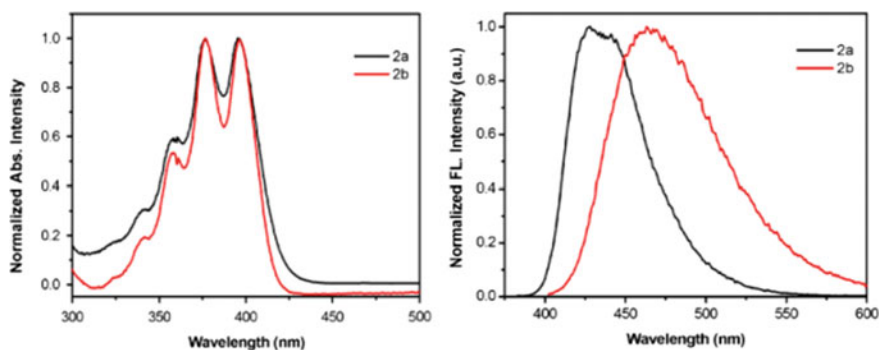


**Fig. 5.** Normalized UV-vis absorption (Left) and FL spectra (Right) of compounds **2** recorded in dichloromethane at about $10^{-5}$ to $10^{-6}$ M at 25 °C

Compared to **2a** and **2b**, the introduction of formyl can cause the increase of the molecular π-conjugate and lead to strong red shift phenomenon, the largest red shift to 47 nm. Obviously, compound **2a** shows a dark blue fluorescence, while compound **2b** shows blue-green fluorescence. Table 2 can express more intuitively the relationship between the maximum absorption wavelength and emission wavelength of two compounds. Further we tested the quantum yields of two compounds, respectively were 0.65 for **2a**, 0.52 for **2b**.

**Table 2.** Photophysical properties of compounds **2a** and **2b**

| Comds. | $\lambda_{max}abs^a$ (nm) | $\lambda_{max}FL^a$ (nm) | Stokes shift$^a$ (nm) | $\Phi_f^b$ | $T_g^c$ (°C) | $T_m^c$ (°C) | $T_d^d$ (°C) | $E_{HOMO}$ $_{(cal)}^e$ (eV) | $E_{LUMO}$ $_{(cal)}^e$ (eV) | $E_{gap}$ $_{(cal)}^e$ (eV) |
|---|---|---|---|---|---|---|---|---|---|---|
| **2a** | 358, 376, 395 | 430 (375) | 55 | 0.65 | – | 286 | 270 | −5.08 | −1.60 | 3.48 |
| **2b** | 358, 376, 395 | 477 (376) | 101 | 0.52 | – | 267 | 307 | −5.46 | −1.95 | 3.51 |

$^a$The maximum absorption wavelength $\lambda_{max}abs$, the maximum emission wavelength $\lambda_{max}FL$ and excitation wavelength (375 nm for **2a**, 376 nm for **2b**), test condition: solvent: dichloromethane, concentration: $10^{-5}$ to $10^{-6}$ M, temperature: 25 °C; $^b$quantum yield, test condition: solvent: dichloromethane, quinine sulfate ($\Phi = 0.55$) soluble in sulfuric acid as the reference standard; $^cT_g$ and $T_m$, using DSC; $^dT_d$, using TGA; $^e$DFT using Gaussian 03

In addition, we studied the influence of different solvents on the photophysical properties. The photophysical properties of compounds **2a** and **2b** were measured respectively in cyclohexane, 1,4-dioxane, THF, methylene chloride, acetonitrile, and N, N-dimethyl formamide (DMF).The results show the ultraviolet absorption spectrum and fluorescence spectrum of compound **2a** are almost the same with the increase of the solvent polarity, which illustrates the solvent polarity has the little effects on the photophysical properties of compound **2a**. However, as shown in Fig. 6, the maximum emission wavelength of compound **2b** in cyclohexane is 431 nm and in DMF is 490 nm and the fluorescence spectrum appears larger redshift (about 59 nm), which shows that the polarity of the solvents have bigger influence on the compound **2b**. This shows that the fluorescence emission spectrum of compound **2b** from nonpolar solvents (cyclohexane) to strong polar solvents (DMF), red shift gradually increased, may be because the strong polar solvent can destroy a faint C–H…O interaction, and cause division of molecular aggregation. In nonpolar solvent, the synergistic effect between π–π and C–H…O interaction can lead to molecular aggregation [15, 16].
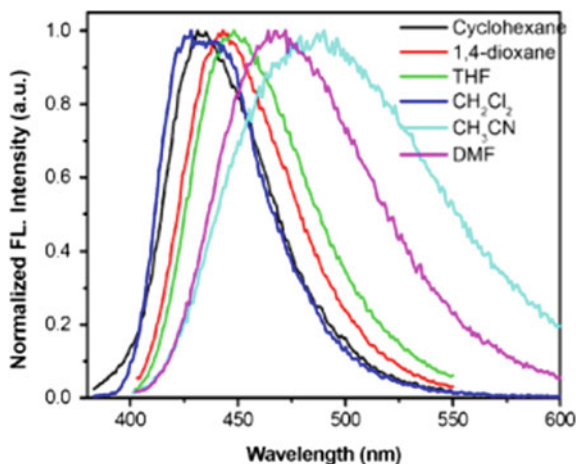
**Fig. 6.** The FL spectra of compounds **2b** in different solvents

## 4.1 Quantum Chemistry Calculation

Using Gaussian 03 of quantum chemistry, the geometry optimization of compound **2a** was operated by density functional method at B3LYP/6-31D(d)level, which can get the most stable molecular geometry and calculate the electronic structure and the frontier orbital. As shown in Fig. 7, compounds **2a** and **2b** in the benzene ring and the level of anthracene ring are almost vertical, the repulsion effects between the space is the least of all, and the molecular structure is the most stable. In addition, the HOMO and LUMO orbit of two compounds mainly concentrate in the anthracene ring part. The HOMO orbital value of **2a** is −5.08 eV, and LUMO is −1.60 eV, $E_{gap} = E_{LUMO} − E_{HOMO} = 3.48$ eV; The HOMO orbit value of **2b** is −5.46 eV, and LUMO is −1.95 eV, $E_{gap} = 3.51$ eV. It shows that the HOMO energy level of compound **2b** (−5.46 eV) containing electron-withdrawing groups –CHO is lower compared to the compound **2a** with electronic-donating groups. And its Stokes shift is larger than **2a** too because of the strong electron-withdrawing groups can increase the oxidation potential of molecules which can lead to lower HOMO energy level [17]. Therefore, the theoretical calculation proves that the redshift of compound **2** between absorption and emission spectrum is in accordance with the experiment results.
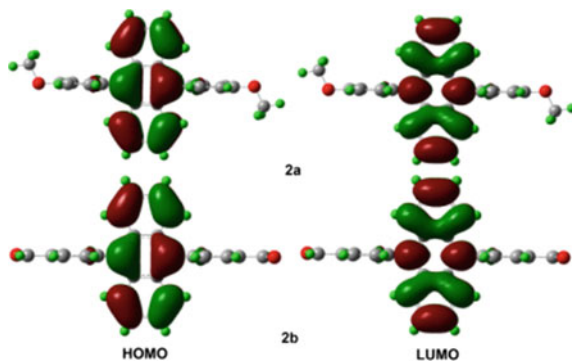
**Fig. 7.** Computed molecular orbital plots (B3LYP/6-31G*) of **2**

## 5    Conclusions

9,10-bis(4-methoxyphenyl) anthracene (**2a**) and 9,10-bis(4-formylphenyl) anthracene (**2b**) were synthesized by Suzuki coupling reaction. The target molecular structure was fully characterized by $^1$H NMR and mass spectra and the thermal stability was researched by TGA and DSC. The results show that two compounds have excellent thermal stability because of the increase of substituents which can benefit to improve thermal stability and the decomposition temperatures ($T_d$) of 9,10-bis(4-methoxyphenyl) anthracene can reach to 307 °C. Further, the UV-vis absorption and FL emission spectra of two compounds were studied detailedly and the results show both compounds **2a** and **2b** can emit blue fluorescence and the emission peak maximum exhibits the red Stokes shift (40 nm) with the increase of π-conjugation. That can be utilized as promising potential blue emitters in organic light-emitting devices (OLEDs) applications. Overall, the anthracene luminescent material with good thermal stability, suitable fluorescence emission wavelength, etc., has hope as a blue emitting light and blue light main material used in electroluminescent devices.

## References

1. Chen JX, Huang XW (2011) OLED display: material and device. Posts and Telecom Press, Beijing
2. Huang W, Mi BX, Gao ZQ (2011) Organic electronics. Science Press, Beijing
3. Uoyama H, Goushi K, Shizu K, Nomura H, Adachi C (2012) Highly efficient organic light-emitting diodes from delayed fluorescence. Nature 492:234–238
4. Du JR, Wang MR, Chen NK, Xie SY, Yu HM, Wu Q (2016) Instability origin and improvement scheme of facial Alq$_3$ for blue OLED application. Chem. Res. Chinese Universities 32(3):423–427

5. Li NQ, Fan ZK, Zhao HR, Quan YW, Chen QM, Ye SH, Li SH, Fan QL, Huang W (2016) A bipolar macrospirocyclic oligomer based on triphenylamine and 4,5-diazafluorene as a solution-processable host for blue phosphorescent organic light-emitting diodes. Dyes Pigments 134:348–357

6. Shao SY, Ding JQ, Wang LX (2016) New applications of poly(arylene ether)s in organic light-emitting diodes. Chin Chem Lett 27:1201–1208

7. Tanaka Y, Takahashi T, Nishide J, Hiraga Y, Nakanotani H, Adachi C (2016) Application of wide-energy-gap material 3,4-di(9H-carbazol-9-yl)benzonitrile in organic light-emitting diodes. Thin Solid Films 619:120–124

8. Yu MQ, Wang SM, Shao SY, Ding JQ, Wang LX, Jing XB, Wang FS (2015) Starburst 4,4′,4″-tris(carbazol-9-yl)-triphenylamine-based deep-blue fluorescent emitters with tunable oligophenyl length for solution-processed undoped organic light-emitting diodes. J Mater Chem C 3:861–869

9. Mallesham G, Balaiah S, Ananth Reddy M, Sridhar B, Punita S, et al. (2014) Design and synthesis of novel anthracene derivatives as n-type emitters for electroluminescent devices: a combined experimental and DFT study. Photoch Photobio Sci 13:342–357

10. Zhao L, Wang SM, Ding JQ, Wang LX (2016) Synthesis and characterization of solution-processible anthracene-based deep-blue fluorescent dendrimers. Chin Sci Bull 61:325–332

11. Sun J, Zhong HL, Xu EJ, Zeng DL, Zhang JH, Xu HG, Zhu WQ, Fang Q (2010) An X-shaped solution-processible oligomer having an anthracene unit as a core: a new organic light-emitting material with high thermostability and efficiency. Org Electron 11:74–80

12. Kang I, Back JY, Kim R, Kim YH, Kwon SK (2012) High efficient and high color pure blue light emitting materials: new asymmetrically highly twisted host and guest based on anthracene. Dyes Pigm 92:588–595

13. Pope M, Kallmann H, Magnante P (1963) Electroluminescence in organic crystals. Chem Phys 38:2042–2043

14. Zhang W, Wang Q, Feng X, Yang L, Wu YK, Wei XF (2017) Anthracene-based derivatives: synthesis, photophysical properties and electrochemical properties. Chem Res Chin Univ 33 (4):603–610

15. Venkataramana G, Sankararaman S (2006) Synthesis and spectroscopic investigation of aggregation through cooperative π–π and C–H···O interactions in a novel pyrene octaaldehyde derivative. Org Lett 8:2739–2742

16. Sciano JC (1989) Handbook of organic photochemistry. CRC Press, Boca Raton, FL

17. Yucel B, Meral K, Ekinci D, Uzunoglu GY, et al (2014) Synthesis and characterization of solution processable 6,11-dialkynyl substituted indeno[1,2-b]anthracenes. Dyes Pigm 100:104–117

# Effect of Reaction Temperature on the Fluorescence Properties of CMC/LaF$_3$: Eu$^{3+}$ Composites

Yuhan Zhong, Guangxue Chen$^{(\boxtimes)}$, and Qing Wang

Key Laboratory of Pulp and Paper, South China University of Technology,
Guangdong, China
chengx@scut.edu.cn

**Abstract.** In this study, sodium carboxymethyl cellulose (CMC) was used as raw material, rare earth chloride was used as inorganic nano luminescent material to prepare a series of lanthanide rare earth ions-doped nanocrystals and composite materials. The photoluminescent materials were prepared via in situ chemical deposition of rare earth ions onto the surface of sodium carboxymethyl cellulose (CMC) with the help of carboxyl groups contained on the surface of sodium carboxymethyl cellulose (CMC). The structure, fluorescence properties and crystalline structure of the composites were characterized by FT-IR spectra (FTIR), field emission scanning electron microscope (FESEM), photoluminescence spectra (PL) and X-ray diffraction (XRD). The results showed that CMC/LaF$_3$: Eu$^{3+}$ composite material was successfully prepared, and its fluorescence intensity can be organically controlled by temperature. The method has mild reaction conditions, facile process without expensive material equipment, and the composite has good fluorescence intensity, which can be used for functional packaging materials.

**Keywords:** Sodium carboxymethyl cellulose · Rare earth ions · Temperature · Fluorescent property

## 1 Introduction

With the development of the economy and the improvement of people's living standards, people's demand for medium and high-end goods is increasing. However, the counterfeit goods has emerged in an endless stream, especially in the fields of medicines, cosmetics, tobacco and alcohol, which not only causes serious economic losses, but also endangers the health of consumers. Therefore, in order to accurately identify the authenticity of products, a variety of anti-counterfeiting technologies are used in industrial production. Fluorescent fiber, as a special fiber that can generate visible light under the excitation of ultraviolet light, has a good anti-counterfeiting effect and can be used as security fiber in the field of anti-counterfeiting labels [1].

Rare earth luminescence is one of the outstanding functions of rare earth compounds. The luminous efficiency of luminescent materials is mainly caused by various factors such as excitation efficiency and power, energy transfer from matrix to activator, and electron radiant transition from activator state energy level to ground state. In recent years, studies have found that a material having a upconversion luminescence

property represented by a lanthanide element have the advantages of high color purity, strong fluorescence signal, long fluorescence lifetime, high stability of coordination structure, and environmental friendliness, which make them detect fluorescence and time. In addition, the increasing number of counterfeit and shoddy products in life has led to an ongoing study of the preparation and properties of nanomaterials [2].

Sodium carboxymethyl cellulose is a cellulose derivative with an ether structure obtained by chemical modification of natural cellulose, which is one of the most widely used natural cellulose derivatives. CMC/metal nanocomposites not only have the characteristics of cellulose macromolecules, but also have the properties of some metals. These kind of nanocomposites are environmentally friendly, non-toxic, low cost, which can meet the requirements of green chemistry and sustainable development [3].

Therefore, CMC-based fluorescent materials have become the hot spot of current research. It is worth mentioning that carboxymethyl cellulose also has good water solubility and light transmittance. Lately, a large number of carboxymethyl cellulose composites have been synthesized. The carbon dots conjugated carboxymethyl cellulose-hydroxyapatite nanocomposite is synthesized by a one-pot method and can be used in various applications such as metal ion sensing, osteogenic activity, bioimaging and drug carriers [4]. A transparent sunlight conversion film based on carboxymethyl cellulose (CMC) and carbon dots (CD) has been developed by dispersing carboxymethyl cellulose in an aqueous solution of CMC [5].

Based on these research backgrounds, carboxymethyl cellulose sodium (CMC) was used as raw material to prepare CMC/LaF$_3$: Eu$^{3+}$ modified materials by in situ adsorption of rare earth ions. The temperature affects the particle size and its distribution, surface area, microstructure etc., which in turn affects its fluorescent properties. As a result, temperature is a very important factor in the synthesis of CMC/LaF$_3$: Eu$^{3+}$ nanocomposites. In this study, CMC/LaF$_3$: Eu$^{3+}$ nanocomposites were prepared under different temperature conditions. The relationship between reaction temperature and nanocomposites fluorescence properties was analyzed.

## 2 Experimental

### 2.1 Materials

Carboxymethyl cellulose (viscosity: 300–600 mPa s; USP) was provided by Tianjin Fuchen Chemical Reagent Factory, europium chloride hexahydrate (99.99%) was acquired from Shanghai Aladdin Co., Ltd., lanthanum chloride hexahydrate (99.99%) and sodium fluoride (NaF, 98.0%) were purchased from Shanghai Maclean Biochemical Technology Co., Ltd.

### 2.2 Preparation of CMC/LaF$_3$: Eu$^{3+}$ Composites

The CMC/LaF$_3$: Eu$^{3+}$ composites were synthesized through direct coprecipitating rare earth ions (La$^{3+}$, Eu$^{3+}$) and fluoride ion (F$^-$) in an aqueous suspension at 50–90 °C. In a typical process, 1.0 g of CMC was dissolved in 50 ml of deionized water at 50–90 °C under vigorous stirring (300 rpm) for 30 min. Then, 10 mL of rare earth aqueous solution

(The molar ratio of $LaF_3$: $Eu^{3+}$ and $Eu^{3+}$ is 7:3) with 0.3 g rare earth ions was introduced and the mixture solution was constantly stirred for 30 min at 50–90 °C. Soon afterwards, aqueous NaF solution (3.2 mmol of NaF dissolved in 30 ml of water) was added dropwise within 30 min and then performed at 50–90 °C for 3 h, directly causing CMC/$LaF_3$: $Eu^{3+}$ composites. The resulting solution was then centrifuged at 4000 rpm for 5 min and rinsed 3 times with deionized water to purify products.

## 2.3   Characterizations

The chemical structures of carboxymethyl cellulose before and after modification were characterized by FT-IR spectra (Spectrum 2000 PerkinElmer spectrometer, USA). Surface morphology were recorded on a field emission scanning electron microscope (FEI Quanta 400F) (FESEM). The photoluminescence (PL) spectra were performed using a fluorescent spectrophotometer (HORIBA Jobin Yvon). Crystal structures were carried out on X-ray diffraction (XRD) using a Philips PW3040/00 X'Pert MPD diffractometer with Cu Kα radiation at the 40 kV range from 5° to 90°. Using the method of Segal et al., the crystallinity index (CI) of the carboxymethyl cellulose before and after modification was calculated from the reflected intensity data [6, 7].

# 3   Results and Discussion

## 3.1   FTIR Spectra

As shown in Fig. 1, structures of CMC and CMC/$LaF_3$: $Eu^{3+}$ composite materials were characterized by FTIR spectroscopy. Compared with the spectrum of CMC in Fig. 1a, a stretching vibration absorption peak of –C=O appeared at 1616 $cm^{-1}$. After the modification of $RE^{3+}$, the peak of –C=O at 1616 $cm^{-1}$ shifted to lower wavenumber of 1597 $cm^{-1}$ [8]. Besides, the absorption peak changes from the original broad peak to a sharp and narrow peak. The changes in these peaks indicated that the carboxyl group in CMC reacted with the rare earth ions, and the CMC/$LaF_3$: $Eu^{3+}$ composites ware successfully synthesized.
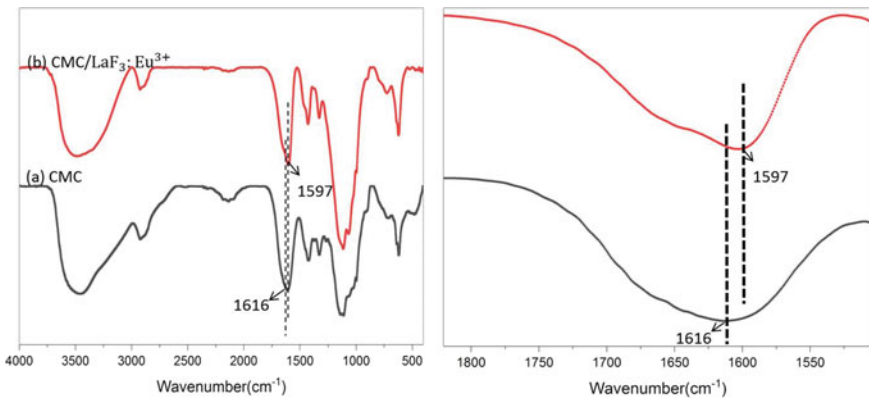


**Fig. 1**   FTIR spectra of **a** CMC and **b** CMC/$LaF_3$: $Eu^{3+}$

### 3.2 SEM Characterization and Analysis

The surface morphology of CMC and CMC/LaF$_3$: Eu$^{3+}$ composites and films obtained by SEM were shown in Fig. 2. Figure 2a shows the surface morpography of the CMC, which has a smooth and uniform surface to provide larger surface area for loading more LaF$_3$: Eu$^{3+}$ nanocrystals. After the rare earth ions embedded in CMC matrix, the LaF$_3$: Eu$^{3+}$ nanocrystals were arranged well on the surface of CMC (Fig. 2b). It can be seen from the results that the free surface of pure CMC film (Fig. 2c) retains a smooth surface, but after the LaF$_3$: Eu$^{3+}$ nanocrystals embedded in CMC substrate, the CMC/LaF$_3$: Eu$^{3+}$ film maintains a homogeneous and compact structure, which further indicates that a strong interaction was formed between LaF$_3$: Eu$^{3+}$ nanocrystals and CMC molecules.
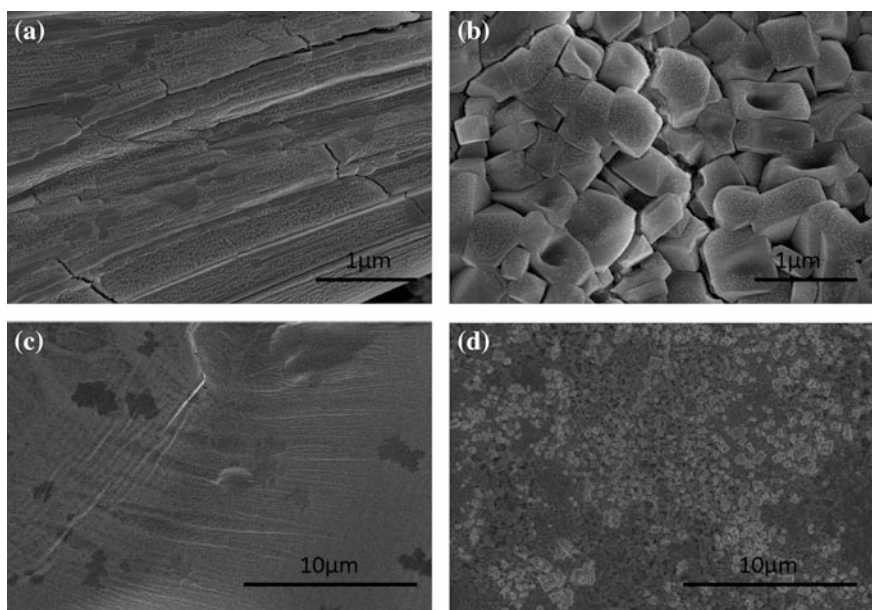


**Fig. 2** SEM images of **a** CMC, **b** CMC/LaF$_3$: Eu$^{3+}$ composite with 0.3 g rare earth ions, **c** CMC film, **d** CMC/LaF$_3$: Eu$^{3+}$ film with 0.3 g rare earth ions

### 3.3 XRD Characterization and Analysis

The crystal structure of CMC/LaF$_3$: Eu$^{3+}$ composite synthesized under different temperature was measured by XRD. After surface modification, the estimated crystallinity index for CMC/LaF$_3$: Eu$^{3+}$ composite synthesized at different temperature was shown in Fig. 3. The crystallinity index increased as the reaction temperature increased, and it reached the maximum when temperature rised to 80 °C. When the temperature exceeded 80 °C, the index decreased. The XRD pattern of the LaF$_3$ crystal agrees with the data reported in the JCPDS standard card (32-0483) for pure hexagonal LaF$_3$

crystals [2, 9]. These results indicated that LaF$_3$: Eu$^{3+}$ nanoparticles doped with rare earth have been well crystallized and embedded in CMC without being changed, which ensured the luminescent properties of the CMC/LaF$_3$: Eu$^{3+}$ composites.
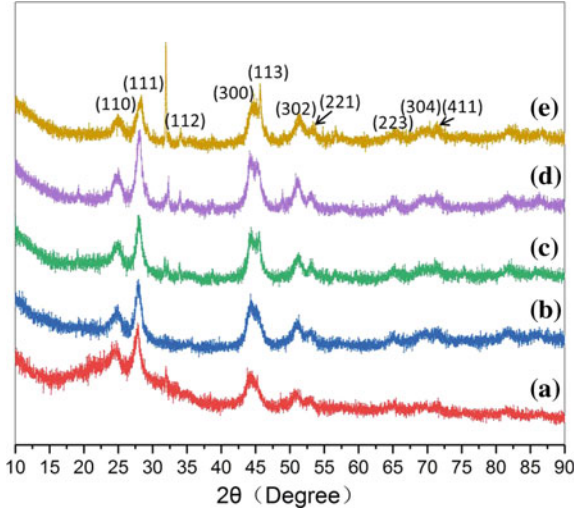


**Fig. 3** XRD patterns of the as-prepared CMC/LaF$_3$: Eu$^{3+}$ composites prepared at: **a** 50 °C, **b** 60 °C, **c** 70 °C, **d** 80 °C, **e** 90 °C

### 3.4   Fluorescence Spectroscopy

The excitation and emission spectrum of the CMC/LaF$_3$: Eu$^{3+}$ composite measured at different temperature was shown in Fig. 4a and b. Figure 4 shows the energy levels of CMC/LaF$_3$: Eu$^{3+}$ composites at 361, 376, 380, 397 and 414 nm corresponded to $^5D_4, ^5G_6, ^5G_2, ^5L_6$ and $^5D_3$ respectively [10]. The main excitation spectrum at 397 nm was attributed to the $^7F_0$-$^5L_6$ transition of Eu$^{3+}$. Under the excitation at 397 nm, the emission spectrum of CMC/LaF$_3$: Eu$^{3+}$composite are at 591 nm, 615 nm, 650 nm and 697 nm, respectively, which emitted red light [11]. Consistent with the previous literature, the main fluorescence peak of Eu$^{3+}$ was located at 591 nm, which was attributed to the magnetic-level transition, which proved that Eu$^{3+}$ was doped to the antisymmetric position of LaF$_3$ nanocrystals [12]. The CMC/LaF$_3$: Eu$^{3+}$ complex shows red color under UV light ($\sim$365 nm), demonstrating that the pre-synthesized CMC/LaF$_3$: Eu$^{3+}$ complex has good fluorescence properties.

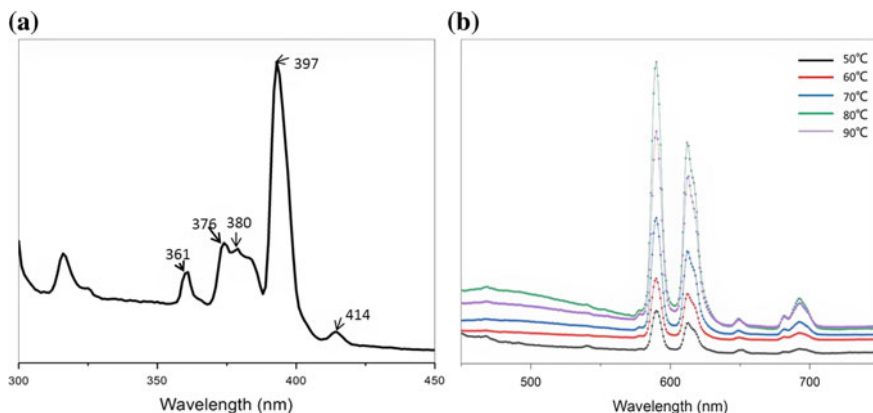**Fig. 4** **a** Excitation spectra of CMC/LaF$_3$: Eu$^{3+}$ composites; **b** Emission spectra of CMC/LaF$_3$: Eu$^{3+}$ composites synthesized at different temperature: 50, 60, 70, 80 and 90 °C

## 4 Conclusions

In this paper, we investigated the effect of temperature on the fluorescence properties of CMC/LaF$_3$: Eu$^{3+}$ composite nanoparticles, and obtained the following conclusions: The CMC/LaF$_3$: Eu$^{3+}$ composite particles synthesized under different temperature were nanoscale, which had high fluorescence properties. When the temperature was 80 °C, the fluorescence intensity of the nanoparticles was the strongest. When the temperature was between 50 and 80 °C, the corresponding fluorescence intensity and fluorescence monochromaticity increased with the increase of temperature; when the temperature was higher than 80 °C, the fluorescence intensity of the nanoparticles showed a downward trend. As a result, the temperature for preparing CMC is preferably between 70 and 80 °C.

## References

1. Wang Qing, Chen Guangxue, Yu Zhaohui (2018) Photoluminescent composites of lanthanide-based nanocrystal-functionalized cellulose fibers for anticounterfeiting applications. ACS Sustain Chem Eng 6(11):13960–13967
2. Wang F, Zhang Y, Fan X, Wang M (2006) One-pot synthesis of chitosan/LaF3: Eu$^{3+}$ nanocrystals for bio-applications. Nanotechnology 17(5):1527–1532
3. Cuba-Chiem LT, Huynh L, Ralston J et al (2008) In situ particle film ATR FTIR spectroscopy of carboxymethyl cellulose adsorption on talc: binding mechanism, pH effects, and adsorption kinetics. Langmuir 24(15):8036–8044

4. Sarkar Chandrani, Chowdhuri AngshumanRay et al (2018) One pot synthesis of carbon dots decorated carboxymethyl cellulose-hydroxyapatite nanocomposite for drug delivery, tissue engineering and $Fe^{3+}$ ion sensing. Carbohyd Polym 181:710–718
5. You Yaqin, Zhang Haoran, Liu Yingliang et al (2016) Transparent sunlight conversion film based on carboxymethyl cellulose and carbon dots. Carbohyd Polym 151:245–250
6. Segal L, Creely J, Martin A, Conrad C (1959) An empirical method for estimating the degree of crystallinity of native cellulose using the X-ray diffractometer. Text Res J 29:786–794
7. Retegi A, Gabilondo N, Peña C, Zuluaga R, Castro C, Gañan P, de la Caba K, Mondragon I (2010) Bacterial cellulose films with controlled microstructure—mechanical property relationships. Cellulose 17:661–669
8. Graf C, Vossen DLJ, Imhof A, van Blaaderen A (2003) A general method to coat colloidal particles with silica. Langmuir 19:6693–6700
9. Goswami M, Das AM (2018) Synthesis of cellulose impregnated copper nanoparticles as an efficient heterogeneous catalyst for CN coupling reactions under mild conditions. Carbohydr Polym 195(1):189–198
10. Chen M, Xie L, Li F, Zhou S, Wu L (2010) Capillary-force induced formation of luminescent polystyrene/(rare-earth-doped nanoparticle) hybrid hollow spheres. ACS Appl Mater Interfaces 2(10):2733–2737
11. Yang R, Zhu Y, Chen F, Dong L, Xiong Z (2017) Luminescent, fire-resistant, and water-proof ultralong hydroxyapatite nanowire based paper for multimode anticounterfeiting applications. ACS Appl Mater Interfaces 9(30):25455–25464
12. Gao D, Tian D, Chong B, Zhang X, Gao W (2014) Rare-earth doped $LaF_3$ hollow hexagonal nanoplates: hydrothermal synthesis and photoluminescence properties. Cryst Eng Comm 16:7106–7114

# Synthesis and Mesomorphism of Triphenylene-Perylene Discotic Mesogenic Dyad

Zhengran Wang, Lina Zhang, Yuwen Feng, Jingze Bi, Huanzhi Yang, Zhenhu Zhang, Chunxiu Zhang[✉], and Jialing Pu

Beijing Institute of Graphic Communication, Beijing, China
zhangchunxiu@bigc.edu.cn

**Abstract.** A novel discotic liquid crystal donor-acceptor dyad was designed and synthesized based on triphenylene and perylene units, which was linked by a flexible alkyl chain. The mesogenic properties were investigated by differential scanning calorimetry (DSC) and polarized optical microscopy (POM), and their chemical structures were determined by ^{1}H-NMR and FT-IR. The discotic liquid crystal compound exhibited good mesomorphic properties and liquid crystal columnar phase properties, providing useful information for organic optoelectronic applications.

**Keywords:** Discotic liquid crystal · Triphenylene · Perylene · Donor-acceptor · Columnar phase properties

## 1 Introduction

Discotic liquid crystals (DLCs) are planar, disc-like molecules that form an ordered array of liquid crystal states under certain conditions [1–4]. Due to DLCs molecules typically have an aromatic chemical structure with several flexible side chains, these molecules tend to self-organize into columns under Van der Waals forces of the side chains and the π–π interactions between the neighboring cores. Triphenylene derivatives is one of the longest-term liquid crystal materials studied because it is easy to synthesize and robust, and it shows an obvious tendency to form column arm mesophase [5–8]. Perylene derivatives, possessing excellent electron affinity and high fluorescence quantum yield, are cheap and easily functionalizable chromophores [9–11]. Until now, only several examples of triphenylene-perylene donor-acceptor were reported. Kumar's group and Cammidge's group investigated perylene derivatives with two triphenylene unit on imides, respectively [12, 13]. They have demonstrated that these compounds exhibit excellent fluorescence emission and mesomorphic properties, but have not investigated the relationship between liquid crystal structure and charge transport properties. According to the above research, We designed a possible way to contact these two discotic liquid crystal molecules with excellent properties through alkyl chain linkage to realize D (donor)–A (accept) transmission system, and control the self-assembly and orientation of molecular units through intermolecular forces. The molecular engineering of covalently linking electron donor (D) and electron acceptor (A) in well-ordered phase-separated D–A molecular systems were relevant for realizing

so-called "molecular heterojunction". Hierarchical self-assembly of DLCs (discotic liquid crystals) through formation of columnar phase is a highly appealing strategy to realize ambipolar charge transport properties.

## 2    Experimental

If not specified, the chemical reagents were analytical reagents which were used in synthesis (Beijing Chemical Reagent Co). The chemical structure was characterized by measurement on a Brucker DMX-300 300 MHz NMR spectrometer and FTIR-8400.

### 2.1    Synthesis of Product 5D5A5

A classical synthetic route was presented which was shown in Fig. 1.
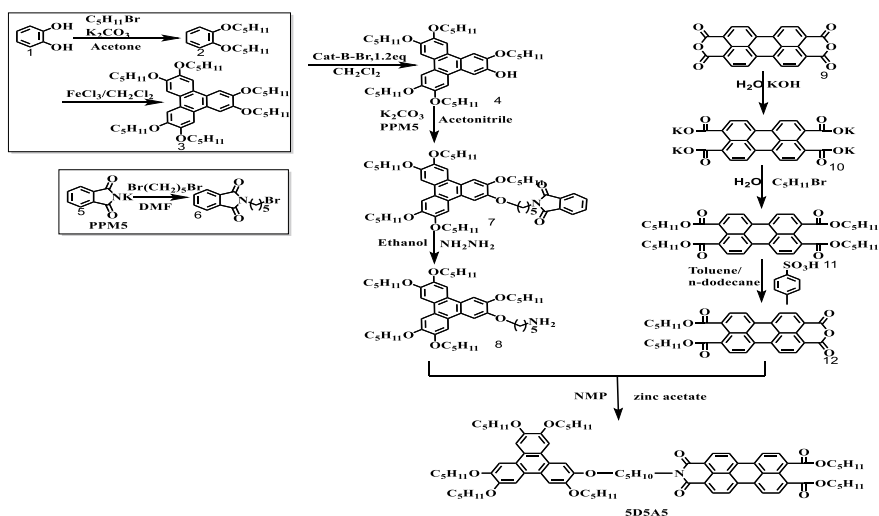


**Fig. 1.**  Synthetic route of compound 5D5A5

## 3    Synthesis of 2-Hydroxy-3,6,7,10,11-Pentabutoxy-Triphenylene

According to the Williamson reaction, phthalic acid was synthesized from catechol and bromo-n-pentane. Then, under the action of ferric trichloride, pentapentyl triphenylene was formed. The compound 4 was synthesized by selective dealkoxy reaction under the action of borane.

## 4    Synthesis of Primary Amine Triphenylene

We use a very low cost phthalimide as a starting material and react with potassium hydroxide in a mixed solvent of water and ethanol to form compound 5 potassium phthalimide. Then, reacting with 1,5-dibromopentane to form compound N-(5-bromopentyl) phthalimide. The compound 7 was synthesized by reaction with the preproduct 2-hydroxy-3,6,7,10,11-pentabutoxy-triphenylene.Finally, the primary amine triphenylene was obtained by reflux with hydrazine hydrate in ethanol.

## 5    Synthesis of Bis-3,4-Anhydride-9,10-Nonanedicarboxylic Acid Di-N-Pentyl Ester

The tetradecyl carboxylic acid dianhydride was used as a starting material, and reacted with potassium hydroxide and 1,5 dibromopentane in an aqueous solution to form a compound 11 perylene tetra-butyl carboxylate. Compound 12 was formed in toluene and n-dodecane solvent.

## 6    Synthesis of Final Product 5D5A5

Finally, compounds 11 and 12 were refluxed in a methylpyrrolidone solvent, and a small amount of anhydrous zinc acetate was added as a catalyst to form the final product 5D5A5.

## 7    Characterization

The DSC curve was measured by a thermal analyzer (Thermal Analysis DSC 2010) and the polarized structure was measured by a Lecia polarized light microscope (POM).

## 8    Results and Discussion

### 8.1    FT-IR and 1H-NMR

FT-IR (cm$^{-1}$): 2948 (C–H), 2860 (C–H), 1714 (C=O), 1691 (O=C–NH), 1261 (C–O)
$^{1}$H-NMR $\delta_H$ (ppm) (400 MHz, CDCl$_3$): 8.37–8.34 (2H, t, H$_{arom}$), 8.17–8.09 (4H, m, H$_{arom}$), 7.99–7.96 (2H, d, H$_{arom}$), 7.62 (4H, s, H$_{arom}$), 7.49 (2H, s, H$_{arom}$), 4.37–4.34 (4H, t, O=C–O–CH$_2$), 4.26–4.08 (14H, m, –O–CH$_2$–, N–CH$_2$,), 1.94–1.79 (18H, m, H$_{aliph}$), 1.56–1.25 (m, 30H, m, H$_{aliph}$), 0.97–0.90 (21H, m, H$_{aliph}$) (Figs. 2 and 3).
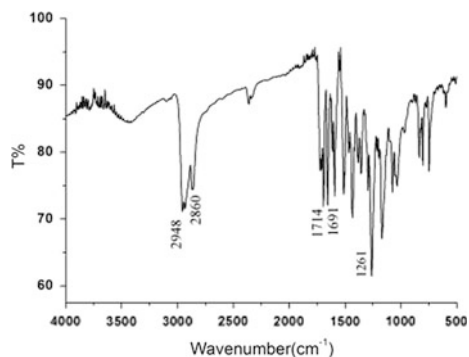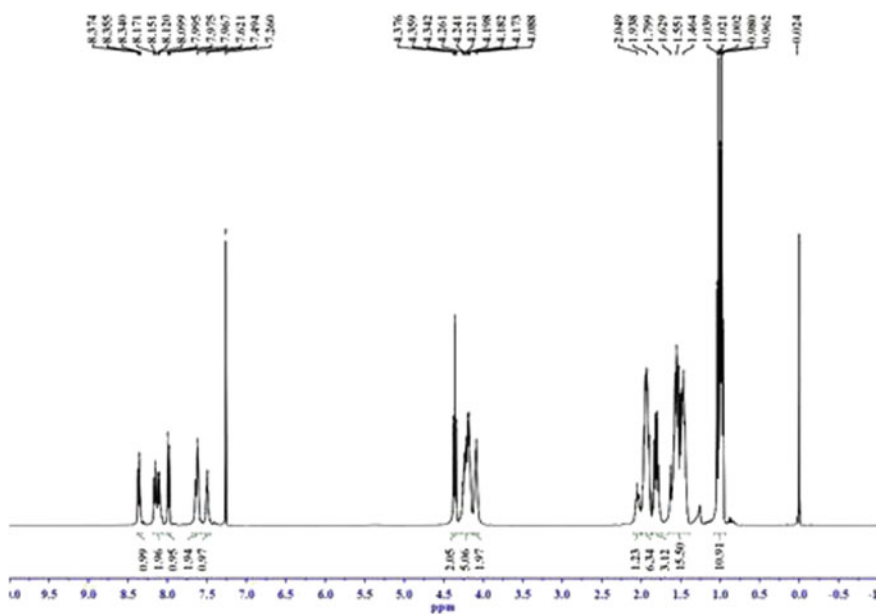
**Fig. 2.** FT-IR of compound 5D5A5



**Fig. 3.** $^1$H-NMR of compound 5D5A5

## 8.2    DSC and POM

The compound 5D5A5 was placed under a polarizing microscope, and the temperature was raised at a rate of 10 °C/min, until raising to 150 °C. Under the observation of a polarizing microscope, the material changes were from dark red powder to isotropic phase, completely clearing into a dark field. Starting from the isotropic liquid phase, the temperature starts to decrease at a rate of 1 °C/min, and enters the re-cooling process. The phenomenon of birefringence occurs at 138.3 °C, which was represented by the mosaic texture of a typical columnar phase and a small amount of pseudo-cone texture.

In order to make a more accurate analysis of the thermal properties of samples, we observed with the DSC curve. The first heating process was to eliminate the thermal history process, so we ignored it. The first cooling curve and the second heating curve were obtained. Compound 5D5A5 exhibited two obvious endothermic peaks at 84.2 °C (transition from crystal state to liquid crystal state) and 144 °C (transition from liquid crystal state to isotropic state). During the first cooling process, two distinct exothermic peaks appeared at 138.3 °C (transition of the isotropic state to the liquid crystal state) and 60 °C (the transition of the liquid crystal state to the crystalline state) (Fig. 4).
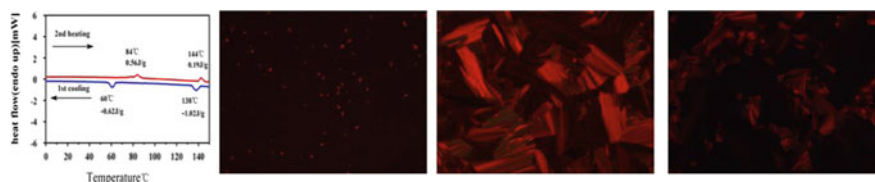


**Fig. 4.** DSC thermogram and texture of compound 5D5A5

# 9 Conclusions

As a result, the target chemical 5D5A5 was characterized in a series of ways. Its chemical structure was confirmed by 1H-NMR and FT-IR. POM was used to observe the columnar structure of the target compound. Combined with DSC test results, the compound showed excellent liquid crystal columnar characteristics and liquid crystal range, which provided a basis for the subsequent application of organic semiconductor devices. The introduction of D–A system improves the clearing temperature and forms highly ordered columnar phase. We will further explore whether the compound has bipolar transport and carrier mobility in subsequent work.

# References

1. Said SM, Mahmood MS, Daud MN, Mohd Sabri MF, Sairi NA (2016) Structure-electronics relations of discotic liquid crystals from a molecular modelling perspective. Liquid Crystals 1–22
2. Gupta M, Pal SK (2016) Triphenylene-based room temperature discotic liquid crystals: a new class of blue light-emitting materials with long range columnar self-assembly. Langmuir, acs.langmuir.5b03353
3. Sergeyev S, Pisula W, Geerts YH (2007) Cheminform abstract: discotic liquid crystals: a new generation of organic semiconductors. Chem Soc Rev 36(12):1902–1929
4. Bisoyi HK, Quan L (2016) Discotic liquid crystals for self-organizing photovoltaics. Nanomaterials for Sustainable Energy

5. Kong X, Dai S, Wang G, Zhang Z, Zhang L, Liao P et al (2017) Synthesis and characterization of mesogenic triphenylene-perylene dyads with phenoxy-alkoxy linkers. Mol Cryst Liq Cryst 650(1):56–64

6. Kouwer PHJ, Pourzand J, Mehl GH (2004) Disc-shaped triphenylenes in a smectic organisation. Chem Commun 35(1):66–67

7. Kumar, & Sandeep. (2005). Triphenylene-based discotic liquid crystal dimers, oligomers and polymers. Liquid Crystals, 32(9), 1089–1113

8. Van DCAM, Siebbeles LDA, Bleyl I, Haarer D, Berlin YA, Zharikov AA, et al (1998) Mechanism of charge transport along columnar stacks of a triphenylene dimer. J Phys Chem B 102(48):9625–9634

9. Wang L, Cui Q, Chen XF, Li Y, Li ZQ, Wang D et al (2013) Novel electric responsive columnar liquid crystals based on perylene tetra sec-alkyl ester derivatives. Aust J Chem 66 (6):692–700

10. Kozma E, Catellani M (2013) Perylene diimides based materials for organic solar cells. Dyes Pigm 98(1):160–179

11. Muth MA, Carrascoorozco M, Thelakkat M (2013) Liquid-crystalline perylene diester polymers with tunable charge-carrier mobility. Adv Func Mater 23(24):4510–4518

12. Gupta SK, Setia S, Sidiq S, Gupta M, Kumar S, Pal SK (2013) New perylene-based non-conventional discotic liquid crystals. RSC Adv 3(30):12060

13. Kong X, He Z, Zhang Y, Mu L, Liang C, Chen B et al (2011) A mesogenic triphenylene-perylene-triphenylene triad. Org Lett 13(4):764–767

# Preparation and Application of Superhydrophobic Surface Materials

Bin Deng[1(✉)], Shisheng Zhou[2], Feng Chen[2], Bin Du[2], Rubai Luo[2], and Huailin Li[2]

[1] Faculty of Mechanical and Precision Instrument Engineering, Xi'an University of Technology, Shaanxi, China
206093ol@qq.com
[2] Faculty of Printing, Packing Engineering and Digital Medial Technology, Xi'an University of Technology, Shaanxi, China

**Abstract.** Superhydrophobic materials have attracted wide attention due to their special wettability on the surface. In this paper, the basic definition, principle, and several common wetting models of superhydrophobic are summarized firstly. Then, the advantages and disadvantages of commonly used methods for preparing superhydrophobic materials are briefly analyzed, including dip coating method, spraying method, template method, chemical vapor deposition method, etching method, electrospinning method, phase separation method, and layer-by-layer assembly method. Finally, the application of superhydrophobic materials in oil-water separation, moisture-proof packaging, self-cleaning, and other fields is summarized and elaborated. The application of smart superhydrophobic materials which can respond to external stimuli such as pH, light, and temperature is also introduced. The purpose is to provide reference for the development of superhydrophobic materials. Preparing excellent superhydrophobic materials in a simple and environmentally friendly way is the key to meet the requirements of current industrial production.

**Keywords:** Superhydrophobic surface · Nanostructures · Chemical modification · Moisture-proof packaging

## 1 Introduction

With the development of industrialization, superhydrophobic surfaces have attracted extensive attention and research. In nature, many plant leaves and animal feathers are superhydrophobic, the most classic of which is the lotus leaf effect. Inspired by the lotus leaf effect, superhydrophobic surfaces are usually constructed by combining micro and nano multilevel structures with low surface energy chemical composition. The superhydrophobic material generally refers to the material whose water contact angle on static surface is greater than 150° and rolling angle is less than 10° [1–4]. Superhydrophobic materials generally have excellent self-cleaning and anti-pollution properties due to their good non-wettability to water. Therefore, they have broad application prospects in daily life and many industrial fields [5–7].

In this paper, the current research status of superhydrophobic materials is briefly described, and some problems that need to be solved are also put forward. It aims to bring help to the future research and promote the further research of superhydrophobic materials.

## 1.1  Definition of Superhydrophobic

The wettability of liquid on solid surface is characterized by contact angle. The contact angle is the angle between the solid-liquid interface and the tangent of the gas-liquid interface along the solid-liquid-gas three-phase contact point. It can be expressed by Young's equation, which describes the wettability of liquids on smooth solid surfaces. The contact angle of 90° is the critical angle for judging the wettability between droplets and solid surfaces. When theta is greater than 90°, it shows that the surface is hydrophobic and vice versa. In fact, there is almost no absolutely smooth surface in nature. The wetting state of liquid on rough solid surface is characterized by Wenzel model and Cassie-Baster model. Wenzel model considers that the apparent contact angle between droplet and solid surface is larger than the intrinsic contact angle due to the increase of surface roughness. While the Cassie-Baster model considers that the droplets are suspended on the concave and convex grooves on the solid surface, and the droplets fall on the solid-liquid-gas three-phase composite interface (Fig. 1).
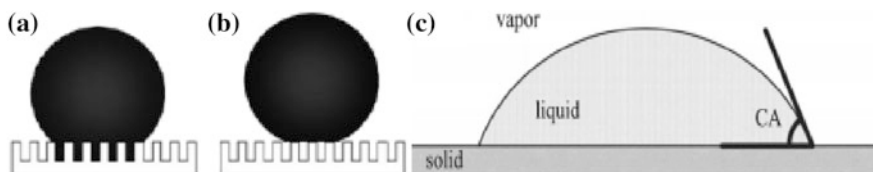


Fig. 1.  **a** Wenzel model, **b** Cassie-Baster model, **c** schematic diagram of contact angle

## 2  Preparation Method of Superhydrophobic Surface

It has been shown that the superhydrophobic property of material surface is determined by its surface energy and surface roughness. Therefore, the superhydrophobic surface can be constructed by using the materials with low surface energy and constructing rough structure. At present, the methods used to construct superhydrophobic surface mainly include dip coating method, spraying method, template method, chemical vapor deposition method, etching method, electrostatic spinning method, phase separation method, and layer by layer self-assembly method. The related methods will be summarized below.

**Dip Coating Method**. At present, the dip coating method is considered to be the most commonly used method to construct the superhydrophobic surface. This method can be applied to the preparation of superhydrophobic surfaces with large substrates and does not require much time. In general, the substrate needs to be impregnated in the prepared superhydrophobic coating for treatment, and then it should be dried and

cured. Superhydrophobic coatings contain solid particles, adhesives, and hydrophobic components that increase surface roughness. Wang et al. [8] firstly prepared silica nanoparticles by sol-gel method, and then the cotton fabric was soaked into a mixture of hydrophobic particles and dopamine hydrochloride for superhydrophobic treatment. The strongly adhered micro/nanoscale roughness with low surface energy imparted the fabric with excellent hydrophobicity and durability. Wang et al. [9] formed a super-hydrophobic surface by soaking the paper into the prepared silica sol. The superhy-drophobic paper had excellent mechanical properties and the functions of acid and moisture resistance.

**Spraying Method**. Superhydrophobic coating can be constructed on the surface of the substrate by spraying method. Hydrophobic nanoparticles are usually mixed with organic reagents and the resulting suspension is sprayed onto the substrate surface. This method is simple, efficient, and has a good application prospect. Lu et al. [10] prepared a coating by mixing two different size ranges of $TiO_2$ nanoparticles in an ethanol solution containing perfluorooctyltriethoxysilane. And then the coating was sprayed onto the filter paper or glass surface. The modified filter paper or glass obtained good hydrophobicity and self-cleaning ability.

**Template Method**. Template method is to fabricate superhydrophobic surface quickly by self-made template or duplicating existing micro-and nano-structures. This method has the advantages of simplicity, efficiency, and large area replication, but the service life of the template is not long. Liu et al. [11] fabricated a transparent super-hydrophobic surfaces by calcining candle-soot-coated polydimethylsiloxane (PDMS) films. The network structures were created on glass. The substrate exhibited a water contact angle of 163° and a high thermal stability.

**Chemical Vapor Deposition**. Chemical vapor deposition involves the chemical reaction of two or more gaseous materials and then the resulting new material is deposited onto the surface of the substrate. Bao et al. [12] proposed a method for fabricating superhydrophobic surfaces, which was developed by coating metal oxide nanoparticles, including ZnO, $Al_2O_3$ and $Fe_3O_4$, on various substrates followed by treatment with PDMS via chemical vapor deposition (CVD) method. Lau et al. [13] prepared hydrophobic vertical array carbon nanotubes (VACNTs) by chemical vapor deposition technology.

**Etching Method**. The etching method is to change the structure of solid surface by physical or chemical methods to form regular or irregular micro-nano size roughness. Then the wetting state of solid surface will be changed. The surface hydrophobicity can be regulated by the method through the operation and design of the surface structure, but the cost is high and it is not suitable for large area preparation. Sung-Woon et al. [14] obtained a superhydrophobic Si surface with a contact angle of 165° via plasma etching by combining the fabrication of microscale rod structures and the deposition of fluorocarbon films on the Si surface.

**Electrostatic Spinning Method**. Electrostatic spinning is a unique fiber manu-facturing process in which polymer solution or its melt is placed in a high-voltage electrostatic field and doped with nanoparticles to form micro-nanofibers under the action of electric field force. It has the advantages of simple manufacturing device, various spinnable materials, and controllable process, which can be used alone or in combination with other methods. Lim et al. [15] used methyltriethoxysilane (MTES) as

an ORMOSIL precursor to prepare silica ($SiO_2$) sol containing methyl groups by sol-gel method. And then the superhydrophobic surface with multifunctionalities and thermal stability was obtained by creating hierarchically electrospun fibrous structures.

**Phase Separation Method.** Phase separation process usually utilizes the different solubility or thermal properties of mixtures to initiate the separation of two or more phases in the system, resulting in micron or nanometer rough structure. The method can be used to prepare uniform and large area superhydrophobic films due to the easy control of experimental conditions and simple operation. It has great practical value, but volatilization of solvents will cause certain environmental pollution. Zhang et al. [16] obtained the poly(vinylidene fluoride) (PVDF) membrane with thermal stability and mechanical stability by using phase separation method and adding ammonia water into the N-methyl-2-pyrrolidone (NMP) solution of PVDF. Obeso et al. [17] precipitated poly(hydroxybutyrate) (PHB) on the surface of cellulose fibers of papers using a phase separation process to obtain a superhydrophobic surface with rough texture at both micro and nano length scales.

**Layer-by-layer Assembly Method.** Layer-by-layer (LBL) assembly method is to assemble nanoparticles or polymer electrolytes onto the substrate by layer-by-layer deposition under the action of electrostatic, coordination bond. This method has the advantages of simple operation, easy control of assembly degree and structure. Shang et al. [18] fabricated highly transparent porous silica coatings on glass substrate through LBL assembly of raspberry-like polystyrene@silica (PS@$SiO_2$) microparticles. Under the action of low surface energy materials, the prepared coatings showed superhydrophilic and superhydrophobicity properties. Gomes et al. [19] proposed a simple technique of LBL of applying polycation chitosan (CH) and polyanion alginates (ALG) to prepare CH/ALG multilayers on cotton samples.

# 3   Application of Superhydrophobic Materials

The special wettability of superhydrophobic materials can make them combine with different substrates so that they can be widely used in oil-water separation, self-cleaning, moisture-proof packaging, and responsive materials.

**Oil-Water Separation.** More and more oily wastewater is produced by modern industrial activities. The consequent environmental problems and the waste of water resources have aroused wide attention. At present, there are many methods for separating oil-water mixture, such as gravity method, centrifugal method, ultrasonic method, adsorption method, and filtration method. But low efficiency and poor stability are the biggest drawbacks of these methods. Oil-water separation is essentially an interfacial problem, so materials with special wettability have been extensively studied. Xu et al. [20] prepared hydrofluoric acid-titanium dioxide (HFA-$TiO_2$) sol by mixing silica nanoparticles ($SiO_2$) with ethanol solution. Then the porous substrates including polyester fabric and polyurethane sponge were coated with the coating solution by a simple dip coating method. The modified coatings showed unusual capabilities for controllable filtration of an oil–water mixture and selective removal of water from bulk oil. Dang et al. [21] fabricated a superhydrophobic polymer that can be applied to cotton fabric, filter paper, and PU by a simple random copolymerization. The wetting

state of the coating can be changed by in situ and ex situ treatment. Thus, the coating can be applied in highly controllable oil/water separation such as continuous separation of oil/water/oil three phase mixtures (Fig. 2).
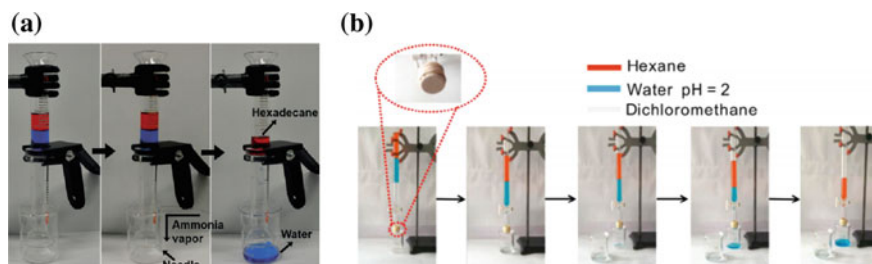


**Fig. 2.** **a** Schematic diagram of continuous separation of oil/water/oil three phase systems, **b** oil-water separation by the functionalized polyester fabric

**Responsive Function**. In order to expand the application field of superhydrophobic materials, more and more researches have been conducted on smart materials that can respond to external stimuli such as temperature, pH, and light [22–25]. Xu et al. [26] prepared superhydrophobic coatings by mixing $SiO_2$ with $TiO_2$ modified by decanoic acid. The superhydrophobic coating presented hydrophobic properties in air and neutral water environment and hydrophilic properties in alkaline solution or ammonia vapor. Xu et al. [27] reported a template lamination method to fabricate multifunctional $TiO_2$-high-density polyethylene (HDPE) nanocomposite surfaces with superhydrophobicity, UV-induced reversible wettability, and selfcleaning properties. Geissler et al. [28] prepared superhydrophobic paper with cellulose stearyl ester (CSE) solution and nano-particles, which could be responded to temperature. The paper would become hydrophilic after heat treatment at 70 °C for 5 min. Cao et al. [29] fabricated thermo and pH dual-controllable mesh by photo initiated free radical polymerization. The coated mesh showed superhydrophilicity and underwater superoleophobicity at certain temperature and pH. While the water resistance of poly(2-(dimethylamino)ethyl methacrylate) (PDMAEMA) hydrogel decreased when the temperature reached above 55 °C or pH was larger than 13 (Fig. 3).

**Moisture-Proof Packaging**. The mechanical properties of paper will be degraded due to the easy absorption of moisture by its fibers when it is used for storage and transportation. In order to widen the application field of paper, the superhydrophobic coating can be combined with paper, so that paper can be used in the field of moisture-proof packaging. A superhydrophobic paper was fabricated by precipitating $TiO_2$ nanoparticles/sodium alginate (ALG) multilayers on paper surface layer-by-layer followed by an adsorption treatment of colloidal carnauba wax. The prepared superhydrophobic paper with excellent moisture-proofing property and high strength stability had a great potential in moisture-proof paper packaging [30]. Li et al. [31] developed a simple method to fabricate superhydrophobic paper which had excellent moisture resistance by depositing carnaubawax onto the surface of cellulose fibers via a phase separation method (Fig. 4).
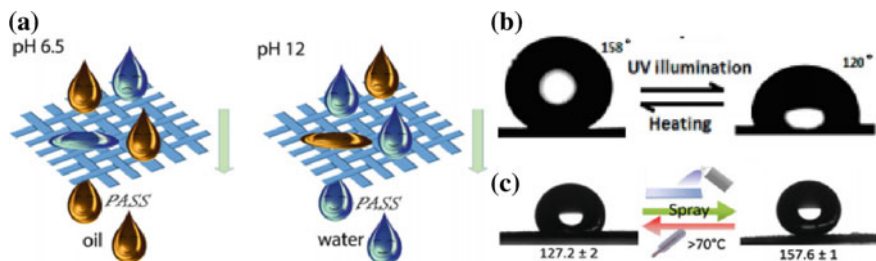
**Fig. 3.** Schematic diagram of **a** surface wettability at different pH, **b** wettability transition of TiO$_2$-polymer nanocomposite surface, **c** wettability transition of superhydrophobic paper treated at different temperatures
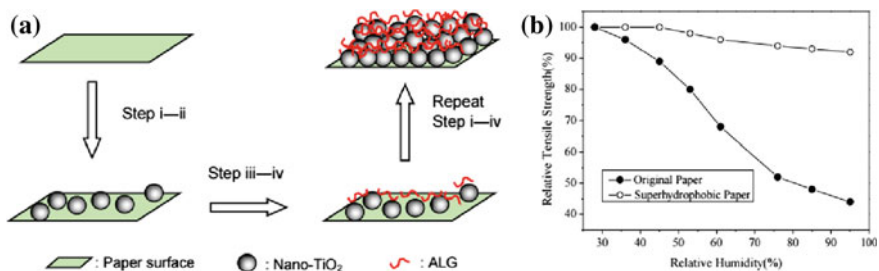


**Fig. 4.** **a** Schematic diagram illustration of the preparation process of TiO$_2$/ALG multilayers on paper surface, **b** relative tensile strength of original paper and superhydrophobic paper under different relative humidity

**Self Cleaning**. The water droplets can roll freely on the surface of the substrate when the contact angle between water droplets and superhydrophobic surface is greater than 150° and the rolling angle is less than 10°, which can realize the self-cleaning characteristics of the material surface. Fu et al. [32] synthesized the quaternary ammonium salts (QAS) functionalized fluorinated copolymer tethered hydroxyl groups. And then the superhydrophobic nanocomposite coatings with self-cleaning properties were prepared by crosslinking fluorine copolymers and poly(urea-formaldehyde) nanoparticles (PUF NPs) nanoparticles with hexamethylene diiso-cyanate. The self-cleaning properties of nano-composite coatings were studied by using copper chloride dihydrate powder as pollutant. Excellent self-cleaning performance was achieved by adding PUF NPs into the copolymer. Chen et al. [33] prepared self-repairing superhydrophobic coatings based on TiO$_2$ with photocatalysis and micro-capsules, which was against UV irradiation and chemically stable. The coatings showed good self-cleaning property to the powder dirt (Fig. 5).
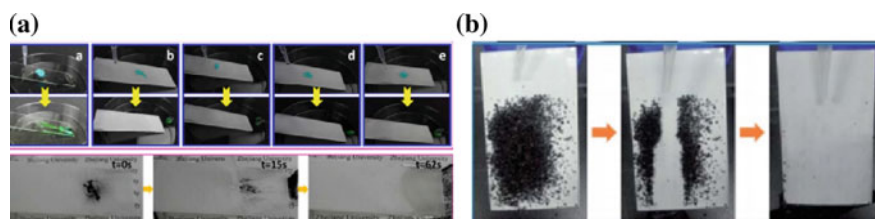
**Fig. 5.** **a** Self cleaning test by copper chloride dihydrate particles, **b** self cleaning ability of the pH-capsules based superhydrophobic surface

## 4  Conclusions

In this paper, the preparation methods and applications of superhydrophobic materials are reviewed in order to provide some reference for the future research of superhydrophobic materials. At present, superhydrophobic materials have been extensively studied, and some achievements have been achieved. However, there are few superhydrophobic materials in the actual production. Actually, there are still some problems to be solved urgently. For example, the preparation of superhydrophobic materials mostly involves fluorine-containing materials, which does not meet the current needs of green development. Although fluorine-containing substances can promote the hydrophobicity, the pollution to the environment and the harm to human health can not be ignored. Therefore, it is a challenge to develop economically and environmentally friendly superhydrophobic materials with excellent superhydrophobic performance, and it is also of great significance for the advancement of superhydrophobic research.

## References

1. Wang B, Liang WX, Guo ZG, Liu WM (2015) Biomimetic super-lyophobic and super-lyophilic materials applied for oil/water separation: a new strategy beyond nature. Chem Soc Rev 44(1):336–361
2. Wang ST, Liu KS, Yao X, Jiang L (2015) Bioinspired surfaces with superwettability: new insight on theory, design, and applications. Chem Rev 115:8230–8293
3. Chu ZL, Feng YJ, Seeger S (2014) Oil/water separation with selective superantiwetting/superwetting surface materials. Angew Chem Int Ed 54(8):2328–2338
4. Xue ZX, Cao YZ, Liu N et al (2014) Special wettable materials for oil/water separation. J Mater Chem A 2:2445–2460
5. Yang C, Wang FJ, Li W et al (2016) Anti-icing properties of superhydrophobic ZnO/PDMS composite coating. Appl Phys A 122(1):1

6. Songok J, Toivakka M (2016) Enhancing capillary driven flow for paper-based microfluidic channels. ACS Appl Mater Interfaces 8(44):30523–30530

7. Zhou X, Kong JH, Sun JT et al (2017) Stable superhydrophobic porous coatings from hybrid ABC triblock copolymers and their anti-corrosive performance. ACS Appl Mater Interfaces 9(35):30056–30063

8. Wang JT, Chen YH (2015) Oil-water separation capability of superhydrophobic fabrics fabricated via combining polydopamine adhesion with lotus-leaf-like structure. J Appl Polym Sci 132(39):42614

9. Wang N, Xiong DS, Pan S et al (2016) Superhydrophobic paper with superior stability against deformations and humidity. Appl Surf Sci 389(32):354–360

10. Lu Y, Sathasivam S, Song JL et al (2015) Robust self-cleaning surfaces that function when exposed to either air or oil. Science 347(6226):1132–1135

11. Liu XJ, Xu Y, Ben KY et al (2015) Transparent, durable and thermally stable PDMS-derived superhydrophobic surfaces. Appl Surf Sci 339:94–101

12. Bao XM, Cui JF, Sun HX et al (2014) Facile preparation of superhydrophobic surfaces based on metal oxide nanoparticles. Appl Surf Sci 303:473–480

13. Lau KKS, Bico J, Teo KBK et al (2003) Superhydrophobic carbon nanotube forests. Nano Lett 3(12):1701–1705

14. Cho SW, Kim JH, Lee HM et al (2016) Superhydrophobic Si surfaces having microscale rod structures prepared in a plasma etching system. Surf Coat Technol 306:82–86

15. Lim HS, Baek JH, Park K et al (2010) Multifunctional hybrid fabrics with thermally stable superhydrophobicity. Adv Mater 22(19):2138–2141

16. Zhang WB, Shi Z, Zhang F et al (2013) Superhydrophobic and superoleophilic PVDF membranes for effective separation of water-in-oil emulsions with high flux. Adv Mater 25 (14):2071–2076

17. Obeso CG, Sousa MP, Song WL et al (2013) Modification of paper using polyhydroxy-butyrate to obtain biomimetic superhydrophobic substrates. Colloids Surf A 416(1):51–55

18. Shang QQ, Zhou YH (2016) Fabrication of transparent superhydrophobic porous silica coating for self-cleaning and anti-fogging. Ceramics Int 42:8706–8712

19. Gomes AP, Mano JF, Queiroz JA et al (2013) Layer-by-layer deposition of antimicrobial polymers on cellulosic fibers: a new strategy to develop bioactive textiles. Polym Adv Technol 24(11):1005–1010

20. Xu ZG, Zhao Y, Wang HX et al (2015) A superamphiphobic coating with an ammonia-triggered transition to superhydrophilic and superoleophobic for oil-water separation. Angew Chem 127(15):4610–4613

21. Dang Z, Liu LB, Li Y et al (2016) In situ and ex situ pH-responsive coatings with switchable wettability for controllable oil/water separation. ACS Appl Mater Interfaces 8(45):31281–31288

22. Xue BL, Gao LC, Hou YP et al (2013) Temperature controlled water/oil wettability of a surface fabricated by a block copolymer: application as a dual water/oil on-off switch. Adv Mater 25:273–277

23. Lee CH, Kang SK, Lim JA et al (2012) Electrospun smart fabrics that display pH-responsive tunable wettability. Soft Matt 8(40):10238

24. Tian DL, Zhang XF, Tian Y et al (2012) Photo-induced water-oil separation based on switchable superhydrophobicity-superhydrophilicity and underwater superoleophobicity of the aligned zno nanorod array-coated mesh films. J Mater Chem 22(37):19652–19657

25. Yin YJ, Guo N, Wang CX, Rao QQ (2014) AlterableSuperhydrophobic–superhy-drophilicwettability of fabric substrates decorated with ion–TiO$_2$ coating via ultraviolet radiation. Ind Eng Chem Res 53(37):14322–14328

26. Xu ZG, Zhao Y, Wang HX et al (2016) Fluorine-free superhydrophobic coatings with pH-induced wettability transition for controllable oil-water separation. ACS Appl Mater Interfaces 8(8):5661–5667
27. Xu QF, Liu Y, Lin FJ et al (2013) Superhydrophobic $TiO_2$-polymer nanocomposite surface with UV-induced reversible wettability and self-cleaning properties. Appl Mater Interfaces 5 (18):8915–8924
28. Geissler A, Loyal F, Biesalski M, Zhang K (2014) Thermo-responsive superhydrophobic paper using nanostructured cellulose stearoyl ester. Cellulose 21(1):357–366
29. Cao YZ, Liu N, Fu CK et al (2014) Thermo and pH dual-responsive materials for controllable oil/water separation. ACS Appl Mater Interfaces 6(3):2026–2030
30. Li P, Li H, Yang J, Meng YH (2016) Facile fabrication of superhydrophobic paper with excellent water repellency and moisture resistance by phase separation. BioResources 11 (3):6552–6565
31. Li H, Yang J, Li P, Lan TQ, Peng LC (2017) A facile method for preparation superhydrophobic paper with enhanced physical strength and moisture-proofing property. Carbohyd Polym 160:9–17
32. Fu YC, Jiang JX, Zhang QH et al (2017) Robust liquid-repellent coatings based on polymer nanoparticles with excellent self-cleaning and antibacterial performances. J Mater Chem A 5:275–284
33. Chen KL, Gu K, Qiang SY, Wang CX (2017) Environmental stimuli-responsive self-repairing waterbased superhydrophobic coatings. RSC Adv 7:543–550

# Synthesis and Mesomorphism of a Triphenylene-Based Discotic Mesogenic Polymer Obtained from Anionic Polymerization

Lina Zhang, Ao Zhang, Jingze Bi, Yuwen Feng, Zhengran Wang, Huanzhi Yang, Zhenhu Zhang, Yi Fang, Yuguang Feng, Chunxiu Zhang[(✉)], and Jialing Pu

Beijing Institute of Graphic Communication, Beijing, China
zhangchunxiu@bigc.edu.cn

**Abstract.** The discotic liquid crystals composed of a rigid aromatic core and peripheral flexible side chains, are easy to be stacked into a one-dimensional ordered column structures by π–π interactions [1–3]. Although the discotic liquid crystals have been studied for many years, the research on discotic liquid crystal polymer (DLCP) is still fundamental, and its performance has not been studied widely in the fields of organic electronics and optoelectronics, such as the application of field-effect transistors, light-emitting diodes, and photovoltaic solar cells. To enrich the studies of the properties of discotic liquid crystal polymers, here we have successfully prepared poly {[3,6,7,10,11-pentakis (hexyloxy)-2-oxytriphenylene] methacrylate} (PMTS) via anionic polymerization for the first time. The chemical structure of the polymer was determined by FT-IR and $^1$H-NMR. The molecular weight of the polymer PMTS was characterized by Gel Permeation Chromatography (GPC). Its number average molecular weight was approximately 32,000 while its weight-average molecular weight was about 36000. The distribution of the molecular weight was 1.4. And then, their thermodynamics and liquid crystal properties were studied by polarizing optical microscopy (POM) and differential scanning calorimetry (DSC).

**Keywords:** Discotic liquid crystal · Anionic polymerization · POM · DSC · GPC

## 1 Introduction

Liquid crystal is an ordered fluid between an anisotropic crystal and an isotropic liquid [4]. According to the molecular weight, it can be divided into polymer liquid crystal and small molecule liquid crystal. Polymer liquid crystals have been extensively studied because of their good application properties [5]. The research of synthesis methods has always been the research focus of polymer liquid crystal [6]. Although it has been studied for many years, the research on discotic liquid crystal polymers is still relatively young, and its performance in the fields of organic electronics and

optoelectronics is still unknown [7]. We successfully prepared poly(pentaoxy)triphenylene methacrylate liquid crystal polymer by anionic polymerization, and determined the chemical structure of the polymer by FT-IR and $^1$H-NMR. The molecular weight of the polymer PMTS was determined by gel permeation chromatography. The thermodynamic properties and liquid crystal properties of the polymer were investigated by polarizingoptical microscopy (POM) and differential scanning calorimetry (DSC). The synthesis of this polymer enriches the synthesis of discotic liquid crystal polymers and the study of liquid crystal properties. The structure of the polymer is given in Fig. 1.
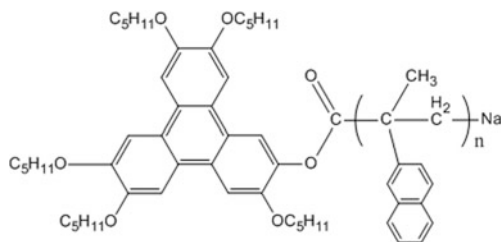


**Fig. 1.** Chemical structure of poly {[3,6,7,10,11-pentakis(hexyloxy)-2-oxytriphenylene] methacrylate}

## 2   Experimental

The reagents used in the reaction are given in Table 1. All chemicals were bought from Aladdin and all solvents were purchased from Aldrich. All chemicals and solvents were used without further purification. Figure 2 shows the specific synthetic steps of the reaction.

**Table 1.**  Experimental reagent

| Reagent name | Purity | Source |
|---|---|---|
| N,N′-dicyclohexylcarbodiimide | Analytical reagent | Aldrich |
| Methacrylic acid | Analytical reagent | Aldrich |
| Ethanol | Analytical reagent | Aldrich |
| Tetrahydrofuran | Analytical reagent | Aldrich |
| Sodium chloride | Analytical reagent | Aladdin |
| Sodium hydroxide | Analytical reagent | Aladdin |
| 4-dimethylaminopyridine | Analytical reagent | Aladdin |
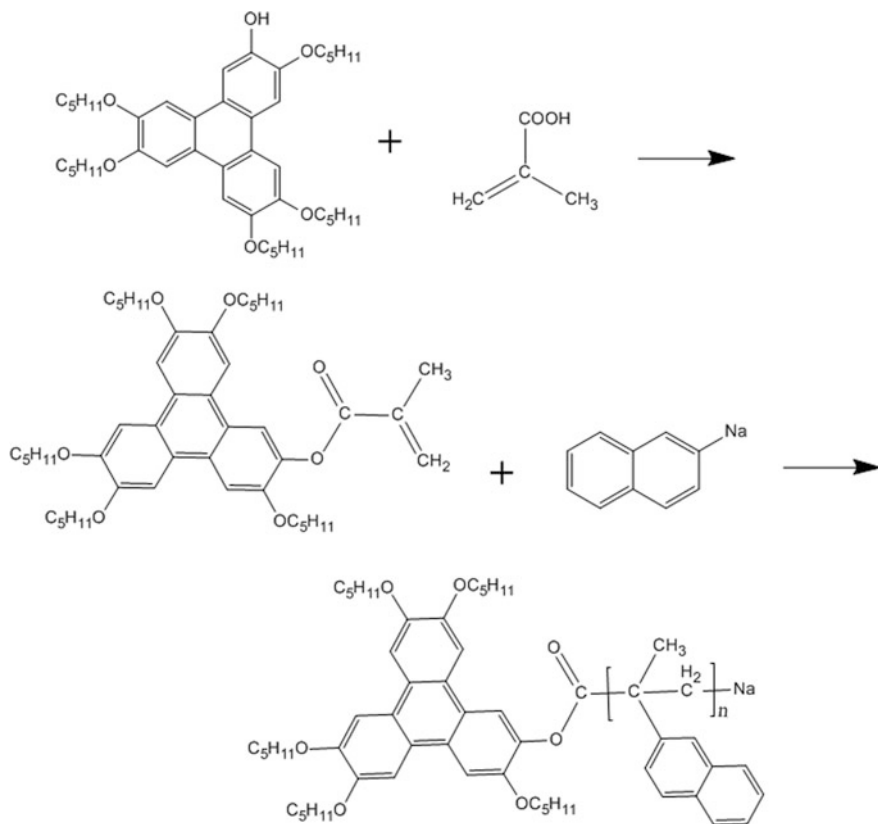
Fig. 2.  Synthesized route of poly {[3,6,7,10,11-pentakis(hexyloxy)-2-oxytriphenylene] methacrylate}

## 2.1   Synthesis of 2-((2-Methylallyl)Peroxy)-3,6,7,10,11-Pentakis (Pentyloxy)Triphenylene

2-hydroxyl-3,6,7,10,11-penta-pentoxytriphenylene (HAT5OH, 2 g, 0.003 mol), metha crylic acid (0.255 g, 0.0028 mol), N,N′-dicyclohexylcarbodiimide (DCC, 0.7342 g) and 4-dimethylaminopyridine (DMAP, 3% by mass) were sequentially added to a 250 ml three-necked flask. The weighed methacrylic acid was slowly added dropwise with a burette under ice bath conditions. After the addition was completed, the ice bath was withdrawn and heating was continued in an oil bath, and the temperature in the reaction flask did not exceed 40 °C. After reacting for 24 h, wash twice with an equal volume of 0.1% sodium hydroxide, then wash twice with saturated sodium chloride, extract and dry, and purify by dry silica gel column. Mix of petroleum ether dichlor-omethane and ethyl acetate. The solution was eluted to give a yellow solid in 45% yield.

^{1}H-NMR (300 MHz, CDCl$_3$): 8.12-7.46 (m, 6H); 6.45 (s, 2H); 4.30-4.16 (m, 10H); 2.14-0.92 (m, 48H).

## 2.2 Synthesis of Poly {[3,6,7,10,11-Pentakis(Hexyloxy)-2-Oxytriphenylene] Methacrylate} (PMTS)

2-((2-methylallyl)peroxy)-3,6,7,10,11-pentakis(pentyloxy)triphenylene, naphthalene sodium, dehydrated tetrahydrofuran was sequentially placed in a glass polymerization tube,and subjected to liquid nitrogen freezing-vacuum- nitrogen-thawed, after repeated three times, the tube was vacuum sealed, the reaction temperature was −5 ∼ 0 °C, and after 6–8 h of reaction, ethanol was added to terminate the reaction. The crude product was purified to give a light brown solid. The final yield was 39%. The results of FT-IR and $^1$H-NMR are shown in Figs. 3 and 4.
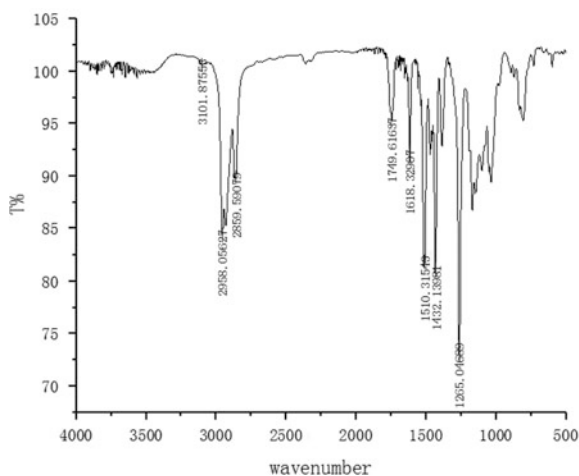


**Fig. 3.** FT-IR spectrum of poly {[3,6,7,10,11-pentakis(hexyloxy)-2-oxytriphenylene] methacrylate}

FT-IR (KBr):$V_{max}$ (cm$^{-1}$):3101 (=C–H); 2985, 2859 (–CH$_3$/–CH$_2$–); 1749 (–C=O); 1618, 1510, 1432 (–C=C–); 1265 (–CH$_3$)
$^1$H-NMR:H (300 MHz, CDCl$_3$) 8.12−7.74 (m, 6H); 6.46 (s, 1H); 5.82 (s, 1H); 4.23 (m, 11H); 2.15−0.97 (m, 50H)

## 3 Results and Discussion

The characterization methods mainly include polarizingoptical microscopy (POM), differential scanning calorimetry (DSC) and gel permeation chromatography (GPC). The liquid crystal properties of the compound were characterized by POM and DSC. The molecular weight distribution was analyzed by gel permeation chromatography (GPC).
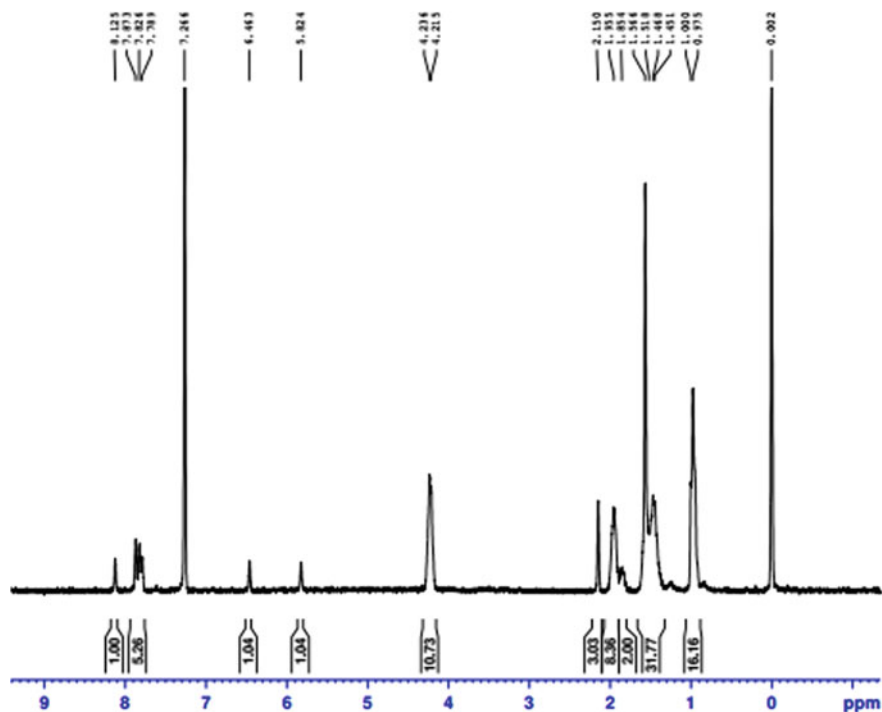
**Fig. 4.** 1H-NMR spectrum of poly {[3,6,7,10,11-pentakis(hexyloxy)-2-oxytriphenylene] methacrylate}

### 3.1    Pom

The sample was heated (10 °C/min) to the isotropic phase, and the cooled (10 °C/min) to the solid phase. The phase transition behavior of the sample was observed, and the texture was captured. During cooling, the sample began to show textures at 140 °C and reached a clearing point at 187 °C. Under the polarizing microscope, we can easily regard this texture as classic sand-like texture. The detailed textures are shown in Fig. 5. Based on the polarized texture we speculated that the sample formed a typical hexagonal columnar phase.

### 3.2    DSC

As shown in Fig. 6, we observed the first endothermic peak at 145.2 °C and the second endothermic peak at 189.6 °C during heating from 0 to 200 °C. Combined with polarizingoptical microscopy (POM) images, we can conclude that the clearing point of the compound is 189.6 °C. During cooling, we also observed two exothermic peaks at
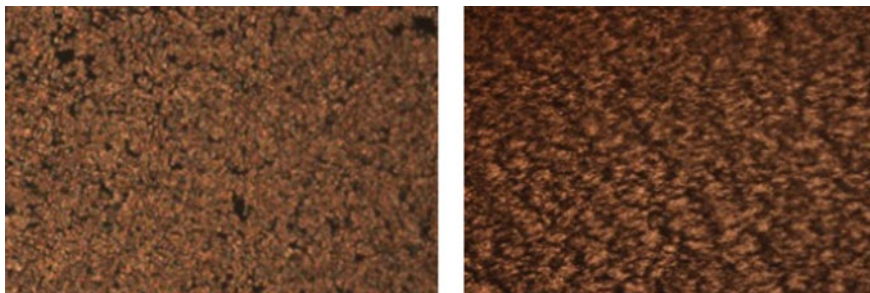
**Fig. 5.** Textures observed at 184.3 °C (left), and 171.9 °C (right) during cooling process
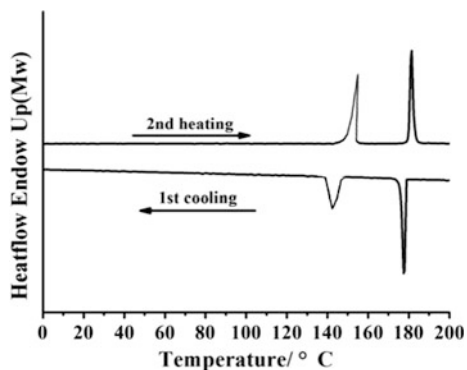


**Fig. 6.** DSCthermogram of poly {[3,6,7,10,11-pentakis(hexyloxy)-2-oxytriphenylene] metha crylate}

141.5 °C and 179.3 °C. Therefore, the compound was converted to a liquid crystal state at 184.3 °C and to a solid state at 137.5 °C. And the phase transition phenomenon appearing in the DSC characterization was basically consistent with the observed results of the polarized light.

## 3.3 GPC

Figure 7 is a GPC curve of the polymer PMTS. It can be seen from the figure that the polymer had a molecular weight distribution of 1.4, where in the number average molecular weight is 32,000, the weight average molecular weight is 34,000, and the molecular weight exhibits a certain gradient.
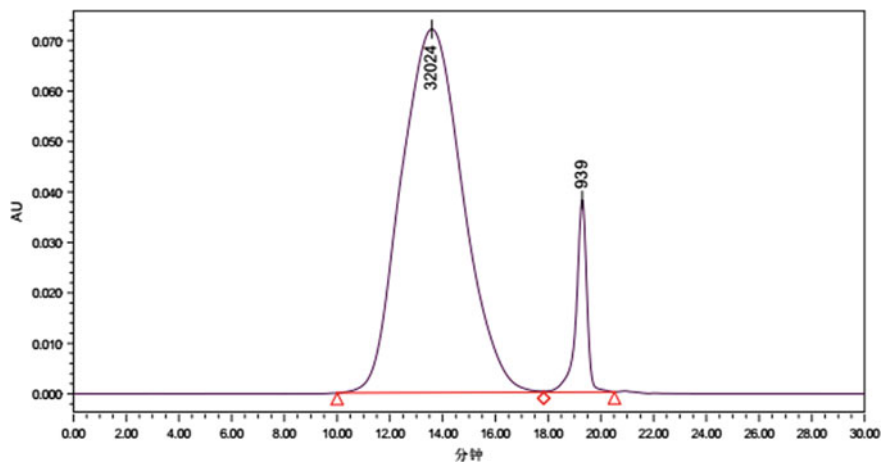
**Fig. 7.** GPC of poly {[3,6,7,10,11-pentakis(hexyloxy)-2-oxytriphenylene] methacrylate}

# 4  Conclusions

In this study, poly(pentaoxy)triphenylene methacrylate (PMTS) liquid crystal polymer has been successfully synthesized by anionic polymerization method and fully characterized by ^{1}HNMR, FT-IR, POM, DSC, and GPC. The results showed that the poly (pentaoxy)triphenylene methacrylate (PMTS) had a hexagonal columnar phase. As shown in Fig. 8, if we were to represent the molecular structure in terms of (a), the self-assembled structure is shown in (b). And the liquid crystal temperature is between 141.2 and 189.6 °C, which can be used as a discotic liquid crystal material.
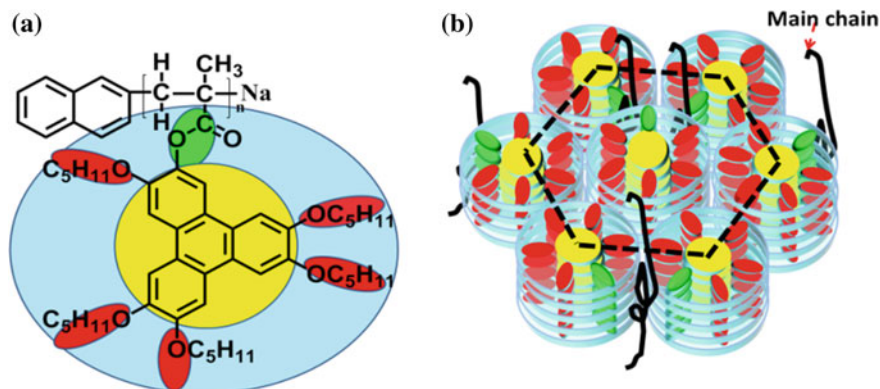


**Fig. 8.** PMTS structure (**a**) and self-assembled structure (**b**)

# References

1. Zhou Q, Wang X (1994) Liquid crystal polymer. Science Press, Beijing, pp 1–56.2
2. Fan Xinghe (2004) Graphic liquid crystal polymer. Beijing Industrial Press, Beijing, pp 3–10
3. Samorì P, Fechtenkötter A, Reuther E, Watson MD, Severin N, Müllen K, Rabe JP (2006) Self-assembly of perylene monoimide substituted hexa-peri-hexabenzocoronenes: Dyads and Triads at surfaces. Adv Mater 18:1317–1321
4. Schmidt-Mende L, Fechtenkotter A, Müllen K, Moons E, Friend RH, MacKenzie1 JD (2001) Self-organized discotic liquid crystals for high-efficiency organic photovoltaics. Science 293:1119–1122
5. Sergeyev S, Pisula W, Geerts YH (2007) Discotic liquid crystals: a new generation of organic semiconductors. Chem Soc Rev 36:1902–1929
6. Ban J-F, Chen S, Zhang H-L (2015) Synthesis and liquid crystalline behavior of side chain liquid crystalline polymers containing triphenylene discotic mesogens with different length flexible spacers. Chin J Polym Sci 33(9):1245–1259
7. Mu B, Wu B, Pan S et al (2015) Hierarchical self-organization and uniaxial alignment of well synthesized side-chain discotic liquid crystalline polymers. Macromolecules 48(8):2388–2398

# DFT Study on the Reactive Species
# of Metalloporphyrin Catalytic Oxidation

Meijuan Cao, Aijing Gao, Zhicheng Sun$^{(\boxtimes)}$, Luhai Li, Lixin Mo,
Ruping Liu, Nan Deng, Rui Fang, and Yumeng Han

Beijing Engineering Research Center of Printed Electronics, Beijing Institute of
Graphic Communication, Beijing, China
sunzhicheng@bigc.edu.cn

**Abstract.** Metalloporphyrin species such as metal porphyrin ($PM^{II}$, $PM^{III}Cl$),
metal(III)-peroxo($PM^{II}\text{-}O_2$), metal(III)-hydroperoxo($PM^{II}\text{-}OH$), and metal(IV)-
oxo($PM^{IV} = O$) are key intermediates in the catalytic activation of dioxygen by
metalloenzymes. It has been difficult to elucidate changes in the structure of the
metal centre during catalysis and factors that control their chemical reactivity
with substrates. The intermediates of metaloporphyrins catalytic circle were
investigated to give insights into the detailed geometric and electronic structure,
thus enhancing the understanding of redox metaloenzymes and their highly
selective roles in biological process. The intermediates of metalloporphyrins
(M = Fe, Mn and Co) including $PM^{II}$, $PM^{III}Cl$, $PM^{II}\text{-}O_2$, $PM^{IV} = O$ and
$PM^{III}OH$ have been investigated using density functional theory method. The
ground state of the intermediates was determined on assessment of relative
energy and the results were are in line with expectations. Geometric structures of
the ground state further confirmed the energetic assessment. The Mulliken
charge and frontier molecular orbitals revealed the behavior of the intermediates
in the catalytic process.

**Keywords:** Density functional theory · Porphyrin intermediates · Ground
state · Mulliken charge · Frontier molecular orbital (FMO)

## 1 Introduction

Recently, metalloporphyrin has been characterized or proposed to catalyze an
impressive range of difficult chemical reactions and a number of new reactive inter-
mediates in metalloporphyrin-catalyzed oxidation process [1–4], including hydroxy-
lation, halogenation, ring closure, desaturation, and electrophilic aromatic substitution.
A theoretical study explored the electronic structure, spin-states, and spin-crossover
reaction of heme-related Fe-porphyrins [5]. And high-valent iron(IV)-oxo species have
been implicated as the key reactive intermediates in the catalytic cycles of alkanes
oxidation by heme and non-heme iron enzymes [6–8] as well as the Mn and Co-oxo
speceis [9–13]. Spectroscopic characterization found a hydroperoxo-heme intermediate
converted from a side-on peroxo to an end-on hydroperoxo complex [14]. The low-spin
end-on ferric peroxo heme intermediate has been proposed as an alternative reactive
intermediate involved in the catalytic cycles of enzymes such as nitric oxide synthase

and cytochrome P450 [15]. Electronic structure of some substituted iron(II) porphyrins has been studied theoretically with intermediate or high spin state [16]. The oxygen activation process on Co, Mn, and Mo porphyrins has been studied by quantum chemical method [17]. A theoretical study was carried out to dioxygen activation by a non-heme iron(II) complex to understand ferric–superoxo complexes [18]. Hydrogen peroxide activated by high-valent heme centers was investigated by density functional theory, implicating its catalytic ability in the catalytic cycle.

The intermediates of electronic and geometric properties in the porphyrin catalytic circle have been calcualted in this work. Firstly, the ground state of the metallopor-phyrin intermediates was evaluated by calculating the relative energy of intermediates. Then, the geometric structure of the ground state intermediates was compared with the experiments and then the ground state was confirmed. Lastly, the electronic property of the intermediates was analyzed to give a deep insight into catalytic behavior of por-phyrin in the oxidation reaction of alkanes.

## 2  Computational Method

Selecting proper calculated methods was essential to obtain reliable molecular structure and properties. All species were optimized with OLYP generalized gradient approxi-mations based on OPTX exchange functiona. OLYP showed good performance for the metal-complex [19, 20]. To obtain accurate results, the triple-$\zeta$ plus polarization slater-type orbital basis sets (TZP) was used and a fine mesh numerical integration of the matrix elements was set on. The sub-valence 3 s and 3p shells of the metal were included the valence set. For C and N atoms, 2 s and 2p were considered as valence shells. The other shells of lower energy, *i.e.* [Ne] for the metal and [He] for C/N, were described as core and kept frozen. The structures of intermediates calculated were listed in Fig. 1.



**Fig. 1.**  The calculated structures of intermediates

## 3    Results and Discussion

### 3.1    Ground State of Intermediates

To determine the ground states of the intermediates, relative energy of the intermediates with various possible spin states was calculated and listed in Table 1. As shown in Table 1, PFe$^{II}$ had an S = 1 ground state which arised from the $(dxy)^2(dz^2)^2(d\pi)^2$ configuration. It is known that Fe$^{II}$ ion (d$^6$) usually has a $^5T_2g$ ground state from view of ligand field. The calculated result was consistent with the experimental and theoretical observations [21, 22]. The S = 2 state was intermediate state which was 112.90 kcal mol$^{-1}$ above the ground state. And the S = 0 state was the high state which was 191.66 kcal mol$^{-1}$ higher relative to the S = 1 ground state. PMn$^{II}$ had an S = 3/2 ground state, which was in good agreement with Liao's theoretical work. The calculations suggested that PCo$^{II}$ had an S = 1/2 ground state which was consistent with the ESR spectra's assignment configuration $(dxy)^2(d\pi)^4(dz^2)^1$.

**Table 1.** Relative energies of the intermediates PM$^{II}$ and PM$^{II}$Cl (M = Fe, Mn and Co)

| Spin states (S) | Electronic figuration | 0 | 1/2 | 1 | 3/2 | 2 | 5/2 | Ground state |
|---|---|---|---|---|---|---|---|---|
| PFe$^{II}$ | d$^6$ | 191.66 | – | 0.00 | – | 112.90 | – | 1 [21, 22] |
| PMn$^{II}$ | d$^5$ | – | 1207.73 | – | 0 | – | 136.53 | 3/2 |
| PCo$^{II}$ | d$^7$ | – | 0 | – | 86.64 | – | – | 1/2 |
| PFe$^{III}$Cl | d$^5$ | – | 44.63 | – | 0.00 | – | 18.38 | 3/2, 5/2 |
| PMn$^{III}$Cl | d$^4$ | 388.57 | – | 68.26 | – | 0 | – | 2 |
| PCo$^{III}$Cl | d$^6$ | 0 | – | 31.51 | – | 63.01 | – | – |

Recently studies reported the oxidative relationships among manganese(IV) molecules that include pairs of hydroxo/oxo ligands. The high-valent iron(IV)-oxo species have been proposed as an oxidant intermediates that abstracts H atom from strong C–H bonds of substrate. As shown in Table 2, PFe$^{IV}$O acted as S = 1 ground state, and S = 2 active state. The intermediates had a high spin (S = 2) iron(IV)–oxo unit with double bond character between the iron ion and oxygen atom. PMn$^{IV}$O had an S = 1/2 ground state with three unpaired electrons distributed 1:2 between manganese and oxygen atoms. The active state was 68.26 kcal.mol-1 above the ground state. By Shaik's two-state theory[30], the S = 2 state PFe$^{IV}$O showed higher reactivity to C-H oxidation. The energetic calculations gave an S = 1/2 ground state PMn$^{IV}$O and an S = 3/2 ground state PCo$^{IV}$O and S = 5/2 active state. The calculated energetics gave reasonable spin sates for high-valent species.

**Table 2.** Relative energies of $PM^{IV}O$ and $PM^{III}OH$ (M = Fe, Mn and Co)

| Spin states (S) | Electronic figuration | 0 | 1/2 | 1 | 3/2 | 2 | 5/2 | Ground state |
|---|---|---|---|---|---|---|---|---|
| $PFe^{IV}O$ | $d^4$ | 84.02 | – | 0.00 | – | 68.26 | – | 1 |
| $PMn^{IV}O$ | $d^3$ | – | 0 | – | 44.63 | – | – | – |
| $PCo^{IV}O$ | $d^5$ | – | 433.21 | – | 0 | – | 147.29 | – |
| $PFeO^{III}H$ | $d^5$ | – | 42.01 | – | 0.00 | – | 44.63 | 3/2 |
| $PMnO^{III}H$ | $d^4$ | 81.39 | – | 31.51 | – | 0 | – | – |
| $PCoO^{III}H$ | $d^6$ | 0 | – | 94.52 | – | 133.90 | – | – |

It was reported that $PMn^{III}OH$ moiety had similar hydrogen abstraction capabilities with $PMn^{IV} = O$[31]. As the reductant of high-valent species, $PFe^{III}OH$ was predicted to be an intermediate (S = 3/2) ground state, which was different from $PFeO^{III}H$[32]. $PMn^{III}OH$ was predicted to be a high-spin ground state (S = 2). By contrast $PCo^{III}OH$ was shown to be a low-spin ground state (S = 0).

### 3.2   Mulliken Charge Analysis

Mulliken charge on $PM^{IV} = O$ and $PM^{III}OH$ were showed in Scheme 1. We can see that the charge of $Co^{IV}$ ion was lower than that of $Fe^{IV}$ and $Mn^{IV}$ ions for high-valent species. The charge on O atom was −0.508 for $PFe^{IV}O$ and $PCo^{IV}O$, but it was only -0.213 for $PMn^{IV}O$. The more negative charge facilitateed $PFe^{IV}O$ and $PCo^{IV}O$ to abstract H atom of C-H bond in alkanes.
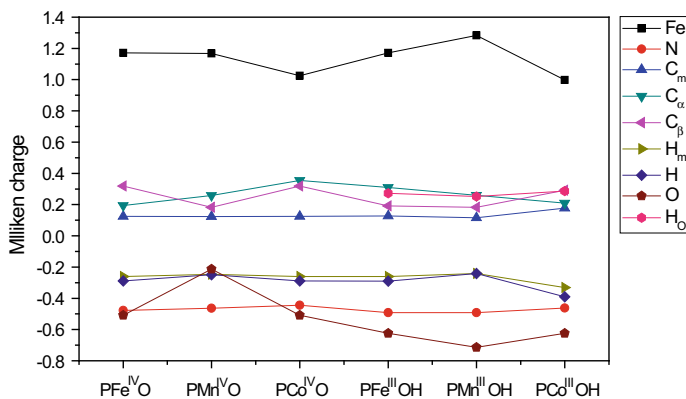


**Scheme 1.** Mulliken charge on $PM^{IV} = O$ and $PM^{III}OH$ (M = Fe, Mn and Co)

The more negative charge on O atoms indicated its strong activity to C-H bond. The O atom of iron-hydroxy species ($PFe^{III}OH$) carried more negative charge than that of the high-valent species. The $PFe^{III}OH$ was considered to combine with the alkane radical in the OH· rebound step. The more negative charge of the O was advantageous

to the iron-hydroxo species combined with alkane radical. The O atoms of PMn$^{III}$OH carried more negative charge than that of PFe$^{III}$OH and PCo$^{III}$OH. Previously iron-hydroperoxo species was considered to be a sluggish oxidants and the oxidizing power of the intermediate can not compete with that of high-valent iron(IV)-oxo species, whereas both iron-oxo and iron-hydroperoxo species have been recently proposed as oxidants in cytochrome P450. The O atom of PFe$^{III}$OH took more negative charge than that of PFe$^{IV}$O. It suggested Fe$^{III}$OH was expected to be a powerfull nucleophilic agent.

### 3.3    Frontier Molecular Orbitals

As shown in Fig. 2, the LUMO of PFe$^{III}$OH was constitute of Fe-dxz and O-px, which formed the $\pi^*$ orbital of PFe$^{III}$OH. The HOMO of PFe$^{III}$OH was made up of Fe-dyz and O-py, forming the $\pi$ orbital of PFe$^{III}$OH. They provided the px,y character perpendicular to the Fe-O bond. PMn$^{III}$OH was observed to $\sigma$ bond with Mn-dx$^2$-y$^2$ and O-p$_x$ orbitals, it provided a character for C-H bond attack along with the Fe-O bond. Finally for the PCo$^{III}$OH, the LUMO was with a character of d$_z^2$ $\sigma$ which had oxo p$_x$ character oriented along the Fe-O bond. The HOMO of PCo$^{III}$OH was d$\pi$ FMO composed of Co-pxz and O-p$_z$ and it facilitatedC-H bond attack perpendicular to Co-O bond. The FMO of PCo$^{III}$OH provided flexible orientation for C-H bond attack and it implied a potential oxidant for PCo$^{III}$OH.



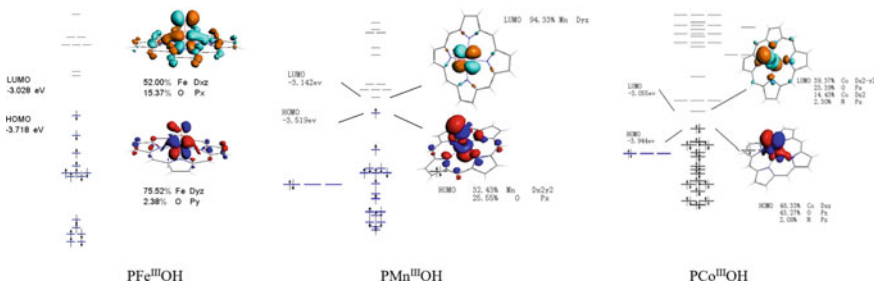**Fig. 2.**  Frontier molecular orbital of PM$^{III}$OH (M = Fe, Mn and Co)

## 4    Conclusions

The ground states of PM$^{II}$ (M = Fe, Mn, and Co) were determined by energy assessment and were confirmed by the experimental results. The geometric structure of intermediates were further analyzed to confirm the ground state. Mulliken charge suggested that the unligated porphyrin was favorable to activate dioxygen.The PMn$^{II}$ showed higher activity to dioxygen than PFeII and PCo$^{II}$. It also indicated that the O atom of iron-hydroxo species (PFe$^{III}$OH) carried more negative charge than that of the high-valent species which showed potential oxidant ability. PCo$^{III}$OH provided flexible orientation for C-H bond attack and it implied a potential oxidant of PCo$^{III}$OH. Frontier molecular orbital analysis found that PCo$^{III}$OH exhibited strong oxidant potential since

the C-H bond provided flexible orientation for C-H bond attack. These distinctly different geometric and electronic properties and relativities of porphyrin intermediates could provide clues to understand these elusive oxidation phenomena and provide the foundation for the efficient design of novel oxidation catalysts.

# References

1. Seo MS, Kim NH, Cho KB, So JE, Park SK, Clemancey M, Garcia-Serres R, Latour JM, Shaik S, Nam WA (2011) Mononuclear nonheme iron(IV)-oxo complex which is more reactive than cytochrome P450 model compound I. Chem Sci 2(6):1039–1045

2. Shin JW, Rowthu SR, Hyun MY, Song YJ, Kim C, Kim BG, Min KS (2011) Monomeric, trimeric, and tetrameric transition metal complexes (Mn, Fe, Co) containing N,N-bis(2-pyridylmethyl)-2-aminoethanol/-ate: preparation, crystal structure, molecular magnetism and oxidation catalysis. Dalton Trans 40:5762–5773

3. Liu W, Groves JT (2010) Manganese porphyrins catalyze selective C–H bond halogenations. J Am Chem Soc 132:12847–12849

4. Ellis Jr PE, Lyons JE (1991) Active iron oxo centers for the selective catalytic oxidation of alkanes. Stud Surf Sci Catal 105:193

5. Ali ME, Sanyal B, Oppeneer PM (2012) Electronic structure, spin-states, and spin-crossover reaction of heme-related Fe-porphyrins: a theoretical perspective. J Phys Chem B 116:5849–5859

6. Kaizer J, Klinker EJ, Oh NY, Rohde J, Song WJ, Stubna A, Kim J, Münck E, Nam W, Que L (2003) Nonheme $Fe^{IV}O$ complexes that can oxidize the C–H bonds of cyclohexane at room temperature. J Am Chem Soc 126:472–473

7. Nam W (2007) High-valent iron(IV)–Oxo complexes of heme and non-heme ligands in oxygenation reactions. Acc Chem Res 40:522–531

8. Altun A, Shaik S, Thiel W (2007) What is the active species of cytochrome P450 during camphor hydroxylation? QM/MM studies of different electronic states of compound I and of reduced and oxidized iron—oxo intermediates. J Am Chem Soc 129:8978–8987

9. Song WJ, Seo MS, DeBeer George S, Ohta T, Song R, Kang M, Tosha T, Kitagawa T, Solomon EI, Nam W (2007) Synthesis, characterization, and reactivities of manganese (V)–oxo porphyrin complexes. J Am Chem Soc 129:1268–1277

10. Charnock JM, Garner CD, Trautwein AX, Bill E, Winkler H, Ayougou K, Mandon D, Weiss R (1995) Characterization of an oxo(porphyrinato)manganese(IV) complex by x-ray absorption spectroscopy. Angewand Chem Int Edn English 34:343–346

11. Arasasingham RD, He GX, Bruice TC (1993) Mechanism of manganese porphyrin-catalyzed oxidation of alkenes. Role of manganese(IV)-oxo species. J Am Chem Soc 115:7985–7991

12. Chen J, Lee Y, Davis KM, Wu X, Seo MS, Cho K, Yoon H, Park YJ, Fukuzumi S, Pushkar YN, Nam W (2013) A mononuclear non-heme manganese(IV)–oxo complex binding redox-inactive metal ions. J Am Chem Soc 135:6388–6391

13. Taguchi T, Gupta R, Lassalle-Kaiser B, Boyce DW, Yachandra VK, Tolman WB, Yano J, Hendrich MP, Borovik AS (2012) Preparation and properties of a monomeric high-spin MnV–oxo complex. J Am Chem Soc 134:1996–1999
14. Liu J, Ohta T, Yamaguchi S, Ogura T, Sakamoto S, Maeda Y, Naruta Y (2009) Spectroscopic characterization of a hydroperoxo-heme intermediate: conversion of a side-on peroxo to an end-on hydroperoxo complex. Angew Chem Int Ed 48:9262–9267
15. Liu J, Shimizu Y, Ohta T, Naruta Y (2010) Formation of an end-on ferric peroxo intermediate upon one-electron reduction of a ferric superoxo heme. J Am Chem Soc 132:3672–3673
16. Liao M, Watts JD, Huang M (2007) Electronic structure of some substituted iron(II) porphyrins. are they intermediate or high spin? J Phys Chem A 111:5927–5935
17. Rutkowska-Zbik D, Tokarz-Sobieraj R, Witko M (2007) Quantum Chemical description of oxygen activation process on Co., Mn. and Mo Porphyrins. J Chem Theor Comput 3:914–920
18. Chen H, Cho K, Lai W, Nam W, Shaik S (2012) Dioxygen activation by a non-heme iron(II) Complex: theoretical study toward understanding ferric-superoxo complexes. J Chem Theor Comput 8:915–926
19. Conradie MM, Conradie J, Ghosh A (2011) Capturing the spin state diversity of iron(III)-aryl porphyrins: OLYP is better than TPSSh. J Inorg Biochem 105:84–91
20. Conradie J, Ghosh A (2007) Electronic structure of trigonal-planar transition-metal-imido complexes: spin-state energetics, Spin-density profiles, and the remarkable performance of the olyp functional. J Chem Theor Comput 3:689–702
21. Liao MS, Scheiner S (2002) Electronic structure and bonding in unligated and ligated Fe-II porphyrins. J Chem Phys 116:3635–3645
22. Mispelter J, Momenteau M, Lhoste JM (1980) Proton magnetic resonance characterization of the intermediate (S = 1) spin state of ferrous porphyrins. J Chem Phys 72:1003

# Research on 3D Printing Efficiency of Sand Table Elements Based on FDM

Qian Deng[1,2], Ruizhi Shi[1(✉)], Fuwei Chen[3], Jilei Chao[1], and Siyang Liu[1]

[1] Information Engineering University, Zhengzhou, China
ruizhishi@sina.com
[2] Henan University of Engineering, Zhengzhou, China
[3] Xi'an University of Technology, Xi'an, China

**Abstract.** The sand table model made by CNC engraving mechanism has short production cycle and high precision, but it is difficult to express the elements of the sand table for important ground objects. To solve this problem, 3D printing technology was introduced into the production of sand table model. The aim of this paper is to improve the printing efficiency of sand table element model. By designing simple 3D models, the influences of forming angle, infill pattern, support type, layer height, placement mode and other parameters on the molding efficiency of 3D printing were studied. By decomposing the elements of sand table into simple models, the shortest printing time was predicted. The results showed that if the forming Angle was larger, more supports and more layers were printed, the printing efficiency would be lower; The higher the infill density was, the more consumable was needed and the longer the printing time was; There was little difference in the time of making small models between "line" and "grid" infill patterns; The printing path of "circle" infill pattern was long and time consuming. When the forming angle was 0°, placed on sidelong, filled with "line or grid" pattern, supported by "line or pillar" pattern, the printing efficiency was high.

**Keywords:** 3D printing · FDM · Printing time · Parameter · Element of sand table

## 1 Introduction

The sand table is made by CNC carving mechanism, and 3D inkjet robot is used to inkjet topographic map on the surface of the sand table model, so that the topographic map elements and the surface of the sand table can be accurately matched. The water system, vegetation, residents, transportation and other elements of the topographic map can be accurately displayed on the sand table [1]. But it's difficult to express important objects on sand table in three dimensions. Take the bridge as an example. If it is printed in the topographic sand table, the symbol of the bridge will be attached to the river of the mountain beam, resulting in the appearance of non-three-dimensional Bridges. Without symbols, important map elements are missing [2, 3]. To solve this problem, 3D printing technology is introduced into the production of sand table. The model of

important ground objects are printed in 3d and added to the corresponding position of the sand table to express important ground objects in three-dimensional form [4, 5].

This paper uses the control variable method to design simple 3D models, and studies the influence of forming angle, infill pattern, support type, layer height and other parameters on the molding efficiency of 3D printing [6]. By decomposing the elements of sand table into simple models, the shortest printing time is predicted to improve the forming efficiency of three-dimensional elements of sand table.

## 2   Equipment

### 2.1   Experimental Materials and Equipment

Instrument: FDM 3D printer, Beijing huitianwei technology co., LTD.
Materials: ABS, PLA, Beijing huitianwei technology co., LTD.
Software: 3D one, Modellight, Beijing huitianwei technology co., LTD.

### 2.2   Experimental Procedure

1. Using 3D one to create a hexahedron, whose size was 20 mm*40 mm*20 mm; Create a cylinder with the height of 20 mm and the diameter of 40 mm. Create a torus with the height of 10 mm, the inner diameter of 20 mm and the outer diameter of 40 mm. Create an ellipsoid with the long axis of 30 mm, the short axis of 10 mm, and the height of 20 mm; Create a cone with the height of 20 mm and the diameter of 20 mm.
2. Modellight was applied to set the forming angle of the model from 0° to 90°, with an interval of 5°. Other parameters: the printed material was "PLA" with the raft was "none", the model support was selected as "everywhere", the support type was "line", the infill pattern was "grid", and the print quality was "low". Print the model and record the printing time, printing layers and material consumption of different models.
3. 3D one was applied to create a hollow model: side length of bottom cuboid was 20 mm, height was 5 mm, side length of upper cuboid was 5 mm and height was 30 mm. As shown in Fig. 1, the model was printed in three different ways: a. sidelong; b. The smallest part of the area serves as the bottom; c. The largest part of the area serves as the bottom.
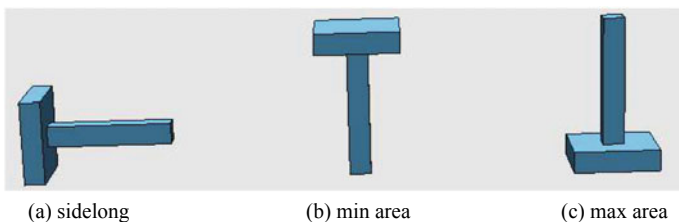


(a) sidelong          (b) min area          (c) max area

**Fig. 1.**  Hollow out model

4. Hori Print Soft was applied to set the infill density of the model from 5% to 95% with an interval of 5%, and the infill types were set "line, grid and circle" respectively; Other parameters: the printing material was "PLA", the raft was selected as "raft 1", the model support was selected as "touching buildplate", the support structure type was "grid", the printing quality was "custom":whose layer height was 0.2 mm, and the edge width was set as 0.8 mm. Print the model and record the printing time, printing layers and material consumption of different models.

5. Modellight was applied to set parameters: the printed material was "PLA", the printing quality was set to "low". Support types were set as follows:

  A. "Bottom support": the infill pattern was "grid", the support type was
     i. set as "pillar, line, surface, tree and grid" respectively. The printing time,
     ii. layers and material consumption of different models were recorded.
  B. "Complete support": the infill pattern was "grid", the support type
     i. was "pillar, line, surface, tree and grid" respectively. The printing time, layers and material consumption of different models were recorded.

6. Apply 3D one to create element models of sand table: building, tree, vehicles, plane, bridge, as shown in Fig. 2.
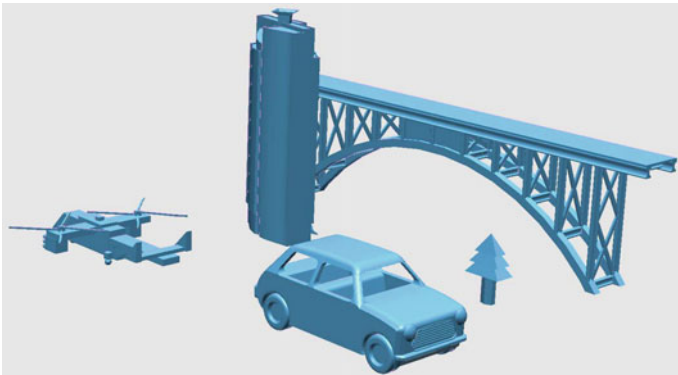


**Fig. 2.** Element models of sand table

7. Set parameters and predict the minimum printing time of the element model.
8. Verify the minimum printing time of the model.

## 3 Results and Discussion

### 3.1 Effect of Infill Density on Forming Efficiency

Figure 3 showed the printing time of infill density from 5% to 100% under different infill types. The trend of hexahedron, cylinder, torus and ellipsoid is almost the same. With the increase of infill density, more materials were consumed, and the printing time
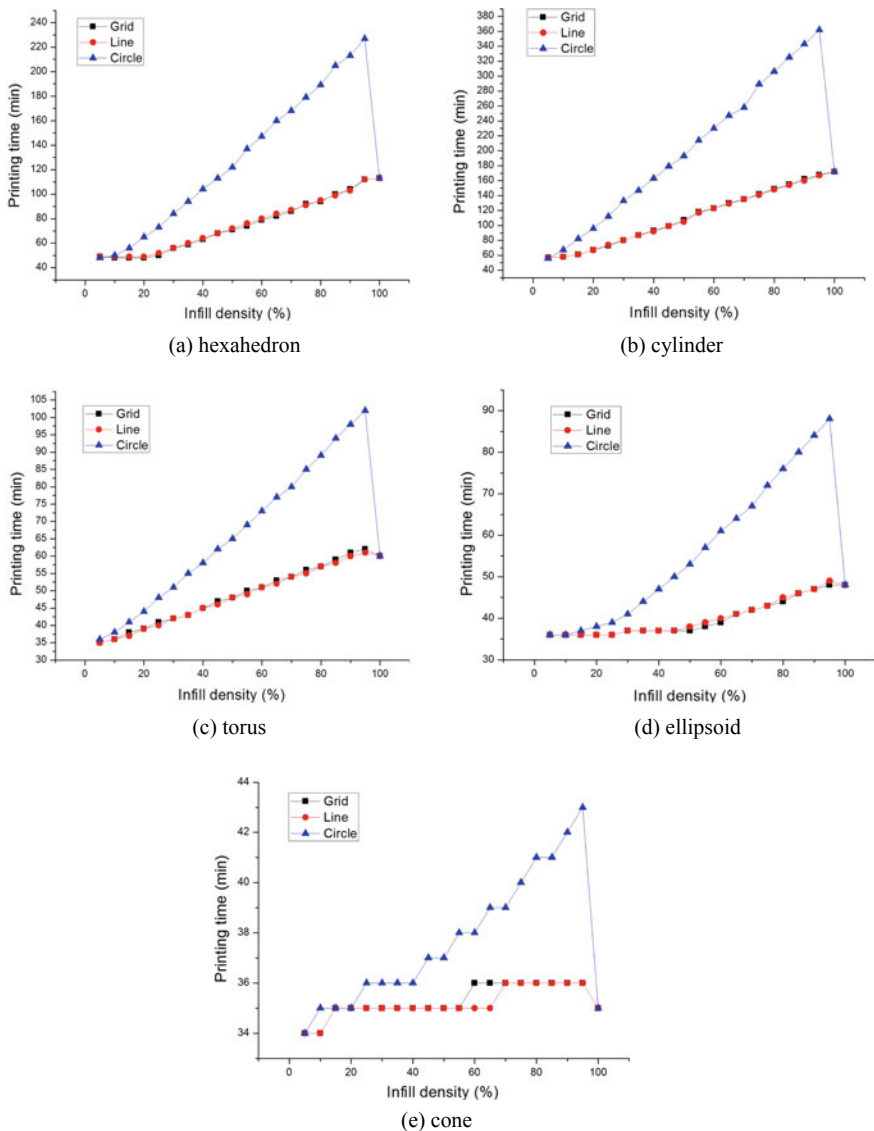
(a) hexahedron

(b) cylinder

(c) torus

(d) ellipsoid

(e) cone

**Fig. 3.** Relationship between infill type and printing time

increased. The model curve of "line" was almost the same as "grid" and the printing time was less than that of the "circle" infill pattern. The model with infill pattern of "circle" took longer time to print and had a higher rate of change. This was because this pattern was complex, the nozzle took longer path and consumed more consumables. Hexahedron: at the infill density of 25%, the "grid" took less time. Choose "grid" pattern when printing this type of model. Torus: at the infill density of 15%, 25% and 45%, "line" need less time. When printing this type of model, chose "line" pattern.

Cone: The printing time of the three infill types presented a step-like change trend with the infill density. The "circle" type need more time, which corresponded to a longer path and more consumables. The "line" pattern was almost the same as the "grid" pattern. At the density of 60% and 65%, "line" pattern took less time than "grid".

## 3.2   Effect of Forming Angle on Forming Efficiency

Figure 4 showed the forming time of five models at different forming angles. Hexa-hedron: when the forming Angle was 0°, the forming time was the shortest, and the area projected into the x-y plane was the largest, no supports were needed. When the forming Angle was 30°, the most supports were needed and the forming time was the longest. When the forming Angle was 35°, the center of gravity was consistent with the geometric center of the current printed model and required less support, so the forming time suddenly became shorter. When the forming Angle was 65°, the printing height was the maximum, so the forming time was longer. Cylinder: when the forming Angle was 0°, the forming time was the shortest. At this angle, the cylinder was placed on the x-y plane with the largest cross-sectional area and no support was needed. When the forming Angle was 25°, the most supports were needed and the forming time was the longest. When the forming Angle was 30°, the center of gravity was consistent with the geometric center of the current printed model, requiring less support and less forming time. When the forming Angle was 75°, the printing height was the maximum and the printing time was longer. Torus: the forming time increased linearly with the molding Angle, reaching the maximum value at 75°, at this Angle model had the most printing layers. When the molding Angle was 0°, the forming time was the shortest, and the area projected into the x-y plane was the largest, no support was needed. Ellipsoidal: with the increase of forming Angle, the forming time increased in a ladder shape, with
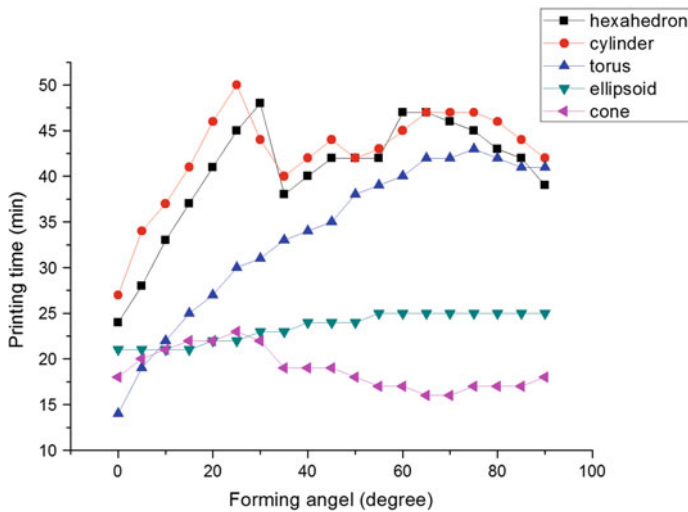


**Fig. 4.**  Relationship between different molding angles and printing time

0° ~ 20° as the minimum value and 55° ~ 90° as the maximum value. The shape of ellipsoid was a sphere, and the support at different angles had little influence on it. The forming time increased with the number of printing layers. Cone: when the forming angle were 65° and 70, the forming time was the shortest and the area projected into the x-y plane was the largest. When the forming Angle was 25°, the forming time was the longest and the layers was the most. The overall trend of change was wavy.

## 3.3  Effect of Placement on Forming Efficiency

The forming time of three different placement showed in Fig. 1 was shown in Table 1. The printing time of "sidelong" was shortest, "min area" was longest.

**Table 1.** Forming time of different placement

| Placement | Sidelong | Min area | Max area |
|---|---|---|---|
| Forming time (min) | 33 | 66 | 44 |

## 3.4  Effect of Support Type on Forming Efficiency

Figure 5 showed the printing time of bottom support and complete support under different support structures of the five models. Hexahedron: The curves of the bottom support and complete support almost coincide, and the printing time of the "grid" support was the same as that of "line" and "surface". The support structure of "tree" required the longest printing time, followed by "pillar". The support structure of "grid" or "line" or "surface" was optional. Cylinder: The curves of the bottom support and complete support almost coincide, and the printing time of the "grid" support structure was the same as that of the "surface" and "pillar". The printing time of "tree" support structure was the longest, "line" support structure was the shortest. The support structure of "line" could be selected. Torus: The printing time of "grid" support structure was the longest when the support type was complete. Under the bottom support type, the print time of "grid" and "surface" support structure was the longest and same. The lowest points of the two types of support were "line" and "pillar". The support structure of "line" or "pillar" with complete support type could be selected. Ellipsoid: The printing time of "grid" support structure under bottom support and complete support was the same. In other types of support structures, the printing time of complete support was longer than that of bottom support. In the case of two support types, "tree" support structure need the longest printing time. Under complete support, "grid", "line" and "surface" support structures had the same time consumption and need the shortest time. The time required for "pillar" support structure type was the shortest under the bottom support. The support structure of "pillar" under bottom support could be selected. Cone: In the case of two support types, the printing time of different support structures was consistent. The printing time of "tree" support was the longest, "grid" and "line" was the shortest. The support structure of "grid" or "line" could be selected.
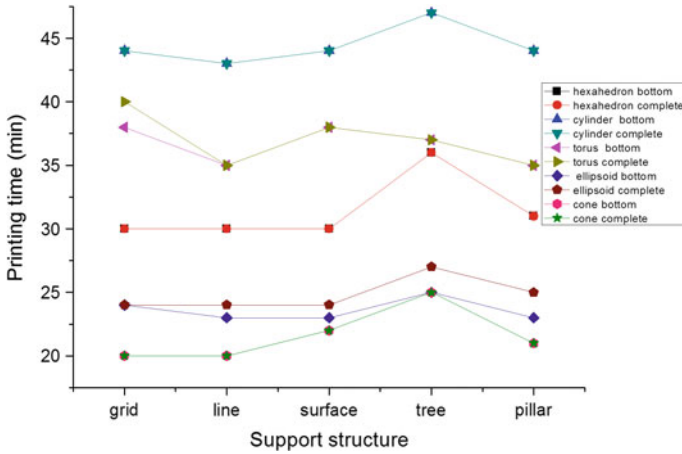
**Fig. 5.** Relationship between support structure and printing time of hexahedron

## 3.5 Prediction and Test of Printing Parameters of Sand Table Element Model

The minimum printing time of five simple models corresponding parameters were shown in Table 2.

**Table 2.** Minimum printing time of five simple models corresponding parameters

| Model | Forming angel | Infill type | Support type | Support structure |
|---|---|---|---|---|
| Hexahedron | 0 | Grid | Bottom | Grid, line, surface |
| Cylinder | 0 | Line | Bottom | Line |
| Torus | 0 | Line | Complete | Line, pillar |
| Ellipsoid | 0 | Grid | Bottom | Pillar |
| Cone | 65, 70 | Line | Bottom | Grid, line |

### 3.5.1 Prediction of Printing Parameters

Prediction of printing parameters of sand table element models based on Table 2 were shown in Table 3. The best placement of car, tree, building and bridge was sidelong. The best placement of plane was max area.

**Table 3.** Prediction of printing parameters of sand table element models

| Model | Model combination | Forming angel | Infill type | Support |
|---|---|---|---|---|
| Car | Hexahedron, cylinder, torus | 0 | line | bottom, line |
| Plane | Hexahedron, cylinder | 0 | line | bottom, line |
| Tree | Hexahedron, cone | 0 | line | bottom, grid |
| Bridge | Hexahedron, torus | 0 | grid | bottom, pillar |
| Building | Hexahedron, ellipsoid | 0 | line | bottom, line |

### 3.5.2    Test of Printing Parameters

The actual data of experiment were shown in Figs. 6 and 7.

These data in Fig. 6 were consistent with the predicted values. Figure 7 showed the forming time of different sand table element model. Although the curves of different models had different trends, the angle corresponded to the shortest time were all at 0°. These data were consistent with the predicted values.
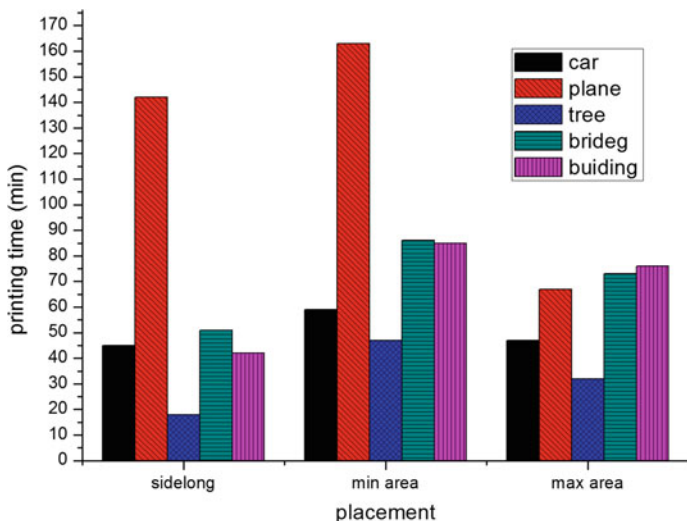


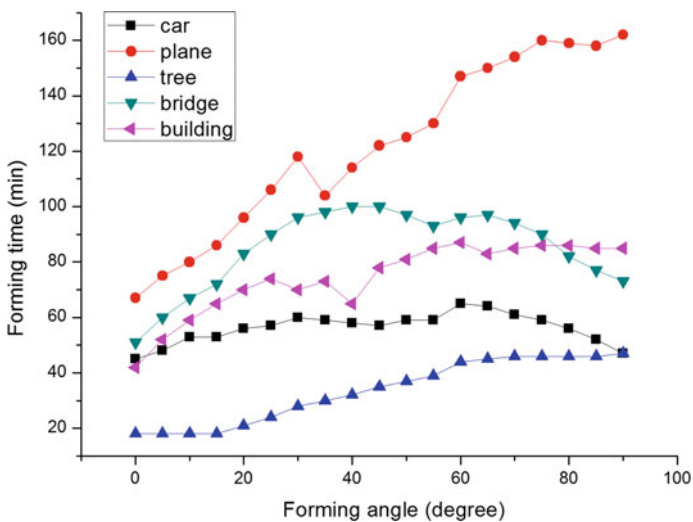**Fig. 6.** Forming time of different model based on different placement



**Fig. 7.** Forming time of different sand table element model

# 4    Conclusions

In this paper, the influence of forming angle, infill rate, infill density, placement mode and support on forming time were studied by using simple models. The results showed that if the forming angle of the model was larger, more supports were needed, and the number of printing layers were more, the printing time was longer. When the forming angle of hexahedron was 30°, cylinder was 25°, torus was 75°, ellipsoid was 55° ∼ 90° and cone was 25°, the corresponding printing time was the longest. The higher the infill density was, the more the printing consumables, the longer the printing time was. There was little difference in the printing time between "line" and "grid" infill patterns, while the printing path of "circle" infill pattern was long and time-consuming. When the model was complex and required a lot of support, the "tree" support structure would save a lot of time. Rules, simple models, "line" support structure required less printing time. When the sand table elements were printed, they were decomposed into simple model, and parameters were set by using the printing rules of the simple model, which could obtain higher printing efficiency.

# References

1. Yang MZ, Wang MX, Ma ZG et al (2017) An automated method for producing 3D true-color terrain sand table model. Geospatial Inf 15(4):89–92
2. Shen YP, Zhai HQ, Ma TG et al (2018) Discussion on the representation method of sand table elements in topographic map. Surv Map Technol Equip 20(2):94–95
3. Yang ZW, Liu Y (2017) Optimal design in 3D printing. J Op Res 21(4):34–56
4. Zhang ZL, Zhang W, Fu J et al (2017) Influence of basic parameters on FDM process. Mod Manuf Technol Equip 7:80–82
5. Liu R, Yan S, Shi S (2018) Analysis of 3D printing technology. Digit Users 24(37):65
6. Zhou GL, Guo DM, Jia ZY et al (2002) Optimization of process parameters of molten deposition. J Dalian Univ Technol 42(4):446–450

# Characterization of Plasma Active Water and Its Sterilization Process Study

Xiaojuan Chen, Hongwei Li, and Yunjin Sun[(✉)]

Beijing Laboratory of Food Quality and Safety, Food Science and Engineering
College, Beijing University of Agriculture, Beijing, China
2270509122@qq.com

**Abstract.** Plasma active water (PAW) has owned a good bacteriostatic performance, which can effectively clean the harmful microorganisms from the surface of fruits and vegetables, and has a wide application in the field of food cold sterilization. Gliding arc discharge was adopted in this study to form PAW liquids, with *Escherichia coli* (*E. coli*) as treatment object, and the sterilization process and the characteristics of PAW was optimized and measured through the determination of hydroxyl free radicals, pH, ORP, conductivity, showing that PAW was a green and residue-free sterilization technology. The experimental results showed that PAW prepared by air discharge had the best sterilization effect, followed by oxygen and nitrogen. PAW through air plasma treatment has a higher ORP value and longer efficiency, which was consistent with the results of pH and conductivity. According to Fenton reaction, PAW contained high concentrations of hydroxyl radical, which was responsible for its good bactericidal effect.

**Keywords:** Low temperature plasma activated water · Glide arc discharge · Sterilization effect · Fenton reaction

## 1 Introduction

Plasma is one kind of discharged gas realized in the atmosphere or vacuum state, which is the fourth state of matter, accounting for 99% of the space of the universe, and widely exists in the natural environment, such as Aurora, Mars, Sun and Thunder and Lightning [1]. Atmospheric plasma is a low-temperature plasma. The active substances produced innerside deionized gas contain electronic, excited molecules, high-energy particles, atoms, reactive oxygen species, active nitrogen and other active ingredients, which have bactericidal effect on bacteria, spores, viruses and fungi [2–5]. Plasma active water (PAW) is a liquid containing some active components of plasma under atmospheric plasma treatment by exposing the liquid to various forms of plasma discharge [6]. Plasma active water can clean various surfaces of food, fresh produce, and so on, and provides an indirect treatment for the storage and fresh preservation in food and agriculture area.

In recent years, PAW has shown many characteristics, such as high efficiency, simple and portable, safety and effect of killing a variety of food borne pathogenic bacteria [7]. Which exists great potential to replace traditional food sterilization

technology and auxiliary. Along with the deepening of the research on the PAW sterilization, sterilization effect of PAW is generally regarded as a good cold sterilization technology due to low temperature (room temperature) processing, no residue, low energy consumption, simple operation, strong sterilization ability and other characteristics, very suitable for processing of heat sensitive material surface. [8]. However, based on the literature research, PAW is a novel sterilization method of low-temperature plasma sterilization, whose sterilization function and sterilization mechanism are still in the preliminary stage and needed to be further studied.

Compared with other low-temperature plasma discharge forms, gliding arc discharge technology, gliding arc discharge can be formed directed through the two naked electrodes, and has strong bactericidal ability, low energy consumption and high efficiency for the potential of industrial application [9]. For example, Zhang et al. studied the treatment of fresh radish with gliding arc discharge, and found that the bactericidal rate of gliding arc discharge reached 92.35% at 170 V within 5 min [10]. This study would adopt gliding arc discharge technology to prepare PAW, investigate the bactericidal effect of PAW, and analyze its internal active components, in order to further reveal its bactericidal mechanism.

## 2 Materials and Method

### 2.1 *Escherichia coli* Inoculation

*Escherichia coli* (*E. coli* ATCC8099) is provided by the China Industrial Microbial Species Management Center. *Escherichia coli* was incubated in a 37 °C and 180 r/min for 12 h, and then mixed with the prepared PAW. After the sterilization treatment of 5–10 min, 1.0 ml of the mixed liquid was extracted into counting medium of total number of colonies, and then cultured in constant temperature horizontal wet box for 24–48 h until the number of colonies can be counted according to the plate count method.

### 2.2 Preparation Instruments of PAW

The atmospheric plasma discharge processor was mainly composed of a power source, a processing chamber, a gas flow test table. There were two parallel copper electrodes in the reaction chamber (length and diameter size of 93 mm and 3.0 mm, respectively). Working gases, such as Air, $O_2$, $N_2$, were introduced from the top of the reactor, and ionized by a voltage of 10 kV between the two copper sheets when passing through the reactor. The samples were placed at the bottom part of the reactor on the sample table (Fig. 1).

Once PAW was prepared, *E. coli* suspension was placed in the plasma activated water with different ratios of 1:1 for 5 min, then adopted 1 ml of mixed liquid into the culture dish, each group is three parallel, and was incubated for 24–48 h in a constant temperature and humidity chamber.
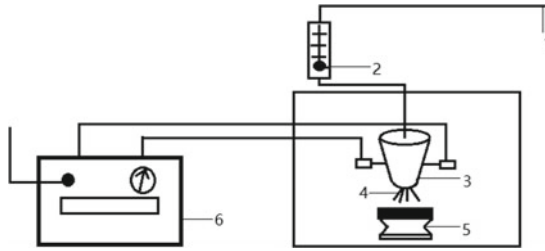
Note :1. Gas source 2. Gas flow meter 3. Reactor
4. Slide arc discharge 5.Sample table 6.power supply

**Fig. 1.** Atmospheric plasma discharge equipment

## 2.3   Methods

### 2.3.1   Determination of ORP Value of Plasma Activated Water

150 ml of sterile deionized water in a 200 ml beaker was treated under plasma equipment with different discharge gases (Air, $N_2$, $O_2$) for 1 min, 2 min, 3 min, 4 min, 5 min. Once prepared, PAW was immediately measured using a HQ30d ORP tester, with three replicates in each set, deionized water as a control.

### 2.3.2   Determination of Hydroxyl Radical Concentration

Using Fenton reaction principle, through hydrogen peroxide reaction to formhydroxyl radicals, and 2,3-dihydroxybenzoic acid formed by the reaction of hydroxyl radicals with salicylic acid can be detected at 510 nm by visible light spectrophotometer (TU-1810, Shanghai Shengke Instrument Equipment Limited), When the salicylic acid added to the solution was fixed, the measured trend of the change of 2,3-dihydroxybenzoic acid and hydroxyl radical was positively correlated.

20 ml of prepared plasma activated water was Pipetted into the culture dish, numbered as 1, 2, 3, 4, 5, 6. After treatment, 13 ml was chosen into a 20 ml centrifuge tube and added 1 ml of iron sulphate solution and 1 ml of salicylic acid. All the treated samples were uniformly subjected to a water bath for 15 min, and the samples were taken at a wavelength of 510 nm by an visible light spectrophotometer, where the absorbance value represented the intensity of 2,3-dihydroxybenzoic acid content.

### 2.3.3   Determination of pH Value

For the determination of pH value, 2 ml of the bacterial suspension was transferred to 18 ml of distilled water, and the pH was measured by pH meter (PHB-4 Shanghai Yidian Scientific Instrument Company limited). Each treatment group was repeated three times.

### 2.3.4   Conductivity Measurement of PAW

Conductivity is an important parameter affecting the efficiency of discharge deactivation [11]. The conductivity of bacterial liquid and distilled water was determined in this

part of the experiment. 2 ml of the bacterial suspension was mixed into 18 ml of distilled water, and measured by conductivity meter (DDS-11A, Shanghai Yidian Scientific Instrument Company limited).

## 3 Results and Discussions

### 3.1 Sterilization Effect of *E. Coli*

PAW formed under different gas discharge radiations, has different bactericidal effects due to different active ingredients. In this study, atmospheric plasma formed through air, nitrogen and oxygen discharges, was used to prepare PAW for *E. coli* inactivation treatment, as shown in Fig. 2. It can be seen that total number of colonies decreased with plasma radiation time, indicating a good sterilization effects. Among air, oxygen and nitrogen of discharge gas species, the sterilization effect of oxygen was the least obvious. When the treatment time was 0–2 min, the sterilization ability of PAW for oxygen discharge gradually increased, and the best sterilization effect was achieved at 2 min, and then remained unchanged. The bactericidal effect of air and nitrogen discharge is obviously better than that of oxygen. After nitrogen discharge treatment for 4 min, total number of colonies decreased to 24 CFU/ml in comparison with 325 CFU/ml of control samples. After 4 min of sterilization the total bacterial colony number reached 0 CFU/ml with obvious bactericidal effect for air discharge, reaching the aseptic state after 5 min treatment. It can be deduced that, if the discharge gas was selected properly, gliding arc discharge technology can completely inactivate *E. coli* within a short time duration of 5 min, indicating a good bactericidal effect. Tian et al. [11] has adopted a direct current atmospheric pressure cold plasma microjet to produce plasma activated water, and found that PAW exhibited stronger disinfection efficiency, which was associated with ORP and conductivity, since the cell membrane integrity and membrane potential of Staphylococcus aureus were destroyed more severely. Shen et al. [12] has adopted argon plasma discharge to inactivate *Staphylococcus aureus* suspended in the liquid, and found that direct plasma treatment for 40 min results in more than 2.0-log cell reduction, which can be contributed to the presence of the presence of hydroxyl radicals and atomic oxygen from the plasma and water interaction. Therefore, it can be deduce that the inactivation efficient would have a close relationship with the characterizes of PAW, as will be further revealed as follows.

### 3.2 Characteristics of PAW Under Different Discharge Gas Species

#### 3.2.1 Conductivity and ORP Evaluation of PAW

According to Nernst equation and electrochemical reaction kinetics, the essential process of plasma and water interaction was a complicatedly redox process. In this study, OPR value was firstly used to test the redox properties of PAW. Figure 3 showed the change of ORP value with the treatment time in different discharge gases. It can be seen that ORP value of PAW prepared by air, nitrogen and oxygen plasma discharge increased with plasma radiation time. Initial ORP value of deionized water was obtained as 379.7 mV, through different gas plasma discharge of air, nitrogen and oxygen, ORP value reached ultimately 558.0 mV, 489.1 and 452.9 mV, respectively,
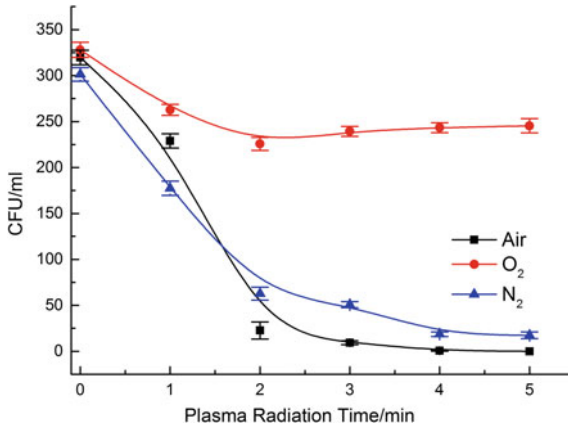
**Fig. 2.** The sterilization effects of PAW on *E. coli* under different discharge gas species

indicating a strong oxidizing effect. ORP from air discharge was the highest, followed by nitrogen discharge, and oxygen discharge water was the lowest, which is much more than that of direct current atmospheric pressure cold plasma microjet results [13].
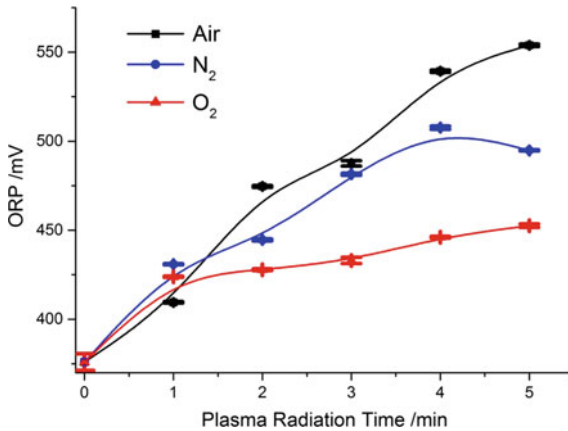


**Fig. 3.** The change of ORP value under air, $N_2$ and $O_2$ plasma activated water under different radiation time

Conductivity of treated liquids reflected the ion concentration and the ability of a solution to conduct a current. The more charged ions in a solution, the greater the conductivity. Figure 4 showed the trend of PAW conductivity variation with discharge power under different gas discharge irradiation. It could be seen that the conductivity of PAW increased with plasma discharge power, during which the conductivity of PAW prepared under air plasma radiation was higher than nitrogen, and oxygen was the lowest. Xin Qing [14] et al. found that the increase of solution conductivity was

resulted from the increment of the concentration of active ions contained in the liquid. With the increment of plasma discharge power, the ion and electron concentration generated by gas ionization increased, leading to the higher conductivity of PAW.
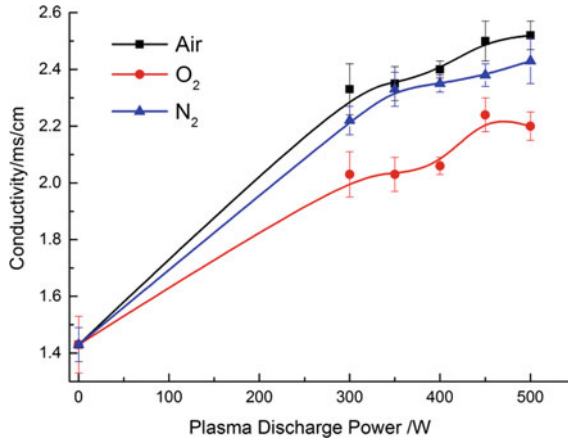


**Fig. 4.** Effect of plasma discharge power on the conductivity of PAW under different gas species

### 3.2.2   Evaluation of pH and Hydroxide of PAW

Figure 5 showed the trend of pH value of PAW under different gas species. As can be seen, the treated water was transferred into acidic liquid after plasma treatment, which had a positive effect on the survival of bacteria. Oxygen plasma has the lowest pH decrement, followed by nitrogen, and air plasma has the largest decrement. Regardless of discharge gas species, when plasma radiation time was kept for 1 min treatment, the pH value dropped rapidly to about 3.5, and then changed gradually down to 3.0 with the treatment time. In fact, this lower pH value was may be due to the interaction and diffusion effect between gliding arc discharge and deionized water surface, since Satoshi et al. has used atmospheric pressure plasmas treating the surface of an aqueous solution to inactivate bacteria suspended in the solution, and found that critical pH value may arise from the equilibrium reaction between $O_2$ and hydroperoxy radicals HOO, which is known to be approximately 4.8 [15].

Figure 6 showed the variation trend of the hydroxide absorption intensity of deionized water treated by gliding arc discharge at different times according to Fenton reaction. As can be seen, the absorption intensity increased gradually with the extension of plasma radiation time. Nitrogen plasma treatment had the largest change in light absorption intensity, followed by air plasma treatment, while oxygen treatment had the smallest influence on light absorption intensity. With the extension of plasma radiation time, both nitrogen and air plasma had a linearly increment, while oxygen plasma had a smaller rise. In addition to hydroxyl radicals, PAW may also contained other active bacteriostatic ingredients, such as nitrite ion and nitration, ozone, etc., which contributed the larger rise of nitrogen or air plasma and would be further verified in future studies [16].
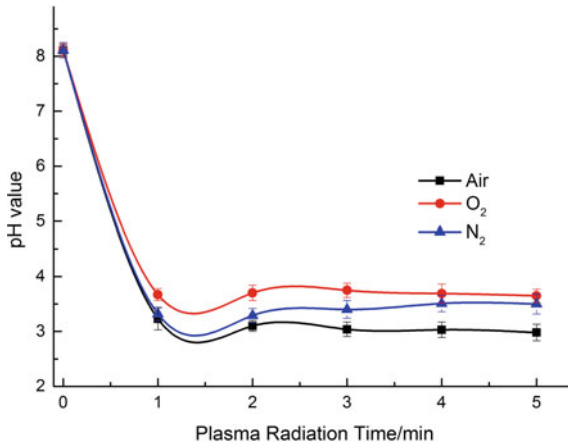
**Fig. 5.** Effect of plasma radiation time on pH value of PAW under different gas species
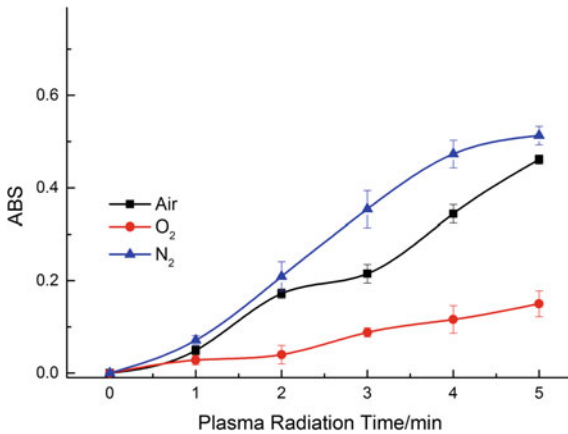


**Fig. 6.** Effect of plasma radiation time on hydroxide absorption of PAW under different gas

## 3.3    Timeliness of Plasma Active Water

Once the plasma is prepared, can its bacteriostatic properties be preserved permanently and thus have a long-term bactericidal effect? This study studied the timeliness of PAW from the respective of ORP variations with storage time. Figure 7 showed ORP variations of PAW under air discharge as a function of storage duration, since strong oxidizing (high ORP value) could damage cell membrane and thus lead to bacterial oxidative damage [11]. Therefore, ORP could be chosen as indicator for sterilization ability of PAW. ORP value of PAW was initially 548.5 mV, showing the redox potential was still very high within first 1–2 h with storage time until ORP value was fed back to the initial state of 350 mV after 5 h. However, ORP value of PAW prepared by air discharge does not change much while that prepared by nitrogen

discharge and oxygen has a similar decreasing trend. It can be concluded that the ORP value of the activated water in the air discharge plasma is higher than that in both the nitrogen and oxygen discharge, which may be caused by more gas components or active substances and indicating a strong timeliness of PAW more than 5 h.
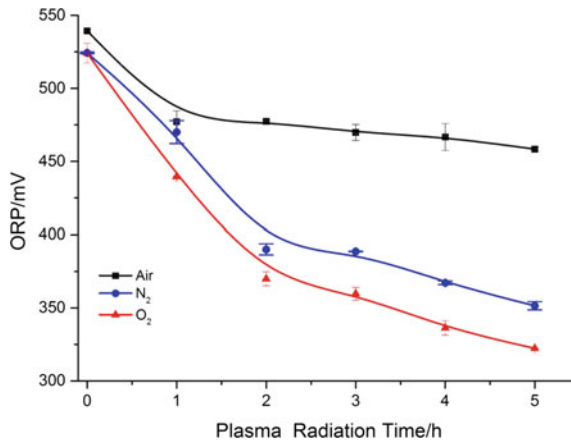


**Fig. 7.** ORP variations of PAW under air discharge as a function of storage duration

## 4    Conclusions

In this study, PAW has been manufactured by gliding arc discharge under different discharge gas species with *E. coli* as treatment object. Sterilization effects showed that bactericidal effect of PAW prepared through air and nitrogen discharge plasma is obviously better than that of oxygen, where the total colony number reached 0 CFU/ml after 4 min plasma radiation duration. The excellent inactivation efficient would have a close relationship with the inner side components of PAW, as was revealed by measuring the characteristics of PAW, such as hydroxyl free radicals, pH, ORP, conductivity. The characterization of PAW showed that the activated water after air plasma irradiation has a higher ORP value and a longer time efficiency, which was consistent with the test results of pH and conductivity. According to reaction, the plasma active water under air plasma may contain high concentration of hydroxyl radicals and other active ingredients, which has a good bactericidal effect, indicating that PAW was a green and residue—free sterilization technology.

# References

1. Conrads H, Schmidt M (2000) Plasma generation and plasma sources. Plasma Sourc Sci Technol 9(4):441–454
2. Kou Y (2015) Experimental study on killing microorganisms in water by pulsed electric field and plasma. Zhejiang University
3. Min J, Yi Z, Huang Y, Zhu J, Yu X (2018) Experimental study on low temperature plasma sterilization based on dielectric barrier discharge of suspended electrodes. Integ Technol 1–6
4. Sun Y, Zhang Z, Wang S (2018) Study on the bactericidal mechanism of atmospheric-pressure low-temperature plasma against *Escherichia coli* and its application in fresh-cut cucumbers. Molecules 23(4):975
5. Brun P, Bernabè G, Marchiori C, et al (2018) Antibacterial efficacy and mechanisms of action of low power atmospheric pressure cold plasma: membrane permeability, biofilm penetration, and antimicrobial sensitization. J Appl Microbiol, J Appl Microbiol 125(2):398–408
6. Misrann Patil S, Moiseev T, et al (2015) In-package atmospheric pressure cold plasma treatment of strawberries. J Food Eng 125:131–138
7. Bo Yang, Chongshan Zhong, Weizhou Wang et al (2019) Research progress of plasma active water in agricultural field. Agric Eng 9(02):101–107
8. Qi Z, Tian E, Song Y, et al (2018) Inactivation of shewanella putrefaciens by plasma activated water. Plasma Chem Plasma Process 38(5):1035–1050
9. Du CM, Yan JH, Cheron B (2007) Decomposition of toluene in a gliding arc discharge plasma reactor. Plasma Sourc Sci Technol 16(4):791
10. Zhiwei Zhang (2018) Bactericidal effect and quality of normal-pressure low-temperature plasma on Staphylococcus aureus on fresh-cut carrots. Grain Oil Food Technol 26(3):50–55
11. Tian Y Marn, Zhang Q et al (2015) Assessment of the physicochemical properties and biological effects of water activated by non-thermal plasma above and beneath the water surface. Plasma Process Polym 12(5):439–449
12. Shen Jie, Sun Qiang, Zhang Zelong, Cheng Cheng, Lan Yan, Zhang Hao, Ying Zimu Xu, Paul KChu (2015) Characteristics of DC gas-liquid phase atmospheric-pressure plasma and bacteria inactivation mechanism. Plasma Process Polym 12:252–259
13. Tian Y, Ma R, Zhang Q, Feng H, Liang Y, Zhang J, Fang J (2015) Assessment of the physicochemical properties and biological effects of water activated by non-thermal plasma above and beneath the water surface. Plasma Process Polym 12:439–449
14. Gerald K (2005) Cell and molecular biology: concepts and experiments. Wiley and Sons, Hoboken
15. Satoshi I, Kitano K, Hamaguchi S (2010) Effects of pH on bacterial inactivation in aqueous solutions due to low-temperature atmospheric pressure plasma application. Plasma Process Polym 7:33–42
16. Peter Bruggeman, Christophe Leys (2009) Non-thermal plasmas in and in contact with liquids. Phys D Appl Phys 42:053001

# Simulation Study on Extinction Characteristics of Gold-Silver Nanoshuttles

Jun Wang[1,2], Shuang Chen[1], Chunyu Chen[1], Yabin Shao[1], Jing Han[1],
Xin Zhao[1], Jijuan Jiang[1], Tong Wu[1], and Yachen Gao[1(✉)]

[1] College of Electronic Engineering, Heilongjiang University, Harbin,
Heilongjiang, China
{wangjun1003, ml3251603662, C_CY2009, shao_yabin,
hanjing1980}@163.com, xinzhiguisu@sina.com,
{935109559, 17l0509490}@qq.com, gaoyachen@hlju.edu.cn
[2] College of Light Industry, Harbin University of Commerce, Harbin,
Heilongjiang, China

**Abstract.** In order to study the extinction characteristics of gold-silver nanoshuttles, finite difference time domain (FDTD) method was used to simulate the models of gold-silver nanoshuttles with different diameter-length ratios, diameters and cone angles. The simulation results show that with the increase of aspect ratio, the longitudinal absorption peak of the gold-silver nanoshuttles shifts red, while its transverse absorption peak does not change significantly; the longitudinal absorption peak also shifts red with the increase of the length of the central nanorod; and the transverse absorption peak of the gold-silver nanoshuttles shifts blue with the increase of the angle of cone.

**Keywords:** Gold-silver nanoshuttles · FDTD · Aspect ratio · Absorption peak

## 1 Introduction

Noble metal nanostructures have attracted much attention due to their remarkable local surface plasmon resonance (LSPR) effect [1–6]. When light waves incident on metal nanostructures, at a certain wavelength, the incident photons resonate with the free electron oscillations transmitted on the surface of nanoparticles, and the absorption spectra show obvious LSPR absorption peaks [7, 8]. The research shows that the location of the absorption peak is not only related to the type of precious metal materials and the shape, size and spacing of nanoparticles, but also sensitive to the surrounding media, so it can be used in the field of sensing. In recent years, the optical properties of metal nanoparticles with different shapes have attracted the attention of researchers, such as nanospheres [3, 9–12], nanorods [13–17], nanotriangles [18–21], nanocages [22, 23], nanodiscs [24], nanotubes [25]. The optical properties of nanomaterials with different structures are obviously different from those of homogeneous structures [26]. However, there are few reports on the optical properties of gold-silver nanoshuttles (Au-Ag NSs). In this paper, the LSPR characteristics of Au-Ag NSs are simulated by the finite-difference time-domain theory (FDTD) [27]. The LSPR absorption spectra of Au-Ag

NSs with different lengths, diameters and cone angles are studied. The LSPR phenomena of the Au-Ag NSs were explored by simulation analysis.

## 2   Simulation Experiment

The simulation object of this experiment is gold-silver nanoshuttle. Its structure consists of gold nanorod and silver nano-cones. Gold nanorod are in the middle, silver nano-cones are on both sides and are shuttle-shaped as a whole. The schematic diagram is shown in Fig. 1. The length of gold nanorod is $L$, the diameter is $D$, and the diameter of the bottom surface of silver nano-cones is the same as that of gold nanorod, and the cone angle is $\theta$.



**Fig. 1.**  Structural schematic diagram of Au-Ag NSs

FDTD Method was used to simulate Au-Ag NSs with different lengths, diameters and cone angles. A water solution substrate with a length of 200 nm, a width of 60 nm and a height of 20 nm is set up. The Au-Ag NSs are put into the water solution substrate, and a monitor is set near the bottom of the substrate for recording data. The light source used in the simulation is plane wave, the wavelength range is 500–2500 nm, the height of the light source is 1000 nm, the size of the simulation grid is 2 nm, the optical constants of Ag and Au are both taken from the CRC model.

## 3   Results and Discussions

Au-Ag NSs of different lengths with diameter of 12 nm and cone angle of 60° were simulated, the simulation results are shown in Fig. 2.

Figure 2 shows that when the diameter and cone angle are fixed, Au-Ag NSs have two resonance absorption peaks, the left side is the longitudinal absorption peak and the right side is the transverse absorption peak. This is due to the different length-diameter ratio of Au-Ag NSs with different lengths and diameters, which results in different distances between the longitudinal and transverse vibration, and then leads to the absorption peak position change. With the increase of the length, the absorption peak shifts red, and the transverse absorption peak shifts significantly. This is due to the increase of the transverse vibration distance of free electrons on the surface of Au-Ag NSs, which leads to the red shift of the transverse absorption peak. In order to facilitate comparison, the position data of longitudinal absorption peaks are collated, the results are shown in Table 1.
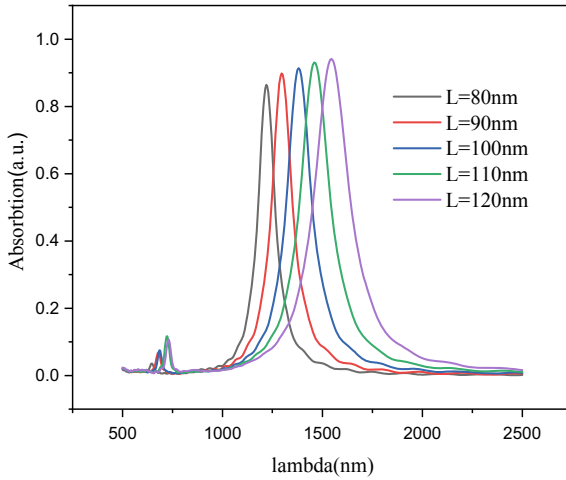
**Fig. 2.** LSPR absorption spectra of Au-Ag NSs with different length (D = 12 nm, θ = 60°)

**Table 1.** LSPR peak tables of Au-Ag NSs with different aspect ratios

| Serial number | D (nm) | L (nm) | θ (°) | LSPR (nm) |
|---|---|---|---|---|
| 1 | 12 | 80 | 60 | 1219 |
| 2 | 12 | 90 | 60 | 1295 |
| 3 | 12 | 100 | 60 | 1382 |
| 4 | 12 | 110 | 60 | 1459 |
| 5 | 12 | 120 | 60 | 1546 |

As can be seen from Table 1, when the length of Au-Ag NSs increases from 80 to 120 nm, the transverse absorption peak shifts from 1219 to 1546, moving 327 nm, and the amount of movement is relatively large. The relationship between the ratio of L to D (aspect ratio) and the data of transverse absorption peak is shown in Fig. 3. In Fig. 3, the position of transverse absorption peak and aspect ratio are linear, and the relationship between them is shown in Eq. (1):

$$P_p = 98.16 \times A_r + 562.20 \tag{1}$$

where, $P_p$ represents the position of the transverse absorption peak and $A_r$ represents the aspect ratio. It can be seen that the transverse absorption peak can be adjusted by adjusting the aspect ratio when the angle of cone is constant.

In order to analyze the influence of cone angle on the position of absorption peaks, Au-Ag NSs with diameter of 12 nm, length of 120 nm and different cone angles were simulated. The results are shown in Fig. 4.

Figure 4 shows that there are two resonance absorption peaks for Au-Ag NSs with the same diameter and length. With the increase of cone angle, the blue shift of
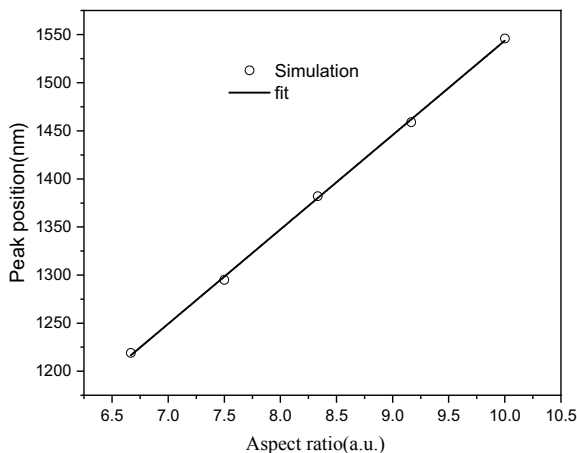
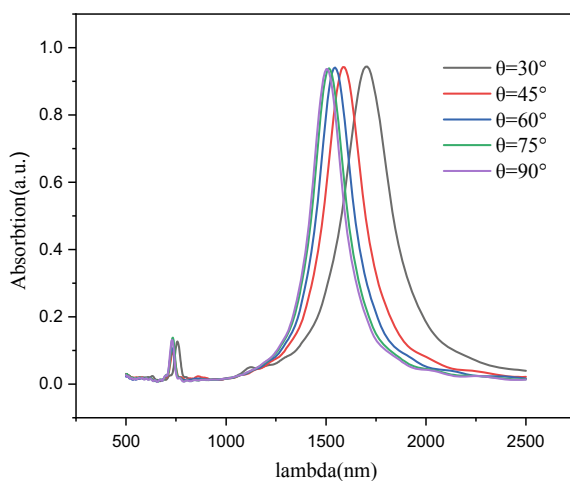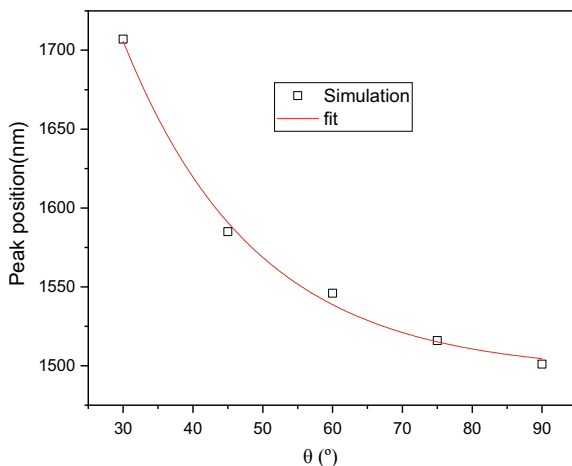**Fig. 3.** Fitting curve between peak position and aspect ratio



**Fig. 4.** LSPR absorption spectra of Au-Ag NSs with different cone angle (D = 12 nm, L = 120 nm)

longitudinal absorption peaks is not obvious, but the blue shift of transverse absorption peaks is significant. This is due to the decrease of nanocone height and the free surface of Au-Ag NSs caused by the increase of cone angle under the same diameter. The smaller the transverse vibration distance of electrons, the shorter the vibration period and the blue shift of the transverse absorption peak. In order to facilitate comparison, the position data of absorption peaks are collated. The results are shown in Table 2.

**Table 2.** LSPR peak tables of Au-Ag NSs with different cone angles

| Serial number | D (nm) | L (nm) | θ (°) | LSPR$_L$ (nm) |
|---|---|---|---|---|
| 1 | 12 | 120 | 30 | 1707 |
| 2 | 12 | 120 | 45 | 1585 |
| 3 | 12 | 120 | 60 | 1546 |
| 4 | 12 | 120 | 75 | 1516 |
| 5 | 12 | 120 | 90 | 1501 |

From Table 2, it can be seen that when the cone angle of Au-Ag NSs increases from 30° to 90°, the transverse absorption peak shifts from 1707 to 1501 and 206 nm, with a relatively large amount of movement. (4) The relationship between cone angle and transverse absorption peak data is shown in Fig. 5.



**Fig. 5.** Fitting curve between peak position and cone angle

As shown in Fig. 5, the position of the transverse absorption peak is exponentially related to the cone angle, as shown in Eq. (2):

$$P_p = 1025.72 \times e^{-\frac{\theta}{18.92}} + 1495.69 \qquad (2)$$

where, *Pp* represents the position of the transverse absorption peak and $\theta$ represents the angle of the cone angle. Thus, the transverse absorption peak can be adjusted by adjusting the angle of the cone angle. In order to observe more intuitively the effect of the change of cone angle on the electric field distribution, the electric field distribution of Au-Ag NSs with different cone angle is shown in Fig. 6.
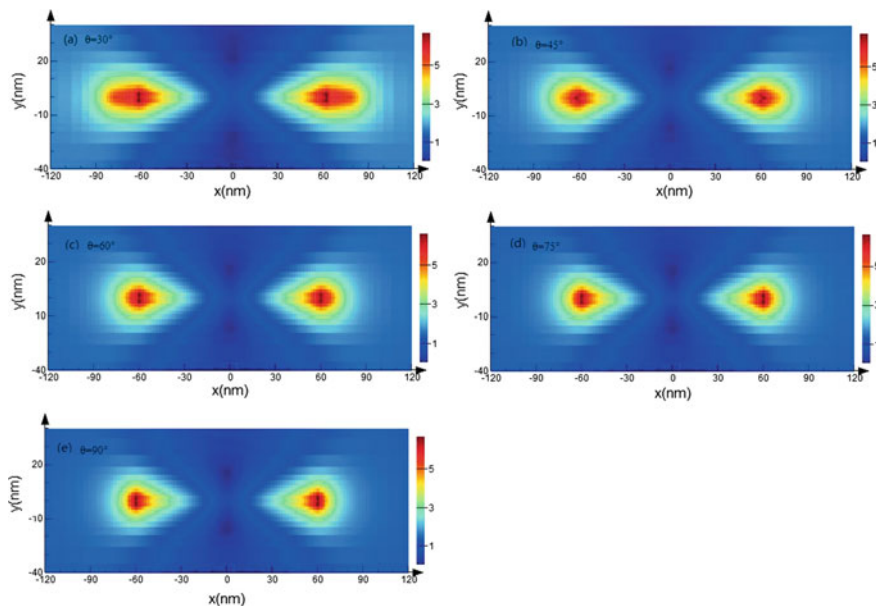
**Fig. 6.** Electric field distribution map of Au-Ag NSs with different cone angles

Figure 6 shows that the electric field intensity along the axis of the nanoshuttle has been significantly enhanced, and the smaller the angle of the cone angle, the sharper the enhancement. This is due to the high charge density at the tip of the nanoshuttle with small angle of the cone angle.

In order to analyze the influence of diameter change on the position of absorption peaks, the simulation of Au-Ag NSs with length 120 nm and cone angle 30° is carried out. The simulation results are shown in Fig. 7.
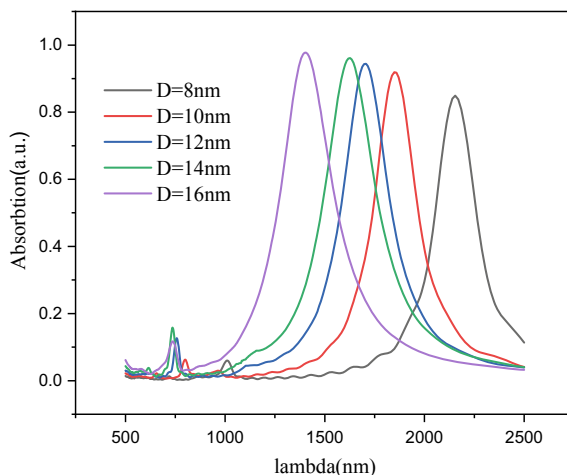


**Fig. 7.** LSPR absorption spectra of Au-Ag NSs with different diameter (L = 120 nm, θ = 30°)

Figure 7 shows that there are two resonance absorption peaks for Au-Ag NSs with the same length and cone angle. With the increase of diameter, the transverse absorption peaks shift blue and move two large ones, which is due to the smaller aspect ratio caused by the increase of diameter when the cone angle remains unchanged. In order to facilitate comparison, the position data of absorption peaks are collated. The results are shown in Table 3.

**Table 3.** LSPR peak tables of Au-Ag NSs with different diameters

| Serial number | D (nm) | L (nm) | θ (°) | $LSPR_L$ (nm) |
|---|---|---|---|---|
| 1 | 8 | 120 | 30 | 2155 |
| 2 | 10 | 120 | 30 | 1848 |
| 3 | 12 | 120 | 30 | 1697 |
| 4 | 14 | 120 | 30 | 1626 |
| 5 | 16 | 120 | 30 | 1400 |

As can be seen from Table 3, when the diameter of Au-Ag NSs increases from 8 to 16 nm, the transverse absorption peak shifts from 2155 to 1400 nm and 755 nm, with a large amount of movement. The broken-line diameters and transverse absorption peaks are shown in Fig. 8.
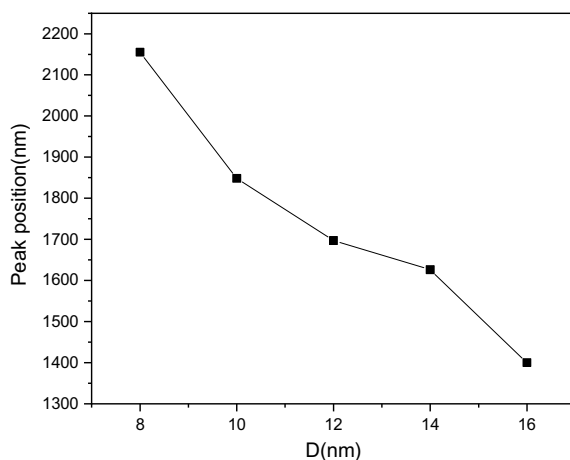


**Fig. 8.** Line graph of the relationship between absorption peak position and diameter

As shown in Fig. 8, the transverse absorption peak decreases with the increase of diameter while the length and cone angle remain unchanged, so the transverse absorption peak can be adjusted by adjusting the diameter size.

# 4   Conclusions

The simulation results show that with the increase of aspect ratio, the longitudinal absorption peak of the Au-Ag NSs shifts red, while its transverse absorption peak does not change significantly; the longitudinal absorption peak also shifts red with the increase of the length of the central nanorod; and the transverse absorption peak of the Au-Ag NSs shifts blue with the increase of the angle of cone.

# References

1. Agrawal A, Cho SH, Zandi O et al (2018) Localized surface plasmon resonance in semiconductor nanocrystals. Chem Rev 118(6):3121–3207
2. Nicoletti O, de la Pena F, Leary RK et al (2013) Three-dimensional imaging of localized surface plasmon resonances of metal nanoparticles. Nature 502(7469):80–84
3. Qiao L, Wang D, Zuo L et al (2011) Localized surface plasmon resonance enhanced organic solar cell with gold nanospheres. Appl Energy 88(3):848–852
4. Sepulveda B, Angelome PC, Lechuga LM et al (2009) LSPR-based nanobiosensors. Nano Today 4(3):244–251
5. Mayer KM, Lee S, Liao H et al (2008) A label-free immunoassay based upon localized surface plasmon resonance of gold nanorods. Acs Nano 2(4):687–692
6. Zhou W, Zhang W, Wang C et al (2010) The analysis of nobel metal nanoparticles LSPR phenomena. Chin J Sens Actuators 23(5): 630–634
7. Kelly KL, Coronado E, Zhao LL et al (2003) The optical properties of metal nanoparticles: the influence of size, shape, and dielectric environment. J Phys Chem B 107(3):668–677
8. Yan QQ, Qin WJ, Wang C et al (2011) Plasmon-enhanced polymer bulk heterojunction solar cells with solution-processable Ag nanoparticles. Optoelectron Lett 7(6):410–414
9. Jayaprakash N, Vijaya JJ, Kaviyarasu K et al (2017) Green synthesis of Ag nanoparticles using Tamarind fruit extract for the antibacterial studies. J Photochem Photobiol B-Biol 169:178–185
10. Shahar T, Feldheim G, Marx S et al (2018) Core-shell nanoparticles for gas phase detection based on silver nanospheres coated with a thin molecularly imprinted polymer adsorbed on a chemiresistor. Nanoscale 10(37):17593–17602
11. El-Khoury PZ, Khon E, Gong Y et al (2014) Electric field enhancement in a self-assembled 2D array of silver nanospheres. J Chem Phys 141(21):17593–17602
12. Zhnag W, Sun H, Liu R Ping et al (2012) Analysis of LSPR extinction properties of two-dimensional Au nanoparticles arrays. J Optoelectron Laser 23(5):1005–1010
13. Dong Q, Wang X, Hu X et al (2018) Simultaneous application of photothermal therapy and an anti-inflammatory prodrug using pyrene-aspirin-loaded gold nanorod graphitic nanocapsules. Angew Chem Int Ed 57(1): 177–181
14. Azimzadeh M, Rahaie M, Nasirizadeh N et al (2016) Anelectrochemical nanobiosensor for plasma miRNA-155, based on graphene oxide and gold nanorod, for early detection of breast cancer. Biosesors Bioelectron 77:99–106
15. Liao J, Li W, Peng J et al (2015) Combined cancer photothermal-chemotherapy based on doxorubicin/gold nanorod-loaded polymersomes. Nanoscale 5(4):345–356

16. Tsai M-F, Chang S-HG, Cheng F-Y et al (2013) Au nanorod design as light-absorber in the first and second biological near-infrared windows for in vivo photothermal therapy. Acs Nano 7(6):5330–5342
17. Zijlstra P, Paulo PMR, Orrit M et al (2012) Optical detection of single non-absorbing molecules using the surface plasmon resonance of a gold nanorod. Nat Nanotechnol 7:379–382
18. Ma, B, Li, P, Chen X et al (2018) Gold nano-triangles as saturable absorbers for a dual-wavelength passively Q-switched Nd:GYSGG laser. Laser Phys 28(7):075802
19. Fletcher G, Arnold MD, Pedersen T et al (2015) Multipolar and dark-mode plasmon resonances on drilled silver nano-triangles. Opt Express 23(14):18002–18013
20. Dharmatti R, Phadke C, Mewada A et al (2014) Biogenic gold nano-triangles: Cargos for anticancer drug delivery. Mater Sci Eng C-Mater Biol Appl 44:92–98
21. Hennemann LE, Kolloch A, Kern A et al (2015) Assessing the plasmonics of gold nano-triangles with higher order laser modes. Beilstein J Nanotechnol 3:674–683
22. Skrabalak SE, Chen J, Sun Y et al (2008) Gold nanocages: synthesis, properties, and applications. Acc Chem Res 41(12):1587–1595
23. Sun H, Su J, Meng Q et al (2017) Cancer cell membrane-coated gold nanocages with hyperthermia-triggered drug release and homotypic target inhibit growth and metastasis of breast cancer. Adv Funct Mater 27(3):1604300
24. Fang Z, Cai J, Yan Z et al (2011) Removing a wedge from a metallic nanodisk reveals a Fano resonance. Nano Lett 11(10):4475–4479
25. Cong C, Wu DJ, Liu XJ et al (2012) Study on the localized surface plasmon resonance properties of bimetallic gold and silver three-layered nanotubes. Acta Phys Sin 61(3):03701-1–03701-7
26. Cheng L, Jiang YG, Huang LQ et al (2016) Optical properties of Ag-Al nanosphere heterodimer. Spectrosc Spectr Anal 36(11):3470–3475
27. Ge DB, Yan YB (2011) Finite-difference time-domain method for electromagnetic waves, 3rd edn. Xi'an Electronic and Science University Press, Xi'an

# Application of Screen Printing to Prepare Photoanode for Dye-Sensitized Solar Cells

Shouzheng Jiao, Zhicheng Sun[(✉)], Furong Li, Jinyue Wen,
Xiaoyang Du, Yutong Ma, Jiani Li, and Luhai Li

Beijing Engineering Research Center of Printed Electronics, School of Printing
and Packaging Engineering, Beijing Institute of Graphic Communication,
Beijing, China
sunzhicheng@bigc.edu.cn

**Abstract.** Dye-sensitized solar cells (DSSCs) have the advantages of low cost, long life and no pollution. In recent years, DSSCs have rapidly developed into solar cells with commercial application prospects. Photoanodes have a critical impact on the performance of DSSCs. In this paper, photoanodes were prepared by screen printing. The size of titanium oxide, number of screen printing layers, mesh number in photoanode were studied. The surface thickness was observed by laser confocal microscopy, and the most suitable screen printing conditions were selected according to the photoelectric conversion efficiency of dye-sensitized solar cells. The researchon the preparation of DSSCs by screen printing provides an effective way for large-area industrial preparation of DSSCs.

**Keywords:** Dye-sensitized solar cells · Photoanodes · Screen printing ·
Titanium dioxide

## 1   Introduction

For more than two decades, researchers have explored the use of a variety of nano-semiconductor materials in dye-sensitized solar cells (DSSCs). From the semiconductor conduction band edge potential and band gap width analysis, suitable semiconductor materials include ZnO [1], $SnO_2$ [1–3], WO and $TiO_2$ and other inorganic oxide semiconductors. These semiconductors can form ester bonds with carboxyl groups in sensitizing dye molecules, facilitating photoinduced electron transfer [4–9]. However, the DSSCs using $TiO_2$ photoanode has the highest photoelectric conversion efficiency. The large surface area and the internal pore structure ensure that the nanocrystalline $TiO_2$ porous semiconductor film absorbs a large amount of dye molecules, thereby increasing the amount of photogenerated electrons.In addition, the internal voids also provide the possibility of reflection of sunlight between the particles in the film. Therefore the absorption rate of the semiconductor film to sunlight can be effectively enhanced.

In 1991, Grätzel et al. first used a metal ruthenium complex as a dye to adsorb a dye-sensitized solar cells on the surface of nanocrystalline $TiO_2$. The photoelectric replacement efficiency of the cells reached 7% [10]. The research of solar cells based

on the principle of dye sensitization has become a hot research direction [11–15]. After nearly two decades of research and improvement, the photoelectric conversion efficiency of DSSCs based on nanoporous $TiO_2$ has exceeded 12% [16]. The nanoporous $TiO_2$ photoanodes can be made of commercial grade nano $TiO_2$ powder. For example, P25 powder, adding a surfactant and a proper amount of solvent to prepare a $TiO_2$ slurry. Then, a layer of $TiO_2$ was deposited on the conductive substrate by screen printing [17], direct coating [18], spin coating [19], etc. The $TiO_2$ electrode was prepared by high temperature sintering activation. The photoanodes prepared by screen printing has a simple process, which can be prepared in a large area to become the most important preparation method of photoanodes. However, there are few reports on the research of the screen printing process parameter system.

In this study, $TiO_2$ photoanodes were prepared by screen printing technology, and the structure of $TiO_2$ photoanodes were optimized by various methods. The effects of screen printing photoanode thickness, photoanode effective area, light absorbing layer particle size, screen mesh number, and number of tests on the performance of dye-sensitized solar cells were compared. Systematic research on screen printing of DSSCs titanium oxide photoanodes in addition to further improving the photoelectric conversion efficiency of DSSCs was also of great significance for commercial applications.

## 2    Experiments

### 2.1    Experimental Materials

Titanium oxide slurry (18-nrt, 30-nrd), N719 photosensitizing dye, Pt slurry were purchased from GreatcellSolarl Co., Ltd., Australia. FTO ($SnO_2$:F) conductive glass (14Ω/sq., thickness 2.2 mm, light transmittance >90%) was purchased from Nippon Sheet Glass Co., Ltd., Japan. LiI (>99%), $I_2$ (>99.9%), guanidiniumthiocyanate (> 99%), 1-propyl-3-methylimidazolium iodide (> 98%), 4-tert-butylpyridine(> 96%), Guanidine thiocyanate (>99%) was purchased from Alfa Aesar Reagent. The screen version was manufactured by Beijing Yingmai Co., Ltd.

## 3    Assembling DSSCs Devices

Before the experiment, FTO glass was ultrasonically cleaned with acetone, ethanol and deionized water, then dried with $N_2$. Then FTO glass was deeply cleanedat UV-$O_3$. The cleaned FTO glass isprepared a photoanodeby screen printed. Prepare a solution photosensitive dye, soak the $TiO_2$ semiconductor electrode prepared above into the dye bath, wrap film Wrap the dyeing bath bottle to isolate moisture, and let it stand in the dark for 24 h. After the sensitization is completed, remove the surface, rinse the surface of the membrane with ethanol solvent, remove the dye that has not been adsorbed, then dry it at low temperature, and store it in the dark.

## 4   Results and Discussion

As shown in Fig. 1a and b, the mesh size was 250 mesh, the effective photoanodes area was 0.16 cm$^2$. The light absorbing layer titanium oxide was 20 nm. The scattering layer has a particle diameter of 200 nm and a printed layer of one. As the number of layers of TiO$_2$ film increases, the short-circuit current of the battery increases greatly. The photoelectric conversion efficiency also increases greatly. However, with the further increase of the number of TiO$_2$ film layers, the short-circuit current and the open circuit voltage both decrease, which leads to a significant decrease in the photoelectric conversion efficiency. As the number of layers of TiO$_2$ film increases, the increase in the number of nano-TiO$_2$ on the photoanodes causes a significant increase in the adsorbed dye molecules, so more photogenerated electrons are generated under illumination. The increase in the path of photogenerated electron transfer increases, and the resistance to transfer and the probability of recombination increase accordingly. Under the combined effect of the above two factors, the cells of different layers of TiO$_2$ photoanodes have a regular change performance. In the 4–5 layers TiO$_2$ film, the rate of photogenerated electrons increases much more than the recombination rate, so the photocurrent shows a significant increase trend. With the thickening of the TiO$_2$ film, the probability of photo-generated electron recombination was significantly increased, so the performance of the cell was degraded. Therefore, four layers of light absorbing layers and one scattering layer was screen printed.
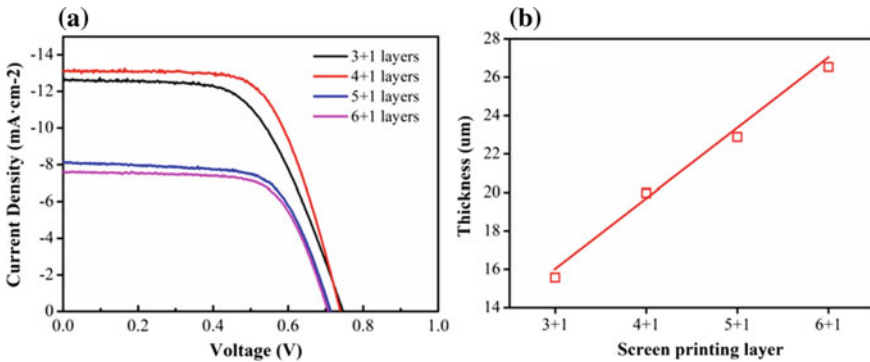


**Fig. 1.** **a** different screen printing layers; **b** Photoanode thickness of different screen printing layers

Compared to small-area devices, large-area DSSC devices (in Fig. 2c) have the same short-circuit current and open-circuit voltage. But large-area DSSC has a low fill factor, as the effective area of the photoanodes increases, during the high-temperature sintering process. The interior is easily heated and uneven, thereby causing cracks which lead to film unevenness. This results in a decrease in the fill factor, resulting in a decrease in photoelectric conversion efficiency. As shown in Fig. 2b, the conversion efficiency of the cell having a particle diameter of 30 nm of the light absorbing layer was significantly lower than that of the cell having a particle diameter of 20 nm.

The devices were prepared by the small particle size $TiO_2$ photoanodewhich has a significantly increased short circuit current of the cell. This is because the large particle size $TiO_2$ has a small specific surface area and a small amount of adsorbed dye, so that the amount of photogenerated electrons generated is small. Therefore, titanium oxide having a particle diameter of 20 nm was used as the light absorbing layer of DSSCs. For the mesh version, we compared the 250 mesh and 120 mesh screens. The light absorbing layer of the 120 mesh screen printed photoanode is 2 layers. The photoanode assembled DSSCs prepared with the 120 mesh screen version still has a higher photoelectric conversion efficiency than the 250 mesh screen plate. However, due to the large mesh size of the 250 mesh screen plate, the quality of the photoanode film prepared by printing is poor. Therefore, the photoelectric conversion efficiency of the 250-mesh screen plate is finally obtained (Fig. 2).
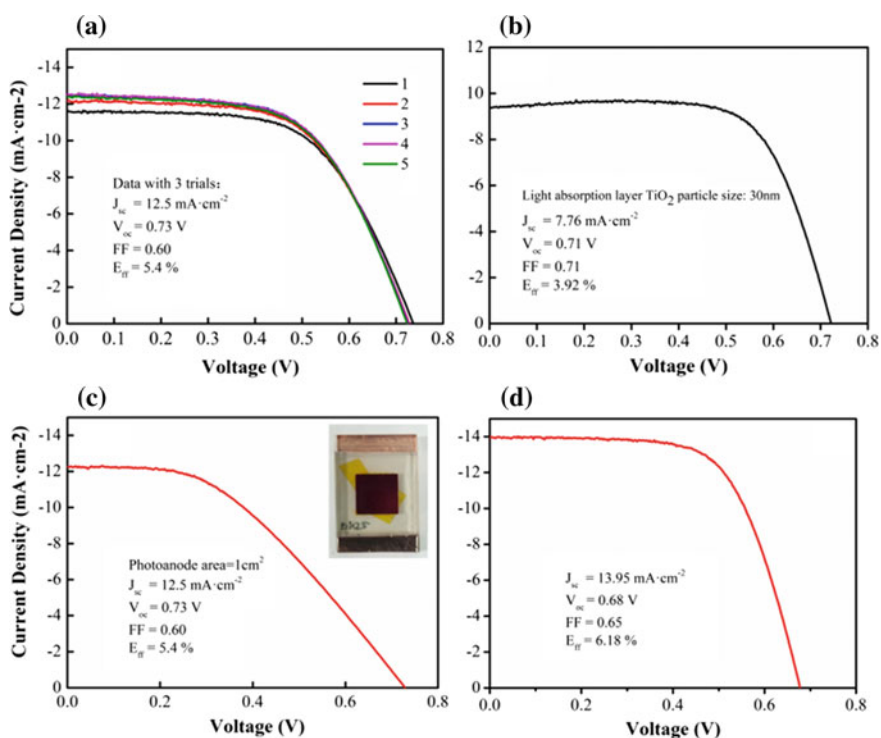


**Fig. 2.** **a** photoanodes with an effective area of 1 cm$^2$; **b** the light absorbing layer is 30 nm $TiO_2$; **c** screen mesh number is 120 mesh; **d** different test times. All of the above J-V curves tests were measured at 100 mW/cm$^2$ intensity simulated sunlight

Fig. 2a shows the J-V curves for different test times. As the number of tests increases, the current density increases from 11.5 mA/cm$^2$ to 12.5 mA/cm$^2$, and the open circuit voltage (Voc) and fill factor (FF) remain almost unchanged. This may be caused by the lag of the redox reaction of the excited state dye and the electrolyte.

When the equilibrium state is reached, a relaxation time is required, and the number of excited electrons is greater than the number of reduced electrons. It is also possible that the photosensitizing dye has two long alkyl chains, which prolongs the electron diffusion channel and increases the probability of electron recombination. However, as the number of excited electrons increases, the number of holes and defects becomes less and less, so the current is gradually increased and the efficiency is increased.

## 5    Conclusions

By comparing the effects of different screen printing parameters on the photoelectric conversion efficiency of DSSCs, the best parameters were obtained: 4 layers of titanium oxide light absorbing layer with a particle size of 20 nm and a layer of 200 nm scattering were prepared by screen printing with 250 mesh. The second time data was taken during the test, and the photoelectric conversion efficiency was as high as 6.30% when the effective area of the photoanodes was 0.16 cm$^2$.

## References

1. Perera VÁS (1999) An efficient dye-sensitized photoelectrochemical solar cell made from oxides of tin and zinc. Chem Commun 1:15–16
2. Bergeron BV, Marton A, Oskam G, Meyer GJ (2005) Dye-sensitized SnO$_2$ electrodes with iodide and pseudohalide redox mediators. J Phys Chem B 109(2):937–943
3. Chappel S, Zaban A (2002) Nanoporous SnO$_2$ electrodes for dye-sensitized solar cells: improved cell performance by the synthesis of 18 nm SnO2 colloids. Sol Energy Mater Sol Cells 71(2):141–152
4. OSA T, Fujihira M (1976) Photocell using covalently-bound dyes on semiconductor surfaces. Nature 264(5584):349
5. Yu J, Fan J, Lv K (2010) AnataseTiO$_2$ nanosheets with exposed (001) facets: improved photoelectric conversion efficiency in dye-sensitized solar cells. Nanoscale 2(10):2144–2149
6. Xu J, Wang G, Fan J, Liu B, Cao S, Yu J (2015) g-C$_3$N$_4$ modified TiO$_2$ nanosheets with enhanced photoelectric conversion efficiency in dye-sensitized solar cells. J Power Sources 274:77–84
7. Hao S, Wu J, Huang Y, Lin J (2006). Natural dyes as photosensitizers for dye-sensitized solar cell. Sol Energy 80(2):209–214
8. Usui H, Tanabe N, Matsui H, Ezure T, Yanagida S (2014) U.S. Patent No. 8,785,765. Washington, DC: U.S. Patent and Trademark Office
9. Miyasaka T, Kijitori Y, Murakami TN, Kimura M, Uegusa S (2002) Efficient nonsintering type dye-sensitized photocells based on electrophoretically deposited TiO$_2$ layers. Chem Lett 31(12):1250–1251

10. O'regan B, Grätzel M (1991) A low-cost, high-efficiency solar cell based on dye-sensitized colloidal TiO$_2$ films. Nature 353(6346):737

11. Freitag M, Teuscher J, Saygili Y et al (2017) Dye-sensitized solar cells for efficient power generation under ambient lighting. Nat Photonics 11(6):372

12. Watson BL, Moore TA, Moore AL, Gust D (2017) Synthesis of a novel building block for the preparation of multi-chromophoric sensitizers for panchromatic dye-sensitized solar cells. Dyes Pigm 136:893–897

13. Zhang W, Wu Y, Bahng HW, Cao Y, Yi C, Saygili Y, Hagfeldt A (2018) Comprehensive control of voltage loss enables 11.7% efficient solid-state dye-sensitized solar cells. Energy Environ Sci 11(7):1779–1787

14. Urbani M, Ragoussi ME, Nazeeruddin MK, Torres T (2019) Phthalocyanines for dye-sensitized solar cells. Coord Chem Rev 381:1–64

15. Ma X, Zheng F, Zhao Y, Wang X, Zhu Z, Fong H (2018) Nanocomposite structures related to electrospunnanofibers for highly efficient and cost-effective dye-sensitized solar cells. Multifunct Nanocomposites Energy Environ Appl 1:113–133

16. Kweon DH, Baek JB (2019) Edge-functionalized graphenenanoplatelets as metal-free electrocatalysts for dye-sensitized solar cells. Adv Mater 31(13):1804440

17. Kumar DK, Swami SK, Dutta V, Chen B, Bennett N, Upadhyaya HM (2019) Scalable screen-printing manufacturing process for graphene oxide platinum free alternative counter electrodes in efficient dye sensitized solar cells. FlatChem 15:100105

18. Zhang J, Freitag M, Hagfeldt A, Boschloo G (2018) Solid-state dye-sensitized solar cells. Molecular devices for solar energy conversion and storage. Springer, Singapore, pp 151–185

19. Butt M, Preuss K, Titirici MM, Rehman H, Briscoe J (2018) Biomass-derived nitrogen-doped carbon aerogel counter electrodes for dye sensitized solar cells. Materials 11(7):1171